รายงานวิจัยฉบับสมบูรณ์

(เล่มที่ 2 ของจำนวน 3 เล่ม)

โครงการ
งานวิจัยขั้นสูงทางการไหลสองสถานะและการเพิ่มความสามารถในการถ่ายเทความร้อน

โดย

ศ. ดร. สมชาย วงศ์วิเศษ

ภาควิชาวิศวกรรมเครื่องกล คณะวิศวกรรมศาสตร์

มหาวิทยาลัยเทคโนโลยีพระจอมเกล้าธนบุรี

วันที่ 31 มีนาคม 2557

Provided for non-commercial research and education use.
Not for reproduction, distribution or commercial use.

This article appeared in a journal published by Elsevier. The attached copy is furnished to the author for internal non-commercial research and education use, including for instruction at the authors institution and sharing with colleagues.

Other uses, including reproduction and distribution, or selling or licensing copies, or posting to personal, institutional or third party websites are prohibited.

In most cases authors are permitted to post their version of the article (e.g. in Word or Tex form) to their personal website or institutional repository. Authors requiring further information regarding Elsevier's archiving and manuscript policies are encouraged to visit:

http://www.elsevier.com/copyright

Author's personal copy

International Communications in Heat and Mass Transfer 39 (2012) 937–944

Contents lists available at SciVerse ScienceDirect

International Communications in Heat and Mass Transfer

journal homepage: www.elsevier.com/locate/ichmt

A correlation development for predicting the pressure drop of various refrigerants during condensation and evaporation in horizontal smooth and micro-fin tubes ☆

M. Balcilar [a], A.S. Dalkilic [b,*], O. Agra [b], S.O. Atayilmaz [b], S. Wongwises [c,d,**]

[a] Computer Engineering Department, Yildiz Technical University, Yildiz, Besiktas, Istanbul 34349, Turkey
[b] Heat and Thermodynamics Division, Department of Mechanical Engineering, Yildiz Technical University (YTU), Yildiz, Besiktas, Istanbul 34349, Turkey
[c] Fluid Mechanics, Thermal Engineering and Multiphase Flow Research Lab. (FUTURE), Department of Mechanical Engineering, King Mongkut's University of Technology Thonburi, Bangmod, Bangkok 10140, Thailand
[d] The Academy of Science, The Royal Institute of Thailand, Sanam Suea Pa, Dusit, Bangkok 10300, Thailand

ARTICLE INFO

Available online 28 May 2012

Keywords:
Artificial neural network (ANN)
Multi-layer perceptron (MLP)
Non-linear least squares (NLS)
Condensation
Evaporation
Correlation development
Micro-fin
Pressure drop

ABSTRACT

This paper predicts the condensation and evaporation pressure drops of R32, R125, R410A, R134a, R22, R502, R507a, R32/R134a (25/75 by wt%), R407C and R12 flowing inside various horizontal smooth and micro-fin tubes by means of the numerical techniques of artificial neural networks (ANNs) and non-linear least squares (NLS). In its analyses, this paper used experimental data from the National Institute of Standards and Technology (NIST) and Eckels and Pate, as presented in Choi et al.'s study provided by NIST. In their experimental setups, the horizontal test sections have 1.587, 3.78, 3.81 and 3.97 m long countercurrent flow double tube heat exchangers with refrigerant flowing in the inner smooth (8, 8.01 and 11.1 mm i.d.) and micro-fin (4.339, 5.45, 7.43 and 8.443 mm i.d.) copper tubes and cooling water flowing in the annulus. Their test runs cover a wide range saturation temperatures, vapor qualities and mass fluxes. The pressure drops are calculated with 1485 measured data points, together with analyses of artificial neural networks and non-linear least squares numerically. Inputs of the ANNs of the best correlation are the measured values of the test sections, such as mass flux, tube length, inlet and outlet vapor qualities, critical pressure, latent heat of condensation, mass fraction of liquid and vapor phases, dynamic viscosities of liquid and vapor phases, hydraulic diameter, two-phase density and the outputs of the ANNs, which comprise the experimental total pressure drops of the evaporation and condensation data from independent laboratories. The total pressure drops of in-tube condensation and in-tube evaporation tests are modeled using the artificial neural network (ANN) method of multi-layer perceptron (MLP) with 12-40-1 architecture. Its average error rate is 7.085%, which came from the cross validation tests of 1485 evaporation and condensation data points. Dependency of the output of the ANNs from 12 numbers of input values is also shown in detail, and new ANN based empirical pressure drop correlations are developed separately for the conditions of condensation and evaporation in smooth and micro-fin tubes as a result of the analyses. In addition, a single empirical correlation for the determination of both evaporation and condensation pressure drops in smooth and micro-fin tubes is proposed with an error rate of 14.556%.

© 2012 Elsevier Ltd. All rights reserved.

1. Introduction

Artificial intelligence methods, which include the genetic algorithm (GA) and artificial neural network (ANN) modeling that have been validated by experimental works, are increasingly being utilized to correlate two-phase flows in tubes. However, the literature still lacks investigations on the prediction of in-tube condensation and evaporation characteristics by means of artificial intelligence techniques. In this paper, artificial neural network analyses were used as one of the numerical solution techniques to determine the important pressure drop characteristics of condensation and evaporation heat transfer. Existing recent numerical studies in these subjects regarding the two-phase flows in the literature are summarized in the following paragraphs.

Balcilar et al. [1,2] numerically investigated the best artificial intelligence method among multi-layer perceptron (MLP), radial basis networks (RBFN), generalized regression neural network (GRNN) and adaptive neuro-fuzzy inference system (ANFIS) to estimate the experimentally measured convective heat transfer coefficient and pressure drop of R134a flowing downward inside a vertical tube during annular flow. Balcilar et al. [3,4] investigated the heat transfer characteristics

☆ Communicated by W.J. Minkowycz.

* Corresponding author.
** Correspondence to: S. Wongwises, The Academy of Science, The Royal Institute of Thailand, Sanam Suea Pa, Dusit, Bangkok 10300, Thailand.
E-mail addresses: dalkilic@yildiz.edu.tr (AS. Dalkilic), somchai.won@kmutt.ac.th (S. Wongwises).

0735-1933/$ – see front matter © 2012 Elsevier Ltd. All rights reserved.
doi:10.1016/j.icheatmasstransfer.2012.05.005

Author's personal copy

Nomenclature

A	coefficients in Eqs. (5), (6) and (7)
Bo	Bond number
d	internal tube diameter, m
f	function
Fr	Froude number
G	mass flux, kg m^{-2} s^{-1}
h_{fg}	latent heat of condensation, kJ kg^{-1}
j	superficial velocity
K_{num}	numerical correction coefficient
L	tube length, m
Pr	Prandtl number
R	ratio of density to dynamic viscosity
Re	Reynolds number
V	volume of fluid
x	average vapor quality
w	mass fraction, m^3 kg^{-1}
We	Weber number
X_{tt}	Lockhart and Martinelli parameter
ΔP	pressure drop, kPa

Greek symbols

α	void fraction
ρ	density, kg m^{-3}
μ	dynamic viscosity, kg m^{-1} s^{-1}
σ	surface tension, N m^{-1}
Ψ	surface tension parameter

Subscripts

eq	equivalent
exp	experiment
g	gas
h	hydraulic
l	liquid
TP	two-phase

of R134a during downward condensation both experimentally and numerically by using the genetic algorithm technique (GA), the unconstrained nonlinear minimization algorithm Nelder–Mead method (NM) and the non-linear least squares error method (NLS) for the optimization of the variables in the study. Demir et al. [5] numerically investigated the forced convection flows of nanofluids by using a computational fluid dynamics (CFD) program in a horizontal tube with constant wall temperature. In addition, Demir et al. [6] developed a generalized neural network correlation for the condensation heat transfer coefficient of alternative refrigerant R600a inside a horizontal tube in their earlier study. The results from the trained network show good agreement with the experimental data and better results than the well-known correlations in the literature. Agra et al. [7] numerically investigated the passive heat transfer enhancement techniques to determine the distribution of temperature and static pressure in the test tubes, the friction factor, the heat flux, temperature difference between the inlet and outlet fluid temperatures, the pressure drop penalty, and convective heat transfer coefficient using a CFD program. Their results were also in-line with the available experimental data in the literature.

Although two-phase flow characteristics of refrigerants have been extensively investigated experimentally in the past; little attention has been paid to determining those numerically, especially with artificial intelligence and CFD techniques in order to predict accurately the pressure drop and related issues inside horizontal smooth and enhanced tubes. Consequently, the chief aim of this study is to model the condensation and evaporation in smooth and micro-fin tubes in the MATLAB program with the methods of multi-layer perceptron (MLP) and non-linear least squares (NLS), then determine the most affected parameters and develop reliable correlations with several sets of basic heat transfer data [8,9] that belong to the flow in smooth and micro-fin tubes. It is believed that the proposed correlations will be useful in predicting the pressure drop characteristics of new smooth and micro-fin tubes without doing additional experiments due to the use of reliable data from independent laboratories.

2. Experimental apparatus and method

Detailed descriptions of the experimental apparatus and summary of test conditions in terms of flow type, refrigerant, mass flux, average pressure, inlet and outlet vapor qualities and number of data points belonging to the data for studying condensation and evaporation of various refrigerants inside horizontal smooth and micro-fin tubes can be found in Choi et al.'s [8] and Eckels and Pate's [9] publication.

3. Calculation procedure for the analyses

3.1. Error analysis

The error analyses' calculation procedure for the average values of the experimental and calculated results of the two-phase pressure drops regarding with R^2 error, proportional error and mean square error (MSE) can be seen from authors' previous publication [1] and their results appear in Tables 1 and 2.

3.2. The generalized artificial neural networks (ANNs) model

As the artificial neural networks (ANNs) are one of the most commonly used and developed models to investigate the relationship between linear or non-linear input–output patterns. These models try to generalize the training group and then estimate the test group. Performance of ANNs is measured with the success of the prediction. There are many described ANN types related with the function approximation in the literature. The most known methods are multi-layer perceptron (MLP), radial basis functions networks (RBFN), generalized regression neural networks (GRNN) and artificial neural fuzzy inference system (ANFIS). The lattermost method is the combination of fuzzy logic decision systems and ANNs.

The detailed information on the ANN analyses of the determination condensation heat transfer coefficient, pressure drop and correlation development can be seen from the authors' previous publications [1–4,6,7]. It should be noted that the authors benefitted from their own experimental database in these publications.

3.3. The non-linear least squares algorithm (NLS)

The non-linear least square (NLS) method allows the user to determine the most optimal non-linear function coefficients in order to fit data collected from an experimental environment to a non-linear function (non-linear curve fitting). This method tries to minimize the mean square error, beginning from the first estimated values determined by the user. Since it advances step by step through optimizing this point, it finds the local minimum and not the global minimum by starting from this initial point. The method is tested by starting from different initial points, and thus the global minimum value of ANN code is determined.

Author's personal copy

Table 1
Elimination of MLP with the architecture 12-10-10-1 according to the error rates for the determination of pressure drop of data [8,9].

Data set	Data of condensation in micro-fin tubes by NIST [8]					Data set	Data of condensation in micro-fin tubes by Eckels and Pate [9]				
1	Error analysis/MLP architecture	ΔP (kPa)				4	Error analysis/MLP architecture	ΔP (kPa)			
		5-5	10-10	20-20	40-40			5-5	10-10	20-20	40-40
	R^2	0.972	0.975	0.949	0.719		R^2	0.962	0.97	0.965	0.952
	MSE	0.149	0.138	0.2768	2.154		MSE	3.131	2.43	2.834	3.985
	Proportional (%)	17.991	18.183	28.599	60.15		Proportional (%)	22.59	20.526	24.13	31.314
Data set	Data of evaporation in micro-fin tubes by NIST [8]					Data set	Data of evaporation in smooth tubes by Eckels and Pate [9]				
2	Error analysis/MLP architecture	ΔP (kPa)				5	Error analysis/MLP architecture	ΔP (kPa)			
		5-5	10-10	20-20	40-40			5-5	10-10	20-20	40-40
	R^2	0.979	0.978	0.982	0.974		R^2	0.928	0.995	0.991	0.987
	MSE	0.24	0.248	0.204	0.29		MSE	12.005	0.625	1.1362	1.785
	Proportional (%)	5.98	6.142	4.934	5.82		Proportional (%)	34.518	17.609	33.645	62.126
Data set	Data of condensation in smooth tubes by Eckels and Pate [9]					Data set	Data of evaporation in micro-fin tubes by Eckels and Pate [9]				
3	Error analysis/MLP architecture	ΔP (kPa)				6	Error analysis/MLP architecture	ΔP (kPa)			
		5-5	10-10	20-20	40-40			5-5	10-10	20-20	40-40
	R^2	0.969	0.988	0.964	0.869		R^2	0.988	0.9942	0.982	0.988
	MSE	0.825	0.322	1.168	3.609		MSE	1.658	1.433	2.65	1.762
	Proportional (%)	21.168	15.286	22.485	50.108		Proportional (%)	19.124	19.524	17.85	20.122

3.4. Correlation development for the two-phase pressure drop

There have been a number of studies on the in-tube condensation and evaporation pressure drops of smooth and enhanced tubes in the literature. The frictional, acceleration, and gravitational components determine the two-phase total pressure drop in tubes. Determination of the void fraction is required to compute the acceleration and gravitational components, and in a similar way, determination of either the two-phase friction factor or the two-phase frictional multiplier is required to compute the frictional component of pressure drop. Generally, empirical methods have been used to compute the two-phase pressure drops in tubes. As a result, Eq. (1) is formed to predict the pressure drops of evaporation and condensation in terms of the above explanations as follows:

$$\Delta P = \left(\frac{G^2 L}{d\rho_{TP}}\right) K_{num} \tag{1}$$

where the numerical correction coefficient (K_{num}) is calculated using the artificial neural network (ANN) with the architecture of multi-layer perceptron (MLP-12-40-1) and non-linear least squares that appear in all tables and figures labeled as f(MLP) and f(NLS), respectively. The following Eqs. (2) and (3) are determined by means of f(NLS). Their coefficients are shown as A_1 to A_{12} in Table 3,

$$K_{num} = \left(\frac{A_1}{1+e^{(A_2 R + A_3)}} + A_4\right) 10^{-8} \tag{2}$$

$$K_{num} = \left(\frac{A_{11}}{1+e^{-Y}} + A_{12}\right) 10^{-8} \tag{3}$$

where the coefficient of Y is estimated as:

$$Y = A_1 \mathrm{Fr} + A_2 \mathrm{We} + A_3 \mathrm{Bo} + A_4 X_{tt} + A_5 \alpha + A_6 \Psi + A_7 \mathrm{Re}_{eq} + A_8 R + A_9 \mathrm{Pr}_l + A_{10} \tag{4}$$

The inputs of all analyses, including MLP architectures with 12-10-10-1 for the determination of pressure drop directly and 12-40-1 (f(MLP)) for the determination of K_{num} in Eq. (1) and non-linear least squares (NLS) for the determination of K_{num} in Eqs. (3) and (4) are shown as follows.

Table 2
Elimination of ANN methods by means of f(ANN) in Eq. (1) according to the error rates for the determination of pressure drop of data [8,9].

Data set	Data of condensation in micro-fin tubes					Data set	Data of evaporation in smooth and micro-fin tubes				
1	Error analysis/MLP architecture	ΔP (kPa)				4	Error analysis/MLP architecture	ΔP (kPa)			
		40	10-10	20-20	40-40			40	10-10	20-20	40-40
	R^2	0.994	0.989	0.981	0.994		R^2	0.93	0.97	0.974	0.975
	MSE	0.028	0.056	0.097	0.036		MSE	7.841	2.574	2.111	2.0697
	Proportional (%)	5.556	6.653	7.523	5.672		Proportional (%)	13.969	14.483	13.966	14.211
Data set	Data of condensation in smooth and micro-fin tubes					Data set	Data of condensation and evaporation in micro-fin tubes				
2	Error analysis/MLP architecture	ΔP (kPa)				5	Error analysis/MLP architecture	ΔP (kPa)			
		40	10-10	20-20	40-40			40	10-10	20-20	40-40
	R^2	0.986	0.987	0.985	0.987		R^2	0.997	0.997	0.996	0.996256
	MSE	0.16	0.144	0.162	0.152		MSE	0.336	0.603	0.796	0.684
	Proportional (%)	3.735	3.484	3.817	3.735		Proportional (%)	7.887	8.959	10.186	9.369
Data set	Data of evaporation in micro-fin tubes					Data set	Data of condensation and evaporation in smooth tubes				
3	Error analysis/MLP architecture	ΔP (kPa)				6	Error analysis/MLP architecture	ΔP (kPa)			
		40	10-10	20-20	40-40			40	10-10	20-20	40-40
	R^2	0.988	0.991	0.995	0.994		R^2	0.986	0.992	0.992	0.989
	MSE	0.308	0.236	0.126	0.22		MSE	2.238	1.406	1.064	4.591
	Proportional (%)	8.256	8.364	7.539	8.143		Proportional (%)	6.774	9.403	7.6	9.381

Author's personal copy

Table 3
Proposed correlations obtained from f(NLS) for condensation and evaporation in smooth and micro-fin tubes using the data points of [8,9].

Type of two-phase flow	Data set	Proposed correlation: $\Delta P = \left(\frac{G^2 L}{d\rho_{TP}}\right)\left(\frac{A_1}{1+e^{(A_2 R+A_3)}}+A_4\right)10^{-8}$	Tube type		R^2	MSE	% Average error
			Smooth	Micro-fin			
Condensation	1	$A_1=-1.17378$, $A_2=0.000167$, $A_3=-11.2363$, $A_4=1.173774$	–	x	0.982	0.101	12.303
	3	$A_1=-1.16593$, $A_2=0.000144$, $A_3=-10.0917$, $A_4=1.165895$	x	–	0.977	0.621	12.665
	4	$A_1=-1.16862$, $A_2=0.065145$, $A_3=-34.1775$, $A_4=1.168633$	–	x	0.962	3.471	18.697
	1–4	$A_1=-1.169$, $A_2=0.080706$, $A_3=-43.954$, $A_4=1.169006$	–	x	0.966	2.071	16.602
	1–3–4	$A_1=-1.16833$, $A_2=0.045122$, $A_3=-29.4969$, $A_4=1.168344$	x	x	0.966	1.746	15.765
Evaporation	2	$A_1=-2.57E\text{-}06$, $A_2=0.324154$, $A_3=-143.636$, $A_4=1.73E\text{-}05$	–	x	0.954	0.522	9.374
	5	$A_1=-9.11E\text{-}06$, $A_2=0.064966$, $A_3=-23.1589$, $A_4=1.96E\text{-}05$	x	–	0.964	5.181	26.089
	6	$A_1=-5.64E\text{-}06$, $A_2=2.661379$, $A_3=-866.67$, $A_4=1.68E\text{-}05$	–	x	0.95	7.965	23.786
	2–5–6	$A_1=-6.51E\text{-}06$, $A_2=0.047376$, $A_3=-18.699$, $A_4=1.77E\text{-}05$	x	x	0.947	2.431	13.983
Condensation and evaporation	1–2–4–6	$A_1=-6.03E\text{-}06$, $A_2=0.032756$, $A_3=-12.5242$, $A_4=1.72E\text{-}05$	–	x	0.961	1.814	13.607
	3–5	$A_1=-1.13E\text{-}05$, $A_2=0.003371$, $A_3=-2.14455$, $A_4=2.02E\text{-}05$	x	–	0.971	2.208	18.703
	1–2–3–4–5–6	$A_1=-0.58331683$, $A_2=0.053697258$, $A_3=-20.9082209$, $A_4=1.707628765$	x	x	0.957	2.119	14.556
	1–2–3–4–5–6	Proposed correlation : $\Delta P = \left(\frac{G^2 L}{d\rho_{TP}}\right)\left(\frac{A_{11}}{1+e^{-Y}}+A_{12}\right)10^{-8}$ $Y = A_1\mathrm{Fr}+A_2\mathrm{We}+A_3\mathrm{Bo}+A_4X_{tt}+A_5\alpha+A_6\Psi+A_7\mathrm{Re}_{eq}+A_8R+A_9\mathrm{Pr}_l+A_{10}$ $A_1=-0.005195717$, $A_2=0.001339146$, $A_3=-0.037830204$, $A_4=-12.67518703$, $A_5=39.32388258$, $A_6=47.21149639$, $A_7=-0.000167776$, $A_8=0.019563285$, $A_9=-16.38509432$, $A_{10}=2.816148392$, $A_{11}=0.662922688$, $A_{12}=1.134726668$	x	x	0.96	1.966	15.471

The all liquid equivalent Re number is determined from:

$$\mathrm{Re}_{eq} = \frac{G_{eq} d_h}{\mu_l}. \tag{5}$$

Equivalent liquid mass flux is defined as:

$$G_{eq} = G\left((1-x) + x\left(\frac{\rho_l}{\rho_g}\right)^{0.5}\right). \tag{6}$$

The ratio of density to dynamic viscosity is defined as:

$$R = \frac{\rho_l \mu_l}{\rho_g \mu_g}. \tag{7}$$

Bond number is defined as:

$$Bo = g\left(\rho_l - \rho_g\right)\left(\frac{(d_h/2)^2}{\sigma}\right). \tag{8}$$

The Froude number is defined as:

$$\mathrm{Fr} = \frac{G^2}{g d_h {\rho_{TP}}^2} \tag{9}$$

where the two-phase density is determined from:

$$\rho_{TP} = \left(\frac{x}{\rho_g} + \frac{1-x}{\rho_l}\right)^{-1}. \tag{10}$$

The Lockhart and Martinelli parameter is expressed as:

$$X_{tt} = \left(\frac{1-x}{x}\right)^{0.9}\left(\frac{\mu_g}{\mu_l}\right)^{0.1}\left(\frac{\rho_g}{\rho_l}\right)^{0.5}. \tag{11}$$

The all liquid Reynolds number equation can be expressed as:

$$\mathrm{Re}_l = \frac{G d_h}{\mu_l}. \tag{12}$$

All gas Reynolds number is defined as:

$$\mathrm{Re}_g = \frac{G d_h}{\mu_g}. \tag{13}$$

The void fraction, α, can be determined from Butterworth's [10] correlation, which was suggested by Choi et al. [8] for the data as follows:

$$\alpha = \frac{1}{1 + 0.28\left(\frac{1-x}{x}\right)^{0.64}\left(\frac{\rho_g}{\rho_l}\right)^{0.36}\left(\frac{\mu_l}{\mu_g}\right)^{0.07}} \tag{14}$$

Author's personal copy

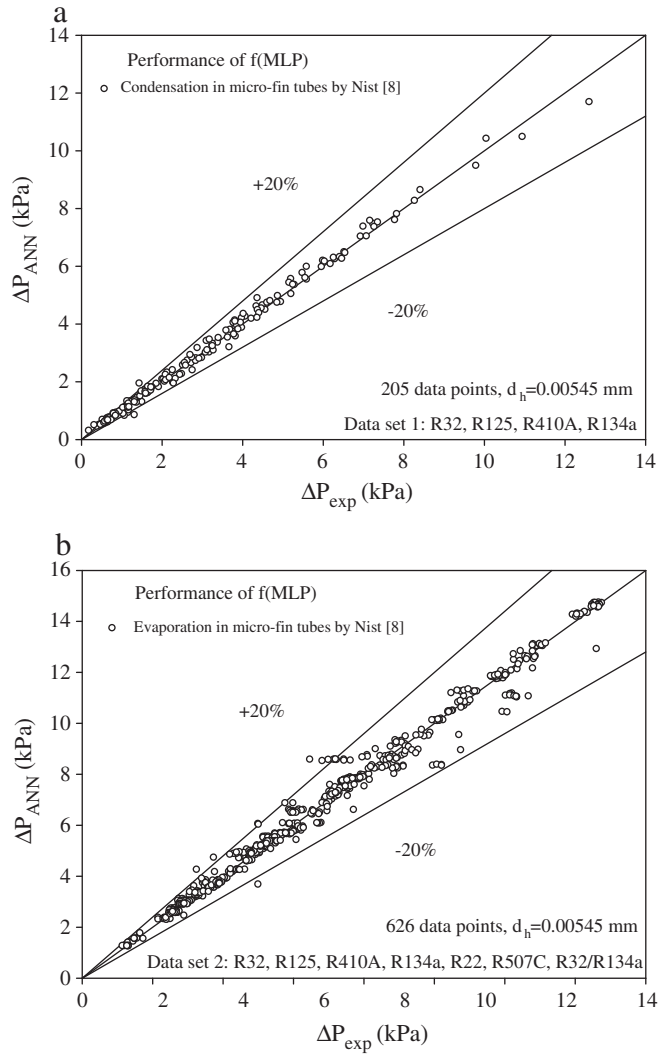

Fig. 1. Comparison of pressure drop values obtained from the condensation (a) and evaporation (b) experiments of NIST [8] in a micro-fin tube and MLP-12-40-1.

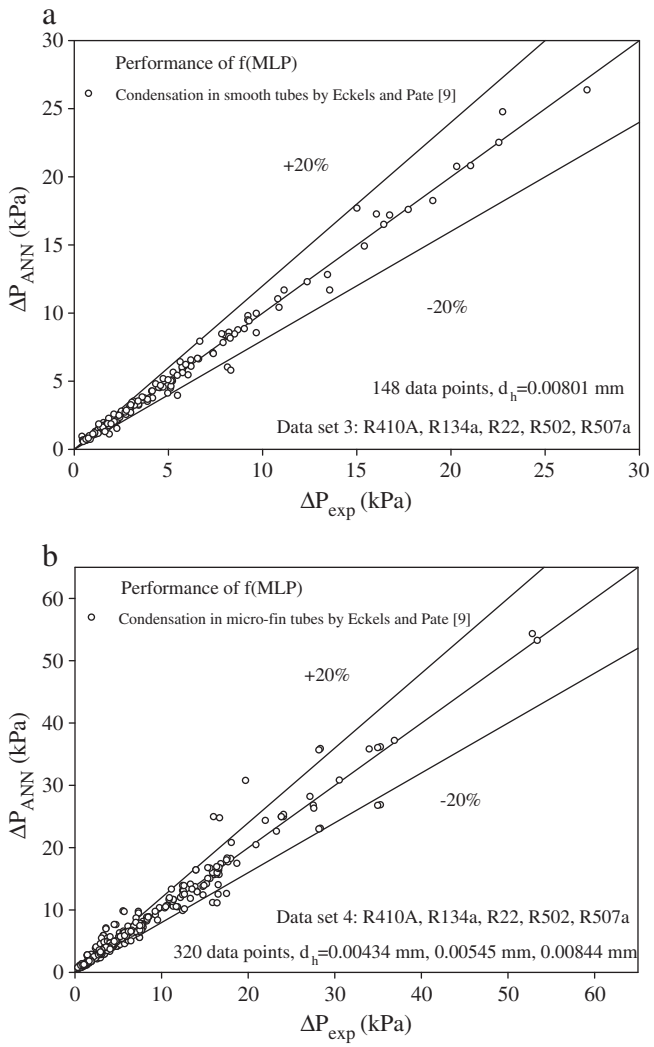

Fig. 2. Comparison of pressure drop values obtained from the condensation experiments of Eckels and Pate [9] in smooth (a) and micro-fin (b) tubes and MLP-12-40-1.

Weber number, We, is used as:

$$\mathrm{We} = \frac{G^2 d_h}{\sigma \rho_{TP}}. \tag{15}$$

Surface tension parameter, ψ, is calculated as:

$$\psi = \frac{j_l \mu_l}{\sigma} \tag{16}$$

where the liquid superficial velocity, j_l, is determined as:

$$j_l = \frac{G(1-x)}{\rho_l(1-\alpha)}. \tag{17}$$

4. Results and discussion

The following paragraphs numerically present the discussion of calculated total pressure drops using the database of National Institute of Standards and Technology (NIST) [8] and Eckels and Pate [9], presented in Choi et al.'s study provided by NIST [8] for the condensation and evaporation of R32, R125, R410A, R134a, R22, R502, R507a, R32/R134a (25/75 by wt%), R407C and R12 in horizontal smooth and micro-fin tubes. It should be noted that detailed explanations and some additional figures and tables containing different experimental parameters related to their studies on the pressure drop calculations can be seen in the applied reference databases [8,9], which demonstrate the accuracy of the experiments. A discussion of the results follows.

There are two-types of neural network analyses in the paper. One of them is developed for the direct determination of the two-phase pressure drop. Its architecture has 2 hidden layers with 10 neurons, and it is shown as MLP 12-10-10-1. This architecture's inputs are mass flux (G), tube length (z), inlet (x_{in}) and outlet (x_{out}) vapor qualities, critical pressure (P_c), latent heat of condensation (h_{fg}), density of liquid (ρ_l) and vapor (ρ_g) phases, dynamic viscosities of liquid (μ_l) and vapor (μ_g) phases, hydraulic diameter (d_h) and the all liquid Reynolds number (Re_l). Another neural network analysis is developed for the calculation of the numerical correction coefficient (K_{num}) in Eq. (1). Its architecture has one hidden layer with forty neurons and it is symbolized as f(MLP) 12-40-1. This architecture's inputs are mass flux (G), tube length (z), inlet (x_{in}) and outlet (x_{out}) vapor qualities, critical pressure (P_c), latent heat of condensation (h_{fg}), mass fraction of liquid (w_l) and vapor (w_g) phases, dynamic viscosities of liquid (μ_l) and vapor (μ_g) phases, hydraulic diameter (d_h) and two-phase density of (ρ_{TP}). These architectures are found as the best architectures of MLP and f(MLP) as a result analyses as shown

Author's personal copy

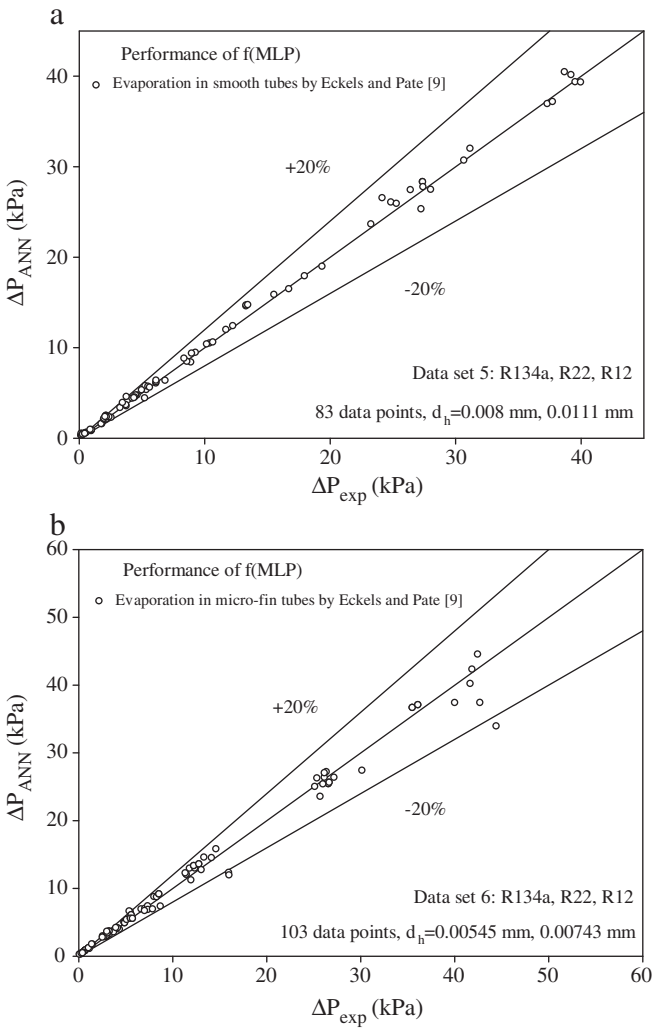

Fig. 3. Comparison of pressure drop values obtained from the evaporation experiments of Eckels and Pate [9] in smooth (a) and micro-fin (b) tubes and MLP-12-40-1.

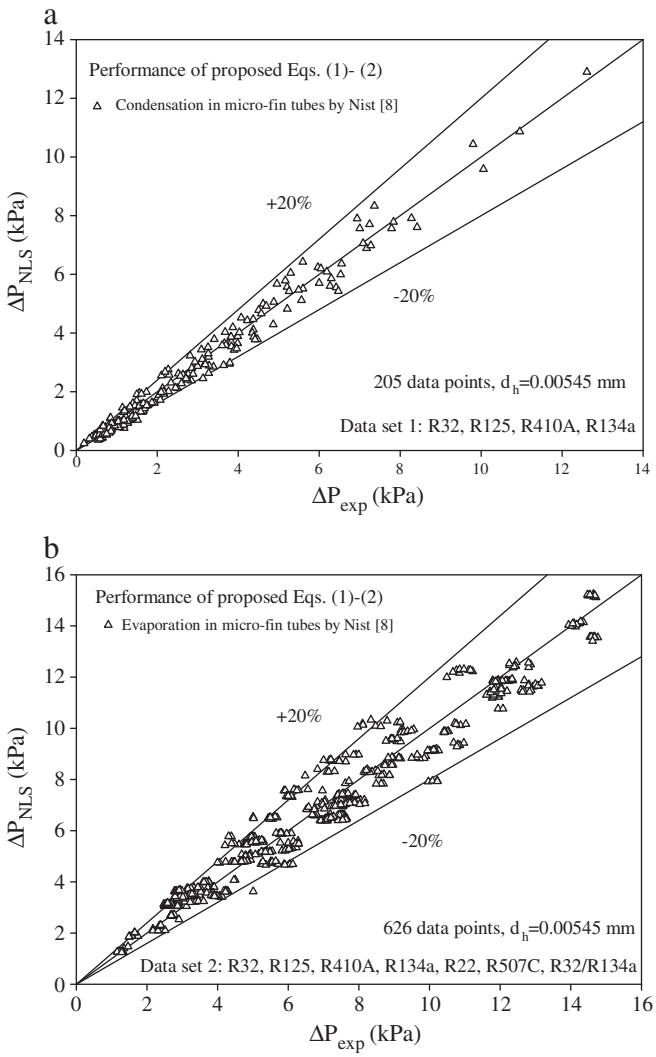

Fig. 4. Comparison of pressure drop values obtained from the comparison of pressure drop values obtained from the condensation (a) and evaporation (b) experiments of NIST [8] in a micro-fin tube and f(NLS).

in Table 2 for MLP and Table 3 for f(MLP). Four-fold cross validation was used for all ANN analyses. It means that 1485 data points (all data of evaporation and condensation in smooth and micro-fin tubes) were divided by four sets randomly and one of the sets selected for the test process, and the rest of them (three sets) were selected for the training process. These processes were continued until there were no untested data sets. Six different data sets of researchers [8,9] are defined in Tables 2 and 3. In terms of the elimination process of different MLPs, the 12-5-5-1, 12-10-10-1, 12-20-20-1 and 12-40-40-1 architectures are tested in Table 2 for MLP, and the 12-40-1, 12-10-10-1, 12-20-20-1 and 12-40-40-1 architectures are tested in Table 3 for f(MLP). It should be noted that although various architectures were tested for elimination, only the typical ones were shown in Tables 2 and 3 due to limited space. Nevertheless, it is possible to derive many results from these tables alone according to the separate databases on the selection of MLP architectures. For instance, the best architecture is found as 12-5-5-1 for data set 1 while the best architecture is found as 12-10-10-1 for data set 4 according to the mean proportional error rates. It should be noted that two of the data sets (one and four) were valid for the condensation in micro-fin tubes. The difference between the results is due to the hardness of generalization in the two-phase flow.

The developed correlations by means of f(NLS) from Eqs. (1) to (4) are the exact form of neural network method of MLP with nine inputs and one hidden neuron. This architecture's inputs are the Froud number (Fr), Weber number (We), Bond number (Bo), Lockhart and Martinelli number (X_{tt}), void fraction, surface tension parameter (Ψ), equivalent Reynolds number (Re_{eq}), the ratio of density to dynamic viscosity (R) and liquid Prandtl number (Pr_l). The initial values of coefficients from Eqs. (2) to (4) were taken from MLP and then they were improved by the method of non-linear least squares (NLS). Approximately 60% and 40% of all data points (1485) were selected for the correlation development set (training) and correlation test set to be used randomly in NLS analyses, respectively. It is obtained from the analyses that f(MLP) with the architecture of 12-40-1 has the lowest mean proportional error rate considering all data with the R^2 value of 0.963. Table 3 shows the coefficients of the proposed equations from Eqs. (1) to (4) according to the flow type, data set, and tube type with the error rates of R^2, MSE and mean proportional error rate in detail. The developed equations of Eqs. (1) and (2) seem to have lower mean deviation than Eqs. (1), (3) and (4) and offer easier applicability with their simpler form than the other ones.

The comparisons between the experimental and predicted values obtained from MLP with the architecture of f(MLP) and the architecture of 12-40-1 and f(NLS) in Eqs. (1) and (2) are illustrated from Figs. 1 to 3 and Figs. 4 to 6, respectively. The condensation and

Author's personal copy

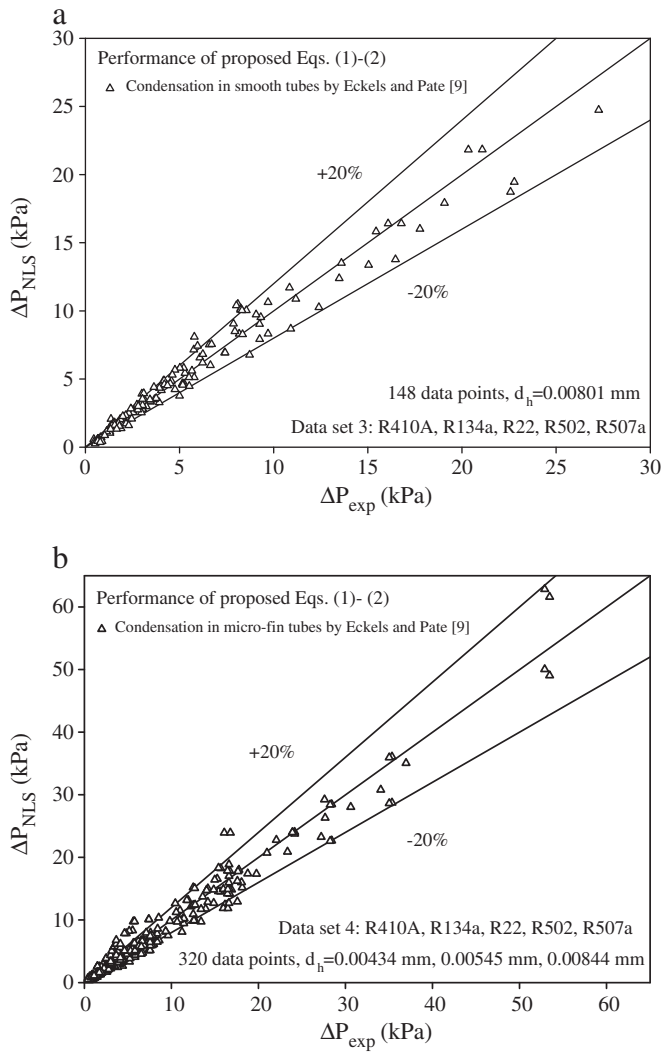

Fig. 5. Comparison of pressure drop values obtained from the condensation experiments of Eckels and Pate [9] in smooth (a) and micro-fin (b) tubes and f(NLS).

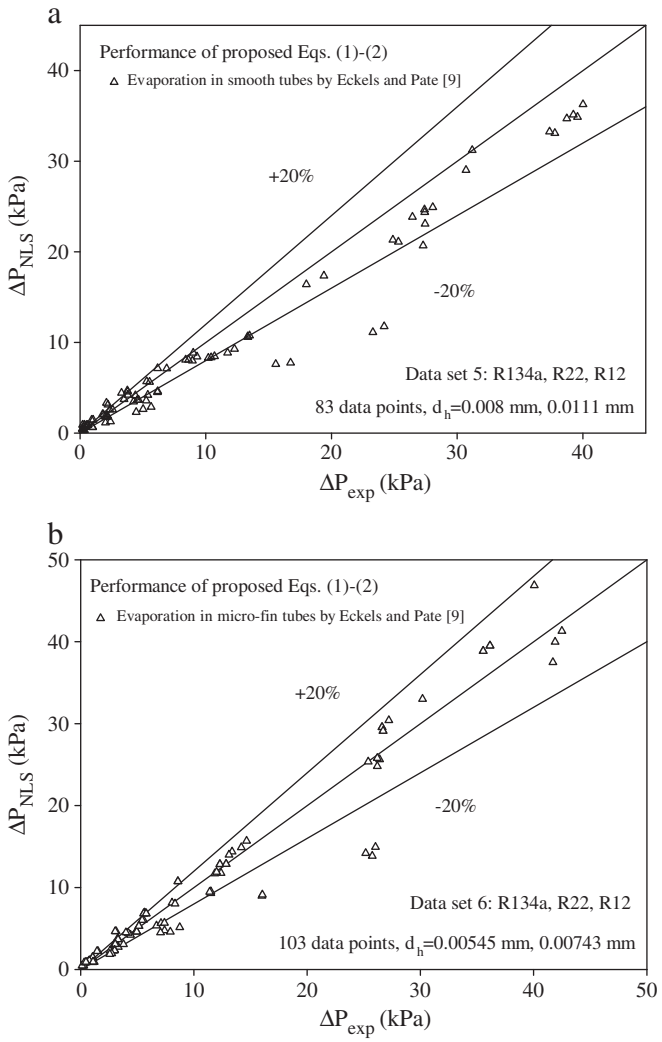

Fig. 6. Comparison of pressure drop values obtained from the evaporation experiments of Eckels and Pate [9] in smooth (a) and micro-fin (b) tubes and f(NLS).

evaporation in micro-fin tube data of NIST [8] are used in Figs. 1 and 4; the condensation in smooth and micro-fin tube data of Eckels and Pate [9] is used in Figs. 2 and 5; the evaporation in smooth and micro-fin tube data of Eckels and Pate [9] is used in Figs. 3 and 6. The data obtained from f(MLP) in Figs. 1 to 3 and NLS in Figs. 4 to 6 have the best results, with a deviation band of ±20%.

Table 4 shows the most predictive combinations of input parameters according to the R^2 values using the method of multi-layer perceptron (MLP) with 12-10-10-1 architecture, including the 1485 experimental data points for condensation and evaporation pressure drop in smooth and micro-fin tubes. In Table 4, when the input parameter number is one, mass flux (G) seems to be dominant on the prediction of pressure drop (ΔP) with the R^2 value of 0.755 for the condensation pressure drop in smooth and micro-fin tubes using data sets 1–3–4. When there are 2 known input parameters, mass flux (G) and the all liquid Reynolds number (Re_l) have the R^2 value of 0.924. When there are 3 known input parameters, mass flux, all liquid Reynolds number (Re_l) and latent vaporization (h_{fg}) have the R^2 value of 0.962. In the same table, when the input parameter number is one, vapor quality (x_{out}) best predicts pressure drop with the R^2 value of 0.473 among others for the evaporation pressure drop in smooth and micro-fin tubes using data sets 2–5–6. When there are 2 known input parameters, mass flux (G) and outlet vapor quality (x_{out}) have the R^2 value of 0.904. This result shows the importance of mass flux. When there are 3 known input parameters, mass flux, outlet vapor quality (x_{out}) and critical pressure have the R^2 value of 0.983. In the same table again, when the input parameter number is one, mass flux (G) best predicts pressure drop with the R^2 value of 0.365 for the evaporation and condensation pressure drops in smooth and micro-fin tubes using data sets 1–2–3–4–5–6. When there are 2 known input parameters, mass flux (G) and liquid dynamic viscosity (μ_l) have the R^2 value of 0.773. This result shows the importance of liquid dynamic viscosity for the investigated data sets. When there are 3 known input parameters, mass flux, mass flux (G), liquid dynamic viscosity (μ_l), and tube length (z) have the R^2 value of 0.88. When there are 4 known input parameters, mass flux, mass flux (G), liquid dynamic viscosity (μ_l), tube length (L) and all liquid Reynolds number (Re_l) have the R^2 value of 0.965. These tables show that the accuracy of the estimated output values by means of input values increases along the increasing number of proper input parameters. In addition, they show the existence of less important input parameters of the method of MLP with the architecture of 12-10-10-1 on the prediction of the pressure drop. Some details on the data sets can be seen on all figures as brief explanations as well as from Choi et al.'s [8] and Eckels and Pate's [9] publications.

5. Conclusion

Numerical analyses have been performed to determine the two-phase pressure drops and to develop reliable correlations of condensation and evaporation in smooth and micro-fin tubes by means of

Author's personal copy

Table 4
The most predictive combinations of input parameters according to the error rates for the determination of measured pressure drop.

Inputs											Input number	Outputs
G	L	x_{in}	x_{out}	P_c	h_{fg}	μ_l	μ_g	d_h	ρ_l	ρ_g	Re_l	R^2 (ΔP)
Condensation pressure drop (ΔP) in smooth and micro-fin tubes using the data sets of 1–3–4 with MLP architecture 12-10-10-1												
						1					1	0.186
1											1	0.755
1							1				2	0.898
1										1	2	0.924
1					1					1	3	0.962
1					1	1				1	4	0.975
1	1				1	1				1	5	0.981
Evaporation pressure drop (ΔP) in smooth and micro-fin tubes using the data sets of 2–5–6 with MLP architecture 12-10-10-1												
						1					1	0.457
			1								1	0.473
			1							1	2	0.865
1			1								2	0.904
1			1	1							3	0.983
1			1	1					1		4	0.990
1			1	1		1			1		5	0.992
Evaporation and condensation pressure drops (ΔP) in smooth and micro-fin tubes using the data sets of 1–2–3–4–5–6 with MLP architecture 12-10-10-1												
						1					1	0.216
1											1	0.365
1										1	2	0.730
1						1					2	0.773
1	1					1					3	0.880
1	1					1				1	4	0.965
1	1					1				1	5	0.978

computational numerical techniques. In order to derive reliable correlations, the well-known experimental databases in the literature [8,9] are used in the analyses. This paper reports that in spite of the numerous studies on the determination of two-phase pressure drop in tubes, application of artificial neural networks (ANN) together with non-linear least squares (NLS) to the in-tube evaporation and condensation for the aim of correlation development does not exist in the literature. For that reason, the content of this study is expected to fill this gap in the literature.

As expected, the neural network approach (MLP) for the aim of correlation development study is found to have equally good results as the non-linear least squares (NLS). The multi-layer perceptron method (f(MLP)) with the architecture of 12-40-1 has better predictability than the classical multi-layer perceptron method (MLP) with the architecture of 12-10-10-1 due to the use of proper input parameters during the correlation development study.

Therefore, this study proposes Eqs. (1) and (2) for practical usage by engineers due to their lower deviation from $\pm 20\%$ and the fact that they are derived for the conditions of evaporation and condensation in smooth and micro-fin tubes separately. These equations are also beneficial for the determination of pressure drops using various databases at the same time that have only one parameter (R). A detailed model of f(MLP) is given to be used in MATLAB directly. This explanation will enable users to predict the two-phase pressure drop with high accuracy.

The pressure drop of evaporation and condensation in smooth and micro-fin tubes is found to be highly dependent upon mass flux, all liquid Reynolds numbers, latent evaporation, outlet vapor quality, critical pressure of refrigerant, liquid dynamic viscosity and tube length as a result of dependency analyses.

Acknowledgments

The second author wishes to thank King Mongkut's University of Technology Thonburi (KMUTT) for providing him with a post-doctoral fellowship. The fifth author is indebted to the Thailand Research Fund and the National Research University Project for their financial support. This paper used NIST's data [8] and Eckels and Pate's [9] experimental data, which were presented in Choi et al.'s [8] study provided by NIST. The authors wish to thank them for their contributions to the subject of in-tube two-phase flow.

References

[1] M. Balcilar, A.S. Dalkilic, S. Wongwises, Artificial neural network (ANN) techniques for the determination of condensation heat transfer characteristics during downward annular flow of R134a inside a vertical smooth tube, International Communications in Heat and Mass Transfer 38 (2011) 75–84.
[2] M. Balcilar, A.S. Dalkilic, S. Wongwises, Determination of condensation heat transfer characteristics of R134a by means of artificial intelligence method, International Mechanical Engineering Congress and Exposition, ASME, November 12–18 2010, USA.
[3] M. Balcilar, A.S. Dalkilic, B. Bolat, S. Wongwises, Investigation of empirical correlations on the determination of condensation heat transfer characteristics using computational numerical methods during downward annular flow of R134a inside a vertical smooth tube, Journal of Mechanical Science and Technology 25 (10) (2011) 1–20.
[4] B. Bolat, M. Balcilar, A.S. Dalkilic, S. Wongwises, Optimization of the relationship between the two-phase friction factor and Reynolds equivalent number model by the means of Genetic Algorithm, ASME/JSME 8th Thermal Engineering Joint Conference, ASME, March 13–17 2011, Hawaii.
[5] H. Demir, A.S. Dalkilic, N.A. Kurekci, W. Duangthongsuk, S. Wongwises, Numerical investigation on the single phase forced convection heat transfer characteristics of TiO_2 nanofluids in a double-tube counter flow heat exchanger, International Communications in Heat and Mass Transfer 38 (2011) 218–228.
[6] H. Demir, O. Agra, Ş.Ö. Atayılmaz, Generalized neural network model of alternative refrigerant (R600a) inside a smooth tube, International Communications in Heat and Mass Transfer 36 (2009) 744–749.
[7] O. Agra, H. Demir, S. Ozgur Atayilmaz, F. Kantas, A.S. Dalkilic, Numerical investigation of heat transfer and pressure drop in enhanced tubes, International Communications in Heat and Mass Transfer 38 (2011) 1384–1391.
[8] J.Y. Choi, M.A. Kedzierski, P.A. Domanski, A generalized pressure drop correlation for evaporation and condensation of alternative refrigerants in smooth and micro-fin tubes, NISTIR 6333 (1999) 1–50.
[9] S.J. Eckels, M.B. Pate, In-tube evaporation and condensation of refrigerant-lubricant mixtures of HFC-134a and CFC-12, ASHRAE Transaction 97 (1991) 62–67.
[10] D. Butterworth, A comparison of some void-fraction relationships for co-current gas–liquid flow, International Journal of Multiphase Flow 1 (1975) 845–850.

Lazarus Godson[1]
Department of Mechanical Engineering,
Karunya University,
Coimbatore, Tamil Nadu 641 114, India
e-mail: godasir@yahoo.co.in

B. Raja
Indian Institute of Information Technology,
Design and Manufacturing (IIITD&M),
Kancheepuram, Chennai,
Tamil Nadu 600 048, India
e-mail: rajab@iiitdm.ac.in

D. Mohan Lal
Department of Mechanical Engineering,
Anna University,
Chennai, Tamil Nadu 600 025, India
e-mail: mohanlal@annauniv.edu

S. Wongwises
Fluid Mechanics, Thermal Engineering and
Multiphase Flow Research Lab. (FUTURE),
Department of Mechanical Engineering,
King Mongkut's University of Technology
Thonburi,
Bangmod, Bangkok 10140, Thailand;
The Academy of Science,
The Royal Institute of Thailand,
Sanam Suea Pa,
Dusit, Bangkok 10300, Thailand
e-mail: somchai.won@kmutt.ac.th

Convective Heat Transfer Characteristics of Silver-Water Nanofluid Under Laminar and Turbulent Flow Conditions

The convective heat transfer coefficient and pressure drop of silver-water nanofluids is measured in a counter flow heat exchanger from laminar to turbulent flow regime. The experimental results show that the convective heat transfer coefficient of the nanofluids increases by up to 69% at a concentration of 0.9 vol. % compared with that of pure water. Furthermore, the experimental results show that the convective heat transfer coefficient enhancement exceeds the thermal conductivity enhancement. It is observed that the measured heat transfer coefficient is higher than that of the predicted ones using Gnielinski equation by at least 40%. The use of the silver nanofluid has a little penalty in pressure drop up to 55% increase 0.9% volume concentration of silver nanoparticles.
[DOI: 10.1115/1.4006027]

Keywords: convective heat transfer, silver, nanofluid, pressure drop, laminar, turbulent, transition

1 Introduction

The last few decades have seen unprecedented growth in field of electronics, communication, and computing technologies, and it is likely to continue unabated into the present century. Recently, high heat flux devices used in avionics and medical engineering demands ultrahigh-performance cooling in thermal management systems. The exponential growth in these areas and their devices through miniaturization and an enhanced rate of operation has brought serious problems in the thermal management of these devices. Conventionally, water, oil and ethylene glycol are used as heat transfer fluids. Though various methods have been used to enhance the performance of a heat transfer device, the poor thermophysical properties affect the enhancement of heat transfer and the compactness of heat exchangers. As a result, there is a strong need to develop advanced heat transfer fluids with higher thermal conductivities and improved heat transfer characteristics. A nanofluid is a new class of heat transfer fluids that manifest enhanced thermal conductivities relative to pure fluids [1]. Besides enhanced heat transfer, nanofluids eliminate most of the problems arising with microsize slurries such as sedimentation, clogging of small channels, erosion, excessive pressure drop, etc. Thus, nanofluids have greater potential for convective heat transfer enhancement and are highly suited to application in practical heat transfer processes.

Focusing on the forced convective heat transfer, the majority of the experimental research focuses on the heat transfer enhancement by using the metal oxide nanoparticles such as aluminum oxide, copper oxide, titanium oxide, silicon oxide, etc., and only a limited research has been done with the use of pure metal nanoparticles such as copper, silver, gold, and carbon nanotube. Pak and Cho [2] investigated the convective heat transfer characteristics of nanofluids (γAl_2O_3–water and TiO_2–water) with $\varphi = 1$–3% in a turbulent regime and showed that the Nusselt number for the nanofluids increased with volume concentration and Reynolds number. Eastman et al. [3] conducted tests to assess the thermal performance of CuO–water with $\varphi = 0.9\%$ under turbulent flow conditions, and the heat transfer coefficient was higher by 15% than that of the base fluid. Wen and Ding [4] assessed the convective heat transfer of nanofluids in the entrance region under laminar flow conditions, γAl_2O_3–water nanofluid ($\gamma = 27$–56 nm; $\varphi = 0.6$–1.6%) under a constant heat flux boundary condition. For nanofluids containing $\varphi = 1.6\%$, the local heat transfer coefficient in the entrance region was found to be 41% higher than that of the base fluid at the same flow rate. It was observed that the enhancement is particularly significant in the entrance region and decreases with axial distance, and the particle migration was found to be the reason for the enhancement. Lai et al. [5] studied the flow behavior of nanofluids (Al_2O_3–deionsed water ; $\gamma = 20$ nm) in a millimeter-sized stainless steel test tube, subjected to constant wall heat flux and a low Reynolds number ($Re < 270$). The maximum Nusselt number enhancement of the nanofluid of 8% at $\varphi = 1\%$ was recorded. Jung et al. [6] conducted convective heat transfer experiments for a nanofluid (Al_2O_3–water) in a rectangular microchannel (50×50 μm) under laminar flow conditions. The convective heat transfer coefficient increased by more than 32% for $\varphi = 1.8\%$ in base fluids. Duangthongsuk and Wongwises [7] reported that the forced convective heat transfer under varied heat flux boundary conditions and pressure drop characteristics of a nanofluid consisting of water and 0.2 vol. % TiO_2 nanoparticles of 21 nm diameter flowing in a horizontal double-pipe counter flow heat exchanger under turbulent flow conditions. The results showed that the convective heat transfer coefficient of nanofluid is slightly higher than that of the base

[1]Corresponding author.

Contributed by the Heat Transfer Division of ASME for publication in the Journal of Thermal Science and Engineering Applications. Manuscript received April 6, 2011; final manuscript received January 24, 2012; published online July 12, 2012. Assoc. Editor: Mehmet Arik.

Copyright © 2012 by ASME

liquid by about 6–11%, and the use of the oxide nanofluid has a little penalty in pressure drop.

Xuan and Li [8] measured the convective heat transfer of the Cu– water nanofluid in a small-hydraulic-diameter flat tube under laminar flow conditions. The Nusselt number of the nanofluid with $\varphi = 0.5\%$ increased by more than 39% compared with that of pure water. Ding et al. [9] tested multiwalled carbon nanotubes (MCNT with $\varphi = 0.1$–1.0% with 0.5 wt % in aqueous solution) in a horizontal tube and obtained a maximum enhancement of heat transfer of 350% at a Reynolds number of 800. Kang et al. [10] investigated heat transfer in a grooved heat pipe using Ag–water and Ag–deionized (DI) water ($\gamma = 10$–35 nm) with particle concentrations ranging from 1 mg/l to 100 mg/l. The results indicated that, after adding a small amount of silver nanoparticles in pure water, the heat pipe wall temperature became lower than that of pipes filled only with pure water. As more nanoparticles became dispersed in the working fluid, the heat pipe wall temperature increase became smaller. The maximum reduction in thermal resistance of a heat pipe operated containing $\gamma = 10$ nm was 52% lower than that of DI–water and while that containing $\gamma = 35$ nm was 81% lower. The enhancement of heat pipe performance was attributed to the increase in effective liquid conductance that flattens the temperature of the fluid.

From the above review, it is observed that the heat transfer enhancement with the use of pure metal nanoparticles with low volume concentration is found to be very much higher than the metal oxide nanoparticles with relatively higher concentrations. This is because the metal nanoparticles posses higher thermal conductivity than the metal oxide ones. High aspect ratio nanoparticles such as carbon nanotubes resulted in greater enhancement in thermal conductivity and the heat transfer coefficient, compared to spherical and low aspect ratio nanoparticles. It is also observed that the use of high concentration metal oxide nanoparticles increases the viscosity and pressure drop leading to the higher pumping power. This issue can be eliminated with the use of low concentration metal nanoparticles. Maiga et al. [11] reported that, with regard to the nanofluid thermal properties, the actual amount of experimental data available in the literature remains surprisingly small, and it is obvious that more works in this area will be published in the near future. So far, all of the convective studies have been performed either in the laminar or turbulent regime or the combination of both. However, no one has studied on the hydrodynamic and heat transfer behavior of nanofluids in the laminar, transition, and the turbulent regime with pure metal nanoparticle such as silver with different concentrations. In this study, the convective heat transfer characteristics of nanofluid suspended with low volume concentrations of silver nanoparticles with 0.3, 0.6, and 0.9 vol. % are investigated. The effect of the Reynolds number and temperature of the flowing nanofluid and mass flow rate and temperature of the chilled water on the heat transfer coefficient are studied.

2 Experiments

2.1 Nanofluid Preparation. In the present study, the two-step method is used for preparation Ag–water nanofluid. The silver nanoparticles are mixed directly with deionized water under ultrasonic vibration without any additive or stabilizer. The ultrasonic vibration is carried out for 8 h using the ultrasonic processor (Roop-Telsonic TEC-40 model, power density-750 W, frequency-20 kHz) in order to make sure complete dispersion of the nanoparticles in the base fluid. The nanofluid was not transparent, and it was looking like black in color. The settling did not occur in 24 h. To validate this, a stability test was conducted by taking some small sample of nanofluid and physically observed if there is any settling occurs. No sedimentation was observed. Hence, the prepared nanofluid is stable for experimentation.

2.2 Effective Thermal Conductivity and Viscosity. A hot wire system is used to measure the thermal conductivity of the nanofluid, which involves a wire suspended symmetrically in a liquid in a vertical cylindrical container. The wire serves both as heating element and as thermometer. Constant current is applied to a thin wire, made of platinum, and the time evolution of its electrical resistance due to the temperature increase is measured. The thermal conductivity of the nanofluid is determined by observing the rate at which the temperature of a very thin platinum wire increases with time after a step change in voltage has been applied to it, thus creating a line source of constant heat flux per unit length. The relative viscosities of nanofluid were measured using Cannon-Fenske Opaque also called as reverse-flow viscometer. It works on the principle of evaluating the time required for a particular quantity of fluid to pass through a capillary bore. The ratio of efflux time of nanofluid to that of base-fluid is regarded as the experimental relative viscosity ratio. The uncertainty of the thermal conductivity and viscosity measurements is found to be around 1.5% and 2%, respectively, and the confidence level is found to be 95%. Detailed methods on the measurement of thermal conductivity and viscosity are given elsewhere in the most recently accepted paper of the present authors [12]. The thermal conductivity and viscosity are correlated as linear and quadratic functions of volume fraction, respectively. The coefficients of silver–water nanofluid for the tested volume concentration and temperature are achieved using linear regression analysis.

2.3 Convective Heat Transfer Coefficient. The experimental setup to measure convective heat transfer coefficient and pressure drop is shown in Fig. 1. The equipment comprises two flow loops: chilled water and nanofluid. Each loop consists of several units such as pump, flow meter, a constant temperature chilled water bath, nanofluid bath with temperature controller, and a test section. The test section is a 2.94 m long tube-in-tube counter flow heat exchanger with heated nanofluid flowing inside the tube while the cooling water flows in the annulus. The inner tube is of 6.3 mm outer diameter and 4.3 mm inner diameter, while the outer tube is having 12.7 mm outer diameter and 10.5 mm as inner diameter. The test section is thermally isolated from its upstream and downstream section by ceramic wool in order to reduce the heat loss along the axial direction. Two RTDs and a differential pressure transmitter are mounted at both ends of the test section to measure the bulk temperatures and pressure drop of the nanofluid. Six RTDs (PT100 RTD sensors with $\pm 0.15\,^{\circ}\mathrm{C}$ accuracy) are mounted on the surface of the wall to measure the temperature distributions along the length of the test section. The nanofluid is heated in an insulated cylindrical tank with a 0.5 kW heating capacity coupled with a proportional integral differential controller (PID-C) to keep the temperature constant inside the nanofluid bath. The hot nanofluid from the bottom of the tank is pumped using a centrifugal pump and then passed through a mass flow meter and fed into the test section in the counter flow direction to the cooling water. The nanofluid flow rate is measured using a Coriolis type mass flow meter with $\pm 0.1\%$ accuracy. Similarly, the water is cooled using an auxiliary cooling system with a 0.5 TR capacity condensing unit and a 1 kW heater coupled with a PID controller in order to keep the temperature of the cooling water constant. The interconnecting tubes in the nanofluid and cooling water loops are provided with necessary insulation to avoid heat loss to the surroundings. The heat infiltration analysis is performed by applying the uncertainty analysis suggested by Moffat [13], and it is seen that the heat leak was less than 5% of the actual heat load, which is insignificant and can be negligible. The inlet and exit temperatures of the cooling water and nanofluids, wall temperatures of the test section, mass flow rates of the cooling water and nanofluid, and the differential pressure in the nanofluid are measured. The experimental test matrix that is used in this study is given below in Table 1.

2.4 Data Reduction. The heat transfer rate from the hot fluid is defined as

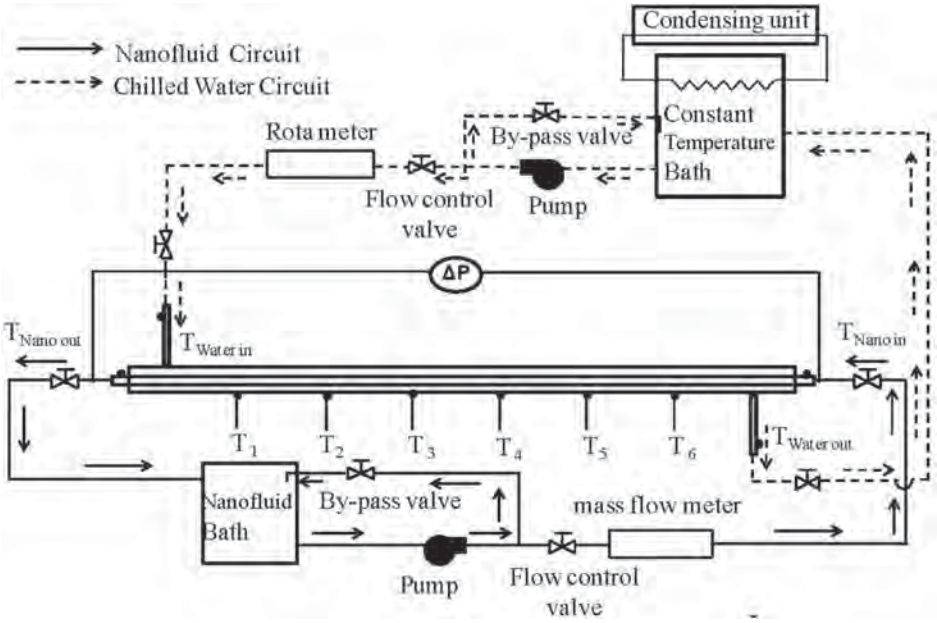

Fig. 1 Schematic diagram of the experimental apparatus

Table 1 Experimental test conditions

D (mm)	Re	T_{nano} (°C)	T_{water} (°C)	m_{water} (kg/s)
4.3	900–12,000	48	26	0.016
		57	30	
		65	35	

$$Q_{h_{nf}} = \dot{m}_{h_{nf}} C_{P_{h_{nf}}} (T_{in_{nf}} - T_{out_{nf}}) \tag{1}$$

where $Q_{h_{nf}}$ is the heat transfer rate of the hot nanofluid and $m_{h_{nf}}$ is the mass flow rate of the hot nanofluid

$$\frac{1}{U_i A_i} = \frac{1}{h_i . Ai} + \frac{\ln(d_o/d_i)}{2\pi kL} + \frac{1}{h_o . A_o} \tag{2}$$

$$Nu_{nf} = \frac{h_{nf} D}{k_{nf}} \tag{3}$$

where $h_i = h_{nf}$ is the heat transfer coefficient of the nanofluid, h_o = heat transfer coefficient of the annulus; k is the thermal conductivity of the copper tube, U_i is the overall heat transfer coefficient of the inner tube, Nu_{nf} is the Nusselt number of the nanofluid, D is the inner diameter of the test tube, and k_{nf} is the thermal conductivity of the nanofluid.

Similar to the heat transfer coefficient, the friction factor of the nanofluid flowing through the test section is calculated using the following equation

$$f_{nf} = \frac{2D\Delta P_{nf}}{L\rho_{nf} u_m^2} \tag{4}$$

where f_{nf} is the friction factor of the nanofluid, ΔP_{nf} is the measured pressure drop of the nanofluid, L is the length of the tube, ρ_{nf} is the density of the nanofluid, and u_m is the mean velocity of the nanofluid.

The thermophysical properties such as the density, specific heat, thermal conductivity, and viscosity of the nanofluid are calculated using the following published correlations.

The density is calculated from Pak and Cho [2] using the following equation

$$\rho_{nf} = \phi\rho_p + (1-\phi)\rho_w \tag{5}$$

The specific heat is calculated from Xuan and Roetzel [14] as follows

$$(\rho C_p)_{nf} = \phi(\rho C_p)_p + (1-\phi)(\rho C_p)_w \tag{6}$$

where $(\rho Cp)_{nf}$ is the heat capacity of the nanofluid, $(\rho Cp)_p$ is the heat capacity of the nanoparticles, and $(\rho Cp)_w$ is the heat capacity of the base fluid.

The thermal conductivity and viscosity of the nanofluid is calculated by the developed correlation given elsewhere in the most recently accepted paper of the present authors in the *Experimental Heat Transfer Journal* [ISSN: 0891-6152]. The thermal conductivity and viscosity are correlated as linear and quadratic functions of volume fraction, respectively. The coefficients of silver–water nanofluid for the tested volume concentration and temperature are achieved using linear regression as shown below

$$\frac{k_{nf}}{k_w} = (0.9692\phi + 0.9508) \tag{7}$$

$$\frac{\mu_{nf}}{\mu_w} = (1.005 + 0.497\phi - 0.1149\phi^2) \tag{8}$$

The properties of the nanofluid shown in the above equations are evaluated from water and nanoparticles at average bulk temperature. The detailed data reduction flow chart is shown below in Fig. 2.

3 Results and Discussion

A data base consisting of 960 data points were generated and the enhancement in heat transfer with respect thermophysical

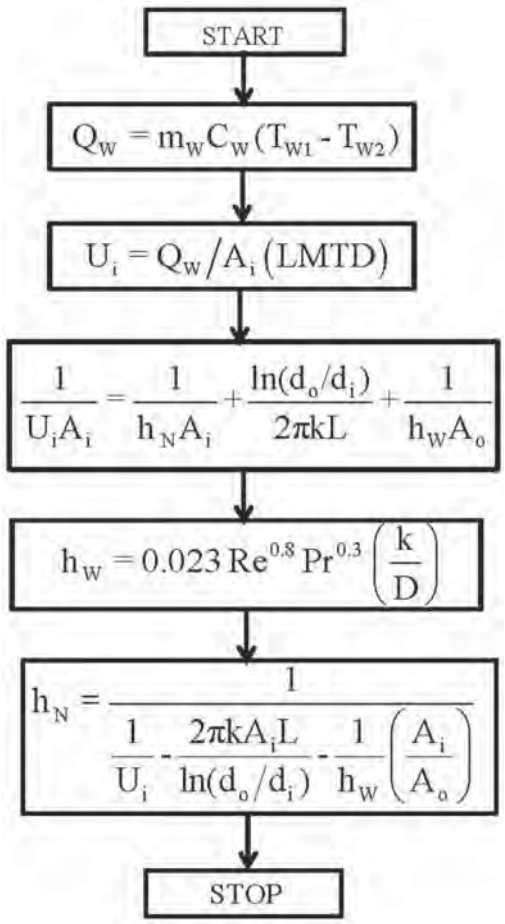

Fig. 2 Data reduction flow chart

properties, mass flow rate, heat flux, concentration, mechanism of heat transfer, etc., are discussed in Secs. 3.1–3.6. The experimental test results of various parameters are shown in Table 2. The test facility is validated with experimental results of water for its repeatability and accuracy. The results are compared with those obtained from the Gnielinski equation [15], and a deviation of ± 4.5% is observed between the experimental and the predicted results.

3.1 Influence of Thermophysical Properties. The thermal conductivity and viscosity ratios as a function of volume concentration and temperature are shown in Fig. 3. The use of nanoparticles dispersed in water gives higher thermal conductivity and viscosity than the base fluid. The thermal conductivity ratio for $\varphi = 0.3$ vol. % increases from 1.09 to 1.43 as the temperature increases from 50 °C to 90 °C; and similarly, for $\varphi = 0.9\%$, the ratio increases from 1.29 to 2.29. This enhancement is expected to reflect in heat transfer coefficient also. The viscosity ratio for $\varphi = 0.3\%$ increases from 1.06 to 1.2, and for $\varphi = 0.9\%$, the ratio increases from 1.23 to 1.43 for the above temperature range. Further, the observed results from the present study have shown that the measured thermal conductivity ratio is larger than that of Masuda et al. [16] and Zhang et al. [17]. Yu et al. [18] reported that the metal oxide particle for $\varphi = 4$–5% produces an enhancement level up to 30%; and the metal particles with less than $\varphi < 1.5\%$ give an enhancement up to 40%. However, the results from the present study show an enhancement of 60% even with $\varphi < 0.9\%$. This shows that the enhancement of thermal conductivity using metal particles is higher than that of the metal oxide particles even at low concentrations. It can be seen the thermal conductivity ratio is significantly higher than the other properties such as density, viscosity, and heat capacity. For 0.3 vol. %, the thermal conductivity ratio is 1.27; and the ratios of density, viscosity, and heat capacity are found to be 1.05, 1.14, and 0.9, respectively. Hence, it clear that the influence of thermal conductivity plays a major role for the heat transfer enhancement.

3.2 Influence of Heat Transfer Mechanism. Brownian motion is a random walk motion of nanoparticles within the base fluid, which results from the collisions between the nanoparticles and the molecules of the base fluid. The nanoparticles themselves can be identified effectively as large molecules when compared with fluid molecules. Also, the nanoparticles are moving with an average kinetic energy equal to that of the fluid molecules with a considerable lower velocity. The Brownian diffusion is found to be the potential mechanism for enhancement of thermal conductivity in the absence of turbulent eddies. Thus, the Brownian motion intensifies with an increase in temperature as per the kinetic theory of particles. The effectiveness of the Brownian motion decreases with an increase in the bulk viscosity and velocity. Heat transfer enhancement through Brownian motion is effective when the bulk flow velocities are very low. At higher flow velocities, the particles travel along with the velocities. It is seen that, with respect to tested flow velocities, the effect of Brownian motion is insignificant. For instant, the required Brownian velocity for silver–water fluid ranges between 0.002 and 0.005 m/s for particle concentration between 0.3% and 0.9%, which is much lower than the lowest tested velocity of 0.12 m/s, which corresponds to a Reynolds number of 800. Even though some literature [19] has exposed the presence of Brownian motion while flow is laminar, the present work reveals that its presence is insignificant under the tested condition. Similarly, the thermophoresis or the Sorét effect, which is due to the diffusion of particles under the effect of a temperature gradient, also seems to be insignificant. The Thermophoresis velocity ranges between 0.0025 and 0.005 m/s, which is very low than the tested flow velocities. Therefore, both effects of thermophoretic and Brownian motion are insignificant under these tested conditions.

3.3 Temperature Distributions. The temperature distribution of the silver–water nanofluid, which flows in the inner tube and the cooling water, which flows in the annulus along the length of the test section for a test condition is shown in Fig. 4. The test mass flow rates 3, 8, and 18 g s^{-1} correspond to laminar, transition, and turbulent flow condition of the nanofluid, respectively. It is observed that, as the mass flow is increased, the logarithmic mean temperature difference (LMTD) decreases. For instance, for a volume concentration of 0.9%, the LMTD is 7.69, 5.63, and 3.73 for laminar, transition, and turbulent regime, respectively. It can also be observed that, for a same flow operating condition, the LMTD decreases as the particle concentration increases. For instance, for a volume concentration of 0.3%, 0.6%, and 0.9%, the LMTD is 4.62, 4.13, and 3.73 for the laminar, transition, and turbulent regime, respectively. Further, it can be noticed that the steepness of the nanofluid curve decreases as the mass flow rate of nanofluid is increased. This steepness in the curve will be reflected in the local and average heat transfer coefficients. The steepness of the curve is higher for entrance region of the laminar flow and lesser for turbulent flow.

3.4 Average Heat Transfer Coefficient. The variation of average heat transfer coefficient ratio on Reynolds number for different concentration is shown in Fig. 5. The heat transfer coefficient ratios for the tested condition are between 1.2 and 1.87 and the ratios increase as Reynolds number increases. The average heat transfer coefficient increases with Reynolds number and particle concentration. For Reynolds number less than 3000, the increase in average heat transfer coefficient with respect to concentration is close to 10% to 15% increase for every increase in

Table 2 Experimental results

			Convective heat transfer coefficient (W/(m^2 K))				Nusselt number				Pressure drop (kPa)			
Re	Mass flow rate (kg/s)	Heat flux (kW/m^2)	Water	0.30%	0.60%	0.90%	Water	0.30%	0.60%	0.90%	Water	0.30%	0.60%	0.90%
$T_{nf}=48\,^{\circ}$C and $T_W=25\,^{\circ}$C														
1107	0.002	3.09	977.57	1198.89	1687.07	1991.90	7.04	8.89	12.19	14.99	0.12	0.31	0.92	1.20
1862	0.003	5.56	1537.92	1834.17	2337.77	2641.00	11.02	13.60	17.28	20.46	0.25	0.45	0.73	1.85
2579	0.004	6.87	1857.12	2299.37	2898.50	3298.55	14.19	17.05	21.66	26.00	0.38	0.68	1.45	2.45
3136	0.005	8.74	2273.91	2773.35	3480.25	3935.93	17.38	20.10	24.21	29.99	0.58	0.92	1.72	3.41
4785	0.008	9.63	3072.34	3723.91	4550.29	4977.12	24.02	28.61	35.57	38.91	1.74	2.11	2.96	4.78
6041	0.011	10.62	3902.91	4414.29	5785.90	6254.69	30.51	34.45	45.24	48.90	3.53	3.92	5.02	5.97
7700	0.014	10.47	4363.73	5134.75	6335.49	6872.25	34.12	41.50	49.53	53.73	5.14	5.80	6.68	7.48
8479	0.017	11.43	5011.34	5739.00	6737.25	7340.27	39.18	46.39	54.24	57.39	7.488	7.92	8.67	9.82
10,115	0.02	11.98	5694.54	6651.48	7631.00	8242.27	44.52	53.06	59.74	64.44	10.69	11.65	12.38	14.07
11,246	0.023	11.51	6176.88	7146.27	8003.65	8771.65	48.29	57.06	63.13	68.74	13.68	15.13	15.14	15.99
$T_{nf}=57\,^{\circ}$C and $T_W=30\,^{\circ}$C														
1107	0.002	3.72	1030.06	1421.87	1975.34	2343.78	8.05	10.99	15.44	18.32	0.09	0.242	0.828	0.94
1862	0.003	6.41	1624.58	1959.01	2496.62	2936.77	12.70	15.38	19.52	22.96	0.16	0.368	0.6555	0.98
2579	0.004	8.63	2028.31	2445.64	3188.32	3647.05	15.86	19.00	24.93	28.51	0.29	0.483	0.7935	1.34
3136	0.005	9.08	2343.51	2720.89	3447.26	3983.24	18.32	20.99	26.95	31.14	0.54	0.777	1.81	2.89
4785	0.008	9.81	3111.99	4119.73	4557.32	5282.83	24.33	31.08	35.63	41.30	1.63	1.932	2.8055	4.74
6041	0.011	9.95	3807.98	4691.56	5509.45	6348.48	29.77	37.26	43.07	49.63	2.89	3.444	4.0595	5.52
7700	0.014	10.63	4462.5	5472.4	6454.32	7256.79	34.89	43.46	50.46	56.73	4.29	5.24	5.4625	7.09
8479	0.017	11.31	4996.61	5984.68	7004.56	7651.32	39.06	47.52	55.33	59.82	6.015	7.14	7.9275	9.65
10,115	0.02	11.74	5577.07	6862.08	7803.36	8463.93	43.60	53.49	61.57	66.17	9.06	10.89	11.431	11.71
11,246	0.023	12.28	6201.98	7461.45	8475.81	9365.81	48.49	58.25	67.19	73.99	13.06	14.16	15.169	15.07
$T_{nf}=65\,^{\circ}$C and $T_W=35\,^{\circ}$C														
1107	0.002	3.82	1105.52	1653.86	2223.24	2715.9	8.64	13	17.23	22.03	0.07	0.21	0.693	0.78
1862	0.003	6.63	1730.89	2257.88	2854.34	3224.43	13.53	17.25	22.35	26.16	0.1	0.294	0.839	0.95
2579	0.004	8.92	2153.36	2879.01	3455.34	3824.94	16.84	21.76	27.22	31.03	0.22	0.357	0.927	2.45
3136	0.005	9.38	2482.25	3198.43	3845.34	4377.78	19.41	24.53	31.20	35.52	0.48	0.567	1.858	3.1
4785	0.008	9.89	3281.26	4289.24	4761.8	5387.36	25.65	32.94	38.63	43.71	1.24	1.523	2.254	4.02
6041	0.011	10.19	4002.12	5275.63	5731.69	6478.47	31.29	40.51	46.50	52.56	2.19	2.457	3.563	5.014
7700	0.014	10.72	4678.09	6175.3	7178.83	7676.71	36.57	47.42	58.24	62.28	4.34	4.125	4.998	6.24
8479	0.017	11.39	5228.52	6574.1	7541.03	8208.71	40.88	52.35	61.99	66.60	4.917	7.01	7.707	8.12
10,115	0.02	12.00	5825.64	7371.69	8633.2	9369.3	45.55	57.7	70.67	76.02	8.79	10.52	10.076	11.36
11,246	0.023	12.42	6467.37	7896.63	8910.69	9861.23	50.56	64.3	73.08	80.88	12.25	13.62	14.355	14.97

concentration of 0.3%. However, for Reynolds numbers between 3000 and 7500, the average heat transfer coefficient increases by 20–30% for the same concentrations. Further, at higher Reynolds number, the average heat transfer coefficient from pure fluid is more than 30%, but with respect to change in concentration, the percentage enhancement is less significant. It can be observed that enhancement in heat transfer with respect to concentration is significant in moderate Reynolds number range from 3000 to 7500, which corresponds to the operating condition for transition from laminar to turbulent. As reported in Ref. [20], the enhancement

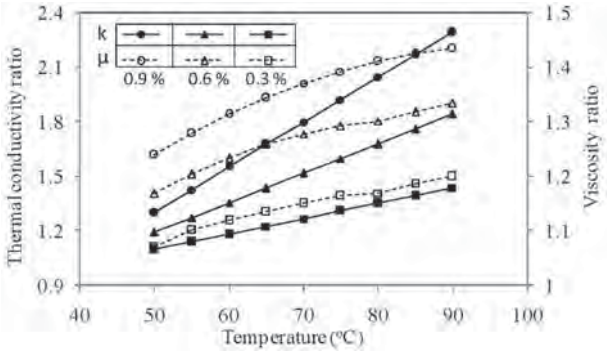

Fig. 3 Thermal conductivity ratio and viscosity ratio of silver-water nanofluids as a function of temperature

heat transfer at Reynolds numbers greater than 7000, which pertains to fully turbulent flow, is less significant.

The comparison between the heat transfer coefficient and the Gnielinski equation is shown in Fig. 6. From the figure, it is clearly seen that the measured heat transfer coefficient of nanofluid is 40% higher than that of the Gnielinski equation. This may be due to the fact that the correlation was established from single phase fluid data and was valid only for the single-phase flow. Similarly, it is observed that the Nu increases with the increase in the Reynolds number and the volume concentration. The enhancement is highly significant in the turbulent region and less significant in the laminar region. Similarly, the enhancement is moderate in the transition region from laminar to turbulent even for small variation in the volume concentration of silver nanoparticles. The attributed reason may be the effect on thermal boundary layer thickness (or thermally fully developed length). Some researchers claimed that one reason for the heat transfer enhancement of nanofluids is reduction of boundary layer thickness and delay in boundary layer development. This effect is more important in turbulent regime. Because, in turbulent regime, the boundary layer develops fast compared to that in laminar flow. For example, for a specific pipe with turbulent flow, the flow along the length of the pipe is almost thermally fully developed. But, with laminar flow, there is a considerable entrance region length. Therefore, using nanofluids, the delay in boundary layer development for turbulent regime is more considerable. Another reason is maybe because of particles migration, which is bigger in turbulent flows. It has been shown in some researches that the nanofluids

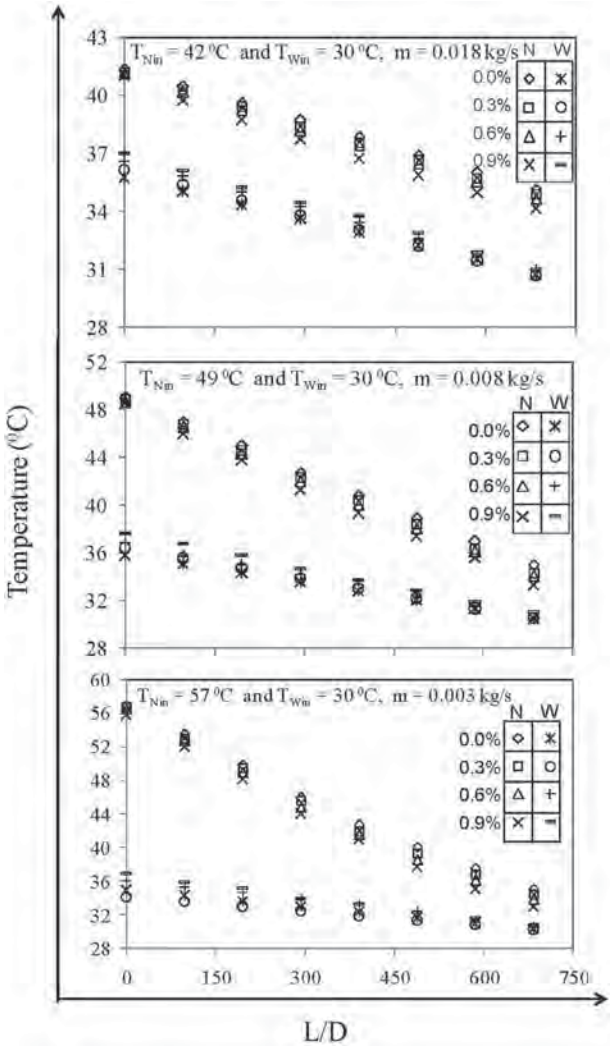

Fig. 4 Variation of temperature of nanofluids against axial positions

are non-Newtonian flows with shear thinning behavior, in which their viscosity decreases when the shear stress increases. Since the wall shear stresses in turbulent regime are so much bigger compared to laminar flow, the viscosity of nanofluid near the wall in

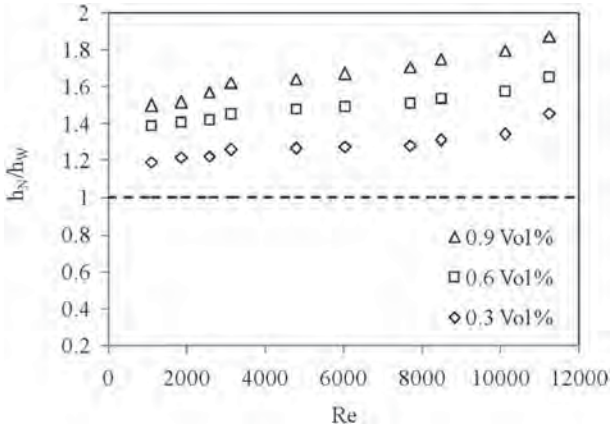

Fig. 5 Variation of heat transfer coefficient ratio (h_n/h_w) against Reynolds number

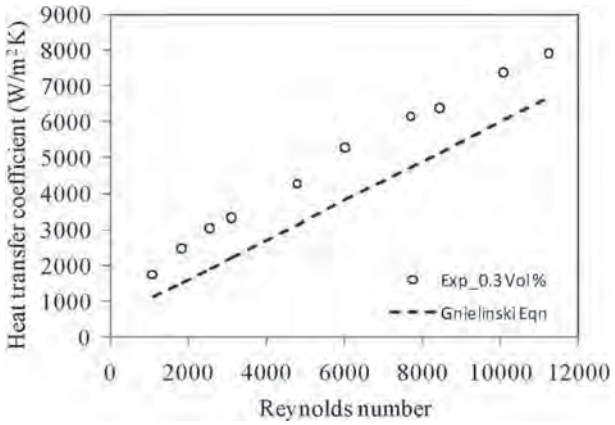

Fig. 6 Comparison of experimental and theoretical heat transfer coefficient

turbulent flow is lower, and as a result, the boundary layer decreases.

Figure 7 shows the variation of the Nusselt number as function of volume fraction and Reynolds numbers of 1800, 4600, and 9500, which corresponds to the laminar, transition, and turbulent flow regimes. It is observed that the Nusselt number increases considerably with both these parameters. Thus, for a given Reynolds number, say Re is 1800, the Nu increases in from 12 to 51 for the lowest tested particle volume fraction of 0.3%. Similarly, the Nusselt number increases from 15 to 55 and 17 to 60 for the Reynolds number varying from of 4600 to 9500, respectively. It is also observed that the increase of Nu with respect to the volume fraction appears less pronounced for low and moderate Reynolds numbers, which is due to the fact that the definition of Nu includes nanofluid thermal conductivity that also increases with particle volume concentration. Further, the Nusselt number increases with the increase in the combination of both high Reynolds number and high particle concentration.

Figure 8 shows the percentage enhancement of heat transfer coefficient with respect to the dimensionless length. The percentage enhancement increases with the increase in the concentration and decreases with the increase in the length. An enhancement of 81.2% and 48.4% is observed at the entrance and the exit regions, respectively, for 0.9 vol. % concentration.

3.5 Local Heat Transfer Coefficient. The variation of local heat transfer coefficient on dimensionless length for different concentration for different flow condition is shown in Fig. 9. The mass flow rates are 3, 8, and 18 g s^{-1} selected in laminar,

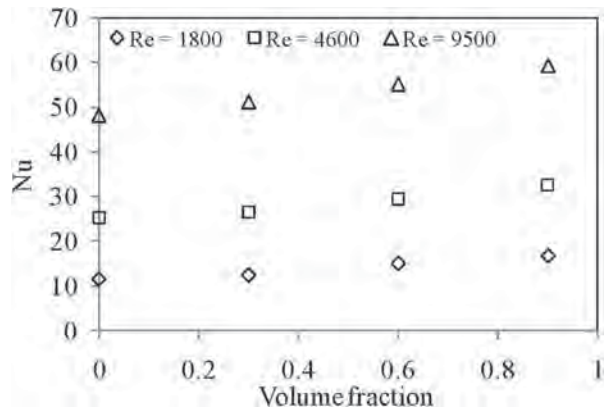

Fig. 7 Effect of volume fraction and Reynolds number on Nusselt number

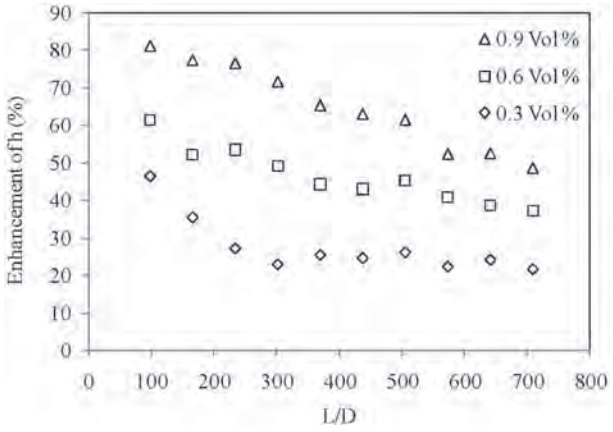

Fig. 8 Enhancement of heat transfer coefficient against axial positions

transition, and turbulent condition, respectively. It can be seen that the local heat transfer coefficient is a strong function of dimensionless length. For the same mass flow rate, the local heat transfer coefficient increases with particle concentration. The decreasing trend of the coefficient is due to the configuration of the test section, which is a counter current heat exchanger. The temperature difference is maximum at a dimensionless length close to 0 and minimum at 1 and so is the heat transfer coefficient. The initial heat transfer coefficient in laminar flow regime cumulatively increases by 15% to 25% from the value of the base fluid. However, in a laminar flow, the percentage increase rapidly decreases as the dimensionless length increases, and the values are almost same at the maximum dimensionless length of 1. Under transition condition, the cumulative percentage increase is spread throughout the dimensionless length as volume concentration is increased, and under the turbulent condition, the increase is drastic. The intense turbulence and thorough mixing of particles at all volume concentration are reasoned for it. Even though, the enhancement of heat transfer is insignificant with respect to Brownian and thermophoresis effects, the particles' capacity of carrying heat in the turbulence flow plays a vital role.

3.6 Pressure Drop. Figure 10 shows the pressure drop as a function of the Reynolds number, which shows that there exists a penalty in pressure drop in the nanofluid used in this study. For instance, a minimum pressure drop of 24% is observed for 0.3 vol. % and, for the nanofluid, average inlet temperature of 57 °C and chilled water temperature of 30 °C. Similarly, a maximum pressure drop of 55% is observed for 0.9 vol. % for the same temperature conditions. The reason may be the use of metal nanoparticles posses a bit higher pressure drop than the use of the metal oxide once, since the viscosity of the pure metal nanoparticles is

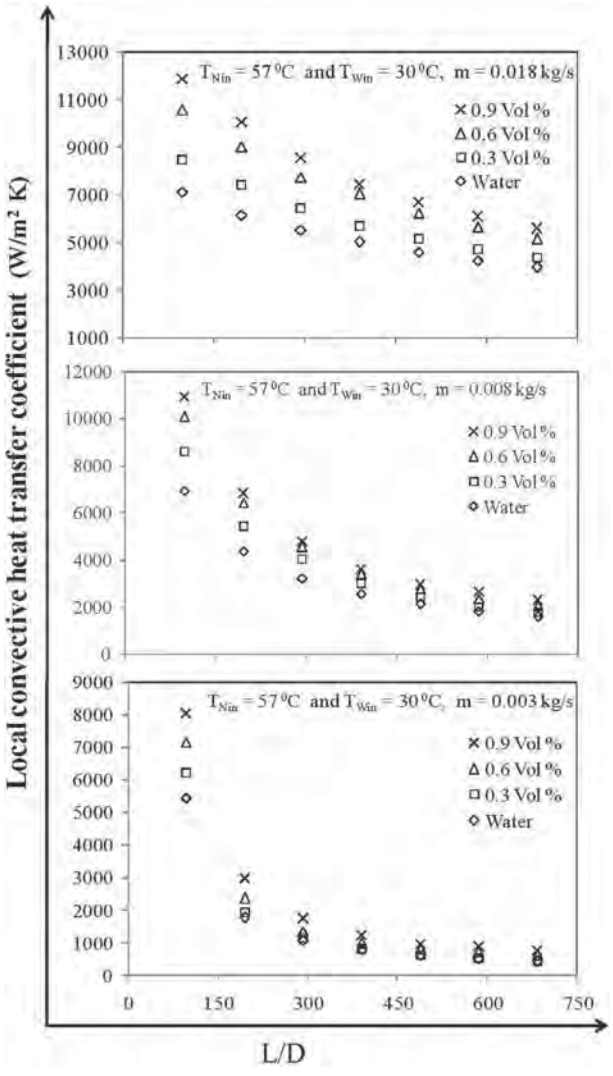

Fig. 9 Variation of local heat transfer coefficients of nanofluids against axial positions

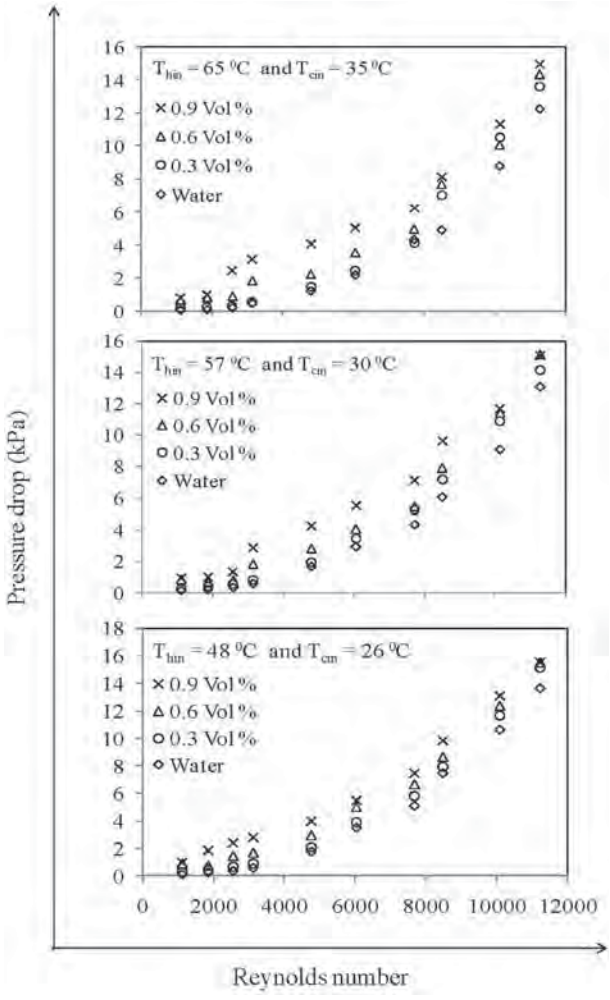

Fig. 10 Variation in pressure drop against Reynolds number

high when compared with that of the oxides. However, it is observed that, for the given conditions, the pressure drop decreases with increase in the temperature. An increase in the nanofluid temperature leads to a decrease in the viscosity of the nanofluid, which results in a reduction in the pressure drop. The important observation is that the nanofluid is actually a two-phase flow, and there need to be more experimental data and correlation to predict the pressure drop of nanofluids, which behaves more like a liquid–solid mixture.

4 Conclusion

The convective heat transfer characteristics of silver–water nanofluid under laminar and turbulent flow conditions are experimentally measured. The use of silver nanoparticles in the base fluid enhances the heat transfer coefficients by 23.5% and 69% for 0.3 and 0.9 vol. % concentrations, respectively. For Reynolds number corresponding to laminar regime, the increase in average heat transfer coefficient with respect to concentration is close to 10% to 15% increase for every increase in concentration of 0.3%. Reynolds numbers corresponding to transition and turbulent regime, the heat transfer coefficient increases by 20% to 30% for the same concentrations. It can be observed that enhancement in heat transfer with respect to concentration is significant in moderate Reynolds number range from 3000 to 7500, which corresponds to the operating condition for transition from laminar to turbulent. The effect of thermophysical properties plays a major role for the heat transfer enhancement. The pressure drop of using the pure metal nanofluid has a little penalty when compared with that of the pure water.

Acknowledgment

The fourth author would like to thank the Thailand Research Fund and the National Research University Project for the financial support.

Nomenclature

A = cross sectional area, m^2
Cp = specific heat, J/(kg K)
D = tube diameter, m
h = heat transfer coefficient, $W/(m^2 K)$
k = thermal conductivity, W/(m K)
m = mass flow rate, kg/s
Nu = Nusselt number
Pr = Prandtl number
q'' = heat flux, W/m^2
Re = Reynolds number
T = temperature, °C

Greek Symbols

β = thermal dispersion coefficient, $N/(m^2 K)$
φ = volume fraction
ρ = density, kg/m^3
μ = dynamic viscosity, kg/(m s)
γ = particle size (nm)

Subscripts

nf = nanofluid
w = tube wall
x = axial distance
bf = base fluid
i = inner wall
o = outer wall

References

[1] Choi, S. U. S., 1995, "Enhancing Thermal Conductivity of Fluids With Nanoparticles in Developments and Applications of Non-Newtonian Flows," ASME FED 231/MD 66, pp. 99–103.
[2] Pak, B. C., and Cho, I. Y., 1998, "Hydrodynamic and Heat Transfer Study of Dispersed Fluids With Sub-Micron Metallic Oxide Particles," Exp. Heat Transfer, **11**, pp. 151–170.
[3] Eastman, J. A, Choi, S. U. S., Li, S., Soyez, G., Thompson, L. J., and DiMelfi, R. J., 1999, "Novel Thermal Properties of Nanostructure Materials," Mater. Sci. Forum, **312**, pp. 629–634.
[4] Wen, D., and Ding, Y., 2005, "Experimental Investigation into the Pool Boiling Heat Transfer of Aqueous Based Alumina Nanofluids," J. Nanopart. Res., **7**, pp. 265–274.
[5] Lai, W. Y., Duculescu, B., Phelan, P. E., and Prasher, R. S., 2006, "Convective Heat Transfer With Nanofluids in a Single 1.02-mm Tube," Proceedings of the ASME International Mechanical Engineering Congress and Exposition, Chicago, pp. 1–8.
[6] Jung, J. Y., Oh, H. S., and Kwak, H. Y., 2006, "Forced Convective Heat Transfer of Nanofluids in Microchannels," Proceedings of the ASME International Mechanical Engineering Congress and Exposition, Chicago, pp. 11–17.
[7] Duangthongsuk, W., and Wongwises, S., 2008, "Effect of Thermo-Physical Properties Models on the Prediction of the Convective Heat Transfer Coefficient for Low Concentration Nanofluid," Int. Commun. Heat Mass Transfer, **35**(10), pp. 1320–1326.
[8] Xuan, Y., and Li, Q., 2004, "Flow and Heat Transfer Performances of Nanofluids Inside Small Hydraulic Diameter Flat Tube," J. Eng. Thermophys., **25**(2), pp. 305–307.
[9] Ding, Y., Alias, G., Wen, D., and Richard, A. W., 2006, "Heat Transfer of Aqueous Suspensions of Carbon Nanotubes (CNT nanofluids)," Int. J. Heat Mass Transfer, **49**, pp. 240–250.
[10] Kang, S. W., Wei, W. C., Tsai, S. H., and Yang, S. Y., 2006, "Experimental Investigation of Silver Nano-Fluid on Heat Pipe Thermal Performance," Appl. Therm. Eng., **26**, pp. 2377–2382.
[11] Maiga, S. E., Palm, S. J., Nguyen, C. T., Roy, G., and Galanis, G., "Heat Transfer Enhancements by Using Nanofluids in Forced Convection Flows," Int. J. Heat Fluid Flow, **26**, pp. 530–546.
[12] Lazarus, G., Raja, B., Lal, D. M., and Wongwises, S., 2010, "Experimental Investigation on the Thermal Conductivity and Viscosity of Silver-Deionized Water Nanofluid," Exp. Heat Transfer, **23**(4), pp. 317–332.
[13] Moffat, R. J., 2000, "Describing the Uncertainties in Experimental Results," Exp. Therm. Fluid Sci., **1**(1), pp. 3–17.
[14] Xuan, Y., and Roetzel, W., 2000, "Conceptions for Heat Transfer Correlation of Nanofluids," Int. J. Heat Mass Transfer, **43**, pp. 3701–3707.
[15] Gnielinski, V., 1976, "New Equations for Heat and Mass Transfer in Turbulent Pipe and Channel Flow," Int. Chem. Eng., **16**, pp. 359–368.
[16] Masuda, H., Ebata, A., Teramae, K., and Hishinuma, N., 1993, "Alteration of Thermal Conductivity and Viscosity of Liquid by Dispersion of Ultra-Fine Particles," Netsu Bussei, **4**, pp. 227–233.
[17] Zhang, X., Gu, H., and Fujii, M., 2007, "Effective Thermal Conductivity and Thermal Diffusivity of Nanofluids Containing Spherical and Cylindrical Nanoparticles," Exp. Therm. Fluid Sci., **31**, pp. 593–599.
[18] Yu, W., France, D. M., Choi, S. U. S., and Routbort, J. L., 2007, "Review and Assessment of Nanofluid Technology for Transportation and Other Applications," Energy Systems Division, Argonne National Laboratory, ANL/ESD/07-9, pp. 1–78.
[19] Buongiorno, J., 2006, "Convective Heat Transfer Enhancement in Nanofluids," Heat and Mass Transfer Conference, HMT-2006-C335, pp. 1–6.
[20] Das, S. K., Choi, S. U. S., Yu, W., and Pradeep, T., 2008, *Nanofluids—Science and Technology*, Wiley, New York.

Provided for non-commercial research and education use.
Not for reproduction, distribution or commercial use.

This article appeared in a journal published by Elsevier. The attached copy is furnished to the author for internal non-commercial research and education use, including for instruction at the authors institution and sharing with colleagues.

Other uses, including reproduction and distribution, or selling or licensing copies, or posting to personal, institutional or third party websites are prohibited.

In most cases authors are permitted to post their version of the article (e.g. in Word or Tex form) to their personal website or institutional repository. Authors requiring further information regarding Elsevier's archiving and manuscript policies are encouraged to visit:

http://www.elsevier.com/copyright

Author's personal copy

Thermochimica Acta 545 (2012) 48–56

Contents lists available at SciVerse ScienceDirect

Thermochimica Acta

journal homepage: www.elsevier.com/locate/tca

Measurement of the thermal conductivity of titania and alumina nanofluids

Thakleaw Yiamsawasd[a], Ahmet Selim Dalkilic[b], Somchai Wongwises[a,c,*]

[a] Fluid Mechanics, Thermal Engineering and Multiphase Flow Research Lab. (FUTURE), Department of Mechanical Engineering, King Mongkut's University of Technology Thonburi, Bangmod, Bangkok 10140, Thailand
[b] Heat and Thermodynamics Division, Department of Mechanical Engineering, Yildiz Technical University (YTU), Yildiz, Besiktas, Istanbul 34349, Turkey
[c] The Academy of Science, The Royal Institute of Thailand, Sanam Suea Pa, Dusit, Bangkok 10300, Thailand

ARTICLE INFO

Article history:
Received 21 January 2012
Received in revised form 18 May 2012
Accepted 20 June 2012
Available online 10 July 2012

Keywords:
Thermal conductivity
Nanoparticle
Nanofluids
Transient hot-wire method

ABSTRACT

This article reports the thermal conductivity of nanofluids experimentally. TiO_2 and Al_2O_3 nanoparticles were suspended in base fluids (water and 20/80 by mass of an ethylene glycol–water mixture) with concentration level of 0–8 vol.%, at a temperature of 15–65 °C. The measurement was done by the transient hot-wire method. The results showed that thermal conductivity of nanofluids increased more with respect to the base fluid and increased with increasing concentration and temperature. When compared with predictions from existing models, thermal conductivity ratio could not be predicted by the models in terms of both concentration and temperature. Finally, a useful correlation for predicting thermal conductivity of Al_2O_3 and TiO_2 nanofluids was presented.

© 2012 Elsevier B.V. All rights reserved.

1. Introduction

At present, modern nanotechnology could synthesize or produce various types of nanoparticles quite easily. Nanoparticles have become important components in several technologies or innovations that are very useful for mankind. Similarly, nanoparticles are also used in heat transfer innovation. A new kind of heat transfer fluid or "nanofluid" has been developed (named by Choi [1]) by suspending nanoparticles of solid substance in general heat transfer fluids.

High conduction heat transfer of solid substance is used to enhance the heat transfer of general working fluids. Nanofluids are also expected to be used appropriately in various forms of mini- and micro-scale heat exchanger, such as in electronic devices, in processors of mobile computers, or in high-capacity military communication devices. They are also used in large-scale heat exchangers or systems that require maximum performance like the heat exchangers of nuclear reactors or high-capacity heat transfer systems.

For real application, the thermal and basic transfer properties of nanofluids should be carefully researched. Therefore, many researchers have studied the thermal properties and transfer capacities of nanofluids, such as thermal conductivity, viscosity, convective heat transfer, and boiling heat transfer. However, there is a basic concept that nanofluids with high thermal conductivity help increase heat transfer capacity. Thus, research on the development and measurement of the thermal conductivity of nanofluids gained special attention over other properties. These studies dealt with the impact or effect of various factors on the increase of thermal conductivity of nanofluids, such as temperature, concentration, shape or size of nanoparticles, and pH. Examples of research on the measurement of thermal conductivity follow.

Masuda et al. [2] studied the thermophysical properties of Al_2O_3–water, SiO_2–water and TiO_2–water nanofluids. The transient hot-wire method was used to measure the thermal conductivity of nanofluids. They found that the thermal conductivity of nanofluids increased dramatically compared with the base fluid. The thermal conductivity of Al_2O_3 nanofluid increased by 32% at the concentration of 4.3 vol.%. They concluded that temperature did not have any effect on the increase of relative thermal conductivity (thermal conductivity ratio).

Lee et al. [3] conducted an experiment to measure the thermal conductivity of Al_2O_3 and CuO suspended in water and ethylene glycol. Particle sizes of Al_2O_3 and CuO were 23.6 nm and 38.4 nm, respectively. The transient hot-wire method was used to measure the thermal conductivity of nanofluids at a concentration range of 1–4 vol.%. Their results indicated that nanofluids had higher thermal conductivity than the base fluid, and it increased with the increasing level of concentration. When compared the experimental results with prediction from Hamilton and Crosser model, it was found that the model could predict thermal conductivity of Al_2O_3 nanofluids, but it could not predict for CuO nanofluids.

* Corresponding author at: Fluid Mechanics, Thermal Engineering and Multiphase Flow Research Lab. (FUTURE), Department of Mechanical Engineering, King Mongkut's University of Technology Thonburi, Bangmod, Bangkok 10140, Thailand. Tel.: +66 2 470 9115; fax: +66 2 470 9111.
E-mail address: somchai.won@kmutt.ac.th (S. Wongwises).

0040-6031/$ – see front matter © 2012 Elsevier B.V. All rights reserved.
http://dx.doi.org/10.1016/j.tca.2012.06.026

Author's personal copy

Wang et al. [4] studied thermal conductivity of Al_2O_3 and CuO nanofluids with a particle size of 20 nm. Each was suspended in water, vacuum pump oil, engine oil, and ethylene glycol. A steady state method was used to measure thermal conductivity. Their results showed that the thermal conductivity of both nanofluids were higher than that of the base fluids and varied with concentration level. The engine oil and ethylene glycol base fluids yielded higher enhancement than other types of base fluids. When compared with the theoretical model, a thermal conductivity ratio of the nanofluids was found to be higher.

Eastman et al. [5] conducted an experiment to measure the thermal conductivity of Cu–ethylene glycol nanofluid with an average copper particle size of 10 nm and concentration level of 0.6 vol.%. A transient hot-wire method was used for measurement. They found that nanofluids had higher thermal conductivity when the concentration level increased. Moreover, acid-added nanofluids had increased thermal conductivity. At a concentration level of 0.3 vol.%, thermal conductivity of acid-added Cu nanofluid increased dramatically by 40%. Their experimental results were higher than those obtained from the classical model. The researchers proposed that the shape of particle also had an effect on the increase of thermal conductivity.

Xie et al. [6] studied the effect of particle size and pH on thermal conductivity of Al_2O_3 nanofluid with particle sizes of 12–300 nm. Deionized water, ethylene glycol, and pump oil were used as base fluid. Transient hot-wire apparatus was used to measure thermal conductivity in this experiment. Their results showed the thermal conductivity of Al_2O_3 nanofluid was higher than that of the base fluid. It also increased with the increase of concentration level, but decreased when pH was lower. Regarding the effect of nanoparticle size, thermal conductivity of the nanofluid was found to vary with particle size. The optimal particle size of 60 nm yielded the highest thermal conductivity enhancements. They also found that the enhanced thermal conductivity ratio decreased when the thermal conductivity of the base fluid increased. When compared with predictions from the classic model, the thermal conductivity used in the experiment was higher.

Das et al. [7] studied the effect of temperature on an increase of thermal conductivity of Al_2O_3 and CuO suspended in water, with a concentration range of 1–4 vol.% at temperatures of 21, 36 and 51 °C. They used the temperature oscillation technique. Their resulted indicated the thermal conductivity of nanofluids increased when the temperature increased. In particular, the thermal conductivity of Al_2O_3–water nanofluid at 4 vol.% increased dramatically when the temperature slightly increased. The experimental results tended to be higher than predictions from the classic model.

Chon and Kihm [8] studied the increase of thermal conductivity of a nanofluid from Brownian motion. Al_2O_3–water nanofluid at the concentration of 1 vol.% was used in this experiment. The particle sizes used were 11, 47, and 150 nm in a temperature range of 20–70 °C. They reported the thermal conductivity of the nanofluid increased more than the base fluid and rose with the increase of temperature. They also found that smaller particle sizes gave higher thermal conductivity. They asserted the increase in thermal conductivity of the nanofluid resulted from Brownian motion or micro-convection mechanism. They argued the increase of temperature caused a greater Brownian motion mechanism.

Hwang et al. [9] conducted an experiment to measure the thermal conductivity of nanofluids. They used multiwalled carbon nanotubes (MWCNT) and CuO and SiO_2 with the base fluid of water and ethylene glycol. The average particle size of the MWCNTs was 10–50 μm long with a diameter of 10–30 nm. The average diameters of the CuO and SiO_2 particles were 35.4 nm and 7 nm, respectively. They used a transient hot-wire method to measure thermal conductivity. They found the thermal conductivity of nanofluids was higher than the base fluid and varied with concentration level. They also found that nanofluids with ethylene glycol as the base fluid had a higher increase in thermal conductivity than water. The MWCNT–ethylene glycol had the highest increase of 11.3% at a concentration level of 1 vol.%.

He et al. [10] studied the heat transfer and upward flow patterns in vertical tubes of TiO_2–water nanofluid. They measured the thermal conductivity and viscosity of TiO_2–water nanofluids. The particle sizes of TiO_2 were 95, 145 and 210 nm with concentration ranges of 1–5 wt.%. They measured the thermal conductivity with a transient hot-wire method. They found that when the concentration level increased, the thermal conductivity of the nanofluid also increased to levels higher than the predictions from the H–C model. They also found smaller particle sizes had higher thermal conductivity than larger particle sizes.

Li and Peterson [11] conducted an experiment on the measurement of thermal conductivity of Al_2O_3 nanofluids with particle sizes of 36 and 47 nm. The nanofluids were suspended in distilled water at temperatures of 27–37 °C and concentration levels of 0.5–6.0 vol.%. They used a steady-state method for measurement. Their experimental results showed the thermal conductivity of nanofluids increased more than the base fluid and increased with the rise of concentration level and temperature. However, the increase was nonlinear. They also found that particle size was an important parameter for the increase of thermal conductivity. Smaller particles had higher increase than larger particle. In this experiment, the temperature of 32 °C and concentration levels of 2 vol.% and 4 vol.% were optimal points that had the highest increase of thermal conductivity. Unfortunately, existing theoretical models could not be used for prediction.

Wang et al. [12] measured thermal conductivity and thermal diffusion of TiO_2 (26 nm) and SiO_2 (23 nm) nanoparticles suspended in distilled water, ethanol, and ethylene glycol. They used a 3ω wire method to measure thermal conductivity. The experiment was conducted with concentration ranges of 1–4 vol.% at temperatures of 18–65 °C. The results indicated the thermal conductivity of nanofluids was higher than the base fluids and increased with the rise of temperature and concentration level. The researchers reported temperature had an obvious effect on the increase of thermal conductivity ratio. The Koo model that referred to a Brownian motion effect and the Ren model that referred to micro convection could not be used for prediction, especially at high temperature.

Zhang et al. [13] studied the thermal conductivity and thermal diffusion of Au–toluene Al_2O_3–water, TiO_2–water, CuO/water and CNT/water nanofluids. The diameters of Au, Al_2O_3, TiO_2, and CuO particles were 1.65, 20, 40, and 33 nm, respectively, with CNF of 10 nm × 150 nm. They measured the thermal conductivity of the nanofluids with a transient short-hot-wire technique. They used concentration levels of 0%, 10%, 20%, and 40% by mass at temperatures of 5–50 °C. Their results showed that the thermal conductivity ratio of nanofluids increased only slightly. The results were similar to the predictions from the model of Hamilton and Crosser in the case of spherical nanoparticles, and the prediction of Yamada and Ota in the case of carbon nanofibers.

Murshed et al. [14] measured the thermal conductivity and viscosity of nanofluids which consisted of 80 and 150 nm Al_2O_3 and 15 nm TiO_2 particles suspended in deionized water and ethylene glycol and 80 nm Al suspended in ethylene glycol (EG) and engine oil (EO). The concentrations ranged from 1 to 5 vol.% at temperatures of 20–60 °C. They used a transient hot-wire technique to measure thermal conductivity. They found nanofluids had higher increases of thermal conductivity than the base fluid and this varied with concentration level and temperature. The researchers also proposed a new model to predict the thermal conductivity of nanofluids which referred to nanolayers as factors of the increase. The model yielded predictions similar to the results of the experiment.

Author's personal copy

Duangthongsuk and Wongwises [15] studied the effect of temperature on thermal conductivity and viscosity of TiO_2-water nanofluids. They experimented with 21 nm TiO_2 particles at temperatures of 15–35 °C with concentration levels of 0.2–2 vol.%. They measured thermal conductivity with the transient hot-wire method. They found the thermal conductivity of TiO_2–water nanofluids increased when concentration levels and temperatures increased.

Turgut et al. [16] used a 3ω method to measure thermal conductivity of TiO_2-deionized water nanofluid with an average TiO_2 nanoparticle diameter of 21 nm. They used a concentration level of 3% by volume and temperature ranges from 13 to 55 °C. They found that thermal conductivity increased by about 7.4% when the concentration level was 3 vol.%. The thermal conductivity ratio did not change with temperature. The experimental results were lower than predictions from the classic model.

From all research mentioned above, the thermal conductivity of nanofluids was found to be higher than the base fluid and increased with concentration level. However, certain important details of the experimental results are still different in many studies. For example, some research found that existing classic models like the Hamilton and Crosser model (H–C model) [17] and Bruggeman model [18] could be used to predict thermal conductivity of nanofluids whereas many researchers found that existing classic models could not be used. Similarly, some parameters showed contrasting effects. For example, Masuda et al. [2] concluded that temperature did not have any effect on the increase in thermal conductivity ratio of nanofluids. This corresponds with Turgut et al. [16]. On the contrary, Das et al. [7], Wang et al. [12] and many other researchers stated that temperature clearly had an effect on the increase in thermal conductivity ratio of nanofluids.

In addition, researchers referred to various theories for the increase in thermal conductivity of nanofluids that conclusions could not be drawn. Hence, there are many different newly-developed models for prediction of thermal conductivity of nanofluids, according to the theories used. For instance, Yu and Choi [19,20] and Xie et al. [21] presented a newly-developed model based mainly on the energy transfer mechanism at the liquid/solid interfacial nanolayer. At the same time, a theory that discusses Brownian motion as cause of the increase in thermal conductivity of nanofluids was also used to develop models in many studies such as Xuan et al. [22], Koo and Kleinstreuer [23], and Jang and Choi [24]. The differences in opinion are quite obvious. Therefore, the measurement of thermal conductivity should be further studied in order to draw clear conclusions in various aspects. Hence, this research aims to conduct an experiment to measure the thermal conductivity of TiO_2 and Al_2O_3 nanofluids suspended in water and ethylene glycol–water mixtures. This study also investigates the effect of concentration level and temperature on the increase in thermal conductivity of nanofluids. Moreover, results gained from the measurement of the thermal conductivity of nanofluids will be compared to predictions from various models and to results from other research. Finally, this study will propose a correlation for predicting the thermal conductivity of nanofluids.

2. Sample preparation

A main purpose in preparing nanofluids is to make suspended nanoparticles diffuse well in the base fluids without precipitation of particles in a short time.

Preparation of nanofluids is an important step. In general, it consists of three methods: control of pH, addition of surfactants or dispersants, and the use of an ultrasonic vibration machine. In this experiment, TiO_2 and Al_2O_3 nanofluids used were supported by the DEGUSSA Company, Germany. The average diameter of TiO_2 nanoparticles was 21 nm and the average diameter of Al_2O_3 particles was 120 nm. Water, and ethylene glycol–water (20/80 wt.%) were used as base fluids. Both TiO_2 and Al_2O_3 were suspended in base fluids with concentration levels of 13.8 and 10.6 vol.%, respectively. Before the experiment, nanofluids were mixed and diluted by adding base fluids to the desired concentration level. After that, the nanofluids were sonicated by an ultrasonic vibrator for 2 h. The addition of surfactants were already done by the manufacturer. The pH of the Al_2O_3–water, Al_2O_3–EG/water, TiO_2–water and TiO_2–EG/water nanofluids were 4, 3, 7 and 6, respectively. The particle size distribution of TiO_2 was also estimated via a transmission electron microscope (TEM) as shown in Fig. 1.

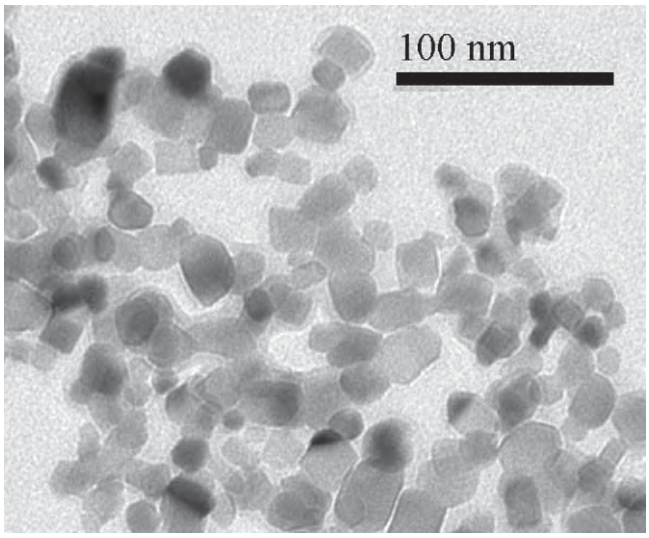

Fig. 1. TEM image of dispersed TiO_2 nanoparticles in water.

3. Experimental apparatus and procedure

The transient hot-wire method is based on measurement of changing temperatures during the heat transfer process of a small-scaled wire which serves both as a heater and temperature sensor of the sample substance. Presumably, small-scale wire has a high thermal diffusion ratio. Heat from the wire will be completely transferred to the surrounding sample substance. When electrical current flows through the wire, it will become a source of heat. The temperature of both the wire and the sample nanofluid will be higher. The increasing rate of temperature depends on the thermal conductivity of the sample substance.

In general, the concept and design for this works are similar to those of Duangthongsuk and Wongwises [15], and Kostic and Simham [25]. The experimental apparatus shown in Fig. 2(a) consists of various main parts. A polypropylene cylinder containing the sample substance is 250 mm long with a diameter of 25 mm. The Teflon-coated platinum wire with a diameter of 76.20 μm and a length of 190 mm was used as a hot wire cell. The thickness of Teflon is 31.75 μm. Based on Healy et al. [26] criteria, the minimum hot wire cell outer boundary diameter was determined as 5.6 mm. The sample substance lump seems to be very large compared with the size of the wire. Based on the 139 mm minimum length of hot-wire recommended by Kierkus et al. [27], the wire seems to be very long and there seems to be no transfer of heat along the wire's length. The both ends of hot wire were well insulated with silicone. The sample substance's temperature is controlled with circulating water in a temperature-control cylinder. The temperature of the sample substance lump was measured with a high-precision thermometer. Changing temperature of the wire was measured using an oscilloscope in form of voltage drops in the bridge resistance

Author's personal copy

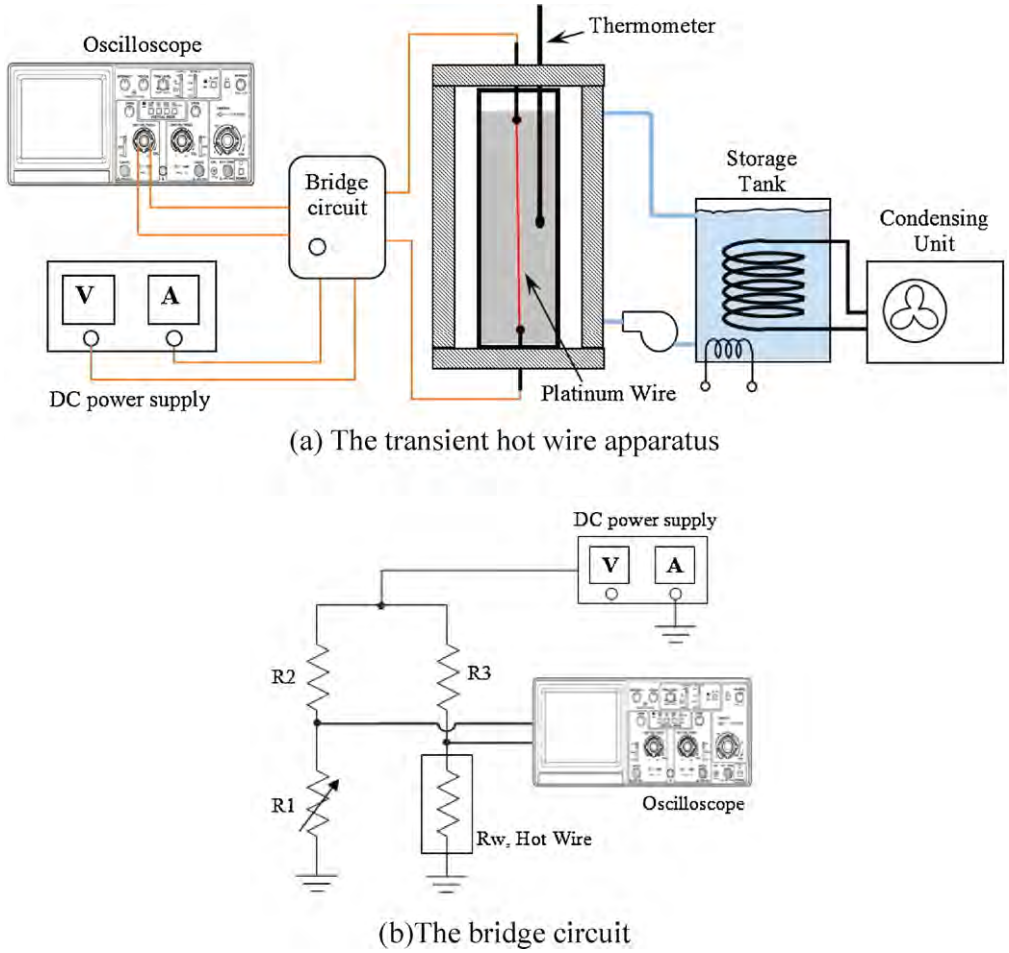

Fig. 2. Schematic diagram of experimental apparatus.

circuit, as shown in Fig. 2(b). A relationship between the temperature and electrical resistance of a platinum wire was presented in Bentley [28]. The thermal conductivity of the sample substance could be calculated from the slope of increase in temperature per logarithmic time interval as follows:

$$k_{nf} = \frac{q}{4\pi(T_2 - T_1)} \ln\left(\frac{t_2}{t_1}\right) \quad (1)$$

where k_{nf} is the thermal conductivity of nanofluids, q is the heat applied to the platinum wire per length unit (W/m), $T_2 - T_1$ (ΔT) is the increased temperature during the test (°C), and t_1 and t_2 are durations of the test (s).

Usually ΔT versus $\ln(t)$ is measured at times from the beginning of heat pulse but only the part which is a straight line is used to calculate the slope which will be used in the calculation of thermal conductivity. The early part of ΔT versus $\ln(t)$ recording is ignored because not only the existence of insulation coating but also the because of the definite C_p of the platinum wire.

4. Results and discussion

Before the measurement of the thermal conductivity of nanofluids, the transient hot-wire method was calibrated by measuring the thermal conductivity of water and the ethylene glycol–water mixture (20/80 wt.%) in temperature ranges of 15–60 °C and comparing the results with the reference standard from ASHRAE [29]. The experimental results tended to correspond with the reference standard. The water sample had the highest deviation of 2.53% with an average deviation of 2.01%. On the other hand, the EG/water (20/80) sample had the highest deviation of 4.04% and an average deviation of 3.46%, as shown in Fig. 3.

The measurement of thermal conductivity of nanofluids with water base fluid shown in Figs. 4 and 5 indicates that thermal conductivity of both Al_2O_3–water and TiO_2–water nanofluids are higher than that of the base fluid and are a function of concentration level and temperature. That is, a higher concentration level of nanoparticles increases the level of thermal conductivity. The

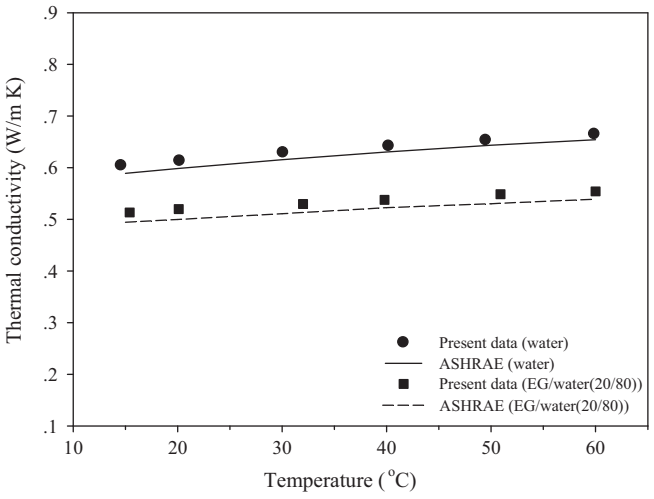

Fig. 3. Comparison of the present data with reference data.

Author's personal copy

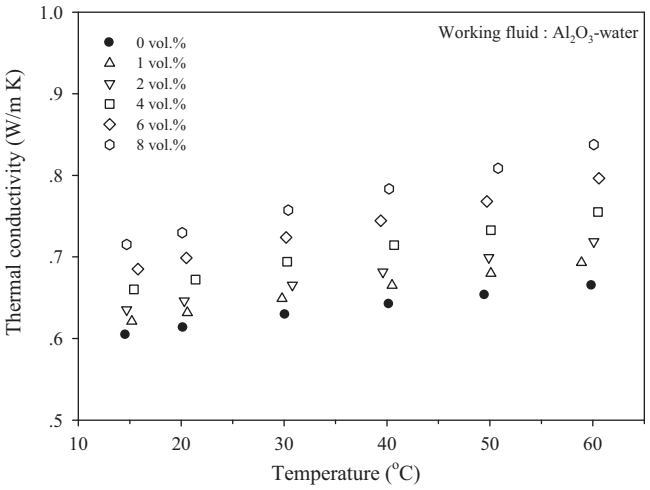

Fig. 4. Thermal conductivity of Al_2O_3–water nanofluid as a function of temperature and concentration.

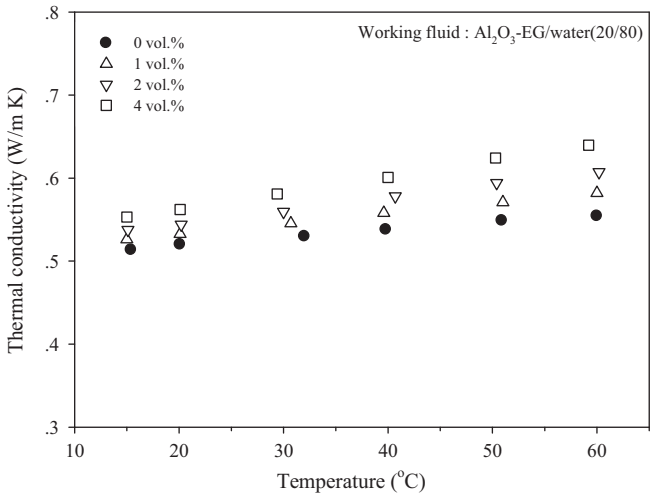

Fig. 6. Thermal conductivity of Al_2O_3–EG/water (20/80) nanofluid as a function of temperature and concentration.

Al_2O_3–water increases by about 5–30% and TiO_2–water increases by about 2–20% in concentration ranges of 1–8 vol.%. Similarly, higher temperature also increases the level of thermal conductivity. Particularly at high concentration level, temperature affects the increase of thermal conductivity more than at low concentration level. However, the effect of increased temperature on the increase of thermal conductivity of TiO_2–water is not great compared to the effect on Al_2O_3–water.

The measurement of the thermal conductivity of nanofluids with an EG/water (20/80) base fluid shown in Figs. 6 and 7 indicates similar results to the water base fluid. The thermal conductivity of Al_2O_3–EG/water (20/80) increases by about 5–20% when the concentration level becomes higher in a range of 1–4 vol.%. The results of TiO_2–EG/water (20/80) show that thermal conductivity increases by about 15% at a concentration level of 4 vol.%. Higher temperature also leads to higher thermal conductivity.

Fig. 8 shows a comparison between the experimental thermal conductivity ratio (relative thermal conductivity) of Al_2O_3–water and results from other studies at various temperatures. The experimental results are different from other studies. Obviously, the experimental thermal conductivity ratio causes lower increases than those from other researches, as evident from the slope of the graph. Particularly, when compared with results from Das et al. [7] and Li and Peterson [11], their results clearly show that the increase of temperature has a dramatic effect on the increase of thermal conductivity ratio of Al_2O_3 nanofluid. Even when compared with results from Murshed et al. [14] and Chon and Kihm [8], who used a similar 150-nm particle size as in this experiment, their thermal conductivity ratio seems to have had higher increases with the rise of temperature.

Similarly, the experimental results of TiO_2–water in Fig. 9 show that the increase of temperature slightly affects the increase of thermal conductivity ratio. This corresponds to results from Masuda et al. [2], Zhang et al. [13], and Turgut al. [16]. In contrast, the results of Wang et al. indicate a higher effect of temperature on the increase of thermal conductivity ratio of TiO_2–water than results from this experiment. It can be seen from Figs. 8 and 9 that the particle size may affect the thermal conductivity of the nanofluid. However, the data are scattered over a large range of the temperature and concentration. Therefore, it is difficult to conclude the trend of the effect of the particle size.

Fig. 10 shows the thermal conductivity ratio of Al_2O_3–water nanofluids at various concentration levels. The thermal conductivity ratio of Al_2O_3–water nanofluid increases when the concentration level increases. The experimental results tend to be similar to those from Wang et al. [4] and Xie et al. [6]. On the

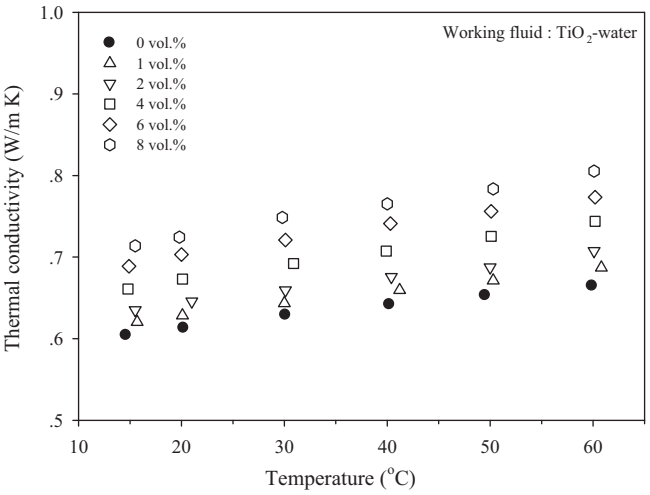

Fig. 5. Thermal conductivity of TiO_2–water nanofluid as a function of temperature and concentration.

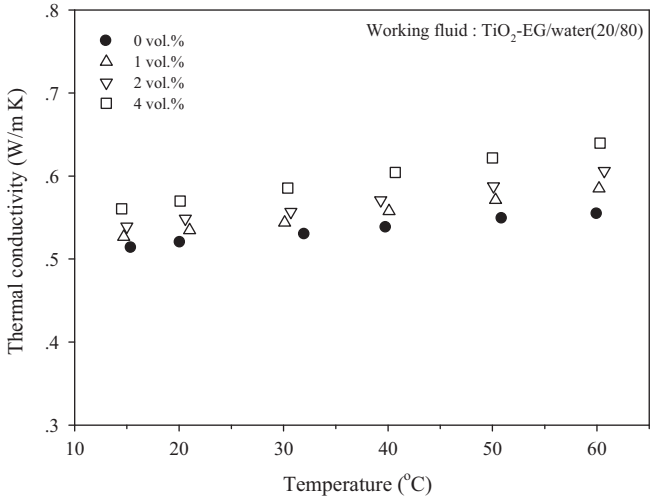

Fig. 7. Thermal conductivity of TiO_2–EG/water (20/80) nanofluid as a function of temperature and concentration.

Author's personal copy

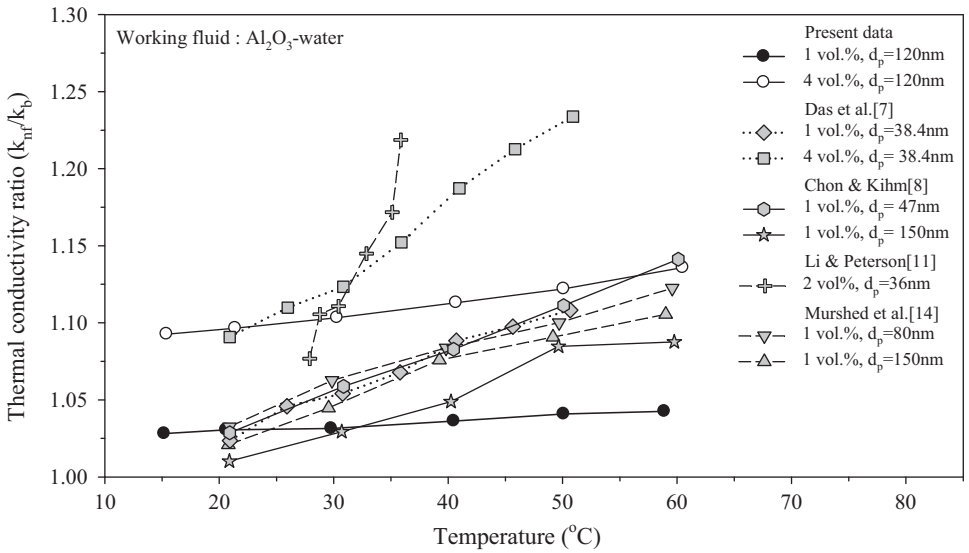

Fig. 8. Effect of temperature on the thermal conductivity ratio of Al_2O_3–water nanofluid.

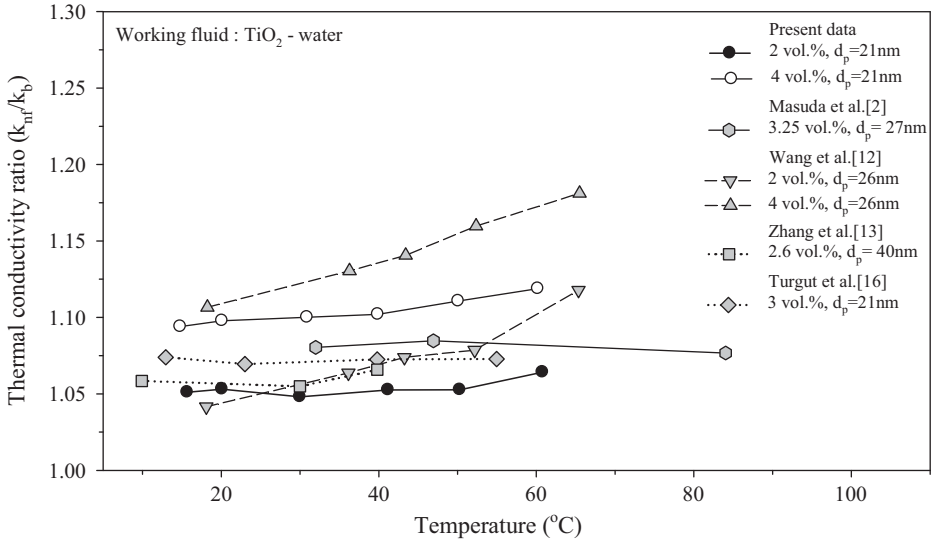

Fig. 9. Effect of temperature on the thermal conductivity ratio of TiO_2–water nanofluid.

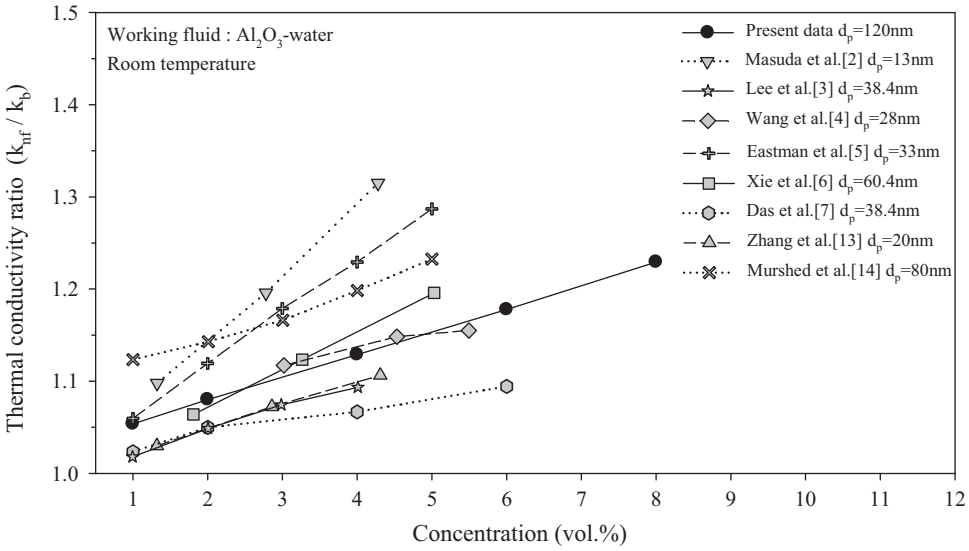

Fig. 10. Effect of concentration on the thermal conductivity ratio of Al_2O_3–water nanofluid.

Author's personal copy

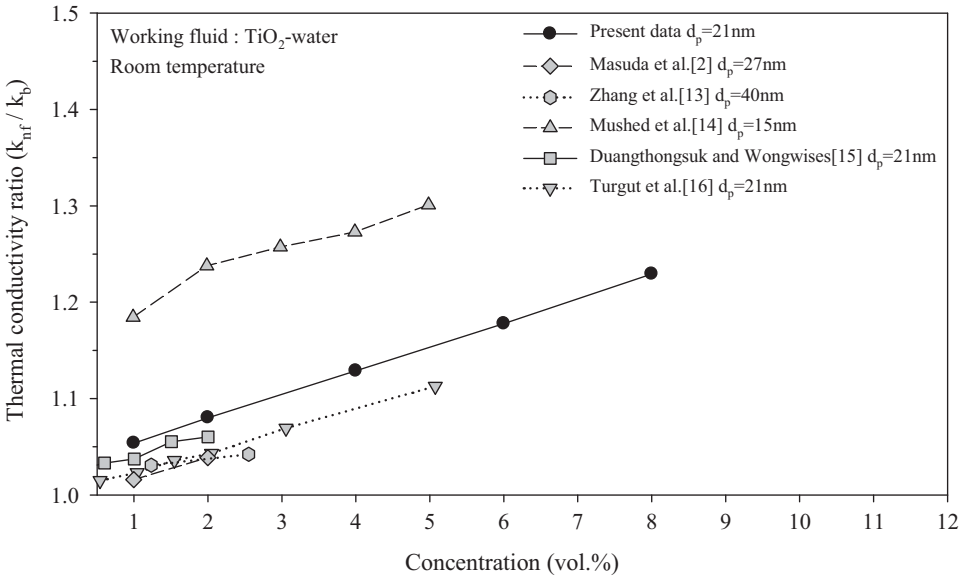

Fig. 11. Effect of concentration on the thermal conductivity ratio of TiO_2–water nanofluid.

other hand, results from Masuda et al. [2], Eastman et al. [5] and Murshed et al. [14] show higher effects. Fig. 11 shows the results of TiO_2–water nanofluids which are similar to those from Masuda et al. [2], Zeng et al. [13], Duangthongsuk and Wongwises [15] and Turgut et al. [16].

Figs. 12–15 show comparisons between the experimental results and predictions from various models popularly used to predict thermal conductivity of nanofluids. For example, the Hamilton and Crosser model (H–C model) [17], popularly used to predict thermal conductivity of two-component mixtures was developed from the Maxwell model [30] by adding a particle shape factor as follows:

$$k_{nf} = \left[\frac{k_p + (n-1)k_b - (n-1)\phi(k_b - k_p)}{k_p + (n-1)k_b + \phi(k_b - k_p)}\right] k_b, \quad \text{when} \quad n = \frac{3}{\psi} \tag{2}$$

where ϕ is the volume fraction, n is a particle shape factor, ψ is the particle sphericity or a ratio of the surface area of a sphere with volume equal to that of the particle, to the surface area of the particle, which are 1 and 0.5 for spherical shape and cylindrical shape, respectively.

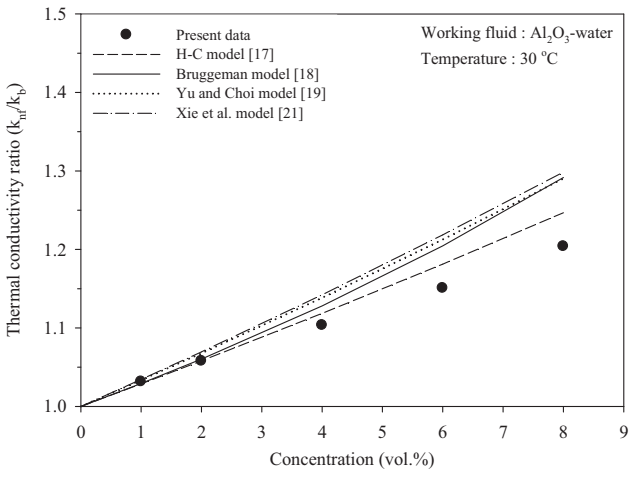

Fig. 12. Comparison of the experimental thermal conductivity ratio of Al_2O_3–water nanofluid with those obtained from various equations.

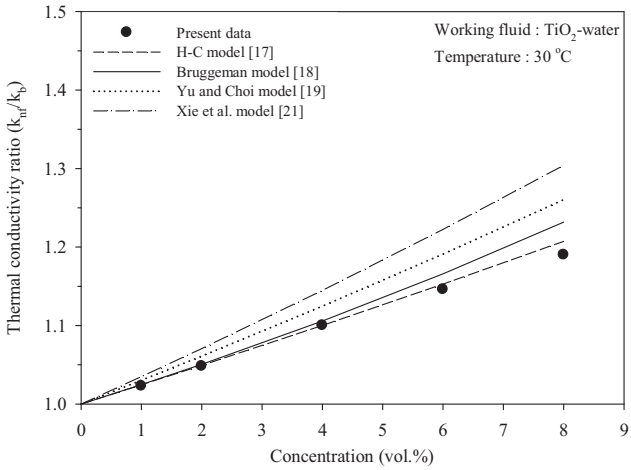

Fig. 13. Comparison of the experimental thermal conductivity ratio of TiO_2–water nanofluid with those obtained from various equations.

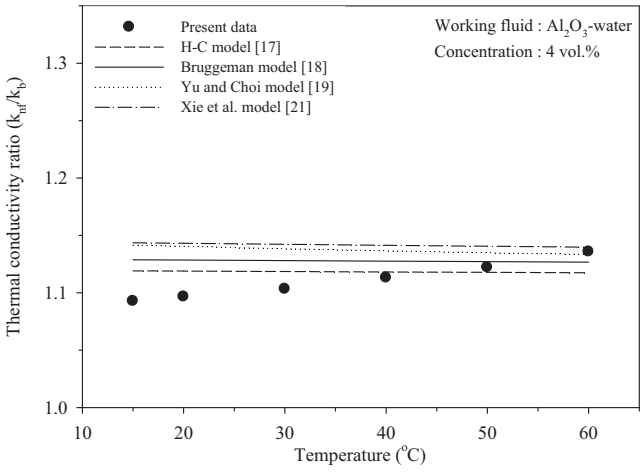

Fig. 14. Comparison of experimental thermal conductivity ratio of Al_2O_3–water nanofluid with those obtained from various equations.

Author's personal copy

Table 1
Coefficients in the correlation for different nanofluids.

Nanofluids	Coefficient				Max. error	Avg. error
	A	*B*	*C*	*D*		
Al_2O_3	0.945867	0.073528	0.036168	−0.00585	2.74%	1.23%
TiO_2	0.916205	0.066817	0.018789	0.016229	2.28%	1.11%

The following Bruggeman's equation [18] is another classic model popularly used to predict thermal conductivity of nanofluids:

$$k_{nf} = \frac{1}{4}[(3\phi-1)k_p + (2-3\phi)k_b] + \frac{k_b}{4}\sqrt{\Delta},$$

$$\text{when } \Delta = \left[(3\phi-1)^2\left(\frac{k_p}{k_b}\right)^2 + (2-3\phi)^2 + 2(2+9\phi-9\phi^2)\left(\frac{k_p}{k_b}\right)\right] \quad (3)$$

The Yu and Choi model [19] is another model that is developed from the Maxwell model. This model includes the mechanism caused by a solid-like nanolayer that coats particles as shown in the following equation:

$$k_{nf} = \left[\frac{k_p + 2k_b + 2\phi(k_p - k_b)(1+\gamma)^3}{k_p + 2k_b + \phi(k_p - k_b)(1+\gamma)^3}\right] k_b \quad (4)$$

where $\gamma = \delta/r_p$ is a ratio of nanolayer thickness ($\delta = 2$ nm) per nanoparticle radius.

Similarly, the Xie et al. model [21] takes the mechanism caused by nanolayer into consideration

$$k_{nf} = \left[1 + 3\Theta\phi_T + \frac{3\Theta^2\phi_T^2}{1-\Theta\phi_T}\right] k_b,$$

$$\text{when } \Theta = \left[\frac{\beta_{llb}(1+\gamma)^3 - \beta_{pl}/\beta_{bl}}{(1+\gamma)^3 + 2\beta_{lb}\beta_{pl}}\right], \quad \beta_{lb} = \left(\frac{k_l - k_b}{k_l + 2k_b}\right),$$

$$\beta_{pl} = \left(\frac{k_p - k_l}{k_p + 2k_l}\right), \quad \beta_{bl} = \left(\frac{k_f - k_l}{k_f + 2k_l}\right) \quad (5)$$

where $\phi_T = \phi(1+\gamma)^3$ is the modified total volume fraction of the original nanoparticle and nanolayer, $k_l = 2k_f$ is the thermal conductivity of nanolayer.

Comparisons on the effect of the concentration show that the increase of thermal conductivity ratio of Al_2O_3–water is different from those obtained by H–C model, Bruggeman model, Yu and Choi model, and Xie et al. model. At low concentration levels, the experimental results are similar to those predicted by the models. However, as shown in Fig. 13, at high concentration levels, the experimental results are lower than those predicted by the models and tend to become steadily lower when the concentration level increases. Comparisons of TiO_2–water in Fig. 13 show that the H–C model could be used to predict the thermal conductivity ratio of TiO_2–water nanofluid with similar results to the experiment, particularly at low concentration levels. However, at high concentration levels, the experimental results tend to be lower than those predicted by the model, similar to the results of the Al_2O_3–water nanofluid.

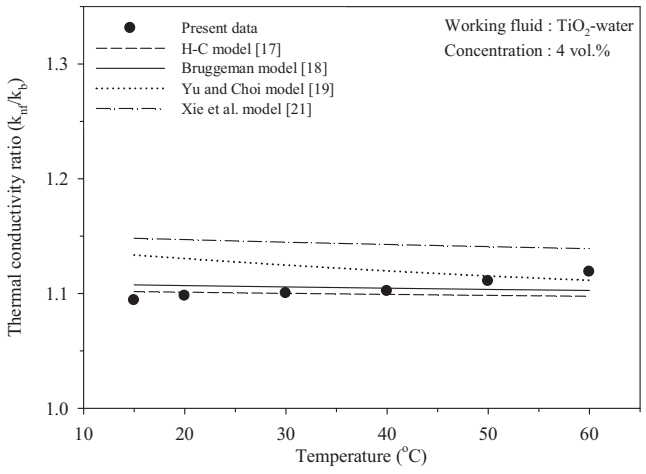

Fig. 15. Comparison of the experimental thermal conductivity ratio of TiO_2–water nanofluid with those obtained from various equations.

Comparisons between experimental results and those obtained from other models, in terms of thermal conductivity ratio of nanofluids with temperature, are shown in Figs. 14 and 15. Fig. 14 shows that other models could not be used to predict the thermal conductivity ratio of the Al_2O_3 nanofluid when temperature changes. The experimental thermal conductivity ratio tends to increase when the temperature increases. On the contrary, predictions from other models show that the thermal conductivity ratio of the Al_2O_3–water nanofluid does not vary with temperature and tends to be lower in some models. However, at low temperature, the experimental results are lower than those predicted by the models. In Fig. 15 which shows the results of TiO_2–water, the experimental results are similar to those predicted by the H–C model and Bruggeman model. However, the experimental thermal conductivity ratio of TiO_2 tends to increase when the temperature increases. On the other hand, the models predict no change with temperature, with a tendency to become lower in Yu and Choi's model.

From comparisons with predictions from other models and with results from other researches mentioned above, the experimental thermal conductivity ratio of nanofluids tends to be lower, especially at high concentration levels. This may be because the nanofluids used in this experiment lack stability in suspension or the nanoparticles cause more clustering with high concentration levels. Taking the increase mechanism of thermal conductivity caused by the solid/liquid nanolayer into account, it could be said that the nanofluids used in this experiment are not influenced by this mechanism, noticeable from a comparison with the models of Yu and Choi and Xie et al. Both models were developed by referring to the mechanism caused by a nanolayer. Reexamination of the effect of temperature shows that thermal conductivity ratio from other models and from some studies does not change with temperature while results from this experiment increase when temperature increases. The increase of the thermal conductivity could result from Brownian motion as discussed by several researchers [7,8,12]. They proposed that when the temperature of the fluid increases, molecules or particles of both liquids and solid will create more turbulence and collision than in low temperature. As a consequence, there is more transfer of energy between molecules or particles which, in turn, affects the thermal property or thermal conductivity.

This paper also presents a correlation for predicting thermal conductivity of the Al_2O_3 and TiO_2 nanofluids in a form of ratio of thermal conductivity between the nanofluid and base fluid ($k_{p,nf}/k_{p,b}$) which can be used in prediction for other base fluids.

Author's personal copy

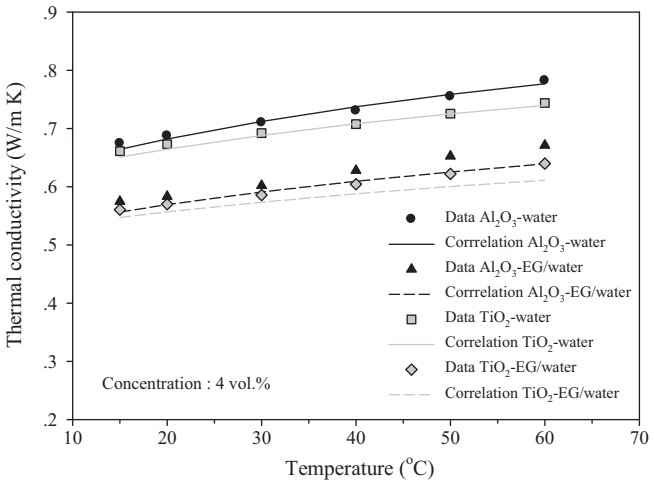

Fig. 16. Comparison of the measured thermal conductivity with proposed correlation.

Effects of temperature, concentration, and thermal conductivity of nanoparticles and base fluid are taken into account in the following equation:

$$\frac{k_{p,nf}}{k_{p,b}} = A\phi^B T^C \left(\frac{k_{p,np}}{k_{p,b}}\right)^D \quad (6)$$

where A, B, C, and D are coefficients of the equation shown in Table 1. This equation could be used with a temperature range of 15–65 °C and a concentration range of 1–8 vol.%. Fig. 16 shows a comparison between thermal conductivity obtained from the experiment and that obtained from the correlation. The results from the predictions are similar to the experimental results with acceptable accuracy.

5. Conclusions

From the calibration by measuring thermal conductivity of water and ethylene glycol, the experimental results are similar to a reference standard from ASHRAE. The developed experimental apparatus for measuring thermal conductivity has acceptable level of precision.

The experimental results show that thermal conductivity of nanofluids is higher than that of the base fluid and varies with temperature and concentration level of nanofluids. The thermal conductivity ratio from this experiment does not correspond with that obtained from predictions using well known models, both in terms of concentration and temperature. The newly- and specifically-developed correlation for predicting thermal conductivity of Al_2O_3 and TiO_2 nanofluids gives similar results to the experiment at acceptable level.

Acknowledgements

The present study was supported financially by the Thailand Research Fund, the Office of the Higher Education Commission and the National Research University Project, whose guidance and assistance are gratefully acknowledged.

References

[1] S.U.S. Choi, Enhancing thermal conductivity of fluids with nanoparticles, ASME Fluids Eng. Div. 231 (1995) 99–103.
[2] H. Masuda, A. Ebata, K. Teramae, N. Hishinuma, Alteration of thermal conductivity and viscosity of liquid by dispersing ultra-fine particles (dispersion of Al_2O_3, SiO_2 and TiO_2 ultra-fine particles), Netsu Bussei (Japan) 7 (4) (1993) 227–233.
[3] S. Lee, S.U.S. Choi, S. Li, J.A. Eastman, Measuring thermal conductivity of fluids containing oxide nanoparticles, J. Heat Transfer 21 (1999) 280–289.
[4] X. Wang, X. Xu, S.U.S. Choi, Thermal conductivity of nanoparticles–fluid mixture, J. Thermophys. Heat Transfer 13 (4) (1999) 474–480.
[5] J.A. Eastman, S.U.S. Choi, S. Li, W. Yu, L.J. Thomson, Anomalously increased effective thermal conductivities of ethylene glycol-based nanofluids containing copper nanoparticles, Appl. Phys. Lett. 78 (2001) 718–720.
[6] H. Xie, J. Wang, T. Xi, Y. Liu, F. Ai, Thermal conductivity enhancement of suspensions containing nanosized alumina particles, J. Appl. Phys. 91 (7) (2002) 4568–4573.
[7] S.K. Das, N. Putta, P. Thiesen, W. Roetzel, Temperature dependence of thermal conductivity enhancement for nanofluids, ASME Trans.: J. Heat Transfer 125 (2003) 567–574.
[8] C.H. Chon, K.D. Kihm, Thermal conductivity enhancement of nanofluids by Brownian motion, J. Heat Transfer 127 (2005) 810.
[9] Y.J. Hwang, Y.C. Ahn, H.S. Shin, C.G. Lee, G.T. Kim, H.S. Park, J.K. Lee, Investigation on characteristics of thermal conductivity enhancement of nanofluids, Curr. Appl. Phys. 6 (2006) 1068–1071.
[10] Y. He, Y. Jin, H. Chen, Y. Ding, D. Cang, H. Lu, Heat transfer and flow behavior of aqueous suspensions of TiO_2 nanoparticles (nanofluids) flowing upward through a vertical pipe, Int. J. Heat Mass Transfer 50 (2007) 2272–2281.
[11] C.H. Li, G.P. Peterson, The effect of particle size on the effective thermal conductivity of Al_2O_3–water nanofluids, J. Appl. Phys. 101 (2007) 044312.
[12] Z.L. Wang, D.W. Tang, S. Liu, X.H. Zheng, N. Araki, Thermal-conductivity and thermal-diffusivity measurements of nanofluids by 3ω method and mechanism analysis of heat transport, Int. J. Thermophys. 28 (2007) 1255–1268.
[13] X. Zhang, H. Gu, M. Fujii, Effective thermal conductivity and thermal diffusivity of nanofluids containing spherical and cylindrical nanoparticles, Exp. Therm. Fluid Sci. 31 (2007) 593–599.
[14] S.M.S. Murshed, K.C. Leong, C. Yang, Investigations of thermal conductivity and viscosity of nanofluids, Int. J. Therm. Sci. 47 (5) (2008) 560–568.
[15] W. Duangthongsuk, S. Wongwises, Measurement of temperature-dependent thermal conductivity and viscosity of TiO_2–water nanofluids, Exp. Therm. Fluid Sci. 33 (2009) 706–714.
[16] A. Turgut, I. Tavman, M. Chirtoc, H.P. Schuchmann, C. Sauter, S. Tavman, Thermal conductivity and viscosity measurements of water-based TiO_2 nanofluids, Int. J. Thermophys. 30 (2009) 1213–1226.
[17] R.L. Hamilton, O.K. Crosser, Thermal conductivity of heterogeneous two component systems, Ind. Eng. Chem. Fundam. 1 (1962) 187–191.
[18] D.A.G. Bruggeman, Berechnung Verschiedener Physikalischer Konstanten von Heterogenen Substanzen I. Dielektrizitatskonstanten und Leitfahigkeiten der Mischkorper aus Isotropen Substanzen, Annalen der Physik 14 (1935) 636–679.
[19] W. Yu, S.U.S. Choi, The role of interfacial layers in the enhanced thermal of nanofluids: a renovated maxwell model, J. Nanopart. Res. 5 (2003) 167–171.
[20] W. Yu, S.U.S. Choi, The role of interfacial layers in the enhanced thermal conductivity of nanofluids: a renovated Hamilton–Crosser model, J. Nanopart. Res. 6 (2004) 355–361.
[21] H. Xie, M. Fujii, X. Zhang, Effect of interfacial nanolayer on the effective thermal conductivity of nanoparticle–fluid mixture, Int. J. Heat Mass Transfer 48 (2005) 2926–2932.
[22] Y. Xuan, Q. Li, W. Hu, Aggregation structure and thermal conductivity of nanofluids, AIChE J. 49 (2003) 1038–1043.
[23] J. Koo, C. Kleinstreuer, A new thermal conductivity model for nanofluids, J. Nanopart. Res. 6 (2004) 577–588.
[24] S.P. Jang, S.U.S. Choi, Role of Brownian motion in the enhanced thermal conductivity of nanofluids, Appl. Phys. Lett. 84 (2004) 4316–4318.
[25] M. Kostic, K.C. Simham, Computerized, transient hot-wire thermal conductivity (HWTC) apparatus for nanofluids, in: Proceedings of the 6th WSEAS International Conference on Heat and Mass Transfer, 2009.
[26] J.J. Healy, J.J. deGroot, J. Kestin, The theory of the transient hot-wire method for measuring thermal conductivity, Physica 82C (1976) 392–408.
[27] W.T. Kierkus, N. Mani, J.E.S. Venart, Radial–axial transient heat conduction in a region bounded internally by a circular cylinder of finite length and appreciable heat capacity, Can. J. Phys. 51 (1973) 1182–1186.
[28] J.P. Bentley, Temperature sensor characteristics and measurement system design, J. Phys. 17 (1984) 430–439.
[29] ASHRAE, ASHRAE Handbook: Fundamentals, American Society of Heating, Refrigerating and Air-Conditioning Engineers Inc., Atlanta, GA, 2005.
[30] J.C. Maxwell, A Treatise on Electricity and Magnetism, vol. 1, third ed., Dover, New York, 1954.

This article was downloaded by: [Uppsala universitetsbibliotek]
On: 19 August 2012, At: 02:19
Publisher: Taylor & Francis
Informa Ltd Registered in England and Wales Registered Number: 1072954 Registered office: Mortimer House, 37-41 Mortimer Street, London W1T 3JH, UK

Heat Transfer Engineering
Publication details, including instructions for authors and subscription information:
http://www.tandfonline.com/loi/uhte20

Experimental Study on the Air-Side Performance of a Multipass Parallel and Counter Cross-Flow L-Footed Spiral Fin-and-Tube Heat Exchanger

Parinya Pongsoi [a] , Santi Pikulkajorn [b] & Somchai Wongwises [a c]

[a] Department of Mechanical Engineering, King Mongkut's University of Technology Thonburi, Bangkok, Thailand

[b] Somchai Industry Co., Ltd., Bangkok, Thailand

[c] The Academy of Science, Royal Institute of Thailand, Dusit, Bangkok, Thailand

Accepted author version posted online: 15 May 2012. Version of record first published: 17 Jul 2012

To cite this article: Parinya Pongsoi, Santi Pikulkajorn & Somchai Wongwises (2012): Experimental Study on the Air-Side Performance of a Multipass Parallel and Counter Cross-Flow L-Footed Spiral Fin-and-Tube Heat Exchanger, Heat Transfer Engineering, 33:15, 1251-1263

To link to this article: http://dx.doi.org/10.1080/01457632.2012.692296

PLEASE SCROLL DOWN FOR ARTICLE

Full terms and conditions of use: http://www.tandfonline.com/page/terms-and-conditions

This article may be used for research, teaching, and private study purposes. Any substantial or systematic reproduction, redistribution, reselling, loan, sub-licensing, systematic supply, or distribution in any form to anyone is expressly forbidden.

The publisher does not give any warranty express or implied or make any representation that the contents will be complete or accurate or up to date. The accuracy of any instructions, formulae, and drug doses should be independently verified with primary sources. The publisher shall not be liable for any loss, actions, claims, proceedings, demand, or costs or damages whatsoever or howsoever caused arising directly or indirectly in connection with or arising out of the use of this material.

Heat Transfer Engineering, 33(15):1251–1263, 2012
Copyright © Taylor and Francis Group, LLC
ISSN: 0145-7632 print / 1521-0537 online
DOI: 10.1080/01457632.2012.692296

Downloaded by [Uppsala universitetsbibliotek] at 02:19 19 August 2012

Experimental Study on the Air-Side Performance of a Multipass Parallel and Counter Cross-Flow L-Footed Spiral Fin-and-Tube Heat Exchanger

PARINYA PONGSOI,[1] SANTI PIKULKAJORN,[2] and SOMCHAI WONGWISES[1,3]

[1]Department of Mechanical Engineering, King Mongkut's University of Technology Thonburi, Bangkok, Thailand
[2]Somchai Industry Co., Ltd., Bangkok, Thailand
[3]The Academy of Science, Royal Institute of Thailand, Dusit, Bangkok, Thailand

This study conducted experiments on the air-side performance of novel L-footed spiral fin-and-tube heat exchangers that were faced with airflow at high Reynolds numbers (3500–13,000). The examined heat exchangers have a multipass parallel-and-counter cross-flow type of water flow arrangement. This flow arrangement is a combination of the parallel cross-flow and the counter cross-flow. This type of water flow arrangement may be the best fit for the reverse-flow system, because it can provide constant heat-exchange effectiveness for every flow reversal direction at the same airflow rate. Ambient air was used as a working fluid on the air side and hot water for the tube side. This way the effect of the number of tube rows on the heat transfer and friction characteristics of L-footed spiral fin-and-tube heat exchangers was clearly observed. The effect of the fin's outside diameter on the pressure drop was also studied. The results show that the number of tube rows has no significant effect on the air-side heat transfer or on friction characteristics at high Reynolds numbers. However, the fin's outside diameter shows a significant effect on the pressure drop. The pressure drop increases as the fin's outside diameter increases for the same number of tube rows.

INTRODUCTION

Heat exchangers are devices that are commonly used for exchanging heat between two fluids of different temperatures without mixing those fluids. Many types of heat exchangers are used in industrial processes. However, one of the most favorable types of heat exchangers is the fin-and-tube heat exchanger. In order to improve the heat transfer performance of this type of heat exchanger, it is very important to consider the heat transfer rate, which is normally limited by the thermal resistance on the air side of the heat exchanger. Improving the fin geometry is one way to augment the heat transfer rate on the air side of the heat exchanger.

The authors are indebted to the Thailand Research Fund, the Energy Policy and Planning Office, the Office of the Higher Education Commission, and the National Research University Project for supporting this study.

Address correspondence to Professor Somchai Wongwises, Department of Mechanical Engineering, Fluid Mechanics, Thermal Engineering and Multiphase Flow Research Laboratory (FUTURE), King Mongkut's University of Technology Thonburi, 126 Pracha-utid Road, Bangkok, Bangmod 10140, Thailand. E-mail: somchai.won@kmutt.ac.th

However, this method may lead to the need for increased fan power because of the pressure drop. Many researchers have studied the effect of the plate fin's geometry, such as plain fin, slit fin, wavy fin, louvered fin, compounded fin, and so on, on heat transfer performance and the friction characteristic. These valuable studies on plate fin-and-tube heat exchangers are detailed in the following section to place this experimental work within the context of previous literature.

Wang et al. [1] tested 49 louver fin-and-tube heat exchangers with different geometrical parameters and proposed a correlation between the heat transfer and the friction characteristic for the louver fin. Yan and Sheen [2] examined 36 fin-and-tube heat exchangers, including 12 plain fin, 12 wavy fin, and 12 louver fin geometries, to study the effects of the number of tube rows and fin pitch on air-side performance. Yan and Sheen then compared the air-side performance of plain, wavy, and louver fin-and-tube heat exchangers. Du and Wang [3] tested 31 samples of superslit fin-and-tube heat exchangers to study the effect of the number of tube rows on air-side performance. They found that the number of tube rows is almost negligible for smaller slit length at Reynolds numbers more than 2000, and they found that friction

factors are relatively independent of the number of tube rows. Wongwises and Chokeman [4] tested 10 herringbone wavy fin-and-tube heat exchangers to investigate the effect of fin pitch and the number of tube rows on air-side performance. A change in fin pitch does not significantly affect heat transfer performance, even though changing the pitch enough will reverse the friction characteristic. The Colburn factor and friction factor decrease with increasing number of tube rows when the Reynolds number is less than 4000. Chokeman and Wongwises [5] examined three herringbone wavy fin-and-tube heat exchangers and conducted experiments to investigate the effect of fin pattern and edge corrugation on air-side heat transfer and friction characteristics. Wen and Ho [6] tested three fin-and-tube heat exchangers, including a plate fin, wavy fin, and compound fin, in a range of airflows corresponding to Reynolds numbers of 600–1200, and Wen and Ho's results strongly suggest the use of compounded fins in the construction of heat exchangers. Pirompugd et al. [7] tested 15 plain fin-and-tube heat exchangers and 18 wavy fin-and-tube heat exchangers, and found that the percentage of the surface that gets wet increases with increasing fin spacing or an increasing number of tube rows along with a decreasing Reynolds number. Pirompugd et al. used the finite circular fin method for data reduction in their experiment.

It can be seen from the literature that many researchers are interested in studying the plate fin-and-tube heat exchanger. On the other hand, there are very few extant studies on the spiral fin-and-tube heat exchanger, as found in references [8–12].

Nuntaphan et al. [8] tested 23 crimped spiral fin-and-tube heat exchangers to analyze the effect of tube diameter, fin spacing, transfer tube pitch, and tube arrangement, and they proposed correlations between heat transfer and friction characteristics in the case of a low Reynolds number. Wongwises and Naphon [9, 10] studied the heat transfer characteristics and the performance of a spirally coiled finned tube heat exchanger under dry-surface and wet-surface conditions. Moreover, they tested heat exchangers that rely on a crimped spiral finned tube. Then Srisawad and Wongwises [11] tested the helically coiled crimped spiral finned tube heat exchanger, focusing on the air-side heat transfer characteristics in dry-surface conditions. Lee et al. [12] studied the air-side heat transfer characteristics of spiral-type circular fin-tube heat exchangers under nonfrosting conditions. They measured these characteristics by varying the fin pitch, the number of tube rows, and the fin alignment.

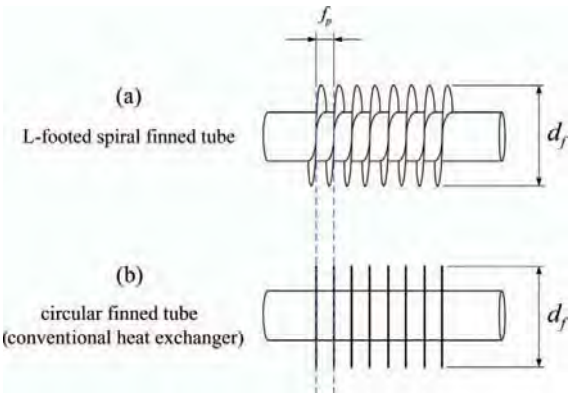

Figure 1 Schematic diagram of (a) the L-footed spiral fin and (b) the circular fin. (Color figure available online.)

The L-footed spiral fin is another type of fin geometry. The base of the fin has an L shape, which provides a large contact area, ensuring a good path for heat transfer from the tube surface to the fin. The spiral fin seems to have a greater heat transfer coefficient than the conventional circular fin, as shown in Figure 1. The L-footed spiral fin-and-tube heat exchanger may be suitable for industrial processes that present a high risk of tube corrosion. To the best of the authors' knowledge, the air-side performance of L-footed spiral fin-and-tube heat exchangers remains unstudied. This study therefore presents the heat transfer performance and frictional characteristics of L-footed spiral fin-and-tube heat exchangers, results that has never before been seen in the literature. Moreover, this study focuses on the effect of the number of tube rows on both copper and aluminum fins with different outside diameters on each fin. The investigation was done at high Reynolds numbers, which correspond to real applications in the industry.

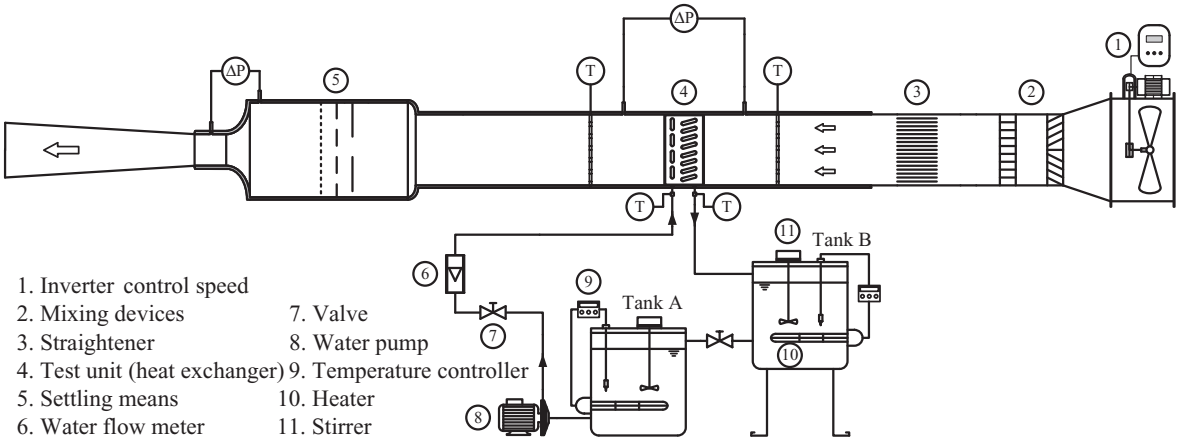

Figure 2 Schematic diagram of the experimental apparatus.

Downloaded by [Uppsala universitetsbibliotek] at 02:19 19 August 2012

In addition, the multipass parallel and counter cross-flow, which is a type of water flow arrangement, was applied in this work. The heat exchangers tested in this work have a combined configuration between the parallel cross-flow and the counter cross-flow: each layer of water flow alternates between the parallel cross-flow and the counter cross-flow. This type of water flow arrangement may be appropriate for reverse-flow heat exchangers used in recuperative systems, because it provides constant heat exchange effectiveness in every direction of flow reversal, which the original parallel cross-flow and counter cross-flow water flow arrangement cannot provide in reverse flow. However, none of the ε–*NTU* relationships match this geometry of water flow arrangement. In order to apply ε–*NTU* methods to this type of water flow arrangement, this work also discusses the effect of using ε–*NTU* relationships on both the multipass parallel cross-flow and the counter cross-flow for this type of water flow arrangement.

EXPERIMENTAL APPARATUS

Figure 2 shows the schematic diagram of the experimental apparatus. Air and hot water were used as working fluids. The main components of the system were the heat exchanger, water

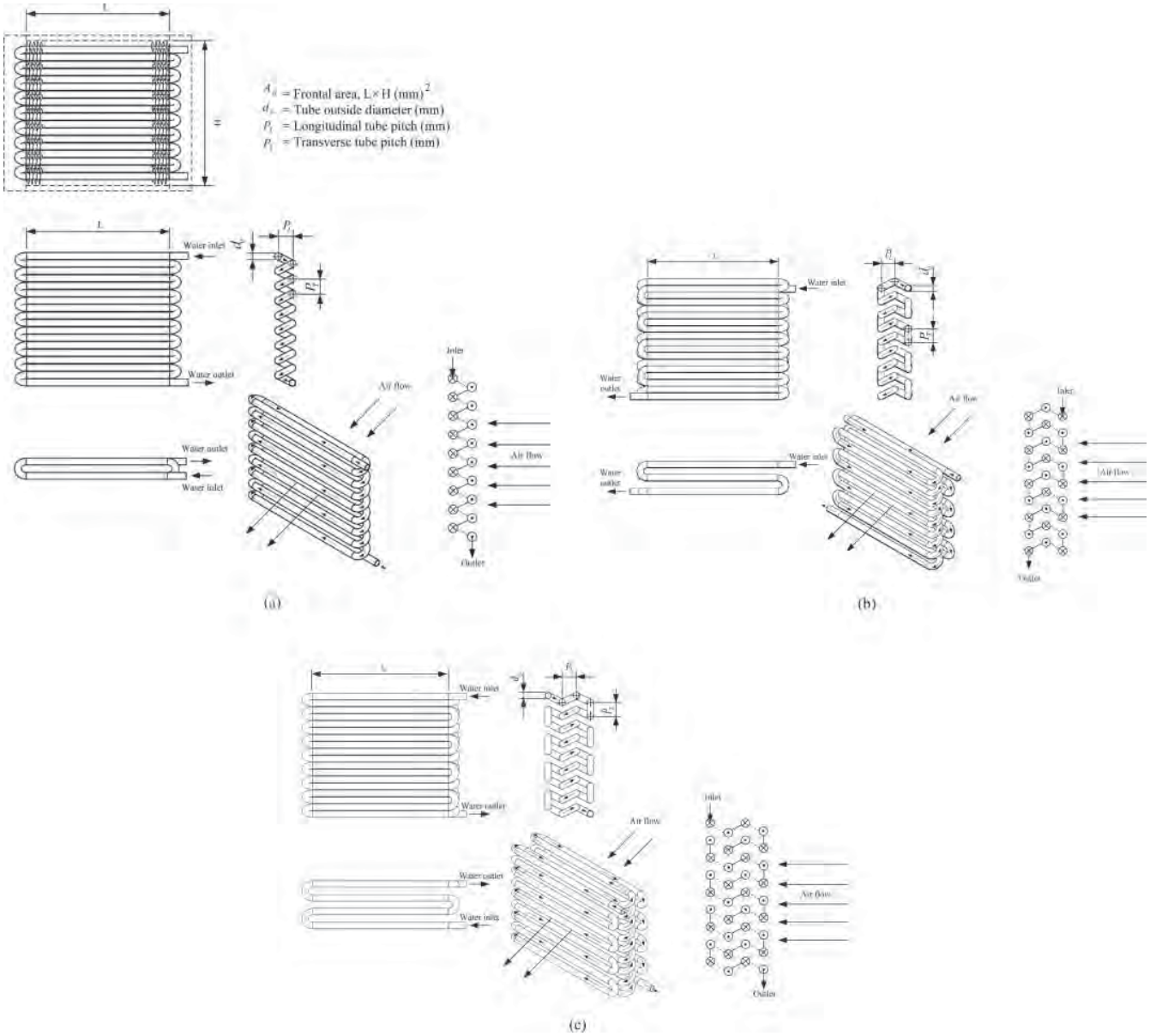

Figure 3 Geometric details of the multipass parallel-and-counter cross-flow heat exchangers and water flow circuit inside the heat exchanger: (a) $N_{row} = 2$, (b) $N_{row} = 3$, and (c) $N_{row} = 4$ (× and • signs indicate that water flows into or out of the paper, respectively).

Downloaded by [Uppsala universitetsbibliotek] at 02:19 19 August 2012

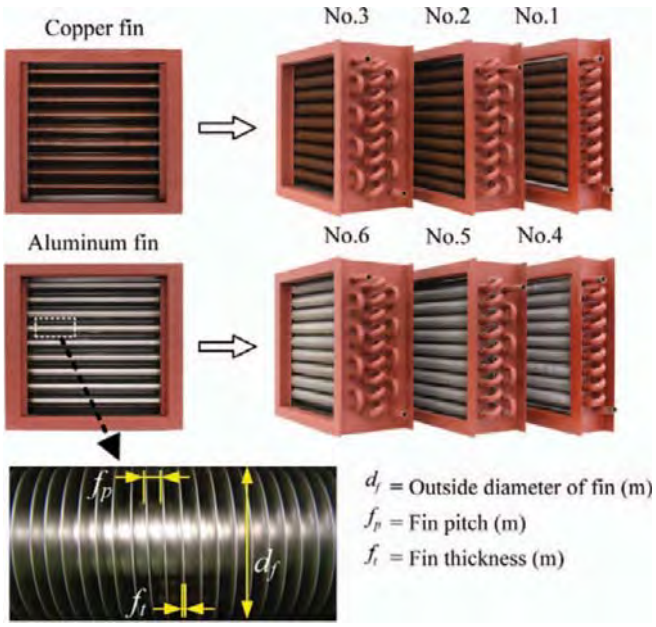

Figure 4 The photos of the tested L-footed spiral fin and tube heat exchangers (numbers 1–6). (Color figure available online.)

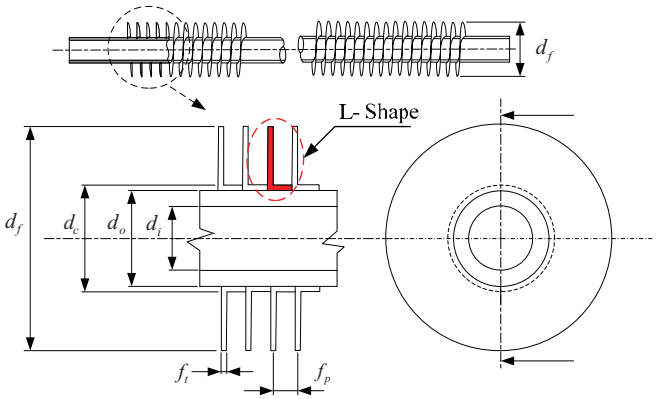

Figure 5 Schematic diagram of the tested L-footed spiral fin. (Color figure available online.)

flow loop, air supply, and the instrumentation and data acquisition system.

The present study's heat exchanger is a type of fin-and-tube heat exchanger. The copper tube is finned with two types of fins: copper fin and aluminum fin. Figure 3 details the water-side circuit and the dimensions of the tested fin and tube heat exchangers. The configuration of the L-footed spiral fin pattern appears in Figures 4 and 5. Finally, the geometric parameters of the heat exchangers are summarized in Table 1.

An open-type wind tunnel was used to push air through the heat exchanger. The connections of the duct were designed so that parts could be changed or repaired quickly and easily. This arrangement operated in a cross-flow with the hot water passing through the heat exchanger. The tunnel was a rectangular air duct fabricated from a steel plate, having the dimensions of 0.43 × 0.48 m. The duct was insulated with a 16-mm-thick Aeroflex standard sheet. Fresh air was drawn into the duct and passed through the mixing device, straightener, and heat exchanger by means of a 2.2-kW axial flow fan. The speed of the fan could be adjusted with an inverter.

Thermocouple probes were located at the air inlet and outlet sections of the heat exchanger. The temperature was measured with 1-mm-diameter probes extending into the duct where the air flowed. The probes consisted of T-type copper–constantan thermocouples grounded to a stainless-steel outer sheath. The measuring points were located at the positions recommended by the ASHRAE standard [13]. The temperature was monitored and recorded continuously. All temperature-measuring devices were well calibrated in a controlled-temperature bath using a standard precision mercury-in-glass thermometer. All sensors were wired directly to terminal control panels mounted on the bench. The airflow rate was detected with a nozzle based on the ISO 5801 standard. The drops in air pressure across the test section and the nozzle were measured with a digital manometer. There were four pressure taps on each wall: an upstream and downstream tap in the test section and in the the nozzle.

To avoid distortion of the air velocity profile, mixing devices and straighteners were installed in the duct. Air velocity and air-velocity fluctuation in the duct were checked with a constant-temperature anemometer 90CN10/C10 (CTA, Dantec) that had an automatic probe setup. Stream Ware software was used to set up the anemometer modules, to perform velocity and directional calibrations, and to provide an experimental platform wherein automatic sequences of hardware setup, data acquisitions, and data reductions could be performed. The probe used in this experiment was a wedge-shaped, right-angled film probe 55R33 with a noncylindrical sensor in a 1 × 0.2-mm sheath. All signals

Table 1 Detailed geometric parameters of the test samples

Number	Fin type	d_i (mm)	d_o (mm)	d_c (mm)	f_p (mm)	f_t (mm)	P_L (mm)	P_T (mm)	d_f (mm)	n_t	A_{fr} (mm)^2	Fin material	N_{row}
1	L-footed	13.5	16.35	16.85	3.25	0.25	35	39	30.5	9	320 × 350	Cu	2
2	L-footed	13.5	16.35	16.85	3.25	0.25	35	40	30.5	9	340 × 360	Cu	3
3	L-footed	13.5	16.35	16.85	3.25	0.25	35	40	30.5	9	340 × 360	Cu	4
4	L-footed	13.5	16.35	16.85	3.25	0.25	35	39	35.0	9	320 × 350	Al	2
5	L-footed	13.5	16.35	16.85	3.25	0.25	35	40	35.0	9	340 × 360	Al	3
6	L-footed	13.5	16.35	16.85	3.25	0.25	35	40	35.0	9	340 × 360	Al	4

Note. Tube layouts of all heat exchangers are staggered layout. Cu = copper, Al = aluminum.

Downloaded by [Uppsala universitetsbibliotek] at 02:19 19 August 2012

Downloaded by [Uppsala universitetsbibliotek] at 02:19 19 August 2012

Table 2 Testing conditions of experimental runs

Inlet-air-dry bulb temperature, °C	31.5 ± 0.5
Inlet-air frontal velocity, m/s	2–6 or Re_{dc} (3500–13,000)
Inlet-water temperature, °C	50–70
Water flow rate, LPM	12–14

were registered by a data acquisition system and finally averaged over the elapsed time.

The hot water flow loop consisted of two storage tanks, an 18-kW electric heater, a centrifugal pump, a control unit and a flow meter with a 0.5 LPM resolution, as shown in Figure 2. The purpose of this loop was to transfer heat to the air flowing through the heat exchanger. The temperature of the hot water in the two tanks was measured with T-type copper–constantan thermocouples and was controlled with the temperature controller. After it had been heated to the required temperature, the hot water was pumped out of storage tank (A), delivered to the heat exchanger, and then returned to storage tank (B), which was used to preheat the water in order to reduce the temperature difference before entering tank (A). The water temperatures at the inlet and outlet of the heat exchanger were measured with 1-mm-diameter probes extending inside the tube where the water flowed. The probes consisted of T-type copper–constantan thermocouples grounded to a stainless-steel outer sheath.

In the experiment, at a specific inlet water temperature, the water flow rate was fixed while the airflow rate was increased. The system was allowed to approach a steady state before any data were recorded. After the system had reached a steady state, the inlet and outlet temperatures of the air passing across the heat exchanger and the water flow rates were determined. All tested conditions of the heat exchangers are shown in Table 2. The accuracies of the direct measurement sensors and uncertainties, which were calculated from the root mean sum square method, are shown in Tables 3 and 4.

DATA REDUCTION

In order to determine the heat transfer characteristics of the heat exchangers from the data recorded under steady-state conditions during each test run, the method of number of transfer units (ε–*NTU*), based on the concept of heat exchanger effectiveness, was applied to determine the *UA* product.

The air-side heat transfer rate is given as:

$$Q_a = m_a c_{P,a} \Delta T_a \tag{1}$$

Table 3 The accuracies of the measurements

Parameters	Accuracy
Inlet-air dry-bulb temperature, °C	±0.1
Pressure drop, Pa	±0.5
Inlet-water temperature, °C	±0.1
Water flow rate, LPM	±0.4 (±0.02 of full scale)

Table 4 Uncertainties of the derived experimental values

Parameters	Maximum uncertainties (%)
Air-side heat transfer rate, Q_a	± 4.96
Water-side heat transfer rate, Q_w	± 3.37
Pressure drop, ΔP	± 2.50
Frontal velocity, V_{fr}	± 3.30
Reynolds number, Re_{dc}	± 3.18
Air-side heat transfer coefficient, h_o	± 8.98
Colburn factor, j	± 12.30
Friction factor, f	± 11.13

The water-side heat transfer rate is given as:

$$Q_w = m_w c_{P,w} \Delta T_w \tag{2}$$

The total rate of heat transfer used in the calculation is averaged from the air side and water side as follows:

$$Q_{ave} = \frac{|Q_a| + |Q_w|}{2} \tag{3}$$

The overall heat transfer coefficient can be written in terms of the total resistance to heat transfer. This total thermal resistance is the sum of the individual thermal resistances, as follows:

$$\frac{1}{UA} = \frac{1}{h_i A_i} + \frac{ln(d_o/d_i)}{2\pi k_t L} + \frac{ln(d_c/d_o)}{2\pi k_f L} + \frac{1}{\eta_o h_o A_o} \tag{4}$$

The ε–*NTU* relationships with one fluid mixed and one fluid unmixed in the cross-flow is employed to determine the overall heat transfer coefficient. According to Figure 3, the multipass parallel and counter cross-flow is a complicated water flow arrangement based on a combination of the multipass parallel cross-flow and the counter cross-flow configurations of water flow. As mentioned earlier, none of the ε–*NTU* relationships match the geometry of the water flow arrangement used in this work. Both relations for the multipass parallel and the counter cross-flow configuration of the water flow arrangement from references [14–19], as shown in Eqs. (5)–(11), were applied in order to calculate the overall heat transfer coefficient. However, the multipass parallel and counter cross-flow used in this experiment is a combination of multipass parallel cross-flow and counter cross-flow. It may be suitable to use the average value of those relations shown in Eq. (11). In addition, the schematic diagram of the heat exchangers algorithm for multipass parallel cross-flow, multipass counter cross-flow, and multipass parallel and counter cross-flow ($N_{row} = 2$, 3, and 4) is shown in Figure 6. In this work, the air-side working fluid (air) is defined as fluid A, and the tube-side working fluid (water) is defined as fluid B. It should be noted that the minimum heat capacity rate (C_{min}) is on the air side (fluid A). Therefore, the following relations are applied in the present calculations.

Multipass parallel cross-flow:

For ($N_{row} = 2$):

$$\varepsilon_p = \left(1 - \frac{K}{2}\right)\left(1 - e^{-2K/C_A^*}\right), \; K = 1 - e^{-NTU_A(C_A^*/2)} \tag{5}$$

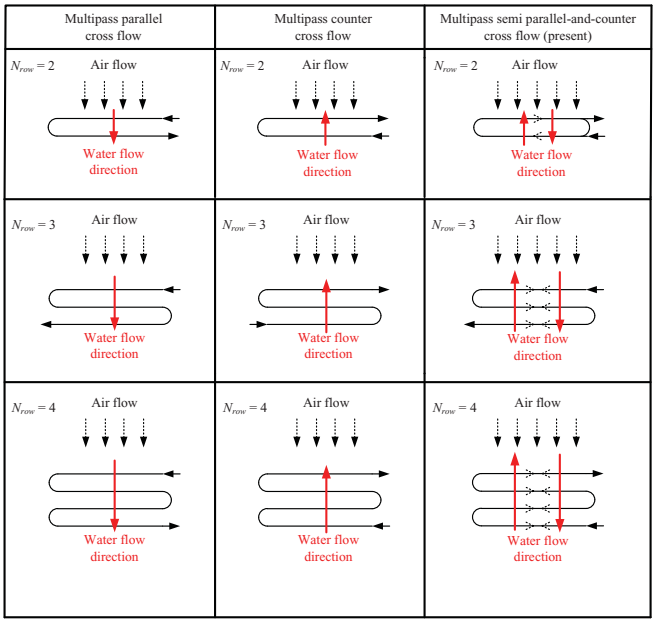

Figure 6 Schematic diagram of the heat exchangers algorithm for multipass parallel cross flow, multipass counter cross flow, and multipass parallel-and-counter cross-flow (N_{row} = 2, 3, and 4). (Color figure available online.)

For ($N_{row}=3$):

$$\varepsilon_p = 1-\left(1-\frac{K}{2}\right)^2 e^{-3K/C_A^*} - K\left[1-\frac{K}{4}+\frac{K}{C_A^*}\left(1-\frac{K}{2}\right)\right] \times e^{-K/C_A^*},\ K = 1-e^{-NTU_A(C_A^*/3)} \tag{6}$$

For ($N_{row}=4$):

$$\varepsilon_p = 1-\frac{K}{2}\left(1-\frac{K}{2}+\frac{K^2}{4}\right) - K\left(1-\frac{K}{2}\right) \times \left(1+2\frac{K}{C_A^*}\left[1-\frac{K}{2}\right]\right)e^{-2K/C_A^*} - \left(1-\frac{K}{2}\right)^3 \times e^{-4K/C_A^*},\ K = 1-e^{-NTU_A(C_A^*/4)} \tag{7}$$

Multipass counter cross-flow:

For ($N_{row}=2$):

$$\varepsilon_c = 1-\left[\frac{K}{2}+\left(1-\frac{K}{2}\right)e^{2K/C_A^*}\right]^{-1},\ K = 1-e^{-NTU_A(C_A^*/2)} \tag{8}$$

For ($N_{row}=3$):

$$\varepsilon_c = 1-\left\{\left(1-\frac{K}{2}\right)^2 e^{3K/C_A^*} + \left[K\left(1-\frac{K}{4}\right) - \left(1-\frac{K}{2}\right)\frac{K^2}{C_A^*}\right]e^{K/C_A^*}\right\}^{-1},\ K = 1-e^{-NTU_A(C_A^*/3)} \tag{9}$$

For ($N_{row}=4$):

$$\varepsilon_c = 1-\left\{\frac{K}{2}\left(1-\frac{K}{2}+\frac{K^2}{4}\right)+K\left(1-\frac{K}{2}\right) \times \left[1-2\frac{K}{C_A^*}\left(1-\frac{K}{2}\right)\right]e^{2K/C_A^*} + \left(1-\frac{K}{2}\right)^3 e^{4K/C_A^*}\right\}^{-1},$$

$$K = 1-e^{-NTU_A(C_A^*/4)} \tag{10}$$

where

$$\varepsilon_A = \frac{\varepsilon_p+\varepsilon_c}{2} \text{ for} N_{row} = 2, 3, \text{ and } 4 \tag{11}$$

Fluid A is mixed (C_{min}); fluid B is unmixed (C_{max}).

$$\varepsilon_A = \varepsilon_B/C_A^* \tag{12}$$

$$C_A^* = \frac{C_A}{C_B} = \frac{1}{C_B^*} \quad \text{for } C^* \le 1 \tag{13}$$

$$NTU_A = \frac{NTU_B}{C_A^*} \tag{14}$$

where $C^* = C_{min}/C_{max}$ is equal to C_c/C_h or C_h/C_c, depending on the value of the hot and cold fluid heat capacity rates.

$$C_{min} = \begin{cases} C_h; C_h < C_c \\ or \\ C_c; C_c < C_h \end{cases} \tag{15}$$

as

$$Q_{max} = (mc_P)_c(T_{h1}-T_{c1}) \text{ if } C_c < C_h \tag{16}$$

or

$$Q_{max} = (mc_P)_h(T_{h1}-T_{c1}) \text{ if } C_h < C_c \tag{17}$$

$$\varepsilon = \frac{Q_{ave}}{Q_{max}} \tag{18}$$

The air-side *UA* tests vary the airflow rate while keeping the water flow rate constant. The *UA* term in Eq. (4) is calculated by using Eq. (20):

$$NTU = \frac{UA}{C_{min}} \tag{19}$$

so that

$$UA = C_{min}(NTU) \tag{20}$$

The tube-side heat transfer coefficient (h_i) is evaluated from the semi-empirical correlation of Gnielinski [20]:

$$h_i = \left(\frac{k_w}{d_i}\right)\frac{(Re_{di}-1000)\,Pr\,(f_i/2)}{1+12.7\sqrt{f_i/2}\left(Pr^{2/3}-1\right)} \tag{21}$$

where the friction factor is given by:

$$f_i = (1.58 ln\, Re_{di} - 3.28)^{-2} \tag{22}$$

Downloaded by [Uppsala universitetsbibliotek] at 02:19 19 August 2012

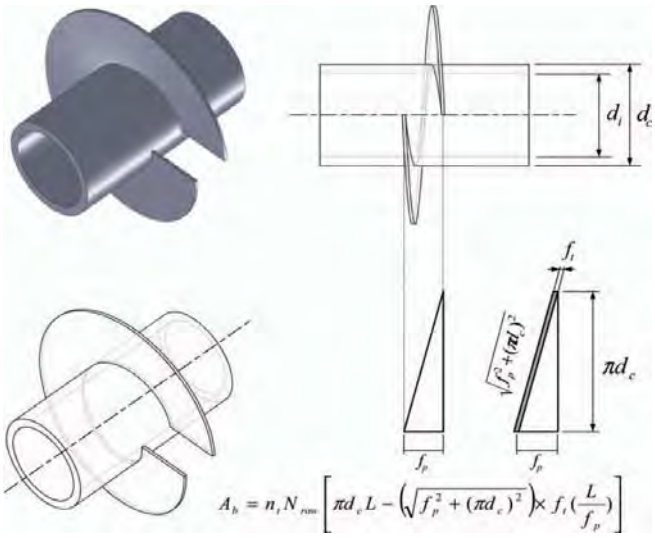

Figure 7 Equation used to determine the unfinned base surface area (A_b). (Color figure available online.)

where $\mathrm{Re}_{di} = \rho V_i d_i/\mu$.

The overall surface effectiveness (η_o), which is defined as the ratio of effective heat transfer area to total heat transfer area, can be expressed in terms of fin efficiency (η), fin surface area (A_f), and total surface area (A_o), as follows:

$$\eta_o = 1 - \frac{A_f}{A_o}(1 - \eta) \tag{23}$$

The relationship among the total surface area of the fin (A_o), the surface area of the fin (A_f), and A_b equals the area of the unfinned base surface (Figure 7). It is determined from Eq. (24).

$$A_b = n_t N_{row}\left[\pi d_c L - \left(\sqrt{f_p^2 + (\pi d_c)^2}\right) \times f_t\left(\frac{L}{f_p}\right)\right] \tag{24}$$

The surface area of fin (A_f) can be estimated by assuming it to be equal to that of the radial fin:

$$A_f = n_t N_{row}\left(\frac{L}{f_p}\right)\left[0.5\pi d_f^2 - 0.5\pi d_c^2 + \pi d_f f_t\right] \tag{25}$$

where $A_o = A_f + A_b$.

The efficiency of a radial fin with a rectangular profile is determined by the method proposed by Gardner [21]:

$$\eta = \frac{2\psi}{\phi(1+\psi)} \frac{I_1(\phi R_o)K_1(\phi R_i) - I_1(\phi R_i)K_1(\phi R_o)}{I_0(\phi R_i)K_1(\phi R_o) + I_1(\phi R_o)K_0(\phi R_i)} \tag{26}$$

where

$$\phi = (r_o - r_i)^{3/2}\left(\frac{2h_o}{k_f A_p}\right)^{1/2} \tag{27}$$

and where A_p is the area in the profile of the fin, as shown in Figure 8:

$$A_p = f_t(r_o - r_i) \tag{28}$$

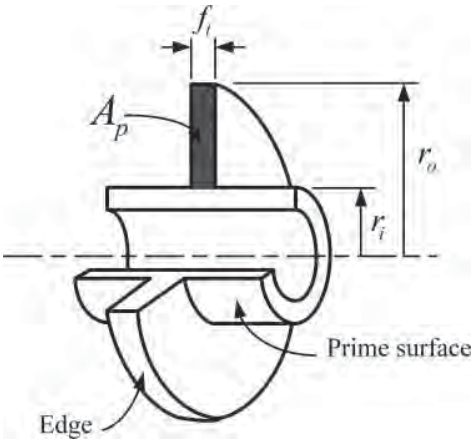

Figure 8 Schematic of the radial fin of the rectangular profile.

The parameters R_o, R_i are given in terms of the radius ratio (ψ):

$$R_o = \frac{1}{1-\psi} \tag{29}$$

and

$$R_i = \frac{\psi}{1-\psi} \tag{30}$$

where

$$\psi = \frac{r_i}{r_o} \tag{31}$$

The air-side heat transfer coefficient (h_o) can then be calculated from Eq. (4).

The air-side heat transfer characteristics of the heat exchanger are presented in terms of nondimensional groups:

$$Re_{dc} = \frac{\rho_a V_{max} d_c}{\mu} \tag{32}$$

$$j = \frac{Nu}{Re_{dc} Pr^{1/3}} = \frac{h_o}{\rho_a V_{max} c_P}(Pr)^{2/3} \tag{33}$$

The flow characteristics determined from the equation proposed by Kays and London [22] are given in terms of the fanning friction factor. The equation includes the entrance and exit pressure losses:

$$f = \left(\frac{A_{min}}{A_o}\right)\left(\frac{\rho_m}{\rho_1}\right)\left[\frac{2\Delta P \rho_1}{G_c^2} - \left(1+\sigma^2\right)\left(\frac{\rho_1}{\rho_2} - 1\right)\right] \tag{34}$$

where σ is the ratio of minimum free flow area to frontal area, A_o is the total heat transfer area and A_{min} is the minimum free flow area.

RESULTS AND DISCUSSION

This section presents the experimental results according to a primary analysis of the energy balance between air and water. The mass flow rate and temperature of both working fluids (air

Downloaded by [Uppsala universitetsbibliotek] at 02:19 19 August 2012

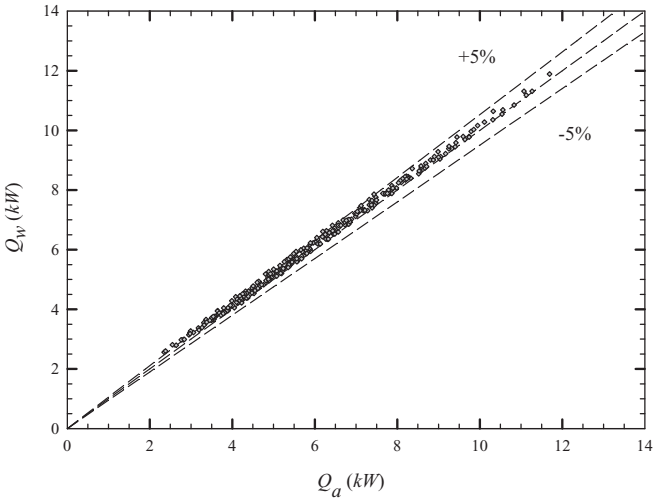

Figure 9 Energy balance between air and water.

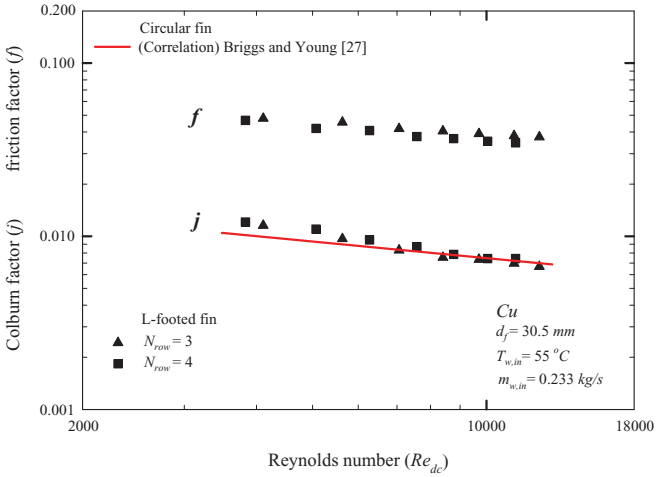

Figure 11 Effect of the number of tube rows on the Colburn factor and the friction factor of L-footed spiral fin-and-tube heat exchangers at $T_{w,in} = 55°C$ and $m_{w,in} = 0.233$ kg/s (copper fin). (Color figure available online.)

and water) were measured to calculate the heat transfer rate using Eqs. (1) and (2). Figure 9 shows that the energy balances between the air and water of the L-footed spiral fin and tube heat exchangers have relative errors of less than 5%. The present database was used to construct the relative errors, and it included 392 data points.

The analyses of air-side heat transfer and friction characteristics of all the heat exchangers examined in this experiment are presented in terms of a dimensionless number that includes the Colburn factor (j) and friction factor (f) plotted against Re_{dc}, which is the Reynolds number based on the fin collar's outside diameter ($d_o + 2f_t$).

As mentioned earlier, Eq. (11) represents the most realistic equation for this multipass parallel and counter cross-flow, so it was used to calculate the Colburn factor (j) for $N_{row} = 2$, 3, and 4. The reason for using Eq. (11) can be explained with Figure 10, which is the comparison chart illustrating the effect of Eqs. (5)–(11) on the variation of heat exchanger effectiveness. The high range of variation of heat exchanger effectiveness between parallel and counter cross-flows occurs at a high value of capacity rate ratio (C^*), which represents a high Reynolds number for the airflow. It may not be suitable for researchers to use one of those equations while operating at high Reynolds numbers. Due to its flow configuration, the heat exchanger effectiveness of multipass parallel cross-flow and counter cross-flow may not be lower or higher than the multipass parallel and the counter cross-flow configuration of the water flow arrangement, respectively. Therefore, Eq. (11) may be the most suitable one for the heat exchanger tested in this work.

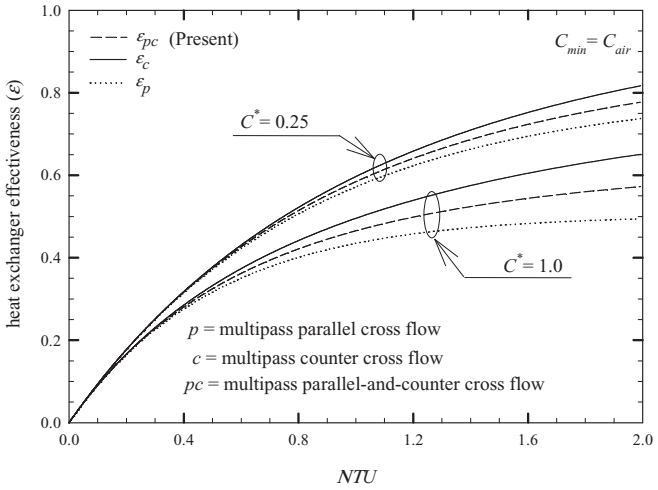

Figure 10 The comparison of the ε–*NTU* relationship at various water flow arrangements.

Figure 11 shows the effect of the number of tube rows on the heat transfer and friction characteristics for a copper fin with an outside diameter of 30.5 mm. The numbers of tube rows of the heat exchanger used in the present work were 3 and 4. As expected, both the Colburn factor (j) and the friction factor (f) decreased with an increasing Reynolds number. However, the number of tube rows has no significant effect on the Colburn factor (j) or the friction factor (f). The present data correspond with those of Rich [23] and Wang et al. [24], who studied the effect of the number of tube rows on the air-side performance of the plain fin. They concluded that the effect of tube rows on the air-side performance diminished as the Reynolds number increased over 2000.

This occurs because the downstream turbulence eddies shed from the tubes and cause good mixing in the downstream fin region. Moreover, the fact that the effect of the number of tube rows on the heat transfer characteristics vanishes for Reynolds numbers over 2000 can also be found in the works of Du and Wang [3] and Wang et al. [25, 26] for the fin-and-tube heat exchangers that have slit, wavy, and louver fins, respectively.

In addition, according to Figure 12, the same phenomenon of the effect of the number of tube rows on the air-side performance

Downloaded by [Uppsala universitetsbibliotek] at 02:19 19 August 2012

Downloaded by [Uppsala universitetsbibliotek] at 02:19 19 August 2012

Table 5 Correlations of the air side performance used for comparing with the experimental data

Round tube				
Authors	Fin types	Surface condition	Correlations	Range of parameters
Wang and Chang [28]	Plain fin	Dry surface	• j – Colburn factor correlation $\frac{j_{N_{row}}}{j_4} = 0.991\left[2.24Re_{dc}^{-0.092}\left(\frac{N_{row}}{4}\right)^{-0.031}\right]^{0.607(4-N_{row})}$ $j_4 = 0.14Re_{dc}^{-0.328}\left(\frac{P_T}{P_L}\right)^{-0.502}\left(\frac{f_p}{d_c}\right)^{0.0312}$; for $N_{row} = 4$	$Re_{dc} = 300 - 8000$ $d_c = 7 - 19.51\,mm$ $f_p = 1.07 - 8.51\,mm$ $N_{row} = 1 - 8$ $P_T = 20.35 - 50.73\,mm$ $P_L = 12.7 - 44.09\,mm$
Wang et al. [24]	Plain fin	Dry surface	• f – Friction factor correlation $f = 1.039Re_{dc}^{-0.418}\left(\frac{f_t}{d_c}\right)^{-0.104}N_{row}^{-0.0935}\left(\frac{f_p}{d_c}\right)^{-0.197}$	$Re_{dc} = 800 - 7500$ $d_c = 10.51\,mm$ $f_p = 1.77 - 3.21\,mm$ $N_{row} = 2 - 6$ $P_T = 25.4\,mm$ $P_L = 22\,mm$
Briggs and Young [27]	Circular fin	Dry surface	• j – Colburn factor correlation $j = 0.134Re_{dc}^{-0.319}\left[\frac{(f_p - f_t)}{\left(\frac{d_f - d_c}{2}\right)}\right]^{0.2}\left[\frac{(f_p - f_t)}{f_t}\right]^{0.11}$	$0.13 \le 2\left[\frac{(f_p - f_t)}{(d_f - d_c)}\right] \le 0.63$ $0.09 \le \frac{1}{2}\left[\frac{(d_f - d_c)}{d_c}\right] \le 0.69$ $0.011 \le \left(\frac{f_t}{d_c}\right) \le 0.15$ $1.54 \le \left(\frac{P_T}{d_c}\right) \le 8.23$

Note. Tube layouts of all correlations are staggered layout.

also occurs with an aluminum fin that has an outside diameter of 35 mm. As shown in Figures 11 and 12, the Briggs and Young correlation [27] (also shown in Table 5) for a circular fin-and-tube heat exchanger was chosen for comparison with the experimental results. It should be noted that the circular fin has the most similar configuration to the tested L-footed spiral fin. However, the difference between these two types of fins is that the tube surface at the base of the circular fin is not covered by the fin, leading to the risk of tube corrosion. As can be seen in Figures 11 and 12, the Briggs and Young correlation [27] gives the same trend of Colburn factor (j) of the circular fin compared with the experimental data with a maximum discrepancy of about 5%.

A comparison of the results for the effect of the number of tube rows on the pressure drop of L-footed spiral fin-and-tube heat exchangers is presented in Figure 13. As expected,

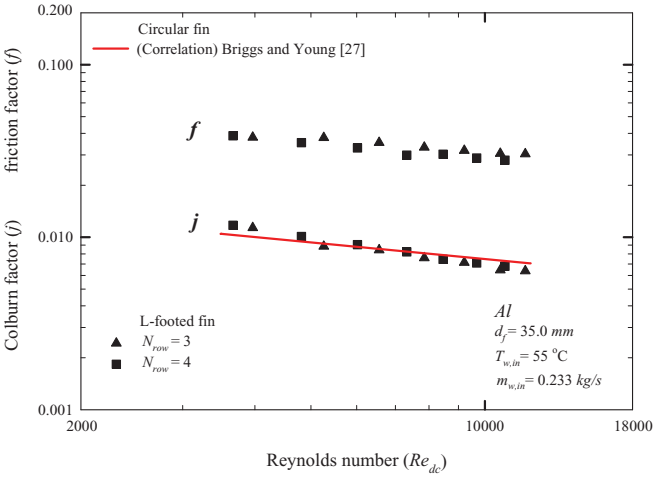

Figure 12 Effect of the number of tube rows on the Colburn factor and friction factor of the L-footed spiral fin and the tube heat exchangers at $T_{w,in} = 55°C$ and $m_{w,in} = 0.233$ kg/s (aluminum fin). (Color figure available online.)

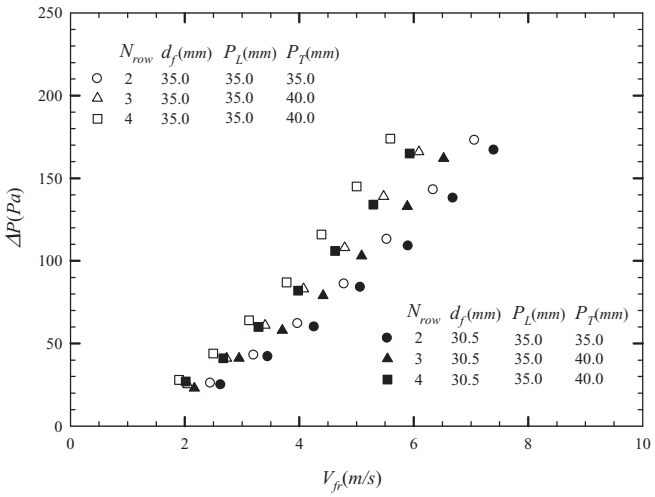

Figure 13 Effect of the fin's outside diameter on the pressure drop of the L-footed spiral fin-and-tube heat exchangers ($N_{row} = 2$, 3, and 4).

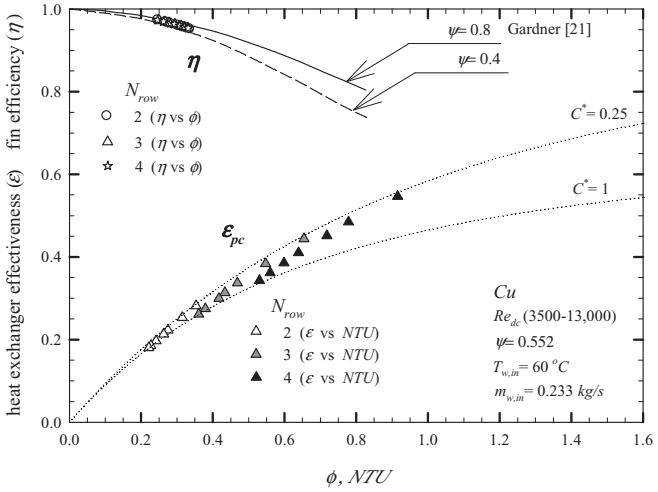

Figure 14 Effect of the number of tube rows on heat exchanger effectiveness (ε) and fin efficiency (η) (copper fin).

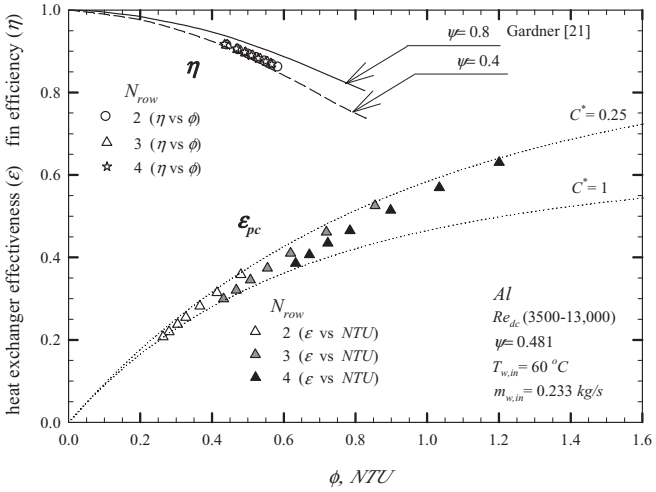

Figure 15 Effect of the number of tube rows on heat exchanger effectiveness (ε) and fin efficiency (η) (aluminum fin).

the pressure drop increases with increasing frontal air velocity while the friction factor, as mentioned earlier, decreases with an increasing Reynolds number. The pressure drop also increases with an increase in the number of tube rows. It can be seen that the pressure drop for $N_{row} = 4$ is higher than for $N_{row} = 3$ by about 22.7–23.4% ($d_f = 30.5$ mm) and 21.5–22.6% ($d_f = 35.0$ mm), respectively. Moreover, the pressure drop increases when d_f increases for the same number of tube rows. When d_f increases from 30.5 mm to 35.0 mm, the pressure drop increases by about 13.3–17.1% (for $N_{row} = 2$), 18.1–18.9% (for $N_{row} = 3$), and 16.3–18.8% (for $N_{row} = 4$) over the range of air frontal velocities (2–6 m/s). The reason for this result can be explained by the increase in the blocking flow area when d_f is increased.

Figure 14 shows the effect of the number of tube rows on the fin efficiency (η) of the copper fin with an outside diameter of 30.5 mm. It can be seen that no significant effect is found under the same experimental conditions. The reason may be explained by Eqs. (26) and (27), which show that an increase in the number of tube rows creates no significant differences in terms of ϕ and fin efficiency (η) at the same Reynolds number because of the characteristics of the efficiency of a radial fin with a rectangular profile, as proposed by Gardner [21].

The plot of heat exchanger effectiveness (ε) for multipass parallel-and-counter cross-flow heat exchangers is also shown in Figure 14. The heat exchanger effectiveness (ε) of a higher number of tube rows is higher than that of a smaller number of tube rows at the same Reynolds number. The causes of this result can be explained by the increase in the heat transfer rate between the air side and the water side with an increase in the number of tube rows. In addition, a trend similar to the one just mentioned occurs with an aluminum fin with an outside diameter of 35 mm, as Figure 15 demonstrates. In addition, Figure 16 shows the influence of the number of tube rows on the average heat transfer rate of L-footed spiral fin and tube heat exchangers. The average heat transfer rate increases with an increasing number of tube rows for both fin materials.

A comparison of the Colburn factor (j) and friction factor (f) is shown in Figure 17 in order to contrast the performance of an L-footed spiral fin to the performances of several plate fin types at high Reynolds numbers. It must be noted that none of the works described in the literature studied radial fins at a high range of Reynolds numbers, so the Colburn factor (j) and friction factor (f) of plate fins in the studies that tested at high Reynolds numbers are used for comparison with the L-footed spiral fin. It was found that the L-footed spiral fin had the same trend in the Colburn factor (j) as a plain fin, slit fin, wavy fin, and louver fin. Moreover, this same trend also occurred in the friction factor (f). It was found that the L-footed spiral fin gave a higher Colburn factor (j) than a plain fin but a lower friction factor than a plain fin. This may be because the L-footed spiral fin mixes the turbulent flow across the spaces between fins more effectively than does a plain fin. Also, the L-footed spiral fin's ability to reduce blockage flow decreases

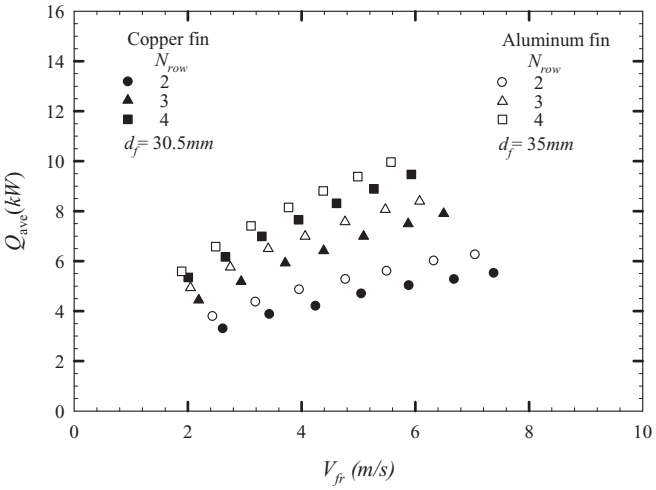

Figure 16 Effect of the number of tube rows on the average heat transfer rate at $T_{w,in} = 65°$C and $m_{w,in} = 0.2$ kg/s.

Downloaded by [Uppsala universitetsbibliotek] at 02:19 19 August 2012

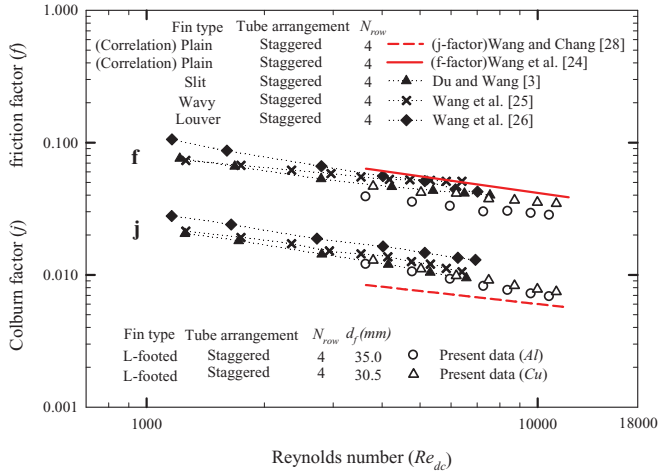

Figure 17 Comparison of j factor and f factor between presented data with correlational and experimental data of several fin types. (Color figure available online.)

with pressure drop, which affects the f factor. Furthermore, the authors found that the j factor and f factor of L-footed spiral fins are about 5–35% and 5–70% different from the plain fin, respectively. As expected, the L-footed spiral fin-and-tube heat exchanger seems to have lower j and f factors when compared to slit, wavy, and louver fin-and-tube heat exchangers, which have more complex fin shapes. In addition, Figure 17 shows only the $N_{row} = 4$ staggered L-footed spiral fins, because N_{row} has no significant effect on the Colburn factor (j) or the friction factor (f), as mentioned earlier. Therefore, the plots for $N_{row} =$ 2 and 3 will result in the same trend, which is not included in this article.

CONCLUSIONS

The objective of this study is to track the heat transfer performance of L-footed spiral fin-and-tube heat exchangers that have multipass parallel-and-counter cross-flows under sensible heating conditions and at a high Reynolds number based on the fin collar's outside diameter (3500–13,000). In total, 6 samples were investigated, each having a fin thickness of 0.25 mm, fin outside diameters (d_f) of 30.5 mm and 35.0 mm, a fin pitch of 3.25 mm, and the number of tube rows (N_{row}) at 2, 3, and 4. The conclusions and related findings of the study are as follows.

- The multipass parallel and counter cross-flow, which is combination of water flow configurations between the parallel cross-flow and the counter cross-flow, was used in this work. This type of multipass parallel-and-counter cross-flow arrangement may be an efficient choice for the reverse-flow heat exchanger that is employed in recuperative systems in modern industrial complexes, because the multipass parallel-and-counter cross-flow heat exchanger provides constant heat exchanger effectiveness under every direction of flow reversal at the same airflow rate.
- This type of water flow arrangement cannot be modeled by only one of the ε–*NTU* relationships for multipass parallel or counter cross-flow configurations because of the high variation in these relations at high Reynolds numbers (the value of C^* approaches 1). On the other hand, at low Reynolds numbers, either relation for the multipass parallel cross-flow or the counter cross-flow arrangement can be used because of the small range of variation. However, this work decided to use the average value of those ε–*NTU* relationships, which may prove to be realistic for this type of water flow arrangement.
- The number of tube rows has no significant effect on the air-side performance (j and f factors) at high Reynolds numbers (3500–13,000).
- The fin's outside diameter has a significant effect on pressure drop. The pressure drop increased as the fin's outside diameter increased for the same number of tube rows.
- It must be noted that all Colburn factors (j) and friction factors (f) calculated in this work use the model of average value of the ε–*NTU* relationships for both the multipass parallel-and-counter cross-flow configurations of water flow arrangement. However, finding the true ε-*NTU* relationships of the multipass parallel-and-counter cross-flow types may present a challenging subject for further investigation.

NOMENCLATURE

A	area, m^2
A_{min}	minimum free flow area, m^2
A_f	surface area of fin, m^2
A_o	total surface area, m^2
A_p	cross-sectional or profile area of fin, m^2
Al	aluminum
c_P	specific heat at constant pressure, J/(kg-K)
C	heat capacity rate, W/K
C^*	capacity rate ratio, dimensionless
C_c	cold-fuid capacity rate, W/K
C_h	hot-fluid capacity rate, W/K
Cu	copper
d_c	fin collar outside diameter, m
d_f	outside diameter of fin, m
d_i	tube inside diameter, m
d_o	tube outside diameter, m
f	Fanning friction factor
f_p	fin pitch, m
f_t	fin thickness, m
G_c	mass flux of the air based on minimum free flow area, kg/m^2-s
H	height, m
h	heat transfer coefficient, W/(m^2-K)
I_0	modified Bessel function solution of the first kind, order 0
I_1	modified Bessel function solution of the first kind, order 1

Downloaded by [Uppsala universitetsbibliotek] at 02:19 19 August 2012

j	Colburn factor
k	thermal conductivity, W/(m-K)
K_0	modified Bessel function solution of the second kind, order 0
K_1	modified Bessel function solution of the second kind, order 1
L	length, m
m	mass flow rate, kg/s
n_t	number of tubes in row
N_{row}	number of tube rows
NTU	number of transfer units, dimensionless
Nu	Nusselt number
P_L	longitudinal tube pitch, m
P_T	transverse tube pitch, m
Pr	Prandtl number
Q	heat transfer rate, W
r_o	radius of tip fin, m
r_i	radius of base fin, m
R	radius function in terms of the radius ratio, dimensionless
Re_{dc}	Reynolds number based on fin collar outside diameter (d_c)
Re_{di}	Reynolds number based on tube inside diameter (d_i)
Re_{do}	Reynolds number based on tube outside diameter (d_o)
T	temperature, °C
T_w	water temperature, °C
U	overall heat transfer coefficient, W/(m^2-K)
V_i	velocity based on tube inside diameter (d_i), m/s
V_{fr}	air frontal velocity, m/s
V_{max}	maximum velocity across heat exchanger, m/s

Greek Symbols

ε	heat exchanger effectiveness
η	fin efficiency
η_o	overall surface effectiveness
ρ	density, kg/m^3
σ	contraction ratio of cross-sectional area
μ	dynamic viscosity of air, Pa-s
ϕ	combination of terms, dimensionless
ψ	radius ratio
ΔP	pressure drop, Pa

Subscripts

1	air-side inlet
2	air-side outlet
a	air
ave	average
b	unfinned base surface
c	multipass counter cross flow or cold fluid
f	fin
fr	frontal ($L \times H$)
h	hot fluid
i	tube-side
in	inlet
m	mean value
max	maximum
min	minimum
o	air-side
p	multipass parallel cross-flow
pc	multipass parallel-and-counter cross-flow
t	tube
w	water

REFERENCES

[1] Wang, C. C., Lee, C. J., Chang, C. T., and Lin, S. P., Heat Transfer and Friction Correlation for Compact Louvered Fin-and-Tube Heat Exchangers, *International Journal of Heat and Mass Transfer*, vol. 42, no. 11, pp. 1945–1956, 1999.

[2] Yan, W. M., and Sheen, P. J., Heat Transfer and Friction Characteristic of Fin-and-Tube Heat Exchangers, *International Journal of Heat and Mass Transfer*, vol. 43, no. 9, pp. 1651–1659, 2000.

[3] Du, Y. J., and Wang, C. C., An Experimental Study of the Airside Performance of the Superslite Fin-and-Tube Heat Exchangers, *International Journal of Heat and Mass Transfer*, vol. 43, no. 24, pp. 4475–4482, 2000.

[4] Wongwises, S., and Chokeman, Y., Effect of Fin Pitch and Number of Tube Rows on the Air Side Performance of Herringbone Wavy Fin and Tube Heat Exchangers, *Energy Conversion and Management*, vol. 46, no. 13–14, pp. 2216–2231, 2005.

[5] Chokeman, Y., and Wongwises, S., Effect of Fin Pattern on the Air-Side Performance of Herringbone Wavy Fin-and-Tube Heat Exchangers, *Heat and Mass Transfer*, vol. 41, no. 7, pp. 642–650, 2005.

[6] Wen, M. Y., and Ho, C. Y., Heat-Transfer Enhancement in Fin-and-Tube Heat Exchanger With Improved Fin Design, *Applied Thermal Engineering*, vol. 29, no. 5–6, pp. 1050–1057, 2009.

[7] Pirompugd, W., Wang, C. C., and Wongwises, S., Correlations for Wet Surface Ratio of Fin-and-Tube Heat Exchangers, *International Journal of Heat and Mass Transfer*, vol. 53, no. 1–3, pp. 568–573, 2010.

[8] Nuntaphan, A., Kiatsiriroat, T., and Wang, C. C., Air Side Performance at Low Reynolds Number of Cross-Flow Heat Exchanger Using Crimped Spiral Fins, *International Communications in Heat and Mass Transfer*, vol. 32, no. 1–2, pp. 151–165, 2005.

[9] Wongwises, S., and Naphon, P., Heat Transfer Characteristics of a Spiral-Coil, Finned Tube Heat Exchanger Under Dry-Surface Conditions, *Heat Transfer Engineering*, vol. 27, no. 1, pp. 25–34, 2006.

[10] Wongwises, S., and Naphon, P., Thermal Performance of a spiral-Coil Finned Tube Heat Exchanger Under

Downloaded by [Uppsala universitetsbibliotek] at 02:19 19 August 2012

Wet-Surface Conditions, *Journal of Mechanical Science and Technology*, vol. 20, no. 2, pp. 212–226, 2006.
[11] Srisawad, K., and Wongwises, S., Heat Transfer Characteristics of a New Helically Coiled Crimped Spiral Finned Tube Heat Exchanger, *Heat Mass Transfer*, vol. 45, no. 4, pp. 381–391, 2009.
[12] Lee, M., Kang, T., and Kim, Y., Air-Side Heat Transfer Characteristics of Spiral-Type Circular Fin-and-Tube Heat Exchangers, *International Journal of of Refrigeration*, vol. 33, no. 2, pp. 313–320, 2010.
[13] ASHRAE, *ASHRAE Handbook—Fundamentals,* American Society of Heating, Refrigerating and Air-Conditioning Engineers, SI-ed., pp.14–15, Inc., Atlanta, GA, chap. 13, 1993.
[14] Stevens, R. A., Fernandez, J., and Woolf, J. R., Mean-Temperature Difference in One, Two, and Three-Pass Crossflow Heat Exchangers, *ASME Trans.*, vol. 79, pp. 287–297, 1957.
[15] Taborek, J., Charts for Mean Temperature Difference Industrial Heat Exchanger Configuration,in *Heat Exchanger Design Handbook*, ed. Schlunder, Hemisphere, Washington, DC, chap. 1.5, 1983.
[16] ESDU 86018, Effectiveness-NTU Relations for the Design and Performance Evaluation of Two-Stream Heat Exchangers, *Engineering Science Data Unit 86018 with Amendment*, London: ESDU International plc, pp. 92–107, 1991.
[17] Chen, T. D., Conklin, J. C., and Baxter, V. D., Comparison of Analytical and Experimental Effectiveness of Four-Row Plate-Fin-Tube Heat Exchangers With Water R-22 and R-410A, *ASME Winter Annual Meeting*, Anaheim, CA, 1998.
[18] Navarro, H. A., and Cabezas-Gomez, L., A New Approach for Thermal Performance Calculation of Cross-Flow Heat Exchanger, *International Journal of Heat and Mass Transfer*, vol. 48, no. 18, pp. 3880–3888, 2005.
[19] Cabezas-Gomez, L., Navarro, H.A., and Saiz-Jabardo, J. M., Thermal Performance of Multipass Parallel and Counter-Cross-Flow Heat Exchangers, *Journal of Heat Transfer*, vol. 129, no. 3, pp. 282–290, 2007.
[20] Gnielinski, V., New Equation for Heat and Mass Transfer in Turbulent Pipe and Channel Flow, *International Chemical Engineering*, vol. 16, pp. 359–368, 1976.
[21] Gardner, K. A., Efficiency of Extended Surface, *ASME Trans.*, vol. 67 pp. 621–631, 1945.
[22] Kays, W. M., and London, A., *Compact Heat Exchangers, 3rd ed.*, McGraw-Hill, New York, 1984.
[23] Rich, D. G., The Effect of the Number of Tube Rows on Heat Transfer Performance of Smooth Plate Fin-and-Tube Heat, *ASHRAE Trans.*, vol. 81, pp. 307–317, 1975.
[24] Wang, C. C., Chang, Y. J., Hsieh, Y. C., and Lin, Y. T., Sensible Heat and Friction Characteristics of Plate Fin-and-Tube Heat Exchangers Having Plane Fins, *International Journal of Refrigeration*, vol. 19, no. 4, pp. 223–230, 1996.
[25] Wang, C. C., Fu, W. L., and Chang, C. T., Heat Transfer and Friction Characteristics of Typical Wavy Fin-and-Tube Heat Exchangers, *Experimental Thermal and Fluid Science*, vol. 14, no. 2, pp. 174–186, 1997.
[26] Wang, C. C., Chi, K. Y., Chang, Y. J., and Chang, Y. P., An Experimental Study of Heat Transfer and Friction Characteristics of Typical Louver Fin-and-Tube Heat Exchangers, *International Journal of Heat Mass Transfer*, vol. 41, no. 4–5, pp. 817–822, 1998.
[27] Briggs, D. E., and Young, E. H., Convective Heat Transfer and Pressure Drop of Air Flowing Across Triangular Pitch Banks of Finned Tubes, *Chemical Engineering Progress Symp. Ser.*, vol. 59–41, no. 41, pp. 1–10, 1963.
[28] Wang, C. C., and Chang, C. T., Heat and Mass Transfer for Plate Fin-and-Tube Heat Exchangers With and Without Hydrophilic Coating, *International Journal of Heat Mass Transfer*, vol. 41, no. 20, pp. 3109–3120, 1998.

Parinya Pongsoi obtained his B.Eng. and M.Eng. from the Department of Mechanical Engineering, King Mongkut's University of Technology, Thonburi, Thailand. He is now a Ph.D. student at the same institute. His current research interests include the heat transfer performance and flow characteristics of fin-and-tube heat exchangers.

Santi Pikulkajorn is currently a plant manager of Somchai Industrial Co., Ltd., Bangkok, Thailand. He received his B.Eng. in mechanical engineering from King Mongkut's University of Technology, North Bangkok.

Somchai Wongwises is a professor of mechanical engineering at King Mongkut's University of Technology, Thonburi, Bangmod, Thailand. He received his Doktor-Ingenieur (Dr.-Ing.) in mechanical engineering from the University of Hannover, Germany, in 1994. His research interests include two-phase flow, heat transfer enhancement, and thermal system design. He is the head of the Fluid Mechanics, Thermal Engineering and Multiphase Flow Research Laboratory (FUTURE).

Downloaded by [Uppsala universitetsbibliotek] at 02:19 19 August 2012

Provided for non-commercial research and education use.
Not for reproduction, distribution or commercial use.

This article appeared in a journal published by Elsevier. The attached copy is furnished to the author for internal non-commercial research and education use, including for instruction at the authors institution and sharing with colleagues.

Other uses, including reproduction and distribution, or selling or licensing copies, or posting to personal, institutional or third party websites are prohibited.

In most cases authors are permitted to post their version of the article (e.g. in Word or Tex form) to their personal website or institutional repository. Authors requiring further information regarding Elsevier's archiving and manuscript policies are encouraged to visit:

http://www.elsevier.com/copyright

Author's personal copy

International Journal of Heat and Mass Transfer 55 (2012) 6555–6566

Contents lists available at SciVerse ScienceDirect

International Journal of Heat and Mass Transfer

journal homepage: www.elsevier.com/locate/ijhmt

Effect of fin pitches on the optimum heat transfer performance of crimped spiral fin-and-tube heat exchangers

Parinya Pongsoi [a], Santi Pikulkajorn [b], Somchai Wongwises [a,c,*]

[a] Fluid Mechanics, Thermal Engineering and Multiphase Flow Research Lab. (FUTURE), Department of Mechanical Engineering, King Mongkut's University of Technology Thonburi, Bangmod, Bangkok 10140, Thailand
[b] Somchai Industry Co., Ltd, Bangkok 10150, Thailand
[c] The Royal Institute of Thailand, Academy of Science, Sanam Suea Pa, Dusit, Bangkok 10300, Thailand

ARTICLE INFO

Article history:
Received 31 December 2011
Received in revised form 18 June 2012
Accepted 20 June 2012
Available online 20 July 2012

Keywords:
Crimped fin
Heat transfer
Heat exchanger
Air–water
Optimum fin pitch

ABSTRACT

This study conducted experiments on the optimized fin pitch for crimped spiral fin-and-tube heat exchangers. The experiments covered a size range of 2.4–6.5 mm, which is the manufacturing limitation for this kind of fin. The water-flow arrangement used in this experiment combined the parallel cross-flow and the counter cross-flow in a two-row configuration. Ambient air was used as the working fluid on the air-side, and hot water was used on the tube-side. The effects of fin pitches on the heat transfer coefficient and pressure drop characteristics were studied. The results clearly showed that the convective heat transfer coefficient (h_o) for a fin pitch of 2.4 mm is relatively low compared with that of other fin pitches with the same air frontal velocity. Using larger fin pitches (i.e., 4.2, 6.2, and 6.5 mm) resulted in negligible differences in the pressure drop. Moreover, this work introduces the parameter of three performances indexes, which can be expressed as the ratio of the desired output to the required input, for optimization purposes. Due to the difference in optimum fin pitch obtained by these performance indexes, an intersection analysis was conducted. The results indicated that the optimum fin pitch is 4.2 mm for this work, which could be valuable for the effective design for industrial thermal-system applications.

© 2012 Elsevier Ltd. All rights reserved.

1. Introduction

The fin-and-tube heat exchanger was designed for thermal systems in many industrial applications involving heat transfer and heating, ventilation, air conditioning, and refrigeration system (HVAC&R) applications that use a forced airflow through a fin-and-tube heat exchanger. Nowadays, the spiral fin-and-tube heat exchanger is the preferred type of heat exchanger for industrial applications. However, the heat transfer rate from the heat exchanger is normally limited by the thermal resistance on the air-side. One way to augment the heat transfer performance of the heat exchanger is to improve its fin geometry, but this method may require more fan power because of the loss associated with the pressure drop.

Many researchers have studied the effects of plate fin geometry—using plain fins, slit fins, wavy fins, louvered fins, compounded fins, circular fins, and conventional spiral fins—on the heat transfer performance and frictional characteristics. On the other hand, the review of the literature indicated that only a few studies indicated the need for research on crimped spiral fin-and-tube heat exchangers [1–7]. The crimped spiral fin features a sine-shaped fin that provides a higher heat transfer rate on the air-side through an increase in the contact surface between the fin base and the tube.

Nuntaphan et al. [1,2] studied the air-side of the crimped spiral fin heat exchanger to analyze the effects of the tubes' diameters, fin spacings, transfer tube pitches, and arrangements, and they proposed a correlation between the heat transfer and friction characteristics in the case of low Reynolds numbers under dry and wet surface conditions. The results showed that the heat transfer coefficient for the dry surface was higher than that for the wet surface. Moreover, heat exchangers using crimped spiral finned tubes were investigated by Srisawad and Wongwises [3], who focused on the air-side performance of helically coiled crimped spiral finned tube heat exchangers in dry surface conditions. Pongsoi et al. [4,5] studied the effects of fin pitch and number of tube rows on the air-side heat transfer characteristics of crimped spiral fin-tube heat exchangers having a multipass parallel and counter cross-flow arrangement under sensible heating conditions at a high Reynolds number, proposed the ε-*NTU* relation equation for this new type of water-flow arrangement, and proposed both heat transfer and friction correlations. Tang et al. [6,7] investigated the air-side heat transfer and friction characteristics of five kinds of fin-and-tube

* Corresponding author at: Fluid Mechanics, Thermal Engineering and Multiphase Flow Research Lab. (FUTURE), Department of Mechanical Engineering, King Mongkut's University of Technology Thonburi, Bangmod, Bangkok 10140, Thailand. Tel.: +66 24709115.
E-mail address: somchai.won@kmutt.ac.th (S. Wongwises).

0017-9310/$ - see front matter © 2012 Elsevier Ltd. All rights reserved.
http://dx.doi.org/10.1016/j.ijheatmasstransfer.2012.06.061

Author's personal copy

Nomenclature

A	area, m^2
A_{min}	minimum free flow area, m^2
A_f	surface area of fin, m^2
A_o	total surface area, m^2
A_p	cross-sectional or profile area of fin, m^2
c_p	specific heat at constant pressure, J/(kg K)
C	heat capacity rate (mc_p), W/K
C^*	capacity rate ratio, dimensionless
C_c	cold-fuid capacity rate, W/K
C_h	hot-fluid capacity rate, W/K
d_f	outside diameter of fin, m
d_i	tube inside diameter, m
d_o	tube outside diameter, m
f	Fanning friction factor, dimensionless
f_p	fin pitch, m
f_t	fin thickness, m
G_c	mass flux of the air based on minimum free flow area, kg/m^2 s
H	height, m
h	heat transfer coefficient, W/(m^2 K)
I_o	modified Bessel function solution of the first kind, order 0
I_1	modified Bessel function solution of the first kind, order 1
k	thermal conductivity, W/(m K)
K_0	modified Bessel function solution of the second kind, order 0
K_1	modified Bessel function solution of the second kind, order 1
L	length, m
m	mass flow rate, kg/s
n	number of tubes in row
N_{row}	number of tube rows
NTU	number of transfer units, dimensionless
P_L	longitudinal tube pitch, m
P_T	transverse tube pitch, m
Pr	Prandtl number, dimensionless
Q	heat transfer rate, W
r_o	radius of tip fin, m
r_i	radius of base fin, m
R	radius function in terms of the radius ratio, dimensionless
Re_{di}	Reynolds number based on tube inside diameter (d_i), dimensionless
Re_{do}	Reynolds number based on tube outside diameter (d_o), dimensionless
T	temperature, °C
U	overall heat transfer coefficient, W/(m^2 K)
V_i	velocity based on tube inside diameter (d_i), m/s
V_{fr}	air frontal velocity, m/s
W_p	fan power, W

Greek symbols

ε	heat exchanger effectiveness
η	fin efficiency
η_o	overall surface effectiveness
ρ	density, kg/m^3
σ	contraction ratio of cross-sectional area
μ	dynamic viscosity of air, Pa s
ϕ	combination of terms, dimensionless
ψ	radius ratio, dimensionless
ΔP	pressure drop, Pa
ζ_1	heat exchanger performance index, W/Pa
ζ_2	system performance index, W/Pa
ζ_3	dimensionless system performance index, dimensionless

Subscripts

1	air-side inlet
2	air-side outlet
a	air
ave	average
b	unfinned base surface
c	multipass counter cross flow or cold fluid
f	fin
fr	frontal ($L \times H$)
h	hot fluid
HX	heat exchanger
i	tube-side
in	inlet
m	mean value
max	maximum
min	minimum
o	air-side
p	multipass parallel cross flow
pc	multipass parallel-and-counter cross flow
Sys	system
t	tube
w	water

heat exchangers crimped spiral fin, plain fin, slit fin, fin with delta-wing longitudinal vortex generators, and mixed fin for which the number of tube rows (N_{row}) was 12 and the diameter of the tubes (d_o) was 18 mm throughout both experimental and numerical investigation. Their results indicated that the crimped spiral fin gave a high pressure drop, but it also provided a higher air-side heat transfer performance than the other types.

According to the literature, several studies have been devoted to the heat transfer and friction characteristics of finned tube heat exchangers under numerous conditions. However, research is needed in the area of the optimal design for fin and tube heat exchangers. Previous researchers [8–10] have extensively observed that the effects of the fin pitch give reliable guidelines for an effective design of the plate and circular fin, in which the other geometric effects, such as fin thickness, longitudinal tube pitch, and transverse tube pitch, show no significance with regard to the optimum fin pitch. Nevertheless, until now, none of the studies in the literature reported on the optimal heat transfer performance of crimped spiral fin-and-tube heat exchangers. Therefore, the purpose of this study is to investigate the optimized fin pitch for a crimped spiral fin-and-tube heat exchanger having a two-row configuration. The fin pitches that were tested covered a size range of 2.4 mm to 6.5 mm, which is the manufacturing limitation for this kind of fin. Finding the optimized fin pitch would be valuable when designing industrial applications in HVAC&R systems, waste heat recovery units (WHRU), and other units and systems.

2. Experimental apparatus

A schematic diagram of the experimental apparatus is shown in Fig. 1. Air and hot water were used as the working fluids. The main

Author's personal copy

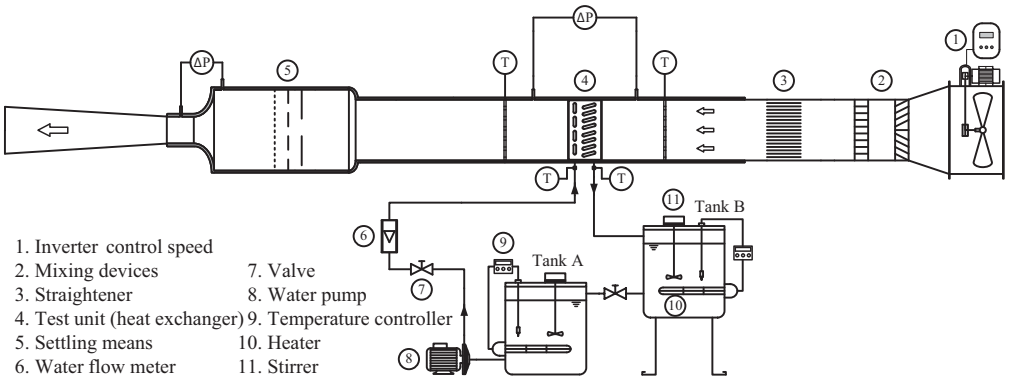

Fig. 1. Schematic diagram of the experimental apparatus.

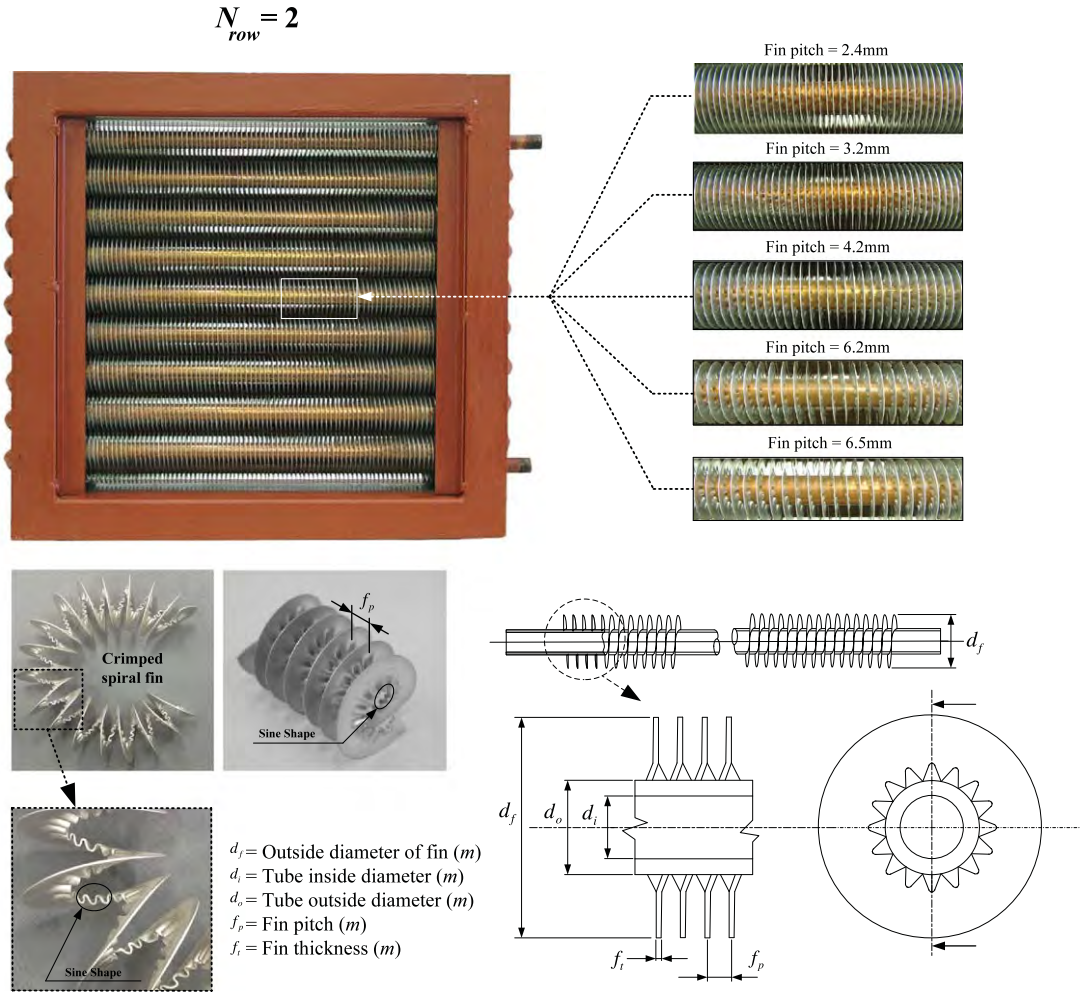

Fig. 2. The photos of the tested crimped spiral fin and tube heat exchangers and schematic diagram of crimped spiral fin.

components of the system were the heat exchanger, water-flow loop, air supply, instrumentation, and data acquisition system.

The present study used a type of fin-and-tube heat exchanger. The copper tubes have a large diameter (about 16 mm), and are very commonly used in ventilator and fan-coil units [11,12]. Moreover, the tubes are also finned with aluminum fins. Photos of the crimped spiral fin pattern are shown in Fig. 2. The water-side circuitry arrangement and detailed dimensions of the tested fin-and-tube heat exchangers are shown in Fig. 3. Finally, the geometric parameters of the heat exchangers are summarized in Table 1.

An open-type wind tunnel was used to push air through the heat exchanger. The connections of the duct were designed so that parts could be changed or repaired quickly and easily. This arrangement operated in a cross-flow with the hot water passing through the heat exchanger. The tunnel was a rectangular air duct fabricated from a 0.43 × 0.48 m steel plate. The duct was insulated with a 16 mm thick Aeroflex standard sheet. The fresh air was drawn into the duct and passed through the mixing device, straightener, and heat exchanger by means of a 2.2 kW axial flow fan. The speed of the fan was adjusted with an inverter.

Author's personal copy

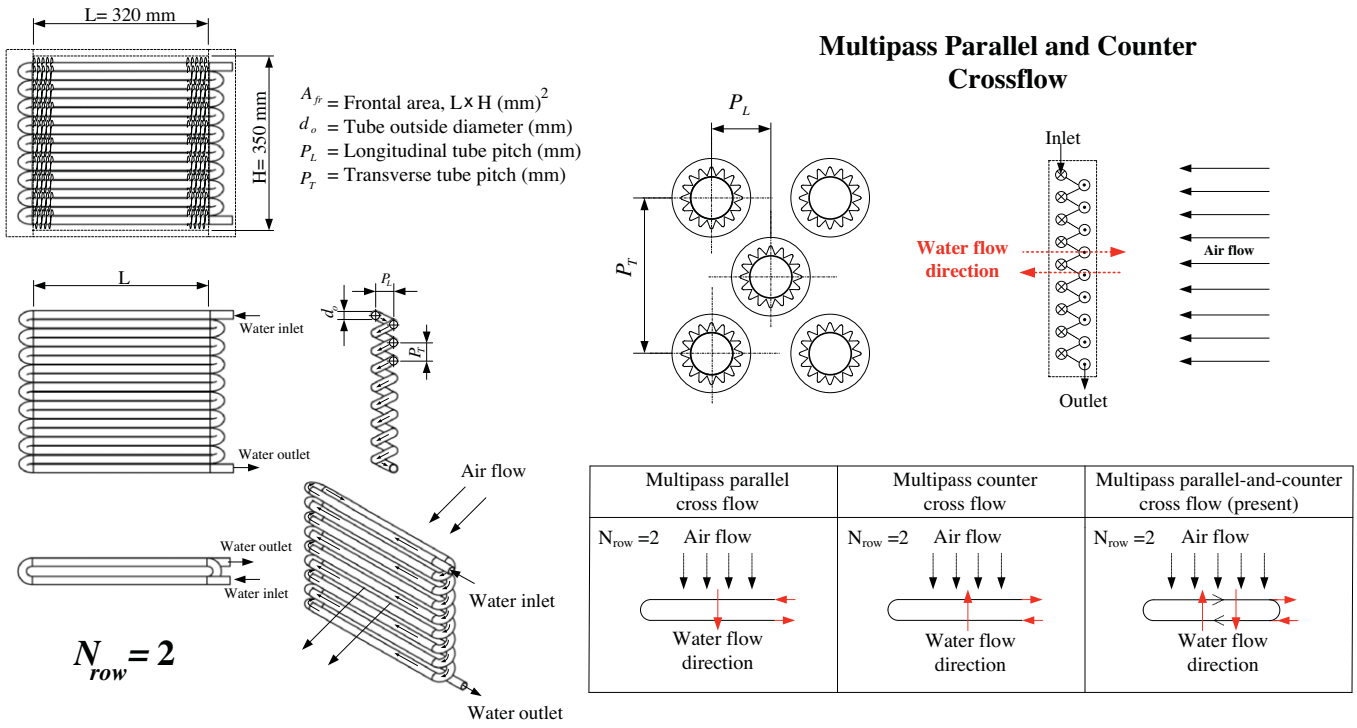

Fig. 3. Geometric details and schematic diagram of the heat exchangers algorithm for multipass parallel cross flow, multipass counter cross flow and multipass parallel-and-counter cross flow (× and • signs indicate that water flows into or out of the paper, respectively).

Table 1
Detailed geometric parameters of the test samples.

No.	Fin type	d_i (mm)	d_o (mm)	d_f (mm)	P_L (mm)	P_T (mm)	f_t (mm)	n_t	N_{row}	f_p (mm)
1–5	Crimped	13.5	16.35	34.8	35	39	0.4	9	2	2.4, 3.2, 4.2, 6.2 and 6.5

Remarks: d_f = outside diameter of fin; d_i = tube inside diameter; d_o = tube outside diameter; f_p = fin pitch; f_t = fin thickness; P_L = longitudinal tube pitch; P_T = transverse tube pitch; n_t = number of tubes in row; N_{row} = number of tube rows.
Notes: Tube layouts of all heat exchangers are staggered layout.

Thermocouple probes were located at the air inlet and outlet sections of the heat exchanger. The temperature was measured with 1 mm diameter probes extending into the duct where the air flowed. The probes were T-type copper-constantan thermocouples grounded to a stainless steel outer sheath. The measuring points were at the positions recommended by the ASHRAE standard [13]. The temperature was monitored and recorded continuously. All temperature-measuring devices were well calibrated in a controlled temperature bath using a standard precision mercury-in-glass thermometer. All sensors were wired directly to terminal control panels mounted on the bench. The air flow rate was detected with a nozzle based on the ISO 5801 standard. The drops in air pressure across the test section and the nozzle were measured with a digital manometer. Four pressure taps were attached on each wall: upstream and downstream taps in the test section and in the nozzle.

To avoid any distortion of the air velocity profile, mixing devices and straighteners were installed in the duct. Air velocity and air velocity fluctuation in the duct were checked with a Constant Temperature Anemometer 90CN10/C10 (CTA, Dantec) that had an automatic probe setup. Stream Ware software was used to set up the anemometer modules, to perform velocity and directional calibrations, and to provide an experimental platform wherein automatic sequences of hardware setup, data acquisitions, and data reductions could be performed. The probe used in this experiment was a wedge-shaped, right-angled film probe 55R33 with a

Table 2
Experimental conditions.

Inlet-air-dry bulb temperature, °C	31.5 ± 0.5
Inlet-air frontal velocity, m/s	2 – 6
Inlet-water temperature, °C	55 – 70
Water flow rate, kg/s	0.2 – 0.233

Table 3
The accuracies of the measurements.

Parameters	Accuracy
Inlet-air dry-bulb temperature, °C	±0.1
Pressure drop, *Pa*	±0.5
Inlet-water temperature, °C	±0.1
Water flow rate, kg/s	±0.4 (±0.02 of full scale)

Table 4
Uncertainties of the derived experimental values.

Parameters	Maximum uncertainties (%)
Air-side heat transfer rate, Q_a	±4.96
Water-side heat transfer rate, Q_w	±3.37
Pressure drop, ΔP	±2.50
Frontal velocity, V_{fr}	±3.30
Air-side heat transfer coefficient, h_o	±8.98

Author's personal copy

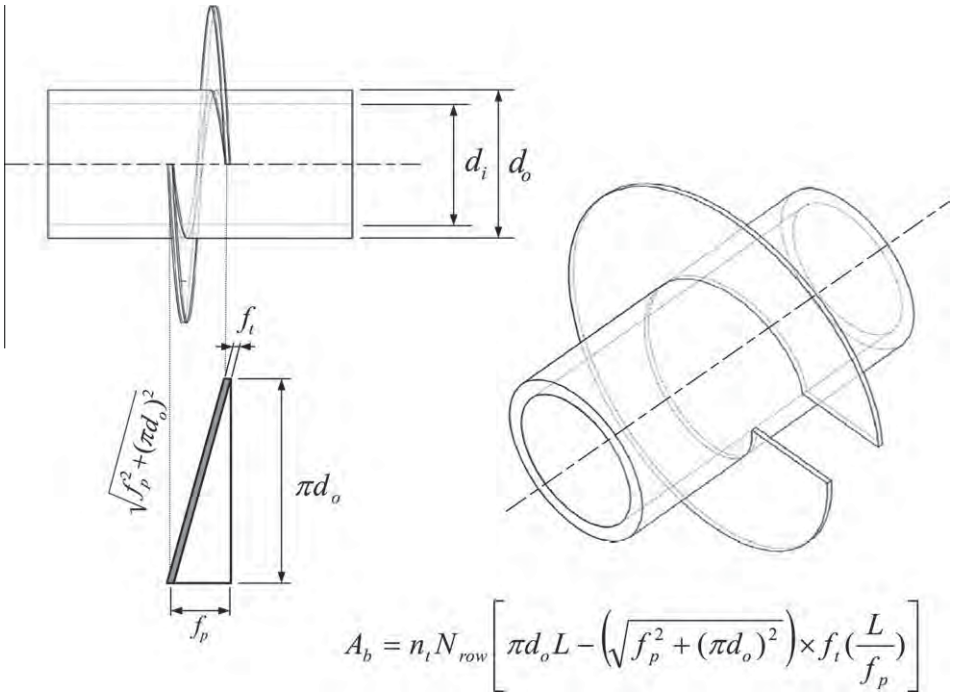

Fig. 4. Details of area of unfinned base surface (A_b) equation.

non-cylindrical sensor in a 1 × 0.2 mm sheath. All signals were registered by a data acquisition system and then averaged over the elapsed time.

The hot-water flow loop consisted of two storage tanks, an 18 kW electric heater, a centrifugal pump, a control unit, and a flow meter with a 0.5 *LPM* resolution (Fig. 1). The purpose of this loop was to transfer heat to the air flowing through the heat exchanger. The temperature of the hot water in the two tanks was measured with T-type copper-constantan thermocouples and was controlled with the temperature controller. After the hot water had been heated to the required temperature, it was pumped out of storage tank (A), delivered to the heat exchanger, and then returned to storage tank (B), which was used to pre-heat the water in order to reduce the temperature difference before entering tank (A). The water temperatures at the inlet and outlet of the heat exchanger were measured with 1 mm diameter probes extending inside the tube where the water flowed. The probes consisted of T-type copper-constantan thermocouples grounded to a stainless steel outer sheath.

In the experiment, at a specific inlet water temperature, the water flow rate was fixed while the air flow rate was increased. The system was allowed to approach a steady state before any data was recorded. After the system reached a steady state, the inlet and outlet temperatures of the air passing across the heat exchanger and the water flow rates were determined. All tested conditions of the heat exchangers are shown in Table 2. It must be noted that for industrial service, the operation velocity is normally much higher, as reported by Xie et al. [11]. Therefore, this study extended the applicable range (V_{fr} up to 6 m s^{-1}). The accuracies of the direct measurement sensors and the uncertainties, which were calculated using the root mean sum square method, are shown in Tables 3 and 4.

3. Data reduction

In order to determine the heat transfer characteristics of the heat exchangers from the data recorded under steady state conditions during each test run, the method of number of transfer units (*ε-NTU*), based on the concept of heat exchanger effectiveness, was applied to determine the *UA* product.

The air-side heat transfer rate is given as:

$$Q_a = m_a c_{P,a} \Delta T_a \tag{1}$$

The water-side heat transfer rate is given as:

$$Q_w = m_w c_{P,w} \Delta T_w \tag{2}$$

The total rate of heat transfer used in the calculation is averaged from the air-side and water-side as follows:

$$Q_{ave} = \frac{|Q_a| + |Q_w|}{2} \tag{3}$$

The overall heat transfer coefficient can be written in terms of the total resistance to heat transfer. This total resistance is the sum of the individual resistances, as follows:

$$\frac{1}{UA} = \frac{1}{h_i A_i} + \frac{ln(d_o/d_i)}{2\pi k_t L} + \frac{1}{\eta_o h_o A_o} \tag{4}$$

The ε-NTU relationships with one fluid mixed and one fluid unmixed in the cross-flow were employed to determine the overall heat transfer coefficient. From Fig. 3, the present mixed circuitry arrangement is a combination of parallel and counter cross-flow. Therefore, the ε-NTU relationships developed by Pongsoi et al. [4] were selected to calculate the heat exchanger effectiveness. This relation combines both the effect of parallel and the counter cross-flow configuration of water-flow arrangement from [14–16], as shown in Eqs. (5)–(7), in order to calculate the overall heat transfer coefficient. However, the multipass parallel and counter cross-flow used in this experiment is a combination of multipass parallel cross-flow and counter cross-flow. It may be suitable to use the average value of those relations shown in Eq. (7). The schematic diagram of the heat exchangers algorithm for multipass parallel cross-flow, multipass counter cross-flow, and multipass parallel and counter cross-flows (Nrow = 2) are shown in Fig. 3. For the present flow configuration, the heat exchanger's

Author's personal copy

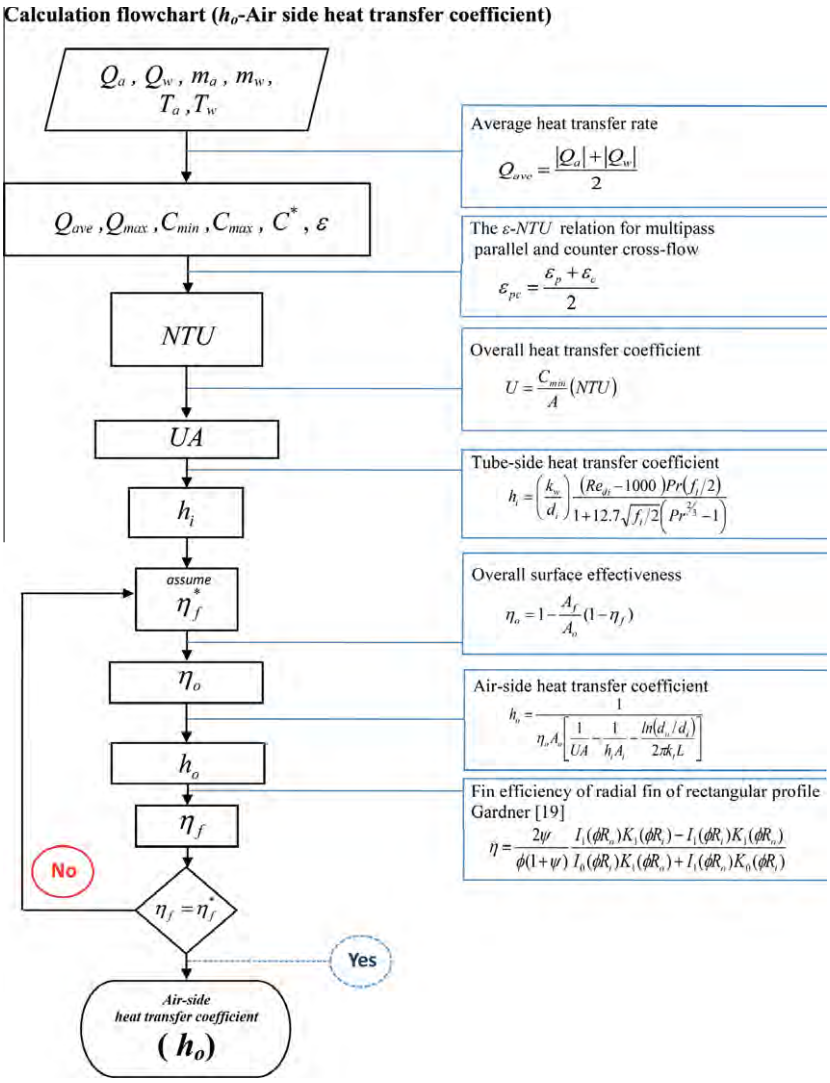

Fig. 5. Flowchart of the data reduction for air-side heat transfer coefficient (h_o).

effectiveness lies between the multipass parallel cross-flow and the counter cross-flow. Note that using inappropriate ε-NTU relationships for complex flow arrangement may lead to an error of up to 10%, as pointed out by Navarro and Cabezas-Gomez [17]. This type of multipass parallel and counter cross-flow arrangement may be an efficient choice for the reverse flow heat exchanger that is employed in recuperative systems in modern industrial complexes.

In this work, the air-side working fluid (air) is defined as fluid A, and the tube-side working fluid (water) is defined as fluid B. It should be noted that the minimum heat capacity rate (Cmin) is on the air-side (fluid A). Therefore, the following relations are applied in the present calculations.

Multipass parallel cross-flow

For (N_{row} = 2):

$$\varepsilon_p = \left(1 - \frac{K}{2}\right)\left(1 - e^{-2K/C_A^*}\right), \quad K = 1 - e^{-NTU_A(C_A^*/2)} \tag{5}$$

Multipass counter cross-flow

For (N_{row} = 2):

$$\varepsilon_c = 1 - \left[\frac{K}{2} + \left(1 - \frac{K}{2}\right)e^{2K/C_A^*}\right]^{-1}, \quad K = 1 - e^{-NTU_A(C_A^*/2)} \tag{6}$$

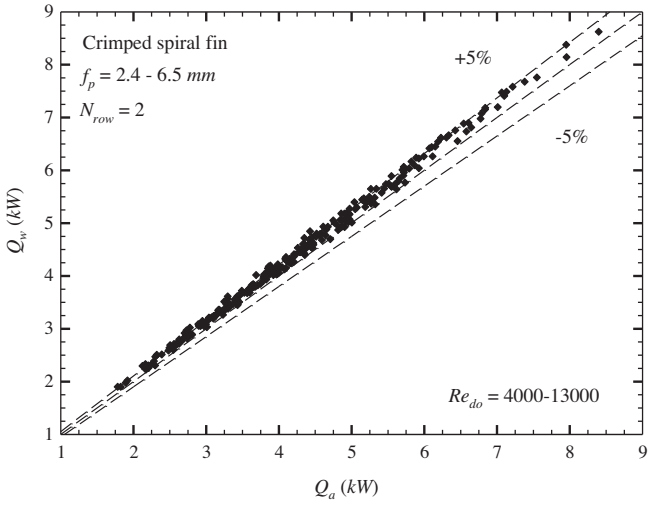

Fig. 6. Energy balance between air and water.

Author's personal copy

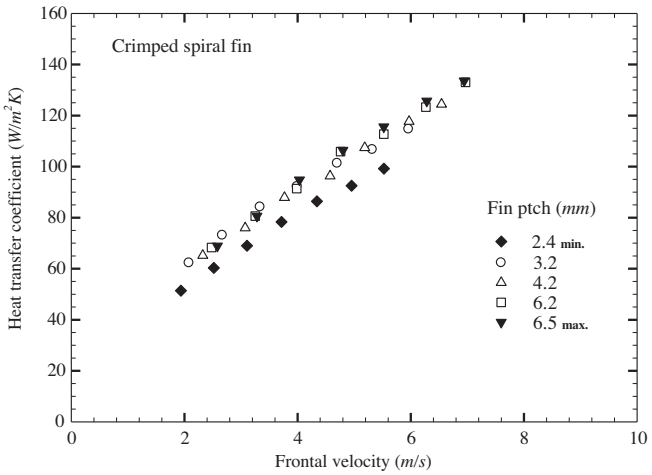

Fig. 7. Effect of fin pitch on the air-side heat transfer coefficient of crimped spiral fin and tube heat exchangers at $T_{w,in}$ = 70 °C and water flow rate of 0.233 kg/s.

where

$$\varepsilon_A = \frac{\varepsilon_p + \varepsilon_c}{2} \tag{7}$$

fluid A is mixed(C_{min}); fluid B is unmixed(C_{max}).

$$\varepsilon_A = \varepsilon_B / C_A^* \tag{8}$$

$$C_A^* = \frac{C_A}{C_B} = \frac{1}{C_B^*} \quad C^* \leqslant 1 \tag{9}$$

$$NTU_A = \frac{NTU_B}{C_A^*} \tag{10}$$

where $C^* = C_{min}/C_{max}$ is equal to C_c/C_h or C_h/C_c, depending on the value of the hot and cold fluid heat capacity rates.

$$C_{min} = C_h; C_h < C_c \tag{11}$$

or

$$C_{min} = C_c; C_c < C_h \tag{12}$$

as

$$Q_{max} = (mc_P)_c(T_{h1} - T_{c1}) \text{ if } C_c < C_h \tag{13}$$

or

$$Q_{max} = (mc_P)_h(T_{h1} - T_{c1}) \text{ if } C_h < C_c \tag{14}$$

$$\varepsilon = \frac{Q_{ave}}{Q_{max}} \tag{15}$$

The UA term in Eq. (4) is calculated by using Eq. (16):

$$UA = C_{min}(NTU) \tag{16}$$

The tube-side heat transfer coefficient (h_i) is evaluated from the semi-empirical correlation of Gnielinski [18]:

$$h_i = \left(\frac{k_w}{d_i}\right) \frac{(Re_{di} - 1000)Pr(f_i/2)}{1 + 12.7\sqrt{f_i/2}\left(Pr^{2/3} - 1\right)} \tag{17}$$

where the friction factor is given by:

$$f_i = (1.58 ln Re_{di} - 3.28)^{-2} \tag{18}$$

where $Re_{di} = \rho V_i d_i/\mu$

The overall surface effectiveness (η_o), which is defined as the ratio of effective heat transfer area to total heat transfer area, can be expressed in terms of fin efficiency (η), fin surface area (A_f), and total surface area (A_o), as follows:

$$\eta_o = 1 - \frac{A_f}{A_o}(1 - \eta) \tag{19}$$

The relationship among the total surface area of the fin (A_o), the surface area of the fin (A_f), and (A_b) equals the area of the unfinned base surface (in Fig. 4). It is determined from Eq. (20):

$$A_b = n_t N_{row}\left[\pi d_o L - \left(\sqrt{f_p^2 + (\pi d_o)^2}\right) \times f_t\left(\frac{L}{f_p}\right)\right] \tag{20}$$

The surface area of fin (A_f) can be estimated by assuming it to be equal to that of the radial fin:

$$A_f = n_t N_{row}\left(\frac{L}{f_p}\right)[0.5\pi d_f^2 - 0.5\pi d_o^2 + \pi d_f f_t] \tag{21}$$

where $A_o = A_f + A_b$

The efficiency of a radial fin with a rectangular profile is determined by the method proposed by Gardner [19]:

$$\eta = \frac{2\psi}{\phi(1+\psi)} \frac{I_1(\phi R_o)K_1(\phi R_i) - I_1(\phi R_i)K_1(\phi R_o)}{I_0(\phi R_i)K_1(\phi R_o) + I_1(\phi R_o)K_0(\phi R_i)} \tag{22}$$

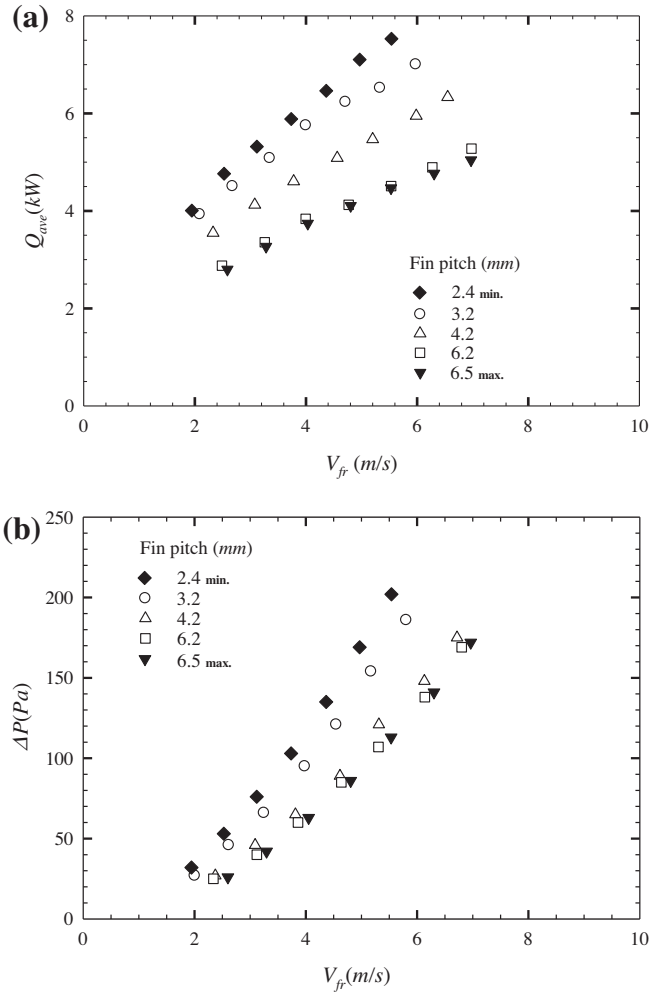

Fig. 8. Effect of fin pitches on (a) the average heat transfer rate and (b) the pressure drop of crimped spiral fin and tube heat exchangers at $T_{w,in}$ = 65 °C and water flow rate of 0.233 kg/s.

Author's personal copy

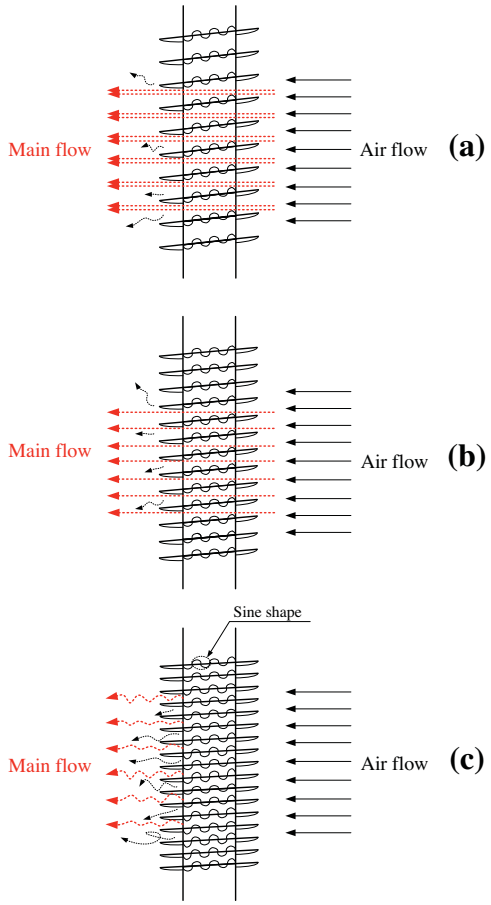

Fig. 9. Schematic showing the flow distribution at fin base of crimped spiral fin (sine shape): (a) f_p = 6.5 and 6.2 mm, (b) f_p = 4.2 mm and (c) f_p = 3.2 and 2.4 mm.

where

$$\phi = (r_o - r_i)^{3/2}\left(\frac{2h_o}{k_f A_p}\right)^{1/2} \tag{23}$$

The air-side heat transfer coefficient (h_o) can then be calculated from Eq. (4). The flow chart with the reduction of the data is shown in Fig. 5.

According to the main purpose of this work, in order to find an optimized fin pitch, the parameter called the performance index must be introduced. In general, the performance index is considered as the ratio of the desired output to the required input. However, there are three performance indexes introduced in this work: the heat exchanger performance index, the system performance index, and the dimensionless system performance index, which can be expressed as below.

The heat exchanger performance index:

$$\zeta_1 = (Q_{ave}/\Delta P)_{HX} \tag{24}$$

which subscript "*HX*" means "heat exchanger".

The system performance index:

$$\zeta_2 = (Q_{ave}/\Delta P)_{Sys} \tag{25}$$

which subscript "*Sys*" means "system".

The dimensionless system performance index:

$$\zeta_3 = (Q_{ave}/W_p)_{Sys} \tag{26}$$

which W_p is fan power.

The pumping (fan) power determined from the equation proposed by Kays and London [20] is given in terms of the fanning friction factor. The equation includes the entrance and exit pressure losses:

$$f = \left(\frac{A_{min}}{A_o}\right)\left(\frac{\rho_m}{\rho_1}\right)\left[\frac{2\Delta P\rho_1}{G_c^2} - (1+\sigma^2)\left(\frac{\rho_1}{\rho_2} - 1\right)\right] \tag{27}$$

where σ is the ratio of minimum free flow area to frontal area, A_o is the total heat transfer area, and A_{min} is the minimum free flow area.

For Eq. (27), if entrance and exit effects are negligible ($\rho_1 = \rho_2$ and $\rho_m = [\rho_1 + \rho_2]/2$), then the friction coefficient can be calculated from

$$f = \frac{A_{min}\rho_m}{A_o}\left[\frac{2\Delta P}{G_c^2}\right] \tag{28}$$

Therefore, the pumping (fan) power is

$$W_p = \frac{G_c A_{min}\Delta P}{\rho_m} \tag{29}$$

The reason for choosing these three performance indexes and how to use them in order to find and optimized the fin pitch will be explained and discussed later in the Results section.

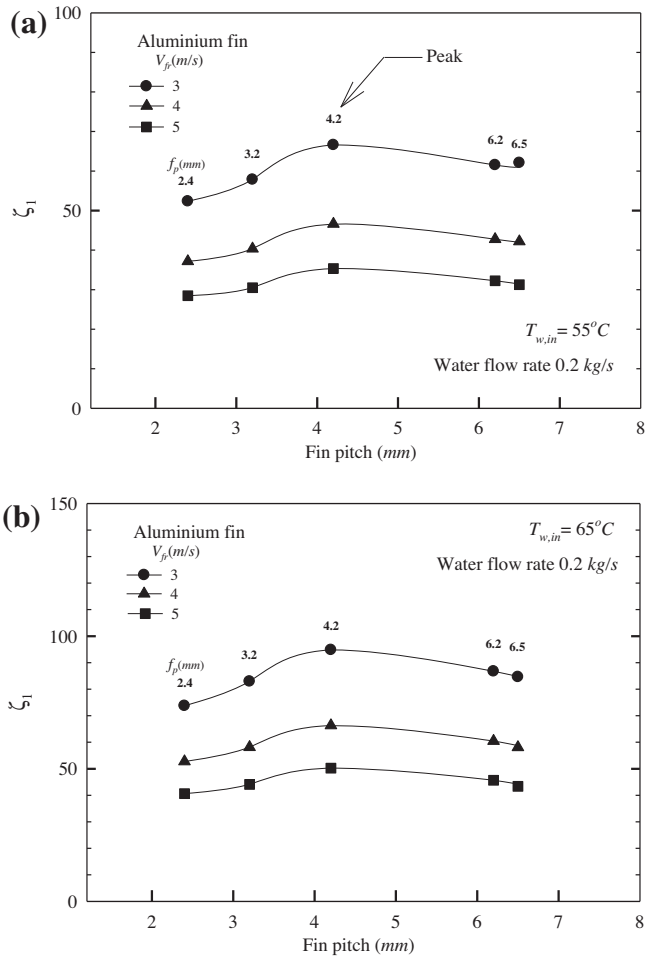

Fig. 10. Effect of fin pitch on the heat exchanger performance index ζ_1 having different inlet-water temperatures (a) 55 °C and (b) 65 °C.

Author's personal copy

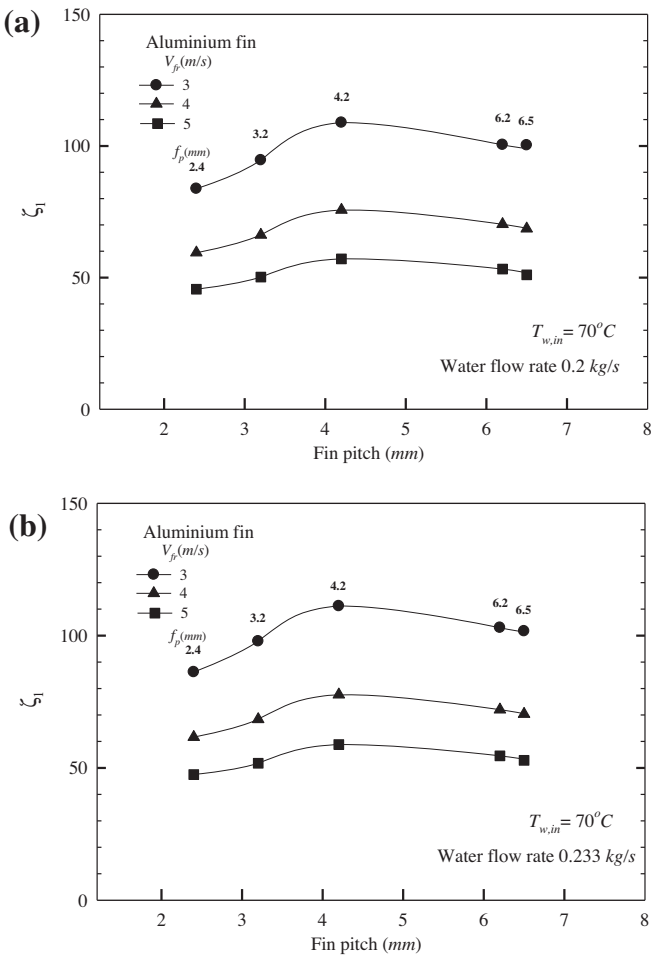

Fig. 11. Effect of fin pitch on the heat exchanger performance index ζ_1 having different water flow rates.

4. Results and discussion

The experimental results of this study are presented based on the energy balances between the air- and water-sides and are used to determine the performance of the crimped spiral fin and tube heat exchangers (Fig. 6). The experiments were conducted following the ANSI/ASHRAE 33 Standards [21] in which the energy unbalance between the air and water of the crimped spiral fin-and-tube heat exchangers, denoting $|Q_a - Q_w|/Q_{ave}$, is less than 0.05. Some experimental data from Pongsoi et al. [4] was also used in this work. The analysis of the heat transfer performance of all the heat exchangers examined are presented in terms of the heat transfer coefficient and pressure drop plotted against the air frontal velocity (V_{fr}). As expected, both the heat transfer and pressure drop increased along with the increasing air frontal velocity. In addition, the experimental results mostly focused on the three performances indexes, ζ_1, ζ_2, and ζ_3, which are important for the analysis of the optimum fin pitch.

Fig. 7 illustrates the effects of fin pitches on the air-side heat transfer coefficient of crimped spiral fin-and-tube heat exchangers having a two-row configuration and fin pitches of 2.4, 3.2, 4.2, 6.2 and 6.5 mm. Test results indicated that the effects of fin pitch on the heat transfer coefficient are very small at 3.2, 4.2, 6.2, and 6.5 mm. In this regard, higher operating velocities promote better mixing and lead to a better heat transfer coefficient, and this phenomenon prevails regardless of a change in the fin pitch. In contrast, for fin pitch 2.4 mm, it can be clearly seen that the heat transfer coefficient lower than other fin pitches, about 11–15% at the same air frontal velocity. This result is similar to that described by Kim and Kim [22] (plate fin or conventional heat exchangers), Mon and Gross [23] (annular fin), and Lee et al. [24] (spiral fin). It is believed to be the result of boundary layer interruption between fin spacing, preventing an increase in heat transfer coefficient. The convection heat transfer coefficient decreases with smaller fin pitches as the boundary layer becomes thicker with a decrease in fin pitch, which can cause easier boundary layer interruption between the fins [24]. However, this phenomenon did not occur at a large fin pitch, as mentioned by Kim and Kim [22].

Fig. 8(a) shows the influence of fin pitches on the average heat transfer rate of crimped spiral fin-and-tube heat exchangers. The average heat transfer rate increases as fin pitch decreases. When f_p decreases from 6.2 mm to 2.4 mm, the average heat transfer rate increases by about <5% (for f_p = 6.2 mm), 27–32% (for f_p = 4.2 mm), 49–55% (for f_p = 3.2 mm), and 65–70% (for f_p = 2.4 mm) to a fin pitch of 6.5 mm over the range of air frontal velocities (2 – 6 m/s). Furthermore, the effects of fin pitch on the average heat transfer rate in case of 6.2 mm and 6.5 mm are negligible. Moreover, Fig. 8(b) shows the effects of fin pitches on the pressure drop of a crimped spiral fin-and-tube heat exchanger. As expected, the pressure drop increases as air frontal velocity increases. Furthermore, using larger fin pitches (i.e., 4.2, 6.2, and 6.5 mm) results in negligible differences in the pressure drop. Over the range of air frontal velocities, it was found that the pressure drops of the f_p = 2.4, 3.2, 4.2, and 6.2 mm are higher than that of the f_p = 6.5 mm by about 78–103%, 52–64%, 11–20% and <8%, respectively. This might be because the main flow at base of the fin can flow along the corrugated channel more effectively compared with smaller fin pitches (i.e., 2.4 mm and 3.2 mm) as illustrated in Fig. 9(a) and (b). On the other hand, the flow distribution at the base of fin (sine shape) in the case of fin pitches of 2.4 mm and 3.2 mm seems to be strongly obstructed by the closer channel of fin pitch as shown in Fig. 9(c), resulting in the highest pressure drop (for f_p = 2.4 mm).

For the optimization of fin pitch, the descriptive analysis is presented for three performances indexes (ζ_1, ζ_2, and ζ_3 These indexes described in this work can be expressed as the ratio of the desired output to the required input, as mention before. However, unlike other thermal systems, the determination of the performance index is too complicated for the heat exchanger. Therefore, in this present work, the performance index will be derived in three terms and will be discussed later in order to determine which one is preferable.

First, the heat exchanger performance index (ζ_1), in which the consideration is a focus only on the heat exchanger section, can be expressed as the ratio of heat absorbed by the air-side to the pressure drop of heat exchanger, which indicates the air flow friction across the heat exchanger. Therefore, (ζ_1) can be described as the performance of the heat exchanger. The effects of fin pitches on the performance index (ζ_1) is shown in Figs. 10 and 11 as having a different inlet-water temperature and a water flow rate, respectively. This figure shows that ζ_1 increases with increasing fin pitch until reaching its maximum value at a fin pitch of 4.2 mm, and then decreases with further increases in the fin pitch. This phenomenon is the same for all air frontal velocity. This might be because by adding fin surface, the flow field is inevitably stabilized, and the contributions of vortices and unstable flow field are also lessened [10]. Moreover, it is commonly known that the pressure drop endures a heat transfer and exhibits a decreasing trend of the heat exchanger performance index with a decreasing fin pitch. The maximum value of ζ_1 means that it is possible to obtain an optimum fin pitch under this criterion when all the other parameters are kept fixed over the range of testing conditions. Actually, using

Author's personal copy

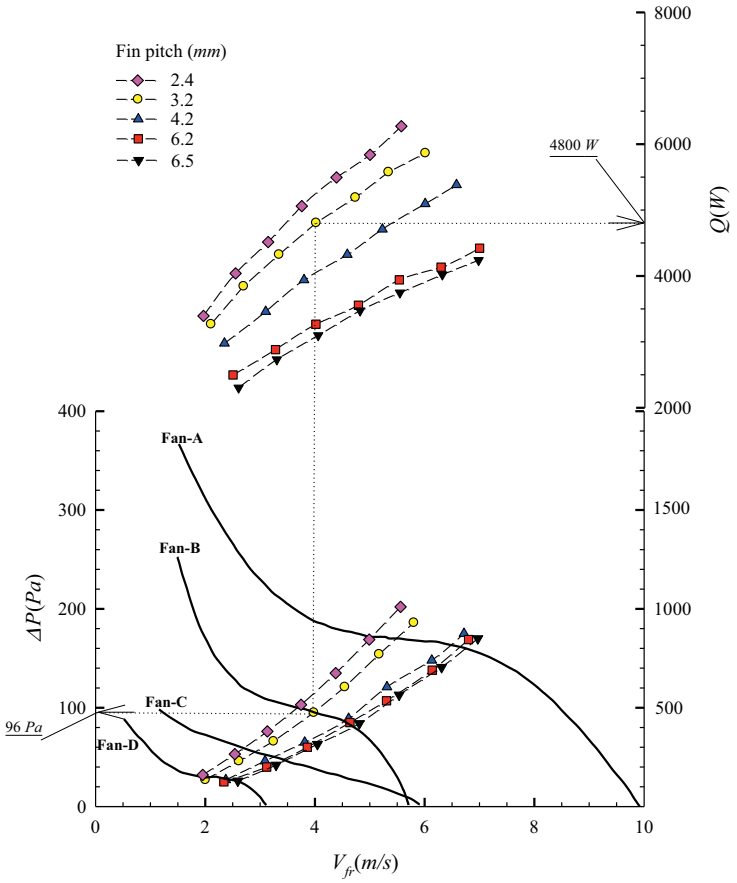

Fig. 12. Axial fan performance curve (P–Q fan curve) with system lines of crimped spiral fin-and-tube heat exchangers having various fin pitches at $T_{w,in}$ = 60 °C and water flow rate of 0.233 kg/s.

a fin pitch higher than 4.2 mm seems to be preferable in terms of production cost because it is cheaper in the sense of having less fin pitch length. However, the value of ζ_1, which is the index to describe the heat exchanger's performance, is relatively lower than that of 4.2 mm. Therefore, it is not recommended to consider only the production cost but also the performance index when designing crimped spiral fin-and-tube heat exchangers.

The next performance index that is derived in this study is the system performance index (ζ_2). Unlike ζ_1, which mainly focuses only in the heat exchanger section, a more advance consideration is developed in order to obtain the performance index that is suitable to describe the whole system, including both the heat exchanger and the pumping fan. Fig. 12 show the axial commercial fan curve fan (P–Q curve) with the system lines of crimped spiral fin-and-tube heat exchangers having various fin pitches. The commercial fan P–Q curve A to D is plotted in Fig. 12, along with the heat exchanger pressure drop, which is referred to as the system line of the heat exchanger. The interception of these two plots could indicate the operating point of heat exchanger. The dashed line in Fig. 12 shows the connection from the operating point to the average heat transfer rate in the case of a fin pitch of 3.2 mm with fan B. The ratio between the average heat transfer rate and the pressure drop at the operating point is introduced as ζ_2. The pressure drop at the operating point obtained for each fin pitch subject to the fan curve is illustrated in Fig. 13(b). Moreover, the obtained average heat transfer rate is also illustrated in Fig. 13(a). In addition, the effect of the fin pitch subject to the actual fan curve on the system performance index is illustrated in Fig. 14. It was found that the system performance index of fin pitches of 2.4, 3.2, and 4.2 mm is similar and significantly higher than those of 6.2 mm and 6.5 mm. The ζ_2 of fin pitch of 2.4, 3.2, and 4.2 mm is generally higher than that of 6.2 mm and 6.5 mm with a maximum discrepancy of about 20% for every fan curve. It is noted that fan A and B is subjected to a high-power fan, and fans C and D are subjected to a low-power fan. The system performance index also decreases with the increasing input power type. The low-power fan gives a higher system performance index than the higher-power one.

Finally, the dimensionless system performance index is introduced. This index is the modification of the system performance index by dividing the average heat transfer rate with pumping (fan) power, which could be expressed as Eq. (30). In the same manner, the dimensionless system performance index could be described as COP for it represents the ratio of the desired heat transfer rate and the provided pumping work. Fig. 15 illustrates the effect of the fin pitch subject to the fan curves on the dimensionless system performance index. Similar to the system performance index, the ζ_3 for a lower-power fan is also greater than that of the higher-power fan. Furthermore, the ζ_3 decreases with increasing fin pitch for all fans. It must be noted that while considering the performance index in term of both ζ_1 and ζ_2, a fin pitch of 4.2 mm seems to be the highest value than that of other cases, illustrating the optimized fin pitch. However, consideration of the performance index in terms of ζ_3 gives an alternate result.

In light of the findings of this study, the value of performance index is validated from the consideration as the ratio of the desired output to the required input, as mentioned above. It can be seen that the fin pitches are key to and directly affect the performance indexes, i.e., the heat exchanger performance index (ζ_1), the system

Author's personal copy

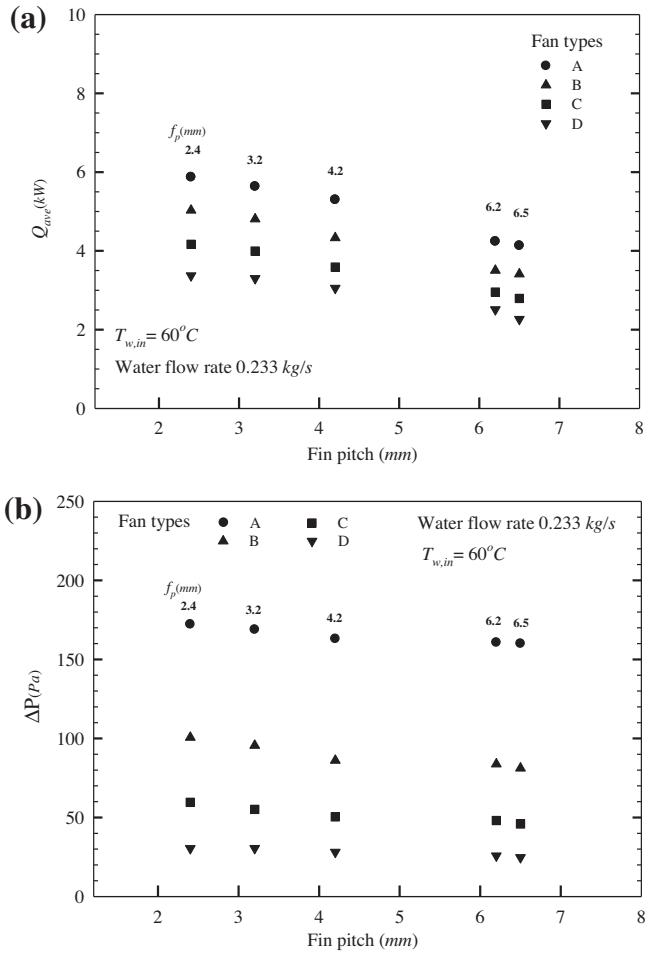

Fig. 13. Effect of fin pitches on (a) the average heat transfer rate and (b) the pressure drop of crimped spiral fin and tube heat exchangers at operating point.

performance index (ζ_2), and the dimensionless system performance index (ζ_3). As the authors have noted, these factors are compared for fin pitches of 2.4, 3.2, 4.2, 6.2, and 6.5 mm in Table 5. It is interesting to note that the fin pitch of 4.2 mm is outstandingly better than other fin pitches. Moreover, as shown in Fig. 16, the results are shown based on the three performance indexes (ζ_1, ζ_2, and ζ_3). This figure can be used to present the optimum fin pitch.

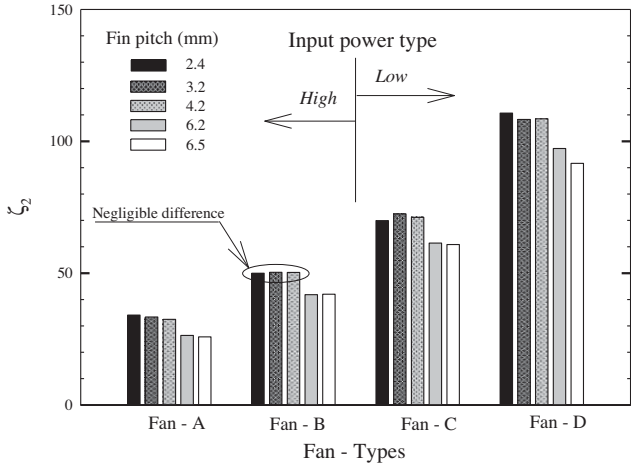

Fig. 14. Effect of fin pitch subjected to fan curve on the performance index ζ_2 at optimum fan operating point ($T_{w,in}$ = 60 °C and water flow rate of 0.233 kg/s).

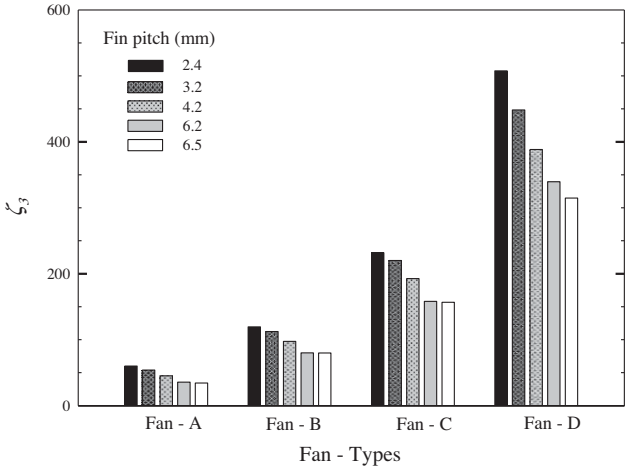

Fig. 15. Effect of fin pitch subjected to pumping (fan) power on the performance index ζ_3 at optimum fan operating point ($T_{w,in}$ = 60 °C and water flow rate of 0.233 kg/s).

Table 5
Characteristics of fin pitch on performances index.

Fin pitches	Heat exchanger performance index (ζ_1)	System performance index (ζ_2)	Dimensionless system performance index (ζ_3)
2.4	Low	High	High
3.2	Low	High	High
4.2*	High*	High*	Intermediate*
6.2	Low	Low	Low
6.5	Low	Low	Low

Note: * Optimum condition.

According to Fig. 16, the intersection area of the three mathematical sets of performance indexes show that the fin pitch of 4.2 mm has good prospects after consideration of each element and of the composition as a whole. Therefore, it is believed that the fin pitch of 4.2 mm is the optimum fin pitch in this study. This report is offered with the expectation that it may be of assistance in designing cost-effective, optimally sized thermal system equipment.

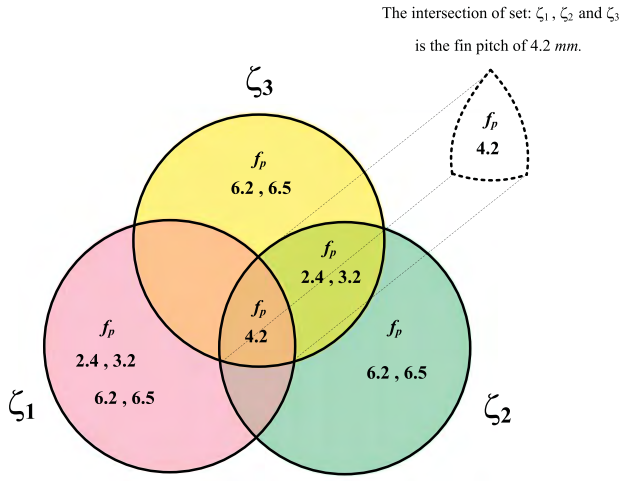

Fig. 16. The intersection of performance index sets defined as the grouping up of the fin pitches.(is the area in the middle of the diagram that represents the intersection point of all two sets and three sets indicating the high and intermediate value of the performance index).

Author's personal copy

5. Conclusion

In this study, an experimental investigation on the optimized fin pitch for crimped spiral fin-and tube-heat exchangers was conducted. The following conclusions based on the tests were obtained:

- It could be clearly seen that the convective heat transfer coefficient (h_o) for a fin pitch of 2.4 mm was relatively low compared to that of the other fin pitches. Furthermore, using larger fin pitches (i.e., 4.2, 6.2, and 6.5 mm) resulted in negligible difference in the pressure drop.
- Three performance indexes are introduced in this work in order to validate the optimum fin pitch. However, the optimum fin pitch obtain by those three are quite different. The heat exchanger performance index (ζ_1) provides the peak value (optimum) at a fin pitch of 4.2 mm, whereas the system performance index (ζ_2) of fin pitches of 2.4, 3.2, and 4.2 mm seem identical. Moreover, the dimensionless system performance index (ζ_3) decreases with increases in the fin pitch.
- Due to the differences in the optimum fin pitch obtained by these performance indexes, the intersection analysis was conducted. The results were that the optimum fin pitch is 4.2 mm (or 6 fins per inch) for this work. Therefore, industrial designers should consider the optimum fin pitch when designing the crimped spiral fin-and-tube heat exchanger.

Acknowledgments

The authors are indebted to the Thailand Research Fund, the Office of the Higher Education Commission and the National Research University Project for supporting this study.

References

[1] A. Nuntaphan, T. Kiatsiriroat, C.C. Wang, Air side performance at low Reynolds number of cross-flow heat exchanger using crimped spiral fins, Int. Commun. Heat Mass Transfer 32 (1–2) (2005) 151–165.
[2] A. Nuntaphan, T. Kiatsiriroat, C.C. Wang, Heat transfer and friction characteristics of crimped spiral finned heat exchangers with dehumidification, Appl. Therm. Eng. 25 (2–3) (2005) 327–340.
[3] K. Srisawad, S. Wongwises, Heat transfer characteristics of a new helically coiled crimped spiral finned tube heat exchanger, Heat Mass Transfer 45 (4) (2009) 381–391.
[4] P. Pongsoi, S. Pikulkajorn, C.C. Wang, S. Wongwises, Effect of fin pitches on the air-side performance of crimped spiral fin-and-tube heat exchangers with a multipass parallel and counter cross-flow configuration, Int. J. Heat Mass Transfer 54 (9–10) (2011) 2234–2240.
[5] P. Pongsoi, S. Pikulkajorn, C.C. Wang, S. Wongwises, Effect of number of tube rows on the air-side performance of crimped spiral fin-and-tube heat exchangers with a multipass parallel and counter cross-flow configuration, International Journal of Heat and Mass Transfer 55 (4) (2012) 1403–1411.
[6] L.H. Tang, G.N. Xie, M. Zeng, M. Lin, Q.W. Wang, A comparative study of fin-and-tube heat exchangers with various fin patterns, ASME Conf. Proc., Heat Transfer Part A and B 4 (2008) 1239–1246.
[7] L.H. Tang, M. Zeng, Q.W. Wang, Experimental and numerical investigation on air-side performance of fin-and-tube heat exchangers with various fin patterns, Exp. Therm. Fluid Sci. 33 (5) (2009) 818–827.
[8] R. Romero-Mendez, M. Sen, K.T. Yang, R. McClain, Effect of fin spacing on convection in a plate fin and tube heat exchanger, Int. J. Heat Mass Transfer 43 (1) (2000) 39–51.
[9] T. Sencic, A. TRP, K. Lenic, Parametric study of operating and geometry characteristics effect on heat transfer in annular finned tube heat exchanger, Eng. Rev. 29 (1) (2009) 25–36.
[10] C.W. Lu, J.M. Huang, W.C. Nien, C.C. Wang, A numerical investigation of the geometric effects on the performance of plate finned-tube heat exchanger, Energ. Convers. Manage. 52 (3) (2011) 1638–1643.
[11] G. Xie, Q. Wang, B. Sunden, Parametric study and multiple correlations on air-side heat transfer and friction characteristics of fin-and-tube heat exchangers with large number of large-diameter tube rows, Appl. Therm. Eng. 29 (1) (2009) 1–16.
[12] Y.C. Liu, S. Wongwises, W.J. Chang, C.C. Wang, Airside performance of fin-and-tube heat exchangers in dehumidifying conditions - Data with larger diameter, Int. J. Heat Mass Transfer 53 (7–8) (2010) 1603–1608.
[13] ASHRAE Handbook Fundamental, American society of heating, Refrigerating and air-conditioning engineers, SI-ed., Inc., Atlanta, chap. 13 (1993) 14–15.
[14] ESDU 86018, Effectiveness-NTU Relations for the design and performance evaluation of two-stream heat exchangers, Engineering science data unit 86018 with amendment, London ESDU International plc, 1991, pp. 92–107.
[15] H.A. Navarro, L. Cabezas-Gomez, A new approach for thermal performance calculation of cross-flow heat exchanger, Int. J. Heat Mass Transfer 48 (2005) 3880–3888.
[16] L. Cabezas-Gomez, H.A. Navarro, J.M. Saiz-Jabardo, Thermal performance of multipass parallel and counter-cross-flow heat exchangers, J. Heat transfer 129 (2007) 282–290.
[17] H.A. Navarro, L. Cabezas-Gomez, Effectiveness-ntu computation with a mathematical model for cross-flow heat exchangers, Braz. J. Chem. Eng. 24 (4) (2007) 509–521.
[18] V. Gnielinski, New eguation for heat and mass transfer in turbulent pipe and channel flow, Int. Chem. Eng. 16 (1976) 359–368.
[19] K.A. Gardner, Efficient of extended surface, ASME Trans. 67 (1945) 621.
[20] W.M. Kays, A. London, Compact Heat Exchangers, third ed., Mcgraw-Hill, New York, 1984.
[21] ANSI/ASHRAE Standard 33-2000, Method of Testing Forced Circulation Air Cooling and Air Heating Coils, 2000.
[22] Y.H. Kim, Y. Kim, Heat transfer characteristics of flate plate finned-tube heat exchangers with large fin pitch, Int. J. Refrig. 28 (6) (2005) 851–858.
[23] M.S. Mon, U. Gross, Numerical study of fin-spacing effects in annular-finned tube heat exchangers, Int. J. Heat Mass Transfer 47 (8–9) (2004) 1953–1964.
[24] M. Lee, T. Kang, Y. Kim, Air-side heat transfer characteristics of spiral-type circular fin- tube heat exchangers, Int. J. of Refrig. 33 (2) (2010) 313–320.

International Communications in Heat and Mass Transfer 39 (2012) 1165–1168

Contents lists available at SciVerse ScienceDirect

International Communications in Heat and Mass Transfer

journal homepage: www.elsevier.com/locate/ichmt

On the thermal cooling of central processing unit of the PCs with vapor chamber ☆

Paisarn Naphon [a,*], Somchai Wongwises [b], Songkran Wiriyasart [a]

[a] Thermo-Fluids and Heat Transfer Enhancement Lab. (TFHT), Department of Mechanical Engineering, Faculty of Engineering, Srinakharinwirot University, 63 Rangsit-Nakhornnayok Rd., Ongkharak, Nakhorn-Nayok, 26120, Thailand

[b] Fluid Mechanics, Thermal Engineering and Multiphase Flow Research Lab. (FUTURE), Department of Mechanical Engineering, King Mongkut's University of Technology Thonburi, 91 Suksawas 48, Bangmod, Bangkok 10140, Thailand

ARTICLE INFO

Available online 20 July 2012

Keywords:
Vapor chamber
Electronics cooling
Central processing unit

ABSTRACT

An experimental investigation on the thermal cooling of vapor chamber for cooling computer processing unit of the personal computer is performed. Two different configurations of the vapor chambers with de-ionized water as working fluid are tested under the real operating conditions of PCs. Parametric studies including different aspect ratios, fill ratios, and operating conditions of PC on the CPU temperature are considered. It was found that the vapor chamber cooling technique has significant effect on the thermal cooling of CPU. Average CPU temperatures obtained from the vapor chamber cooling system are 4.1%, 6.89% lower than those from the conventional cooling system for no load and 90% operating loads, respectively. In additional, this cooling system requires 6.89%, 10.53% lower energy consumption for no load and 90% operating loads, respectively. The results of this study are of technological importance for the efficient design of cooling systems of the personal computers or electronic devices to enhance cooling performance.

© 2012 Elsevier Ltd. All rights reserved.

1. Introduction

Higher performance processor will have larger heat generation. In order to ensure reliable operation, therefore, the PCs or electronics devices must be operated in the specific temperature ranges. For effective cooling the heat must spread to a larger surface area and away from the processor, as there is usually restricted space available in the vicinity of the processor. The best known device for effective heat transfer with lowest thermal resistance is vapor chamber. The heat transfer characteristics of the vapor chamber have been widely studied by researchers. Hsieh et al. [1] analyzed the thermal resistance of vapor chamber heat sink with and without pillar for electronic cooling. Hu and Tang [2] investigated the flow and thermal characteristics of a microphase-change cooling system with a microgroove evaporator. The results indicated that the liquid fill ratio has a significant influence on thermal resistance in the cooling system. Liu et al. [3] investigated startup of a novel two-phase cooling loop. Wang et al. [4] studied the micro-capillary pumped loop system for a cooling high-power device. Xie et al. [5] experimentally investigated a novel high-performance integrated heat pipe–heat sink for high-flux chip cooling. Hsieh et al. [6] examined the spreading thermal resistance of a flat vapor chamber. Vin and Astrain [7] studied the development of a thermoelectric refrigerator with two-phase thermosyphons. Chang et al. [8] experimentally investigated the effects of the evaporation surfaces, fill ratios of working fluid and input heating powers on the thermal performance of the heat pipe cooling system with the thermal resistance model. Chen et al. [9] presented a numerical investigation of a plate-fin heat sink embedded with a vapor chamber, subject to the influence of concentrated heat sources. Zhang et al. [10] numerically and experimentally investigated the flat two-phase thermosyphon. Ma et al. [11] developed an innovative one-side actuating piezoelectric micropump to drive liquid in a cooling system for a laptop. Vasiliev et al. [12] studied the loop heat pipe for cooling of high-power electronic components. Ming et al. [13] experimentally and numerically investigated the grooved vapor chamber. Khandekar et al. [14] investigated the multiple quasi-steady states in a closed loop pulsating heat pipe. Orian et al. [15] predicted the heat transfer coefficients for calculations of various heat and mass transfer processes. Kang et al. [16] experimentally investigated the nanofluids on sintered heat pipe thermal performance. Tsai et al. [17] experimentally investigated the effects of heat source, fill ratio of working fluid, and evaporator surface structure on the thermal performance of the vapor chamber. Wang et al. [18] considered the thermal performance of the vapor chamber for the high-power LEDs. Wong et al. [19] studied a novel vapor chamber with inner groove surface. Wang et al. [20] analyzed the thermal characteristics for board-level high-performance package equipped with vapor chamber. Li et al. [21,22] investigated effects of the width, height and number of fins and of the Reynolds number on the thermal performance and surface temperature distributions of vapor chamber. Harmand et al. [23] presented a theoretical investigation of a flat heat pipe for cooling electronic components. Wang et al. [24] analyzed the pressure-difference phenomenon between the condensing and boiling sections of a heat pipe. Reyes et al. [25]

☆ Communicated by W.J. Minkowycz.

* Corresponding author.
E-mail address: paisarnn@swu.ac.th (P. Naphon).

0735-1933/$ – see front matter © 2012 Elsevier Ltd. All rights reserved.
doi:10.1016/j.icheatmasstransfer.2012.07.013

experimentally and theoretically studied the vapor chamber based heat spreader. Naphon and Wongwises [26] studied the jet nanofluids impingement system for cooling computer processing unit. Attia and El-Assal [27] experimentally investigated of the effects of different working fluids, different charge ratios on the thermal performance of the vapor chamber. Ji et al. [28] studied the vapor chamber performance with sintering the copper foams pieces. Choi et al. [29] studied a new CPU cooler design based on an active cooling heat sink combined with heat pipes.

As mentioned above, the numerous papers presented the study on the heat transfer characteristics of the vapor chamber. However, the trend of the processor performance and heat dissipation increased significantly every year. Heat dissipation increased but in contrary the size of the processor reduced and thus the heat flux is critically high. In 2000, the heat flux is about 10–15 W/cm^2 and could reach over 150 W/cm^2 by year 2012. The purpose of this paper is to study the thermal cooling of central processing unit of personal computers with the vapor chamber. As compared to other cooling devices such as fans, thermoelectric module, liquid pump loop device, the vapor chamber cooling technique has simple structures, has no moving parts and does not use electricity. In addition, selection of the working fluid is based on the operating temperature of the application. For computer application, the operating temperatures are normally between 50 and 100 °C. Effects of operating condition of PC, the fill ratio, and aspect ratio on the CPU temperature and energy consumption are considered.

2. Experimental apparatus and method

The test loop consists of a set of PC, a set of vapor chamber cooling system and data acquisition system. A schematic diagram of the vapor chamber cooling system is shown in Fig. 1. The vapor chamber cooling system consists of the vapor chamber, heat sink unit, and axial fan unit. The details of the vapor chamber are listed as shown in Table 1. The schematic diagram of the vapor chamber unit is shown in Fig. 2. The vapor chamber is fabricated from copper plate which consists of bottom copper plate, wick sheet, sinter column, and top copper plate. The wick sheet and the sinter column are fabricated from the copper powder. The bottom copper plate is the evaporator section that may be mounted on CPU of the PC to absorb the

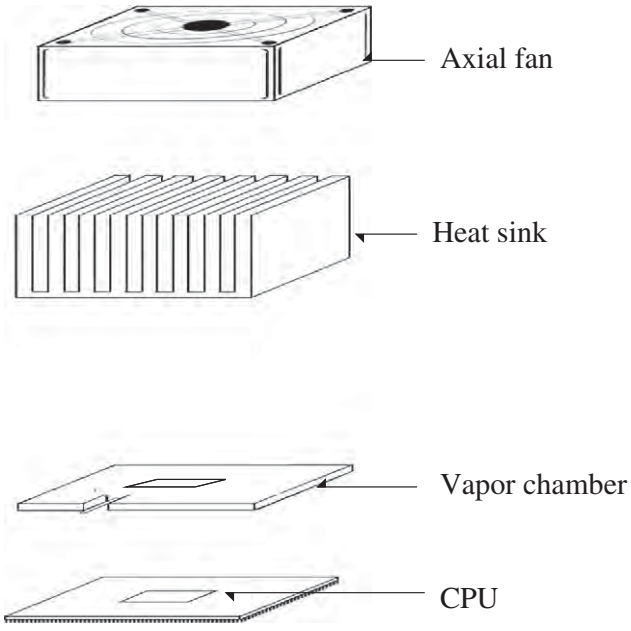

Fig. 1. Schematic diagram of the vapor chamber cooling system.

Table 1
Details of the vapor chambers.

Vapor chamber	Vapor chamber size (mm*mm*mm)	Fill ratio	Copper plate size (mm*mm*mm)
Model A	–	–	60*60*3.8
Model B	32*32*2.2	10%	60*60*3.8
Model C	32*32*2.2	20%	60*60*3.8
Model D	56.8*56.8*2.2	20%	60*60*3.8

generated heat, and the other is the condenser section which heat is transferred to heat sink and air, respectively. In order to minimize thermal resistance between the CPU-vapor chamber, vapor chamber heat sink unit, a thin film of high thermal conductivity grease is applied at their junction interface. There are two vapor chambers with different aspect ratio (CPU surface area to bottom plate surface area) that are tested in the present study. The working fluid (de-ionized water) is evaporated on the heated side and condensed on the cooling side and then returns to the evaporator section under gravity. Type T copper-constantan thermocouples with an accuracy of 0.1% of full scale are employed to measure the temperatures. Four type T copper-constantan thermocouples are applied to measure the vapor chamber temperature. One thermocouple is applied to observe the ambient temperature. A groove within the chamber walls is machined and the high conductivity cement is utilized to embed the thermocouples within the chamber wall. The CPU temperature is measured by two type T copper-constantan thermocouples. All thermocouples are pre-calibrated with dry box temperature calibrator.

Experiments were conducted with various fill ratios, aspect ratios and operating condition of PC. The supplied load into the CPU was adjusted to achieve the desired level by setting the operating conditions of PC: no load and 50% and 90% operating loads. The energy consumption of the PC was measured by the watt-hour meter with an accuracy of 0.2% of full scale. The temperatures at each position and energy consumption were recorded in the period time of 200 min. Data collection was carried out using a data acquisition system (DataTaker).

3. Results and discussion

Initially experiments are performed with the conventional cooling system (copper plate) which forms the basis for comparison of the results with vapor chamber cooling technique. After installing all components, the experiments are performed with different vapor chamber models, different fill ratios and under different operating conditions of personal computer. Fig. 3 shows the variation of the CPU temperature for different operating loads. Model A represents the cooling system in the sensible heat term (copper plate) while others represent the conventional cooling system in the latent heat term (vapor chamber). It can be seen that the CPU temperatures obtained from three vapor chamber models are similar to the one from the conventional cooling system. Model A, which represents the conventional cooling system with copper plate, gives the highest CPU temperature among all the models. This is because the latent heat term has significant effect on the thermal cooling of the CPU. In addition, the CPU temperature rapidly increases as the operating condition load increases. However, this effect becomes relatively less as the operating load >50%.

Fig. 4 shows the variation of the CPU temperature for different models. The total volume of the vapor chamber for the present study is measured to be about 8000 ml. The heat phenomenon by working fluid in the vapor chamber, the working fluid absorbs heat from heat source (CPU) and evaporates in the evaporator (bottom plate). The evaporating fluid moves toward the condenser, and then condenses in the condenser (top plate). For a given operating load and aspect ratio, it can be seen that model C with fill ratio of 20%

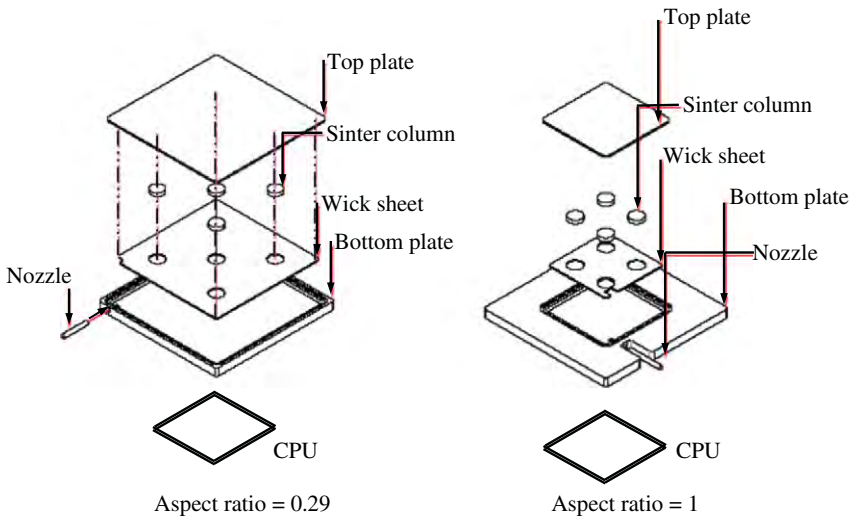

Fig. 2. Schematic diagram of the vapor chamber details.

gives the CPU temperature lower than those from model B with fill ratio of 10%. It may be due to low fill ratio, and the dry out phenomenon might happen. The condensing liquid cannot promptly reflow at this operating load. Therefore, model B gives the CPU temperatures higher than those from model C. In addition, effect of aspect ratio (CPU surface area to bottom plate surface area) on the CPU temperature is also shown in Fig. 4. For model C, there is only the thin liquid film in the heat input region. For model D, however, due to the local boiling and the effect of capillary pressure of the vapor chamber, the liquid film at the heat input region is much thinner than that at the other region (heat input region outside). The thermal resistance of the phase change heat transfer will also increase with the thickness of the liquid film. For a given fill ratio, therefore, model C with an aspect ratio of 1 gives the CPU temperature lower than those from model D with an aspect ratio of 0.29.

The total thermal resistance of the vapor chamber cooling technique is the summation of the contact resistance, the evaporation resistance, the condensation resistance, and the convection resistance. For the same operating condition of PC, the thermal resistance for the CPU with the conventional cooling technique and with the vapor chamber cooling technique is expressed as

$$R_{con} = \frac{T_{CPU,con} - T_{ambient}}{Q} \tag{1}$$

$$R_{vc} = \frac{T_{CPU,vc} - T_{ambient}}{Q} \tag{2}$$

The thermal resistance ratio can be written as

$$\frac{R_{vc}}{R_{con}} = \frac{T_{CPU,vc} - T_{ambient}}{T_{CPU,con} - T_{ambient}} \tag{3}$$

Fig. 5 shows the variation of the thermal resistance ratio for different models and different operating loads. At a lower operating load, the heat is mainly transferred through natural convection. The increasing operating load induces a larger superheat, which activates and intensifies nucleate boiling and consequently leads to higher heat transfer efficiency. Therefore, the thermal resistance at higher operating load condition is higher than those at lower operating load condition. In addition, the thermal resistance with the conventional cooling technique is higher than those with the vapor chamber cooling technique which corresponds to the variation of the CPU temperature as mentioned above.

The CPU temperature and the energy consumption obtained from 20% fill ratio of the vapor chamber cooling system are compared with those from the conventional liquid cooling system for the operating time of 200 min. It can be seen from Table 2 that the CPU

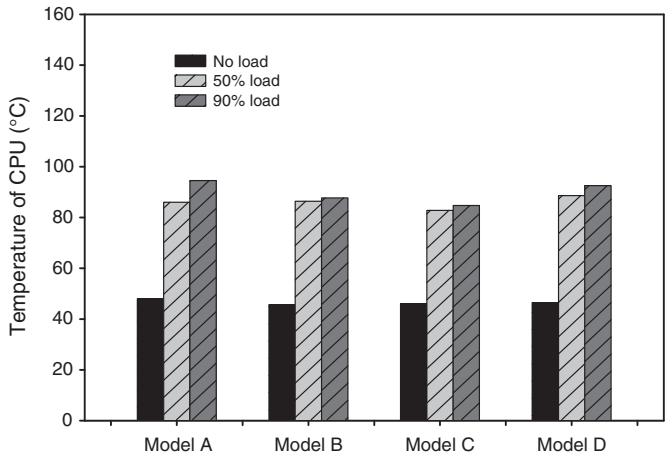

Fig. 3. Variations of CPU temperature for different models of vapor chamber.

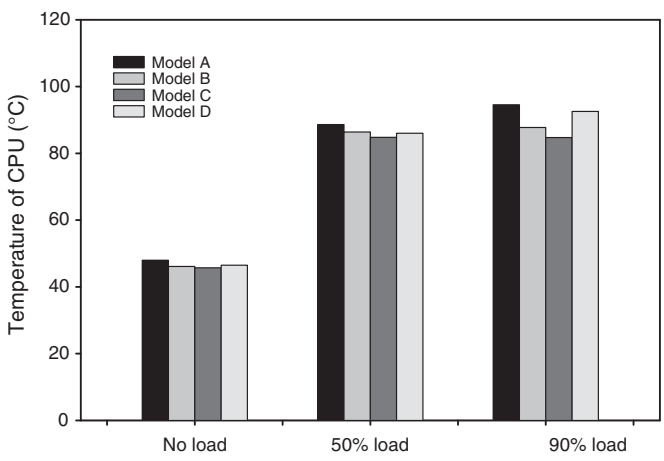

Fig. 4. Variations of CPU temperature for different operating conditions of PC.

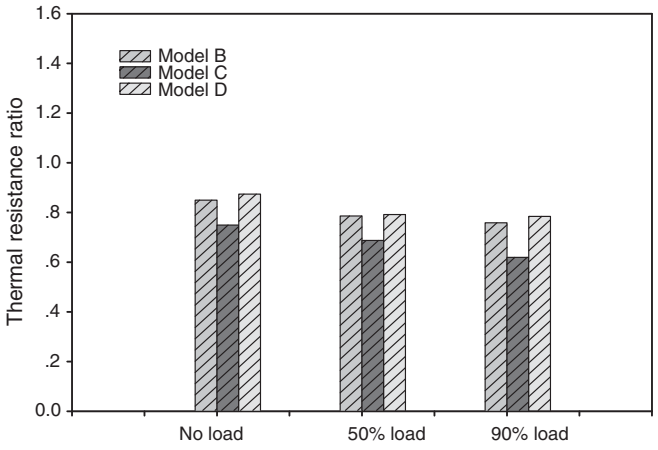

Fig. 5. Variations of thermal resistance ratio for different operating conditions of PC.

temperatures obtained from the vapor chamber cooling system are 4.1%, 6.89% lower than those from the conventional cooling system for no load and 90% operating loads, respectively. In addition, the energy consumption also decreases 6.89%, 10.53% for no load and 90% operating loads, respectively.

4. Conclusions

The space limitation, air cooling limitation and high level of the generated heat are the encountered problems of the cooling system development of the CPU or electronic devices. The vapor chambers have many advantages as compared to other cooling devices such as fans, thermoelectric module, liquid pump loop device: it has simple structures, has no moving parts and does not use electricity. In addition, selection of the working fluid is based on the operating temperature range of the applications. It is found that the CPU temperatures and the energy consumption of the CP obtained from the vapor chamber cooling system are lower than those from the conventional liquid system. The results of this study are expected to lead to guidelines that will allow the design of a cooling system with improved thermal cooling performance for ensuring that these devices are in the specific temperature ranges.

Acknowledgements

The authors would like to express their appreciation to the Excellent Center for Sustainable Engineering (ECSE) of the Srinakharinwirot University (SWU) and the King Mongkut's University of Technology Thonburi (KMUTT) for providing financial support for this study. The authors also wish to acknowledge Fujikura Electronics (Thailand) Ltd. for their assistance in some of the vapor chamber samples.

Table 2
Comparison of the CPU temperature and the energy consumption between the conventional cooling system and 20% fill ratio of the vapor chamber cooling system.

Cooling techniques	CPU temperature (°C)	Energy consumption (W·h)
No load operating condition with the conventional cooling system	47.5	150
No load operating condition with vapor chamber cooling system	45.6	140
Full load operating condition with the conventional cooling system	94.5	300
Full load operating condition with vapor chamber cooling system	88.2	270

References

[1] S.S. Hsieh, R.Y. Lee, J.C. Shyu, S.W. Chen, Analytical solution of thermal resistance of vapor chamber heat sink with and without pillar, Energy Conversion and Management 48 (2007) 2708–2717.
[2] X. Hu, D. Tang, Experimental investigation on flow and thermal characteristics of a microphase-change cooling system with a microgroove evaporator, International Journal of Thermal Sciences 46 (2007) 1163–1171.
[3] J. Liu, N.Q. Pei, K.H. Guo, Z.H. He, T.X. Li, J.M. Gu, Experimental investigation on startup of a novel two-phase cooling loop, Experimental Thermal and Fluid Science 32 (2008) 939–946.
[4] C.T. Wang, T.S. Leu, T.M. Lai, Micro capillary pumped loop system for a cooling high power device, Experimental Thermal and Fluid Science 32 (2008) 1090–1095.
[5] X.L. Xie, Y.L. He, W.Q. Tao, H.W. Yang, An experimental investigation on a novel high-performance integrated heat pipe–heat sink for high-flux chip cooling, Applied Thermal Engineering 28 (2008) 433–439.
[6] S.S. Hsieh, R.Y. Lee, J.C. Shyu, S.W. Chen, Thermal performance of flat vapor chamber heat spreader, Energy Conversion and Management 49 (2008) 1774–1784.
[7] J.G. Vin, D. Astrain, Development of a thermoelectric refrigerator with two-phase thermosyphons and capillary lift, Applied Thermal Engineering 28 (2008) 1514–1521.
[8] Y.W. Chang, C.H. Cheng, J.C. Wang, S.L. Chen, Heat pipe for cooling of electronic equipment, Energy Conversion and Management 49 (2008) 3398–3404.
[9] Y.S. Chen, K.H. Chien, T.C. Hung, C.C. Wang, Y.M. Ferng, B.S. Pei, Numerical simulation of a heat sink embedded with a vapor chamber and calculation of effective thermal conductivity of a vapor chamber, Applied Thermal Engineering 29 (2009) 2655–2664.
[10] M. Zhang, Z. Liu, G. Ma, S. Cheng, Numerical simulation and experimental verification of a flat two-phase thermosyphon, Energy Conversion and Management 50 (2009) 1095–1100.
[11] H.K. Ma, B.R. Chen, J.J. Gao, C.Y. Lin, Development of an OAPCP-micropump liquid cooling system in a laptop, International Communications in Heat and Mass Transfer 36 (2009) 225–232.
[12] L. Vasiliev, D. Lossouarn, C. Romestant, A. Alexandre, Y. Bertin, Y. Piatsiushyk, V. Romanenkov, Loop heat pipe for cooling of high-power electronic components, International Journal of Heat and Mass Transfer 52 (2009) 301–308.
[13] Z. Ming, L. Zhongliang, M. Guoyuan, The experimental and numerical investigation of a grooved vapor chamber, Applied Thermal Engineering 29 (2009) 422–430.
[14] S. Khandekar, A.P. Gautam, P.K. Sharma, Multiple quasi-steady states in a closed loop pulsating heat pipe, International Journal of Thermal Sciences 48 (2009) 535–546.
[15] G. Orian, M. Jelinek, A. Levy, Heat transfer to sub-cooled binary solution in horizontal tube, Applied Thermal Engineering 29 (2009) 661–669.
[16] S.W. Kang, W.C. Wei, S.H. Tsai, C.-C. Huang, Experimental investigation of nanofluids on sintered heat pipe thermal performance, Applied Thermal Engineering 29 (2009) 973–979.
[17] T.E. Tsai, H.H. Wu, C.C. Chang, S.L. Chen, Two-phase closed thermosyphon vapor-chamber system for electronic cooling, International Communications in Heat and Mass Transfer 37 (2010) 484–489.
[18] J.C. Wang, R.T. Wang, T.L. Chang, D.S. Hwang, Development of 30 watt high-power LEDs vapor chamber-based plate, International Journal of Heat and Mass Transfer 53 (2010) 3990–4001.
[19] S.C. Wong, K.C. Hsieh, J.D. Wu, W.L. Han, A novel vapor chamber and its performance, International Journal of Heat and Mass Transfer 53 (2010) 2377–2384.
[20] T.H. Wang, C.C. Lee, Y.S. Lai, Thermal characteristics evaluation for board-level high performance flip-chip package equipped with vapor chamber as heat spreader, Microelectronic Engineering 87 (2010) 2463–2467.
[21] H.Y. Li, M.H. Chiang, C.I. Lee, W.J. Yang, Thermal performance of plate-fin vapor chamber heat sinks, International Communications in Heat and Mass Transfer 37 (2010) 731–738.
[22] H.Y. Li, M.H. Chiang, Effects of shield on thermal-fluid performance of vapor chamber heat sink, International Journal of Heat and Mass Transfer 54 (2011) 1410–1419.
[23] S. Harmand, R. Sonan, M. Fakès, H. Hassan, Transient cooling of electronic components by flat heat pipes, Applied Thermal Engineering 31 (2011) 1877–1885.
[24] R.T. Wang, J.C. Wang, Analyzing the pressure-difference phenomenon between the condensing and boiling sections in a heat pipe cooling system, International Communications in Heat and Mass Transfer 39 (2012) 390–398.
[25] M. Reyes, D. Alonso, J.R. Arias, A. Velazquez, Experimental and theoretical study of a vapour chamber based heat spreader for avionics applications, Applied Thermal Engineering 37 (2012) 51–59.
[26] P. Naphon, S. Wongwises, Experimental study of jet nanofluids impingement system for cooling computer processing unit, Journal of Electronics Cooling and Thermal Control 1 (2012) 1–7.
[27] A.A.A. Attia, B.T.A. El-Assal, Experimental investigation of vapor chamber with different working fluids at different charge ratios, Ain Shams Engineering Journal (in press).
[28] X. Ji, J. Xu, A.M. Abanda, Copper foam based vapor chamber for high heat flux dissipation, Experimental Thermal and Fluid Science 40 (2012) 93–102.
[29] J. Choi, M. Jeong, J. Yoo, M. Seo, A new CPU cooler design based on an active cooling heat sink combined with heat pipes, Applied Thermal Engineering 44 (2012) 50–56.

Send Orders of Reprints at reprints@benthamscience.org

Current Nanoscience, 2012, *8*, 949-969

Forced Convective Heat Transfer of Nanofluids - A Review of the Recent Literature

A.S. Dalkilic[a,*], N. Kayacı[a], A. Celen[a], M. Tabatabaei[a], O. Yıldız[a], W. Daungthongsuk[b] and S. Wongwises[c,d]

[a]*Heat and Thermodynamics Division, Department of Mechanical Engineering, Yildiz Technical University, Yildiz, Istanbul, 34349, Turkey;* [b]*Department of Mechanical Engineering, Faculty of Engineering, South-East Asia University,* [c]*Fluid Mechanics, Thermal Engineering and Multiphase Flow Research Lab. (FUTURE), Department of Mechanical Engineering, Faculty of Engineering, King Mongkut's University of Technology Thonburi, Bangmod, Bangkok, 10140, Thailand;* [d]*The Academy of Science, The Royal Institute of Thailand, Sanam Suea Pa, Dusit, Bangkok 10300, Thailand*

Abstract: The forced convection of fluids has been investigated by numerous researchers, both experimentally and numerically. A good understanding of characteristics of nanofluid flowhas thoroughly been investigated in these studies. Since the nanoparticles behave more like a single-phase fluid than a solid–liquid mixture, it is assumed that nanofluids are ideally suited in the applications as their usage causes little or no penalty in pressure drop. In recent years, many researchers have tried to fill the gaps on this subject in the literature. To meet the demand for improving the performance of heat transfer equipment, re-examination of the individual components is considered to be essential. The addition of the nanoparticles to the base fluid is one of the significant issues for the optimal performance of heat transfer systems. This paper reports on most of the forced convective heat transfer literature occurring both in-tubes and in-channels regarding the use and preparation of nanofluids. The peer reviewed papers published in citation index journals up to 2012 have been selected for review in the paper. Classification of the papers has been performed according to the publication years. The critical information on the theoretical, experimental and numerical works is presented comprehensively for each paper.

Keywords: Nanofluids, ultrafine, effective thermal conductivity, effective viscosity, forced convective heat transfer.

1. INTRODUCTION

Performance of heat transfer equipment can be improved with studies related to a significant increase in heat flux and miniaturization. In many industrial applications such as power generation, microelectronics, heating processes, cooling processes and chemical processes, water, mineral oil and ethylene glycol are used as heat transfer fluid. Effectiveness and high compactness of heat exchangers are obstructed by the lower heat transfer properties of these common fluids as compared to most solids. It is obvious that solid particles having thermal conductivities several hundred times higher than these conventional fluids must be used in the heat transfer applications. To improve thermal conductivity of a fluid, suspension of ultrafine solid particles in the fluid can be acreative idea. Different types of particles (metallic, non-metallic and polymeric) can be added into fluids to form slurries. Due to the fact that sizes of these suspended particles are in the millimeter or even micrometer scale, some serious problems such as the clogging of flow channels, erosion of pipelines and an increase in pressure drop can occur. Moreover, they often suffer from rheological and instability problems. Especially, the particles tend to settle rapidly. For that reason, though the slurries have better thermal conductivities but they are not practical.

Many published articles show that the heat transfer coefficient of nanofluids is much higher than the common-base fluid giving little or no penalty in pressure drop. The main reasons for the heat transfer enhancement of the nanofluids may roughly be listed as follow: the suspended nanoparticles increase the thermal conductivity of the fluids, and the chaotic movement of ultrafine particles increases fluctuation and turbulence of the fluids that accelerates the energy exchange process. Furthermore, that the numerous correlations for single-phase fluid have clearly failed to predict the heat transfer coefficients of nanofluids that might have been caused by the complicated phenomena coexisting in the main flow. However, some sophisticated correlations for predicting the heat transfer performance of nanofluids have been established. At present, the uses of the nanofluids are still in early stages of development. Therefore, urgent theoretical and experimental research works is needed to clearly understand and accurately predict their hydrodynamic and thermal characteristics. Generally, many researchers indicated that nanofluids behave like pure fluids because the suspended particles are ultra-fine. However, at present, no formulated advanced theory exists to explain the behavior of nanofluids by considering them as multi-component materials. Moreover, several attempts have been discussed to determine the physical properties of nanofluids in the literature. They are shown in Table **1** for their dynamic viscosity [1-7] and Table **2** for their thermal conductivity [8-19]. It should be noted that there are some deviations among the results which will be obtained from the correlations in Tables **1** and **2**.

*Address correspondence to this author at the Heat and Thermodynamics Division, Department of Mechanical Engineering, Yildiz Technical University, Yildiz, Istanbul, 34349, Turkey; Tel: +9 0212 2597070;
Fax: +9 0212 2616659; E-mail: dalkilic@yildiz.edu.tr

2. EXPERIMENTAL APPROACH

The heat transfer coefficient of the nanofluids can be calculated as follows:

$$Nu_{nf} = \frac{h_{nf} D}{k_{nf}} \tag{1}$$

$$h_{nf} = \frac{q}{T_w - T_f} \tag{2}$$

In the literature, the experimental results usually show that the flow velocity and volume fraction affected the convective heat transfer coefficient of the nanofluids as well as being higher than the base fluid at the same conditions. The Nusselt number of thenanofluid with 2% volume fraction of Cu particles can be 60% higher as compared to water. Moreover, at various volume fractions the Dittus-Boelter equation is not valid for the prediction of the Nusselt number of the nanofluids. According to experimental data, new heat transfer correlations, for the prediction of the heat transfer coefficient of nanofluids flowing in a tube, have been given by Qiang and Yimin [20] in the following forms for laminar and turbulent flows respectively:

$$Nu_{nf} = 0.4328\left(1.0 + 11.285\phi^{0.754} Pe_d^{0.218}\right) \mathrm{Re}_{nf}^{0.333} \mathrm{Pr}_{nf}^{0.4} \tag{3}$$

1875-6786/12 $58.00+.00 © 2012 Bentham Science Publishers

Table 1. Some Dynamic Viscosity and Specific Heat Correlations of Nanofluids in Recent Literature

Researcher	Correlation
Putra *et al*. [1]	$\mu_{nf}=2.9*10^{-7}*T^2-2*10^{-4}*T+3.4*10^{-2}$ For % 1 $\mu_{nf}=3.4*10^{-7}*T^2-2.3*10^{-4}*T+3.9*10^{-2}$ For % 4
Tang *et al*. [2]	$\mu_{nf}=2.761*10^{-6}*e^{1713/T}$
Tseng and Chen [3]	$\mu_{nf} = \mu_{bf} x\,0,4513 e^{0,6965\phi}$
Chen *et al*. [4]	$\mu_{nf} = \mu_{bf}\left[1+10,6\phi+(10,6\phi)^2\right]$
Nguyen *et al*. [5]	$\mu_{nf} = \mu_{bf} x\,0,904 e^{0,1482\phi}$ $\mu_{nf} = \mu_{bf}(1 + 0,025\phi + 0,015\phi^2)$
Khanafer and Vafai [6]	$\mu_{nf} = \mu_{bf}(1,0538 + 0,1448\phi_p - 3,363x10^{-3} T - 0,0147\phi_p + 6,735x10^{-5} T^2 - 1,337\frac{\phi_p}{T})$
Duanghongsuk and Wongwises [7]	$\mu_{nf} = \mu_{bf}(1,013 + 0,092\phi_p + 0,015\phi_p^2)$

$$Nu_{nf} = 0.0059\left(1.0 + 7.6286\phi^{0.6886} Pe_d^{0.001}\right)\mathrm{Re}_{nf}^{0.9238}\,\mathrm{Pr}_{nf}^{0.4} \quad (4)$$

Where, Nu is the Nusselt number, Pe the Peclet number, Re the Reynolds number, and Pr the Prandtl number.

$$\mathrm{Pe}_d = \frac{u_m d_p}{\alpha_{nf}} \quad (5)$$

$$\mathrm{Re}_{nf} = \frac{u_m D}{\upsilon_{nf}} \quad (6)$$

$$\text{And } \mathrm{Pr}_{nf} = \frac{\upsilon_{nf}}{\alpha_{nf}} \quad (7)$$

To calculate Pe and Pr parameters, the thermal diffusivity of the nanofluid can be defined as follows:

$$\alpha_{nf} = \frac{k_{nf}}{\left(\rho C_p\right)_{nf}} = \frac{k_{nf}}{(1-\phi)\left(\rho C_p\right)_f + \phi\left(\rho C_p\right)_d} \quad (8)$$

In the view of the pressure drop, the results show that the friction factor of the nanofluid being almost equal to those of water under the same flow velocity does not vary with the volume fraction. It means that the usage of the nanofluids does not change required pump power and the single-phase friction factor correlation can be used for more accurate predictions. The friction factor of the nanofluids can be determinedas follows:

$$\lambda_{nf} = \frac{\Delta P_{nf} D}{L}\frac{2g}{u_m^2} \quad (9)$$

Yang *et al*. [21] conducted experiments related to the convective heat transfer coefficient of graphite nanoparticles dispersed in liquid for laminar flow in a horizontal tube heat exchanger. In their study, they used nanoparticles of different sources and focused on an aspect ratio (l/d) of about 0.02 (like a disc), avoiding the addition of large aspect ratio particles into a fluid since it may dramatically increase viscosity compared with the single-phase. In their study, two different nanofluids were used. The experiments were performed for different volume flow rates changing between 62-507 cm^3/min, the heating fluid temperature changing between 50-70 ^oC and the Reynolds number changing between 5-110. The purpose of this study was to define the effect of the volume fraction, fluid temperature, Reynolds number, nanoparticle source and type of base fluid on the convective heat transfer coefficient.

The following calculations are performed to evaluate the heat transfer coefficient of the nanofluids.

The heat transfer rate into the nanofluids is calculated as follows:

$$Q_{nf} = \dot{m} Cp\left(T_{out} - T_{in}\right) \quad (10)$$

The heat transfer rate from the heating fluids is calculated as follows:

$$Q_{hf} = \dot{m}_{hf} Cp_{hf}\left(T_{out} - T_{in}\right)_{hf} \quad (11)$$

The energy balance between the process fluid and the heating fluid was found to be at a difference of about 25%. This is common for small-scale experimental setup equipment.

The heat transfer coefficient of the nanofluids (h_{nf}) can be defined by using overall heat transfer resistance relationship:

$$\frac{1}{U} = \frac{1}{h_{nf}\left(A_i/A_o\right)} + \frac{D_o}{2k}\ln\frac{D_o}{D_i} + \frac{1}{h_o} \quad (12)$$

The overall heat transfer coefficient can then be determined as follows:

$$U = \frac{Q}{A_o \Delta T_{lm}} \quad (13)$$

Table 2. Some Thermal Conductivity Correlations of Nanofluids in Recent Literature

Researcher	Correlation
Yu and Choi [8]	$k_{nf} = k_f * \frac{k_{pe} + 2k_f + 2\phi(k_{pe} - k_f)(1+\beta)^3}{k_{pe} + 2k_f - \phi(k_p - k_f)(1+\beta)^3}$, $\beta = \frac{h}{r}$, $h < 10nm \longrightarrow \beta = 0.1$
Godson *et al*. [9]	$k_{nf} = 0.9692 * \phi + 0.9508$
Prasher *et al*. [10]	$k_{nf} = k_f * \frac{1 + A\phi\, Re^m\, Pr^{0,333} * (1+2\alpha) + 2\phi(1-\alpha)}{(1+2\alpha) - \phi(1-\alpha)}$,$\alpha = \frac{2R_b k_f}{d_p}$, $A = 40000$,$m = 2.5$, $R_b = 0.77 \times 10^{-8}$
Koo and Kleinstreuer [11]	$k_{nf} = k_{MG} + 5 \times 10^4\ \beta\phi\rho_p\, C_p \sqrt{\frac{K_B T}{\rho_p D}}\ f(T,\phi)$, $k_{MG} = k_f * \left(1 + \frac{3\phi\left(\frac{k_p}{k_f} - 1\right)}{\left(\frac{k_p}{k_f} + 2\right) - \phi\left(\frac{k_p}{k_f} - 1\right)}\right)$ $f(T,\phi) = (-6.04\phi + 0.4705) * T + (1722.3\phi - 134.63), \beta = 0.0137(100\phi)^{-0.8229} \rightarrow \phi \le 1\%$
Li and Peterson [12]	$k_{nf} = k_f + k_f(0.764\phi - 0.0187\,(T - 273.15) - 0.462)$ For Al_2O_3 $k_{nf} = k_f + k_f(3.761\phi + 0.0179\,(T - 273.15) - 0.307)$ For CuO
Palm and Roy [136]	Al_2O_3 $\left(\begin{array}{l} k_{nf} = 0.003352T - 0.3708 \quad For\ \phi = \%1 \\ k_{nf} = 0.004961T - 0.8078 \quad For\ \phi = \%4 \end{array}\right)$
Nguyen *et al*. [13]	$k_{nf} = k_f\,(4.97\phi^2 + 2.72\phi + 1)$ For Al_2O_3 $k_{nf} = k_f\,(28.905\phi^2 + 2.827\phi + 1)$ For CuO
Bhattacharya *et al*. [14]	$k_{nf} = k_p\phi + (1-\phi)k_f$
Buongiorno [15]	$k_{nf} = k_f\,(1 + 7.47\phi)$
Kim *et al*. [16]	$k_{nf} = 0.65 + 4{,}864 \times 10^{-7} T^3$
Timofeeva *et al*. [17]	$k_{nf} = k_f(1 + 3\phi)$
Chon *et al*. [18]	$k_{nf} = k_f * (1 + 64.7\phi^{0.746}\,(d_f/d_p)^{0.369}(k_p/k_f)^{0.747}\, Re^{1.2321}\, Pr^{0.9955})$ $Pr = \frac{\mu}{\rho_{BF}\alpha}, Re = \frac{\rho_{BF} V d_p}{\mu} = \frac{\rho_{BF} K_B T}{3\pi\mu^2 L_{BF}}, \mu = 2{,}414 \times 10^{-5} \times 10^{\left(\frac{247}{T-140}\right)}$
Murshed *et al*. [19]	$k_{nf} = \frac{k_f * (1 + 0.27\phi^{4/3}\,(\frac{k_p}{k_f} - 1)(1 + \frac{0.52\phi}{1 - \phi^{1/3}}\,(\frac{k_p}{k_f} - 1)}{1 + \phi^{4/3}\,(\frac{k_p}{k_f} - 1)(\frac{0.52}{1 - \phi^{1/3}} + 0.27\phi^{1/3} + 0.27)}$

Monrad and Pelton's equation [22] can be used to estimate the outside heat transfer coefficient, h_o, for turbulent flow in annuli as follows:

$$Nu = 0.020\,Re^{0.8}\,Pr^{1/3}\left(D_2/D_1\right)^{0.53} \tag{14}$$

Subscript 1 and 2 refer to the outer and inner diameter of the annulus, respectively. The equivalent diameter, being represented by D_e, was used instead of the typical diameter (D).

$$D_e = \frac{D_{i,a}^2 - D_o^2}{D_o} \tag{15}$$

By modifying the Seider-Tate equation [23], all of the experimental data can be used to develop a new heat transfer correlation for predicting the heat transfer coefficient of nanofluids flowing laminar in a more convenient form as follows:

$$\Omega = Nu_{nf}\,Pr_{nf}^{-1/3}\left(\frac{L}{D}\right)^{1/3}\left(\frac{\mu_f}{\mu_w}\right)^{-0.14} = a\,Re_{nf}^{b} \tag{16}$$

where a and b are the various constants depending on the experimental conditions.

The Nusselt number and heat transfer coefficient of the nanofluids are calculated by the means of following equations:

$$Nu_{nf,x} = \frac{h_{nf,x} D}{k_{nf}} \tag{17}$$

$$h_{nf,x} = \frac{q}{T_{w,x} - T_{f,x}} \tag{18}$$

The fluid temperature (19)

In the literature, the results showed that Reynolds number and volume fraction are very important parameters for the local heat transfer coefficient. Particularly, the entrance region showed that the use of nanofluids revealed a significant increase in the heat transfer coefficient causing a decrease in the thermal boundary layer thickness and a decrease along the tube length. This behavior indicated that "smart entrance" must be created to improve performance of nanofluids. Furthermore, the Shah correlation for laminar flow and the Dittus-Boelter equation for turbulent flow did not match with the Nusselt number between the experimental results and the calculated values.

Similar to the experimental investigation, many researchers tried to formulate the suitable correlations for the prediction of the thermal conductivity of the nanofluid. Since several challenges such as dispersion, Brownian force, sedimentation and friction force between the fluid and the solid particles may coexist in the main flow it becomes hard to generate any formulated theory for the prediction of the accurate heat transfer behavior of the nanofluid. Nanofluid is considered more like a fluid rather than a liquid-solid mixture by some researchers. There are few articles treating the nanofluid as to have the multiphase feature.

3. LITERATURE REVIEW OF RECENT YEARS

The studies on the use of particles of nanometer dimension were first continuously conducted by a research group at the Argonne National Laboratory approximately a decade ago. Choi [24] was possibly the first researcher who called the fluids with particles of nanometer scale 'nano-fluids'.

Nanofluids have better rheological and stability properties, significantly higher thermal conductivities and no penalty in pressure drop as compared with suspended particles of millimeter-or-micrometer scale.

In recent years, the nanofluid has emerged as an alternative heat transfer fluid for heat transfer applications showing a significant potential for heat transfer improvement. It has been expected to be suitable for the engineering application without severe problems in pipeline and with little or no penalty in pressure drop. According to earlier researches, thermal conductivity has come into the limelight as most studied transport properties of the nanofluid. The convective heat transfer of nanofluids has comparatively been less acclaimed in literature therefore the number of the publications dealing with the convective heat transfer of nanofluids is limited. The most productive research has been continuously carried out by the following studies.

3a. Somestudies of 2012

Alizad *et al*. [25] investigated thermal performance, transient behavior and operational start-up characteristics of flat-shaped heat pipes by using nanofluids. They used three different primary nanofluid of CuO, Al_2O_3, and TiO_2. They benefitted from a comprehensive analytical model having detailed heat transfer characteristics inside the condensation and evaporation sections of the tube. The thermal performance of either the flat-plate or disk-shaped heat pipes was increased by higher concentration of nanoparticles.

Bobbo *et al*. [26] showed some viscosity data for nanofluids. They used water as base fluid and two different primary nanofluids such as single wall carbonnanohorn (SWCNH) and titanium dioxide (TiO_2). They determined viscosity of nanofluids using arhometer experimentally and benefitted from the function of the nanoparticles' mass fraction and the shear rate. Therefore they accounted the possible non-Newtonian behavior for the nanofluid. As a result, different empirical correlations were proposed in their study.

Buschmann [27] studied on ceramic nanofluid's thermal conductivity and heat transfer characteristics. He observed that heat transfer could be increased by using nanofluids in the thermal entrance with test rig. It was revealed that when the thermal conductivity of five different ceramic nano fluids were measured by means of a sophisticated ring gap apparatus the dynamic viscosity was found to be enhanced successfully.

Yang *et al*. [28] enhanced the heat and mass transfer on the ammonia water absorption refrigeration system. They yielded three different nanofluids by inserting the mixture of carbon black with emulsifier OP-10, $ZnFe_2O_4$ with sodium dodecyl benzene sulfonate (SDBS), and Fe_2O_3 with SDBS to the ammonia water solution, respectively. It was found that key parameters for this study werethe content of surfactant and nanoparticles, their interaction, and also the dispersion type that affected the viscosity of ammonia water nanofluid. They correlated mainly two models to predict the viscosity of ammonia water nanofluid.

Colangelo *et al*. [29] intended to observe the diathermic oil based nanofluids being used in many areas such as renewable energy, cogeneration and cooling systems. They used the diathermic oil with CuO, Al_2O_3, ZnO and Cu particles having different shapes and concentrations from 0% to 3.0%. It was found that the heat transfer performance of diathermic oil increased more than that of the water for the same nanoparticle concentrations.

Jamshidi *et al*. [30] investigated the heat transfer rate and pressure drop in helical coils in their study. They assumed that thermophysical properties of nanofluid did not depend on volume fraction and temperature. They utilized from a numerical simulation and Taguchi method to obtain the optimum condition for desired parameter values. Results showed that the use of nanofluids enhanced the thermal-hydraulic performance of helical tube. Although, temperature dependent properties changed with the optimum particle volume fraction, nanofluids were not varied by the optimized shape factor.

Giraldo *et al*. [31] investigated the thermal behavior of a nanofluid loaded with alumina nanoparticles and developed a direct numerical simulation of the flow. They utilized from the boundary element method to solve moving boundary problems. They observed that strong convective currents occurred as a result of the presence of the nanoparticles, which in time increased the total heat flow in the cavity particle concentration. Particle concentration increased the total heat flow influencing both the conductive part of heat transfer and the convective part expectedly.

Özerinç *et al*. [32] studied the application of some empirical correlations of forced convection heat transfer developed for the flow of pure fluids and nanofluids. They compared their results with existing theories in the literature and their model underestimated the heat transfer as a result of the numerical solution pointing that single-phase assumption with temperature-dependent thermal conductivity and thermal dispersion being the certain way of heat transfer enhancement analysis of nanofluids in convective heat transfer.

Yu *et al*. [33] investigated the thermophysical properties and convective heat transfer of Al_2O_3-polyalphaolefin (PAO) nanofluids includingboth the spherical and the rod-like nanoparticles. They determined the viscosity and thermal conductivity of the nanofluids and compared their predictions with several existing theories in the literature. Their results showed that in a convective flow, the shear-induced alignment and specific motion of the particles should be regarded to truly interpret the experimental data of the nanofluids including non-spherical nanoparticles.

Farahani and Kowsary [34] intended to clarify a heat conduction method used for defining the local convective boiling heat transfer coefficient of pure water and copper based nanofluid flowing in a mini channel by utilizing three different concentrations of nanoparticles being 5 mg/L, 10 mg/L and 50 mg/L. They tried to solve the IHCP using sequential specification function method by calculating the space-variable convective heat transfer coefficient. Their results acknowledged two dimensional SFS method to have the optimum experiments for the determination of boiling heat transfer coefficients of pure water and nanofluid flowing in mini channel.

Cimpean and Pop [35] studied on the steady fully developed mixed convection flow of a nanofluid in a channel filled with a porous medium. They used some equations to solve the problem those being non-dimensional and based mainly on the mixed convection parameter, the Péclet number, the inclination angle of the channel to the horizontal and the nanoparticle volume fraction. Their results showed that nanofluid greatly enhanced the heat transfer, even for small additions of nanoparticles in the base water fluid.

Leong *et al.* [36] studied on the flow of nanofluids in shell and tube heat recovery exchangers in a biomass heating plant. They benefited from the literature that included heat exchanger specification, nanofluid properties and mathematical formulations. They found that use of nanofluids augmented the convective and overall heat transfer coefficient as compared to the ethylene glycol or water based fluids shown in Fig. (**1**).

Mahbubul *et al*. [37] investigated different characteristics of viscosity of nanofluids such as nanofluid preparation methods, temperature, particle size and shape, and volume fraction effects. They found that viscosity's augmentation depended on volume concentration, increase and decrease of the temperature rise. They observed that viscosity improved with volume fraction for different concentration of Al_2O_3, TiO_2 as shown in Fig (**2**).

Wenzheng *et al*. [38] studied a Molecular Dynamics simulation on Couette flow of nanofluids and showed the microscopic flow characteristics through visual observation and statistic analysis. They presented the even-distributed liquid argon atoms near solid surfaces of nanoparticles those which might have been appeared as a reform to base liquid had contributed to heat transfer enhancement. Nanoparticles moved rapidly in the shear direction accompanying with motions of rotation and vibration in the other two directions in the process of Couette flow. The motions of nanoparticles were reinforced significantly when the shearing velocity was grown. More enhanced heat transferring in nanofluids obtained by the motions of nanoparticles could disturb the continuity of fluid and strengthen partial flowing around nanoparticles.

3b. Somestudies of 2011

Ahmed *et al*. [39] investigated the characteristics of heat transfer and pressure drop belonging to copper-water nanofluid flow in an isothermally heated corrugated channel. Their model included the equations of continuity, momentum and energy for laminar flow in curvilinear coordinates using the Finite Difference (FD) approach. Reynolds number and nanoparticle volume fraction varied from 100 to 1000 and from 0 to 0.05 in their study, respectively. They studied the effects of using nanofluid on the heat transfer and pressure drop inside the channel. Their results showed that increase in the volume fraction of the nanoparticle and Reynolds number caused both an increase in heat transfer enhancement and a slight increase in pressure drop. They highlighted the effect of Reynolds number for different nanoparticle volume fraction on average Nusselt number enhancement in Fig. (**3**).

Akbarinia *et al*. [40] investigated the heat transfer enhancement at low Reynolds numbers using Al_2O_3-water nanofluid flows in two-dimensional rectangular microchannels. Their results showed that the major enhancement in Nusselt number was not only due to the increase in the nanoparticle concentrations but also due to the increase in the inlet velocity to reach a constant Reynolds number. They reported that constant Reynolds number studies of nanofluids had not sufficient approach to evaluate the heat transfer and the skin friction factor due to the use of nanofluids.

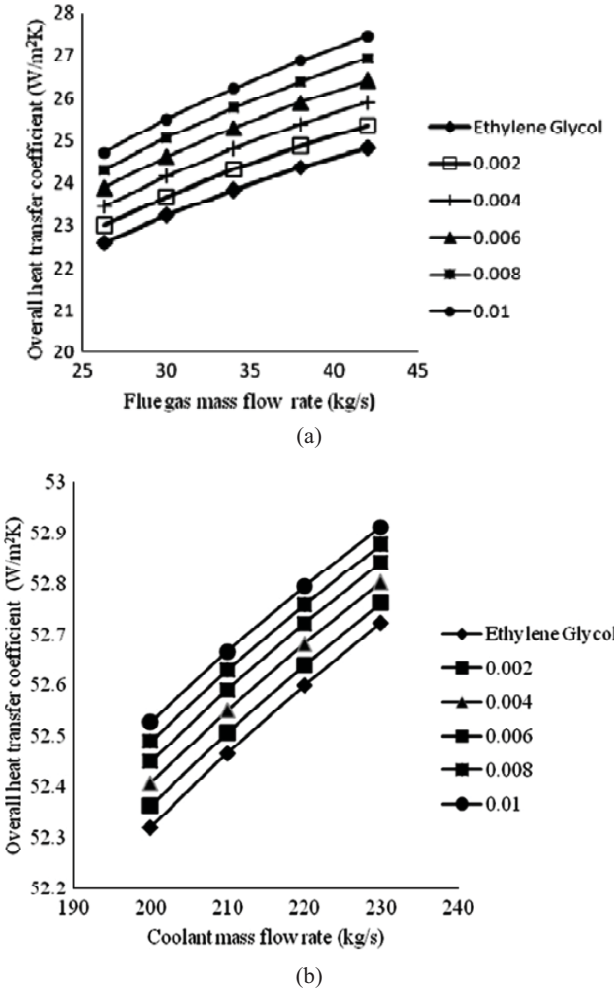

Fig. (1). The effect of flue gas mass flow rate and (**a**) coolant mass flow rate (**b**) on overall heat transfer coefficient [From Leong *et al*. [36], with permission from Elsevier]

In the studies made by Bianco *et al*. [41], turbulent forced convection flow of water-Al_2O_3 nanofluid in a circular tube was calculated numerically depending on a constant and uniform heat flux at the wall. Their study was based on two different approaches: single and two-phase models, with particle diameterequal to 38 nm. It was calculated that convective heat transfer coefficient for nanofluids was greater than that of the base liquid. Their study showed that heat transfer enhancement increased with the particle volume concentration and Reynolds number. Comparisons with correlations in literature were carried out obtaining a very good agreement.

Corcione [42] put forward two empirical correlations and discussed them for predicting the effective thermal conductivity and dynamic viscosity of nanofluids using a high number of experimental data available in the literature. It was observed that at the constant nanoparticle material and the base fluid, the ratio between the thermal conductivities of the nanofluid and the pure base liquid increased by increasing the nanoparticle volume fraction and the temperature, and decreasing the nanoparticle diameter. Moreover, the ratio between the dynamic viscosities of the nanofluid and the

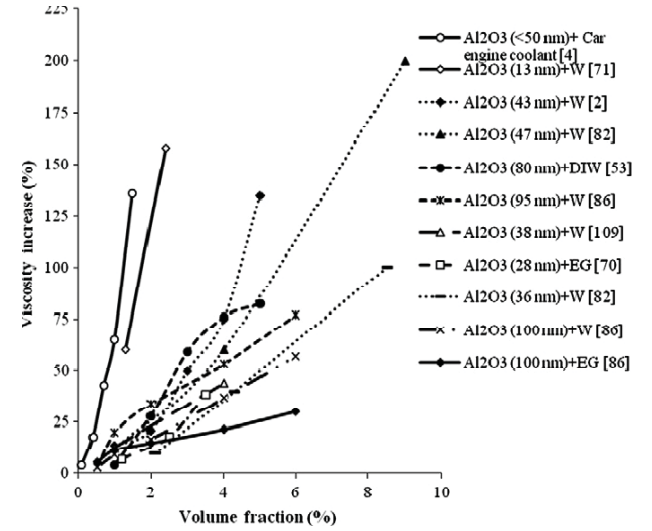

(a)

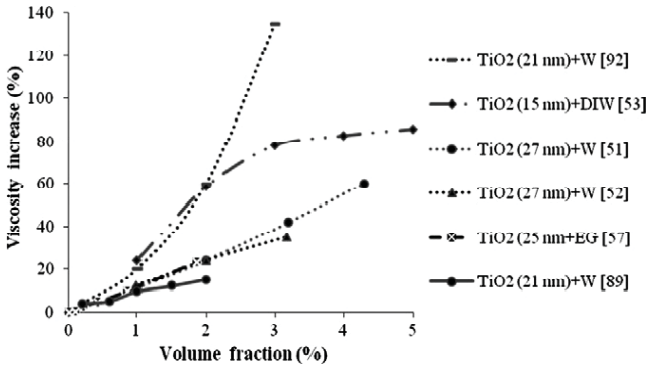

(b)

Fig. (2). Viscosity increases with the increase of volume fraction for different concentration of Al_2O_3 (**a**) TiO_2 (**b**) [From Mahbubul *et al*. [37], with permission from Elsevier].

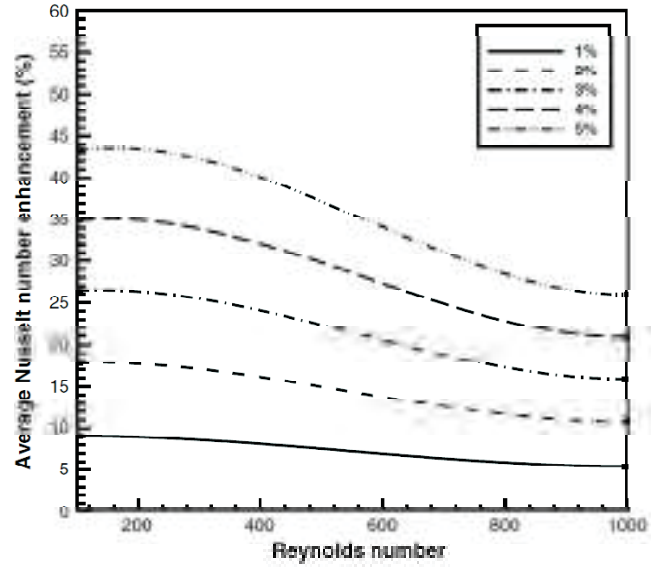

Fig. (3). Average Nusselt number enhancement vs. Reynolds for different nanoparticle volume fractions [From Ahmed *et al.* [39], with permission from Elsevier].

pure base liquid increased with increasing the nanoparticle volume fraction, and decreasing the nanoparticle diameter in the case of those practically being not dependent on temperature.

Firouzfar *et al*. [43] used nanoparticles to investigate the heat transfer mechanisms concerning the thermal conductivity increase, brownian motion, dispersion, and fluctuation of nanoparticles especially near the wall which led an increase in the energy exchange rates and augmented the heat transfer rate between the fluid and the wall of evaporator section. Their experimental results showed that addition of silver nanofluid in methanol led to energy saving around 8.8-31.5% for cooling and 18-100% for reheating the supply air stream in an air conditioning system.

Gherasim *et al*. [44] presented heat transfer enhancement capabilities of coolants using suspended nanoparticles (Al_2O_3 dispersed inwater) inside a confined impinging jet cooling device in their numerical study. A good agreement was found between numerical results and available experimental data. Their study reported heat transfer enhancement being possible in their application using nanofluids. It was observed that the mean Nusselt number increased with increasing particle volume fraction and Reynolds number and also it decreased with increasing in disk spacing. The study deduced that a significant increase in pumping power might impose some limitations on the efficient use of this type of nanofluid in a radial flow configuration.

Hojjat *et al*. [45] experimentally investigated the forced convective heat transfer using dispersing γ-Al_2O_3, CuO, and TiO_2 nanoparticles in an aqueous solution of carboxymethyl cellulose (CMC). Their experimental apparatus included a uniformly heated circular tube under turbulent flow conditions passing through these nanofluids. Their results showed that the local and average heat transfer coefficients of nanofluids were larger than those of the base fluid. A new correlation was therefore proposed for the prediction of the Nusselt number of non-Newtonian nanofluids as a function of the Reynolds and the Prandtl numbers.

Hojjat *et al*. [46], by using γ-Al_2O_3, TiO_2 and CuO nanoparticles in a 0.5 wt% of carboxymethyl cellulose (CMC) aqueous solution calculated thermal conductivity of base fluid and nanofluids with various nanoparticle loadings at different temperatures experimentally. Their results showed that the thermal conductivity varied exponentially with the nanoparticle concentration. In their study, they developed an ANN model for the thermal conductivity as a function of the temperature.

Hojjat *et al*. [47] investigated the forced convection heat transfer of non-Newtonian nanofluids in a circular tube with constant wall temperature condition under turbulent flow conditions of three types of nanofluids (γ-Al_2O_3, TiO_2 and CuO nanoparticles) in the base fluid experimentally. Their base material was the aqueous solution of carboxymethyl cellulose (CMC). Their results showed convective heat transfer coefficient of nanofluids being higher than that of the base fluid.

Huminic and Huminic *et al*. [48] used CuO and TiO_2 nanoparticles with the diameters of 24 nm dispersed in water with volume concentrations of 0.5-3 vol.% as the working fluid in their experiment and investigated three-dimensional analysis on the heat transfer characteristics of double-tube helical heat exchangers using nanofluids under laminar flow conditions. Experimental calculations showed that at 2% CuO nanoparticles in water and same mass flow rate in inner tube and annulus, the heat transfer rate of the nanofluid was found to be approximately 14% greater than that of pure water, while the heat transfer rate of water in the annulus was calculated approximately 19% greater than those nanofluids which were flowing through the inner tube.

Huminic and Huminic [49] studied the heat transfer characteristics of two-phase closed thermosyphon (TPCT) with iron oxide-nanofluids. The TPCT with the de-ionic water and nanofluids (water and nanoparticles) were tested. Effects of TPCT inclination

angle, operating temperature and nanoparticles concentration levels on the heat transfer characteristics of TPCT were investigated. The nanoparticles were found to have a significant effect on the enhancement of heat transfer characteristics of TPCT. The heat transfer characteristics of TPCT of the nanofluids were compared with those of the based fluid. Their experimental results focused on iron oxide-water nanofluid as the working fluid, heat transfer rate, evaporation and condensation heat transfer coefficients and thermal resistances. Different nanoparticle concentration levels in suspension within the two-phase closed thermosyphon, operating temperatures and inclination angles of the heat pipe (30-90°) were experimentally examined and the results were compared with those of pure water.

Jung *et al*. [50] developed binary nanofluids using nanoparticle suspensions to enhance the heat and mass transfer performance of absorption refrigeration cycles. To stabilize the nanoparticles in a strong electrolyte, polymer was used as a steric stabilizer. The effective thermal conductivities of the binary nanofluids with the concentrations of nanoparticle up to 0.1 vol% were measured by means of the transient hot wire method. The study revealed that the dispersion stability of nanofluids was a dominant factor for enhancing the thermal conductivity of binary nanofluids while thermal conductivity was found to be changing with time. It was also observed that thermal conductivity of H_2O/LiBr binary mixture with Al_2O_3 nanoparticles increased with increasing the particle volume concentration and was enhancedat 2.2% at 0.1 vol% concentration conditions.

Khanafer and Vafai [51] came up with a study related with the critical synthesis of the variants within the thermophysical properties of nanofluids. This study showed that it was not clear which analytical model should be used to describe the thermal conductivity of nanofluids. Their results showed that the effective thermal conductivity and viscosity of nanofluids could be estimated using the classical equations at low volume fractions.

Lee *et al.* [52] determined the transmission of electron microscopy and scanning of electron microscope images for characterizing the shape and size of SiC nanoparticles. The dispersion behavior for SiC/deionized water (DIW) nanofluids was investigated under different pH values and characterized with the zeta potential values. The isoelectric point of SiC/DIW nanofluid was determined concerning colloidal stability. Thermal conductivity and viscosity as a function of volume fraction were investigated.

Asirvatham *et al*. [53] performed experiments to investigate the convective heat transfer of nanofluids using silver-water nanofluids under laminar, transition and turbulent flow regimes in a horizontal 4.3 mm inner-diameter tube-in-tube counter-current heat transfer test section. The volume concentration of the nanoparticles was found to be varying from 0.3% to 0.9% in steps of 0.3%. The effects of thermo-physical properties, inlet temperature, volume concentration, and mass flow rate on heat transfer coefficient were investigated. Experiments showed that the suspended nanoparticles remarkably increased the convective heat transfer coefficient, by as much as 28.7% and 69.3% for 0.3% and 0.9% of silver content, respectively. Heat transfer coefficient clearly augmented with an increase in the combination of particle loading and Reynolds number as shown in Fig. (**4**). Based on the experimental results, a correlation was developed to predict the Nusselt number of the silver-water nanofluid, within ±10% deviation band between experimental and predicted values. Predicted and experimental Nusselt numbers were shown in the range of Reynolds number from 800 to 12000, Prandtl number from 4 to 10 and volume concentration from 0 to 2% in Fig. (**5**).

Ebrahimnia-Bajestan [54] presented a numerical investigation on the heat transfer performance and pressure drop of nanofluids flowing through a straight circular pipe during laminar flow regime

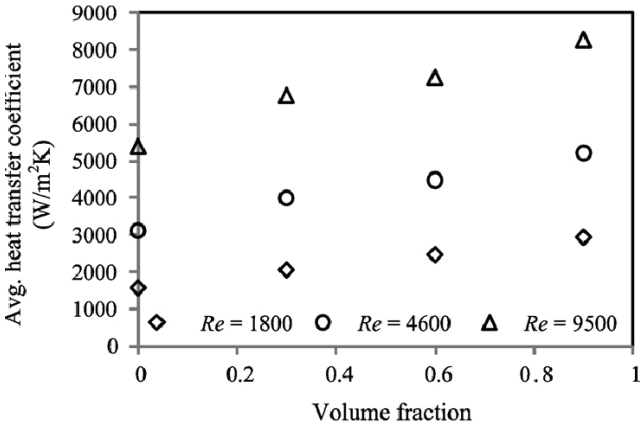

Fig. (4). Heat transfer coefficient increases with volume fraction [From Asirvatham *et al*. [53], with permission from Elsevier].

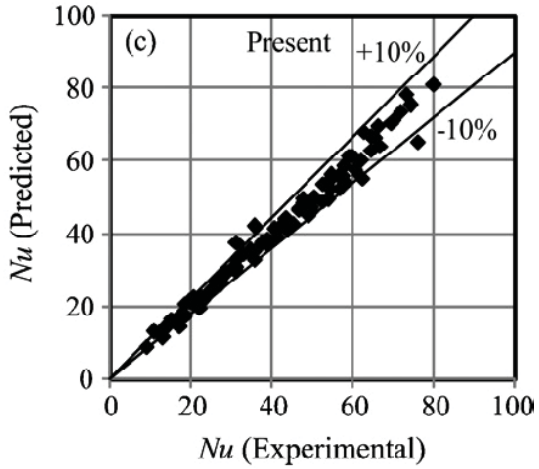

Fig. (5). Variations of Predicted and Experimental Nusselts numbers [From Asirvatham *et al*. [53], with permission from Elsevier].

and constant heat flux boundary condition. Al_2O_3, CuO, carbon nanotube (CNT) and titanate nanotube (TNT) nanoparticles dispersed in water and ethylene glycol/water with particle concentrations ranging between 0 and 6 vol.% were used as working fluids for simulating the heat transfer and flow behaviours of nanofluids. The proposed model was validated with the available experimental data and correlations. The effects of particle concentrations, particle diameter, particles' Brownian motions, Reynolds number, type of the nanoparticles and base fluid on the heat transfer coefficient and pressure drop of nanofluids were determined and discussed in detail. The results indicated that the particle volume concentration, Brownian motion and aspect ratio of nanoparticles increased the heat transfer coefficient while the nanoparticle diameter was found to have an opposite effect on the heat transfer coefficient. They listed temperature increase, pressure drop, and pumping power for different nanofluids flow conditions in Table **3**. Finally, the present study provided some considerations for the appropriate choice of the nanofluids for practical applications.

Raisi *et al*. [55] numerically studied method for both slip and non-slip boundary conditions in the thermal performance of a microchannel, cooled with either pure water or a Cu-water nanofluid on the flow field and heat transfer. They assumed that the microchannel should be partially heated at a constant temperature and cooled by forced convection of a laminar flow at a relatively lower

Table 3. Temperature increase, Pressure drop and Pumping power is listed for different nanofluids flow conditions [Ebrahimnia-Bajestan *et al.* [54], with permission from Elsevier]

Type of working fluids	Re	d_p (nm)	ϕ (vol.%)	ΔT (°C)	ΔP (Pa)	Pump power (W)
Al_2O_3/60% EG/water	1460	20	4	0.56	43240	1.38
60% EG/water	1460	–	–	0.68	26240	0.69
CNT/water	1460	$L_p/d_p > 100$	0.038	0.9	9625	0.16
CuO/water	1460	20	6	1.05	8838	0.12
CuO/water	1460	20	4	1.52	3830	0.04
TNT/water	1460	$d_p = 10$, $L_p = 100$	0.6	1.8	2241	0.017
Al_2O_3/water	1460	100	6	2.05	2020	0.014
Al_2O_3/water	1460	40	6	2.06	2020	0.014
Al_2O_3/water	1460	20	6	2.08	2020	0.014
CuO/water	1460	20	2	2.18	1670	0.011
Al_2O_3/water	1460	40	4	2.39	1416	0.008
Al_2O_3/water	1460	20	4	2.39	1417	0.008
Al_2O_3/water	1460	20	3	2.52	1188	0.007
Water	1620	–	–	2.6	974	0.005
Al_2O_3/water	1460	20	2	2.72	996	0.005
Al_2O_3/water	1460	100	2	2.72	995	0.005
Al_2O_3/water	1460	40	2	2.73	995	0.005
Water	1460	–	–	2.78	869	0.004
Al_2O_3/water	1000	20	4	3.44	936	0.004
Water	1000	–	–	4.08	572	0.002
Al_2O_3/water	500	20	4	6.91	438	0.0009
Water	500	–	–	8.19	266	0.0004

temperature. The effects of pertinent parameters such as Reynolds number, solid volume fraction, and slip velocity coefficient on the thermal performance of the microchannel ewere investigated. The heat transfer rate was significantly affected by the solid volume fraction and slip velocity coefficient at high Reynolds numbers.

Heris *et al*. [56] numerically studied laminar flow-forced convective heat transfer of Al_2O_3/water nanofluid in a triangular duct under constant wall temperature condition. The effects of parameters were investigated such as diameter of nanoparticles, concentration, and Reynolds number on the enhancement of nanofluids heat transfer. By comparing heat transfer between nanofluid and pure fluid it was found that in non-circular ducts the low heat transfer rate was one of the limitations of these systems and use of nanofluid instead of pure fluid because of its potential to increase heat transfer of system could compensate this problem. They obtained that the nanofluid Nusselt number increased with increasing concentration of nanoparticles and decreasing its diameter. Also, the enhancement of the fluid heat transfer became better at high Re in laminar flow with the addition of nanoparticles.

Vincenzo *et al*. [57] numerically studied the developing turbulent forced convection flow of a water-Al_2O_3 nanofluid in a square tube in constant and uniform wall heat flux. The particlesize equal to 38 nm was used in nanofluid flow. The optimal working condition was obtained during an entropy generation analysis for the given geometry under given boundary conditions. A simple analytical procedure was proposed to evaluate the entropy generation and its results were compared with the numerical calculations. The optimal Reynolds number was determined on minimizing entropy generation.

Demir *et al*. [58] numerically investigated forced convection flows of nanofluids consisting of water with TiO_2 and Al_2O_3 nanoparticles in a horizontal tube with constant wall temperature. The horizontal test section was modeled and solved using a CFD program. Palm *et al*.'s correlations were used to determine the nanofluid properties. A single-phase model having two-dimensional equations was employed with either constant or temperature dependent properties to study the hydrodynamics and thermal behaviors of the nanofluid flow. The numerical investigation was performed for a constant particle size of Al_2O_3 as a case study after the validation of its model by means of the experimental data of Duangthongsuk and Wongwises with TiO_2 nanoparticles. The velocity and temperature vectors were presented both in the entrance and fully developed region. The variations in the fluid temperature, local heat transfer coefficient and pressure drop along tube length had been shown in the paper. Effects of nanoparticles concentration and Reynolds number on the wall shear stress, Nusselt number, heat transfer coefficient and pressure drop were highlighted. Numerical results showed the heat transfer enhancement due to presence of the nanoparticles in the fluid concerning the results of the experimental study used for the validation process of the numerical model.

3c. Somestudies of 2010

Nanoparticles of magnetite Fe_3O_4 have been synthesized at various pH values by a method of co-precipitation in Abareshi *et al.* [59]'s study. The characteristic properties of the products were determined by transmission electronic microscopy, Fourier infrared spectroscopy and X-ray diffraction. By using a vibrating sample magnetometer, the magnetic properties of the products were found. According to the obtained results, particles being cubic in shape exhibited super paramagnetic properties at room temperature. Fe_3O_4 nanoparticles were dispersed in water as a base fluid in the presence of a dispersant which was tetramethyl ammonium hydroxide and so the magnetic nanofluids were prepared. As a function of temperature and volume fraction, the thermal conductivity of the nanofluids was measured. The thermal conductivity values of the nanofluids were obtained in terms of volume fraction and temperature. It was found by the results that an increase in the thermal conductivity ratio of the nanofluids resulted in an increase in temperature and volume fraction. As it has been demonstrated in Fig. (**6**), that the thermal conductivity was increased by 11.5% at most at 40°C for the nanofluids having 3 vol% nanoparticles because of the Brownian motion of nanoparticles intensified at high temperatures. Then the experimental results were evaluated and discussed according to the theoretical models.

Under turbulent flow conditions, the measurement of heat transfer characteristics of Gama-Al_2O_3 and TiO_2/water nanofluids was performed in a shell and tube heat exchanger in Farajollahi *et al.* [60]'s study. It was investigated how the heat characteristics were affected by Peclet number, volume concentration of suspended nanoparticles, and particle type. It was evident from the obtained result that when the nanoparticles were added to the base fluid, heat transfer characteristics were significantly enhanced. When the heat transfer behavior of two nanofluid was compared, it was found that at a definite Peclet number, TiO_2/water nanofluid showed greater heat transfer characteristics at its optimum nanoparticle concentration than the heat transfer characteristics of Gama-Al_2O_3/water nanofluid. However, better rate of heat transfer behavior at higher nanoparticle concentrations of Gama-Al_2O_3/water nanofluid was obtained.

By using a CFD approach, under constant wall temperature condition in a circular tube, the laminar convective heat transfer of nanofluids was studied in a numerical way in Fard *et al.* [61]'s study. Single phase and two-phase models were used for the determination of the temperature, flow field, and calculation of heat transfer coefficient. The effects of some important parameters such as nanoparticle sources, nanoparticle volume fraction and nanofluid's Peclet number on heat transfer rate were investigated. The result showed that as the particle concentration increased, heat transfer coefficient also increased. According to their simulation results, it was seen that when their model was compared to the single phase model, better predictions for heat transfer rate were obtained from the two phase approach.

According to Do *et al.* [62]'s study, thermal performance of nanofluids was investigated by testing circular screen mesh of wick heat pipes experimentally. In their study, water-based Al_2O_3 nano-

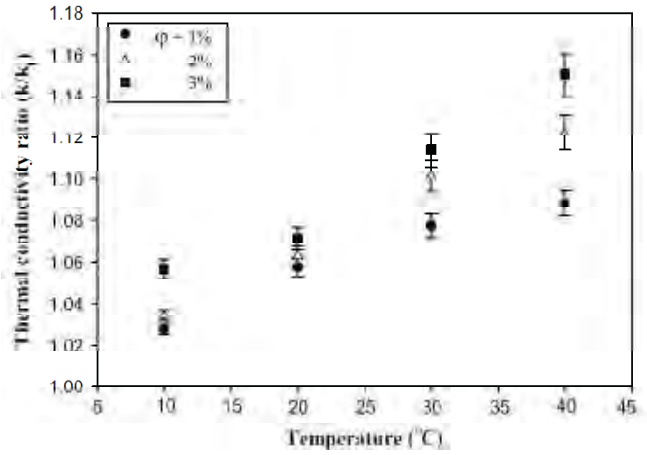

Fig. (6). The effect of temperature at different volume fractions of Fe_3O_4 on the thermal conductivity ratio (k/kf) [From Abareshi *et al.* [59], with permission from Elsevier].

fluids were used by the volume fraction of 1.0 and 3.0 vol.%. According to their study, the use of water based Al_2O_3 nanofluids instead of DI water could accomplish the maximum heat transfer rate of pipe. The thin porous coating layer formed by nanoparticles suspended in nanofluids at wick structures was observed experimentally. It was observed that the coating layer formed by nanoparticles at the evaporator section was the primary mechanism on the enhancement of the thermal performance for the heat pipe due to the fact that the layer could not only extend the evaporation surface with high heat transfer performance but could also improve the surface wettability and capillary wicking performance.

According to Henderson *et al.* [63]'s study, the experiments were performed at low vapor quality (x<20%) with a specific range of mass flux (100<G<400 kg/m^{2}s) for the flow boiling of R-134a and R134a/polyolester mixtures. By using direct dispersion of SiO_2 nanoparticles in R-134a, when compared with pure R-134a, it was observed that the heat transfer coefficient decreased as much as 55%. This degradation was stemmed from, partly, the difficulties in producing a stable dispersion. It was concluded that nanoparticles insignificantly affected the flow pressure drop with the R-134a/POE/CuO nanofluid.

According to Godson *et al.* [64]'s study, the unique features of nanofluids, such as enhancement of heat transfer, improvement in thermal conductivity, increase in surface volume ratio, Brownian motion, thermophoresis, etc. were summarized. Additionally, the recent research in experimental and theoretical studies on forced and free convective heat transfer in nanofluids, their thermophysical properties and applications were summarized. This article identified the challenges and opportunities for future research.

In Kima *et al.* [65]'s study, it was shown that prior studies of pool boiling had demonstrated that nanofluids could improve critical heat flux (CHF) by as much as 200 %. It was observed that heat transfer coefficient increased with the increasing in mass and heat flux during flow boiling. Test section was examined by a confocal microscopy and this technique showed nanoparticle deposition occurring on the boiling surface. The number of micro cavities on the surface, and also the surface wettability were changed by this deposition. In order to estimate the ensuing nucleation site density changes, a simple model was used; however, a successful correlation between the nucleation site density and the heat transfer coefficient could not be obtained.

In Lotfi *et al*. [66]'s study, water and Al_2O_3 nanoparticle mixtures under forced convective condition were studied numerically. Agreeable correlations of computed results were validated. Eulerian model was implemented to observe two phase flow field as a first study in the literature. The two-phase and single phase models were used in the mixture model formulation. According to calculated experimental values, the mixture model was found to be more precise. It should be noted that Nusselt numbers for single-phase model and the two-phase Eulerian model could not be predicted accurately in the study.

In Meibodi *et al*. [67]'s study, modeling of the thermal conductivity of the suspensions was performed by means of the resistance model approach. In this model, Brownian motion, interfacial layer and also a new mechanism were considered. They reported that this model migh be used without any adjustable parameter for estimating the upper and lower limits of nanofluid thermal conductivity. Data of thermal conductivity for CuO nanofluids were acquired experimentally and according to the results, proposed model was found to be consistent with the data. Their model was used to detect the various mechanisms' portions on the thermal conductivity of nanofluids. The results were found to be compatible with the basic knowledge about nanofluids' thermal conductivity mechanism.

According to the theory in Meibodi *et al*. [68]'s study, convective heat transfer coefficient depended on the parameters of velocity and temperature profiles. Within this study, friction factor and convection coefficient were utilized to compare the profiles for both nanofluids and base fluids. To reach this aim, Al_2O_3/water and carbon nanotube/water were preferred. It was demonstrated that the velocity profile of a nanofluid was similar to that of its base fluid. It was suggested that the only responsible variable for unpredictable convective heat transfer coefficient of nanofluids was the alteration of temperature profile for nanofluids.

In Meibodi *et al*. [69]' study, thermal conductivity and stability of carbon nanotube (CNT)/water mixture nanofluid were investigated and an optimum condition for the production and application of nanofluids was also proposed. They revealed a plethora of parameters such as size, shape and source of nanoparticles, surfactants, power of ultrasonic, time of ultrasonication, elapsed time after ultrasonication, pH, temperature, particle concentration and surfactant concentration, which affected this property. It was demonstrated that significant factors on the thermal conductivity and stability were not precisely similar to one another.

Paul *et al*. [70] presented various techniques for the measurement of nanofluid thermal conductivity and developed a unique thermal conductivity measurement device that propped up the thermal comparator principle. The constructional details were elaborated as well. After completing their research they presented some suggestions to enhance the reliability of the measurement of thermal conductivity. Their results indicated that they benefited from the transient hot-wire technique for measuring thermal conductivity.

Paul *et al*. [71] studied on preparation of the nano-gold dispersed water based nanofluid using the chemical reduction method. They described crystallite size, particle size/shape/morphology, and purity of the nanoparticles by benefiting from X-ray diffraction, scanning and transmission electron microscopy and energy dispersion spectroscopy, respectively. It was found that an increase in concentration and a decrease in size of nanoparticles augmented the heat transfer. They observed the maximum enhancement under 48% at 0.00026 vol.% concentration and 21 nm average particle size conditions.

Qu *et al*. [72] analyzed the thermal performance of an oscillating heat pipe (OHP) containing the effects of filling ratios, mass fractions of alumina particles, and power inputs loaded with base water and spherical Al_2O_3 particles of 56 nm in diameter. It was found that the alumina nanofluids enhanced the OHP's thermal performance, with an optimal mass fraction of 0.9 wt.% for maximal heat transfer increase. When the input power was 58.8 W at 70% filling ratio and 0.9% mass fraction, the maximal thermal re-

sistance was decreased by 0.14 °C/W (or 32.5%) in comparison to the pure water.

Rao [73] presented a brief overview of the important scientific disciplines about nanofluids such as stability properties, phase diagram, rheology and applications. He predicted about future development of this area.

Raykar and Singh [74] investigated to estimate the effective thermal conductivity (ETC) of CNT nanofluids by means of a differential effective medium theory together with Brownian motion. Their results showed that augmentation of ETC, correlated with Brownian motion was remarkably greater in dilute nanofluids.

Roberts and Walker [75] studied on the mixture of alumina/water's performance of different volume loadings using a commercially available electronics cooling system. Their results indicated that convective heat transfer increased with the addition of nanoparticles in the commercial cooling system with nanoparticles' volume loadings up to 1.5% by volume. They also observed nanoparticle suspensions from hours to weeks depending on the particle's size.

Rostamani *et al*. [76] numerically investigated the turbulent flow of nanofluids with different volume concentrations of nanoparticles being copper oxide (CuO), alumina (Al_2O_3) and oxide titanium (TiO_2) flowing along two-dimensional duct under constant heat flux condition. They used water as based fluid. It was found that when the volume concentration was increased the wall shear stress and heat transfer rates augmented. As it can be observed in Fig. (**7a**), the wall shear stress increased with increasing volume concentrations for TiO_2-water nanofluid. Also the wall shear stress has been shown for the comparison of three different nanofluids at the Reynolds number of 40,000 and 3% volume concentration in Fig. (**7b**). Nusselt number was affected more from CuO nanoparticles than Al_2O_3 and TiO_2 nanoparticles to get a constant volume concentration and Reynolds number.

Singh *et al*. [77] analyzed entropy generation owing to the flow and heat transfer by using nanofluids theoretically. They used alumina-water nanofluids and mainly three diameters of tube such as a microchannel (0.1 mm), a minichannel (1 mm) and a conventional channel (10 mm) for the sensitivity of entropy. Their results showed that entropy generation behaviour of nanofluids in the microchannel and conventional channel were estimated accurately by the reduced equation with the help of order of magnitude analysis. In conclusion, they reported the existence of an optimum diameter where the entropy generation rate was found to be the minimum for a specific nanofluid during both laminar and turbulent flow.

Sundar and Sharma [78] studied on the measurement of thermal conductivity and viscosity of Al_2O_3 nanofluid via experiments at different volume concentrations and temperatures and verification of them. Researchers inserted a plain tube with twisted tape and tried to obtain the convective heat transfer coefficient and friction factor at various volume concentrations experimentally. According to the results, the heat transfer coefficient and friction factor, which had 0.5% volume concentration of nanofluid and twist ratio of five conditions, increased heat transfer and friction factor 33.51% and 1.096 times respectively in comparison to the base fluid of water.

Vajjha *et al*. [79] developed new correlations for the determination of convective heat transfer and the friction factor. They used nanoparticles of aluminum oxide, copper oxide and silicon dioxide dispersed in 60% ethylene glycol and 40% water by mass. Researchers measured the properties in the fully developed turbulent regime for the mentioned three nanofluids at several particle volumetric concentrations. They calculated the rheological and the thermophysical properties such as viscosity, density, specific heat and thermal conductivity primarily and then utilized form these properties to improve new correlation as a function of these properties and the particle volumetric concentration.

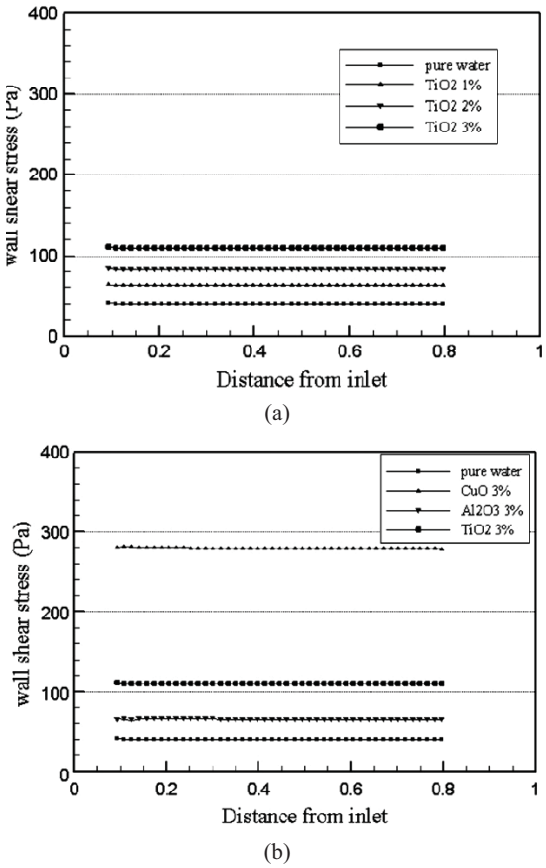

Fig. (7). Effect of the nanoparticle on wall shear stress (**a**: volume concentration for TiO_2 nanofluid, **b**: Comparison for different nanoparticles at same conditions) [From Rostamani *et al*. [76], with permission from Elsevier].

Vajjha *et al.* [80] analyzed three-dimensional laminar flow and heat transfer with some mixtures containing Al_2O_3 and CuO particles/ethylene glycol and water and also compared these fluids' performance to the base fluid. They developed a new correlation about the determination of viscosity and thermal conductivity of nanofluids as a function of particle volumetric concentration and temperature. It was found that the heat transfer coefficient and the friction factor augmentation increased with the increasing in nanofluids' volumetric concentrations at several Reynolds numbers.

Wei *et al.* [81] investigated the chemical solution method to produce CuS/Cu_2S nanofluids and tried to obtain their thermal conductivity. They mentioned the increase or decrease of the thermal conductivity of nanofluids with proper references.

Wei and Wang [82] presented a microfluidic chemical solution technique, to produce Cu nanofluids. The method changed batch-based macro reactors in the conventional chemical solution method by continuous-flow of microfluidic micro reactors, thus they provided the production of nanofluids with several microstructures. The results showed that Cu nanofluids produced by this technique, had higher stability performance even after more than 100 h.

Yang and Lai [83] benefited from a single-phase approach and focused on creating mathematical model to simulate the forced convection flow of Al_2O_3-water nanofluid in the radial flow cooling system. They indicated that the heat transfer coefficient augmentation depended on increasing of the Reynolds number and the nanoparticle volume fraction, but the pressure drop increase depended more on the increase of particle concentration.

Yu *et al*. [84] investigated preparation of stable ethylene glycol based copper nanofluids via a two-step method. They utilized polyvinyl pyrrolidone as dispersant that could remain stable for a long term. They observed that thermal conductivity significantly increased for the determined nanofluids. The results showed that they achieved 46% increase for the enhancement ratio under 0.5 vol.% at 50 °C conditions. In addition, they suggested 15 min waiting time at least for getting correct thermal conductivities of ethylene glycol based copper nanofluids.

The applied areas and developing process of nanofluids were thoroughly summarized by Wong and Leon [85]'s review paper. Their paper investigated the current and future applications of nanofluids as heat transfer applications (industrial cooling applications, smart fluids, nuclear reactors, extraction of geothermal power and other energy sources), automotive applications (nanofluid coolant, nanofluid in fuel, brake and other vehicular nanofluids), electronic applications (cooling of microchips), biomedical applications (nanodrug delivery, cancer theraupetics, cryopreservation, nanocryosurgery, sensing and imaging) and other applications (nanofluid detergent) generally and also mentioned the increased heat transfer properties by means of nanofluids which made them appropriate for such applications.

Duangthongsuk and Wongwises [86] reported a comparison of the differences between using measured and computed thermophysical properties to describe the heat transfer performance of TiO_2-water nanofluids. In this study, TiO_2 nanoparticles with average diameters of 21 nm and a particle volume fraction of 0.2-1 vol.% were used. The thermal conductivity and viscosity of nanofluids were measured by using transient hot-wire apparatus and a Bohlin rotational rheometer, respectively. The well-known correlations calculating the thermal conductivity and viscosity of nanofluids were used for describing the Nusselt number of nanofluids and were compared with the results from the measured data. The results showed that the use of the models of thermophysical properties for calculating the Nusselt number of nanofluids gave similar results to use of the measured data. Where there was a lack of measured data on thermophysical properties, the most appropriate models for computing the thermal conductivity and viscosity of the nanofluids were the models of Yu and Choi and Wang *et al*., respectively.

Duangthongsuk and Wongwises [87] reported the heat transfer coefficient and friction factor of the TiO_2-water nanofluids flowing in a horizontal double tube counter-flow heat exchanger under turbulent flow conditions, experimentally. TiO_2 nanoparticles with diameters of 21 nm dispersed in water with volume concentrations of 0.2-2 vol.% were used as the test fluid. The results showed that the heat transfer coefficient of nanofluid being higher than that of the base liquid increased with an increase in the Reynolds number and particle concentrations. The heat transfer coefficient of nanofluids was found to be approximately 26% greater than that of pure vol.%, and the results also showed that the heat transfer coefficient of the nanofluids at a volume concentration of 2.0 vol.% was approximately 14% lower than that of base fluids for given conditions. For the pressure drop, the results showed that the pressure drop of nanofluids being slightly higher than that of the base fluid increased with the increasing in volume concentrations. Finally, the new correlations were especially proposed for predicting the Nusselt number and friction factor of the nanofluids.

3d. Somestudies of 2009

Bergman [88] studied laminar, internal forced convection by using nanofluids. The work included the descriptions of nanofluid's specific heat experimentally and explaining their two effects. One of them was about the increased thermal conductivity and the other was about the reduced specific heat of the nanofluid in comparison to its base liquid. To measure heat transfer augmentation, he presented a dimensionless effectiveness number to observe the nanofluid's performance and compared it with base fluid. The results illustrated the use of different nanofluids, that could either increase or decrease thermal performance.

Bianco *et al*. [89] investigated a numerical method in laminar forced convection flow of a water-Al_2O_3 nanofluid in a circular tube used to have a constant and uniform heat flux at the wall. The work was examined with a single and two-phase model by employing either constant or temperature-dependent properties. The size of particles was 100 nm. The maximum difference between single and two-phase models was resulted about 11% in the average heat transfer coefficient. Nanofluids` convective heat transfer coefficient was higher than that of its base liquid. The particle volume concentration increased the heat transfer enhancement but it increased wall shear stress values at the same time. In their study, temperature dependents models had higher heat transfer coefficients and lower shear stresses. They found that the heat transfer always increased with increasing both Reynolds number and shear stress.

He *et al*. [90] studied numerically single phase method and combined it with Euler and Lagrange method on the convective heat transfer of TiO_2 nanofluids those flowing through a straight tube under the laminar flow conditions. They observed the effects of nanoparticles' concentrations, Reynolds number, and various nanoparticle sizes on the flow and the convective heat transfer behavior. It was found that heat transfer of nanofluids increased remarkably in the entrance region. As the numerical results were found to be in good agreement with the experimental data, a reasonable good agreement was accomplished.

Hwang *et al*. [91] quantified the pressure drop and convective heat transfer coefficient of water-based Al_2O_3 nanofluids flowing through a uniformly heated circular tube in the fully developed laminar flow regime. According to the experimental results, they found a good agreement with analytical predictions from the Darcy's equation for single-phase flow for the nanofluid's friction factor. They illustrated the flattening of velocity profile, induced from large gradients in bulk properties such as nanoparticle concentration, thermal conductivity and viscosity in numerical solutions. It was suggested that this flattening of velocity profile had a suitable mechanism for the convective heat transfer coefficient enhancement exceeding the thermal conductivity enhancement.

Jung *et al*. [92] quantitated convective heat transfer coefficient and friction factor of nanofluids in rectangular microchannels. They experimentally studied the effect of the volume fraction of the nanoparticles on the convective heat transfer and fluid flow in microchannels where Aluminum dioxides (Al_2O_3) with diameter of 170 nm nanofluids at different particle volume fractions were flowing. They measured the convective heat transfer coefficient of the Al_2O_3 nanofluid in laminar flow regime that increased up to 32% comparing with the distilled water at a volume fraction of 1.8 volume percent without friction loss. It was established that the measured Nusselt number increased with increasing the Reynolds number in laminar flow regime. The measured Nusselt number was correlated with Reynolds number and Prandtl number by virtue of the thermal conductivity of nanofluids was measured to be less than 0.5. They found that Nusselt number and Friction factor changed various volume fractions of nanoparticles in different dimension of micro-channels as shown in Fig. (**8**).

Kakaç and Pramuanjaroenkij [93] researched literature works on convective heat transfer on the enhancement of heat transfer of nanofluids. The objective of their review study was to compile the significant published articles on the enhancement of the forced convection heat transfer of nanofluids.

Kim *et al*. [94] study showed to examine the effect of nanofluids on convective heat transfer experimentally through a circular straight tube with a constant heat flux condition in the laminar and turbulent flow regime. They studied the effects of thermal conduc tivity and supernatant nanoparticles of the nanofluids on convective heat transfer under differentflow regimes. Thermal conductivity and

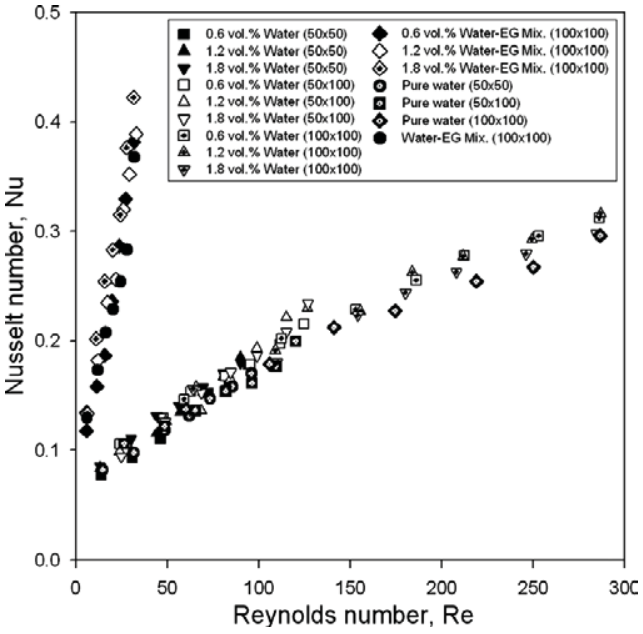

(a)

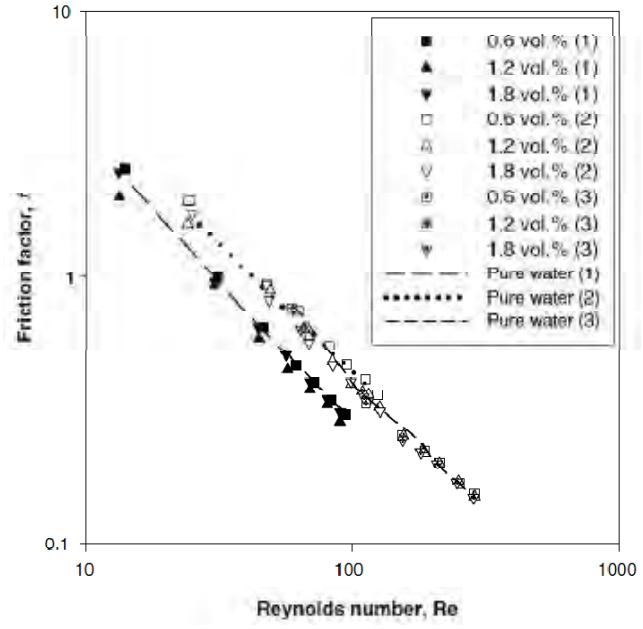

(b)

Fig. (8). Variation of Nusselt number (**a**) and Friction factor (**b**) on Reynolds number in various volume fraction in different dimensions of microchannels of (1)50*50μm^2 (2)50*100 μm^2 (3)100*100 μm^2 [From Jung *et al.*[92], with permission from Elsevier].

convective heat transfer coefficient were increased up to 8% and 20% respectively, in alumina nanofluids including 3 vol% of suspended particles. They reported that the thermal conductivity of nanofluids was similar to that of water, and the convective heat transfer coefficient increased by only 8% in laminar flow in amorphous carbonic nanofluids. It was determined that the augmentation of the convective heat transfer was much greater than that of the thermal conductivity of nanofluids on account of the movements of nanoparticles at the entrance region.

Kulkarni *et al.* [95] investigated measurements of convective heat transfer and viscosity of nanofluids, and estimated how they performed heating buildings in cold regions. They perfromed experimental works using copper oxide, aluminum oxide and silicon dioxide nanofluids, each in an ethylene glycol and water mixture. They obtained some calculations for conventional finned-tube heat exchangers utilizing in buildings in cold regions. The use of nanofluids in heat exchangers decreased volumetric and mass flow rates and resulted in an overall pumping power savings in their study. It was found that the use of nanofluids to heat buildings decreased the size of the heat transfer system and reduced the accompanying pressure loss and the subsequent pumping power. It was observed that the volume concentration increased with the nanofluid viscosity at a specific temperature. Fig. (**9a** and **9b**) indicate the comparison of viscosity and pressure loss of Al_2O_3, CuO, SiO_2 and EG/Water at same particle volumetric concentration.

Mintsa *et al*. [96] researched the effects of particle volume fraction, temperature and particle size to measure the effective thermal conductivity of alumina/water and copper oxide/water nanofluids. Readings at ambient temperature as well as over a relatively large temperature range were performed for different particle volume fractions up to 9%. As a result, they obtained an increase in the effective thermal conductivity with an increase in particle volume fraction and with a decrease in particle size. The relative increase in thermal conductivity was also claimed to be more at high temperatures.

Murshed *et al*. [97] researched a combined static and dynamic mechanisms based on a model for anticipating the effective thermal conductivity of nanofluids. In their study, the model incorporated the effects of particle size, nanolayer, Brownian motion, particle surface chemistry and interaction potential which were about the static and dynamic mechanisms responsible for the enhanced effective thermal conductivity of nanofluids. Also, the model was found to have logically a good agreement with the experimental results of various types of nanofluids

Namburu *et al*. [98] studied a numerical analysis of turbulent flow and heat transfer of three different nanofluids (CuO, Al_2O_3 and SiO_2) in an ethylene glycol and water mixture flowing through a circular tube under constant heat flux condition. They correlated new correlations for viscosity up to 10% volume concentration for these nanofluids as a function of volume concentration and temperature from the experiments. They found out that calculation results had formalized with existing well known correlations. They obtained that nanofluids including smaller diameter nanoparticles had higher viscosity and Nusselt number. They compared the convective heat transfer coefficients of CuO, $Al_2O_3$and SiO_2 nanofluids with each other. They said that Nusselt number improved by 35% for 6% CuO nanofluids over the base fluid at a constant Reynolds number.

Rea *et al*. [99] studied on laminar convective heat transfer and viscous pressure loss of alumina-water and zirconia-water nanofluids in a flow loop with a vertical heated tube. They observed that the heat transfer coefficients of entrance region and fully developed region increased as 17% and 27%, respectively, and for alumina-water nanofluid at 6% vol according to pure water. Furthermore, the zirconia-water nanofluid's heat transfer coefficient increased as 2% in the entrance region and 3% in the fully developed region at 1.32 vol %. They found that the measured pressure loss for the nanofluids was generally much greater than for pure water .It was indicated that the measured nanofluid's heat transfer coefficient and pressure loss were in good agreement with the conventional model predictions of laminar flow.

Pantzali *et al*. [100] studied the efficiency of nanofluids as coolants. Nanoparticles were mixed for testing nanofluid's thermo-

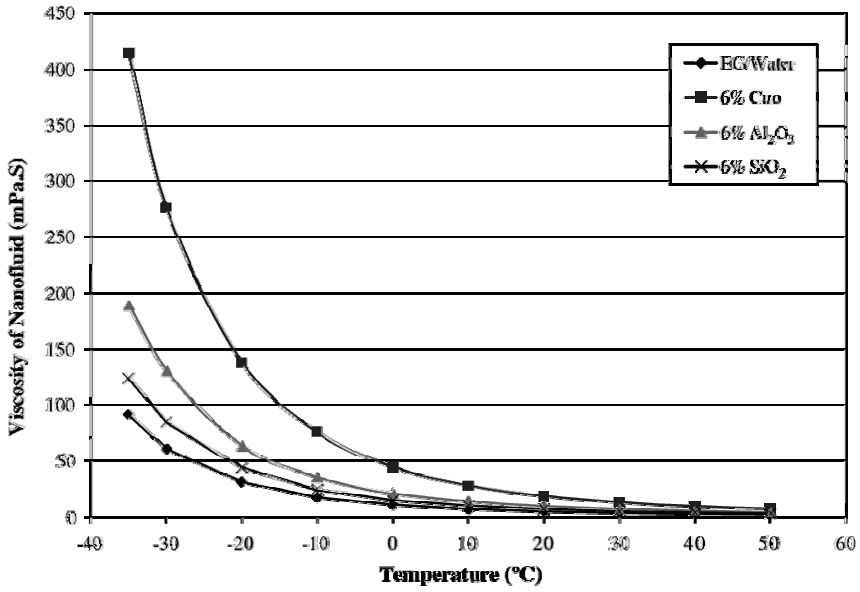

(a)

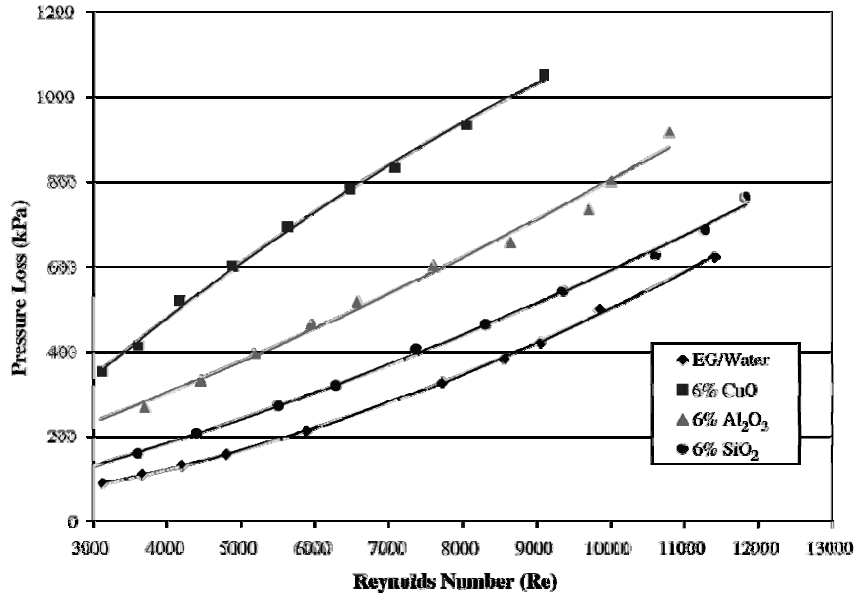

(b)

Fig. (9). The viscosity variation of different nanofluids of same concentration and the base fluid in terms of temperature (**a**) Pressure loss of different nanofluids in terms of conventional glycol/water mixture (**b**) [From D.P. Kulkarni *et al*. [95], with permission from Elsevier].

physical properties. They used a typical nanofluid, namely a 4% CuO suspension in water and investigated nanofluid's performance in a commercial herringbone-type PHE experimentally. They showed the type of flow inside the heat exchanger equipment and also its influence on the efficiency of a nanofluid as coolant. The heat exchanger performance depended on the fluid viscosity due to its significance. They obtained large volumes of required nanofluids and reported that turbulent flow was usually developed in industrial heat exchangers.

Xie and Chen [101] produced homogeneous and stable nanofluids using suspended and well dispersible multi-walled carbon nanotubes (CNTs) into ethylene glycol base fluid. They said that CNT nanofluids improved the thermal conductivity and the enhancement ratios increased with increasing the nanotube loading and their temperature. Their work showed that the straightness ratio, aspect ratio and aggregation had collective effect on the thermal conductivity of CNT nanofluids.

Pantzali *et al*. [102] investigated the effect of the use of a nanofluid in a miniature plate heat exchanger (PHE) with modulated surface both experimentally and numerically. Firstly, they worked on thermophysical properties (i.e., thermal conductivity, heat capacity, viscosity, density and surface tension) of a typical nanofluid (CuO in water, 4% v/v), then the effect of surface modulation on heat transfer augmentation and friction losses were researched by simulating the existing miniature PHE as well as a notional similar PHE with flat plate using a CFD code. Conclusively, they studied the effect of the nanofluid on the PHE performance in comparison to that of a conventional cooling fluid (i.e., water). As a result of

their study, the required nanofluid volumetric flow rate for a given heat duty was found to be lower than that of water causing lower pressure drop. Shortly, they concluded that the use of smaller equipment and less pumping power were required. Since the total volume of the equipment was the main issue, use of the nanofluids seemed to be a promising solution towards designing efficient heat exchanging systems. The only disadvantages were the high price and the possible instability of the nanoparticle suspensions.

Vajjha and Das [103] investigated the determination of the thermal conductivity of three nanofluids comprising aluminum oxide, copper oxide and zinc oxide nanoparticles dispersed in a base fluid of 60:40 (by mass) ethylene glycol and water mixture. According to evaluated particle volumetric concentration being up to 10% and the temperature range of the experiments varied from 298 to 363 K the results indicated an increase in the thermal conductivity of nanofluids compared to the base fluids with an increasing volumetric concentration of nanoparticles parallel with the thermal conductivity that also increased substantially with an increase in temperature. By using their experimental data for comparisons with various existing models to determine thermal conductivity they developed a model that was a refinement of an existing model, that incorporated the classical Maxwell model and the Brownian motion effect to account for the thermal conductivity of nanofluids as a function of temperature, particle volumetric concentration, the properties of nanoparticles, and the base fluid with these experimental data.

Wen *et al*. [104] carried out a critical review of research on heat transfer applications of nanofluids with the aim of identifying the limiting factors so as to boost their development.

Hadjov [105] studied spherical nanoparticles with a conductive interface in the self-consisted scheme for forecasting the thermal conductivity of nanofluids. They adopted a flux jump in the particle-fluid interface opposite to the temperature jump that was assumed in the case of thermal barrier resistance. Upper and lower bounds to the homogenized suspension thermal conductivity were gained by their working to the particle packing.

Ali *et al*. [106] numerically studied two-dimensional turbulent convective heat transfer behavior of alumina nanoparticle dispersed in water flow in a horizontal circular pipe at constant wall temperature. The finite-volume method was employed considering the full range of flow at the entrance length and at the fully developed region. They showed that the shear stress was observed to be increasing at any x station along the pipe as the concentration of nanoparticle increased and achieved its higher value at the beginning of the pipe at the entrance region and then dropped to an asymptotic value at the fully developed region. When the velocity increased, both Nusselt number and the shear stress were observed to be increasing. As a result Reynolds number was observed to decrease as the concentration increased at fixed inlet velocity.

Duangthongsuk and Wongwises [107] reported the thermal conductivity and dynamic viscosity of nanofluids experimentally. TiO_2 nanoparticles dispersed in water with volume concentration of 0.2-2 vol.% were used in their study. A transient hot-wire apparatus was used for measuring the thermal conductivity of nanofluids whereas the Bohlin rotational rheometer (Malvern Instrument) for measuring the viscosity of nanofluids. The data were collected for temperatures ranging from 15 °C to 35 °C. The results showed that the measured viscosity and thermal conductivity of nanofluids increased as the particle concentrations increased and were found to be higher than the values of the base liquids. Furthermore, thermal conductivity of nanofluids increased by increasing nanofluid temperatures and, conversely, the viscosity of nanofluids decreased by increasing temperature of nanofluids. Moreover, the measured thermal conductivity and viscosity of nanofluids were found to be quite different from the predicted values evaluated from the existing correlations and the data reported by other researchers. Finally, new thermophysical correlations were proposed for predicting the thermal conductivity and viscosity of nanofluids.

Duangthongsuk and Wongwises [108] reported an experimental study on the forced convective heat transfer and flow characteristics of a nanofluid consisting of water and 0.2 vol.% TiO_2 nanoparticles. The heat transfer coefficient and friction factor of the TiO_2-water nanofluid flowing in a horizontal double-tube counter flow heat exchanger under turbulent flow conditions were investigated. They utilized Degussa P25 TiO_2 nanoparticles of about 21 nm diameter in their study. The results showed that the convective heat transfer coefficient of nanofluid was found to be slightly higher than that of the base liquid by about 6-11%. The heat transfer coefficient of the nanofluid increased with an increase in the mass flow rate of the hot water and nanofluid, and it also increased with a decrease in the nanofluid temperature, and the temperature of the heating fluid showed no significant effect on the heat transfer coefficient of the nanofluid. It was also noted that the Gnielinski equation failed to predict the heat transfer coefficient of the nanofluid. Finally, the use of the nanofluid presented a little penalty in pressure drop.

3e. Somestudies of 2008

Bi *et al*. [109] studied nanoparticles in the working fluid for observing domestic refrigerator's reliability and performance. They utilized from mineral oil/TiO_2 nanoparticle mixtures such as the lubricant instead of Polyol-ester (POE) oil in the 1,1,1,2-tetrafluoroethane (HFC134a) used in refrigerator. Researchers analyzed that the refrigerator performance regarding the energy consumption and freezing capacity was enhanced with the use of nanoparticles. Their results showed that HFC134a and mineral oil with TiO_2 nanoparticles worked normally and securely in the refrigerator. They also observed that the refrigerator had higher performance than the HFC134a and POE oil system,and the use of nanoparticles with 0.1% mass fraction reduced energy consumption 26.1% compared to the HFC134a and POE oil system.

Hwang *et al*. [110] tested homogeneous dispersion of nanoparticles in nanofluids. They investigated various physical treatment techniques based on two step methods comprising ultrasonic bath, ultrasonic disruptor and high-pressure homogenizer to confirm their versatility for preparing stable nanofluids. They used CB (carbon black) and Ag nanoparticles with the diameter of 330nm to 585nm. Their results indicated that Ag nanoparticle, which was generated by the modified magnetron sputtering system, dispersed homogeneously and sustained its stability in the silicon oil based fluid.

Karthikeyan *et al*. [111] studied on synthesizing of CuO nanoparticles having average diameter of 8 nm by using a simple precipitation technique and observed thermal properties of the suspensions. They utilized from water and ethylene glycol as based fluids and 1 vol.% CuO nanoparticles. Their results showed that thermal conductivity increased with increasing finer particle size and mono dispersity of nanoparticles. They obtained some results from experiments that of thermal conductivity being significantly affected from the nanoparticles size, polydispersity, cluster size and the volume fraction of particles.

Khandekar *et al*. [112] studied on a closed two-phase thermosyphon's overall thermal resistance. They selected pure water and various water based nanofluids (of Al_2O_3, CuO and laponite clay) as working fluids. The results indicated that all these nanofluids had worse thermal performance than pure water. In additionto all nanofluids on copper substrate, having the same average roughness as that of the thermo syphon container pipe was greater than that of pure water.

Lee *et al*. [113] synthesized and characterized aqueous nanofluids including low volume concentrations of Al_2O_3 nanoparticles from 0.01 to 0.3 vol.%. Their results pointed out that those alumina nanoparticles had the highest dispersion and stabilization performance in DI water at 5 h of ultrasonic vibration. They observed that

the temperature increased with decreasing the Al_2O_3-water nano fluids' viscosity. In addition, Al_2O_3-water nano fluids' viscosity indicated a nonlinear correlation with the concentration even in the low volume concentration (from0.01 to 0.3 vol.%.).

Murshed *et al*. [114] searched the existing theories in the literature on thedetermination of nanofluids' properties such as synthesis methods, potential application areas, experimental and analytical studies on the effective thermal conductivity, effective thermal diffsivity, convective heat transfer, and electrokinetic properties and compared them with each other.

Oh *et al*. [115] investigated 3-omega (3 w) method as new application to measure the thermal conductivity of nanofluids and they provided information about it. Their new theoretical model was proposed instead of the transient hot wire method for the determination of thermal conductivity. They tested the effective thermal conductivity of Al_2O_3 nanofluids in DI water and EG at room temperature. Furthermore, thermal response showed interesting effects owing to agglomeration and sedimentation of nanoparticles.

Kang *et al*. [116] studied on measuring the vapor absorption rate and heat transfer rate for falling film flow of binary nanofluids, being tested at the same conditions with pure water, and tried to observe the changes of heat and mass transfer. They used some parameters such as base fluid concentration of LiBr, the concentration of nanoparticles in weight %, and nano-particle constituents. They prepared the mixture of H_2O/LiBr solution with nanoparticles of Fe and Carbon nanotubes (CNT). Their results illustrated that the mass transfer increase was more than the heat transfer augmentationin the binary nanofluids with Fe and CNT and the properties of mass transfer of CNT nanoparticles were better than those of Fe nanoparticles.

Lu and Fan [117] studied on molecular dynamics (MD) simulation method, applicable for a stationary nanofluids of the volume fractions less than 8%. They used this method to simulate nanofluids' thermophysical properties such as thermal conductivity and viscosity. They compared experimental data with numerical results and obtained good results. They found it very useful to estimate some thermal properties of nanofluids. Their results also showed that thermal conductivity and the viscosity of nanofluids depended on the volume fraction and the size of nanoparticles.

Nguyen *et al*. [118] focused on the temperature and particle volume concentration's impact on the dynamic viscosity for the water-Al_2O_3 mixture experimentally. They benefited from piston-type device used as a commercial viscometer for temperatures at room condition. Their results indicated an enhancement on the nanofluid dynamic viscosity in respect with particle volume fraction; however temperature increase showed a negative effect on it.

Chen *et al*. [119] presented the properties of the effective thermal conductivity, their rheological behavior and forced convective heat transfer of the nanofluids. They found that thermal conductivity increased as 3% at 25 °C and 5% at 40 °C for the 2.5 wt.% nanofluid. They observed that nanofluidsincluding spherical titanium nanoparticles had better properties of thermal conductivity and convective heat transfer coefficient. They also suggested new systems to increase the convective heat transfer coefficient.

3f. Somestudies of 2007

Ding *et al*. [120] experimentally studied on the forced convective heat transfer using aqueous and ethylene glycol-based spherical titanium nanofluids, and aqueous-based titanate nanotubes, carbon nanotubes and nano-diamond nanofluids.. They accomplished to formulate these nanofluid's specifications. They indicated that all the formulated nanofluids performed a higher effective thermal conductivity than those predicted by the conventional theories. Apart from the ethylene glycol-based titanium nanofluids, all other nanofluids were observed to be non-Newtonian. They reported that the convective heat transfer coefficient enhancement was substantially higher than the thermal conduction enhancement. However, they indicated deterioration of the convective heat transfer for ethylene glycol-based titanium nanofluids at low Reynolds numbers. They recommended the effective thermal conductivity as to be responsible for the experimental observations.

Zhang *et al*. [121] accomplished to measure the effective thermal conductivity and thermal diffusivity of Au/toluene, Al_2O_3/water, TiO_2/water, CuO/water and CNT/water nanofluids by utilizing from the transient short-hot-wire technique. In their study, the average diameters of Au, Al_2O_3, TiO_2 and CuO spherical particles were 1.65, 20, 40 and 33 nm, respectively. Also the average length and diameter of CNFs were 10 l m and 150 nm, respectively. According to results obtained, the effective thermal conductivities of the nanofluids indicated no abnormal enhancements.

Ko *et al*. [122] published an experimental investigation on the flow characteristics of the aqueous suspensions of carbon nanotubes (CNTs). They tried to measure pressure drop to obtain stable nanotube suspensions by utilizing two methods. They studied the effects of CNT loading and various preparation methods and measured the pressure drops in a horizontal tube and viscosities of nanofluids. They found that the CNT nanofluids prepared by the acid treatment had much smaller viscosity than the ones made with surfactant at the same volume fraction. They indicated that the friction factor of stabilized CNT nanofluids (by adding surfactant) was much greater than that of CNT nanofluids prepared by acid treatment, and nanofluids had greater friction factors than distilled water under laminar flow conditions. It was found that the friction factors of nanofluids were inversely similar to that of the base fluids. As the flow rate improved under turbulent flow conditions,they noticed that nanofluids had low friction factors than pure water flows at definite range of flow rates.

Mansour *et al*. [123] studied the uncertainty impacts regarding with the physical properties of water-Al_2O_3 nanofluid on the determination of the thermohydraulic performance for both laminar and turbulent fully developed forced convection in a tube with uniform wall heat flux. They suggested many experimental data necessary to determine the real potential of nanofluid.

Hong *et al*. [124] firstly reported that the thermal conductivity (TC) and heat transfer of nanofluids could be enhanced by the external magnetic field. The nanofluids contained carbon nanotubes (CNTs) and magnetic-field-sensitive nanoparticles of Fe_2O_3. The sensible explanation for these interesting determinations was that the Fe_2O_3 particles formed aligned chains under applied magnetic field that helped to connect the nanotubes. In that magnetic field, the particles slowly moved and formedlarge clumps of particles, and caused clumping of CNTs, then decreased the TC.

Li and Peterson [125] pointed out the Brownian motion of the nanoparticles in these suspensions as one of the potential contributors to this enhancement and the mechanisms that could contribute considerable discussion and debate to this subject. The mixing effect of the base fluid in the immediate vicinity of the nanoparticles caused by the Brownian motion was examined, modeled and was also compared with the experimental data in the literature. Moreover, simulation results showed the effective thermal conductivity of nanofluids being affected by this mixing effect.

Yoo *et al*. [126] prepared some nanofluids such as T_iO_2, Al_2O_3, F_e, and WO_3compounds in a two-step procedure by dispersing in a base fluid. The transient hot wire method was used for the calculation of thermal conductivity. These nanofluids' thermal conductivities were analyzed and then compared with each other.

Avsec and Oblak [127] proposed a mathematical model for the calculation of thermophysical properties of nanofluids on the basis of statistical nanomechanics. In this study, they indicated two calculation methods to describe the properties such as classical and statistical mechanics. It was reported that the classical mechanics had no insight into the microstructure of the substance. On the other

hand, it calculated the properties of state both on the basis of molecular motions in a space and on the basis of the intermolecular interactions. On the contrary to the classical mechanics, they suggested that the statistical mechanics calculated the thermomechanic properties of state on the basis of intermolecular interactions between particles in the same system of molecules. They illustrated that the systems were composed of a very large number of particles. The results of the analysis were compared with experimental data that indicated a relatively good agreement.

He *et al*. [128] studied different particle (agglomerate) sizes in stable aqueous TiO_2 nanofluids and calculated their static thermal conductivity and rheological behavior. Heat transfer and flow behavior were investigated in a vertical pipe during both laminar and turbulent flow regimes. Thermal conduction was observed to increase with addition of nanoparticles into the base liquid but decreased with increasing particle (agglomerate) size. Increasing particle (agglomerate) size and particle concentration caused to grow the constant viscosity. In both the laminar and turbulent flow regimes, convective heat transfer coefficient increased with increasing nanoparticle concentrations.

Lee and Mudawar [129] experimentally studied water-based nanofluids containing small concentrations of Al_2O_3 in the microchannel cooling. They investigated the high thermal conductivity of nanoparticles in the single-phase heat transfer coefficient, especially for laminar flow. In the entrance region of micro-channels, maximum heat transfer coefficients were obtained. Greater sensitivity to heat flux was caused by higher concentrations.

Wang and Mujumdar [130] reviewed convective heat transfer using suspensions of nanometer-sized solid particles in base liquids. The transport properties and heat transfer characteristics of the suspension were found to be significantly dependable to the suspended nanoparticles.

Trisaksri and Wongwises [131] reviewed the literature on the general heat transfer characteristics of nanofluids. It was found that only a few papers had discussed on the convective heat transfer of nanofluids. The purpose of this article was to review the literature mentioning convective heat transfer of nanofluids, such as the experimental and theoretical investigations.

Daungthongsuk and Wongwises [132] reviewed suspension of ultrafine particles in a conventional base fluid which tremendously enhanced the heat transfer characteristics of the original fluid. They reported that nanofluids were expected to be ideally suited in practical applications as their use incurred little or no penalty in pressure drop because the nanoparticles were ultrafine, therefore, appearing to behave more like a single-phase fluid than a solid-liquid mixture. The purpose of their article was to summarize the published subjects respectively with the investigating forced convective heat transfer of the nanofluids both experimentally and numerically.

3g. Somestudies of 2006

Hwang *et al*. [133] showed the higher effective thermal conductivity of nanofluid consisting of nanoparticles dispersed in base fluid than those dispersed in its pure fluid. They used four kinds of nanofluids such as multiwalled carbon nanotube (MWCNT) in water, CuO in water, SiO_2 in water, and CuO in ethylene glycol. They used transient hot-wire method to measure the thermal conductivities. They reported that the increase in thermal conductivity enhancement of water-based MWCNT nanofluid was 11.3% at a volume fraction of 0.01. According to their results, the thermal conductivities of both particles and the base fluid affected the thermal conductivity enhancement of nanofluids.

Hwang *et al*. [134] used the nanoparticles of multi-walled carbon nanotube (MWCNT), fullerene, copper oxide, silicon dioxide and silver to improve the thermal conductivity and lubrication. DI water, ethylene glycol, oil, silicon oil and poly-a-olefinoil (PAO) were taken as the base fluids. They measured the thermal conductivity and kinematic viscosity to investigate the thermo-physical properties of nanofluids. UV-vis spectrophotometer was used to check the stability estimation of nanofluid. They found that the increase in particle volume fraction displayed a positive effect on the increase in thermal conductivity of nanofluid that increased with increasing particle volume fraction.

Liu *et al*. [135] presented a study on the enhancement of the thermal conductivity of water in the presence of copper (Cu) using the chemical reduction method. They reported that their method was used firstly for the synthesis of nanofluids containing Cu nanoparticles in water. Their results showed that Cu-water nanofluids having low concentration of nanoparticles had higher thermal conductivities than those of the water base fluid without Cu. Beside this, thermal conductivity was improved up to 23.8% for Cu nanoparticles at a volume fraction of 0.001 (0.1 vol.%).

Palm *et al*. [136] investigated the heat transfer enhancement capabilities of coolants' laminar forced convection flow with suspended metallic nanoparticles inside typical radial flow cooling systems. They obtained significant heat transfer enhancement with the use of these fluid/solid particle mixtures. They also indicated the noticeable differences between the use of constant property of nanofluids (temperature independent) and nanofluids with temperature dependent properties.

Heris *et al*. [137] investigated the laminar flow convective heat transfer of nanofluids containing CuO and Al_2O_3 oxide nanoparticles in water through circular tube with constant wall temperature boundary condition. They experimentallyshowed that homogeneous model should be used for the prediction of nanofluids properties concerning the determination of the single phase heat transfer coefficient enhancement. Al_2O_3-water nanofluids were noted to have higher heat transfer enhancement with the increase in the volume fraction.

3h. Somestudies of 2005

Xuan *et al*. [138] determined heat transfer process and flow properties of Cu-water nanofluid flowing inside a channel by using the thermal Lattice Boltzmann model. Because they took into consideration the molecular dynamics and bridged the gap of macroscopic or microscopic challenge of the nanofluids, this method showed a significant advantage. Two existing methods used for application of this method to model the thermal fluid flow problem were the multispeed (MS) and the double-distribution-function (DDF). In this study, double-distribution-function (DDF) was used that led to two separate distribution functions as follows: The temperature was treated as a passive diffusing scalar, that was simulated by a distribution function notdependent on density distribution, respectively. The feature point of the Lattice Boltzmann method was the assumption that the particles mesoscopically located at a series of lattices and their distributions corresponding to the Boltzmann distribution. The viscosity dissipation term in the Lattice Boltzmann equation for energy transport was neglected in order to simulate heat transfer characteristics of the nanofluid. According to numerical results, for 1% volume fraction the Nusselt number of Cu-water nanofluid was calculated 27% higher than that of pure water at the same Reynolds number. Furthermore, random motion of the particles suspended in the fluid could be seen along the main flow direction because of fluctuations of the Nusselt number of the nanofluid.

Liu *et al*. [139] studied thermal conductivity enhancements in ethylene glycol and synthetic engine oil using multiwalled carbon nanotubes (MWNTs). The volume concentration of CNT-ethylene glycol suspensions and synthetic engine oil suspensionswere below 1.0 and 2.0 vol.% respectively. They used a modified transient hot wire method to measure the thermal conductivities of the CNT suspensions and observed significant increase in CNT-ethylene glycol suspensions' thermal conductivities in comparison to the ethylene glycol base fluid without CNT. They noted that CNT–

synthetic engine oil suspensions gave the similar results with CNT-ethylene glycol suspensions. They obtained 12.4% enhancement on thermal conductivity for CNT-ethylene glycol suspensions at a volume fraction of 0.01 (1 vol.%) and 30% enhancement at a volume fraction of 0.02 (2 vol.%) for CNT-synthetic engine oil suspension, thermal conductivity was enhanced by 30% at a volume fraction of 0.02 (2 vol.%). As a result of their analysis, the thermal conductivity ratio of CNT-synthetic engineoil suspension was found to be having a noticeably higher value than that of the CNT-ethylene glycolsuspension.

Maiga *et al*. [140] used two particular geometrical configurations, namely a uniformly heated tube and a system of parallel, coaxial and heated disks to study the laminar forced convection flow of nanofluids numerically. By using the mixtures of water-γAl_2O_3 and Ethylene Glycol-γAl_2O_3they obtained a significant increase in the heat transfer coefficient in the presence of nanoparticles dispersed into the base fluids. They also illustrated that the heat transfer coefficient increased with increasing the particle concentration having severe effects on the wall shear stress that increased considerably with the particle loading. The Ethylene Glycol-γAl_2O_3 nanofluids were found to have a better heat transfer enhancement and adverse effects on the wall shear stress than water-γAl_2O_3.

3i. Somestudies of 2004

Wen and Ding [141] performed experiments in order to calculate the convective heat transfer coefficient of γ-Al_2O_3 nanoparticles suspended in deionized water in a copper tube for laminar flow. Under a constant wall heat flux condition, nanoparticles having 0.6 %, 1.0 %, and 1.6 % concentrations were tested in their study. In the experiments, straight copper tube with 4.5±0.02 mm inner diameter, 6.4±0.05 mm outer diameter and 970 mm length was used as a test section. A flexible silicon rubber having 300W heating capacity was used to maintain a constant heat flux boundary condition. A peristaltic pump was used to deliver a maximum flow rate of 10 l/min. The flow rate was controlled by adjusting rotational speed of the pump. Sodium dodecylbenzene sulfonate (SDBS) was used as a dispersant in order to stabilize the nanoparticles.

Maiga *et al*. [142] reported numerical method and a mathematical formulation for water-γAl_2O_3 and ethylene glycol-γAl_2O_3 to determine the forced convective heat transfer and wall shear stress for the laminar and turbulent regions of water-γAl_2O_3 and ethylene glycol-γAl_2O_3 flowing inside a uniformly heated tube. The solid-liquid mixture was considered as a single-phase, so the slip velocity between the phases was neglected. Moreover, symmetry in flow and the local thermal equilibrium of the mixture were considered. To define heat flux and stresses of the nanofluids for the turbulent flow, the Reynolds-averaged Navier-Stokes equation and κ-ε turbulent model were used. In the numerical simulations, the heated tube having 0.01m diameter and 1.0 m length was used. The conditions of laminar flow were as follows: the Reynolds number was fixed at 250 and the constant heat flux was varied between 10-250 W/m^2. The conditions of turbulent flow were as follows: the constant heat flux was fixed at 500,000 W/m^2 and the Reynolds number was varied in the range of 10,000-50,000.

Roy *et al*. [143] performed a numerical investigation to analyze the heat transfer and wall shear stress for radial laminar flow in a cooling system of water-γAl_2O_3 nanofluids compared with some base fluids such as water, glycol, and oil. All assumptions used in this study being similar to those reported by Maiga *et al*. [142] marked the nanofluid as an incompressible fluid.

Nguyen *et al*. [144] introduced a numerical simulation to determine the efficiency of water-γAl_2O_3 and ethylene glycol-γAl_2O_3 nanofluids for the cooling of a high-heat output microprocessor under laminar forced flow inside a heat sink. The simulation set-up comprised of a 50x50x10 mm rectangular slot having a 3x48 mm fluid flow cross-section. In this article, assumptions were uniform velocity and temperature profile at the inlet section and laminar flow. The contact area for exchange heat was 10x10 mm. The numerical results showed that Reynolds number and the volume fraction were mainly parameters affecting average heat transfer coefficient of nanofluids and ethylene glycol-γAl_2O_3 nanofluid had higher heat transfer coefficient than that of the water-γAl_2O_3 nanofluid.

Ali *et al*. [145] reported the mathematical and numerical formulation to determine heat and mass transfer between air and falling solution film in a cross-flow heat exchanger for the dehumidification and cooling process. Effect of Cu nanoparticles to the heat and mass transfer process were tested by adding them into the solution. In this study, two models from available literature were used. Moreover, the assumptions of this article were laminar and steady state flow. Constant film thickness, thermal properties of the air and the solution were constant except for the thermal conductivity of the solution, gravitational force of the air was neglected for fully developed velocity profile of fluids. According to he results of the study, the dehumidification and cooling process increased with high Cu particle volume fraction, low air Reynolds number, decrease in the channel width, increase in the height and length of the channel. In addition, it was revealed that an increase in Cu volume fraction led to more stability of the solution.

Ali and Vafai [146] suggested the numerical and mathematical formulations in order to analyze the effects of the inclination angel of parallel-and-counter-flow on heat and mass transfer between air and falling desiccant film having Cu nanoparticles suspended. They used the same assumptions in the two approach models as those used in the previous paper such as the simulated conditions used in this study being low and high air Reynolds number for the inclined parallel flow arrangement and low and high air Reynolds number for the inclined counter flow configuration.

Zhu *et al*. [147] developed a method for the preparation of copper nanofluids using the base fluid of ethylene glycol with $CuSO_4 \cdot 5H_2O$ with $NaH_2PO_2 \cdot H_2O$ under microwave irradiation. They investigated the effects of $CuSO_4$concentration with the addition of NaH_2PO_2 and microwave irradiation on the reaction rate and the properties of Cu nanofluids by transmission of electron microscopy, infrared analysis, and sedimentation measurements. They obtained nonagglomerated and stably suspended Cu nanofluids at the end of their analysis.

3j. Somestudies of 2003 and Previous Studies

Li and Xuan [148] and Xuan and Li [149] used an experimental set up in order to determine the convective heat transfer coefficient and friction factor parameters of nanofluids for laminar and turbulent flow in a tube. Deionized water with a dispersion of Cu particles with under 100nm diameter was used in this study. The effect of the nanoparticle concentration on the heat transfer coefficient was determined for different particle volume percentages being 0.3, 0.5, 0.8, 1, 1.5 and 2%. The Reynolds number of the nanofluids varied between 800 and 25,000. The experimental set up was consisted of a test section, a pipeline, a pump, a cooler, a fluid collection and a reservoir tank. A straight brass tube having 800 mm length and 10 mm inner diameter was used and a 3.5 kW electric heater was placed to test section for getting a constant wall heat flux boundary condition. A fatty acid was used to prevent the aggregation of the nanoparticles in the base fluid.

Xuan and Li [149] suggested a method for preparing some nanofluid samples and presented theoretical study of thermal conductivity. The transient hot-wire method was used for measurements in their study. For determining the heat transfer performance of nanofluids flowing in a tube, they proposed a single phase or dispersion model. Cu particles having a diameter of 100 nm were used as nanoparticles where base fluids are water and mineral oil. The particles in the mineral oil and water were stabilized by using oleic acid and laureate salt respectively. For Cu-mineral oil, suspension stabilization time was nearly 1 week and suspension had no sedimentation with a fill of 22 wt%. For Cu-water, suspension with 9

wt% laureate salt, vibrated by an ultrasonic vibrator, the results indicated that the nanoparticles could suspend more 30 h than in stationary state. This behavior implied that particle stability and dispersion were affected by fluid viscosity. Furthermore, this study showed that and Crosser model [150] and Wasp model [151] can be used for predicting thermal conductivity in the absence of a sophisticated formula. According to measurements obtained by using transient hot-wire method, the thermal conductivity was observed to be significantly varied with the volume fraction of the particles. The heat transfer enhancement was evaluated with two different ways the single-phase model and two-phase model. The single phase model assumed that both the liquid and particle phases being in thermal equilibrium were flowing at the same velocity. This model beingsimple required less computation time. The two-phase model provided opportunity to understand functions of liquid phase and solid phase in the heat transfer process but required a long time for computation and a high performance computer.

The purpose of their work aimed to develop a modified single-phase model to determine the heat transfer process of nanofluids flowing in tubes.

Xuan and Roetzel [152] presented two different approaches to define some fundamentals for predicting the convective heat transfer coefficient of nanofluids under the assumption that they behaved like a single-phase liquid rather than a normal solid-liquid mixture. In their study, the effects of thermal dispersion and transport properties of the nanofluid were covered. The first model treated as a single-phase and the other model treated as a multi-phase fluid and dispersed fluid. It was assumed that liquid phase and the particles being in thermal equilibrium state were devoid of slip velocity between them. The nanofluid acted as a common pure liquid. This implied that the all equation of energy continuity, and motion for a single-phase fluid had been applied directly to the nanofluid.

Similar to the Xuan and Li model [153], the Hamilton and Crosser model [150] and Wasp model [151] provided rough results for predicting the thermal conductivity of nanofluid. For a modified conventional approach, known as dispersion model, the slip velocity between the solid-liquid mixture could not be zero because of many factors such as gravity, Brownian force, friction force between the solid-liquid mixture, Brownian diffusion, sedimentation, and dispersion happening simultaneously in the main flow.

Xue [154] presented a model of the effective thermal conductivity for nanofluids, based on Maxwell theory and average polarization theory, considering the interface effect between the solid particles and the base fluid in nanofluids. They found that their theoretical results were in good agreement with the experimental data on the effective thermal conductivity of nanotube/oil nanofluid and Al_2O_3/water nanofluid.

4. CONCLUSIONS

Nanofluid has been classified as a new class of heat transfer fluids engineered by dispersing metallic or non-metallic nanoparticleswith a typical size of less than 100 nm in the conventional heat transfer fluids. Their use remarkably augments the heat transfer potential of the base liquids thus offering an opportunity to the engineers for the development of highly compact and effective heat transfer equipmentfor many industrial applications, nuclear reactors, transportation, electronics as well as biomedicine and food.

Nanofluid is consideredas an innovative heat transfer fluid with superior potential for enhancing the heat transfer performance of conventional fluids. This review presents the recent studies of single phase and two-phase nanofluid flows in tubes and channels and also helps to determine the physical properties of nanofluids chronologically. According to the most recent experimental papers, heat transfer performance of the base fluid can significantly be increased by the suspended nanoparticles since heat transfer coefficient of the nanofluid was found to be larger than that of its base fluid for the same Reynolds number. The volume fraction of nanoparticles increases the heat transfer feature of a nanofluid. Pressure drop and friction factors of nanofluids are also larger than its base fluids. Besides of many attempts made to determine the nanofluids' thermal conductivity and viscosity, being important thermophysical properties no definitive agreements have emerged on these properties. Moreover, there is a lack of studies on the mixture flows of nano particles with the refrigerants as pressurized flows in tubes or channels due to the hardness in the experimental conditions.

CONFLICT OF INTEREST

The authors confirm that this article content has no conflicts of interest.

ACKNOWLEDGEMENTS

The authors would like to thank King Mongkut's University of Technology Thonburi (KMUTT), the Thailand Research Fund, the Office of Higher Education Commission and the National Research University Project for the financial support. Especially, the first author wishes to thank KMUTT for providing him with a Post-doctoral fellowship.

REFERENCES

[1] Putra, N.; Roetzel W.; Das, S. K. Natural convection of nano-fluids. *Int. J. Heat Mass Transfer*., **2003**, *39*, 775-784.

[2] Tang, G.Y.; Yang, C.; Chai, J.C.; Gong, H.Q. Joule heating effect on electroosmotic flow and mass species transport in a microcapillary. *Int. J. Heat and Mass Transfer*., **2004**, *47*, 215-227.

[3] Tseng, W.J.; Chen, C.N. Effect of polymeric dispersant on rheological behavior of nickel–terpineol suspensions. *Mater. Sci. Eng*., **2003**, A *347* (1–2), 145-153.

[4] Chen, H.; Ding, Y.; He, Y.; Tan, C. Rheological behaviour of ethylene glycol based titania nanofluids. *Chem. Phys. Lett.*, **2007**, *444* (4–6), 333-337.

[5] Nguyen, C.; Desgranges, F.; Roy, G.; Galanis, N.; Mare, T.; Boucher, S.; Anguemintsa, H. Temperature and particle-size dependent viscosity data for water-based nanofluids – hysteresis phenomenon. *Int. J. Heat Fluid Flow*., **2007**, *28* (6), 1492-1506.

[6] Khanafer, K.; Vafai, K. A. critical synthesis of thermophysical characteristics of nanofluids. *Int. J. Heat Mass Transfer*, **2011**, *54,* 4410-4428.

[7] Duangthongsuk, W.; Wongwises, S. Measurement of temperature-dependent thermal conductivity and viscosity of TiO2–water nanofluids. *Exp. Therm. Fluid Sci*., **2009**, 33, 706–714.

[8] Yu, W.; Choi, S.U.S. The role of interfacial layers in the enhanced thermal conductivity of nanofluids: a renovated Maxwell model. *J. Nanopart. Res.*, **2003**, *5*, 167-171.

[9] Godson, L.; Raja, B.; Lal, M.D.; Wongwises, S. Experimental investigation on the thermal conductivity and viscosity of silver-deionized water nanofluid. *Exp. Heat Transfer.*, **2010**, *23*, 317-332.

[10] Prasher, R.; Bhattacharya, P.; Phelan, P.E. Thermal conductivity of nanoscale colloidal solutions (nanofluids). *Phys. Rev. Lett.*, **2005**, *94*, 025901-1–025901-4.

[11] Koo J., Kleinstreuer,C. A new thermal conductivity model for nanofluids. *J. Nanopart. Res.*, **2004**, *6*, 577-588.

[12] Li, C.H.; Peterson, G.P. Experimental investigation of temperature and volume fraction variations on the effective thermal conductivity of nanoparticle suspensions (nanofluids). *J. Appl. Phys.*, **2006**, *99*, 084314.

[13] Maiga, S.E.B.; Nguyen, C.T.; Galanis, N.; Roy, G. Heat transfer behaviours of nanofluids in a uniformly heated tube. *Superlattice. Microst.*,**2004**, *35*, 543-557.

[14] Bhattacharya, P.; Saha, S.K.; Yadav, A.; Phelan, P.E.; Prasher, R.S. Brownian dynamics simulation to determine the effective thermal conductivity of nanofluids. *J. Appl. Phys.*, **2004**, *95*, 6492-6494.

[15] Buongiorno, J. Convective transport in nanofluids. *J. Heat Transf.*, **2006**, *128*, 240-251.

[16] Kim, D.; Kwon, Y.; Cho, Y.; Li, C.; Cheong S., Hwang Y., Lee J., Hong D., Moon S., Convective heat transfer characteristics of nanofluids under laminar and turbulent flow conditions. *Curr. Appl. Phys.*, **2009**, *9* (2), 119-123.

[17] Timofeeva, E. V.; Gavrilov, A. N.;McCloskey, J.M.;Tolmachev, Y.V. Thermal conductivity and particle agglomeration in alumina nanofluids: Experiment and Theory. *Phys. Rev. E*, **2007,** *76*, 061203.

[18] Chon, C.H.; Kihm, K.D.; Lee, S.P.; Choi, S.U.S. Empirical correlation finding the role of temperature and particle size for nanofluid (Al2O3) thermal conductivity enhancement. *Appl. Phys. Lett.*, **2005**, *87*.

[19] Murshed, S.M.S.; Leong, K.C.; Yang, C. A model for predicting the effective thermal conductivity of nanoparticles–fluid suspensions, *Int. J. Nanosci*., **2006**, *5,* 23-33.

[20] Qiang, L.; Yimin, X. Convective heat transfer and flow characteristics of Cu-water nanofluid. *Sci. China Ser. E*, **2002**, *45*, 408-416.

[21] Yang, Y.; Zhang, Z.G.; Grulke, E.A.; Anderson, W.B.; Wu, G. Heat Transfer properties of nanoparticle-in-fluid dispersions (Nanofluids) in laminar flow. *Int. J. Heat Mass Transfer*., **2005**, *48*, 1107-1116.

[22] Monrad, C.C; Pelton, J.F. Heat transfer by convection in annular spaces. *Trans. Am. Inst. Chem. Eng.,* **1942**, *38*, 593-611.

[23] Sieder, E.N.; Tate, G.E. Heat transfer and pressure drop of liquids in tubes. *Ind. Eng. Chem.*, **1936**, *28*, 1429-1435.

[24] Choi, U.S. Enhancing thermal conductivity of fluids with nanoparticle. *ASME FED 231*, **1995**, *231*, 99-103.

[25] Alizad, K.; Vafai, K.; Shafahi M. Thermal performance and operational attributes of the startup characteristics of flat-shaped heat pipes using nanofluids. *Int. J. Heat Mass Transfer*, **2012,** *55*, 140-155.

[26] Bobbo, S.; Fedele, L.; Benetti, A.; Colla, L.; Fabrizio, M.; Pagura, C.; Barison, S. Viscosity of water based SWCNH and TiO_2 nanofluids. *Exp. Therm. Fluid Sci.*, **2012,** *36*, 65-71.

[27] Buschmann, M. H.; Thermal conductivity and heat transfer of ceramic nano fluids. *Int. J. Therm. Sci.*, **2011**, Article in Press-Corrected Proof.

[28] Yang, L.; Du, K.; Ding, Y. H.; Cheng, B.; Li, Y. J. Viscosity-prediction models of ammonia water nanofluids based on various dispersion types. *Powder Technol.,* **2012**, *215-216*, 210-218.

[29] Colangelo, G.; Favale E.; Risi A.; Laforgia, D. Results of experimental investigations on the heat conductivity of nanofluids based on diathermic oil for high temperature applications. *Appl. Energy*, **2011**, Article in Press-Corrected Proof..

[30] Jamshidi, N.; Farhadi, M.; Sedighi, K.; Ganji, D. D. Optimization of design parameters for nanofluids flowing inside helical coils. *Int. Commun. Heat Mass Trans.,* **2011***, 39*, 311-317.

[31] Giraldo, M.; Sanin, D.; Flórez, W. F. Heat transfer in nanofluids: A computational evaluation of the effects of particle motion. *Appl. Math. Comput.,* **2011**, Article in Press-Corrected Proof.

[32] S. Özerinç, A .G. Yazıcıoglu, S. Kakaç, Numerical analysis of laminar forced convection with temperature-dependent. *Int. J. Therm. Sci.*, **2011**, Article in Press-Corrected Proof.

[33] Yu, L.; Liu, D.; Botz, F. Laminar convective heat transfer of alumina-polyalphaolefin nanofluids containing spherical and non-spherical nanoparticles. *Exp. Therm. Fluid Sci*., **2011**, *37*, 72-83.

[34] Farahani, S.D.; Kowsary, F. Estimation local convective boiling heat transfer coefficient in mini channel. *Int. Commun. Heat Mass Trans.*, **2011**, *39*, 304-310

[35] Cimpean, D. S.; Pop, I. Fully developed mixed convection flow of a nanofluid through an inclined channel filled with a porous medium. *Int. J. Heat Mass Transfer*, **2012**, *55*, 907-914.

[36] Leong, K.Y.; Saidur, R.; Mahlia, T.M.I.; Yau, Y.H. Modeling of shell and tube heat recovery exchanger operated with nanofluid based coolants. *Int. J. Heat and Mass Transfer*, **2012**, *55*, 808-816.

[37] Mahbubul, I.M.; Saidur, R.; Amalina, M.A. Latest developments on the viscosity of nanofluids. *Int. J. Heat Mass Transfer,* **2012**, *55*, 874-885.

[38] Wenzheng, C.; Minli, B.; Jizu, L.; Xiaojie, Li. On the microscopic flow characteristics of nanofluids by molecular dynamics simulation on Couette Flow. *Open Fuels Energy Sci. J.*, **2012**, *5*, 21-27.

[39] Ahmed, M.A.; Shuaib, N.H.; Yusoff, M.Z.; Al-Falahi A.H. Numerical investigations of flow and heat transfer enhancement in a corrugated channel using nanofluid. *Int. Commun. Heat Mass Trans.,* **2011**, *38*, 1368-1375.

[40] Akbarinia, A.; Abdolzadeh, M.; Laur, R. Critical investigation of heat transfer enhancement using nanofluids in microchannels with slip and non-slip flow regimes. *Appl. Therm. Eng.*, **2011**, *31*, 556-565.

[41] Bianco, V.; Manca, O.; Nardini, S. Numerical investigation on nanofluids turbulent convection heat transfer inside a circular tube. *Int. J. Therm. Sci*., **2011**, *50*, 341-349.

[42] Corcione, M. Empirical correlating equations for predicting the effective thermal conductivity and dynamic viscosity of nanofluids. *Energy Convers. Manage.*, **2011**, *52*, 789-793.

[43] Firouzfar, E.; Soltanieh, M.; Noie, S.H.; Saidi, S.H. Energy saving in HVAC systems using nanofluid. *Appl. Therm. Eng*., **2011**, *31*, 1543-1545.

[44] Gherasim, I.; Roy; G., Nguyen, C.T.; Vo-Ngoc, D. Heat transfer enhancement and pumping power in confined radial flows using nanoparticle suspensions (nanofluids). *Int. J. Therm. Sci.,* **2011**, *50*, 369-377.

[45] Hojjat, M.; Etemad, S.Gh.; Bagheri, R.; Thibault. J. Convective heat transfer of non-Newtonian nanofluids through a uniformly heated circular tube. *Int. J. Therm. Sci.,* **2011**, *50*, 525-531.

[46] Hojjat, M.; Etemad, S.Gh.; Bagheri, R.; Thibault, J. Thermal conductivity of non-Newtonian nanofluids: Experimental data and modeling using neural network. *Int. J. Heat Mass Trans*., **2011**, *54*, 1017-1023.

[47] Hojjat, M.; Etemad, S.Gh.; Bagheri, R.; Thibault. Turbulent forced convection heat transfer of non-Newtonian nanofluids. *Exp. Therm. Fluid Sci.,* **2011***, 35*, 1351-1356.

[48] Huminic, G.; Huminic, A. Heat transfer characteristics in double tube helical heat exchangers using nanofluids. *Int. J. Heat Mass Tran.,* **2011***, 54*, 4280-4287.

[49] Huminic, G.; Huminic, A. Heat transfer characteristics of a two-phase closed thermosyphons using nanofluids. *Exp. Therm. Fluid Sci.,* **2011***, 35,* 550-557.

[50] Jung, J.Y.; Cho, C.; Lee, W.H.; Kang, Y.T. Thermal conductivity measurement and characterization of binary nanofluids. *Int. J. Heat Mass Trans.,* **2011***, 54*, 1728-1733.

[51] Khanafer, K.; Vafai, K. A critical synthesis of thermophysical characteristics of nanofluids. *Int. J. Heat Mass Trans.,* **2011***, 54*, 4410-4428.

[52] Lee, S.W.; Park, S.D.; Kang, S.; Bang, I.C.; Kim, J.H. Investigation of viscosity and thermal conductivity of SiC nanofluids for heat transfer applications. *Int. J. Heat Mass Trans.,* **2011**, *54*, 433-438.

[53] Asirvatham, L.G.; Raja, B.; Lal, D.M.; Wongwises, S., Convective heat transfer of nanofluids with correlations. *Particuology*, **2011**, *9*, 626-631.

[54] Ebrahimnia-Bajestan, E.; Niazmand, H.; Duangthongsuk, W; Wongwises, S. Numerical investigation of effective parameters in convective heat transfer of nanofluids flowing under a laminar flow regime. *Int. J. Heat Mass Trans.,* **2011***, 54*, 4376-4388.

[55] Raisi, A.; Ghasemi, B.; Aminossadati, S. M. A Numerical study on the forced fonvection of laminar nanofluid in a microchannel with both slip and No-slip conditions. *Numer. Heat Tr. A-Appl.*, **2011**, *59*, 114-129.

[56] Heris, S; Z.;Noie, S.H.; Talaii, E.; Sargolzaei, J. Numerical investigation of Al2O3/water nanofluid laminar convective heat transfer through triangular ducts. *Nanoscale Res. Lett.*,**2011**, *6*,1-10.

[57] Vincenzo, B.; Nardini, S.; Manca, O. Enhancement of heat transfer and entropy generation analysis of nanofluids turbulent convection flow in square section tubes. *Nanoscale Res. Lett.,* **2011**, *6*, 1-12.

[58] Demir, H.; Dalkilic, A.S.; Kürekci, N.A.; Wongwises, D. S. Numerical investigation on the single phase forced convection heat transfer characteristics of TiO_2 nanofluids in a double-tube counter flow heat exchanger. *Int. J. Commun. Heat Mass Trans*., **2011**, *38*, 218-228.

[59] Abareshi, M.; Goharshadi, E.; Zebarjad, S.M.; Fadafan, H.K.; Youssefi, A. Fabrication characterization and measurement of thermal conductivity of Fe_3O_4 nanofluids. *J. Magn. Magn.Mater*., **2010**, *322*, 3895-3901.

[60] Farajollahi, B. I; Etemad, S.Gh.; Hojjat, M. Heat transfer of nanofluids in a shell and tube heat exchanger. *Int. J. Heat Mass Trans*., **2010,** *53*, 12-17.

[61] Fard, H. M.; Esfahany, M.N.; Talaie, M.R. Numerical study of convective heat transfer of nanofluids in a circular tube two-phase model versus single-phase model. *Int. J. Commun. Heat Mass Trans*., **2010**, *37*, 91-97.

[62] Do, K.H.; Ha, H.J.; Jang, S.P. Thermal resistance of screen mesh wick heat pipes using the water-based Al_2O_3 nanofluids. *Int. J. Heat Mass Trans*., **2010**, *53*, 5888-5894.

[63] Henderson, K.; Park, Y.G.; Liu, L.; Jacobi, A.M. Flow-boiling heat transfer of R-134a-based nanofluids in a horizontal tube, *Int. J. Heat Mass Trans.*, **2010**, *53*, 944-951.

[64] Godson, L.; Raja, B.; Lal, D.M.; Wongwises, S. Enhancement of heat transfer using nanofluids-An overview. *Renew. Sust. Energ. Rev.*, **2010**, *14*, 629-641.

[65] Kima, S.J.; McKrella, T.; Buongiornoa, J.; Hu, L.W Subcooled flow boiling heat transfer of dilute alumina, zinc oxide, and diamond nanofluids at atmospheric pressure. *Nucl. Eng. Des.*, **2010**, *240*, 1186-1194.

[66] Lotfi, R.; Saboohi, Y.; Rashidi, A.M. Numerical study of forced convective heat transfer of Nanofluids: Comparison of different approaches. *Int. J. Commun. Heat Mass Trans.,* **2010***, 37*, 74-78.

[67] Meibodi, M.E.; Sefti, M.V.; Rashidi, A.M.; Amrollahi, A.; Tabasi, M.; Kalal, H.S. Simple model for thermal conductivity of nanofluids using resistance model approach . *Int. J. Commun. Heat Mass Trans. ,* **2010**, *37*, 555-559.

[68] Meibodi, M.E.; Sefti, M.V.; Rashidi, A.M.; Amrollahi, A.; Tabasi, M.; Kalal, H.S. An estimation for velocity and temperature profiles of nanofluids in fully developed turbulent flow conditions. *Int. J. Commun. Heat Mass Trans.,* **2010**, *37*, 895-900.

[69] Meibodi, M.E.; Sefti, M.V.; Rashidi, A.M.; Amrollahi, A.; Tabasi, M.; Kalal, H.S. The role of different parameters on the stability and thermal conductivity of carbon nanotube/water nanofluids. *Int. J. Commun. Heat Mass Trans.*, **2010***, 37*, 319-323.

[70] Paul, G.; Chopkar, M.; Manna, I.; Das, P.K. Techniques for measuring the thermal conductivity of nanofluids: A review. *Renew. Sust. Energ. Rev.*, **2010**, *14*, 1913-1924.

[71] Paul, G.; Pal, T.; Manna, I. Thermo-physical property measurement of nano-gold dispersed water based nanofluids prepared by chemical precipitation technique. *J. Colloid Interf. Sci.*, **2010**, *349*, 434-437.

[72] Qu, J.; Wu, H.Y.; Cheng, P. Thermal performance of an oscillating heat pipe with Al_2O_3-water nanofluids. *Int. J. Commun. Heat Mass Trans.,* **2010***, 37*, 111-115.

[73] Rao, Y. Nanofluids: Stability, phase diagram, rheology and applications, *Particuology*, **2010**, 549-555.

[74] Raykar, V.S.; Singh, A.K. Dispersibility dependence of thermal conductivity of carbon nanotube based nanofluids. *Phys. Lett. A*, **2010**, *374*, 4618-4621.

[75] Roberts, N.A.; Walker, D.G. Convective performance of nano fluids in commercial electronics cooling systems. *Appl. Therm. Eng.*, **2010**, *30*, 2499-2504.

[76] Rostamani, M.; Hosseinizadeh, S.F.; Gorji, M.; Khodadadi, J.M. Numerical study of turbulent forced convection flow of nano fluids in a long horizontal duct considering variable properties. *Int. J. Commun. Heat Mass Trans*., **2010**, *37*, 1426-1431.

[77] Singh, P.K.; Anoop, K.B.; Sundararajan, T.; Das, S. K. Entropy generation due to flow and heat transfer in nanofluids. *Int. J. Heat Mass Trans*., **2010**, *53*, 4757-4767.

[78] Sundar, L.S. R; Sharma, K.V. Turbulent heat transfer and friction factor of Al_2O_3 Nanofluid in circular tube with twisted tape inserts. *Int. J. Heat Mass Trans*., **2010**, *53*, 1409-1416.

[79] Vajjha, R. S.; Das, D. K.; Kulkarni, D.P. Development of new correlations for convective heat transfer and friction factor in turbulent regime for nanofluids. *Int. J. Heat Mass Trans*., **2010**, *53* 4607-4618.

[80] Vajjha, R.S.; Das, D.K.; Namburu, P. K. Numerical study of fluid dynamic and heat transfer performance of Al_2O_3 and CuO nanofluids in the flat tubes of a radiator. *Int. J. Heat Fluid Fl.*, **2010**, *31*, 613-621.

[81] Wei, X.; Kong, T.; Zhu, H.; Wang, L. CuS/Cu_2S nanofluids: Synthesis and thermal conductivity. *Int. J. Heat Mass Trans*., **2010**, *53*, 1841-1843.

[82] Wei, X.; Wang, L. Synthesis and thermal conductivity of microfluidic copper nanofluids. *Particuology*, **2010**, *8*, 262-271.

[83] Yang, Y.T.; Lai, F.H. Numerical study of heat transfer enhancement with the use of nanofluids in radial flow cooling system. *Int. J. Heat Mass Trans*., **2010**, *53*, 5895-5904.

[84] Yu W., Xie H., Chen L., Li Y. Investigation on the thermal transport properties of ethylene glycol-based nanofluids containing copper nanoparticles. *Powder Technol.*, **2010**, *197*, 218-221.

[85] Wong, K.V.; Leon, O.D. Applications of Nanofluids: Current and Future. *Adv. Mech. Eng.*, **2010**, 1-11.

[86] Duangthongsuk, W; Wongwises, S. Comparison of the effects of measured and computed thermophysical properties of nanofluids on heat transfer performance. *Exp. Therm. Fluid Sci.,* **2010***, 34*, 616-624.

[87] Duangthongsuk, W; Wongwises, S. An experimental study on the heat transfer performance and pressure drop of TiO_2-water nanofluids flowing under a turbulent flow regime. *Int. J. Heat Mass Trans*., **2010**, *53*, 334-344.

[88] Bergman, T.L. Effect of reduced specific heats of nanofluids on single phase, laminar internal forced convection. *Int. J. Heat Mass Trans*., **2009**, *52*, 1240-1244.

[89] Bianco, V.; Chiacchio, F.; Manca, O.; Nardini, S. Numerical investigation of nanofluids forced convection in circular tubes. *Appl. Therm. Eng.*, **2009**, *29*, 3632-3642.

[90] He, Y.; Men, Y.; Zhao, Y.; Lu, H.; Ding, Y. Numerical investigation into the convective heat transfer of TiO2 nanofluids flowing through a straight tube under the laminar flow conditions. *Appl. Therm. Eng.,* **2009***, 29*, 1965-1972.

[91] Hwang, K.S.; Jang, S.P.; Choi, S.U.S. Flow and convective heat transfer characteristics of water-based Al2O3 nanofluids in fully developed laminar flow regime. *Int. J. Heat Mass Trans*., **2009**, *52*, 193-199.

[92] Jung, J.Y.; Oh, H.S; Kwak, H.Y. Forced convective heat transfer of nanofluids in microchannels. *Int. J. Heat Mass Trans*., **2009***, 52*, 466-472.

[93] Kakaç S., Pramuanjaroenkij, A., Review of convective heat transfer enhancement with nanofluids. *Int. J. Heat Mass Trans*., **2009**, *52*, 3187-3196.

[94] Kim, D.; Kwon, Y.; Cho, Y.; Li, C.; Cheong, S.; Hwang, Y.; Lee, J.; Hong, D.; Moon S. Convective heat transfer characteristics of nanofluids under laminar and turbulent flow conditions. *Curr. Appl. Phys*., **2009**, *9*, e119-e123.

[95] Kulkarni, D.P.; Das, D.K.; Vajjha, R.S. Application of nanofluids in heating buildings and reducing pollution. *Appl. Energ.*, **2009**, *86*, 2566-2573.

[96] Mintsa, H.A; Roy, G.; Nguyen, C.T.; Doucet, D. New temperature dependent thermal conductivity data for water-based nanofluids. *Int. J. Therm. Sci.*, **2009**, *48*, 363-371.

[97] Murshed, S.M.S.; Leong, K.C.; Yang, C. A combined model for the effective thermal conductivity of nanofluids. *Appl. Therm. Eng.*, **2009**, *29*, 2477-2483.

[98] Namburu, P.K.; Das D. K., Tanguturi, K.M.; Vajjha, R.S. Numerical study of turbulent flow and heat transfer characteristics of nanofluids considering variable properties*. Int. J. Therm. Sci.*, **2009**, *48*, 290-302.

[99] Rea, U.; McKrell, T.; Hu, L.W. Buongiorno J., Laminar convective heat transfer and viscous pressure loss of alumina-water and zirconia-water nanofluids. *Int. J. Heat Mass Trans*., **2009**, *52*, 2042-2048.

[100] Pantzali, M.N.; Mouza, A.A.; Paras, S.V. Investigating the efficacy of nanofluids as coolants in plate heat exchangers (PHE), *Chem. Eng. Sci*., **2009**, *64*, 3290-3300.

[101] Xie, H.; Chen, L. Adjustable thermal conductivity in carbon nanotube nanofluids. *Phys. Lett.*, **2009**, *373*, 1861-1864.

[102] Pantzali, M.N.; Kanaris, A.G.; Antoniadis, K.D.; Mouza, A.A.; Paras, S.V. Effect of nanofluids on the performance of a miniature plate heat exchanger with modulated surface. *Int. J. Heat Fluid Fl.*, **2009**, *30*, 691-699.

[103] Vajjha, R.S.; Das, D. K. Experimental determination of thermal conductivity of three nanofluids and development of new correlations. *Int. J. Heat Mass Trans*., **2009**, *52*, 4675-4682.

[104] Wen D., Lin G., Vafaei S., Zhang K., Review of nanofluids for heat transfer applications. *Particuology,* **2009**, *7*, 141-150.

[105] Hadjov, K.B. Modified self-consisted scheme to predict the thermal conductivity of nanofluids. *Int. J. Therm. Sci.,* **2009***,* 48, 2249-2254.

[106] Ali, M.; Zeitoun, O. Nanofluids forced convection heat transfer inside circular tubes. *Int. J. Nanoparticles*, **2009**, *2*, 164-172.

[107] Duangthongsuk, W.; Wongwises, S. Measurement of temperature-dependent thermal conductivity and viscosity of TiO2-water nanofluids.*Exp. Therm. Fluid Sci*., 2009, *33*,706-714.

[108] Duangthongsuk, W.; Wongwises, S. Heat transfer enhancement and pressure drop characteristics of TiO_2-water nanofluid in a double-tube counter flow heat exchanger. *Int. J. Heat Mass Trans*., **2009**, *52*, 2059-2067.

[109] Bi, S.S.; Shi, L.; Zhang, L.L Application of nanoparticles in domestic refrigerators. *Appl. Therm. Eng.*, **2008**, *28*, 1834-1843.

[110] Hwang, Y., Lee, J. K.; Lee, J.K.; Jeong, Y.M.; Cheong, S.; Ahn, Y.C.; Kim, S. H. Production and dispersion stability of nanoparticles in nanofluids. *Powder Technol*., **2008**, *186*, 145-153.

[111] Karthikeyan, N.R.; Philip, J.; Raj, B. Effect of clustering on the thermal conductivity of nanofluids. *Mater. Chem. Phys.,* **2008**, *109*, 50-55.

[112] Khandekar, S.; Joshi, Y.M.; Mehta, B. Thermal performance of closed two-phase thermosyphon using nanofluids. *Int. J. Therm. Sci.,* **2008***, 47*, 659-667.

[113] Lee, J.H; Hwang, K.S.; Jang, S.P; Lee, B.H.; Kim, Ho, J.; Choi, S.U.S. Effective viscosities and thermal conductivities of aqueous nanofluids containing low volume concentrations of Al_2O_3 nanoparticles. *Int. J. Heat Mass Trans*., **2008**, *51*, 2651-2656.

[114] Murshed, S.M.S.; Leong, K.C.; Yang, C. Thermophysical and electrokinetic properties of nanofluids - A critical review. *Appl. Therm. Eng.,* **2008**, *28*, 2109-2125.

[115] Oh, D.W.; Jain, A.; Eaton, J. K.; Goodson, K. E.; Lee, J. S. Thermal conductivity measurement and sedimentation detection of aluminum oxide nanofluids by using the 3 w method. *Int. J. Heat Fluid Fl*., **2008**, *29*, 1456-1461.

[116] Kang, Y.T.; Kim, H. J.; Lee, K.I. Heat and mass transfer enhancement of binary nanofluids for H_2O/LiBr falling film absorption process. *Int. J. Refrig.*,**2008**, *31*, 850-856.

[117] Lu, W.Q.; Fan, Q.M. Study for the particle's scale effect on some thermophysical properties of nanofluids, by a simplified molecular dynamics method. *Eng. Anal. Bound. Elem.*, **2008**, *32*, 282-289.

[118] Nguyen, C.T.; Desgranges, F.; Galanis, N.; Roy, G.; Maré, T.; Boucher, S.; Mintsa, H. A. Viscosity data for Al_2O_3–water nanofluid-hysteresis: is heat transfer enhancement using nanofluids reliable. *Int. J. Therm. Sci.,* **2008***, 47*, 103-111.

[119] Chen, H.; Yang, W.; He, Y.; Ding, Y.; Zhang, L.; Tan, C.; Lapkin, A. A.; Bavykin, D. V. Heat transfer and flow behavior of aqueous suspensions of titanate nanotubes (nanofluids). *Powder Technol.,* **2008**, *183*, 63-72.

[120] Ding, Y.; Chen, H.; He, Y.; Lapkin, A.; Yeganeh, M.; Šiller, L.; Butenko, Y. V. Forced convective heat transfer of nanofluids. *Adv. Powder Technol.*, **2007**, *18*, 813-824.

[121] Zhang, X.; Gu, H.; Fujii, M.; Effective thermal conductivity and thermal diffusivity of nanofluids containing spherical and cylindrical nanoparticles. *Exp. Therm. Fluid Sci.,* **2007***, 31*, 593-599.

[122] Ko, G.H.; Heo, K.; Lee, K.; Kim, D.S.; Kim, C.; Sohn, Y. Choi M., An experimental study on the pressure drop of nanofluids containing carbon nanotubes in a horizontal tube. *Int. J. Heat Mass Trans*., **2007**, *50*, 4749-4753.

[123] Mansour, R.B.; Galanis, N.; Nguyen, C.T. Effect of uncertainties in physical properties on forced convection heat transfer with nanofluids. *Appl. Therm. Eng.*, **2007**, *27*, 240-249.

[124] Hong, H.; Wright, B.; Wensel, J.; Jin, S.; Ye, X.R.; Roy, W. Enhanced thermal conductivity by the magnetic field in heat transfer nanofluids containing carbon nanotube. *Synthetic Met.*, **2007**, *157*, 437-440.

[125] Li, C.H.; Peterson, G.P. Mixing effect on the enhancement of the effective thermal conductivity of nanoparticle suspensions (nanofluids). *Int. J. Heat Mass Trans.*, **2007**, 50, 4668-4677.

[126] Yoo, D.H.; Hong, K.S.; Yang, H.S. Study of thermal conductivity of nanofluids for the application of heat transfer fluids. *Thermochim. Acta*, **2007**, *455*, 66-69.

[127] Avsec, J.; Oblak, M. The calculation of thermal conductivity, viscosity and thermodynamic properties for nanofluids on the basis of statistical nanomechanics. *Int. J. Heat Mass Trans.*, **2007**, *50*, 4331-4341.

[128] He, Y.; Jin, Yi; Chen, H.; Ding, Y.; Cang, D.; Lu, H. Heat transfer and flow behavior of aqueous suspensions of TiO_2 nanoparticles (nanofluids) flowing upward through a vertical pipe. *Int. J. Heat Mass Trans.*, **2007**, *50*, 2272-2281.

[129] Lee, J.; Mudawar, I. Assessment of the effectiveness of nanofluids for single-phase and two-phase heat transfer in micro-channels. *Int. J. Heat Mass Trans.*, **2007**, *50*, 452-463.

[130] Wang, X.Q.; Mujumdar, A.S. Heat transfer characteristics of nanofluids: a review. *Int. J. Therm. Sci.,* **2007***, 46*, 1-19.

[131] Trisaksri, V.; Wongwises S. Critical review of heat transfer characteristics of nanofluids. *Renew. Sust. Ener. Rev.,* **2007***, 11*, 512-523.

[132] Daungthongsuk W.; Wongwises S.; A critical review of convective heat transfer of nanofluids. *Renew. Sust. Ener. Rev.*, **2007**, *11*, 797-817.

[133] Hwang, Y.J.; Ahn, Y.C.; Shin, H.S.; C.G. Lee; G.T. Kim; H.S. Park; J.K. Lee Investigation on characteristics of thermal conductivity enhancement of nanofluids. *Curr. Appl. Phys.*, **2006**, *6*, 1068-1071.

[134] Hwang, Y.; Park, H.S.; Lee, J.K.; Jung, W.H. Thermal conductivity and lubrication characteristics of nanofluids. *Curr. Appl. Phys.*, **2006**, *6* S1, e67-e71.

[135] Liu, M.S.; Lin, M.C.C.; Tsai, C.Y.; Wang, C.C. Enhancement of thermal conductivity with Cu for nanofluids using chemical reduction method. *Int. J. Heat Mass Trans.*, **2006**, *49*, 3028-3033.

[136] Palm, S.J.; Roy, G.; Nguyen, C.T.; Heat transfer enhancement with the use of nanofluids in radial flow cooling systems considering temperature-dependent properties. *Appl. Therm. Eng.*, **2006**, *26*, 2209-2218.

[137] Heris, S. Z.; Etemad, S.G.; Esfahany, M.N. Experimental investigation of oxide nanofluids laminar flow convective heat transfer. *Int. J. Commun. Heat Mass Trans.*, **2006**, *33*, 529-535.

[138] Xuan, Y.; Yu, K.; Li, Q. Investigation on flow and heat transfer of nanofluids by the thermal Lattice Boltzmann model. *Prog. Comput. Fluid Dy.*, **2005**, *5*, 13-19.

[139] Liu, M.S.; Lin, M.C.C.; Huang, I.T. Wang C.C., Enhancement of thermal conductivity with carbon nanotube for nanofluids. *Int. J. Commun. Heat Mass Trans.*, **2005**, *32*, 1202-1210.

[140] Maiga, S.E.B.; Palm, S.J.; Nguyen, C.T.; Roy, G.; Galanis, N. Heat transfer enhancement by using nanofluids in forced convection flows. *Int. J. Heat Fluid Fl.,* **2005**, *26*, 530-546.

[141] Wen, D.; Ding, Y. Experimental investigation into convective heat transfer of nanofluids at the entrance region under laminar flow conditions. *Int. J. Heat Mass Trans.*, **2004**, *47*, 5181-5188.

[142] Maiga, S.E.B.; Nguyen, C.T.; Galanis, N.; Roy, G. Heat transfer behaviours of nanofluids in a uniformly heated tube. *Superlattice. Microst.,* **2004***, 35*, 543-557.

[143] Roy, G.; Nguyen, C.T.; Lajoie, P.R. Numerical investigation of laminar flow and heat transfer in a radial flow cooling system with the use of nanofluids. *Superlattice. Microst.*, **2004**, *35*, 497-511.

[144] Nguyen, C.T.; Roy, G.; Maiga, S.E.B.; Lajoie, P.R. Heat transfer enhancement by using nanofluidsfor cooling of high output microprocessor. *www.electronicscooling.com/html/ 2004_nov_techbrief.html*, **2004**.

[145] Ali, A.; Vafai, K.; Khaled, A.R.A. Analysis of heat and mass transfer between air and falling film in a cross flow Configuration. *Int. J. Heat Mass Trans.*, **2004**, *47*, 743-755.

[146] Ali, A.; Vafai K. An investigation of heat and mass transfer between air and desiccant film in an inclined parallel and counter flow channels. *Int. J. Heat Mass Trans.*, **2004**, *47*, 1745-1760.

[147] Zhu, H.T.; Lin, Y.S.; Yin, Y.S. A novel one-step chemical method for preparation of copper nanofluids. *J. Colloid Interf. Sci.,* **2004**, *277*, 100-103.

[148] Li Q., Xuan Y., Convective heat transfer and flow characteristics of cu-water nanofluid, *Sci. China Ser E*, **2002**, *45*, 408-416.

[149] Xuan Y., Li Q., Investigation on convective heat transfer and flow features of nanofluids. *ASME J. Heat Transfer*, **2003**, *125*, 151-155.

[150] Hamilton R.L., Crosser O.K., Thermal conductivity of heterogeneous two-component systems. *I & EC Fundamentals*, **1962**, *1*, 187-191.

[151] Wasp E.J., Solid-liquid flow slurry pipeline transportation. Trans Tech Publications, **1977**.

[152] Xuan, Y.; Roetzel, W. Conceptions for heat transfer correlation of nanofluids. *Int. J. Heat Mass Trans.*, **2000**, *43*, 3701-3707.

[153] Xuan Y., Li Q., Heat transfer enhancement of nanofluids. *Int. J. Heat Fluid Fl.*, **2000**, *21*, 58-64.

[154] Xue, Q.Z. Model for effective thermal conductivity of nanofluids. *Phys. Lett.*, **2003**, *307*, 313-317.

Received: January 22, 2012 **Revised: April 24, 2012** **Accepted: July 18, 2012**

Send Orders of Reprints at reprints@benthamscience.org

Current Nanoscience, **2012,** *8,* **939-944**

Measurement of Specific Heat of Nanofluids

T. Yiamsawasd[a], A.S. Dalkilic[b] and S. Wongwises[a,c*]

[a]*Fluid Mechanics, Thermal Engineering and Multiphase Flow Research Lab. (FUTURE), Department of Mechanical Engineering, Faculty of Engineering, King Mongkut's University of Technology Thonburi, Bangmod, Bangkok 10140, Thailand;* [b]*Heat and Thermodynamics Division, Department of Mechanical Engineering, Yildiz Technical University (YTU), Yildiz, Besiktas, Istanbul 34349, Turkey;* [c]*The Academy of Science, The Royal Institute of Thailand, Sanam Suea Pa, Dusit, Bangkok 10300, Thailand*

Abstract: This article reports an experiment on specific heat measurement of nanofluids using a calorimeter of the comparison type. The measurement is based on a differential thermal analysis technique. The studied TiO_2 and Al_2O_3 nanoparticles are dispersed in base fluids which are pure water and a mixture of ethylene glycol/water (20/80 wt.%). Concentrations between 0 and 8 vol.% and temperatures are between 15 and 65°C. Results show that the measured specific heat of nanofluids is lower than that of the base liquid decreases as the particle concentrations increases. Furthermore, the specific heat of nanofluids was found to increase with increasing temperatures. When compared with predicted values from existing correlations and data reported by other researchers, measurements are compatible with the prediction from the thermal equilibrium model presented by Xuan and Roetzel. Finally, new correlations are proposed for predicting the specific heat of Al_2O_3 and TiO_2 nanofluids.

Keywords: Specific heat, nanofluids, nano particle, base fluid.

INTRODUCTION

Nanofluids are innovative working fluids gained from dispersing nanometer-sized solid particles in common working fluids. These solid particles with high thermal conductivity are expected to enhance heat transfer with long-term stability in suspensions and minimal effect on pressure drop. The term 'nanofluids' was firstly defined by Choi in 1995 [1] and was widely used since then. Nanofluids are expected to be used in mini- and micro-scaled heat exchangers, such as electrical and electronic appliances and computers. However, their relevant properties should be studied, especially thermal properties. This will be very useful for the effective use of nanofluids and for further analysis and development thereof.

Past studies have shown great interest in nanofluids. Initially, most studies focused on thermal conductivity [1-10], viscosity [6-11], and convective heat transfer [12-17]. Unfortunately, there are only a few studies that are concerned with specific heat. Actually, specific heat is one of the most important basic thermal properties that deserves attention. It can be used to calculate for example, the sensible heat transfer rate, Prandtl numbers and thermal diffusivity for predicting heat transfer performance of heat exchangers. Therefore, specific heat of nanofluids should be studied together with other properties.

Below are recent experimental studies about specific heat of nanofluids.

Namburu *et al.* [11] conducted an experiment to measure specific heat and viscosity of silicon dioxide nanofluids suspended in 60/40 by weight mixture of ethylene glycol/water. Particles sizes of SiO_2 examined were 20, 50 and 100 nm, with concentration range of 0 to 10 vol. %. A specially designed electrical heater calorimeter was used to measure the specific heat of nanofluids. Their experiment showed that specific heat of silicon dioxide nanofluids decreased when concentration increased. At the concentration of 10 vol.%, the specific heat decreased by about 12% when compared to the base fluid.

*Address correspondence to this author at the Fluid Mechanics, Thermal Engineering and Multiphase Flow Research Lab. (FUTURE), Department of Mechanical Engineering, King Mongkut's University of Technology Thonburi, Bangmod, Bangkok 10140, Thailand; Tel: +662-470-9115;
Fax: +662-470-9111; E-mail: somchai.won@kmutt.ac.th

Zhou and Ni [18] measured the specific heat of Al_2O_3-water nanofluids with an Al_2O_3 particle size of 45 nm at a temperature of 33°C and a concentration range of 0 to 21.7 vol.%. A differential scanning calorimeter was used for measurement. Their study revealed that when the concentration increased, the specific heat of Al_2O_3-water nanofluids decreased. When compared to the existing correlation, the experimental result was found to be compatible with the prediction from the thermal equilibrium model of Xuan and Roetzel [19], whereas the ideal gas mixtures model of Pak and Cho [5] provided different results.

Vajjha and Das [20] measured the specific heat of 3 types of nanofluids that consisted of Al_2O_3 (44 nm) and ZuO (77 nm) particles suspended in 60/40 % by mass of ethylene glycol-water mixture, and SiO_2 (20 nm) particles suspended in deionized water. A specially designed electrical heating calorimeter was used in a temperature range of 42 to 82°C and a concentration range of 0 to 10 vol.%. Results showed that the specific heat of all 3 types of nanofluids decreased when the concentration increased. On the contrary, the specific heat increased when the temperature increased. However, their results were found to be incompatible with results from the ideal gas mixtures of Pak and Cho and from the thermal equilibrium model of Xaun and Roetzel.

Nelson *et al.* [21] conducted an experiment on thermal properties, as well as flow and forced convection heat transfer characteristics, of exfoliated graphite nanoparticles suspended in polyalphaolfin. The specific heat was measured at the concentration of 0.6 wt.% with a particle diameter of 20 nm and a thickness of 100 nm in a temperature range of 45 to 90°C, using differential scanning calorimeter techniques. They found that the specific heat of nanofluids increased by about 50% when compared to the base fluid and increased with increasing temperature.

Zhou *et al.* [22] measured the specific heat and volumetric heat capacity of CuO-EG nanofluids at a concentration range of 0.1 to 0.6 vol.%. They concluded that when concentration increased, the specific heat of CuO-EG decreased gradually. Volumetric heat capacity was found to change minimally. Their results were compatible with the prediction from the thermal equilibrium model of Xuan and Roetzel, while the ideal gas mixtures model of Pak and Cho could not predict.

Shin and Bernejee [23] measured the specific heat of nanofluids which were used in solar thermal energy storage. Silica nanoparti-

1875-6786/12 $58.00+.00 **© 2012 Bentham Science Publishers**

cles (1 wt.%) suspended in a eutectic of lithium carbonate and potassium carbonate mixture (62/38 % by weight). The silica nanoparticles with an average size of 35 nm were tested in a temperature range of 525 to 555°C using a differential scanning calorimeter. They found that the specific heat of nanofluids increased by about 19–24% when compared with the base fluid. Temperature had little effect on the change of the specific heat of nanofluids used in this experiment.

It can be clearly seen from the study on the nanofluids mentioned above that there are various types of apparatus or measurement techniques used to determine the specific heat of nanofluids and the results obtained from those techniques were also different. Thus, other techniques could be developed to measure the specific heat of nanofluids in order to determine compatibility. To the best of the authors' knowledge, a differential thermal analysis technique has never been found before to be used with nanofluids. In the present study, this technique will be applied to measure the specific heat of nanofluids. The results will be compared with those reported in literature. The correlations for determining the specific heat of nanofluids are also proposed for practical applications.

PREPARATION OF NANOFLUIDS

The preparation of nanofluids is an important step. Generally, there are three methods of nanofluids preparation: pH control, addition of surfactants or dispersants, and use of ultrasonic vibration. The purpose of nanofluids preparation is to suspend nanoparticles stably in base fluids without precipitation of particles in short duration [2].

TiO_2 and Al_2O_3 nanofluids used in the present study were supplied by DEGUSSA Company. The average diameter of the TiO_2 particles is 21 nm and the average diameter of the Al_2O_3 particles is 120 nm. Table **1** shows the density and specific heat of nanoparticles used in the present study determined using Ref. [24] and Ref. [25] for density and specific heat, respectively. Both are suspended in water base fluid with concentrations of 13.8 and 10.6 vol.%. The base fluids used in this research are pure water and ethylene glycol-water mixture at 20/80 wt %. Before the experiment, the nanofluids supplied by the manufacturer were mixed and diluted by adding base fluid to reach the desired concentrations. Then, ultrasonic vibration was used for about 2 hours to create dispersion. Preparation by pH control and addition of surfactants was done discretely by the manufacturer.

Table 1. Properties of Nanoparticles

Nanoparticles	Density (kg/m^3)	Specific heat at 33 °C (kJ/kg K)
TiO_2	4157	0.715
Al_2O_3	3970	0.795

The photograph of TiO_2 nanoparticles taken from the transmission electron microscope (TEM) is shown in Fig. (**1**). The particle size distribution is also shown in Fig. (**2**). Initially, it was found that both nanoparticles have a circular shape, with an average diameter of 21 nm for TiO_2 and of 120 nm for Al_2O_3 which are very similar to the information provided by the manufacturer.

EXPERIMENTAL APPARATUS AND PROCEDURES

In this study, a calorimeter of the comparison type used to measure the specific heat of nanofluids was newly developed. The measurement was based on differential thermal analysis technique as shown in Fig. (**3**). Temperature differences obtained from heating between the reference liquid and the tested nanofluids together with known properties of the reference liquid can be used to determine the specific heat.

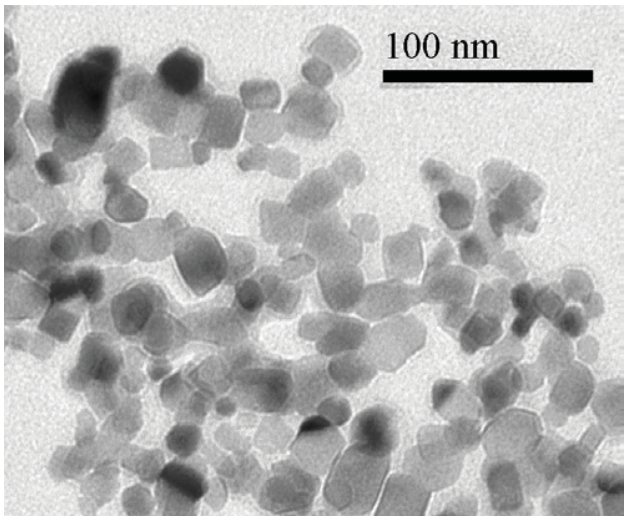

Fig. (1). TEM image of dispersed TiO_2 nanoparticles in water [From Suriyawong and Wongwises [26], with permission from Elsevier].

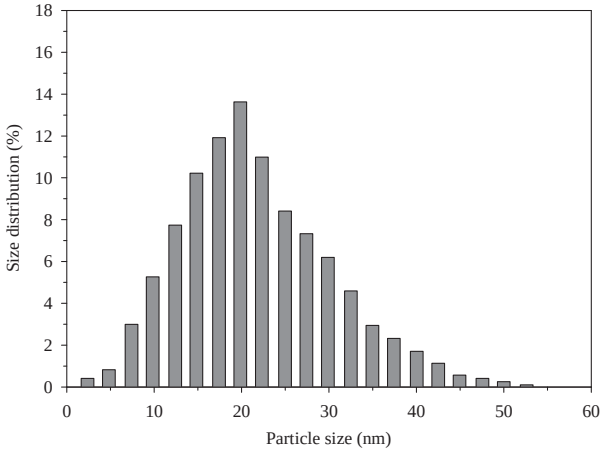

Fig. (2). Size distribution of TiO_2.

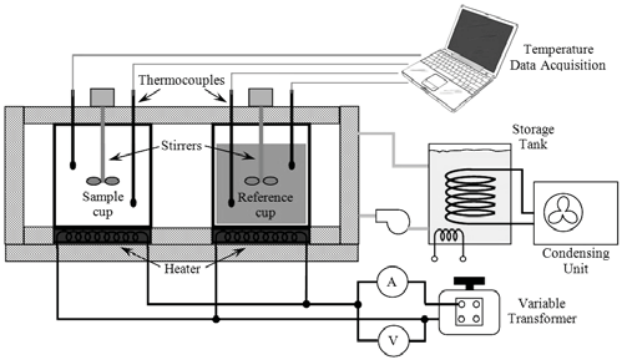

Fig. (3). Schematic diagram of experimental apparatus.

Important components shown in Fig. (**3**) are cups for sample and reference substances that are specially designed in symmetrical sizes. The cups are made from stainless steel with high conductivity

and high sensibility to temperature change. Both cups are placed in temperature control sleeves connected to a hot-cold water tank. Heat for each cup is fed from the bottom of each cup with a 30-watt electrical plate heater. The heater's coils are specially designed to have equal resistance. Heat can be controlled by variable transformers. Each cup has a small propeller with a low speed to create an evenly dispersed temperature and to prevent sedimentation and agglomeration of nanoparticles. The temperatures of both substances are measured with T-type thermocouples installed at the top and the bottom of the cup are recorded precisely via a computerized data logger every 3 seconds.

The experiment began by measuring an equal volume of the prepared nanofluids and reference substances. Both substances were weighed for use in calculation. Next, the substances were put in each cup carefully. The lids of the cups and the temperature control sleeves were then closed. Next, the level of the thermocouples, as well as the level and speed of the propeller, were adjusted and checked. Cooling water was put into the sleeves to adjust the starting temperature of both substances. When the desired starting temperature was reached, the cooling water was poured out of the sleeves and the heater was turned on. The temperature was recorded immediately. The temperature change of the nanofluids and reference substance were observed during the experiment. The experiment was stopped when the final temperature was reached. Both cups were cleaned, along with the other components that came in contact with nanofluids, before repeating the experiment.

Based on the differential thermal analysis, both sample and reference substances received an equal amount of heat. Therefore, specific heat of nanofluids $\left(C_{p,nf}\right)$ could be calculated from

$$Q_{nf} = Q_{ref}$$

$$m_{nf} C_{p,nf} \Delta T_{nf} = m_{ref} C_{p,ref} \Delta T_{ref}$$

$$C_{p,nf} = \frac{m_{ref} C_{p,ref} \Delta T_{ref}}{m_{nf} \Delta T_{nf}} \quad (1)$$

where $C_{p,ref}$ is the specific heat of reference substance; m_{nf} and m_{ref} are the masses of the nanofluids and the reference substances, respectively; and ΔT_{nf} and ΔT_{ref} are the temperature changes during the experiment of the nanofluids and the reference substances, respectively.

RESULTS AND DISCUSSION

Before the experiment, the developed apparatus was calibrated by measuring the specific heat of the water sample and a 20/80 % by weight mixture of ethylene glycol (EG)/water in the temperature range of 15 to 65°C. Results were then compared with the standard values from ASHRAE [27] and were found to be similar. The water sample had a maximum deviation of 1.4% with an average deviation of 1.36%. The EG/water mixture had maximum deviation of 3.21% with average deviation of 2.24%, as shown in Fig. (**4**).

This section discusses the effect of the concentration and temperature on the specific heat of nanofluids with water and mixture of ethylene glycol as base fluids, tested at concentrations of 1, 2, 4, 6 and 8 vol.% in a temperature range of 15 to 65°C. Fig. (**5**(a)) shows that the specific heat of Al_2O_3-water is a function of concentration and temperature. The experimental results indicated that specific heat decreased by about 20% when the concentration increased to 8 vol.%. In terms of temperature, the specific heat increased only slightly when the temperature increased. Fig. (**5**(b)) shows similar results of TiO_2-water. That is, the increasing concentration caused specific heat to decrease by about 5 to 23% at the concentrations of 1 to 8 vol.%. The increasing temperature also caused a slight increase in specific heat.

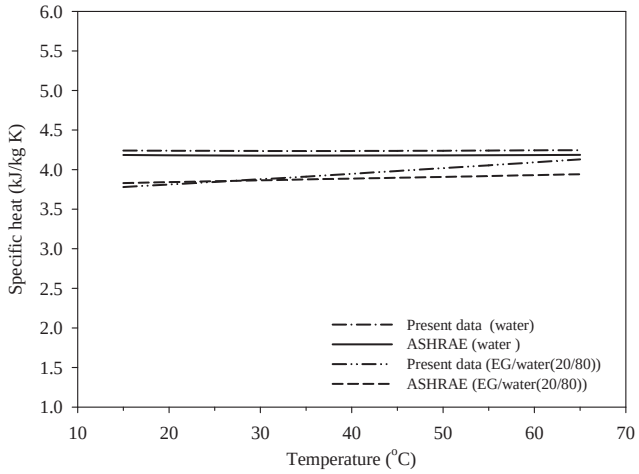

Fig. (4). Comparison of the measured specific heat with reference data.

This research also studied the effect of base fluid on the specific heat of nanofluids. Hence, apart from the water-based nanofluids, the EG/water (20/80)-based fluid was also examined. Al_2O_3-EG/water and TiO_2-EG/water at the concentrations of 1, 2 and 4 vol.% in a temperature range of 15 to 65°C were tested. Figs. (**6**(a) and **6**(b)) show that for both Al_2O_3-EG/water and TiO_2-EG/water the increasing concentrations caused the specific heat to decrease by about 3 to 11% in a concentration range of 1 to 4 vol.%. The specific heat tended to increase when the temperature increased.

From the experimental results of all four types of nanofluids mentioned above, the decrease of the specific heat of nanofluids when the concentration increased could directly result from the fact that the specific heat of nanoparticles mixed is much lower than that of the base fluid. As a result, the overall specific heat of nanofluids decreases. In terms of temperature, the increase of specific heat with the increasing temperature is similar to that of the base fluid. Basically, the specific heat of the base fluids increases when the temperature increases. Different from the base fluids, the specific heat of nanoparticles slightly increases with the increasing temperature. As a result the slope of the experimental lines shown in Figs. (**5** and **6**) are almost the same.

This section compares the experimental results with the prediction from existing models and data obtained from other researches. The widely used models of Pak and Cho [5] assume that nanofluids are homogeneous substances that could be calculated by mixing theory as follows:

$$C_{p,nf} = \phi C_{p,np} + (1-\phi) C_{p,b} \quad (2)$$

where $C_{p,nf}$ is the specific heat of nanofluids; $C_{p,np}$ is the specific heat of nanoparticles; $C_{p,b}$ is the specific heat of the base fluid; and ϕ is the concentration by volume.

Another widely used model of Xuan and Roetzel [19] assumes that the heat transfer process between nanoparticles and the base fluid is thermal equilibrium, as follows:

$$C_{p,nf} = \frac{\phi \rho_{np} C_{p,np} + (1-\phi) \rho_b C_{p,b}}{\phi \rho_{np} + (1-\phi) \rho_b} \quad (3)$$

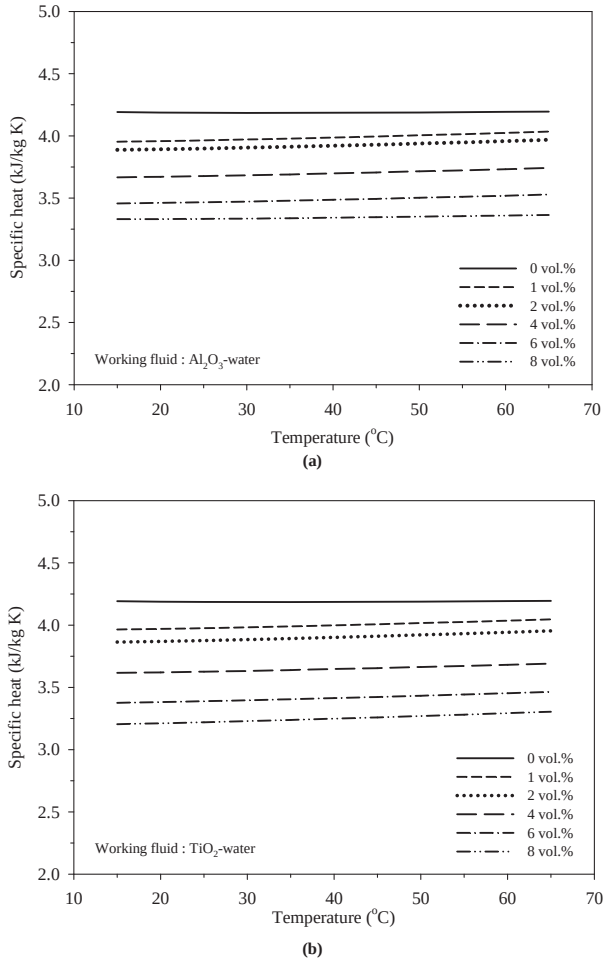

Fig. (5). The specific heat of water-base nanofluids as a function of temperature and volume fraction.

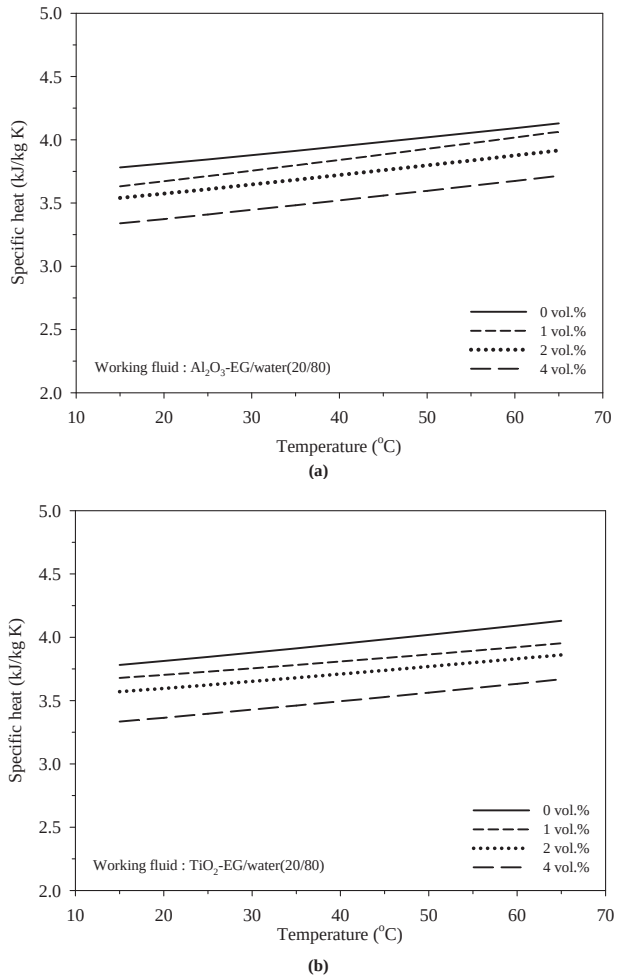

Fig. (6). The specific heat of EG/water (20/80)-base nanofluids as a function of temperature and volume fraction.

where ρ_{np} is the density of the nanoparticles, and ρ_b is the density of the base fluid.

Vajjha and Das [20] also present a correlation developed from the experiment to measure the specific heat of Al_2O_3, ZnO, and SiO_2 nanofluids as follows:

$$C_{p,nf} = \frac{\left((AT) + B(\frac{C_{p,np}}{C_{p,b}}) \right)}{C + \phi} \quad (4)$$

where *T* is the temperature of the nanofluids, and *A*, *B*, and *C* are coefficients shown in Table **2**.

Table 2. Coefficients in Vajjha and Das Model

Nanoparticle	Coefficients		
	A	**B**	**C**
Al_2O_3	0.0008911	0.5179	0.4250
SiO_2	0.001769	1.1937	0.8021
ZnO	0.0004604	0.9855	0.299

Fig. (**7**(a)) shows the specific heat of Al_2O_3-water nanofluids at various concentrations. Results are similar to those from the model of Xuan and Roetzel. However, the model of Pak and Cho could not be used to predict, particularly at high concentrations. On the other hand, the model of Vajjha and Das gave lower values, particularly at low concentrations. In terms of temperature, the experimental results are also similar to those from the model of Xuan and Roetzel. The model of Pak and Cho gave higher values, whereas the model of Vajjha and Das gave lower values, particularly in the lower temperature ranges, as shown in Fig. (**7**(b)). Similarly, the experimental results of TiO_2-water nanofluids, shown in Figs. (**8**(**a**) and **8**(**b**)), also correspond with the prediction from the model of Xuan and Roetzel, both in terms of concentration and temperature. From all comparisons, it could be said that the sample nanofluids used in this experiment are in a thermal equilibrium during the experiment. Therefore, the specific heat gained from the experiment is similar to the prediction of the thermal equilibrium model presented by Xuan and Roetzel. This could be confirmed with the experiment of Zhon and Ni, who measured Al_2O_3-water nanofluids and obtained similar results to the prediction from the model of Xuan and Roetzel, as shown in Fig. (**7**(a)). Moreover, Zhou *et al*. [21] also concluded from their experiment in measuring the specific heat of CuO-EG nanofluids that the specific heat of CuO-water was also similar to those predicted by the thermal equilibrium model.

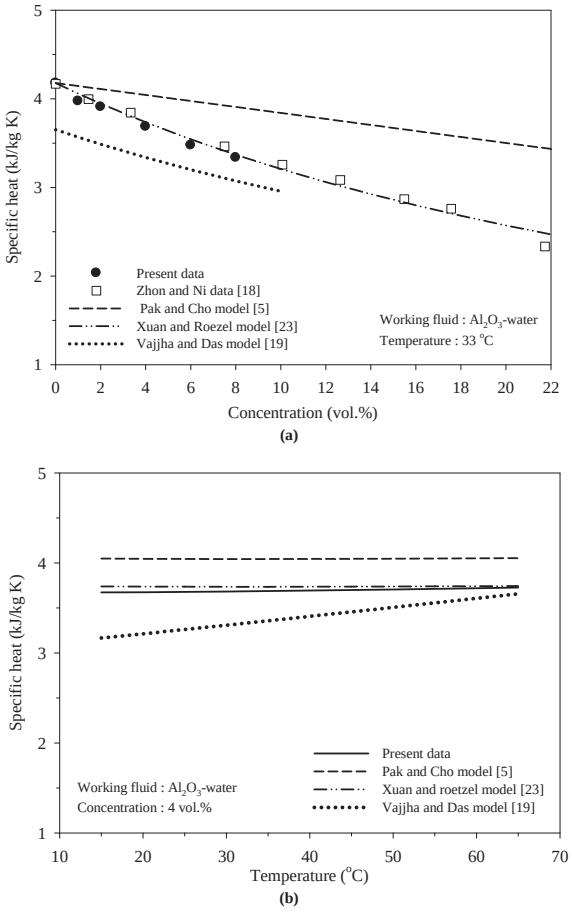

Fig. (7). Comparison of the measured specific heat with those obtained from various researchers.

This research presents a correlation to predict specific heat of Al_2O_3 and TiO_2 nanofluids in a form of specific heat ratio between nanofluids and base fluid $\left(C_{p,nf}/C_{p,b}\right)$ that could be applied to other base fluids. This model considers the effects of temperature, concentration, the specific heat of nanoparticles, and the specific heat of the base fluid as follows:

$$\frac{C_{p,nf}}{C_{p,b}} = A\phi^B T^C \left(\frac{C_{p,np}}{C_{p.b}}\right)^D \quad (5)$$

where A, B, C, and D are the coefficients shown in Table **3**. The model could be used in a temperature range of 15 to 65°C and a concentration range of 1 to 8 vol.%. Fig. (**9**) shows a comparison between experimental specific heat and predictions from the correlation (Eq. (5)). It could be seen that the predicted value is similar to the experimental value at a verifiable and acceptable level.

Table 3. The Coefficients in Presented Correlation for Different Nanofluids

Nanofluid	Coefficients				Max. error	Avg. error
	A	B	C	D		
Al_2O_3	1.249458	-0.05846	0.006467	-0.17236	1.77%	0.79%
TiO_2	1.387402	-0.06425	0.001124	-0.21159	1.82%	0.85%

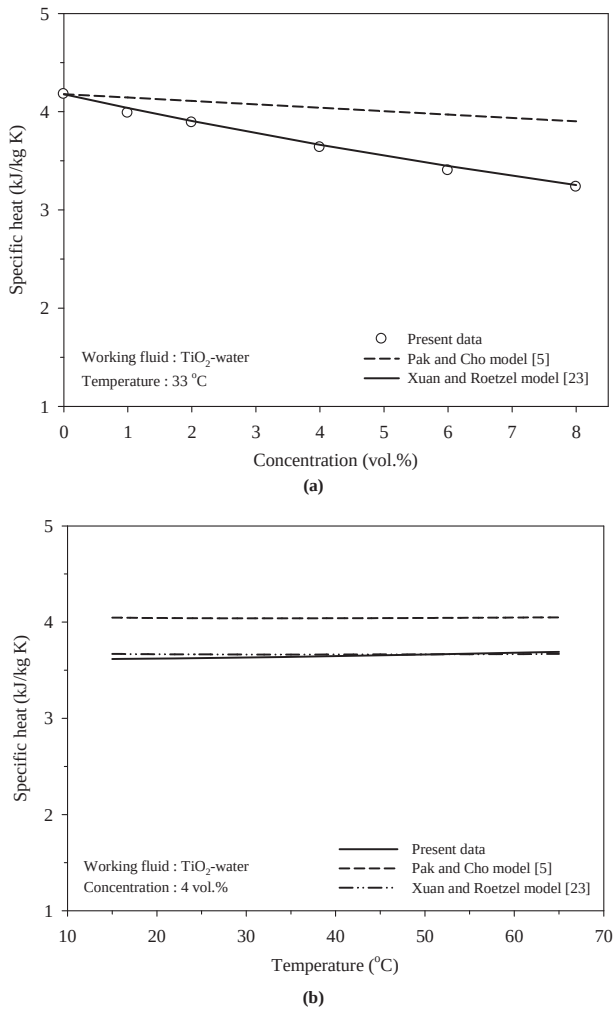

Fig. (8). Comparison of the measured specific heat of TiO_2-water nanofluids with those obtained from various researchers.

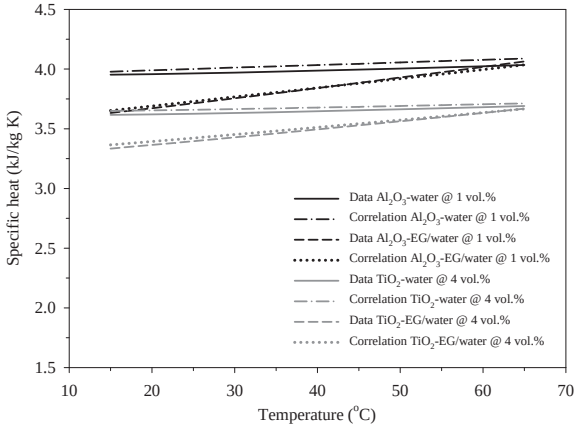

Fig. (9). Comparison of the measured specific heat with the proposed correlations.

CONCLUSIONS

From the calibration of measuring specific heat of water and ethylene glycol, the results are similar to the standard values from

ASHRAE. The developed specific heat measurement apparatus also has an acceptable precision level.

The experimental results indicate that the specific heat of nanofluids is lower than the base fluid and tends to decrease when concentration increases. On the other hand, the increasing temperature causes the specific heat of nanofluids to increase. These experimental results are compatible with the prediction from the thermal equilibrium model of Xuan and Roetzel. This research also presents a newly developed correlation to predict the specific heat of Al_2O_3 and TiO_2 nanofluids.

CONFLICT OF INTEREST

The authors confirm that this article content has no conflicts of interest.

ACKNOWLEDGEMENTS

The present study was supported by the Thailand Research Fund (TRF), the Office of the Higher Education Commission and the National Research University Project whose guidance and assistance are gratefully acknowledged.

REFERENCES

[1] Choi, S.U.S. Enhancing thermal conductivity of fluids with nanoparticles. *ASME FED*, **1995**, *231*, 99-103.

[2] Das, S.K.; Putta, N.; Thiesen, P.; Roetzel, W. Temperature Dependence of Thermal Conductivity Enhancement For Nanofluids. *ASME Trans. J. Heat Transfer*, **2003**, *125*, 567-574.

[3] Eastman, J.A.; Choi, S.U.S.; Li, S.; Yu, W.; Thomson, L.J. Anomalously increased effective thermal conductivities of ethylene glycol-based nanofluids containing copper nanoparticles. *Appl. Phys. Lett.*, **2001**, *78*, 718-720.

[4] Wang, X.; Xu, X.; Choi, S.U.S. Thermal Conductivity of Nanoparticles-Fluid Mixture. *J. Thermophys. Heat Transfer*, **1999**, *13*, 474-480.

[5] Pak, B. C.; Cho, Y. I. Hydrodynamic and Heat Transfer Study of Dispersed Fluids with Submicron Metallic Oxide Particles. *Exp. Heat Transfer*, **1998**, *11*, 151-170.

[6] Murshed, S.M.S.; Leong, K.C.; Yang, C. Investigations of Thermal Conductivity and Viscosity of Nanofluids. *Int. J. Therm. Sci.*, **2008**, *47*, 560-568.

[7] Duangthongsuk, W.; Wongwises, S. Measurement of temperature-dependent thermal conductivity and viscosity of TiO_2-water nanofluids. *Exp. Therm. Fluid Sci.*, **2009**, *33*, 706-714.

[8] Yu, W.; Xie, H.; Li, Y.; Chen, L. Experimental investigation on thermal conductivity and viscosity of aluminum nitride nanofluid. *China Particuol.*, **2011**, *9*, 187-191.

[9] Nguyen, C.T.; Desgranges, F.; Roy, G.; Galanis, N.; Mare, T.; Boucher, S.; Mintsa, H.A. Temperature and particle-size dependent viscosity data for water-based nanofluids – Hysteresis phenomenon. *Int. J. Heat Fluid Flow*, **2007**, *28*, 1492-1506.

[10] Masuda, H.; Ebata, A.; Teramae, K.; Hishinuma, N. Alteration of Thermal Conductivity and Viscosity of Liquid by Dispersing Ultra-Fine Particles (Dispersion of Al_2O_3, SiO_2 and TiO_2 Ultra-Fine Particles). *Netsu Bussei (Japan)*, **1993**, *7*, 227-233.

[11] Namburu, P.K.; Kulkarni, D.P.; Dandekar, A.; Das, D.K. Experimental investigation of viscosity and specific heat of silicon dioxide nanofluids. *Micro Nano Lett.*, **2007**, *2*, 67-71.

[12] Yang, Y.; Zhang, Z.G.; Grulke, E.A.; Anderson, W.B.; Wu, G. Heat Transfer Properties of Nanoparticle-in-Fluid Dispersions (Nanofluids) in Laminar Flow. *Int. J. Heat Mass Transfer*, **2005**, *48*, 1107-1116.

[13] Xuan, Y.; Li, Q. Investigation on Convective Heat Transfer and Flow Features of Nanofluids. *ASME J. Heat Transfer*, **2003**, *125*, 151-155.

[14] Nguyen, C.T.; Roy, G.; Gauthier, C.; Galanis, N. Heat Transfer Enhancement Using Al_2O_3-Water Nanofluid for Electronic Liquid Cooling System. *Appl. Therm. Eng.*, **2007**, *28*, 1501-1506.

[15] Heris, S.Z.; Etemad, S.G.; Esfahany, M.N. Experimental Investigation of Oxide Nanofluids Laminar Flow Convective Heat Transfer. *Int. Commun. Heat Mass Transfer*, **2006**, *33*, 529-535.

[16] He, Y.; Jin, Y.; Chen, H.; Ding, Y.; Cang, D.; Lu, H. Heat Transfer and Flow Behavior of Aqueous Suspensions of TiO_2 Nanoparticles (Nanofluids) Flowing Upward Through a Vertical Pipe. *Int. J. Heat Mass Transfer*, **2007**, *50*, 2272-2281.

[17] Duangthongsuk, W.; Wongwises, S. An experimental study on the heat transfer performance and pressure drop of TiO_2-water nanofluids flowing under a turbulent flow regime. *Int. J. Heat Mass Transfer*, **2010**, *53*, 334-344.

[18] Zhou, S.; Ni, R Measurement of the Specific Heat Capacity of Water-Based Al_2O_3 Nanofluid. *Appl. Phys. Lett.*, **2008**, *92*, 093123.

[19] Xuan, Y.; Roezel, W. Conceptions for Heat Transfer Correlations of Nanofluids. *Int. J. Heat Mass Transfer*, **2000**, *43*, 3701-3707.

[20] Vajjha, R.S.; Das, D.K. Specific Heat Measurement of Three Nanofluids and Development of New Correlations. *ASME J. Heat Transfer*, **2009**, *131*, 071601

[21] Nelson, I.C.; Banerjee, D.; Rengasamy, P. Flow Loop Experiments Using Polyalphaolefin Nanofluids. *J. Thermophys. Heat Transfer*, **2009**, *23*, 752-761.

[22] Zhou, L.P.; Wang, B.X.; Peng, X.F.; Du X.Z.; Yang Y.P. Research Article on The Specific Heat Capacity of CuO Nanofluid. *Adv. Mech. Eng.*, **2010**, *2010*, 172085.

[23] Shin, D.; Banerjee, D. Enhanced Specific Heat of Silica Nanofluid. *ASME J. Heat Transfer*, **2011**, *133*, 024501.

[24] Incropera, F.P.; DeWitt, D.P. *Introduction to Heat Transfer*, 3rd ed.; Wiley, New York: **1996**.

[25] Touloukian, Y.S.; Buyco, F.H. In: *Thermophysical Properties of Matter*; Specific Heat Nonmetallic Solids; IFI/Plenum, New York: **1970**; Vol. *5*

[26] Suriyawong, A.; Wongwises, S. Nucleate Pool Boiling Heat Transfer Characteristics of TiO_2-Water Nanofluids at Very Low Concentrations. *Exp. Therm. Fluid Sci.*, **2010**, *34*, 992-999.

[27] ASHRAE, *ASHRAE Handbook: Fundamentals*, American Society of Heating, Refrigerating and Air-Conditioning Engineers Inc., Atlanta, GA, **2005**.

Received: October 22, 2011 **Revised: June 17, 2012** **Accepted: July 11, 2012**

International Journal of Air-Conditioning and Refrigeration
Vol. 20, No. 4 (2012) 1230003 (20 pages)
© World Scientific Publishing Company
DOI: 10.1142/S2010132512300030

World Scientific
www.worldscientific.com

A REVIEW ON THE HEAT-TRANSFER PERFORMANCE AND PRESSURE-DROP CHARACTERISTICS OF VARIOUS ENHANCED TUBES

S. LAOHALERTDECHA*, A. S. DALKILIC† and S. WONGWISES*,‡,§
*Fluid Mechanics, Thermal Engineering and Multiphase Flow Research Lab. (FUTURE)
Department of Mechanical Engineering, Faculty of Engineering
King Mongkut's University of Technology Thonburi (KMUTT) Bangmod
Bangkok, 10140, Thailand
†Heat and Thermodynamics Division, Department of Mechanical Engineering
Yildiz Technical University, Yildiz, Besiktas, Istanbul, 34349, Turkey
‡The Academy of Science, The Royal Institute of Thailand
Sanam Suea Pa, Dusit, Bangkok 10300, Thailand
§somchai.won@kmutt.ac.th

Received 11 May 2012
Revised 28 August 2012
Accepted 3 September 2012
Published 4 December 2012

The enhanced tube is a kind of the passive technique for improving the thermal performance of the heat exchangers with a little increase of the friction penalty. They have stated to use instead of the common smooth tubes for designing of the heat exchangers. The size of these heat exchangers can be reduced considerably by using the enhanced tubes instead of smooth tubes. Normally, they are divided into four groups: the corrugated tube, ribbed tube, grooved tube, and fluted tube. Compared with the common smooth tube, many researchers reported that use of the enhanced tubes dramatically increases the heat-transfer performance, both theoretically and experimentally. Focusing on the advantages of the enhanced tubes, this article summarizes the published studies on the heat-transfer and pressure-drop characteristics of the enhanced tubes, both experimental and quantitative investigations.

Keywords: Enhanced tubes; heat-transfer performance; pressure drop; heat exchanger.

Nomenclature

D : Diameter (m)
e : Corrugation depth (m)
f : Friction factor
G : Mass flux ($\mathrm{kg \cdot m^{-2} \cdot s}$)
h : Heat transfer coefficient ($\mathrm{W \cdot m^{-2} \cdot K}$)
L : Length of the test tube (m)
Nu : Nusselt number
p : Corrugation pitch (m)
Pr : Prandtl number
Re : Reynolds number

§Corresponding author.

t : Corrugation width (m)
x : Quality

Greek Letters

β : Helix angle (degree)

Subscripts

avg : Average
i : Inside
o : Outside

1. Introduction

The surface area of heat exchangers has a directly significant effect on their heat-transfer performance. Improvements to make heat transfer equipment more energy-efficient would need to focus on miniaturization on the one hand and an astronomical increase in heat flux on the other. Normally, heat-transfer enhancement techniques necessarily reduce the thermal resistance in a conventional heat exchanger by promoting a higher convection heat-transfer coefficient in order to minimize the size of the heat exchanger.

In general, enhancement techniques can be divided into two categories — active and passive techniques. The active technique requires external forces such as an electric field or acoustic or surface vibration, whereas the passive technique requires special surface geometries, such as a rough surface, extended surface, or fluid additives. Enhanced heat-transfer surfaces or "enhanced tubes" are one of the passive techniques, in which the surface is modified in such a way as to promote turbulence in the flow field and increase the heat-transfer surface.

These tubes can be employed in many heat exchangers to enhance the heat-transfer performance of both the inside and outside tubes, by mixing and also limiting the fluid boundary layers close to the heat transfer surfaces. Nowadays, enhanced tubes such as spirally corrugated tubes, ribbed tubes, grooved tubes, and fluted corrugated tubes are typically selected to replace conventional smooth tubes in the designs of industrial heat exchangers. They are expected to increase the heat-transfer performance of the heat-transfer equipment with only a very small increase in the pressure-drop penalty.

The heat transfer and pressure drop characteristics of the various refrigerants flowing through different type of the enhanced tubes under condensation process were summarized and reported in Ref. 1. The effects of tube orientation, tube geometry, flow pattern, oil mixture and void fraction on the condensation heat transfer performance and pressure drop were presented.

The purpose of this article is to review the literature mentioning heat-transfer performance and pressure-drop characteristics of the enhanced tubes, both experimental and theoretical studies. Various categories of enhanced tubes will be investigated i.e., corrugated tubes, ribbed tubes, grooved tubes, and fluted tubes. In addition, heat transfer characteristics of a new type of enhanced tube named "Vipertubes" are also presented. Each type is described in detail in the following sections.

2. Corrugated Tubes

This type of tube has a corrugated surface. The overall heat-transfer coefficient has been remarkably improved because of the turbulent flow effect on the inner surface and outer surface of the tube caused by the corrugation. The details of corrugated tubes are shown in Fig. 1. Many experimental investigations have been performed to investigate the effects of corrugation pitch, corrugation depth, and tube diameter on the heat-transfer and pressure-drop characteristics of the corrugated tubes. The heat transfer and flow characteristics of corrugated tubes have been reviewed as described below.

Mimura and Isozaki[2] reported the effect of shapes of corrugated tubes on the experimentally observed heat-transfer and flow characteristics. For heat-transfer experiments, steam is condensed on the

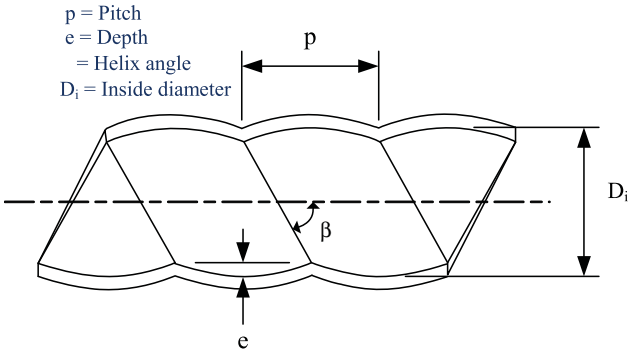

Fig. 1. Schematic diagram of the corrugated tubes.

outside of a horizontally corrugated tube made from 90−10 cupronickel. Similarly, pressure drop is measured under isothermal cold-flow conditions. The results indicated that the heat-transfer coefficient decreased with increasing corrugated pitch. At the ratio of depth to tube diameter of 0.05, the maximum heat-transfer coefficient was obtained. Moreover, the dual-start corrugated tubes gave a slightly higher heat-transfer coefficient than those of the single-start tubes. The friction factor equation was presented by considering the effect of pitch and depth. Finally, the correlation between the tube side heat-transfer coefficient and pressure drop in the corrugated tube was proposed.

Ganeshan and Rao[3] presented an experimental study on the heat-transfer behavior and friction characteristics of hot water flowing through a smooth tube and seven spirally corrugated tubes. The corrugated tubes of one to four helical starts and having constant helix angle of 65° were used as the test sections. They were different geometrical aspect ratios of e/d, p/e and p/d. The experimental data demonstrated that the heat-transfer coefficient of the four-start corrugated tube was larger than the smooth tube by about 100% at a Prandtl number of 4.3. Similarly, at a higher Prandtl number of 109, a 150% increase in the heat transfer coefficient was obtained.

Thien and Khan[4] reported the friction factor of an Oldroyd-type fluid flowing inside a sinusoidally corrugated tube, experimentally and quantitatively. The boundary element method was used to solve the problem and a Deborah number up to 20 was used in their study. The numerical results showed that the friction factor increased with the Deborah number. The results also gave reasonably agreement with the measured data.

Asako *et al.*[5] studied the heat transfer and flow characteristics of corrugated ducts with rounded corners, quantitatively. The results with the rounded corners were compared with the straight duct results. Three assigned corrugation angles and four aspect ratios of corrugated ducts are used as the test section. The simulation conditions were as follows: (1) Reynolds number between 100 and 1000 and (2) a fixed Prandtl number of 0.7. Their results indicated that rounding of the corners led to decreases in both the friction factor and the Nusselt number.

Honda and colleagues[6] investigated heat transfer and flow behaviors of R-11 and R-113 flowing in the annulus of a horizontal double-tube condenser during the condensation process. A corrugated tube with an outside diameter of 19.1 mm and installed with wire fins on the outer surface is used as the inner tube; three smooth tubes with inner diameter of 24.8, 27.2, and 29.9 mm are used as the outer tube. The mass velocity of working fluids were between 50 and $300\,\mathrm{kg}\cdot\mathrm{m}^{-2}\cdot\mathrm{s}$. The Lockhart−Martinelli parameters were used to calculate the frictional pressure gradient and then compared with the measured data. The experimental results showed that the local heat-transfer coefficient was two to 13 times higher than those for horizontal annuli with a smooth and corrugated inner tube. Moreover, the measured data was used to develop the correlation for predicting the local heat-transfer coefficient based on the surface tension controlled flow and the vapor shear controlled-flow model.

Burdette *et al.*[7] presented an upper-convected Maxell (UCM) model for predicting the flow behavior of working fluid flowing through an axisymmetric corrugated tube with a sinusoidally varying cross-section. The explicitly elliptic momentum equation (EEME) was used to solve the problem, and the results showed an agreement with the spectral/finite difference calculations.

Zimparov *et al.*[8] experimentally investigated the heat transfer and frictional pressure drop of a power plant condenser. One smooth tube and 25 spirally corrugated brass tubes were used as the test sections. The corrugated pitch varied from 6.5 to 16.9 mm, the ridge height varied from 0.44 to 1.18 mm, and the spiral angle ranged from 68° to 85°. Performance evaluation criteria were used to estimate the benefit of the spirally corrugated tubes.

Zimparov *et al.*[9] introduced a mixing-length model for predicting the heat-transfer coefficient and the Fanning friction factor of water flowing through a corrugated tube. A Reynolds number between 10^4 and 6×10^4 and a Prandtl number between 2.2 and 3.4 were used as the test conditions.

Gopalan and Ponnalagasamy[10] reported a steady laminar flow of a suspension in a corrugated tube with asymmetric and symmetric wavy wall, numerically. The effects of Reynolds number, Peclet number, wave number and the volume fraction of the particles on the flow were presented. The simulation results indicated that the mixing phenomenon due to secondary flow increased the flow of a relatively large volume fraction of low diffusive particles. In addition, their results also illustrated that

the pressure drop of corrugated tubes is higher than that of the smooth tube and decreased with increases in the diffusive particles.

Hinton and Conklin[11] experimentally studied the condensing heat-transfer and pressure drop characteristics of R-22 and non-azeotropic refrigerant mixture (NARM) of 75 wt.% R-143a and 25 wt.% R-124 flowing through a condenser made from common smooth tubes and then compared with the spirally corrugated tubes. The double-tube counter flow heat exchanger is used as the test section, in which refrigerant flows inside the internal tube and the water circulates in the annulus. Their results showed that the average heat transfer coefficient for the corrugated tube was higher than that for the smooth tube by about 40% for R-22 and 70% for NARM. Similarly, the pressure drop of the corrugated tube working with R-22 and NARM was roughly 23% and 36% larger than that of the smooth tube, respectively.

Chen *et al.*[12] experimentally investigated the heat-transfer and friction characteristics of four-start spirally corrugated tubes. A double-pipe counter flow heat exchanger was used as the test section. In their study, the non-symmetric nature of the corrugation angles along the longitudinal direction was reported. Then, the measured data were compared with the neural network analysis. The differences in heat transfer and friction loss due to effect of the corrugation angles were observed. Moreover, the heat transfer coefficient correlation based on a neural network model was proposed by considering the effect of the corrugation angles.

Dong *et al.*[13] reported the heat transfer and friction characteristics of water and oil flowing through four spirally corrugated tubes under turbulent flow, experimentally. The dimensions of the test tubes are shown in Table 1. The test conditions were conducted for the Reynolds number between 6000 and 93,000 for water and 3200 and 19,000 for oil. Compared with the common smooth tube, the experimental data indicated that the spirally corrugated tubes gave higher heat-transfer coefficient and friction factor by about 30% to 120% and 60% to 160%, respectively, as shown in Fig. 2. Moreover, the increase of e/d has a greater effect on the increase of the friction factor and heat transfer coefficient than the increase of p/d.

Table 1. The dimensions of the corrugated tubes.[13] [From Ref. 13, with permission from Elsevier.]

Number	p (mm)	e (mm)	β (degree)	D_i (mm)	L (mm)
1	10	0.39	78.8	16.04	500
2	10	0.32	78.8	16.12	500
3	10	0.69	82.1	22.82	500
4	12	0.7	79.0	20.08	500

Zimparov[14,15] experimentally investigated the heat-transfer and pressure-drop characteristics of water flow in single-start and three-start spirally corrugated tubes combined with five twisted tape inserts. The effects of height to diameter ratio and relative pitch were presented. The extended performance evaluation criteria equation was used to evaluate the multiplicative effect. At a given condition, the measured data illustrated that the heat-transfer coefficient and friction factor of spirally corrugated tubes combined with twisted tape inserts were higher than those for the conventional smooth tube.

Rainieri and Pagliarini[16] presented experimental study on the convective heat-transfer performance of corrugated wall tubes with axial symmetrical and helical corrugations with various pitch values. The effects of the wall roughness and fluid property variation were determined. Figure 3 presents a photo of the corrugated tubes. The Reynolds number ranged from 90 to 800, and ethylene glycol was used as the working fluid. The experimental data showed that the helical corrugation promoted a significant swirl component. However, an as much significant heat-transfer enhancement was not associated. Moreover, variation of fluid properties with temperature promoted the transition to an unstable flow.

Barba *et al.*[17] reported an experimental study on heat-transfer and pressure-drop characteristics of ethylene glycol flowing through a corrugated tube. The corrugated tube was obtained from a circular SS AISI 304 smooth tube, through a cold mechanical bucking, indenting the smooth tube without abrasion and mass removal as shown in Fig. 4. A Reynolds number ranging from 100 to 800 was tested. In comparison to the smooth tube, their results showed that the Nusselt number of the corrugated tube was significantly increased throughout the test run. However, for pressure drop consideration, the results also showed that using the corrugated tube caused increases in the friction factor by about 1.83 to 2.45. Moreover, the Nusselt number and friction factor correlations were proposed.

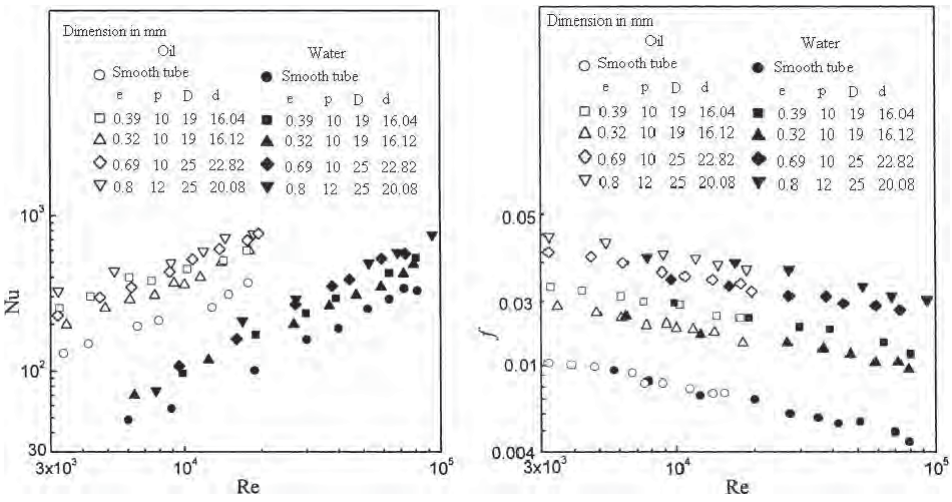

Fig. 2. Nusselt number and friction factor versus Reynolds number.[13] [From Ref. 13, with permission from Elsevier.]

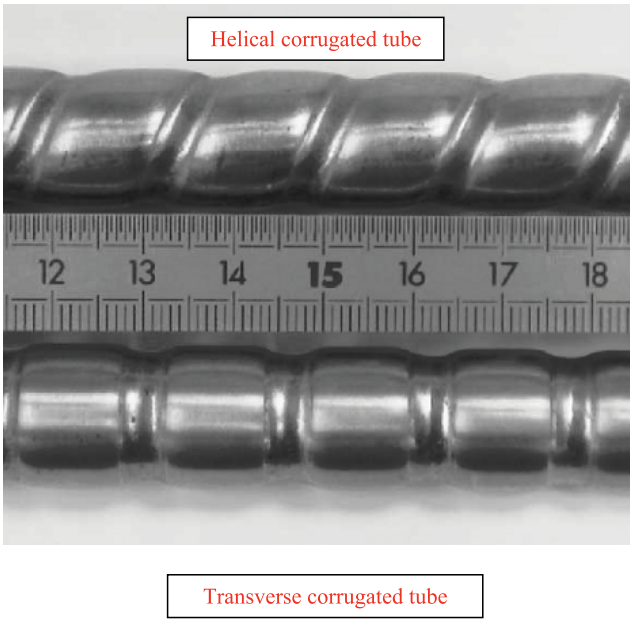

Fig. 3. Helical and transverse corrugated tubes.[16] [From Ref. 16, with permission from Elsevier (color online).]

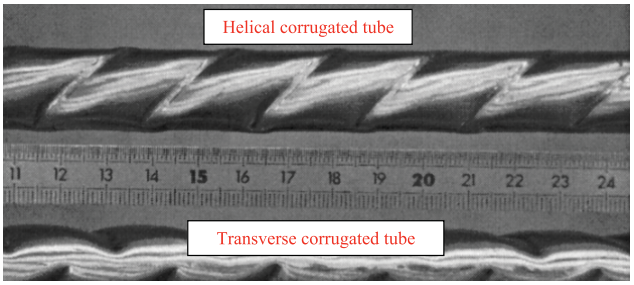

Fig. 4. Helical and transverse corrugated tubes.[17] [From Ref. 17, with permission from Elsevier (color online).]

Vicente and colleagues[18] determined the heat-transfer performance and friction characteristics of water and ethylene glycol flow in 10 corrugated tubes under turbulent flow. In this study, the Prandtl number was in the range of 2.5 to 100. The effect of rib height and spiral pitch was also investigated. Their data indicated that the severity index can be used to identify the effects of roughness on flow behaviors. Moreover, based on the experimental data, the Nusselt number and Fanning friction factor correlations were proposed as function of flow and geometry dimensionless parameters.

Zimparov[18] proposed a simple mathematical model for predicting the friction factor in the case of a spirally corrugated tube combined with a twisted tape insert under a fully developed turbulent flow region. This model was first suggested by Smithberg and Landis. In this study, the flow field was divided into two regions: (1) a helicoidal core flow and (2) a twisting boundary layer flow. Their simulation results demonstrated that the wall roughness had a significant effect on both the axial velocity and tangential velocity, which led to swirl-mixing phenomena. Moreover, their data were compared with 570 experimental data points obtained from the testing of 57 tubes. The results also indicated that the majority of the data falls within $\pm 15\%$ of the proposed model. This means that the proposed model can be used to predict the friction factor in the cases of smooth pipe, smooth pipe with a twisted tape inserts, a corrugated tube, and a corrugated tube combined with twisted tape inserts for turbulent flow regime.

The ongoing work of Zimparov[20] was to present a simple mathematical model created by Smithberg and Landis for predicting the heat-transfer coefficients of a spirally corrugated tube combined with a twisted tape insert in fully developed turbulent flow regime. The effects of both axial and tangential boundary layer were considered. Their results demonstrated that the wall roughness had simultaneous effects on the axial velocity and secondary fluid motion. Similar to the case of friction factor, the proposed model was compared with the 544 measured data obtained from Bergles *et al.*[21] for heat-transfer coefficient. The results showed that the proposed model gave reasonably good agreement with the measured data and deviations of $\pm 15\%$ were obtained.

Vicente *et al.*[18] reported an experimental study on the heat-transfer and pressure-drop characteristics of water and ethylene glycol flowing through corrugated tubes under laminar and transition flow regime. For laminar flow condition, their results indicated that the Nusselt number depended on both the natural convection and the entrance effect, and corrugated tube increases heat-transfer performance by about 30% at high Rayleigh numbers. Similarly, the friction factors in corrugated tubes were 25% larger than those of a smooth tube. Moreover, they reported that roughness of the corrugated tube accelerated the transition to a critical Reynolds number below 1300.

Targanski and Cieslinski[22] studied the evaporation heat-transfer coefficient and pressure drop of pure R407C and R407C/oil mixtures flow in two smooth tubes, corrugated tube and micro-finned tube, experimentally. The dimensions of the test sections are shown in Table 2. The experiments were conducted at saturation temperature of 0°C and mass flux varied between 250 and 500 $\mathrm{kg \cdot m^{-2} \cdot s}$. Their experimental data showed that two enhanced tubes gave a larger heat-transfer coefficient than the smooth tube, as well as a pressure drop. The average heat-transfer coefficient in the micro-finned tube and corrugated tube was up to 50% and 20%, respectively, higher than in the smooth tube. Similarly, pressure drop in the micro-finned tube and corrugated tube was up to 40% and 80%, respectively, higher than in the smooth tube, as shown in Fig. 5. Moreover, compared with pure R407C and R407C/oil mixtures, higher heat-transfer coefficients for pure R407C were obtained.

Table 2. The dimensions of the corrugated tubes[22] (from Ref. 22, with permission from Elsevier).

Number	Tube description	h (mm)	D_i (mm)	L (mm)
1	Smooth	—	8	2000
2	Smooth	—	8.8	2000
3	Corrugated	0.45	8.8	2000
4	Micro-fin	0.2	8.92	2000

Rozzi *et al.*[23] presented an experimental investigation on the convective heat transfer and friction losses in helically corrugated tubes. A shell and tube heat exchanger was used as the test apparatus. Whole milk, cloudy orange juice, apricot, and apple puree were tested under heating and cooling conditions. The experimental data showed that the use of helically corrugated tube had no effect on the heat-transfer performance for a Reynolds number less than 800. For a Reynolds number ranging from 800 to the limit of the transition flow regime, larger heat-transfer coefficients for corrugated tubes were obtained. Moreover, the results indicated that heat-transfer coefficients for corrugated tubes were moderately higher than those for smooth tubes and very high pressure drops were also obtained.

Dalkilic *et al.*[24] showed an experimental comparison of the laminar film condensation heat transfer coefficients of R134a in vertical smooth and micro-fin tubes having inner diameters of 7 mm and lengths of 500 mm at a mass flux of 29 $\mathrm{kg\,m^{-2}\,s^{-1}}$ and the pressures between 0.8 and 0.9 MPa. The original smooth tube heat transfer model was modified by a well-known friction factor to account for the heat transfer enhancement effects due to the presence of micro-fins, shown in Fig. 6(a), on the internal wall surface during annular flow regime conditions. Alterations of the local heat transfer coefficient, and condensation rate along the tube length during downward condensing film were determined. Their results show that the interfacial shear stress is found to have significance for the laminar condensation heat transfer of R134a under the given conditions due to its better predictive performance than the classical solution neglecting the interfacial shear stress effect. A comparison of the convective heat transfer coefficients was done according to the condensing pressures as shown in Fig. 6(b).

In 2010 and 2011, the work of Laohalertdecha and Wongwises[25–29] presented an experimental investigation on the heat-transfer coefficient and pressure-drop characteristics of refrigerant R134a flowing through the corrugated tubes under evaporation and condensation processes. The dimensions of the corrugated tubes are shown in Table 3, while

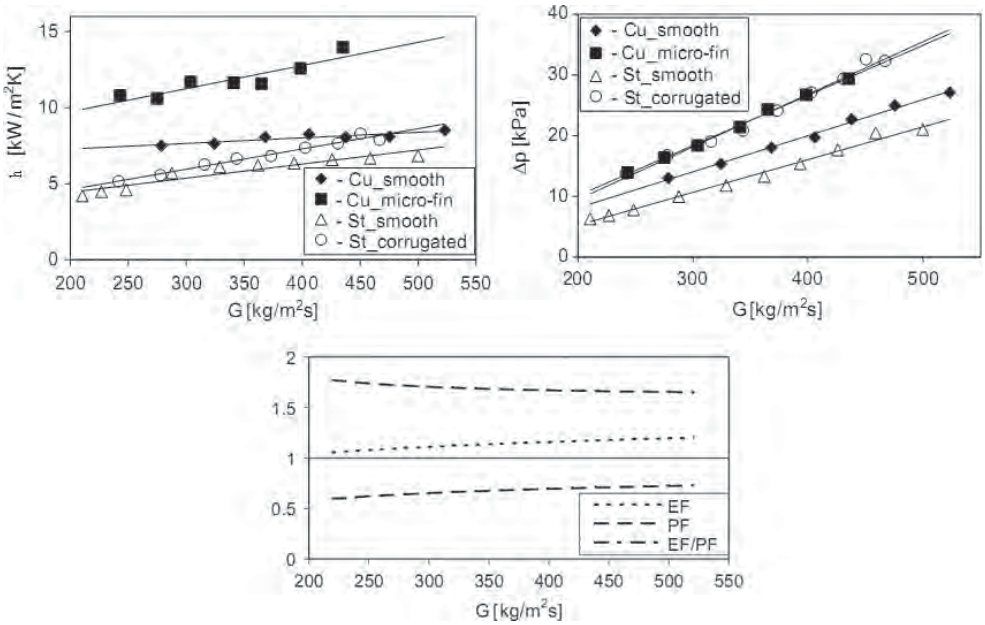

Fig. 5. Average heat transfer coefficient, pressure drop, enhancement factor and penalty factor versus mass flux for R407C.[22] [From Ref. 22, with permission from Elsevier.]

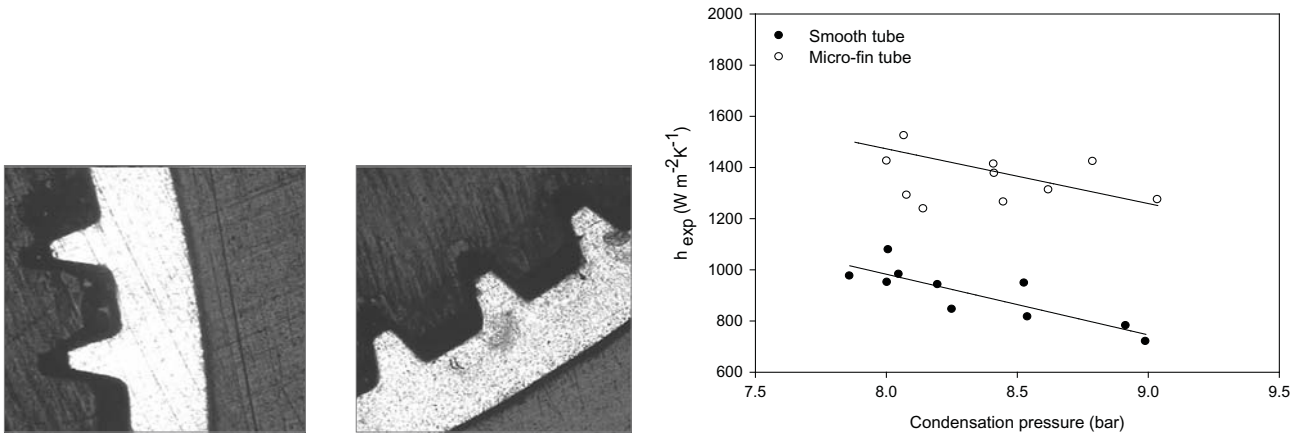

(a) (b)

Fig. 6. Cross-section of the micro-fin tube by electron microscope (100×) (a) and Comparison of average experimental convective heat transfer coefficients of the smooth and micro-fin tubes for the mass flux of 29 kg $m^{-2}s^{-1}$ at pressures of 0.77−0.90 MPa (b)[24] [From Ref. 24, with permission from Turk Isı Bilimi Teknigi Dernegi.]

Table 3. The dimensions of the corrugated tubes.[25−29] [From Refs. 25−27 and 29 with permission from Elsevier and Ref. 28, with permission from ASME.]

Number	p (mm)	e (mm)	β (degree)	β (degree)	D_i (mm)	L (mm)
1	5.08	1	79.47	79.47	8.7	2000
2	5.08	1.25	79.47	79.47	8.7	2000
3	5.08	1.5	79.47	79.47	8.7	2000
4	8.46	1.5	74.20	74.20	8.7	2000
5	6.35	1.5	76.56	76.56	8.7	2000

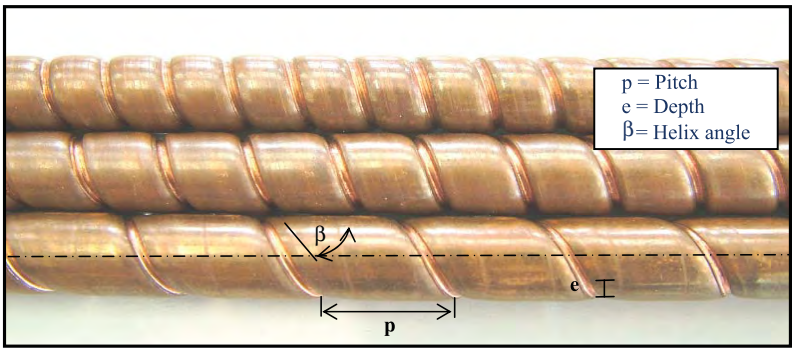

Fig. 7. The photograph of the corrugated tubes.[25–29] [From Refs. 25–29, with permission from Elsevier (color online).]

the photograph of corrugated tubes is displayed in Fig. 7. The tube-in-tube heat exchanger was used as the test section, in which R134a flows inside the corrugated tube and water flows in the annulus. The experimental results demonstrated that the corrugated tube gave higher heat-transfer performance and pressure drop than those of the smooth tube, by about 50% and 70%, respectively. The effect of pitch and depth on the heat-transfer performance and friction characteristics were reported and then compared with the common smooth tube, as illustrated in Fig. 8. Moreover, the new heat transfer and two-phase friction factor correlations were proposed for predicting the Nusselt number and two-phase friction factor for corrugated tubes. Moreover, the two-phase heat transfer coefficient and friction factor correlations were also proposed based on the measured data of R134a flowing through the corrugated tubes under evaporation process.

Aroonrat and Wongwises[30] studied the heat-transfer and friction characteristics of the pure refrigerant HFC-134a during evaporation inside a vertical corrugated tube, experimentally. The double-tube test sections were 0.5 m long with refrigerant flowing in the inner tube and hot water flowing in the annulus. The inner tubes were one smooth tube and two corrugated tubes, which were constructed from smooth copper tube with 8.7 mm inner diameter. The test runs were performed at evaporating temperatures of 10°C, 15°C, and 20°C, heat fluxes of 20, 25, and 30 $kW \cdot m^{-2}$, and mass fluxes of 200, 300, and 400 $kg \cdot m^{-2} \cdot s$. The effects of heat flux, mass flux, and evaporation temperature on the heat-transfer coefficient and two-phase friction factor were also discussed. It was found that the percentage increases of the heat-transfer coefficient and the two-phase friction factor of the corrugated tubes compared with those of the smooth tube are approximately zero to 10% and 70% to 140%, respectively.

Khoeiki *et al.*[31] studied the effect of inclination angle on the heat transfer performance of R134a flows inside a corrugated tube under condensation condition. Inclination angle ranging between −90° and 90°, mass flux varied from 87 to 253 kg/m^2s were tested. The experimental data illustrated that the inclination angle of the test section had a significant effect on the condensation heat transfer coefficient. The highest condensation heat transfer coefficient was obtained at inclination of 30° which was about 140% larger than that at the inclination of −90°. Moreover, a new empirical correlation of the heat-transfer coefficient of R134a flowing inside the corrugated tube with different inclination angles was proposed.

Rainieri *et al.*[32] presented an experimental investigation on the convective heat transfer performance of coiled corrugated tubes for highly viscous fluids such as glycerol and ethylene glycol. The test tube with diameter of 14 mm, curvature ratio of 0.06, corrugation depth of 1 mm, and pitch of 16 mm was used as the test section. The results indicated that the wall curvature could increase the heat transfer performance. Moreover, the wall corrugation had significant effect on the heat transfer performance for only the higher Reynolds number (150–1500).

Garcia *et al.*[33] reported the artificial roughness shape affecting the heat transfer enhancement of corrugated tubes, dimpled tubes and wire coils. The experimental data from their previous works for heat transfer and pressure drop in laminar, transition and turbulent flow regimes were used to compare with the analytical results. The results showed

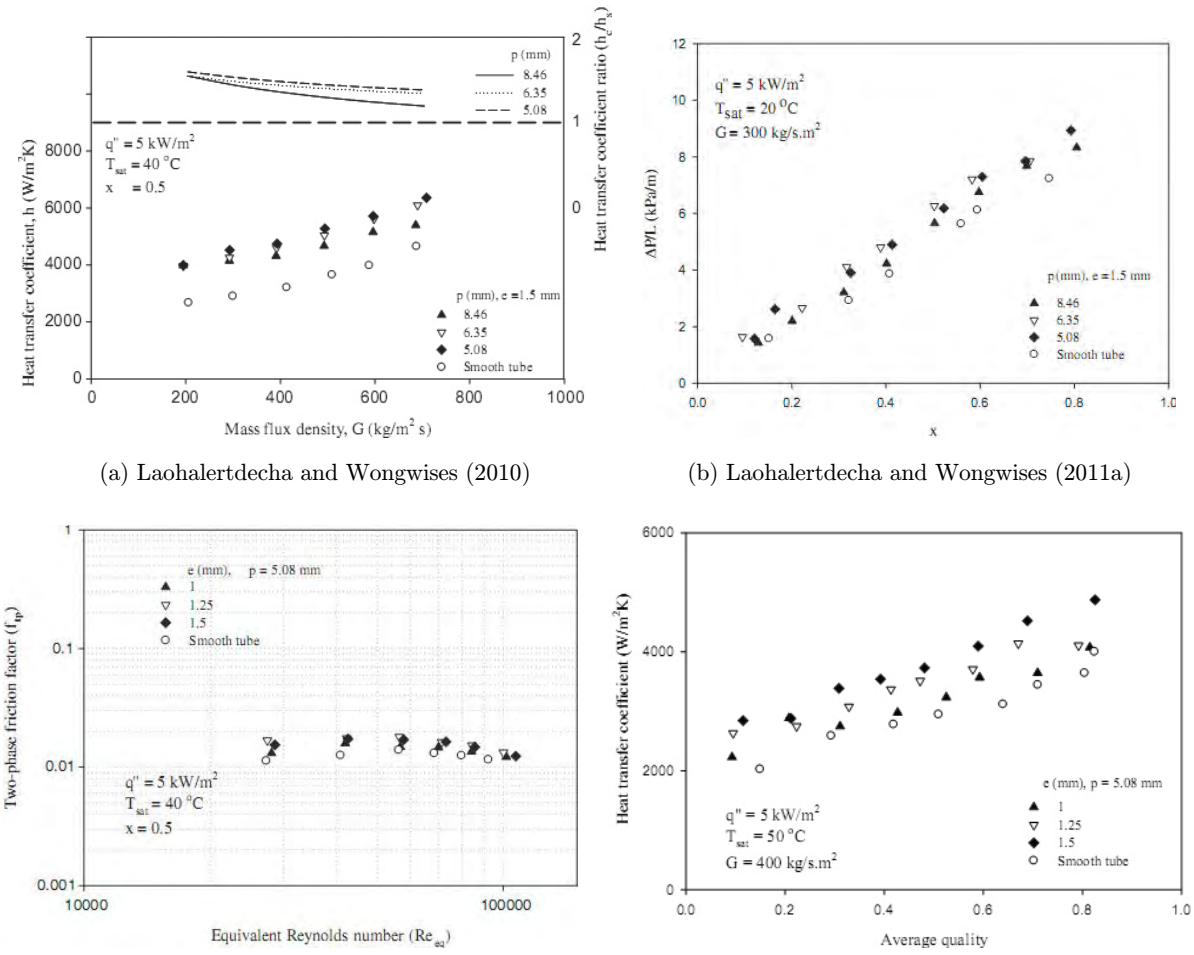

(a) Laohalertdecha and Wongwises (2010)

(b) Laohalertdecha and Wongwises (2011a)

(c) Laohalertdecha and Wongwises (2011b)

(d) Laohalertdecha and Wongwises (2011c)

Fig. 8. The effects of pitch and depth on heat transfer and flow characteristics. [From Refs. 25–28, with permission from Elsevier and ASME.]

that the shape of the artificial roughness had larger effect on the pressure drop than the heat transfer performance. Moreover, they also recommended that the smooth tube should be used for Reynolds number less than 200, wire coil for Reynolds number ranging between 200 and 2000. For Reynolds number larger than 2000, the employment of corrugated and dimpled tubes gave an advantage over the wire coils.

As mentioned above, it is clearly seen that numerous papers are currently available on the single-phase behavior, both experimentally and quantitatively. There are only a few research works that attempt to study the heat-transfer and flow characteristics of the refrigerant two-phase flow. Thus, the research works with respect to the thermal performance and flow characteristics of the refrigerant two-phase flow flowing through fluted tubes with different configurations are required in order to address their performance.

3. Ribbed Tubes

The schematic diagram of an internally finned or ribbed tube is shown in Fig. 9. In an internally finned or ribbed tube, it is difficult to geometrically identify a difference between fin and rib. Normally, both names are assumed to refer to the same geometry. The internal fin or rib geometry is defined by the fin height, the mean fin thickness, pitch of the fin and the apex angle, and the helix angle of the fin. Publications on the heat-transfer and flow characteristics of fluid flow in ribbed tubes are summarized as follows.

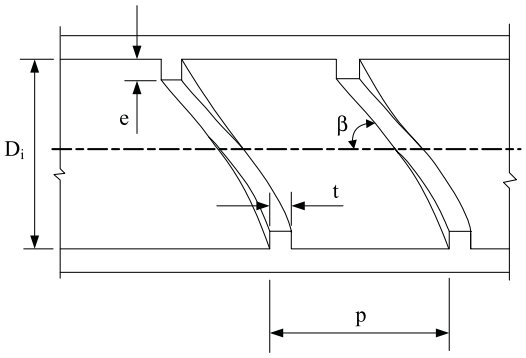

Fig. 9. Schematic diagram of the ribbed tube.

Morris and Rahmat-Asadi[34] conducted an experimental study to investigate the forced convection heat transfer in rotating ribbed tubes. The effect of internal ribs and orthogonal mode rotation on heat transfer was presented. The dimensions of the ribbed tubes are shown in Table 4. Typical three-rib geometries used in turbine rotor blade cooling channels were used as the test tubes. Their experimental data indicated that rotating ribbed tubes increase the heat-transfer performance compared with a common smooth tube as shown in Fig. 10. This behavior is due to the rotation Coriolis-induced secondary flows, which led to the increase in heat-transfer performance on the trailing edge of the tube compared with the leading edge. Finally, the effects of centripetal buoyancy and Coriolis forces were investigated.

Ravigururajan and Bergles[35] use generalized ribbed tube correlations to optimize the thermal performance of heat exchangers based on performance evaluation criteria (PEC). At a given pumping power and surface area, the maximum heat transfer was considered. Similarly, the minimum surface area was taken into account for the case of constant heat load and pumping power. The PEC with their relayed constraint equations were calculated by using a simple iterative procedure. Their simulation results indicated that the Reynolds number and

Table 4. The dimensions of the ribbed tubes.[34] [From Ref. 34, with permission from Elsevier.]

Number	p (mm)	e (mm)	D_i (mm)	L (mm)
1	20	2	10	130
2	15	1.5	10	130
3	10	1	10	130

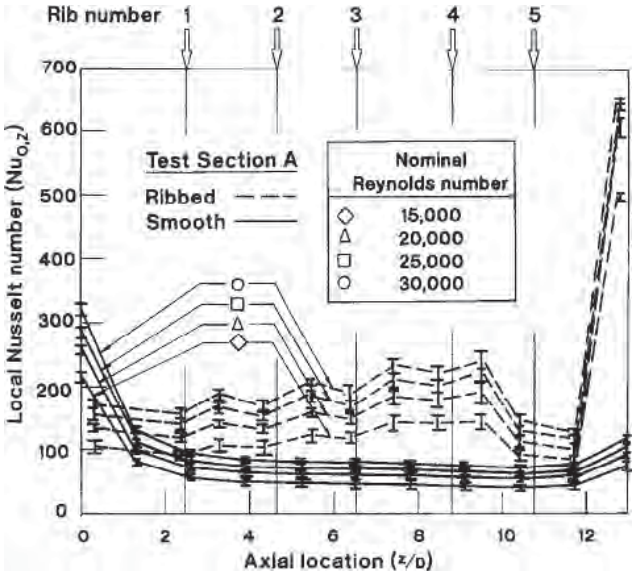

Fig. 10. The effect of ribs on measured local Nusselt number distribution.[34] [From Ref. 34, with permission from Elsevier.]

Prandtl number had a tiny effect on the heat-transfer enhancement. On the contrary, the use of the ribbed tubes can improve the thermal performance, which is useful for designing the enhanced heat exchangers.

Cho and Liu[36] presented an experimental study to investigate the possibility of the electronic anti-fouling (EAF) technique to control precipitation fouling in a spirally ribbed tube used in a common refrigerator. Two new tubes, one with the EAF treatment and another without EAF treatment, were used for testing the fouling tendency of the test tubes. Their measured data showed that the EAF technique could be used to control precipitation fouling that takes place in a spirally ribbed tube.

Chang and Su[37] experimentally investigated the heat-transfer performance of a reciprocating helical tube fitted with full circumferential ribs, which is commonly used in piston designs for a marine diesel engine. The effects of the Reynolds number, Dean number, pulsating number, buoyancy number, and five different reciprocating frequencies on the local heat transfer were tested. The results demonstrated that the presence of Dean vortices caused the increase in local heat-transfer coefficient on the outer surface, even with the agitated flow field caused by ribs under a reciprocating environment. Moreover, the pulsating force and reciprocating buoyancy had also significant effects on the heat-transfer coefficient due to the modified vortex flow

Table 5. The dimensions of the ribbed tubes.[38] [From Ref. 38, with permission from Elsevier.]

Number	p (mm)	e (mm)	D_i (mm)	L (mm)
1	9	0.4–0.6	11.69	1620

structures in the ribbed coils. Finally, an empirical correlation for predicting the heat transfer in the ribbed coils was proposed by considering the effect of pulsating force and reciprocating buoyancy force.

Cheng and Xia[38] presented the critical heat flux (CHF) for water flow in a conventional smooth tube and a four-head spiral internally ribbed tube, experimentally. The test tubes were located in the vertical direction and were heated by an electric power supply. The dimensions of the test tubes are shown in Table 5. The effects of mass flux and pressure on the CHF were investigated. The measured data demonstrated that the increase of wall temperature at which CHF occurs in the spirally internally ribbed tube is less than that of the smooth tube. For both the smooth tube and the spirally internally ribbed tube, fluid enthalpy decreases with the increase of pressure as shown in Fig. 11.

Li and Webb[39] presented long-term cooling tower water fouling data for seven helically ribbed tubes with inner diameter of 15.54 mm, experimentally. The effects of rib starts, helix angle, and height were determined. Based on internal dimensions, there are only two ranges of fouling characteristics, the linear range and nonlinear range. The experimental results showed that the ratio of the enhanced-to-plain tube fouling resistance rose with increases in the product of area indexes and efficiency indexes in the linear range, and the linear relationship fell in a nonlinear range. In addition, the semi-theoretical fouling correlations as a function of the product of area indexes and efficiency indexes and the linear multiple regression correlations as a function of geometric variables and Reynolds number were proposed. These correlations could be used to evaluate the fouling potential of enhanced tubes in actual cooling water situations.

Kim *et al.*[40] experimentally investigated the CHF for flow boiling of R-134a flowing through rifled tubes with four heads and six heads in vertical direction. The test section was shown in Fig. 12. The results were then compared with the data for smooth tube and calculated values from Bowing and Katto correlations. The inner diameters of both the rifled tube and the smooth tube were 17.04 mm. The experimental test runs were conducted at outlet pressure ranging from 13 to 23.9 bar, mass flux ranging from 285 to 1300 $\mathrm{kg \cdot m^{-2} \cdot s}$, and inlet subcooling temperature of five to 40°C. The experimental data showed that the CHF in the rifled tube was approximately 40% to 60% greater than that of the smooth tube and rose with increasing mass flux as well as outlet pressure as shown in Fig. 13.

Naphon and co-workers[41] reported the heat-transfer and pressure-drop characteristics of helical rib tubes, experimentally. The double-tube counter flow heat exchanger was used as the test section, in which hot water flowed inside the test tube and cold water flowed in the annulus. The effects of helical rib height and helical rib pitch were presented. Their results indicated that the heat-transfer coefficient

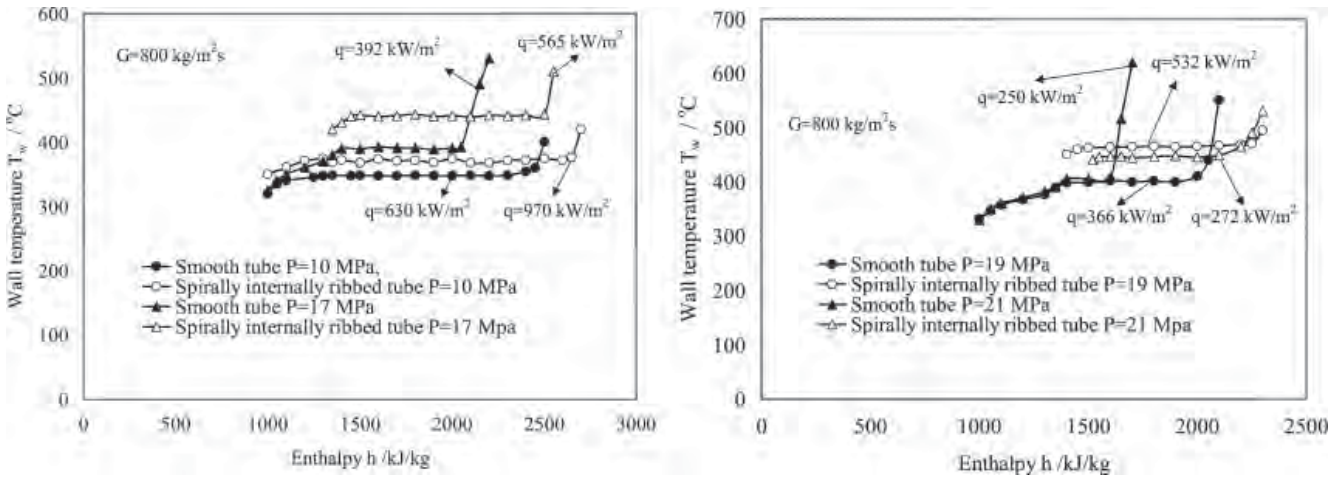

Fig. 11. Variation of wall temperatures with enthalpy.[38] [From Ref. 38, with permission from Elsevier.]

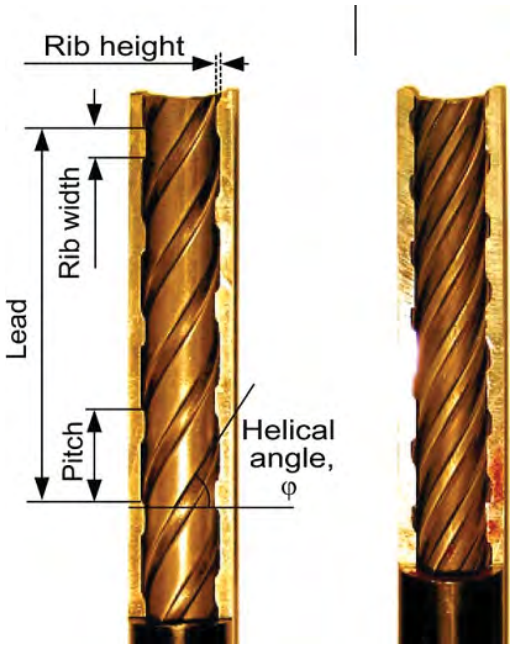

Fig. 12. Cross sectional view of rifled tubes and geometric parameters.[40] [From Ref. 40, with permission from Elsevier (color online).]

and pressure of helical rib tube were significantly higher than that of the smooth tube approximately 10% to 70% and 10% to 280%, respectively. The heat-transfer coefficient rose with increases in the Reynolds number and the helical rib depth, and also rose with decreases in the helical rib pitches. Similarly, the friction factor of the helical ribbed tube rose with an increase in helical rib depth and decreased with increases in the Reynolds number and helical rib pitch. Moreover, they also proposed the heat transfer and friction factor correlation for predicting the Nusselt number and friction characteristics of the helical ribbed tube as a function of helical rib dept and helical rib pitch. The proposed correlations gave good agreement between measured data and calculated values, and the majority of the data fell within $\pm 15\%$ of the proposed equations.

Recently, Ji *et al.*[42] presented an experimental investigation on the heat transfer and friction factor of 16 internal helically ribbed tubes with different geometrical parameters under turbulent flow regime. Reynolds number ranged from 10,000 to 100,000 and Prandtl number varied between 4.98 and 8.22 were tested. A correlation for predicting the average heat transfer coefficient of the ribbed tubes was proposed based on the Gnielinski correlation by replacing the friction factor with the measured friction factor of the internally ribbed tubes. The results indicated that the proposed equation was very appropriate for practical engineering design and gave vary good accuracy.

Similar to the corrugated tubes, a number of researchers reported on the heat-transfer and flow features of ribbed tubes with single-phase flow of

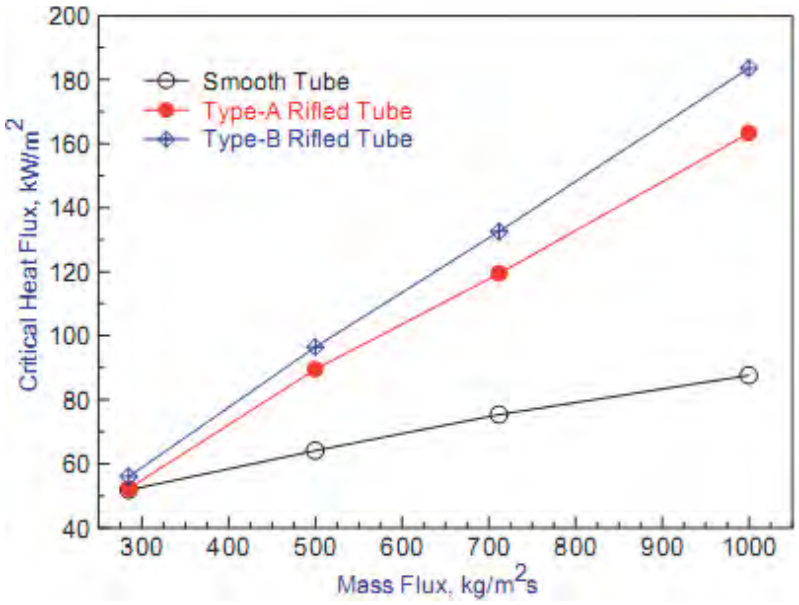

Fig. 13. CHF versus mass flux for one smooth tube and two rifled tubes at 16.5 bar.[40] [From Ref. 40, with permission from Elsevier (color online).]

liquids, both experimentally and quantitatively. Therefore, the two-phase flow data are required to certify the heat transfer and flow characteristics of ribbed tubes.

4. Grooved Tubes

As shown in Fig. 14, internally grooved tubes having an internal surface including many grooves to increase the heat-transfer performance have been used in many applications. The internal surface of an internally grooved tube includes many ribs helically extending along the tube in an axial direction and a groove is formed between each adjacent pair of ribs. Publications on the heat-transfer and flow characteristics of single-phase flow in internally grooved tubes are summarized as follows.

Graham *et al.*[43] presented an experimental study on the heat-transfer and pressure-drop characteristics of R-134a flowing through an axially grooved tube during the condensation process. The measured data were compared with the data for a smooth tube and a common grooved tube with an 18° helix angle. A grooved tube with an inner diameter of 8.91 mm was used as the test section and tested at the mass flux range from 75 to 450 $\mathrm{kg \cdot m^{-2} \cdot s}$. At a mass flux of 75 $\mathrm{kg \cdot m^{-2} \cdot s}$, their results showed that the axially grooved tube gave higher heat-transfer performance than that of a smooth tube smaller than the common grooved tube with an 18° helix angle. In contrast, at a mass flux of 150 $\mathrm{kg \cdot m^{-2} \cdot s}$, the results indicated that the heat-transfer performance of axially grooved tubes was larger than those of both smooth tubes and helically ribbed tubes. For the pressure drop, their data showed that the pressure drops of axially grooved tubes agreed well with those of the helically ribbed tubes.

Herman and Kang[44] presented an experimental study on the unsteady temperature field in the grooved channel with curved vanes (GCV) using holographic interferometry. The heat-transfer performance of GCV was compared with the basic grooved channel (BGC). Their experimental data indicated that addition of the curved vane above the downstream end of the heated block gave higher heat-transfer performance than that of BGC by a factor of approximately 1.5 to 3.5 times. This behavior due to the GCV tube accelerated the flow between the curved vane and the heated block and the large recirculation region in the groove was eliminated. At the Reynolds number of 450, flow transition from steady to oscillatory regime took place. Moreover, their data also showed that the pressure drop for the GCV tube was three to five times greater than those of the BGC tube.

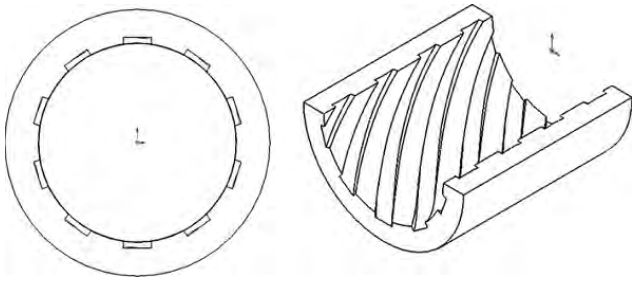

Fig. 14. Schematic diagram of the grooved tube.[51] [From Ref. 51, with permission from Springer.]

Goto *et al.*[45,46] investigated the local condensation and evaporation heat-transfer coefficient of R410A and R22 flow inside the five different kinds of internally grooved tubes placed in the horizontal direction. The test conditions were conducted at a refrigerant mass flow rate ranging from 130 to 400 $\mathrm{kg \cdot m^{-2} \cdot s}$ for both R410A and R22 and the vapor pressures of 2.41 MPa for R410A and 1.53 MPa for R22. The measured data indicated that the local heat-transfer coefficients of the herringbone grooved tube were two times larger than those of the helical tube for both R410A and R22. Moreover, they also proposed the new heat-transfer correlations for predicting the Nusselt number of R410A and R22 flowing in the helical micro-finned tube and herringbone micro-finned tube. Compared with the measured data, good correspondence between the experimental values and the calculated values by the proposed equations were obtained and the majority of the data fell within ± 20% of the proposed equation.

Zhang *et al.*[47] reported the evaporation heat-transfer characteristics of R417A flowing inside horizontal two internally grooved tubes with various geometrical parameters compared with common smooth tube and micro-finned tube correlations, experimentally. The experimental conditions used in their study were summarized as follows: mass flow rate ranged from 176 to 344 $\mathrm{kg \cdot m^{-2} \cdot s}$; heat flux ranged from 11 to 32 $\mathrm{kW \cdot m^{-2}}$; evaporation temperatures ranged from 0°C to 5.5°C; and vapor quality ranged from 0.2 to 1. The effects of the above parameters were presented. The results demonstrated that the evaporation heat-transfer coefficient of R417A was lower than that of the R22 and

significantly smaller in internally grooved tubes than the conventional smooth tube. This means that the heat-transfer enhancement was more effective for pure refrigerant than that for the non-azeotropic refrigerant mixtures. Compared with the calculated values from the existing correlations, the results indicated that the modified Kattan model gave better agreement with the measured data than the standard Kattan model. Moreover, the Koyama and Wellsandt model for micro-finned tubes overestimated the evaporation heat-transfer coefficient, especially for R417A.

Zhang *et al.*[48] presented an experimental investigation on the local heat-transfer coefficient of R417A flowing through internally grooved tubes during the evaporation process, experimentally. Two internally grooved tubes with different geometrical parameters were tested and then compared with the common smooth tube and the existing correlations. Their data showed that the existing micro-finned tube correlations could not be used to predict the local evaporation heat-transfer coefficient of the internally grooved tubes. They also proposed a new correlation based on the modified Kattan model for computing the heat-transfer coefficient of non-azeotropic refrigerant R417A. Compared with the measured data, a deviation of $\pm 30\%$ was obtained for vapor quality less than 0.8.

Bilen *et al.*[49] experimentally studied the heat-transfer and friction characteristics of air flowing inside internally grooved tubes with circular, trapezoidal and rectangular configurations under turbulent flow regime. The geometrical parameters of the grooved tubes are shown in Fig. 15. A Reynolds number ranging from 10,000 to 38,000 was tested. At the highest Reynolds number, the results indicated that the Nusselt number for internally grooved tubes was larger than that for a common smooth tube by about 47% for a rectangular groove, 58% for a trapezoidal groove, and 63% for a circular groove. Moreover, the thermal performance for all internally grooved tubes was shown to be higher than that of a smooth tube — approximately 1.24−1.28 times for a circular groove, 1.22−1.25 times for a trapezoidal groove, and 1.13−1.26 times for a rectangular groove. In addition, the friction factors of all grooved tubes were nearly the same, and the friction factor was independent of the Reynolds number for grooved tubes as shown in Fig. 16.

Bharadwaj *et al.*[50] presented an experimental study on the heat-transfer and pressure-drop characteristics of water flowing through a 75-start spirally grooved tube with twisted tape insert under laminar and turbulent flow regimes. Their results showed that the Nusselt number of the spirally grooved tube without twisted tape insert was 400% and 140% higher than that of a smooth tube for laminar and turbulent flow regime, respectively. Similarly, for the spirally grooved tube with twisted tape insert, maximum heat-transfer enhancements of 600% and 140% were obtained for laminar and

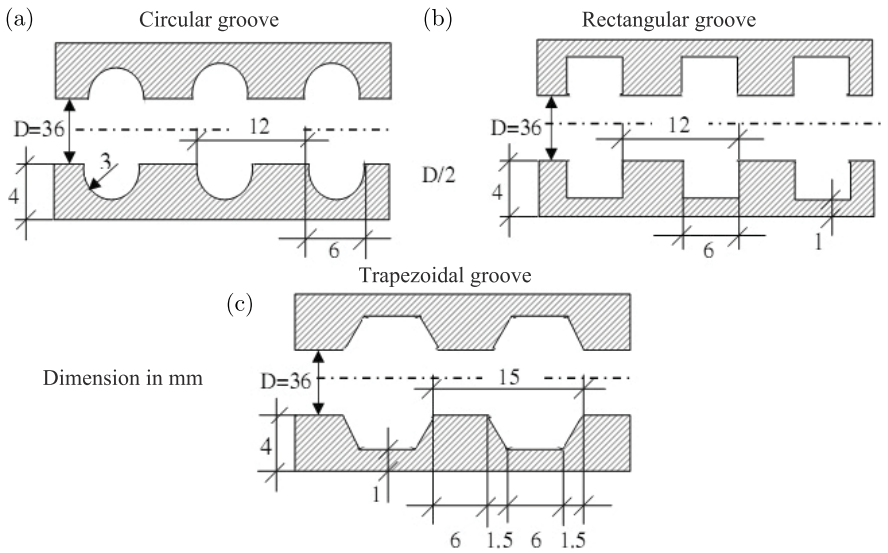

Fig. 15. The geometric shapes of the grooved tubes.[49] [From Ref. 49, with permission from Elsevier.]

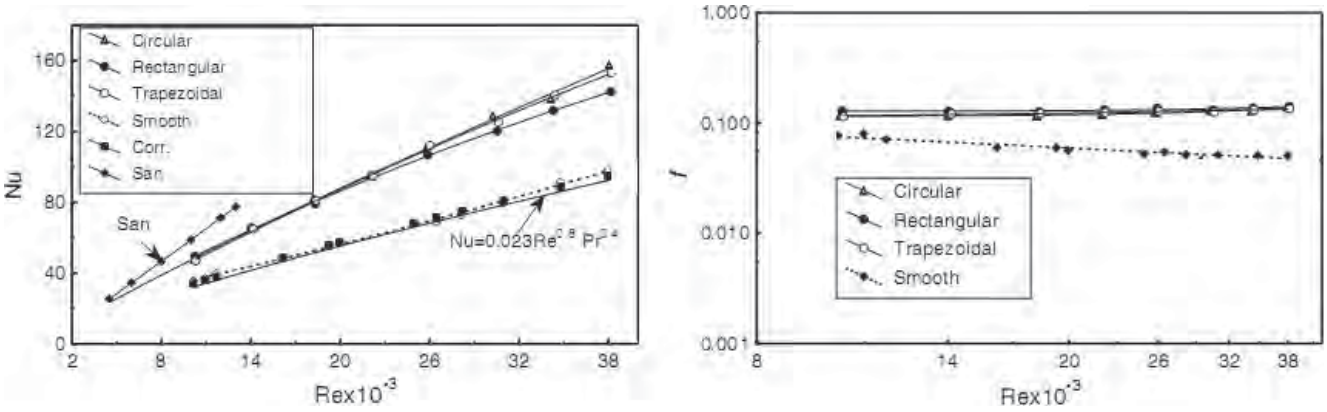

Fig. 16. Variation of the Nusselt number and friction factor with the Reynolds number.[49] [From Ref. 49, with permission from Elsevier (color online).]

turbulent flow regime, respectively. Moreover, the pressure drop of internally grooved tubes was larger than that of the smooth conventional smooth tube.

Wongwises *et al.*[51] reported the evaporation heat-transfer coefficient and pressure drop of R-134a flowing inside internally grooved tubes, experimentally. Four grooved tubes with different configurations made from stainless steel were tested under a condition of constant heat flux. The effects of groove pitch, mass flux, heat flux, and saturation temperature on heat-transfer coefficient and frictional pressure drop were presented. The measured data showed that the grooved tubes gave higher heat-transfer coefficient and frictional pressure drop than those of the common smooth tube.

As mentioned above, many researchers have been focused on the heat-transfer and friction characteristics of two-phase refrigerants flowing through horizontal internally grooved tubes under both evaporation and condensation processes. However, heat-transfer and pressure-drop characteristics of internally grooved tubes in other directions should be studied.

5. Fluted Tubes

From the configuration of the fluted tube, it is evident that they are quite similar to the corrugated tubes. However, from the point view of the authors, there are small differences between the two enhanced tubes. If the ratio of corrugation to cross-sectional area is greater than one, it is a fluted tube; however, if this ratio is less than one, it is a corrugated tube. The published articles describe the heat-transfer enhancements of the fluted tubes as follows.

Aly and Bedrose[52] introduced a theoretical study of heat-transfer performance of stagnant water vapor condensed on both vertical and horizontal spirally fluted tubes. In this study, two regions of fluted tubes, namely the valley and the crest, were separately considered; the condensation process was started on the flute crest and then ran down to the valley by gravity and surface tension. The motion equation and energy balance equation were taken into account to examine the relationships between condensate flow rate and film thickness. Their simulation results indicated that the spirally fluted tube gave five times higher heat-transfer performance than a smooth tube in the case of horizontal direction and about three times higher in the case of vertical direction. Moreover, the calculated Nusselt number from the proposed model coincided well with the experimental results for integral finned tubes and the majority of the data fell within $\pm 20\%$ of the proposed model. Similarly, for vertical tubes, an agreement between the predicted value and the measured data can be seen and the majority of the data fell within $\pm 5\%$ of the proposed model.

Kang *et al.*[53] presented an experimental system to formulate the new flooding correlations for both vertical and horizontal directions as a function of declination angle for a fluted tube with a twisted insert. Figure 17 depicts the sketch of the fluted tube and geometrical parameters. In their study, twisted tubes made from plastic were inserted inside the fluted tube to accelerate the absorption rate in counter-current absorption. Water−ethyl alcohol solution flows downward in the fluted tube, whereas air flows counter-current in an upward direction. For the inclination angle less than 60°, the results

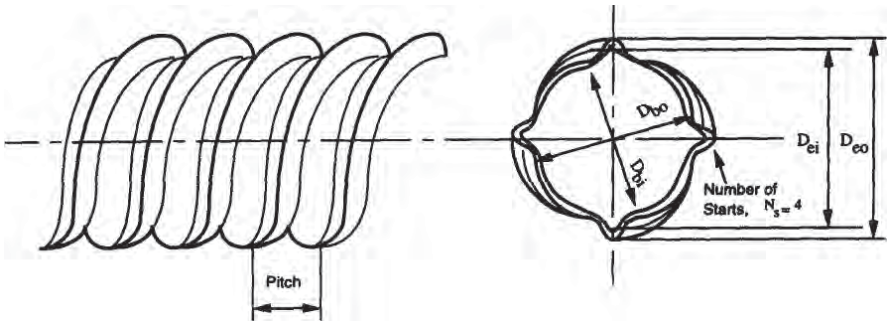

Fig. 17. Schematic diagram of the fluted tube.[53] [From Ref. 53, with permission from Elsevier.]

indicated that flooding was created from the top of the tube. On the contrary, it was initiated from the bottom of the tube for an inclination angle greater than 60°. The position of the twisted insert had no significant effect on the flooding mechanism in the case of a horizontal tube, whereas it had a small effect in the case of a vertical tube. Moreover, for the fluted tube with a twisted insert, the results indicated that the flooding vapor velocity reached a maximum for the inclination angle between 40° and 60° and superficial liquid velocities less than $0.01178\,\mathrm{m}\cdot\mathrm{s}^{-1}$. However, in the case of superficial liquid velocities greater than $0.01178\,\mathrm{m}\cdot\mathrm{s}^{-1}$, the superficial flooding vapor velocity increased with the inclination angle.

Wang and colleagues[54] reported experimental results that illustrated the heat-transfer performance of carbon-steel spirally fluted tubes replacing the conventional copper smooth tubes that corrode easily due to the feed water of boiler. The dimensions of the fluted tubes are shown in Table 6. Compared with the common carbon-steel smooth tube, the experimental results showed that the heat-transfer coefficient of the carbon-steel spirally fluted tube was 10% to 17% higher than that of the smooth tube and it was very close to that of the copper smooth tubes, as shown in Fig. 18.

Qi *et al.*[55] presented an experimental study that evaluated the drag reduction and heat-transfer

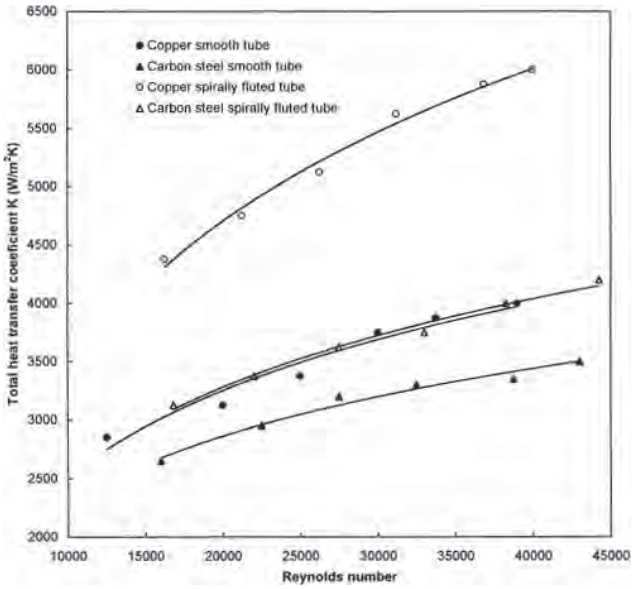

Fig. 18. Heat transfer coefficient versus Reynolds number.[54] [From Ref. 54, with permission from Elsevier.]

enhancement of a fluted tube. Tube-in-tube heat exchanger was used as the test section for cationic surfactant solution Ethoquad T13-50/NaSal (5 mM/8.75 mM) and zwitterionic/anionic reduction surfactant solution SPE98330 (1500 ppm). The results indicated that use of the fluted inner tube increased the heat-transfer coefficient for both surfactant solutions. Moreover, cationic surfactant solution

Table 6. The dimensions of the fluted tubes.[54] [From Ref. 54, with permission from Elsevier.]

Number	Tube description	e (mm)	p (mm)	D_o (mm)	D_i (mm)	β (degree)	L (mm)
1	Copper (Smooth)	—	—	16	13	—	650
2	Carbon steel (Smooth)	—	—	16	13	—	650
3	Copper (Fluted)	0.25	15.6	16	13	40	650
4	Carbon steel (Fluted)	0.25	15.6	16	13	40	650

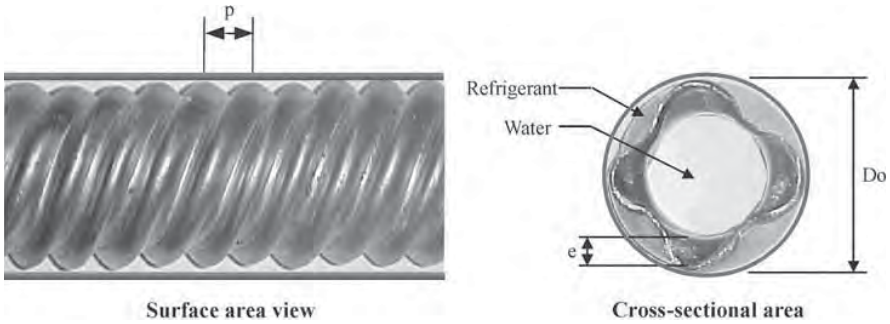

Fig. 19. Photograph of the fluted tube.[56] [From Ref. 56, with permission from Elsevier.]

gave a higher pressure-drop penalty than the zwitterionic/anionic solution.

Rousseau and co-workers[56] presented a mathematical formulation and numerical method to investigate the heat-transfer and pressure-drop characteristics of fluted-tube refrigerant-to-water condensers. Figure 19 shows the photo of the fluted tube. In this model, the surface area was divided into three regions: superheated, two-phase, and subcooled regions, in which all properties of refrigerant and water can be calculated. The proposed model was formulated based on the effectiveness-NTU method. For the water side, the existing empirical correlations for friction factor and heat-transfer coefficient were used. Unfortunately, for the refrigerant side, they reported that there are no available correlations for calculating the friction factor and heat-transfer coefficient of the fluted tube-in-tube condenser. Thus, the existing correlations for smooth tubes, combined with an enhancement ratio based on available correlations for helical coils, as well as an enhancement factor based on empirical data for fluted tube condenser were employed. Data for two commercial fluted tube heat exchangers were used to validate the proposed model. The average difference between the measured and the predicted pressure drop was about 7.27%. Similarly, the difference in the log mean temperature was roughly 4.41%.

As mentioned above, for the fluted tube, a number of researches studied the single-phase heat transfer and flow behaviors for conventional heat transfer fluids. The heat-transfer and pressure-drop characteristics for two-phase flow of refrigerants in the fluted tubes are required for practical applications.

6. Vipertubes

Vipertube is a new type of enhanced tube which produced by Vipertex^{TM} company under ASTM standard. The configuration of the Vipertubes is shown in Fig. 20. Kukulka *et al.*[57] was the first research group who presented the heat-transfer enhancement and fouling characteristics of a series of the Vipertubes. These tubes were made from stainless steel tube (Type 304L) with outer diameter of 1.905 cm and length of 0.9144 m. From their experiment with water, the measured data illustrated that the enhancement ratio of the Vipertubes was

Fig. 20. Photograph of the Vipertube.[57] [From Ref. 57, with permission from Elsevier (color online).]

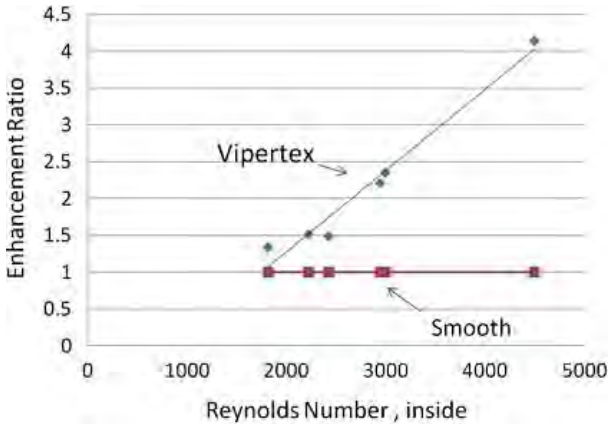

Fig. 21. Heat transfer enhancement ratio versus Reynolds number.[57] [From Ref. 57, with permission from Elsevier (color online).]

varied between 1 and 4, for Reynolds number ranging from 2000 to 5000. This enhancement is due to several factors such as increasing of fluid turbulence, secondary flow, disturbing of the thermal boundary layer and increasing of the heat transfer area. Moreover, the Vipertubes was designed to minimize the effect of fouling. Some results were shown in Fig. 21.

7. Conclusions

As discussed, different types of the enhanced tubes (corrugated tube, ribbed tube, grooved tube and fluted tube) have great potential for heat-transfer enhancement and are highly suited to applications in practical heat-transfer processes. This offers an opportunity for engineers to develop highly compact and effective heat-transfer equipment. Several published articles show that the heat-transfer coefficients of the enhanced tubes are much higher than the conventional smooth tubes and give only marginal drops in pressure. An important reason for the heat-transfer enhancement of the enhanced tubes is the modified rough surface, which causes increases in the turbulence mixing intensity in the flow field, and also by limiting the growth of fluid boundary layers close to the heat transfer surfaces, which leads to increases in heat-transfer performance. Moreover, from the review of the published literature, many researchers reported the heat-transfer performance and pressure-drop characteristics of the enhanced tubes working with single-phase fluids. Only some researchers reported on the use of two-phase flow refrigerants as working fluids for both evaporation and condensation processes. Many researchers suggested that the enhanced tubes have higher potential for replacing the conventional smooth tubes normally used in heat-transfer equipment. This is a great opportunity for researchers to discover new ways for increasing the heat-transfer performance of the enhanced tubes in order to meet high compactness and high heat flux of the heat exchangers. Moreover, new types of enhanced tubes such as Vipertube should be investigated in order to meet highest heat transfer performance and lowest. This is a challenge task of researchers and heat exchanger manufacturer.

Acknowledgments

The authors would like to express their appreciation to the Thailand Research Fund, the Office of the Higher Education Commission and the National Research University Project for providing financial support. Especially, the second author wishes to thank KMUTT for providing him with a Post-doctoral fellowship.

References

1. A. S. Dalkilic and S. Wongwises, Intensive literature review of condensation inside smooth and enhanced tubes, *Int. J. Heat Mass Transfer* **52** (2009) 3409−3426.
2. K. Mimura and A. Isozaki, Heat transfer and pressure drop of corrugated tubes, *Desalination* **22** (2001) 131−139.
3. S. Ganeshan and M. R. Rao, Studies on themohydraulics of single and multi-start spirally corrugated tubes for water and time independent power law fluids, *Int. J. Heat Mass Transfer* **25** (1982) 1013−1022.
4. P. P. Thien and M. M. K. Khan, Flow of an Oldroyd-type fluid through a sinusoidally corrugated tube, *J. Non-Newtonian Fluid Mech.* **24** (1987) 203−220.
5. Y. Asako, H. Nakamura and M. Faghri, Heat transfer and pressure drop characteristics in a corrugated duct with rounded corners, *Int. J. Heat Mass Transfer* **31** (1988) 1237−1245.
6. H. Honda, S. Nozu, Y. Matsuoka, T. Aoyama and H. Nakata, Condensation of R-11 and R-113 in the annuli of horizontal double-tube condensers with an enhanced inner tube, *Exp. Ther. Fluid Sci.* **2** (1989) 173−182.

7. S. R. Burdette, P. J. Coates, R. C. Armstrong and R. A. Brown, Calculations of viscoelastic flow through an axisymmetric corrugated tube using the explicitly elliptic momentum equation formulation (EEME), *J. Non-Newtonian Fluid Mech.* **33** (1989) 1−23.
8. V. Zimparov, N. L. Vulchanov and L. B. Delov, Heat transfer and friction characteristics of spirally corrugated tubes for power plant condensers-1. Experimental investigation and performance evaluation, *Int. J. Heat Mass Transfer* **34** (1991a) 2187−2197.
9. V. Zimparov, N. L. Vulchanov and L. B. Delov, Heat transfer and friction characteristics of spirally corrugated tubes for power plant condensers-2. A mixing-length model for predicting fluid friction and heat transfer, *Int. J. Heat Mass Transfer* **34** (1991b) 2199−2206.
10. N. P. Gopalan and R. Ponnalagasamy, Investigation on laminar flow of a suspension in corrugated straight tubes, *Int. J. Eng. Sci.* **30** (1992) 631−644.
11. D. L. Hinton and J. C. Conklin, Condensation of refrigerants flowing inside smooth and corrugated tubes, *Fourth ASME/JSME Thermal Engineering Joint Conference*, Hawaii, March 1995, pp. 19−24.
12. X. D. Chen, S. K. Nguang and A. E. Bergles, Characterization of the effect of corrugation angles on hydrodynamic and heat transfer performance of four-start spiral tubes, *J. Heat Transfer* **123** (2001) 1149−1158.
13. Y. Dong, L. Huixiong and C. Tingkuan, Pressure drop, heat transfer and performance of single phase turbulent flow in spirally corrugated tubes, *Exp. Therm. Fluid Sci.* **24** (2001) 131−138.
14. V. Zimparov, Enhancement of heat transfer by a combination of three-start spirally corrugated tubes with a twisted tape, *Int. J. Heat Mass Transfer* **44** (2001) 551−574.
15. V. Zimparov, Enhancement of heat transfer by a combination of single-start spirally corrugated tubes with a twisted tape, *Exp. Therm. Fluid Sci.* **25** (2002) 535−546.
16. S. Rainieri and G. Pagliarini, Convective heat transfer to temperature dependent property fluids in the entry region of corrugated tubes, *Int. J. Heat Mass Transfer* **45** (2002) 4525−4536.
17. A. Barba, S. Rainieri and M. Spica, Heat transfer enhancement in a corrugated tube, *Int. Comm. Heat Mass Transfer* **29** (2002) 313−322.
18. P. G. Vicente, A. Garcia and A. Viedma, Mixed convection heat transfer and isothermal pressure drop in corrugated tubes for laminar and transition flow, *Int. Comm. Heat Mass Transfer* **31** (2004a) 651−662.
19. V. Zimparov, Prediction of friction factor and heat transfer coefficients for turbulent flow in corrugated tubes combined with twisted tape inserts. Part 1: Friction factor, *Int. J. Heat Mass Transfer* **47** (2004) 589−599.
20. V. Zimparov, Prediction of friction factor and heat transfer coefficients for turbulent flow in corrugated tubes combined with twisted tape inserts. Part 2: Heat transfer coefficients, *Int. J. Heat Mass Transfer* **47** (2004) 385−393.
21. A. E. Bergles, R. A. Lee and B. B. Mikic, Heat transfer in rough tubes with twisted tape swirl flow, *Trans. ASME, J. Heat Transfer* **91** (1969) 443−445.
22. W. Targanski and J. T. Cieslinski, Evaporation of R407C/Oil mixtures inside corrugated and microfin tubes, *Appl. Therm. Eng.* **27** (2007) 2226−2232.
23. S. Rozzi, R. Massini, G. Paciello, G. Pagliarini, S. Raineiri and A. Trifiro, Heat treatment of fluid foods in a shell and tube heat exchanger: Comparison between smooth and helically corrugated wall tubes, *J. Food Eng.* **79** (2007) 249−254.
24. A. S. Dalkiliç, İ. Teke, S. Wongwises, Heat transfer enhancement during downward laminar flow condensation of R134a in vertical smooth and micro-fin tubes, *Isi Bilimi Ve Teknigi Dergisi/Journal of Thermal Science and Technology* **32** (2012) 19v31.
25. S. Laohalertdecha and S. Wongwises, The effects of corrugation pitch on the condensation heat transfer coefficient and pressure drop of R-134a inside horizontal corrugated tube, *Int. J. Heat Mass Transfer* **53** (2010) 2924−2931.
26. S. Laohalertdecha and S. Wongwises, An experimental study into the evaporation heat transfer and flow characteristics of R-134a refrigerant flowing through corrugated tubes, *Int. J. Ref.* **34** (2011a) 280−291.
27. S. Laohalertdecha and S. Wongwises, Condensation heat transfer and flow characteristics of R-134a flowing through corrugated tubes, *Int. J. Heat Mass Transfer* **54** (2011b) 2673−2682.
28. S. Laohalertdecha and S. Wongwises, Effects of pitch and depth on the condensation heat transfer of R-134a flowing through corrugated tubes, *Proc. ASME/JSME 2011 8th Therm. Eng. Con.*, Hawaii, USA (2011c).
29. S. Laohalertdecha, A. S. Dalkilic and S. Wongwises, Correlations for evaporation heat transfer coefficient and two-phase friction factor for R-134a flowing through horizontal corrugated tubes, *Int. J. Heat Mass Transfer* **38** (2011d) 1406−1413.
30. K. Aroonrat and S. Wongwises, Evaporation heat transfer and friction characteristics of R-134a flowing downward in a vertical corrugated tube, *Exp. Therm. Fluid Sci.* **35** (2011) 20−28.
31. D. Khoeiki, M. A. Akhavan-Behabadi and A. Saboonchi, Experimental study on condensation heat transfer of R-134a flow in corrugated tubes with

different inclinations, *Int. Comm. Heat Mass Transfer* **39** (2012) 138−143.
32. S. Rainieri, F. Bozzoli and G. Pagliarini, Experimental investigation on the convective heat transfer in straight and coiled corrugated tubes for highly viscous fluids: Preliminary results, *Int. J. Heat Mass Transfer* **55** (2012) 498−504.
33. A. Garcia, J. P. Solano, P. G. Vicente and A. Viedma, The influence of artificial roughness shape on heat transfer enhancement: Corrugated tubes, dimpled tubes and wire coils, *App. Therm. Eng.* **35** (2012) 196−201.
34. W. D. Morris and W. F. Rahmat-Asadi, Convective heat transfer in rotating ribbed tubes, *Int. J. Heat Mass Transfer* **39** (1996) 2253−2266.
35. T. S. Ravigururajan and A. E. Bergles, Optimization of fin-tube enhancement for large evaporation and condensers, *Energy* **39** (1996) 421−432.
36. Y. I. Cho and R. Liu, Control of fouling in a spirally-ribbed water chilled tube with electronic anti-fouling technology, *Int. J. Heat Mass Transfer* **42** (1999) 3037−3046.
37. S. W. Chang and L. M. Su, Heat transfer of reciprocating helical tube fitted with full circumferential ribs, *Int. J. Heat Mass Transfer* **44** (2001) 3025−3042.
38. L. Cheng and G. Xia, Experimental study of CHF in a vertical spirally internally ribbed tube under the condition of high pressures, *Int. J. Therm. Sci.* **41** (2002) 396−400.
39. W. Li and R. L. Webb, Fouling characteristics of internal helical-rib roughness tubes using low-velocity cooling tower water, *Int. J. Therm. Sci.* **45** (2002) 1685−1691.
40. C. H. Kim, I. C. Bang and S. H. Chang, Critical heat flux performance for flow boiling of R-134a in vertical uniformly heated smooth tube and rifled tubes, *Int. J. Heat Mass Transfer* **48** (2005) 2868−2877.
41. P. Naphon, M. Nuchjapo and J. Kurujareon, Tube side heat transfer coefficient and friction factor characteristics of horizontal tubes with helical rib, *Energ. Convers. Manag.* **47** (2006) 3031−3044.
42. W. T. Ji, D. C. Zhang, Y. L. He and W. Q. Tao, Prediction of fully developed turbulent heat transfer of internal helically ribbed tubes — an extension of gnielinski equation, *Int. J. Heat Mass Transfer* **55** (2012) 1375−1384.
43. D. Graham, J. C. Chato and T. A. Newell, Heat transfer and pressure drop during condensation of refrigerant 134a in an axially grooved tube, *Int. J. Heat Mass Transfer* **42** (1999) 1935−1944.
44. C. Herman and E. Kang, Heat transfer enhancement in a grooved channel with curved vanes, *Int. J. Heat Mass Transfer* **45** (2002) 3741−3757.
45. M. Goto, N. Inoue and N. Ishiwatari, Condensation and evaporation heat transfer of R410A inside internally grooved horizontal tubes, *Int. J. Ref.* **24** (2001) 628−638.
46. M. Goto, N. Inoue and R. Yonemoto, Condensation heat transfer of R410a inside internally grooved horizontal tubes, *Int. J. Ref.* **26** (2003) 410−416.
47. X. Zhang, X. Zhang, Y. Chen and X. Yuan, Heat transfer characteristics for evaporation of R417a flowing inside horizontal smooth and internally grooved tubes, *Energ. Convers. Manag.* **49** (2008) 1731−1739.
48. X. Zhang, C. Ji and X. Yuan, Prediction method for evaporation heat transfer of non-azeotropic refrigerant mixtures flowing inside internally grooved tubes, *Appl. Therm. Eng.* **28** (2008) 1974−1983.
49. K. Bilen, M. Cetin, H. Gul and T. Balta, The investigation of groove geometry effect on heat transfer for internally grooved tubes, *Appl. Therm. Eng.* **29** (2009) 753−761.
50. P. Bharadwaj, A. D. Khondge and A. W. Date, Heat transfer and pressure drop in a spirally grooved tube with twisted tape insert, *Int. J. Heat Mass Transfer* **52** (2009) 1938−1944.
51. S. Wongwises, J. Kaew-On, S. Laohalertdecha, W. Duangthongsuk and K. Sakamatapan, Evaporation Heat Transfer and Flow Characteristics of R-134a Flowing Through Internally Grooved Tubes. Heat Mass Transfer DOI 10.1007/s00231-010-0748-6 (2010).
52. N. H. Aly and S. D. Bedrose, Enhanced film condensation of steam on spirally fluted tubes, *Desalination* **101** (1995) 295−301.
53. Y. T. Kang, R. Stout and R. N. Christensen, The effects of inclination angle on flooding in a helically fluted tube with a twisted insert, *Int. J. Mult. Flow.* **23** (1997) 1111−1129.
54. L. Wang, D. W. Sun, P. Liang, L. Zhuang and Y. Tan, Heat transfer characteristics of carbon steel spirally fluted tube for high pressure preheaters, *Energ. Convers. Manag.* **41** (2000) 993−1005.
55. Y. Qi, Y. Kawaguchi, Z. Lin, M. Ewing, R. N. Christensen and J. L. Zakin, Enhanced heat transfer of drag reducing surfactant solutions with fluted tube-in-tube heat exchanger, *Int. J. Heat Mass Transfer* **44** (2001) 1495−1505.
56. P. G. Rousseau, M. V. Eldik and G. P. Greyvenstein, Detailed simulation of fluted tube water heating condenser, *Int. J. Ref.* **26** (2003) 232−239.
57. P. J. Kukulka, R. Smith and K. G. Fuller, Development and evaluation of enhanced heat transfer tubes, *Appl. Therm. Eng.* **31** (2011) 2141−2145.
58. P. G. Vicente, A. Garcia and A. Viedma, Experimental investigation on heat transfer and frictional characteristics of spirally corrugated tubes in turbulent flow at different Prandtl number, *Int. J. Heat Mass Transfer* **47** (2004b) 671−681.

International Journal of Air-Conditioning and Refrigeration
Vol. 20, No. 4 (2012) 1250019 (11 pages)
© World Scientific Publishing Company
DOI: 10.1142/S2010132512500198

World Scientific
www.worldscientific.com

NUMERICAL AND EXPERIMENTAL INVESTIGATION OF THE FLOW CHARACTERISTICS OF R134a FLOWING THROUGH ADIABATIC HELICAL CAPILLARY TUBES

SUKKARIN CHINGULPITAK[*,‡], JATUPORN KAEW-ON[†,‡] and SOMCHAI WONGWISES[‡,§]

[*]*The Joint Graduate School of Energy and Environment*
King Mongkut's University of Technology Thonburi
Bangmod, Bangkok 10140, Thailand

[†]*Physics Department, Faculty of Science*
Thaksin University, Papayom, Phattalung 93110, Thailand

[‡]*Fluid Mechanics, Thermal Engineering and Multiphase Flow Research Lab. (FUTURE)*
Department of Mechanical Engineering
Faculty of Engineering
King Mongkut's University of Technology Thonburi
Bangmod, Bangkok 10140, Thailand
[§]*somchai.won@kmutt.ac.th*

Received 10 July 2012
Accepted 1 October 2012
Published 14 December 2012

This paper presents numerical and experimental results of the flow characteristics of R134a flowing through adiabatic helical capillary tubes. The local pressure distribution along the length of the capillary tubes is measured at inlet pressures ranging from 10 to 14 bar, mass flow rates from 8 to 20 kg h^{-1}, and degrees of subcooling from 0.5°C to 15°C. The theoretical model is based on conservation of mass, energy and the momentum of the fluids in the capillary tube. The model is divided into three regions: subcooled liquid region, metastable liquid region and equilibrium two-phase region and can be applied for various tube geometries, new alternative refrigerants and critical or noncritical flow conditions. The model is validated by comparing results from the present experimental data with that of the available literature. Based on the comparison results, the model used in the present study provides reasonable agreement with the experimental data.

Keywords: Capillary; expansion valve; R134a; vapor pressure; two-phase flow.

[§]Corresponding author.

Nomenclature

A : Cross-sectional area of capillary tube, m^2
d_i : Capillary tube internal diameter, m
D_C : Coil diameter, m
f : Friction factor
g : Gravitational acceleration, $m\,s^{-2}$
G : Mass flow rate per unit area, $kg\,s^{-1}\,m^{-2}$
h : Specific enthalpy, $J\,kg^{-1}$
k : Entrance loss coefficient
L : Length, m
m : Mass flow rate, $kg\,h^{-1}$
P : Pressure, bar
Re : Reynolds number
s : Specific entropy, $J\,kg^{-1}\,K^{-1}$
T : Temperature, °C
V : Velocity, $m\,s^{-1}$
x : Quality

Greek Letters

ΔT_{sub} : Degree of subcooling, °C
ε : Roughness, m
ν : Specific volume, $m^3\ kg^{-1}$
μ : Dynamic viscosity, $kg\,m^{-1}\ s^{-1}$
ρ : Density, $kg\,m^{-3}$

Subscripts

evap : Evaporator
f : Liquid phase
g : Gas phase
i : Capillary inlet condition
in : Inlet
ml : Metastable liquid
sp : Single-phase
tp : Two-phase
vap : Vaporization

1. Introduction

A capillary tube is an important device in small vapor-compression refrigeration and air conditioning systems used to reduce refrigerant pressure from the condenser to the evaporator. The nominal size of the capillary tube typically ranges between 0.5 and 2.0 mm in diameter and 1−6 m in length. This type of tube is widely used in household refrigerators due to its simplicity, cost-effectiveness, no maintenance requirement, no moving parts and low starting torque. For several decades, the flow characteristics of various refrigerants flowing through capillary tubes have been studied both experimentally and theoretically and primarily for straight capillary tubes. However, in practical applications, household refrigerator systems use a helical capillary tube in order to reduce installation space. To the best of the authors' knowledge, there has been minimal experimental investigation of the differences that might exist for straight and helical tube structures. The available papers regarding numerical and experimental investigations of refrigerant flow in coiled capillary tubes are summarized as follows:

Kim *et al.*[1] presented experimental results of mass flow rate and proposed the mass flow rate correlation based on the Buckingham π theorem. They performed tests at condensing temperatures of 40°C, 45°C and 50°C and subcooling temperature of 1.5°C, 5°C and 10°C. They concluded that the mass flow rates of R22 were lower than those of R407C and R410A by about 4% and 23%, respectively. Moreover, the mass flow rates of the coiled capillary tubes were lower than those of straight capillary tubes, especially at smaller coil diameters. In the case of a 40 mm coil diameter, the mass flow rates of the coiled capillary tubes were approximately 9% lower than those for straight capillary tubes.

Zhou and Zhang[2] theoretically and experimentally investigated the performance of coiled adiabatic capillary tubes and compared the results with straight capillary data for R22. They found that the mass flow rate of a straight capillary tube was approximately 10% more than that of a coiled adiabatic capillary tube with a coil diameter of 40 mm. Moreover, the results showed that the mass flow rate of the refrigerant increased significantly with increases in the coil diameter. However, little change was observed for coil diameters larger than 300 mm.

Valladares[3] presented a numerical simulation describing the flow characteristics of coiled adiabatic capillary tubes based on a finite volume formulation. The numerical model was evaluated for various aspects such as type of fluid (pure substances and mixtures), geometry, metastable regions, critical or noncritical flow conditions and transient behavior. The prediction showed 97.7% agreement of 211 data points evaluated within an error of ± 10%.

Park *et al.*[4] studied the flow characteristics of coiled capillary tubes for R22 and proposed a mass flow rate correlation for coiled capillary tubes. In the same operating conditions, the results showed that the mass flow rates of the coiled capillary tubes decreased by about 5−16% less than those of the straight capillary tubes. The correlation was

developed on the basis of experimental data such as the effects of inlet condition, refrigerant properties and coiled tube geometry. For both straight and coiled capillary tubes, the results showed that the proposed correlation gave reasonable agreement with the experimental data for R22, R407C and R410A.

Mittal *et al.*[5] presented an experimental investigation of coiling effect on the flow characteristics of R407C in an adiabatic helical capillary tube. They observed that the coiling of capillary tubes (coil diameters of 60, 100 and 140 mm) significantly influenced the mass flow rate. From the experimental results, the mass flow rates through the coiled capillary tubes decreased about 5−10% less than those through the straight capillary tubes. In addition, the authors also proposed correlations to predict the mass flow rate of R407C flowing through straight and helical capillary tubes. When compared with experimental data, the majority of the results fell within 10% of their proposed correlation.

Chingulpitak and Wongwises[6] applied a mathematical model to study the flow characteristics of alternative refrigerants in adiabatic helical capillary tube. The model presented is based on conservation of mass, energy and momentum of fluids in the capillary tube. The developed model is validated by comparison with the experimental data from Kim *et al.*[1] for R22, R407C and R410A and Zhou and Zhang for R22.[2,7] The results obtained from the present model show reasonable agreement with the experiment data. Chingulpitak and Wongwises[8,9] studied the effects of various geometries of helical capillary tubes and compared the flow characteristics of refrigerants in straight and helical capillary tubes. The results show that for coil diameters of 40 to 300 mm, the mass flow rate of refrigerants increases rapidly by about 6−7%. For coil diameters between 300 and 600 mm, the increase in mass flow rate of refrigerant is small (about 1−2%). The comparison between the straight and helical capillary tubes showed that the length of the helical capillary tube was 20% shorter than that of the straight capillary tube under the same operating conditions.

Zhou and Zhang[10] studied the inlet pressure fluctuation characteristics of R22 in adiabatic helical and straight capillary tubes. Their results show that the pressure fluctuation for straight capillary tubes is less prominent than for helical ones. In the case of a small coil diameter, the inlet pressure fluctuation is weak. Moreover, the results show that the fluctuation amplitude decreases as the preset inlet pressure increases.

Up to now, as described above, there have been only two works, carried out by Zhou and Zhang[2] and Valladares,[3] dealing with the metastable region in the simulation of refrigerant flow in coil capillary tube. Although some information is currently available, there still remains room to discuss, for example, there are no information regarding local pressure and temperature distributions obtained from either simulation or experiment available yet, the effects of various relevant parameters on flow characteristics also remain unstudied. In this paper, the main concern is to present an experimental and theoretical study for predicting the refrigerant flow characteristics including metastable region in adiabatic helical capillary tubes. R134a which is current widely used but has never been investigated before in helical capillary tube, is studied. The influence of parameters such as inlet pressure, degree of subcooling, capillary tube diameters and coil diameters on local pressure and mass flow rate along the capillary tube length are also investigated. Flashing process behavior and the delay of refrigerant vaporization are also discussed.

2. Experimental Apparatus and Method

A schematic diagram of experimental apparatus is shown in Fig. 1. The main refrigeration system components consist of a compressor, condenser, capillary tube, evaporator and other accessory parts, including the oil separator, liquid receiver, filter/drier, sight glass, subcooler and accumulator. A two-cylinder single stage reciprocating compressor, driven by an electric motor, was used to circulate the refrigerant. The speed of the motor was varied so as to provide a wide range of mass flow rates by means of an inverter. More details of the experimental apparatus are available from Kaew-on *et al.*[11]

The details of the test capillary tube dimensions are presented in Fig. 2. The inlet pressure and inlet temperature were measured at the inlet header. Similarly, the outlet pressure and outlet temperature were obtained from the outlet header. Seven points of the capillary tube were drilled for the installation of pressure taps. Also, seven T-type

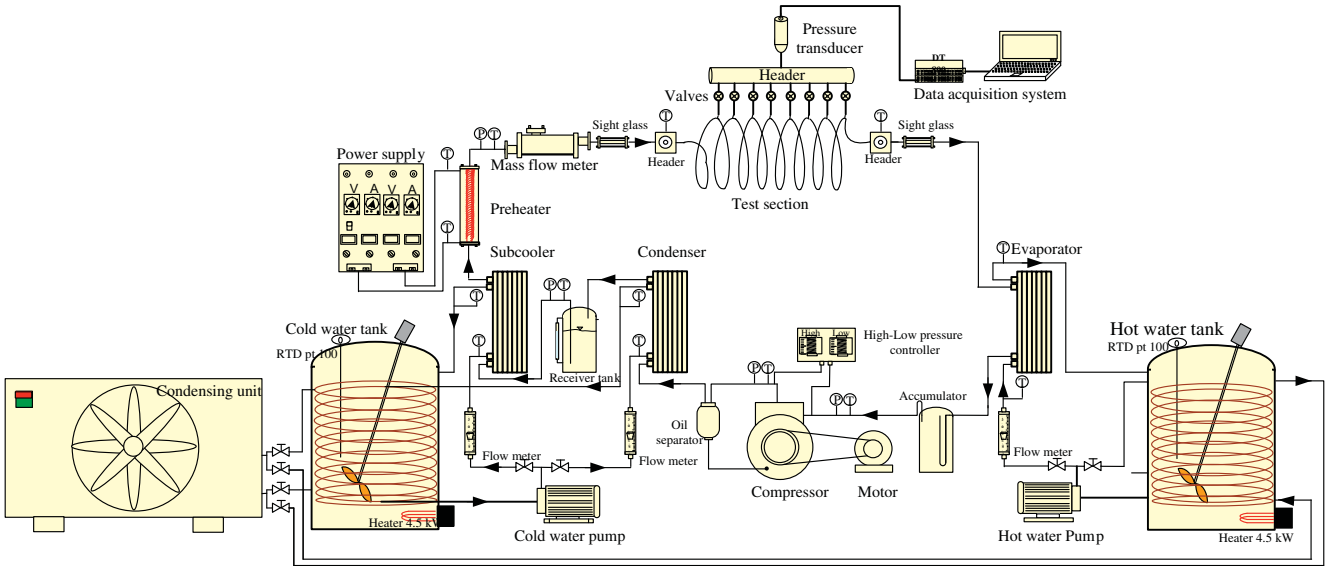

Fig. 1. Schematic diagram of the experimental apparatus.[11]

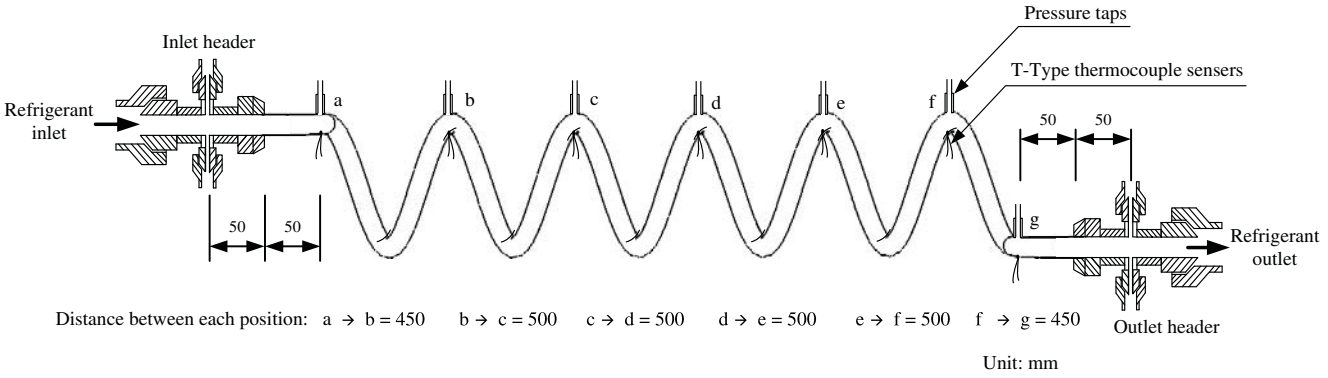

Fig. 2. Schematic diagram of the test section.

thermocouples were installed in the same sections as the pressure taps. The thermocouples were insulated with an Aeroflex standard sheet to reduce the effect of heat transfer on measurement. The range of experimental conditions and the details of test sections are listed in Table 1.

Table 1. The details of test sections and experimental conditions.

Items	Details
Refrigerant	R134a
Capillary diameter, d_i, mm	1.07, 1.27, 1.62
Coil diameter, D_c, mm	25, 50, 100
Capillary length, L, m	3.05
Inlet pressure, P_{in}, bar	10, 12, 14
Degree of subcooling, ΔT_{sub}, °C	0.5−10.5
Mass flow rate, m, kg/h	7−18

3. Mathematical Modeling

In mathematical modeling, the flow characteristics of refrigerant are analyzed by applying the fundamental principles of thermodynamics and fluid mechanics.[6,12] The proposed model assumes that the helical capillary tube is a horizontal capillary tube with constant coil diameter, inner diameter and roughness. Also, the flow inside is considered to be adiabatic, one-dimensional, steady, metastable region and homogeneous two-phase flow. The flow characteristics of refrigerant in a helical capillary tube can be divided into a single-phase flow region,

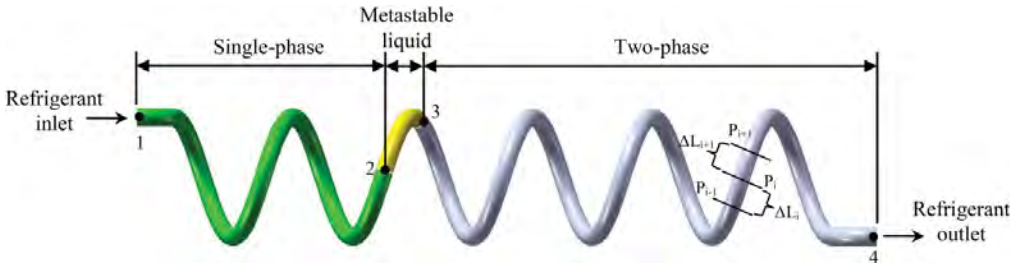

Fig. 3. Schematic diagram of an adiabatic helical capillary tube.

metastable liquid region and a two-phase flow region. The theoretical flow model of refrigerant through the capillary tube is based on the conservation of mass, energy and momentum of fluids in the helical capillary tube. For convenience, the developed model is briefly reviewed.

3.1. *Single-phase flow region*

The single-phase flow region represents the position from the inlet of the capillary tube to the position where the pressure drops to the saturated pressure (points 1 and 2 in Fig. 3). From our previous work,[6] the single-phase length is calculated as follows:

$$L_{\mathrm{sp}} = \frac{d_i}{f_{\mathrm{sp}}}\left[\frac{2}{\rho V^2}(P_1 - P_3) - k - 1\right], \tag{1}$$

where f_{sp} is the single-phase friction factor and k is the entrance loss coefficient (for square edged, $k = 0.5$).

The friction factor of coil capillary tube (f_c) proposed by Mori and Nakayama[13] presented in Eq. (2), is used to calculate the single-phase friction factor.

$$f_c = \frac{C_1(d_i/D_c)^{0.5}}{[\mathrm{Re}(d_i/D_c)^{2.5}]^{1/6}}\left\{1 + \frac{C_2}{[\mathrm{Re}(d_i/D_c)^{2.5}]^{1/6}}\right\}, \tag{2}$$

where

$$\begin{aligned} C_1 &= 1.88411177 \times 10^{-1} + 85.2472168(\varepsilon/d_i) \\ &\quad - 4.63030629 \times 10^{4}(\varepsilon/d_i)^2 \\ &\quad + 1.31570014 \times 10^{7}(\varepsilon/d_i)^3, \\ C_2 &= 6.79778633 \times 10^{-2} + 25.3880380(\varepsilon/d_i) \\ &\quad - 1.06133140 \times 10^{4}(\varepsilon/d_i)^2 \\ &\quad + 2.54555343 \times 10^{6}(\varepsilon/d_i)^3, \end{aligned}$$

and

$$\mathrm{Re} = \frac{\rho V d_i}{\mu}. \tag{3}$$

3.2. *Metastable-liquid flow region*

The metastable phenomenon occurs when the pressure of the liquid approaches the saturation pressure, but the fluid is still in the liquid phase (points 2 and 3 in Fig. 3). The pressure of vaporization (P_{vap}) is calculated using the correlation proposed by Chen *et al.*,[14] as follows;

$$\frac{(P_{\mathrm{sat}} - P_{\mathrm{vap}})\sqrt{kT_{\mathrm{sat}}}}{\sigma^{1.5}} = 0.679\left(\frac{\nu_g}{\nu_g - \nu_l}\right)\mathrm{Re}^{0.914}\left(\frac{\Delta T_{sc}}{T_c}\right)^{-0.208}\left(\frac{d_i}{D'}\right)^{-3.18}, \tag{4}$$

where D' is the reference length $\left(\sqrt{\frac{kT_{\mathrm{sat}}}{\sigma}} \times 10^4\right)$, and k is the Boltzmann constant ($1.380662 \times 10^{-23}\,\mathrm{J\,K^{-1}\,mol^{-1}}$).

According to the recommendation by Zhou and Zhang,[2] the metastable liquid region length is evaluated in the same way as the single-phase region.

3.3. *Two-phase flow region*

The flow in this region is assumed to be homogeneous flow. The fundamental equations used for this section are conservation of mass, energy and momentum. The following equations are based on the control volume considerations in the two-phase region. Also, calculation of the two-phase length can be followed from our previous model.[6]

$$dL = \frac{2d_i}{f_{\mathrm{tp}}}\left[-\frac{\rho dP}{\rho V^2} + \frac{d\rho}{\rho}\right]. \tag{5}$$

The two-phase friction factor can be calculated using Eq. (2), in the same way as the single-phase region, where the Reynolds number in the two-phase region is determined by

$$\mathrm{Re}_{\mathrm{tp}} = \frac{Vd_i}{\mu_{\mathrm{tp}}\nu_{\mathrm{tp}}}\,, \tag{6}$$

where

$$V = G\nu_{\mathrm{tp}} = G\big(x\nu_g + (1-x)\nu_f\big)\,. \tag{7}$$

The two-phase dynamic viscosity correlation proposed by McAdams *et al.*[15] is presented as follows:

$$\frac{1}{\mu_{\mathrm{tp}}} = \frac{x}{\mu_g} + \frac{1-x}{\mu_f}\,. \tag{8}$$

4. Solution Methodology

The solution methodology used in the present stydy is modified from Wongwises and Pirompak,[12] Bansal and Rupasingh.[16]

For the two-phase region, as shown in Fig. 3, the capillary tube between points 3 and 4 can be divided into numerous sections. Since P_3 is known (the pressure of vaporization, P_{vap}), the pressure in any section, i, can be expressed as

$$P_i = P_3 - i\Delta P\,. \tag{9}$$

The entropy of each section can be calculated from

$$s_i = s_{if}(1-x) + s_{ig}\,x\,. \tag{10}$$

The calculation is done section by section along the capillary tube until the entropy reaches its maximum value. At this point, the fluid velocity is equal to the local speed of sound and the flow is choked. The pressure of the element, where the entropy has the maximum value, $(P_i)_{s\,\max}$, is then compared to the evaporator pressure, P_{evap}, as follows:

if $P_{i,s\max} > P_{\mathrm{evap}}$ then $P_4 = P_{i,s\max}$ and if $P_{i,s\max} < P_{\mathrm{evap}}$ then $P_4 = P_{\mathrm{evap}}$.

Thus, from Eq. (5) the two-phase length (L_{tp}) can be expressed as follows:

$$L_{\mathrm{tp}} = d_i\left[\frac{-2}{G^2}\int_{P_3}^{P_{s\max}}\frac{\rho}{f_{\mathrm{tp}}}dp + 2\int_{P_3}^{P_{s\max}}\frac{d\rho}{\rho f_{\mathrm{tp}}}\right]. \tag{11}$$

Finally, the total length of the capillary tube is a summation of the single-phase, metastable liquid region and two-phase lengths, which is defined as follows:

$$L_{\mathrm{total}} = L_{\mathrm{sp}} + L_{\mathrm{ml}} + L_{\mathrm{tp}}\,. \tag{12}$$

All refrigerant properties are taken from the REFPROP version 6.01 computer program,[17] and are developed in the pressure function.

5. Results and Discussion

5.1. *Mathematical model verification*

To validate the present model, comparison is made with the available experimental data from Ref. 7. As shown in Fig. 4, a comparison between the present numerical result and experimental data from Ref. 7 for R22 was used to validate the temperature distribution along the capillary tube length. In the subcooled liquid region, the temperature remains nearly constant along the tube, while rapidly decreasing after the refrigerant flashes. This is due to the delay of vaporization. However, the actual point of inception of vaporization did not occur at the end of the subcooled liquid region. The result shows that the calculated tube length of R22 deviates from the experimental results. However, the results also indicate that the tendency of temperature distribution along the capillary tube length obtained from the present model shows reasonable agreement with previous data.

5.2. *Comparison of the present model and the Chingulpitak and Wongwises model*[6]

Figure 5 shows the comparison of simulation results of our previous model[6] with the present model. It is

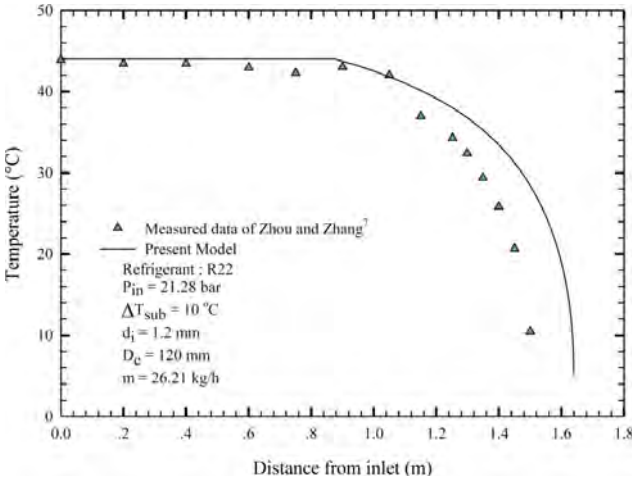

Fig. 4. Comparison of present numerical results with experimental data.

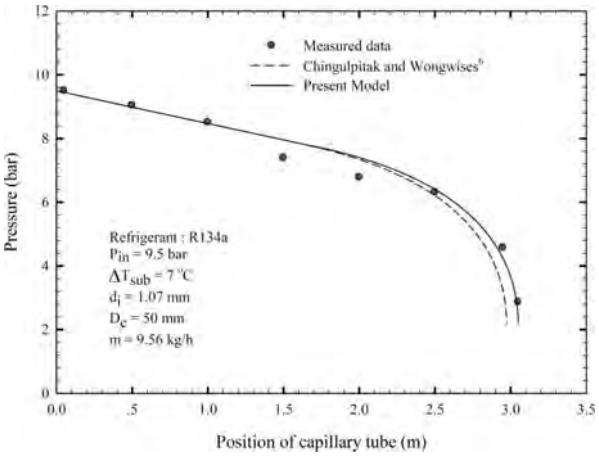

(a)

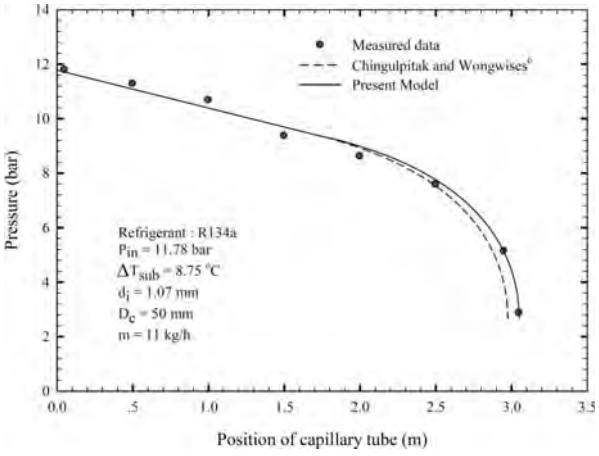

(b)

Fig. 5. Comparison of the present model and nonmetastable region model proposed by Chingulpitak and Wongwises[6] with experimental data.

clear that the pressure distribution along the helical capillary tube obtained from the present model gives a better prediction than those of our previous model.[6] This is due to the fact that the previous model was developed excluding a metastable liquid region. The metastable phenomenon is an effect on increasing the capillary tube's length in the single-phase region.

5.3. *Pressure distributions*

5.3.1. *Effect of inlet pressure on pressure distribution*

The variations of refrigerant pressure along the capillary tube at different inlet pressures are depicted in Fig. 6. It is apparent that the pressure drop of

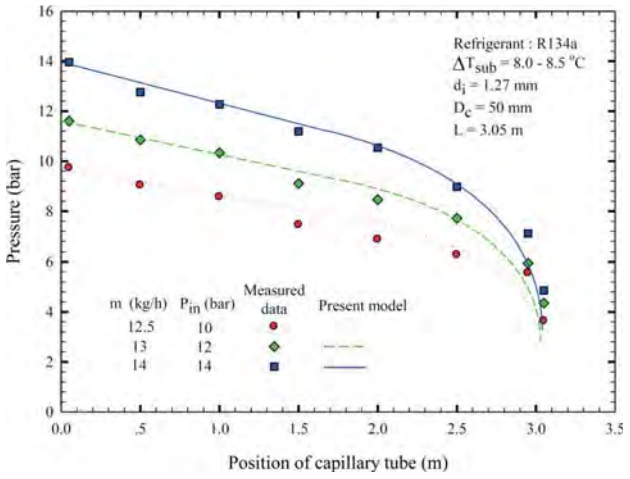

Fig. 6. Effect of inlet pressure on the pressure distribution along the capillary tube length.

refrigerant increases as the inlet pressure increases. The enlargement of inlet pressure led to an increased difference between inlet and outlet pressure, resulting in an increase of refrigerant mass flow rate and velocity. Therefore, the frictional and accelerational pressure drop inside the capillary tube increased.

5.3.2. *Effect of coil and inner diameters on pressure distribution*

The effects of coil and inner diameters on pressure distribution are presented in Fig. 7. In Fig. 7(a), the results show that decreases in pressure for all conditions have similar profiles. Thus, it can be concluded that coil diameter has no significant effect on pressure distribution in the range of the present study. However, in terms of inner diameter, the pressure drop along the capillary tube decreased with increasing capillary tube diameter, as shown in Fig. 7(b).

5.3.3. *Effect of degree of subcooling on pressure distribution*

At the same inlet pressure and dimensions of capillary tube, the effect of degree of subcooling on pressure distribution along the capillary tube is presented in Fig. 8. It is evident from this data that the single-phase length increases with increasing subcooling temperature. In the subcooled liquid region, the pressure drop remains nearly constant along the tube, while it decreases rapidly after the refrigerant flashes.

From the comparison results, the present model gives a good tendency of pressure distribution along

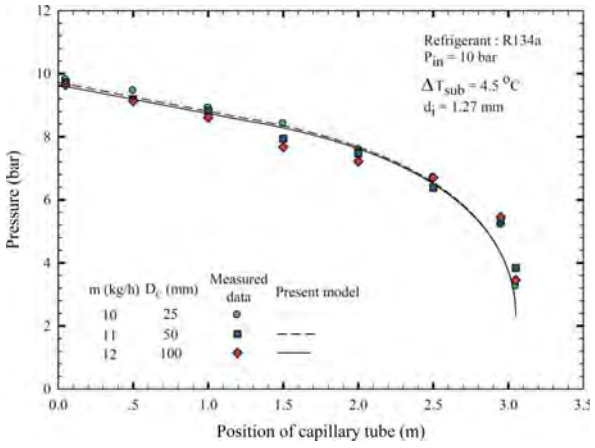

(a)

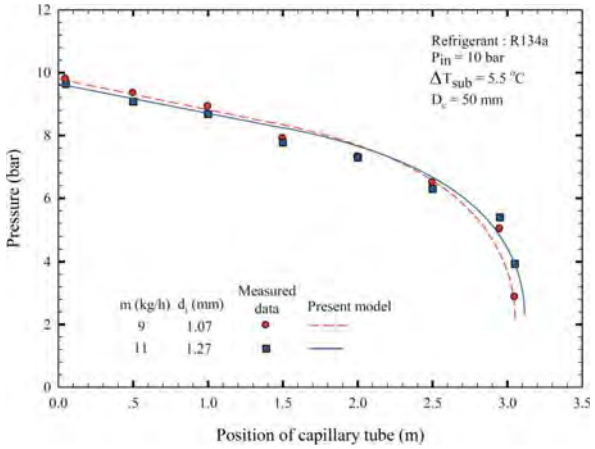

(b)

Fig. 7. Effect of the relevant parameters on pressure distribution of the R134a through the capillary tubes (a) effect of coil diameters and (b) effect of inner diameters.

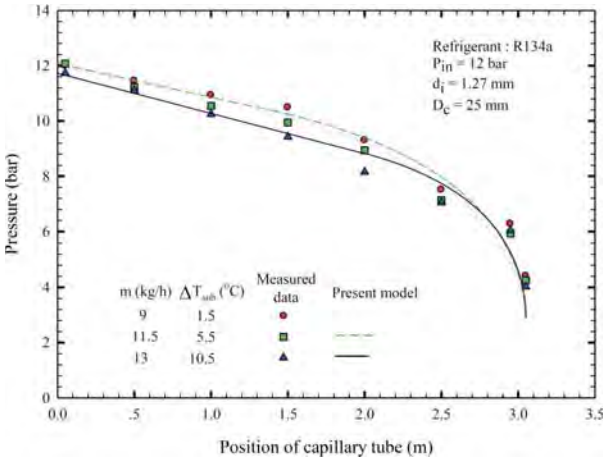

Fig. 8. Effect of degree of subcooling on pressure distribution of the R134a through the capillary tube.

the tube's length compared with experimental data. The present model can be used to predict the flow characteristics of R134a flowing through adiabatic helical capillary tube.

5.4. *The mass flow rate*

5.4.1. *Effect of inlet pressure on mass flow rate*

In Fig. 9(a), the variation of mass flow rates for capillary inlet pressures of 10 and 12 bar with varying degrees of subcooling is presented. The results show that for a given capillary diameter, the mass flow rate increased with an increase of inlet pressure. At higher inlet pressures, the driving force was also higher and resulted in an increase of mass flow rate. Moreover, the comparison of the predicted mass flow rates with the measured data at inlet pressure 10 and 12 bar shows that the present model gives a mean absolute error of 2.1% and 4.1%, respectively.

5.4.2. *Effect of coil diameters on mass flow rate*

As shown in Fig. 9(b), the variation of mass flow rates with coil diameters of 50 and 100 mm is presented. Here, the refrigerant mass flow rate increased with an increase in coil diameter. At 4.5°C of subcooling, the refrigerant mass flow rate of the helical capillary tube from coil diameters of 50 to 100 mm, increased by 9%. Comparison of mass flow rates obtained from the present model with the measured data at coil diameter 50 and 100 mm shows that the present model gives a mean absolute error of 5.9% and 2.1%, respectively.

5.4.3. *Effect of degree of subcooling and inner diameter on mass flow rate*

Figure 9(c) shows mass flow rates and degrees of subcooling for capillary tube diameters of 1.07 and 1.27 mm, inlet pressure of 10 bar and coil diameter of 50 mm. The results show that the mass flow rate increased with increasing degree of subcooling. This phenomenon can be explained by the fact that the increase in mass flow rate was a result of increased liquid length for high inlet subcooling. Moreover, the results also indicate that the effect of capillary tube diameter on the refrigerant mass flow rate is clear and significant. The results show that the mass flow

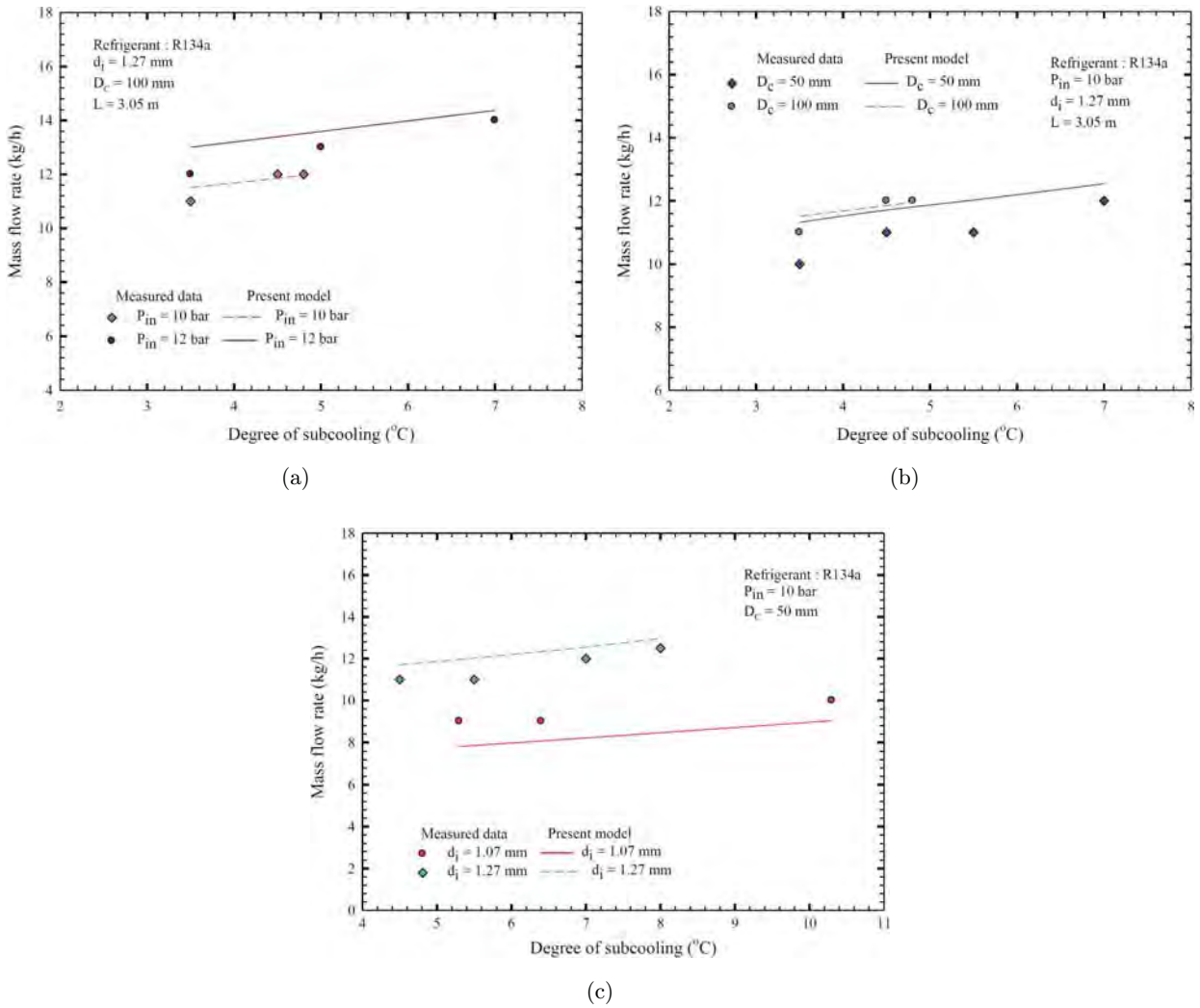

Fig. 9. Effect of the relevant parameter on the mass flow rate of the R134a through the capillary tubes (a) effect of inlet pressure, (b) effect of coil diameter and (c) effect of degree of subcooling and capillary tube diameter.

rates dramatically increased with an increase in capillary tube diameter.

5.5. *Effect of the choked flow condition on pressure distribution and total capillary tube length*

As shown in Fig. 10, with an inner diameter of 1.62 mm, the pressure distribution along capillary tube length of the present model with a mass flow rate 18.1 kg h^{-1} fits very well with the measured data, although the numerical result gives the total capillary tube length longer than that of the measured data by about 11.14%. On the other hand, a mass flow rate of 19.1 kg h^{-1} gives the best result for the total capillary tube length but this mass flow

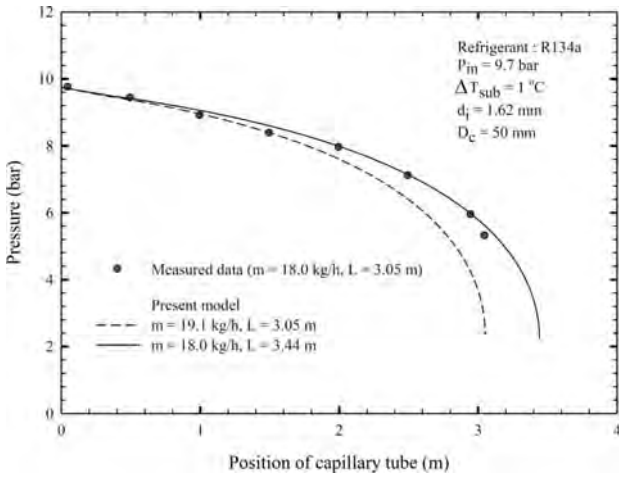

Fig. 10. Comparison of measured pressure distribution with present numerical results at different mass flow rate.

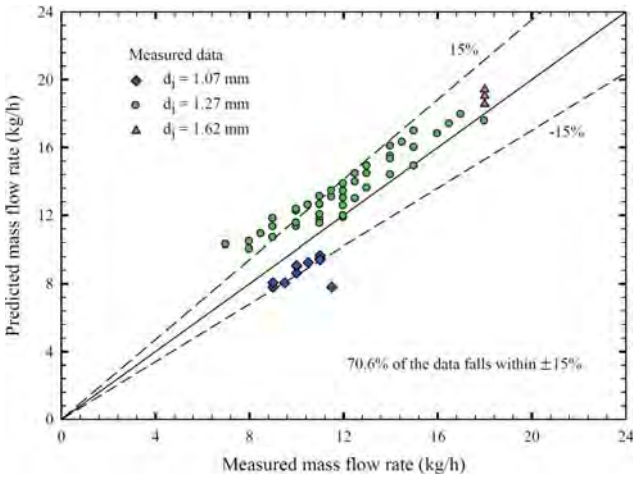

Fig. 11. Comparison of mass flow rate obtained from the present model with measured data for R134a.

rate failed with the tendency of pressure distribution inside the helical capillary tube. This is due to the fact that the present model is limited at the choked flow condition for any computation. Therefore, the pressure profile of refrigerant in the capillary tube should be considered for accuracy of the comparison between the simulation and experiment results. In addition, considering the pressure distribution at any position along capillary tube length is one of the main purposes of the present experiment.

In Fig. 11, the comparison of the predicted mass flow rates with all of the present measured data for R134a shows that 70.6% of the 58 data points are within $\pm 15\%$.

6. Conclusion

In this study, the flow characteristics of R134a flowing through adiabatic helical capillary tubes were theoretically and experimentally investigated. From the measured mass flow rate data, the capillary tube diameter has a more significant effect on mass flow rate than the other variables. For example, at 5.5°C of subcooling, as the capillary tube diameter increased from 1.07 mm to 1.27 mm, the refrigerant mass flow rate increased by 22.2%. Similarly, at 4.5°C of subcooling, the refrigerant mass flow rate of the helical capillary tube from coil diameters of 50 mm to 100 mm increased by 9%. In terms of the theoretical study, the present model was validated by comparing its results with the experimental data. The comparison results show that the proposed model, including metastable liquid region, can be used to predict the flow characteristics of R134a flowing through an adiabatic helical capillary tube, and specifically, local pressure distribution along the tube's length.

Acknowledgments

The authors are indebted to the Thailand Research Fund, the Office of the Higher Education Commission and the National Research University Project for supporting this study.

References

1. S. G. Kim, M. S. Kim and S. T. Ro, Experimental investigation of the performance of R22 R407C and R410A in several capillary tubes for air-conditioners, *Int. J. Ref.* **25** (2002) 521−531.
2. G. Zhou and Y. Zhang, Numerical and experimental investigations on the performance of coiled adiabatic capillary tubes, *Appl. Therm. Eng.* **26** (2006) 1106−1114.
3. O. G. Valladares, Numerical simulation and experimental validation of coiled adiabatic capillary tubes, *Appl. Therm. Eng.* **27** (2007) 1062−1071.
4. C. Park, S. Lee, H. Kang and Y. Kim, Experimentation and modeling of refrigerant flow through coiled capillary tubes, *Int. J. Ref.* **30** (2007) 1168−1175.
5. M. K. Mittal, R. Kumar and A. Gupta, An experimental study of the flow of R-407C in an adiabatic helical capillary tube, *Int. J. Ref.* **33** (2010) 840−847.
6. S. Chingulpitak and S. Wongwises, Two-phase flow model of refrigerants flowing through helically coiled capillary tubes, *Appl. Therm. Eng.* **30** (2010) 1927−1936.
7. G. Zhou and Y. Zhang, Experimental investigation on hysteresis effect of refrigerant flowing through a coiled adiabatic capillary tube, *Energy Convers. Manage.* **47** (2006) 3084−3093.
8. S. Chingulpitak and S. Wongwises, Effects of coil diameter and pitch on the flow characteristics of alternative refrigerants flowing through adiabatic helical capillary tubes, *Int. Commun. Heat Mass Transfer* **37** (2010) 1305−1311.
9. S. Chingulpitak and S. Wongwises, A comparison of flow characteristics of refrigerants flowing through adiabatic straight and helical capillary tubes, *Int. Commun. Heat Mass Transfer* **38** (2011) 398−404.
10. G. Zhou and Y. Zhang, Inlet pressure fluctuation characteristics of coiled adiabatic capillary tubes, *Appl. Therm. Eng.* **33–34** (2012) 183−189.

11. J. Kaew-on, K. Nilpuang, S. Chingulpitak and S. Wongwises, Experimental investigation of R134A flowing through adiabatic helically coiled capillary tubes, *Int. J. Air-conditioning Ref.* **20** (2012) 1−11.
12. S. Wongwises and W. Pirompak, Flow characteristics of pure refrigerants and refrigerant mixtures in adiabatic capillary tubes, *Appl. Therm. Eng.* **21** (2001) 845−861.
13. Y. Mori and W. Nakayama, Study on forced convective heat transfer in curved pipes (2nd, report turbulent region), *Int. J. Heat Mass Transfer* **10** (1967) 37−59.
14. Z. H. Chen, R. Y. Li, S. Lin and Z. Y. Chen, A correlation for metastable flow of refrigerant 12 through capillary tubes, *ASHRAE Trans.* **96** (1990) 550−554.
15. W. H. McAdams, W. K. Wood and R. L. Bryan, Vaporization inside horizontal tubes. II, Benzence-oil mixture, *Trans. ASME* **64** (1942) 193.
16. P. K. Bansal and A.S. Rupasinghe, A homegeneous model for adiabatic capillary tubes, *Appl. Therm. Eng.* **18** (1998) 207−219.
17. M. O. McLinden, S. A. Klein and E. W. Lemmon, REFPROP — thermodynamic and transport properties of refrigerants and refrigerant mixtures, NIST Standard Reference Database — version 6.01 (1998).

Provided for non-commercial research and education use.
Not for reproduction, distribution or commercial use.

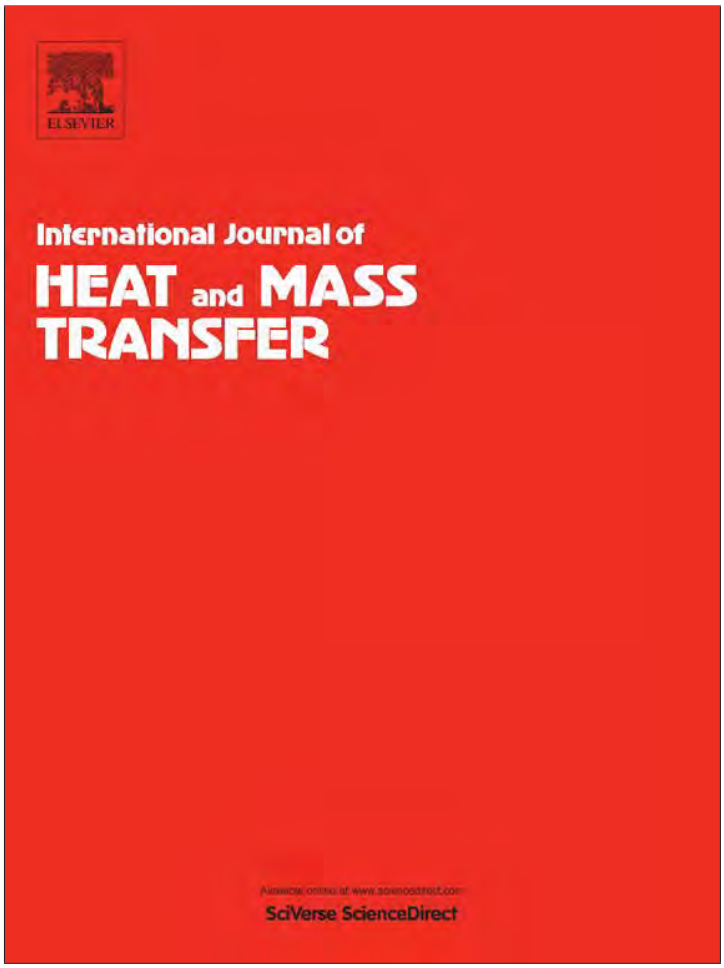

(This is a sample cover image for this issue. The actual cover is not yet available at this time.)

This article appeared in a journal published by Elsevier. The attached copy is furnished to the author for internal non-commercial research and education use, including for instruction at the authors institution and sharing with colleagues.

Other uses, including reproduction and distribution, or selling or licensing copies, or posting to personal, institutional or third party websites are prohibited.

In most cases authors are permitted to post their version of the article (e.g. in Word or Tex form) to their personal website or institutional repository. Authors requiring further information regarding Elsevier's archiving and manuscript policies are encouraged to visit:

http://www.elsevier.com/copyright

Author's personal copy

International Journal of Heat and Mass Transfer 57 (2013) 582–594

Contents lists available at SciVerse ScienceDirect

International Journal of Heat and Mass Transfer

journal homepage: www.elsevier.com/locate/ijhmt

A review of the applications of nanofluids in solar energy

Omid Mahian [a], Ali Kianifar [a], Soteris A. Kalogirou [b], Ioan Pop [c,*], Somchai Wongwises [d,e]

[a] Department of Mechanical Engineering, Engineering Faculty, Ferdowsi University of Mashhad, Mashhad, Iran
[b] Department of Mechanical Engineering and Materials Science and Engineering, Cyprus University of Technology, Cyprus
[c] Department of Mathematics, Babeş-Bolyai University, 400084 Cluj-Napoca, CP 325, Romania
[d] Fluid Mechanics, Thermal Engineering and Multiphase Flow Research Lab. (FUTURE), Department of Mechanical Engineering, Faculty of Engineering, King Mongkut's University of Technology Thonburi, Bangmod, Bangkok 10140, Thailand
[e] The Academy of Science, The Royal Institute of Thailand, Sanam Suea Pa, Dusit, Bangkok 10300, Thailand

ARTICLE INFO

Article history:
Received 27 May 2012
Received in revised form 26 August 2012
Accepted 11 October 2012

Keywords:
Nanofluids
Solar energy
Efficiency
Economic and environmental considerations
Challenges

ABSTRACT

Utilizing nanofluids as an advanced kind of liquid mixture with a small concentration of nanometer-sized solid particles in suspension is a relatively new field, which is less than two decades old. The aim of this review paper is the investigation of the nanofluids' applications in solar thermal engineering systems. The shortage of fossil fuels and environmental considerations motivated the researchers to use alternative energy sources such as solar energy. Therefore, it is essential to enhance the efficiency and performance of the solar thermal systems. Nearly all of the former works conducted on the applications of nanofluids in solar energy is regarding their applications in collectors and solar water heaters. Therefore, a major part of this review paper allocated to the effects of nanofluids on the performance of solar collectors and solar water heaters from the efficiency, economic and environmental considerations viewpoints. In addition, some reported works on the applications of nanofluids in thermal energy storage, solar cells, and solar stills are reviewed. Subsequently, some suggestions are made to use the nanofluids in different solar thermal systems such as photovoltaic/thermal systems, solar ponds, solar thermoelectric cells, and so on. Finally, the challenges of using nanofluids in solar energy devices are discussed.

© 2012 Elsevier Ltd. All rights reserved.

Contents

1. Introduction . . . 583
2. Applications of nanofluids in solar energy . . . 583
 2.1. Collectors and solar water heaters . . . 583
  2.1.1. Efficiency of nanofluid-based solar collectors . . . 584
  2.1.2. Economic and environment considerations . . . 588
 2.2. Other applications . . . 588
  2.2.1. Thermal energy storage . . . 588
  2.2.2. Solar cells . . . 589
  2.2.3. Solar stills . . . 589
3. Future work . . . 589
 3.1. Parabolic trough systems . . . 590
 3.2. Photovoltaic/thermal systems . . . 590
 3.3. Solar thermoelectric cells . . . 590
 3.4. Solar ponds . . . 591
 3.5. Other possibilities . . . 591
4. Challenges . . . 591
 4.1. High cost . . . 591
 4.2. Instability and agglomerating . . . 592
 4.3. Pumping power and pressure drop . . . 592
 4.4. Erosion and corrosion of components . . . 592

* Corresponding author. Tel.: +40 264405300; fax: +40 264591906.
E-mail address: popm.ioan@yahoo.co.uk (I. Pop).

0017-9310/$ - see front matter © 2012 Elsevier Ltd. All rights reserved.
http://dx.doi.org/10.1016/j.ijheatmasstransfer.2012.10.037

Author's personal copy

5. Conclusion . . . 592
Acknowledgments . . . 592
References . . . 592

1. Introduction

Common fluids such as water, ethylene glycol, and heat transfer oil play an important role in many industrial processes such as power generation, heating or cooling processes, chemical processes, and microelectronics. However, these fluids have relatively low thermal conductivity and thus cannot reach high heat exchange rates in thermal engineering devices. A way to overcome this barrier is using ultra fine solid particles suspended in common fluids to improve their thermal conductivity. The suspension of nano-sized particles (1–100 nm) in a conventional base fluid is called a nanofluid. Choi first used the term "nanofluid" in 1995 [1]. Nanofluids, compared to suspensions with particles of millimeter-or-micrometer size, show better stability, rheological properties, and considerably higher thermal conductivities.

In recent years, many researchers have investigated the effects of nanofluids on the enhancement of heat transfer in thermal engineering devices, both experimentally and theoretically. Researchers have also applied a variety of preparation methods, characteristics, and different models used for the calculation of thermophysical properties of nanofluids (i.e., thermal conductivity, viscosity, density, specific heat capacity) [2–9]. Some investigators have also summarized the effects of nanofluids on flow and heat transfer in natural and forced convection in different systems [10–13]. The enhanced thermal behavior of nanofluids could provide a basis for an enormous innovation for heat transfer intensification, which is of major importance to a number of industrial sectors including transportation, power generation, micromanufacturing, thermal therapy for cancer treatment, chemical and metallurgical sectors, as well as heating, cooling, ventilation and air-conditioning. Nanofluids are also important for the production of nanostructured materials for the engineering of complex fluids as well as for cleaning oil from surfaces due to their excellent wetting and spreading behavior (Ding et al. [14]). Another application of the nanofluid flow is in the delivery of nano-drug as suggested by Kleinstreuer et al. [15].

Saidur et al. [16] reviewed the potential of nanofluids in the improvement of heat transfer in refrigeration systems. The authors concluded that more studies are required to find the reasons behind the considerable improvements in heat transfer whereas an insignificant increase in pressure occurs. Thomas and Sobhan [17] presented experimental studies on nanofluids, with emphasis on the techniques of measuring the effective thermal conductivity. Escher et al. [18] investigated the applications of nanofluids in cooling electronics. Recently, applications of computer simulations and computational fluid dynamics (CFD) used to model systems employing nanofluids were reviewed and analyzed by Abouali and Ahmadi [19] and Kamyar et al. [20]. Ahn and Kim [21] also published a review on the critical heat flux of nanofluids for both convective flow boiling and pool boiling applications. In another publication, Saidur et al. [22] reviewed the general applications of nanofluids in some fields such as cooling of electronics, heat exchangers, medical applications, fuel cells, nuclear reactors, and many more. They also mentioned briefly the applications of nanofluids in solar water heaters. They investigated challenges in using nanofluids, including an increased pressure drop and pumping power, long-term stability of nanoparticles dispersion, and the high cost of nanofluids.

In recent years, the use of solar energy has had a remarkable edge. The perceived shortage of fossil fuels as well as environmental considerations will constrain the use of fossil fuels in the future. Therefore, researchers are motivated to find alternative sources of energy. This has become even more popular as the price of fossil fuels continues to rise. The earth receives in just about 1 h more energy from the sun than that consumed by the entire world for 1 year. Most solar energy applications are financially viable while small systems for individual use require just a few kilowatts of power [23,24]. It is important to apply solar energy to a wide range of applications and provide solutions through the modification of the energy proportion, improving energy stability, increasing energy sustainability, and enhancing system efficiency [25]. This paper presents a review of former studies on the application of nanofluids in solar thermal engineering systems. The former works on applications of nanofluids in solar energy are mainly related to their applications in collectors. Therefore, this review mainly investigates the effects of nanofluids on the efficiency improvement of solar collectors as well as on economic and environmental considerations regarding the usage of these systems. Other applications of nanofluids in thermal energy storage, solar cells, and solar stills are also reviewed. Some suggestions also are made for future works in this field. In addition, the existing challenges of using nanofluids in solar energy applications are discussed. Finally, the authors wish to mention that in contrast with the comprehensive references on nanofluids mentioned above much less is known about the application of nanofluids in solar energy applications. It should be reiterated here that, as this is the first systematic review paper on this subject, it is desirable to provide as complete details as possible. However, in an attempt to reduce the overall length of the paper, without compromising the technical quality, only some very important questions for problems of practical applications have been briefly described.

2. Applications of nanofluids in solar energy

Initially, the application of nanofluids in collectors and water heaters are investigated from the efficiency, economic, and environmental aspects. Some studies conducted on thermal conductivity and optical properties of nanofluids are also briefly reviewed, because these parameters can determine the capability of nanofluids to enhance the performance of solar systems.

2.1. Collectors and solar water heaters

Solar collectors are particular kind of heat exchangers that transform solar radiation energy into internal energy of the transport medium. These devices absorb the incoming solar radiation, convert it into heat, and transfer the heat to a fluid (usually air, water, or oil) flowing through the collector. The energy collected is carried from the working fluid, either directly to the hot water or space conditioning equipment or to a thermal energy storage tank, from which it can be drawn for use at night or on cloudy days [26]. Solar water heaters are the most popular devices in the field of solar energy. As mentioned in the introduction, the nanofluid-based solar collectors are investigated in two aspects. In the first, these devices are studied from the efficiency viewpoint, and in the second, from economic and environmental viewpoints.

Author's personal copy

2.1.1. Efficiency of nanofluid-based solar collectors

Tyagi et al. [27] investigated theoretically the effects of different parameters on the efficiency of a low-temperature nanofluid-based direct absorption solar collector (DAC) where the working fluid is a mixture of water and aluminum nanoparticles. A schematic of the direct absorption collector is shown in Fig. 1. The upper side of this collector is covered by a glass while the lower side is well insulated, so it is adiabatic. The efficiency of the collector is obtained by the following equation:

$$\eta = \frac{useful\ gain}{available\ energy} = \frac{\dot{m}c_p(\overline{T}_{out} - \overline{T}_{in})}{AG_T} \quad (1)$$

where $\dot{m}$ is the mass flow rate of the fluid flowing through the collector; c_p is the specific heat; and $\overline{T}_{in}$ and $\overline{T}_{out}$ are the mean fluid inlet and outlet temperatures, respectively. A is the cover area of the collector, and G_T is the solar flux incident on the solar collector. In the analysis, they assumed that the values of $\overline{T}_{in}$, G_T, and $\dot{m}$ to be 35 °C, 1000 W/m^2, and 1.2 kg/s, respectively.

Tyagi et al. [27] plotted the variation of collector efficiency as a function of the particle volume fraction (%), where the volume fraction varies from 0.1% to 5% (see Fig. 2). Their results showed that by adding nanoparticles to the working fluid, the efficiency increases remarkably for low values of volume fraction of nanoparticles. They attributed the increase of collector efficiency to the increase in attenuation of sunlight passing through the collector due to the nanoparticles addition that leads to the increase of collector efficiency. However, for a volume fraction higher than 2%, the efficiency remains nearly constant, so adding more nanoparticles is not beneficial. Tyagi et al. [27] also investigated the effects of nanoparticles size on the collector efficiency where the volume fraction is equal to 0.8%. The results revealed that the efficiency increases slightly with an increase in the size of nanoparticles (see Fig. 3).

Otanicar et al. [28] investigated both experimentally and numerically the effects of different nanofluids (carbon nanotubes, graphite, and silver) on the performance of a micro scale direct absorption solar collector (DASC). The schematic of the experimental set up showing also the dimensions of the collector is presented in Fig. 4. Fig. 5 shows the variation of collector efficiency with volume fraction for different materials, estimated using Eq. (1). The DASC data are compared to a conventional collector configuration where the solar energy is absorbed on a black plate surface. As

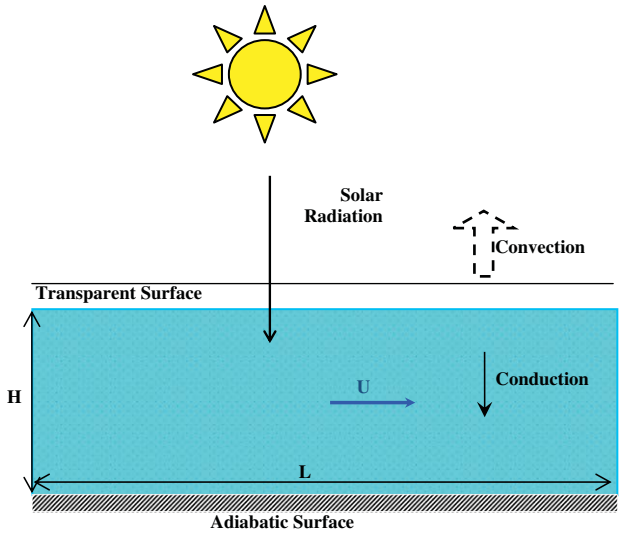

Fig. 1. Schematic of the nanofluid-based direct absorption solar collector (Reprinted from Tyagi et al. [27], with permission from ASME).

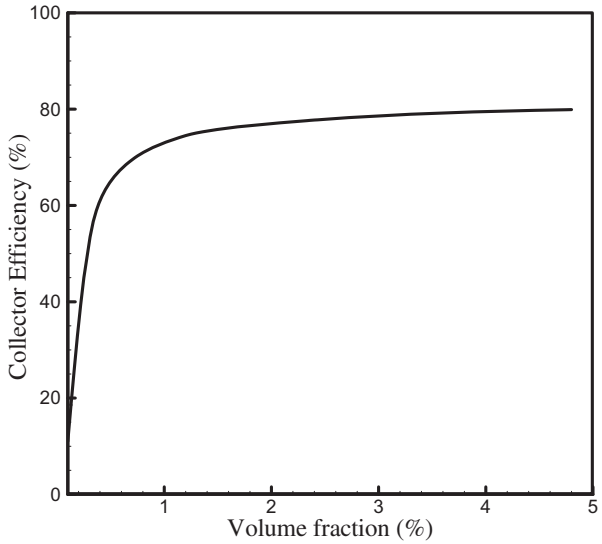

Fig. 2. Effect of particle volume fraction on collector efficiency (Reprinted from Tyagi et al. [27], with permission from ASME).

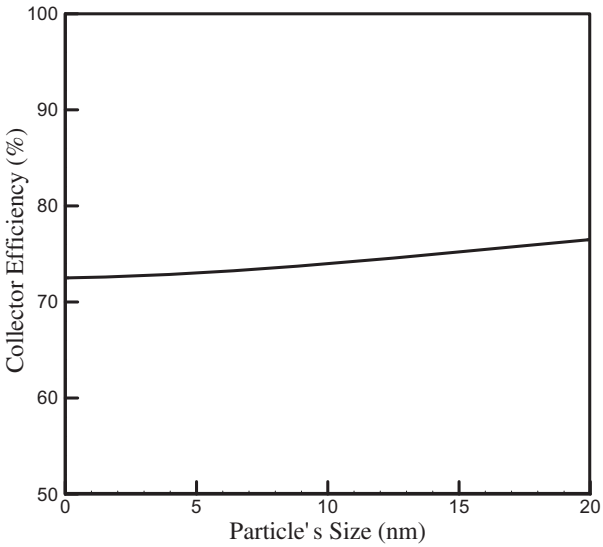

Fig. 3. Effect of nanoparticles size on collector efficiency (Reprinted from Tyagi et al. [27], with permission from ASME).

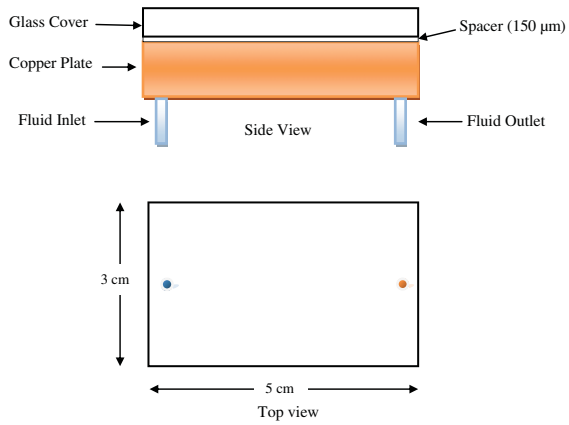

Fig. 4. Experimental schematic of the microsolar thermal collector (Reprinted with permission from Otanicar et al. [28]. Copyright 2010, American Institute of Physics).

Author's personal copy

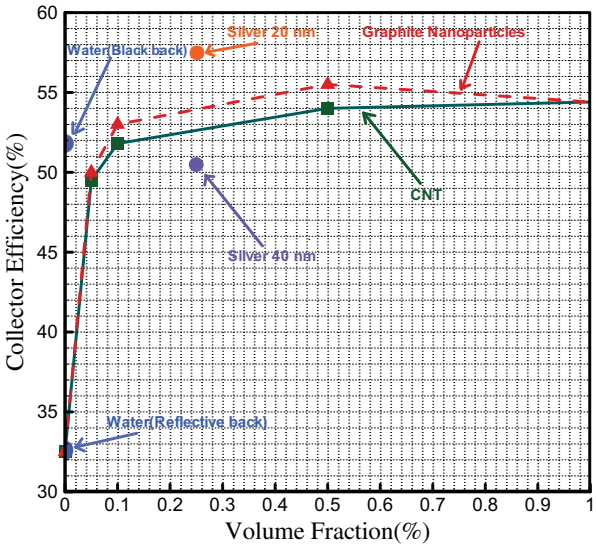

Fig. 5. Experimental microsolar thermal collector: steady-state collector efficiency (Reprinted with permission from Otanicar et al. [28]. Copyright 2010, American Institute of Physics).

shown, adding small quantities of nanoparticles leads to the remarkable enhancement of the efficiency until a volume fraction of approximately 0.5%. After a volume fraction of 0.5%, the efficiency begins to level off and even decrease slightly with increasing volume fraction. The authors attributed this reduction to the high increase of the fluid absorption at high particle loadings. The main difference in the steady-state efficiency between nanofluids occurs in silver particles when the size of the particles is between 20 and 40 nm. When halving the size from 40 to 20 nm, a 6% efficiency increase is found. The effect of particle size on efficiency is shown in Fig. 6 for silver nanoparticles. Unlike the results obtained by Tyagi et al. [27], with increase in size of nanoparticles, the efficiency of the collector decreases.

Taylor et al. [29] compared a nanofluid-based concentrating solar thermal system with a conventional one. Their results show that the use of a nanofluid in the receiver can improve the

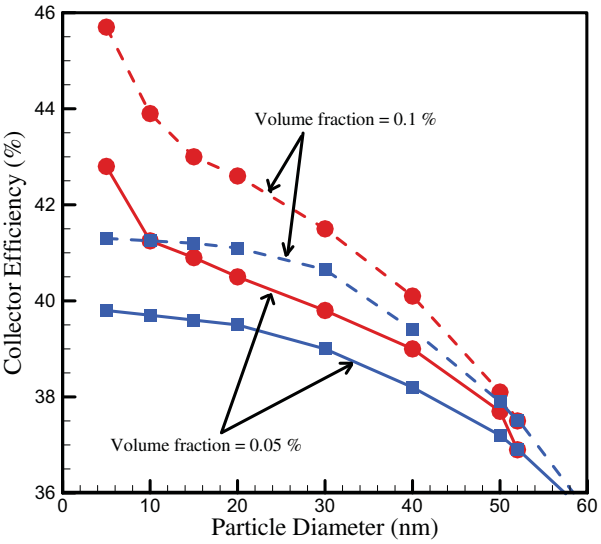

Fig. 6. Collector efficiency as a function of silver nanoparticle diameter (squares: bulk properties; circles: size-dependent properties and volume fraction (Reprinted with permission from Otanicar et al. [28]. Copyright 2010, American Institute of Physics).

efficiency by 10%. They also concluded that for 10–100 MWe power plants, using graphite/therminol VP-1 nanofluid with volume fractions approximately to 0.001% or less could be beneficial. The authors estimated that combining a nanofluid receiver with a solar thermal power tower with the capacity of 100 MWe operating in a solar resource like Tucson, Arizona, could generate $3.5 million more per year. Taylor et al. [29] considered two notional designs of potential nanofluid receivers, designated as A and B, as shown in Fig. 7.

He et al. [30] investigated the light-heat conversion characteristics of two nanofluids, water–TiO_2 and water–carbon nanotube (CNT), in a vacuum tube solar collector under sunny and cloudy weather conditions. The experimental results show a very good light heat conversion characteristic of the CNT–H_2O nanofluid with the weight concentration of 0.5%. Because of the better light-heat conversion characteristics of the CNT–H_2O nanofluid compared to the TiO_2–H_2O nanofluid, the temperature of the CNT–H_2O nanofluid is higher than that of the TiO_2–H_2O one. This means that the CNT–H_2O nanofluid is more suitable than the TiO_2–H_2O to be utilized in a vacuum tube solar collector.

Li et al. [31] studied the effects of three different nanofluids, Al_2O_3/water, ZnO/water, and MgO/water, on the performance of a tubular solar collector. Their results show that ZnO–H_2O nanofluid with 0.2% volume concentration is the best selection for the collector. Taylor et al. [32] investigated the optical property characterization of graphite, silver, copper, gold, and aluminum nanoparticles in water and VP1 as the based fluids to determine their potential to be used in direct absorption solar collectors. They revealed that over 95% of incoming sunlight can be absorbed (in a nanofluid thickness $\geqslant$10 cm) with very low nanoparticle volume fractions (less than 1×10^{-5}, or 10 ppm).

Khullar et al. [33] investigated theoretically a nanofluid-based concentrating parabolic solar collector (NCPSC) and compared the results obtained with the experimental results of conventional concentrating parabolic solar collectors operating under similar conditions. They used Aluminum nanoparticles with 0.05 vol.% suspended in Therminol VP-1 as the base fluid for the analysis. Fig. 8 shows the schematic of the nanofluid-based concentrating parabolic solar collector (NCPSC) that they considered in their work. They found that the thermal efficiency of NCPSC compared to a conventional parabolic solar collector is about 5–10% higher under the same weather conditions (see Fig. 9).

Yousefi et al. [34] experimentally investigated the effects of Al_2O_3/water nanofluid on the efficiency of a flat-plate solar collector. They examined the effects of two different weight fractions of the nanofluid, including 0.2% and 0.4%, where the diameter of particles was 15 nm. In addition, they studied the effects on efficiency of Triton X-100 used as a surfactant. The photograph and specifications of the flat-plate collector tested are presented in Fig. 10 and Table 1, respectively.

Yousefi et al. [34] conducted the experiments using a schematic setup shown in Fig. 11. Their findings are as follows:

1. The efficiency of the solar collector with 0.2% weight fraction (wt.) nanofluid is greater than that with water by 28.3% (see Fig. 12).
2. For a wide range of the reduced temperature parameter $(T_i - T_a)/G_T$, the efficiency of collector with 0.2% wt.% nanofluid is higher compared to 0.4 wt.% (see Fig. 12).
3. Using surfactant leads to a 15.63% enhancement of the efficiency.

Later, Yousefi et al. [35], using the same experimental setup as in their previous work [34], examined the effects of water–Multi wall carbon nanotubes (MWCNT) – Water nanofluid on the efficiency of the flat plate collector. They observed that:

Author's personal copy

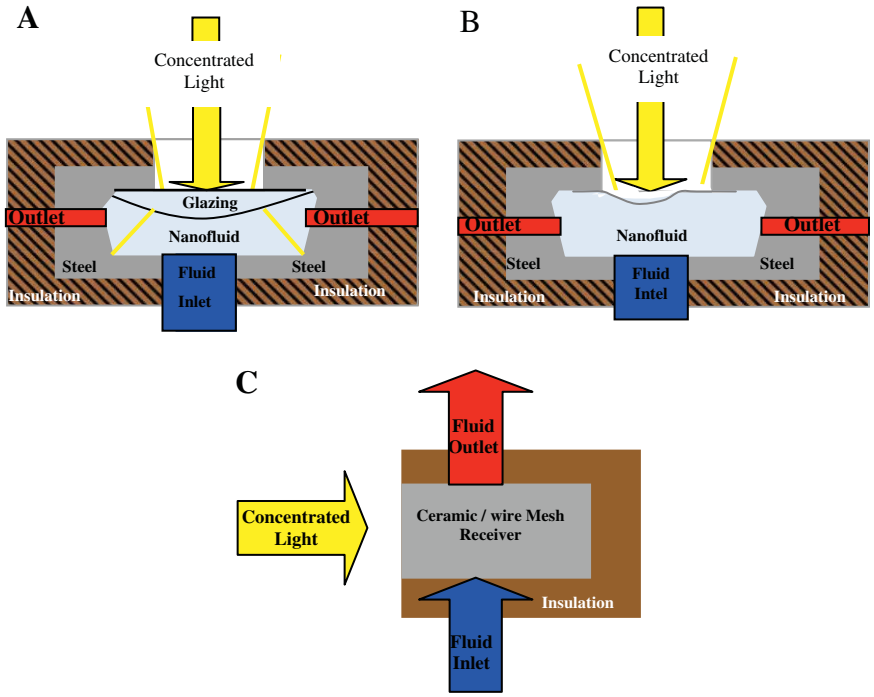

Fig. 7. (a) Conceptual design of a nanofluid concentrating collector with glazing. (b) Conceptual design of a nanofluid concentrating collector without glazing. (c) Conceptual drawing of a conventional power tower solid surface absorber (Reprinted with permission from Taylor et al. [29]. Copyright 2011, American Institute of Physics).

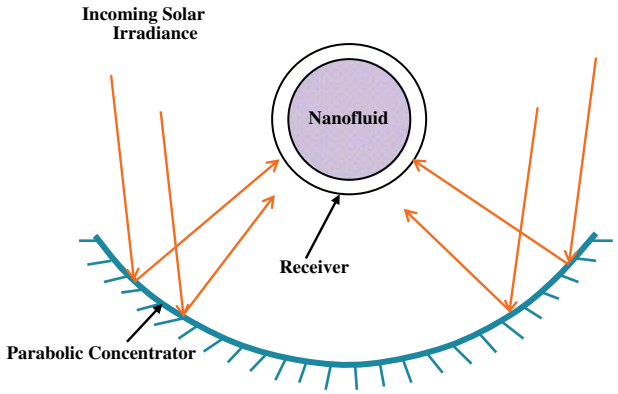

Fig. 8. Schematic of nanofluid-based concentrated parabolic solar collector (NCPSC) (Reprinted from Khullar et al. [33], with permission from ASME).

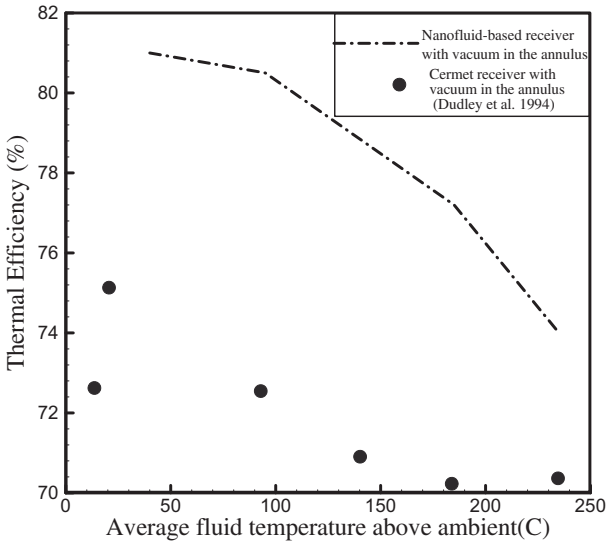

Fig. 9. Comparison of thermal efficiency as a function of average fluid temperature above ambient for NCPSC with conventional linear parabolic solar collector (Reprinted from Khullar et al. [33], with permission from ASME).

1. The efficiency of the collector by using of MWCNT–water nanofluid without surfactant is remarkably increased for 0.4 wt.% nanofluid, whereas with 0.2 wt.% the efficiency reduces compared to water as the working fluid.
2. For 0.2 wt.% nanofluid, using surfactant increases the efficiency of the collector compared to water.

In another study, Yousefi et al. [36], investigated the effects of pH variation of the MWCNT–water nanofluid on the efficiency of the flat plate collector. They used 0.2 wt.% MWCNT with various pH values −3.5, 6.5, and 9.5 – and Triton X-100 as an additive. They found that a bigger difference between the pH of nanofluid and pH of isoelectric point leads to higher efficiency. The isoelectric point is the point at which the molecules carry no electrical charge. For MWCNT, the pH of the isoelectric point is 7.4. The effects of pH variation of H_2O–MWCNT nanofluid on the efficiency of the flat plate collector are presented in Fig. 13.

In the following, some previous works are reviewed in which the potential of nanofluids for use in solar energy system is performed through the study of optical properties and thermal conductivity of nanofluids. Link and El-Sayed [37] reviewed the optical properties of gold nanoparticles. Particularly, they studied the shape and size dependence of radiative, and photothermal properties of gold nanocrystals. Khlebtsov et al. [38] investigated the effects of the size, shape, and structure of gold and silver nanoparticles on the optical properties of the nanofluids and perceived that the shape and size of the nanoparticle have great effect on the optical properties of a nanofluid. Sani et al. [39] reported the

Author's personal copy

Fig. 10. Flat-plate collector used by Yousefi et al. (Reprinted from Yousefi et al. [34], with permission from Elsevier).

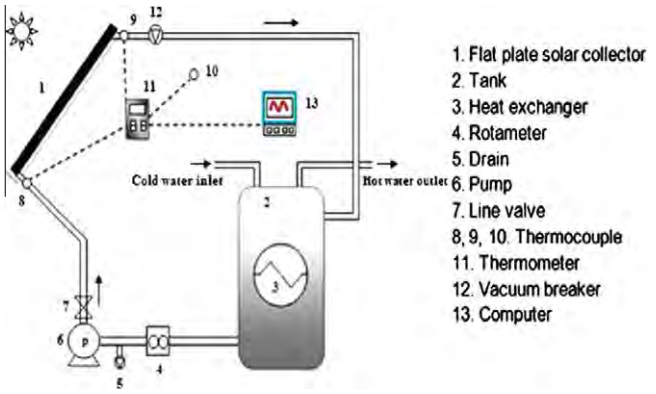

Fig. 11. Schematic of the experiment used by Yousefi et al. (Reprinted from Yousefi et al. [34], with permission from Elsevier).

Table 1
The specifications of the flat-plate collector (Reprinted from Yousefi et al. [34], with permission from Elsevier).

Specification	Dimension/value	Unit
Occupied area	200 × 94 × 9.5	cm
Absorption area	1.51	m^2
Weight	38.5	kg
Frame (Al6063 extruded)	–	–
Glass (float)	t = 4	mm
Header pipe (Cu)	Ø22, t = 0.9	mm
Connector riser pipe to absorber sheet (Cu)	Ø10, t = 0.9	mm
Absorption sheet:	–	–
Thermal emission:	7	%
Solar absorption:	96.2	%
Coating method:	Vacuum magnetron sputtering	–

optical characterization of a new fluid consisting of single-wall carbon nanohorns and ethylene glycol for solar energy applications. They concluded that carbon nanohorns could enhance remarkably the sunlight absorption with respect to pure base-fluid. The results obtained are compared with those obtained for fluids suspending more conventional carbon forms, i.e., carbon-black particles. They found that nanohorn spectral features are considerably more favorable than those of amorphous carbon for a specific application. This result shows that using carbon nanohorn-based nanofluids in thermal solar devices leads to the enhancement of efficiency and compactness in the systems. Mercatelli et al. [40,41] investigated the potential of single-wall carbon nanohorns nanoparticles with two different base fluids including water and glycol. Their measurements showed that these nanofluids are very suitable for direct absorption solar devices because only about 5% of the total extinction is scattered by SWCNH particles. In another work, Mercatelli et al. [42] applied a simple spectrophotometric to estimate the spectral scattering albedo of SWCNHs/water nanofluid. Recently, Saidur et al. [43] investigated the potential of Aluminum/water nanofluid to use in direct absorption solar collectors. They concluded that Aluminum/water nanofluid with 1% volume fraction improves considerably the solar absorption so that it is a fine solution for a direct solar collector. To use of the nanofluid they suggested, although the particle size has no effect on the extinction coefficient of nanofluid, in order to have Rayleigh scattering the size of nanoparticles should be less than 20 nm. They also found that the extinction coefficient varies linearly with volume fraction. Lenert and Wang [44] and Lenert [45] presented a combined theoretical and experimental work to optimize the efficiency of liquid-based solar receivers seeded with carbon-coated absorbing nanoparticles. They concluded that the efficiency of nanofluid volumetric receivers increases with increasing solar concentration and nanofluid height. Colangelo et al. [46] measured the thermal conductivities of CuO, Al_2O_3, ZnO and Cu with different shapes and volume fraction by 3%, where water and diathermic oil are as the base fluids, to evaluate their potential to use for high temperature applications such as in solar collectors. They found that the thermal conductivity enhancement of the nanofluids with diathermic oil is higher than that with water, with the same nanoparticles and at the same conditions. They also concluded that the thermal conductivity is reduced with increasing the size of particles. Kameya and Hanamura [47] found experimentally that the solar radiation absorption for the nanofluid of Ni/alkyl naphthalene with 0.1% volume fraction is much higher than the base fluid. Gan and Qiao [48] investigated the optical properties of ethanol-based nanofluids containing multiwalled carbon nanotubes (MWCNTs), carbon and aluminum nanoparticles. They concluded that MWCNTs leads to more absorption than aluminum and carbon nanoparticles. Finally, Gan and Qiao [49] found that for ethanol-based nanofluids, the radiation absorption for nanofluids

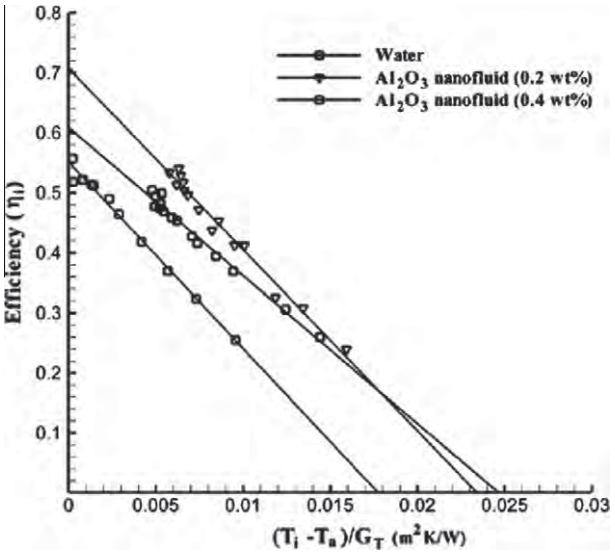

Fig. 12. The efficiencies of solar collectors for Al_2O_3 nanofluid without surfactant and for water (Reprinted from Yousefi et al. [34], with permission from Elsevier).

Author's personal copy

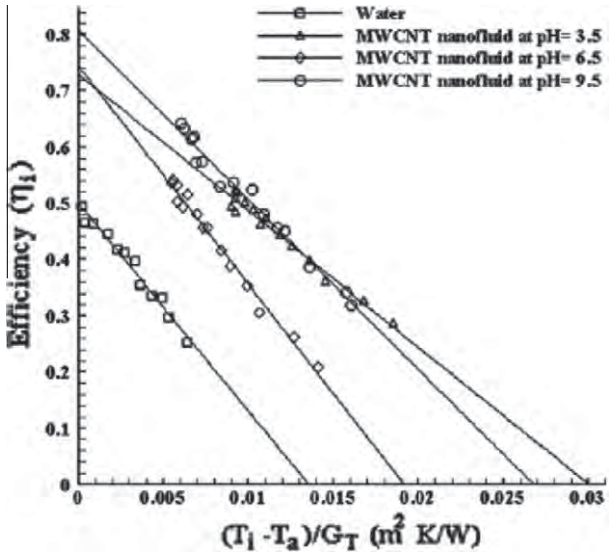

Fig. 13. The efficiency of the flat-plate solar collector with MWCNT nanofluid as a base fluid at three pH values compared water at a 0.0333 kg/s mass flow rate (Reprinted from Yousefi et al. [36], with permission from Elsevier).

containing Al_2O_3 nanoparticles is higher than nanofluids containing aluminum nanoparticles.

2.1.2. Economic and environment considerations

An accepted way to determine the economic and environmental impacts of a product is life cycle assessment [50]. This section presents the economic and environment considerations of nanofluid-based collectors. Otanicar and Golden [50] compared the environmental and economic aspects of using a conventional solar collector against a nanofluid based collector located in Phoenix, Arizona. The economic analysis shows that the capital cost and maintenance costs of the nanofluid-based solar collector compared to the conventional one are $120 and $20 higher, respectively (see Table 2). However, because of the higher efficiency and annual solar fraction of the nanofluid-based solar collector, the fuel cost savings per year, for both electricity and natural gas, is greater than that of the conventional solar collector. Moreover, due to the high cost of nanofluids compared the conventional collector, the payback period for a nanofluid-based collector is longer, but at the end of its useful life, it has the same life cycle savings as a conventional collector.

Embodied energy for both solar collectors, including conventional and nanofluid-based collectors, are compared in Table 3. The embodied energy for the nanofluid-based collector is about 9% lower. Additionally, from an environmental point of view, as shown in Table 4, the manufacturing of the nanofluid-based solar collector leads to 34 kg fewer CO_2 emissions while during its operation it saves 50 kg year when compared to the conventional solar collector. The magnitudes of other emissions including SO_x and NO_x are very small, so the differences are not considerable. Over the 15-year expected lifetime of the solar collectors, the nanofluid-based solar collector would offset more than 740 kg of CO_2 in comparison to a conventional collector. The authors concluded that more than one million metric tons of CO_2 could be offset per year if the usage of nanofluid-based solar collector systems for hot water heating increases by 50% in Phoenix, Arizona.

Khullar and Tyagi [51] examined the potential of the nanofluid-based concentrating solar water heating system (NCSWHS) as an alternative for systems based on fossil fuels. Using NCSWHS leads to annual electricity and liquefied petroleum gas (LPG) savings of approximately 1716 kWh/household/year and 206 kg/household /year, respectively, which produces significant economic benefits. In addition, they concluded that based on the annual estimation, CO_2 emissions are reduced by about 2.2×10^3 kg of CO_2/household/year. The use of nanofluid-based collectors is beneficial to reduce the environment problems. Table 5 summarizes the most important results obtained from the former works concerning the application or potential of nanofluids to use in solar collectors.

2.2. Other applications

In this section, other applications of nanofluids in solar energy systems including their applications in thermal energy storage materials, solar cells, and solar stills are reviewed. It should be noted that the reported works in this field are very scarce.

2.2.1. Thermal energy storage

Typical solar thermal-energy storage facilities require the storage medium to have high heat capacity and thermal conductivity. However, few materials are available with these properties and applicable in high temperatures. Recently, Shin and Banerjee [52] reported the anomalous enhancement of specific heat capacity of high-temperature nanofluids. They found that Alkali metal chloride salt eutectics when is doped with silica nanoparticles at 1% mass concentration increases the specific heat capacity of the nanofluid by 14.5%, so that this material can be a suitable one to use in solar thermal-energy storage facilities. One of techniques of storing solar energy is the application of PCMs. Among lots of PCMs available, paraffin is the most suitable due to its desirable characteristics, including large latent heat capacity, negligible super cooling and low cost. However, the inherent low thermal conductivity (0.21–0.24 W/mK) strongly prevents possible applications [53]. Wua et al. [53] numerically investigated the melting processes of Cu/paraffin nanofluids PCMs. Their results revealed that with 1 wt.% Cu/paraffin, the melting time can be saved by 13.1%. Therefore, they concluded that adding nanoparticles is an efficient technique to enhance the heat transfer in latent heat thermal energy storage system.

Table 2
Economic comparisons for conventional and nanofluid-based solar collectors (Reprinted with permission from Otanicar and Golden [50]. Copyright (2009) American Chemical Society).

Parameter	Conventional solar collector {$}	Nanofluid solar collector {$}
Independent costs	200.00	200.00
Area based costs	397.80	327.80
Nanoparticles		188.79
Total capital (one time cost)	597.80	716.59
Total maintenance (for 15 year life)	96.23	115.35
Total costs	694.03	831.94
Electricity cost saving per year	270.13	278.95
Years until electricity savings = costs	2.57	2.98
Natural gas cost saving per year	80.37	83.02
Years until natural gas savings = costs	8.64	10.02
Electricity price		
November_March (per kWh)	0.08	0.08
May_October (per kWh)	0.09	0.09
Daily service charge	0.25	0.25
Gas price		
Rate (per therm)	0.74	0.74
Monthly service charge	9.70	9.70

Author's personal copy

Table 3
Embodied energy comparisons for conventional and nanofluid-based solar collectors (Reprinted with permission from Otanicar and Golden [50]. Copyright (2009) American Chemical Society).

Description	Embodied energy index (MJ/kg)	Conventional solar collector		Nanofluid-based solar collector	
		Mass (kg)	Embodied energy content (MJ)	Mass (kg)	Embodied energy (MJ)
Insulation					
Polyester	53.7	1.74	93.22	1.74	93.22
Fiberglass	30.3	3.26	98.75	3.26	98.75
Glass	15.9	14.20	225.76	28.40	451.52
Copper pipe					
Collector	70.6	4.97	350.72	0.00	0.00
Manifold	70.6	3.48	245.57	3.48	245.57
Aluminum extrusion	201.0	0.56	111.58	0.56	111.58
Aluminum backplate	199.0	2.12	421.75	2.12	421.75
Steel backplate	34.8	0.00	0.00	5.97	207.65
Sealant	87.0	0.70	60.90	0.70	60.90
Black paint	90.4	0.30	27.12	0.30	27.12
Casing paint	90.4	0.90	81.36	0.90	81.36
Screws	34.8	0.00	0.04	0.00	0.04
Copper absorber	70.6	4.05	285.80	0.00	0.00
Nanoparticles	246.8	0.00	0.00	0.06	15.55
Thermal fluid	17.0	5.84	99.28	5.84	99.28
Conversion rate (27%)			567.50		516.86
Total		42.10	2669.34	53.32	2431.14

Table 4
Embodied energy emissions and consumer phase operational energy (Reprinted with permission from Otanicar and Golden [50]. Copyright (2009) American Chemical Society).

Emissions	Pollution from collector embodied energy		Saving of solar energy	
	Conventional (kg)	Nanofluid-based (kg)	Conventional (kg/year)	Nanofluid-based (kg/year)
Carbon dioxide (CO_2)	599.77	564.94	1500.89	1550.33
Sulfur oxides (SO_x)	0.51	0.48	0.83	0.85
Nitrogen oxides (NO_x)	0.84	0.79	1.53	1.58

2.2.2. Solar cells

Cooling of solar cells can improve the efficiency of such solar devices. Nanofluids can be used as a solution to cool the solar cells. Elmir et al. [54] simulated the cooling of a silicon solar cell using the finite element method. They considered the solar panel as an inclined cavity (with a slope of 30°) and solved the equations in Cartesian coordinate system. They used Al_2O_3/water nanofluid for their analysis, where the thermal conductivity and viscosity of the nanofluid are estimated using the models of Wasp [55] and Brinkman [56], respectively. As seen in Fig. 14, they concluded that using nanofluids leads to the increase of the average Nusselt number, and, hence, the rate of cooling increases with increases in volume fraction. Of course, it should be noted that the thermophysical properties, which are used in this study, are old and they do not predict the thermal conductivity and viscosity of nanofluids correctly. Therefore, it is suggested that in the future works, temperature-dependent models, or at least newer temperature-independent models are used to calculate the thermophysical properties of nanofluids. For example, to calculate the viscosity of nanofluids, the models and relation presented by Maiga et al. [57], Buongiorno [58], Nguyen et al. [59], Koo and Kleinstreuer [60], and Duangthongsuk and Wongwises [61] can be used. To estimate the thermal conductivity of nanofluids, the relations presented by Maiga et al. [57], Xuan et al. [62], Jang and Choi [63], Koo and Kleinstreuer [64], Chon et al. [65], Duangthongsuk and Wongwises [61] and Yiamsawasd et al. [66] can be applied.

2.2.3. Solar stills

Potable water demand is increasing due to rapid population increase and due to uncontrolled pollution of freshwater resources. According to the World Health Organization, nearly 2.8 billion people (approximately 40% of the world population) currently have no access to safe drinking water, and water-borne diseases account for 90% of all infectious diseases in the developing world [67]. In arid remote regions in the world, the provision of fresh water is more critical. In these regions, solar desalination systems can solve part of the problem where solar energy is available. Solar stills can be used to avoid the greenhouse gas emissions from the production of fresh water [68]. Many researches have carried out research on solar stills, and different methods are applied to improve their productivity. Recently, Gnanadason et al. [69] reported that using nanofluids in a solar still can increase its productivity. The schematic of their experimental set-up is shown in Fig. 15. They investigated the effects of adding carbon nanotubes (CNTs) to the water inside a single basin solar still. Their results revealed that adding nanofluids increases the efficiency by 50%. Nevertheless, they have not mentioned the amount of nanofluid added to the water inside the solar still. Regarding the addition of nanofluids to the solar still, the economic viability should be considered. In literature, some works reported that adding dyes to solar stills could improve the efficiency. For instance, Nijmeh et al. [70] concluded that adding violet dye to the water inside the solar still increases the efficiency by 29%, which is considerable. On the other hand, it is evident that nanofluids (especially CNTs) compared to dyes are more expensive, hence this may be a challenge on using nanofluids in solar stills, because in this type of use of nanofluids in solar stills the nanofluids have no flow in a closed loop so that they could be recovered.

3. Future work

The above review shows that the application of nanofluids in solar energy applications is still in its infancy. Nanofluids can be used in many fields of solar energy. Here, some suggestions are presented for future work in the area. The authors hope that these

Author's personal copy

Table 5
Summary of former works on the application or potential of nanofluids to use in solar collectors.

Author(s) and type of study	Collector type	Nanofluid type and nanoparticle size	Results
Tyagi et al. [27] (Theoretically)	Non-concentrating direct absorption	Aluminum/water (0–20 nm)	–Efficiency remarkably increases for volume fraction less than 2% –Efficiency remains nearly constant for volume fraction higher than 2% –Efficiency increases slightly with an increase in the size of nanoparticles
Otanicar et al. [28] (Theoretically and experimentally)	Non-concentrating micro scale direct absorption	Graphite/water (30 nm) silver/water (20 and 40 nm) carbon nanotube/water (6–20 nm diameter, 1000–5000 nm length)	–Efficiency considerably increases for volume fractions less than 0.5% –Efficiency for volume fractions higher than 0.5% may even decrease –Efficiency increases by 6%, with decreasing the nanoparticle size in Silver/Water nanofluid
Taylor et al. [29] (Theoretically and experimentally)	Concentrating direct absorption	Graphite/therminol VP-1 aluminum/therminol VP-1 silver/therminol VP-1 copper/therminol VP-1 (10–100 nm)	–Efficiency increases up to 10% by using a nanofluid in the receiver –Using graphite/therminol VP-1 nanofluid with volume fractions less than 0.001% is beneficial for 10–100 MWe power plants
He et al. [30] (Experimentally)	Vacuum tube	TiO_2/water (5–10 nm) CNT/water (10–50 nm diameter, 100–1000 nm length)	–CNT/water nanofluid is more suitable than the TiO_2/water to be used in a vacuum tube solar collector
Li et al. [31] (Experimentally)	Tubular	Al_2O_3/water ZnO/water MgO/water(size < 20 nm)	–ZnO/water nanofluid with 0.2% volume concentration is the best selection for the collector
Taylor et al. [32] (Theoretically and experimentally)	Direct absorption	Graphite/water and graphite/VP1 aluminum/water and aluminum/VP1 copper/water and copper/VP1 silver/water and silver/VP1 gold/water and silver/VP1	–Over 95% of incoming sunlight can be absorbed for nanofluid thickness $\geqslant$ 10 and nanoparticle volume fractions less than 1×10^{-5}
Khullar et al. [33] (Theoretically)	Concentrating Parabolic	Aluminum/therminol VP-1 (5 nm)	–Thermal efficiency of nanofluid concentrating parabolic collectors compared to a conventional parabolic solar collector is about 5–10% higher
Yousefi et al. [34] (Experimental)	Flat plate	Al_2O_3/water (15 nm) Triton X-100 is used as a surfactant	–Efficiency of the solar collector with 0.2% weight fraction (wt) nanofluid is higher than that with water by 28.3%. –Efficiency increases by15.63% using the surfactant
Yousefi et al. [35] (Experimental)	Flat plate	Water-Multi wall carbon nanotubes (MWCNT)/water (10–30 nm) Triton X-100 is used as a surfactant	–Efficiency of the collector increases remarkably for 0.4 wt.% nanofluid, whereas with 0.2 wt.% the efficiency reduces compared to water –For 0.2 wt.% nanofluid, using surfactant increases the efficiency of the collector compared to water
Yousefi et al. [36] (Experimental)	Flat plate	Water-Multi wall carbon nanotubes (MWCNT)/water with various pH values: 3.5, 6.5, and 9.5 Triton X-100 is used as a surfactant	–A bigger difference between the pH of nanofluid and pH of isoelectric point leads to higher efficiency
Otanicar and Golden [50] (Theoretical)	Direct absorption	Graphite/water and propylene glycol	–Using a nanofluid-based solar collector leads to fewer CO_2 emissions compared to the conventional solar collector
Khullar and Tyagi [51] (Theoretical)	Concentrating direct absorption	Aluminum/water	–Using this type of collector leads to fewer CO_2 emissions by 2.2×10^3 kg in 1 year

proposals will be helpful for the development on the use of nanofluids in the solar thermal devices.

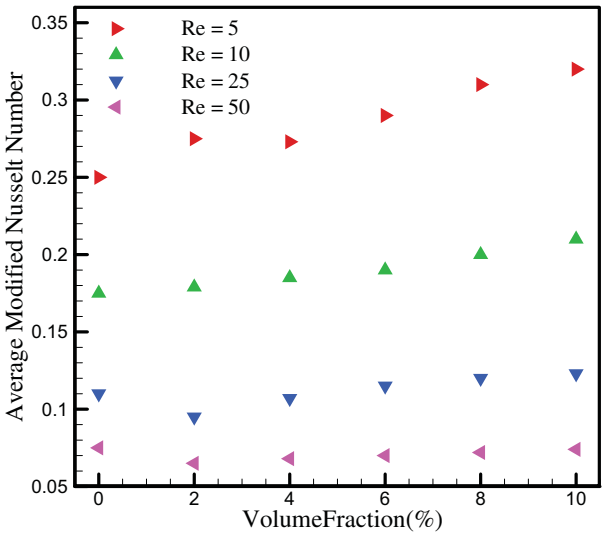

Fig. 14. Effects of volume fraction on Nusselt number for cooling a solar cell (Reprinted from Elmir et al. [54], with permission from Elsevier).

3.1. Parabolic trough systems

As mentioned, only a theoretical work has been done on parabolic trough collectors, therefore some experimental studies can be performed on the effects of nanofluids on the efficiency of parabolic trough systems.

3.2. Photovoltaic/thermal systems

A photovoltaic/thermal (PV/T) system is a hybrid structure that converts part of the sun's radiation to electricity and part to thermal energy [71]. One can investigate experimentally the effects of using different nanofluids on the cooling rate, and, hence, the efficiency of the PV/T systems. In this area, the effects of different volume fractions, nanoparticle size on the efficiency of the system can be studied. A review of the literature shows that many researches have been carried out on the potential of nanofluids for cooling of different thermal systems such as electronic devices [72–74], automobile radiator [75], and micro channel heat sinks [76]. Therefore, using nanofluids to cool the PV/T system may be reasonable.

3.3. Solar thermoelectric cells

In recent years, interest in the development of solar thermoelectric systems has been considerably increased [77]. The

Author's personal copy

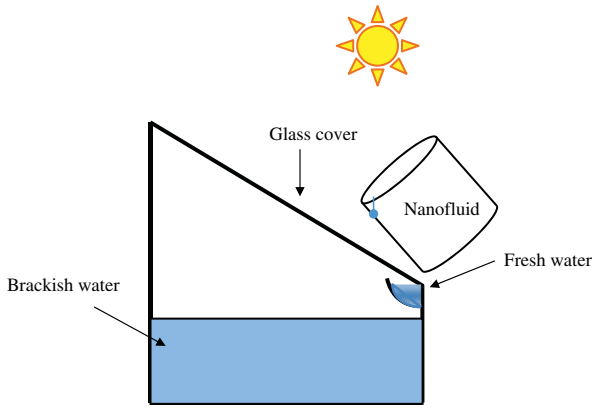

Fig. 15. Schematic of the experimental set up used by Gnanadason et al. [69].

thermoelectric cells can be used to convert the solar energy to electricity due to the temperature difference between two hot and cold surfaces. A greater temperature difference between the hot and cold surfaces of the thermoelectric cell leads to a bigger electricity production. The authors would like to suggest an experimental set-up to investigate the effects of nanofluids on the performance of such systems. Fig. 16 shows the schematic of the set-up, which is a development of the work done by Fan et al. [77]. In this work, a dish concentrates the solar radiation on the thermoelectric cells installed on the focal point of the dish. In this way the effects of different nanofluids with various mass flow rates on the efficiency of the solar thermoelectric cell can be studied.

3.4. Solar ponds

Salinity gradient solar ponds are great bodies of water between 2–5 m deep, which could collect solar radiation and store it in the form of heat [78,79].

Heat can be extracted from the solar ponds and has been used for industrial process heating, space heating, and power generation. In all these applications heat is extracted from the bottom of the solar pond which is at a temperature of about 50–60 °C higher than the top surface of the solar pond [80,81]. Concerning the application of nanofluids in solar ponds an experimental set up is proposed in Fig. 17. As seen, a nanofluid flows through a heat exchanger mounted at the bottom of the solar pond to absorb the heat. It expects that nanofluids could enhance the rate of heat removal from the bottom of the solar pond.

3.5. Other possibilities

The above suggestions are only a few of the possible applications relating to the use of nanofluids in solar energy. Besides the above ideas, nanofluids also can be used in solar cooling systems, solar absorption refrigeration systems, and a combination of different solar devices. Here, for instance, the authors would like to suggest some Refs. [82–86], in which there is a potential to use a nanofluid as the working fluid. In addition, in numerical studies such as the simulation of solar cell cooling, which it is mentioned in Section 2.2.2, new models can be used to calculate the thermophysical properties. Additionally, the nanofluid can be considered as a two-phase mixture [87].

4. Challenges

The possible challenges for the application of nanofluids in solar thermal devices are mentioned briefly in the following sections.

4.1. High cost

The first possible challenge in the use of nanofluids in solar thermal devices is the high cost of nanofluids because of difficulties in production. The high cost of nanofluids to use in thermal engineering systems such as heat exchangers is emphasized as a disadvantage in some works [88,89].

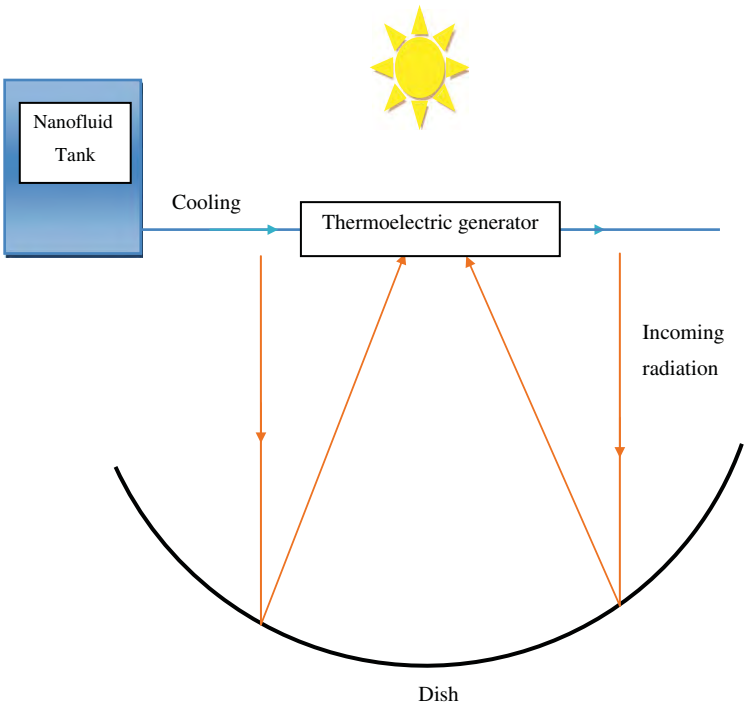

Fig. 16. The experimental set-up proposed for using nanofluids in thermoelectric cells.

Author's personal copy

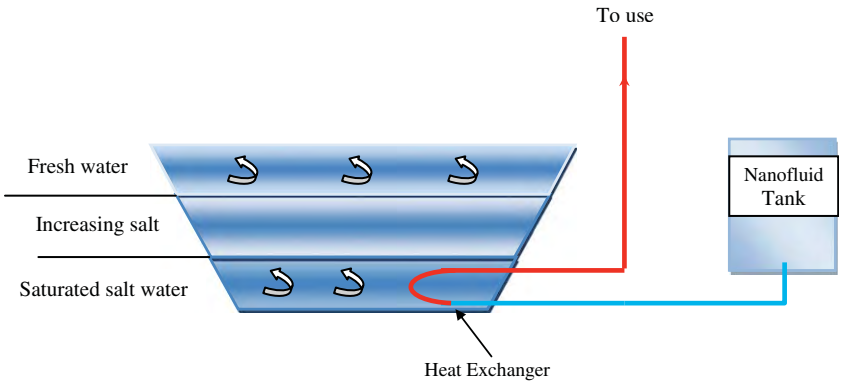

Fig. 17. The experimental set-up proposed for using nanofluids in solar ponds.

4.2. Instability and agglomerating

Instability and agglomerating of the nanoparticles is another problem. Therefore, using nanofluids in solar systems with natural circulation (such as thermosiphons) where there is no pump to circulate the fluid, is not reasonable. It should be also noted that for high temperature gradients the agglomeration of nanoparticles seems to be more serious [90]. Therefore, exact investigations are needed for an appropriate selection of a nanofluid for applications in high temperatures.

4.3. Pumping power and pressure drop

Using a nanofluid with higher viscosity compared to the base fluid leads to the increase of pressure drop and consequently the increases in the required power for pumping. For example, Duangthongsuk and Wongwises [91] found during their experiments that the pressure drop under a turbulent regime increases with an increase in volume fraction of TiO_2/water nanofluid. In another experimental research, Razi et al. [92] also concluded that using CuO/oil nanofluid increases the pressure drop under a laminar regime.

4.4. Erosion and corrosion of components

Existing of nanoparticles in nanofluid may lead to corrosion and erosion of thermal devices in a long time. Celata et al. [93] recently investigated the effects of nanofluid flow effects on erosion and corrosion of metal surfaces. They conducted their experiments for TiO_2, Al_2O_3, SiC, ZrO_2 nanoparticles with water as the base fluid where the nanofluids flow in pipes with three different materials, i.e., aluminum, copper and stainless. They concluded that the nanofluids have no effect on the erosion of the stainless pipe, while the aluminum pipe has highest erosion. They also found that ZrO_2 and TiO_2 nanoparticles lead to highest erosion while SiC nanoparticles results in lowest erosion.

5. Conclusion

Nanofluids are advanced fluids containing nano-sized particles that have emerged during the last two decades. Nanofluids are used to improve system performance in many thermal engineering systems. This paper presented a review of the applications of nanofluids in solar thermal engineering. The experimental and numerical studies for solar collectors showed that in some cases, the efficiency could increase remarkably by using nanofluids. Of course, it is found that using a nanofluid with higher volume fraction always is not the best option (Yousefi et al. [34]). Therefore, it is suggested that the nanofluids in different volume fractions should be tested to find the optimum volume fraction. It is also seen that the available theoretical works give different results on the effects of particle size on the efficiency of the collectors (see Refs. [27,28]). It is worth to carry out an experimental work on the effect of particle size on the collector efficiency. It is also concluded that some factors such as adding surfactant to nanofluid and a suitable selection of the pH of nanofluid are effective in the collector efficiency. From the economic and environmental point of view, the previous studies showed that using nanofluids in collectors leads to a reduction in CO_2 emissions and annual electricity and fuel savings. Some other reported works of applications of nanofluids in solar cells, solar thermal energy storage, and solar stills are also reviewed. It is also stressed that for the numerical study of solar systems (for example cooling of solar cells), it is better to use the new thermophysical (temperature-dependent) models and two phase mixture models for the nanofluid to have a more exact prediction of the system performance. This review reveals that the application of nanofluids in solar energy is yet in its infancy. Therefore, some proposals are presented to develop the use of nanofluids in different solar systems such as solar ponds, solar thermoelectric cells, and so on. Finally, the most important challenges on the use of nanofluids in solar systems including high costs of production, instability and agglomeration problems, increased pumping power and erosion are mentioned. These challenges may be reduced with the development of nanotechnology in the future.

Acknowledgments

The fifth author wishes to thank the Thailand Research Fund, and the National Research University Project for support for his study. Also, the valuable help of Prof. Akbarzadeh and Dr. Singh from RMIT University, Australia, and Dr. Tyagi from the School of Mechanical, Materials and Energy Engineering, Indian Institute of Technology Ropar, India is appreciated.

References

[1] U.S. Choi, Enhancing thermal conductivity of fluids with nanoparticles, ASME FED 231 (1995) 99–103.
[2] Y. Li, J. Zhou, S. Tung, E. Schneider, S. Xi, A review on development of nanofluid preparation and characterization, Powder Technol. 196 (2009) 89–101.
[3] J.H. Lee, S.H. Lee, C.J. Choi, S.P. Jang, S.U.S. Choi, A review of thermal conductivity data, mechanics and models for nanofluids, Int. J. Micro–Nano Scale Transport 1 (2010) 269–322.
[4] A. Ghadimi, R. Saidur, H.S.C. Metselaar, A review of nanofluid stability properties and characterization in stationary conditions, Int. J. Heat Mass Transfer 54 (2011) 4051–4068.

Author's personal copy

[5] G. Ramesh, N.K. Prabhu, Review of thermo-physical properties, wetting and heat transfer characteristics of nanofluids and their applicability in industrial quench heat treatment, Nanoscale Res. Lett. 6 (2011) 334.
[6] K. Khanafer, K. Vafai, A critical synthesis of thermophysical characteristics of nanofluids, Int. J. Heat Mass Transfer 54 (2011) 4410–4428.
[7] J. Fan, L. Wang, Review of heat conduction in nanofluids, ASME J. Heat Transfer 133 (2011) 040801.
[8] R.S. Vajjha, D.K. Das, A review and analysis on influence of temperature and concentration of nanofluids on thermophysical properties, heat transfer and pumping power, Int. J. Heat Mass Transfer (2012), http://dx.doi.org/10.1016/j.ijheatmasstransfer.2012.03.048.
[9] V. Trisaksri, S. Wongwises, Critical review of heat transfer characteristics of nanofluids, Renew. Sustain. Energy Rev. 11 (2007) 512–523.
[10] W. Daungthongsuk, S. Wongwises, A critical review of convective heat transfer of nanofluids, Renew. Sustain. Energy Rev. 11 (2007) 797–817.
[11] S. Kakaç, Pramuanjaroenkij, Review of convective heat transfer enhancement with nanofluids, Int. J. Heat Mass Transfer 52 (2009) 3187–3196.
[12] L. Godson, B. Raja, D. Mohan, S. Wongwises, Enhancement of heat transfer using nanofluids – An overview, Renew. Sustain. Energy Rev. (2009), http://dx.doi.org/10.1016/j.rser.2009.10.004.
[13] J. Sarkar, A critical review on convective heat transfer correlations of nanofluids, Renew. Sustain. Energy Rev. 11 (2011) 3271–3277.
[14] Y. Ding, H. Chen, L. Wang, C.-Y. Yang, Y. He, W. Yang, W.P. Lee, L. Zhang, R. Huo, Heat transfer intensification using nanofluids, Kona, Nr. 25 (2007) 23–38.
[15] C. Kleinstreuer, J. Li, J. Koo, Microfluidics of nano-drug delivery, Int. J. Heat Mass Transfer 51 (2008) 5590–5597.
[16] R. Saidur, S.N. Kazi, M.S. Hossain, M.M. Rahman, H.A. Mohammed, A review on the performance of nanoparticles suspended with refrigerants and lubricating oils in refrigeration systems, Renew. Sustain. Energy Rev. 15 (2011) 310–323.
[17] S. Thomas, C. Sobhan, A review of experimental investigations on thermal phenomena in nanofluids, Nanoscale Res. Lett. 6 (2011) 377.
[18] W. Escher, T. Brunschwiler, N. Shalkevich, A. Shalkevich, T. Burgi, B. Michel, D. Poulikakos, On the cooling of electronics with nanofluids, ASME J. Heat Transfer 133 (2011) 051401.
[19] O. Abouali, G. Ahmadi, Computer simulations of natural convection of single phase nanofluids in simple enclosures: a critical review, Appl. Therm. Eng. 36 (2012) 1–13.
[20] A. Kamyar, R. Saidur, M. Hasanuzzaman, Application of computational fluid dynamics (CFD) for nanofluids, Int. J. Heat Mass Transfer (2012), http://dx.doi.org/10.1016/j.ijheatmasstransfer.2012.03.052.
[21] H.S. Ahn, M.H. Kim, A review on critical heat flux enhancement with nanofluids and surface modification, ASME J. Heat Transfer 134 (2012) 024001.
[22] R. Saidur, K.Y. Leong, H.A. Mohammad, A review on applications and challenges of nanofluids, Renew. Sustain. Energy Rev. 15 (2011) 1646–1668.
[23] M. Thirugnanasambandam, S. Iniyan, R. Goic, A review of solar thermal technologies, Renew. Sustain. Energy Rev. 14 (2010) 312–322.
[24] A. Sharma, A comprehensive study of solar power in India and World, Renew. Sustain. Energy Rev. 15 (2011) 1767–1776.
[25] S. Mekhilef, R. Saidur, A. Safari, A review on solar energy use in industries, Renew. Sustain. Energy Rev. 15 (2011) 1777–1790.
[26] S.A. Kalogirou, Solar Energy Engineering: Processes and Systems, Elsevier, Oxford, 2009.
[27] H. Tyagi, P. Phelan, R. Prasher, Predicted efficiency of a low-temperature nanofluid – based direct absorption solar collector, J. Solar Energy Eng. 131 (2009) 041004.
[28] T.P. Otanicar, P.E. Phelan, R.S. Prasher, G. Rosengarten, R.A. Taylor, Nanofluid-based direct absorption solar collector, J. Renew. Sustain. Energy 2 (2010) 033102.
[29] R.A. Taylor, P.E. Phelan, T.P. Otanicar, C.A. Walker, M. Nguyen, S. Trimble, R. Prasher, Applicability of nanofluids in high flux solar collectors, J. Renew. Sustain. Energy 3 (2011) 023104.
[30] Y. He, S. Wang, J. Ma, F. Tian, Y. Ren, Experimental study on the light-heat conversion characteristics of nanofluids, Nanosci. Nanotechnol. Lett. 3 (2011) 494–496.
[31] Y. Li, H. Xie, W. Yu, J. Li, Investigation on heat transfer performances of nanofluids in solar collector, Mater. Sci. Forum 694 (2011) 33–36.
[32] R.A. Taylor, P.E. Phelan, T.P. Otanicar, R. Adrian, R.P. Prasher, Nanofluid optical property characterization: towards efficient direct absorption solar collectors, Nanoscale Res. Lett. 6 (2011) 225.
[33] V. Khullar, H. Tyagi, P.E. Phelan, T.P. Otanicar, H. Singh, R.A. Taylor, Solar energy harvesting using nanofluids-based concentrating solar collector, in: Proceedings of MNHMT2012 3rd Micro/Nanoscale Heat & Mass Transfer International Conference on March 3–6, Atlanta, Georgia, USA, 2012.
[34] T. Yousefi, F. Veysi, E. Shojaeizadeh, S. Zinadini, An experimental investigation on the effect of Al_2O_3–H_2O nanofluid on the efficiency of flat-plate solar collectors, Renew. Energy 39 (2012) 293–298.
[35] T. Yousefi, F. Veysi, E. Shojaeizadeh, S. Zinadini, An experimental investigation on the effect of MWCNT–H_2O nanofluid on the efficiency of flat-plate solar collector, Exp. Therm. Fluid Sci. 39 (2012) 207–212.
[36] T. Yousefi, F. Veysi, E. Shojaeizadeh, S. Zinadini, An experimental investigation on the effect of pH variation of MWCNT–H2O nanofluid on the efficiency of a flat-plate solar collector, Solar Energy 86 (2012) 771–779.
[37] S. Link, M.A. El-Sayed, Shape and size dependence of radiative, non-radiative and photothermal properties of gold nanocrystals, Int. Rev. Phys. Chem. 19 (2000) 409–453.
[38] N. Khlebtsov, L. Trachuk, A. Mel'nikov, The effect of the size, shape, and structure of metal nanoparticles on the dependence of their optical properties on the refractive index of a disperse medium, Optics Spectrosc. 98 (1) (2005) 77–83.
[39] E. Sani, L. Mercatelli, S. Barison, C. Pagura, F. Agresti, L. Colla, P. Sansoni, Potential of carbon nanohorn-based suspensions for solar thermal collectors, Solar Energy Mater. Solar Cells 95 (2011) 2994–3000.
[40] L. Mercatelli, E. Sani, G. Zaccanti, F. Martelli, D.P. Ninni, S. Barison, C. Pagura, F. Agresti, D. Jafrancesco, Absorption and scattering properties of carbon nanohorn-based nanofluid for direct sunlight absorbers, Nanoscale Res. Lett. 6 (1) (2011) 282.
[41] L. Mercatelli, E. Sani, D. Fontani, G. Zaccanti, F. Martelli, D.P. Ninni, Scattering and absorption properties of carbon nanohorn-based nanofluids for solar energy applications, J. Euro. Optical Soc. 6 (2011) 11025.
[42] L. Mercatelli, E. Sani, A. Giannini, D.P. Ninni, F. Martelli, G. Zaccanti, Carbon nanohorn-based nanofluids: characterization of the spectral scattering albedo, Nanoscale Res. Lett. 7 (2012) 96.
[43] R. Saidur, T.C. Meng, Z. Said, M. Hasanuzzaman, A. Kamyar, Evaluation of the effect of nanofluid-based absorbers on direct solar collector, Int. J. Heat Mass Transfer 55 (2012) 589–5907.
[44] A. Lenert, E.N. Wang, Optimization of nanofluid volumetric receivers for solar thermal energy conversion, Solar Energy (2011).
[45] A. Lenert, Nanofluid-based receivers for high-temperature, high-flux direct solar collectors. M.Sc. Thesis, Massachusetts Institute of Technology, 2010.
[46] G. Colangelo, E. Favale, A. de Risi, D. Laforgia, Results of experimental investigations on the heat conductivity of nanofluids based on diathermic oil for high temperature applications, Appl. Energy 97 (2012) 828–833.
[47] Y. Kameya, K. Hanamura, Enhancement of solar radiation absorption using nanoparticle suspension, Solar Energy 85 (2011) 299–307.
[48] Y. Gan, L. Qiao, Optical properties and radiation-enhanced evaporation of nanofluid fuels containing carbon-based nanostructures, Energy Fuels 26 (2012) 4224–4230.
[49] Y. Gan, L. Qiao, Radiation-enhanced evaporation of ethanol fuel containing suspended metal nanoparticles, Int. J. Heat Mass Transfer 55 (2012) 5777–5782.
[50] T.P. Otanicar, J. Golden, Comparative environmental and economic analysis of conventional and nanofluid solar hot water technologies, Environ. Sci. Technol. 43 (2009) 6082–6087.
[51] V. Khullar, H. Tyagi, A study on environmental impact of nanofluid based concentrating solar water heating system, Int. J. Environ. Studies 69 (2012) 220–232.
[52] D. Shin, D. Banerjee, Enhancement of specific heat capacity of high-temperature silica-nanofluids synthesized in alkali chloride salt eutectics for solar thermal-energy storage applications, Int. J. Heat Mass Transfer 54 (2011) 1064–1070.
[53] S. Wua, H. Wanga, S. Xiaoa, D. Zhub, Numerical simulation on thermal energy storage behavior of Cu/paraffin nanofluids PCMs, Energy Procedia 31 (2012) 240–244.
[54] M. Elmir, R. Mehdaoui, A. Mojtabi, Numerical simulation of cooling a solar cell by forced convection in the presence of a nanofluid, Energy Procedia 18 (2012) 594–603.
[55] F.J. Wasp, Solid–Liquid Slurry Pipeline Transportation, Trans. Tech, Berlin, 1977.
[56] H.C. Brinkman, The viscosity of concentrated suspensions and solutions, J. Chem. Phys. 20 (1952) 571.
[57] S. Maiga, S.J. Palm, C.T. Nguyen, G. Roy, N. Galanis, Heat transfer enhancement by using nanofluids in forced convection flows, Int. J. Heat Fluid Flow 26 (2005) 530–546.
[58] J. Buongiorno, Convective transport in nanofluids, ASME J. Heat Transfer 128 (2006) 240–250.
[59] C.T. Nguyen, F. Desgranges, G. Roy, N. Galanis, T. Maŕe, S. Boucher, H.A. Mintsa, Temperature and particle-size dependent viscosity data for waterbased nanofluids– hysteresis phenomenon, Int. J. Heat Fluid Flow 28 (2007) 1492–1506.
[60] J. Koo, C. Kleinstreuer, Laminar nanofluid flow in microheat-sinks, Int. J. Heat Mass Transfer 48 (2005) 2652–2661.
[61] W. Duangthongsuk, S. Wongwises, Measurement of temperature-dependent thermal conductivity and viscosity of TiO2–water nanofluids, Exp. Therm. Fluid Sci. 33 (2009) 706–714.
[62] Y. Xuan, Q. Li, W. Hu, Aggregation structure and thermal conductivity of nanofluids, AIChE J. 49 (2003) 1038–1043.
[63] S.P. Jang, S.U.S. Choi, Role of Brownian motion in the enhanced thermal conductivity of nanofluids, Appl. Phys. Lett. 84 (2004) 4316–4318.
[64] J. Koo, C. Kleinstreuer, A new thermal conductivity model for nanofluids, J. Nanopart. Res. 6 (2004) 577–588.
[65] C.H. Chon, K.D. Kihm, S.P. Lee, S.U.S. Choi, Empirical correlation finding the role of temperature and particle size for nanofluid (Al_2O_3) thermal conductivity enhancement, Appl. Phys. Lett. 87 (2005) 153107.
[66] T. Yiamsawasd, A. Dalkilic, S. Wongwises, Measurement of the thermal conductivity of titania and alumina nanofluids, Thermochim. Acta 545 (2012) 48–56.
[67] O. Mahian, A. Kianifar, Mathematical modeling and experimental study of a solar distillation system, Proc. Inst. Mech. Eng., Part C J. Mech. Eng. Sci. 225 (2011) 1203–1212.
[68] A. Kianifar, S. Zeinali Heris, O. Mahian, Exergy and economic analysis of a pyramid shaped solar water purification system: active and passive cases, Energy 38 (2012) 31–36.

Author's personal copy

[69] M.K. Gnanadason, P.S. Kumar, S. Rajakumar, M.H.S. Yousuf, Effect of nanofluids in a vacuum single basin solar still, I.J.AERS 1 (2011) 171–177.
[70] S. Nijmeh, S. Odeh, B. Akash, Experimental and theoretical study of a single-basin solar still in Jordan, Int. Commun. Heat Mass Transfer 32 (2005) 565–572.
[71] A. Bouzoukas, New approaches for cooling photovoltaic/thermal (PV/T) systems, Ph.D Thesis, University of Nottingham, 2008.
[72] C.T. Nguyen, G. Roy, C. Gauthier, N. Galanis, Heat transfer enhancement using Al_2O_3–water nanofluid for an electronic liquid cooling system, Appl. Therm. Eng. 27 (2007) 1501–1506.
[73] M. Elmir, R. Mehdaoui, A. Mojtabi, A vertical magneto-convection in square cavity containing Al_2O_3/water nanofluid: cooling of electronic compounds, Energy Procedia 18 (2012) 724–732.
[74] A. Ijam, R. Saidur, Nanofluid as a coolant for electronic devices (cooling of electronic devices, Appl. Therm. Eng. 32 (2012) 76–82.
[75] S.M. Peyghambarzadeh, S.H. Hashemabadi, M. Seifi Jamnani, S.M. Hoseini, Improving the cooling performance of automobile radiator with Al_2O_3/water nanofluid, Appl. Therm. Eng. 31 (2011) 1833–1838.
[76] T. Hung, W. Yan, Enhancement of thermal performance in double-layered microchannel heat sink with nanofluids, Int. J. Heat Mass Transfer 55 (2012) 3225–3238.
[77] H. Fan, R. Singh, A. Akbarzadeh, Electric power generation from thermoelectric cells using a solar dish concentrator, J. Electron. Mater. 40 (2011). pages !.
[78] H. Tabor, Z. Weinberger, Nonconvecting solar ponds, in: J.F. Kreider, F. Kreith (Eds.), Solar Energy Handbook, McGraw-Hill, New York, 1980.
[79] J. Hull, C.E. Nielsen, P. Golding, Salinity Gradient Solar Ponds, CRC Press, Boca Raton, FL, 1989.
[80] J. Andrews, A. Akbarzadeh, Enhancing the thermal efficiency of solarponds by extracting heat from the gradient layer, Solar Energy 78 (2005) 704–716.
[81] R. Singh, S. Tundee, A. Akbarzadeh, Electric power generation from solar pond using combined thermosyphon and thermoelectric modules, Solar Energy 85 (2011) 371–378.
[82] M. Ozgoren, M. Bilgili, O. Babayigit, Hourly performance prediction of ammoniaewater solar absorption refrigeration, Appl. Therm. Eng. 40 (2012) 80–90.
[83] M. Balghouthi, M.H. Chahbani, A. Guizani, Investigation of a solar cooling installation in Tunisia, Appl. Energy 98 (2012) 138–148.
[84] T.S. Ge, Y.J. Dai, Y. Li, R.Z. Wang, Simulation investigation on solar powered desiccant coated heat exchanger cooling system, Appl. Energy 93 (2012) 532–540.
[85] Z.S. Lu, R.Z. Wang, Z.Z. Xia, X.R. Lu, C.B. Yang, Y.C. Ma, G.B. Ma, Study of a novel solar adsorption cooling system and a solar absorption cooling system with new CPC collectors, Renew. Energy 50 (2013) 299–306.
[86] Y.J. Dai, R.Z. Wang, L. Ni, Experimental investigation and analysis on a thermoelectric refrigerator driven by solar cells, Solar Energy Mater. Solar Cells 77 (2003) 377–391.
[87] M. Alinia, D.D. Ganji, M. Gorji-Bandpy, Numerical study of mixed convection in an inclined two sided lid driven cavity filled with nanofluid using two-phase mixture mode, Int. Commun. Heat Mass Transfer 38 (2011) 1428–1435.
[88] M.N. Pantzali, A.A. Mouza, S.V. Paras, Investigating the efficacy of nanofluids as coolants in plate heat exchangers (PHE), Chem. Eng. Sci. 64 (2009) 3290–3300.
[89] J. Lee, I. Mudawar, Assessment of the effectiveness of nanofluids for singlephase and two-phase heat transfer in micro-channels, Int. J. Heat Mass Transfer 50 (2007) 452–463.
[90] R.A. Taylor, P.E. Phelan, R.J. Adrian, A. Gunawan, T.P. Otanicar, Characterization of light-induced, volumetric steam generation in nanofluids, Int. J. Therm. Sci. 56 (2012) 1–11.
[91] W. Duangthongsuk, S. Wongwises, An experimental study on the heat transfer performance and pressure drop of TiO_2–water nanofluids flowing under a turbulent flow regime, Int. J. Heat Mass Transfer 53 (2010) 334–344.
[92] P. Razi, M.A. Akhavan-Behabadi, M. Saeedinia, Pressure drop and thermal characteristics of CuO-base oil nanofluid laminar flow in flattened tubes under constant heat flux, Int. Commun. Heat Mass Transfer 38 (2011) 964–971.
[93] G.P. Celata, F.D. Annibale, A. Mariani, Nanofluid Flow Effects on metal surfaces, Energia Ambiente e Innovazione 4–5 (2011) 94–98.

Provided for non-commercial research and education use.
Not for reproduction, distribution or commercial use.

This article appeared in a journal published by Elsevier. The attached copy is furnished to the author for internal non-commercial research and education use, including for instruction at the authors institution and sharing with colleagues.

Other uses, including reproduction and distribution, or selling or licensing copies, or posting to personal, institutional or third party websites are prohibited.

In most cases authors are permitted to post their version of the article (e.g. in Word or Tex form) to their personal website or institutional repository. Authors requiring further information regarding Elsevier's archiving and manuscript policies are encouraged to visit:

http://www.elsevier.com/copyright

Author's personal copy

Experimental Thermal and Fluid Science 45 (2013) 8–15

Contents lists available at SciVerse ScienceDirect

Experimental Thermal and Fluid Science

journal homepage: www.elsevier.com/locate/etfs

An experimental investigation of the heat transfer and pressure drop characteristics of a circular tube fitted with rotating turbine-type swirl generators

Weerapun Duangthongsuk [a,b], Somchai Wongwises [b,c,*]

[a] Department of Mechanical Engineering, South-East Asia University, Bangkok, Thailand
[b] Fluid Mechanics, Thermal Engineering and Multiphase Flow Research Lab. (FUTURE), Department of Mechanical Engineering, Faculty of Engineering, King Mongkut's University of Technology Thonburi, Bangmod, Bangkok 10140, Thailand
[c] The Academy of Science, The Royal Institute of Thailand, Sanam Suea Pa, Dusit, Bangkok 10300, Thailand

ARTICLE INFO

Article history:
Received 17 March 2012
Received in revised form 6 July 2012
Accepted 9 September 2012
Available online 2 November 2012

Keywords:
Heat transfer coefficient
Pressure drop
Swirl generator
Passive technique

ABSTRACT

Heat transfer enhancement and flow behaviors in horizontal circular tubes installed with five rotating turbine-type swirl generators (RTSG) are presented experimentally. This type of RTSG is an innovative design that has not been seen in the previous research. Deionized water is used as a working fluid and flows through the test section under turbulent flow conditions. A smooth, stainless steel tube 9.2 mm in ID, 0.4 mm in thickness, and 2.3 m in length is used as the test section. RTSG made from aluminum, with a twisted angle of 60° and a length of 2 cm, are located at 0.46 m equally distant along the test section. When fluid flows through the RTSG, continuously free rotations are observed, and swirl flow after RTSG is created. A DC power supply is used to supply heat load to the test section. Compared with a common, plain tube (without rotating swirl devices), the experimental results indicate that the local heat transfer coefficient of the tube with RTSG inserts is higher than that of the common, plain tube, and they increase when the working fluid flows through the RTSG. Similarly, the wall temperatures of the tube with RTSG inserts are lower than those of the common tube. However, the pressure drop of the tube fitted with RTSG is significantly greater than that of the common, plain tube.

© 2012 Elsevier Inc. All rights reserved.

1. Introduction

Heat transfer enhancement techniques are ways to increase heat transfer performance and minimize the size and cost of heat exchangers. A variety of approaches is concluded by Goldstein et al. [1]. Normally, there are two heat transfer enhancement techniques. The first is a passive technique, and the other is an active technique. The passive technique requires special surface geometries, such as a rough surface, an extended surface, fluid additives, displaced insert devices, or swirl flow devices, whereas the active technique requires external forces, such as an electrical field, stirring of the fluid, fluid and surface vibration, or jet impingement. Focusing on passive techniques, displaced insert devices or swirl flow devices can be equipped inside and outside of the tubes to generate swirl flow, thereby reducing the thermal boundary layer thickness, which leads to an increase in heat transfer performance. However, the addition of some devices into the main flow can cause an increase in the natural pressure drop. A significant increase in heat transfer performance and reduction of the pressure drop to the minimum value are the most suitable ways to improve the heat transfer performance of heat exchangers. As a result, a number of researchers have tried to investigate the heat transfer performance and flow characteristics of conventional tubes with the insertion of swirl flow devices. Several existing articles describing these attempts follow.

Garcia et al. [2] reported on an experimental investigation of heat transfer enhancement of a circular tube with different helical-wire-coil inserts. Water and water-propylene glycol were used as working fluids, along with flowing under laminar, transition, and turbulent flow regimes. Under turbulent flow conditions, their results showed that heat transfer performance and the pressure of wire coils were four times and nine times higher, respectively, than those for plain tubes. However, at a low Reynolds number, the wire coils behaved like smooth tubes. Under transition flow conditions, the heat transfer rate of the wire coils was 200% higher than that of the smooth tube, without a decrease in pumping power. Correlations for predicting the Fanning friction factor and Nusselt number were also proposed.

Tandiroglu [3] reported on the effect of flow geometry parameters on transient forced convective heat transfer of an experimental round tube with baffle inserts. Air was used as a working fluid, and flowing took place under constant heat flux and turbulent flow regimes. Time-averaged Nusselt number and time-averaged pressure drop correlations were also proposed.

* Corresponding author at: Fluid Mechanics, Thermal Engineering and Multiphase Flow Research Lab. (FUTURE), Department of Mechanical Engineering, King Mongkut's University of Technology Thonburi, Bangmod, Bangkok 10140, Thailand.
E-mail address: somchai.won@kmutt.ac.th (S. Wongwises).

0894-1777/$ - see front matter © 2012 Elsevier Inc. All rights reserved.
http://dx.doi.org/10.1016/j.expthermflusci.2012.09.009

Author's personal copy

Nomenclature

A	area, m^2
C_p	specific heat, J/kg K
D	diameter, m
f	friction factor
h	heat transfer coefficient, W/m^2 K
I	electric current (A)
k	thermal conductivity, W/m K
L	length of the test tube, m
$\dot{m}$	mass flow rate, kg/s
Nu	Nusselt number
Pr	Prandtl number
ΔP	Pressure drop, Pa
Q	heat transfer rate, W
Re	Reynolds number
T	temperature, °C
u	velocity, m/s
V	electric voltage, V

Greek symbols

ε	roughness, m
ρ	density, kg/m^3
μ	viscosity, kg/ms

Subscript

ave	average
elec	electric
f	fluid
in	inlet
m	mean
out	outlet
s	surface
w	tube wall
x	local distance

Sivashanmugam and Suresh [4] experimentally investigated the heat transfer performance and friction factor of a round tube fitted with a full-length helical screw element with different twist ratios and spacer lengths. Their data indicated that the helical screw inserts with spacers provided higher heat transfer enhancement than those in the round tube only under turbulent flow conditions, and less of a reduction in pumping power was observed. Moreover, the empirical equations for Nusselt number and friction factor were performed.

Chang et al. [5] reported on an experimental study on the local heat transfer coefficient and pressure drop characteristics of a circular tube with a broken twisted tape insert. The data showed that the use of the broken twisted tape insert could increase the heat transfer coefficient and friction factor. Finally, the local Nusselt number and Fanning friction factor correlations for the tube fitted with broken twisted tape were presented.

Garcia et al. [6] reported on the heat transfer performance and pressure drop characteristics of an experimental smooth tube with three different wire coils inserts. The test fluids flowed under laminar and transition conditions. Their results indicated that the use of wire coils did not increase the heat transfer performance at a Reynolds number less than 200. However, at a Reynolds number ranging between 200 and 1000, the heat transfer coefficients of the wire coil inserts were much larger than those of the conventional smooth tube. At a Reynolds number of 1000, eight times the heat transfer coefficient over the smooth tube was obtained.

Kurtbas et al. [7] investigated the effects of propeller-type turbulators fitted into a circular tube on the entropy generation rate and exergy loss rate. The experimental data indicated that the Nusselt number and exergy loss rate of a round tube with propeller-type turbulator inserts were higher than those of a smooth tube.

Sarac and Bali [8] reported on an experimental investigation into the heat transfer and pressure drop characteristics of a circular tube fitted with a decaying swirl flow. Their data showed that a round tube with decaying swirl flow inserts provided higher heat transfer performance than a smooth tube by approximately 18.1–163%.

Gul and Evin [9] reported on an experimental investigation of the heat transfer and friction characteristics under decaying turbulent swirl flow conditions generated by a short helical tape fitted at the entrance of the test section. Their measured data demonstrated that the use of helical tape inserted into the tube led to a significant increase in the heat transfer rate, compared with a circular tube. Moreover, the number of helical channels and the helical angle had no significant effects on heat transfer performance.

Akhavan-Behabadi et al. [10] carried out an experimental study on the heat transfer enhancement and pressure drop characteristics due to twisted tape inserts in a horizontal evaporator of R-134a. The experiments were carried out for four tubes with different twist ratios and refrigerant mass flux.

Kurtbas et al. [11] experimentally investigated the heat transfer performance and pressure drop characteristics of a circular tube fitted with a conical injector-type swirl generator (CITSG). The results demonstrated that the heat transfer enhancement ratio of CITSG decreased with increasing Reynolds number. The director angle and the director diameter and width decreased with increasing CITSG angle.

Akhavan-Behabadi et al. [12] studied the heat transfer coefficient and pressure drop of a round tube with coiled wire inserts during the heating of engine oil. The results showed that the use of coiled wire inserted into the round tube provided higher heat transfer augmentation than the plain tube, by approximately 2.2–3.2 times, and there was an increase in the friction factor. Heat transfer correlations for coiled wire inserts were proposed.

Khali et al. [13] experimentally studied the heat transfer and pressure drop characteristics of turbulent swirling air flow through a sudden expansion pipe. Their data showed that the sudden expansion pipe with a swirl generator inserts remarkably 40% increased the heat transfer performance of the tested pipe. Moreover, the Nusselt number and friction factor correlations for swirl flow were proposed.

In the last year, Zohir et al. [14] examined the heat transfer enhancement and pressure drop characteristics of a sudden expansion pipe experimentally implanted with a propeller-type swirl generator and a spiral spring for turbulent air flow. The measured data showed that the tube with the propeller inserts provided a higher heat transfer rate and a larger pressure drop than the plain tube, by roughly 1.69 times and 1.5 times, respectively. The Nusselt number correlations for propeller inserts were also presented.

Ibrahim [15] presented an experimental investigation on the heat transfer and friction factor characteristics of flat tubes with full-length helical screw-tape inserts. The results indicated that the Nusselt number and friction factor of a flat tube decreased with increasing spacer length, as did the twist ratio. The Nusselt number and friction factor correlations were also presented.

Patil and Babu [16] experimentally studied the heat transfer and pressure drop characteristics of a double-pipe counter flow

Author's personal copy

heat exchanger fitted with full-length twisted tape and full-length screw tape inserts. Their data indicated that the Nusselt number of the screw tape and twisted tape inserts was higher than that of the plain tube, by approximately 5.3 and 2.85 times, respectively. Similarly, the friction factor of the screw tape and twisted tape inserts was found to be 14 and 7.7 times, respectively, that of the plain duct.

As mentioned above, it has been seen that the use of some devices inserted in plain tubes resulted in better heat transfer performance than with a common plain tube. These devices also generate higher pressure drops than that of plain tubes, by roughly four to five times, due to their being fixed or their not freely rotating. Only the research of Kurtbas et al. [7], and Zohir et al. [14] has been concerned with freely rotating swirl devices. However, the sizes of their test tubes have varied from 40 to 100 mm, which are rather large and the fluid used in their studies are air. This research aimed to investigate the heat transfer performance and pressure drop characteristics of a small, round tube (ID = 9.2 mm) fitted with rotating turbine-type swirl generators (RTSGs) at five positions along the test section. These types of RTSG inserts are new designs that have never been seen before in the available literature. Five RTSG with twist angles of 60° were made from aluminum. The length of each RTSG was 2 cm, with thickness of 0.5 mm and diameter of 6.6 mm, and each RTSG had four blades. When the working fluid flowed through the RTSG, continuously free rotation took place, and swirl flow after each RTSG was created. They were expected to improve the heat transfer performance and result in a small decrease in pressure drop. The experimental data for the RTSG inserts were compared with conventional plain tubes.

2. Experimental apparatus and procedures

The experimental apparatus used in this research is shown schematically in Fig. 1. It mainly consisted of two test sections: the first section was the common plain tube, and the other was the tube with RTSG inserts. Moreover, it consisted of two cooling tanks, a pump with a speed controller, and a rotameter. De-ionized water was used as the working fluid flowing under constant heat flux and turbulent flow conditions. The test section was made from stainless steel and was 2.3 m in length, 10 mm in outer diameter, and 0.4 mm in thickness. For the test section with RTSG inserts, five RTSG were mounted at x/L of 0.0, 0.2, 0.4, 0.6 and 0.8, respectively. RTSG with twist angles of 60° were made from aluminum material with 2 cm in length, 0.5 mm thickness, and 6.6 mm in outer diameter, and each RTSG had four blades. Each RTSG was installed inside the transparency tube for observation of the rotation of the RTSG. When the fluid was forced through the RTSG, continuously free rotation was observed, and swirl flow was produced after the RTSG. The detail of the RTSG is shown in Fig. 2. To measure the pressure drop and the bulk temperature of the de-ionization, the differential pressure transmitter and a T-type thermocouple were mounted at both ends of the test section. Similarly, 10 T-type thermocouples were mounted at different longitudinal positions on the outer surface to measure the wall temperature along the test tube. For the thermocouple fixations at the outer wall of the test section, the thermal insulation tape was used to bind the thermocouple end around the tube. The positions of the wall temperature measurements and the RTSG locations are depicted in Fig. 3. A DC power supply was used to supply the heat load to the test section. Cooling tank No. 1, with a 3.52 kW cooling capacity, a 4 kW electric heater, and an RTD with a temperature controller were used to keep the water temperature constant at a desired value. Similarly, cooling tank No. 2, with an 5.28 kW cooling capacity, and an RTD with a temperature controller was used to cool the water temperature leaving from the test section to the setting temperature of tank No. 1. The water flow rate was measured by a rotameter and was controlled by adjusting the rotation speed of the pump. Finally, in order to minimize the

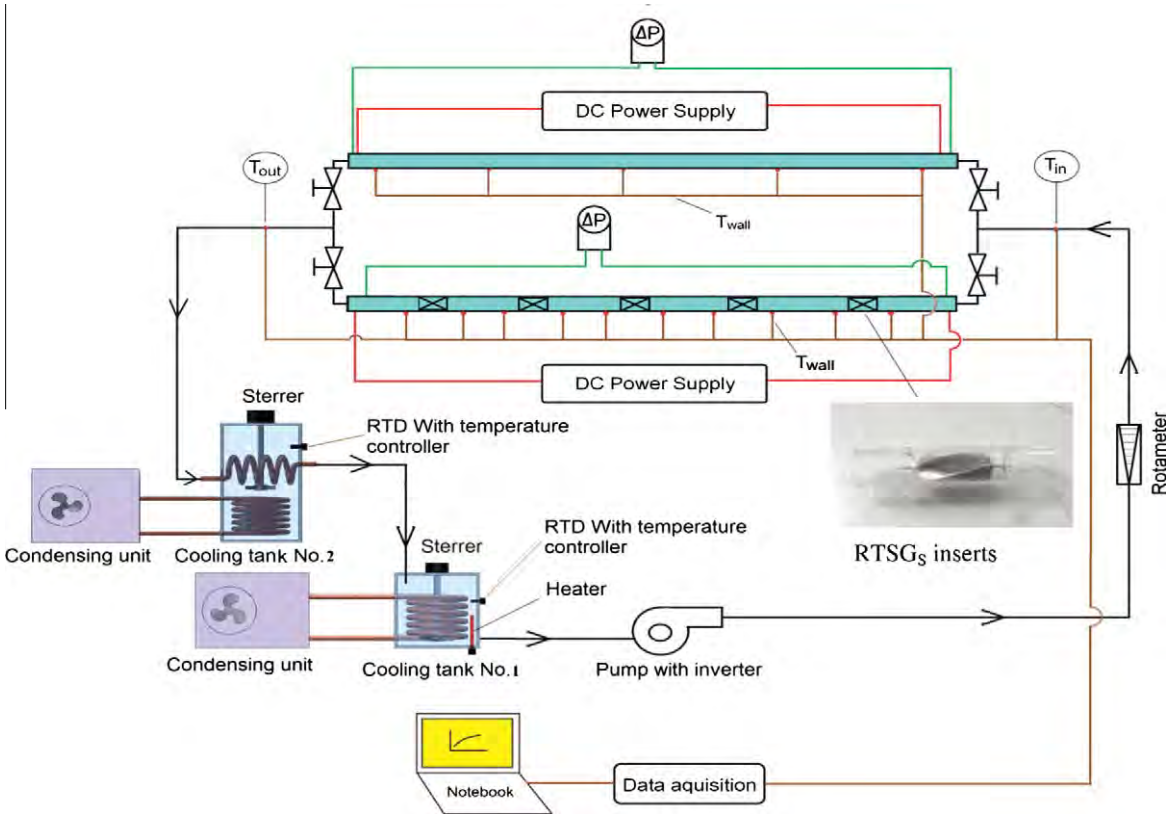

Fig. 1. Schematic diagram of the experimental apparatus used in the present study.

Author's personal copy

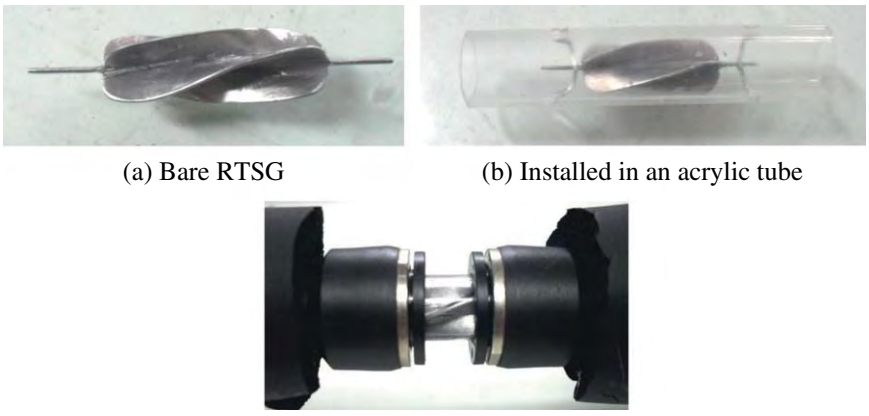

(a) Bare RTSG (b) Installed in an acrylic tube

(c) After fitting in the experimental system

Fig. 2. Configuration of the RTSG used in this study.

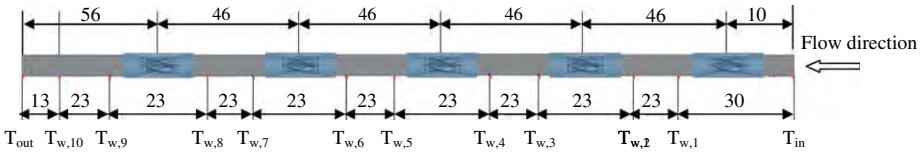

Fig. 3. Position of the wall temperature measurement and the $RTSG_S$ insert (Unit: cm).

Table 1
The dimensions of the test section and testing conditions used in the present study.

Parameter	Quantity
1. Tube length (m)	2.3
2. Outside diameter (mm)	10
3. Tube thickness (mm)	0.4
4. Inlet fluid temperature (°C)	15
5. Wall heat flux (kW/m^2)	15
6. Reynolds number	4500–9500
7. Volume flow rate (LPM)	2–4

heat loss along the test section, the elastomer type insulator with thickness of 20 mm and thermal conductivity of 0.04 W/mK was used to insulate the outer surface of the tube. The dimensions of the test tube and operating conditions are shown in Table 1.

In the present study, the differential pressure transmitter was calibrated using an air-operated dead weight tester. The uncertainty of the pressure measurement was ±0.030 kPa. All of the temperature-measuring devices were well calibrated in a controlled temperature bath, using standard precision mercury glass thermometers. The uncertainty of the temperature measurements as recorded by the data acquisition system was ±0.1 °C. The rotameter was specially calibrated by the manufacturer, and its accuracy was ±7% of full scale. In the present study, the root mean sum square method was used to estimate the uncertainty of the measured data. Therefore, the uncertainty of the measured heat transfer coefficient was approximately 5%.

The experiments were conducted with various flow rates of water. A Reynolds number ranging between 4500 and 9500 was employed. Heat flux was kept at 15 kW/m^2. The inlet water temperature was kept at 15 °C. During each experiment, the heat transferred from the test section was kept at a desired value by adjusting the voltage regulator. The system was allowed to approach a steady state before any data were recorded. After stabilization, the wall temperatures and the inlet and outlet temperatures of the water and the pressure drop across the test section and flow rates of water were all recorded.

3. Data reduction

The accuracy and reliability of the experimental system were tested before measuring the convective heat transfer coefficient and the pressure drop of the round tube fitted with RTSG. Thus, a plain circular tube was tested. The experimental results of the convective heat transfer coefficient and pressure drop were compared with the predicted values obtained from Gnielinski's equation and Colebrook's equation, respectively, which are defined as follows.

The Gnielinski equation [17] is defined as:

$$Nu = \frac{(f/8)(\mathrm{Re}-1000)\mathrm{Pr}}{1+12.7(f/8)^{0.5}(\mathrm{Pr}^{2/3}-1)}, \tag{1}$$

where Nu is the Nusselt number, Re is the Reynolds number, Pr is the Prandtl number, and f is the friction factor.

The Colebrook equation [18] is defined as:

$$\frac{1}{\sqrt{f}} = -2.0\log\left(\frac{\varepsilon/D}{3.7}+\frac{2.51}{\mathrm{Re}\sqrt{f}}\right), \tag{2}$$

The pressure drop across the test section is defined as:

$$\Delta P = f\frac{Lu_m^2}{2D}g, \tag{3}$$

where ΔP is the measured pressure drop, L is the length of the tube, D is the inner diameter of the tube, and u_m is the mean velocity of fluid.

Then, the heat transfer performance of RTSG could be computed from the following equation.

The heat supplied to the test section can be calculated from:

$$Q_{elec} = VI, \tag{4}$$

The heat transfer rate into the fluid was computed from:

$$Q_f = \dot{m}Cp(T_{out}-T_{in}), \tag{5}$$

Author's personal copy

The average heat transfer rate was described as follows:

$$Q_{ave} = \frac{Q_{elec} + Q_f}{2}, \tag{6}$$

where Q_{elec} and Q_f are the heat transfer rate of electric power and the fluid, respectively, Q_{ave} is the average heat transfer rate, V is the electric voltage, I is the electric current, $\dot{m}$ is the mass flow rate of the fluid, Cp is the specific heat, and T_m and T_{out} are the temperature of the water at the inlet and exit, respectively, of the test section. However, the difference between electric power input and energy absorbed by working fluids is approximately less than 2.0%.

The local heat transfer coefficient and the local Nusselt number are evaluated from the following equations:

$$h_x = \frac{q}{(T_w - T_f)_x}, \tag{7}$$

$$Nu_x = \frac{h_x D}{k}, \tag{8}$$

The bulk fluid temperature along the test section is calculated from:

$$T_{f,2} = T_{f,1} + \frac{q\pi Dx}{\dot{m}C_P}, \tag{9}$$

where h_x is the local heat transfer coefficient, T_{wall} is the average wall temperature of the tube, q is the wall heat flux, T_f is the bulk temperature of the fluid at each section, x is the length of the each section, Nu_x is the local Nusselt number, A_S is the surface area of the test tube, and k is the thermal conductivity of the fluid.

The average heat transfer coefficient (h_{ave}) can be computed by using the following equation:

$$h_{ave} = \frac{1}{L}\int_{x_1}^{x_2} h_x dx = \frac{1}{L}\sum_{i=1}^{n}\frac{1}{2}(h_{x,i} + h_{x,i+1})x_i, . \tag{10}$$

Moreover, the Reynolds number can be calculated by using the following equation:

$$\mathrm{Re} = \frac{\rho u_m D}{\mu}, \tag{11}$$

where ρ is the density, and μ is the viscosity of the fluids.

Similarly, the Prandtl number is defined as:

$$\mathrm{Pr} = \frac{\mu Cp}{k}. \tag{12}$$

For cases of pressure drop, the measured pressure drops of RTSG were compared with the conventional plain tube.

4. Results and discussion

As shown in Figs. 4 and 5, an agreement between the experimental results and the calculated values for the common, plain tube could be seen.

Fig. 6a and b shows the variation of the wall temperature along the test section for the common, plain tube and the RTSG inserts, respectively. For common plain tube, the results showed that the wall temperature increased with the increasing distance of the test section. This result was due to the heat from the electric power continuously transmitted to the test section, which resulted in an increase of the wall temperature. However, for the case of the RTSG inserts, abnormal behavior was obtained. As shown in Fig. 6b, the wall temperature of the test tube decreased after the fluid flowed past the RTSG. This result might due to fluid swirl flow freely rotating after each RTSG, which led to higher heat transfer rate from the tube wall. Thus, the lower wall temperature after the RTSG was obtained.

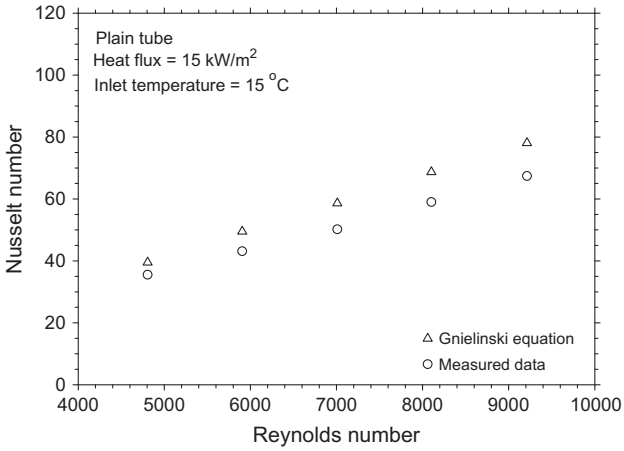

Fig. 4. Comparison between the measured Nusselt number and that calculated from Gnielinski equation.

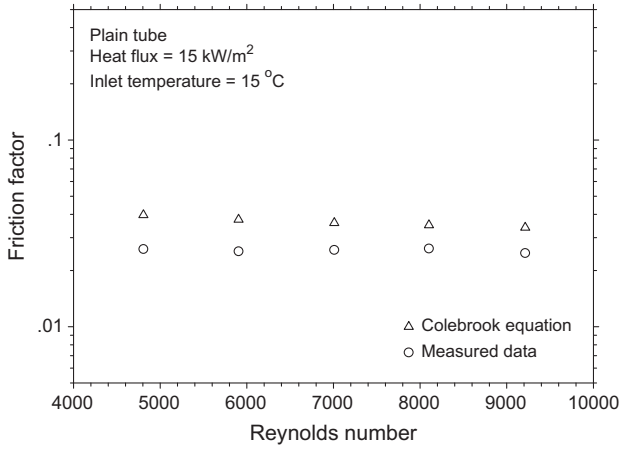

Fig. 5. Comparison between the measured friction factor and that calculated from Colebrook equation.

Fig. 7 shows the comparisons between the local wall temperatures obtained from the common, plain tube and those obtained from the RTSG inserts. The results showed that the wall temperature of the RTSG inserts was lower than that of the common, round tube. This result means that the use of RTSG inserted inside the round tube provide better thermal performance than the conventional plain tube.

Similarly, the variation of the water temperatures along the test tube for the common round tube and the tube fitted with $RTSG_S$ was shown in Fig. 8a and b, respectively. The data indicated that the water temperature along the test section increases with increasing the tube length and varied linearly with the length of the test section. This result was caused from heat supplied to the test tube continuously transferring to the fluid, which led to increase in the water temperature.

Comparison of the water temperature along the test section between common plain tube and RTSG inserts was shown in Fig. 9. The results showed that the tube with RTSG inserts gave lower water temperature than those of the common plain tube. This behavior caused from use of the RTSG inserted into the common tube led to decrease in the wall temperature which resulted decrease in the water temperature at the same time which described in Fig. 7.

Fig. 10a and b shows the variation in the local heat transfer coefficient along the test tube as a function of the volume flow

Author's personal copy

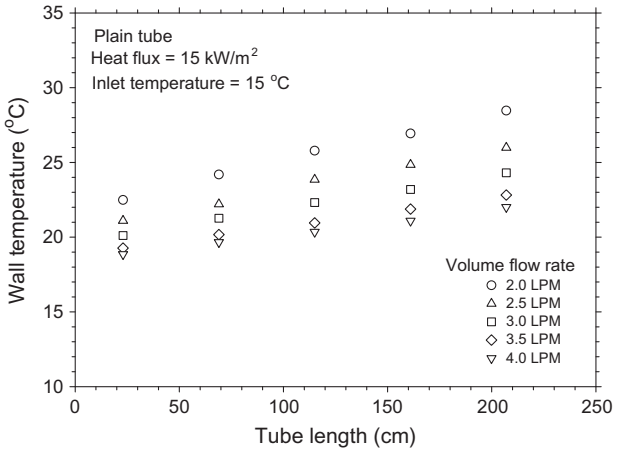

(a) For the common plain tube

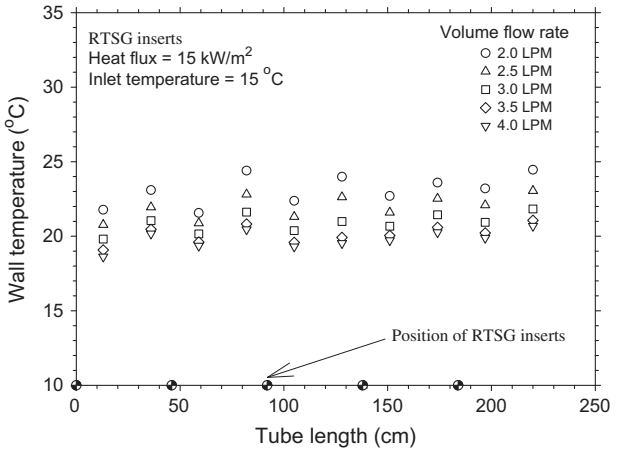

(b) For RTSG inserts

Fig. 6. Variation of the wall temperatures along the test section.

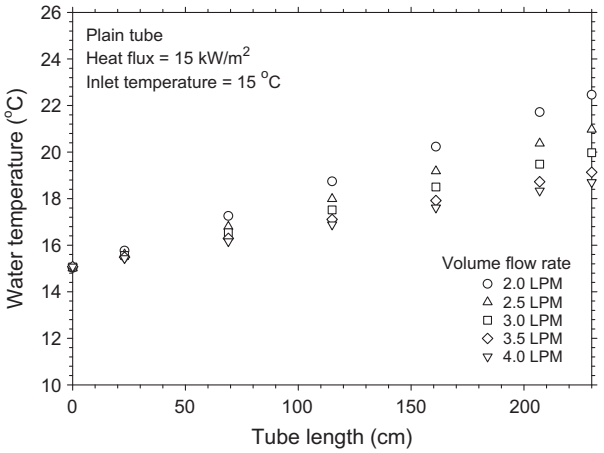

(a) For the common plain tube

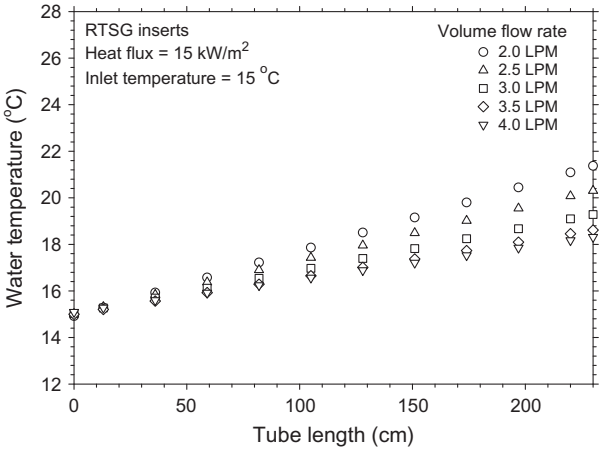

(b) For RTSG inserts

Fig. 8. Variation of the water temperatures along the test section.

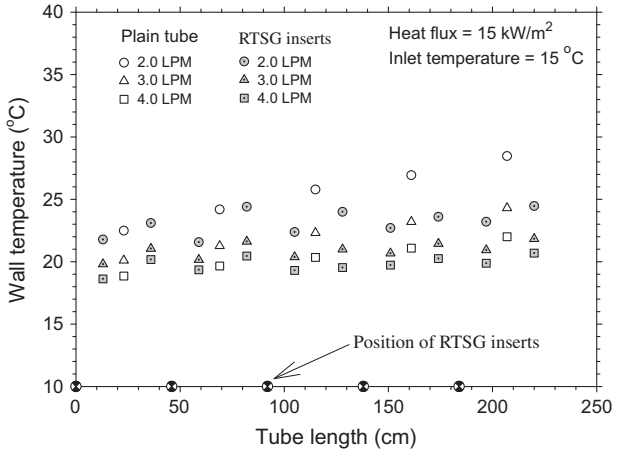

Fig. 7. Comparison of the wall temperature along the test section between the plain tube and the tube fitted with RTSG.

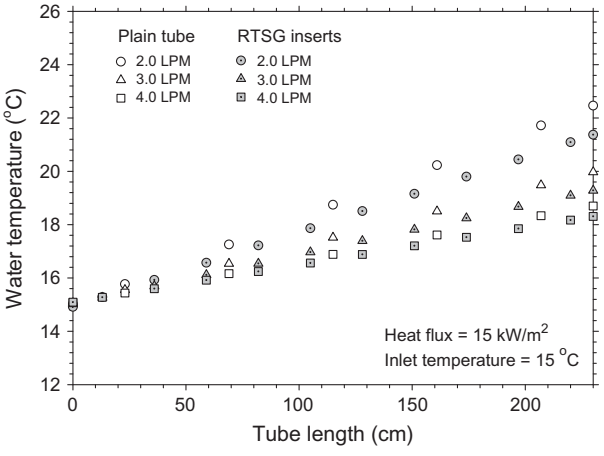

Fig. 9. Comparison of the water temperature along the test section between the plain tube and the RTSG inserts.

rates for the common, plain tube and the RTSG inserts, respectively. For the common, plain tube, the results indicated that the local heat transfer coefficient increased with the increasing volume flow rate and remained constant along the tube length. However, for the case of RTSG inserts, abnormal heat transfer behavior could be clearly seen. From the measured data, it was seen that the heat transfer coefficient of the round tube fitted with RTSG increased with increasing tube length. Moreover, focusing on the position behind the RTSG, a significantly higher heat transfer coefficient is obtained. This result was due to the swirling flow after the RTSG, creating higher heat transfer performance.

Author's personal copy

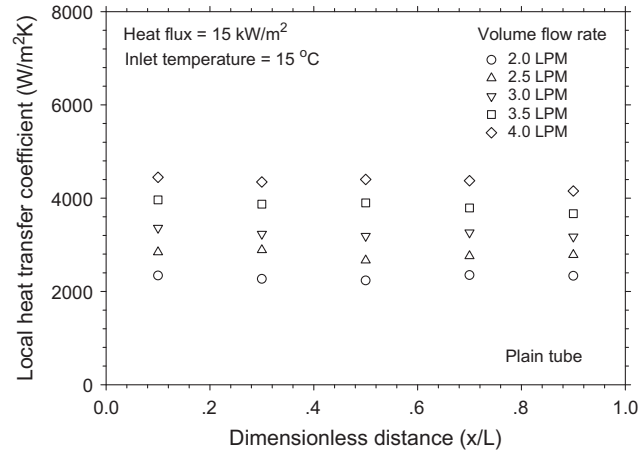

(a) For the common plain tube

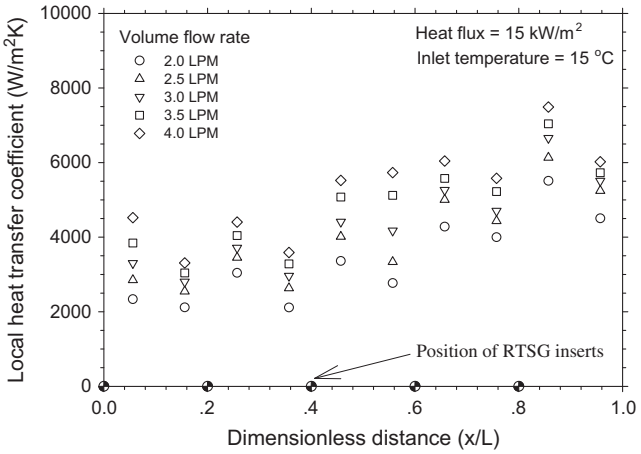

(b) For RTSG inserts

Fig. 10. Local heat transfer coefficient along the test section at different volume flow rates.

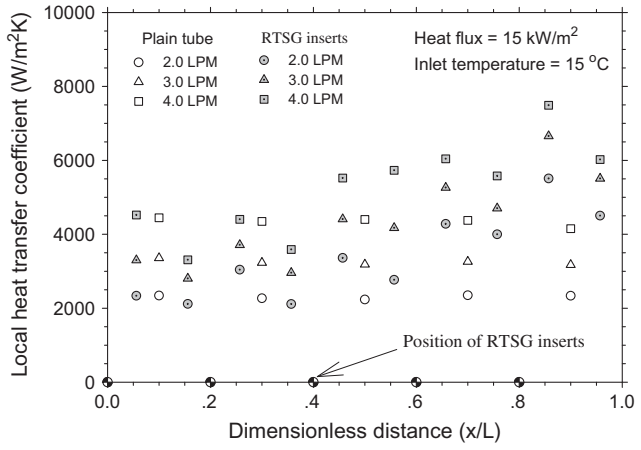

Fig. 11. Comparison of the local heat transfer coefficient between the plain tube and the RTSG inserts.

Fig. 11 also shows comparisons between the local heat transfer coefficients obtained from the common, plain tube and those obtained from the tube fitted with RTSG. The results indicated that the use of RTSG inserted inside a common, round tube provided

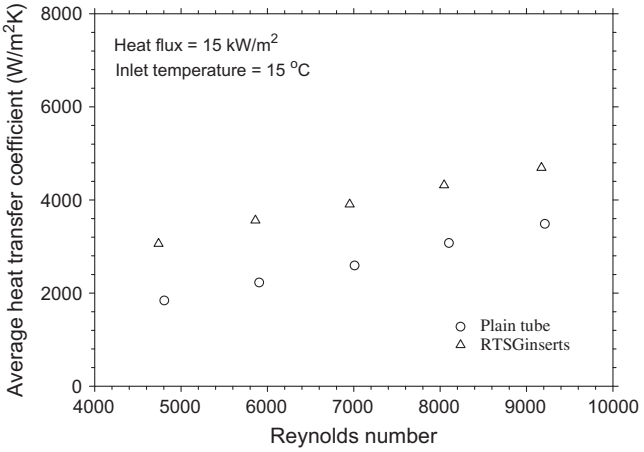

Fig. 12. Comparison of the average heat transfer coefficient between the plain tube and the RTSG inserts.

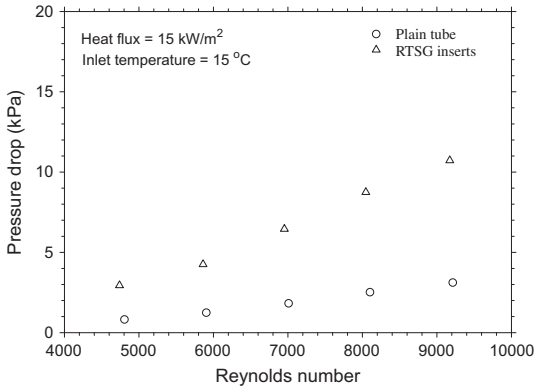

Fig. 13. Comparison of the pressure drop obtained from the common, plain tube and that of the RTSG inserts.

significantly higher heat transfer performance than the plain tube. The results were described in the above sub-section.

Similarly, a comparison of the average heat transfer coefficient between the common, plain tube and the RTSG inserts, as a function of the Reynolds number, is shown in Fig. 12. The measured results showed that the average heat transfer coefficient of the RTSG inserts was approximately 35–37% higher than that of the plain tube and increases with increasing Reynolds number. The reason for this was given in the preceding section. This result was due to the fact that the swirl flow was created after the RTSG in which led to enhance the heat transfer performance.

The pressure drops of the common plain, tube and the tube fitted with RTSG are shown in Fig. 13. The results show that the pressure drop of the RTSG inserts was larger than that of the plain tube by roughly 2.5 times. However, this value was still smaller than in the previous work of other researchers. This behavior, due to a freely rotating device, was used in the present study. Moreover, different distances (short-length tabulators) of RTSG were installed in the round tube, and its configuration could not resist the flow as could a propeller.

5. Conclusions

The heat transfer enhancement and pressure drop characteristics of a plain tube fitted with a rotating turbine-type swirl generator (RTSG) were experimentally investigated. This type of RTSG is

Author's personal copy

an innovative design that has not been seen in the previous research. The measured data for RTSG inserts were compared with the data for the common, plain tube. Important conclusions have been obtained and summarized as follows:

- The tube with RTSG inserts creates abnormal behaviors of the local heat transfer coefficients which increase after the flow passes the RTSG;
- the use of RTSG inserted into the round tube at different locations provided a significantly higher average heat transfer coefficient than that of the common, plain tube by roughly 35%;
- the wall temperatures and water temperature of the round tube with RTSG inserts were lower than those of the common, plain tube, and they significantly decreased after the fluid flowed past the RTSG; and
- the pressure drops of the tube with RTSG inserted were higher than those of the conventional, plain tube by approximately 2.5 times. However, this value was less than that seen in the previous literature, due to the freely rotating device used in the present study.

Acknowledgments

The authors would like to express their appreciation to the Office of Research, South-East Asia University, the Thailand Research Fund, the Office of the Higher Education Commission and the National Research University Project for providing financial support. The authors also wish to thank Mr. Arnont Kamlangsuea and Mr. Theindham Kaenak for their help during our study.

References

[1] R.J. Goldstein, W.E. Ibele, S.V. Patankar, T.W. Simon, T.H. Kuehn, P.J. Strykowski, K.K. Tamma, J.V.R. Heberlein, J.H. Davidson, J. Bischof, F.A. Kulacki, U. Kortshagen, S. Garrick, V. Srinivasan, Heat transfer—A review of 2003 literature, International Journal of Heat and Mass Transfer 49 (2006) 451–534.
[2] A. Garcia, P.G. Vicente, A. Viedma, Experimental study of heat transfer enhancement with wire coil inserts in laminar-transition-turbulent regimes at different Prandtl numbers, International Journal of Heat and Mass Transfer 48 (2005) 4640–4651.
[3] A. Tandiroglu, Effect of flow geometry parameters on transient heat transfer for turbulent flow in a circular tube with baffle inserts, International Journal of Heat and Mass Transfer 49 (2006) 1559–1567.
[4] P. Sivashanmugam, S. Suresh, Experimental studies on heat transfer and friction factor characteristics of turbulent flow through a circular tube fitted with regularly spaced helical screw-tape inserts, Applied Thermal Engineering 27 (2007) 1311–1319.
[5] S.W. Chang, T.L. Yang, J.S. Liou, Heat transfer and pressure drop in tube with broken twisted tape insert, Experimental Thermal and Fluid Science 32 (2007) 489–501.
[6] A. Garcia, J.P. Solano, P.G. Vicente, A. Viedma, Enhancement of laminar and transitional flow heat transfer in tubes by means of wire coil inserts, International Journal of Heat and Mass Transfer 50 (2007) 3176–3189.
[7] I. Kurtbas, A. Durmus, H. Eren, E. Turgut, Effect of propeller type swirl generators on the entropy generation and efficiency of heat exchangers, International Journal of Thermal Sciences 46 (2007) 300–307.
[8] B.A. Sarac, T. Bali, An experimental study on heat transfer and pressure drop characteristics of decaying swirl flow through a circular pipe with a vortex generator, Experimental Thermal and Fluid Science 32 (2007) 158–165.
[9] H. Gul, D. Evin, Heat transfer enhancement in circular tubes using helical swirl generator insert at the entrance, International Journal of Thermal Sciences 46 (2007) 1297–1303.
[10] M.A. Akhavan-Behabadi, R. Kumar, A. Mohammadpour, M. Jamali-Asthiani, Effect of twisted tape insert on heat transfer and pressure drop in horizontal evaporators for the flow of R-134a, International Journal of Refrigeration 32 (2009) 922–930.
[11] I. Kurtbas, F. Gulcimen, A. Akbulut, D. Buran, Heat transfer augmentation by swirl generators inserted into a tube with constant heat flux, International Communications in Heat and Mass Transfer 36 (2009) 865–871.
[12] M.A. Akhavan-Behabadi, R. Kumar, M.R. Salimpour, R. Azimi, Pressure drop and heat transfer augmentation due to coiled wire inserts during laminar flow of oil inside a horizontal tube, International Journal of Thermal Sciences 49 (2010) 373–379.
[13] A. Khali, A.E. Zohir, A.M. Farid, Heat transfer characteristics and friction of turbulent swirling air flow through abrupt expansion, American Journal of Scientific and Industrial Research 1 (2) (2010) 364–374.
[14] A.E. Zohir, A.A. Abdel Aziz, M.A. Habib, Heat transfer characteristics in a sudden expansion pipe equipped with swirl generators, International Journal of Heat and Fluid Flow 32 (2011) 352–361.
[15] E.Z. Ibrahim, Augmentation of laminar flow and heat transfer in flat tubes by means of helical screw-tape inserts, Energy Conversion and Management 52 (2011) 250–257.
[16] S.V. Patil, P.V. Vijay Babu, Performance comparison of twisted tape inserts in square duct, in: Proceedings of the International Conference on Advanced Science, Engineering and Information Technology (Malaysia), 2011, pp. 50–55.
[17] V. Gnielinski, New equations for heat and mass transfer in turbulent pipe and channel flow, International Chemical Engineering 16 (1976) 359–368.
[18] C.F. Colebrook, Turbulent flow in pipes, with particular reference to the transition between the smooth and rough pipe laws, Journal of the Institution of Civil Engineers, London 11 (1939) 133–156.

International Communications in Heat and Mass Transfer 40 (2013) 32–35

Contents lists available at SciVerse ScienceDirect

International Communications in Heat and Mass Transfer

journal homepage: www.elsevier.com/locate/ichmt

Application of two-phase vapor chamber technique for hard disk drive cooling of PCs ☆

P. Naphon [a,*], S. Wongwises [b], S. Wiriyasart [a]

[a] Thermo-Fluids and Heat Transfer Enhancement Lab. (TFHT), Department of Mechanical Engineering, Faculty of Engineering, Srinakharinwirot University, 63 Rangsit-Nakhornnayok Rd., Ongkharak, Nakhorn-Nayok, 26120, Thailand

[b] Fluid Mechanics, Thermal Engineering and Multiphase Flow Research Lab. (FUTURE), Department of Mechanical Engineering, King Mongkut's University of Technology Thonburi, 91 Suksawas 48, Bangmod, Bangkok 10140, Thailand

ARTICLE INFO

Available online 22 October 2012

Keywords:
Vapor chamber
Electronics cooling
Hard disk drive

ABSTRACT

The internal mechanism of the hard disk drive is seriously damaged if it is subjected to forces outside the environmental specifications. The results of the investigation on the thermal cooling of vapor chamber for cooling hard disk drive of the personal computer are presented. It was found that the vapor chamber cooling technique has a significant effect on the thermal cooling of a hard disk drive. The average hard disk drive temperature with the vapor chamber cooling system is 15.21%, which is lower than those without the vapor chamber cooling system. The results of this study are of technological importance for the efficient design of cooling systems of personal computers or electronic devices to enhance cooling performance.

© 2012 Elsevier Ltd. All rights reserved.

1. Introduction

In recent years, the generated heat of PCs or electronic devices has been increasing along with the enhancement of CPU performance, memory capacity, and other devices. Therefore, the cooling system cools not only the CPU, but also others devices such as the HDD. In order to ensure the specified lifetime guarantee, most HDD suppliers do not allow the case temperature of the HDD to exceed 60 °C. For effective cooling the heat must spread to a larger surface area and away from those devices, as there is usually restricted space available. The heat transfer characteristics of the vapor chamber have been widely studied by researchers. Liu et al. [1] investigated on the startup of a novel two-phase cooling loop. Wang et al. [2] studied on the micro capillary pumped loop system for cooling high power devices. Xie et al. [3] experimentally investigated on a novel high-performance integrated heat pipe–heat sink for high-flux chip cooling. Hsieh et al. [4] examined the spreading thermal resistance of a flat vapor chamber. Vin and Astrain [5] studied on the development of a thermoelectric refrigerator with two-phase thermosyphons. Chang et al. [6] experimentally investigated the effects of the evaporation surfaces, fill ratios of working fluid and input heating powers on the thermal performance of the heat pipe cooling system with the thermal resistance model. Chen et al. [7] presented a numerical investigation of a plate-fin heat sink embedded with a vapor chamber, subject to the influence of concentrated heat sources. Zhang et al. [8] numerically and experimentally investigated on the flat two-phase thermosyphon. Vasiliev et al. [9] studied on the loop heat pipe for cooling of high-power electronic components. Ming et al. [10] experimentally and numerically investigated on the grooved vapor chamber. Tsai et al. [11] experimentally investigated on the effects of heat source, fill ratio of working fluid, and evaporator surface structure on the thermal performance of the vapor chamber. Wang et al. [12] considered the thermal performance of the vapor chamber for high-power LEDs. Wong et al. [13] studied on a novel vapor chamber with an inner groove surface. Wang et al. [14] analyzed the thermal characteristics for a board-level high performance package equipped with a vapor chamber. Li et al. [15,16] investigated the effects of the width, height and number of fins on the thermal performance of the vapor chamber. Reyes et al. [17] experimentally and theoretically studied on the vapor chamber based heat spreader. Attia et al. [18] experimentally investigated the effects of different working fluids, and different charge ratios on the thermal performance of the vapor chamber. Ji et al. [19] studied on the vapor chamber performance with sintering of the copper foam pieces. Choi et al. [20] studied a new CPU cooler design based on an active cooling heat sink combined with heat pipes.

As mentioned above, the numerous papers present studies on the heat transfer characteristics of the vapor chamber for cooling electronics devices. However, there are no researches present for the study on the thermal cooling of the hard disk drive (HDD). Therefore, the purpose of this paper is to study the thermal cooling of hard disk drives of personal computers with the vapor chamber. For computer applications, the operating temperatures are normally between 50 and 100 °C. Effects of the operating condition of a PC, and the fill ratio on the hard disk drive temperature are considered.

2. Experimental apparatus and method

The test loop consists of a set of PCs, and a set of vapor chamber cooling system and data acquisition system. A schematic diagram of

☆ Communicated by W.J. Minkowycz.

* Corresponding author.
E-mail address: paisarnn@swu.ac.th (P. Naphon).

0735-1933/$ – see front matter © 2012 Elsevier Ltd. All rights reserved.
http://dx.doi.org/10.1016/j.icheatmasstransfer.2012.10.014

the vapor chamber cooling system is shown in Fig. 1. The vapor chamber cooling system consists of the vapor chamber, the heat sink unit, and the axial fan unit. The vapor chamber is fabricated from a copper plate which consists of a bottom copper plate, a wick sheet, a sinter column, and a top copper plate. The wick sheet and the sinter column are fabricated from the copper powder. The bottom copper plate is the evaporator section that may be mounted on the hard disk drive of the PC to absorb the generated heat, and the other is the condenser section in which heat is transferred to the heat sink and air, respectively. In order to minimize thermal resistance between the HDD-vapor chamber and vapor chamber-heat sink unit, a thin film of high thermal conductivity grease is applied at their junction interface. The working fluid (de-ionized water) is evaporated on the heated side and condensed on the cooling side and then returns to the evaporator section under gravity. Type T copper-constantan thermocouples with an accuracy of 0.1% of full scale are employed to measure the temperatures. Four type T copper-constantan thermocouples are applied to measure the vapor chamber temperature (T_{vc}). Two thermocouples are applied to observe the air temperature in the computer case (T_{case}). A groove within the chamber walls is machined and the high conductivity cement is utilized to embed the thermocouples within the chamber wall. The hard disk drive temperature is measured by four type-T copper-constantan thermocouples (T_{hdd}). All thermocouples are pre-calibrated with a dry box temperature calibrator.

Experiments were conducted with various fill ratios and operating conditions of the PC. The supplied load into the hard disk drive was adjusted to achieve the desired level by setting the operating conditions of the hard disk drive: no load, 50%, and 100% operating loads. The temperatures at each position were recorded in a time period of 200 min. Data collection was carried out using a data acquisition system.

3. Results and discussion

The hard disk drive, with a 5.5-in. size, and two rotating disks with a nominal speed of 15,000 rpm, is tested in the present study. The hard disk drive was supported with insulation blocks under each corner.

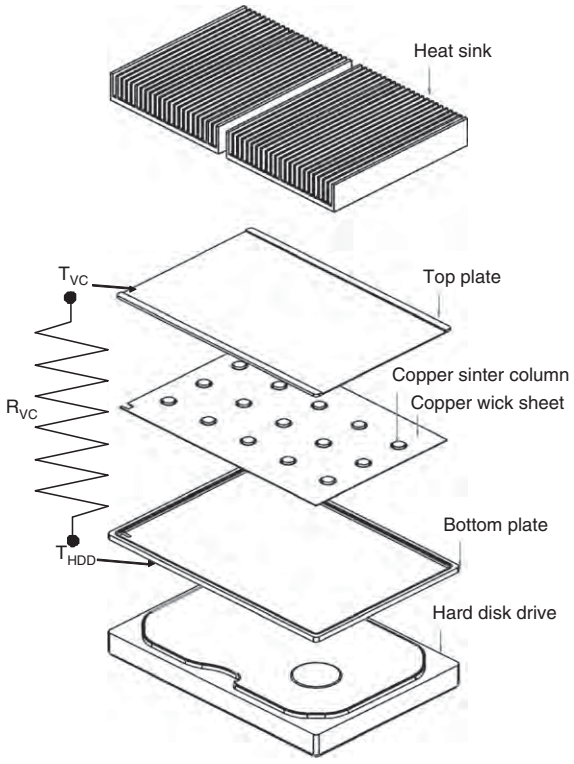

Fig. 1. Schematic diagram of the vapor chamber cooling system.

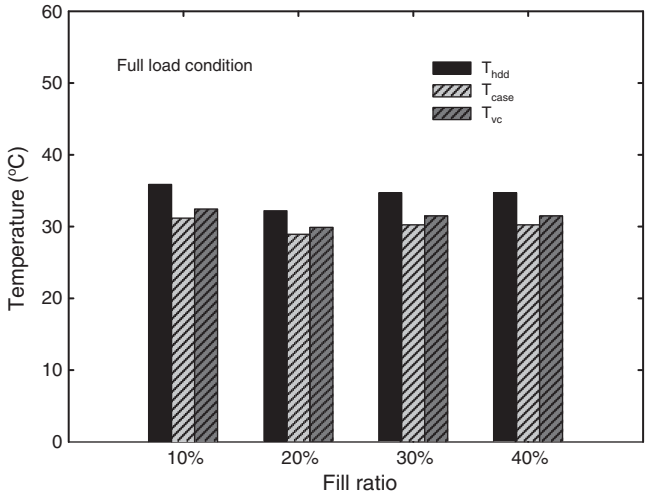

Fig. 2. Variation of HDD, vapor chamber and air temperatures for different fill ratios.

Both the top and bottom surfaces of the hard disk drive were exposed to the quiescent environment of the laboratory room with constant temperature of 26 °C. Initially experiments are performed without the vapor chamber cooling system which forms the basis for comparison of the results with the vapor chamber cooling technique. In order to ensure long life and reliable operations, hard disk drives are all designed to function only in specific temperature ranges. Fig. 2 shows the variation of the temperature of the HDD, vapor chamber and air in the computer temperatures for the different of fill ratios of the working fluid. For all fill ratios of the working fluid, it can be seen that the HDD temperatures are higher than those of the vapor chamber and air on the computer temperature. The full load operation of the HDD can be done by setting the writing data into both partitions of the HDD.

Fig. 3 shows the variation of the hard disk drive temperature for different fill ratios of the working fluid. It can be seen the HDD without the vapor chamber the cooling system gives a temperature higher than those with the vapor chamber cooling system. The values of the heat input to the system by various components depend on the operating condition of the hard disk drive. In general, the heat within the hard disk drive operation is mainly generated by the spindle motor, voice coil motor, magnetic read/write head sensor, and windage loss. Therefore, the HDD temperatures without the operating load are lower than those with the operating load. At a lower operating load, however, the heat is mainly transferred through natural

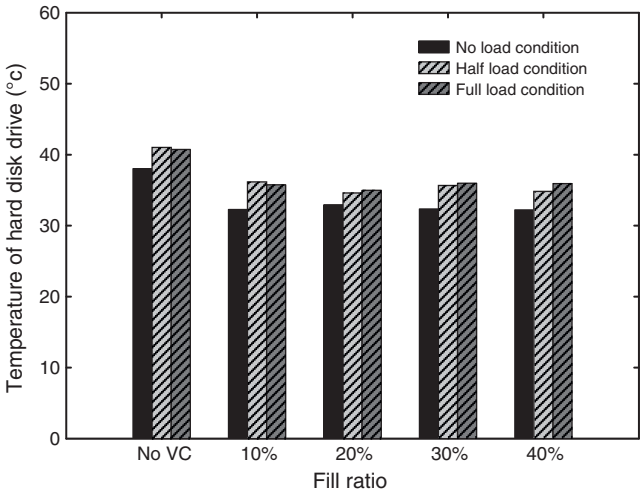

Fig. 3. Variation of HDD temperatures for different fill ratios.

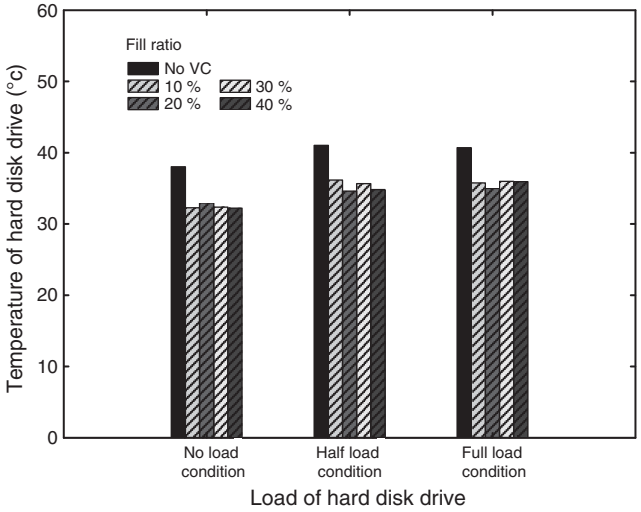

Fig. 4. Variation of HDD temperatures for different operating conditions of HDD.

convection. The increasing operating load induces a larger superheat, which activates and intensifies nucleate boiling and consequently leads to higher heat transfer efficiency. Therefore, a higher operating load of the hard disk drive has a slight effect on the hard disk drive temperature.

Fig. 4 shows the variation of hard disk drive temperature for different operating conditions of HDD. For a given operating load, it can be seen that the HDD temperatures of the HDD with the vapor chamber cooling system are lower than those without the vapor chamber cooling system. In addition, the hard disk drive with a fill ratio of 20% gives the lowest HDD temperature among the other fill ratios. It may be due to the low fill ratio that the dry out phenomenon might happen. The condensing liquid cannot promptly reflow at this operating load. For a higher fill ratio, there is a thin liquid film in the heat input region. The thermal resistance of the phase change heat transfer will also increase with the thickness of the liquid film. Therefore, the vapor chamber with a 20% fill ratio of the vapor chamber gives the lowest HDD temperature among the other fill ratios.

Fig. 5 shows the variation of vapor chamber temperature for different operating conditions of HDD. The average vapor chamber temperature is obtained from the top plate temperature and the bottom plate temperature of the vapor chamber. It can be seen that the fill

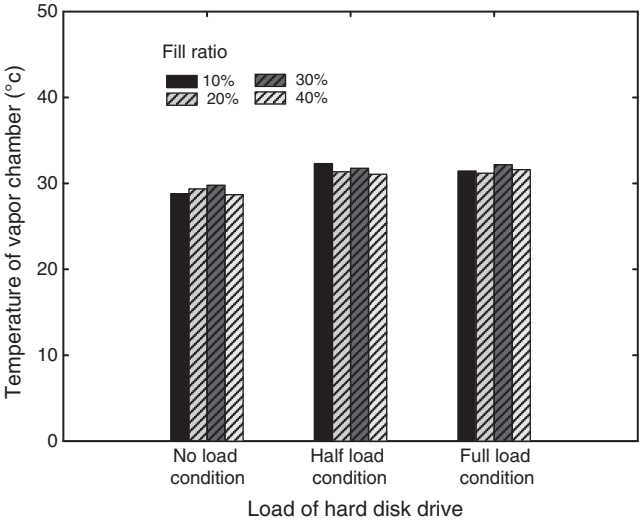

Fig. 5. Variation of vapor chamber temperatures for different operating conditions of HDD.

Table 1
Comparison of the energy consumption and hard disk drive temperature between the hard disk drive with and without vapor chamber cooling system.

Hard disk condition	Energy consumption	Hard disk drive temperature (°C)
HDD with 20% fill ratio for no load condition	+28.57%	−14.16%
HDD with 20% fill ratio for full load condition	+14.81%	−16.21%

ratio of the working fluid has a significant effect on the vapor chamber temperature. The heat phenomenon by the working fluid in the vapor chamber shows how the working fluid absorbs heat from heat source (HDD) and evaporates in the evaporator (bottom plate). The evaporating fluid moves toward the condenser, and then condenses in the condenser (top plate).

The HDD temperature and the energy consumption obtained from the HDD with the vapor chamber cooling system are compared with those without the vapor chamber cooling system. As seen in Table 1, the plus symbol represents the higher values while the minus symbol is represents the lower values as compared with those without the vapor chamber cooling system. It can be seen that the HDD temperatures obtained from the HDD with vapor chamber cooling system are lower than those without vapor chamber cooling system and with the same explanation as mentioned above. However, the energy consumption also increases.

4. Conclusions

Temperature is often quoted as the most important environmental factor affecting hard disk drive reliability. However, the space limitation and air cooling limitation are the encountered problems of the cooling system development of the hard disk drive or electronic devices. The vapor chambers have many advantages as compared to other cooling devices such as fans, thermoelectric modules, and liquid pump loop devices, which are that it has a simple structure, no moving parts and does not use electricity. In addition, selection of the working fluid is based on the operating temperature range of the applications. It is found that the HDD with the vapor chamber cooling system gives HDD temperatures lower than those without the vapor chamber cooling system.

Acknowledgments

The authors would like to express their appreciation to the Excellent Center for Sustainable Engineering (ECSE) of the Srinakharinwirot University (SWU) and the King Mongkut's University of Technology Thonburi (KMUTT) for providing financial support for this study. The authors also wish to acknowledge Fujikura Electronics (Thailand) Ltd. for their assistance in some of the vapor chamber samples.

References

[1] J. Liu, N.Q. Pei, K.H. Guo, Z.H. He, T.X. Li, J.M. Gu, Experimental investigation on startup of a novel two-phase cooling loop, Experimental Thermal and Fluid Science 32 (2008) 939–946.
[2] C.T. Wang, T.S. Leu, T.M. Lai, Micro capillary pumped loop system for a cooling high power device, Experimental Thermal and Fluid Science 32 (2008) 1090–1095.
[3] X.L. Xie, Y.L. He, W.Q. Tao, H.W. Yang, An experimental investigation on a novel high-performance integrated heat pipe–heat sink for high-flux chip cooling, Applied Thermal Engineering 28 (2008) 433–439.
[4] S.S. Hsieh, R.Y. Lee, J.C. Shyu, S.W. Chen, Thermal performance of flat vapor chamber heat spreader, Energy Conversion and Management 49 (2008) 1774–1784.
[5] J.G. Vin, D. Astrain, Development of a thermoelectric refrigerator with two-phase thermosyphons and capillary lift, Applied Thermal Engineering 28 (2008) 1514–1521.
[6] Y.W. Chang, C.H. Cheng, J.C. Wang, S.L. Chen, Heat pipe for cooling of electronic equipment, Energy Conversion and Management 49 (2008) 3398–3404.
[7] Y.S. Chen, K.H. Chien, T.C. Hung, C.C. Wang, Y.M. Ferng, B.S. Pei, Numerical simulation of a heat sink embedded with a vapor chamber and calculation of effective

thermal conductivity of a vapor chamber, Applied Thermal Engineering 29 (2009) 2655–2664.
[8] M. Zhang, Z. Liu, G. Ma, S. Cheng, Numerical simulation and experimental verification of a flat two-phase thermosyphon, Energy Conversion and Management 50 (2009) 1095–1100.
[9] L. Vasiliev, D. Lossouarn, C. Romestant, A. Alexandre, Y. Bertin, Y. Piatsiushyk, V. Romanenkov, Loop heat pipe for cooling of high-power electronic components, International Journal of Heat and Mass Transfer 52 (2009) 301–308.
[10] Z. Ming, L. Zhongliang, M. Guoyuan, The experimental and numerical investigation of a grooved vapor chamber, Applied Thermal Engineering 29 (2009) 422–430.
[11] T.E. Tsai, H.H. Wu, C.C. Chang, S.L. Chen, Two-phase closed thermosyphon vapor-chamber system for electronic cooling, International Communications in Heat and Mass Transfer 37 (2010) 484–489.
[12] J.C. Wang, R.T. Wang, T.L. Chang, D.S. Hwang, Development of 30 Watt high-power LEDs vapor chamber-based plate, International Journal of Heat and Mass Transfer 53 (2010) 3990–4001.
[13] S.C. Wong, K.C. Hsieh, J.D. Wu, W.L. Han, A novel vapor chamber and its performance, International Journal of Heat and Mass Transfer 53 (2010) 2377–2384.
[14] T.H. Wang, C.C. Lee, Y.S. Lai, Thermal characteristics evaluation for board-level high performance flip-chip package equipped with vapor chamber as heat spreader, Microelectronic Engineering 87 (2010) 2463–2467.
[15] H.Y. Li, M.H. Chiang, C.I. Lee, W.J. Yang, Thermal performance of plate-fin vapor chamber heat sinks, International Communications in Heat and Mass Transfer 37 (2010) 731–738.
[16] H.Y. Li, M.H. Chiang, Effects of shield on thermal-fluid performance of vapor chamber heat sink, International Journal of Heat and Mass Transfer 54 (2011) 1410–1419.
[17] M. Reyes, D. Alonso, J.R. Arias, A. Velazquez, Experimental and theoretical study of a vapour chamber based heat spreader for avionics applications, Applied Thermal Engineering 37 (2012) 51–59.
[18] A.A.A. Attia, B.T.A. El-Assal, Experimental investigation of vapor chamber with different working fluids at different charge ratios, Ain Shams Engineering Journal, 2 (2012) 289–297.
[19] X. Ji, J. Xu, A.M. Abanda, Copper foam based vapor chamber for high heat flux dissipation, Experimental Thermal and Fluid Science 40 (2012) 93–102.
[20] J. Choi, M. Jeong, J. Yoo, M. Seo, A new CPU cooler design based on an active cooling heat sink combined with heat pipes, Applied Thermal Engineering 44 (2012) 50–56.

Provided for non-commercial research and education use.
Not for reproduction, distribution or commercial use.

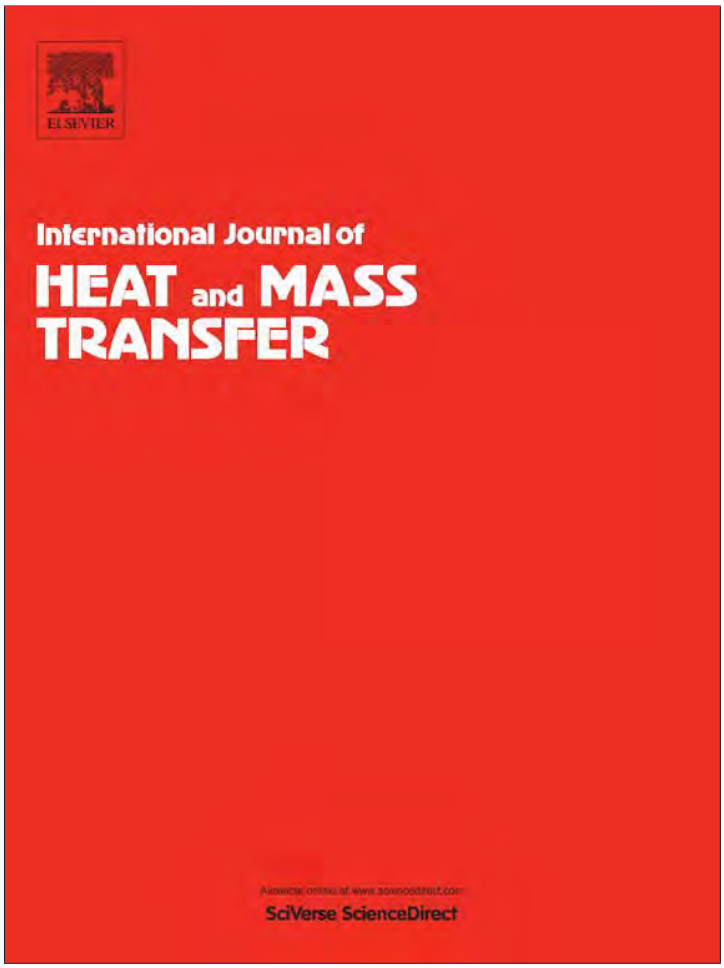

(This is a sample cover image for this issue. The actual cover is not yet available at this time.)

This article appeared in a journal published by Elsevier. The attached copy is furnished to the author for internal non-commercial research and education use, including for instruction at the authors institution and sharing with colleagues.

Other uses, including reproduction and distribution, or selling or licensing copies, or posting to personal, institutional or third party websites are prohibited.

In most cases authors are permitted to post their version of the article (e.g. in Word or Tex form) to their personal website or institutional repository. Authors requiring further information regarding Elsevier's archiving and manuscript policies are encouraged to visit:

http://www.elsevier.com/copyright

Author's personal copy

International Journal of Heat and Mass Transfer 59 (2013) 75–82

Contents lists available at SciVerse ScienceDirect

International Journal of Heat and Mass Transfer

journal homepage: www.elsevier.com/locate/ijhmt

Effect of fin pitches on the air-side performance of L-footed spiral fin-and-tube heat exchangers

Parinya Pongsoi [a], Patcharapit Promoppatum [a], Santi Pikulkajorn [b], Somchai Wongwises [a,c,*]

[a] Fluid Mechanics, Thermal Engineering and Multiphase Flow Research Lab (FUTURE), Department of Mechanical Engineering, Faculty of Engineering, King Mongkut's University of Technology Thonburi, Bangmod, Bangkok 10140, Thailand
[b] Somchai Industry Co., Ltd., Bangkok 10150, Thailand
[c] The Academy of Science, The Royal Institute of Thailand, Sanam Suea Pa, Dusit, Bangkok 10300, Thailand

ARTICLE INFO

Article history:
Received 24 August 2012
Received in revised form 15 November 2012
Accepted 21 November 2012

Keywords:
L-footed fin
Heat transfer
Heat exchanger
Air–water
Extended surface

ABSTRACT

The purpose of this experimental investigation is to investigate the effects of fin pitch (i.e., f_p of 2.4, 3.2, and 4.2 mm) on the air-side heat transfer performance and frictional characteristics of L-footed spiral fin-and-tube heat exchangers at high Reynolds numbers (Re_{dc}) of 4000–15,000. A determinant of the parallel cross-flow and the counter cross-flow is the flow arrangement of the test heat exchangers. Ambient air and hot water are used as a working fluid on the air- and the tube-side, respectively. The results indicate that the air-side heat transfer coefficient and Colburn factor are independent of fin pitch. However, fin pitch does have an influential effect on the average heat transfer rate, pressure drop, and friction factor. In terms of industrial applications, the correlation of the Colburn factor and friction factor are proposed for practical applications.

© 2012 Elsevier Ltd. All rights reserved.

1. Introduction

The heat exchangers are used in two main methods of heat transfer (convection and conduction modes). Many types of heat exchangers are used in industrial applications, such as intercoolers, boilers, economizers, air and liquid pre-heaters, evaporating and condensing heat exchangers, etc. Fin and tube heat exchangers are among the more favored types of heat exchangers. This kind of heat exchanger is designed for enhancing heat transfer performance. This enhancement is very important for thermo-economic analysis. Moreover, this heat transfer enhancement is normally limited by the thermal resistance on the heat exchanger's air-side. Arguably, fin configuration improvement is one of the most effective ways to augment the heat transfer rate on heat exchangers' air-side.

Over the years, the spiral fin has been studied by a number of researchers. Some examples related to this subject can be found in [1–13].

Nuntaphan et al. [1] tested crimped spiral fin-and-tube heat exchangers to analyze the effect of tube arrangement, transverse tube pitch, fin pacing, tube diameter, and they proposed heat transfer and friction characteristics correlations under wet conditions at low Reynolds numbers. Wongwises and Naphon [2,3] studied the heat transfer characteristics and the performance of a spirally coiled finned tube heat exchanger under dry-surface and wet surface conditions. Moreover, they tested heat exchangers that rely on a crimped spiral finned tube. Then, Srisawad and Wongwises [4] tested the helically coiled crimped spiral finned tube heat exchanger, aiming on the heat transfer performance in dry-surface conditions. Pongsoi et al. [5–7] studied the effect of number of tube rows and fin pitches on the air-side heat transfer characteristics and the optimized fin pitch of crimped spiral fin-tube heat exchangers having multipass parallel and counter cross-flow under sensible heating conditions and purpose the ε-*NTU* relation equation for this new water flow arrangement. In addition, the correlation of Colburn factor (j) and friction factor (f) of crimped spiral fin-and-tube heat exchangers at high Reynolds number were proposed in this study. Hamakawa et al. [8] investigated the flow around the fin and vortex shedding from the fin tube by using smoke wire technique. According to results, the spiral fin seemed to have more heat transfer over the conventional circular fin by the influence of downstream rotational vortices. Lee et al. [9,10] studied the air-side heat transfer characteristics of spiral-type circular fin-tube heat exchangers under frosting and non-frosting conditions. They measured these characteristics by varying the fin pitches, the number of tube rows and the fin alignments. Kawaguchi et al. [11] studied the effects of fin pitches on the serrated finned tube bank on

* Corresponding author at: Fluid Mechanics, Thermal Engineering and Multiphase Flow Research Lab (FUTURE), Department of Mechanical Engineering, Faculty of Engineering, King Mongkut's University of Technology Thonburi, Bangmod, Bangkok 10140, Thailand. Tel.: +66 24709115.
E-mail address: somchai.won@kmutt.ac.th (S. Wongwises).

0017-9310/$ - see front matter © 2012 Elsevier Ltd. All rights reserved.
http://dx.doi.org/10.1016/j.ijheatmasstransfer.2012.11.071

Author's personal copy

Nomenclature

A	area, m^2
A_{min}	minimum free flow area, m^2
A_o	total surface area, m^2
A_p	cross-sectional or profile area of fin, m^2
Al	aluminum
c_P	specific heat at constant pressure, J/(kg K)
d_c	fin collar outside diameter, m
d_f	fin outside diameter, m
d_i	tube inside diameter, m
d_o	tube outside diameter, m
f	Fanning friction factor, dimensionless
f_p	fin pitch, m
f_t	fin thickness, m
G_c	mass flux of the air based on minimum free flow area, kg/m^2 s
H	height, m
h	heat transfer coefficient, $W/(m^2 K)$
I_0	modified Bessel function solution of the first kind, order 0
I_1	modified Bessel function solution of the first kind, order 1
j	Colburn factor, dimensionless
k	thermal conductivity, W/(m K)
K_0	modified Bessel function solution of the second kind, order 0
K_1	modified Bessel function solution of the second kind, order 1
L	length, m
m	mass flow rate, kg/s
M	data point
n_t	number of tubes in row
N_{row}	number of tube rows
NTU	number of transfer units, dimensionless
Nu	Nusselt number, dimensionless
P_L	longitudinal tube pitch, m
P_T	transverse tube pitch, m
Pr	Prandtl number, dimensionless
Q	heat transfer rate, W
r_o	radius of tip fin, m
r_i	radius of base fin, m
R	radius function in terms of the radius ratio, dimensionless
Re_{dc}	Reynolds number based on fin collar outside diameter (d_c)
T	temperature, °C
U	overall heat transfer coefficient, $W/(m^2 K)$
V_{fr}	air frontal velocity, m/s
V_{max}	maximum velocity across heat exchanger, m/s

Greek symbols

ε	heat exchanger effectiveness
η	fin efficiency
η_o	overall surface effectiveness
ρ	density, kg/m^3
σ	contraction ratio of cross-sectional area
μ	dynamic viscosity of air, Pa s
ϕ	combination of terms, dimensionless;
ψ	radius ratio
ΔP	pressure drop, Pa

Subscripts

1	air-side inlet
2	air-side outlet
a	air
ave	average
corr	correlation
c	multipass counter cross flow or cold fluid
exp	experiment
f	fin
h	hot fluid
i	tube-side
m	mean value
max	maximum
o	air-side
p	multipass parallel cross flow
pc	multipass parallel-and-counter cross flow
t	tube
w	water

the pressure drop characteristics for higher improvement of heat transfer than circular spiral finned tube. Næss [12] investigated the effects of tube layout and fin geometry on the heat transfer and pressure drop performance of serrated fin and tube heat exchangers. Moreover, Lemouedda et al. [13] studied the optimization of fin serration, fin twisting and the number of segments by numerical calculations for serrated spiral fin-and-tube heat exchangers.

The L-footed spiral fin is one of several types of fin configurations. The base of the fin has an L-shape, which provides a large contact area, ensuring a good path for heat transfer from the tube surface to the fin. The spiral fin seems to have a greater heat transfer coefficient than the conventional circular fin. The L-footed spiral fin-and-tube heat exchanger may be suitable for industrial processes that present a high risk of tube corrosion. Despite its importance in many applications, the air-side performance of L-footed spiral fin-and-tube heat exchangers has received little attention in the literature. To the best of our knowledge, Pongsoi et al. [14] is the only work dealing with this issue. In the present study, the primary concern is to study the heat transfer performance and frictional characteristics of L-footed spiral fin-and-tube heat exchangers at high Reynolds numbers in industrial applications. The effect of fin pitch on the performance of the L-footed spiral fin and tube heat exchangers, which have not yet appeared in the available literature, are presented.

2. Data reduction

In this experimental work, air and hot water were used as working fluids. The main components of the system were the heat exchanger, water flow loop, air supply, and the instrumentation and data acquisition system. In addition, detailed descriptions of the essential components are available from Pongsoi et al. [7].

The test samples are a type of fin-and-tube cross-flow heat exchanger. The copper tube is finned with an aluminum fin. Fig. 1 details the water-side circuit and the dimensions of the tested fin-and-tube heat exchangers. Additionally, the schematic diagram of the heat exchangers algorithm for multi-pass parallel cross-flow, multi-pass counter cross-flow, and multi-pass parallel and counter cross-flows ($N_{row} = 2$) are shown in the previous figure. For the present flow configuration, the heat exchanger's effectiveness lies between the multi-pass parallel cross-flow and the counter cross-flow. Finally, the geometric parameters of the heat exchangers are

Author's personal copy

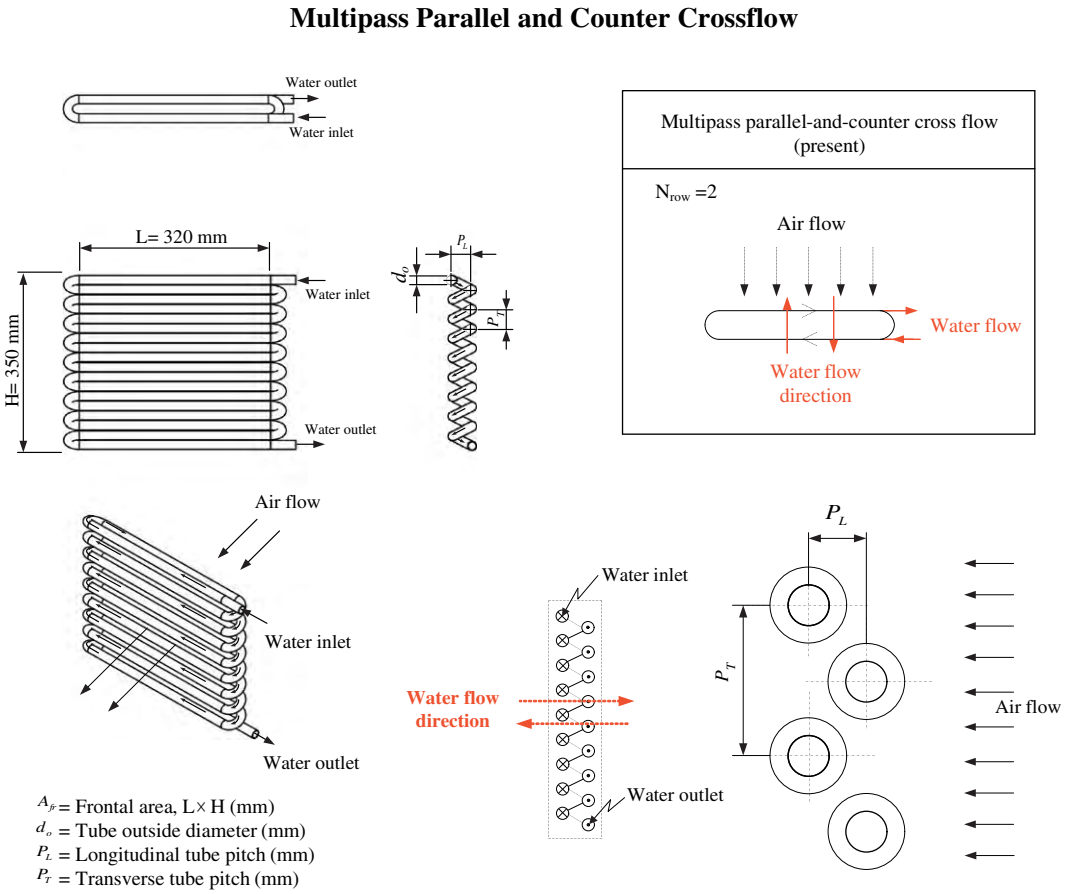

Fig. 1. Geometric details and schematic diagram of the heat exchangers algorithm for multipass parallel cross flow, multipass counter cross flow and multipass parallel-and-counter cross flow (× and ● signs indicate that water flows into or out of the paper, respectively).

Table 1
Detailed geometric parameters of the test samples.

No.	Fin type	d_i (mm)	d_c (mm)	d_f (mm)	P_L (mm)	P_T (mm)	f_t (mm)	n_t	N_{row}	Fin material	f_p (mm)
1	L-footed	13.5	16.85	34.8	35	39	0.25	9	2	Al	**2.4**
2	L-footed	13.5	16.85	34.8	35	39	0.25	9	2	Al	**3.2**
3	L-footed	13.5	16.85	34.8	35	39	0.25	9	2	Al	**4.2**

Remarks: d_f = Outside diameter of fin; d_i = Tube inside diameter; d_c = fin collar outside diameter; f_p = Fin pitch; f_t = Fin thickness; P_L = Longitudinal tube pitch; P_T = Transverse tube pitch; n_t = number of tubes in row; N_{row} = number of tube rows.
Notes: Tube layouts of all heat exchangers are staggered layout and all test sections have a tube outside diameter (d_o) of 16.35 mm.

summarized in Table 1, while the photographs and schematic diagram of L-footed spiral finned tube are shown in Fig. 2.

In the experiment, at a specific inlet water temperature, the water flow rate was fixed while the air flow rate was increased. The system was allowed to approach a steady state before any data was recorded under the experimental conditions shown in Table 2. After the system reached a steady state, the inlet and outlet temperatures of the air passing across the heat exchanger and the water flow rates were determined.

The overall heat transfer coefficient can be written in terms of the total resistance to heat transfer. This total resistance is the sum of the individual resistance values, as follows:

$$\frac{1}{UA} = \frac{1}{h_i A_i} + \frac{ln(d_o/d_i)}{2\pi k_t L} + \frac{ln(d_c/d_o)}{2\pi k_f L} + \frac{1}{\eta_o h_o A_o} \quad (1)$$

The multipass parallel and counter cross-flow used in this experiment is a combination of multipass parallel cross-flow and counter cross-flow. It may be suitable to use the average value of the heat exchanger effectiveness relations shown in Eq. (4). The air-side working fluid and the tube-side working fluid (water) are defined as fluid *A* and fluid B, respectively. It should be noted that the minimum heat capacity rate (C_{min}) is on the air-side (Fluid *A*). Therefore, the following relations are applied in the present calculation.

Multipass parallel cross-flow

For (N_{row} = 2);

$$\varepsilon_p = \left(1 - \frac{K}{2}\right)\left(1 - e^{-2K/C_A^*}\right), \quad K = 1 - e^{-NTU_A(C_A^*/2)} \quad (2)$$

Multipass counter cross-flow

For (N_{row} = 2);

$$\varepsilon_c = 1 - \left[\frac{K}{2} + \left(1 - \frac{K}{2}\right)e^{2K/C_A^*}\right]^{-1}, \quad K = 1 - e^{-NTU_A(C_A^*/2)} \quad (3)$$

where

$$\varepsilon_A = \frac{\varepsilon_p + \varepsilon_c}{2} \quad (4)$$

Author's personal copy

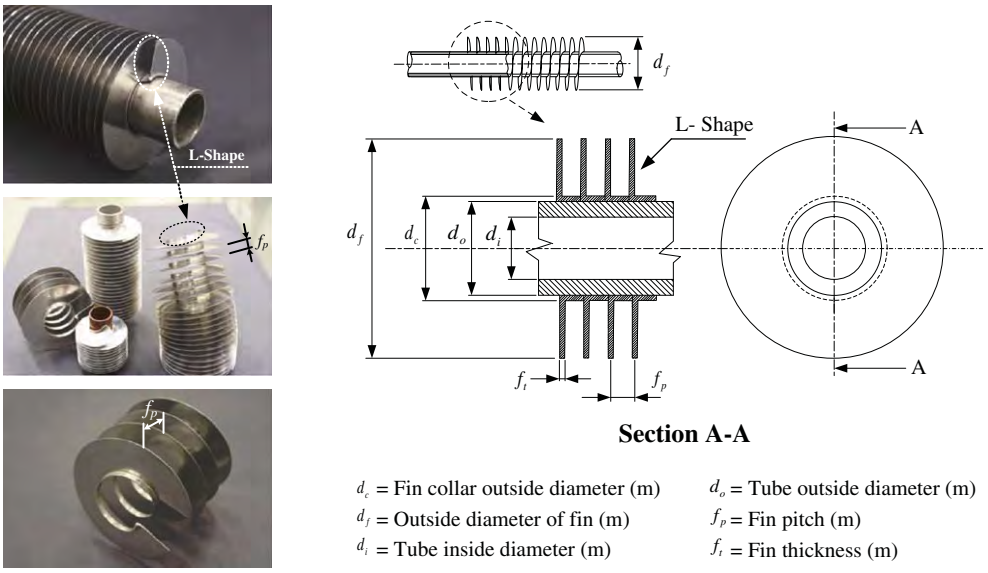

Fig. 2. Photographs and schematic diagram of L-footed spiral finned tube.

Table 2
Experimental conditions.

Inlet-air-dry bulb temperature, °C	31.5 ± 0.5
Inlet-air frontal velocity, m/s	2–8 or Re_{dc} (4000–15000)
Inlet-water temperature, °C	55–70
Water flow rate, LPM	12–14 or (0.2–0.233 kg/s)

Fluid A is mixed (C_{min}); Fluid B is unmixed (C_{max}).

$$\varepsilon_A = \varepsilon_B / C_A^* \tag{5}$$

$$C_A^* = \frac{C_A}{C_B} = \frac{1}{C_B^*}; \quad C^* \leqslant 1 \tag{6}$$

$$NTU_A = \frac{NTU_B}{C_A^*} \tag{7}$$

where $C^* = C_{min}/C_{max}$ is equal to C_c/C_h or C_h/C_c, depending on the value of the hot and cold fluid heat capacity rates.

$$C_{min} = C_h; \quad C_h < C_c \tag{8}$$

or

$$C_{min} = C_c; \quad C_c < C_h \tag{9}$$

as

$$Q_{max} = (mc_P)_c(T_{h1} - T_{c1}) \text{ if } C_c < C_h \tag{10}$$

or

$$Q_{max} = (mc_P)_h(T_{h1} - T_{c1}) \text{ if } C_h < C_c \tag{11}$$

$$\varepsilon = \frac{Q_{ave}}{Q_{max}} \tag{12}$$

The UA term in Eq. (1) is calculated by using Eq. (13):

$$UA = C_{min}(NTU) \tag{13}$$

The efficiency of a radial fin with a rectangular profile is determined by Gardner's [15] proposed method:

$$\eta = \frac{2\psi}{\phi(1+\psi)} \frac{I_1(\phi R_o)K_1(\phi R_i) - I_1(\phi R_i)K_1(\phi R_o)}{I_0(\phi R_i)K_1(\phi R_o) + I_1(\phi R_o)K_0(\phi R_i)} \tag{14}$$

where

$$\phi = (r_o - r_i)^{3/2}\left(\frac{2h_o}{k_f A_p}\right)^{1/2} \tag{15}$$

and where A_p is the area in the profile of the fin, as shown in Fig. 8:

$$A_p = f_t(r_o - r_i) \tag{16}$$

The parameters R_o, R_i are given in terms of the radius ratio (ψ):

$$R_o = \frac{1}{1-\psi} \tag{17}$$

and

$$R_i = \frac{\psi}{1-\psi} \tag{18}$$

where

$$\psi = \frac{r_i}{r_o} \tag{19}$$

The tube-side heat transfer coefficient (h_i) is calculated from the semi-empirical correlation of Gnielinski [16]:

$$h_i = \left(\frac{k_w}{d_i}\right)\frac{(Re_{di} - 1000)Pr(f_i/2)}{1 + 12.7\sqrt{f_i/2}\left(Pr^{2/3} - 1\right)} \tag{20}$$

where the friction factor is given by:

$$f_i = (1.58 \ln Re_{di} - 3.28)^{-2} \tag{21}$$

where $Re_{di} = \rho V d_i/\mu$.

The air-side heat transfer coefficient (h_o) can then be calculated from Eq. (1).

The heat transfer characteristics of the heat exchanger are presented in terms of non-dimensional groups:

$$Re_{dc} = \frac{\rho_a V_{max} d_c}{\mu} \tag{22}$$

$$j = \frac{Nu}{Re_{dc}Pr^{1/3}} = \frac{h_o}{\rho_a V_{max} c_P}(Pr)^{2/3} \tag{23}$$

The flow characteristics determined from the equation proposed by Kays and London [17] are given in terms of the fanning friction factor. The equation includes the entrance and exit pressure losses:

$$f = \left(\frac{A_{min}}{A_o}\right)\left(\frac{\rho_m}{\rho_1}\right)\left[\frac{2\Delta P \rho_1}{G_c^2} - (1+\sigma^2)\left(\frac{\rho_1}{\rho_2} - 1\right)\right] \tag{24}$$

Author's personal copy

where σ is the ratio of minimum free flow area to frontal area, A_o is the total heat transfer area, and A_{min} is the minimum free flow area.

The uncertainties are calculated from the root mean sum square method. The maximum uncertainties are 11% for the j-factor and 10% for the f-factor. The highest uncertainties were associated with the lowest Reynolds numbers.

3. Results and discussion

The primary analysis of the experimental data involved the energy balance between air and water. The energy balance related to systems, which investigated both heat transfer rates. The energy balance between the air and water associated with the L-footed spiral fin-and-tube heat exchangers had relative errors less than 5% (or $|Q_a - Q_w|/Q_{ave} < 0.05$). In addition, it is found that the ranges of the fin efficiency (η) and the heat exchanger effectiveness (ε) are 0.87–0.94 and 0.14–0.36, respectively. The air-side heat transfer and friction characteristics of all heat exchangers were examined in this experiment, which were presented in terms of the average heat transfer rate (Q_{ave}), air-side heat transfer coefficient (h_o), and pressure drop (ΔP) with air frontal velocity (V_{fr}). Moreover, the terms of a dimensionless number included the Colburn factor (j)

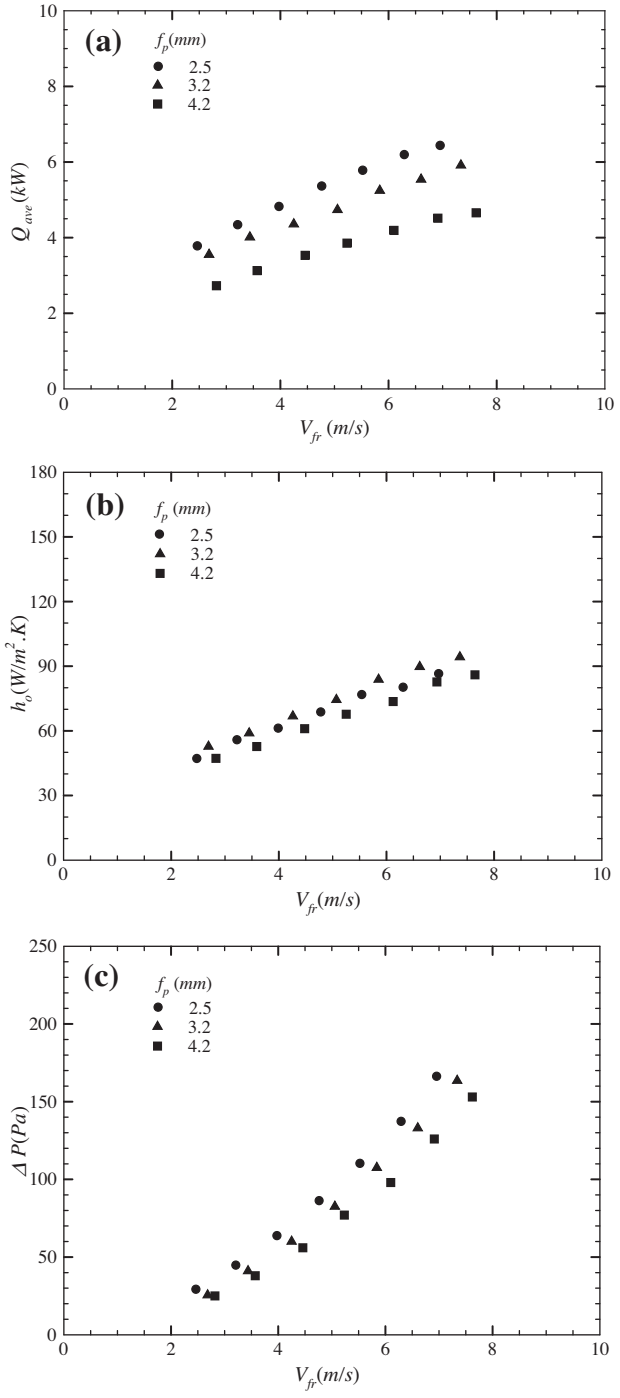

Fig. 3. Effect of fin pitches on the average heat transfer rate (a), heat transfer coefficient (b) and pressure drop (c) of L-footed spiral fin and tube heat exchangers. ($T_{w,in}$ = 65 °C/$m_{w,in}$ = 0.2 kg/s).

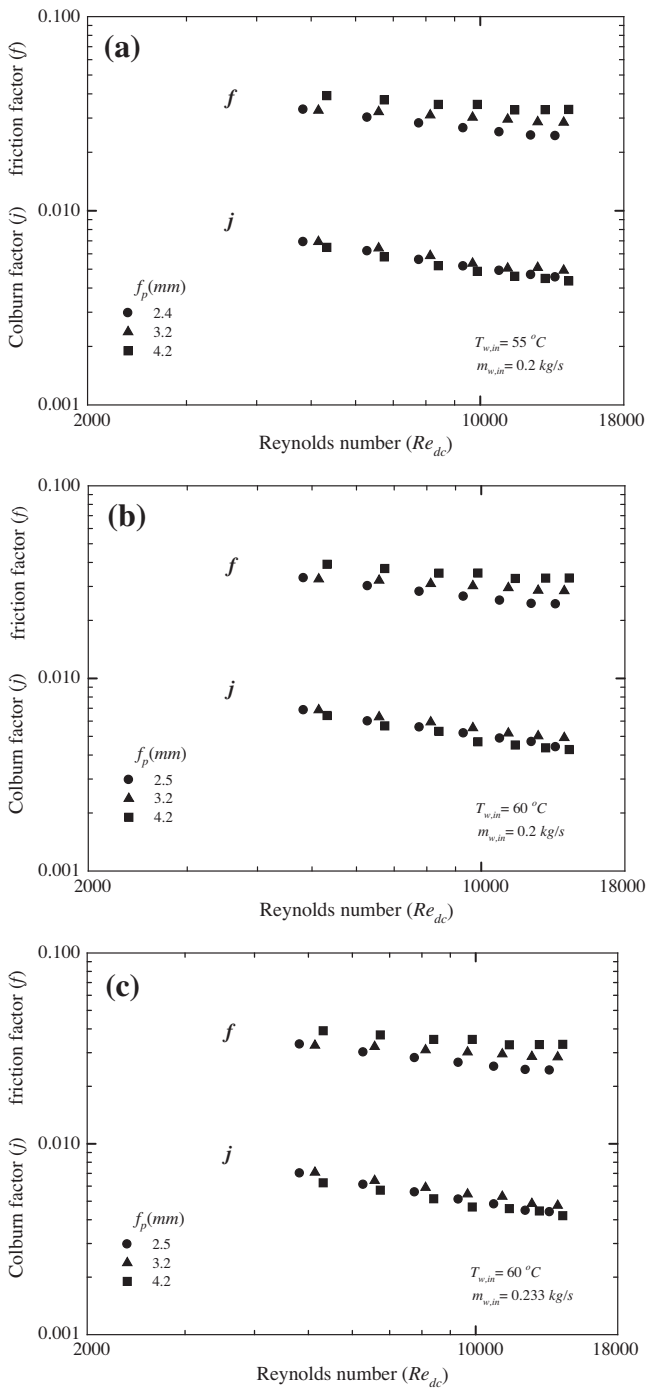

Fig. 4. Effect of fin pitches on the Colburn factor and friction factor at $T_{w,in}$ = 55 °C/$m_{w,i}$ = 0.2 kg/s (a), $T_{w,in}$ = 60 °C/$m_{w,in}$ = 0.2 kg/s (b) and $T_{w,in}$ = 60 °C/$m_{w,in}$ = 0.233 kg/s (c).

Author's personal copy

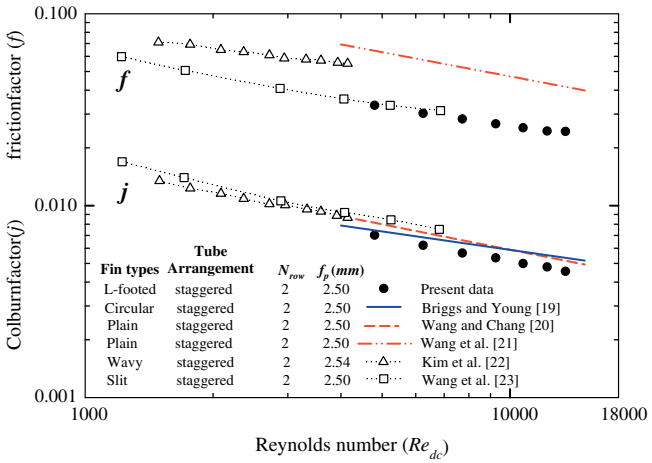

Fig. 5. Comparison of Colburn factor and friction factor between present data with correlational and experimental data of several fin types.

and friction factor (f) plotted against Re_{dc}, which was the Reynolds number based on the fin collar's outside diameter ($d_o + 2f_t$).

Fig. 3 shows the effect of the fin pitches on the average heat transfer rate, air-side heat transfer coefficient, and pressure drop for an aluminum fin with an outside fin collar diameter of 16.85 mm and outside fin diameter of 34.8 mm. This study has extended the fin pitches of 2.4, 3.2, and 4.2 mm. The results show that the average heat transfer rate, air-side heat transfer coefficient, and pressure drop increase with increasing air frontal velocity. Fig. 3(a) depicts the effect of fin pitches on average heat transfer rate. It was found that the average heat transfer rate of $f_p = 2.4$ and 3.2 mm are higher than that for $f_p = 4.2$ mm by about 37% and 26%, respectively, over the range of air frontal velocities. This is be because the surface heat transfer area of the smaller fin pitch is generally higher than that of larger ones which leads to the increasing of the average heat transfer rate.

However, Fig. 3(b) shows that the fin pitches had an insignificant effect on the air-side heat transfer coefficient. The present data correspond with Pongsoi et al. [5], who studied the effect of fin pitch on the air-side performance of the crimped spiral fin. Furthermore, as illustrated in Fig. 3(c), when f_p decreases from 4.2 to 2.4 mm, the pressure drop increases by about 18% (for $f_p = 3.2$) and 38% (for $f_p = 2.4$). The reason for this is increasing pressure blocking the flow area due to decreasing fin pitch.

The examination on the effect of fin pitch in the dimensionless terms is shown in Fig. 4. As expected, both the Colburn factor (j) and the friction factor (f) decrease with increasing Reynolds number over the range of operating conditions. The result shows that the fin pitch has a negligible effect on the Colburn factor (j), which is supported by findings in other research [5,6,18]. This phenomenon occurs because the high Reynolds number accentuates the good mixing, leading to better heat transfer performance, regardless of fin pitch changes.

In terms of the friction factor, it is clear that at Reynolds numbers greater than 6000, fin pitch has a significant effect (i.e., the friction factor is higher for a larger fin pitch than for a smaller fin pitch). According to Eq. (24), the ratio of minimum free-flow area and the total heat transfer area (A_{min}/A_o) and mass flux of air (G_c) showed that A_o significantly increases as fin pitch is changed from 4.2 to 3.2 or 2.4 mm. Conversely, the reduction of A_{min} is comparatively small. For these reasons, the friction factor signals a detectable rise for greater fin pitch. In summary, a large fin pitch increases the ratio of minimum free-flow area and the total heat transfer area (A_{min}/A_o), but decreases mass flux of the air (G_c). A low value of G_c will make the friction factor higher. It should be noted that the dynamic effects (A_{min}/A_o and G_c) have a more pronounced effect upon the friction factor than the air-side pressure drop (ΔP). Nevertheless, the effect of fin pitch on the friction factor tends to vanish at Reynolds numbers less than about 6000.

Initial validation comparison for the air-side heat transfer and flow characteristics of the performance of an L-footed spiral fin contrast with the performance of several plate fin types (circular [19], plain [20,21], wavy [22], and slit [23] fin) at high Reynolds numbers, as shown in Fig. 5. It was found that the present data and other fin types produce similar trends and slopes of the Colburn factor, which decrease with an increasing Reynolds number. However,

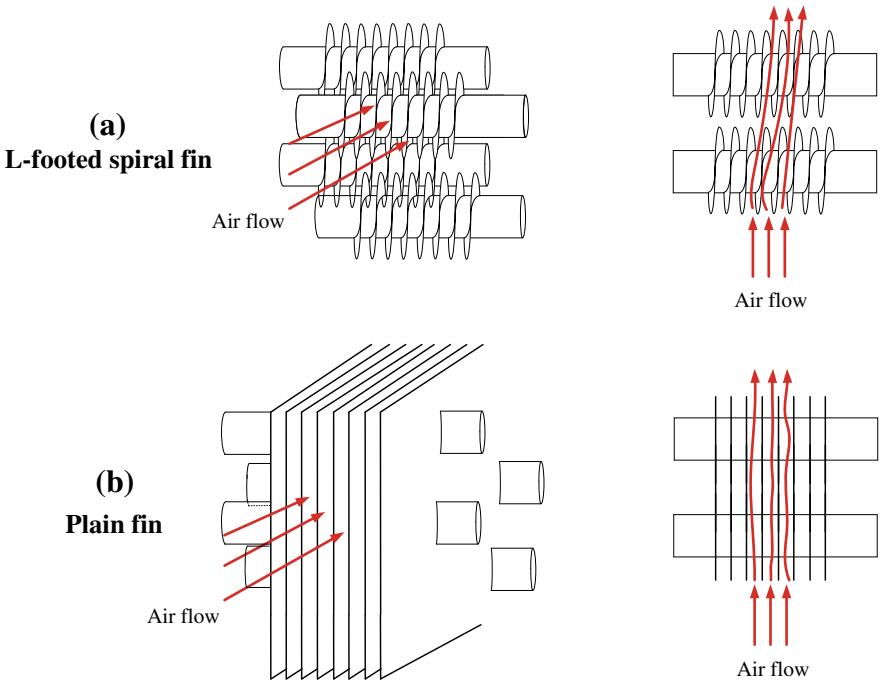

Fig. 6. Schematic showing the flow distribution (a) L-footed spiral fin (b) plain fin.

Author's personal copy

significant difference existed between an L-footed fin and plain fin on the friction factor. The authors found that the friction factor of L-footed spiral fins is about 80–90% different from the plain fin (conventional heat exchanger). As demonstrated in Fig. 6, the plain fin experiences single flow though channels. Therefore, this phenomenon might occur from the geometry of the plain fin that leads to contact surface friction greater than that of L-footed spiral fins.

Finally, empirical correlations for the Colburn factor (j) and the friction factor (f) are proposed in this study which parallel actual industrial applications operated at high Reynolds numbers. It must be noted that fin pitches have a negligible influence on the Colburn factor, as mentioned above. Thus, the fin pitch is not included in the Colburn factor correlation. The present data is correlated as suggested by Pongsoi et al. [6] in the form of $j = aRe_{dc}^{b}$ and $f = aRe_{dc}^{b}\left(\frac{f_p}{d_c}\right)^{c}$, where a, b, and c are the empirical constants obtained from least-square fitting of the experimental data. According to the data analysis, friction factor correlation was also associated with fin pitch. Therefore, the present correlation for f factor is modified by including the dimensionless fin pitch (f_p) normalized by the tube's outside diameter (d_c). The computable correlations for the Colburn and friction factors were suggested according to the form:

$$j_{corr} = 0.2150Re_{dc}^{-0.4059} \tag{25}$$

$$f_{corr} = 0.4852Re_{dc}^{-0.2156}\left(\frac{f_p}{d_c}\right)^{0.4771} \tag{26}$$

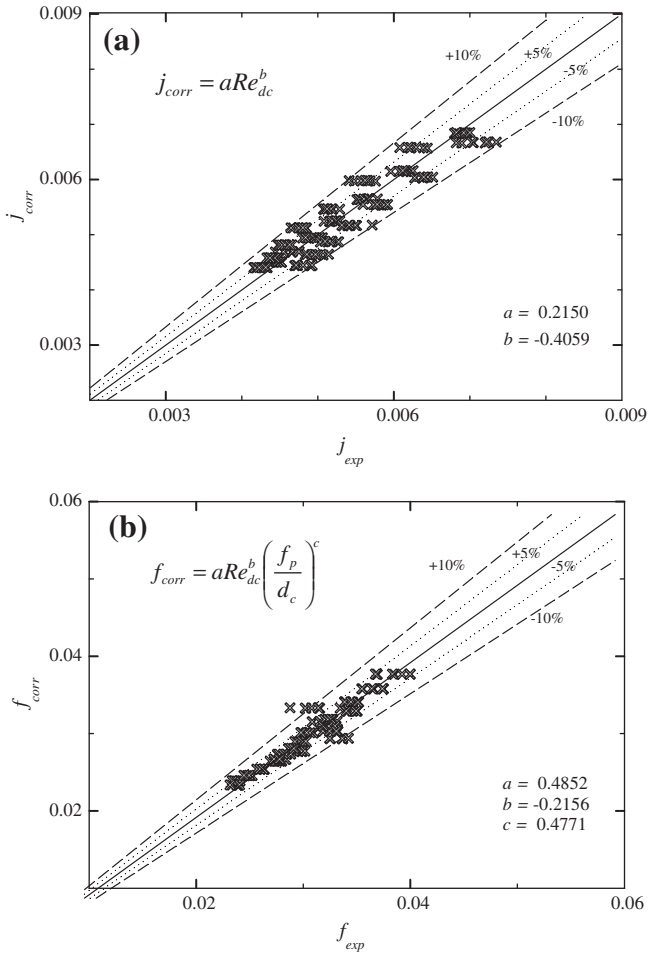

Fig. 7. Comparison of the proposed correlations with experimental data: (a) Colburn factor and (b) friction factor.

$$\text{Mean deviations} = \frac{1}{M}\left[\sum_{1}^{M}\frac{|\Phi_{corr} - \Phi_{exp}|}{\Phi_{exp}}\right] \times 100\% \tag{27}$$

Fig. 7 shows the comparison of the proposed correlations with experimental data. The correlation Eqs. (25) and (26) describe 100% and 95% of the j and f factors, respectively, to be within ±10%. The proposed heat transfer and friction correlations have mean deviations in Eq. (27) of 4.29% and 2.12%, respectively. However, these correlations can be used not only for parallel-and-counter cross-flow types of water flow arrangements, but also used for parallel cross-flow, counter cross-flow, and pure cross-flow.

4. Conclusions

This research determined the extent of the probable effect of fin pitch on the heat transfer performance of L-footed spiral fin-and-tube heat exchangers. Total test sections have a fin thickness of 0.25 mm, outside fin diameter (d_f) of 34.8 mm, two tube rows (N_{row}) and various fin pitches from 2.4, 3.2, and 4.2 mm (i.e., 10, 8, and 6 fpi, respectively), which are the manufacturing limitations for this kind of fin. The test samples were multi-pass parallel-and-counter cross-flows arrangement under sensible heating conditions and examined at a high Reynolds number (4000–15,000) based on the fin collar's outside diameter. In summary, the following major conclusions emerged from this study:

- It was confirmed that the average heat transfer rate, air-side heat transfer coefficient, and pressure drop increase with increasing Reynolds numbers. In addition, the effect of fin pitch on average heat transfer rate and pressure drop were considered significant. On the contrary, results suggest that the air-side heat transfer coefficient is independent of fin pitch.
- Fin pitch has no significant effect on the Colburn factor (j factor) at high Reynolds numbers (4000–15,000).
- The effect of fin pitch on the friction factor is negligible at Reynolds numbers lower than 6000. In other words, a detectable increment in friction factor is found for greater fin pitch when the Reynolds number is more than 6000.
- A correlation is proposed for the Colburn factor (j) and friction factor (f) for L-footed spiral fin-and-tube heat exchangers at high Reynolds number. The mean deviations of the proposed Colburn and friction factors correlations are 4.29% and 2.12%, respectively.
- The authors hope that future research will use this study as a foundation for enhancing our understanding of the effect of fin pitch on L-footed spiral fin-and-tube heat exchangers.

Acknowledgments

The authors are indebted to the Thailand Research Fund, the Office of the Higher Education Commission and the National Research University Project for supporting this study.

References

[1] A. Nuntaphan, T. Kiatsiriroat, C.C. Wang, Heat transfer and friction characteristics of crimped spiral finned heat exchangers with dehumidification, Appl. Therm. Eng. 25 (2005) 327–340.
[2] S. Wongwises, P. Naphon, Heat transfer characteristics of a spiral-coil, finned tube heat exchanger under dry-surface conditions, Heat Transfer Eng. 27 (1) (2006) 25–34.
[3] S. Wongwises, P. Naphon, Thermal performance of a spiral-coil finned tube heat exchanger under wet-surface conditions, J. Mech. Sci. Technol. 20 (2) (2006) 212–226.
[4] K. Srisawad, S. Wongwises, Heat transfer characteristics of a new helically coiled crimped spiral finned tube heat exchanger, Heat Mass Transfer 45 (4) (2009) 381–391.

Author's personal copy

[5] P. Pongsoi, S. Pikulkajorn, C.C. Wang, S. Wongwises, Effect of fin pitches on the air-side performance of crimped spiral fin-and-tube heat exchangers with a multipass parallel and counter cross-flow configuration, Int. J. Heat Mass Transfer 54 (9–10) (2011) 2234–2240.
[6] P. Pongsoi, S. Pikulkajorn, C.C. Wang, S. Wongwises, Effect of number of tube rows on the air-side performance of crimped spiral fin-and-tube heat exchangers with a multipass parallel and counter cross-flow configuration, Int. J. Heat Mass Transfer 55 (4) (2012) 1403–1411.
[7] P. Pongsoi, S. Pikulkajorn, S. Wongwises, Effect of fin pitches on the optimum heat transfer performance of crimped spiral fin-and-tube heat exchangers, Int. J. Heat Mass Transfer 55 (23–24) (2012) 6555–6566.
[8] H. Hamakawa, K. Nakashima, T. Kudo, E. Nishida, T. Fukano, Vortex shedding from a circular cylinder with spiral fin, J. Fluid Sci. Technol. 3 (6) (2008) 787–795.
[9] M. Lee, T. Kang, Y. Kim, Air-side heat transfer characteristics of spiral-type circular fin-and-tube heat exchangers, Int. J. Refrig. 33 (2) (2010) 313–320.
[10] M. Lee, T. Kang, Y. Joo, Y. Kim, Heat transfer characteristics of spirally-coiled circular fin-tube heat exchangers operating under frosting conditions, Int. J. Refrig. 34 (1) (2011) 328–336.
[11] K. Kawaguchi, K. Okui, Y. Asai, Y. Hasegawa, Effects of serrated fin and fin pitch on pressure drop of the finned tube banks, Turbomachinery 32 (2004) 551–559.
[12] E. Næss, Experimental investigation of heat transfer and pressure drop in serrated-fin tube bundles with staggered tube layouts, Appl. Therm. Eng. 30 (2010) 1531–1537.
[13] A. Lemouedda, A. Schmid, E. Franz, M. Breuer, A. Delgado, Numerical investigations for the optimization of serrated finned-tube heat exchangers, Appl. Therm. Eng. 31 (2011) 1393–1401.
[14] P. Pongsoi, S. Pikulkajorn, S. Wongwises, Experimental study on the air-side performance of a multipass parallel and counter cross-flow L-footed spiral fin-and-tube heat exchanger, Heat Transfer Eng. 33 (15) (2012) 1251–1263.
[15] K.A. Gardner, Efficient of extended surface, ASME Trans. 67 (1945) 621.
[16] V. Gnielinski, New equation for heat and mass transfer in turbulent pipe and channel flow, Int. Chem. Eng. 16 (1976) 359–368.
[17] W.M. Kays, A. London, Compact Heat Exchangers, third ed., Mcgraw-Hill, New York, 1984.
[18] S. Wongwises, Y. Chokeman, Effect of fin pitch and number of tube rows on the air side performance of herringbone wavy fin and tube heat exchangers, Energy Convers. Manage. 46 (2005) 2216–2231.
[19] D.E. Briggs, E.H. Young, Convective heat transfer and pressure drop of air flowing across triangular pitch banks of finned tubes, Chem. Eng. Prog. Symp. Ser. 59 (41) (1963) 1–10.
[20] C.C. Wang, C.-T. Chang, Heat and mass transfer for plate fin-and-tube heat exchangers with and without hydrophilic coating, Int. J. Heat Mass Transfer 41 (1998) 3109–3120.
[21] C.C. Wang, Y.J. Chang, Y.C. Hsieh, Y.T. Lin, Sensible heat and friction characteristics of plate fin-and-tube heat exchangers having plane fins, Int. J. Refrig. 19 (4) (1996) 223–230.
[22] N.H. Kim, J.H. Ham, J.P. Cho, Experimental investigation on the airside performance of fin-and-tube heat exchangers having herringbone wave fins and proposal of a new heat transfer and pressure drop correlation, J. Mech. Sci. Technol. 22 (2008) 545–555.
[23] C.C. Wang, W.H. Tao, C.J. Chang, An investigation of the airside performance of the slit fin-and-tube heat exchangers, Int. J. Refrig. 22 (1999) 595–603.

This article was downloaded by: [S. Wongwises]
On: 16 January 2013, At: 20:32
Publisher: Taylor & Francis
Informa Ltd Registered in England and Wales Registered Number: 1072954 Registered office: Mortimer House, 37-41 Mortimer Street, London W1T 3JH, UK

Experimental Heat Transfer: A Journal of Thermal Energy Generation, Transport, Storage, and Conversion

Publication details, including instructions for authors and subscription information:
http://www.tandfonline.com/loi/ueht20

Experimental Study on Evaporative Heat Transfer and Pressure Drop of R-134a Flowing Downward Through Vertical Corrugated Tubes with Different Corrugation Pitches

K. Aroonrat [a] , A. S. Dalkilic [b] & S. Wongwises [a c]

[a] Fluid Mechanics, Thermal Engineering and Multiphase Flow Research Lab (FUTURE), Department of Mechanical Engineering, Faculty of Engineering, King Mongkut's University of Technology Thonburi, Bangmod, Bangkok, Thailand

[b] Heat and Thermodynamics Division, Department of Mechanical Engineering, Yildiz Technical University (YTU), Yildiz, Besiktas, Istanbul, Turkey

[c] The Academy of Science, The Royal Institute of Thailand, Sanam Suea Pa, Dusit, Bangkok, Thailand

To cite this article: K. Aroonrat , A. S. Dalkilic & S. Wongwises (2013): Experimental Study on Evaporative Heat Transfer and Pressure Drop of R-134a Flowing Downward Through Vertical Corrugated Tubes with Different Corrugation Pitches, Experimental Heat Transfer: A Journal of Thermal Energy Generation, Transport, Storage, and Conversion, 26:1, 41-63

To link to this article: http://dx.doi.org/10.1080/08916152.2011.631080

PLEASE SCROLL DOWN FOR ARTICLE

Full terms and conditions of use: http://www.tandfonline.com/page/terms-and-conditions

This article may be used for research, teaching, and private study purposes. Any substantial or systematic reproduction, redistribution, reselling, loan, sub-licensing, systematic supply, or distribution in any form to anyone is expressly forbidden.

The publisher does not give any warranty express or implied or make any representation that the contents will be complete or accurate or up to date. The accuracy of any instructions, formulae, and drug doses should be independently verified with primary sources. The publisher shall not be liable for any loss, actions, claims, proceedings,

demand, or costs or damages whatsoever or howsoever caused arising directly or indirectly in connection with or arising out of the use of this material.

Downloaded by [S. Wongwises] at 20:32 16 January 2013

Experimental Heat Transfer, 26:41–63, 2013
Copyright © Taylor & Francis Group, LLC
ISSN: 0891-6152 print/1521-0480 online
DOI: 10.1080/08916152.2011.631080

Downloaded by [S. Wongwises] at 20:32 16 January 2013

EXPERIMENTAL STUDY ON EVAPORATIVE HEAT TRANSFER AND PRESSURE DROP OF R-134a FLOWING DOWNWARD THROUGH VERTICAL CORRUGATED TUBES WITH DIFFERENT CORRUGATION PITCHES

K. Aroonrat,[1] A. S. Dalkilic,[2] and S. Wongwises[1,3]

[1]Fluid Mechanics, Thermal Engineering and Multiphase Flow Research Lab (FUTURE), Department of Mechanical Engineering, Faculty of Engineering, King Mongkut's University of Technology Thonburi, Bangmod, Bangkok, Thailand

[2]Heat and Thermodynamics Division, Department of Mechanical Engineering, Yildiz Technical University (YTU), Yildiz, Besiktas, Istanbul, Turkey

[3]The Academy of Science, The Royal Institute of Thailand, Sanam Suea Pa, Dusit, Bangkok, Thailand

This study reports an experimental investigation of evaporative heat transfer and pressure drop of R-134a flowing downward inside vertical corrugated tubes with different corrugation pitches. The double tube test section is 0.5 m long with refrigerant flowing in the inner tube and hot water flowing in the annulus. The inner tubes are comprised of one smooth tube and three corrugated tubes with different corrugation pitches of 6.35, 8.46, and 12.7 mm. The test runs are performed at evaporating temperatures of 10°C, 15°C, and 20°C; heat fluxes of 20, 25, and 30 kW/m^2; and mass fluxes of 200, 300, and 400 kg/m^{2}s. The experimental data obtained from the smooth tube are plotted with flow pattern map for vertical flow. Comparisons between smooth and corrugated tubes on the heat transfer and pressure drop are also discussed. It is observed that the heat transfer coefficient and frictional pressure drop obtained from the corrugated tubes are higher than those from the smooth tube. Furthermore, the heat transfer coefficient and frictional pressure drop increase as the corrugation pitch decreases. The maximum heat transfer enhancement factor and penalty factor are up to 1.22 and 4.0, respectively.

Keywords vertical, evaporative, heat transfer, pressure drop, corrugated tube

INTRODUCTION

Heat exchangers are devices used to implement the exchange of heat between two fluids that are at different temperatures and separated by a solid wall. They are commonly used in a wide range of applications, such as refrigeration and air-conditioning systems, power plants, and the chemical process industry. The aim in designing a heat exchanger is to reduce the heat transfer surface area required for a given application and thus reduce the heat exchanger size and material cost or to increase the heat

Received 6 September 2011; accepted 13 September 2011.

Address correspondence to S. Wongwises, Department of Mechanical Engineering, Faculty of Engineering, King Mongkut's University of Technology Thonburi, 126 Pracha-utid Road, Bangmod, Bangkok 10140, Thailand. E-mail: somchai.won@kmutt.ac.th

NOMENCLATURE

A	surface area of the test section (m^2)
c_p	specific heat at constant pressure (J/kg K)
d	tube diameter (m)
e	depth of corrugation (mm)
f	friction factor
g	gravitational acceleration (m/s^2)
G	mass flux (kg/m^2s)
h	heat transfer coefficient (W/m^2K)
i	specific enthalpy (J/kg)
i_{fg}	specific enthalpy of vaporization (J/kg)
J_g	superficial gas velocity, Gx/ρ_g (m/s)
J_l	superficial liquid velocity, $G(1-x)/\rho_l$ (m/s)
k	thermal conductivity (W/m K)
m	mass flow rate (kg/s)
p	pitch of corrugation (mm)
P	pressure (Pa)
Q	heat transfer rate (W)
q''	heat flux (kW/m^2)
Re	Reynolds number
T	temperature (°C)
x	vapor quality
z	axial coordinate (m)

Greek Symbols

α	void fraction
ΔP	pressure drop (Pa/m)
θ	helix angle (°)
μ	dynamic viscosity (kg/m s)
ρ	density (kg/m^3)

Subscripts

avg	average
eq	equivalent
F	frictional term
g	gas/vapor
G	gravitational term
i	inside
in	inlet
l	liquid
M	momentum term
o	outside
out	outlet
ph	pre-heater
ref	refrigerant
sat	saturation
tp	two-phase
TS	test section
w	water
wi	inner wall

Downloaded by [S. Wongwises] at 20:32 16 January 2013

exchanger effectiveness for a given surface area. In recent years, many researchers use the heat transfer enhancement techniques to improve the performance of the heat exchanger. In general, heat transfer enhancement techniques can be categorized as active and passive methods. Active methods are those that use the addition of external power—such as electric field, mechanical vibration, and injection—to facilitate the desired flow modification and concomitant improvement in the rate of heat transfer. Passive methods employ special surface geometries, such as rough surfaces, extended surfaces, and swirl flow devices. Rough surfaces are utilized in many configurations to promote turbulence rather than increase the heat transfer area. A corrugated tube has corrugation on the surface to increase the heat transfer coefficient by mixing the flow boundary layer and increasing the turbulence level of fluid flow.

In past decades, many researchers have thoroughly analyzed the heat transfer and flow characteristics of refrigerants in a horizontal smooth tube. Heat transfer enhancement of refrigerant using horizontal enhanced tubes has been the subject of some research, for example, Thors and Bogart [1]. However, there are not many investigations concerning the heat transfer and pressure drop of refrigerant in vertical tubes. Several experimental studies have been performed on condensation heat transfer and flow characteristics of refrigerant in vertical tube (Briggs et al. [2], Ma et al. [3], and Dalkilic et al. [4–8]). Publications on boiling heat transfer and flow characteristics of refrigerant flow in vertical tubes are summarized as follows.

Downloaded by [S. Wongwises] at 20:32 16 January 2013

Shah [9] proposed equations to fit his chart correlation, used for the estimation of heat transfer coefficients during saturated boiling of water, R-11, R-12, R-22, R-113, and cyclohexanein tubes and annuli. The correlation was shown to be applicable to both horizontal and vertical tubes. Gungor and Winterton [10] presented a new general correlation for forced-convection boiling that has been developed with a large data bank. This data bank consists of more than 4,300 data points for water, refrigerants, and ethylene glycol, covering 7 fluids and 28 authors, mostly for saturated boiling in vertical and horizontal tubes. Kandlikar [11] proposed the correlation for predicting saturated flow boiling heat transfer coefficients inside horizontal and vertical tubes. The correlation has been developed with 5,246 data points for water, refrigerants, and cryogenic fluids from 24 experimental investigations. Lee and Chang [12] investigated the heat transfer characteristics in the post-dryout region for the boiling of up-flow of R-134a in vertical smooth tubes and rifled tubes. Aroonrat and Wongwises [13] investigated the heat transfer and friction characteristics of pure refrigerant R-134a during evaporation inside vertical corrugated tubes. One smooth tube and two corrugated tubes were tested.

Among the above-described works, most experimental investigations focused on the heat transfer and flow characteristics of refrigerant flow inside vertical smooth tubes. There have been some works dealing with the flow in vertical enhanced tubes. In addition, there has been only one work—Aroonrat and Wongwises [13]—concerning the heat transfer and flow characteristics of R-134a during downward evaporation inside vertical corrugated tubes. Although some information is currently available, there still remains room for further research. In particular, the effects of corrugation pitch on the evaporative heat transfer and pressure drop characteristics of R-134a flow through vertical corrugated tubes remain unstudied. As a consequence, the objective of this current work is to study the effect of corrugation pitch on the evaporative heat transfer and pressure drop characteristics of R-134a flowing downward through vertical corrugated tubes. This article presents experimental data that have never been seen before on heat transfer and pressure drop.

EXPERIMENTAL APPARATUS AND METHOD

Figure 1 shows a schematic diagram of the test apparatus. The refrigerant loop consists of a pre-heating loop, test section, heating loop, and chilling loop. The refrigerant is forced by a gear pump controlled by an inverter. The refrigerant then passes through a filter/dryer, a refrigerant flow meter, a pre-heater, and a sight glass, and then enters the test section. The pre-heater controls the inlet quality before entering the test section; it consists of a spiral counter-flow tube-in-tube heat exchanger that is designed to supply heat to prepare an inlet quality for the vaporization of the refrigerant. Leaving the test section, the refrigerant vapor then condenses inside a sub-cooler and is collected in a receiver. After exiting the chilling loop, the refrigerant returns from a two-phase refrigerant to a sub-cooled state. Finally, the refrigerant returns to the refrigerant pump, completing the cycle.

Details of the test section are shown schematically in Figure 2. The test section is a vertical counter-flow double-tube heat exchanger with refrigerant flowing downward in the inner tube and heating water flowing upward in the annulus. Four different inner copper tubes, which are one smooth tube and three corrugated tubes having different corrugation pitches, are tested. The inner diameter and outer diameter of the inner tube

Downloaded by [S. Wongwises] at 20:32 16 January 2013

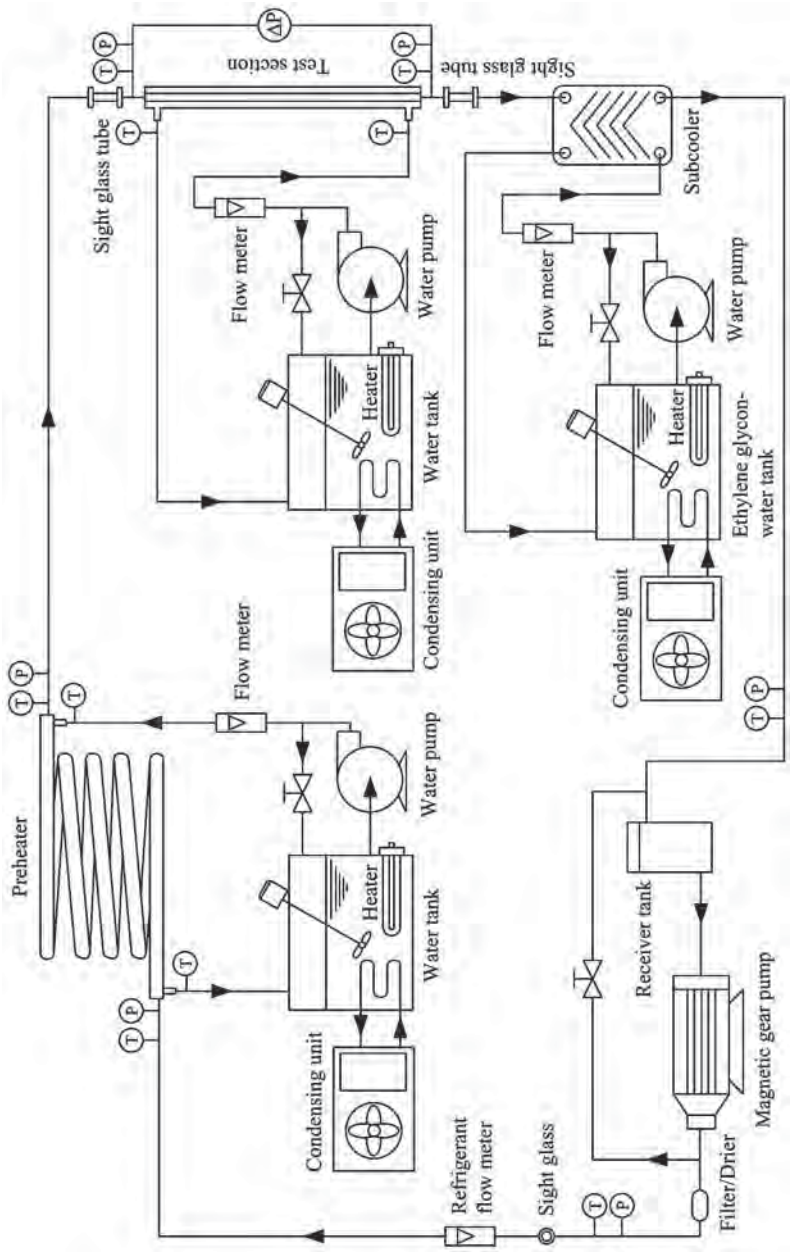

Figure 1. Schematic diagram of the experimental apparatus.

Downloaded by [S. Wongwises] at 20:32 16 January 2013

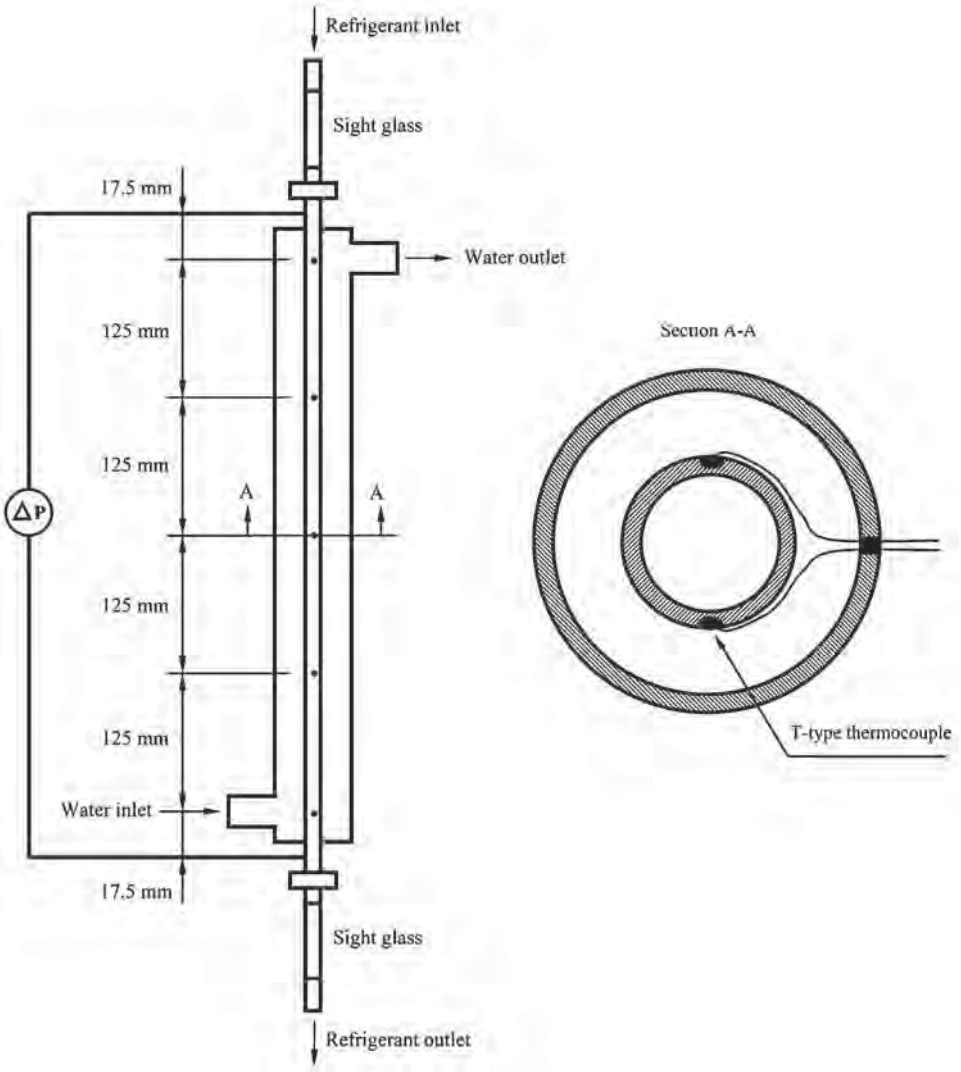

Figure 2. Schematic diagram of the test section.

are 8.7 and 9.52 mm, respectively. The length of the test section is 500 mm. Figure 3 shows the sketch and the actual photograph of the corrugated tube. The dimensions of the test section are listed in Table 1. T-type thermocouples are installed at the inlet and outlet of the test section to measure the saturation temperature of the refrigerant. Similarly, the differential pressure transducer is installed to measure the pressure drop across the test section. The length between the pressure taps is 850 mm. There are ten thermocouples located at five positions along the test section; all of the wall thermocouples are affixed with special glue having low thermal conductivity. The test section is well insulated with a proper material to minimize the heat loss. All of the thermocouples are well calibrated

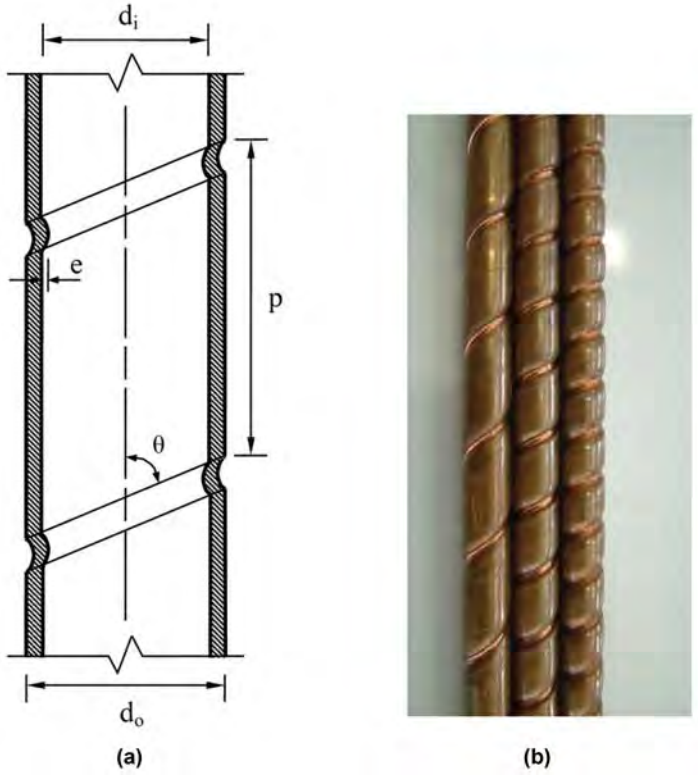

Figure 3. Corrugated tube: (a) sketch and (b) actual photograph. (color figure available online)

Downloaded by [S. Wongwises] at 20:32 16 January 2013

by standard thermometers with a precision of 0.1°C. The refrigerant flow meter is a variable area type and is specially calibrated in the range of 0.2–3.4 liters per minute (LPM) for R-134a by the manufacturer, as is the differential pressure transducer.

In the experiments, the inlet quality of the test section is varied by small increments. The imposed heat flux, mass flux, and saturation temperature are kept constant at the

Table 1. Dimensions of the test sections

		Corrugated tube		
Parameters	Smooth tube	Corrugation pitch 1	Corrugation pitch 2	Corrugation pitch 3
Outer diameter (mm)	9.52	9.52	9.52	9.52
Inner diameter (mm)	8.7	8.7	8.7	8.7
Length of test section (mm)	500	500	500	500
Inside tube area (mm^2)	13,665.9	15,362.2	15,951.1	16,582.8
Corrugation pitch (mm)	—	12.7	8.46	6.35
Corrugation depth (mm)	—	1	1	1
Helix angle (°)	—	53.875	64.07	69.95

Table 2. Experimental conditions

Controlled variable	Evaporation
Mass flux (kg/m^{2}s)	200, 300, 400
Heat flux (kW/m^2)	20, 25, 30
Saturation temperature (°C)	10, 15, 20
Tested tube material	Copper
Refrigerant	R-134a
Average vapor quality	0.2–0.8

desired values. The system is allowed to approach a steady state before any data are recorded. During experiments, the temperature and pressure are continuously recorded along the test section by the data acquisition system. The range of experimental conditions tested in this study is listed in Table 2. The uncertainties of measured quantities and calculated parameters calculated from the root mean sum square method are shown in Table 3.

Downloaded by [S. Wongwises] at 20:32 16 January 2013

DATA REDUCTION

The following calculation is employed to determine the vapor quality of the refrigerant entering and exiting the test section, heat transfer coefficient, and two-phase friction factor from the data recorded during each test run at steady-state conditions.

The Inlet Vapor Quality of the Test Section ($x_{TS,in}$)

The inlet vapor quality of the test section ($x_{TS,in}$) can be defined as

$$x_{TS,in} = \frac{i_{TS,in} - i_{lT_{TS,in}}}{i_{fgT_{TS,in}}}, \tag{1}$$

where $i_{lT_{TS,in}}$ and $i_{fgT_{TS,in}}$ are the enthalpy of the saturated liquid and the enthalpy of vaporization, respectively, based on the temperature at the test section inlet; $i_{TS,in}$ is

Table 3. Uncertainties of measured quantities and calculated parameters

Parameter	Uncertainty
Temperature, T	± 0.1
Frictional pressure drop, ΔP_F	± 10 %
Mass flow rate of refrigerant, m_{ref}	± 2% Full scale
Heat transfer rate of test section, Q_{TS}	± 15 %
Heat transfer rate of pre-heater, Q_{ph}	± 10 %
Average heat transfer coefficient, h_{avg}	± 15 %
Two-phase friction factor, f_{tp}	± 13 %
Average quality, x_{avg}	± 8 %
Equivalent Reynolds number, Re_{eq}	± 6 %

the enthalpy of refrigerant at the test section inlet, which is calculated by the following equation:

$$i_{TS,in} = i_{ph,in} + \frac{Q_{ph}}{m_{ref}}, \tag{2}$$

where $i_{ph,in}$ is the inlet enthalpy of the liquid refrigerant before entering the pre-heater, m_{ref} is the mass flow rate of the refrigerant, and Q_{ph} is the heat transfer rate in the pre-heater:

$$Q_{ph} = m_{w,ph} c_{p,w} (T_{w,in} - T_{w,out})_{ph}, \tag{3}$$

with $m_{w,ph}$ as the mass flow rate of water entering the pre-heater.

Downloaded by [S. Wongwises] at 20:32 16 January 2013

The Outlet Vapor Quality of the Test Section ($x_{TS,out}$)

The outlet vapor quality of the test section ($x_{TS,out}$) can be defined as

$$x_{TS,out} = \frac{i_{TS,out} - i_{lT_{TS,out}}}{i_{fgT_{TS,out}}}, \tag{4}$$

where $i_{TS,out}$ is the refrigerant enthalpy at the test section outlet, $i_{lT_{TS,out}}$ is the enthalpy of the saturated liquid based on the temperature at the test section outlet, and $i_{fgT_{TS,out}}$ is the enthalpy of vaporization based on the temperature at the test section outlet. As a consequence, the outlet enthalpy of the refrigerant flow is calculated as

$$i_{TS,out} = i_{TS,in} + \frac{Q_{TS}}{m_{ref}}, \tag{5}$$

where the heat transfer rate Q_{TS} in the test section is obtained from

$$Q_{TS} = m_{w,TS} c_{p,w} (T_{w,in} - T_{w,out})_{TS}, \tag{6}$$

where $m_{w,TS}$ is the mass flow rate of the water entering the test section, and $(T_{w,in} - T_{w,out})_{TS}$ is the difference in water temperature between the outlet and inlet positions.

Average Heat Transfer Coefficient (h_{avg})

The average heat transfer coefficient (h_{avg}) can be calculated using the following equation:

$$h_{avg} = \frac{Q_{TS}}{A_i (T_{i,avg,wi} - T_{avg,sat})}, \tag{7}$$

where $T_{avg,sat}$ is the average temperature of the refrigerant at the test section inlet and outlet, $T_{i,avg,wi}$ is the average temperature of the inner wall, and A_i is the inside surface area of the test section.

Downloaded by [S. Wongwises] at 20:32 16 January 2013

Nusselt Number (Nu)

The Nusselt number is calculated as follows:

$$\mathrm{Nu} = \frac{h_{avg} d_i}{k_l}, \tag{8}$$

where k_l is thermal conductivity of liquid refrigerant.

Two-Phase Friction Factor (f_{tp})

The total pressure gradient is the sum of three contributions: the gravitational pressure gradient, the momentum pressure gradient, and the frictional pressure gradient, as follows:

$$\left(\frac{dP}{dz}\right)_T = \left(\frac{dP}{dz}\right)_F + \left(\frac{dP}{dz}\right)_G + \left(\frac{dP}{dz}\right)_M. \tag{9}$$

Pressure drop due to gravity can be determined from

$$\left(\frac{dP}{dz}\right)_G = -g\left[(1-\alpha)\rho_l + \alpha\rho_g\right], \tag{10}$$

where the void fraction α can be determined from the Zivi correlation [14], as follows:

$$\alpha = \frac{1}{1 + \dfrac{(1-x)}{x}\left(\dfrac{\rho_g}{\rho_l}\right)^{2/3}}. \tag{11}$$

The momentum pressure gradient can be defined as follows:

$$\left(\frac{dP}{dz}\right)_M = G^2 \frac{d}{dz}\left[\frac{(1-x)^2}{\rho_l(1-\alpha)} + \frac{x^2}{\rho_g \alpha}\right]. \tag{12}$$

The two-phase frictional pressure gradient can be obtained by subtracting the gravitational and momentum terms from the total measured pressure drop, as follows:

$$\left(\frac{dP}{dz}\right)_F = \left(\frac{dP}{dz}\right)_T - \left(\frac{dP}{dz}\right)_G - \left(\frac{dP}{dz}\right)_M. \tag{13}$$

The two-phase friction factor is calculated by the following equation based on the equivalent Reynolds number:

$$f_{tp} = \left(\frac{dP}{dz}\right)_F \frac{\rho_l d_i^3}{2\,\mathrm{Re}_{eq}^2\,\mu_l^2}, \tag{14}$$

where the equivalent Reynolds number is determined from

$$\mathrm{Re}_{eq} = \frac{G_{eq} d_i}{\mu_l}, \tag{15}$$

and equivalent mass flux is defined as

$$G_{eq} = G\left[(1-x) + x\sqrt{\frac{\rho_l}{\rho_g}}\right]. \tag{16}$$

RESULTS AND DISCUSSION

The present study is performed to investigate the effect of corrugation pitch on the heat transfer coefficient and pressure drop of R-134a during evaporation inside vertical corrugated tubes. The experimental data obtained from this work are not from the dry-out region. Before measuring the two-phase heat transfer coefficient and pressure drop during evaporation of refrigerant in the test section, the experimental results obtained from the smooth tube are checked by sight glass at the inlet and outlet of the test section, and they are also checked with the flow pattern maps for vertical flow. Figures 4–6 show the flow pattern map of Hewitt and Roberts [15], Taitel et al. [16], and Mishima and Ishii [17] with the plotted experimental data of the current study, respectively. They are observed that more than 90% of the data points locate in the region of annular flow regime.

Heat Transfer Coefficient

The experimental data obtained from the smooth tube are validated by comparing the present heat transfer coefficient data with the correlations for vertical flow proposed by Shah [9], Gungor and Winterton [10], Kandlikar [11], Wright [18], Schrock and

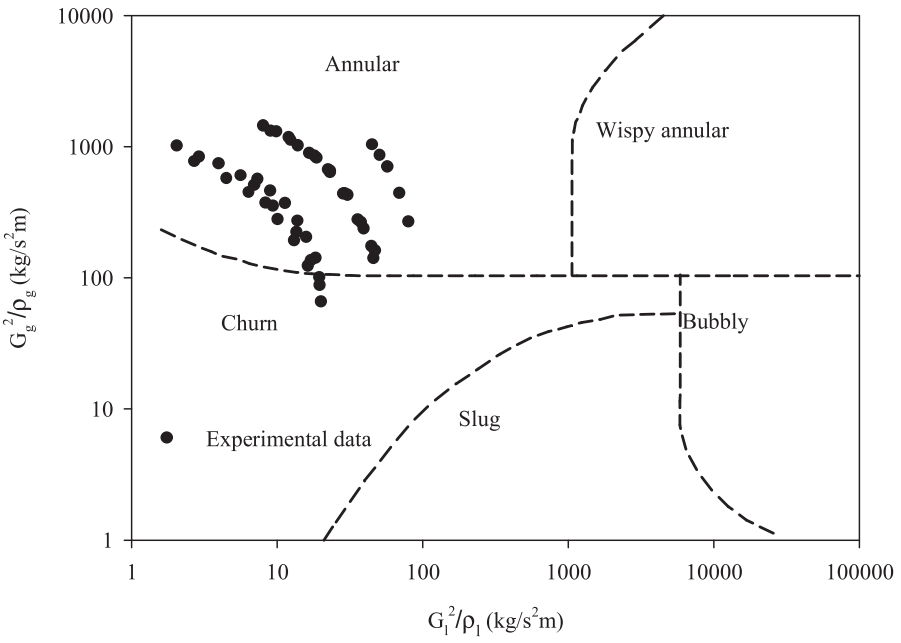

Figure 4. Flow pattern identification of the experimental data by means of Hewitt and Roberts [15] flow regime map.

Downloaded by [S. Wongwises] at 20:32 16 January 2013

Downloaded by [S. Wongwises] at 20:32 16 January 2013

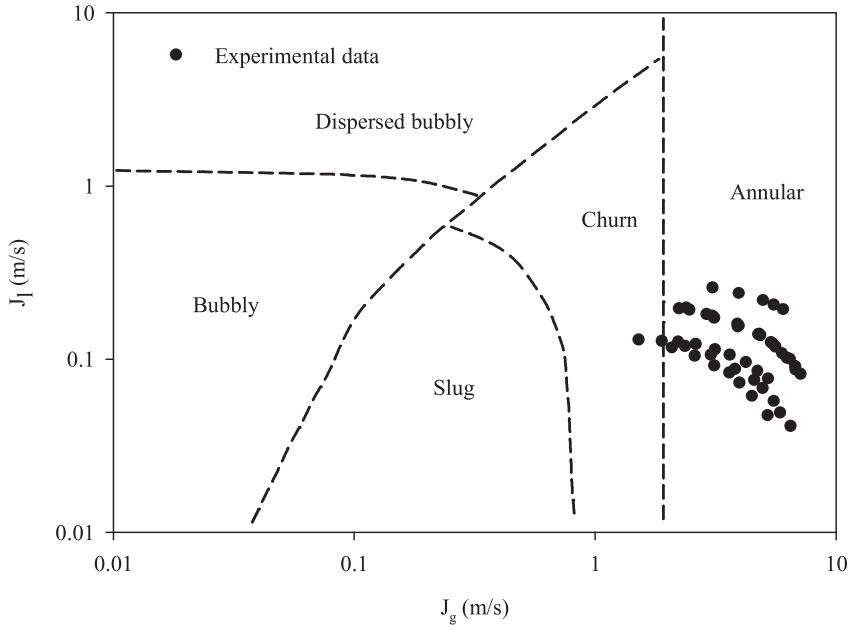

Figure 5. Flow pattern identification of the experimental data by means of Taitel et al. [16] flow regime map.

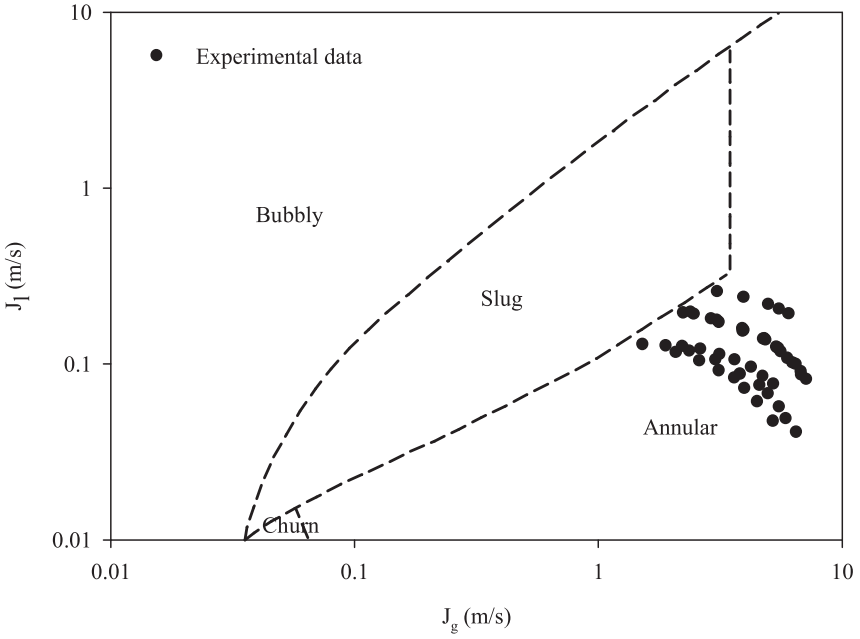

Figure 6. Flow pattern identification of the experimental data by means of Mishima and Ishii [17] flow regime map.

Grossman [19], and Pujol and Stenning [20], as shown in Figure 7. It is observed that almost all of data correlate within the deviation of ± 30%.

Figure 8 shows the relationship between average heat transfer coefficient and average quality in the smooth tube and corrugated tube having different corrugation pitches of 6.35, 8.46, and 12.7 mm at heat flux of 20 kW/m^2, saturation temperature of 20°C, and mass fluxes of 200 kg/m^{2}s. It can be observed that higher average vapor quality results in a higher average heat transfer coefficient. This occurs because at high vapor quality, the velocity of the vapor flow is high, resulting in high shear stress at the interface between the vapor and liquid film. The increasing shear stress causes more entrainment of droplets, making the liquid film thinner. As a result, thermal resistance is decreased. In addition, during evaporation, the liquid film boils and turns to vapor, which, in turn, increases the velocity of two-phase flow. For these reasons, the average heat transfer coefficient tends to increase as the average vapor quality increases.

Figure 9 shows the variation of the average heat transfer coefficient as a function of the mass flux at the heat flux of 20 kW/m^2, the average vapor quality of 0.35, and the saturation temperature of 20°C. It is observed that the average heat transfer coefficient increases with increasing mass flux. This occurs because the velocity of the vapor and liquid film increase as the mass flux increases, and therefore, the average heat transfer coefficient also increases.

As seen from these figures, the heat transfer coefficients obtained from the corrugated tubes are higher than those from the smooth tube. This can be explained by the fact that the corrugated surface promotes more turbulence by increasing the mixing of the refrigerant flow. Further, it is speculated that the rotational flow produced by the

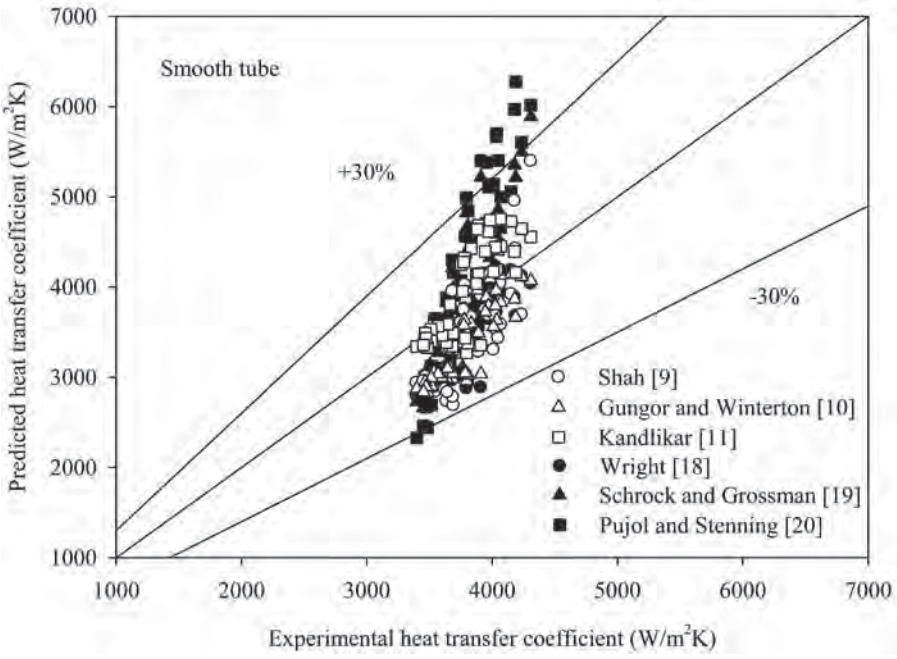

Figure 7. Comparison of experimental heat transfer coefficient data with existing correlations.

Downloaded by [S. Wongwises] at 20:32 16 January 2013

Downloaded by [S. Wongwises] at 20:32 16 January 2013

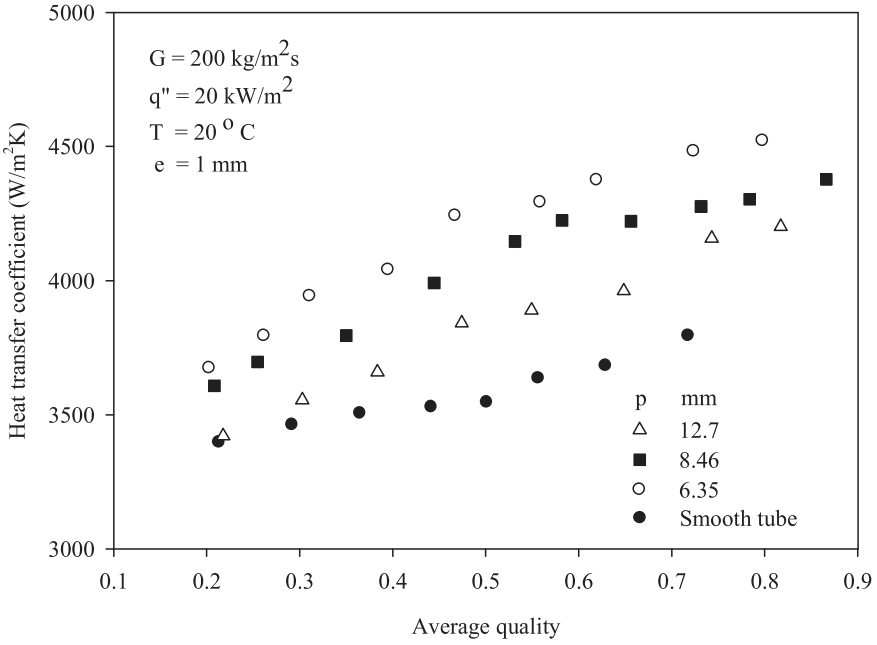

Figure 8. Average heat transfer coefficient as a function of average quality for $G = 200$ kg/m^{2}s, $q'' = 20$ kW/m^2, and $T = 20°$C.

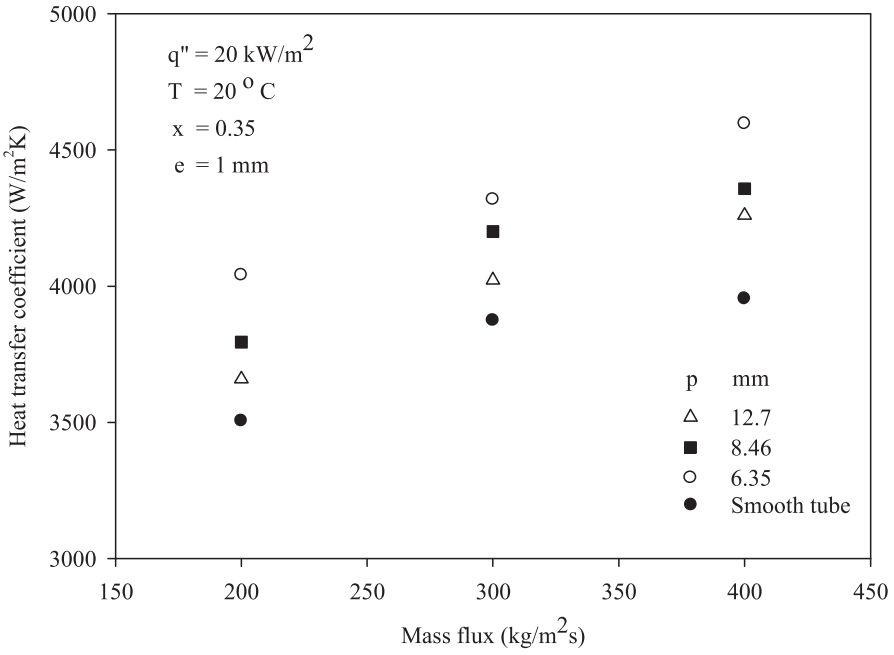

Figure 9. Average heat transfer coefficient as a function of mass flux for $x = 0.35$, $q'' = 20$ kW/m^2, and $T = 20°$C.

corrugation causes the liquid film to become thinner as a result of enhancing heat transfer. Moreover, the heat transfer coefficient increases with the decrease of corrugation pitch. This occurs because the tube with lower corrugation pitch produces more turbulence of the fluid flow and increases the heat transfer area. Hence, the highest heat transfer coefficient is achieved by the tube with the lowest corrugation pitch. The maximum heat transfer enhancement is obtained up to 22% for a pitch of 6.35 mm, 16% for a pitch of 8.46 mm, and 11% for a pitch of 12.7 mm in comparison with the smooth tube at the mass flux of 200 kg/m^{2}s, the heat flux of 20 kW/m^2, and the saturation temperature of 20°C.

The heat transfer enhancement factors as a function of vapor quality are shown in Figures 10 and 11, defined as the ratio of the heat transfer coefficient for a corrugated tube to that of a comparable smooth tube. The heat transfer enhancement factor is calculated by a linear regression analysis using a least-squares method to determine the best-fitting straight line. It is found that the heat transfer enhancement factor increases as the average vapor quality increases. This can be explained by the effect of corrugation on the heat transfer coefficient, which is weak in low vapor quality region but becomes stronger at high vapor quality. At low vapor quality, the liquid film thickness is higher than that at high vapor quality, and, as a result, the turbulence effects produced by the corrugation depth are reduced. When the liquid film thickness is close to the corrugation depth, the periodic liquid wave caused by corrugation pitch produces an unstable liquid flow, which maximizes thermal efficiency and turbulent effects [21]. The heat transfer enhancement factor varies from 1.09 to 1.22 for a pitch of 6.35 mm, 1.06 to 1.16 for a pitch of

Downloaded by [S. Wongwises] at 20:32 16 January 2013

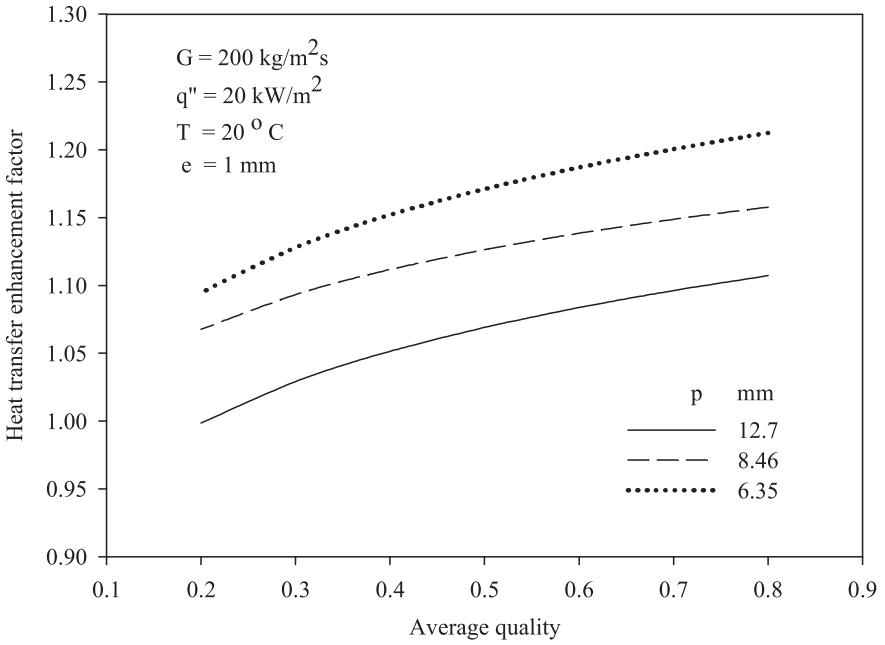

Figure 10. Heat transfer enhancement factors as a function of average quality for $G = 200$ kg/m^{2}s, $q'' = 20$ kW/m^2, and $T = 20$°C.

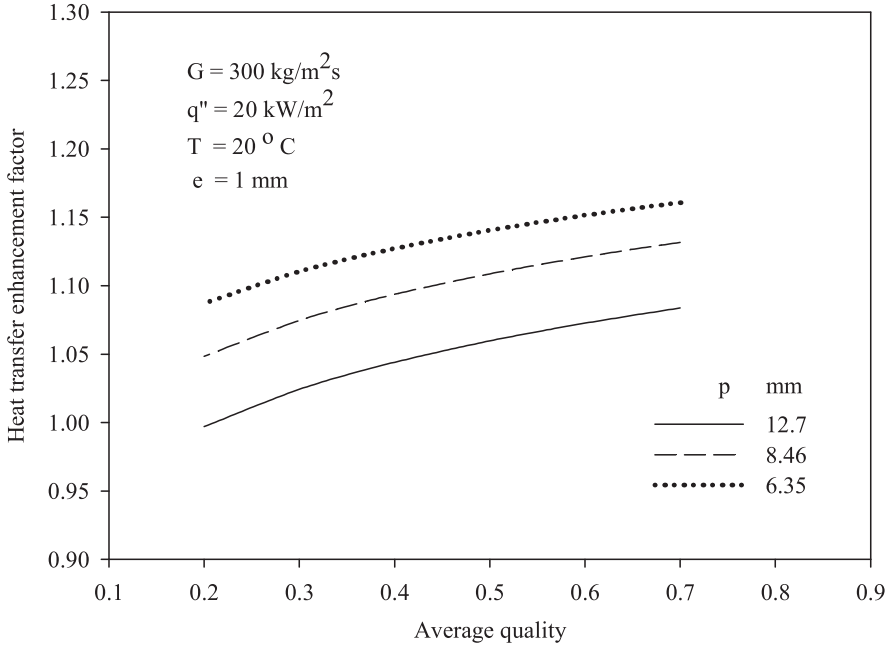

Figure 11. Heat transfer enhancement factors as a function of average quality for $G = 300$ kg/m^{2}s, $q'' = 20$ kW/m^2, and $T = 20$°C.

8.46 mm, and 1.00 to 1.11 for a pitch of 12.7 mm at the mass flux of 200 kg/m^{2}s, heat flux of 20 kW/m^2, and saturation temperature of 20°C.

Figure 12 shows a comparison of the experimental data for the corrugated tube with the proposed correlations. The correlation is expressed as a function of Nusselt number, equivalent Reynolds number, corrugation pitch, and inside diameter as follows:

$$\mathrm{Nu} = 35.948\,\mathrm{Re}_{eq}^{0.237}\left(\frac{p}{d_i}\right)^{-0.114}. \tag{17}$$

As shown in Figure 12, the results show that more than 95% of data fall within a deviation of ± 5%.

Pressure Drop

Figure 13 compares the frictional pressure drop for the smooth tube with the correlations from literature. The correlations proposed by Lockhart and Martinelli [22] and Chisholm [23] are in agreement with the present data within 30%. About 70% of the data are captured within 30% by Laohalertdecha et al.'s [24] correlation, while the Friedel [25], and Quibén and Thome [26] correlations underestimate the data by more than 30%.

The variation of the frictional pressure drop with average quality in smooth and corrugated tubes is illustrated in Figure 14. The frictional pressure drop increases with increasing vapor quality. This occurs because at higher vapor quality, the higher velocity

Downloaded by [S. Wongwises] at 20:32 16 January 2013

Downloaded by [S. Wongwises] at 20:32 16 January 2013

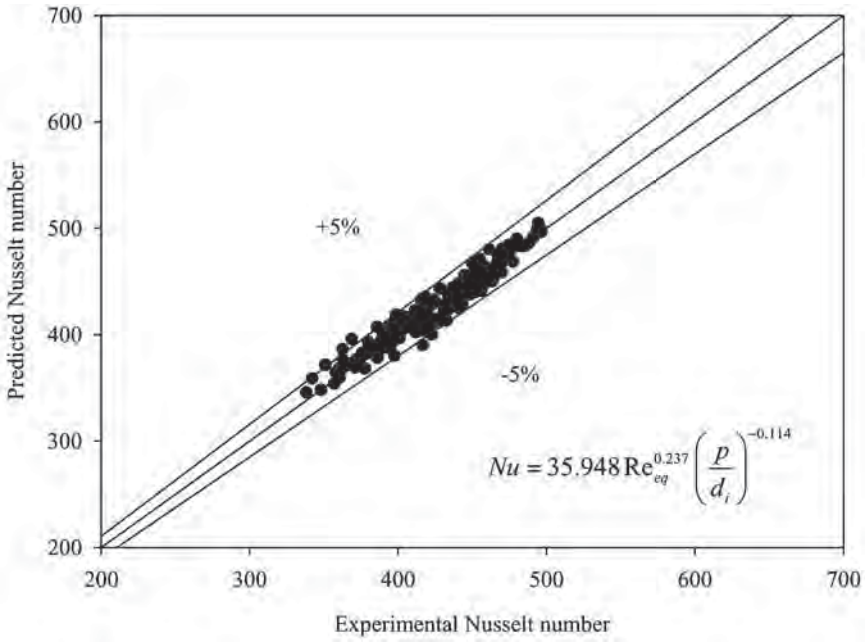

Figure 12. Predicted Nusselt number using the proposed correlation versus the experimental data.

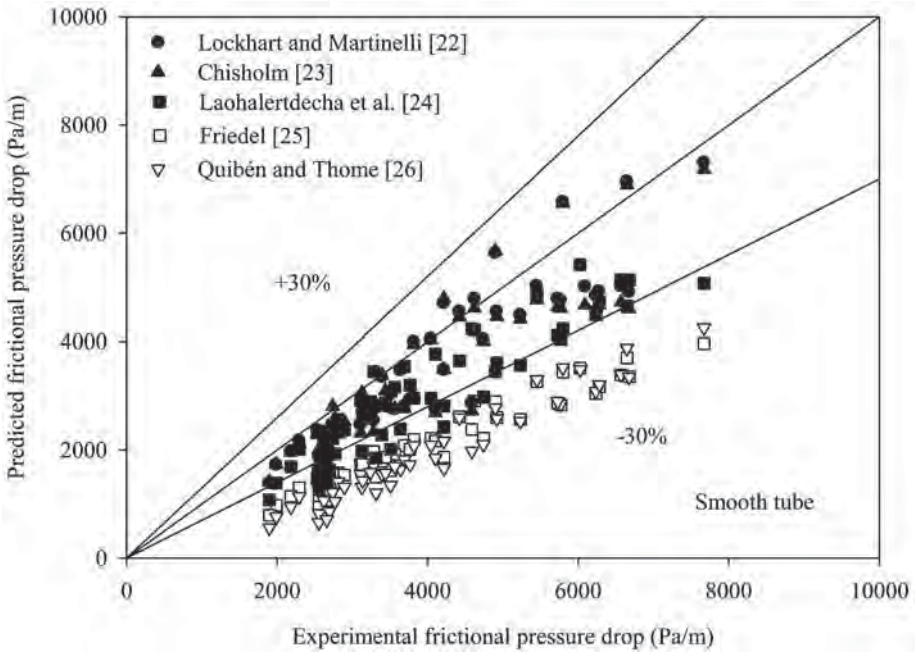

Figure 13. Comparison of experimental frictional pressure drop data with existing correlations.

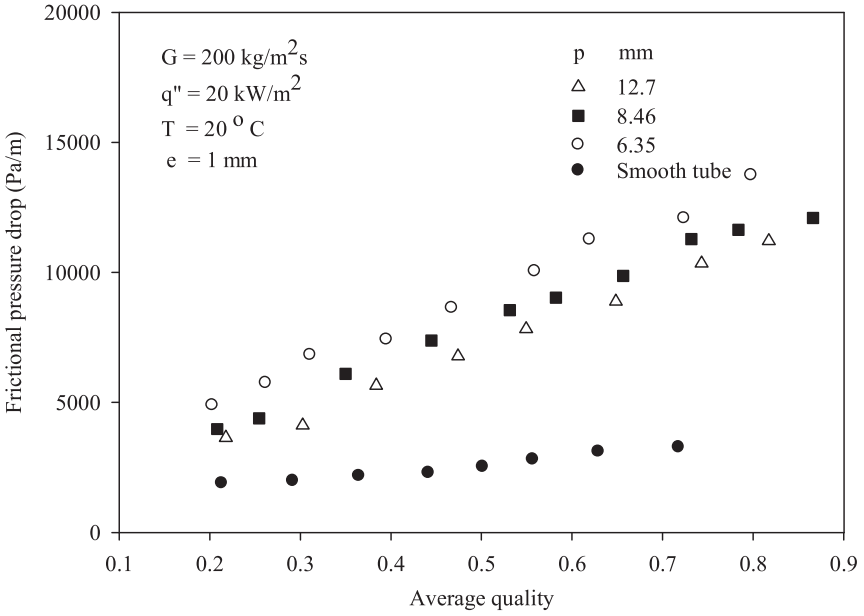

Figure 14. Frictional pressure drop as a function of average quality for $G = 200$ kg/m^{2}s, $q'' = 20$ kW/m^2, and $T = 20°$C.

of vapor flow causes more shear stress at the interface of the vapor and liquid film. Moreover, the secondary flow that becomes stronger at higher vapor velocity will produce more entrainment and redeposition of droplets, causing more flow turbulence.

Figure 15 illustrates the variation of the frictional pressure drop as a function of the saturation temperature at the heat flux of 20 kW/m^2, average vapor quality of 0.45, and mass flux of 200 kg/m^{2}s. The frictional pressure drop decreases significantly as the evaporating temperature increases. This is because when the evaporating temperature increases, the viscosity of liquid film decreases, resulting in lower flow resistance. Consequently, the frictional pressure drop decreases as the evaporating temperature increases.

As shown in Figures 14 and 15, the frictional pressure drops for the corrugated tubes are higher than those for the smooth tube. This is due to the pressure-drop augmentation in corrugated tubes that is produced by (1) drag forces exerted on the flow field by the corrugation, (2) flow blockage due to area reduction, (3) turbulence augmentation, and (4) rotational flow produced by the corrugation [27]. The figures also show the effect of the corrugation pitch at constant corrugation depth of 1 mm on the frictional pressure drop. These plots show that the higher frictional pressure drop is obtained from the tube with lower corrugation pitch; lower corrugation pitch results in increased corrugation surface, more turbulence of the fluid flow, and more pressure loss. The maximum value of frictional pressure drop is obtained from the tube having a corrugation pitch of 6.35 mm up to 300% in comparison with the smooth tube at the mass flux of 200 kg/m^{2}s, heat flux of 20 kW/m^2, and saturation temperature of 20°C.

The relationship between the two-phase friction factor and the equivalent Reynolds number is demonstrated in Figure 16. The two-phase friction factor decreases with

Downloaded by [S. Wongwises] at 20:32 16 January 2013

Downloaded by [S. Wongwises] at 20:32 16 January 2013

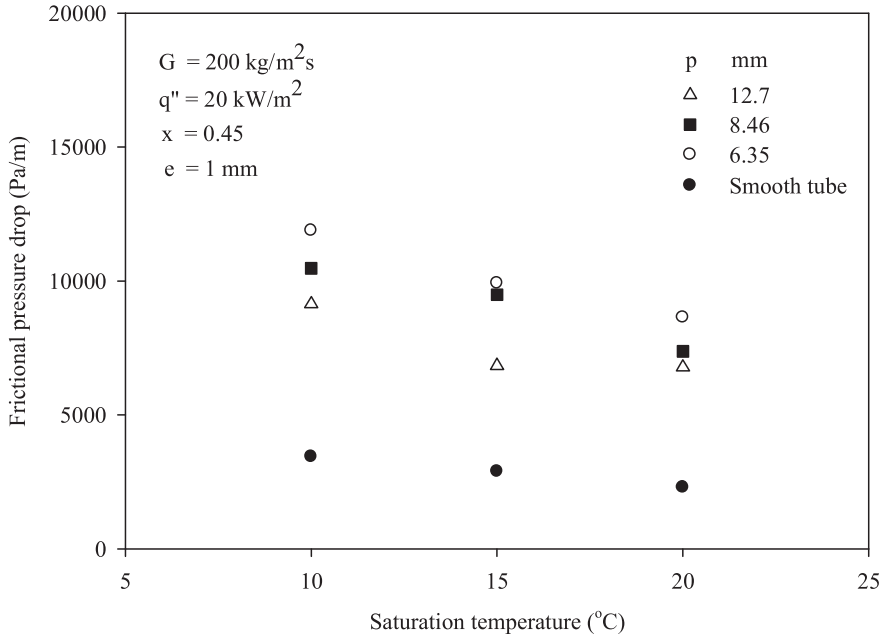

Figure 15. Frictional pressure drop as a function of saturation temperature for $G = 200$ kg/m^{2}s, $q'' = 20$ kW/m^2, and $x = 0.45$.

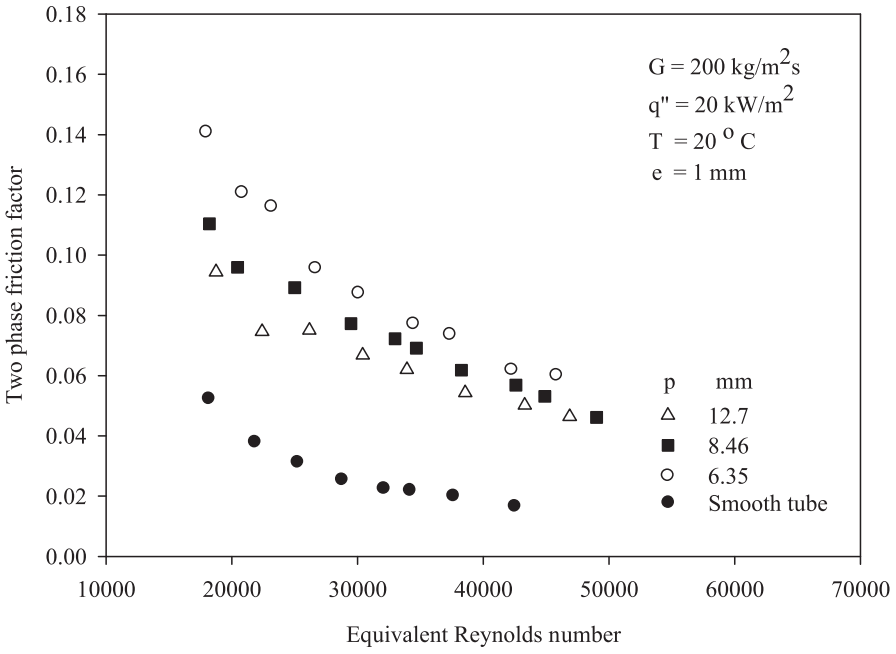

Figure 16. Two-phase friction factor as a function of equivalent Reynolds number for $G = 200$ kg/m^{2}s, $q'' = 20$ kW/m^2, and $T = 20°$C.

Downloaded by [S. Wongwises] at 20:32 16 January 2013

increasing equivalent Reynolds number. This is because both the frictional pressure drop and equivalent Reynolds number increase with increasing vapor quality. According to Eq. (14), the equivalent Reynolds number dominates the two-phase friction factor. Therefore, the increase in average quality causes the two-phase friction factor to decrease. Figure 16 also shows that the two-phase friction factor for the corrugated tubes is higher than that for the smooth tube. In addition, the two-phase friction factor tends to increase as the corrugation pitch decreases. The reason for this is similar to the above-mentioned explanation concerning the frictional pressure drop.

Figures 17 and 18 illustrate the variation of the penalty factor with the average vapor quality. The penalty factor is defined as the ratio of the frictional pressure drop for a corrugated tube to that of a comparable smooth tube. The penalty factor increases with a rise of the average vapor quality. This is because the turbulence effects produced by corrugation depth are strong at high vapor quality as a result of more pressure loss. The penalty factor ranges from 2.8 to 4.0 for a pitch of 6.35 mm, 2.2 to 3.5 for a pitch of 8.46 mm, and 1.8 to 3.2 for a pitch of 12.7 mm at the mass flux of 200 kg/m^{2}s, heat flux of 20 kW/m^2, and saturation temperature of 20°C.

Figure 19 shows the experimental two-phase friction factor plotted against predicted two-phase friction factor obtained from Eq. (18). It is found that about 90% of the data fall within a deviation of ± 15%:

$$f_{tp} = 37.337\,\mathrm{Re}_{eq}^{-0.594}\left(\frac{p}{d_i}\right)^{-0.301} . \tag{18}$$

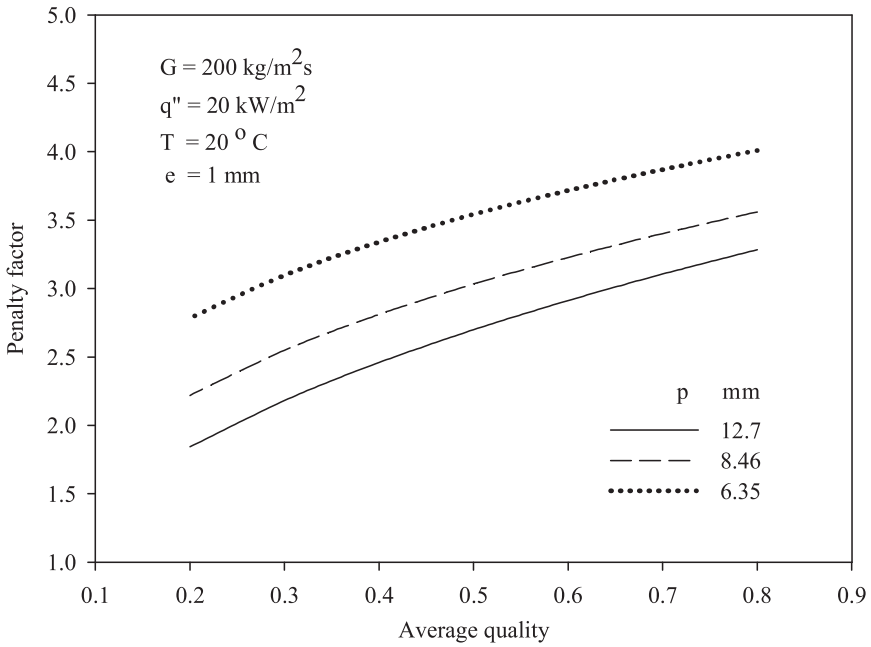

Figure 17. Penalty factors as a function of average quality for $G = 200$ kg/m^{2}s, $q'' = 20$ kW/m^2, and $T = 20$°C.

Downloaded by [S. Wongwises] at 20:32 16 January 2013

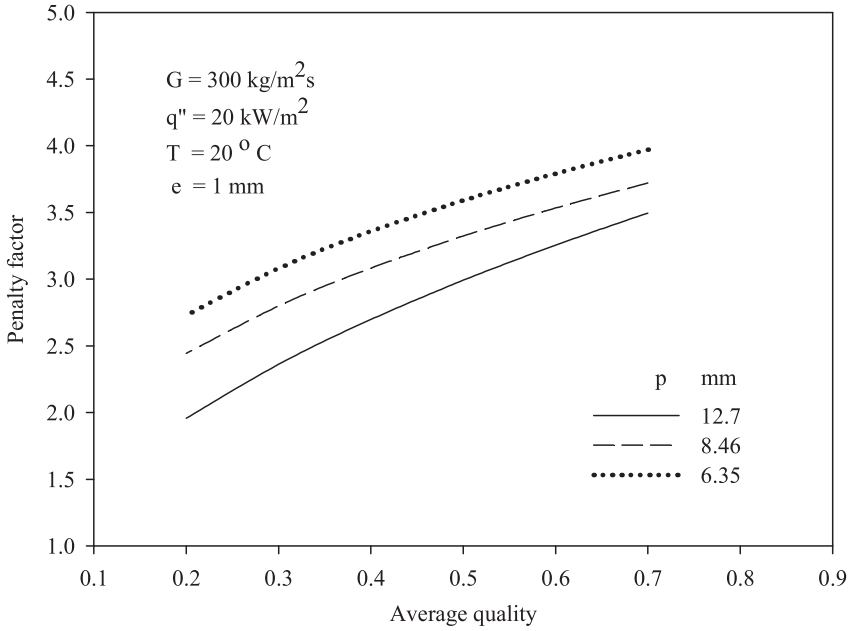

Figure 18. Penalty factors as a function of average quality for $G = 300$ kg/m^{2}s, $q'' = 20$ kW/m^2, and $T = 20$°C.

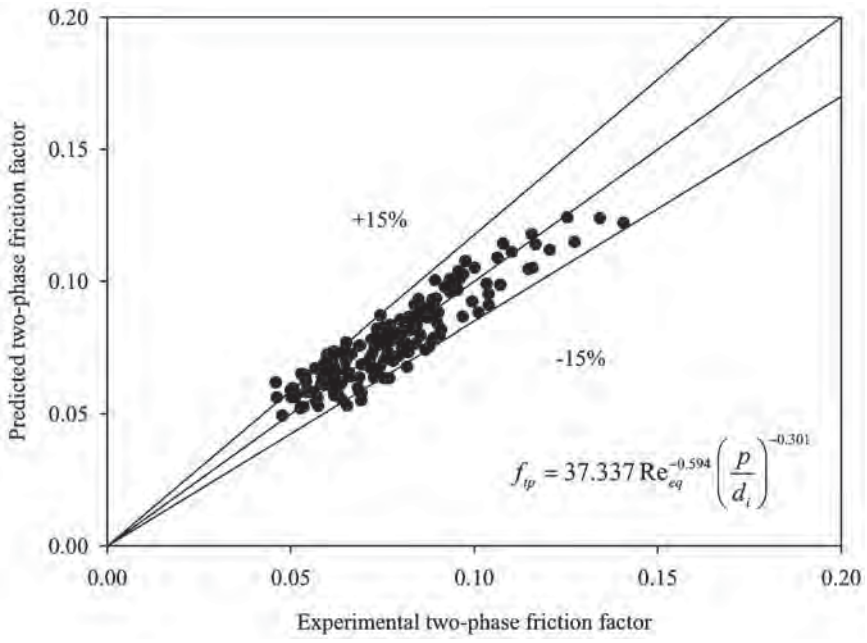

Figure 19. Predicted two-phase friction factor using the proposed correlation versus the experimental data.

CONCLUSION

This study is conducted to investigate the evaporative heat transfer and pressure drop characteristics of R-134a flow through vertical smooth and corrugated tubes with different corrugation pitches. The conclusions follow.

1. The experimental data obtained from the smooth tube are plotted with a flow pattern map for vertical flow proposed by Hewitt and Roberts [15], Taitel et al. [16], and Mishima and Ishii [17]. It is observed that more than 90% of the data points locate in the region of annular flow regime.
2. The heat transfer coefficient tends to increase with increasing average vapor quality and mass flux. The heat transfer coefficient obtained from the corrugated tube is higher than that from the smooth tube. Moreover, the heat transfer coefficient increases with the decrease of corrugation pitch.
3. The frictional pressure drop increases with increasing vapor quality, while it decreases significantly as the evaporating temperature increases. The two-phase friction factor decreases with increasing equivalent Reynolds number. The frictional pressure drops for the corrugated tube is higher than that for the smooth tube. In addition, the higher frictional pressure drop is obtained from the tube with lower corrugation pitch.
4. The heat transfer enhancement factor and penalty factor increase with a rise of the average vapor quality. The heat transfer enhancement factor varies from 1.09 to 1.22, 1.06 to 1.16, and 1.00 to 1.11, while the penalty factor ranges from 2.8 to 4.0, 2.2 to 3.5, and 1.8 to 3.2 for a pitch of 6.35 mm, 8.46 mm, and 12.7 mm, respectively.

Downloaded by [S. Wongwises] at 20:32 16 January 2013

ACKNOWLEDGMENTS

The present study was supported financially by the Thailand Research Fund and the National Research University Project, whose guidance and assistance are gratefully acknowledged.

REFERENCES

1. P. Thors and J. Bogart, In Tube Evaporation of HCFC-22 with Enhanced Tubes, *J. Enhanced Heat Transf.*, vol. 1, pp. 365–377, 1994.
2. A. Briggs, C. Kelemenis, and J. W. Rose, Condensation of CFC-113 with Downflow in Vertical Internally Enhanced Tubes, *Proceedings of 11th IHTC*, Keongju, Korea, pp. 23–28, August 23–28, 1998.
3. X. Ma, A. Briggs, and J. W. Rose, Heat Transfer and Pressure Drop Characteristics for Condensation of R113 in a Vertical Micro-Finned Tube with Wire Insert, *Int. Commun. Heat Mass Transf.*, vol. 31, pp. 619–627, 2004.
4. A. S. Dalkilic, S. Laohalertdecha, and S. Wongwises, Two-Phase Friction Factor in Vertical Downward Flow in High Mass Flux Region of Refrigerant HFC-134a During Condensation, *Int. Commun. Heat Mass Transf.*, vol. 35, pp. 1147–1152, 2008.

5. A. S. Dalkilic, S. Laohalertdecha, and S. Wongwises, Effect of Void Fraction Models on the Two-Phase Friction Factor of R134a During Condensation in Vertical Downward Flow in a Smooth Tube, *Int. Commun. Heat Mass Transf.*, vol. 35, pp. 921–927, 2008.
6. A. S. Dalkilic, S. Laohalertdecha, and S. Wongwises, Effect of Void Fraction Models on the Film Thickness of R134a During Downward Condensation in a Vertical Smooth Tube, *Int. Commun. Heat Mass Transf.*, Vol. 36, pp. 172–179, 2009.
7. A. S. Dalkilic, S. Laohalertdecha, and S. Wongwises, Experimental Investigation of Heat Transfer Coefficient of R134a During Condensation in Vertical Downward Flow at High Mass Flux in a Smooth Tube, *Int. Commun. Heat Mass Transf.*, vol. 36, pp. 1036–1043, 2009.
8. A. S. Dalkilic, S. Yildiz, and S. Wongwises, Experimental Investigation of Convective Heat Transfer Coefficient During Downward Laminar Flow Condensation of R134a in a Vertical Smooth Tube, *Int. J. Heat Mass Transf.*, vol. 52, pp. 142–150, 2009.
9. M. M. Shah, Chart Correlation for Saturated Boiling Heat Transfer Equation and Further Study, *ASHRAE Trans.*, vol. 88, pp. 185–196, 1982.
10. K.E. Gungor and R. H. S. Winterton, A General Correlation for Flow Boiling in Tubes and Annuli, *Int. J. Heat Mass Transf.*, vol. 29, pp. 351–358, 1986.
11. S. G. Kandlikar, A General Correlation for Saturated Two-Phase Flow Boiling Heat Transfer Inside Horizontal and Vertical Tubes, *ASME J. Heat Transf.*, vol. 112, pp. 219–228, 1990.
12. S. K. Lee and S. H. Chang, Experimental Study of Post-Dryout with R-134a Upward Flow in Smooth Tube and Rifled Tubes, *Int. J. Heat Mass Transf.*, vol. 51, pp. 3153–3163, 2008.
13. K. Aroonrat and S. Wongwises, Evaporation Heat Transfer and Friction Characteristics of R-134a Flowing Downward in a Vertical Corrugated Tube, *Exp. Thermal Fluid Sci.*, vol. 35, pp. 20–28, 2011.
14. S. M. Zivi, Estimation of Steady-State Steam Void-Fraction by Means of the Principle of Minimum Entropy Production, *ASME J. Heat Transf.*, vol. 86, pp. 247–252, 1975.
15. G. F. Hewitt and D. N. Roberts, *Studies of Two-Phase Flow Patterns by Simultaneous X-Ray and Flash Photography*, AERE-M 2159, Her Majesty's Stationery Office, London, 1969.
16. Y. Taitel, D. Barnea, and A. E. Dukler, Modelling Flow Pattern Transitions for Steady Upward Gas-Liquid Flow in Vertical Tubes, *AIChE J.*, vol. 26, pp. 345–354, 1980.
17. K. Mishima and M. Ishii, Flow Regime Transition Criteria for Upward Two-Phase Flow in Vertical Tubes, *Int. J. Heat Mass Transf.*, vol. 27, pp.723–737, 1984.
18. R. M. Wright, *Down Flow Forced Convection Boiling of Water in Uniformly Heated Tubes*, UCRL-9744, University of California, Berkeley, CA, 1961.
19. V. E. Schrock and L. M. Grossman, Forced Convection Boiling in Tubes, *Nuclear Sci. Eng.*, vol. 12, pp. 474–481, 1962.
20. L. Pujol and A. H. Stenning, Effects of Flow Directions on the Boiling Heat Transfer Coefficients in Vertical Tubes, in E. R. Rhodes and D. S. Scott (Eds.), *Co-Current Gas-Liquid Flow*, Plenum Press, New York, pp. 401–453, 1969.
21. R. Yun, Y. Kim, K. Seo, and H. Y. Kim, A Generalized Correlation for Evaporation Heat Transfer of Refrigerants in Micro-Fin Tubes, *Int. J. Heat Mass Transf.*, vol. 45, pp. 2003–2010, 2002.
22. R. W. Lockhart and R. C. Martinelli, Proposed Correlation of Data for Isothermal Two-Phase Two Component Flow in Pipes, *Chem. Eng. Progress*, vol. 45, pp. 39–48, 1949.
23. D. Chisholm, Pressure Gradients Due to Friction During the Flow of Evaporating Two-Phase Mixtures in Smooth Tubes and Channels, *Int. J. Heat Mass Transf.*, vol. 16, pp. 347–358, 1973.
24. S. Laohalertdecha, A. S. Dalkilic and S. Wongwises, Correlations for Evaporation Heat Transfer Coefficient and Two-Phase Friction Factor for R-134a Flowing Through Horizontal Corrugated Tubes, *Int. Commun. Heat Mass Transf.*, vol. 38, pp. 1406–1413, 2011.

Downloaded by [S. Wongwises] at 20:32 16 January 2013

25. L. Friedel, Improved Friction Pressure Drop Correlations for Horizontal and Vertical Two-Phase Pipe Flow, Paper E2, *The European Two-Phase Flow Group Meeting*, Ispra, Italy, June 5–8, 1979.
26. J. M. Quibén and J. R. Thome, Flow Pattern Based Two-Phase Frictional Pressure Drop Model for Horizontal Tubes, Part II: New Phenomenological Model, *Int. J. Heat Fluid Flow*, vol. 28, pp. 1060–1072, 2007.
27. P. G. Vicente, A. Garcia, and A. Viedma, Experimental Investigation on Heat Transfer and Friction Factor Characteristics of Spirally Corrugated Tubes in Turbulent Flow at Different Prandtl Number, *Int. J. Heat Mass Transf.*, vol. 47, pp. 671–681, 2004.

Downloaded by [S. Wongwises] at 20:32 16 January 2013

Technical Note

Performance of Two-Stage Upflow Anaerobic Sludge Blanket Reactor Treating Wastewater from Latex-Processing Factory

S. Phoolphundh[1]; K. Hathaisamit[2]; and S. Wongwises[3]

Abstract: In this study, a relatively high-rate treatment (hydraulic retention time ≤2.5 days) of latex-processing wastewater was achieved in a two-stage upflow anaerobic sludge blanket reactor. A maximum acid production rate of 1.8 $g\,L^{-1}\,d^{-1}$ acetic acid was obtained when the acidogenic reactor was operated over a hydraulic retention time (HRT) of 4 hr. Total chemical oxygen demand (COD) and sulfate removal efficiencies of the system were 51.6 and 75.9%, respectively, when the methanogenic reactor was operated over an HRT of 24 h. The specific acidogenic activity of granular sludge in the acidogenic and methanogenic reactor varied between 1.33–2.02 g COD g volatile suspended solids $(VSS)^{-1}\,d^{-1}$, and the specific methanogenic activity ranged from 0.0078 to 0.0138 $g\,COD\text{-}CH_4\,g\,VSS^{-1}\,d^{-1}$. Microbial diversity monitoring using the denaturing gradient gel electrophoresis technique revealed that there was more sulfate-reducing bacteria in both reactors than *archea* bacteria. **DOI: 10.1061/(ASCE)EE.1943-7870.0000604.** © *2013 American Society of Civil Engineers.*

CE Database subject headings: Reactors; Wastewater management; Sludge.

Author keywords: Acidogenic reactor; Latex-processing wastewater; Methanogenic reactor; Sulfate reduction; Two-stage upflow anaerobic sludge blanket system.

Downloaded from ascelibrary.org by Kasetsart University on 01/10/13. Copyright ASCE. For personal use only; all rights reserved.

Introduction

Thailand is the leading natural rubber producer in the world. According to a report from the Thailand Office of Agricultural Economics (2009), there are approximately 27,200 square kilometres of rubber tree plantations in Thailand, 75% of which are located in the southern region. Latex concentrate, which is produced by centrifugation of rubber latex (sap), is generally used as a raw material for an enormous variety of products, e.g., sheet rubber, gloves, and tires. Wastewater from concentrated latex factories is a significant source of pollution because of its high organic content and sulphate concentration. Rubber latex wastewater is widely treated by an anaerobic process. A major problem associated with the anaerobic treatment of sulfate-rich wastewater is the production of sulfide by sulphate-reducing bacteria (SRB), which may lead to process failure. One of the strategies to accomplish the successful treatment of sulfate-containing wastewater is the separation of sulfide production and methanogenesis through a two-stage anaerobic digestion process (Lens et al. 1998). The resulting sulfide will be removed during the first stage (acidification) via stripping that can easily occur as a result of the low pH (approximately 5.0–6.5) in the reactor. This reduces the toxicity of sulfide to methane-producing bacteria (MPB) and acetogenic bacteria (AB) in the second stage (methanogenesis). This study attempted to determine the effect of hydraulic retention time (HRT) in an acidogenic reactor and methanogenic reactor on volatile fatty acid (VFA) production, chemical oxygen demand (COD) removal, sulfate reduction, and biogas production, to evaluate the performance of a two-stage upflow anaerobic sludge blanket (UASB) reactor on treating wastewater from a concentrated latex-processing factory.

Materials and Methods

Experimental Setup and Operation

A laboratory-scale two-stage UASB system, consisting of an acidogenic (A) reactor and a methanogenic reactor (M), was used in this study. The working volume of the A and M reactors was 2.9 and 4.1 L, with an inner diameter of 5 cm and a height of 96 and 120 cm, respectively. Fig. 1 is a schematic diagram of the two-stage UASB system. Both reactors were separated by an effluent tank that received the effluent from the A reactor and provided the feed for the M reactor. A water displacement-type gas meter was connected to the M reactor to measure the volume of produced biogas. One-third of each reactor was inoculated with granular sludge from a full-scale UASB reactor belonging to a beverage company (Sermsuk Co., Ltd., Pathumthani province, Thailand). The concentration of total suspended solids (TSS) and volatile suspended solids (VSS) of the seed sludge were 39 and 36 g/L, respectively. The latex-processing wastewater used in this study was taken from the first anaerobic pond at the wastewater treatment plant of Srithepthai Latex Co., Ltd. (Rayong province, Thailand), and was stored at 4°C before use. The characteristics of this latex-processing wastewater are shown in Table 1.

During the start-up period, seed sludge in both reactors was acclimatized by continuously fed with diluted latex-processing wastewater

[1]Dept. of Microbiology, Faculty of Science, King Mongkut's Univ. of Technology Thonburi, 126 Prachauthid Rd., Thungkru, Bangkok 10140, Thailand (corresponding author). E-mail: sivawan.pho@kmutt.ac.th

[2]Environmental Science, Faculty of Science and Technology, Bansomdejchaopraya Rajabhat Univ., Isaraphab Rd., Dhonburi, Bangkok 10600, Thailand.

[3]Dept. of Mechanical Engineering, Faculty of Engineering, King Mongkut's Univ. of Technology Thonburi, 126 Prachauthid Rd., Thungkru, Bangkok 10140, Thailand.

Note. This manuscript was submitted on September 21, 2011; approved on June 11, 2012; published online on August 3, 2012. Discussion period open until June 1, 2013; separate discussions must be submitted for individual papers. This technical note is part of the ***Journal of Environmental Engineering***, Vol. 139, No. 1, January 1, 2013. © ASCE, ISSN 0733-9372/2013/1-141-146/$25.00.

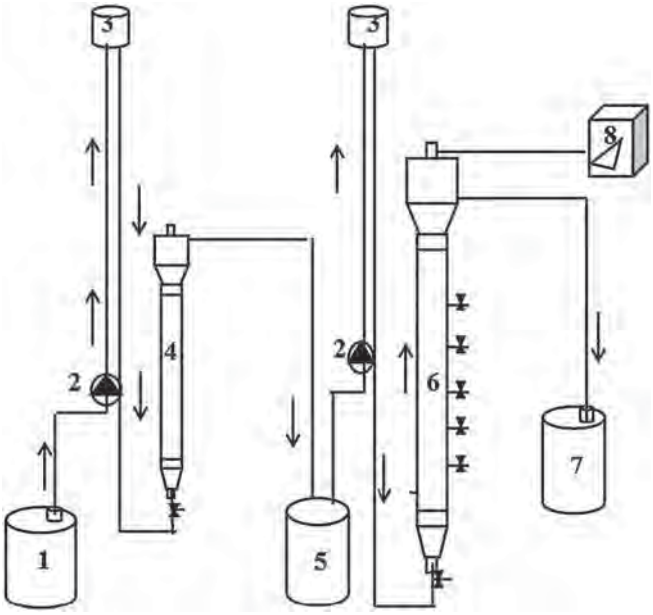

Fig. 1. Schematic diagram of two-stage UASB system: (1) influent tank, (2) feed pump, (3) control level tank, (4) acidogenic reactor, (5) effluent tank 1, (6) methanogenic reactor, (7) effluent tank 2, (8) gas meter

Table 1. Characteristics of Latex-Processing Wastewater in the First Anaerobic Pond of Srithepthai Latex Co., Ltd.

Parameters	Units	Value
pH	—	4.8–7.1
COD	mg/L	5,240–12,450
Sulfate	mg/L as SO_4^{-2}	1,889–4,210
Ammonia-N	mg/L as N	523–1,435
TKN	mg/L as N	816–1,970
Phosphate	mg/L as P	80–164
SS	mg/L	840–1,125
VSS	mg/L	670–924

(30% of the designated concentration, ≅6,000 mg COD/L) and the reactors were operated at HRT of 24 h. A stepwise increase of influent COD concentration from 30 to 50, 70, and 100% was conducted when ≥70% of COD removal efficiency at each dilution was attained. Tap water was used to prepare diluted wastewater and sodium bicarbonate solution was added to increase the pH of wastewater to neutral values (6.5–7.2). After the acclimation period, the pH and COD concentration of the influent were controlled at 5.5–6.0 and 6,000 mg/L, respectively. In Phase I of the experiment, the A reactor was first operated at HRT of 8 h and then was stepwise decreased to 6 and 4 h, respectively, while the M reactor was operated at HRT of 18 h. The steady state of each HRT was defined by the constant effluent COD and VFA concentrations. The HRT that permitted the highest VFA production rate will be used as the HRT for the A reactor of the two-stage UASB system in Phase II of the experiment. The HRT of the M reactor will be varied from 24, 32, and 56 h to maintain the HRT of the system at 28, 36, and 60 h, respectively.

Analysis

The measurement of COD, Total Kjeldahl Nitrogen (TKN), SO_4^{2-}, TSS, VSS, pH, and alkalinity in influent and effluent samples from both reactors was performed according to the *Standard Methods for Examination of Water and Wastewater* [American Public Health Association (APHA) 1992]. The VFA was determined by both direct titration and the use of a gas chromatograph (PerkinElmer, Auto System XL) equipped with a flame ionization detector (FID) and capillary column (Aquawax). The temperatures of the column, the injection port and the FID detector were 120, 180, and 250°C, respectively. The contents of CH_4 and CO_2 in the biogas was analyzed by another gas chromatograph (Shimadzu, GC-148) equipped with a thermal conductivity detector and a stainless-steel column (Porapak Q). The temperatures of the column, the injection port, and the detector were 45, 100, and 120°C, respectively. At the end of each HRT, sludge was taken from the A and M reactors to assess the specific acidogenic activity (SAA) and specific methanogenic activity (SMA) in a 120-mL serum bottle using glucose and acetic acid, respectively, as substrate (Soto et al. 1993). The external structure of the granular sludge from both reactors was examined using the JEOL scanning electron microscope (SEM), with the granules prepared according to Kalyuzhnyi et al. (1996). Sample sludge for DNA extraction was taken from the A and M reactors when each steady state was reached, and was stored in a refrigerator before use. Polymerase chain reaction-denaturing gel gradient electrophoresis (PCR-DGGE) was performed according to a previously published method (O-Thong et al. 2007).

Results and Discussion

Effect of HRT on Acidification in the UASB Reactor

Acidification and VFAs

The suitable HRT of A reactors in the two-stage anaerobic digestion process treating wastewater with a high COD concentration has been reported in the range of 6–24 h (Chathanee 1988). In the present study, it was found that the VFA concentration in the effluent decreased with the increasing HRT (Fig. 2) when the UASB reactors were operated at HRTs of 8 and 18 h. Because effluent VFA concentration is the sum of VFA production during acidification of the substrate and bacterial VFA degradation, this result indicated that the degradation of VFA in the reactor exceeded its production. Therefore, the HRTs of the experimental UASB reactors were lowered to 4 and 6 h in an attempt to achieve a high VFA concentration (especially of acetic acid) in the A reactor. The effluent VFA concentrations were found to be 8.9 and 2.67%, respectively, higher than those in the influent (Fig. 2). The concentration of each VFA, as determined by gas chromatography (data not shown), revealed that the acetic acid concentration in the

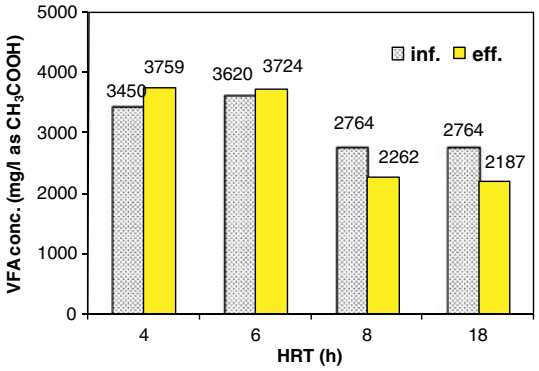

Fig. 2. VFA concentration in the influent and effluent at each HRT of the UASB reactor under acidogenic conditions

J. Environ. Eng. 2013.139:141-146.

Downloaded from ascelibrary.org by Kasetsart University on 01/10/13. Copyright ASCE. For personal use only; all rights reserved.

effluent (1,783–2,907 mg/L) at each HRT was higher than the concentrations of propionic and butyric acids. This will be of benefit to the MPB in the second stage, because MPB can use acetic acid, formic acid, H_2, methanol, and methylamine as a substrate, but not VFAs that have a C atom > 2, e.g., propionic acid or butyric acid (Speece 1995). Butyrate is easily degraded to acetate by butyrate-oxidizing bacteria [Eq. (1)], whereas the degradation of propionate to acetate is thermodynamically infeasible unless the by-product, hydrogen, is removed by the hydrogen-consuming bacteria (Shin et al. 2001). However, the SRB are able to grow with a variety of organic carbon and sulfur compounds, including propionate [Eq. (2)]:

$$2\,\text{butyrate} + 4\,H_2O \longrightarrow 4\,\text{acetate} + H^+ + 4\,H_2 \quad (1)$$

$$4\,\text{propionate} + 3SO_4^{2-} \longrightarrow 4\,\text{acetate} + 4HCO_3^- + 3HS^- + H^+ \quad (2)$$

The reduction of propionic acid in the effluent, even for the short HRTs (4 and 6 h) observed in this study, may be attributable to the cooperation between propionate-degrading bacteria, hydrogen-consuming bacteria, and the activity of the SRB in the reactor.

COD removal and Sulfate Reduction

Generally, organic matter in sulfate-rich wastewater will be removed via sulfate reduction and methanogenesis in an anaerobic bioreactor (Hulshoff Pol et al. 1998). The SRBs obtain the energy for growth through oxidation of the organic substrate, and use sulfate as the terminal electron acceptor. The experimental results illustrate that COD and sulfate removal efficiency increased with the increasing HRT, in that 16–55% of COD and 23–35% of sulfate were removed (Fig. 3). The MPB and SRB were reported to be very competitive for substrate at a COD/SO_4^{2-} ratio of between 1.7 and 2.7, but which one will be dominant depends on the experimental conditions (Hao et al. 1996). Considering the COD/SO_4^{2-} ratio of this study (2.12–2.97) and the operating conditions of the reactor (pH 5.5, short HRT), which were not conducive to the optimal function of the MPB, it can be assumed that the reduction of COD concentration at each HRT was more because of the activity of the SRB than that of the MPB. The COD demand for SRB is in the range of 0.7 to 1.5 g $COD/g\,SO_4^{2-}$, depending on the C-source used as substrate (Hao et al. 1996). The increasing of alkalinity and pH (pH 7–8) in the effluent was observed although the influent pH was controlled at between pH 5.4–5.9. This may due to the degradation of protein and ammonia in latex-processing wastewater by the hydrolytic bacteria, which leads to the formation of NH_4HCO_3 [Eqs. (3) and (4)]. Moreover, the alkalinity could come from HCO_3^- alkalinity, HS^- alkalinity, and volatile acid alkalinity, which occur from sulfate reduction [Eqs. (5) and (6)]:

$$\text{Org-N} + H_2O \longrightarrow NH_3 + CO_2 \quad (3)$$

$$NH_3 + CO_2 + H_2O \longrightarrow NH_4HCO_3 \quad (4)$$

$$SO_4^{2-} + \text{organic matter} \xrightarrow{\text{SRB}} HS^- + H_2O + HCO_3^- \quad (5)$$

$$CH_3COO^- + SO_4^{2-} \xrightarrow{\text{SRB}} 2HCO_3^- + HS^- \quad (6)$$

Considering all the results, the suitable HRT for the acidification stage was 4 h, because a high degree of acidification and acetic acid concentration was achieved at this HRT. Although the COD removal efficiency at this HRT was rather low (<20%), the sulfate reduction efficiency was at the same level as it had been over HRTs of 6 and 8 h (Fig. 3). Moreover, effluent pH (6.5–7.5) and alkalinity

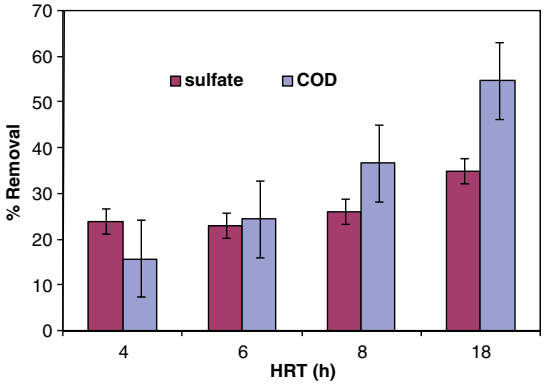

Fig. 3. COD and sulfate removal efficiency at each HRT of the UASB reactor under acidogenic conditions

at HRT of 4 h were optimal for the MPB; therefore, the effluent from the aforementioned conditions could feed directly to the methanogenic reactor without any alkaline addition.

Performance of the Two-stage UASB Reactor Treating Latex-Processing Wastewater

COD and Sulfate Removal Efficiency

The A reactor in the two-stage UASB system was constantly operated over an HRT of 4 h, while the HRTs of the M reactor were varied at 24, 32, and 56 h, respectively. The performance of the two-stage UASB system for each HRT, treating wastewater from a latex-processing factory, is shown in Table 2. The COD removal efficiency of the system was found to increase with the increasing HRT, in which 87.3% of COD was removed for HRT of 60 h [Fig. 4(a)]. A significantly decreased SS concentration was also observed after each stage of treatment. Suspended solids in the latex-processing wastewater are primarily rubber particles, which occur from the skim crepe recovery by adding H_2SO_4 to the skim latex. The decrease of SS concentration was presumably due to the degradation of the rubber particles, which resulted in the formation of rubber scum. It was noticed that most of the COD removal took place in the M reactor; however, the methane content of the biogas could be analyzed only at HRT of 28 h. It was found that the gas outlet in the gas-liquid-solid separator (GSS) of the methanogenic reactor was covered with a lot of rubber scum, which led to the loss of biogas with the effluent. The decrease in the VFA content was also consistent with the increase in efficiency of COD removal.

An increase in sulfate removal efficiency from 71 to 83% was observed when the HRT of the system increased from 28 to 36 h [Fig. 4(b)]. Corresponding to the COD removal, most of the sulfate reduction at those HRTs occurred in the M reactor. It can be presumed that the SRB shared contribution with MPB on COD removal in the M reactor, despite the presence of favorable conditions for the MPB in the reactor. Such results were not surprising, because in the anaerobic treatment of wastewater in the presence of sulfate, hydrogenotrophic SRB (HSRB) has a higher growth rate, substrate affinity, and cell yield than hydrogenotrophic MPB (HMPB) (Oude Elferink et al. 1994; Colleran et al. 1995). Acetate-utilizing SRB (ASRB) has a thermodynamic and kinetic advantage over acetate-utilizing MPB (AMPB) in its competition for acetate (Widdel 1988). In contrast to the COD removal, a remarkably low sulfate-reduction efficiency of only 17% was observed in the M reactor, operating for HRT of 56 h. A lower sulfate concentration in the A reactor (901 mg/L), which resulted in a

J. Environ. Eng. 2013.139:141-146.

Downloaded from ascelibrary.org by Kasetsart University on 01/10/13. Copyright ASCE. For personal use only; all rights reserved.

Downloaded from ascelibrary.org by Kasetsart University on 01/10/13. Copyright ASCE. For personal use only; all rights reserved.

Table 2. Performance of the Two-Stage UASB Reactor Treating Latex-Processing Wastewater at Each HRT

Parameters[a]	HRT 28 h			HRT 36 h			HRT 60 h		
	Influent	Acid tank (4 h)	Methane tank (24 h)	Influent	Acid tank (4 h)	Methane tank (32 h)	Influent	Acid tank (4 h)	Methane tank (56 h)
pH	5.41 ± 0.21	7.01 ± 0.3	8.00 ± 0.17	5.84 ± 0.22	7.83 ± 0.51	8.56 ± 0.13	6.2 ± 0.52	8.3 ± 0.24	8.9 ± 0.13
COD	6, 394 ± 380	5, 460 ± 449	3, 093 ± 461	6, 660 ± 817	5, 230 ± 596	2, 140 ± 499	5, 821 ± 452	3, 887 ± 373	742 ± 181
VFA	3, 450 ± 329	3, 759 ± 314	2, 297 ± 236	3, 385 ± 932	3, 261 ± 1, 081	1, 260 ± 763	2, 631 ± 567	2, 217 ± 228	239 ± 74
Acetic acid	1,346	2,664	1,251	1,693	2,392	1,496	1,740	1,820	53
Propionic acid	1,032	309	n.d.[b]	1,062	284	40	878	141	n.d.[b]
Butyric acid	126	11	n.d.[b]	75	50	n.d.[b]	18	n.d.[b]	n.d.[b]
Alkalinity	2, 220 ± 80	2, 848 ± 206	4, 120 ± 460	2, 495 ± 699	2, 903 ± 900	3, 768 ± 1470	2, 249 ± 609	2, 971 ± 249	2, 943 ± 286
Sulfate	2, 987 ± 257	2, 270 ± 82	859 ± 302	2, 938 ± 999	2, 037 ± 622	506 ± 333	1, 767 ± 333	901 ± 185	807 ± 183
Sulfide	—	38 ± 15	132 ± 39	—	77 ± 28	139 ± 28	—	142 ± 25	56 ± 11
SS	955 ± 320	531 ± 304	252 ± 116	926 ± 157	344 ± 57	94 ± 16	742 ± 122	349 ± 98	66 ± 26
CH_4 (%)	—	7.14	48.98	—	n.a.[c]	n.a.[c]	—	n.a.[c]	n.a.[c]
CO_2 (%)	—	2.41	3	—	n.a.[c]	n.a.[c]	—	n.a.[c]	n.a.[c]

[a]The units of all parameters are mg/L, except pH, CH_4, CO_2.
[b]Not detected.
[c]Could not analyzed (because GSS was blocked by rubber scum).

Fig. 4. Removal efficiency of the two-stage UASB reactor at each HRT: (a) COD removal efficiency; (b) sulfate removal efficiency

COD/SO_4^{2-} ratio of 4.31, might be the reason for the low sulfate reduction efficiency, because MPB outcompeted SRB for available electron donors when the COD/SO_4^{2-} ratio of the wastewater was greater than 2.7 (Hao et al. 1996). Thus, it can be presumed that the degradation of COD in the M reactor operating at HRT of 56 h was primarily due to MPB.

Nevertheless, relatively low methane content in the biogas and low SMA were detected. Visser et al. (1996) found that sludge granules were 50% inhibited at H_2S concentrations of 250 and 90 mg L^{-1} at pH values of 6.4–7.2 and 7.8–8.0, respectively. The methane production of MPB was thought to be inhibited by sulfide toxicity, because the sulfide concentration in the effluent from the acidogenic reactor was 142 mg L^{-1} (Table 2). Moreover, it was noticeable that both the COD removal and sulfate reduction efficiency of the A reactor, even when it operated constantly for HRT of 4 h, increased as the HRT of the system increased from 28 to 36 and 60 h. This might be explained by two reasons: (1) the acclimation of microorganisms to the latex-processing wastewater; and (2) a rapid increase of SRB and acidogenic bacteria in the reactor, because the maximum specific growth rates (μ_{max}) of SRB and acidogenic bacteria were 0.85–2.0 and 0.05–7.2 day^{-1}, respectively (Speece 1995).

The COD removal efficiency of the two-stage UASB system in this study was compared to that of the anaerobic hybrid reactor (one stage) that treated latex-processing wastewater from the same source (Wongkittiwimol 2000). The average COD removal efficiencies when the anaerobic hybrid reactor was operated at HRTs of 36, 60, 96, and 144 h were 41, 59, 81, and 84%, respectively. It was found that the two-stage UASB system had higher removal efficiency than the anaerobic hybrid reactor for the same HRT. For example, a COD removal efficiency of 87.3% could be achieved by the two-stage UASB system at an HRT of 60 h, whereas the same level of efficiency was attained only when the anaerobic hybrid reactor was operated under HRT longer than

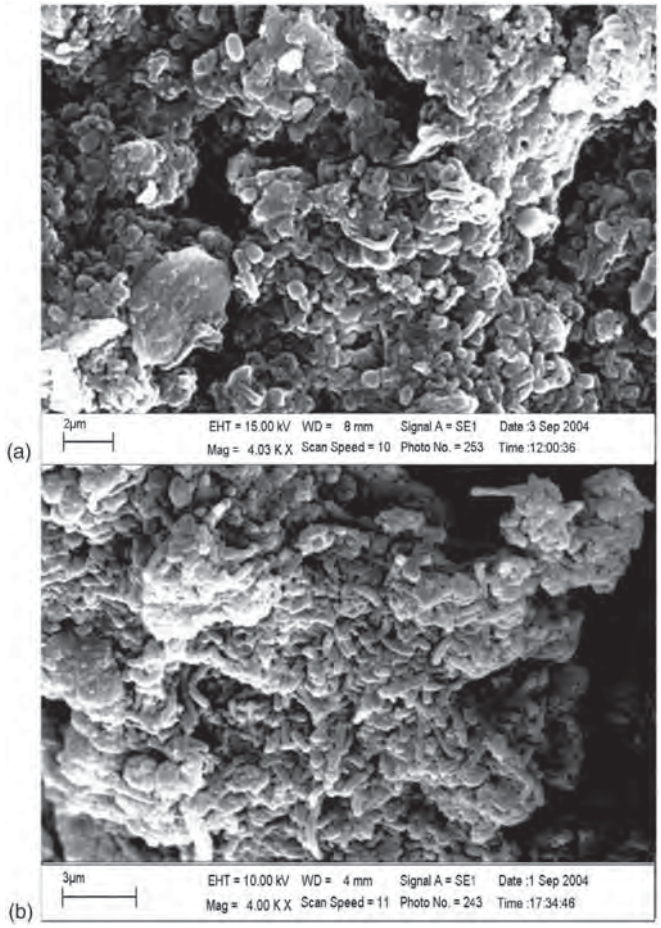

Fig. 5. Scanning electron micrograph of the surface of sludge from: (a) A reactor; (b) M reactor

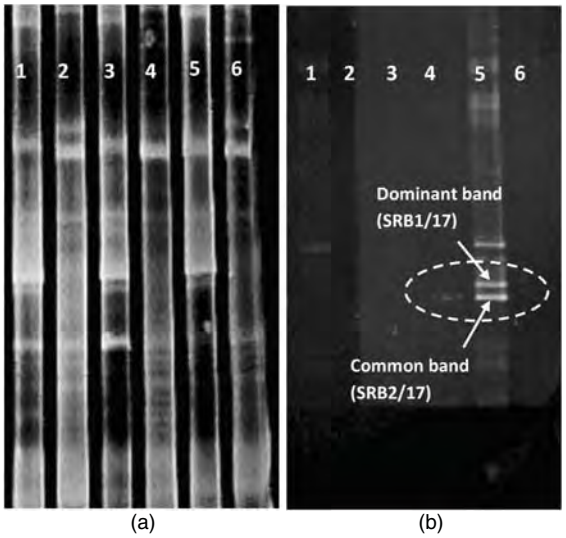

Fig. 6. DGGE profiles of 16S rRNA genes in sludge from the A reactor (columns 1, 3, 5: HRT 4 h) and the M reactor (column 2: HRT 24 h; column 4: HRT 32 h; column 6: HRT 56 h): (a) *archae* bacteria (571 bps); (b) sulfate reducing bacteria (522 bps)

4 days (96 h). This highlights the advantages of the two-stage UASB system, in which the accumulation of VFA and the interference or inhibition of the SRB in relation to the MPB could be reduced in the first stage of the system.

Sludge Morphology and Sludge Activity

The morphology of the sludge from both the acidogenic and the methanogenic reactor, as examined by SEM, revealed that the surfaces of most granules were covered by rubber polymer. A heterogeneous population of rod and filament bacteria was found on the surfaces of both types of sludge. Acidogenic granules predominantly consisted of short-rod bacteria [Fig. 5(a)], whereas networks of long multicellular filaments appeared to colonize the surface of the methanogenic sludge [Fig. 5(b)].

The SAA of sludge from the A reactor was between 1.705–1.835 g COD g VSS^{-1} d^{-1}, and the SAA of the M sludge was slightly broader (1.326–2.024 g COD g VSS^{-1} d^{-1}). Compared to the maximum acidogenic activity in pure cultures and in mixed cultures from anaerobic reactors in the literature (Henze and Harremoes 1983; Soto et al. 1993), the SAA of the tested sludge was 5–10 times lower. Unexpectedly low SMA in the range of 0.0078 to 0.0138 g COD-CH_4 g VSS^{-1} d^{-1}, accompanied by methane content of 25–36% in the biogas, was obtained from the acidogenic and the methanogenic sludge. It was hypothesized that the MPB in the UASB reactor, particularly the M reactor, were eliminated or inhibited by the other bacteria. The monitoring of the microbial community, using a denaturing gradient gel electrophoresis (DGGE) technique, revealed that MPB could still be detected in both the A and M reactors (Fig. 6), but were dominated by the SRB. This was clearly observed in the acidogenic sludge when the system was operated at HRT of 36 h. The ability of SRB to use several intermediates of the anaerobic process (e.g., propionate, butyrate, and acetate) as energy sources in the presence of sulfate, coupled with their high substrate affinity (Hao et al. 1996), were supposed to be the reasons for the overwhelming numbers of SRB in the M reactor. This assumption was confirmed by the SAA of the sludge from the M reactor, which was at the same level as the sludge from the A reactor, and by the high sulfate-reduction efficiency concomitant with the COD removal in the methanogenic reactor at HRTs of 28 and 36 h (Fig. 4).

Conclusions

Latex-processing wastewater was successfully treated in a two-stage UASB reactor. Maximum COD removal efficiency of 87% was achieved at HRT of 60 h and 83% sulfate reduction efficiency was observed at HRT of 36 h. Most of the COD removal was attributable to SRB rather than MPB. Not much difference was observed between the SAA of the acidogenic and methanogenic sludge, which indicates the existence of acetogenic, methanogenic, and sulfate-reducing bacteria in the methanogenic reactor. Microbial community monitoring by the DGGE technique confirmed the domination of SRB in both reactors.

Acknowledgments

The authors would like to express their acknowledgement to the Thailand Research Fund, the Office of the Higher Education Commission and the National Research University Project for the financial support. A grateful thank is also for Dr. Srisuda Dhamwichukorn for her helping hand in PCR-DGGE analysis and the Department of Microbiology, King Mongkut's University of Technology Thonburi for providing the facilities for this study.

J. Environ. Eng. 2013.139:141-146.

Downloaded from ascelibrary.org by Kasetsart University on 01/10/13. Copyright ASCE. For personal use only; all rights reserved.

References

American Public Health Association (APHA). (1992). *Standard methods for the examination of water and wastewater*, 18th ed., APHA/American Water Works Association/Water Environment Federation, Washington DC.

Chathanee, C. (1988). "Tapioca wastewater treatment by two-stage anaerobic digestion process." Master's thesis, Biotechnology, Chulalongkorn Univ., Bangkok, Thailand, 35–46 (in Thai).

Colleran, E., Finnegan, S., and Lens, P. (1995). "Anaerobic treatment of sulphate-containing waste streams." *Antonie Leeuwenhoek*, 67(1), 29–46.

Hao, O. J., Chen, J. M., Huang, L., and Buglass, R. L. (1996). "Sulfate-reducing bacteria." *Crit. Rev. Env. Sci. Technol.*, 26(2), 155–187.

Henze, M., and Harremoes, P. (1983). "Anaerobic treatment of wastewater in fixed film reactors—A literature review." *Water Sci. Technol.*, 15, 1–101.

Hulshoff Pol, L. W., Lens, P. N. L., Stams, A. J. M., and Lettinga, G. (1998). "Anaerobic treatment of sulphate-rich wastewaters." *Biodegradation*, 9(3–4), 213–224.

Kalyuzhnyi, S. V., et al. (1996). "Organic removal and microbiological features of UASB-reactor under various organic loading rates." *Bioresour. Technol.*, 55(1), 47–54.

Lens, P. N. L., Visser, A., Janssen, A. J. H., Hulshoff Pol, L. W., and Lettinga, G. (1998). "Biotechnological treatment of sulfate-rich wastewaters." *Crit. Rev. Env. Sci. Tech.*, 28(1), 41–88.

O-Thong, S., Prasertsan, P., Intrasungkha, N., Dhamwichukorn, S., and Birkeland, N. (2007). "Improvement of biohydrogen production and treatment efficiency on palm oil mill effluent with nutrient supplementation at thermophilic condition using an anaerobic sequencing batch reactor." *Enzyme Microb. Technol.*, 41(5), 583–590.

Oude Elferink, S. J. W. H., Visser, A., Hulshoff Pol, L. W., and Stams, A. J. M. (1994). "Sulfate reduction in methanogenic bioreactors." *FEMS Microb. Rev.*, 15(2–3), 119–136.

Shin, H. S., Han, S. K., Song, Y. C., and Lee, C. Y. (2001). "Performance of UASB reactor treating leachate from acidogenic fermenter in the two-phase anaerobic digestion of food waste." *Water Res.*, 35(14), 3441–3447.

Soto, M., Mendez, R., and Lema, J. M. (1993). "Methanogenic and non-methanogenic activity tests: Theoretical basis and experimental set up." *Water Res.*, 27(8), 1361–1376.

Speece, R. E. (1995). *Anaerobic biotechnology for industrial wastewater*, Archae Press, Nashville, TN.

Thailand Office of Agricultural Economics. (2009). ⟨http://www.oae.go.th/download/prcai/Rubber09.xls⟩ (Jun. 27, 2011).

Visser, A., Hulshoff Pol, L. W., and Lettinga, G. (1996). "Competition of methanogenic and sulfidogenic bacteria." *Water Sci. Technol.*, 33(3), 99–110.

Widdel, F. (1988). "Microbiology and ecology of sulfate- and sulphur reducing bacteria." *Biology of anaerobic microorganisms*, A. J. B. Zehnder, ed., Wiley, New York, 469–586.

Wongkittiwimol, A. (2000). "Treatment of concentrated latex wastewater in the anaerobic hybrid reactor." Master's thesis, Faculty of Engineering, King Mongkut's Univ. of Technology Thonburi, Bangkok, Thailand.

Downloaded from ascelibrary.org by Kasetsart University on 01/10/13. Copyright ASCE. For personal use only; all rights reserved.

J. Environ. Eng. 2013.139:141-146.

Send Orders of Reprints at bspsaif@emirates.net.ae

56 *Current Nanoscience,* **2013,** *9,* **56-60**

Pool-Boiling Heat Transfer Characteristics of Al_2O_3-Water Nanofluids on a Horizontal Cylindrical Heating Surface

Weerapun Duangthongsuk[a,b], Taklaew Yiamsawasd[a], Ahmet Selim Dalkilic[c] and Somchai Wongwises[a,d*]

[a]*Fluid Mechanics, Thermal Engineering and Multiphase Flow Research Lab. (FUTURE), Department of Mechanical Engineering, Faculty of Engineering, King Mongkut's University of Technology Thonburi, Bangmod, Bangkok 10140, Thailand;* [b]*Department of Mechanical Engineering, South-East Asia University, Bangkok, Thailand;* [c]*Heat and Thermodynamics Division, Department of Mechanical Engineering, Yildiz Technical University (YTU), Yildiz, Besiktas, Istanbul 34349, Turkey;* [d]*The Academy of Science, The Royal Institute of Thailand, SanamSueaPa, Dusit, Bangkok 10300, Thailand*

Abstract: This research involved conducting an experiment on pool boiling characteristics of Al_2O_3–water nanofluid. The experimental concentration ranged between 0.00005 and 0.03 %vol. The pressure used was at 1 and 2 atm. The boiling surface was a horizontal copper cylinder with a diameter of 28.5 mm, a length of 90 mm, and surface roughness of 3.14 μm. The main purpose of this research was to study the effect of the nanofluid's concentration and pressure on the heat transfer coefficient and on heat flux, by comparing with water. Calibration of the experimental apparatus with water revealed that the experimental results corresponded to the prediction by Rohsenow's equation. Results from the experiment on pool boiling of nanofluids indicated that the heat transfer coefficient of Al_2O_3–water nanofluid was lower than that of water and tended to decrease when the concentration was higher.

Keywords: Pool boiling, nanofluid, heat transfer coefficient, particle concentration.

1. INTRODUCTION

Heat exchangers are important energy devices commonly found in various industries. They include steamers, heat ventilators in mechanical or electronic devices, coolers, air-conditioners, and other types of devices. At present, the world is facing energy problems. Therefore, many researchers are interested in design and development of devices that use energy more efficiently, including heat exchangers. Working fluids used with heat exchangers include both phase-change (between liquid and vapor) and non phase-change types. The phase-change type produces better heat transfer, compared with the non-phase change type. Pool-boiling heat transfer is one of the mechanisms that occur in heat exchangers. Examples of pool-boiling heat exchangers are heat pipes in heat exchanger units of processors in mobile computers or military communication devices, and fire-tube steamers in industrial factories. Development of pool-boiling heat exchangers maybe carried out in two parts: 1) development of the heating surface and 2) development of the working substance used in the system. The first and most widely used for nucleate pool boiling was developed by Rohsenow [1]. The effects of the surface were taken into account in the correlation. The development of a working substance used in pool-boiling heat exchangers has been carried out in many ways. At present, one of the methods that many researchers are interested in is the addition of solid nanoparticles with high conductivity into base fluids in order to increase thermal conductivity of working fluids. Choi [2] termed the fluids obtained from the addition of solid nanoparticles into abase fluid as "Nanofluid." Regarding the use of nanofluids in forced heat transfer, many researchers have reported increases in the heat transfer coefficient by about 7% to 40% [3-10]. This is because nanofluids have higher conductivity than base fluids. However, only a few studies have used nanofluids with pool-boiling heat transfer, and their results are still inconsistent. Studies concerning specific characteristics of pool boiling of nanofluids in the past decade are summarized here.

*Address correspondence to this author at the Fluid Mechanics, Thermal Engineering and Multiphase Flow Research Lab. (FUTURE), Department of Mechanical Engineering, Faculty of Engineering, King Mongkut's University of Technology Thonburi, Bangmod, Bangkok 10140, Thailand;
Tel: +662-470-9115; Fax: +662-470-9111;
E-mail: somchai.won@kmutt.ac.th

Das *et al*. [11] studied specific characteristics of pool-boiling heat transfer of nanofluids by adding 58.4 mm Al_2O_3 particles to Al_2O_3–water nanofluid at a concentration of 0.1–4 vol.%. The heating surface was a horizontal tube with a diameter of 20 mm and surface roughness of 0.4 to 1.15 μm. Their experimental results showed that the pool boiling heat transfer performance was increased when level of surface roughness increased. However, when the concentration of the nanofluid was increased, the specific characteristics of the heat transfer decreased.

You *et al*. [12] studied the increase incritical heat flux caused by pool boiling of an Al_2O_3–water nanofluid with concentrations of 0.001–0.05 g/l. The heating surface was a horizontal 10x10 mm^2 square copper plate. During the experiment, pressure and temperature were fixed at 2.89 psi and 60°C, respectively. Their results showed that the critical heat flux of the nanofluid was higher than that of water and that it also increased with the increase of the nanofluid's concentration. They found that the critical heat flux increased by 200% at a concentration of 0.05 g/l.

Li *et al*. [13] studied pool-boiling heat transfer characteristics under atmospheric-pressured subcooled boiling of 25 mm silicon dioxide nanoparticles suspended in water at concentrations of 0.05–0.5 wt.%. The heating surface was platinum wire with a diameter of 0.1mm. They found that the pool-boiling heat transfer of SiO_2–water nanofluid was higher than that of water that it varied with the nanofluid's concentration level. In addition, they found that the critical heat flux also increased when the concentration increased.

Vassallo *et al*. [14] studied the pool-boiling heat transfer characteristics of a SiO_2–water nanofluid with Si-deionized size of 15 nm, 50 nm, and 3 μm, and with concentration levels of 0.5–9 vol.%. The heating surface was nickel-chromium wire with a diameter of 0.4 mm and a length of 75 mm. The experiment at atmospheric pressure showed that the critical heat flux of the nanofluid was higher than that of the base fluid, and that it increased when concentration levels of the particles increased.

Bang and Chang [15] studied specific characteristics of nucleate pool-boiling heat transfer of an Al_2O_3–water nanofluid with particle size of 47 nm and concentration levels of 0.5–4 vol.%. The heating surface consisted of 4×100 mm^2 rectangular copper plates placed both horizontally and vertically. Their results showed that increases in the nanofluid's concentration lowered the pool-boiling heat

1875-6786/13 $58.00+.00 © 2013 Bentham Science Publishers

transfer coefficient. However, the critical heat flux was higher than that of water. Analysis from photography revealed that at heat flux higher than 100 kW/m^2, the boiling pattern of the nanofluid was less vigorous than water. They also found that the horizontal heating surface produced higher heat flux than the vertical one.

Kim *et al*. [16] studied the critical heat flux of pool-boiling nanofluids at atmospheric pressure. The 85 nm TiO_2 particles were suspended in water at concentration levels of 0.00001–0.1 vol.%. The heating surface was 0.2 mm nickel-chromium wire. The effect of a heating surface covered with nanoparticles was also studied. They found that the critical heat flux of the nanofluid was higher than that of the base fluid and that the critical heat flux increased when the heating surface was covered with nanoparticles.

Nguyen *et al*. [17] studied specific characteristics of pool-boiling heat transfer of an Al_2O_3–distilledwater nanofluid at atmospheric pressure. The particle size was 47 nm and the concentration level was 0.5–2 vol.%. The heating surface was a horizontal 24 mm-diameter chromium-coated copper disc. Their results showed that when the nanofluid's concentration increased, its pool-boiling heat transfer capacity decreased, compared to water.

Kim *et al*. [18] studied the pool-boiling heat transfer of three-types of nanofluids: Al_2O_3, ZrO_2 and SiO_2 particles suspended in water at concentrations of 0.001–0.1 vol.%. Two types of heating surfaces were used: stainless steel wire with a diameter of 0.381mm and a length of 120mm, and a horizontal 5x45mm^2 plate. The experiment was carried out at atmospheric pressure. The researchers found that the critical heat flux increased with the increase of concentration and heat transfer coefficient was higher than that of water. For all nanofluids, the enhancement of critical heat flux (CHF) is obtained, up to 52% for alumina nanofluids, up to 75% for zirconia nanofluids and up to 80% for silica nanofluids.

Kiu *et al*. [19] studied pool-boiling heat transfer of nanofluids with 50nm CuO and 35 nm SiO_2 particles, each suspended in water and in ethyl alcohol with concentrations of 0.5 wt.%. The heating surface was a horizontal 20mm-diameter copper disc. Their results showed that the critical heat flux of nanofluids was higher than that of the base fluids.

Golubovic *et al*. [20] studied the effect of concentration levels on the critical heat flux of BiO_2–water and Al_2O_3–water nanofluids at a concentration range of 0.0005714–0.0064615 g/l. The heating surface was nickel-chromium wire with a diameter of 0.64 mm and a length of 50 mm, applied at atmospheric pressure. They found that the critical heat flux varied as concentration levels increased, and that it was overall higher than that of water. The CHF was increased by 50% when Al_2O_3 nanoparticles were suspended in pure distilled water and by 33% when BiO particles were suspended.

Trisaksri and Wongwises [21] studied the specific characteristics of pool-boiling heat transfer of a nanofluid with 21nm-diameter TiO_2 nanoparticles suspended in R141b refrigerant at concentrations of 0.01–0.05 vol.%. The heating surface was a horizontal cylinder with a diameter of 28.5 mm and length of 90mm,appliedat pressure levels of 200 to 500 kPa. The researchers concluded that the pool-boiling heat transfer coefficient decreased when the nanofluid's concentration increased, but it increased with increases in the pressure level.

Suriyawong and Wongwises [22] studied pool-boiling heat transfer characteristics of a TiO2–water nanofluid at very low concentration levels (0.00005–0.01 vol.%). The heating surface was made from copper and aluminum, with roughness of 0.2 and 4 μm, applied at atmospheric pressure. In the case of the copper surface, it was found that at concentrations of 0.00005–0.0001 vol.%, the heat transfer coefficient was higher than that of the base fluid. On the other hand, at concentrations higher than 0.0001 vol.%, the heat transfer coefficient was lower than that of the base fluid. In the case of the aluminum surface, the heat transfer coefficient was found to be lower than that of the base fluid at every concentration level. Regarding roughness, a surface roughness of 0.2μm produced a higher heat transfer than roughness of 4μm.

Cieslinski and Kaczmarczyk [23] studied pool-boiling heat transfer of Al_2O_3–water and Cu–water nanofluids at concentrations of 0.01%, 0.1% and 1% by weight. The heating surface was a horizontal smooth-surfaced tube made from copper and stainless steel with a diameter of 10 mm. The effects of concentration level and of surface material on heat transfer characteristics were studied at atmospheric pressure. They found that the concentration level had very little effect on the boiling heat transfer coefficient of Al_2O_3–water and Cu–water nanofluids on the copper heating surface. Additionally, the type of surface material used seemed to have no effect on boiling heat transfer of Cu–water at a concentration of 0.1 wt.%. However, at other concentration levels of both Al_2O_3–water and Cu–water, the boiling heat transfer coefficient on the stainless steel tube was higher than that onthe copper tube at the same heat flux.

From the above review of the literature, there are seemingly very few studies concerning the specific characteristics of pool-boiling heat transfer of nanofluids, and their results are inconsistent. Some researchers reported that the heat transfer coefficient varied with the concentration level of the nanofluid [12-14, 16, 18- 20], while some reported an inverse variation with concentration levels [11, 15, 17, 21, 22]. Every experiment was conducted at atmospheric pressure, except the experiment by Trisaksri and Wongwises [21], who also observed the effects of pressure. Thus, the researchers in the current study aimed to conduct additional experiments on pool-boiling heat transfer in order to clarify the inconsistent results mentioned above. This research uses a nanofluid with $A1_2O_3$ nanoparticles suspended in water at concentrations of 0.00005–0.03 vol.% and at pressure levels of 1 and 2 atm. The heating surface used is a horizontal copper cylinder.

2. PREPARATION OF THE NANOFLUID

The Al_2O_3–water nanofluidused in this study is a product supplied by DEGUSSA Company Limited (Thailand) under the code of AeroDisp. W630. The 120nm-diameter Al_2O_3 particles are suspended in water at a concentration of 30 wt.%. In order to study the effect of the concentration level, the fluidis diluted by addition of base water to obtain concentration levels of 0.00005, 0.0001, 0.005 and 0.03 vol.%. To attaineven dispersion of particles in the base fluid, an ultrasonic vibrator is used for sonication for 2 hours before every experiment. The preparation of the nanofluid with pH-control and the addition of surfactants were accomplished by the manufacturer without revealing information about the process.

3. EXPERIMENTAL APPARATUS AND PROCEDURES

The experimental apparatus includes a pressure vessel, a water-cooling unit, a boiling heating surface, and a DC power supply, as shown in Fig. (**1**).

The pressure vessel containing the nanofluid used in the experiment is made from stainless steel with a diameter of 10 cm, a height of 30 cm, and a thickness of 1 cm. Its outer surface is coated with insulator to prevent heat loss. A cooling coil and a pressure gauge are installed on top of the vessel to control the pressure level and to condense the upward flow of vapors into liquid, in order to maintain a stable concentration throughout the experiment. The control is done by adjusting the flow rate of cold water pumped from the cooling unit. A T-type thermocouple is also installed on top of the vessel to measure the temperature of the fluid mass.

The heating surface, as shown in Fig. (**2**), consists of a 2-kilowatt heater stick buried inside the copper cylinder (28.5 mm diameter and 90 mm length). Both ends of the copper cylinder are covered with insulators to force heat from the heater to the heating surface on its side only (radially). Four sets of T-type thermocouple are installed along the length at even intervals to measure surface

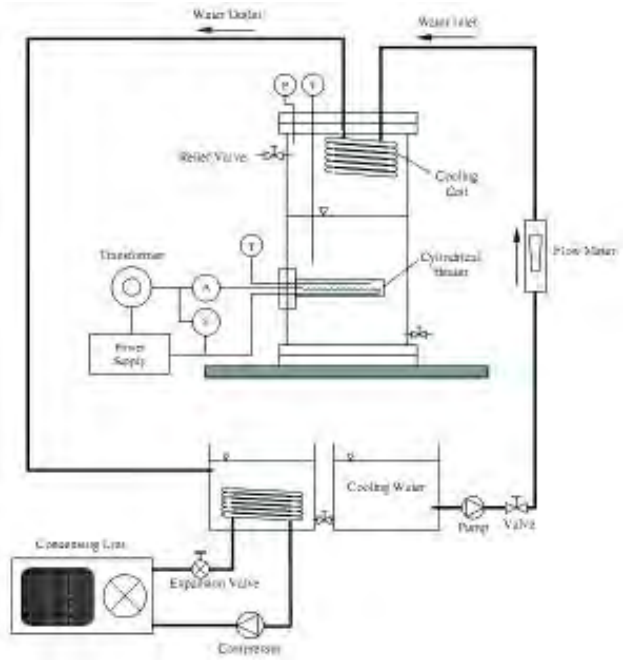

Fig. (1). Schematic diagram of experimental apparatus [Trisaksri and Wongwises [21], with permission from Elsevier].

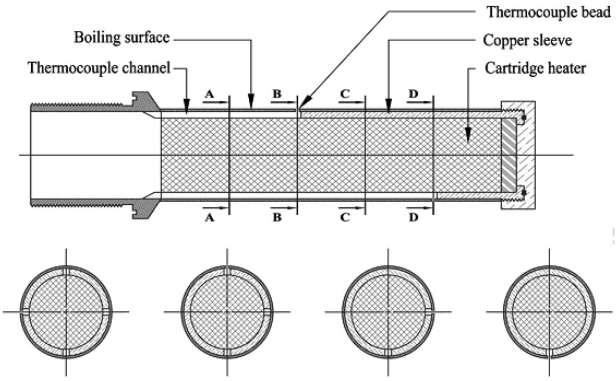

Fig. (2). Cross-sectional view of the heating surface [Trisaksri and Wongwises [21], with permission from Elsevier].

temperature of the tested unit. Each set is placed at an angle of 90 degrees radially. The thermocouples are specially designed so that only the small temperature gauge head is fixed directly onto the outer heating surface, while other signal wires are concealed inside to prevent interference on the heating surface and movement of vapor bubbles during the boiling process.

4. DATA REDUCTION

The heat transfer coefficient and the heat flux of pool boiling may be calculated with the following equations.

The heat flux q (W/m^2) maybe calculated with Eq. (1).

$$q = \frac{IV}{A} \tag{1}$$

where I is electrical current(Amp), V is voltage(Volt), and A is heating surface(m^2).

The average heat transfer coefficient of pool boiling, $h_b(W/m^2K)$ maybe calculated with Eq. (2).

$$h_b = \frac{q}{T_h - T_{sat}} \tag{2}$$

where T_{sat} is the saturated temperature of working fluids (^oC)and T_h is the average temperature of the heating surface, which maybe calculated with Eq. (3).

$$T_h = \frac{T_{h,top} + 2T_{h,side} + T_{h,bottom}}{4} \tag{3}$$

where $T_{h,top}$, $T_{h,side}$ and $T_{h,bottom}$ are temperatures at each location as shown in Fig. (**2**).

The uncertainties of the heat flux, heating surface temperature and heat transfer coefficient are ±2.92%, ±2.39% and ±5.89%, respectively.

Regarding calibration of the experimented apparatus, Rohsenow's equation [1] is used with water as the working fluid, as follows:

$$q = \mu_l h_{fg} \left[\frac{g(\rho_l - \rho_v)}{\sigma} \right]^{0.5} \left[\frac{C_p (T_h - T_{sat})}{C_{sf} h_{fg} \Pr_l^n} \right]^3 \tag{4}$$

where μ is viscosity of fluid, ρ is density of fluid, σ is surface tension of fluid, C_p is specific heat, h_{fg} is latent heat, Pr is Prandtl number, and C_{sf} and n are constants between heating surface and fluid. In the case of the copper surface and water, the constants are 0.031 and 1.0, respectively. The subscripts l and v represent the liquid phase and vapor phase, respectively.

5. RESULTS AND DISCUSSION

Before the experiment on boiling of the nanofluid, the invented apparatus was calibrated to confirm its accuracy by testing with water. The test results were compared with calculations from Rohsenow's equation [1] and data from the experiments of other researchers, as shown in Fig. (**3**). The calibration results confirmed that data gained from the invented apparatus were consistent with calculations from Rohsenow' sequation and with measurements by other researchers.

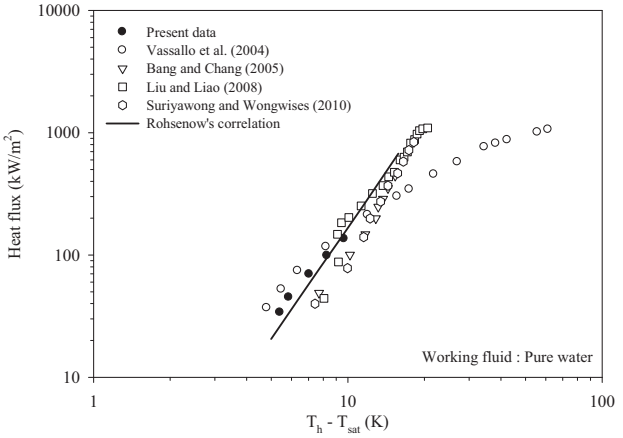

Fig. (3). Comparison of present data with Rohsenow's correlation and various researchers.

Fig. (**4**) shows boiling curves ofAl_2O_3–water nanofluidat various concentration levels. At the same heat flux, the boiling curves tend to move in a direction to the right when concentration levels of nanoparticles increased or when differences in temperature between the heating surface and the fluid increased. It could be said that the

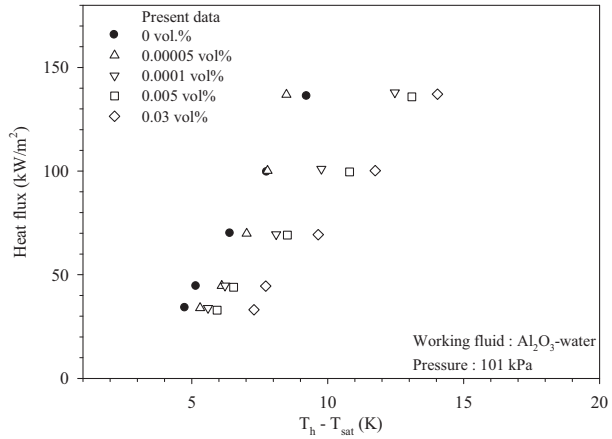

Fig. (4). Boiling curves for Al_2O_3-water nanofluid at 101 kPa.

onset of nucleate boiling is slower. That is, the heat transfer coefficient is lower than the water base fluid and decreases when the concentration increases, as clearly evident in Fig. (**5**). However, at a concentration of 0.00005 vol.%, it was found that at high heat flux, the heat transfer tended to be higher than that of the base fluid. Regarding heat flux, it was found that at the same concentration level, the heat transfer coefficient varied with heat flux in both water and nanofluidat every concentration level.

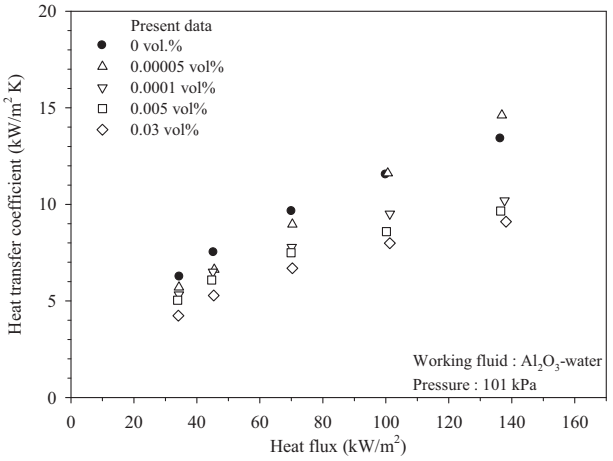

Fig. (5). Boiling heat transfer coefficient for Al_2O_3-water nanofluid at 101 kPa.

The results of the experiment on the pool-boiling heat transfer of an Al_2O_3–water nanofluid were compared with those of other studies, as shown in Fig. (**6**). Correspondence was found with the studies by Das *et al*. [11] and by Cieslinski and Kaczmarczyk [23]. Both of those studies used a horizontal copper cylinder boiling surface similar to that used in this research. It can be seen in the figure that when the concentration increases, the boiling curves tend to move in a direction to the right. In other words, the heat transfer coefficient tends to decrease and is lower than the base fluid. This could be clearly seen in Fig. (**7**), where the experimental results are presented in terms of heat transfer enhancement, which is a ratio between heat the transfer coefficient of nanofluid and the heat transfer coefficient of the base fluid. This figure also shows that at a low concentration level of 0.00005 vol.%, the heat transfer coefficientis higher than that of the base fluid. This is consistent with Suriyawong and Wongwises [22], who found that heat transfer

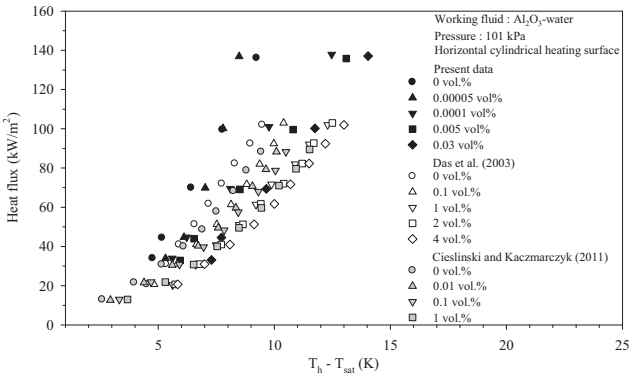

Fig. (6). Comparison of experimental boiling curves with those reported by various researchers.

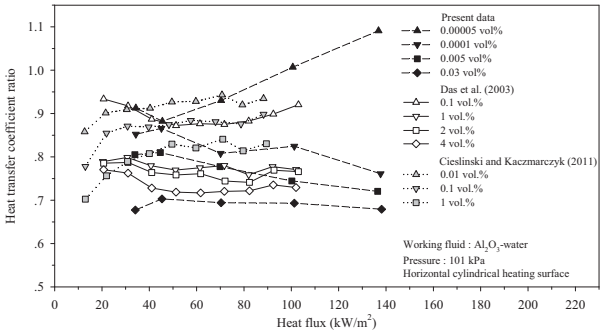

Fig. (7). Comparison of experimental pool boilingheat transfer enhancement with those reported by various researchers.

coefficient of TiO_2-water nanofluid was higher than the base fluid at low concentration levels (between 0.00005 to 0.01 vol.%), but decreased at high concentration level.

Fig. (**8**) shows the effect of pressure on the boiling curve of Al_2O_3–water nanofluid at a concentration of 0.00005 vol.%. The experiment reveals that when the pressure of a fluid increases, the boiling curvetends to move in the left direction, which means that the heat transfer coefficient is higher. Fig. (**9**) shows consistency with the study of Trisaksri and Wongwises [21] who found that the heat transfer coefficient of TiO_2–R141b decreased when the pressure decreased.

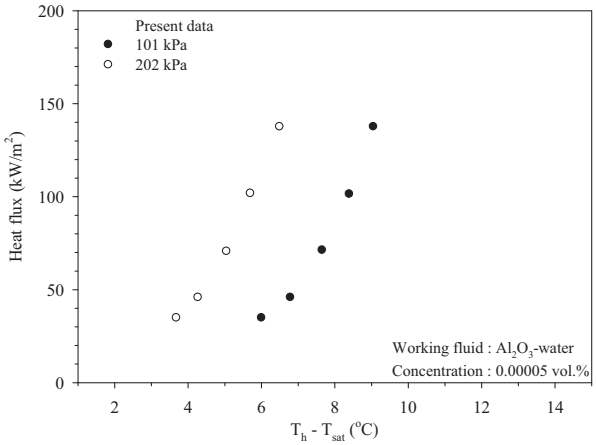

Fig. (8). Variation of boiling curves of nanofluid with pressures.

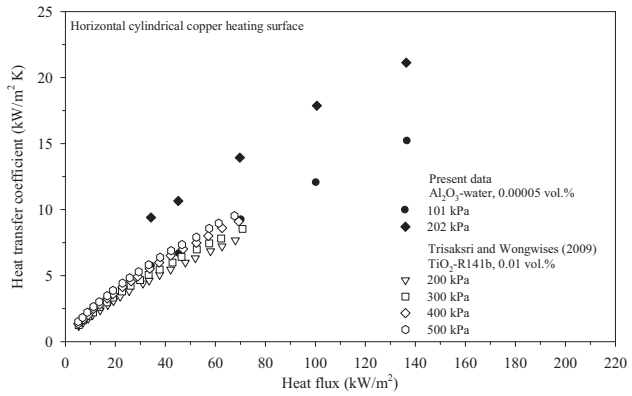

Fig. (9). Variation of heat transfer coefficient with heat flux at different pressures.

The fact that pool-boiling heat transfer coefficient of nanofluid used in this experiment is lower than the water base fluid and decreases when the concentration increases could occur because nanoparticles cover or clog up tiny pores on the heating surface and reduce nucleation site. Normally, these tiny pores produce nucleate bubbles which flow upward and help with circulation and turbulence of fluid that lead to better heat transfer. Moreover, the cover of nanoparticles on heating surface also increases thermal resistance which decreases its heat transfer coefficient.

6. CONCLUSIONS

This research studies pool-boiling heat transfer characteristics of Al_2O_3–water nanofluid with the concentration of 0.00005, 0.0001, 0.005 and 0.03 vol.% at the pressure levels of 1 and 2 atm. The heating surface used is a horizontal copper cylinder. The results from the experiment could be concluded as follows:

- The use ofAl_2O_3–water nanofluid does not help in increasing pool-boiling heat transfer coefficient when compared to water. It also decreases when the concentration increases.
- The heat transfer coefficient decreases when the pressure level decreases.

CONFLICT OF INTEREST

The authors confirm that this article content has no conflicts of interest.

ACKNOWLEDGEMENTS

The authors would like to express their appreciation to the Thailand Research Fund, the Office of the Higher Education Commission and the National Research University Project for providing financial support. The authors also thank Mr. Prawitt Kerdpermdee, Mr. Pumpat Jaturapattanapum and Mr. Theanthum Kaenak for their help in the experimental works.

REFERENCES

[1] Rohsenow, W.M. A method of correlation heat transfer data for surface boiling liquids. *ASME Transaction*, **1952**, *77,* 969.

[2] Choi, S.U.S. Enhancing thermal conductivity of fluids with nanoparticle. *ASME FED*, **1995**, *231*, 99-103.

[3] Duangthongsuk, W.; Wongwises, S. A critical review of convective heat transfer of nanofluids. *Renew. Sustain. Energy Rev.*, **2007**, *11*, 797-817.

[4] Pak, B. C.; Cho, Y. I. Hydrodynamic and heat transfer study of dispersed fluids with submicron metallic oxide particles. *Exp. Heat Transfer*, **1998**, *11*, 151-170.

[5] Xuan, Y.; Li, Q. Investigation on convective heat transfer and flow features of nanofluids. *ASME J. Heat Transfer*, **2003**, *125*, 151.

[6] Wen, D.; Ding, Y. Experimental investigation into convective heat transfer of nanofluids at the entrance region under laminar flow conditions. *Int. J. Heat Mass Transfer*, **2004**, *47*, 5181.

[7] He, Y.; Jin, Y.; Chen, H.; Ding, Y.; Cang, D.; Lu, H. Heat transfer and flow behavior of aqueous suspensions of TiO_2 nanoparticles (nanofluids) flowing upward through a vertical pipe. *Int. J. Heat Mass Transfer*, **2007**, *50*, 2272.

[8] Duangthongsuk, W.; Wongwises, S. Effect of thermophysical properties models on the prediction of the convective heat transfer coefficient for low concentration nanofluid. *Int. Commun. Heat Mass Transfer*, **2008**, *35*, 1320.

[9] Duangthongsuk, W.; Wongwises, S. Heat transfer enhancement and pressure drop characteristics of TiO_2-water nanofluid in a double-tube counter flow heat exchanger. *Int. J. Heat Mass Transfer*, **2009**, *52*, 2059.

[10] Duangthongsuk, W.; Wongwises, S. An experimental study on the heat transfer performance and pressure drop of TiO_2-water nanofluids flowing under a turbulent flow regime. *Int. J. Heat Mass Transfer*, **2010**, *53*, 334-344.

[11] Das, S.K.; Putra, N.; Roetzel, W. Pool boiling characteristics of nanofluids. *Int. J. Heat Mass Transfer*, **2003**, *46*, 851-862.

[12] You, S.M.; Kim, J.H.; Kim, K.H. Effect of nanoparticles on critical heat flux of water in pool boiling heat transfer. *Appl. Phys. Lett.*, **2003**, *83*, 3374-3376.

[13] Li, C.H.; Wang, B.X.; Peng, X.F. On the pool boiling of subcoolednano-particle suspensions. *paper presented in the 6th International Symposium on Heat Transfer*, Beijing, China, **2004**.

[14] Vassallo, P.; Kumar, R.; Amico, S.D. Pool boiling heat transfer experiments in silica–water nanofluids. *Int. J. Heat Mass Transfer*, **2004**, *47*, 407-411.

[15] Bang, I.C.; Chang, S.H. Boiling heat transfer performance and phenomena of Al_2O_3-water nanofluids from a plain surface in a pool. *Int. J. Heat Mass Transfer*, **2005**, *48*, 2407-2419.

[16] Kim, H.; Kim, J.; Kim, M. Experimental study on characteristics of water-TiO_2 nanofluids. *Nucl. Eng. Technol.*, **2006**, *38*, 61-68.

[17] Nguyen, C.T.; Galanis, N.; Roy, G.; Divoux, S.; Gillbert, D. Pool boiling characteristics of water-Al_2O_3 nanofluid, *paper presented in the 13th International Heat transfer conference*, Sydney, Australia, **2006**.

[18] Kim, S.J.; Bang, I.C.; Buongiorno, J.; Hu, L.W. Surface wettability change during pool boiling of nanofluids and its effect on critical heat flux. *Int. J. Heat Mass Transfer*, **2007**, *50*, 4105-4116.

[19] Liu, Z.; Liao, L. Sorption and agglutination phenomenon of nanofluids on a plain heating surface during pool boiling. *Int. J. Heat Mass Transfer*, **2008**, *51*, 2593-2602.

[20] Golubovic, M.N.; Madhawa, H.D.; Hettiarachchi, M.; Worek, W.M.; Minkowycz, W.J. Nanofluids and critical heat flux, experimental and analytical study. *Appl. Therm. Eng.*, **2009**, *29*, 1281-1288.

[21] Trisaksri, V.; Wongwises, S. Nucleate pool boiling heat transfer of TiO_2-R141b nanofluids. *Int. J. Heat Mass Transfer*, **2009**, *52*, 1582-1588.

[22] Suriyawong, S.; Wongwises, S. Nucleate pool boiling heat transfer characteristics of TiO_2-waternanofluids at very low concentrations. *Exp. Therm. Fluid Sci.*, **2010**, *34*, 992-999.

[23] Cieslinski, J.T.; Kaczmarczyk, T.Z. Pool boiling of water-Al_2O_3 and water-Cu nanofluids on horizontal smooth tubes. *Nanoscale Res. Lett.*, **2011**, *6*, 1-9.

Received: April 2, 2012 **Revised: September 13, 2012** **Accepted: October 14, 2012**

Send Orders of Reprints at bspsaif@emirates.net.ae

Current Nanoscience, **2013**, *9*, 61-80

Determination of the Single-Phase Forced Convection Heat Transfer Characteristics of TiO_2Nanofluids Flowing in Smooth and Micro-Fin Tubes by Means of CFD and ANN Analyses

N. Kayaci[1], M. Balcilar[2], M. Tabatabaei[1], A. Celen[1], O. Yıldız[3], A.S. Dalkilic*,[1] and S. Wongwises[4]

[1]*Heat and Thermodynamics Division, Department of Mechanical Engineering,Yildiz Technical University (YTU), Yildiz, Besiktas, Istanbul 34349, Turkey;* [2]*Computer Engineering Departmant, Yildiz Technical University (YTU), Davutpasa, Esenler, Istanbul 34220, Turkey;* [3]*Department of Mechanical Engineering, Kocaeli University, Umuttepe Campus, Kocaeli, 41380, Turkey;* [4]*Fluid Mechanics, Thermal Engineering and Multiphase Flow Research Lab. (FUTURE), Department of Mechanical Engineering, Faculty of Engineering, King Mongkut's University of Technology Thonburi (KMUTT), Bangmod, Bangkok 10140, Thailand*

Abstract: A numerical study including a validation process with experimental data was performed on the forced convection flows of nanofluids; the object of study was water containing TiO_2 nanoparticles in smooth and micro-fin tubes at a constant wall temperature. Constant heat flux and temperature-dependent properties were used to determine the hydrodynamics and thermal behaviors of the nanofluid flow;a single-phase numerical model was used to solve two-dimensional equations by means of a CFD program for the water flow, contained in a smooth tube and in various micro-fin tubes having various helix angles (0^o, 18^o). An extensive literature review on the determination of the physical properties (k, μ, ρ, Cp) of nanofluids is given in this paper. Multilayer Perceptron (MLP), one of theartificial neural network (ANN) methods, was used to determine the most agreeable physical propertiesof TiO_2 nanofluids among correlations. The inputs ofthe ANN analyses were the correlations of physical properties, the average temperature and velocity of water in the test tubes, and the nanoparticle concentrations, while the outputs were shear stress, friction factor, heat flux, convective heat transfer coefficient, and pressure drop. After obtaining the best combination of physical properties of TiO_2 nanofluids from the ANN analyses, the numerical model was validated by means of a CFD program,with the experimental smooth tube data as a case study; it was also validatedas a simulation studyfor several micro-fin tubes through a CFD program. This paper shows temperature, pressure, and velocity distributions in the investigated tubes; in addition, average and local experimental, theoretical, and numerical values in the smooth and micro-fin tubes are compared with oneanother in terms of friction factors, shear stresses, convective heat transfer coefficients, and pressure drops, according to various nanoparticle concentrations.

Keywords: Heat transfer coefficient, Pressure drop, ANN, Nanofluid, Single-phase flow, CFD.

1. INTRODUCTION

Thermal conductivity is an important parameter that expresses the heat transfer performance of a heat transfer fluid. Due to their low thermal conductivity, conventional heat transfer fluids (e.g. water, oil, ethylene glycol mixtures) restrict the enhancement of performance and compactness in heat exchangers used in the electronic, automotive, and aerospace industries. One solution for improving the thermal conductivity of a fluid is to suspend small solid particles in the fluid. Since the thermal conductivity of solid metals is higher than that of fluids, the suspended particles are expected to be able to increase thermal conductivity and heat transfer performance. Experimental studies on the thermal conductivity of nanofluids have been performed by many researchers. Slurries are formed by adding metallic, non-metallic and polymeric particles to fluids. Due to the large size of these suspended particles (on the millimeter scale), problems such as abrasion and clogging can occur. For this reason, such large particles cannot offer a workable solution for heat transfer enhancement. Recently, progress in manufacturing technologies has made possible the production of particles on the nanometer scale (i.e., particle diametersranging from 10 to 100 nm). These smaller-sized particles allow uniform and stable suspensions to form; thus, nanofluidsprovide higher heat transfer enhancement than do existing techniques. The first continuous studies on the use of particles of nanometer dimension were conducted by a research group at the Argonne National Laboratory approximately a decade ago. Choi [1] was likely the first researcher who called the fluids with nanometer particles 'nano-fluids'. The term 'nanofluid' thus refers to a two-phase mixture usually composed of a continuous liquid phase and of dispersed nanoparticles in suspension.

Xuan and Li [2] stated that nanofluids are easily fluidized and can almostbe considered a fluid due to their tiny particle size, despite their character as atwo-phase mixture. For this reason, nanofluid flow can be treated as a single-phase flow. Maxwell [3] assumed that the fluid phase and the particles are in thermal equilibrium and move at the same velocity under certain conditions,given the ultra-fine and lowvolume fraction of the solid particles. Advantages of a single-phase flow include its simplicity and its lowerrequired computational time. It should be emphasizedthat physical properties of nanofluids have a strong impact on experimental, numerical, and theoretical solutions. The most well-known nanoparticles are Al_2O_3, CuO, TiO_2, each of which is used, together with the base fluids of water and ethylene glycol, in the experimental work of many researchers. Across the range ofparticle sizes and types of base fluids, the enhancement of thermal conductivity has beenachievedunder all experimental conditions with these nanoparticles.

The following paragraph summarizes some of the recent studies presented by researchers on the flow of nanofluids. The review paper of Daungthongsuk and Wongwises [4] summarized published resultson the forced convective heat transfer of nanofluids inboth experimental and numerical investigation. Daungthongsuk and Wongwises [5] reported that the thermal conductivity of nanofluids increased with increasing nanofluid temperatures and, conversely, that the viscosity of nanofluids decreased with increasing nanofluid temperatures. Duangthongsuk and Wongwises [6] studied the differences between using measured and computed thermophysical

*Address correspondence to this author at the Heat and Thermodynamics Division, Department of Mechanical Engineering, Yildiz Technical University (YTU), Yildiz, Besiktas, Istanbul 34349, Turkey; Tel: +9 0212 3832819; Fax: +9 0212 2616659; E-mail: dalkilic@yildiz.edu.tr

1875-6786/13 $58.00+.00 © 2013 Bentham Science Publishers

properties to describe the heat transfer performance of TiO_2-water nanofluids; they concluded that measuring the thermophysical properties of nanofluids is an important way to address the transport behavior of nanofluids.Duangthongsuk and Wongwises [7] also conducted an experimental study on the heat transfer performance and pressure drop results of TiO_2-water nanofluids under a turbulent flow regimen. Their results indicated that the dispersion of nanoparticles into the base liquid increases the thermal conductivity and viscosity of the nanofluids, and that this augmentation increases with increasing particle concentrations. Daungthongsuk and Wongwises [8] further reported their study on the forced convective heat transfer and flow characteristics of a nanofluid consisting of water and 0.2vol.%TiO_2 nanoparticles. According to their results, the heat transfer coefficient of the nanofluid increases with an increase in the mass flow rate of the hot water and nanofluid; increases with a decrease in the nanofluid temperature; and does not significantly respond to the temperature of the heating fluid. Duangthongsuk and Wongwises [9] also studied the role of thermophysical properties models in the prediction of convective heat transfer coefficientsin low concentration nanofluids. They reported that precise values for thermal and physical properties such as specific heat, viscosity, and thermal conductivity are required in order to study the heat transfer behavior of the nanofluids. Daungthongsuk *et al*. [10] presented an experimental study on the heat transfer and pressure drop characteristics of Al_2O_3-water nanofluids flowing through a microchannel heat sink (MCHS). The study investigated the effects of the Reynolds number and of particle concentrations on the heat transfer and flow behavior of the nanofluids. Results indicatedan increase in the heat transfer performance of MCHS both with an increase in the Reynolds number and with an increase in particle concentration. Suriyawong and Wongwises [11] studied the nucleate pool-boiling heat transfer of TiO_2-water nanofluids experimentally. Nanofluids with varying concentrations of 0.00005, 0.0001, 0.0005, 0.005, and 0.01vol.% were employed in their study. The experiments explored the effects of nanofluid concentrations and of the heating and roughnessof the surface material on the nucleate pool-boiling characteristics and on the heat transfer coefficient under ambient pressure. In the case ofaheated copper surface tested at a concentration of 0.0001vol.%, results showed a higher nucleate pool-boiling heat transfer coefficient than was obtained with the base fluid. Trisaksri and Wongwises [12] investigated the nucleate pool-boiling heat transfer of a refrigerant-basednanofluid at different nanoparticle concentrations and pressures. TiO_2 nanoparticles were mixed with the refrigerant HCFC 141b at 0.01, 0.03 and 0.05vol.%, and pool-boiling experiments on nanofluids were compared tofindings on the base refrigerant. Results indicated that the nucleate pool-boiling heat transfer deteriorated with increasing particle concentrations, especially at high heat fluxes.

This paragraph summarizes some of the recent studies presented on the CFD analyses of in-tube flows. Dalkilic *et al*. [13-14] presented theoretical flow models for homogeneous and separated flows applied to in-tube condensation to predict the pressure drop characteristics of R134a. Numerical analyses were performed by means of a CFD program to determine average and local homogeneous wall shear stresses and friction factors [15]. Refrigerant-side total pressure drops, frictional pressure drops, friction factors, and wall shear stresses were determined within a ±30% error band. Demir *et al*. [16] numerically investigated laminar and turbulent forced convection flows of a nanofluid consisting of water and Al_2O_3 particles in a horizontal smooth tube with constant wall temperature. Their CFD15 results demonstrated a heat transfer enhancement due to the presence of the nanoparticles in the fluid. Demir *et al*. [17] studied numerically the single-phase forced convection heat transfer characteristics of TiO_2 nanofluids in a double-tube counter-flow heat exchanger. In their paper, they used Palm *et al*.'s [18] correlations to determine the thermophysical properties of the nanofluids. Their CFD [15] results indicateda heat transfer enhancement due to the presence of the nanoparticles in the fluid,agreeing with the results of the experimental study used in the validation process for the numerical model. Agra *et al*. [19] investigated the heat transfer and pressure drop characteristics of smooth, corrugated, and helically finned tubes by using Fluent CFD software [15] and Gambit software [15] to plot and mesh models of the test tubes. The problem under investigation was a two-dimensional (axisymmetric), steady forced turbulent convection flow of water flowing inside straight and enhanced circular tubes. Their paper compared numerical results with experimental data and with the Blasius equation. It was seen that the Fluent CFD [15] program predicted the experimental data more accurately than did the Blasius equation.

The following paragraph summarizes some of the recent studies presented on the artificial intelligence analyses of in-tube flows. Balcilar *et al*. [20] used computational numerical methods such as artificial neural networks (ANNs) to determine the compatibility of the most suitable coefficients of the correlations with the majority of experimental data; Balcilar *et al*. [21] and Bolat *et al*. [22] studied heat transfer characteristics in their analyses by means of ANNs. The inputs of the ANNs are the measured values of test sections such as mass flux, heat flux, temperature differences between the tube wall and the saturation temperature, and average vapor quality, while the outputs are the experimental condensation heat transfer coefficient and the pressure drop measured in the analysis. Balcilar *et al*. [23-24] investigated the nucleate pool-boiling heat transfer characteristics of TiO_2 nanofluids to determine the effects of the important parameterson the heat transfer coefficient, and also to formreliable empirical correlations based on the neural network analysis. Balcilar *et al*. [25] predicted the condensation and evaporation pressure drops of R32, R125, R410A, R134a, R22, R502, R507a, R32/R134a (25/75 by wt%), R407C, and R12, flowing inside various horizontal smooth and micro-fin tubes, by means of the numerical techniques of ANNs and of non-linear least squares (NLS). Total pressure drops within in-tube condensation and in-tube evaporation tests were modeled using the ANN method of multi-layer perceptron (MLP) with a 12-40-1 architecture. In light of cross-validation tests of 1485 evaporation and condensation data points,the average error rate of this method was 7.085%.

For some time now, many studies have concentrated on proposing a model to predict the heat transfer enhancement of nanofluids. It should be noted, however, that there has not yet been a paper on the investigation of the proper physical properties of nanofluids by ANN analyses. In the remainder of this paper, the most agreeable physical properties (k, μ, ρ, c_p) of nanofluids will be analyzed through experimental data, making use ofnearly all correlations in the current literature. To this end, two ANN models with different input values were developed using experimental results to determine the most suitable physical properties among these correlations. Smooth and micro-fin tubes were drawn in SOLIDWORKS [26] software and then imported into ANSYS Fluent [27] software for CFD analysis. Prior to thesimulation of the micro-fin tubes in the CFD program, the smooth-tube model was validated using the agreeable physical properties obtained from ANN analyses and experimental data from the forced convection of TiO_2nanofluids, which were calculated and measured for heat transfer coefficients and pressure drops. Temperature distributions, pressure and velocity of the inner surface and of the fluids at the inlet and outlet sections of the tube, friction factors, wall shear stresses, pumping powers and particle concentrations, local heat transfer coefficients, and pressure drops along the tubes were also obtained from the numerical study for smooth and micro-fin tubes. Last of all,this paper demonstrates a heat transfer enhancement and an increase in pressure drop and pumping power due to the presence of the nanofluids and the micro-fin tubes.

2. SAMPLE PREPARATION

In the present study, nanofluids provided by a commercial source (DEGUSSA, VP Disp. W740x) were used as working fluid. The fluid mixture was composed of TiO_2 nanoparticles with an average diameter of 21 nm dispersed in water. The original particle concentration was 40 wt.%. In order to produce other required particle volume fractions, dilution with water and stirring action were employed. An ultrasonic vibrator was used to sonicate the solution continuously for about 2 h in order to break down the agglomeration of the nanoparticles. The desired volume concentrations used in this study were 0.2%, 0.6%, and 1.0%, with pH values of 7.5, 7.1, and 7.0, respectively. From these pH values it can be seen that the solution chemistry of nanofluids is nearly neutral. A transmission electron microscope (TEM) was used to approximate the size of the primary nanoparticles. As Fig. (**1**) shows, it is clear that the primary size of the nanoparticles was approximately spherical, with an average diameter of around 21 nm.

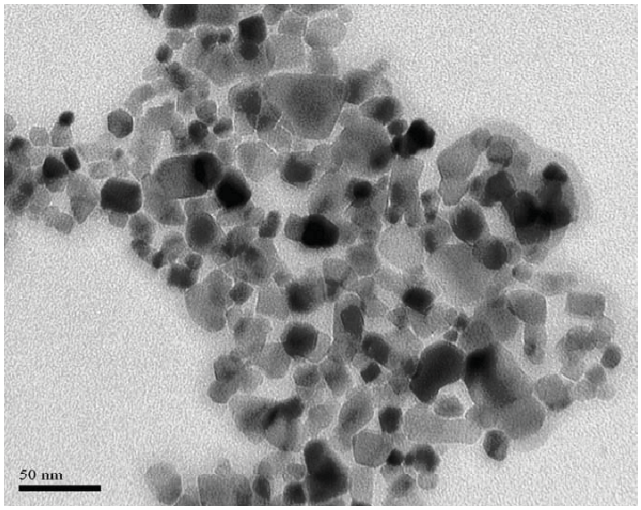

Fig. (1). TEM image of dispersed TiO_2 nanoparticles in water [From Duangthongsuk and Wongwises [6], with permission from Elsevier].

3. EXPERIMENTAL APPARATUS

The experimental system used in the present study is shown schematically in Fig. (**2a**). It consisted mainly of a test section, two receiver tanks, a magnetic gear pump, a hot water pump, a cooler tank, a hot water tank, and a collection tank. The test section was a 1.5 m long counter-flow horizontal double-tube heat exchanger with nanofluid flowing inside the tube and hot water flowing in the annular. The inner tube was made from smooth copper tubing with a 9.53 mm outer diameter and a 0.7 mm thickness, while the outer tube was made from PVC tubing and has a 33.9 mm outer diameter and a 3 mm thickness. The test section was thermally isolated from its upstream and downstream sections by plastic tubes in order to reduce the heat loss along the axial direction. The differential pressure transmitter and the T-type thermocouple were mounted at both ends of the test section to measure the nanofluid's pressure drop and bulk temperature,respectively. Thermocouples were mounted in sets of three, equally spaced around the tube circumference, at different longitudinal positions along the surface of the inner tube wall. The inlet and exit temperatures of the hot water were measured using T-type thermocouples inserted directly into the flow. The 60 L receiver tanks,made of stainless steel, stored the nanofluid and hot water leaving the test section. The cooler tank had a 4.2 kW cooling capacity, and a thermostat was used to keep the nanofluid temperature constant. As with the cooler tank, a 3 kW electric heater with a thermostat was installed to keep the temperature of the hot water constant. The nanofluid flow rate was controlled by adjusting the rotation speed of the magnetic gear pump. The hot water flow rate was measured by a rotameter, while the nanofluid flow rate wascalculated from the exact time required for the entire mass of nanofluid to be discharged. For each pump speed, five measurements were taken. Averagesare given for all data in the present study.

A portable programmable calibrator was used to calibrate all T-type thermocouples, with a maximum precision of 0.1 °C. The nanofluid mass flow rates were determined by electronic balance, with an uncertainty of ±0.0006 kg. Maximum uncertainty of the nanofluid mass flow rate was evaluated at 2.2%; this was taken into account in calculating the uncertainty of the Nusselt number.

The uncertainty of the hot water mass flow rate was evaluated $\pm$7% (full scale). As noted above, the uncertainty of the measured Nusselt number can readily be seen to depend on measurements of temperature, nanofluid flow rate, and hot water flow rate. The uncertainty of the measured Nusselt number was evaluated using the root mean sum square method, and was found to be 5%.

During the test run, wall temperatures of the test section, mass flow rates of the hot water and nanofluid, and the inlet and exit temperatures of the hot water and nanofluid were measured.

A view of the geometrical parameters of the micro-fin tubes is given in Fig. (**2b**). The dimensional parameters of the investigated tubes are given in Table **4**.

4. DATA REDUCTION

4.1. Thermal and Physical Properties of Nanofluids

The determination of nanofluid properties is known to be a widespread pursuit in current research. Some correlations have been developed toward this end by Williams *et al*. [28]. The measurement of physical properties has been undertaken by several researchers within the literature,including Rea *et al*. [29] and Duangthongsuk and Wongwises [7].

Tables **1**, **2**, and **3** provide a summary of the current literature on almost all empiricalcorrelations for nanofluid dynamic viscosity [30-53], thermal conductivity [3, 18, 54-68], and specific heat capacity at constant pressure [3, 54, 69-70], respectively.

It should be noted that the density of the nanofluid was calculated from Pak and Cho's [48] correlation, as follows:

$$\rho_{nf} = \rho_s.\phi + (1-\phi).\rho_w \tag{1}$$

4.2. Governing Dimensionless Numbers, Heat Flux, the Heat Transfer Coefficient, and the Nusselt Number

As test fluid flows through ducts, the heat transfer surface surrounds and guides the stream, and the convection process is said to be internal. The velocity distribution in a duct has two distinct regions in laminar flow: first, the entrance region, where the walls are lined by successive boundary layers, and second, farther downstream, the fully developed region, where longitudinal velocity is independent of position along the duct. It is assumed that duct geometry does not change with longitudinal position. The flow through a straight duct ceases to be laminar when the Reynolds number (Re) exceeds approximately 2300, and the turbulent flow becomes fully developed hydrodynamically and thermally after a relatively short entrance distance [71].

The Reynolds number (Re) and the Prandtl number are used in theoretical analysis [18]; the particle volume fraction (φ) and the ratios k_p/k_{bf} and Cp_p/Cp_{bf} are used to characterize the problem, and can be calculated as follows:

$$\mathrm{Re} = \frac{2Q}{\pi d\nu} \tag{2}$$

$$\mathrm{Pr} = \frac{C_p\mu}{k} \tag{3}$$

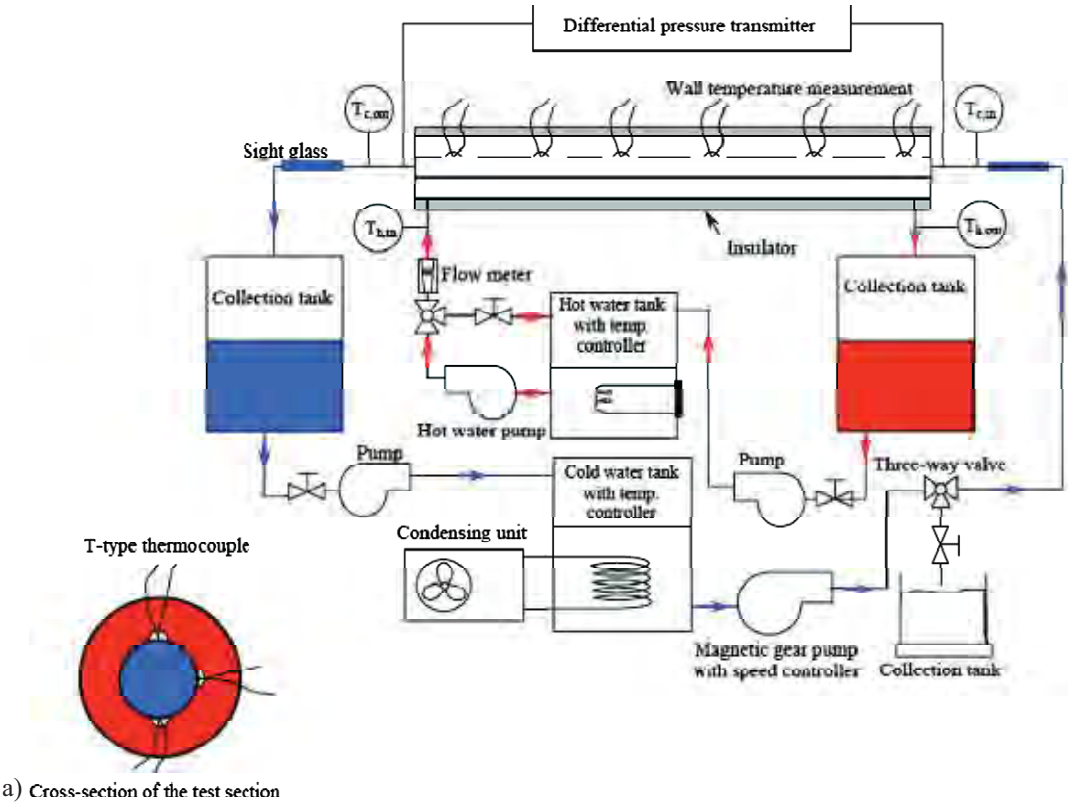

Fig. (2). Schematic diagram of the experimental apparatus (**a**) [From Duangthongsuk and Wongwises [6], with permission from Elsevier] and view of geometrical parameters of micro-fin tubes (**b**).

In the fully developed region, the friction factor is defined as in the laminar flow:

$$f = \frac{64}{\mathrm{Re}} \tag{4}$$

Petukhov [72] discovered a formula for the friction factor in turbulent flow, as follows:

$$f = (0.970 \ln \mathrm{Re} - 1.64)^{-2} \tag{5}$$

By using the Darcy friction factor, wall shear stress can be calculated as below:

$$\tau = \frac{f \rho V_{avg}^2}{8} \tag{6}$$

Table 1. Some Dynamic Viscosity Correlations of Nanofluids in Literature

Researcher	Correlation
(1) Einstein [30]	$\mu_{eff} = (1 + 2.5\varphi)\mu_f$
(2) Brinkman [31]	$\mu_{eff} = \mu_{bf}(1 - \varphi)^{2.5}$
(3) Batchelor [32]	$\mu_{eff} = (1 + \eta\varphi + k_H\varphi^2)\mu_f = (1 + 2.5\varphi + 6.2\varphi^2)\mu_f$
(4) Graham [33]	$\mu_{eff} = (1 + 2.5\varphi)\mu_f + \left[\frac{4.5}{(h/r_p)(2+h/r_p)(1+h/r_p)^2}\right]\mu_f$
(5) Kitano *et al*. [34]	$\mu_{eff} = \mu_{bf}\left[1-(\varphi-\varphi_m)\right]^{-2}$
(6) Bicerano *et al*. [35]	$\mu_{nf} = \mu_{bf}\left[1+\eta\phi+k_H\phi^2)\right]$
(7) Wang *et al*. [36]	$\mu_{nf} = \mu_{bf}\left[1+7,3\phi+123\phi^2\right]$
(8) Tseng and Chen [37]	$\mu_{nf} = \mu_{bf}\,0,4513e^{0,6965\phi}$
(9) Chen *et al*. [38]	$\mu_{nf} = \mu_{bf}\left[1+10,6\phi+(10,6\phi)^2\right]$
(10)-(11) Nguyen *et al*. [39]	$\mu_{nf} = \mu_{bf}\,0,904e^{0,1482\phi}$ $\mu_{nf} = \mu_{bf}(1 + 0,025\phi + 0,015\phi^2)$
(12) Khanafer and Vafai [40]	$\mu_{nf} = \mu_{bf}(1,0538 + 0,1448\phi - 3,363x10^{-3}T - 0,0147\phi + 6,735x10^{-5}T^2 - 1,337\frac{\phi}{T})$
(13) Duanghongsuk and Wongwises [5]	$\mu_{nf} = \mu_{bf}(1,013 + 0,092\phi + 0,015\phi^2)$
(14) Vand [41]	$\mu_{nf}=\mu_{bf}e^{2.5\phi+2.7\phi^2/(1-0.609\phi)}$
(15) Mooney [42]	$\mu_{nf} = \mu_{bf}e^{(\frac{2.5*\phi_m*\phi}{1-\phi})}$
(16)-(17) Krieger [43-44]	$\mu_{nf} = \mu_{bf}(\frac{\phi_m}{1-\phi})^a$ $\mu_{nf} = \mu_{bf}(\frac{\phi_m}{1-\phi})^{1.82}$
(18) Frankel and Acrivos [45]	$\mu_{nf} = \mu_{bf}1.125(\frac{\phi}{\phi_m})^{1/3}/(1-(\frac{\phi}{\phi_m})^{1/3})$
(19) Miler *et al*. [46]	$\mu_{nf} = \mu_{bf}(537.42\phi - 0.188)$
(20) Chow [47]	$\mu_{nf} = \mu_{bf} * (e^{\frac{2.5*\phi}{1-\phi}}) + (A*\phi^2)/(1 - A*\phi^2*\phi_m)$
(21) Pak and Cho [48]	$\mu_{nf} = \mu_{bf}(108.2\phi^2 + 5.45\phi + 1)$

(Table 1) Contd….

Researcher	Correlation
(22) Liu [49]	$\mu_{nf} = \mu_{bf}((\frac{1-\phi}{\phi_m})^2 + (\frac{k_1 - 2}{\phi_m})\phi + (\frac{k_2 - 6}{\phi_m^2})\phi^2)$
(23)-(24) Wang *et al*. [50]	$\mu_{nf} = \mu_{bf}(123\phi^2 + 7.3\phi + 1)$ $\mu_{nf} = \mu_{bf}(306\phi^2 - 0.19\phi + 1)$
(25) Davalos *et al*. [51]	$\mu_{nf} = \mu_{bf}(6.17\phi^2 + 2.5\phi + 1)$
(26)-(27) Putra *et al*. [52]	$\mu_{nf} = 2.9x10^{-7}xT^2 - 2x10^{-4}xT + 3.4x10^{-2}$ for %1 $\mu_{nf} = 3.4x10^{-7}xT^2 - 2.3x10^{-4}xT + 3.9x10^{-2}$ for %4
(28) Tang *et al*. [53]	$\mu_{nf} = 2.761x10^{-6}xe^{1713/T}$

Table 2. Some Thermal Conductivity Correlations of Nanofluids in Literature

Researcher	Correlation
(1) Maxwell [3]	$k_{nf}=k_f * \frac{k_p+2k_f+2\phi(k_p-k_f)}{k_p+2k_f-\phi(k_p-k_f)}$
(2) Hamilton and Crosser [54]	$k_{nf}=k_f * \frac{k_p+(n-1)k_f-(n-1)\phi(k_f-k_p)}{k_p+(n-1)k_f+\phi(k_f-k_p)}, n=\frac{3}{\Psi}, \Psi=\frac{\phi\rho_f}{\rho_p+\phi\rho_f-\phi\rho_p}$
(3) Hui *et al*. [55]	$k_{nf}=\frac{1}{4}[(3\phi-1)k_p+(2-3\phi)k_f]+\frac{k_p}{4}\sqrt{\Delta},$ $\Delta=(3\phi-1)^2(\frac{k_p}{k_f})^2+(2-3\phi)^2+2(2+9\phi-9\phi^2)(\frac{k_p}{k_f})$
(4) Xuan and Li [56]	$k_{nf}=k_f \frac{k_p+2k_f-2\phi(k_f-k_p)}{k_p+2k_f+\phi(k_f-k_p)}$
(5) Yu and Choi [57]	$k_{nf}=k_f * \frac{k_{pe}+2k_f+2\phi(k_{pe}-k_f)(1+\beta)^3}{k_{pe}+2k_f-\phi(k_p-k_f)(1+\beta)^3}$, $\beta=\frac{h}{r}$, h<10nm,β=0.1
(6) Godson *et al*. [58]	$k_{nf} = 0.9692\phi + 0.9508$
(7) Prasher *et al*. [59]	$k_{nf}=k_f \frac{1+A\phi\ Re^m\ Pr^{0,333}*(1+2\alpha)+2\phi(1-\alpha)}{(1+2\alpha)-\phi(1-\alpha)}$,$\alpha=\frac{2R_bk_f}{d_p}$, A=40000 ,m=2.5 , $R_b=0.77.10^{-8}$
(8) Koo and Kleinstreuer [60]	$k_{nf}=k_{MG}+5\times10^4\ \beta\phi\rho_p\ C_p\sqrt{\frac{K_B\ T}{\rho_p D}}\ f(T,\phi),\ k_{MG}=k_f\left(1+\frac{3\phi\left(\frac{k_p}{k_f}-1\right)}{\left(\frac{k_p}{k_f}+2\right)-\phi\left(\frac{k_p}{k_f}-1\right)}\right)$ $f(T,\phi)=(-6.04\phi+0.4705).T+(1722.3\phi-134.63),\beta=0.0137(100\phi)^{-0.8229}\rightarrow\phi\le1\%$
(9)-(10) Li and Peterson [61]	$k_{nf}=k_f+k_f(0.764\phi-0.0187\ (T-273.15)-0.462)$ For Al_2O_3 $k_{nf}=k_f+k_f(3.761\phi+0.0179\ (T-273.15)-0.307)$ For CuO
(11)-(12) Palm [18]	Al_2O_3 $\left(\begin{array}{l}k_{nf}=0.003352T-0.3708 \text{ For } \phi=\%1\\ k_{nf}=0.004961T-0.8078 \text{ For } \phi=\%4\end{array}\right)$
(13)-(14) Maiga *et al*. [62]	$k_{nf}=k_f(4.97\phi^2+2.72\phi+1)$ For Al_2O_3 $k_{nf}=k_f(28.905\phi^2+2.827\phi+1)$ For CuO

(Table 2) Contd….

Researcher	Correlation
(15) Bhattacharya *et al*. [63]	$k_{nf}=k_p\phi+(1-\phi)k_f$
(16) Buongiorno [64]	$k_{nf}=k_f\ (1+7.47\phi)$
(17) Kim *et al*. [65]	$k_{nf}=0.65+4{,}864\times10^{-7}T^3$
(18) Timofeeva *et al*. [66]	$k_{nf}=k_f(1+3\phi)$
(19) Chon *et al*. [67]	$k_{nf}=k_f\ .(1+64.7\phi^{0.746}\ (d_f/d_p\ )^{0.369}(k_p/k_f)^{0.747}\mathrm{Re}^{1.2321}\ \mathrm{Pr}^{0.9955})$ $\mathrm{Pr}=\frac{\mu}{\rho_{BF}\alpha},\mathrm{Re}=\frac{\rho_{BF}Vd_p}{\mu}=\frac{\rho_{BF}K_BT}{3\pi\mu^2L_{BF}},\mu=2.414\times10^{-5}\times10^{(\frac{247}{T-140})}$
(20) Murshed *et al*. [68]	$k_{nf}=\frac{k_f(1+0.27\phi^{4/3}\ (\frac{k_p}{k_f}-1)(1+\frac{0.52\phi}{1-\phi^{1/3}}\ (\frac{k_p}{k_f}-1)}{1+\phi^{4/3}\ (\frac{k_p}{k_f}-1)(\frac{0.52}{1-\phi^{1/3}}+0.27\phi^{1/3}+0.27)}$

Table 3. Some Specific Heat Capacity Correlations of Nanofluids in Literature

Researcher	Correlation
(1) Maxwell [3]	$Cp_{nf}=(1-\varphi)Cp_{nf}(1+2.5\varphi_p)\mu_f$
(2) Hamilton and Crosser [54]	$Cp_{nf}=\frac{\phi.\rho_s.Cp_s+(1-\phi).\rho_w.Cp_w}{\rho_{nf}}$
(3) Yang *et al*. [69]	$\frac{Cp_{eff}}{Cp_f}=(1-\phi)+\phi\frac{Cp_n}{Cp_f}$
(4) Yu *et al*. [70]	$Cp_{nf}=\frac{\varphi(p_s)Cp_s+(1-\varphi).(\rho.c_p)}{\varphi\rho_p+(1-\varphi).\rho_{bf}}$

Because of viscous effects, pressure loss occurs, and is expressed for all types of fullydeveloped internal flows as follows:

$$\Delta P_L=f\frac{L}{D}\frac{\rho V_{avg}^2}{2} \quad (7)$$

When a pressure drop occurs, the pumping power required to overcome flow resistance can be determined as follows:

$$W_P=\dot{Q}.\Delta P \quad (8)$$

Heat flux in the test section is determined as follows:

$$q"=\frac{m_wC_{p,w}(T_i-T_o)}{\pi dL} \quad (9)$$

The heat transfer coefficient of the base fluid and the nanofluid can be calculated as follows:

$$h=\frac{q"}{(T_w-T_{f,m})} \quad (10)$$

The Nusselt numberfor the base fluid and the nanofluid can be calculated as follows:

$$Nu=\frac{hd}{k} \quad (11)$$

4.3. Numerical method - CFD Approach

The ANSYS Fluent program [15] is commonly used software in CFD analysis, and a detailed description of its mathematical models can be found in the Fluent User's Guide. The program uses a technique based on control volume theory to convert governing equations into algebraic equations so that they can be solved numerically, providing a significant research solution [27]. The control volume technique works by integrating the governing equations for each control volume, and then by discretizing the equations that conserve each quantity based on the control volume.

Classic single-phase conservation equations found a solution in the control volume approach, since governing equations could be given numerical solutions after being converted into a set of algebraic equations. This addressed some of the entailments of governing equations, including convection terms, diffusion terms, and other quantities, which were not properly addressed in a second-order upwind scheme. All scalar values and velocity components are calculated at the center of control volume interfaces, where grid

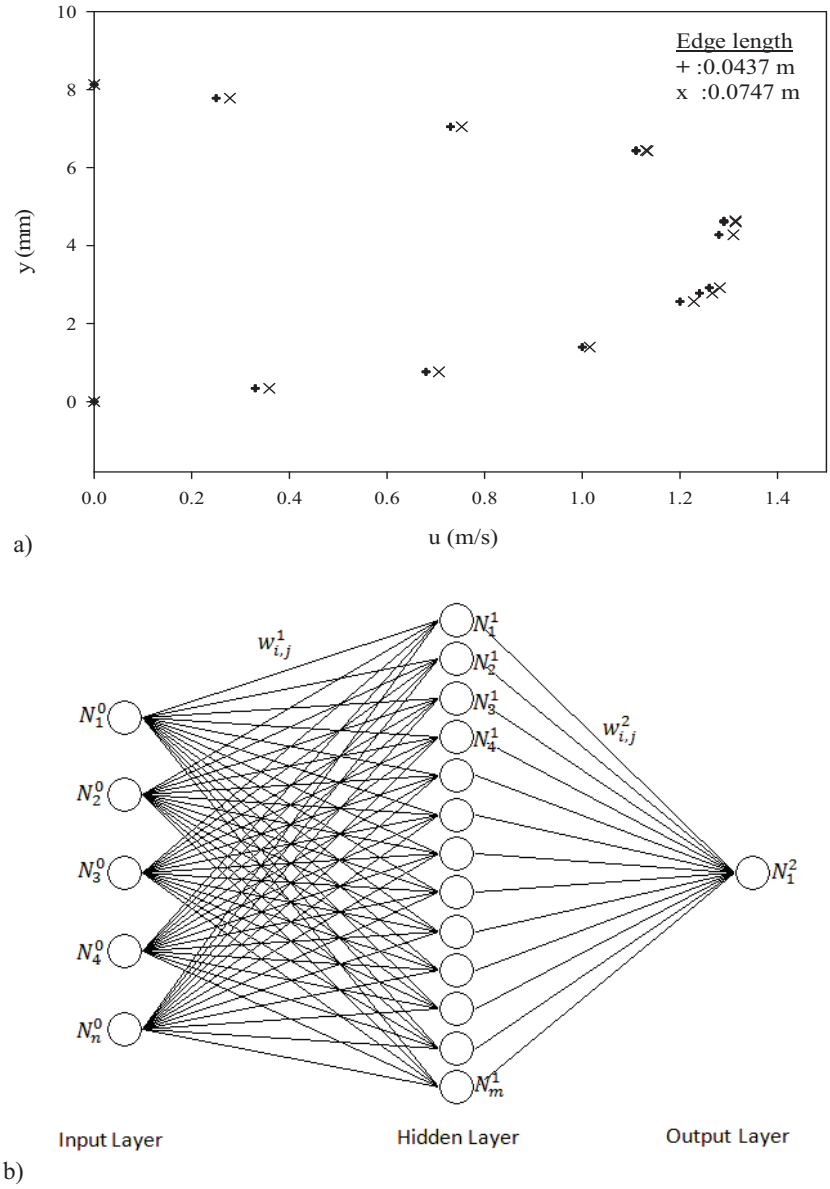

Fig. (3). Achieving the grid independency for velocity profiles at Re=8895.2 (**a**) and schematic representation of MLP (**b**) for the numerical part of the study.

schemes are used extensively. The Semi-Implicit Method for Pressure Linked Equations (SIMPLE) was used to pair pressure and velocity. A point-implicit (Gauss-Seidel) linear equation solver, in conjunction with an algebraic multigrid method, was employed in the Fluent CFD program [15] to solve the linear systems resulting from discretization schemes. k-ε turbulence models were chosen in the viscous model. Residuals were thoroughly monitored during the iterative process, and all solutions were considered to have converged when the residuals for each governing equation fell below 10^{-6}. Boundary conditions were defined for the velocity inlet at the pipe inlet and for the pressure outlet at the pipe exit; turbulence intensity and hydraulic diameter were defined for the turbulence parameters. Constant heat flux was applied to the pipe surface. To show grid-independent solutions, two different edge lengths were used in the tetrahedrons grid type for Re=8895.2. Fig. (**3a**) shows the velocity profile distributions of the two, which are nearly identical.

4.4. Numerical Method- ANN Approach

An artificial neural network (ANN) is an information-processing system that has certain performance characteristics in common with biological neural networks. Artificial neural networks have been developed as generalizations of mathematical models of human cognition or neural biology, based on the assumptions as follows [73].

- Information processing occurs at many simple elements called neurons
- Signals are passed between neurons over connection links
- Each connection link has an associated weight, which, in a typical neural net, multiplies the signal transmitted
- Each neuron applies an activation function (usually non-linear) to its net input (sum of weighted input signals) to determine its output signal.

The ANN is the most widely used model, and is able to find linear and non-linear relationships between input and output patterns. To find a relationship between input and output sets, well-known training sets are first used to generalize concerning a relationship. Once a generalization is made, the ANN tries to predict the outputs of a new test set. The performance metrics of the ANN are measured by the quality of its test set predictions. There are many types of ANN in function approximation literature, including the Multi-Layer Perceptron (MLP), the Radial Basis Functions Networks (RBFN), the Generalized Regression Neural Network (GRNN), and the decision-making system based on human 'fuzzy logic', the ANN Artificial Neural Fuzzy Inference System (ANFIS).

4.4.1. Multi-layer Perceptron

A multilayer perceptron (MLP) is a feedforward artificial neural network model that maps sets of input data onto a set of appropriate output. An MLP consists of multiple layers of nodes in a directed graph, with each layer fully connected to the next one. Except for the input nodes, each node is a with a nonlinear activation function. MLP utilizes a supervised learning technique called back propagation for training the network [74-75].

The MLP consists of three different layers, the input layer, the hidden layer, and the output layer. The input layer's neuron number and the output layer's neuron number are equal to the dimensions of the input variables and output variables, respectively. The number of the hidden layer and the number of any hidden layer's neuron may be manipulated at will; if the number of the hidden layer and any hidden layer's neuron increases, then the non-linear feature of the model will increase as well. A schematic representation of the MLP model is shown in Fig. (**3b**).

Let Nbe the number of input parameters used for the estimation of displacement, and M the neuron number in the hidden layer;let the inputs of the MLP (0^{th} layer outputs) be shown as $\left\{N_1^0, N_2^0, ...N_n^0\right\}$, the output values of the hidden layer (1^{st} layer outputs) as $\left\{N_1^1, N_2^1, ...N_m^1\right\}$, the output values of the output layer (2^{nd} layer outputs, predicted value) as N_1^2, the connection weight of the i^{th} neuron of the input layer to the j^{th} neuron of the hidden layer as $w_{i,j}^1$, the j^{th} neuron of the l^{st} layer's bias value as b_j^l, andthe l^{st} layer's transfer function as f_l ;the j^{th} neuron of the l^{st} layer's output is then calculated as in Eq. (12):

$$N_j^l = f_l\left(b_j^l + \sum_i N_i^{l-1}.w_{i,j}^l\right) \tag{12}$$

In the literature, there are many different kinds of transfer functions,including purelin, tansig, logsig, and so on. If the training output set is shown by D, then the error function of the prediction is calculated as in Eq. (13):

$$J = \frac{1}{2}\sum\left(N^{out} - D\right)^2 \tag{13}$$

The optimization method appliedin Eq. (12) in order to find the w and b values, and to yield a minimum value of J, is called the MLP learning algorithm. The mean of training calculates optimal w and b values by way of the training set. The Gradient Descent, Gradient Descent with Momentum, Conjugate Gradient, Quasi-Newton, and Levenberg-Marquardt methods are well-known learning algorithmswithin the literature.

4.4.2. Validation and Performance Metrics

Validation is a supervised learning method using data points obtained from experiments, and must be performed in order to gauge the success of learning algorithms. The most well-known validation methods are the hold-out, the k-fold cross, and the leave-one-out cross-validation methods.

In the k-fold cross-validation method, n number data obtained from experimentationare divided randomly into k number sets,each data cluster having equal elements and each being numbered from 1 to k.

$$\upsilon_i \in \{1,2,..k\} \qquad i=1..n \tag{14}$$

Data whose υ_i values are equal to 1 are first placed in the test set, while data whose υ_i values are different from 1 are placed in the training set. The suggested method is then to train using the training set and to examine using the test set. The researcher's next step is to send data with a υ_i value of 2 to the test set and data with υ_i values different from 2 to the training set. The method is repeated once again with a new training set and a new testing set, and the process continues until all folds are tested [76].

To determine the most appropriate inputs for this process, the mean squared error (MSE) and the coefficient of correlation determination (R) metrics are used as performance criteria for the validation sets. If n is the number of experimental data, y is the value of the experiment, and $\hat{y}$ is the prediction of the MLP, then the formulations of MSE and R are shown in Eq. (15) and Eq. (16), respectively.

$$mse = \frac{1}{n}\sum_{i=1}^{n}\left(y_i - \hat{y}_i\right)^2 \tag{15}$$

$$R = \frac{n.\sum(y.\hat{y}) - \sum(\hat{y}).\sum(y)}{\sqrt{\left(n.\sum y^2 - \left(\sum y\right)^2\right).\left(n.\sum \hat{y}^2 - \left(\sum \hat{y}\right)^2\right)}} \tag{16}$$

4.4.3. Application of Multi-Layer Perceptron

To simulate the behavior of liquids flowing inside a pipe, CFD software processes 7 different inputs: the physical properties of nanofluids (k,μ,C_p,ρ),volume fraction, and the average temperature and velocity of the water. This simulation produces the outputs $h,\tau,\Delta P$, and Q. These outputs are maximally compatible with the experimental data, defined in the literature in terms of 20 different thermal conductivity correlations, 28 different dynamic viscosity correlations, and 4 different specific correlations of heat at constant pressure. To determine which combination of these correlations should be used, all of the possibilities can be tested individually. So many options can so prolong the simulation process as to make it infeasible; if the MLP model can simulate CFD software, however, finding relationships between the inputs and outputs of the CFD software within acceptable limits, the MLP model can be used instead of CFD software to determine the best input combination.

Because the CFD software requires 7 inputs and produces 4 outputs, the MLP requires 7 input neurons and 4 output neurons. In practice, the selected architecture of MLP has only 1 hidden layer with 5 neurons, as shown in Fig. (**3b**).; the MLP also has an available 7-5-4 architecture. The back-propogation model can be used, along with the Levenberg-Marquardt methods,as a learning algorithm. The transfer functions of the hidden layer (1st layer) and the output layer (2nd layer) are tansig and purelin, respectively, shown in Eq. (17):

$$f(x) = \frac{2}{1+e^{-2x}} - 1 \qquad f(x) = x \tag{17}$$

The validation process was performed by the 2-fold cross-validation method, using data groups according to test results and R criteria.

5. RESULTS AND DISCUSSION

The commercial software package ANSYS Fluent [27] was employed in the numerical study. Investigated tubes were plotted in the SolidWorks program [26], and were imported to ANSYS Geometry as shown in Fig. (**4a**) and Fig. (**4b**). After the investigated tubes were imported to ANSYS Geometry, they were forwarded for meshing in the ANSYS Meshing program. The mesh influences the accuracy, convergence, and speed of the solution. Furthermore, the time required to create a mesh model often represents a significant portion of the time required to acquire results from the solutions; this means that the better and more automated the meshing tools, the better the solution. The mesh performed for the investigated tubes is shown in Fig. (**4c**) and Fig. (**4d**).

Two different ANN models were developed to determine the best combination of physical properties for the TiO_2 nanofluid. The inputs of the ANN model 1 analyses were the correlations of physical properties, the average temperature and velocity of water in the test tube, and the nanoparticle concentration, while the outputs of the analyses were shear stress, friction factor, heat flux, convective heat transfer coefficient, and pressure drop. The inputs of the ANN model 2 analyses were the correlations of physical properties and the inlet and outlet temperature and velocity of the water in the test tube, while the outputs were the convective heat transfer coefficient and the pressure drop. The success of the ANN models are represented in Table **5**. The changes inthe numerical and experimental results ofthe ANN models are shown in Figs. (**5a** and **5b**) and (Figs. **6a** and **6b**). All results seemed to be successful within the ±5% deviation band. The most substantiated correlations were obtained from the ANN 1 model for the physical properties (k, μ, Cp) of nanofluids. They are given below:

$$k_{nf}=k_p\phi+(1-\phi)k_f \quad (18)$$

$$\mu_{nf}=\mu_{bf}(306\phi^2-0.19\phi+1) \quad (19)$$

$$Cp_{nf}=(1-\phi)Cp_{nf}(1+2.5\phi_p)\mu_f \quad (20)$$

These equations were obtained from ANN results; Eq. (18) is the thermal conductivity correlation of Bhattacharya *et al*. [63], numbered 15 in Table **2**; Eq. (19) is the viscosity correlation of Wang *et al*. [50], numbered 24 in Table **1**; and Eq. (20) is the heat capacity correlation of Maxwell [3], numbered 1 in Table **3**.

The validation process for numerical models is performed by means of the experimental data [6], as shown in Fig. (**7**) regarding heat transfer characteristics. Fig. (**7**) clearly demonstrates that the numerical model of ANSYS Fluent [27] is in substantialagreement with experimental values [6] in the calculation of the heat transfer coefficient (within a ±25% range) and of the pressure drop (within a ±10% range) for the in-tube single-phase flow of pure water and nanofluid with TiO_2 volume concentrations of 0.2, 0.6, and 1%. Table **6** further shows error rates of less than 1.56% and 2.02% between experimental and numerical temperatures at the outlet section and at the surface, respectively. It should be noted that experimental and numerical studies are conducted for Re numbers between 4516 and 15681 and for surface heat fluxes between 7233 and 13340 W m^{-2}.

The velocity of the fluid in contact with the pipe wall is essentially zero, and it increases with increasing distance from the wall. The velocity profile depends upon the surface condition of the pipe wall;a smoother wall results in a more uniform velocity profile than does a rough pipe wall. The pressure of the fluid in contact with the pipe wall is likewise small, and likewise increases with increasing distance from the wall. The pressure of the fluid has its maximum value at the entrance of pipe and decreases with increasing distance from the entrance. The temperature of the fluid has its maximum value on the wall, since a constant heat flux is applied to the pipe surface. The temperature of the fluid has its minimum value at the entrance of pipe and increases with increasing distance fromthe entrance, due to the constant heat flux. The ANSYS Fluent CFD [27] program was used in numerical analyses to develop velocity, pressure, and temperature profiles at various locations, and was applied to φ=1% to the smooth tube (Fig. **8**), to the micro-fin tube with a helix angle of 0º (Fig. **9**), and to the micro-fin tube with a helix angle of 18º (Fig. **10**).

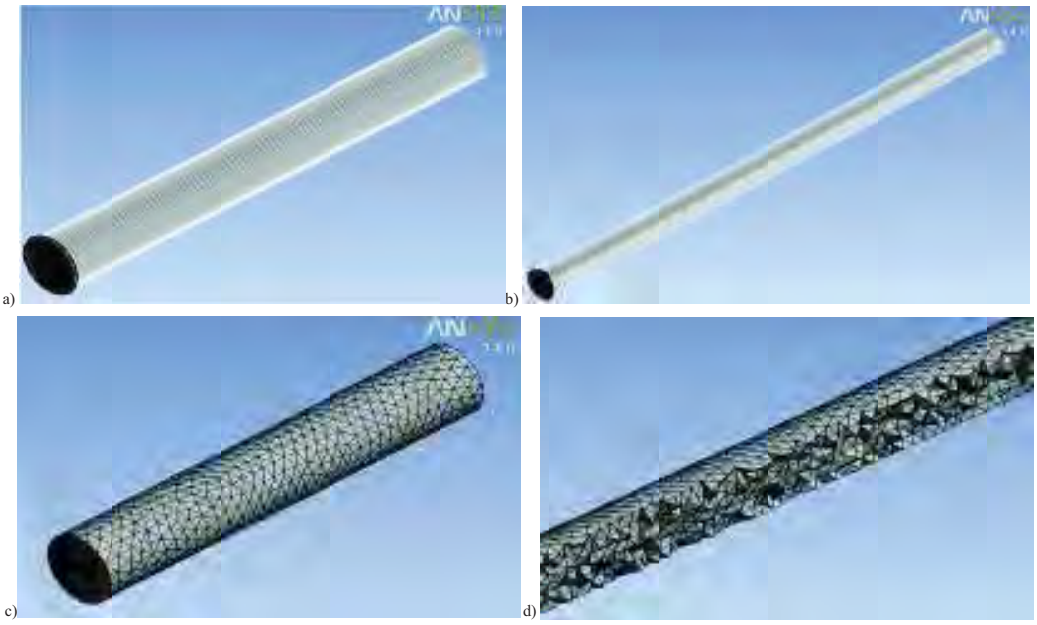

Fig. (4). Views of different helix angles of micro-fin tubes 0º (**a**), 18º (**b**), and views of meshing (**c**) and detailes of meshing (d) for smooth tube.

Table 4. Geometrical Parameters of the Investigated Tubes

Tubes	Smooth	Micro-fin 1	Micro-fin 2
a(°)	-	0	18
Θ(°)	-	36	36
e (mm)	-	0.435	0.435
p (mm)	-	0.378	0.378
n_f	-	60	60
s (mm)	-	0.293	0.293
di (mm)	8.13	8.13	8.13
do (mm)	9.13	9.13	9.13
L (m)	1.5	1.5	1.5
A (mm^2)	38311.7	92180.86	96210

Table 5. The Best Inputs Obtained from ANN Analyses and Numbered in Tables 1-2-3

k ($W\ m^{-1}K^{-1}$)	μ ($kg\ m^{-1}s^{-1}$)	c_p ($J\ kg^{-1}K^{-1}$)	R^2
12	24	1	0.967465
10	10	2	0.963421
6	7	2	0.961502
12	11	2	0.960374
13	8	1	0.958547
16	9	2	0.958514
14	27	2	0.958276
5	3	2	0.957927
11	11	3	0.957073
1	7	2	0.956864

a-) considering the determination of shear stress, friction factor, heat flux, convective heat transfer coefficient and pressure drop as outputs (ANN model 1)

k ($W\ m^{-1}K^{-1}$)	μ ($kg\ m^{-1}s^{-1}$)	c_p ($J\ kg^{-1}K^{-1}$)	R^2
18	2	2	0.99290234
6	21	2	0.99105436
11	1	4	0.99006633
15	1	2	0.98885878
6	1	1	0.98860543
19	26	3	0.9881786
7	12	1	0.98806904
8	28	2	0.98798953
6	7	2	0.98795459
16	2	4	0.98774095

b-) considering the determination of pressure drop and convective heat transfer coefficient as outputs (ANN model 2)

Table 6. Comparison of Experimental and Numerical Temperatures at Outlet Section and at Surface Using Pure Water with 0.2%, 0.6% and 1% TiO_2 Particles Data [4]

Concentration (%)	$T_{o,exp}$(°C)	$T_{o,num}$(°C)	Error Rate (%)	$T_{s,exp}$(°C)	$T_{s,num}$(°C)	Error Rate (%)
Pure water	26.6	26.9	1.26	27.4	27.8	1.45
0.2 %	27.0	27.4	1.52	27.85	28.4	1.97
0.6 %	27.2	27.6	1.56	28.13	28.7	2.02
1 %	27.0	27.4	1.45	27.75	28.2	1.62

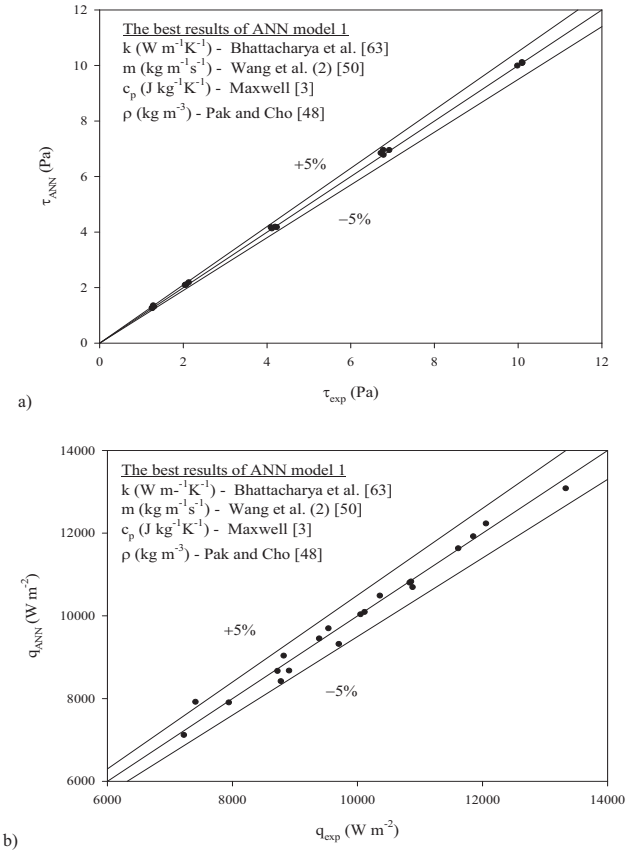

Fig. (5). The best results of ANN model 1 regarding with the shear stress (**a**) and heat flux (**b**).

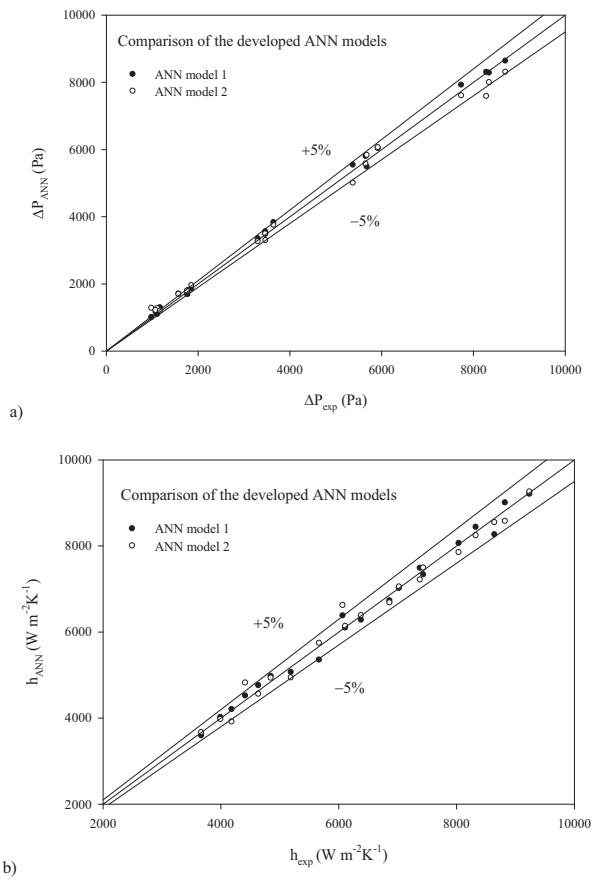

Fig. (6). Comparison of the developed ANN models regarding with the pressure drop (**a**) and convective heat transfer coefficient (**b**).

The variation in the local heat transfer coefficients along the pipe length for the flow of pure water, and for the nanofluids with different particle weight concentrations inside the smooth tube, are shown in Fig. (**11a**). This figure indicates that the additionof solid nanoparticles to the pure water did in fact lead to an increase in the local heat transfer coefficient for the flow inside the smooth tube. As has been shown before, the addition of nanoparticles improves the thermal conductivity of the base fluid. The convective heat transfer enhancement from the nanofluid may be due to an increase in thermal conductivity or to the random movement and dispersion of nanoparticles in the nanofluid. Disordered movements of the solid particles in the flow will alsoupset the thermal boundary layer formation on the tube wall surface, causing the development of the thermal boundary layer to lag and higher heat transfer coefficientsto obtain at the thermal entrance region. Here too, it appears that adding nanoparticles will improve the local heat transfer coefficient in a fluid flow. At higher weight concentrations of nanofluids, both the thermal conductivity of the TiO_2-water mixture and the disturbance effect of the solid nanoparticles will increase; nanofluids with higher weight concentrations will therefore haveeven higher convective heat transfer coefficients.

Fig. (**11b**) further demonstrates that nanofluids display better heat transfer performance when they flow inside micro-fin tubes with helix angles of 0º and 18º than when they flow insidesmooth tubes. The results clearly indicate that the highest heat transfer coefficientswere obtained for micro-fin tubeswith a helix angle of 18º and a volume concentration of 1%; these results are compatible withother current findings in the literature. (Fig. **11c**), furthermore, compares heat transfer coefficients between smooth and micro-fin tubes, and shows that the heat transfer coefficients of micro-fin tubeswith a helix angle of 18º are higher those of than micro-fin tubeswith a helix angle of 0º at nearly the same Reynolds numbers,

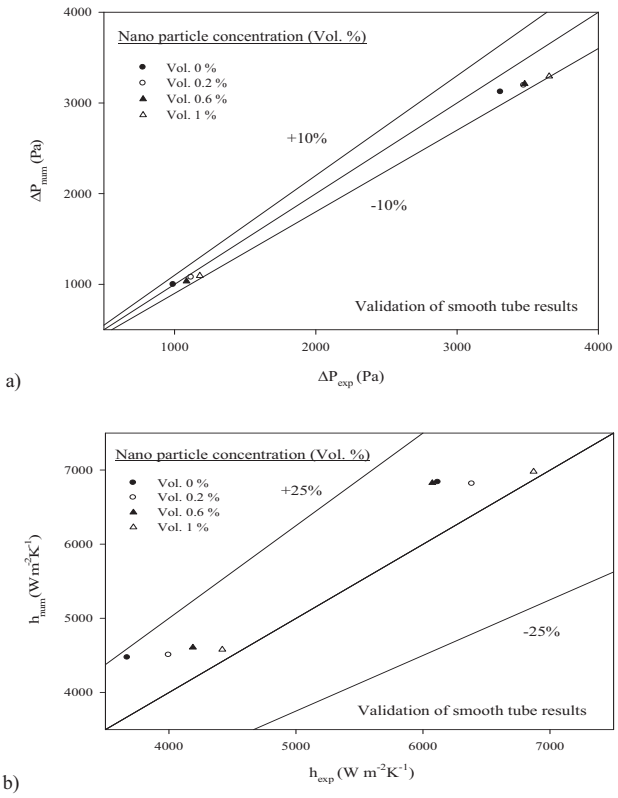

Fig. (7). Comparison of experimental and numerical pressure drops (**a**) and heat transfer coefficients (**b**) and using pure water with 0.2%, 0.6% and 1% TiO_2 particles data [6].

heat flux, and volume concentrations along the pipe. Similarly, the heat transfer coefficients of micro-fin tubes with a helix angle of 0º are higher than those of the smooth tubes.

Fig. (**12a**) shows a remarkable increase in the pressure drop of nanofluids with 0.2, 0.6, and 1 wt.% particle concentrations compared to pure water when flowing inside smooth and micro-fin tubes. This trend tends to continue for nanofluids at higher weight fractions. This is due to the fact that suspending solid particles in a fluid generally increases dynamic viscosity relative to the base fluid. Since viscosity stands in direct relation to pressure drop, the higher viscosity naturally leads to an increased pressure drop. Experimental results show that the pressure drop of micro-fin tubes with a helix angle of 18º is higher than that of micro-fin tubes with a helix angle of 0º. Moreover, the pressure drop of micro-fin tubes with a helix angle of 0º is higher than that of the smooth tubes. More exactly, the pressure drop of micro-fin tubes with a helix angle of 18º is 21.5% higher than that of smooth tubes, and the pressure drop of micro-fin tubes with a helix angle of 0º is 15.5% higher than that of smooth tubes at φ=1%.

From Fig. (**12b**), it is evident that the friction factor increases with increasing concentrations of nanoparticles because of the rise in working fluid viscosity. As was previously observed, nanofluids in smooth tubes with concentrations of 0.2%, 0.6%, and 1% provide friction factors higher than those of base fluids by 1.5, 5.1, and 5.8%, respectively. Similarly, nanofluids in micro-fin tubes with a helix angle of 18º, and with concentrations of 0.2%, 0.6%, and 1%, provide friction factors higher than those of base fluids by around 0.33%, 2.2% and 3.2%, respectively. It can be observed from Fig. (**12c**) that wall shear stress increases with the increasing volume concentration of the nanoparticles; the Reynolds number of the flow also increases as the inclusion of nanoparticles raises the viscosity of the mixture.

As the numbers indicate, nanofluids in smooth tubes with concentrations of 0.2%, 0.6%, and 1% induced a wall shear stress higher than that of the base fluid by around 2.2, 2.7% and 5.2%, respectively. Likewise, nanofluids in micro-fin tubes with a helix angle of 18º, and with concentrations of 0.2%, 0.6% and 1%, induced a wall shear stress higher than that of the base fluid by around 1%, 1.2%, and 4.2%, respectively. According to Fig. (**12c**), the wall shear stress of micro-fin tubes with a helix angle of 18º is 21.1% higher than that of smooth tubes, and the wall shear stress of micro-fin tubes with a helix angle of 0º is 3.77% higher at φ=0.6 % than that of smooth tubes. Fig. (**12d**) shows, finally, a remarkable increase in pumping power due to the increase in the pressure drop of the nanofluid in a large cross-section of the micro-fin tubes. The results show that the pumping power of micro-fin tubes with a helix angle of 18º is higher than that of micro-fin tubes with a helix angle of 0º; similarly, the pumping power of micro-fin tubes with a helix angle of 0º is higher than that of smooth tubes. In all, the characteristics of in the sub-figures of Fig. (**12**) are found to be compatible with other current findings in the literature.

6. CONCLUSION

This study investigated the heat transfer characteristics of pure water and of a water-TiO_2 mixture flowing inside smooth tubes, as a validation study, and inside micro-fin tubes, as a simulation study, with various volume concentrations investigated for forced flow conditions using two- dimensional governing equations. The conclusions of this study can be outlined as follows:

- The heat transfer coefficient was slightly increased with increasing nanofluid volume concentration.
- Micro-fin tubes with helix angles of 0° and 18° enhanced the heat transfer coefficient significantly under the same flow conditions, yielding at φ=1% mean heat transfer coefficients higher than those of smooth tubes by 23.5% and 32.5%, respectively.
- Compared to micro-fin tubes with a helix angle of 0°, the mean heat transfer coefficient and pressure drop of micro-fin tubes with a helix angle of 18° increased at φ=1% by 11.8% and 7.55%, respectively.
- Nanofluids with concentrations of 0.2%, 0.6%, and 1% in micro-fin tubes with a helix angle of 18º yielded friction factors higher than those of the base fluid by approximately 0.33%, 2.2%, and 3.2%, respectively.
- The wall shear stress of micro-fin tubeswith a helix angle of 18º was 21.1% higher at φ=0.6% than those of smooth tubes, and the wall shear stress of micro-fin tubeswith a helix angle of 0º was 3.77% higher than that of smooth tubes.
- The pumping power of micro-fin tubeswith a helix angle of 18º was 68.8% higher at φ=1% than that of smooth tubes and 11.5% higher than that of micro-fin tubeswith a helix angle of 0º.
- Nanofluids at higher volume concentrations showed both higher heat transfer enhancement and higher pressure drop. Therefore, judicious decisions should be taken to select a nanofluid that will balance the heat transfer enhancement and the pressure drop penalty.

As this study has also found, the proven tools of computational fluid dynamics (CFD) will make it feasible for researchers to analyze different geometrical configurations and various nanofluids without needing to perform additional experimental studies, once they have performed their validation process on the experimental data.

a)

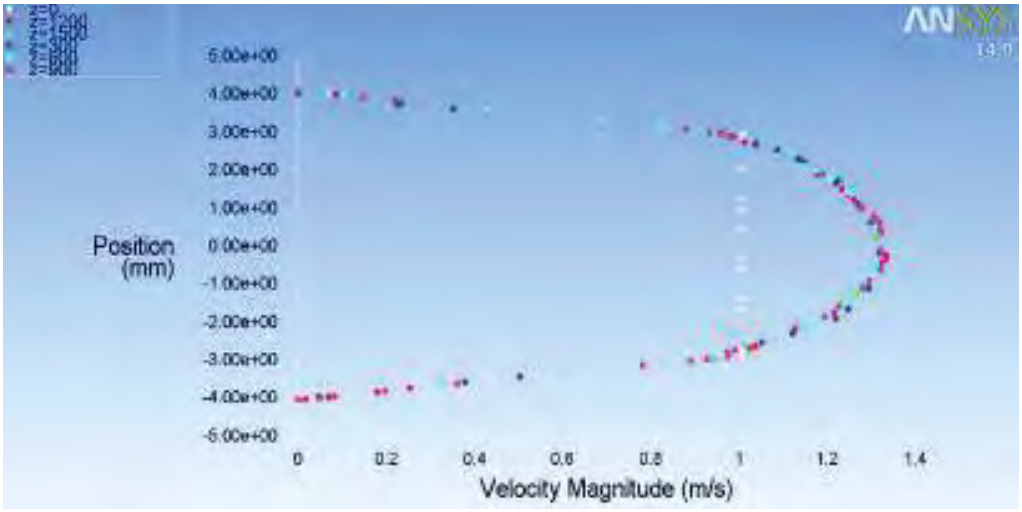

b)

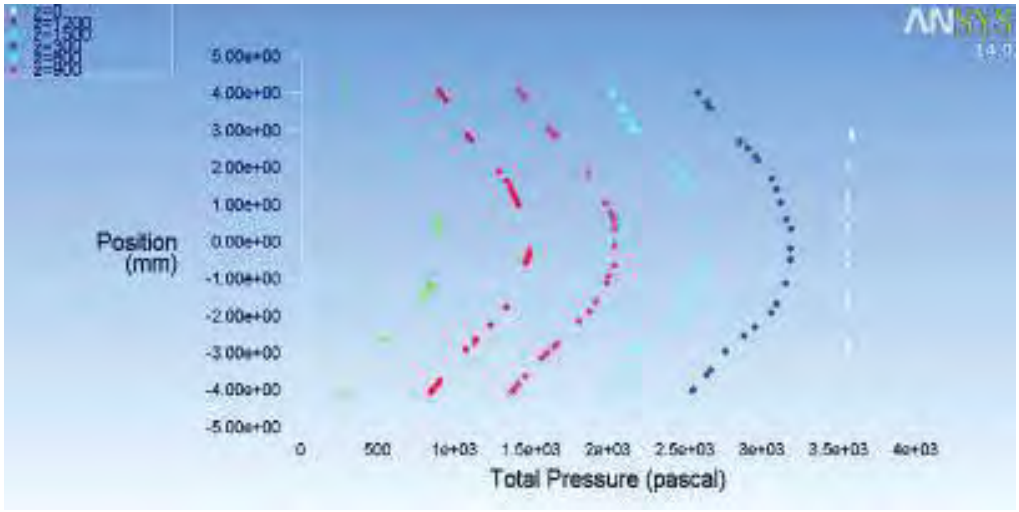

c)

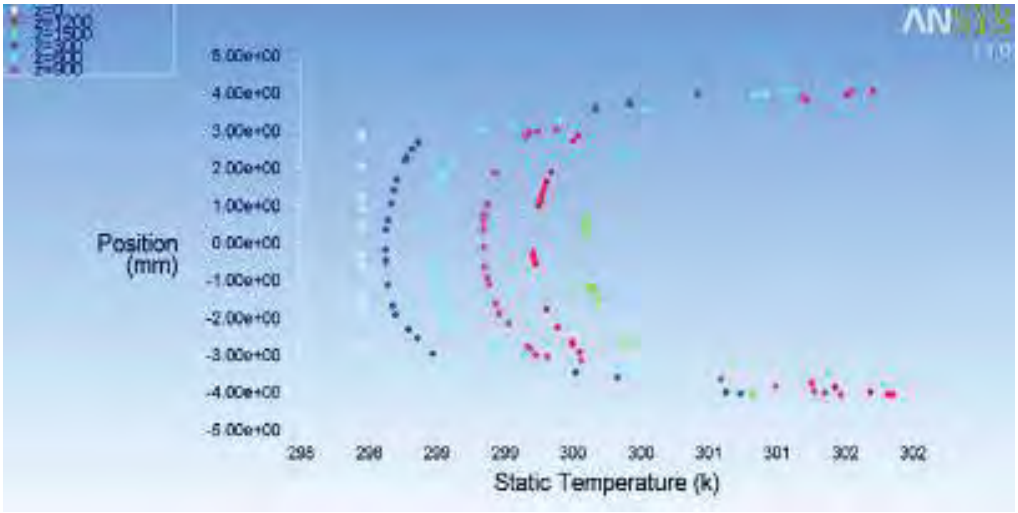

Fig. (8). Velocity profile (**a**), pressure profile (**b**) and temperature profile (**c**) at various locations in smooth tube.

a)

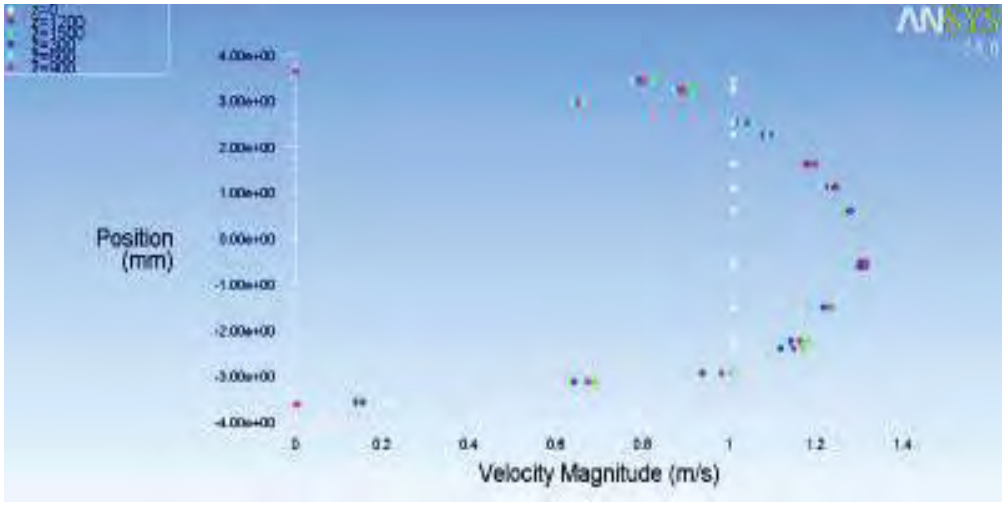

b)

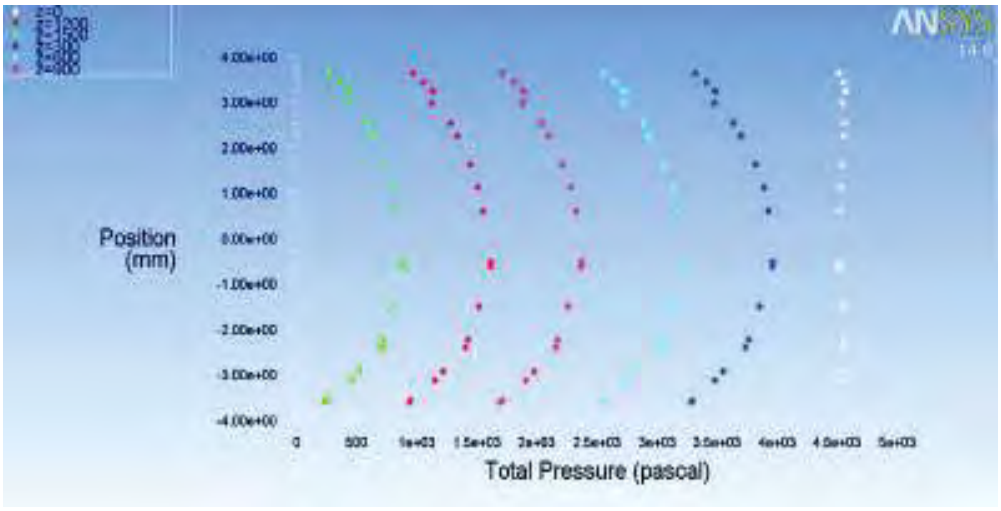

c)

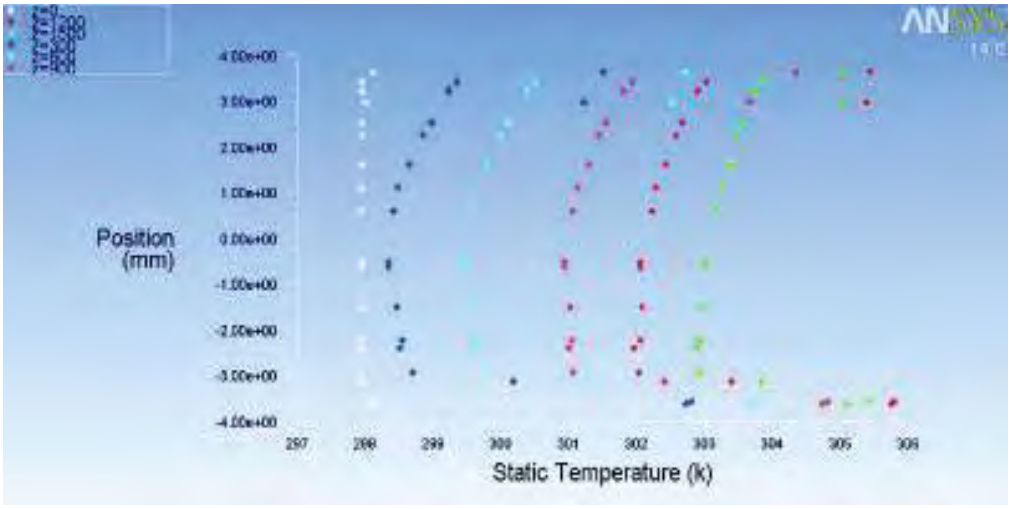

Fig. (9). Velocity profile (**a**), pressure profile (**b**) and temperature profile (**c**) at various locations in micro-fin tube having helix angle 0º.

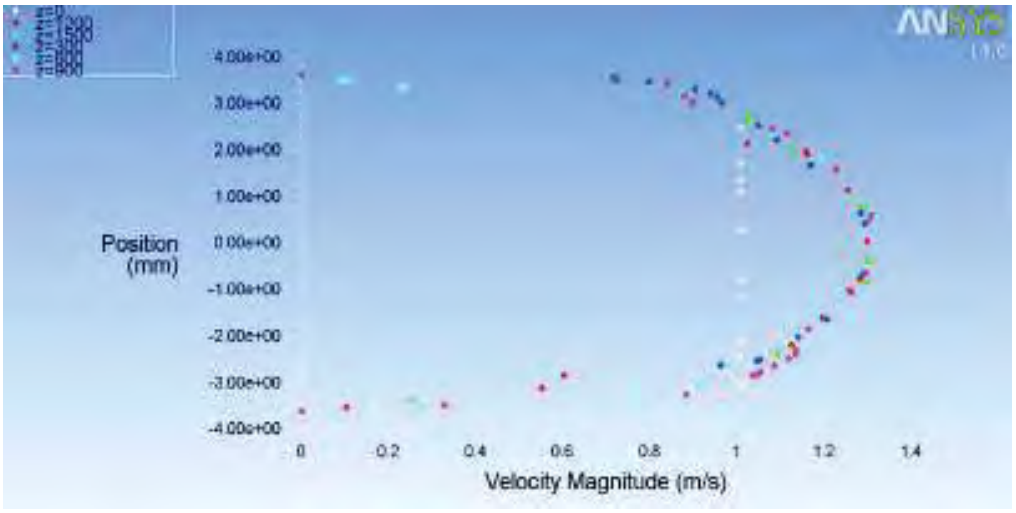

a)

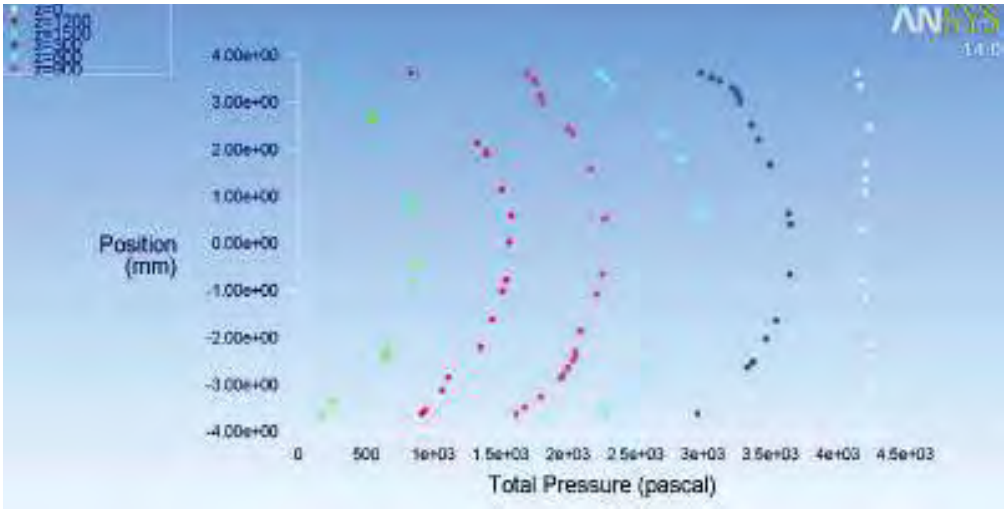

b)

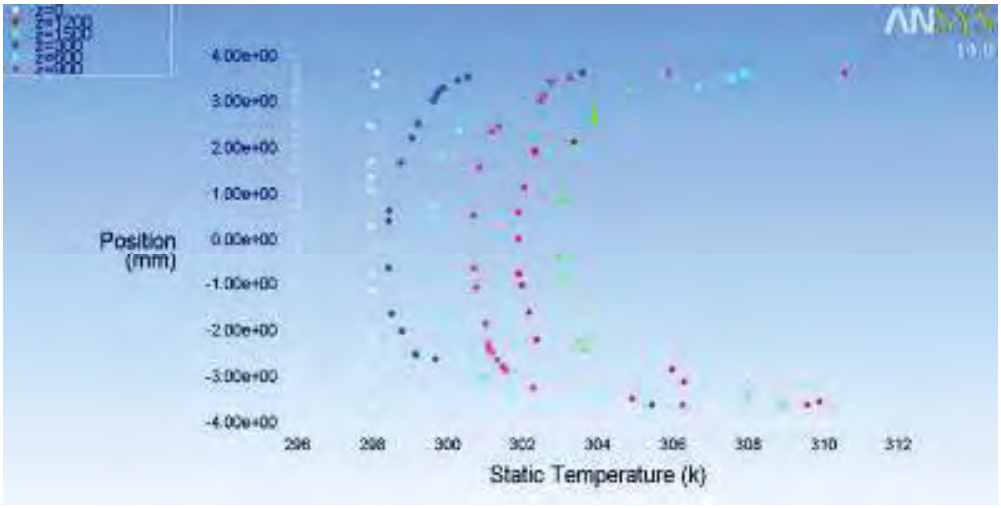

c)

Fig. (10). Velocity profile (a), pressure profile (**b**) and temperature profile (**c**) at various locations in micro-fin tube having helix angle 18º.

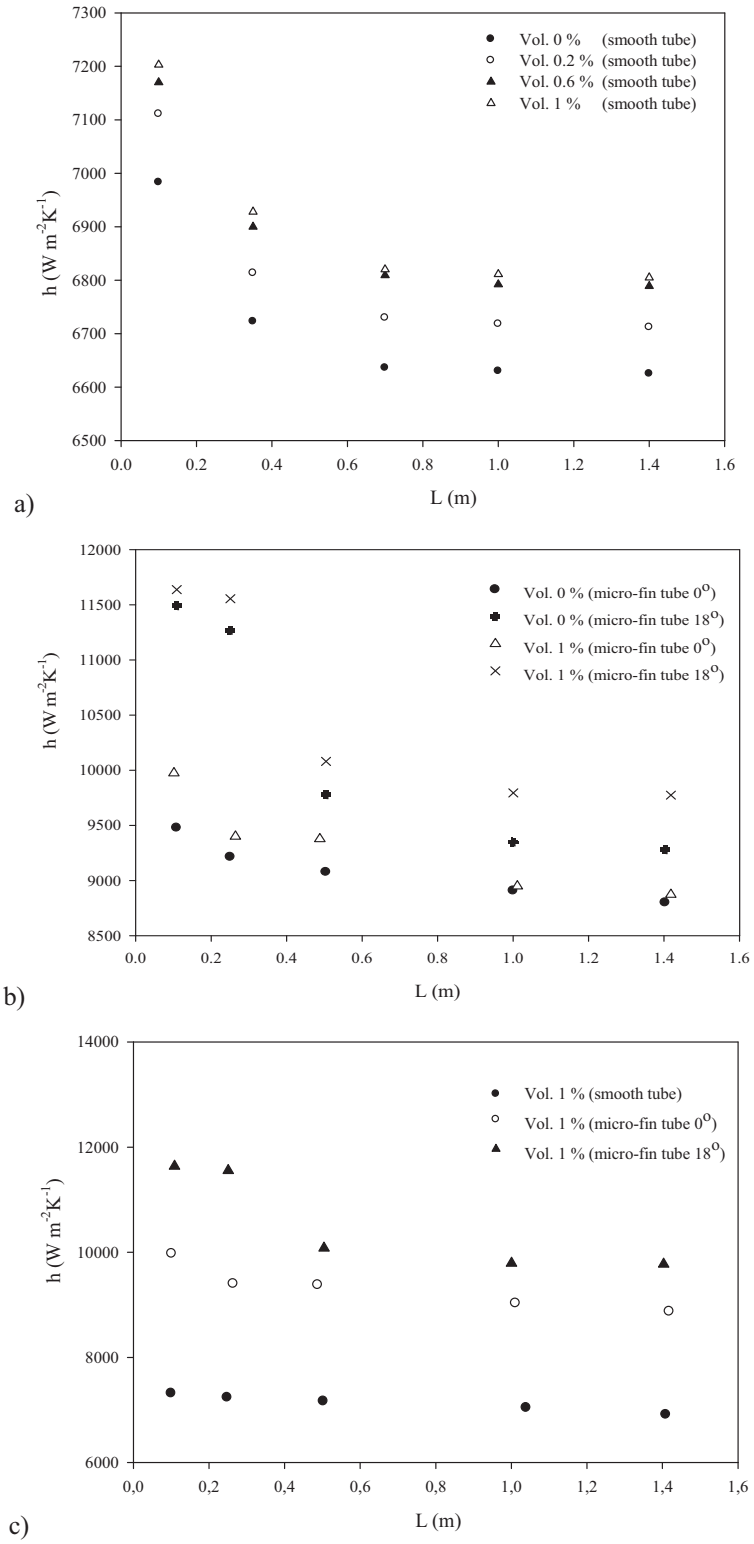

Fig. (11). Variations in heat transfer coefficient of smooth tube (**a**), micro-fin tubes (**b**) and smooth-micro-fin tubes (**c**) on volume concentration along the tube length.

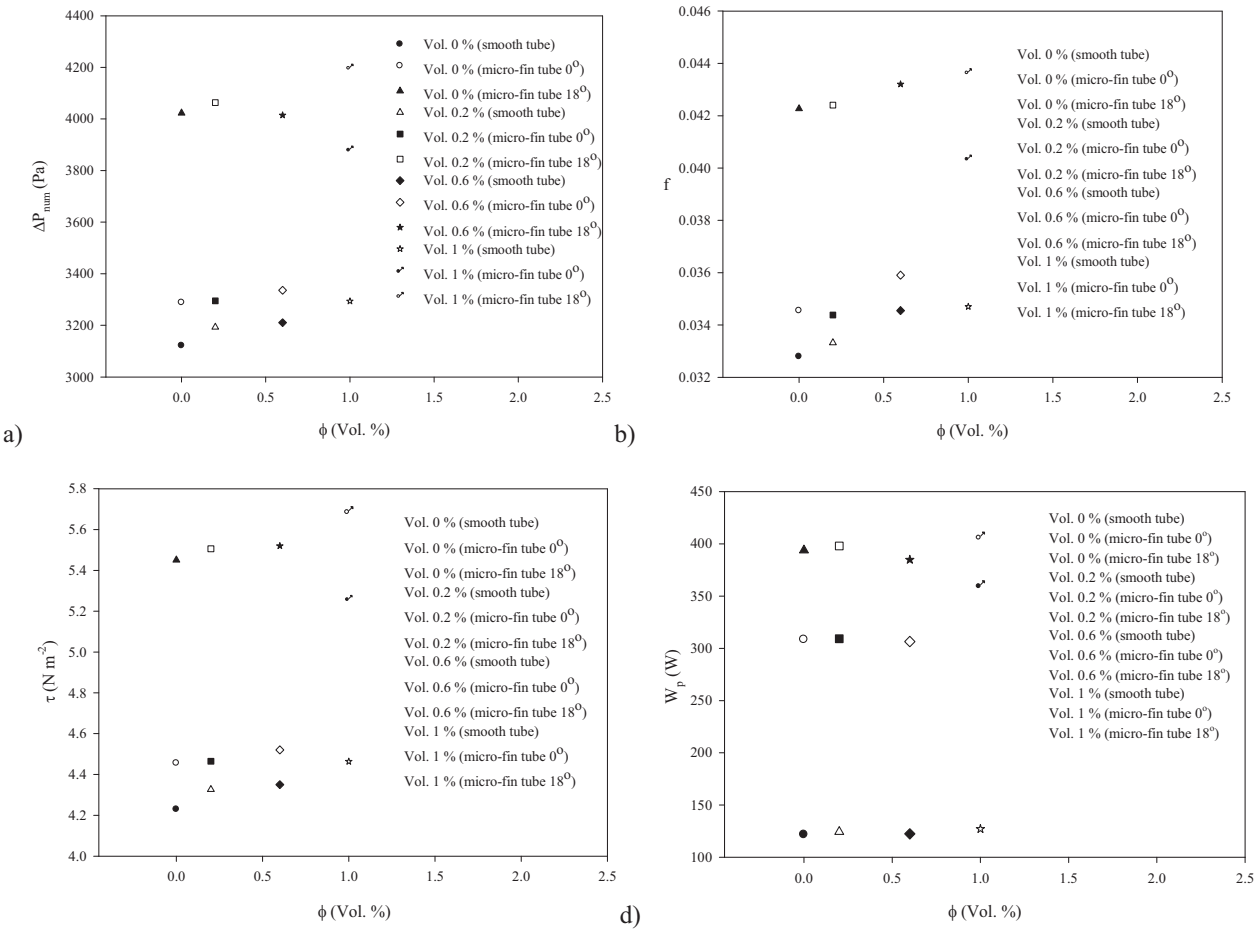

Fig. (12). Variations in pressure drop (**a**), friction factor (**b**), wall shear stress (**c**) and pumping power (**d**) of smooth tube and micro-fin tubes on different volume.

CONFLICT OF INTEREST

The authors confirm that this article content has no conflicts of interest.

ACKNOWLEDGEMENTS

The authors would like to express their appreciation to the Thailand Research Fund (TRF) and The National Research University Project for providing financial support for this study. Especially, the First author wishes to thank KMUTT for providing him with a Postdoctoral fellowship. The authors also wish to thank DEGUSSA AG, Germany for the valuable donation of the nanoparticles used in the present study. This research has been supported by Yıldız Technical University Scientific Research Projects Coordination Department. Project Number: 29-06-01-01.

NOMENCLATURE

Cp	=	Specific heat [J $kg^{-1}K^{-1}$]
d	=	Internal tube diameter [m]
h	=	Heat transfer coefficient [W $m^{-2}K^{-1}$]
k	=	Thermal conductivity [W $m^{-1}K^{-1}$]
k_H	=	Huggins coefficient.
L	=	Length of test tube [m]
m	=	Mass flow rate [kg s^{-1}],
Nu	=	Nusselt number
ΔP	=	Pressure drop [Pa]
Pr	=	Prandtl number
Re	=	Reynolds number
Q	=	Heat transfer rate [W]
q"	=	Heat flux [W m^{-2}]
T	=	Temperature [°C]
μ	=	Dynamic viscosity [Pa.s]
ρ	=	Density [kg m^{-3}]
τ	=	Shear stress [N m^{-2}]
φ	=	Volume fraction [%]
$φ_m$	=	maximum particle packing fraction
ν	=	Kinematic viscosity [m^2 s^{-1}]
m	=	Mass [kg]
f	=	Friction factor
W	=	Work [J]
P	=	Pressure [Pa]
A	=	Area [m^2]
u	=	Average velocity [m/s]
n	=	Number of fins

e = Height of fin [m]
p = Distance between micro-fins [m]
Q = Flow rate

SUBSCRIPTS

avg = Average
bf = Base fluid
nf = Nano fluid
exp = Experimental
ext = External
f = Fluid
h = Hot
i = Inlet
m = Mean
nf = Nanofluid
num = Numerical
p = Particle
r = Radius of particle
s = Surface
o = Outlet
w = Water

REFERENCES

[1] Choi, U.S. Enhancing thermal conductivity of fluids with nanoparticles. *ASME FED,* **1995**, *66*, 99-103.

[2] Xuan, Y.; Li, Q. Heat transfer enhancement of nanofluids. *Int. J. Heat Fluid Fl.*, **2000**, *21*, 58-64.

[3] Maxwell, J.C. *Electricity and Magnetism*.; Clarendon Press: Oxford UK, **1873**.

[4] Daungthongsuk, W.; Wongwises, S. A critical review of convective heat transfer of nanofluids. *Renew. Sustain. Energy Rev.,* **2007**, *11*, 797-817.

[5] Duangthongsuk, W.; Wongwises, S.Measurement of temperature-dependent thermal conductivity and viscosity of TiO_2-water nanofluids. *Exp. Therm. Fluid Sci.*, **2009**, *32*, 706-714.

[6] Duangthongsuk, W.; Wongwises, S. Comparison of the effects of measured and computed thermophysical properties of nanofluids on heat transfer performance. *Exp. Therm. Fluid Sci.*, **2010**, *34*, 616-624.

[7] Duangthongsuk, W.; Wongwises, S. An experimental study on the heat transfer performance and pressure drop of TiO_2-water nanofluids flowing under a turbulent flow regime. *Int. J. Heat Mass Trans.,* **2010**, *53*, 334-344.

[8] Duangthongsuk, W.; Wongwises, S. Heat transfer enhancement and pressure drop characteristics of TiO2-water nanofluid in a double-tube counter flow heat exchanger. *Int. J. Heat Mass Tran.*, **2009**, *52*, 2059-2067.

[9] Duangthongsuk, W.; Wongwises, S. Effect of thermophysical properties models on the predicting of the convective heat transfer coefficient for low concentration nanofluid. *Int. Commun. Heat Mass.,* **2008**, *35*, 1320-1326.

[10] Duangthongsuk, W.; Dalkilic, A.S.; Wongwises, S. Convective heat transfer of Al2O3-water nanofluids in a microchannel heat sink. *Curr. Nanosci.,* **2012**, *8,* 317-322.

[11] Suriyawong, A.; Wongwises, S., Nucleate pool boiling heat transfer characteristics of TiO_2-water nanofluids at very low concentrations. *Exp. Therm. Fluid Sci.*, **2010**, *34*, 992-999.

[12] Trisaksri, V.; Wongwises, S. Nucleate pool boiling heat transfer of TiO2–R141b nanofluids. *Int. J. Heat Mass Trans.*, **2009**, *52*, 1582-1588.

[13] Dalkilic, A.S.; Kürekci, N.A.; Wongwises, S. Effect of void fraction and friction factor models on the prediction of pressure drop of R134a during downward condensation in a vertical tube. *Heat Mass Transfer*., **2012**, *48*, 123-139.

[14] Dalkilic, A.S.; Kürekci, N.A.; Wongwises , S. Prediction of two-phase friction factor of refrigerants inside a horizontal tube using CFD analysis for the homogeneous condensation flow.*ASME-JSME-KSME Joint Fluids Engineering Conference, ASME-JSME-KSME.*, **2011**, *July 24-29*, Japan.

[15] Fluent release 6.2.16, Fluent Incorporated, **2005.**

[16] Demir, H.; Dalkilic, A.S.; Kurekci , N.A.; Kelesoglu, B.; Wongwises, S. A numerical investigation of nanofluids forced convection flow in a horizontal smooth tube. *Int. Heat Transfer Con.* ASME. , **2010**, *August 8-13*, USA.

[17] Demir, H.; Dalkilic, A.S.; Kurekci , N.A.; Kelesoglu, B.; Wongwises, S., Numerical investigation on the single phase forced convection heat transfer characteristics of TiO_2nanofluids in a double-tube counter flow heat exchanger. *Int. Commun. Heat Mass.,* **2011**, *38*, 218-228.

[18] Palm, S.J.; Roy, G.; Nguyen, C.T. Heat transfer enhancement with the use of nanofluids in radial flow cooling systems considering temperature-dependent properties. *Appl. Therm. Eng.*, **2006**, *26*, 2209-2218.

[19] Ağra, Ö.; Demir, H.; Atayılmaz, Ş.Ö.; Kantaş, F.; Dalkılıç, A.S. Numerical investigation of heat transfer and pressure drop in enhanced tubes. *Int. Commun. Heat Mass.,* **2011**, *38*, 1384-1391.

[20] Balcılar, M.; Dalkılıç, A.S.; Bolat, B.; Wongwises, S. Investigation of empirical correlations on the determination of condensation heat transfer characteristics during downward annular flow of R134a inside a vertical smooth tube using artificial intelligence algorithms. *J. Mec. Sci. Technol.,* **2011**, *25*, 2683-2701.

[21] Bolat, B.; Balcilar , M.; Dalkilic, A.S.; Wongwises, S. Optimization of the relationship between the two-phase friction factor and Reynolds equivalent number model by the means of Genetic Algorithm. *ASME/JSME 8th Thermal Engineering Joint Conference. ASME.,* **2011**, *March 13-17*, Hawaii.

[22] Balcilar, M.; Dalkilic, A.S.; Wongwises S. Artificial neural network (ANN) techniques for the determination of condensation heat transfer characteristics during downward annular flow of R134a inside a vertical smooth tube.*Int. Commun. Heat Mass.,* **2011**, *38*, 75-84.

[23] Balcilar, M.; Dalkilic, A.S.; Wongwises S. Determination of condensation heat transfer characteristics of R134a by means of artificial intelligence method. *International Mechanical Engineering Congress and Exposition, ASME*., **2010,** *November 12-18*, USA.

[24] Balcilar, M.; Dalkilic, A.S.; Suriyawong, A.; Yiamsawas , T.; Wongwises, S. Investigation of pool boiling of nanofluids using artificial neural networks and correlation development techniques. *Int. Commun. Heat Mass.,* **2012**, *39*, 424-431.

[25] Balcilar, M.; Dalkilic, A.S.; Agra, O.; Atayilmaz, S.O.; Wongwises, S. A correlation development study on the prediction of pressure drop during condensation and evaporation of various refrigerants in horizontal smooth and micro-fin tubes. *Int. Commun. Heat Mass.,* **2012**, *39*, 937-944.

[26] SolidWorks, SolidWorks Corporation, 300 Baker Avenue, Concord, MA 01742. Available from: http://www.solidworks.com/.

[27] ANSYS Fluent, ANSYS Inc., 10 Cavendish Court Lebanon, NH 03766 Available from: http://www.ansys.com/.

[28] Williams, W.C.; Buongiorno, J.; Hu, L.W. Experimental investigation of turbulent convective heat transfer and pressure loss of alumina/water and zirconia/water nanoparticle colloids (nanofluids) in horizontal tubes. *J. Heat Transf*., **2008**, *130*, 042412.

[29] Rea, U.; McKrell, T.; Hu, L.; Buongiorno, J. Laminar convective heat transfer and viscous pressure loss of alumina-water and zirconia-water nanofluids.*Int. J. Heat Mass Tran.,* **2009**, 52, 2042-2048.

[30] Einstein, A. Eineneuebestimmung der moleküldimensionen.*Ann Phys-Newyork***., 1906**, *324*, 289-306.

[31] Brinkman, H. The viscosity of concentrated suspensions and solutions.*J. Chem. Phys.*, **1952**, *20*, 571-581.

[32] Batchelor, G. The effect of brownian motion on the bulk stress in a suspension of spherical particles.*J. Fluid Mech.,* **1977**, *83*, 97-117.

[33] Graham, A.L. On the viscosity of suspensions of solid spheres.*J. ApplSci Res*., **1981**, *37*, 275-286.

[34] Kitano, T.; Kataoka, T.; Shirota, T. An empirical equation of the relative viscosity of polymer melts filled with various inorganic fillers. *The Journal RheologicaActa*., **1981** , *20*, 207-209.

[35] Bicerano, J.; Douglas, J.F.; Brune, D.A. Model for the viscosity of particle dispersions. *J. Macromol Sci-Rev. M.,* **1999**, *39*, 561-642.

[36] Wang, X.; Xu, X.; Choi, S.U.S. Thermal conductivity of nanoparticle–fluid mixture. *J.Thermophys Heat Tr*., **1999**, *13*, 474-480.

[37] Tseng, W.J.; Chen, C.N. Effect of polymeric dispersant on rheological behavior of nickel-terpineol suspensions.*Mat. Sci. Eng.A-Struct*, **2003**, *347*, 145-153.

[38] Chen, H.; Ding, Y.; He, Y.; Tan, C. Rheological behaviour of ethylene glycol based titanianofluids. *Chem. Phys. Lett.*, **2007**, *444*, 333-337.

[39] Nguyen, C.; Desgranges, F.; Roy, G.; Galanis, N.; Mare, T.; Boucher, S.; Anguemintsa, H. Temperature and particle-size dependent viscosity data for water-based nanofluids-hysteresis phenomenon. *Int. J. Heat Fluid Fl.*, **2007**, *28*, 1492-1506.

[40] Khanafer, K.; Vafai, K. A critical synthesis of thermophysical characteristics of nanofluids.*Int. J. Heat Mass Tran.*, **2011**, *54*, 4410-4428.

[41] Vand , V. Viscosity of solutions and suspensions I. Theory, *J. Phys. Colloid Chem.*, **1948**, *52*, 277-299.

[42] Mooney, M. The viscosity of a concentrated suspension of spherical particles. *J. Coll. Sci. Imp. U. Tok***., 1951**, 6-8.

[43] Krieger , I. M.; Dougherty, T. J. A mechanism for non-newtonian flow in suspensions of rigid spheres. *J. Rheol.*, **1959**, *3*, 137-152.
[44] Krieger, I.M. Rheology of monodisperse lattices., *Adv. Colloid Interfac.*, **1972**, *3*, 111-136.
[45] Frankel, N.A.; Acrivos, A. On the viscosity of a concentrated suspension of solid spheres. *Chem. Eng. Sci.*, **1967**, *22*, 847-853.
[46] Miller, A.; Gidaspow, D.; Dense, D. Vertical gas-solid flow in a pipe. *AIChE journal*, **1992**, *38*, 1801-1815.
[47] Chow , T.S. Viscosities of concentrated dispersions.*Phys. Rev. E.*, 1993, *48*, 1977-1983.
[48] Pak, B.C.; Cho, Y.I. Hydrodynamic and heat transfer study of dispersed fluids with submicron metallic oxide particles.*Exp. Heat Transfer.*, **1998**, *11*, 151-170.
[49] Liu, S. Particle dispersion for suspension flow. *Chem. Eng. Sci.*, **1999**, *54*, 873-891.
[50] Wang, X.; Xu, X. Choi S.U.S., Thermal conductivity of nanoparticle-fluid mixture, *J. Thermophys. Heat Tr.*, **1999**, *13*, 474-480.
[51] Davalos, L.A.; Orozco, L.A.; Castillo, L.F. Del. Hydrodynamic behavior of suspensions of polar particles. *Encycl. Surf. Colloid Sci.*, **2002**, *4*, 2375-2396.
[52] Putra, N.; Roetzel, W.; Das, S.K. Natural convection of nano-fluids.*Heat Mass Transfer*., **2003**, *39*, 775-784.
[53] Tang, G.Y.; Yang, C.; Chai, J.C.Gong, H.Q. Joule heating effect on electroosmotic flow and mass species transport in a microcapillary. *Int. J. Heat Mass Trans.*, **2004**, *47*, 215-227.
[54] Hamilton, R.L.; Crosser , O.K. Thermal conductivity of heterogeneous two component systems.*Ind. Eng. Chem.*, **1962**, *1*, 187-191.
[55] Hui , P.M.; Zhang, X.; Markworth , A.J.; Stroud, D. Thermal conductivity of graded composites: numerical simulations and an effective medium approximation. *J. Mater. Sci.*, **1999**, *34*, 5497-5503.
[56] Xuan, Y.; Li , Q. Heat transfer enhancement of nanofluids.*Int. J. Heat Fluid Fl.*, **2000**, 21, 58-64.
[57] Yu, W.; Choi, S.U.S. The role of interfacial layers in the enhanced thermal conductivity of nanofluids: a renovated Maxwell model. *J. Nanopart. Res.*, **2003**, *5*, 167-171.
[58] Godson, L.; Raja, B.; Mohan, D. Lal; Wongwises, S. Experimental investigation on the thermal conductivity and viscosity of silver-deionized water nanofluid. *Exp. Heat Transfer.*, **2010**, *23*, 317-332.
[59] Prasher, R.; Bhattacharya, P.; Phelan, P.E. Thermal conductivity of nanoscale colloidal solutions (nanofluids). *Phys. Rev. Lett.*, **2005**, *94*, 025901-1–025901-4.
[60] Koo, J.; Kleinstreuer, C. A new thermal conductivity model for nanofluids. *J. Nanopart. Re.,* **2004**, *6,* 577-588.
[61] Li, C.H.; Peterson, G.P. Experimental investigation of temperature and volume fraction variations on the effective thermal conductivity of nanoparticle suspensions (nanofluids). *J. Appl. Phys.*, **2006**, 99-084314.
[62] Maiga, S.E.B.; Nguyen, C.T.; Galanis, N.; Roy, G. Heat transfer behaviours of nanofluids in a uniformly heated tube. *Superlattice Microst.*, **2004**, *35*, 543-557.
[63] Bhattacharya, P.; Saha, S.K.; Yadav, A.; Phelan, P.E.; Prasher, R.S. Brownian dynamics simulation to determine the effective thermal conductivity of nanofluids. *J. Appl. Phys.,* **2004**, *95*, 6492-6494.
[64] Buongiorno, J. Convective transport in nanofluids. *J. Heat Transf.*, **2006**, *128*, 240-251.
[65] Kim, D.; Kwon, Y.; Cho, Y.; Li, C.; Cheong, S.; Hwang, Y.; Lee, J.; Hong, D.; Moon, S. Convective heat transfer characteristics of nanofluids under laminar and turbulent flow conditions.*Curr. Appl. Phys.*, **2009**, *9 (2)*, 119-123.
[66] Elena, V.; Timofeeva, V.; Gavrilov, N.A.; McCloskey, J.M.; Tolmachev, Y.V. Thermal conductivity and particle agglomeration in alumina nanofluids: Experiment and Theory. *Phys. Rev. E.*, **2007,** *76*, 061203.
[67] Chon, C.H.; Kihm, K.D.; Lee, S.P.; Choi, S.U.S. Empirical correlation finding the role of temperature and particle size for nanofluid (Al_2O_3) thermal conductivity enhancement. *Appl. Phys. Lett.*, **2005**, 87.
[68] Murshed, S.M.S.; Leong, K.C.; Yang, C. A. model for predicting the effective thermal conductivity of nanoparticles–fluid suspensions. *Int. J. Nanosci.*, **2006**, *5*, 23-33.
[69] Yang, Y.; Zhang, Z.G.; Grulke, E.A.; Anderson, W.B.; Wu, G. Heat transfer properties of nanoparticle-in-fluid dispersions (nanofluids) in laminar flow.*Int. J. Heat Mass Trans.,* **2005**, 1107-1116
[70] Yu , W.; France, D.M.; Routbort, J.L.; SUS., Choi., Review and comparison of nanofluid thermal conductivity and heat transfer enhancements. *Heat Transfer Eng.*, **2008**, *29 5*, 432-460.
[71] Bejan, A.; Tsatsaronics, G.; Moran, M. Thermal design and optimization, Wiley-Interscience Publication:**1996**.
[72] Petukhov, B. S. Heat transfer and friction in turbulent referred to in handbook of single-phase convective pipe flow with variable physical properties. In Heat Transfer, ed. T. F. Irvine and J. P.New York: Wiley Interscience, 1987. Hartnett, Vol. 6, Academic Press:New York, **1970.**
[73] Fausett, L., *Fundamentals of Neural Networks, Architectures, Algorithms, and Application; Prentice-HallInc. Press*, **1994**.
[74] Rosenblatt , F., *Principles of Neurodynamics: Perceptrons and the Theory of BrainMechanisms*; Washington DC: Spartan Books, **1961**.
[75] Rumelhart D.E., G. E., Hinton, R.J., Williams, *Learning internal representations by error propagation.In D. E. Rumelhart& J. L. McClelland (Eds.), Parallel Distributed Processing1*, **1986**, pp. 318-362.
[76] Alpaydin, E.*Introduction to Machine Learning*, (T. Dietterich, C. Bishop, D. Heckerman, M. Jordan, & M. Kearns, Eds.) Machine Learning , **2004**, *56*, pp.387-99.

Received: August 22, 2012 **Revised: October 16, 2012** **Accepted: October 25, 2012**

Provided for non-commercial research and education use.
Not for reproduction, distribution or commercial use.

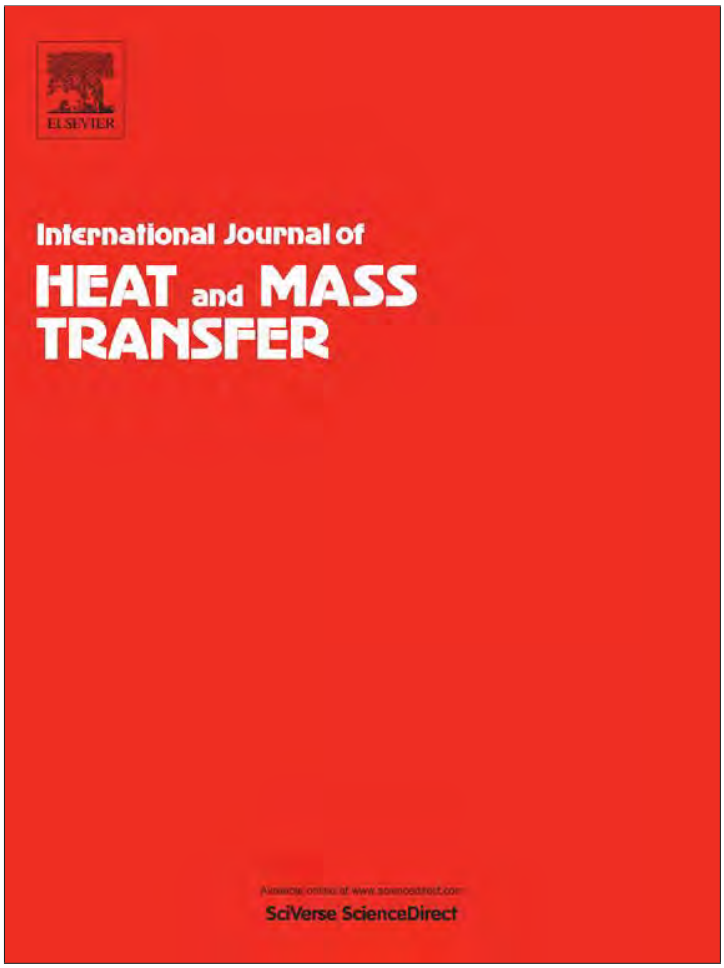

(This is a sample cover image for this issue. The actual cover is not yet available at this time.)

This article appeared in a journal published by Elsevier. The attached copy is furnished to the author for internal non-commercial research and education use, including for instruction at the authors institution and sharing with colleagues.

Other uses, including reproduction and distribution, or selling or licensing copies, or posting to personal, institutional or third party websites are prohibited.

In most cases authors are permitted to post their version of the article (e.g. in Word or Tex form) to their personal website or institutional repository. Authors requiring further information regarding Elsevier's archiving and manuscript policies are encouraged to visit:

http://www.elsevier.com/copyright

Author's personal copy

International Journal of Heat and Mass Transfer 60 (2013) 201–209

Contents lists available at SciVerse ScienceDirect

International Journal of Heat and Mass Transfer

journal homepage: www.elsevier.com/locate/ijhmt

Heat transfer performance of screen mesh wick heat pipes using silver–water nanofluid

Lazarus Godson Asirvatham [a,*], Rajesh Nimmagadda [a], Somchai Wongwises [b,c]

[a] Department of Mechanical Engineering, Karunya University, Coimbatore 641 114, Tamil Nadu, India
[b] Fluid Mechanics, Thermal Engineering and Multiphase Flow Research Lab (FUTURE), Department of Mechanical Engineering, Faculty of Engineering, King Mongkut's University of Technology Thonburi,126 Bangmod, Tongkru, Bangkok 10140, Thailand
[c] The Academy of Science, The Royal Institute of Thailand, Sanam Suea Pa, Dusit, Bangkok 10300, Thailand

ARTICLE INFO

Article history:
Received 3 May 2012
Received in revised form 6 November 2012
Accepted 10 November 2012

Keywords:
Silver
De-ionized water
Nanofluid
Thermal resistance
Evaporation and condensation heat transfer coefficients
Dry-out condition

ABSTRACT

This study presents the improvement in heat transfer performance of a heat pipe using silver nanoparticles dispersed in DI (De-Ionized) water. The nanoparticles suspended in conventional fluids have superior heat transfer capability due to improved thermal conductivity. The heat pipes are tested for heat inputs ranging from 20 W to 100 W in five steps, which is suitable for removing heat from power transistors in electronics and processors in computers. The effect of various operational limits and test parameters such as heat inputs, volume fraction, vapour temperature on the thermal resistance, evaporation and condensation heat transfer coefficients, are experimentally investigated. The tested silver nanoparticles volume concentration ranged from 0.003% to 0.009% with average nanoparticle diameter of 58.35 nm. The experimental results are evaluated in terms of performance metrics by direct measurement of vapour temperatures in the centre core of heat pipe. A substantial reduction in thermal resistance of 76.2% is observed for 0.009 vol.% concentration of silver nanoparticles. Further an enhancement in the evaporation heat transfer coefficient of 52.7% is observed for the same concentration. The use of nanoparticles enhances the operating range of heat pipe by 21% compared with that of DI water.

© 2012 Elsevier Ltd. All rights reserved.

1. Introduction

Heat pipes and their applications in thermal management have been studied for decades. They constitute an efficient compact tool to dissipate substantial amount of heat from various engineering systems including electronics cooling [1,2] like computers, laptop notebooks etc. In fact, virtually every notebook computer manufactured today uses at least one heat pipe assembly, typically designed to carry 30 W of power. The results of reports from various researchers [3] concludes that the conventional working fluids such as DI water, methanol etc. in heat pipes possess limited heat transport capabilities which arises due to working fluid transport properties. To overcome these limitations, the thermo physical properties of working fluid have to be improved. An innovative way to enhance liquid thermal conductivity is the dispersion of highly conductive solid nanoparticles within the base fluid. This new generation of conductive fluids with nanoparticles is referred to as nanofluid [4,5]. Taehyun Cho et al. [6] investigated thermal conductivity of fluids suspended with silver nanoparticles. The observation concludes an improvement in thermal conductivity by 10%, 16% and 18% for respective concentrations of 1000, 5000 and 10000 ppm.

Das et al. [7] investigated the increase in thermal conductivity with temperature and volume fraction for Al_2O_3 and CuO nanoparticles dispersed in water. The increase in effective thermal conductivity of nanofluids between 20 and 40 °C is found to be 15% for each type nanofluid. It was observed that in comparison with distilled water, the addition of nanoparticles gives a better enhancement with temperature for low volume fraction of particles. Terekhov et al. [8] reviewed experimental and theoretical results on heat transfer mechanism in nanofluids and concluded significant divergences in data of different researchers and possible reasons for this divergence. Lee et al. [9] used transient hot wire method to measure thermal conductivities of oxide nanofluids. The results shows that nanofluids have higher thermal conductivity than base fluid and the enhancement observed is 5%–60% increment in thermal conductivity for volume fraction ranging from 0.1% to 5%. Paisarn Naphon et al. [10] experimentally investigated titanium nanofluids on heat pipe thermal efficiency. The heat pipes with the de-ionic water, alcohol, and nanofluids (alcohol and nanoparticles) are tested. The titanium nanoparticles with diameter of 21 nm are used in the present study. Effects of percentage charge amount of working fluid, heat pipe tilt angle and percentage

* Corresponding author. Tel.: +91 422 2614430; fax: +91 422 2615615.
E-mail addresses: godson@karunya.edu, godasir@yahoo.co.in (L.G. Asirvatham), rajesh.mech335@gmail.com (R. Nimmagadda), somchai.won@kmutt.ac.th (S. Wongwises).

0017-9310/$ - see front matter © 2012 Elsevier Ltd. All rights reserved.
http://dx.doi.org/10.1016/j.ijheatmasstransfer.2012.11.037

Author's personal copy

Nomenclature

A	surface area (m^2)
C_p	specific heat (J/kg K)
d	outer diameter (m)
h	heat transfer coefficient (W/m^2 K)
K	thermal conductivity (W/m K)
L	length (m)
m	mass flow rate (kg/s)
Q	heat load (W)
q	heat flux (kW/m^2)
R	thermal resistance (°C/W)
ΔT	temperature difference (°C)
$\overline{T}$	average temperature (°C)
U	uncertainty

Subscript

A	adiabatic
C	condenser
CT	condenser temperature
CW	cooling water
c/s	cross-sectional
E	evaporator
EC	evaporator and condenser
ET	evaporator temperature
eff	effective
H.P	heat pipe
Inlet	inlet to condenser
nf	nanofluid
p	particle
Surf	surface
Vap	vapour
vs	vapour and surface
w	water

Greek Symbols

φ	volume fraction
ρ	density (kg/m^3)
μ	dynamic viscosity (kg/m-s)
Δ	increment

nanoparticles volume concentrations on the thermal efficiency of heat pipe are considered. For the heat pipe with 0.10% nanoparticles volume concentration, the thermal efficiency is 10.60% higher than that with the base fluid.

Riehl [11] has observed that a higher heat transfer coefficient can be seen when using nanoparticles in water under low heat input conditions. Tsaia et al. [12] investigated the influence of particle size on the heat pipe thermal performance. The study is based on the structural characteristics of gold nanoparticles of various sizes dispersed in aqueous solution on heat pipe thermal resistance. The thermal resistance of heat pipe ranges from 0.17 to 0.215 °C/W with different nanoparticle solutions. Furthermore, the thermal resistance of the heat pipes with nanoparticle solution is lower than that with DI water. Shafahi et al. [3] used a two-dimensional analysis to study the thermal performance of a cylindrical heat pipe using Al_2O_3, CuO, and TiO_2 nanoparticles suspended in water as the working fluid. The existence of optimum mass concentration to improve heat transfer performance is obtained as 5%, 15% and 7% for Al_2O_3, CuO, and TiO_2 respectively. It was found that smaller nanoparticles with particle diameter of 10 nm have a more pronounced effect on the temperature gradient along the heat pipe when compared to 40 nm. Kang et al. [13] used dilute dispersion of silver nano particles in pure water as working fluid in a circular heat pipe. The diameters of the nano particles used are 10 and 35 nm, respectively. The results showed that the nanofluid as working fluid in heat pipe can transport heat up to 70 W and is higher than pure water by about 20 W. Do et al. [14] investigated the effect of water-based Al_2O_3 nanofluids on the thermal performance of circular screen mesh wick heat pipes. The volume fraction of the nanoparticles used are 1 and 3 vol.%. It is found that the thermal resistance at the evaporator-adiabatic section decreases by 40% when using nanofluid with volume fraction of 3.0 vol.%. It is also shown that the use of water based Al_2O_3 nanofluids enhances the maximum heat transport rate of heat pipes. Do and Jang [15] evaluated the thermal performance of a heat pipe with rectangular grooved wick using water-based Al_2O_3 nanofluid. They found that the thin porous coating layer formed by nanoparticles is the key effect for higher heat transfer. The results showed the feasibility of enhancing the thermal performance up to 100% although water-based Al_2O_3 nanofluids with the concentration less than 1.0% is used as working fluid.

Yang et al. [16] carried out an experiment to study the heat transfer performance of a horizontal micro-grooved heat pipe using CuO–water nanofluids. Mass concentration of CuO nanoparticles ranging from 0.5 to 2.0 wt.% having the average diameter of 50 nm and the operating pressure varying from 7.45, 12.38 and 19.97 kPa, are respectively used. The experimental results showed that the CuO–water nanofluids can improve the thermal performance of the heat pipe at optimum mass concentration of 1 wt.%. Under an operating pressure of 7.45 kPa, the heat transfer coefficients of the evaporator can be averagely enhanced by 46% and the CHF (critical heat flux) can be maximally enhanced by 30% compared with those of the heat pipe using DI water. Guo-Shan Wang et al. [17] have carried out an experimental study on thermal performance of a cylindrical miniature grooved heat pipe using aqueous CuO nanofluids for two different operating conditions. One was the steady operating processes with constant cooling conditions and the other was the unsteady start up processes with constant cooling conditions. The start up characteristics of the heat pipe using nanofluids was especially compared with that of the heat pipe using water. The experimental results are useful for designing miniature grooved heat pipes using nano-fluids as the working liquid. It was found that the thermal performance of the heat pipe had a remarkable increase by adding CuO nanoparticles into the base liquid. For unsteady start-up process, substituting the nanofluid for water as the working fluid, cannot only improve the thermal performance, but also reduce significantly the start-up time. The total heat resistance was reduced by 50% and heat removal capacity increases by 40% for nanofluid based heat pipe when compared with that of heat pipe using water. Park et al. [18] and Shung-Wen Kang et al. [19] also observed in another study that silver nanofluid grooved heat pipe thermal performance was higher than that for a conventional grooved heat pipe with water as working fluid.

It is found from the above mentioned literature [10,12,13] that all the researchers have observed an enhancement in the thermal performance of heat pipes using nanofluids. It is also observed that most of the previous investigations have been performed with high concentrations of metal oxide nanoparticles [3,14–16]; and very little amount of work has been carried out with the use of pure metal nanoparticles in predicting the thermal performance of heat pipes. It is also reported that use of high concentration

Author's personal copy

nanoparticles will block the wick due to the deposited nanoparticles and causes more resistance on the returning fluid to reach from condenser to evaporator. This eventually results in early evaporator dry out and causes heat pipe failure. Moreover, the earlier experiments have been performed by measuring only the wall temperature to evaluate the heat transfer performance of heat pipes. Interestingly, it is observed from the present study that there exist 5.8 °C difference between the wall and vapour temperatures measured at the core of the evaporator. Hence, there is a need to analyze the performance of heat pipes by considering the effect of the temperature difference between the wall and the vapour core which have never before appeared in the open literature. Therefore, the present study aims to experimentally analyze the thermal performance of heat pipe using low volume concentration (0.003%, 0.006% and 0.009%) of pure metal (silver) nanoparticles by measuring both the vapour and wall temperatures at the same time in all the three regions. The effect of heat load on the quantities such as thermal resistance, axial temperature distribution, evaporation, condensation heat transfer coefficients, effective thermal conductivity etc. are experimentally analyzed on the basis of vapour core and wall temperatures are discussed and presented.

2. Experimentation

2.1. Experimental setup

The schematic layout of test facility to measure the effect of nanoparticle concentration on the performance of heat pipe is shown in Fig. 1. The test section is made up of copper with outer diameter and length as 10 and 180 mm, respectively. The wall thickness, lengths of evaporator section, adiabatic section and condenser section of the heat pipes are 0.5, 50, 50 and 80 mm, respectively. Two layers of copper wick with a wire diameter of 0.105 mm and mesh number 100/inch is wrapped inside the heat pipe. 30% of the total volume of the heat pipe is charged with working fluid to completely saturate the wick. The condenser section of the het pipe was inserted horizontally into a cooling chamber made up of acrylic material. The test set up also consists of a pump and flow meter (with an uncertainty of ±10 ml) to circulate cooling water at a constant flow rate of 260 ml per minute through the condenser section. A constant temperature chilled water bath is used to maintain the inlet temperature of the circulating cooling water at 24 °C for all the test sections at various heat loads to obtain performance accuracy. The temperatures of the cooling water circulating through the condenser section are recorded by using two T-type thermocouples fixed at inlet and outlet of the condenser. A total of eight thermo couple sensors with T-type thermocouples of uncertainty ±0.5 °C are fixed along the test section include two in evaporator, three in adiabatic and three in condenser section, respectively. These sensors will directly measure the vapour temperature which is passing through the centre core of the heat pipe from evaporator section to condenser section. The evaporator and condenser surface temperatures are measured by fixing four T-type thermocouples two on each section.

The heat input to the heat pipe is applied using a digital wattmeter (with an uncertainty of ±0.5 W) connected to an electric heater wounded on the evaporator section. A 220 V A.C supply is used to energize the heater. The evaporator and adiabatic sections of the heat pipe are completely insulated using glass wool to minimize the heat loss. The temperature readings of the test section are recorded by connecting thermo couples to data logger [Model-(DA 100-13-1F), Yokogawa-N 200]. The entire data acquisition system is monitored and controlled by using a P.C.

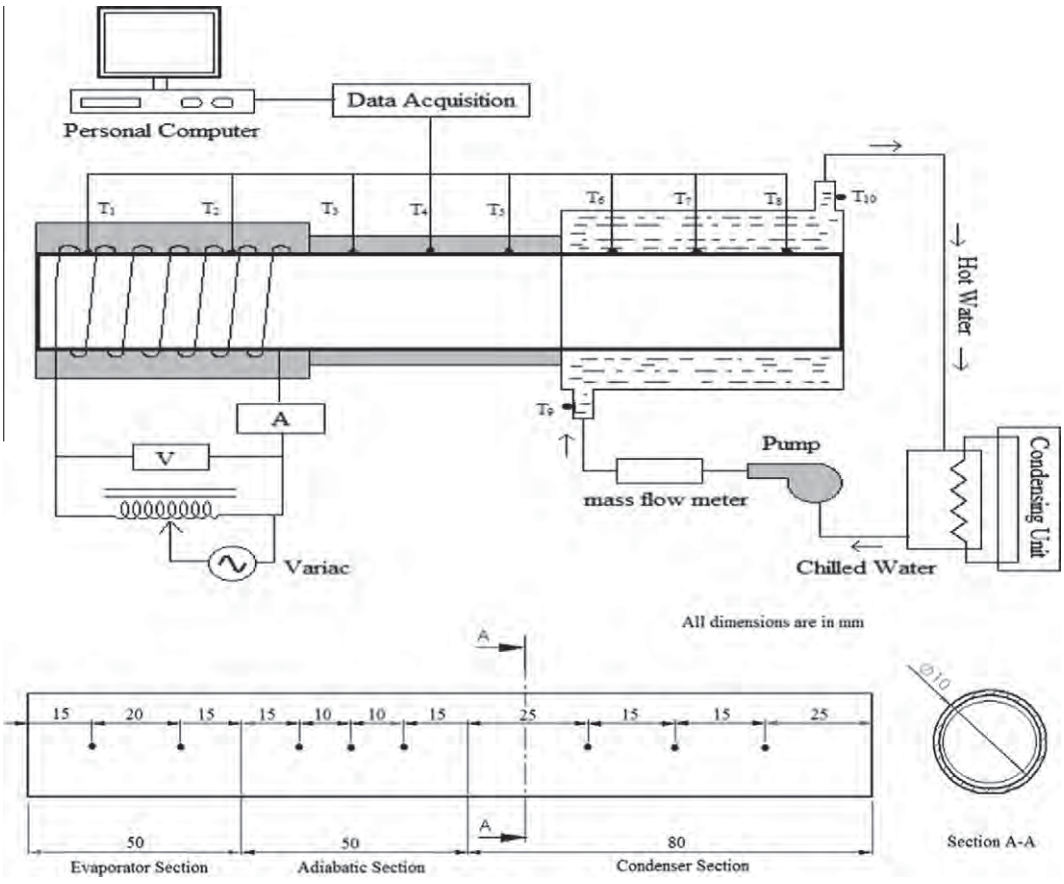

Fig. 1. Schematic diagram of the experimental apparatus.

Author's personal copy

2.2. Experimental procedure

2.2.1. Nanofluid preparation

The nanoparticles used in the present study is silver (manufactured by Sigma Aldrich; The Product Number - 576832, Silver nano-powder, <100 nm, 99.5% metals). A two step method is used to prepare silver–water nanofluid. The nanoparticles are mixed directly with De-ionized water without addition of any surfactant. The nanofluids are sonicated well for about 1 h in an ultra sonicator at sound frequencies of 50–60 kHz to ensure uniform and stable dispersion of nanoparticles in base fluid. The silver nanoparticles are further characterized by using scanning electron microscope (SEM) and particle size analyzer to study the size distribution and morphology. Fig. 2 shows the SEM image of 0.009 vol.% concentration of silver nanoparticles taken at 45,000X magnification. The size of the nanoparticles is marked in the SEM image. It is found that the size of the silver nanoparticles vary from 51 nm to 67 nm in some places. It is clearly seen that the nanoparticles are well dispersed with certain level of agglomeration. It is also observed that the size of the agglomerated nanoparticles exceed 100 nm in some places. Hence, the agglomerated nanoparticles are finely grinded in a ball grinder before adding to base fluid for sonication. Similarly, the size of the silver nanoparticles is measured using the particle size analyzer and shown in Fig. 3. It is clearly observed from the figure that the majority of the nanoparticles have the average size of 110–120 nm with an intensity of 13% and it is also seen from the peak that 10% of the nanoparticles have the size varying between 40 and 60 nm with 1.5% intensity. This justifies the average size of the silver nanoparticles used for the present study.

2.2.2. Experimental test

The experiments are conducted using four identical heat pipes in horizontal orientation which are fabricated as per mentioned dimensions. One of the heat pipes is filled with De-ionized water and remaining three heat pipes are filled with three different concentrations of silver–water nanofluid. The tests on all the four heat pipes are conducted under identical operating conditions such as constant flow rate and inlet temperature of the cooling water circulating through the condenser section. The power supply was turned on and the heater was energized with a heat load of 20 W. The steady state vapour temperature reading as well as surface temperature reading is recorded using data acquisition system. The input heat load is incremented gradually in equal steps from 20 W to beyond 100 W until dry out condition is reached.

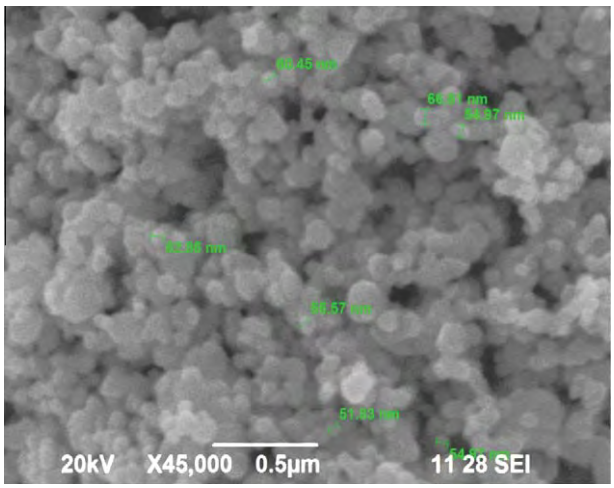

Fig. 2. SEM image of 0.009 vol.% concentration of silver nanoparticles.

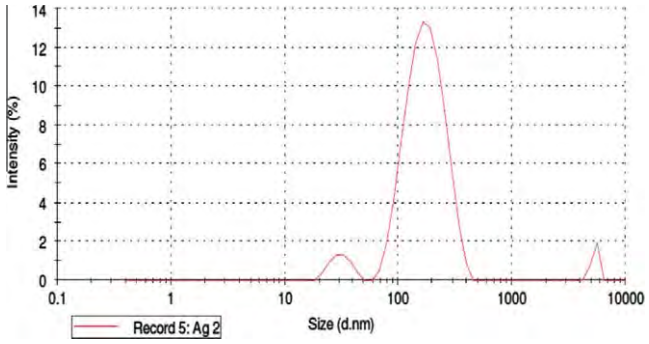

Fig. 3. Size distribution by intensity of the silver nanoparticles.

The heat input at which dry out condition is observed is assumed as maximum heat transport capability of heat pipe. At this condition the vapour temperature difference between evaporator and condenser abruptly increases.

2.3. Thermo physical properties of nanofluid

The thermo-physical properties of silver water nanofluid are calculated as follows.

The density is calculated from Pak and Cho [21] using the following equation:

$$\rho_{nf} = \varphi\rho_p + (1-\varphi)\rho_w \tag{1}$$

The specific heat is calculated from Xuan and Roetzel [22] as follows:

$$(\rho C_p)_{nf} = \varphi(\rho C_p)_p + (1-\varphi)(\rho C_p)_w \tag{2}$$

where $(\rho C_p)_{nf}$ is the heat capacity of the nanofluid, $(\rho C_p)_p$ is the heat capacity of the nanoparticles and $(\rho C_p)_w$ is the heat capacity of the base fluid.

The other properties such as viscosity and thermal conductivity are measured using the following equations proposed by the present authors. The detailed measurement techniques and procedure are given elsewhere [23] in a published literature for reference

$$\frac{\mu_{nf}}{\mu_w} = (1.005 + 0.497\varphi - 0.1149\varphi^2) \tag{3}$$

$$\frac{K_{nf}}{K_W} = (0.9692\varphi + 0.9508) \tag{4}$$

2.4. Data reduction

$$R_{H,P} = \frac{\overline{T}_{E,Vap} - \overline{T}_{C,Vap}}{Q} \tag{5}$$

The thermal resistance of heat pipe ($R_{H,P}$) is defined as the ratio of vapour temperature difference measured between evaporator and condenser ($\overline{T}_{E,Vap} - \overline{T}_{C,Vap}$) to the applied heat load (Q)

$$h_C = \frac{Q}{A_C \Delta T_C} \quad \text{where } A_C = \pi d_C L_C, \quad \Delta T_C = \overline{T}_{C,Vap} - \overline{T}_{C,Surf} \tag{6}$$

The condenser heat transfer coefficient (h_C) is defined as the ratio of heat load (Q) to the product of condenser surface area (A_C) and the temperature difference (ΔT_C) between vapour ($\overline{T}_{C,Vap}$) and surface ($\overline{T}_{C,Surf}$) in the condenser region. In the condenser region the vapour temperature ($\overline{T}_{C,Vap}$) is higher than the surface temperature ($\overline{T}_{C,Surf}$) due to heat rejection

Author's personal copy

$$h_E = \frac{Q}{A_E \Delta T_E} \quad \text{where } A_E = \pi d_E L_E, \quad \Delta T_E = \overline{T}_{E,Surf} - \overline{T}_{E,Vap} \tag{7}$$

The evaporator heat transfer coefficient (h_E) is defined as the ratio of applied heat load (Q) to the product of evaporator surface area (A_E) and the temperature difference (ΔT_E) between surface ($\overline{T}_{E,Surf}$) and vapour ($\overline{T}_{E,Vap}$) in the evaporator region. In the evaporator region the surface temperature ($\overline{T}_{E,Surf}$) is higher than the vapour temperature ($\overline{T}_{E,Vap}$) due to heat addition

$$K_{eff} = \frac{1}{A_{c/s,H,P} R_{H,P}} \quad \text{where } A_{c/s,H,P} = \frac{\pi}{4} d^2 \tag{8}$$

The effective thermal conductivity of heat pipe is defined as the inverse of product of cross sectional area of the heat pipe ($A_{c/s,H,P}$) and the thermal resistance of heat pipe ($R_{H,P}$).

2.4.1. Uncertainty analysis of measured parameters

$$\frac{\Delta Q}{Q} = \left[\left(\frac{\Delta V}{V}\right)^2 + \left(\frac{\Delta I}{I}\right)^2 + \left(\frac{\Delta L_E}{L_E}\right)^2 + \left(\frac{\Delta d_E}{d_E}\right)^2 \right]^{1/2} \tag{9}$$

Uncertainty in heat flux is calculated using Eq. (9). It is calculated based on the uncertainties in the applied voltage (ΔV), applied current (ΔI) to the heater coil. It also includes the uncertainties in the measured length (ΔL_E) and diameter (Δd_E) of the evaporator region over which heater coil is wrapped. The least count of the vernier calipers used to measure this length and diameter is taken as the uncertainty value

$$\frac{\Delta R}{R} = \left[\left(\frac{\Delta Q}{Q}\right)^2 + \left(\frac{\Delta(\Delta T)}{\Delta T_{EC}}\right)^2 \right]^{1/2} \tag{10}$$

Uncertainty in calculated thermal resistance is done using the Eq. (10). It depends on uncertainty in heat applied (ΔQ) and uncertainty in the measured temperature difference between evaporator and condenser ($\Delta(\Delta T)$). The actual temperature difference measured is found to be (ΔT_{EC})

$$\frac{\Delta h}{h} = \left[\left(\frac{UQ}{Q}\right)^2 + \left(\frac{U\Delta T}{\Delta T_{VS}}\right)^2 \right]^{1/2} \tag{11}$$

Uncertainty in the calculated heat transfer coefficient is made using Eq. (11). The calculation is done by taking into consideration all the uncertainties in the parameters on which heat transfer coefficient depends. The various uncertainties on which this heat transfer coefficient depends are uncertainty in the applied heat load (UQ) and uncertainty in the measured temperature difference between surface and vapour ($U\Delta T$). All these calculations are done to eliminate the experimental errors and the obtained results are taken from a standardized experimental test facility. The maximum uncertainties in thermal resistance and heat transfer coefficient are found to be 5.57% and 6.64%.

3. Results and discussion

The experiments are conducted for various heat loads (20, 40, 60, 80, 100 W) with heat pipes kept in horizontal position. The vapour temperatures as well as the surface temperature readings are recorded using thermocouples connected to a data acquisition system. The experimental results are compared between base fluid and nanofluid for all the concentrations and the enhancement in heat transfer performance with respect to concentration, heat load, thermo physical properties etc. are discussed in the following sub sections. Many day-to-day experiments have been conducted with the base fluid to check the repeatability in the experimental readings and found that the deviation between day1 and day2 reading is found to be less than 1.4%. The operating conditions of all the heat pipes such as evaporator heat load, cooling water inlet temperature and circulation rate are maintained constant for effective comparison of the results. Table 1 gives the experimental conditions chosen for the present study.

Table 1
Experimental conditions.

Working fluid charged (ml)	Q (W)	m_{CW} (kg/s)	$T_{CW,Inlet}$ (°C)
3.5	20	4.3333×10^{-3}	24
	40	4.3333×10^{-3}	24
	60	4.3333×10^{-3}	24
	80	4.3333×10^{-3}	24
	100	4.3333×10^{-3}	24

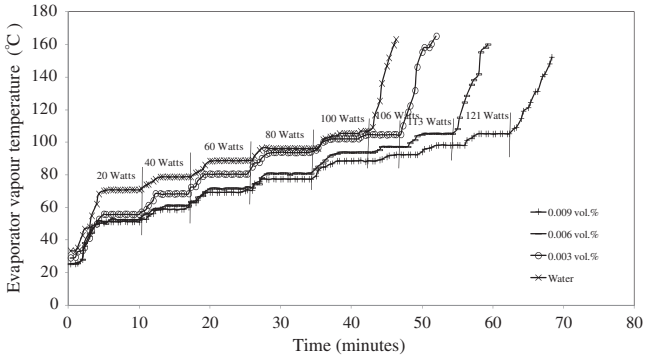

Fig. 4. Vapour temperature in the evaporator with respect to time in minutes.

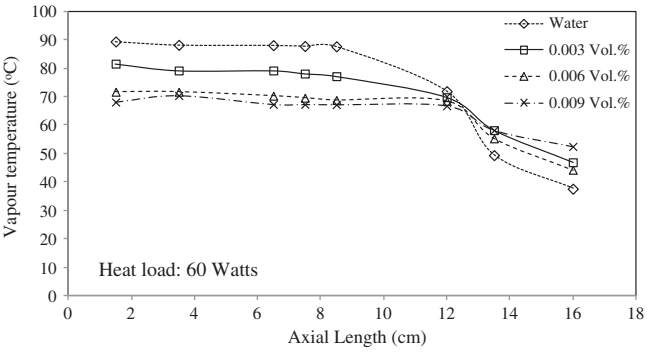

Fig. 5. Vapour temperature distribution with respect to axial length.

The vapour temperature in the evaporator section as a function of time for various heat loads and concentrations are shown in Fig. 4. It is observed that the steady state has been attained approximately after 15–20 min. The steady state temperature reading is taken for the analysis and data reduction. The dry out condition is observed beyond 100 W for heat pipes with DI water as working fluid. The vapour temperature reading decreases with the increase in concentration of nanofluid. This drop in temperature increases the operating range of heat pipe beyond 100 W, with nanofluid. It is also seen that for 0.003 and 0.006 vol.%, dry out is observed near 106 and 113 W. Whereas for heat pipe with 0.009 vol.% the dry out appears beyond 121 W. This shows that an increment of 21% in heat transfer capability is observed by using nanofluid as working fluid in heat pipe. The vapour temperature distribution along the axial length of the heat pipe for heat load of 60 W is shown in Fig. 5. It is clearly seen that a reduction in vapour temperature is observed by using nanofluids due to high thermal

Author's personal copy

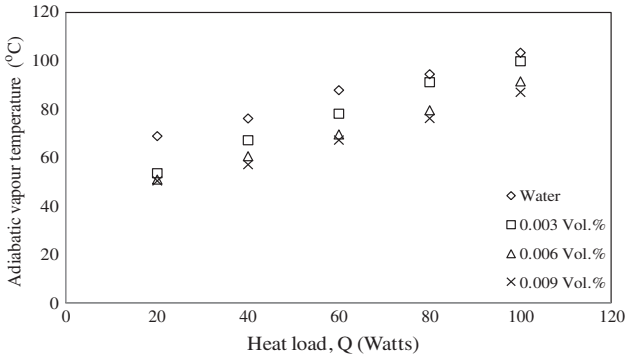

Fig. 6. Variation in adiabatic vapour temperature as a function of heat load.

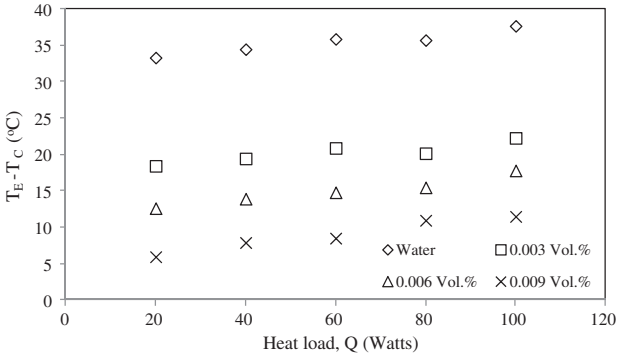

Fig. 8. Evaporator and condenser vapour temperature difference as a function of heat load.

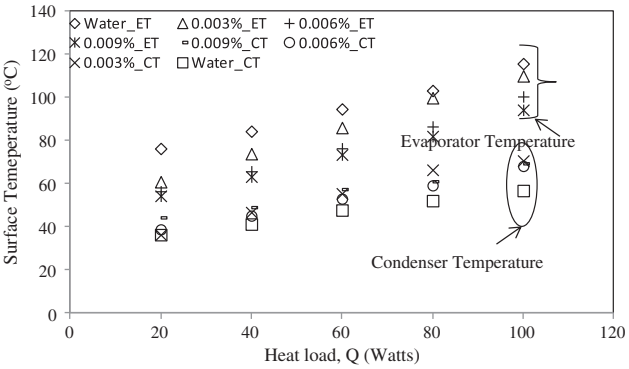

Fig. 7. Evaporator and condenser surface temperature as a function of heat load.

conductivity of silver nanoparticles. This reduces the vapour temperature inside the heat pipe. 19.5 °C temperature difference is observed in the evaporator for maximum concentration of the heat pipe when compared with DI water. Subsequent slight drop in vapour temperature is also observed in condenser section for a constant cooling water flow rate at constant inlet temperature. A slight drop of 1–2 °C is observed between evaporator and adiabatic chamber due to losses. The low vapour temperature for constant heat input indicates that an increment in the operating range of the heat load when compared with that of base fluid heat load.

The adiabatic vapour temperature as a function of heat load is shown in Fig. 6. It is observed from the figure that the adiabatic vapour temperature which is also called as operating temperature of heat pipe increases as heat load on the evaporator section increases and decreases as volume concentration of nanoparticles in base fluid increases. The reduction in this temperature indicates an effective heat transfer capability due to addition of additives in base fluid. 21.54% reduction is observed in case of heat pipe operating with 0.009 vol.% concentration. This increases the operating range of the heat pipe beyond 100 W which is the maximum heat load in the case of water based heat pipe. Similarly a reduction of 9.49% and 18.25% is observed respectively for 0.003 and 0.006 vol.% concentration when compared to heat pipe operating with water. The surface temperatures of evaporator and condenser with respect to various heat loads are shown in Fig. 7. The evaporator surface temperature increases with increment in heat load and decreases with increment in volume concentration of nanoparticles. This reduction in surface temperature enhances and aids faster cooling rate of the heat dissipating components. It is found that for the maximum volume concentration of 0.009%, the decrement in the evaporator surface temperature is 21 °C for input heat load of 60 W. Similarly the evaporator surface temperatures of heat pipes with volume concentration of 0.003% and 0.006% is reduced by 8.6 and 18.2 °C when compared to heat pipe with DI water. The lowering of the evaporator surface temperature with the increase in the volume concentration of nanoparticles permits the heat pipe with additional heat flow rate before reaching dry out condition. It is also found that the increase in volume concentration of nanoparticles in base fluid increases the condenser surface temperature due to effective heat rejection in condenser section.

The temperature difference between evaporator and condenser as a function of heat load is shown in Fig. 8. It is observed that the temperature difference between evaporator and condenser gradually decreases with respect to the increase in the concentration level of nano particles for a given heat load. It is found that for a constant temperature difference between evaporator and condenser the use of nanofluid allows the heat pipe to operate under larger heat loads. It is also seen that the temperature difference reduces by 72.57%, 56.39% and 42% respectively for 0.009, 0.006 and 0.003 vol.% of silver water nanofluid when compared to heat pipe operating with DI water. This reduction in temperature difference enhances an increment in heat transport capability of heat pipe. The reason for this is that the nanoparticles suspended in water forms a porous coating in the evaporator region. This increases the surface roughness and cause enhancement in the bubble formation, growth and collapse. The porous coating formed on the screen mesh wick eventually increases the evaporator heating surface and leads to high heat transfer. It also increases the pumping capability of the wick. Researchers like Kim et al. [24] and Yang et al. [16] indicated that the formation of coating layer by nanoparticles reduces the contact angle and increases the surface wettability and surface roughness. It is observed that the porous coating layer formed on the wick surface reduces the evaporator vapour temperature by increasing the evaporator heating surface. It also increases the wick capillary pumping ability and eventually induces liquid suction due to capillary wicking into the evaporator region, which enhances the maximum heat transport rate This eventually reduces the vapour temperature difference between evaporator and condenser.

The thermal resistances of the heat pipes are calculated based on the vapour temperatures to quantitatively evaluate the thermal performance of heat pipes using silver–water nanofluids. As shown in Fig. 9 the thermal resistances of heat pipes using both the base fluid and nanofluids are high at low heat loads as thick liquid film resides in the evaporator section. However the thermal resistance decreases rapidly as heat load increases. This reduction in thermal resistance of heat pipes using silver–water nanofluid is more when compared with that of the heat pipe operating with DI water. 40% reduction in thermal resistance is observed for 0.003 vol.% silver nanofluid when compared with that of DI water. It is also observed

Author's personal copy

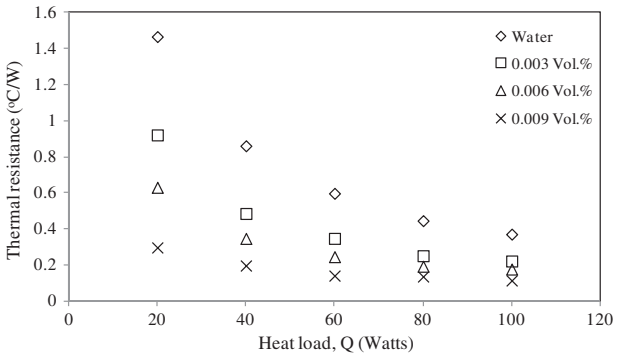

Fig. 9. Variation in thermal resistance as a function of heat load.

that this reduction in thermal resistance gradually increases as concentration of nanoparticles in base fluid increases. However for the maximum concentration of 0.009 vol.% of silver nanofluid, 76% reduction in thermal resistance is observed when compared with DI water. The thin porous coating layer formed by nanoparticles, not only improve the maximum heat transport rate but also significantly reduce the thermal resistance of the heat pipe using nanofluids is considered to be the main reason for the decrease in the thermal resistance of the heat pipe. Similar results have also been observed by Do et al. [14].

In order to check formation of the porous coating layer by addition of silver nanoparticles in the screen mesh wick surface of the evaporator region, a SEM image has been taken with the plain wick and the one with the addition of nanoparticles after conducting the experiments. The Fig. 10(a), shows the SEM image of the plain screen mesh wick surface without adding the nanoparticles. It is observed from the figure that the walls of the wick surface are found to be smooth and does have any pores or coating. However, the Fig. 10(b) shows the SEM image of the screen mesh wick surface with 0.009 vol.% of silver–water nanofluids. It clearly seen from the figure that there exists the porous coating layer which is formed by silver nanoparticles on the wick surface. This observation shows evidence for the formation of the thin porous coating layer at screen mesh wick of the evaporation region. The coating layer on the mesh wick surface provides an additional evaporating surface where high heat transfer rates occur. This drastically reduces the thermal resistance of the mesh wicked heat pipe and increases the capillary pumping ability to pull the liquid to the mesh wick surface. This leads to the enhancement in the heat transport rate of the of the heat pipe when using the silver–water nanofluid. The effective thermal conductivity of heat pipes with respect to various heat loads is shown in Fig. 11. It is clearly seen that the effective thermal conductivity of heat pipe increases with respect to heat load and concentration. The enhancement observed is 73.5% for 0.009 vol.% concentration of silver–water nanofluid. This concludes effective heat transfer is possible through the heat pipes employed with nanofluids. Similarly the heat pipes operating with 0.003 and 0.006 vol.% gives 42.4% and 56.8% increment in conductivity when compared with water based heat pipe.

The evaporation heat transfer coefficient as a function of heat flux is shown in Fig. 12. It is found that the evaporation heat transfer coefficients of heat pipe with silver–water nanofluid is higher when compared with that of the heat pipe with DI water for the same heat flux. The increment in nanoparticles volume concentration in base

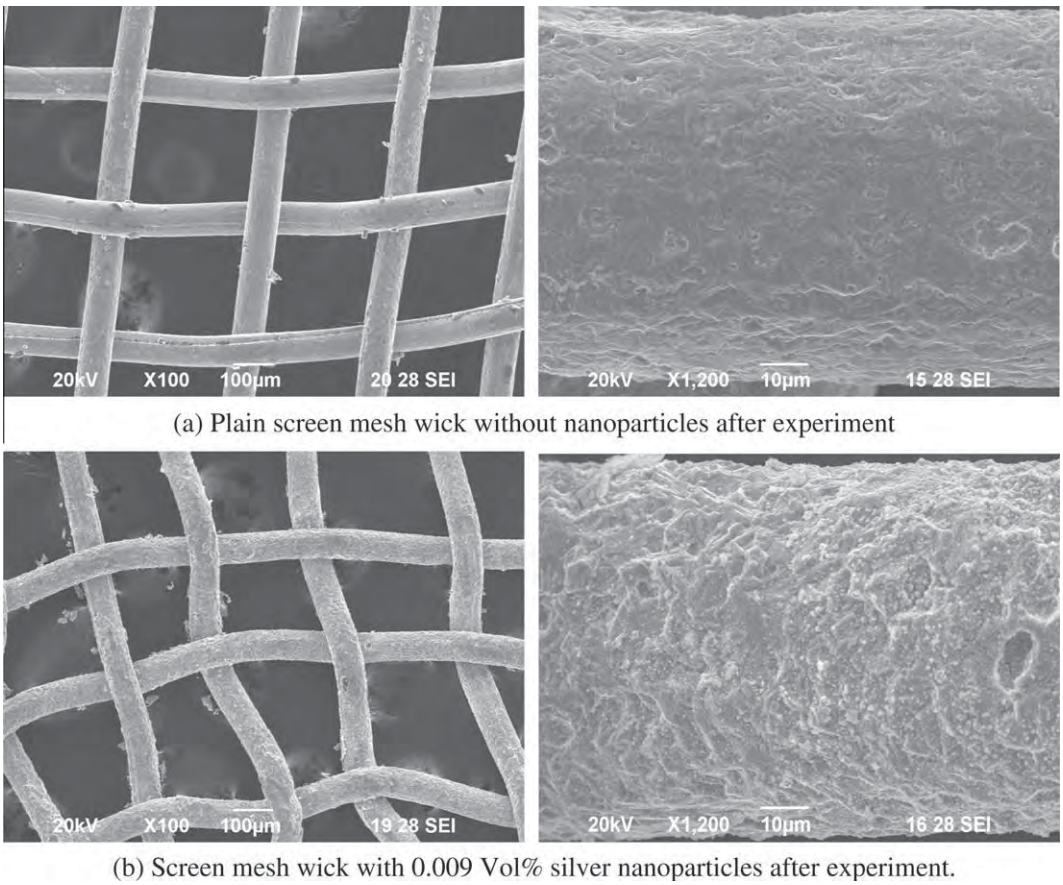

Fig. 10. SEM image of the screen mesh wick surface (a) plain screen mesh wick without nanoparticles after experiment; (b) Screen mesh wick with 0.009 vol.% silver nanoparticles after experiment.

Author's personal copy

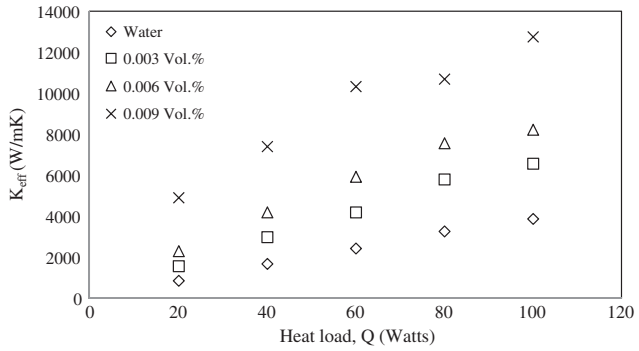

Fig. 11. Effective thermal conductivity of heat pipe as a function of heat load.

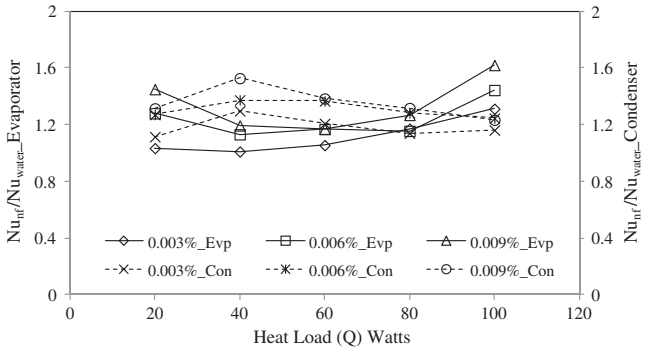

Fig. 13. Nusselt number ratio of evaporator and condenser as a function of heat load.

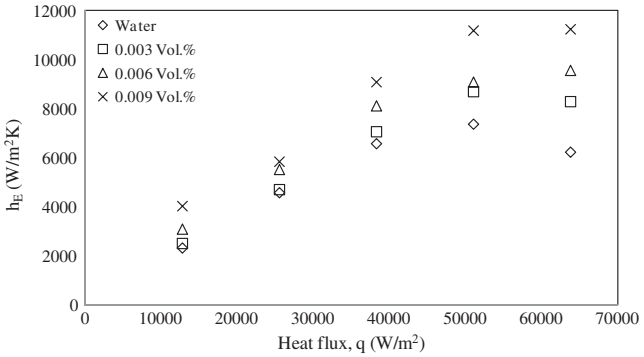

Fig. 12. Evaporation heat transfer coefficient with respect to the heat flux.

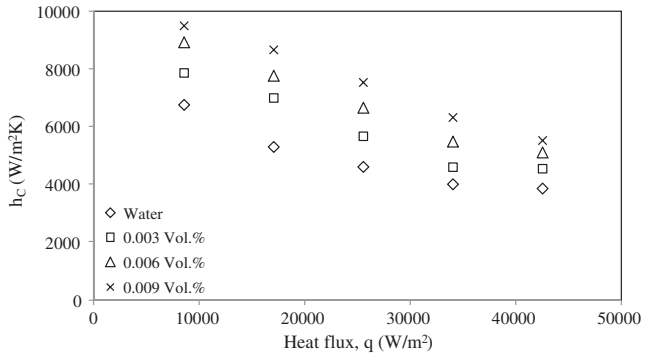

Fig. 14. Condensation heat transfer coefficient with respect to the heat flux.

fluid increases the evaporation heat transfer coefficient. For 0.009 vol.%, concentration an increment of 52.7% in evaporation heat transfer coefficient is observed experimentally when compared to heat pipe with DI water. It is mainly due to less temperature difference between the evaporator surface and vapour core. This concludes that the effective heat transfer is possible through heat pipes employed with nanofluids as working fluid. It is also found and clearly observed from Fig. 12 that the evaporation heat transfer coefficient of DI water based heat pipe decreases as the heat flux increases beyond 50 kW/m^2 due to reaching out of partial dry out condition. The reason for this is that the evaporator region is completely filled with vapour, since the optimum heat transport capacity of heat pipe is reached near 100 W; the heat pipe tends to move closer to the dry-out condition. Due to this partial dry out condition the temperature difference between evaporator surface and vapour increases and tends the heat transfer coefficient to decrease. However, for heat pipes with silver water nanofluid, the evaporation heat transfer coefficient still increases beyond the heat flux of 50 kW/m^2 because of higher heat transport capability employed with the presence of nanoparticles. From the observed results it is significantly seen that the presence of nanoparticles decreases the wall and the vapour temperatures which in turn increases the operating range of the pipe to higher heat flux when compared with that of the DI water.

The Nusselt number ratio of evaporator and condenser drawn respectively in the primary and secondary axis against heat load is shown in Fig. 13. It is observed that the Nusselt number ratio of both evaporator and condenser increases with the increase in the volume concentration of silver nanoparticles. At higher heat load the Nusselt number ratio for evaporator is found to be higher when compared with that of condenser Nusselt number ratio. As Nusselt number is a dimensionless parameter which depends on heat transfer coefficient, thermal conductivity of working fluid and characteristic length. It is found that at low heat load say for example (40 W) the Nusselt number ratio of condenser is more when compared with that of the evaporator. The reason is that the temperature difference (ΔT) between the wall surface and vapour core in the evaporator is high at low heat load and the temperature difference between the vapour core and the wall surface is less in the condenser section. This increases the heat transfer coefficient in the condenser which is directly proportional to the Nusselt number ratio at low heat loads and the inverse effect is found in the case of evaporator.

The condensation heat transfer coefficient as a function of heat flux is shown in Fig. 14. It is found that at low heat flux say for example (12 kW/m^2) the condensation heat transfer coefficient is more when compared with that of the evaporation heat transfer coefficient. The reason is that the temperature difference (ΔT) between the wall surface and vapour core in the evaporator is high at low heat flux and the temperature difference between the vapour core and the wall surface is less in the condenser section. Also the surface area of the condenser is more than the evaporator; since the length is 1.5 times the length of the evaporator section. As the heat flux increases the (ΔT) in evaporator decreases due to the formation of large number of small nucleation sites by the nanoparticle layer deposited on the heating surface. This eventually increases the evaporation heat transfer coefficient. However in condenser the (ΔT) increases with respect to heat flux, which results in a decrement in the condensation heat transfer coefficient. A similar trend of results has also been observed and reported in the published literature by Liu et al. [20]. Meantime, on an average the enhancement of the condensation heat transfer coefficient is also quite similar to that of the evaporation heat transfer coefficient for the same nanofluid. On the other hand, the condensation heat transfer coefficient curves has the similar trend for both water

Author's personal copy

and nanofluids at the present operating pressure, that describes actually a heat transfer characteristic of the convective condensation. The mode of heat transfer in evaporator and condenser is convective. The main reasons for the enhancement of heat transfer effect of nanofluid based heat pipes are:

1. The highly conductive nanoparticles in base fluid will increase the effective thermal conductivity of nanofluid.
2. During heat pipe operation, the working fluid travels through the porous wick and the nanoparticles present in it forms a coating layer on the wick and on the heating surface. This enhances the heat transfer effect of heat pipe.
3. The random motion (Brownian motion) of nanoparticles in base fluid causes the particles to collide with each other and with particles of DI water. This will enhance the heat transfer effect by convection. This Brownian motion is significant at higher temperatures.

4. Conclusion

The heat transfer performance of heat pipe using silver–water nanofluid with volume concentrations of 0.003%, 0.006% and 0.009% is experimentally investigated. It is clearly seen that by using silver–water nanofluid, the operating range of heat pipe increases beyond 100 W which is the maximum heat transport range for DI water based heat pipe. The dry out condition is observed near 106, 113 and 121 W respectively for 0.003, 0.006 and 0.009 vol.% concentrations. It is also observed that the thermal resistance of heat pipe decreases with the use of silver–water nanofluid, which in turn increases the effective thermal conductivity by 42.4%, 56.8% and 73.5% respectively for 0.003, 0.006, 0.009 vol.% concentrations. It is also observed that the evaporation and condensation heat transfer coefficients increases with the increases in the concentration of silver nanoparticles. Similarly, the difference between evaporator wall temperature and vapour temperature near a heat load of 60 W is observed to be 5.8, 5.4, 4.7 and 4.2 °C respectively for DI water, 0.003, 0.006 and 0.009 vol.% concentrations of the silver nanoparticles indicating the improved performance of heat pipes.

Acknowledgements

The authors would like to thank Mr. Seelan, Mr. P. Augustine and Mr. Jeyakumar of Karunya University for helping in the fabrication of the experimental test facility. The third author would like to thank the Thailand Research Fund for the supporting.

References

[1] Mariya Ivanova, Yvan Avenas, Christian Schaeffer, Jean-Bernard Dezord, Juergen Schulz-Harder, Heat pipe integrated in direct bonded copper (DBC) technology for cooling of power electronics packaging, IEEE Trans. Power Electron. 21 (6) (2006) 1541–1547.

[2] R. Sonan, S. Harmand, J. Pelle, D. Leger, M. Fakès, Transient thermal and hydrodynamic model of flat heat pipe for the cooling of electronics components, Int. J. Heat Mass Transfer 51 (25–26) (2008) 6006–6017.

[3] Maryam Shafai, Vincenzo Bianco, Kambiz Vafai, Oronzio Manca, An investigation of the thermal performance of cylindrical heat pipes using nanofluids, Int. J. Heat Mass Transfer 53 (2010) 376–383.

[4] S.U.S. Choi, Enhancing thermal conductivity of fluids with nanoparticles, ASME FED 231 (1995) 99–105.

[5] S. Kakac, A. Pramuanjaroenkij, Review of convective heat transfer enhancement with nanofluids, Int. J. Heat Mass Transfer 52 (2009) 3187–3196.

[6] Taehyun cho, Ilhyun Baek, Jonghee Lee, Sangdo Park, Preparation of nanofluids containing suspended silver particles for enhancing fluid thermal conductivity of fluids, J. Ind. Eng. Chem. 11 (3) (2005) 400–406.

[7] S.K. Das, N. Putra, P. Thiesen, W. Roetzel, Temperature dependence of thermal conductivity enhancement for nanofluids, J. Heat Transfer 125 (2003) 567–574.

[8] V.I. Terekhov, S.V. Kalinina, V.V. Lemanov, The mechanism of heat transfer in nanofluids, state of the art (review). Part 1. Synthesis and properties of nanofluids, Thermophys. Aeromech. 17 (1) (2010).

[9] S. Lee, S.U.S. Choi, S. Li, J.A. Eastman, Measuring thermal conductivity of fluids containing oxide nanoparticles, J. Heat Transfer 121 (1999) 280–289.

[10] Paisarn Naphon, Pichai Assadamongkol, Teerapong Borirak, Experimental investigation of titanium nanofluids on the heat pipe thermal efficiency, Int. Commun. Heat Mass Transfer 35 (10) (2008) 1316–1319.

[11] R.R. Riehl, Analysis of loop heat pipe behavior using nanofluid, in: Heat Powered Cycles International Conference (HPC), New Castle, UK, 2006, Paper: 06102.

[12] C.Y. Tsaia, H.T. Chiena, P.P. Dingb, B. Chanc, T.Y. Luhd, P.H. Chena, Effect of structural character of gold nanoparticles in nanofluid on heat pipe thermal performance, Mater. Lett. 58 (2004) 1461–1465, http://dx.doi.org/10.1016/j.matlet.2003.10.009.

[13] S. Kang, W. Wei, S. Tsai, C. Huang, Experimental investigation of nanofluids on sintered heat pipe thermal performance, Appl. Therm. Eng. 29 (5–6) (2009) 973–979.

[14] K. Do, H. Ha, S. Jang, Thermal resistance of screen mesh wick heat pipes using the water-based Al_2O_3 nanofluids, Int. J. Heat Mass Transfer 53 (25–26) (2010) 5888–5894.

[15] K.H. Do, S.P. Jang, Effect of nanofluids on the thermal performance of a flat micro heat pipe with a rectangular grooved wick, Int. J. Heat Mass Transfer 53 (9–10) (2010) 2183–2192.

[16] X.F. Yang, Z. Liu, J. Zhao, Heat transfer performance of a horizontal micro grooved heat pipe using CuO nanofluid, J. Micromech. Microeng. 18 (3) (2008) 035038.

[17] Guo-Shan Wang, Bin Song, Zhen-Hua Liu, Operation characteristics of cylindrical miniature grooved heat pipe using aqueous CuO nanofluids, Exp. Therm. Fluid Sci. 34 (8) (2010) 1415–1421.

[18] K.H. Park, W.H. Lee, K.W. Lee, I.H. Baek, S.H. Rhi, D.R. Shin, Study on the operating characteristics in small size heat pipe using nanofluids, in: Proceedings of the Third IASME/WSEAS International Conference on Heat Transfer, Thermal Engineering and Environment, Corfu Greece, August 20–25 (2005) pp. 106–109.

[19] Shung-Wen Kang, Wei-Chiang Wei, Sheng-Hong Tsai, Shih-Yu Yang, Experimental investigation of silver nanofluid on heat pipe thermal performance, Appl. Therm. Eng. 26 (17–18) (2006) 2377–2382.

[20] Zhen-Hua Liu, Yuan-Yang Li, Ran Bao, Compositive effect of nanoparticle parameter on thermal performance of cylindrical micro-grooved heat pipe using nanofluids, Int. J. Therm. Sci. 50 (2011) 558–568.

[21] Bock Choon Pak, I. Young Cho, Hydrodynamic and heat transfer study of dispersed fluids with sub-micron metallic oxide particles, Exp. Heat Transfer 11 (2) (1998) 151–170.

[22] Yimin Xuan, Wilfried Roetzel, Conceptions for heat transfer correlation of nanofluids, Int. J. Heat Mass Transfer 43 (19) (2000) 3701–3707.

[23] L. Godson, B. Raja, D. Mohan lal, S. Wongwises, Experimental investigation of thermal conductivity and viscosity of silver-deionized water nanofluid, Exp. Heat Transfer 23 (4) (2010) 317–332.

[24] H.D. Kim, J. Kim, M.H. Kim, Experimental studies on CHF characteristics of nanofluids at pool boiling, Int. J. Multiphase Flow 33 (2007) 691–706.

JOURNAL OF THERMOPHYSICS AND HEAT TRANSFER
Vol. 27, No. 1, January–March 2013

Entropy Generation Between Two Rotating Cylinders with Magnetohydrodynamic Flow Using Nanofluids

Omid Mahian*
Islamic Azad University, 91735 Mashhad, Iran
Shohel Mahmud†
University of Guelph, Guelph, Ontario N1G 2W1, Canada
and
Somchai Wongwises‡
King Mongkut's University of Technology Thonburi, Bangmod, Bangkok 10140, Thailand

DOI: 10.2514/1.T3908

Downloaded by UNIVERSITY OF WATERLOO on February 10, 2013 | http://arc.aiaa.org | DOI: 10.2514/1.T3908

The flow between two cylinders where one or both of the cylinders rotate has many practical applications such as swirl nozzles, rotating electrical machines, rotating disks, standard commercial rhymesters, and chemical and mechanical mixing equipment. In this paper, the effect of using TiO_2-water nanofluid ($\phi \leq 2\%$) on entropy generation between two corotating cylinders in the presence of magnetohydrodynamic flow is investigated. An analytical approach is applied to solve the simplified governing equations in the cylindrical coordinate system. To calculate the thermal conductivity and viscosity of the nanofluid, two correlations, which are based on the experimental data, are used. The velocity field is obtained as modified Bessel functions, and then, using the expansions of these Bessel functions with three terms, the temperature field and, subsequently, the entropy generation rate are estimated. The results are presented for various parameters, including the entropy generation number (N_S), Bejan number (Be), Hartmann number (M), Brinkman number (Br), and a group parameter ($\frac{\Omega}{Br}$). From the results, it is concluded that, at low Brinkman numbers (depending on the value of $\frac{\Omega}{Br_f}$), the average entropy generation number $(N_S)_{ave}$ decreases with the increase in nanoparticle volume fraction.

Nomenclature

Be	=	Bejan number
Br	=	Brinkman number
B_0	=	constant magnetic flux density
C_p	=	specific heat
E	=	electric field
Ec	=	Eckert number
J	=	electric current
k	=	thermal conductivity
M	=	Hartmann number
N_F	=	entropy generation number, fluid friction
N_H	=	entropy generation number, heat transfer
N_m	=	entropy generation number, magnetohydrodynamic flow
N_S	=	entropy generation number, total
$N_{S,a}$	=	augmentation entropy generation number
Pr	=	Prandtl number
Q	=	electric charge density
R	=	dimensionless radius
r	=	radius
$\dot{S}'''_{\text{gen}}$	=	entropy generation rate
T	=	temperature
u	=	peripheral velocity
$\boldsymbol{V}$	=	velocity vector
α	=	thermal diffusivity
Γn	=	constants of integration, $n = 1 \times$ to $\times$ 12
θ	=	dimensionless temperature
λ	=	velocity ratio
μ	=	dynamic viscosity
Π	=	radius ratio
ρ	=	density
ϕ	=	volume fraction of nanoparticles
Ω	=	dimensionless temperature difference
ω	=	angular velocity
$\forall$	=	volume

Subscripts

ave	=	average (overall value)
f	=	base fluid
nf	=	nanofluid
0	=	value at the inner cylinder
1	=	value at the outer cylinder

Received 27 February 2012; revision received 29 May 2012; accepted for publication 31 May 2012; published online 29 November 2012. Copyright © 2012 by the American Institute of Aeronautics and Astronautics, Inc. All rights reserved. Copies of this paper may be made for personal or internal use, on condition that the copier pay the $10.00 per-copy fee to the Copyright Clearance Center, Inc., 222 Rosewood Drive, Danvers, MA 01923; include the code 1533-6808/12 and $10.00 in correspondence with the CCC.

*Graduate Student, Young Researcher's Club, Mashhad Branch; omid.mahian@gmail.com (Corresponding Author).
†Assistant Professor, School of Engineering.
‡Professor, Fluid Mechanics, Thermal Engineering, and Multiphase Flow Research Laboratory (FUTURE), Department of Mechanical Engineering, Faculty of Engineering.

I. Introduction

IN THE last three decades, many studies have been conducted on the analysis of the second law of thermodynamics with the aim of entropy generation minimization to improve the performance of thermal engineering systems. Bejan [1,2] investigated the different effective factors behind entropy generation in heat transfer engineering, in which the destruction of useful energy (exergy) of a system occurs through entropy generation. Recently, Naterer and Camberos [3] presented past analytical methods of entropy generation minimization to numerical simulations involving more complex configurations and experimental measurement techniques. Of course, it should be noted that some researchers during the analysis of heat exchangers concluded that the minimum entropy generation is not always related to the optimal performance. Therefore, the parameter of heat exchanger effectiveness should be considered to examine the real performance of heat exchanges for avoiding the entropy generation paradox [4–7].

In recent years, various methods have been used to improve the performance of thermal engineering systems. One of these methods is using a nanofluid as the working fluid in heat transfer devices.

Downloaded by UNIVERSITY OF WATERLOO on February 10, 2013 | http://arc.aiaa.org | DOI: 10.2514/1.T3908

Nanofluid is the name given to a fluid in which nanometer-sized particles (1–100 nm) are suspended [8]. The enhancement of heat transfer using nanofluids is a relatively new field within the past decade. Currently, research groups worldwide are focusing on the properties of various nanofluids and their applications in different thermal engineering systems and devices [9]. For more recent studies on nanofluids, readers can refer to some research articles and review papers in which various models to calculate the thermophysical properties of nanofluids and their applications are reviewed [10–14]. Relatively little information is currently available on the effects of flow and heat transfer of nanofluids on entropy generation.

Here, the main studies concerning the second-law analysis of the flow and heat transfer of nanofluids are presented. Singh et al. [15] conducted an analytical analysis of entropy generation due to the flow and heat transfer of water-alumina nanofluids in different regimes within channels (with different sizes), including microchannels, minichannels, and conventional channels. Their results indicated that there is an optimum channel type in which entropy generation is minimized. They also found that using a water-alumina nanofluid with high viscosity in microchannels with laminar flow, as well as in minichannels and conventional channels with turbulent flow, is not beneficial. Li and Kleinstreuer [16] numerically investigated entropy generation due to the steady laminar flow of pure water and water-CuO nanofluids in trapezoidal microchannels. They determined that using nanofluids with very low particle loading reduces entropy generation at low Reynolds numbers. Feng and Kleinstreuer [17] considered the flow of an alumina-water nanofluid with heat transfer in a parallel disk system. They found that the total entropy generation rate decreases with an increase in the volume fraction of nanofluid.

Moghaddami et al. [18] analytically studied entropy generation due to water-Al_2O_3 and ethylene gylcol-Al_2O_3 nanofluid flow inside a circular pipe with constant heat flux for both laminar and turbulent regimes. Their results revealed that adding a volume fraction of nanofluids is effective only when irreversibility caused by heat transfer is dominant. Concerning the turbulent flow of water-Al_2O_3 nanofluid, they concluded that adding nanoparticles only for Reynolds numbers smaller than 40,000 decreases entropy generation, whereas for Reynolds numbers bigger than 80,000, entropy generation becomes higher in magnitude. Shahi et al. [19] studied numerically entropy generation due to the natural convection cooling of a heat source within a cavity filled by water-Cu nanofluid, in which the heat source can be mounted at different positions on the walls of the cavity. They investigated the effects of the Rayleigh number, nanoparticle concentration, and the position of the heat source on entropy generation. Esmaeilpour and Abdollahzadeh [20] investigated entropy generation numerically due to the natural convection of Cu-water nanofluids with a volume fraction from 0 to 10% inside a two-dimensional wavy enclosure. Their results showed that, with the addition of nanoparticles to a base fluid, the entropy generation rate decreases. Bianco et al. [21] presented a numerical analysis of the turbulent forced-convection flow of water-Al_2O_3 nanofluids inside a square tube with constant and uniform wall heat flux. They determined analytically the optimum Reynolds number at which entropy production becomes smallest. Recently, Falahat and Vosough [22] investigated entropy generation through a coiled tube heat exchanger with uniform wall heat flux conditions in both laminar and turbulent regimes using water-Al_2O_3 nanofluid. They obtained the optimum conditions based on the entropy generation sense for both laminar and turbulent regimes.

A review of the literature shows that there is no analytical report concerning the effect of using nanofluids on entropy generation between two concentric rotating cylinders in the presence of magnetohydrodynamic (MHD) flow. The flow between two cylinders where one or both of the cylinders rotate has many practical applications, such as swirl nozzles, rotating electrical machines, rotating disks, standard commercial rhymesters, and chemical and mechanical mixing equipment. In addition, the flow and heat transfer in annuli, where the outer cylinder rotates and the inner one is stationary, is an important research subject in many engineering applications, such as in the petroleum, food, and automobile industries [23,24].

Yilbas [23] conducted an entropy generation analysis for a rotating outer cylinder and differentially heated isothermal boundary condition assuming a linear velocity distribution in the annuli. Mahmud and Fraser [24,25] investigated entropy generation inside the cylindrical annular space with different boundary conditions. They simplified and solved governing equations in cylindrical coordinates to obtain analytical expressions for dimensionless entropy generation and the Bejan number as a function of the parameters involved in the problem. In another work, Mirzazadeh et al. [26] focused on entropy generation induced by the flow of a nonlinear viscoelastic fluid between concentric rotating cylinders.

Using an external magnetic field is of significant importance in many industrial applications, particularly as a control mechanism in material manufacturing [27]. In addition, the study of flow and heat transfer in a closed cavity or a channel in the presence of a magnetic field is important because of engineering applications such as the cooling of nuclear reactors, MHD micropumps, electronic packages, and microelectronic devices. In the past decade, the study of MHD flow and its effect on entropy generation in related systems has received extensive attention because of its importance in industry, as mentioned previously. Some works that investigated the effect of MHD flow on entropy generation for various flows and geometries are mentioned.

Salas et al. [28] analyzed the second law for MHD induction devices such as electromagnetic pumps and electrical generators. Ibanez et al. [29] optimized the operation conditions for an alternate MHD generator based on the global entropy generation rate. Mahmud et al. [30] studied the effect of a transverse magnetic field on entropy generation inside a vertical channel made of two parallel plates by considering mixed convection inside the channel. Later, Tasnim et al. [31] considered the same problem for porous media. Mahmud and Fraser [32] investigated the second law analytically for a mixed convection–radiation interaction in a vertical porous channel in the presence of MHD flow. Mahmud and Fraser [33] examined the problem of entropy generation in a fluid-saturated porous cavity for laminar natural convection heat transfer where the magnetic field is assumed to act along the direction of the force of gravity.

Ibanez and Cuevas [34] applied the approach of entropy generation minimization by considering joule dissipation, heat conduction, and viscosity to optimize the MHD flow between two infinite parallel walls with limited electrical conductivity. Mahmud and Fraser [35] presented a general relation for entropy generation for a single-plate thermoacoustic system that was exposed to a transverse magnetic field. Ibanez and Cuevas [36] considered a stationary buoyant MHD flow of a liquid metal immersed in a magnetic field through a vertical rectangular duct with thin conducting or insulating walls.

Arikoglu et al. [37] investigated the effect of slip and joule dissipation on entropy generation in a single rotating disk in the presence of MHD flow by a seminumerical analytical solution method, in which the magnetic field is constant and acts only in the axial direction. In addition, the effect of a magnetic field on entropy generation in a microchannel was investigated by Ibanez and Cuevas [38].

As mentioned, the aim of this study is to investigate the effect of using nanofluids on entropy generation between two rotating cylinders in the presence of MHD flow. The governing equations in cylindrical coordinates are simplified and analytically solved using isothermal boundary conditions to obtain the average entropy generation in the annulus.

II. Description of the Problem

The geometry of the cylindrical annulus considered is indicated in Fig. 1. A Newtonian nanofluid fills the gap between the inner and outer cylinders, which are of radii r_0 and r_1 and with constant surface temperatures of T_0 and T_1, respectively. The inner and outer cylinders can rotate with constant angular velocities of ω_0 and ω_1, respectively. A magnetic field (B_0) constantly acts in parallel to the axial direction

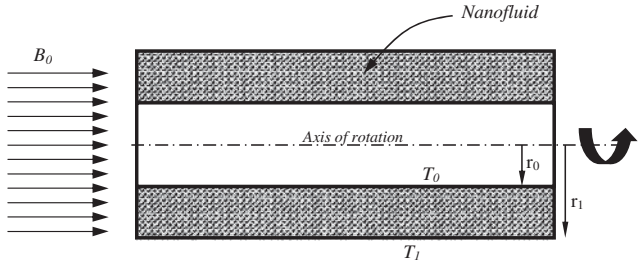

Fig. 1 Schematic diagram of the problem under consideration.

of the cylinders while the flow between the cylinders is laminar and steady.

It is assumed that the fluid and nanoparticles are in thermal equilibrium and that no slip occurs between them. It should be remarked that, in practical situations, most nanofluids used for enhancement of heat transfer are made up of very fine particles, normally less than 40 nm. Hence, the nanofluids can be considered to behave like a conventional, homogeneous, single-phase fluid [39]. Also, the thermophysical properties of the nanofluid are assumed to be constant. In the present work, TiO_2-water nanofluid is considered in the analysis.

III. Problem Formulation and Analysis

A. First Law Analysis

With the assumption of no relative axial motion between the cylinders and ignoring the radial velocity component compared to the tangential one, the momentum equation in cylindrical coordinates is simplified as follows:

$$\left(\frac{\partial^2 u_\theta}{\partial r2}+\frac{1}{r}\frac{\partial u_\theta}{\partial r}-\frac{u_\theta}{r^2}\right)-\frac{\sigma B_0^2}{\mu_{\rm nf}}u_\theta=0 \tag{1}$$

where u_θ is the tangential velocity component and σ is the fluid's electrical conductivity. The energy equation disregarding the convection term becomes (see Jiji [40] for details)

$$\frac{k_{\rm nf}}{r}\frac{\partial}{\partial r}\left(r\frac{\partial T}{\partial r}\right)=-\mu_{\rm nf}\left(\frac{\partial u_\theta}{\partial r}-\frac{u_\theta}{r}\right)^2 \tag{2}$$

The boundary conditions for the momentum and energy equations are as follows:

$$\begin{aligned} &r=r_0\colon\ u_\theta=u_0=r_0\omega_0 \quad \text{and} \quad T=T_0\\ &r=r_1\colon\ u_\theta=u_1=r_1\omega_1 \quad \text{and} \quad T=T_1 \end{aligned} \tag{3}$$

To calculate the thermal conductivity ($k_{\rm nf}$) and viscosity ($\mu_{\rm nf}$) of the nanofluid, the Duangthongsuk and Wongwises equations [41], which are based on experimental results, are considered as follows:

$$\frac{k_{\rm nf}}{k_f}=1.0204+0.0249\phi \tag{4}$$

$$\frac{\mu_{\rm nf}}{\mu_f}=1.013+0.092\phi-0.015\phi^2 \tag{5}$$

In the previous relation, ϕ is the volume fraction of nanoparticles, and k_f and μ_f are the thermal conductivity and viscosity of the base fluid, respectively. It should be stated that Eqs. (4) and (5) are valid for 0.2–2 vol % of TiO_2-water nanofluid. These relations are obtained for 25° C, but in this work, the properties of nanofluids are assumed to be independent of temperature.

Using the following dimensionless parameters and considering the outer cylinder as the reference,

$$\begin{aligned} &R=\frac{r}{r_1},\quad U=\frac{u_\theta}{r_1\omega_1},\quad \theta=\frac{T-T_1}{T_0-T_1},\quad \Pi=\frac{r_0}{r_1},\\ &\lambda=\frac{\omega_0}{\omega_1}\quad Pr_f=\frac{\mu_f C_{p,f}}{k_f},\quad Ec_f=\frac{(r_1\omega_1)^2}{C_{p,f}\Delta T},\quad M^2=\frac{\sigma B_0^2}{\mu_f}r_1^2 \end{aligned} \tag{6}$$

The governing equations in dimensionless form can be expressed as follows: Momentum equation:

$$\begin{aligned} &R^2\frac{\partial^2 U}{\partial R^2}+R\frac{\partial U}{\partial R}-\left[1+\left(\frac{\mu_f}{\mu_{\rm nf}}\right)M^2R^2\right]U=0 R=\Pi\colon\ U=\Pi\lambda\\ &R=1\colon\ U=1 \end{aligned} \tag{7}$$

Energy equation:

$$\begin{aligned} &\frac{1}{R}\frac{\partial}{\partial R}\left(R\frac{\partial\theta}{\partial R}\right)=-Ec_f Pr_f\left(\frac{\mu_{\rm nf}}{\mu_f}\right)\left(\frac{k_f}{k_{\rm nf}}\right)\left(\frac{\partial U}{\partial R}-\frac{U}{R}\right)^2\quad R=\Pi\colon\ \theta=1\\ &R=1\colon\ \theta=0 \end{aligned} \tag{8}$$

where M is the Hartmann number, Ec_f is the Eckert number, and Pr_f is the Prandtl number. By noting that the multiplication of $(\mu_f/\mu_{\rm nf})$ by M^2 is a positive quantity, and then by considering $H^2=(\mu_f/\mu_{\rm nf})M^2$, the solution of the momentum equation is obtained as follows:

$$U(R)=\Gamma_1 I_1(HR)+\Gamma_2 K_1(HR) \tag{9}$$

where $I_1(HR)$ is known as the modified Bessel function of the first kind, of order 1, and $K_1(HR)$ as the modified Bessel function of the second kind, of order 1. The constants of integration Γ_1 and Γ_2 can be calculated while applying the boundary conditions; therefore, the constants are obtained as follows:

$$\begin{aligned} \Gamma_1&=\frac{\Pi\lambda K_1(H)-K_1(H\Pi)}{I_1(H\Pi)K_1(H)-K_1(H\Pi)I_1(H)}\\ \Gamma_2&=\frac{\Pi\lambda I_1(H)-I_1(H\Pi)}{K_1(H\Pi)I_1(H)-I_1(H\Pi)K_1(H)} \end{aligned} \tag{10}$$

To find the temperature field from Eq. (8), the expansions of the Bessel functions $I_1(HR)$ and $K_1(HR)$, with three terms, are used as follows:

$$\begin{aligned} I_1(HR)&\cong\frac{1}{2}HR+\frac{(HR)^3}{16}+\frac{(HR)^5}{384}\\ K_1(HR)&\cong\frac{1}{HR}+\left[\frac{1}{2}\ln\left(\frac{HR}{2}\right)-\frac{1}{4}(-2\gamma+1)\right](HR)\\ &\quad+\left[\frac{1}{16}\ln\left(\frac{HR}{2}\right)-\frac{1}{32}\left(\frac{5}{2}-2\gamma\right)\right](HR)^3 \end{aligned} \tag{11}$$

in which

$$\gamma\approx 0.57722\ldots$$

By substituting the values of $I_1(HR)$ and $K_1(HR)$ for the expansions in the velocity distribution equation [Eq. (9)], and using the new velocity distribution in Eq. (8), the temperature gradient that is required in the entropy generation analysis is given as follows:

Downloaded by UNIVERSITY OF WATERLOO on February 10, 2013 | http://arc.aiaa.org | DOI: 10.2514/1.T3908

$$\frac{\partial\theta}{\partial R}=\frac{\Gamma_3}{R}+\left(\frac{\mu_{\rm nf}}{\mu_f}\right)\left(\frac{k_f}{k_{\rm nf}}\right)\frac{Br_f}{R}\times\left[\begin{array}{l}2\Gamma_2^2\ \ln\left(\frac{HR}{2}\right)+\frac{2\Gamma_2^2}{H^2R^2}+\Gamma_5(HR)^6\ \ln\left(\frac{HR}{2}\right)\\+\Gamma_6(HR)^6-\frac{1}{384}\Gamma_2^2(HR)^6\left[\ln\left(\frac{HR}{2}\right)\right]^2\\+\Gamma_7(HR)^2+\Gamma_8(HR)^4-\frac{1}{32}\Gamma_2^2(HR)^4\ \ln\left(\frac{HR}{2}\right)\\+\Gamma_9(HR)^8-\frac{1}{3072}\Gamma_1\Gamma_2(HR)^8\ \ln\left(\frac{HR}{2}\right)-\frac{1}{92{,}160}(HR)^{10}\Gamma_1^2\end{array}\right]\tag{12}$$

In this equation, Br_f is the Brinkman number that is the multiplication of Ec_f by Pr_f. Also, Γ_3 is the constant of integration and the constants Γ_5 to Γ_9 are in terms of Γ_1, Γ_2, and γ as follows:

$$\begin{aligned}\Gamma_5&=\frac{11}{2304}\Gamma_2^2-\frac{1}{192}\Gamma_1\Gamma_2-\frac{1}{192}\Gamma_2^2\gamma\\\Gamma_6&=\frac{11}{2304}\Gamma_2^2\gamma+\frac{7}{2304}\Gamma_1\Gamma_2-\frac{1}{384}\Gamma_2^2\gamma^2-\frac{1}{384}\Gamma_1^2\\&\quad-\frac{125}{55,296}\Gamma_2^2-\frac{1}{192}\Gamma_1\Gamma_2\gamma\\\Gamma_7&=\frac{1}{4}\Gamma_2^2\gamma-\frac{7}{16}\Gamma_2^2+\frac{1}{4}\Gamma_1\Gamma_2\\\Gamma_8&=\frac{1}{32}\Gamma_2^2-\frac{1}{32}\Gamma_2^2\gamma-\frac{1}{48}\Gamma_1\Gamma_2\\\Gamma_9&=\frac{7}{24,576}\Gamma_1\Gamma_2-\frac{1}{3072}\Gamma_1\Gamma_2\gamma-\frac{1}{3072}\Gamma_1^2\end{aligned}$$

Therefore, the temperature field is given by integrating Eq. (12) as follows:

$$\theta=\Gamma_4+\Gamma_3\ \ln(R)\quad+\left(\frac{\mu_{\rm nf}}{\mu_f}\right)\left(\frac{k_f}{k_{\rm nf}}\right)Br_f\left\{\begin{array}{l}\Gamma_{10}(HR)^6+\Gamma_{11}(HR)^8+\Gamma_{12}(HR)^4+\frac{1}{2}\Gamma_7(HR)^2-\frac{1}{921{,}600}\Gamma_1^2(HR)^{10}\\+\Gamma_2^2\left[\ln\left(\frac{HR}{2}\right)\right]^2-\frac{\Gamma_2^2}{(HR)^2}+\frac{1}{6}\Gamma_5\ \ln\left(\frac{HR}{2}\right)(HR)^6-\frac{1}{2304}\Gamma_2^2\left[\ln\left(\frac{HR}{2}\right)\right]^2(HR)^6\\+\frac{1}{6912}\Gamma_2^2\ \ln\left(\frac{HR}{2}\right)(HR)^6-\frac{1}{128}\Gamma_2^2\ \ln\left(\frac{HR}{2}\right)(HR)^4-\frac{1}{24{,}576}\Gamma_1\Gamma_2\ \ln\left(\frac{HR}{2}\right)(HR)^8\end{array}\right\}\tag{13}$$

The constants of integration Γ_3 and Γ_4 will be readily obtained using isothermal boundary conditions. To conserve space, the expressions for Γ_3 and Γ_4 are not presented here due to length constraints. Constants Γ_{10}, Γ_{11}, and Γ_{12} are given as follows:

$$\Gamma_{10}=-\frac{1}{36}\Gamma_5+\frac{1}{6}\Gamma_6-\frac{1}{41,472}\Gamma_2^2\quad\Gamma_{11}=\frac{1}{8}\Gamma_9+\frac{1}{196,608}\Gamma_1\Gamma_2$$
$$\Gamma_{12}=\frac{1}{4}\Gamma_8+\frac{1}{512}\Gamma_2^2$$

B. Entropy Generation Analysis

In the presence of a magnetic field, the local volumetric entropy generation rate can be expressed as follows (see [37] with a similar analysis):

$$\dot{S}'''_{\rm gen}=\frac{k_{\rm nf}}{T_1^2}[\nabla T]^2+\frac{\mu_{\rm nf}}{T_1}\phi+\frac{1}{T_1}[(J-QV)(E+V\times B)]\tag{14}$$

where

$$J=\sigma(E+V\times B)\tag{15}$$

In Eq. (14), ϕ is viscous dissipation, J is the electric current, Q is the electric charge density, V is the velocity vector, E is the electric field, and B is the magnetic induction. Assuming that QV is negligible compared with J, and disregarding E in comparison with $V\times B$, the entropy production rate [Eq. (14)] decreases in this case to

$$\dot{S}'''_{\rm gen}=\frac{k_{\rm nf}}{T_1^2}\left(\frac{\partial T}{\partial r}\right)^2+\frac{\mu_{\rm nf}}{T_1}\left[r\frac{\partial}{\partial r}\left(\frac{u}{r}\right)\right]^2+\frac{\sigma B_0^2}{T_1}u^2\tag{16}$$

Equation (16) shows that entropy generation is due to three effects: a conductive effect ($k_{\rm nf}$), a viscous effect ($\mu_{\rm nf}$), and a magnetic effect (B_0). Defining N_S as the entropy generation number, the dimensionless form of Eq. (16) can be expressed as follows:

$$\begin{aligned}N_S&=\frac{\dot{S}'''_{\rm gen}}{\left(\frac{\mu_{\rm nf}\omega_1^2}{T_1}\right)}=\frac{\Omega}{Br_f}\left(\frac{k_{\rm nf}}{k_f}\right)\left(\frac{\mu_f}{\mu_{\rm nf}}\right)\left(\frac{\partial\theta}{\partial R}\right)^2+\left(R\frac{\partial}{\partial R}\left(\frac{U}{R}\right)\right)^2+H^2U^2\\&=N_H+N_F+N_M\end{aligned}\tag{17}$$

where Ω is the dimensionless temperature difference, which equals $\Delta T/T_1$. On the right side of Eq. (17), the first term ($=N_H$) is the local entropy generation due to heat transfer irreversibility, the second term ($=N_F$) is the local entropy generation due to fluid friction irreversibility, and the last term ($=N_M$) is the local entropy generation due to the magnetic field. To calculate the entropy generation number N_S in Eq. (17), the terms N_F and N_M are determined directly by using Eq. (9) without any approximation, unlike the term N_H, in which the temperature gradient is obtained using approximation.

To evaluate the irreversibility distribution, the parameter Be (Bejan number), which is the ratio of entropy generation due to heat transfer to the overall entropy generation [42], is defined as follows:

$$Be=\frac{N_H}{N_H+N_F+N_M}\tag{18}$$

The Bejan number varies from 0 to 1. Subsequently, $Be=0$ reveals that the irreversibility due to fluid friction and magnetic field dominates, whereas $Be=1$ indicates that the irreversibility due to heat transfer is dominant. It is obvious that $Be=0.5$ is the case in which the irreversibility due to heat transfer is equal to fluid friction and magnetic field contributions in the entropy production.

The volumetric averaged entropy generation rate, $(N_S)_{\rm ave}$, can be obtained using Eq. (17) as follows:

$$(N_S)_{\rm ave}=\frac{1}{\forall}\int_{\forall}N_S\,{\rm d}\forall=\frac{2}{(1-\Pi^2)}\int N_SR\,{\rm d}R\tag{19}$$

or

$$(N_S)_{\rm ave}=\frac{2}{(1-\Pi^2)}\int(N_H+N_F+N_M)R\,{\rm d}R\tag{20}$$

From this relation, it is possible to evaluate the contributions of heat transfer, fluid friction, and the magnetic field in the averaged entropy

Downloaded by UNIVERSITY OF WATERLOO on February 10, 2013 | http://arc.aiaa.org | DOI: 10.2514/1.T3908

Downloaded by UNIVERSITY OF WATERLOO on February 10, 2013 | http://arc.aiaa.org | DOI: 10.2514/1.T3908

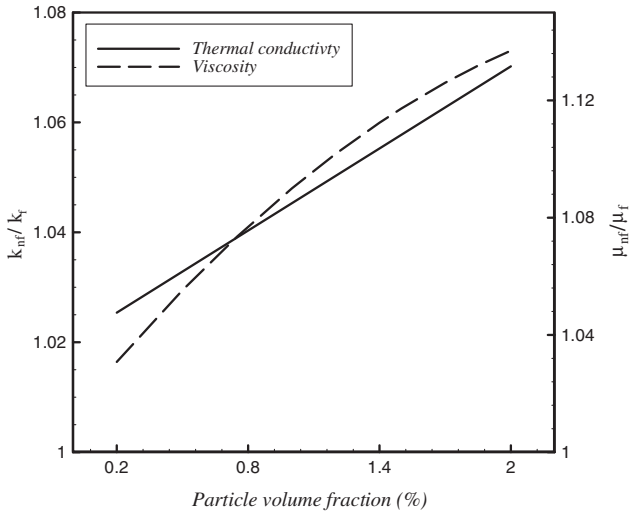

Fig. 2 Variations of the thermal conductivity and viscosity ratios with particle volume fraction.

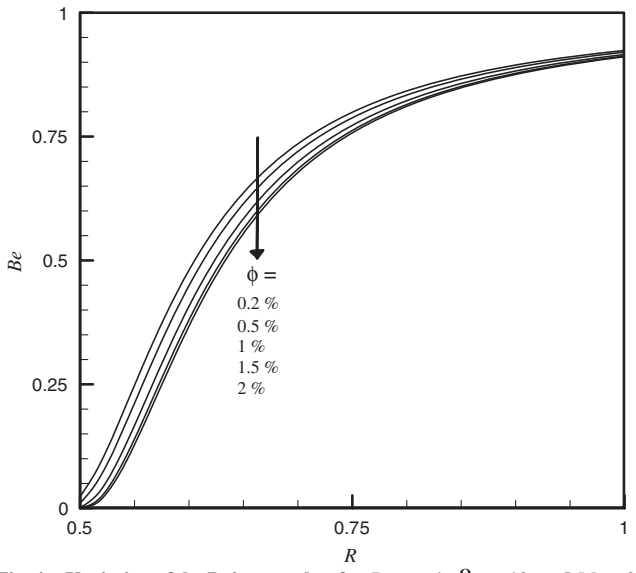

Fig. 4 Variation of the Bejan number for $Br_f = 1, \frac{\Omega}{Br_f} = 10$, and $M = 0$ at different nanoparticle volume fractions.

generation. It should be noted that, in practical applications, the inner cylinder is assumed at rest, and therefore the velocity ratio ($\lambda = \frac{\omega_0}{\omega_1}$) becomes zero. It is also assumed that the radius ratio ($\Pi = \frac{r_0}{r_1}$) is equal to 0.5.

IV. Results and Discussion

Figure 2 shows the variations of the thermal conductivity ratio ($\frac{k_{nf}}{k_f}$) and the viscosity ratio ($\frac{\mu_{nf}}{\mu_f}$) of the nanofluid with the particle volume fraction for TiO_2-water nanofluid. It was observed that, as the particle volume fraction increased up to 2 vol %, the thermal conductivity and viscosity increased by ~7 and ~14%, respectively.

The variation of the entropy generation number (N_S) with radial distance (R) is shown in Fig. 3 for $Br_f = 1$, $\frac{\Omega}{Br_f} = 10$, $M = 0$, and volume fraction (ϕ) from 0.2 to 2%. The figure reveals that the temperature and velocity gradients are highest on the inner cylinder, whereas the minimum gradients occur on the outer cylinder. As shown, with the increase in volume fraction, the entropy generation number falls in the gap due to the decreasing temperature gradients in the annulus. In this case, the temperature gradients decrease, because with an increase in the volume fraction the effective thermal conductivity increases. Consequently, the thermal conductance in the gap enhances, and the irreversibility due to heat transfer decreases. It also is seen that the decreasing tendency in the entropy generation number is more obvious between $\phi = 0.5\%$ to $\phi = 1\%$ compared with $\phi = 1.5\%$ to $\phi = 2\%$. This is because the effects of viscosity and fluid friction are higher at high volume fractions than at low volume fractions; therefore, the decreases in entropy generation decrease.

The variation of the Bejan number with radial distance is displayed in Fig. 4 for the same conditions of Fig. 3. As shown in Fig. 4, the Bejan number falls in the annulus in response to an increase in the particle volume fraction. This phenomenon can be described by considering the definition of the Bejan number in Eq. (18). When the particle volume fraction increases, the effective viscosity in the annulus increases; hence, the irreversibility due to fluid friction (N_F) increases. Thus, Be decreases with an increase in N_F, because N_F is in the denominator of Eq. (18). On the other hand, increasing the volume fraction leads to the increase of effective thermal conductivity; hence, the irreversibility due to heat transfer (N_H) decreases. Therefore, the Bejan number decreases due to the increase in nanoparticle loading, and the Bejan number is maximized on the

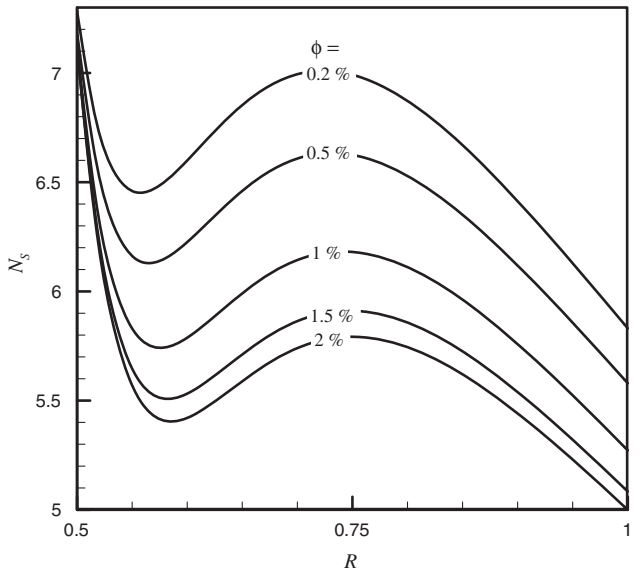

Fig. 3 Variation of the entropy generation number for $Br_f = 1$, $\frac{\Omega}{Br_f} = 10$, and $M = 0$ at different nanoparticle volume fractions.

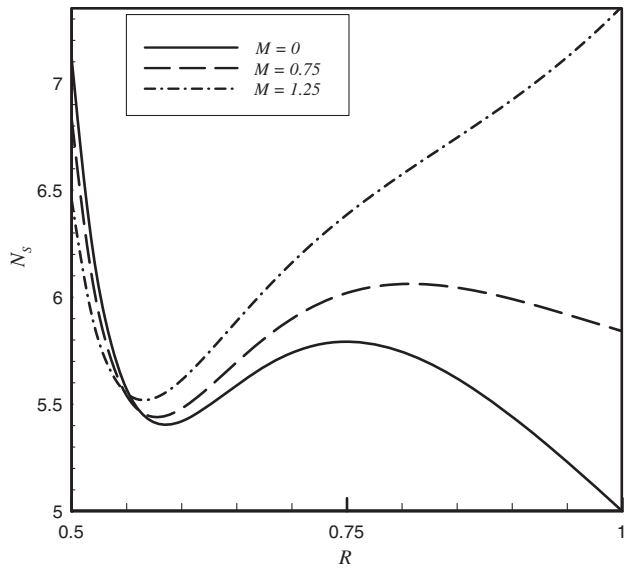

Fig. 5 Variation of the entropy generation number for $Br_f = 1$, $\frac{\Omega}{Br_f} = 10$, $\phi = 2\%$, and different values of the Hartmann number.

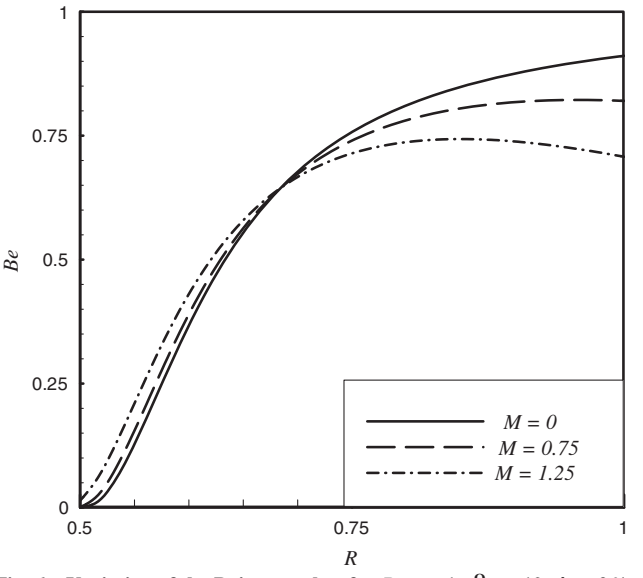

Fig. 6 Variation of the Bejan number for $Br_f = 1$, $\frac{\Omega}{Br_f} = 10$, $\phi = 2\%$, and different values of the Hartmann number.

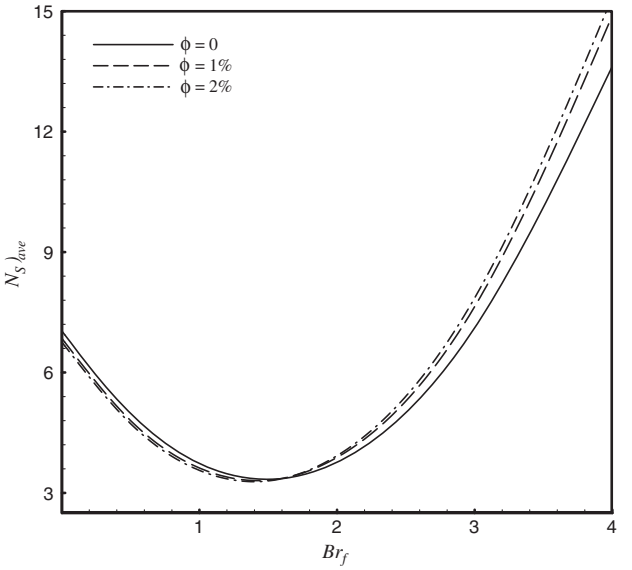

Fig. 8 Effect of nanoparticle loading on the average entropy generation number at different Brinkman numbers for $\frac{\Omega}{Br_f} = 1$.

outer cylinder. This indicates that in regions near the outer cylinder, the contribution of heat transfer to entropy generation is greater than in other regions.

The variation of the entropy generation number with radial distance is indicated in Fig. 5 for $Br_f = 1$, $\frac{\Omega}{Br_f} = 10$, $\phi = 2\%$, and three different values of the Hartmann number. It was found that the entropy generation number in the vicinity of the inner cylinder decreased a little with an increase in the Hartmann number from 0 to 1.25, whereas, with movement toward the outer cylinder, the entropy generation number increased with the increasing intensity of the magnetic field. In other words, as the Hartmann number increases, the gradients near the outer cylinder increase. In this case, an enhanced magnetic field leads to a decrease in the fluid velocity, and consequently, the boundary layer thickness in the annulus decreases. This leads to the increases in the velocity gradients.

Figure 6 shows the variation of the Bejan number with radial distance for the same conditions of Fig. 5. It was observed that an increase in the Hartmann number decreased the contribution of heat transfer in entropy generation near the outer cylinder; thus, Be decreased. In addition, it was found that because high values of shear stresses and high viscous dissipations are dominant near the inner cylinder, the Bejan number tends toward zero.

In this section, the effect of different parameters on average entropy generation is investigated. The effect of particle loading on the average entropy generation number at different Brinkman numbers from 0.001 to 4 is illustrated in Fig. 7 for $\frac{\Omega}{Br_f} = 0.1$ and $M = 1$. For $Br_f \leq 2.7$, the average entropy generation number decreased with an increase in ϕ; for $Br_f > 2.7$, $(N_S)_{\text{ave}}$ increases with the nanoparticle loading. The Brinkman number determines the relative significance between dissipation effects and fluid conduction effects (see White [43]). At high Brinkman numbers, the dissipation effects dominate conduction effects; hence, an increase in particle volume fraction is more effective in the irreversibility due to fluid friction, and consequently the average entropy generation increases. It also is shown that there is an optimum Brinkman number at which the average entropy generation is minimized. This optimum point can be obtained readily by the following relation:

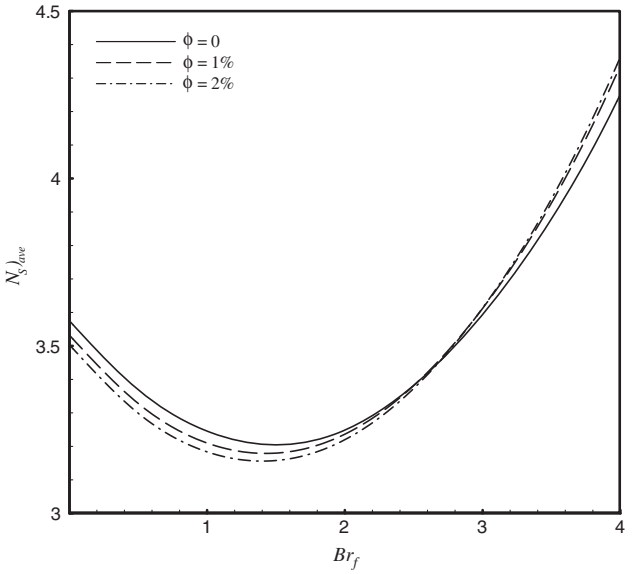

Fig. 7 Effect of nanoparticle loading on the average entropy generation number at different Brinkman numbers for $\frac{\Omega}{Br_f} = 0.1$.

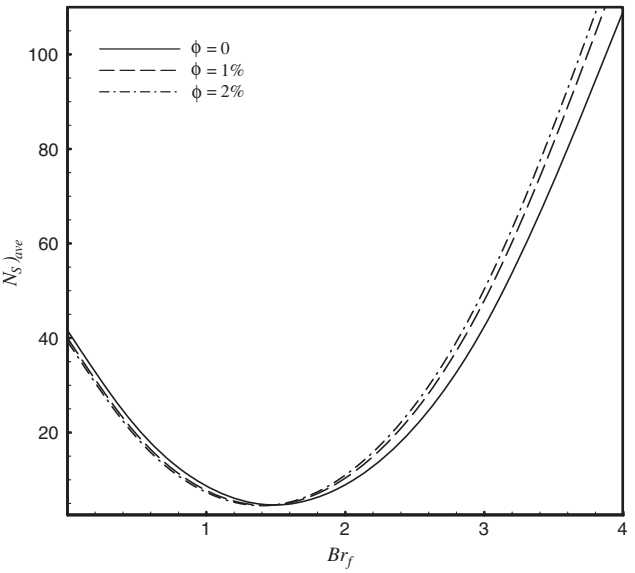

Fig. 9 Effect of nanoparticle loading on the average entropy generation number at different Brinkman numbers for $\frac{\Omega}{Br_f} = 10$.

Downloaded by UNIVERSITY OF WATERLOO on February 10, 2013 | http://arc.aiaa.org | DOI: 10.2514/1.T3908

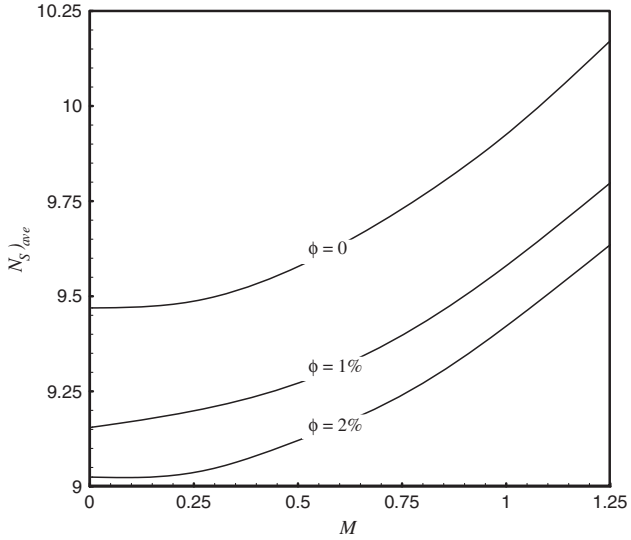

Fig. 10 Variation of the average entropy generation number with the Hartmann number for $Br_f = 0.1$ and $\frac{\Omega}{Br_f} = 2$.

$$\frac{(\partial N_S)_{\text{ave}}}{\partial Br_f} = 0 \quad \text{or} \quad \frac{\partial(\int_{0.5}^{1} N_S R\, \mathrm{d}R)}{\partial Br_f} = 0 \tag{21}$$

The optimum Brinkman number is approximately equal to 1.5.

Figures 8 and 9 present the variation of $(N_S)_{\text{ave}}$ with the Brinkman number for $M = 1$, $\frac{\Omega}{Br_f} = 1$, and $\frac{\Omega}{Br_f} = 10$. In these two cases, as in the previous case, the optimum Brinkman number at which entropy generation is minimized is approximately 1.5. However, unlike the previous case, the range of the Brinkman number at which increasing ϕ results in decreasing$(N_S)_{\text{ave}}$ decreases from 2.7 to 1.5. With increasing $\frac{\Omega}{Br_f}$, the average entropy generation increases, as expected.

The results of Figs. 7–9 have significance for industrial applications as follows. When the Brinkman number is small and the outer cylinder rotates at low speed, the addition of nanoparticles leads to a reduction in entropy generation of the system. By contrast, the addition of nanoparticles is not recommended when the outer cylinder rotates at high speeds.

The variation of the average entropy generation number with the Hartmann number is presented in Fig. 10 for $Br_f = 0.1$ and $\frac{\Omega}{Br_f} = 2$. As mentioned in the previous section, the average entropy generation decreases for Brinkman numbers of less than 1.5 with an increase in the nanoparticle volume fraction. This fact also is shown in Fig. 10. The decreasing tendency in entropy generation is more obvious between $\phi = 0$ and $\phi = 1\%$, because the viscous dissipation effects are smaller at lower particle volume fractions. Hence, the addition of nanoparticles leads to more reduction in entropy generation.

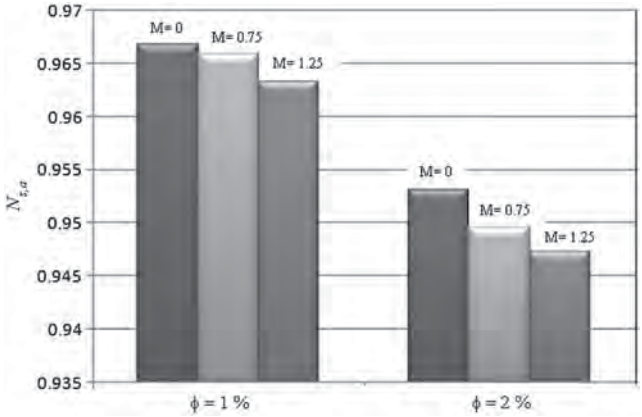

Fig. 11 Augmentation entropy generation number for $Br_f = 0.1$ and $\frac{\Omega}{Br_f} = 2$.

It also is shown in the figure that, with the augmentation of the magnetic field, the average entropy generation increases. The presence of the magnetic field makes a resistive force similar to the drag force, which acts in the opposite direction of fluid movement. This reduces the fluid velocity, leads to the increase in viscous dissipation, and results in more internal heating of the working fluid. Consequently, there is an increase of the entropy generation. As shown, the profiles of $(N_S)_{\text{ave}}$ for different values of ϕ are parallel and regular.

The proper effect of the augmentation method (here, adding nanoparticles) on the thermodynamic performance of the thermal system can be appraised by comparing the irreversibility before and after using the augmentation method. For this purpose, the augmentation entropy generation number is defined as follows [22]:

$$N_{S,a} = \frac{N_S}{N_{S,0}} \tag{22}$$

where $N_{S,0}$ indicates the degree of irreversibility when the volume fraction is zero (distilled water). According to Eq. (22), adding nanoparticles is advantageous with respect to the second law of thermodynamics when $N_{S,a}$ values are less than 1. Figure 11 presents the variation of augmentation entropy generation number at different Hartmann numbers and volume fractions (1 and 2%) for the conditions of Fig. 10. The figure shows that the augmentation entropy generation decreases with an increase in volume fraction and the Hartmann number. Therefore, for this case, the following suggestion can be given. With respect to the second law of thermodynamics, adding nanoparticles to the working base fluid is more justifiable with increasing intensity of magnetic field than in the case in which the magnetic field is poor.

V. Conclusions

An analytical analysis of the second law of thermodynamics is presented to investigate the effect of using TiO_2-water nanofluid (up to 2 vol %) on entropy generation between two rotating cylinders in the presence of magnetohydrodynamic flow. The governing equations in a cylindrical coordinate system are simplified and solved to obtain analytical expressions for the velocity and temperature fields and, consequently, the entropy generation rate. To calculate the thermophysical properties of the nanofluid, including thermal conductivity and viscosity, the Duangthongsuk and Wongwises models, which are based on experimental data, have been used. The results for the local entropy generation analysis reveal that entropy generation is highest near the inner cylinder due to the maximum gradients of velocity and temperature. In addition, with an increase in the Hartmann number (magnetic field), entropy generation in the vicinity of the inner cylinder decreases, whereas in other regions, the entropy generation number is raised. The results show that, at low Brinkman numbers (depending on the value of $\frac{\Omega}{Br_f}$), the average entropy generation number decreases with the addition of nanoparticle volume fraction. It also was found that the increase in the Hartmann number results in an increase in the average entropy generation number. Hence, with respect to the second law of thermodynamics, using nanofluids for the flow between two rotating cylinders in the presence of a magnetohydrodynamic field is suggested only at low Brinkman numbers.

Acknowledgments

The third author would like to thank the Thailand Research Fund and the National Research University Project for support.

References

[1] Bejan, A., "Second-Law Analysis in Heat Transfer and Thermal Design," *Advances in Heat Transfer*, Vol. 15, 1982, pp. 1–58. doi:10.1016/S0065-2717(08)70172-2

[2] Bejan, A., *Entropy Generation Minimization*, CRC Press, Boca Raton, FL, 1996.

Downloaded by UNIVERSITY OF WATERLOO on February 10, 2013 | http://arc.aiaa.org | DOI: 10.2514/1.T3908

[3] Naterer, G. F., and Camberos, J. A., *Entropy Based Analysis and Design of Fluids Engineering Systems*, CRC Press, Boca Raton, FL, 2008.
[4] Shah, R. K., and Skiepko, T., "Entropy Generation Extrema and their Relationship with Heat Exchanger Effectiveness—Number of Transfer Unit Behavior for Complex Flow Arrangements," *Journal of Heat Transfer*, Vol. 126, No. 6, 2004, pp. 994–1002. doi:10.1115/1.1846694
[5] Guo, Z. Y., Liu, X. B., Tao, W. Q., and Shah, R. K., "Effectiveness–Thermal Resistance Method for Heat Exchanger Design and Analysis," *International Journal of Heat and Mass Transfer*, Vol. 53, Nos. 13–14, 2010, pp. 2877–2884. doi:10.1016/j.ijheatmasstransfer.2010.02.008
[6] Guo, J., and Xu, M., "The Application of Entransy Dissipation Theory in Optimization Design of Heat Exchanger," *Applied Thermal Engineering*, Vol. 36, 2012, pp. 227–235. doi:10.1016/j.applthermaleng.2011.12.043
[7] Cheng, X., and Liang, X., "Computation of Effectiveness of Two-Stream Heat Exchanger Networks Based on Concepts of Entropy Generation, Entransy Dissipation and Entransy-Dissipation-Based Thermal Resistance," *Energy Conversion and Management*, Vol. 58, 2012, pp. 163–170. doi:10.1016/j.enconman.2012.01.016
[8] Yu, W., France, D. M., Routbort, J. L., and Choi, S. U. S., "Review and Comparison of Nanofluid Thermal Conductivity and Heat Transfer Enhancements," *Heat Transfer Engineering*, Vol. 29, No. 5, 2008, pp. 432–460. doi:10.1080/01457630701850851
[9] Yu, W., France, D. M., Smith, D. S., Singh, D., Timofeeva, E. V., and Routbort, J. L., "Heat Transfer to a Silicon Carbide/Water Nanofluid," *International Journal of Heat and Mass Transfer*, Vol. 52, Nos. 15–16, 2009, pp. 3606–3612. doi:10.1016/j.ijheatmasstransfer.2009.02.036
[10] Trisaksri, V., and Wongwises, S., "Critical Review of Heat Transfer Characteristics of Nanofluids," *Renewable and Sustainable Energy Reviews*, Vol. 11, No. 3, 2007, pp. 512–523. doi:10.1016/j.rser.2005.06.005
[11] Duangthongsuk, W., and Wongwises, S., "A Critical Review of Convective Heat Transfer of Nanofluids," *Renewable and Sustainable Energy Reviews*, Vol. 11, No. 5, 2007, pp. 797–817. doi:10.1016/j.rser.2005.06.005
[12] Godson, L., Raja, B., Mohan Lal, D., and Wongwises, S., "Enhancement of Heat Transfer Using Nanofluids—An Overview," *Renewable and Sustainable Energy Reviews*, Vol. 14, No. 2, 2009, pp. 629–641. doi:10.1016/j.rser.2009.10.004
[13] Saidur, R., Leong, K. Y., and Mohammad, H. A., "A Review on Applications and Challenges of Nanofluids," *Renewable and Sustainable Energy Reviews*, Vol. 15, No. 3, 2011, pp. 1646–1668. doi:10.1016/j.rser.2010.11.035
[14] Khanafer, K., and Vafai, K., "A Critical Synthesis of Thermophysical Characteristics of Nanofluids," *International Journal of Heat and Mass Transfer*, Vol. 54, Nos. 19–20, 2011, pp. 4410–4428. doi:10.1016/j.ijheatmasstransfer.2011.04.048
[15] Singh, P. K., Anoop, K. B., Sundararajan, T., and Das, S. K., "Entropy Generation Due to Flow and Heat Transfer in Nanofluids," *International Journal of Heat and Mass Transfer*, Vol. 53, Nos. 21–22, 2010, pp. 4757–4767. doi:010.1016/j.ijheatmasstransfer.2010.06.016
[16] Li, J., and Kleinstreuer, C., "Entropy Generation Analysis for Nanofluid Flow in Microchannels," *Journal of Heat Transfer*, Paper 122401, Vol. 132, No. 12, 2010
[17] Feng, Y., and Kleinstreuer, C., "Nanofluid Convective Heat Transfer in a Parallel-Disk System," *International Journal of Heat and Mass Transfer*, Vol. 53, No. 21–22, 2010, pp. 4619–4628. doi:10.1016/j.ijheatmasstransfer.2010.06.031
[18] Moghaddami, M., Mohammadzade, A., and Varzane Esfehani, S. A., "Second Law Analysis of Nanofluid Flow," *Energy Conversion and Management*, Vol. 52, No. 2, 2011, pp. 1397–1405. doi:10.1016/j.enconman.2010.10.002
[19] Shahi, M., Mahmoudi, A. H., and Raouf, A. H., "Entropy Generation Due to Natural Convection Cooling of a Nanofluid," *International Communications in Heat and Mass Transfer*, Vol. 38, No. 7, 2011, pp. 972–983. doi:10.1016/j.icheatmasstransfer.2011.04.008
[20] Esmaeilpour, M., and Abdollahzadeh, M., "Free Convection and Entropy Generation of Nanofluid Inside an Enclosure with Different Patterns of Vertical Wavy Walls," *International Journal of Thermal Sciences*, Vol. 52, 2012, pp. 127–136. doi:10.1016/j.ijthermalsci.2011.08.019
[21] Bianco, V., Nardini, S., and Manca, O., "Enhancement of Heat Transfer and Entropy Generation Analysis of Nanofluids Turbulent Convection Flow in Square Section Tubes," *Nanoscale Research Letters*, Vol. 6, 2011, p. 252. doi:10.1186/1556-276X-6-252
[22] Falahat, A., and Vosough, A., "Effect of Nanofluid on Entropy Generation and Pumping Power in Coiled Tube," *Journal of Thermophysics and Heat Transfer*, Vol. 26, No. 1, 2012, pp. 141–146. doi:10.2514/1.T3771
[23] Yilbas, B. S., "Entropy Analysis of Concentric Annuli with Rotating Outer Cylinder," *International Journal of Exergy*, Vol. 1, No. 1, 2001, pp. 60–66. doi:10.1016/S1164-0235(01)00011-5
[24] Mahmud, S., and Fraser, R. A., "Second Law Analysis of Heat Transfer and Fluid Flow Inside a Cylindrical Annular Space," *International Journal of Exergy*, Vol. 2, No. 4, 2002, pp. 322–329. doi:10.1016/S1164-0235(02)00078-X
[25] Mahmud, S., and Fraser, R. A., "Analysis of Entropy Generation Inside Concentric Cylindrical Annuli with Relative Rotation," *International Journal of Thermal Sciences*, Vol. 42, No. 5, 2003, pp. 513–521. doi:10.1016/S1290-0729(02)00051-0
[26] Mirzazadeh, M., Shafaei, A., and Rashidi, F., "Entropy Analysis for Non-Linear Viscoelastic Fluid in Concentric Rotating Cylinders," *International Journal of Thermal Sciences*, Vol. 47, No. 12, 2008, pp. 1701–1711. doi:10.1016/j.ijthermalsci.2007.11.002
[27] Jery, A. E., Hidouri, N., Magherbi, M., and Brahim, A. B., "Effect of an External Oriented Magnetic Field on Entropy Generation in Natural Convection," *Entropy*, Vol. 12, No. 6, 2010, pp. 1391–1417. doi:10.3390/e12061391
[28] Salas, H., Cuevas, S., and Haro, M. L., "Entropy Generation Analysis of Magnetohydrodynamic Induction Devices," *Journal of Physics D: Applied Physics*, Vol. 32, No. 20, 1999, pp. 2605–2608. doi:10.1088/0022-3727/32/20/304
[29] Ibanez, G., Cuevas, S., and Haro, M. L., "Optimization Analysis of an Alternate Magnetohydrodynamic Generator," *Energy Conversion and Management*, Vol. 43, No. 14, 2002, pp. 1757–1771. doi:10.1016/S0196-8904(01)00133-9
[30] Mahmud, S., Tasnim, S. H., and Mamun, M. A. H., "Thermodynamic Analysis of Mixed Convection in a Channel with Transverse Hydromagnetic Effect," *International Journal of Thermal Science*, Vol. 42, No. 8, 2003, pp. 731–740. doi:10.1016/S1290-0729(03)00040-1
[31] Tasnim, S. H., Mahmud, S., and Mamun, M. A. H., "Entropy Generation in a Porous Channel with Hydromagnetic Effect," *Energy*, Vol. 2, No. 4, 2002, pp. 300–308. doi:10.1016/S1164-0235(02)00065-1
[32] Mahmud, S., and Fraser, R. A., "Mixed Convection-Radiation Interaction in a Vertical Porous Channel: Entropy Generation," *Energy*, Vol. 28, No. 15, 2003, pp. 1557–1577. doi:10.1016/S0360-5442(03)00154-3
[33] Mahmud, S., and Fraser, R. A., "Magnetohydrodynamic Free Convection and Entropy Generation in a Square Porous Cavity," *International Journal of Heat and Mass Transfer*, Vol. 47, Nos. 14–16, 2004, pp. 3245–3256. doi:10.1016/j.ijheatmasstransfer.2004.02.005
[34] Ibanez, G., and Cuevas, S., "Optimum Wall Conductance Ratio in Magnetoconvective Flow in a Long Vertical Rectangular Duct," *International Journal of Thermal Science*, Vol. 47, No. 8, 2008, pp. 1012–1019. doi:10.1016/j.ijthermalsci.2007.09.003
[35] Mahmud, S., and Fraser, R. A., "The Thermoacoustic Irreversibility for a Single-Plate Thermoacoustic System," *International Journal of Heat and Mass Transfer*, Vol. 49, Nos. 19–20, 2006, pp. 3448–3461. doi:10.1016/j.ijheatmasstransfer.2006.02.051
[36] Ibanez, G., and Cuevas, S., "Optimum Wall Conductance Ratio in Magnetoconvective Flow in a Long Vertical Rectangular Duct," *International Journal of Thermal Science*, Vol. 47, No. 8, 2008, pp. 1012–1019. doi:10.1016/j.ijthermalsci.2007.09.003
[37] Arikoglu, A., Ozkol, I., and Komurgoz, G., "Effect of Slip on Entropy Generation in a Single Rotating Disk in MHD Flow," *Applied Energy*, Vol. 85, No. 12, 2008, pp. 1225–1236. doi:10.1016/j.apenergy.2008.03.004
[38] Ibanez, G., and Cuevas, S., "Entropy Generation Minimization of a MHD (Magnetohydrodynamic) Flow in a Microchannel," *Energy*, Vol. 35, No. 10, 2010, pp. 4149–4155. doi:10.1016/j.energy.2010.06.035

Downloaded by UNIVERSITY OF WATERLOO on February 10, 2013 | http://arc.aiaa.org | DOI: 10.2514/1.T3908

[39] Mansour, R. B., Galanis, N., and Nguyen, C. T., "Effect of Uncertainties in Physical Properties on Forced Convection Heat Transfer with Nanofluids," *Applied Thermal Engineering*, Vol. 27, No. 1, 2007, pp. 240–249. doi:10.1016/j.applthermaleng.2006.04.011
[40] Jiji, L. M., *Heat Convection*, Springer-Verlag, Berlin, 2006.
[41] Duangthongsuk, W., and Wongwises, S., "Measurement of Temperature-Dependent Thermal Conductivity and Viscosity of TiO_2 Water Nanofluids," *Experimental Thermal and Fluid Science*, Vol. 33, No. 4, 2009, pp. 706–714. doi:10.1016/j.expthermflusci.2009.01.005
[42] Paoletti, S., Rispoli, F., and Sciubba, E., "Calculation of Exergetic Losses in Compact Heat Exchanger Passages," *American Society of Mechanical Engineers, Advanced Energy Systems Division*, Vol. 10, No. 2, 1980, pp. 21–29.
[43] White, F. M., *Viscous Fluid Flow*, McGraw–Hill, New York, 1974.

Downloaded by UNIVERSITY OF WATERLOO on February 10, 2013 | http://arc.aiaa.org | DOI: 10.2514/1.T3908

HVAC&R Research (2013) **19**, 159–174
Copyright © 2013 ASHRAE.
ISSN: 1078-9669 print / 1938-5587 online
DOI: 10.1080/10789669.2012.751812

Taylor & Francis
Taylor & Francis Group

Numerical simulation of refrigerants flowing through short-tube orifices during flashing process

KITTI NILPUENG[1,2] and SOMCHAI WONGWISES[2,3,*]

[1]*Department of Mechanical Engineering, South East Asia University, Bangkok 10160, Thailand*
[2]*Fluid Mechanics, Thermal Engineering and Multiphase Flow Research Lab (FUTURE), Department of Mechanical Engineering, Faculty of Engineering, King Mongkut's University of Technology Thonburi, Bangmod, Bangkok 10140, Thailand*
[3]*The Academy of Science, The Royal Institute of Thailand, Sanam Suea Pa, Dusit, Bangkok 10300, Thailand*

A numerical simulation for calculating the flashing flow characteristics of refrigerants inside short-tube orifices is presented. The refrigerant flow behaviors along short-tube orifices are separated into three sections: subcooled liquid region, metastable liquid region, and two-phase region. Annular two-phase flow pattern is developed from the mass, energy, and momentum equation. The present simulation is corroborated by comparison with the experimental data. The selection charts are also presented to estimate the refrigerant mass flow rate along short-tube orifices in practical applications.

Introduction

Expansion device is one of four main parts of refrigeration system. The functions are two-fold: (1) to reduce the refrigerant pressure from high pressure in condenser to low pressure in evaporator and (2) to control the refrigerant flow rate from the condenser to the evaporator. Short-tube orifice is a constant-restriction type of expansion device commonly used in domestic and automobile air conditioners. It is a short and narrow tube with length-to-diameter ratio of 3–20 and lengths of 10–13 mm (0.394–0.512 in.) for domestic air conditioners. Length-to-diameter ratio and diameter of short-tube orifices are 21–35 mm (0.827–1.378 in.) and 1–2 mm (0.039–0.079 in.) for automobile air conditioners (ASHRAE 1998). The benefits of using short-tube orifices are low starting torque of the compressor, high reliability, low cost, and simplicity. However, it is found that to obtain the optimum air conditioner performance, the refrigerant flow inside the short-tube orifice should be choked. Moreover, after the size of a short-tube orifice is selected to install into an air-conditioning system, it will be suitable for only one design condition. This means that the refrigerant flow rate and pressure drop cannot be satisfied under different operating conditions. Therefore, a design tool for estimating the refrigerant mass flow rate along the short-tube orifice at a given operating condition is very necessary.

During the past decades, the numerical analysis on the refrigerant flashing flow through short-tube orifices has been reported in the publications. It is separated into two classifications: semi-empirical models and theoretical models. Semi-empirical models are generated in the form of simple equations with the correction factor created from experimental data. It was found that a single-phase orifice equation (ASME 1971) has been proposed by most previous researchers as follows:

$$\dot{m} = CA\sqrt{\frac{2\rho(P_{up} - P_{down})}{(1-\beta^4)}}. \quad (1)$$

As shown in Equation 1, it was found that the mass flow rate was a function of downstream pressure (P_{down}), upstream pressure (P_{up}), short-tube orifice flow area (A), upstream density (ρ), and the orifice diameter-to-tube diameter ratio (β). The correction factor, which was combined in the single-phase orifice equation, was presented into two forms: orifice constant correlation (C) and downstream pressure correlation. The first one was dependent on the difference of upstream pressure and downstream pressure, downstream vapor quality, ratio of length to diameter, and degree of subcooling (Mei 1982; Pasqua 1953; Tu et al. 2006). The other one was dependent on the ratio of length to diameter, upstream temperature, downstream pressure, and upstream pressure (Aaron and Domanski 1990; Kim 1993; Kim et al. 2002; Liu et al. 2004). A generalized mass flow rate correlation of alternative refrigerant through short-tube orifices was proposed in few publications (Choi et al. 2004). The correlation in power law form, which was included with dimensionless parameters, was generated and proposed. Buckingham Pi theorem was used to create the dimensionless parameters.

Although the semi-empirical models can be used to calculate the refrigerant mass flow rate through short-tube orifices, they cannot be used to indicate the physical meaning of refrigerant flow mechanism; the accuracy of the models are valid only over the testing conditions. Therefore, theoretical

Received June 14, 2012; accepted November 9, 2012
Kitti Nilpueng, D.Eng, is lecturer and researcher. **Somchai Wongwises, PhD, Dr-Ing**, is professor.
*Corresponding author e-mail: somchai.won@kmutt.ac.th

models have been proposed to simulate the characteristic of refrigerant through short-tube orifice by some researchers. Eight critical flow models were compared with the experimental data of HCFC-22 and HFC-134a by Kim and O'Neal (1995). These models were divided into three classes: homogeneous equilibrium models (HEMs), nonhomogeneous equilibrium models (NEMs), and homogeneous frozen models (HFMs). A comparison between the experimental data and calculated results of models showed that the HFM gave the best agreement except at outlet qualities below 0.06. A nonequilibrium two-fluid model, which consisted of mass, momentum, and energy equations for each phase, was represented for predicting the refrigerant flow behavior through short-tube orifices by Yang and Zhang (2005). Based on the measured mass flow rates of HFC-134a, CFC-12, HCFC-22, HFC-410A, and HFC-407C, it was found that the two-fluid model gave an acceptable prediction with a deviation of $\pm 20\%$. However, in the case of supercritical carbon dioxide (CO_2), Zhang and Yang (2005) reported that the difference of interphase temperature and velocity in two-phase region between gas and liquid were small. Therefore, the nonhomogeneous and nonequilibrium flow behavior inside the short-tube orifice was insignificant. They also concluded that the accuracy of the two-fluid model was similar to that of the HEM. The fluid-dynamic flow characteristic of CO_2 through short-tube orifices was simulated by Garcia-Valladares (2006). He developed the governing equations from the continuity equation, energy equation, entropy equation, and momentum equation. The simulation has been solved by a finite volume formulation. The numerical results showed good acceptance with the measured results.

As mentioned above, it is observed that the theoretical model is more attractive than the semi-empirical model because it can show the physical meaning of the refrigerant along the short-tube orifice. However, the theoretical model is rather difficult to solve when it includes the complicated equations and correlations. As a result, only a few research works have been reported and it is still not clear which one is the best.

The objective of this research work is to develop the numerical model for estimating the flashing flow of refrigerant along the short-tube orifice. The assumptions of metastable liquid flow and annular flow pattern in a two-phase section are applied in this model. The numerical results of refrigerant flow rate and distribution of pressure inside a short tube orifice are verified with the experimental data. Moreover, the short-tube orifice selection charts are presented to estimate the refrigerant mass flow rate along short-tube orifices in practical applications.

Mathematical modeling

The refrigerant flow behavior inside a short-tube orifice is shown diagrammatically in Figure 1. It is separated into three sections: subcooled liquid region, metastable liquid region, and two-phase region. To simulate the refrigerant flow behavior along the short-tube orifice, a present model is developed from the mass, energy, and momentum equation with the following assumptions:

- one dimensional steady flow;
- adiabatic flow; and
- the short-tube orifice diameter and surface roughness is constant.

Subcooled liquid region

As shown in Figure 1, the steady flow energy equation for subcooled liquid region (points 1–3) can be expressed as:

$$\frac{P_1}{\rho_1 g} + \frac{V_1^2}{2g} + z_1 = \frac{P_3}{\rho_3 g} + \frac{V_3^2}{2g} + z_3 + h_L. \tag{2}$$

For an incompressible fluid ($\rho_2 \cong \rho_3 = \rho_L$), the continuity equation is written as:

$$\dot{m} = \rho_2 V_2 A = \rho_3 V_3 A = \rho V A, \tag{3}$$

where h_L is the head loss due to the sudden contraction and friction of the tube wall. It is determined by the following equation:

$$h_L = k\frac{V^2}{2g} + f_{sp}\frac{L}{D}\frac{V^2}{2g}, \tag{4}$$

where k is the entrance loss coefficient and f_{sp} is the friction factor for single-phase flow. It is calculated from the Colebrook

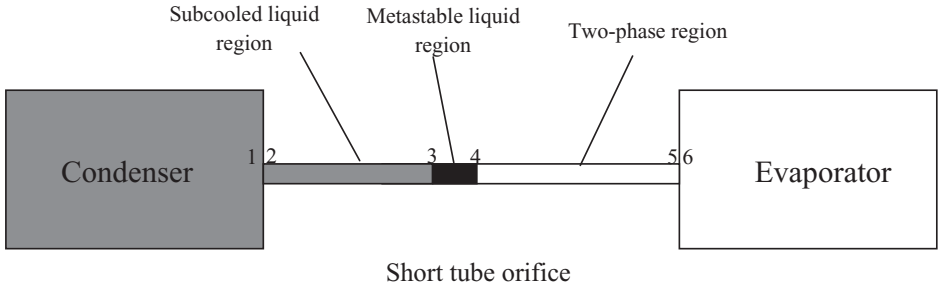

Fig. 1. Schematic diagram a short-tube orifice (color figure available online).

formula as follows:

$$\frac{1}{\sqrt{f_{sp}}} = 1.14 - 2\log\left[\frac{\varepsilon}{D} + \frac{9.3}{\mathrm{Re}\sqrt{f_{sp}}}\right], \quad (5)$$

where

$$\mathrm{Re} = \rho V D/\mu. \quad (6)$$

For a horizontal short-tube orifice ($z_2 = z_3$), substituting Equation 4 into Equation 2, the subcooled liquid length can be estimated from:

$$L_{sub} = \left[(P_1 - P_3)\frac{2}{\rho V^2} - (k+1)\right]\frac{D}{f_{sp}}, \quad (7)$$

where P_3 is the saturation pressure corresponding to the upstream temperature.

Metastable liquid region

The experimental data from prior studies (Kim 1993; Nilpueng and Wongwises 2009) show that even the pressure was decreased lower than the saturation pressure; the refrigerant inside the short-tube orifice was liquid. This indicates that the inception of vaporization is delayed. This flow phenomenon is defined as metastable liquid flow. Considering the length of the metastable liquid region (points 3–4) in Figure 1, it can be calculated based on the steady flow energy equation as follows:

$$L_{mt} = \left[\frac{2}{\rho V^2}(P_3 - P_4)\right]\frac{D}{f_{sp}}, \quad (8)$$

where P_4 is the actual pressure of vaporization. In this model, two empirical correlations of actual pressure of vaporization (P_υ) are applied as follows:

- *Chen et al. correlation* (Chen et al. 1990):
  The Chen et al. correlation was developed based on the flow of R12 through capillary tubes for predicting the actual pressure of vaporization. In this study, it is applied as follows:

$$\frac{(P_s - P_\upsilon)\sqrt{kT_s}}{\sigma^{3/2}} = 0.679\left(\frac{\upsilon_G}{\upsilon_G - \upsilon_L}\right)\mathrm{Re}^{0.914} \times \left(\frac{\Delta T_{sub}}{T_c}\right)^{-0.208}\left(\frac{D}{D'}\right)^{-3.18}, \quad (9)$$

  where D' is the reference length ($\sqrt{kT_s/\sigma}\times 10^4$), T_c is the refrigerant critical temperature, and k is the Boltzman constant (1.380662×10^{-23}). The thermodynamic properties are determined at saturation condition.
- *Lackme correlation* (Lackme 1979):

$$P_\upsilon = k_1 P_s, \quad (10)$$

  where the average value of k_1 ($k_1 = 0.93$) is applied in this study.

Two-phase region

The model is developed from the separated flow model presented by Collier and Thome (1996). The flow pattern of the vapor core is covered by the liquid film (annular flow) is applied in this model (Wongwises and Suchatawat 2002). The governing equations of annular flow are developed from the mass, energy, and momentum equation. The continuity equation for two-phase flow is presented in the following relationship:

$$\frac{d\dot{m}_L}{dz} + \frac{d\dot{m}_G}{dz} = \frac{d\dot{m}}{dz} = 0. \quad (11)$$

The momentum equation for each phase can be expressed as:

$$\frac{d(\dot{m}_L V_L)}{dz} = -\tau_{Lw}C_{Lw} + \tau_i C_i - A_L\frac{dP}{dz} + V_L\frac{d\dot{m}_L}{dz}, \quad (12)$$

$$\frac{d(\dot{m}_G V_G)}{dz} = -\tau_i C_i - A_G\frac{dP}{dz} + V_G\frac{d\dot{m}_G}{dz}. \quad (13)$$

The momentum transfer between liquid and vapor is:

$$\tau_i C_i + V_L\frac{d\dot{m}_L}{dz} - \tau_i C_i + V_G\frac{d\dot{m}_G}{dz} = 0. \quad (14)$$

Combining Equations 12 and 13 by using the relation of the momentum transfer between liquid and vapor (Equation 14), the following is obtained:

$$\frac{d(\dot{m}_L V_L + \dot{m}_G V_G)}{dz} = -\tau_{Lw}C_{Lw} - (A_L + A_G)\frac{dP}{dz}. \quad (15)$$

If Equation 15 is rearranged with the following basic relationships:

$$G = \frac{\dot{m}}{A} = \rho V = \frac{V}{\upsilon}, \quad \dot{m}_G = GAx, \dot{m}_L = GA(1-x),$$
$$\alpha = \frac{A_G}{A}, (1-\alpha) = \frac{A_L}{A}, \quad V_G = \frac{Gx}{\rho_G\alpha}, V_L = \frac{G(1-x)}{\rho_L(1-\alpha)},$$

then it can be written as:

$$-\left(\frac{dP}{dz}\right) = \frac{\tau_{Lw}C_{Lw}}{A} + G^2\frac{d}{dz}\left[\frac{x^2\upsilon_G}{\alpha} + \frac{(1-x)^2\upsilon_L}{(1-\alpha)}\right]. \quad (16)$$

The two-phase frictional pressure gradient is calculated by using the Lockhart Martinelli correlation as follows:

$$\left(\frac{dP_F}{dz}\right)_{TP} = \frac{\tau_{Lw}C_{Lw}}{A} = \phi_L^2\left(\frac{dP_F}{dz}\right)_L. \quad (17)$$

The two-phase multiplier is:

$$\phi_L^2 = 1 + \frac{C}{X} + \frac{1}{X^2}. \quad (18)$$

The value of constant C depends on the flow condition of the gas and liquid phase. It is varied from 5 to 20. The Martinelli parameter can be expressed as:

$$X^2 = \frac{(dP_F/dz)_L}{(dP_F/dz)_G}, \tag{19}$$

when

$$\left(\frac{dP_F}{dz}\right)_L = \frac{2f_L G_L^2}{\rho_L D}, \tag{20}$$

$$\left(\frac{dP_F}{dz}\right)_G = \frac{2f_G G_G^2}{\rho_G D}. \tag{21}$$

The void fraction is expressed in the following equation:

$$\alpha = \frac{x\upsilon_G}{(1-x)\upsilon_L S + x\upsilon_G}. \tag{22}$$

In this equation, three empirical correlations of slip ratio, which are used to indicate the difference between liquid and vapor velocities, are considered as follows:

- *Chisholm correlation* (Chisholm 1973):

$$S = \left[1 - x\left(1 - \frac{\rho_L}{\rho_G}\right)\right]^{1/2}. \tag{23}$$

- *Miropolskiy et al.* correlation (Miropolskiy et al. 1970):

$$S = 1 - \frac{13.5(1 - P/P_c)}{Fr_L^{5/12}\mathrm{Re}_L^{1/6}}, \tag{24}$$

where

$$Fr_L = G^2\upsilon_L^2/gD \quad \text{and} \quad \mathrm{Re}_L = GD/\mu_L.$$

- *Zivi correlation* (Zivi 1964):

$$S = \left(\frac{\rho_L}{\rho_G}\right)^{1/3}. \tag{25}$$

As shown in Equation 16, the accelerational pressure gradient, which is the last term of the equation, can be expanded as:

$$\begin{aligned}\frac{\mathrm{d}}{\mathrm{d}z}\left[\frac{x^2\upsilon_\mathrm{G}}{\alpha} + \frac{(1-x)^2\upsilon_\mathrm{L}}{(1-\alpha)}\right] &= \frac{\mathrm{d}x}{\mathrm{d}z}\left\{\left[\frac{2x\upsilon_\mathrm{G}}{\alpha} - \frac{2(1-x)\upsilon_\mathrm{L}}{(1-\alpha)}\right]\right.\\ &\left.+\left(\frac{\partial\alpha}{\partial x}\right)_P\left[\frac{(1-x)^2\upsilon_\mathrm{L}}{(1-\alpha)^2} - \frac{x^2\upsilon_\mathrm{G}}{\alpha^2}\right]\right\}\\ &+\frac{\mathrm{d}P}{\mathrm{d}z}\left\{\left[\frac{x^2}{\alpha}\frac{\mathrm{d}\upsilon_\mathrm{G}}{\mathrm{d}P} + \frac{(1-x)^2}{(1-\alpha)}\frac{\mathrm{d}\upsilon_\mathrm{L}}{\mathrm{d}z}\right]\right\}\\ &+\left(\frac{\partial\alpha}{\partial P}\right)_x\left[\frac{(1-x)^2\upsilon_\mathrm{L}}{(1-\alpha)^2} - \frac{x^2\upsilon_\mathrm{G}}{\alpha^2}\right].\end{aligned} \tag{26}$$

Therefore, Equation 16 can be expressed as:

$$A_1\left(-\frac{\mathrm{d}P}{\mathrm{d}z}\right) - A_2\left(\frac{\mathrm{d}x}{\mathrm{d}z}\right) = B_1, \tag{27}$$

where

$$\begin{aligned}A_1 &= 1 + G^2\left\{\left[\frac{x^2}{\alpha}\frac{\mathrm{d}\upsilon_\mathrm{G}}{\mathrm{d}P} + \frac{(1-x)^2}{(1-\alpha)}\frac{\mathrm{d}\upsilon_\mathrm{L}}{\mathrm{d}z}\right]\right.\\ &\left.+\left(\frac{\partial\alpha}{\partial P}\right)_x\left[\frac{(1-x)^2\upsilon_\mathrm{L}}{(1-\alpha)^2} - \frac{x^2\upsilon_\mathrm{G}}{\alpha^2}\right]\right\},\\ A_2 &= G^2\left\{\left[\frac{2x\upsilon_\mathrm{G}}{\alpha} - \frac{2(1-x)\upsilon_\mathrm{L}}{(1-\alpha)}\right]\right.\\ &\left.+\left(\frac{\partial\alpha}{\partial x}\right)_P\left[\frac{(1-x)^2\upsilon_\mathrm{L}}{(1-\alpha)^2} - \frac{x^2\upsilon_\mathrm{G}}{x^2}\right]\right\},\\ B_1 &= \frac{\tau_{Lw}C_{Lw}}{A}.\end{aligned}$$

Based on the assumptions of adiabatic flow, steady state steady flow, no energy transfer by work, and horizontal short-tube orifice, the liquid and vapor energy equations are expressed as:

$$\begin{aligned}\frac{d}{dz}\left[\dot{m}_L\left(h_L + \frac{V_L^2}{2}\right)\right] &= -q''_{Lw}C_{Lw} + q''_i C_i + \tau_i V_i C_i\\ &+\left(h_L + \frac{V_L^2}{2}\right)\frac{d\dot{m}_L}{dz},\end{aligned} \tag{28}$$

$$\begin{aligned}\frac{d}{dz}\left[\dot{m}_G\left(h_G + \frac{V_G^2}{2}\right)\right] &= -q''_i C_i - \tau_i V_i C_i\\ &+\left(h_G + \frac{V_G^2}{2}\right)\frac{d\dot{m}_G}{dz}.\end{aligned} \tag{29}$$

At the interface between liquid and vapor, the conservation of energy is written as:

$$\begin{aligned}q''_i C_i + \tau_i V_i C_i + \left(h_L + \frac{V_L^2}{2}\right)\frac{d\dot{m}_L}{dz} - q_i C_i - \tau_i V_i C_i\\ +\left(h_G + \frac{V_G^2}{2}\right)\frac{d\dot{m}_G}{dz} = 0.\end{aligned} \tag{30}$$

Combining Equations 28 and 29 with using the relationship of energy at the interfacial (Equation 30), the following is obtained:

$$\frac{d}{dz}(\dot{m}_G h_G + \dot{m}_L h_L) + \frac{d}{dz}\left[\dot{m}_G\frac{V_G^2}{2} + \dot{m}_L\frac{V_L^2}{2}\right] = -q''_{Lw}C_{Lw}. \tag{31}$$

In this work, the energy transfer by heat from the tube wall to liquid film is neglected ($q''_{Lw} \approx 0$). This is because the axial conduction along the wall is very slight (Chisholm 1973).

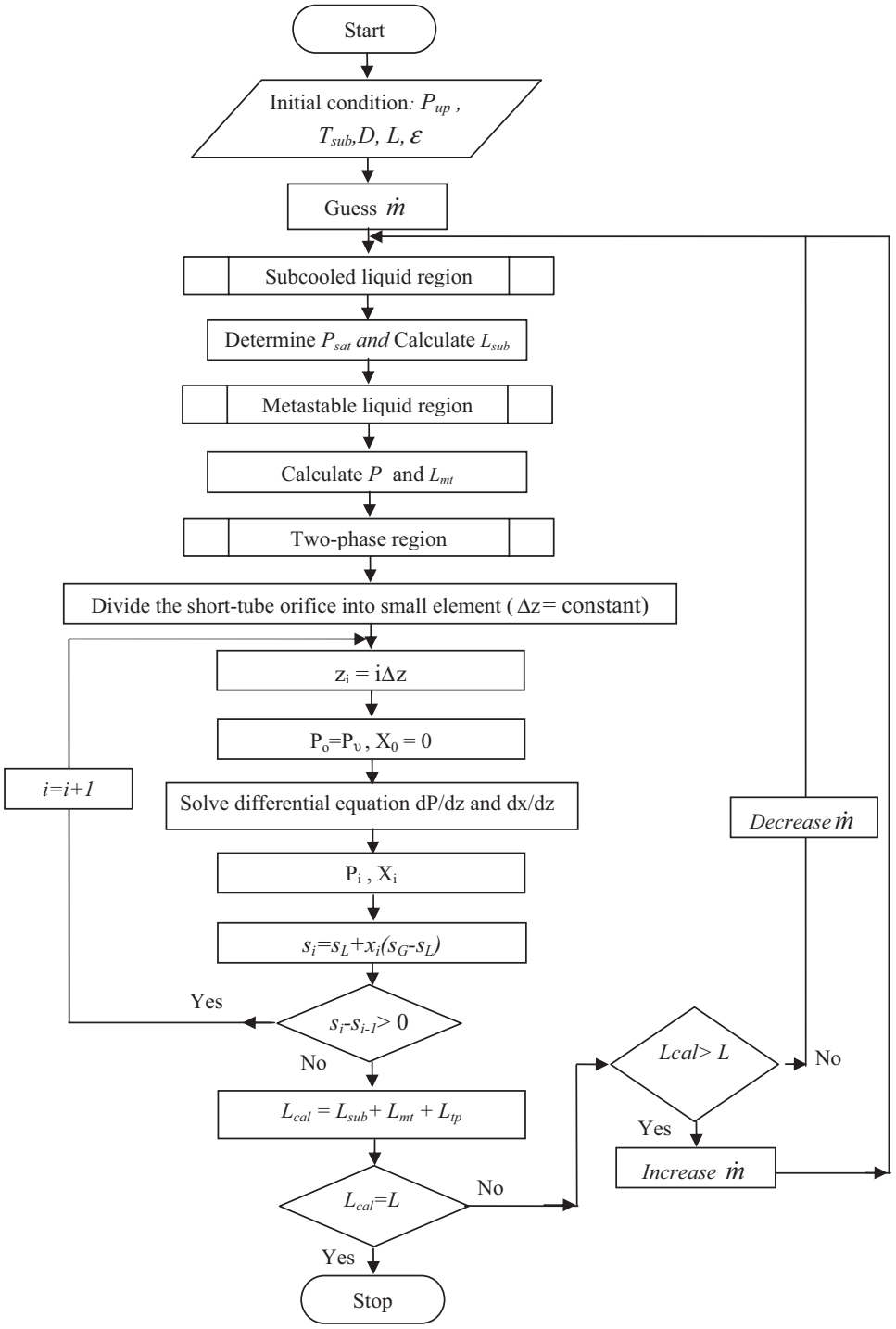

Fig. 2. Flow chart for calculating the critical mass flow rate inside short-tube orifice.

Substituting the basic two-phase relationship into Equation or 31, it can be expressed as:

$$\frac{d}{dz}\left[(GAx)h_G + GA(1-x)h_L\right] + \frac{1}{2}\frac{d}{dz}\left[GAx\,V_G^2 + GA(1-x)\,V_L^2\right] = 0 \qquad (32)$$

$$x\frac{dh_G}{dz} + h_G\frac{dx}{dz} + (1-x)\frac{dh_L}{dz} - h_L\frac{dx}{dz} + \frac{1}{2}\left[2xV_G\frac{dV_G}{dz} + V_G^2\frac{dx}{dz} + 2(1-x)V_L\frac{dV_L}{dz} - V_L^2\frac{dx}{dz}\right] = 0, \qquad (33)$$

Table 1. Testing conditions of the experimental data.

Refrigerant	Short-tube orifice diameter (mm)	Short-tube orifice diameter (in.)	Short-tube orifice length (mm)	Short-tube orifice length (in.)	Upstream pressure (kPa)	Upstream pressure (psi)	Degree of subcooling (°C)	Degree of subcooling (°F)	Downstream pressure (kPa)	Downstream pressure (psi)
HFC-134a										
• Kim (1993)	1.097–1.731	0.043–0.068	9.48–24.47	0.037–0.963	890–1459	129.1–211.6	2.8–13.9	5.04–25.02	310–483	44.9–70.1
• Singh et al. (2001)	1.22–1.71	0.048–0.067	13.1–38.4	0.515–1.512	1020–2140	147.9–310.4	0.6–24.5	1.08–44.1	3.4–5.2	49.3–75.4
• Nilpueng and Wongwises (2009)	0.961–1.2	0.037–0.047	10–20	0.394–0.787	900–1300	130.5–188.6	1–12	1.8–21.6	300–400	43.5–58.0
HFC-407C										
• Payne and O'Neal (1998)	1.097–1.94	0.043–0.076	12.68–25.39	0.499–0.999	1526–2273	221.3–329.6	0.28–11.28	0.50–20.3	630–770	91.4–111.7
HFC-410A										
• Payne and O'Neal (1999)	1.097–1.983	0.043–0.078	12.67–25.57	0.498–1.01	2130–3179	308.9–461.1	0.479–11.18	0.862–20.12	800–1100	116.0–159.5
• Kim et al. (2005)	1.097–1.799	0.043–0.071	12.7	0.5	2349–2617	340.7–379.6	1.792–11.03	3.225–19.85	772–1274	111.9–184.8

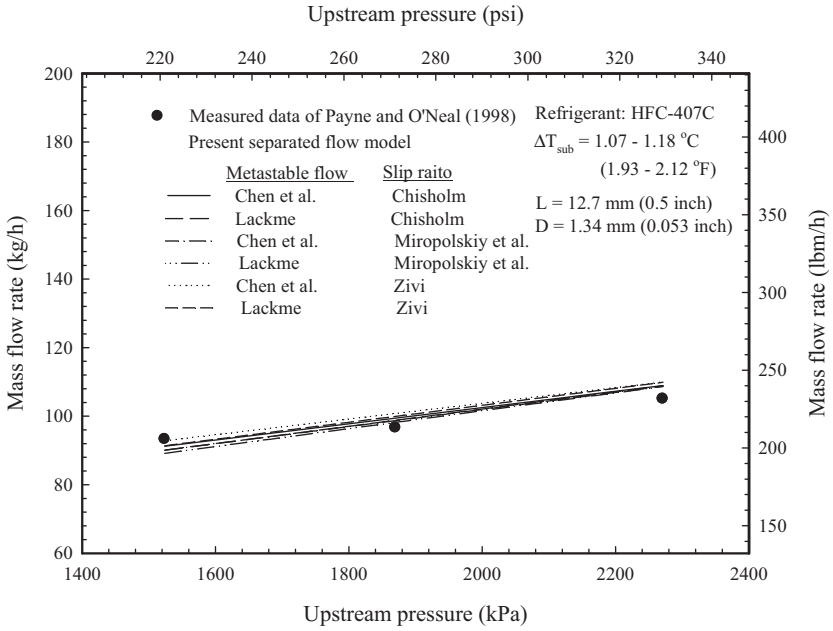

Fig. 3. Comparison of the numerical results with the measured mass flow rate at different upstream pressure.

where

$$\frac{dV_G}{dz} = G\left[\frac{x}{\alpha}\frac{d\upsilon_G}{dP}\frac{dP}{dz} + \frac{\upsilon_G}{\alpha}\frac{dx}{dz} - \frac{x\upsilon_G}{\alpha^2}\left(\left(\frac{\partial\alpha}{\partial P}\right)_x\frac{dP}{dz} + \left(\frac{\partial\alpha}{\partial x}\right)_p\frac{dx}{dz}\right)\right] \tag{34}$$

and

$$\frac{dV_L}{dz} = G\left\{\frac{1}{(1-\alpha)}\left[(1-x)\frac{d\upsilon_L}{dP}\frac{dP}{dz} - \upsilon_L\frac{dx}{dz}\right] + \frac{(1-x)\upsilon_L}{(1-\alpha)^2}\left[\left(\frac{\partial\alpha}{\partial P}\right)_x\frac{dP}{dz} + \left(\frac{\partial\alpha}{\partial x}\right)_p\frac{dx}{dz}\right]\right\}. \tag{35}$$

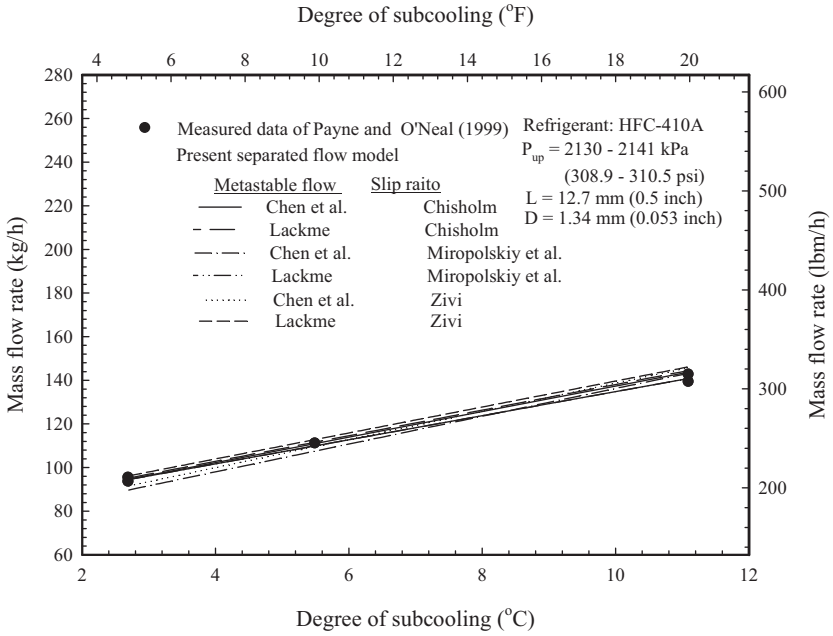

Fig. 4. Comparison of the numerical results with the measured mass flow rate at different degree of subcooling.

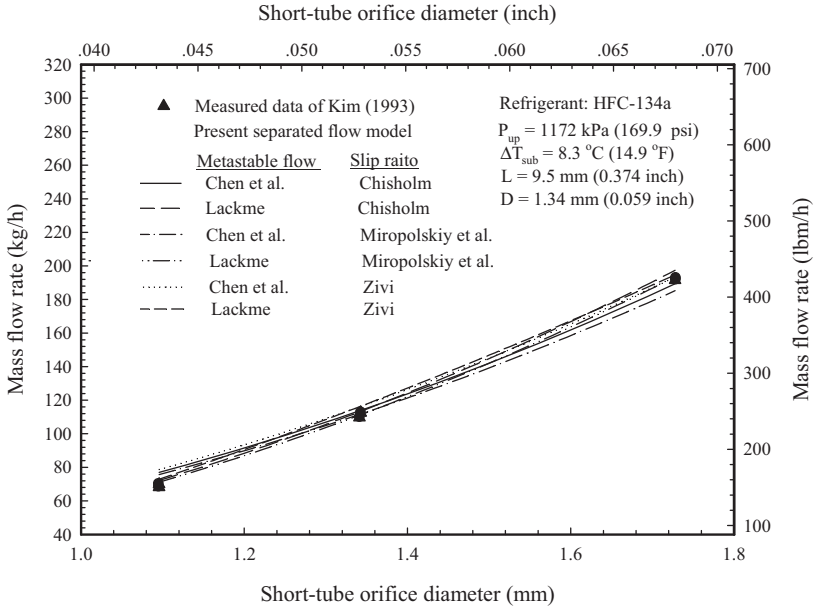

Fig. 5. Comparison of the numerical results with the measured mass flow rate at different short-tube orifice diameter.

Substituting Equations 34 and 35 into Equation 33 gives the following:

$$
\begin{aligned}
&(h_G - h_L)\frac{dx}{dz} + x\frac{dh_G}{dP}\frac{dP}{dz} + (1-x)\frac{dh_L}{dP}\frac{dP}{dz} + Gx\left(\frac{Gx\upsilon_G}{\alpha}\right)\\
&\times\left[\frac{x}{\alpha}\frac{d\upsilon_G}{dP}\frac{dP}{dz} + \frac{\upsilon_G}{\alpha}\frac{dx}{dz} - \frac{x\upsilon_G}{\alpha^2}\left(\left(\frac{\partial\alpha}{\partial P}\right)_x\frac{dP}{dz}\right.\right.\\
&\left.\left.+\left(\frac{\partial\alpha}{dx}\right)_p\frac{dx}{dz}\right)\right] + \frac{1}{2}\left[\frac{Gx\upsilon_G}{\alpha}\right]^2\frac{dx}{dz} + (1-x)G\\
&\times\left[\frac{G(1-x)\upsilon_L}{1-\alpha}\right]\left\{\frac{(1-x)}{(1-\alpha)}\frac{d\upsilon_L}{dP}\frac{dP}{dz} - \frac{\upsilon_L}{1-\alpha}\frac{dx}{dz}\right.\\
&\left.+\frac{(1-x)\upsilon_L}{(1-\alpha)^2}\left[\left(\frac{\partial\alpha}{\partial P}\right)_x\frac{dP}{dz} + \left(\frac{\partial\alpha}{\partial x}\right)_p\frac{dx}{dz}\right]\right\}\\
&-\frac{1}{2}\left[\frac{G(1-x)\upsilon_L}{1-\alpha}\right]^2\frac{dx}{dz} = 0. \qquad (36)
\end{aligned}
$$

Therefore, Equation 36 can be written as:

$$A_3\left(-\frac{dP}{dz}\right) - A_4\left(\frac{dx}{dz}\right) = B_2, \qquad (37)$$

where

$$
\begin{aligned}
A_3 &= \left\{x\frac{dh_G}{dP} + (1-x)\frac{dh_L}{dP} + \frac{G^2x^3\upsilon_G}{\alpha^2}\frac{d\upsilon_G}{dP}\right.\\
&\quad + \frac{G^2(1-x)^3\upsilon_L}{(1-\alpha)^2}\frac{d\upsilon_L}{dP}\\
&\quad \left. - \left[\frac{G^2x^3\upsilon_G^2}{\alpha^3} - \frac{G^2(1-x)^3\upsilon_L^2}{(1-\alpha)^3}\right]\left(\frac{\partial\alpha}{\partial P}\right)_x\right\},\\
A_4 &= \left\{(h_G - h_L) + \frac{3}{2}\frac{G^2x^2\upsilon_G^2}{\alpha^2} - \frac{3}{2}\frac{G^2(1-x)^2\upsilon_L^2}{(1-\alpha)^2}\right.\\
&\quad \left. - \left[\frac{G^2x^3\upsilon_G^2}{\alpha^3} - \frac{G^2(1-x)^3\upsilon_L^2}{(1-\alpha)^3}\right]\left(\frac{\partial\alpha}{\partial x}\right)_P\right\}, \quad B_2 = 0.
\end{aligned}
$$

Table 2. Mean absolute deviations between measured and calculated mass flow rate with different correlations.

	Actual pressure of vaporization correlation	Slip ratio correlation	HFC-134a (%)	HFC-407C (%)	HFC-410A (%)
1.	Chen et al.	Chisholm	8.32	12.94	16.67
2.	Chen et al.	Miropolskiy et al.	8.89	12.45	16.16
3.	Chen et al.	Zivi	9.13	14.10	17.68
4.	Lackme	Chisholm	9.03	12.20	15.43
5.	Lackme	Miropolskiy et al.	9.02	11.74	14.83
6.	Lackme	Zivi	9.08	13.19	16.41

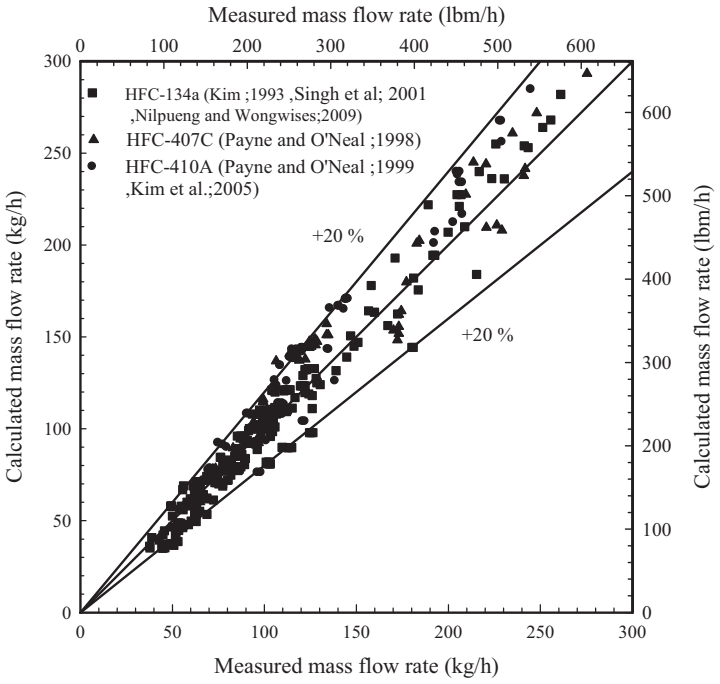

Fig. 6. Measured mass flow rateversus calculated massflow rate obtained from present model with Lackme (1979) and Miropolskiy et al. (1970) correlation.

According to Equations 27 and 37, the system of differential and equations is solved by the following equations:

$$-\frac{dP}{dz} = \frac{A_4 B_1 - A_2 B_2}{A_1 A_4 - A_2 A_3} \tag{38}$$

$$\frac{dx}{dz} = \frac{A_3 B_1 - A_1 B_2}{A_1 A_4 - A_2 A_3}. \tag{39}$$

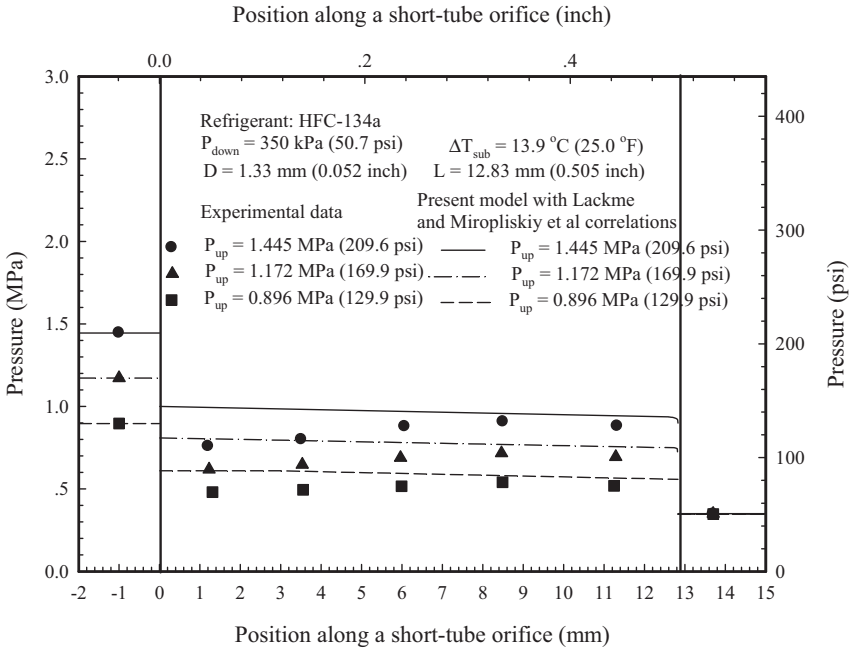

Fig. 7. Comparison of measured pressure distribution with numerical results at different upstream pressure.

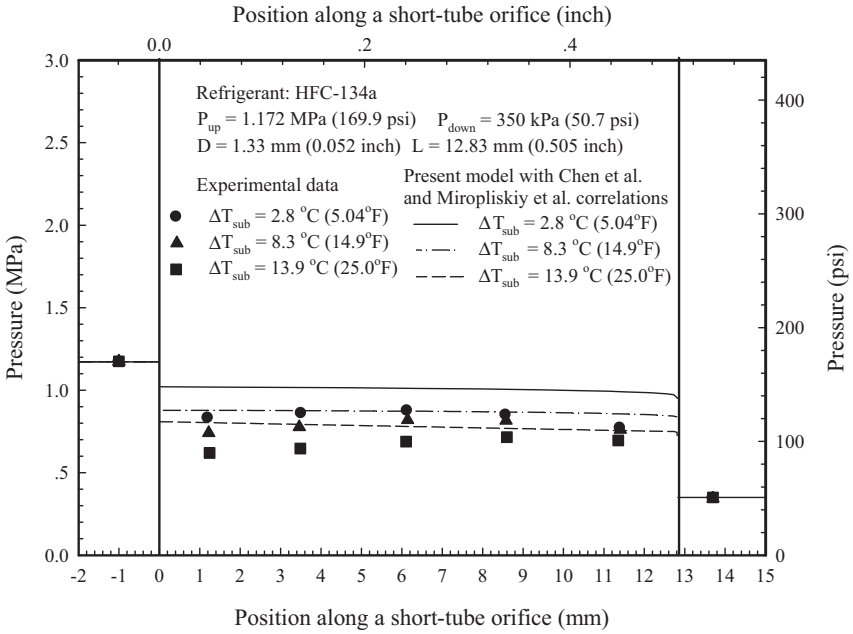

Fig. 8. Comparison of measured pressure distribution with numerical results at different degree of subcooling.

Solution method

The calculation procedure of the mass flow rate inside the short-tube orifice is presented by using the flow chart as shown in Figure 2. The thermodynamic properties and initial conditions, including upstream pressure, diameter, length, and degree of subcooling are specified. The thermodynamic properties of refrigerants are computed as a function of the pressure by using REFPROP (McLinden et al. 1998). As described above, the refrigerant flow behavior inside the short-tube orifice is separated into three sections, subcooled liquid region, metastable liquid region, and two-phase region. The surface roughness of drawn brass ($\varepsilon = 0.0000015$ m [0.0000049 ft.]) is assumed and used for Equation 5. To calculate the subcooled liquid length, the saturation pressure corresponding to the inlet temperature and friction factor obtained from the Colebrook equation are determined and applied into Equation 7. Similarly, the metastable liquid length is calculated by using Equation 8 with the correlation of actual pressure of vaporization. In this study, two correlations of actual vapor pressure obtained from Lackme (1979) and Chen et al. (1990) are considered. In the case of a two-phase region, short-tube orifice length is separated into numerous sections. The refrigerant pressure, which is calculated at the ending of the metastable liquid flow, is the initial condition of two-phase flow region. The fourth-order Runge-Kutta method is used to solve the system of differential equations, which are presented by Equations 38 and 39. The computation of each section is run until the choked flow phenomenon is appeared. Under choked flow condition, the refrigerant velocity reaches sonic speed and the entropy at the exit plane is equal to the maximum value. To verify the appearance of choked flow, the entropy increment at the exit plane of tube is inspected. That is, the choked flow occurs as the entropy increment is negative. The entropy of two-phase flow of each section can be estimated by:

$$s_i = s_L(1 - x_i) + s_G x_i. \tag{40}$$

After the choked flow appears, the length of the two-phase region can be calculated by:

$$L_{tp} = \Delta z n, \tag{41}$$

where n is number of sections. Therefore, the calculated length is the summation of lengths in the subcooled liquid region, metastable liquid region and two-phase flow:

$$L_{cal} = L_{sub} + L_{mt} + L_{tp}. \tag{42}$$

To obtain the critical mass flow rate under a given short-tube orifice length, the iteration procedure is done until the calculated length (L_{cal}) and the actual length are equal. That is, as the calculated length is higher than the actual length, the mass flow rate is increased. Conversely, the mass flow rate decreases when the calculated length is less than the actual length.

Results and discussion

To confirm the accuracy of the present model, the numerical results of mass flow rate and distribution of pressure inside the short-tube orifice are compared with the experimental data under choked flow conditions. The present model with three correlations of slip ratio (Chisholm 1973; Miropolskiy et al. 1970; Zivi 1964) and two correlations of actual pressure of vaporization (Chen 1990; Lackme 1979) are proved. The experimental data, which are used to validate the numerical results,

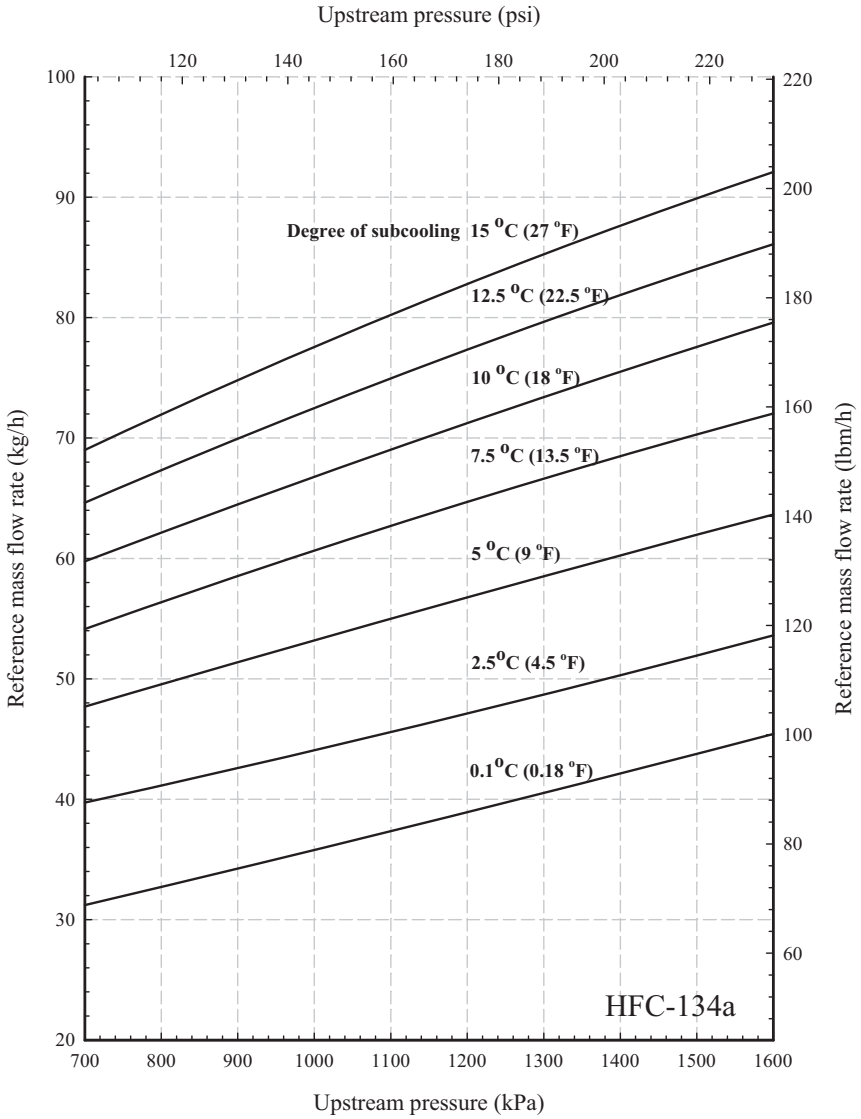

Fig. 9. Short-tube orifice selection chart generated from the present model for HFC-134a ($D = 1.1$ mm (0.043 in.) and $L = 12.7$ mm (0.5 in.)).

include 279 data points for HFC-134a (Kim 1993; Nilpueng and Wongwises 2009; Singh et al. 2001), 122 data points for HFC-407C (Payne and O'Neal 1998), and 95 data points for HFC-410A (Payne and O'Neal 1999; Kim et al. 2005). The testing conditions of experimental data are listed in Table 1.

The comparisons between the experimental and calculated mass flow rate at different upstream pressures are presented in Figure 3. It is found that the calculated results show good agreement with the experimental data, especially, the model with correlations of Lackme (1979) and Miropolskiy et al. (1970), which gives the MAD (mean absolute deviation) of 4.78%. It is also clear that the mass flow rate obtained from the present model increases in direct proportion as the upstream pressure is increased. This is because, based on the numerical results, the difference of pressure across the short-tube orifice is increased as the upstream pressure increases. This leads to an increase of mass flow rate. On the other hand, it is also observed that the upstream density is decreased when the upstream pressure is increased which results in the decrease of mass flow rate. However, the influence of the difference of pressure across the short-tube orifice dominates the influence of refrigerant density, which results in an increase of the refrigerant flow rate. In addition, based on the calculations in the present model, it is found that the prediction of underpressure (Ps - Pv) obtained from Lackme correlation is higher than that obtained from Chen correlation, about 42.5%.

Figure 4 shows the effect of degree of subcooling on the mass flow rate by comparing the experimental data with the numerical results. The tendency of calculated mass flow rate and experimental results is consistent. The prediction of the present model using Chen et al. (1990) and Miropolskiy et al. (1970) correlations gives the smallest mean absolute deviation (MAD), which is 1.32%. The numerical results indicate that the mass flow rate proportionally enhanced when the degree

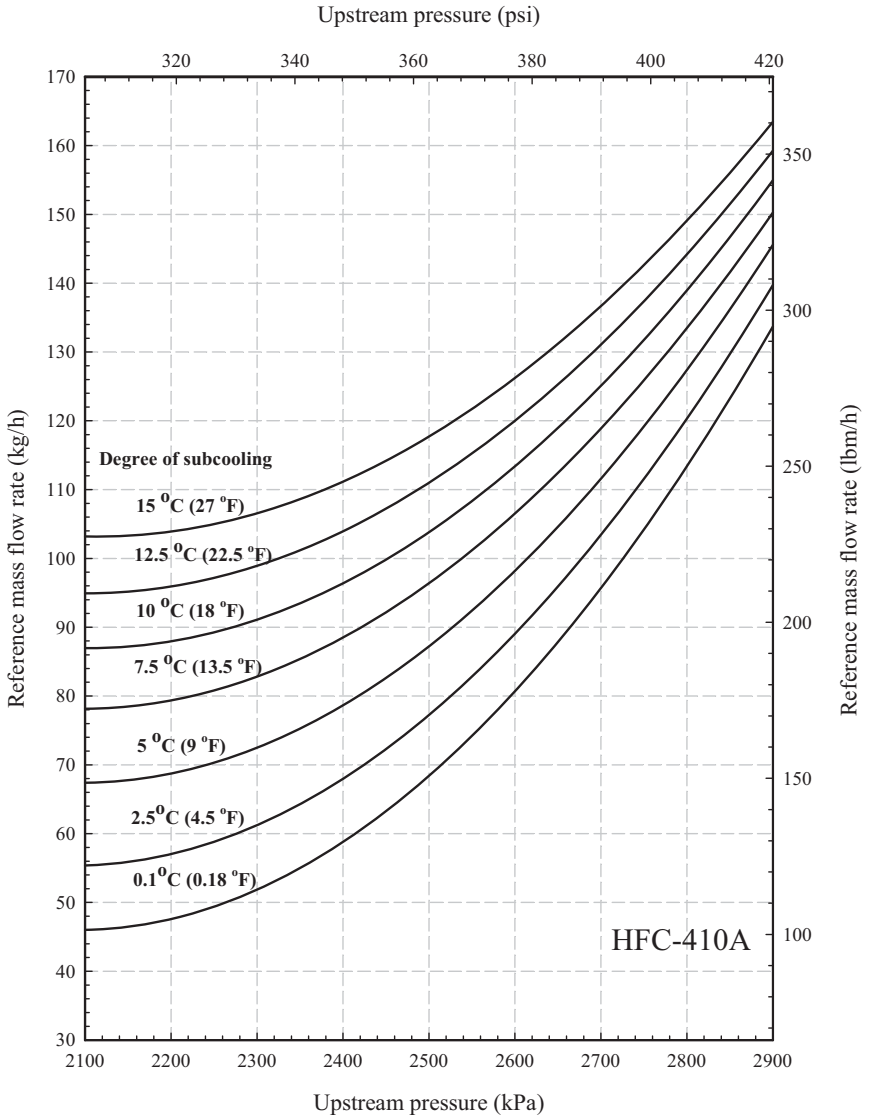

Fig. 10. Short-tube orifice selection chart generated from thepresent model for HFC-410A ($D = 1.1$ mm (0.043 in.) and $L = 12.7$ mm (0.5 in.)).

of subcooling increased. This is because the increase of degree of subcooling results in an increase of upstream density and the difference of pressure across the short-tube orifice, which results in an increase of mass flow rate.

The influence of short-tube orifice diameter on the mass flow rate is presented in Figure 5. It is found that the mass flow rate is strongly increased by enlarging short-tube orifice diameter. This is because the increase of diameter results in an increase of cross-sectional flow area. All of the calculated results give acceptable predictions compared with the measured data. However, the proposed model with Chen et al. (1990) and Miropolskiy et al. (1970) correlation shows the best prediction with MAD of 4.52%.

As mentioned above, the tendency of numerical results is estimated and compared with the experimental data at different sizes of short-tube orifice and working conditions. However, to verify the accuracy of the model at the same condition, the MAD between the numerical results and all experimental data is also examined. Based on the 496 data points of experimental results of HFC-134a, HFC-407C, and HFC-410A, the MAD of mass flow rate are estimated as showed in Table 2. It is found that the present model with Chen et al. (1990) and Chisholm (1973) gives the best prediction for HFC-134a, whereas the present model with Lackme (1979) and Miropolskiy et al. (1970) gives the best prediction for HFC-407C and HFC-410A. However, for all refrigerant types, the present model with the correlations of Lackme (1979) and Miropolskiy et al. (1970) shows the best calculation with MAD of 11.86%. In addition, the calculated results from the model with Lackme (1979) and Miropolskiy et al. (1970) correlations is compared with the measured mass flow rate (Figure 6). It is found that the present model can describe 98.2% of mass flow rate within

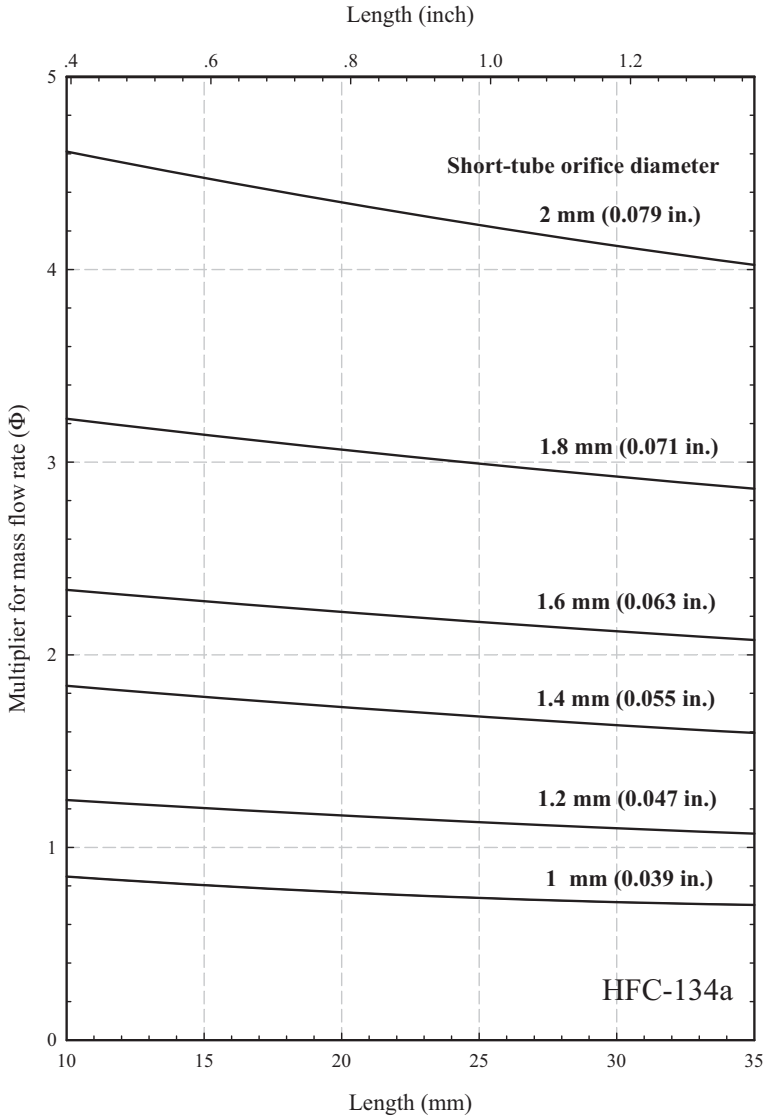

Fig. 11. Multiplier for mass flow rate to be applied to Figure 9 for other diameter and lengths of short-tube orifice.

±20%. Comparing the accuracy of this model with the two-fluid model (Yang and Zhang 2005), it is found that, for the two-fluid model, the relative deviations of 94% data are within 20%. This indicates that the relative deviation obtained from both models is similar. However, it can be noted that the two-fluid model is rather complicated when it is included with the six governing equations.

Figure 7 depicts the relationship between the pressure distribution and upstream pressure obtained from experimental data and the present model with the correlation of Lackme (1979) and Miropolskiy et al. (1970). The average of pressure distribution along the short-tube orifice is enhanced with increasing the upstream pressure. It is also discovered that the pressure decreases suddenly at the inlet, while it slightly increases over a short length and gradually decreases thereafter inside the short-tube orifice. This phenomenon indicates that the vena contracta occur inside the short tube- orifice. The reasons for the variation of pressure inside the short-tube are due to the increase of flow area after the vena contracta, and wall shear stress. In the model, the equation of head loss at the inlet section indicates the loss of flow due to sudden contraction after the refrigerant flow past the inlet section. However, the model does not include the flow behavior at the vena contracta. As a consequence, the variation of pressure obtained from numerical model is inconsistent with experimental results at the vena contracta, whereas it agrees with experimental results after the vena contracta. The large pressure drop at the outlet section can be explained by choked flow phenomenon. Under the choked flow condition, the pressure at the exit plane reaches the infinity value. In addition, the numerical results give an average overestimation of 9.54%. It is also found that the calculated mass flow rate shows good agreement with the experimental data with a MAD of 3.12%.

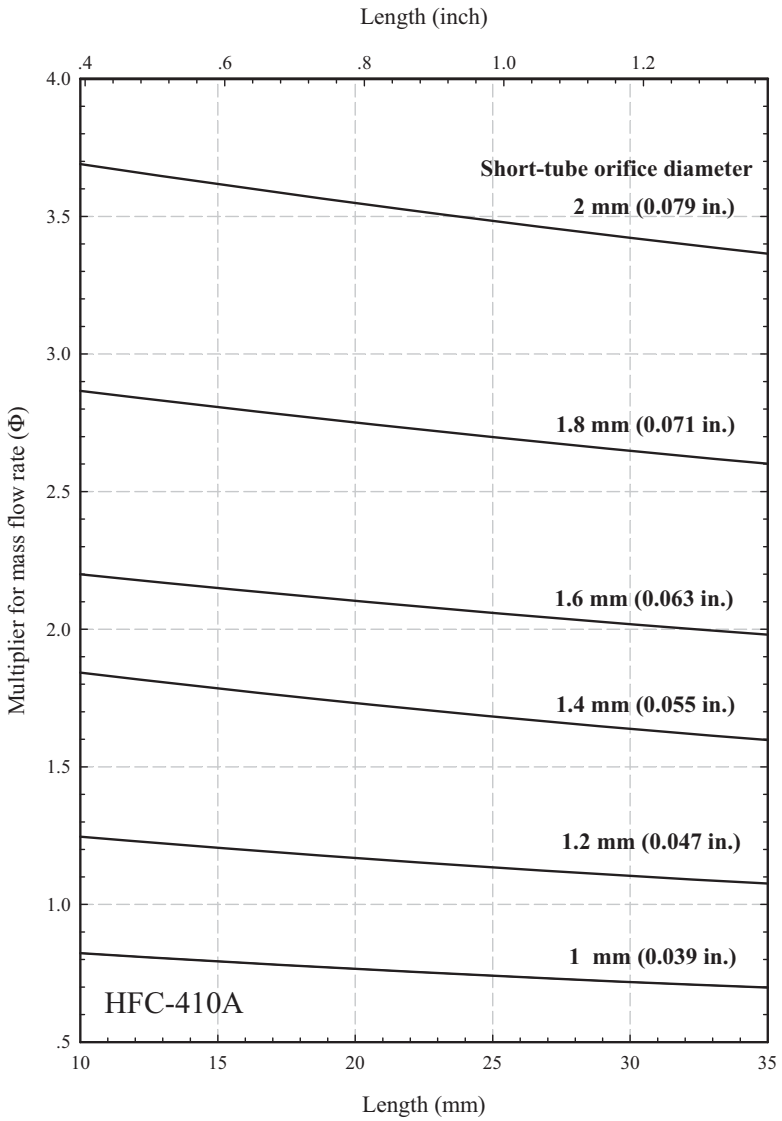

Fig. 12. Multiplier for mass flow rate to be applied to Figure 10 for other diameter and lengths of short-tube orifice.

The comparison of pressure distribution inside the short-tube orifice obtained from numerical and experimental results at different degrees of subcooling are shown in Figure 8. The present model gives an average over-prediction of 11.98%. It can be seen that the increase of degree of subcooling results in the decrease of average pressure along the short-tube orifice. This is due to, based on the numerical calculation, the difference of upstream and critical pressure, and upstream density is increased as the degree of sub-cooling is increased. These effects result in an increase of the refrigerant velocity. Therefore, the average refrigerant pressure along the short-tube orifice decreases. In addition, the predicted mass flow rate agrees well with the experimental data and gives the MAD of 2.64%.

In order to utilize the present numerical model in practical applications, the selection charts, which are generated for various condenser pressures and degree of sub-cooling at given short-tube orifice diameters and lengths, are presented for HFC-134a and HFC-410A. The proposed charts are similar to the rating chart for flow through capillary tube developed by ASHRAE (1998). For a short-tube orifice having a diameter of 1.1 mm (0.043 in.) and a length of 12.7 mm (0.5 in.), the mass flow rate can be estimated directly from selection charts (Figures 9 and 10) by specifying the condenser pressures and degree of subcooling. However, under the different size of diameter and length, the multiplier obtained from correction charts is required (Figures 11 and 12). Based on the proposed selection charts, the MAD of the mass flow rate is 9.48% and 16.04% for HFC-134a and HFC-410A, respectively.

Conclusion

The numerical simulation for calculating the flashing flow of refrigerant along the short-tube orifices is presented. The

precision of the present model is verified with 496 data points of experimental results of HFC-134a, HFC-407C, and HFC-410A. The results show that the calculated mass flow rate and pressure distribution through the short-tube orifice give reasonable agreement with the experimental data. The proposed model with the correlation of Lackme (1979) and Miropolskiy et al. (1970) shows the best prediction with MAD of 11.86%. This implied that the proposed model with appropriate correlations of slip ratio and actual vapor pressure can be used to calculate the refrigerant flow characteristic inside the short-tube orifice. Moreover, based on the present model with Lackme (1979) and Miropolskiy et al. (1970) correlations, the selection charts are also proposed to calculate the refrigerant mass flow rate along short-tube orifices.

Acknowledgments

The present study is supported by the Thailand Research Fund, the Office of the Higher Education Commission, and the National Research University Project whose guidance and assistance are gratefully acknowledged.

Nomenclature

A = cross section area of tube, m^2 (ft^2)
C = circumference of tube, m (ft)
D = diameter of tube, m (ft)
f = friction factor
g = gravitational acceleration, m/s^2 (ft/s^2)
G = mass flux, kg/m^2 s (lbm/ft^2 s)
h = specific enthalpy, J/kg (Btu/lbm)
L = length, m (lbm)
$\dot{m}$ = mass flow rate, kg/s (lbm/s)
P = pressure, Pa (psi)
q'' = heat flux, W/m^2 (Btu/lbm^2 h)
Re = Reynolds number
S = slip ratio
s = specific entropy, J/kg K (Btu/lbm °R)
T = temperature, K (°R)
V = velocity, m/s (ft/s)
x = vapor quality
z = horizontal position, m (ft)

Greek symbols

α = void fraction
ε = wall roughness, m (ft)
μ = dynamic viscosity, kg/m s (lb s/ft^2)
ρ = density, kg/m^3 (lbm/ft^3)
σ = surface tension, N/m (lb/ft)
τ = shear stress, N/m^2 (lb/ft^2)
υ = specific volume, m^3/kg (ft^3/lbm)

Subscripts

G = vapor phase
L = liquid phase
in = inlet condition
i = liquid-vapor interface
Lw = liquid-wall interface
mt = metastable region
s = saturated condition
sp = single-phase
sub = subcooling
tp = two-phase
v = vaporization

References

Aaron, A.A.20, and P.A. Domanski. 1990. Experimentation analysis and correlation of refrigerant-22 flow through short tube restrictors. *ASHRAE Transactions* 96:729–42.

ASHRAE. 1998. *ASHRAE Handbook*—Refrigeration, chap. 45. Atlanta, GA: ASHRAE.

ASME. 1971. *Fluid Meters—Their Theory and Application*. New York: American Society of Mechanical Engineers.

Chen, Z.H., R.Y. Li, S.Lin, and Z.Y. Chen. 1990. A correlation for metastable flow of refrigerant 12 through capillary tubes. *ASHRAE Transactions* 96:550–4.

Chisholm, D. 1973. Pressure gradient due to friction during the flow of evaporating two-phase mixture in smooth tube and channel. *International Journal of Heat and Mass Transfer* 16:347–58.

Choi, J., J.T. Chung, and Y. Kim. 2004. A generalized correlation for two-phase flow of alternative refrigerants through short tube orifices. *International Journal of Refrigeration* 27:393–400.

Collier, J.G., and J.R. Thome. 1996. *Convective Boiling and Condensation, 3rd ed.* Oxford University Press, New York.

Garcia-Valladares, O. 2006. Numerical simulation of trans-critical carbon dioxide (R744) flow through short tube orifices. *Applied Thermal Engineering* 144–51.

Kim, Y. 1993. Two-phase flow of HFC134a and HCFC22 through short tube orifices. Ph.D. Thesis, Texas A&M University, College Station, TX.

Kim, Y., and D.L. O'Neal. 1995. A comparison of critical flow models for estimating two-phase flow of HCFC22 and HFC134a through short tube orifices. *International Journal of Refrigeration* 18:447–55.

Kim, Y.C., W.V. Payne, D.L. O'Neal, and M. Farzad. 2002. Refrigerant flow through flexible short tube orifices. *HVAC&Research* 8:179–90.

Kim, Y., V. Payne, J. Choi, and P. Domanski. 2005. Mass flow of R410A through short tube working near the critical point. *International Journal of Refrigeration* 28:547–53.

Lackme, C. 1979. Incompleteness of the flashing of supersaturated liquid and sonic ejection of the produced phases. *International Journal of Multiphase Flow* 5:131–41.

Liu, J.P., Y.M. Niu, J.P. Chen, Z.J. Chen, and X. Feng. 2004. Experimental and correlation of R744 two-phase flow through short tubes. *Experimental Thermal and Fluid Science* 28:565–73.

McLinden, M.O., S.A. Klein, and E.W. Lemmon. 1998. REFPROP-thermodynamic and transport properties of refrigerant and refrigerant mixtures. NIST Standard Reference Database, Version 6.01.

Mei, V.C. 1982. Short-tube refrigerant flow restrictors. *ASHRAE Transactions* 88:157–69.

Miropolskiy, Z.L., R.I. Shneyerova, and A.I. Karamysheva. 1970. Vapour void fraction in steam fluid mixture flowing in heated and unheated channels. *International Heat Transfer Conference, Paris, France, August 31–September 5,* paper B4.75.

Nilpueng, K., and S. Wongwises. 2009. Experimental investigation of two-phase flow characteristics of HFC-134a through short-tube orifices. *International Journal of Refrigeration* 32:854–64.

Pasqua, P.F. 1953. Metastable flow of Freon-12. *Refrigeration Engineering* 61:1084–8.

Payne, W.V., and D.L. O'Neal. 1998. Mass flow characteristics of R407C through short-tube orifices. *ASHRAE Transactions* 104:197–209.

Payne, W.V., and D.L. O'Neal. 1999. Multiphase flow of refrigerant 410A through short tube orifices. *ASHRAE Transactions* 105: 66–74.

Singh, G.M., P.S. Hrnjak, and C.W. Bullard. 2001. Flow of refrigerant R134a through orifice tubes. *HVAC&R Research* 7: 245–62.

Tu, X., P.S. Hrnjak, and C.W. Bullard. 2006. Refrigerant 134a liquid flow through micro-scale short tube orifices with/without phase change. *Experimental Thermal and Fluid Science* 30:253–62.

Wongwises, S., and M. Suchatawat. 2002. A simulation for predicting the refrigerant flow characteristics including metastable region in adiabatic capillary tubes. *International Journal of Energy Research* 27:93–109.

Yang, L., and C.-L. Zhang. 2005. Two-fluid model of refrigerant two-phase flow through short tube orifice. *International Journal of Refrigeration* 28:419–27.

Zhang, C-L., and L. Yang. 2005. Modeling of supercritical CO_2 flow through short tube orifice. *Journal of Fluid Engineering, Transactions of ASME* 127:1194–8.

Zivi, S.M. 1964. Estimation of steady-state steam void fraction by means of the principle of minimum entropy production. *ASME Journal of Heat Transfer* 86:247–52.

Provided for non-commercial research and education use.
Not for reproduction, distribution or commercial use.

This article appeared in a journal published by Elsevier. The attached copy is furnished to the author for internal non-commercial research and education use, including for instruction at the authors institution and sharing with colleagues.

Other uses, including reproduction and distribution, or selling or licensing copies, or posting to personal, institutional or third party websites are prohibited.

In most cases authors are permitted to post their version of the article (e.g. in Word or Tex form) to their personal website or institutional repository. Authors requiring further information regarding Elsevier's archiving and manuscript policies are encouraged to visit:

http://www.elsevier.com/copyright

Author's personal copy

International Communications in Heat and Mass Transfer 42 (2013) 62–68

Contents lists available at SciVerse ScienceDirect

International Communications in Heat and Mass Transfer

journal homepage: www.elsevier.com/locate/ichmt

Heat transfer and single-phase flow in internally grooved tubes ☆

K. Aroonrat [a], C. Jumpholkul [a], R. Leelaprachakul [b], A.S. Dalkilic [c], O. Mahian [d], S. Wongwises [a,e,*]

[a] Fluid Mechanics, Thermal Engineering and Multiphase Flow Research Lab. (FUTURE), Department of Mechanical Engineering, Faculty of Engineering, King Mongkut's University of Technology Thonburi, Bangmod, Bangkok 10140, Thailand
[b] Thai-German Products Public Company Limited, Thailand
[c] Heat and Thermodynamics Division, Department of Mechanical Engineering, Yildiz Technical University (YTU), Yildiz, Besiktas, Istanbul 34349, Turkey
[d] Young Researchers Club, Mashhad Branch, Islamic Azad University, Mashhad, Iran
[e] The Academy of Science, The Royal Institute of Thailand, Sanam Suea Pa, Dusit, Bangkok 10300, Thailand

ARTICLE INFO

Available online 20 December 2012

Keywords:
Nusselt number
Friction factor
Grooved tube
Type 304 stainless steel

ABSTRACT

This study investigates heat transfer and flow characteristics of water flowing through horizontal internally grooved tubes. The test tubes consisted of one smooth tube, one straight grooved tube, and four grooved tubes with different pitches. All test tubes were made from type 304 stainless steel. The length and inner diameter of the test tube were 2 m and 7.1 mm, respectively. Water was used as working fluid, heated by DC power supply under constant heat flux condition. The test runs were performed at average fluid temperature of 25 °C, heat flux of 3.5 kW/m^2, and Reynolds number range from 4000 to 10,000. The effect of grooved pitch on heat transfer and pressure drop was also investigated. The performance of the grooved tubes was discussed in terms of thermal enhancement factor. The results showed that the thermal enhancement factor obtained from groove tubes is about 1.4 to 2.2 for a pitch of 0.5 in.; 1.1 to 1.3 for pitches of 8, 10, and 12 in., respectively; and 0.8 to 0.9 for a straight groove.

© 2012 Elsevier Ltd. All rights reserved.

1. Introduction

The energy crisis plays a major role on human lifestyle in today's world. Utilizing energy efficiently by improving heat transfer performance of a heat exchanger is one method to correct this problem. Moreover, heat exchanger size and material cost are reduced for the given application. In recent years, several researchers use heat transfer enhancement techniques to increase performance of the heat exchanger. One heat transfer enhancement technique modified the surface to promote turbulent flow and increase the heat transfer area; this is known as “rough surface technique”. Many kinds of tubes with enhanced surfaces—that is, grooved tubes—are made using this technique. Internally grooved tubes provide swirl to facilitate better fluid mixing and reduce the boundary layer thickness in comparison to a smooth tube. They are widely used instead of smooth tubes in heat exchangers because they are easy to manufacture and yield effective heat transfer augmentation.

Over the years, experimental studies on heat transfer and flow characteristics of fluid flow inside straight tubes have been carried out by numerous researchers. However, there have been few investigations concerned with heat transfer and pressure drop of internally grooved tubes. Publications on heat transfer and flow characteristics of fluid flow in internally grooved tube are summarized as follows.

A study of heat transfer and pressure drop during condensation of R134a in an axially grooved copper tube was conducted by Graham et al. [1]. In comparison with the enhancement factor of a helically grooved tube, the enhancement factor for an axially grooved tube was significant lower at mass flux of 75 kg/m^{2}s, whereas it was higher over a mass flux range of 150–450 kg/m^{2}s. Goto et al. [2] measured heat transfer coefficient and pressure drop of R410A and R22 during evaporation and condensation inside internally grooved tubes. The obtained heat transfer data reported that the evaporation and condensation heat transfer coefficient of a herring-bone grooved tube was higher than that of a spiral grooved tube. Zhang et al. [3,4] experimented with evaporation heat transfer of R417A (R125/R134a/R600) flowing inside horizontal smooth and two internally grooved tubes with different geometrical parameters. All tested tubes were made of copper. The study's results revealed that the heat transfer coefficient of R417A obtained from internally grooved and smooth tubes were lower than that of R22. Based on the data of R417A, an empirical correlation for microfin tubes was developed by introducing the enhancement factors into the modified Kattan model. Bharadwaj et al. [5] presented heat transfer and pressure drop characteristics of water flowing inside 75-start spirally grooved copper tube with a twisted tape insert. In this experiment, laminar to fully turbulent ranges of Reynolds numbers were considered. In comparison with a smooth tube, the heat transfer enhancement obtained from a grooved tube—with and without twisted tape—increased

☆ Communicated by W.J. Minkowycz.

* Corresponding author at: The Academy of Science, The Royal Institute of Thailand, Sanam Suea Pa, Dusit, Bangkok 10300, Thailand.
E-mail address: somchai.won@kmutt.ac.th (S. Wongwises).

0735-1933/$ – see front matter © 2012 Elsevier Ltd. All rights reserved.
http://dx.doi.org/10.1016/j.icheatmasstransfer.2012.12.001

Author's personal copy

Nomenclature

A	Surface area of the test section (mm^2)
C_p	Specific heat at constant pressure (J/kg-K)
d	Tube diameter (mm)
e	Grooved depth (mm)
f	Friction factor
h	Heat transfer coefficient (W/m^2-K)
I	Electric current (A)
k	Thermal conductivity (W/m-K)
L	Length of the test tube (mm)
m	Mass flow rate (kg/s)
Nu	Nusselt number
P	Pressure (Pa)
Pr	Prandtl number
p	Grooved pitch (mm)
Q	Heat transfer rate (W)
q″	Heat flux (kW/m^2)
Re	Reynolds number
r	Radius (mm)
T	Temperature (°C)
u	Flow velocity at the inlet of test tube (m/s)
V	Electric voltage (V)
w	Grooved width (mm)

Greek symbols

μ	Dynamic viscosity (kg/m-s)
β	Helix angle (deg)
ρ	Density (kg/m^3)
ε	Tube roughness (mm)
ΔP	Pressure drop (Pa/m)

Subscripts

avg	Average
e	Electric heater
f	Water
i	Inside
in	Inlet
l	Liquid
o	Outside
out	Outlet
ss	Stainless steel type 304
wi	Inner wall
wo	Outer wall

largely in laminar and moderately in turbulent range of Reynolds numbers. Bilen et al. [6] investigated the Nusselt number and friction factor of air flowing through a grooved tube with different geometric grooved shapes: circular, trapezoidal, and rectangular. These grooved tubes were made of stainless steel and had an inner diameter of 36 mm. The test runs were performed in the Reynolds number range from 10,000 to 38,000. Correlations of Nusselt number and friction factor were obtained for different grooved tubes. An experimental investigation on the thermal performance of an inclined grooved copper heat pipe using water-based CuO nanofluid as the working fluid was performed by Lui et al. [7]. The experimental results showed that the inclination angle had a strong effect on heat transfer performance of heat pipes using both water and nanofluid. The thermal performance of an inclined grooved heat pipe was strengthened by using CuO nanofluid.

Wongwises et al. [8] presented the experimental investigations of evaporative heat transfer coefficient and pressure drop of R-134a flowing inside internally grooved tubes. One smooth tube and four grooved tubes, made from stainless steel, were tested. The study indicated that the grooved tubes had a significant effect on the heat transfer coefficient and pressure drop augmentations.

Among several papers described above, most experimental studies focused on heat transfer and flow characteristics of fluid flowing inside copper grooved tubes. The flow and heat transfer studies in stainless steel grooved tubes have received relatively little attention in literature. To the best of the authors' knowledge, aside from the authors' previous paper, there has been only one work—carried out by Bilen et al. [6]—dealing with stainless steel grooved tubes. However, the experimental work carried out by Bilen et al. [6] focused on the flow of air, which seems not applicable in real use.

As a consequence, the objective of this current work is to study the heat transfer and flow characteristics of water flowing through internally grooved tubes made from stainless steel. The effect of grooved pitch on heat transfer and pressure drop was also investigated. Experimental data that have never been published are presented on heat transfer and pressure drop.

2. Experimental apparatus

The experimental system used for this study is shown schematically in Fig. 1. It was mainly comprised of a test tube, DC power supply, storage tank No. 1, storage tank No. 2, magnetic gear pump, and a rotameter. In this experiment, the temperature of the fluid inside storage tank No.1 was adjusted to about 25 °C. Condensing unit No. 1 and heater was used to keep the fluid temperature constant. The fluid was forced through the loop by a magnetic gear pump, which could be adjusted for flow rate by using an inverter. The test section was heated uniformly by the regulated DC power supply for a constant heat flux condition. The voltage and electrical current values were measured by a multimeter. Leaving the test section, the fluid was collected in storage tank No. 2. This storage tank was equipped with condensing unit No. 2 and a heater to reduce the temperature of the fluid to about 25 °C. Finally, the fluid returned to storage tank No. 1 to complete the cycle.

Fig. 2 shows a schematic diagram of the test section. The test sections were comprised of one smooth tube (SMT), one straight grooved tube (SGT), and four helical grooved tubes having different pitches of 0.5 (GT0.5), 8 (GT8), 10 (GT10), and 12 in. (GT12)—all made from stainless steel type 304. The sketch of the grooved tube is shown in Fig. 3, and the dimensions of the test sections are listed in Table 1. The differential pressure transmitter was mounted at both ends of the test section to measure the pressure drop. The inlet and exit temperature of the fluid were measured directly by using T-type thermocouples. The eight thermocouples were installed at different longitudinal positions on the surface of the test section to measure the wall temperatures. These thermocouples were fixed on the outer surface of the test section using heat-resistant tape (NITOFLON No. 973UL-S). The test section was insulated with fiberglass and rubber insulation to prevent heat loss in a radial direction. All of the thermocouples were well calibrated by standard thermometers with a precision of 0.1 °C. In addition, the differential pressure transducer was specially calibrated by the manufacturer.

When the system approached the steady state, we recorded the pressure drop of the fluid along the test section, the electrical power supply to the test section, the wall temperature of the test section, and the inlet and exit temperatures of the fluid at the test section. The range of experimental conditions tested in this study is listed in Table 2. The uncertainties of measured quantities and calculated parameters calculated from the root mean sum square method are shown in Table 3.

3. Data reduction

The following calculation was employed to determine the Reynolds number, the Nusselt number, and friction factors from the data recorded during each test run at steady state conditions.

Author's personal copy

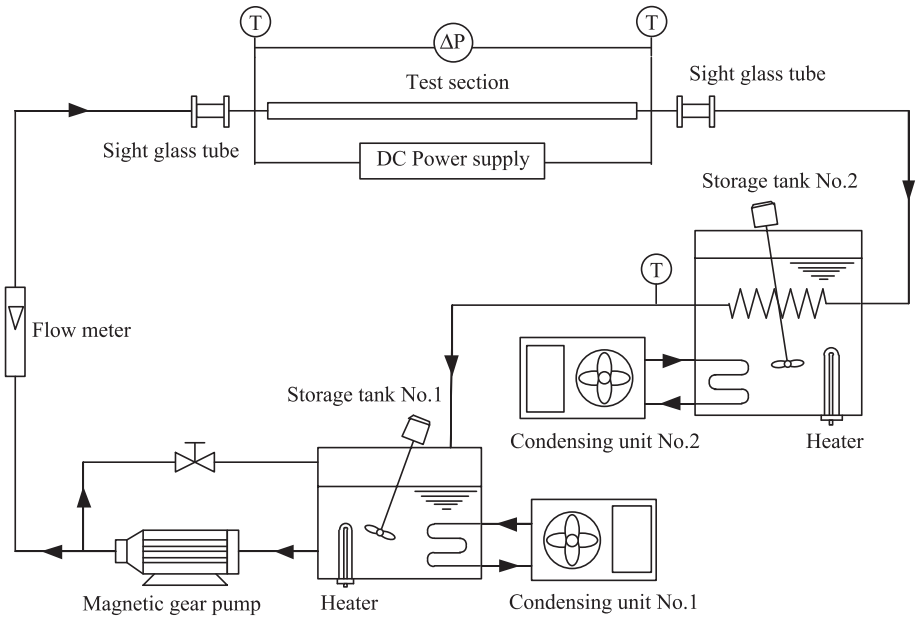

Fig. 1. Schematic diagram of the experimental apparatus.

3.1. Reynolds number (Re)

The Reynolds number was defined based on the inner diameter and flow velocity at the inlet of the test tube as

$$Re = \frac{\rho u d_i}{\mu} \tag{1}$$

where ρ is the density of water, u is the flow velocity of water at the inlet of the test section, d_i is the inner diameter of the test tube, and μ is dynamic viscosity of water.

3.2. Nusselt number (Nu)

The Nusselt number was calculated as follows:

$$Nu = \frac{h_{avg} d_i}{k_l} \tag{2}$$

where h_{avg} is the average heat transfer coefficient of water flowing inside the test section, and k_l is thermal conductivity of liquid water. The average *heat transfer coefficient* was determined by using the following equation:

$$h_{avg} = \frac{Qe}{A_i\left(T_{avg,wi} - T_{avg,f}\right)} \tag{3}$$

where $T_{avg,f}$ is the average temperature of water at the test section inlet and outlet, $T_{avg,wi}$ is the average temperature of the inner wall, A_i is the actual inside surface area of the test section, and Q_e is the electrical energy supplied to the test tube, which was obtained from:

$$Q_e = VI \tag{4}$$

where I and V are the current and voltage of the electric heater, respectively. The heat gained by the fluid inside the test tube (Q_f) can be calculated as

$$Q_f = m_f c_p\left(T_{f,out} - T_{f,in}\right) \tag{5}$$

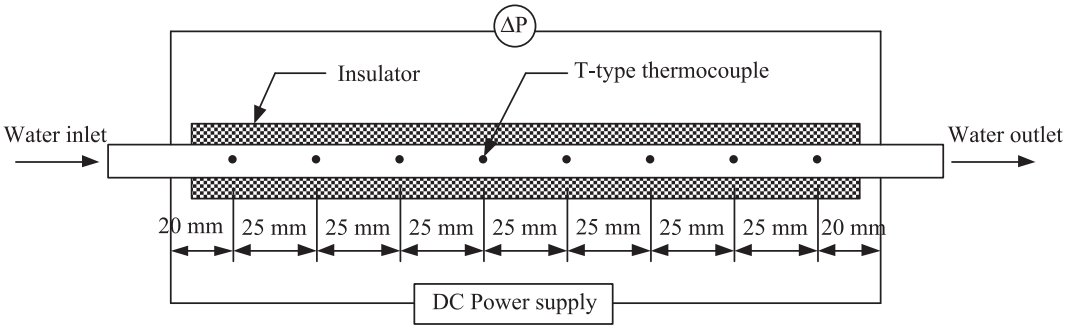

Fig. 2. Schematic diagram of the test section.

Author's personal copy

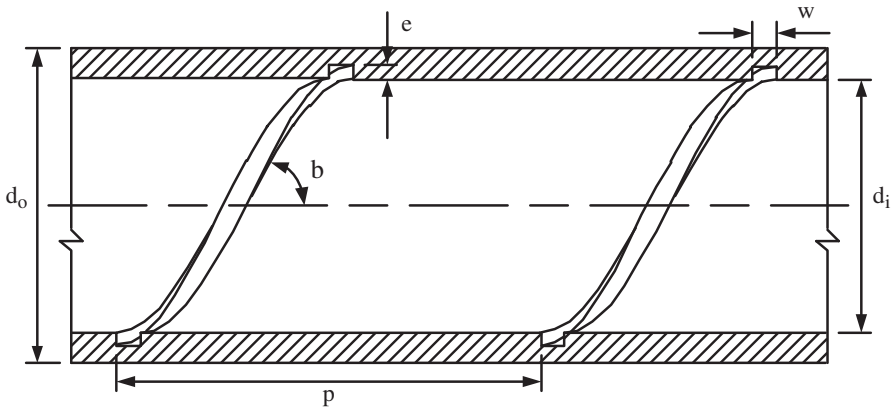

Fig. 3. Sketch of a grooved tube.

where m_f is the mass flow rate of the water entering the test section, and ($T_{f,out}$-$T_{f,in}$) is the difference in water temperature between the outlet and inlet positions. In this experiment, the heat gained by water flowing inside the test section was within 10% lower than the electrical energy supplied to the test tube.

The outer wall temperatures (T_{wo}) were measured by eight thermocouples installed at the outer wall of the test tube. These outer wall temperatures were used to determine the inner wall temperatures (T_{wi}), which can be solved by using the one-dimensional heat conduction equation in cylindrical coordinates as

$$T_{wi} = T_{wo} - \frac{Q_e\left(1n\frac{r_o}{r_i}\right)}{2\pi L k_{ss}} \tag{6}$$

where k_{ss} is the thermal conductivity of stainless steel, and L is the test tube length.

3.3. Friction factor (f)

The friction factor (f) for fully developed flow in a circular tube was determined by measuring the pressure drop across the test tube, as follows:

$$f = \frac{\Delta P}{\left(\frac{L}{d_i}\right)\frac{\rho u^2}{2}} \tag{7}$$

where ΔP is the pressure drop between the entrance and exit of the test tube measured by the differential pressure transmitter.

4. Results and discussion

The present study was performed to investigate the effect of pitch on the heat transfer coefficient and pressure drop of water inside grooved tubes. Before measuring the Nusselt number of water in grooved tubes, the measured Nusselt number for the plain tube was confirmed by comparing with correlation results provided by Dittus and Boelter [9] and Gnielinski [10]. The Dittus–Boelter equation is defined as

$$Nu = 0.023\ Re^{0.8}Pr^{0.4} \tag{8}$$

The correlation proposed by Gnielinski is expressed as follows:

$$Nu = \frac{\left(\frac{f}{8}\right)(Re-1000)Pr}{1+12.7\left(\frac{f}{8}\right)^{0.5}\left(Pr^{\frac{2}{3}}-1\right)} \tag{9}$$

The friction factor obtained from the smooth tube was compared with the correlations proposed by Blasius [11] and Colebrook [12].

The Blasius equation was presented in the following form:

$$f = 0.316Re^{-\frac{1}{4}} \tag{10}$$

The Colebrook equation was defined as

$$\frac{1}{\sqrt{f}} = -2.0\log\left(\frac{\frac{\varepsilon}{d_i}}{3.7}+\frac{2.51}{Re\sqrt{f}}\right) \tag{11}$$

As shown in Figs. 4 and 5, these indicate that the data trends correspond to these correlation results.

4.1. Nusselt number

Fig. 6 represents the relationship between the Nusselt number and Reynolds number in the smooth tube, straight grooved tube, and the helical grooved tubes having different pitches of 0.5, 8, 10, and 12 in. at heat flux of 3.5 kW/m^2, average fluid temperature of 25 °C, and the

Table 1
The details of the test sections.

Test tube	e (mm)	w (mm)	p (mm)	β (Degree)	d_o (mm)	d_i (mm)	N_s	A_c (mm^2)	A_i (mm^2)	L (mm)
SMT	–	–	–	–	9.5	7.1	–	39.6	44,611	2000
SGT	0.2	0.2	–	–	9.5	7.1	12	42	54,210	2000
GT0.5	0.2	0.2	12.7	60	9.5	7.1	10	41.6	61,497	2000
GT8	0.2	0.2	203	6.3	9.5	7.1	10	41.6	52,658	2000
GT10	0.2	0.2	254	5	9.5	7.1	10	41.6	52,641	2000
GT12	0.2	0.2	305	4.2	9.5	7.1	10	41.6	52,632	2000

Remarks: e = grooved depth, w = grooved width, p = grooved pitch, β = helix angle, d_o = outside diameter, d_i = inside diameter, N_s = number of start, A_c = cross section area, A_i = inside surface area, L = length.

Author's personal copy

Table 2
Experimental conditions.

Controlled variable	Range
Flow rate (l/min)	1.2–3.2
Heat flux (kW/m^2)	3.5
Average temperature (°C)	25
Test section material	Stainless steel type 304
Working fluid	Water

range of Reynolds number from 4000 to 10,000. It was observed that the Nusselt number increased with increasing Reynold numbers for all cases. In addition, the Nusselt number obtained from the helical grooved tubes was higher than those from the smooth tube. This occurred because the helical grooved tube provided heat transfer enhancement by increasing the mixing of fluid inside the groove, caused by flow separation and recirculation. Moreover, the helical groove also generated a swirl effect on the fluid in the vicinity of the tube wall. The thermal boundary layers of fluid flow inside the helical grooved tube became thinner than that of the smooth tube. For these reasons, augmentation in heat transfer was achieved. Fig. 6 also shows that the Nusselt number increased with the decrease of the grooved pitch. This can be explained by the fact that the tube with lower grooved pitch produced higher turbulence levels of fluid flow. Hence, the tube with the lowest grooved pitch resulted in the highest Nusselt number. However, for the tube with pitches of 8, 10, and 12 in., it can be seen that the variation of grooved pitch had an insignificant effect on the Nusselt number due to very small differences in helix angle. Nevertheless, in the case of the straight grooved tube, the Nusselt number data was slightly lower than that of the smooth tube—about 5%, which falls in the range of uncertainty. Therefore, it is supposed that no enhancement in heat transfer is obtained from this tube due to no flow recirculation and the swirl effect induced by the straight grooved tube. A maximum heat transfer enhancement was obtained up to about 260% for a pitch of 0.5 in. and 25% for pitches of 8, 10, and 12 in. in comparison with the smooth tube.

The Nusselt number ratio as a function of Reynolds number is shown in Fig. 7; it is defined as the ratio of the Nusselt number for a grooved tube to that of the smooth tube. For helical grooved tubes, the Nusselt number ratio tended to increase with the increasing Reynolds number. This is because more flow recirculation and fluid mixing was caused by the groove at a higher Reynolds number. As a result, the increasing rate of the Nusselt number obtained from the tube with a helical groove was higher than that of the smooth tube. As shown in Fig. 7, the Nusselt number ratio varied from 2 to 3.6 for a pitch of 0.5 in., and about 1.0 to 1.3 for the pitches of 8, 10, and 12 in.

4.2. Friction factor

Fig. 8 explains the variation of friction factor with the Reynolds number in the smooth tube, straight grooved tube, and helical grooved tube with different pitches of 0.5, 8, 10, and 12 in. It was found that the friction factor decreased gradually as the Reynolds

Table 3
Uncertainties of measured quantities and calculated parameters.

Parameter	Uncertainty
Temperature (°C)	±0.1
Volume flow rate (l/min)	±0.1
Pressure drop (Pa)	±7
Electric current (A)	±1
Voltage (V)	±0.1
Electric power (W)	±4%
Nusselt number	±18%
Friction factor	±1%

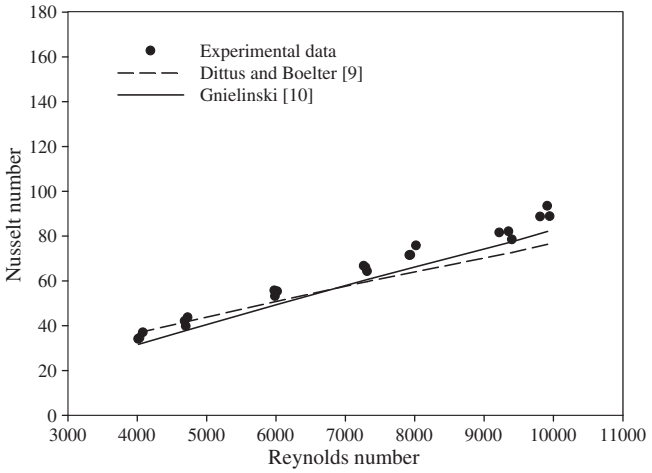

Fig. 4. Comparison of experimental Nusselt number data of smooth tube with existing correlations.

number increased. Moreover, the friction factors for the helical grooved tubes were higher than those for the smooth tube. This implies that the helical groove tubes produced more flow disturbance by the occurrence of the swirl flow and flow recirculation produced by the groove, which led to higher frictional pressure drop. The effect of the grooved pitch on the friction factor is also revealed in this figure. The higher friction factor was obtained from the tube with a lower pitch; lower pitch resulted in increased surface area, more turbulence augmentation, and more friction loss. However, the friction factor values obtained from the tube with pitches of 8, 10, and 12 in. almost coincided with those of the smooth tube.

It can be speculated that the flow separation and swirl effect provided by the helical groove have an insignificant effect on the pressure drop if the helix angle is small. Unlike the Nusselt number, the friction factor obtained from the straight grooved tube was slightly higher than that of the smooth tube or the tubes with pitches of 8, 10, and 12 in. This can be explained that an increase in surface area by the straight groove causes more friction loss, leading to a higher friction factor. The maximum value of friction factor is obtained from the tube having a pitch of 0.5 in. up to 70% in comparison with the smooth tube.

Fig. 9 illustrates the friction factor ratio as a function of the Reynolds number. The friction factor ratio is defined as the ratio of the friction factor obtained from grooved tube to that of a comparable smooth tube. It was observed that the friction factor ratio for a pitch

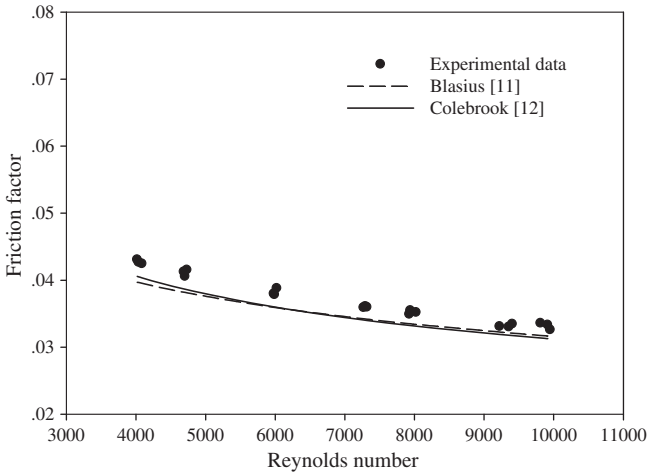

Fig. 5. Comparison of experimental friction factor data of smooth tube with existing correlations.

Author's personal copy

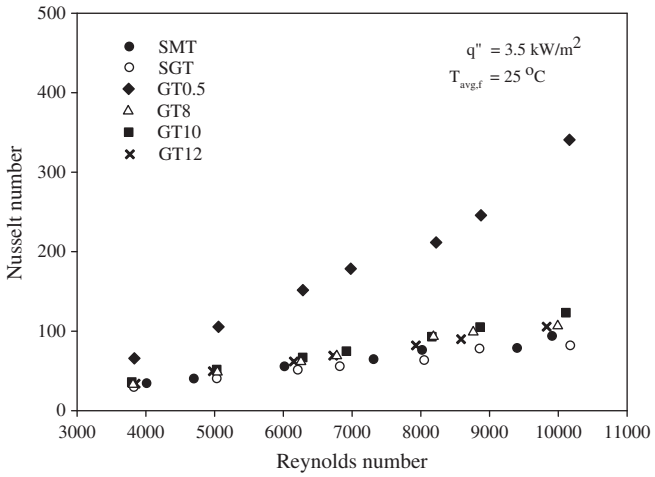

Fig. 6. Nusselt number as a function of Reynolds number for $q'' = 3.5$ kW/m^2 and $T_{avg,f} = 25$ °C.

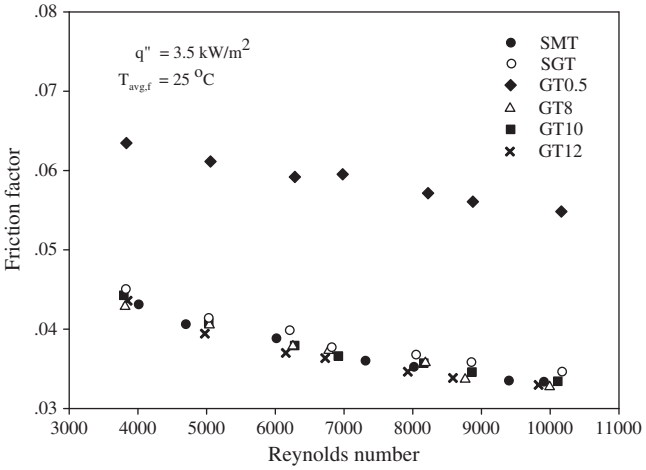

Fig. 8. Friction factor as a function of Reynolds number for $q'' = 3.5$ kW/m^2 and $T_{avg,f} = 25$ °C.

of 0.5 in. increased with the rise of the Reynolds number, whereas the ratio of friction factor of other groove tubes had nearly the same value in all ranges of Reynolds number. This implies that the tube with a smaller grooved pitch created stronger turbulence in the fluid flow at a higher Reynolds number. As a result, the increasing rate of friction factor ratio of tubes with smaller pitch was higher than that of a larger pitch. In addition, for a straight grooved tube and a tube with pitches of 8, 10, and 12 in., the turbulence level of fluid flow induced by the groove was weak. Therefore, the friction factor ratios of these tubes were almost equal as the Reynolds number increased. The highest friction factor ratio was gained from the tube with a pitch of 0.5 in., which was around 1.4 to 1.7 times.

4.3. Thermal performance factor

The performances of grooved tubes were investigated in terms of thermal enhancement factor, η, defined as the ratio between the Nusselt number ratio to friction factor ratio. The thermal enhancement factors of various grooved tubes were plotted against the Reynolds number, as shown in Fig. 10. It is observed that all helical grooved tubes had thermal enhancement factors greater than 1. Moreover, the thermal enhancement factor tended to increase with increasing of the Reynolds number. This indicates that these tubes provided higher increasing rate of Nusselt number ratio than that of the friction factor ratio. Hence, the helical grooved tubes yielded more advantage at a higher Reynolds number. In the case of the straight grooved tube, the thermal enhancement factor was lower than 1. The thermal performance obtained from the groove tubes was about 1.4 to 2.2 for a pitch of 0.5 in.; 1.1 to 1.3 for pitches of 8, 10, and 12 in.; and 0.8 to 0.9 for a straight groove.

5. Conclusion

We carried out an experimental study on heat transfer and flow characteristics of water flowing through horizontal internally grooved tubes. The effect of the grooved pitch on the Nusselt number and friction factor were investigated. The conclusions are as follows:

1. The Nusselt number and friction factor obtained from the helical grooved tubes were higher than those from the smooth tube. Moreover, the Nusselt number and friction factor increased with the decrease of the grooved pitch. However, for the tube with pitches of 8, 10, and 12 in., the variation of grooved pitch had an insignificant effect on the Nusselt number and friction factor. In the case of the straight grooved tube, no enhancement in heat transfer was obtained. Unlike the Nusselt number, the friction factor obtained from the straight grooved tube was slightly higher than those of the smooth tube and the tube with pitches of 8, 10, and 12 in.

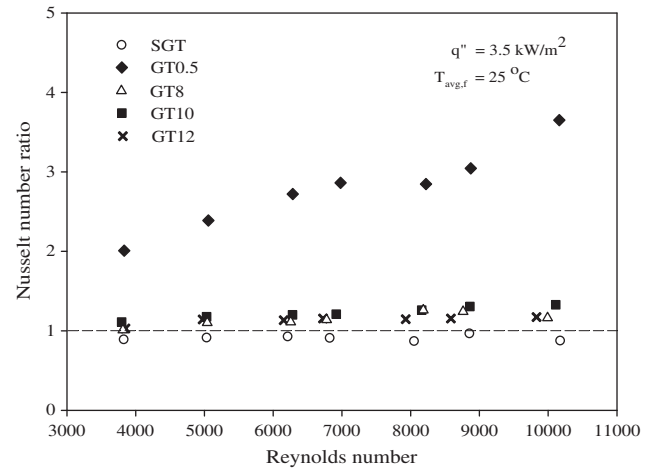

Fig. 7. Variation of Nusselts number ratio with Reynolds number for $q'' = 3.5$ kW/m^2 and $T_{avg,f} = 25$ °C.

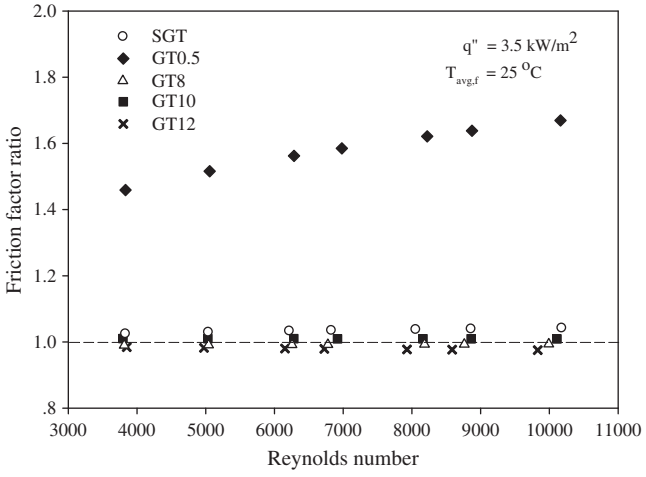

Fig. 9. Variation of friction factor ratio with Reynolds number for $q'' = 3.5$ kW/m^2 and $T_{avg,f} = 25$ °C.

Author's personal copy

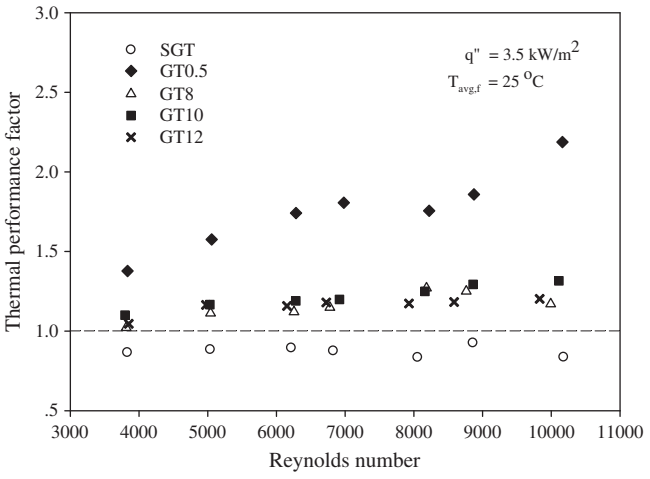

Fig. 10. Thermal performance factor as a function of Reynolds number for $q'' = 3.5$ kW/m^2 and $T_{avg,f} = 25$ °C.

2. For the helical grooved tubes, the Nusselt number ratio tended to increase with increasing Reynolds number. The Nusselt number ratio varied from 2 to 3.6 for a pitch of 0.5 in., and about 1.0 to 1.3 for the pitches of 8, 10, and 12 in. The friction factor ratio for a pitch of 0.5 in. increased with the rise in Reynolds number, whereas the ratio of friction factor of other groove tubes had nearly the same value in all ranges of Reynolds number. The highest friction factor ratio was gained from the tube with a pitch of 0.5 in., around 1.4 to 1.7 times.
3. The thermal enhancement factor was greater than 1 for the helical grooved tubes, while it was lower than 1 for the straight grooved tube. The thermal performance obtained from the groove tubes was about 1.4 to 2.2 for a pitch of 0.5 in.; 1.1 to 1.3 for pitches of 8, 10, and 12 in.; and 0.8 to 0.9 for the straight groove.

Acknowledgments

The present study was supported financially by the Thailand Research Fund, the Office of the Higher Education Commission, and the National Research University Project, whose guidance and assistance are gratefully acknowledged. The third and fourth authors wish to thank the Department of Mechanical Engineering, King Mongkut's University of Technology Thonburi for providing them with research fellowships.

References

[1] D. Graham, J.C. Chato, T.A. Newell, Heat transfer and pressure drop during condensation of refrigerant 134a in an axially grooved tube, International Journal of Heat and Mass Transfer 42 (1999) 1935–1944.
[2] M. Goto, N. Inoue, R. Yonemoto, Condensation heat transfer of R410A inside internally grooved horizontal tubes, International Journal of Refrigeration 26 (2003) 1731–1739.
[3] X. Zhang, X. Zhang, Y. Chen, X. Yuan, Heat transfer characteristics for evaporation of R417A flowing inside horizontal smooth and internally grooved tubes, Energy Conversion and Management 49 (2008) 1731–1739.
[4] X. Zhang, C. Ji, X. Yuan, Prediction method for evaporation heat transfer of non-azeotropic refrigerant mixtures flowing inside internally grooved tubes, Applied Thermal Engineering 28 (2008) 1974–1983.
[5] P. Bharadwaj, A.D. Khondge, A.W. Date, Heat transfer and pressure drop in a spirally grooved tube with twisted tape insert, International Journal of Heat and Mass Transfer 52 (2009) 1938–1944.
[6] K. Bilen, M. Cetin, H. Gul, T. Balta, The investigation of groove geometry effect on heat transfer for internally grooved tubes, Applied Thermal Engineering 29 (2009) 753–761.
[7] Z.H. Liu, Y.Y. Li, R. Bao, Thermal performance of inclined grooved heat pipes using nanofluids, International Journal of Thermal Sciences 49 (2010) 1680–1687.
[8] S. Wongwises, S. Laohalertdecha, J. Kaew-on, W. Duangthongsuk, K. Aroonrat, K. Sakamatapan, Evaporation heat transfer and flow characteristics of R-134a flowing through internally grooved tubes, Heat Mass Transfer 47 (2011) 629–640.
[9] F.W. Dittus, L.M.K. Boelter, Heat transfer in automobile radiators of the tubular type, University of California Publications in Engineering 2 (1930) 443–461.
[10] V. Gnielinski, New equations for heat and mass transfer in turbulent pipe and channel flow, International Journal of Chemical Engineering 16 (1976) 359–368.
[11] P.R.H. Blasius, Das Aehnlichkeitsgesetz bei Reibungsvorgangen in Flüssigkeiten, Forschungsheft 131 (1913) 1–41.
[12] C.F. Colebrook, Turbulent flow in pipes, with particular reference to the transition region between smooth and rough pipe laws, Journal of the Institution of Civil Engineers 11 (1939) 133–156.

Experimental Thermal and Fluid Science 46 (2013) 232–244

Contents lists available at SciVerse ScienceDirect

Experimental Thermal and Fluid Science

journal homepage: www.elsevier.com/locate/etfs

An experimental investigation of flow boiling heat transfer of R-134a in horizontal and vertical mini-channels

Sira Saisorn [a,c], Jatuporn Kaew-On [b,c], Somchai Wongwises [c,d,*]

[a] King Mongkut's Institute of Technology Ladkrabang, Chumphon Campus, Chumphon 86160, Thailand
[b] Department of Physics, Faculty of Science, Thaksin University, Phattalung 93110, Thailand
[c] Fluid Mechanics, Thermal Engineering and Multiphase Flow Research Lab. (FUTURE), Department of Mechanical Engineering, Faculty of Engineering, King Mongkut's University of Technology Thonburi, Bangmod, Bangkok 10140, Thailand
[d] The Academy of Science, The Royal Institute of Thailand, Sanam Suea Pa, Dusit, Bangkok 10300, Thailand

ARTICLE INFO

Article history:
Received 20 January 2012
Received in revised form 23 December 2012
Accepted 23 December 2012
Available online 2 January 2013

Keywords:
Flow boiling
Flow pattern
Micro-scale channel
Heat transfer

ABSTRACT

Flow boiling experiments with R-134a flowing in horizontal and vertical mini-channels are performed to obtain flow visualization and heat transfer data. A 1.75 mm diameter channel with a length of 600 mm is used as test section. Two sets of the horizontal flow and vertical upward flow data are presented based on a mass flux range of 200–1000 kg/m^2 s, a heat flux range of 1–80 kW/m^2 and a saturation pressure range of 7–13 bar. Flow visualization and heat transfer results show heat transfer coefficient depending on flow pattern. The results also indicate that flow regime transition and heat transfer coefficient tend to depend on flow direction under the certain experimental conditions. In addition, the comparisons between the experimental data and the predictions recommended for either macro-scale flow boiling or micro-scale flow boiling are presented in this work.

© 2012 Elsevier Inc. All rights reserved.

1. Introduction

Research on flow boiling heat transfer in micro-scale channel has gained significant attention in engineering community because of the utilization of latent heat of vapourization in their compact sizes. Flow boiling in micro-scale channel has been applied to energy and process systems including high heat-flux compact heat exchangers, and cooling devices of various types of equipment such as high performance micro-electronics, high-powered lasers, and so on. For compact heat exchanger, small channels can provide a larger contact area and support working under high pressure conditions. The application of micro-scale channels in flow boiling process can remove larger amounts of thermal energy when compared with single-phase flow approach. Various beneficial advantages are also discussed in Ribatski et al. [1]. Capillary force or surface tension is likely to play an important role in two-phase flow and heat transfer characteristics, resulting in significant differences in the flow phenomena between macro-scale channels and micro-scale channels.

The criteria for the classification of small channels have been given by different investigators. For instance, arbitrary channel classifications associated with the hydraulic diameter, D_h have been proposed. Mehendale et al. [2] employed the hydraulic diameter as an important parameter for defining the heat exchangers as follows:

- Micro-heat exchanger: 1 μm $\leqslant D_h \leqslant$ 100 μm
- Meso-heat exchanger: 100 μm $\leqslant D_h \leqslant$ 1 mm
- Compact heat exchanger: 1 mm $\leqslant D_h \leqslant$ 6 mm
- Conventional heat exchanger: $D_h >$ 6 mm

Kandlikar [3] proposed criteria for different-sized channels used in engineering applications:

- Micro-channels: 10 μm $\leqslant D_h \leqslant$ 200 μm
- Mini-channels: 200 μm $\leqslant D_h \leqslant$ 3 mm
- Conventional channels: $D_h >$ 3 mm

The criteria based on different dimensionless parameters have also been proposed in the literature. The confinement number recommended by Kew and Cornwell [4], for instance, was proposed to be related with some physical aspects of flow boiling. The confinement number is defined as

$$C_o = \frac{D_b}{D_h} \tag{1}$$

where D_h is hydraulic diameter and D_b is nominal bubble size or capillary length which is expressed by

* Corresponding author at: Fluid Mechanics, Thermal Engineering and Multiphase Flow Research Lab. (FUTURE), Department of Mechanical Engineering, Faculty of Engineering, King Mongkut's University of Technology Thonburi, Bangmod, Bangkok 10140, Thailand. Tel.: +66 2 470 9115; fax: +66 2 470 9111.
E-mail address: somchai.won@kmutt.ac.th (S. Wongwises).

0894-1777/$ - see front matter © 2012 Elsevier Inc. All rights reserved.
http://dx.doi.org/10.1016/j.expthermflusci.2012.12.015

Nomenclature

B_o	boiling number, $B_o = q/Gi_{LG}$
C_{CO}	convection number, $C_{CO} = (\rho_G/\rho_L)^{0.5}((1-x)/x)^{0.8}$
C_o	confinement number as defined in Eq. (1)
C_p	specific heat at constant pressure (J/kg K)
D	channel diameter (m)
D_b	capillary length (m)
D_h	hydraulic diameter (m)
F	factor
Fr	Froude number, $Fr = G^2/\rho^2 gD$
F_{Fl}	fluid-surface parameter
f	friction factor
G	mass flux (kg/m^2 s)
g	gravitational acceleration (m/s^2)
h	heat transfer coefficient (W/m^2 K)
i	specific enthalpy (J/kg)
i_{LG}	latent heat of vapourization (J/kg)
k	thermal conductivity (W/m K)
MAE	mean absolute error, $MAE = \frac{1}{N}\sum_1^N\left(\frac{\lvert h_{pre}-h_{exp}\rvert}{h_{exp}}\times 100\right)$
N	number of experimental data
Nu	Nusselt number, $Nu = hD_h/k$
Pr	Prandtl number, $Pr = \mu C_p/k$
ΔP_{sat}	saturation pressure difference (Pa)
q	heat flux (W/m^2)
Re	Reynolds number, $Re = GD_h/\mu$
S	nucleate boiling suppression factor
T	temperature (°C)
ΔT_{sat}	wall superheat (K)
We	Weber number, $We = G^2 D_h/\rho\sigma$
x	vapour quality

Greek symbols

χ	Lockhart–Martinelli parameter
λ	Bond number, $\lambda = g(\rho_L - \rho_G)D_h^2/\sigma$
μ	dynamic viscosity (N s/m^2)
ρ	density (kg/m^3)
σ	surface tension (N/m)

Subscripts

A	annular flow
CB	coalescing bubble flow
conv	convection boiling contribution
exp	experimental value
G	vapour phase
GO	all-vapour
IB	isolated bubble flow
in	inner
L	liquid phase
LO	all-liquid
loc	local
nb	nucleate boiling contribution
pre	predicted value
S–P	plug–slug flow
sat	saturation
wall	wall surface

$$D_b = \sqrt{\frac{\sigma}{g(\rho_L - \rho_G)}} \tag{2}$$

The confinement number above 0.5 implies that the micro-scale effects are important for a given channel diameter. In Eq. (2), σ stands for surface tension, g is gravitational acceleration, ρ_L and ρ_G are, respectively, liquid and vapour densities.

The combination of non-dimensional number was used by Harirchian and Garimella [5] to propose the transition criterion. They indicated micro-scale flow corresponding to the conditions for which $\lambda^{0.5} \times Re_L$ is lower than 160.

Tibirica and Ribatski [6] reported that the channel with a diameter of 2.3 mm was considered as the one in which the transition between macro- and micro-scale flow boiling phenomena took place when halocarbon refrigerants were used as working fluids under Earth's gravity. It should be noting that referring to Ong and Thome [7], the term "mini-channel" found in the literature is loosely given for the flow phenomena that might take place at the transition from macro-scale flow to micro-scale flow.

Despite a number of criteria being proposed, a clear physical criterion that relates the channel diameter to the fluid flow mechanisms is still not available and, hence, further investigation should be performed to meet a more general definition dealing with channel classification.

With regard to two-phase flow research, there have been a relatively small number of publications in the area of small channels compared with those done for macro-scale channels. On the contrary, many recent publications have dealt with small scale channels, but the two-phase characteristics are not completely understood. Recent works concerned with two-phase heat transfer characteristics in micro-scale channels are outlined in the following paragraphs.

A number of researchers such as Lee and Lee [8], Sumith et al. [9] and Qu and Mudawar [10] have reported that flow boiling heat transfer is substantially controlled by convective boiling. Inconsistently, there were such publications as Lazarek and Black [11], Wambsganss et al. [12], Tran et al. [13], Kew and Cornwell [4] and Bao et al. [14], which indicated nucleate boiling as predominant heat transfer mechanism. With 3899 data points from 14 research works in the literature, Bertsch et al. [15] proposed heat transfer prediction method for flow boiling in micro-channels. Their correlation was based on the method of Chen [16], which was done by accounting for nucleate boiling mechanism and two-phase force convection contribution for predicting heat transfer coefficient. Please note that Thome [17] analyzed the experimental data, based on studies published before 2007.

Huo et al. [18] studied experimentally boiling heat transfer of R-134a flowing in 2.01 and 4.26 mm diameter channels. The test section was placed vertically. In the range of low vapour quality, the heat transfer coefficient in both tubes increased with increasing heat flux and saturated pressure but was independent of vapour quality. These results were attributed to nucleate boiling being the dominant heat transfer mode. Over other ranges of vapour quality, however, the dominant heat transfer mode was not addressed as a result of inconsistency in the experimental data. Under the same controlled conditions, they found that the nucleate boiling heat transfer coefficient was higher for the 2.01 mm tube than for the 4.26 mm tube.

Lee and Mudawar [19] carried out experiments to explore flow boiling heat transfer characteristics of R-134a refrigerant in rectangular micro-channels having 231 μm wide and 713 μm deep. In this study, different heat transfer mechanisms were addressed for three different vapour quality regions. Bubbly/slug flow, slug flow and annular flow were observed in their work.

Yun et al. [20] were concerned with flow boiling heat transfer characteristics in rectangular channels with hydraulic diameters ranging from 1.08 to 1.54 mm. Working fluids tested were CO_2 and R-134a. Generally, the average heat transfer coefficient of

CO_2 increased by around 53% as compared with that of R-134a. The effect of heat flux on heat transfer coefficient was much more obvious for CO_2 than for R-134a. The dry-out region, indicated by the reduction in the heat transfer coefficient, was developed early as mass flux increases. It was also noted that the effect of mass flux on heat transfer coefficient was less significant than that of heat flux. As expected, the heat transfer coefficient increased with a decrease in hydraulic diameter.

Kandlikar and Balasubramanian [21] studied experimentally the flow boiling of water in micro-channels. Hydraulic diameter for each channel was 0.333 mm. The observed flow patterns including bubbly flow, plug flow, churn flow and annular flow tend to appear alternately with time even at a given flow condition. It should be noted that the plug flow and slug flow are characterized by the diameters of elongated bubbles. The diameters of elongated bubbles which are similar in size to the channel diameter refer to slug flow, and those which are smaller than the channel diameter refer to plug flow [22]. Regarding the experimental data, they indicated the channel orientation affecting the flow pattern transition and the heat transfer coefficient which was found to be compatible with nucleate boiling mechanism.

Shiferaw et al. [23] compared their flow boiling data with existing correlations. Their data points were obtained from experiments with R-134a fluid flowing in circular channels with diameters of 4.26 and 2.01 mm. The comparison revealed that existing correlations did not predict their data very well.

Shiferaw et al. [24] conducted flow boiling experiments using R-134a as working fluid. The test section having a diameter of 1.1 mm was placed vertically. An insignificant influence of mass flux and vapour quality on heat transfer coefficient was observed. However, the heat transfer coefficient increased with increasing heat flux and saturation pressure.

The experiments for boiling heat transfer of water flow through rectangular micro-channels were carried out by Lee and Garimella [25]. The channel width ranging from 102 to 997 μm with the channel depth of around 400 μm was considered in their work and working fluid was deionized water. They found that at heat flux larger than 30 W/cm^2, the heat transfer coefficient was nearly independent with heat flux.

Three different refrigerants, R-134a, R-236fa and R-245fa, were tested for flow boiling in a 1.03 mm diameter tube by Ong and Thome [26]. Trends apparent in the data were investigated, showing that the heat transfer coefficient depended on heat flux at low vapour quality and on mass flux at high vapour quality. In terms of the refrigerants tested at low vapour quality, R-134a exhibited the highest heat transfer coefficient followed by R-236fa and R-245fa, respectively.

Arcanjo et al. [27] obtained flow visualization data for flow boiling of R-134a and R-245fa in a horizontal tube having a diameter of 2.32 mm. Slug flow, churn flow and annular flow were observed. According to their report, the flow pattern transitions were affected by working fluid and saturation temperature.

Saisorn et al. [28] performed flow visualization study for R-134a refrigerant during flow boiling in a circular channel having a diameter of 1.75 mm. Slug flow, throat-annular flow, churn flow, annular flow and annular-rivulet flow were observed and found to influence the flow boiling heat transfer process. Slug flow appeared with the lowest heat transfer coefficient in comparison to the other flow regimes. Annular-rivulet flow showed a relatively high heat transfer coefficient but a local dry-out region was observed at high vapour qualities, which has been undesirable for a thermal design approach dealing with a cooling system implemented with small channels. Moderate values of heat transfer coefficient were given by throat-annular flow, churn flow and annular flow which might be good choices for the development of the micro-scale devices. Besides, their flow pattern data were compared with the transition lines by Triplett et al. [29] for two-phase air–water flow through a 1.45 mm diameter channel. In general, the comparisons showed inconsistencies between the flow pattern map established from two-phase gas-liquid flow and that from phase-change process. Such inconsistencies were also reported by Yang and Shieh [30] and Martin-Callizo et al. [31]. Yang and Shieh [30] performed flow visualization with air–water mixture and refrigerant R-134a, and the comparison between such two cases were discussed. Martin-Callizo et al. [31] conducted the visualization of R-134a during flow boiling in a tube with a diameter of 1.33 mm. Their test section was made from a quartz glass tube coated externally by Indium Tin Oxide (ITO) which was served as the resistive coating over which a potential difference generated by a DC power supply was applied. Their flow pattern data were also compared with the transition lines by Triplett et al. [29], indicating that the agreement was not satisfactory. However, the two-phase gas-liquid flow pattern map tends to be compatible with the flow regime map based on condensation flow process. In micro-channels, for instance, Saisorn and Wongwises [32] reported the fair agreement between their gas–liquid flow pattern data and the transition lines of Garimella et al. [33] for condensation flow.

Ong and Thome [34] experimentally investigated flow boiling heat transfer of three refrigerants in channels of 1.03, 2.20 and 3.04 mm diameters. R-134a, R-236fa and R-245fa were used as working fluids in their study. The channel with higher confinement number, i.e. smaller diameter, gave heat transfer coefficients with lower dependency on heat flux. The heat transfer coefficient was also found to strongly depend on flow pattern. The heat transfer coefficient for R-134a showed the highest dependence on heat flux but R-245fa yielded the lowest heat flux dependency while R-236fa was positioned in between the other two refrigerants.

Two single rectangular channels were used for flow boiling experiments carried out by Soupremanien et al. [35]. In their work, the test sections of different two aspect ratios having the same hydraulic diameter of 1.4 mm were employed and the Forane®365 HX was used as working fluid. They observed bubbly flow, plug flow, plug/slug flow, churn/annular flow and annular flow in both channels. For lower aspect ratio of 0.143, they detected instabilities with flow reversals in plug/slug flow regime. The instabilities also appeared in the other channel with a higher aspect ratio (0.43) but were observed in churn/annular flow regime. Another point to note was that the heat transfer coefficient for the aspect ratio of 0.143 was higher than that for the aspect ratio of 0.43 under low heat flux conditions. The opposite trend was found at high heat flux conditions. In other words, the heat transfer coefficient was found to be higher for the aspect ratio of 0.43.

Wang et al. [36] studied heat transfer performance for flow boiling of dielectric fluid HFE-7100. A multiport micro-channel with a hydraulic diameter of 0.825 mm was used in the study. They reported that the heat transfer performance was always deteriorated when the experiments were conducted based on the downward flow arrangements.

The recent studies, previously mentioned, mainly explored the heat transfer mechanisms in small channels with various diameters and working fluids. The effects of such parameters as mass flux and heat flux on flow boiling phenomena have been reported in several publications whereas the important information dealing with the gravitational aspect is still lacking, especially in the channel thought to be in the transition range between macro-scale channel and micro-scale channel [37]. The present experimental study, which is a continuation of the authors' previous work, is therefore carried out to compare the heat transfer results obtained from the horizontal channel with those from the vertical upward flow channel under the same test conditions with a channel diameter of 1.75 mm. The discussions are presented based on two-phase flow pattern and heat transfer coefficient.

2. Experimental apparatus and procedure

This study is a continuation of the authors' previous work. The experiments are carried out using the apparatus and instruments shown in Figs. 1 and 2. A detailed description of the experimental setup can be seen in Saisorn et al. [28]. For a better understanding, however, the corresponding details are described as follows. For the refrigerant circulating loop, as seen in Fig. 1, liquid refrigerant is pumped by a variable speed gear pump. The refrigerant then passes in series through a filter/dryer, a refrigerant flow meter, pre-heater, sight glass tube, and enters the test section attached to the rigid frame having adjustable connector which is served for channel orientation purpose. Horizontal flow and vertical upward flow are conducted in current work. The inlet quality before entering the test section is controlled by the pre-heater with a DC power supply used to apply heat. Leaving the test section, the

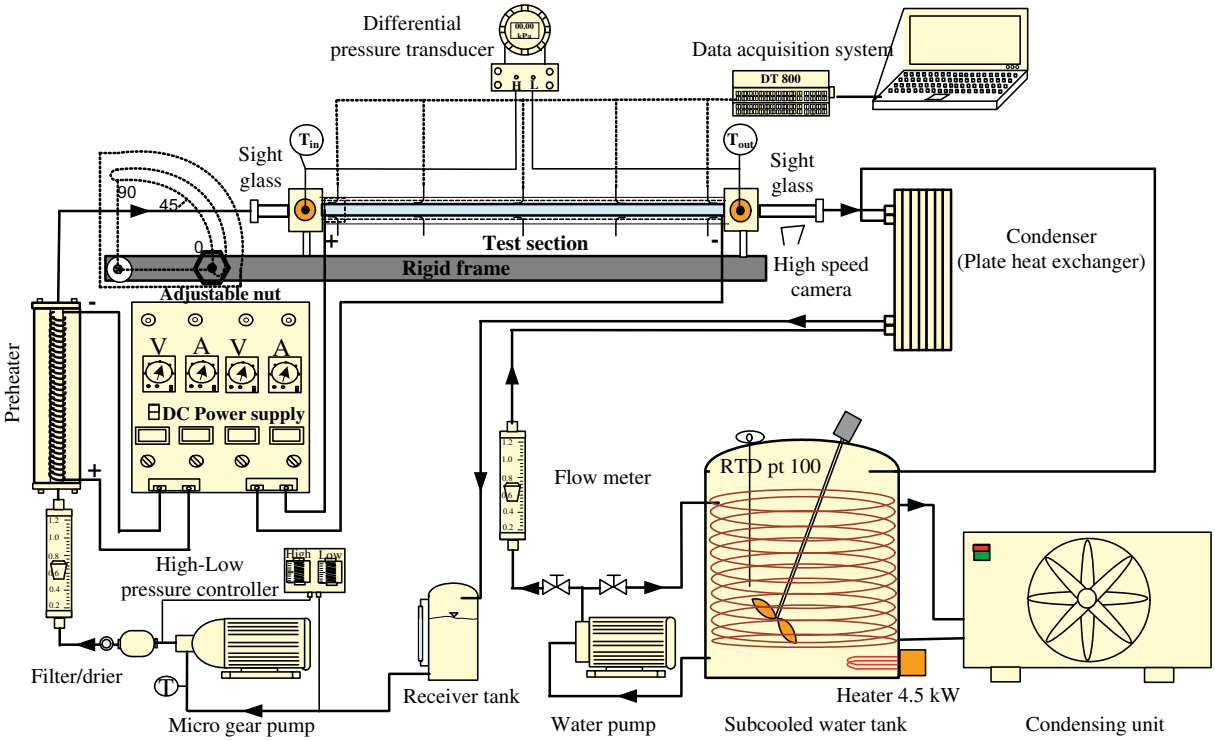

Fig. 1. Schematic diagram of experimental apparatus.

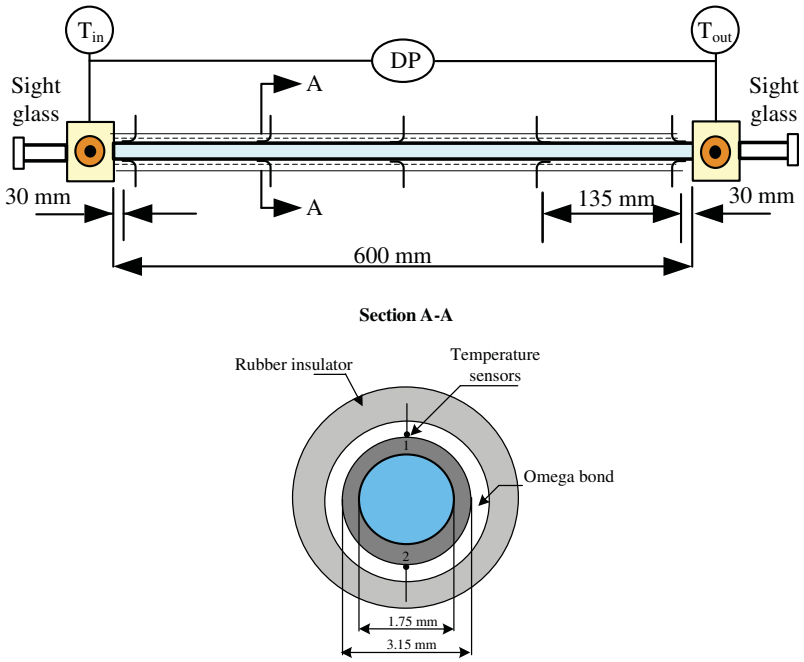

Fig. 2. Schematic diagram of the test section.

refrigerant vapour subsequently condenses in a condenser which is a plate heat exchanger and then is collected in a receiver and returns to the refrigerant pump to complete the cycle. Instrumentation is installed at various positions, as shown in Fig. 1, to monitor the state of the refrigerant. All the signals from the thermocouples and pressure transducer are recorded by the data acquisition system.

Fig. 2 shows a schematic diagram of the test section, a stainless steel tube which is 600 mm long and 1.75 mm in diameter. A regulated DC power supply generating 80 A at 12 V is used to apply heat to the test section. The voltage and electric current values are measured by a multi-meter (Fluke 336 model) which has an uncertainty of ±2% for voltage and ±1% for current. T-type thermocouples are installed at the inlet and outlet of the test section to measure the system temperature. The 10 thermocouples are installed on the top and bottom sides at equal distances along the tube to measure the wall temperature. All thermocouples on the tube surface are fixed with special glue. The test section is well insulated by means of rubber foam with a thermal conductivity of 0.04 W/m K. A variable area type flow meter is specially calibrated in the range of 0.02–0.2 LPM for R-134a by the manufacturer. All relevant instruments installed in the experimental apparatus, including the thermocouples and pressure transducer are well calibrated.

A 1.75 mm diameter transparent tube is installed to match up with the test section outlet and to serve as a viewing window for flow visualization. The detailed formation of each flow pattern is registered by a high quality camera (Fujifilm FinePix S7000) having shutter speeds of 1/15–1/10,000 s. The camera together with an adjustable light source consisting of 150 W halogen lamp and dimmer are placed normal to the viewing section.

In this work, the experiments were conducted in such a way that the heat applied to the test section is varied in small increments, while the refrigerant flow rate, saturation pressure, and inlet vapour quality in the test section are kept constant at the desired value. The system is allowed to approach a steady state before the flow pattern and relevant data are recorded. The steady state condition is verified by plotting a number of temperatures measured by the T-type thermocouples installed at pre-heater and test section, against time. Their variations are within the error range for a time of at least 120 s. During the experiment, the temperature and pressure are continuously recorded along the test section on the data acquisition system. The temperature profiles help us to know the limits of useful data because a large increase in wall temperature and saturation temperature at the test section outlet is observed when dry-out occurs. The range of experimental conditions is presented in Table 1. The uncertainties in the measured quantities and calculated parameters are shown in Table 2.

Table 1
Experimental conditions.

Refrigerant	R-134a
Diameter (mm)	1.75
Length (mm)	600
Mass flux (kg/m^2 s)	200–1000
Heat flux (kW/m^2)	1–80
Saturation pressure (bar)	7–13
Test section material	Stainless steel

Table 2
Uncertainties of measured quantities and calculated parameters.

Parameter	Uncertainty
Channel diameter	±0.05 (mm)
Temperature	±0.1 (°C)
Mass flow rate of refrigerant	±1.42%
Heat transfer rate of test section	±2.25%
Heat transfer rate of pre-heater	±2.25%
Heat transfer coefficient	±8.12%

3. Results and discussion

In this section, the two-phase flow patterns are presented at first. The flow regime maps are subsequently presented, and the corresponding heat transfer results come in last.

3.1. Flow patterns

The visual observation of flow patterns is carried out through a viewing window which is a transparent tube, installed to match up with the test section outlet. The flow regime map is developed based on the observed flow patterns which are registered by a high quality camera (Fujifilm FinePix S7000) having shutter speeds of 1/15–1/10,000 s. The camera together with an adjustable light source, comprising mainly of 150 W halogen lamp and dimmer, are aligned across the viewing section. The alignment of the flow visualization system is normal to the viewing section.

In the present work, the two-phase flow pattern observations are performed under a mass flux range of 200–1000 kg/m^2 s, a heat flux range of 1–80 kW/m^2 and saturation pressures of 8 and 10 bar. Similar to horizontal flow results reported in Saisorn et al. [28], slug flow, throat-annular flow, churn flow, annular flow and annular-rivulet flow are also observed in vertical upward flow experiments as illustrated in Fig. 3. Slug flow, elongated bubbles which are larger in length than the channel diameter, corresponds to isolated bubble flow. Throat-annular flow, considered as a unique flow pattern in micro-scale flow, and churn flow, defined as the occurrence of disruptive region associated with intense mixing of the two phases, correspond to coalescing bubble flow. Annular flow is characterized by the flowing of the liquid film on the tube wall and continuous vapour in the tube core whereas annular-rivulet flow deals with the situation that annular flow is observed alternately with flowing of a rivulet-like liquid stream on the tube surface. Besides, the local heat transfer coefficients, which illustrate heat transfer mechanisms in various flow patterns, can also be obtained based on the present experimental setup as follows.

Heat flux, q, transferred to the test section is provided by the regulated DC power supply generating 80 A at 12 V. T-type thermocouples are installed at the inlet and outlet of the test section to measure the refrigerant temperatures. Since, during experiments, the two-phase conditions for flow boiling are provided at the test section inlet by using pre-heater as shown in Fig. 1, the saturation pressures at the test section inlet and outlet are obtained based on the corresponding saturation temperatures. Regarding the assumption of a linear variation of the saturation pressure along the tube, the local saturation temperatures, $T_{sat,loc}$, can subsequently be obtained.

As presented in Fig. 2, the 10 T-type thermocouples are installed on the top and bottom sides at equal distances along the tube to measure the tube surface temperature. For each position where the thermocouple is installed on the tube surface, the inner wall temperature at a given position is determined using the equations for steady-state one-dimensional heat conduction through the tube wall with internal heat generation. At a given distance, hence, the average temperature of the inner wall at the top and bottom sides stands for the local temperature on the inner wall, $T_{wall,in,loc}$. Finally, the local heat transfer coefficient, h_{loc}, for flow boiling of R-134a along the test section is determined using the following equation.

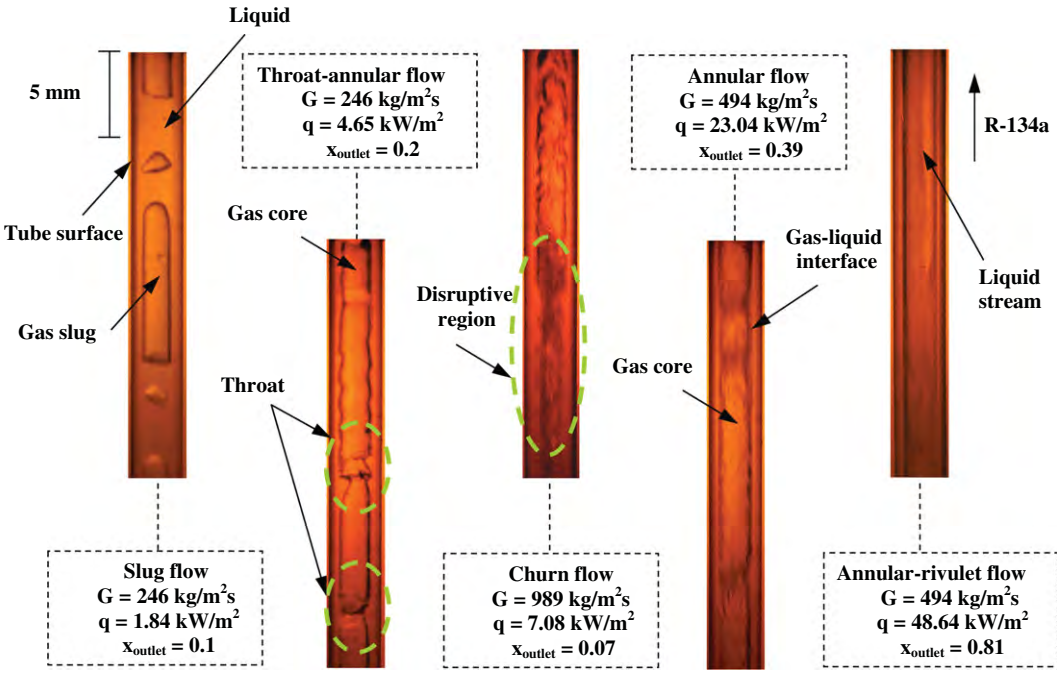

Fig. 3. Flow patterns for vertical upward flow (8 bar).

$$h_{loc} = \frac{q}{(T_{wall,in,loc} - T_{sat,loc})} \quad (3)$$

The local vapour quality is determined based on thermodynamic properties, i.e.

$$x = \frac{(i - i_L)}{i_{LG}} \quad (4)$$

where i_L is the specific enthalpy of the saturated liquid, i_{LG} represents the latent heat of vaporization and the local fluid enthalpy, i is determined from an energy balance.

As shown in Fig. 1, the working fluid i.e. R-134a, is preheated and became two-phase fluid before entering the test section. The two-phase fluid leaving the pre-heater can also be observed in the transparent tube installed at the test section inlet. In this work, the heat transfer data were taken simultaneously with the flow pattern information as illustrated in Fig. 4. During experiments, inlet vapour quality in the test section was kept constant at the desired value which corresponded to slug flow regime. As presented in Fig. 4a ($G = 246$ kg/m^2 s), slug flow corresponding to low heat flux condition took place in the entire test section as observed in the transparent tubes installed at the inlet and outlet of the test section. Some fluctuations during slug flow regime were mainly attributed to the intermittent behaviour resulting from liquid slugs and elongated bubbles zones. As heat flux increased, the slug flow, observed in the test section inlet, tended to undergo a change to throat-annular flow when the fluid entered the heated length of the test section. The throat-annular flow persisted over the entire test section because there was no drastic change in the corresponding local heat transfer coefficient. Similar explanation could be applicable to annular flow. Regarding this observation, the flow pattern, observed in the transparent tube installed at the test section outlet, became fairly apparent to represent flow regime taking place along the channel. Fig. 4b ($G = 742$ kg/m^2 s) shows the heat transfer data for different flow patterns, i.e. churn flow, annular flow and annular-rivulet flow. In a similar way, each of them could also be taken as the flow regime for the entire test section. It should be noted that the substantial decrease in the heat transfer coefficients for annular-rivulet flow resulted from local

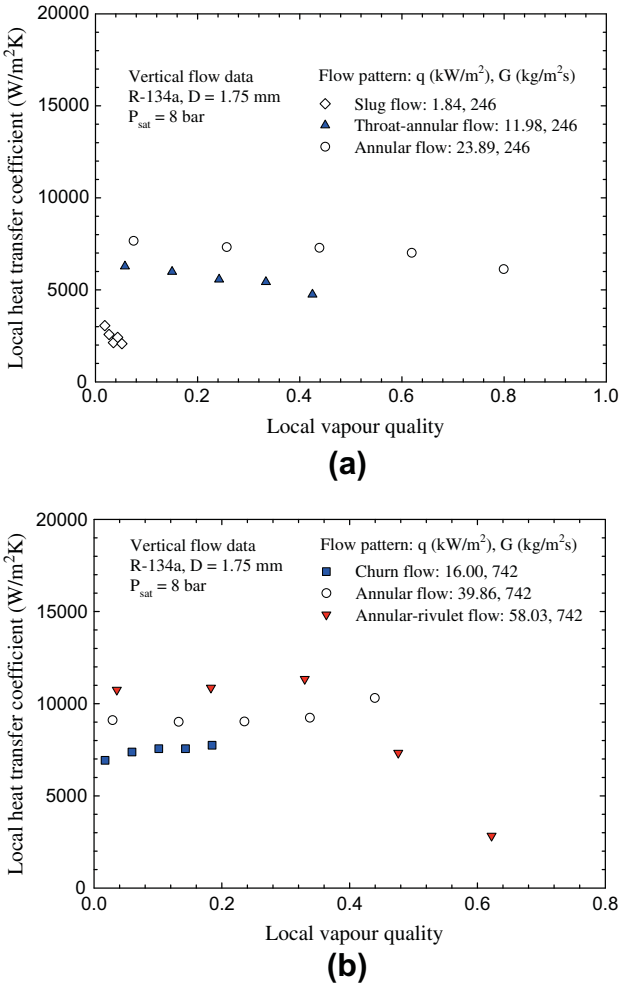

Fig. 4. Local heat transfer coefficient data for various flow patterns.

dry-out region. Similar characteristics are also observed for the horizontal flow experiments. Notably, slug flow may not be a good choice for designing the cooling system owing to its lowest heat transfer coefficient in comparison to the other flow regimes. Moreover, throat-annular flow, churn flow and annular flow tend to be more useful than annular-rivulet flow in which local dry-out region is observed.

3.2. Flow regime maps

The usual method in the presentation of flow pattern data is to classify the flow pattern by visual observation and plot the data as a flow pattern map in terms of system parameters. The present flow pattern maps in terms of mass flux, G, and vapour quality, x, are presented in this section. With similar experimental conditions and size of the test section, the previous data obtained by Ong and Thome [26], are compared with the present work as shown in Fig. 5. According to their classification methodology, bubbly flow and plug–slug flow can be classified as isolated bubble regime whereas slug flow, churn flow and throat-annular flow (or slug-annular flow named by Kawaji and Chung [38]) can be referred to as coalescing bubble regime. In general, the present slug flow/churn flow transition fairly agrees with their isolated bubble/coalescing bubble transition line. However, their annular flow regime tends to develop early as vapour quality increases. The shift in the flow regime transition is due to the difference in the channel diameter. The present flow pattern maps for both horizontal and vertical flows are presented in Fig. 6. The solid lines presented with the flow pattern names in the figure represent the boundaries of the flow patterns and transitions from one flow pattern to another. Naturally, due to the fact that the flow patterns do not change suddenly, the transition lines should be represented as broad transition bands. As depicted in Fig. 6a, at a saturation pressure of 8 bar, the vertical upward flow results are compared with the transition lines for the horizontal flow data. The regions of both slug flow and annular-rivulet flow for vertical upward flow fairly agree with those for horizontal flow while throat-annular flow data and some annular flow results are found to be located on the throat-annular flow regime for horizontal flow. Although the churn-annular flow transition is shifted, the deviation is not considered as remarkably obvious due to the nature at the vicinity of the transitions between flow patterns as previously discussed. As a consequence of the comparisons, the channel orientation under a saturation pressure of 8 bar tends to have no significant effect on the two-phase flow regime. With a saturation pressure of 10 bar as presented in Fig. 6b, however, it is found that the flow regime

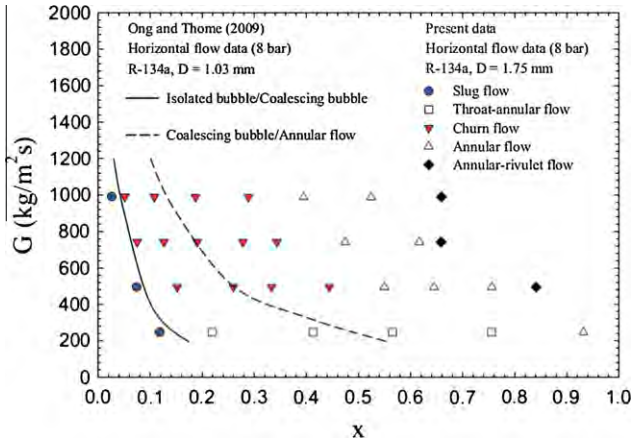

Fig. 5. Comparison of the present flow patterns with the data from Ong and Thome [26].

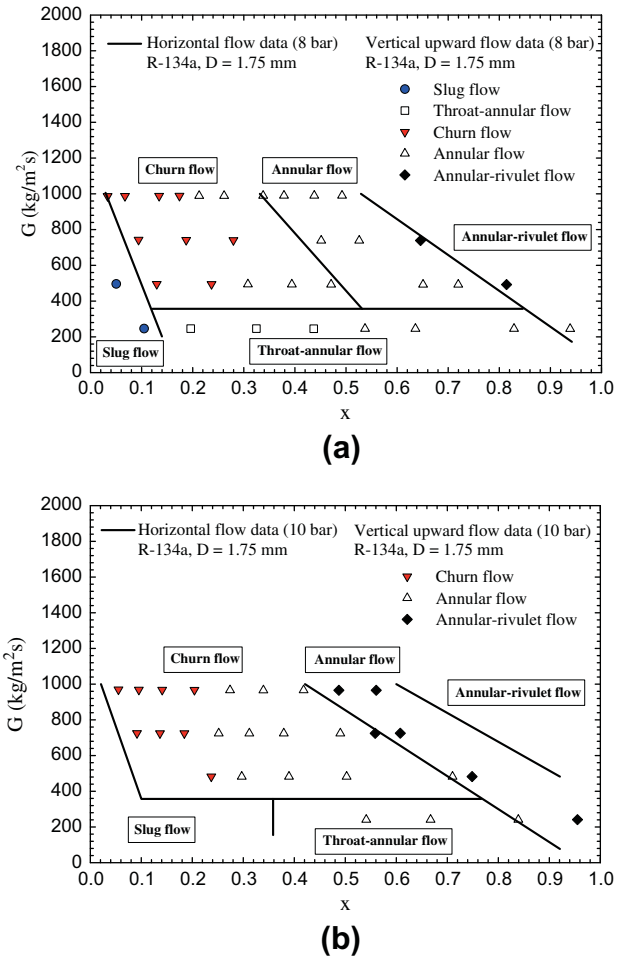

Fig. 6. Flow regime maps.

for the vertical upward flow does not correspond to the flow regime for horizontal flow case. Since, as addressed in Kandlikar [39], flow boiling phenomena are affected by interactions among five major forces including surface tension, inertia, gravity, viscous and evaporation momentum forces, the relative effects of these forces under different saturation pressure may cause discrepancy in the boiling process. As the saturation pressure increases, the reduced surface tension force and the decrease in evaporation momentum force may result in the flow regime transitions sensitive to gravitational effect. In other words, as saturation pressure increases, the gravitation taking place in the vertical upward flow becomes important, causing the flow regime transition for vertical upward flow different from the horizontal flow case.

In the present experimental conditions carried out in a 1.75 mm diameter channel, the gravity has less impact on the flow regime during saturation pressure of 8 bar while the flow transitions are affected by the channel orientation under saturation pressure of 10 bar. It seems that micro-to-macro-scale transition can take place in this channel size and become sensitive to the saturation pressure as previously discussed. This finding agrees well with Ong and Thome [7] who concluded that the micro-to-macro-scale transition for R-134a was located in diameters between 1 mm and 2 mm. Such diameter range corresponds to confinement number ranging from 0.4 to 1, covering the present conditions having the value of around 0.5.

Ong and Thome [7] also proposed the new flow pattern transition lines aimed to predict both macro- and micro-scale flow patterns for 0.5–3.04 mm channels. Dimensionless numbers were

introduced in the prediction method to account for such different effects as gravity, inertia and surface tension. The followings are their flow pattern transition lines.

Isolated bubble/coalescing bubble (IB/CB) was presented by

$$x_{IB/CB} = 0.36C_o^{0.2}\left(\frac{\mu_G}{\mu_L}\right)^{0.65}\left(\frac{\rho_G}{\rho_L}\right)^{0.9}Re_{GO}^{0.75}B_o^{0.25}We_{LO}^{-0.91} \quad (5)$$

Coalescing bubble/annular (CB/A) was expressed as

$$x_{CB/A} = 0.047C_o^{0.05}\left(\frac{\mu_G}{\mu_L}\right)^{0.7}\left(\frac{\rho_G}{\rho_L}\right)^{0.6}Re_{GO}^{0.8}We_{LO}^{-0.91} \quad (6)$$

Plug–slug/coalescing bubble (S–P/CB) was established when $x_{S-P/CB} < x_{CB/A}$ and Co < 0.34, and was given by

$$x_{S-P/CB} = 9C_o^{0.2}\left(\frac{\rho_G}{\rho_L}\right)^{0.9}Fr_{LO}^{-1.2}Re_{LO}^{0.1} \quad (7)$$

Plug–slug/annular (S–P/A) was used when $x_{S-P/CB} > x_{CB/A}$ and $C_o < 0.34$, and was represented by

$$x_{S-P/A} = x_{CB/A} \quad (8)$$

Referring to Eqs. (5)–(8), B_o represents boiling number, μ_L is liquid viscosity, u_G is vapour viscosity, Re_{GO} is all-vapour Reynolds number, Re_{LO} represents all-liquid Reynolds number, We_{LO} is all-liquid Weber number, We_{GO} is all-vapour Weber number, and Fr_{LO} denotes all-liquid Froude number.

The present results are compared with the transition lines of Ong and Thome [7] as illustrated in Fig. 7. The present data are in good agreement with their macro-micro-scale flow pattern maps even at the saturation pressure of 10 bar.

3.3. Average heat transfer coefficients

During the experiments, heat flux, q, transferred to the test section is provided by regulated DC power supply generating 80 A at 12 V. As depicted in Fig. 2, the 10 T-type thermocouples are installed on the top and bottom sides at equal distances along the tube to measure the tube surface temperatures. For each position where the thermocouple is installed on the tube surface, the inner wall temperature at a given position is determined using the equations for steady-state one-dimensional heat conduction through the tube wall with internal heat generation. The average value of the inner wall surface temperature, T_{wall}, of the test section is subsequently obtained using the arithmetic mean of the temperatures along the tube. In addition to the wall temperature, T-type thermocouples are also installed at the inlet and outlet of the test section to determine the average temperature of the refrigerant, T_{sat}. According to the above details, the heat transfer coefficient, h, for the entire 0.6 m long tube is obtained using the following equation.

$$h = \frac{q}{(T_{wall} - T_{sat})} \quad (9)$$

The experimental heat transfer coefficients for both horizontal flow and vertical upward flow plotted as a function of heat flux for different constant values of mass flux are presented in Fig. 8. In general, heat flux shows significant role on the heat transfer coefficient. Notably, the sharp drop on the heat transfer coefficients for heat flux higher than 40 kW/m^2 is indicative of partial dry-out region appearing in the annular-rivulet flow. As shown in Fig. 8a, the heat transfer coefficient data corresponding to horizontal flow are mostly less dependent on mass flux, indicating that the dominance of forced convection is not obvious although liquid laminar-vapour turbulent flow (G = 246 kg/m^2 s) and liquid turbulent-vapour turbulent flow (G = 494, 742 kg/m^2 s) are established in this work. Under the same experimental conditions, i.e. confinement number of around 0.5, on the contrary, the heat

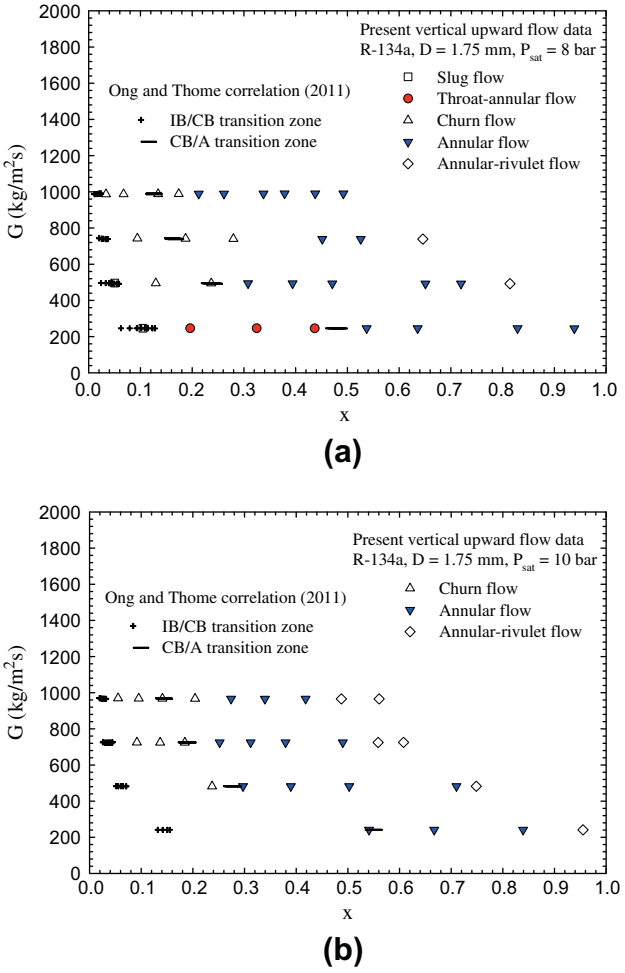

Fig. 7. Comparison of the observed flow patterns with the transition lines by Ong and Thome correlation [7].

transfer coefficient for vertical upward flow presented in Fig. 8b shows the dependence on mass flux. This behaviour observed reveals that for vertical upward flow, as mass flux increases, the flow inertia is concurrent with the buoyancy force, leading to reinforce the convective contribution.

Fig. 9a and b shows respectively the effect of saturation pressure on the heat transfer coefficient in horizontal flow and vertical upward flow. During the experiments carried out under the pressures ranging from 7 to 13 bar, the heat transfer coefficient for both orientations tends to decrease with increment of saturation pressure across the experimental range of heat flux. Choi et al. [40], Kaew-On and Wongwises [41], and Saisorn et al. [28] also reported the similar trend which may be attributed to the following reasons. As the saturation pressure increases, the smaller latent heat of vapourization and the lower liquid viscosity can contribute the thinner liquid film on the tube wall to break easier than that taking place under lower saturation pressure, leading to a decrease in heat transfer coefficient.

Based on different flow patterns, the horizontal flow and vertical upward flow results are presented in Figs. 10 and 11. The flow patterns seem to influence the flow boiling heat transfer process. The figures indicate that heat transfer coefficient is relatively low for slug flow regime and continuously increases to the value associated with annular flow, but decreases thereafter when the annular-rivulet flow, which corresponds to local dry-out region, is established.

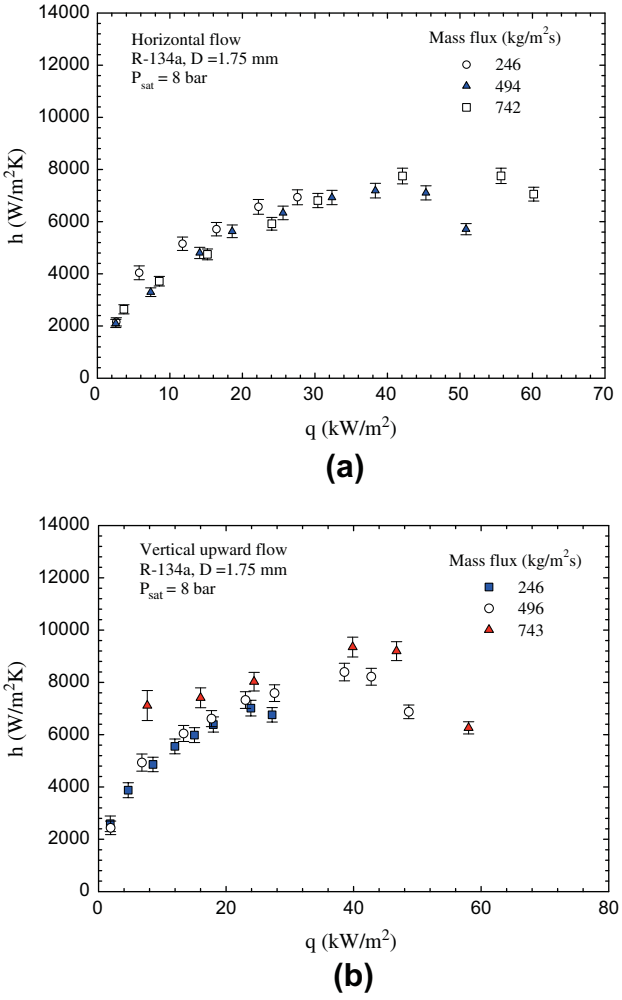

Fig. 8. Heat flux versus heat transfer coefficient for different mass flux values.

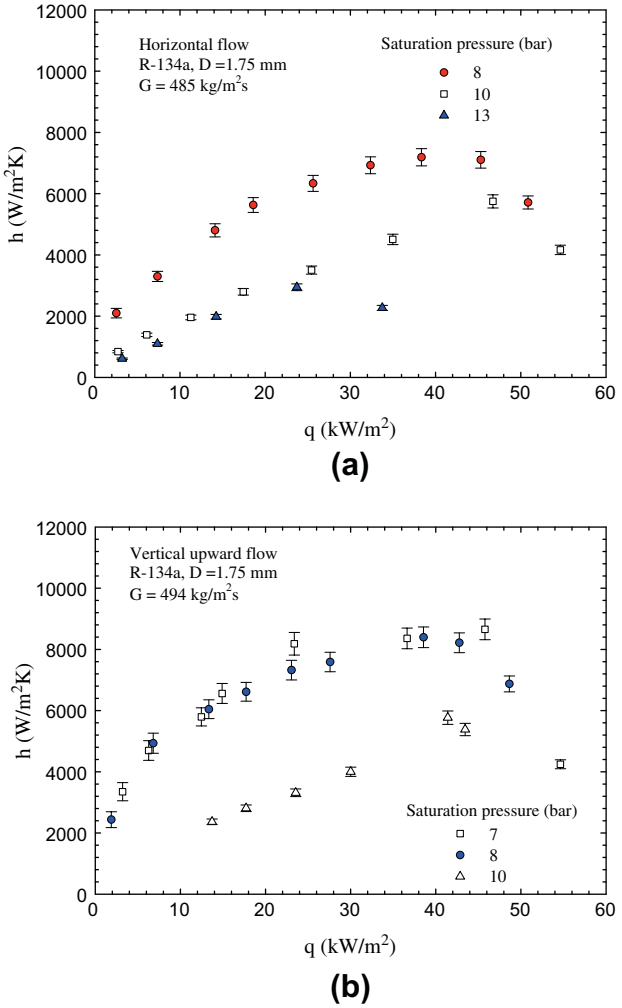

Fig. 9. Heat flux versus heat transfer coefficient for different saturation pressures.

For a saturation pressure of 8 bar, the channel orientation has no influence on the heat transfer coefficient during laminar liquid flow taking place at a mass flux of 246 kg/m^2 s as shown in Fig. 10a. In turbulent liquid region where mass flux values are of 495 and 743 kg/m^2 s, nevertheless, the heat transfer coefficient is higher for vertical upward flow than for horizontal flow case. The relatively high heat transfer coefficient for the vertical flow case presented in Fig. 10b and c is mainly due to the buoyancy promoting the vapour flow.

These observed characteristics should be examined by the macro-to-micro-scale criteria. For boiling process, the confinement number was recommended by Kew and Cornwell [4] to be used as the transition criterion for checking whether the micro-scale effects are important. The confinement number below 0.5 stands for macro-scale channel. In the present work, the confinement number for all mass flux under a saturation pressure of 8 bar is slightly above 0.5, presumably indicating the dominance of micro-scale effects for which gravity should be insignificant. However, this criterion only agrees well with the results obtained at a mass flux of 246 kg/m^2 s.

Interestingly, the macro-scale and micro-scale behaviours, which are observed at different mass flux values, are exactly identified by the criterion recently developed by Li and Wu [42]. In addition to surface tension and gravitational forces taken into account in the criterion of Kew and Cornwell [4], the viscous and inertia forces were also considered by Li and Wu [42]. The authors proposed micro-scale flow becoming important when the combined non-dimensional number, $\lambda Re_L^{0.5}$, was smaller than 200. On the other hand, the macro-scale flow was addressed at the value larger than 200. λ represents Bond number and Re_L is liquid Reynolds number. Based on the experimental data, the values of the combined non-dimensional number are 162.02, 235.98 and 303.76 for mass flux of 246, 495 and 743 kg/m^2 s, respectively, which is compatible with the present observations depicted in Fig. 10a–c.

Fig. 11 illustrates the experimental results for a saturation pressure of 10 bar. The vertical upward flow results are almost identical to those for the horizontal flow even at high mass flux. At this pressure, the criteria proposed by Kew and Cornwell [4], and by Li and Wu [42] indicate the macro-scale flow region ($C_o < 0.5$, $\lambda Re_L^{0.5} > 200$) although the dependence on mass flux is not observed. The emerging phenomena may possibly be dominated by the thin wall liquid film becoming easily broken at high pressure for both horizontal and vertical flows as previously discussed. Fig. 11 also indicates annular flow in vertical upward flow to appear earlier than in horizontal flow, which results in early dryout taking place in annular-rivulet flow. It is likely that the more important role of inertia and buoyant forces in comparison to low surface tension during high saturation pressure may contribute to the early continuous vapour core in vertical upward flow.

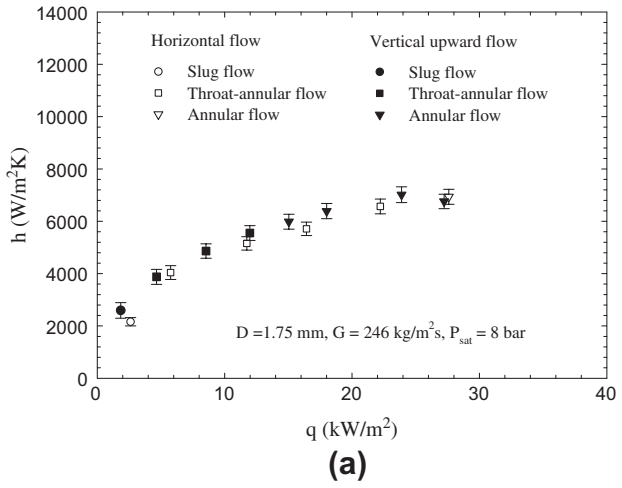

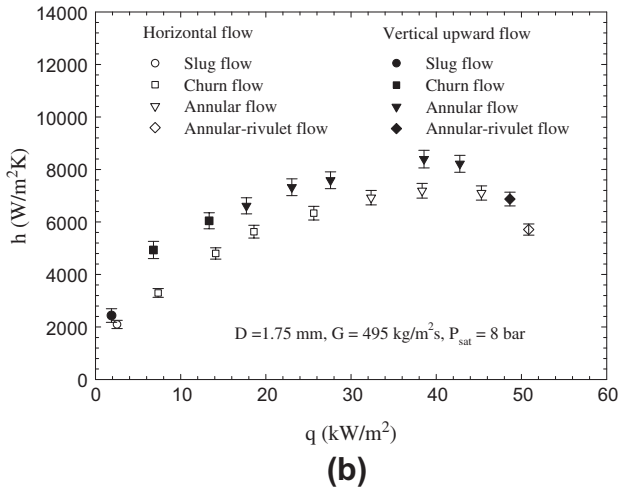

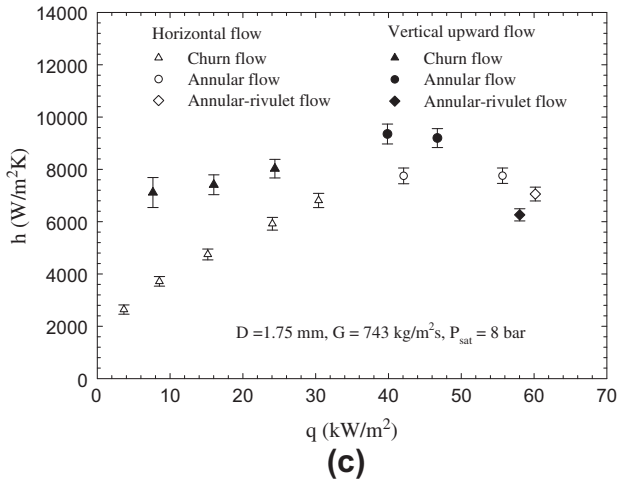

Fig. 10. Heat transfer coefficients for horizontal and vertical upward flow (8 bar).

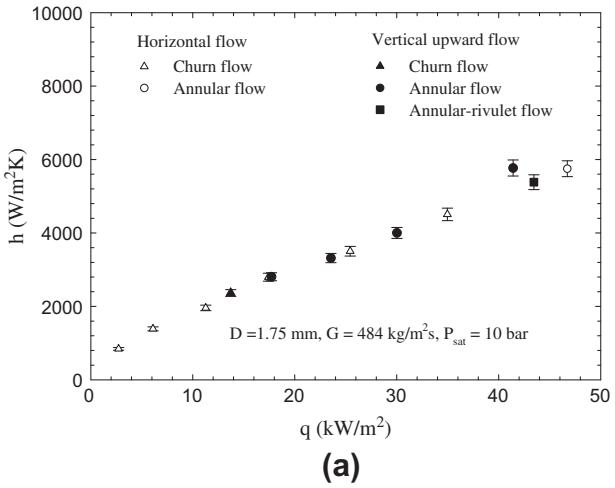

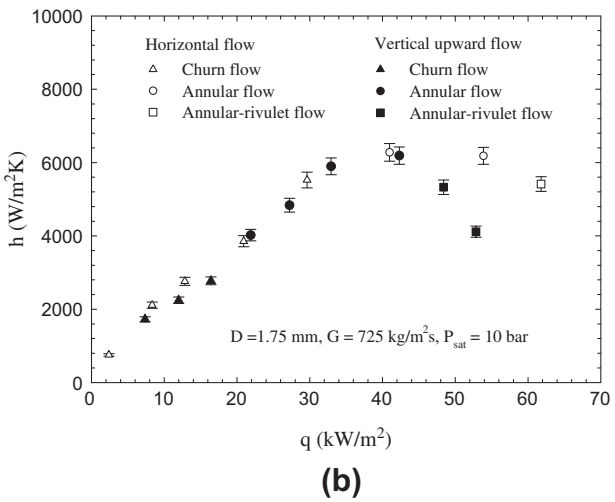

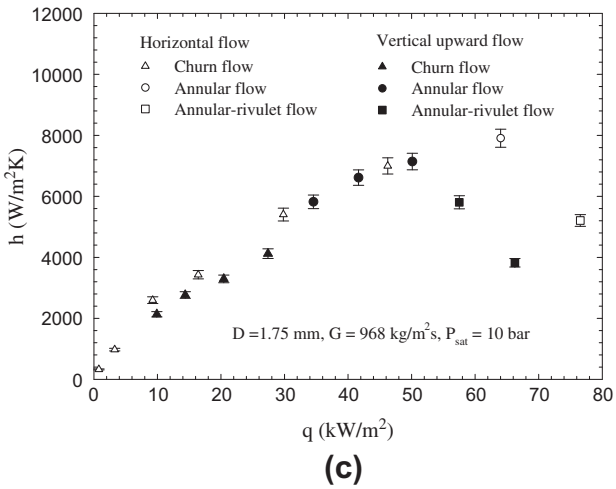

Fig. 11. Heat transfer coefficients for horizontal and vertical upward flow (10 bar).

3.4. Comparison of the predictive methods with the experimental data

Since the macro-scale and micro-scale behaviours were observed during the present work, both macro-scale and micro-scale correlations for flow boiling heat transfer were used to compare with the experimental data. Chen correlation [16] has been chosen for macro-scale flow because it is widely used and taken as a benchmark in the literature [43]. For micro-scale flow correlations, Kandlikar and Balasubramanian [44], and Sun and Mishima [45] have been chosen because the database, including working fluid and parameter range, which was used to develop their predictions, is compatible with our experimental conditions.

The prediction method of Chen [16] recommended for macro-scale flow boiling, and those for micro-scale flow boiling proposed by Kandlikar and Balasubramanian [44], and by Sun and Mishima [45] are compared with the present heat transfer coefficient data.

One of the widely used correlations for macro-scale channels, which is taken as a benchmark in the flow boiling literature, was proposed by Chen [16]. An additive concept for nucleate boiling and forced convective mechanisms was introduced in the correlation which is expressed as:

$$h = h_{nb}S + h_L F \tag{10}$$

where F is a two-phase convection multiplier which is calculated as:

$$F = \begin{cases} 1 & \text{for } \frac{1}{\chi} \leqslant 0.1 \\ 2.35\left(\frac{1}{\chi} + 0.213\right)^{0.736} & \text{for } \frac{1}{\chi} > 0.1 \end{cases} \tag{11}$$

χ in Eq. (11) represents the Lockhart-Martinelli parameter determined by:

$$\chi = \left(\frac{1-x}{x}\right)^{0.9}\left(\frac{\rho_G}{\rho_L}\right)^{0.5}\left(\frac{\mu_L}{\mu_G}\right)^{0.1} \tag{12}$$

The nucleate boiling suppression factor, S, is expressed as:

$$S = \frac{1}{1 + 2.53 \times 10^{-6}\mathrm{Re}_L^{1.17}} \tag{13}$$

The liquid-phase heat transfer coefficient, h_L, is given by:

$$h_L = 0.023 Re_L^{0.8}\left(\frac{\mu_L C_{p_L}}{k_L}\right)^{0.4}\left(\frac{k_L}{D}\right) \tag{14}$$

and nucleate boiling heat transfer coefficient, h_{nb}, is determined from the following equation:

$$h_{nb} = 0.00122\Delta T_{sat}^{0.24}\Delta P_{sat}^{0.75}\left(\frac{k_L^{0.79}C_{p_L}^{0.45}\rho_L^{0.49}}{\sigma^{0.5}\mu_L^{0.29}i_{LG}^{0.24}\rho_G^{0.24}}\right) \tag{15}$$

In Eqs. (12)–(15), $\mathrm{Re_L}$ is liquid Reynolds number, C_{p_L} is liquid specific heat capacity, k_L is liquid thermal conductivity, D is channel diameter, i_{LG} is latent heat of vapourization, ΔT_{sat} is wall superheat and ΔP_{sat} stands for the difference between the saturation pressures calculated from wall temperature and fluid temperature.

Kandlikar and Balasubramanian [44] modified the correlation proposed by Kandlikar [46] for macro-scale channels to extend the prediction to micro-scale channels which correspond to the neglected Froude number.

For all-liquid Reynolds numbers higher than 100, their correlation can be expressed as shown below.

$$h = \text{larger of}\begin{cases} h_{nb} \\ h_{conv} \end{cases} \tag{16}$$

where the heat transfer coefficient based on nucleate boiling contribution, h_{nb}, and that on forced convective contribution, h_{conv}, are given by Eqs. (17) and (18), respectively.

$$h_{nb} = 0.6683C_{CO}^{-0.2}(1-x)^{0.8}h_{LO} + 1058.0B_o^{0.7}(1-x)^{0.8}F_{FI}h_{LO} \tag{17}$$

$$h_{conv} = 1.136C_{CO}^{-0.9}(1-x)^{0.8}h_{LO} + 667.2B_o^{0.7}(1-x)^{0.8}F_{FI}h_{LO} \tag{18}$$

where C_{CO} represents convection number, F_{FI} stands for a fluid-surface dependent parameter which is equal to 1 for all fluids tested with stainless steel tubes, and h_{LO} for all-liquid flow heat transfer coefficient which is found from Eqs. (19)–(21):

$$h_{LO} = \frac{\mathrm{Re_{LO}Pr}_L(f/2)(k_L/D)}{1 + 12.7(\mathrm{Pr}_L^{2/3} - 1)(f/2)^{0.5}} \quad \text{for } 10^4 \leqslant \mathrm{Re_{LO}} \leqslant 5 \times 10^6 \tag{19}$$

$$h_{LO} = \frac{(\mathrm{Re_{LO}} - 1000)\mathrm{Pr}_L(f/2)(k_L/D)}{1 + 12.7(\mathrm{Pr}_L^{2/3} - 1)(f/2)^{0.5}} \quad \text{for } 3000 \leqslant \mathrm{Re_{LO}} \leqslant 10^4 \tag{20}$$

$$h_{LO} = \frac{\mathrm{Nu}\,k_L}{D} \quad \text{for } \mathrm{Re_{LO}} \leqslant 1600 \tag{21}$$

Pr_L is the liquid Prandtl number and f appearing in Eqs. (19) and (20) is the friction factor determined by:

$$f = [1.58\ln(\mathrm{Re_{LO}}) - 3.28]^{-2} \tag{22}$$

It is noted that, for laminar flow in a circular channel with constant surface heat flux, the Nusselt number indicated in Eq. (21) is

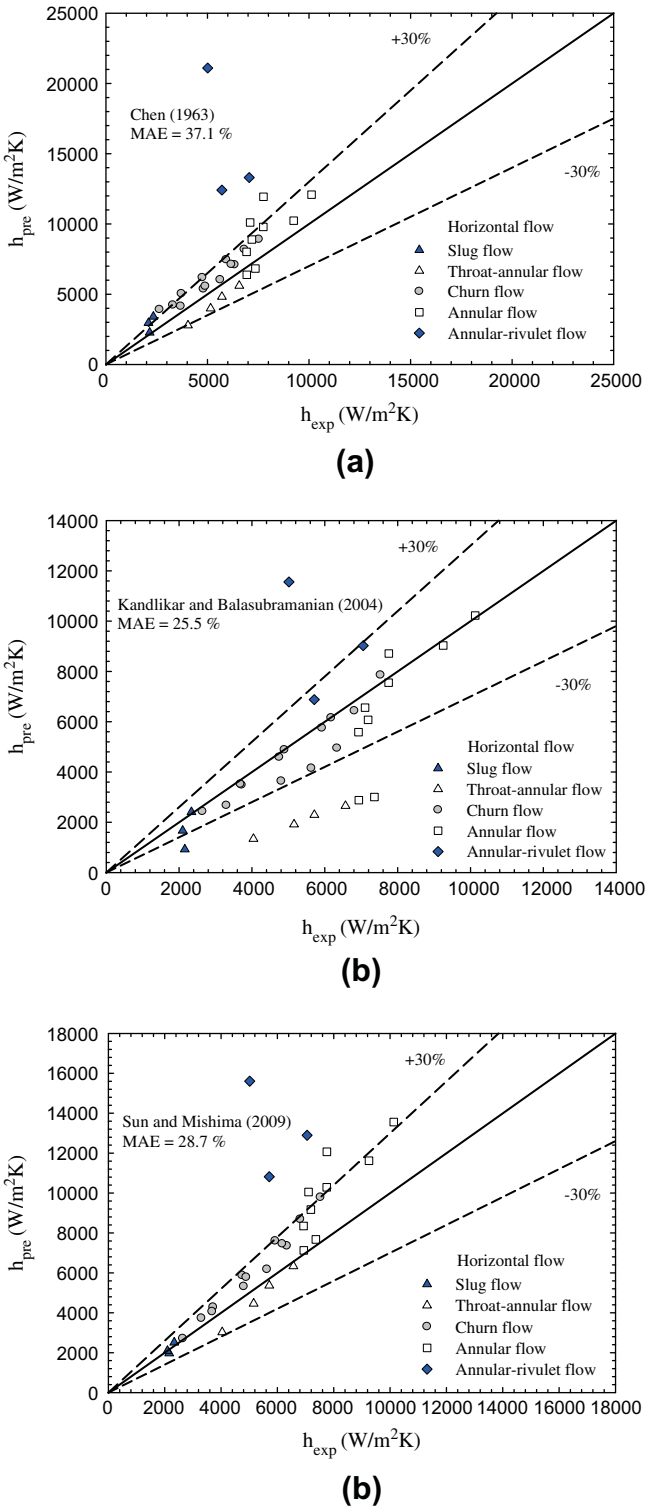

Fig. 12. Comparison between measured and calculated heat transfer coefficient for horizontal flow (8 bar) using different correlations: (a) Chen [16], (b) Kandlikar and Balasubramanian [44] and (c) Sun and Mishima [45].

equal to 4.36. In the case of the transition region, the all-liquid flow heat transfer coefficient is established using a linear interpolation between Re_{LO} of 1600 and 3000.

They also proposed a two-phase heat transfer coefficient for very low Reynolds number ($Re_{LO} \leqslant 100$) which is recommended as:

$$h = h_{nb} = 0.6683 C_{CO}^{-0.2} (1-x)^{0.8} h_{LO} + 1058.0 B_o^{0.7} (1-x)^{0.8} F_{FI} h_{LO} \quad (23)$$

where h_{LO} is found from Eq. (21).

Sun and Mishima [45] compiled existing 2505 flow boiling data based on several working fluids and channel diameters ranging from 0.21 to 6.05 mm. Lazarek and Black correlation [11] was modified to predict the heat transfer coefficient as follow.

$$h_{TP} = \frac{6 Re_{LO}^{1.05} B_o^{0.54} k_L}{D_h We_{LO}^{0.191} \left(\frac{\rho_L}{\rho_G}\right)^{0.142}} \quad (24)$$

Comparisons between the present results and the predictions are presented respectively for horizontal flow and vertical upward flow in Figs. 12 and 13 in which the mean absolute errors (MAE) standing for the predictive accuracy of the corresponding correlations are indicated.

For horizontal flow as depicted in Fig. 12, the method of Sun and Mishima [45] yields the best prediction capturing 78.13% of the data within ±30% error band (MAE of 28.6%), followed by the method developed by Kandlikar and Balasubramanian [44] predicting 75% of the data within ±30% error band (MAE of 25.5%). Chen correlation [16] gives rough prediction, with MAE of 37.1% and 68.75% of the predicted data falling within ±30% error band. It seems from Fig. 12 that the micro-scale channel correlations proposed by Kandlikar and Balasubramanian [44], and by Sun and Mishima [45] are more useful than Chen correlation [16] developed for macro-scale flow. Sun and Mishima method [45] can be used to predict the flow boiling heat transfer under slug flow, throat-annular flow and churn flow while Kandlikar and Balasubramanian [44] gives fair prediction for churn flow, annular flow and annular-rivulet flow.

Fig. 13 depicts the comparison results based on the vertical upward flow. Chen correlation [16] works best with MAE of 24.4% and 81.82% of the predicted data falling within ±30% error band. The other two prediction methods for micro-scale channels fail to accurately predict the data for vertical upward flow. With this channel diameter (D = 1.75 mm), although the channel is small, the important role of gravity for the vertical upward flow may cause the heat transfer characteristics to be close to those for ordinarily sized channels.

For system pressure higher than 8 bar, however, the predictions with MAE of up to 300% are obtained for both horizontal and vertical directions. During high saturation pressure, as discussed in previous section, such substantially poor predictions are possibly due to the unstable liquid film near the tube wall, which is not taken into account in these correlations.

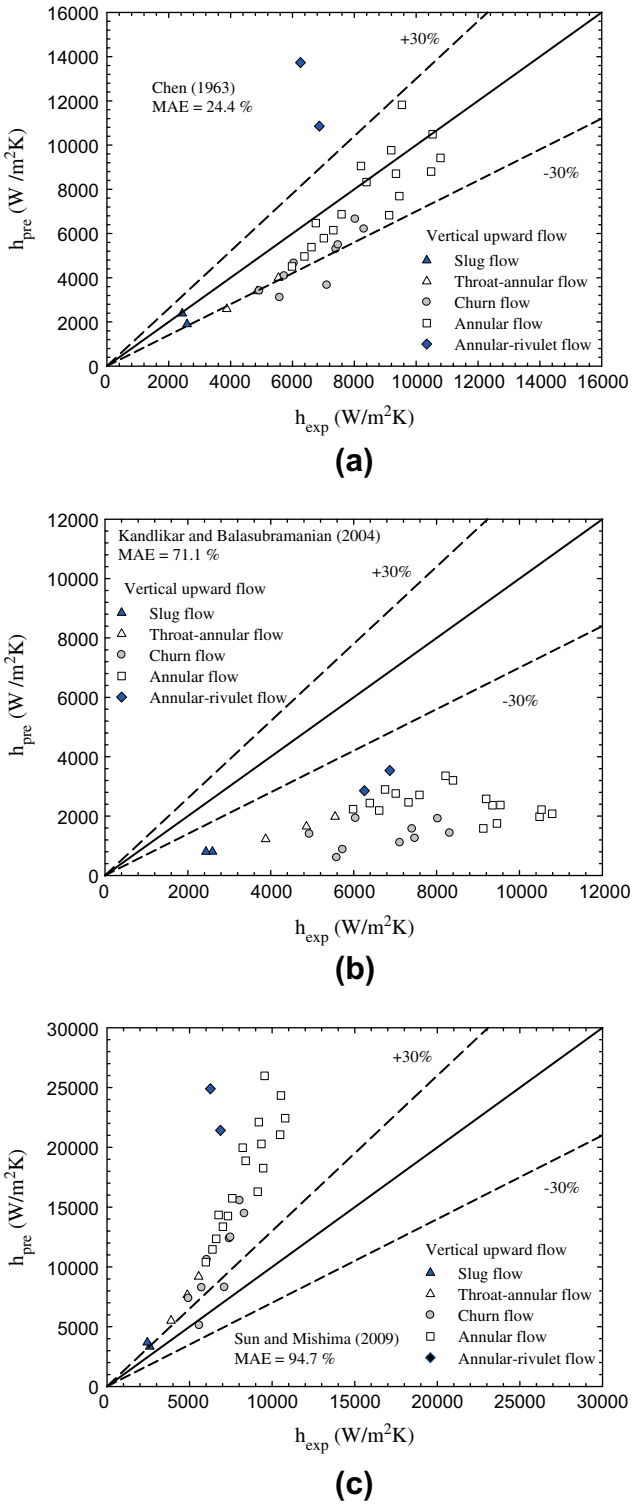

Fig. 13. Comparison between measured and calculated heat transfer coefficient for vertical upward flow (8 bar) using different correlations: (a) Chen [16], (b) Kandlikar and Balasubramanian [44] and (c) Sun and Mishima [45].

4. Conclusion

Two-phase flow and heat transfer characteristics of R-134a during flow boiling in circular mini-channels are presented in this paper. The experiments are carried out to obtain flow pattern and heat transfer coefficient data for horizontal and vertical channels having a diameter of 1.75 mm. The conclusion from the present work can be given as follows.

1. The flow visualization results show different flow patterns including slug flow, throat-annular flow, churn flow, annular flow and annular-rivulet flow. Based on heat transfer coefficient data, the results also indicate that throat-annular flow, churn flow and annular flow tend to be useful for cooling applications.
2. The change in saturation pressure seems to cause the flow regime transitions to be sensitive to the channel orientation.
3. The heat transfer data obtained reveal that the heat transfer coefficient for vertical upward flow is higher than for horizontal

flow. However, the gravitational effect tends to be insignificant when the mass flux is low.

Acknowledgements

The authors would like to express their appreciation to the Thailand Research Fund, KMITL Research Fund and the National Research University Project for providing financial support for this study.

References

[1] G. Ribatski, L. Wojtan, J.R. Thome, An analysis of experimental data and prediction methods for two-phase frictional pressure drop and flow boiling heat transfer in micro-scale channels, Exp. Therm. Fluid Sci. 31 (2006) 1–19.
[2] S.S. Mehendale, A.M. Jacobi, R.K. Ahah, Fluid flow and heat transfer at micro- and meso-scales with application to heat exchanger design, Appl. Mech. Rev. 53 (2000) 175–193.
[3] S.G. Kandlikar, Fundamental issues related to flow boiling in mini-channels and micro-channels, Exp. Therm. Fluid Sci. 26 (2002) 389–407.
[4] P.A. Kew, K. Cornwell, Correlations for the prediction of boiling heat transfer in small-diameter channels, Appl. Therm Eng. 17 (1997) 705–715.
[5] T. Harirchian, S.V. Garimella, A comprehensive flow regime map for microchannel flow boiling with quantitative transition criteria, Int. J. Heat Mass Transfer 53 (2010) 2694–2702.
[6] C.B. Tibirica, G. Ribatski, Flow boiling heat transfer of R134a and R245fa in a 2.3 mm tube, Int. J. Heat Mass Transfer 53 (2010) 2459–2468.
[7] C.L. Ong, J.R. Thome, Macro-to-microchannel transition in two-phase flow: Part 1-Two-phase flow patterns and film thickness measurements, Exp. Therm. Fluid Sci. 35 (2011) 37–47.
[8] H.J. Lee, S.Y. Lee, Heat transfer correlation for boiling flows in small rectangular horizontal channels with low aspect ratios, Int. J. Multiphase Flow 27 (2001) 2043–2062.
[9] B. Sumith, F. Kaminaga, K. Matsumura, Saturated flow boiling of water in a vertical small tube, Exp. Therm. Fluid Sci. 27 (2003) 789–801.
[10] W. Qu, I. Mudawar, Flow boiling heat transfer in two-phase microchannel heat sinks; experimental investigation and assessment of correlation methods, Int. J. Heat Mass Transfer 46 (2003) 2755–2771.
[11] G.M. Lazarek, S.H. Black, Evaporative heat transfer, pressure drop and critical heat flux in a small diameter vertical tube with R-113, Int. J. Heat Mass Transfer 25 (1982) 945–960.
[12] M.W. Wambsganss, D.M. France, J.A. Jendrzejczyk, T.N. Tran, Boiling heat transfer in a horizontal small-diameter tube, J. Heat Transfer 115 (1993) 963–972.
[13] T.N. Tran, M.W. Wambsganss, D.M. France, Small circular- and rectangular-channel boiling with two refrigerants, Int. J. Multiphase Flow 22 (1996) 485–498.
[14] Z.Y. Bao, D.F. Fletcher, B.S. Haynes, Flow boiling heat transfer of Freon R11 and HCFC123 in narrow passages, Int. J. Heat Mass Transfer 43 (2000) 3347–3358.
[15] S.S. Bertsch, E.A. Groll, S.V. Garimella, A composite heat transfer correlation for saturated flow boiling in small channels, Int. J. Heat Mass Transfer 52 (2009) 2110–2118.
[16] J.C. Chen, A correlation for boiling heat transfer to saturated fluid in convective flow, ASME paper, 63-HT-34, 1963, pp. 1–11.
[17] J.R. Thome, Boiling in microchannels: a review of experiment and theory, Int. J. Heat Fluid Flow 25 (2004) 128–139.
[18] X. Huo, L. Chen, Y.S. Tian, T.G. Karayiannis, Flow boiling and flow regimes in small diameter tubes, Appl. Therm Eng. 24 (2004) 1225–1239.
[19] J. Lee, I. Mudawar, Two-phase flow in high-heat-flux micro-channel heat sink for refrigeration cooling applications: Part II – heat transfer characteristics, Int. J. Heat Mass Transfer 48 (2005) 941–955.
[20] R. Yun, Y. Kim, M.S. Kim, Convective boiling heat transfer characteristics of CO_2 in microchannels, Int. J. Heat Mass Transfer 48 (2005) 235–242.
[21] S.G. Kandlikar, P. Balasubramanian, An experimental study on the effect of gravitational orientation on flow boiling of water in 1054 197 m parallel minichannels, J. Heat Transfer 127 (2005) 820–829.
[22] J.R. Thome, Engineering Data Book III. Wolverine Tube Inc, 2004. <http://www.wlv.com/products/databook/db3/data/db3ch12.pdf> (Chapter 12).
[23] D. Shiferaw, X. Huo, T.G. Karayiannis, D.B.R. Kenning, Examination of heat transfer correlations and a model for flow boiling of R134a in small diameter tubes, Int. J. Heat Mass Transfer 50 (2007) 5177–5193.
[24] D. Shiferaw, T.G. Karayiannis, D.B.R. Kenning, Flow boiling in a 1.1 mm tube with R134a: experimental results and comparison with model, Int. J. Therm. Sci. 48 (2009) 331–341.
[25] P.-S. Lee, S.V. Garimella, Saturated flow boiling heat transfer and pressure drop in silicon microchannel arrays, Int. J. Heat Mass Transfer 51 (2008) 789–806.
[26] C.L. Ong, J.R. Thome, Flow boiling heat transfer of R134a, R236fa and R245fa in a horizontal 1.030 mm circular channel, Exp. Therm. Fluid Sci. 33 (2009) 651–663.
[27] A.A. Arcanjo, C.B. Tibirica, G. Ribatski, Evaluation of flow patterns and elongated bubble characteristics during the flow boiling of halocarbon refrigerants in a micro-scale channel, Exp. Therm. Fluid Sci. 34 (2010) 766–775.
[28] S. Saisorn, J. Kaew-On, S. Wongwises, Flow pattern and heat transfer characteristics of R-134a refrigerant during flow boiling in a horizontal circular mini-channel, Int. J. Heat Mass Transfer 53 (2010) 4023–4038.
[29] K.A. Triplett, S.M. Ghiaasiaan, S.I. Abdel-Khalik, D.L. Sadowski, Gas–liquid two-phase flow in microchannels Part I: two-phase flow patterns, Int. J. Multiphase Flow 25 (1999) 377–394.
[30] C.-Y. Yang, C.-C. Shieh, Flow pattern of air–water and two-phase R-134a in small circular tubes, Int. J. Multiphase Flow 27 (2001) 1163–1177.
[31] C. Martin-Callizo, B. Palm, W. Owhaib, R. Ali, Flow boiling visualization of R-134a in a vertical channel of small diameter, J. Heat Transfer 132 (2010) 1–8.
[32] S. Saisorn, S. Wongwises, The effects of channel diameter on flow pattern, void fraction and pressure drop of two-phase air–water flow in circular micro-channels, Exp. Therm. Fluid Sci. 34 (2010) 454–462.
[33] S. Garimella, J.D. Killion, J.W. Coleman, An experimentally validated model for two-phase pressure drop in the intermittent flow regime for circular microchannels, J. Fluid Eng. 124 (2002) 205–214.
[34] C.L. Ong, J.R. Thome, Macro-to-microchannel transition in two-phase flow: Part 2-Flow boiling heat transfer and critical heat flux, Exp. Therm. Fluid Sci. 35 (2011) 873–886.
[35] U. Soupremanien, S.L. Person, M. Favre-Marinet, Y. Bultel, Influence of the aspect ratio on boiling flows in rectangular mini-channels, Exp. Therm. Fluid Sci. 35 (2011) 797–809.
[36] C.-C. Wang, W.-J. Chang, C.-H. Dai, Y.-T. Lin, K.-S. Yang, Effect of inclination on the convective boiling performance of a microchannel heat sink using HFE-7100, Exp. Therm. Fluid Sci. 36 (2012) 143–148.
[37] S. Saisorn, S. Wongwises, A critical review of recent investigations on flow pattern and heat transfer during flow boiling in micro-channels, Front. Heat Mass Transfer 3 (2012) 013006, http://dx.doi.org/10.5098/hmt.v3.1.3006.
[38] M. Kawaji, M. Chung, Adiabatic gas–liquid flow in microchannels, Microscale Thermophys. Eng. 8 (2004) 239–257.
[39] S.G. Kandlikar, Scale effects on flow boiling heat transfer in microchannels: a fundamental perspective, Int. J. Therm. Sci. 49 (2010) 1073–1085.
[40] K.-I. Choi, A.S. Pamitran, J.-T. Oh, Two-phase flow heat transfer of CO_2 vaporization in smooth horizontal minichannels, Int. J. Refrigeration 30 (2007) 767–777.
[41] J. Kaew-On, S. Wongwises, Experimental investigation of evaporation heat transfer coefficient and pressure drop of R-410A in a multiport mini-channel, Int. J. Refrigeration 32 (2009) 124–137.
[42] W. Li, Z. Wu, A general criterion for evaporative heat transfer in micro/mini-channels, Int. J. Heat Mass Transfer 53 (2010) 1967–1976.
[43] W. Zhang, T. Hibiki, K. Mishima, Correlation for flow boiling heat transfer in mini-channels, Int. J. Heat Mass Transfer 47 (2004) 5749–5763.
[44] S.G. Kandlikar, P. Balasubramanian, An extension of the flow boiling correlation to transition, laminar, and deep laminar flows in minichannels and microchannels, Heat Transfer Eng. 25 (2004) 86–93.
[45] L. Sun, K. Mishima, An evaluation of prediction methods for saturated flow boiling heat transfer in mini-channels, Int. J. Heat Mass Transfer 52 (2009) 5323–5329.
[46] S.G. Kandlikar, A general correlation for two-phase flow boiling heat transfer coefficient inside horizontal and vertical tubes, J. Heat Transfer 112 (1990) 219–228.

Fundamental Basis and Application of Cold-Room Project Design: A Turkish Case Study

A. S. Dalkilic, N. A. Kurekci, O. Kincay & S. Wongwises

Arabian Journal for Science and Engineering

ISSN 1319-8025
Volume 38
Number 5

Arab J Sci Eng (2013) 38:1115-1130
DOI 10.1007/s13369-012-0534-5

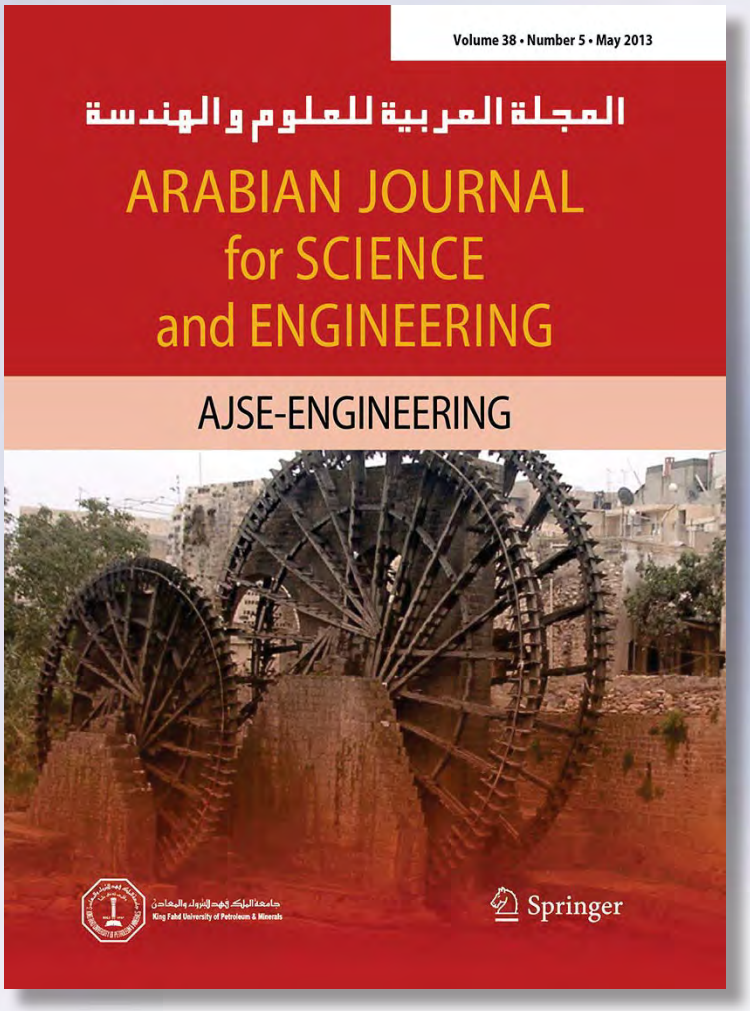

Springer

Your article is protected by copyright and all rights are held exclusively by King Fahd University of Petroleum and Minerals. This e-offprint is for personal use only and shall not be self-archived in electronic repositories. If you wish to self-archive your article, please use the accepted manuscript version for posting on your own website. You may further deposit the accepted manuscript version in any repository, provided it is only made publicly available 12 months after official publication or later and provided acknowledgement is given to the original source of publication and a link is inserted to the published article on Springer's website. The link must be accompanied by the following text: "The final publication is available at link.springer.com".

Author's personal copy

Arab J Sci Eng (2013) 38:1115–1130
DOI 10.1007/s13369-012-0534-5

RESEARCH ARTICLE - MECHANICAL ENGINEERING

Fundamental Basis and Application of Cold-Room Project Design: A Turkish Case Study

A. S. Dalkilic · N. A. Kurekci · O. Kincay · S. Wongwises

Received: 26 March 2011 / Accepted: 2 May 2011 / Published online: 10 January 2013
© King Fahd University of Petroleum and Minerals 2013

Abstract In this paper, cold-room systems in Turkey's various regions were analyzed as case studies to demonstrate the application of the proposed model. They were also compared with each other in terms of the alteration of alternative refrigerants and insulation thickness and energy and exergy analyses of the cold rooms' refrigeration system. The coefficients of performance (COP), refrigerant charge rates, volumetric refrigeration capacity and capacities of each component of the refrigeration system for the refrigerants CFC-12, HCFC-22 and their alternatives, such as HFC-134A, HFC-404A, HFC-407C, HFC-410A and HFC-507, were determined by considering the effects of the main parameters of the performance analysis, such as refrigerant type, degree of subcooling, superheating and compressor efficiency. The first law efficiencies, exergy efficiencies and irreversibility rates were also obtained and discussed in this theoretical study. Based on the results of the energy analyses, all the alternative refrigerants have a slightly lower COP and require lower refrigerant charge rates than CFC-12 and HCFC-22 for condensation temperatures ranging from36–47 °C. The investigated large cities in Turkey have an evaporation temperature of −6 °C regarding the preserved product and various ambient temperatures of these largest cities of Turkey range from 31–42 °C in the case studies. Based on the results of the exergy analyses, the compressor has the greatest irreversibility, followed by the expansion valve, condenser and evaporator as the components of the refrigeration system.

Keywords Cold room · Heat transfer · Refrigerant · Exergy · Case study

A. S. Dalkilic (✉) · N. A. Kurekci · O. Kincay
Heat and Thermodynamics Division,
Department of Mechanical Engineering,
Yildiz Technical University, Yildiz, Besiktas,
Istanbul 34349, Turkey
e-mail: dalkilic@yildiz.edu.tr

S. Wongwises (✉)
Fluid Mechanics, Thermal Engineering
and Multiphase Flow Research Lab. (FUTURE),
Department of Mechanical Engineering,
Faculty of Mechanical Engineering,
King Mongkut's University of Technology Thonburi,
Bangmod, Bangkok 10140, Thailand
e-mail: somchai.won@kmutt.ac.th

الخلاصة

تم - في هذه الورقة العلمية- تحليل نظم الغرفة الباردة في مناطق مختلفة في تركيا ودراسة الحالة لبيان تطبيق الأنموذج المقترح. وتمت أيضا مقارنة بعضها ببعض من حيث تغيير غازات التبريد البديلة ، وسمك العزل، وتحاليل الطاقة ، والطاقة القصوى في نظام تبريد الغرفة الباردة. وتم إيجاد معاملات الأداء (COP)، ومعدلات شحن المبردات، وقدرة التبريد الحجمي، وقدرات كل عنصر من عناصر نظام التبريد لمبردات CFC-12، 22-HCFC وبدائلها، مثل A134-HFC، A404-HFC، C407 -HFC، A410 HFC و507-HFC ، وذلك من خلال النظر في الآثار المترتبة على المعالم الرئيسية لتحليل الأداء، مثل نوع المبردات، ودرجة التبريد الجزئي، والتسخين الفائق ، وكفاءة الضاغط. كما تم الحصول على كفاءات القانون الأول، و كفاءة الطاقة القصوى ، ومعدلات الرجعة ومناقشتها في هذه الدراسة النظرية. وبناء على نتائج تحليلات الطاقة فإن كل من المبردات البديلة لها COP أقل قليلا، وتتطلب معدلات شحن المبردات أقل من-CFC 12 و HCFC 22- لحرارات تكثيف تمتد من 36 مئوية إلى 47 مئوية. إن المدن الكبيرة في تركيا التي تم التحقيق فيها لديها درجة حرارة تبخر -6 مئوية بشأن المنتج المحافظ عليه ودرجات الحرارة المحيطة المختلفة لهذه المدن الكبرى في تركيا التي تمتد من 31 إلى 42 مئوية في دراسات الحالة. وبناء على نتائج تحاليل الطاقة القصوى فإن الضاغط لديه أكبر لا رجعة، يليه صمام التوسع، والمكثف والمبخر ومكونات نظام التبريد.

Author's personal copy

Abbreviations

A	Area, m^2
CFCs	Chlorofluorocarbons
COP	Coefficient of performance
C_{p1}	Specific heat for the temperature above the freezing temperature, J kg^{-1} K^{-1}
C_{p3}	Specific heat for the temperature after freezing process, J kg^{-1} K^{-1}
E	Exergy rate, kW
e	Specific exergy, kJ kg^{-1}
E_Q	Rate of exergy of heat input, kW
E_W	Rate of exergy of power output, kW
F	Defrost factor
GWP	Global warming potential
h	Enthalpy, kJ kg^{-1}
h_i	Inner convective heat transfer coefficient, W m^{-2} K^{-1}
h_d	Outer convective heat transfer coefficient, W m^{-2} K^{-1}
H_d	Air alteration coefficient
HCFCs	Hydro chlorofluorocarbons
HCs	Hydrocarbons
HFCs	Hydro fluorocarbons
I	Rate of irreversibility, kW
k	Thermal conductivity, W m^{-2} K^{-1}
K	Total heat transfer coefficient, W m^{-2} K^{-1}
L	Length, m
l	Freezing heat of product, W kg^{-1}
m	Mass flow rate, kg s^{-1}
m_e	Exergy flow rate of working fluid, kg s^{-1}
m_p	Mass of product, kg
n_{eh}	Total number of electric heaters in the cold room
n_{em}	Total number of electric motors in the cold room
n_p	Total number of people in the cold room
ODP	Ozone depletion potential
P	Pressure, MPa
R	Refrigerant
s	Entropy, kJ kg^{-1} K^{-1}
Q	Heat rejection rate, kW
Q_i	Heat generation of a person, kW
T	Temperature, °C or K
T_0	Environmental reference temperature, °C or K
t_{41}	Total working duration of people in the cold room, h
t_{42}	Illumination time for a day, h
t_{43}	Total working time of an electric motor, h
W	Isentropic compression work, kNm kg^{-1}
W_1	Power of illumination, kJ
W_2	Power of electric motors, kJ
W_3	Power of electric heaters, kJ
ΔT	Temperature difference, K

Greek Symbols

ρ	Density, kg m^{-3}
η	Efficiency
δ	Efficiency defects

Subscripts

afp	After freezing point of product
cl	Ceiling
CL	Cooling load
CR	Cold room
comp	Compressor
cond	Condensing/condenser
E	Exergy
evap	Evaporating/evaporator
fl	Floor
fp	Freezing point
gen	Generation
in	Inside
out	Outside
T	Total
tv	Throttling valve
1	Evaporator superheat
2	Compressorsuperheat
3	Condensersaturated liquid
4	Evaporator saturated mixture

1 Introduction

The refrigeration process is the main process of cold-room systems, which provide proper preservation temperatures to preserve the quality of products. The product is usually a type of perishable food within a certain isolated volume. In addition, many types of medical and perishable products are stored in the same way. It is important for designers to pay attention to the cooling load and the freezing temperatures, which prevent the growth of bacteria. Further, they should know the correct and appropriate type of compressor and condenser to be used in the cold-room system in advance. There are numerous details to plan at the design stage, such as efficient cold-storage space, its location with regard to transportation time from the cold room to the market area, product types stored together at the same time, building materials and seasonal temperature changes of its location.

Many investigations have conducted research on substitutes for CFC-12 and CFC-22. Chlorine atoms cannot be contained in the chemical structure of candidate refrigerants due to their harmful effects, such as ozone layer depletion and global warming. Since the discovery of the depletion of the earth's ozone layer and as a result of the 1992 United

Author's personal copy

Nations Environment Program meeting, the use of CFC-11 and CFC-12 has been phased out. They were used primarily in conventional refrigeration and air conditioning equipments. Besides this, HCFCs is expected to be prohibited after 2030 [1]. HFC-134A and HFC-152A were proposed as replacements of CFC-12 by the American Household Appliances Manufacturers (AHAM) [2]. They can be used as alternative refrigerants in domestic refrigeration due to their specifications of non-toxicity, flammability classes as A1 for R134A and A2 for R152A, and better ozone-depleting potential (ODP) and global-warming potential (GWP). The commercial refrigerant propane/isobutane blends have been utilized in small systems as substitutes for CFC-12 in recent years. Moreover, R407C is acceptable as a short-term replacement for R22 due to its having similar properties to R22.

Wongwises et al. [3] performed an experimental study on the application of hydrocarbon mixtures to replace HFC-134A in automotive air conditioners. The hydrocarbons investigated were propane (R290), butane (R600) and isobutane (R600A). The measured data were obtained from an automotive air conditioning test facility that utilized HFC-134A as the refrigerant. Wongwises and Chimres [4] conducted an experimental study on the application of a mixture of propane, butane, and isobutene to replace HFC-134A in a domestic refrigerator. The results showed that a 60/40 propane/butane mixture was the most appropriate alternative refrigerant. Wongwises and Pirompak [5] reported the results of simulations using an adiabatic capillary tube model developed to study the flow characteristics in adiabatic capillary tubes used as control devices in refrigerating systems and validated by the usage of alternative refrigerants and their mixtures. Wongwises et al. [6] presented a theoretical comparison of the flow characteristics of numerous pairs of refrigerants flowing through adiabatic capillary tubes. For all pairs, numerical results showed that the traditional refrigerants consistently gave lower pressure drops for both single-phase and two-phase flow than the environmentally acceptable alternative refrigerants, which resulted in longer tube lengths. Dalkilic and Wongwises [7] performed a theoretical performance study on a traditional vapor compression refrigeration system with refrigerant mixtures based on HFC-134A, HFC-152A, HFC-32, HC-290, HC-1270, HC-600 and HC-600A for various ratios. They compared their findings with CFC-12, CFC-22, and HFC-134A as possible alternative replacements. Results showed that all the alternative refrigerants investigated in the analysis had a slightly lower performance coefficient (COP) than CFC-12, CFC-22 and HFC-134A. Dalkilic and Wongwises [8] compared a single-stage vapor compression refrigeration system with an actual vapor compression cycle, a single-stage process with an internal heat exchanger and a two-stage process with an economizer using HCFC-22 and CFC-502 and their alternatives, such as HFC-134A, HFC-32, HFC-152A, HFC-404A, HFC-407C, HFC-507 and HFC-410A. Some of the alternative refrigerants' COP values were found to be higher than those of their base traditional pure refrigerants. The effects of the main parameters of the performance analysis, such as refrigerant type, degree of subcooling and superheating on the performance coefficient, refrigerant charge rate and volumetric refrigeration capacity, were investigated for various operating conditions as case studies. Dalkilic [9] presented a comparison of CFC-12, HCFC-22, CFC-502 and their alternatives, such as HFC-134A, HFC-152A, HFC-404A, HFC-407C, HC-290, HC-600A, R717 (ammonia) and three mixtures composed of HFC-134A, HFC-152A, HC-600A and HC-290. His theoretical performance study on a cascade refrigeration system was conducted using two refrigeration cycles connected through a heat exchanger in the middle of the cycle working as an evaporator for the high-pressure cycle and a condenser for the low-pressure cycle. The separate usage of R717 and HFC-152A for the high-pressure and low-pressure sections of the cascade system, respectively, was found to be superior in the analysis to determine the COP and refrigerant charge rates.

Exergy can be defined as a potential or quality of energy. Based on a review of the literature, it seems that the determination of a sustainable quality assessment of energy is possible. There is a relationship among the laws of thermodynamics and exergy. There are specific applications that require the simultaneous calculation of exergy and energy. Dopazo et al. [10] investigated a cascade refrigeration system with CO_2 and NH_3 as working fluids in the low- and high-temperature stages, respectively. Determinations of COP and exergetic efficiency and optimization studies based on the optimum CO_2 condensing temperature have also been performed. Lee et al. [11] used CO_2 and R717 in a cascade refrigeration system to determine the optimal condensing temperature of the cascade condenser, given various design parameters, to maximize the COP and minimize the exergy destruction of the system. They found that the maximum COP increased with evaporating temperature, but decreased as the condensing temperature or temperature difference between the brine and the refrigerant increased. Kanoglu [12] performed an exergy analysis of the multistage cascade refrigeration cycle used for natural gas liquefaction. The equations of exergy destruction and exergetic efficiency for the main cycle components, such as evaporators, condensers, compressors and expansion valves, were developed in his study.

In this study, a single-stage vapor compression refrigeration cycle for some well-known pure refrigerants was investigated to conduct energy and exergy analyses of the cycle at various insulation thicknesses (i.e., 75, 100 and 125 mm) and condenser and evaporator temperatures, according to the largest cities of Turkey in different climatic regions. Graphical presentations are shown to determine high-performance

Author's personal copy

Table 1 Outside design temperatures in summer in the investigated cities of Turkey [16,17]

City	Dry-bulb thermometer temperature (°C)	Wet-bulb thermometer temperature (°C)	Soil temperature (°C)
Erzurum	31	23	15
İstanbul	33	24	20
Ankara	35	21	20
Antalya	39	28	25
Diyarbakır	42	23	25

refrigerants for the preserved product's specified evaporating temperature of −6 °C. Also, condensing temperatures ranged from 36–47 °C, and the various ambient temperatures of Erzurum, Istanbul, Ankara, Antalya and Diyarbakır ranged from 31–42 °C in the cycle. In addition, the fundamental basis and application of cold-room project design are discussed as a sample case study for the simulation of a cold room under specified operating conditions (see Table 1). Accordingly, the main aim of this study was to analyze the single-stage refrigeration cycle to show the differences in refrigeration system components' capacities based on the specified preserved product and various refrigerants. Thus, the use of less energy for the refrigeration system can be obtained and efficiency can be increased by determining the total irreversibility rates and rational efficiency values as a result of the analyses. The specifications of low potentials of ODP and GWP make investigated refrigerants preferable for use in actual refrigeration systems.

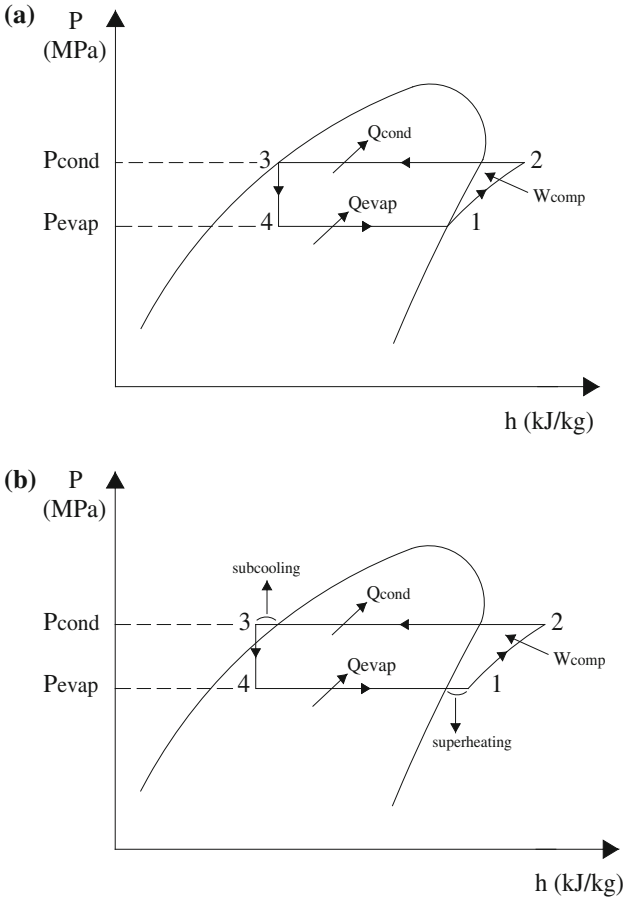

Fig. 1 The ideal vapor-compression refrigeration cycle **a** with P-h diagram **b** for the performance analysis of alternative refrigerants

2 Theoretical Computation Model

The ideal refrigeration cycle [13] shown in Fig. 1 was considered for the working substances that changed phases during the cycle. Actual refrigeration cycle systems have some deviations from the ideal one due to actual pressure losses due to fluid flow and heat transfer exchange in the surroundings. Cycle performance determination is performed to ease theoretical calculations by means of several assumptions: steady-state operating conditions, negligible alterations of kinetic and potential, an adiabatic (well-insulated) heat exchanger, saturated liquid at the outlet of the condenser, saturated vapor at the inlet of the compressor, neglect of pressure drops and heat loss in the environment from evaporators and condensers (see Fig. 1a), isenthalpic flow across the expansion valves and the assumed isentropic efficiency for the compressor. Theoretical investigations were performed using REFPROP [14] and SOLKANE [15] to determine the related physical properties of the refrigerant cycle states in accordance with the various refrigerants. The superheated state of vapor exists at the inlet of the compressor (see Fig. 1b). The pressure of the liquid at the outlet of the condenser is lower than the pressure at the inlet. In addition, there is a greater-than-ideal pressure drop between the condenser and the expansion valve, whereas a larger pressure drop occurs in the evaporation line in actual systems.

2.1 Case Study

In this study, the cold room was used for storing 100,000 kg of pears, requiring preservation at a temperature of –1 °C (−1.6 ÷ –0.5 °C), as recommended by the Intervention Board for Agricultural Products in Turkey. The cold room's dimensions were 14 × 18 × 4.5 m^3 (1,134 m^3) for the preserved product in terms of the planning of efficient preservation conditions in the room considering the product blocks and forklift turnings. The relative humidity of the cold room was set at 90 % for pear preservation (90–95 %). The temperature difference between the cold room and the evaporator was assumed to be 5 K. The evaporator's steady-state temperature was fixed at −6 °C in terms of the preserved products. The ambient temperatures were selected for the investigated cities, such as 31, 33, 35, 39 and 42 °C. Further, the saturation temperatures of the

Author's personal copy

Table 2 The detailed specifications of the construction materials of the cold room

Material	L (m)	k ($W m^{-1} K^{-1}$)	h_i ($W m^{-2} K^{-1}$)	h_d ($W m^{-2} K^{-1}$)	K ($W m^{-2} K^{-1}$)
Outer walls					
Tile	0.01	0.78	9	23	0.32
Internal plastering	0.02	0.87			
Hollow brick	0.23	0.45			
Polyurethane	0.1	0.041			
External plastering	0.03	1.4			
Inner walls					
Tile	0.01	0.78	9	9	0.31
Internal plastering	0.02	0.87			
Hollow brick	0.23	0.45			
Polyurethane	0.1	0.041			
External plastering	0.03	1.4			
Floor					
Terrazzo tile	0.035	1.05	8	∞	0.33
Cement finish	0.03	1.4			
Lean concrete	0.2	1.2			
Polyurethane	0.1	0.041			
Lean concrete	0.2	1.2			
Blockage	0.15	1.74			
Ceiling					
Internal plastering	0.02	0.87	6	23	0.31
Polyurethane	0.1	0.041			
Beton	0.2	0.65			
Asphalt insulation	0.03	0.13			
Door					
Sheet iron (2 pieces)	0.004	46.5	9	23	0.56
Fagus	0.04	0.2			
Polyurethane	0.05	0.041			
Fagus	0.04	0.2			

condenser were calculated as 36, 38, 40, 44 and 48 °C. All assumptions regarding the investigated cities and preserved products were obtained from Duruk and Sarıbatı [16], whereas the conditions of Turkey were acquired from Özkol [17].

The system's cooling load was calculated by means of heat gained from all surfaces and the preserved products in the cold room as shown in Eq. (1). The cold room's heat gained per hour was the sum of the following heat transfer rates: the heat transfer rate from the walls surrounding the cooled volume, ceiling and floor; the heat transfer rate from air alterations; the heat transfer rate from the preserved products and the heat transfer rate from the heat sources in the cold room. The unknown heat gains were usually considered as shown in Eq. (2). A 10 % increase was added to the total value of the system's cooling load, which was equal to the evaporator's heat rejection rate from the cold room. The heat gains can be calculated respectively as follows:

$$Q_T = Q_{11} + Q_{12} + Q_{13} + Q_{21} + Q_{31} + Q_{32} + Q_{33} + Q_{34} + Q_{41} + Q_{42} + Q_{43} + Q_{44} \quad (1)$$

$$Q_{CL} = 1.1 Q_T \quad (2)$$

The total heat transfer coefficient was calculated using Eq. (3) as follows

$$\frac{1}{K} = \frac{1}{h_i} + \sum_{i=1}^{n} \frac{L_i}{k_i} + \frac{1}{h_d} \quad (3)$$

The total heat transfer coefficient in Eqs. (4, 6, 8) was modified according to the manner of heat loss for the walls, floor, ceiling and door. Their construction materials are shown in Table 2 for the insulation material with 100-mm thickness. The temperatures of the cold-room system were considered with a machine room ($T_{out} + 5$ °C), an entrance (T_{out}) and an office ($T_{out} - 8$ °C). The floor (T_{soil}) and the ceiling ($T_{out} - 5$ °C) were examined according to the dry bulb temperature

Author's personal copy

Table 3 Infiltration rates to be added to the outside temperature due to the effect of sun light [16,17]

Way/color	East	South	West	Plan glass
Dark	4	3	4	10
Normal	3	2	3	8
Light	2	1	2	5

of the investigated cities (T_{out}) in Table 1. Whereas the temperature differences in these equations were calculated by means of the related neighbor volumes' temperatures, the infiltration rates from the sun light (see Table 3) were added to the outside temperature (T_{out}).

2.1.1 Heat Transfer Rate from the Walls (Q_{11})

The heat transfer rate from the total wall surfaces was determined for the inner and outer walls, whose directions were north, east, south and west, separately. The average heat conduction coefficient of the cold room's walls was calculated as follows:

$$Q_{11} = A_{out} K_{out} \Delta T_{11} \tag{4}$$

where the temperature difference was the difference between the inside and outside temperatures.

$$\Delta T_{11} = T_{out} - T_{in} \tag{5}$$

In addition, the value of the average heat conduction coefficient was usually between 0.3 and 0.6 $W\,m^{-2}\,K^{-1}$

2.1.2 Heat Transfer Rate from the Floor (Q_{12})

The heat gained from the floor of the cold room was calculated in a similar way as that from the walls of the cold room:

$$Q_{12} = A_{fl} K_{fl} \Delta T_{12} \tag{6}$$

where the temperature difference was the difference between the floor and inside temperatures.

$$\Delta T_{12} = T_{fl} - T_{in} \tag{7}$$

2.1.3 Heat Transfer Rate from the Ceiling (Q_{13})

The heat gained from the outside to the inside of the cold room related to the surface of the ceiling was determined as follows:

$$Q_{13} = A_{cl} K_{cl} \Delta T_{13} \tag{8}$$

Table 4 Sample case study for the comparison of various refrigerants with the insulation thickness of 100 mm for the different cities at $T_{CR} = -1$ °C, $T_{evap} = -6$°C, $\Delta T_{subcooling} = 0$°C, $\Delta T_{superheating} = 0$°C and $\eta_{comp} = 1$

City	Refrigerant	h_1 (kJ kg^{-1})	h_2 (kJ kg^{-1})	h_3 (kJ kg^{-1})	h_4 (kJ kg^{-1})	h_5 (kJ kg^{-1})	h_6 (kJ kg^{-1})	m (kg h^{-1})	Q_{evap} (kW)	Q_{cond} (kW)	W_{comp} (kW)	COP
Diyarbakır $T_{out} = 42$ °C $T_{cond} = 47$ °C	R12	350.77	377.88	377.88	246.47	246.47	350.77	1455.88	42.18	53.14	10.96	3.85
	R22	402.65	440.33	440.33	258.95	258.95	402.65	1056.7	42.18	53.24	11.06	3.81
	R134a	394.97	429.39	429.39	266.93	266.93	394.97	1185.94	42.18	53.52	11.34	3.72
	R407c	406.57	445.89	445.89	263.79	263.79	406.57	1063.51	42.18	53.80	11.62	3.63
	R410A	419.38	460.42	460.42	279.65	279.65	419.38	1086.72	42.18	54.57	12.39	3.40
	R404a	362.77	391.51	391.51	271.29	271.29	362.77	1659.9	42.18	55.43	13.25	3.18
	R507	358.94	386.84	386.84	271.91	271.91	358.94	1744.78	42.18	55.70	13.52	3.12
Erzurum $T_{out} = 31$ °C $T_{cond} = 36$ °C	R12	350.77	372.92	372.92	235.14	235.14	350.77	1013.09	32.54	38.77	6.23	5.22
	R22	402.65	433.23	433.23	244.43	244.43	402.65	740.387	32.54	38.83	6.29	5.17
	R134a	394.97	423.23	423.23	250.54	250.54	394.97	811.078	32.54	38.91	6.37	5.11
	R407c	406.57	438.69	438.69	245.63	245.63	406.57	727.874	32.54	39.03	6.49	5.01
	R410A	419.38	452.73	452.73	258.69	258.69	419.38	729.006	32.54	39.29	6.75	4.82
	R404a	362.77	386.51	386.51	252.65	252.65	362.77	1063.78	32.54	39.56	7.02	4.64
	R507	358.94	381.99	381.99	253.15	253.15	358.94	1107.33	32.54	39.63	7.09	4.59

Author's personal copy

where the temperature difference was the difference between the ceiling and inside temperatures.

$$\Delta T_{13} = T_{\mathrm{cl}} - T_{\mathrm{in}} \tag{9}$$

2.1.4 Heat Transfer Rate from Air Alteration (Q_{21})

Some amount of heat transfer occurred when the door of the cold room was opened to the outside or a place with a different temperature than the inside of the cold room. This situation brought an additional cooling load to the system, which was calculated as:

$$Q_{21} = H_{\mathrm{d}}\, V (h_{\mathrm{out}} - h_{\mathrm{in}}) \rho_{\mathrm{air}} \tag{10}$$

where the air alteration coefficient (H_{d}) was assumed to be 1.7 times/24 h for this application.

2.1.5 The Heat Transfer Rate from Preserved Products (Q_{31}, Q_{32}, Q_{33})

The cooling load from the preserved product can be evaluated in three sections, which are summarized below briefly. These sections depended upon the type of product. The specific heats of the pears before and after the freezing point are 3.61 and 1.88 $\mathrm{kJ\,kg^{-1}\,K^{-1}}$, respectively. The latent heat of freezing and the heat of respiration are 277 $\mathrm{kJ\,kg^{-1}}$ and 0.005 $\mathrm{W\,kg^{-1}}$ for pears.

First, the heat rejection rate from the preserved products for the temperature above the freezing temperature was calculated as:

$$Q_{31} = m C_{\mathrm{p1}} \Delta T_{31} \tag{11}$$

where the temperature difference was the same as in Eq. (5).

Second, the heat rejection rate from the preserved products during the freezing temperature was shown as:

$$Q_{32} = m_{\mathrm{p}}\, l \tag{12}$$

Third, the heat rejection rate from the preserved products was calculated after the freezing process as:

$$Q_{33} = m C_{\mathrm{p3}}\, \Delta T_{33} \tag{13}$$

where the temperature difference was the difference between the freezing temperature and the temperature after the freezing process.

$$\Delta T_{33} = T_{\mathrm{fp}} - T_{\mathrm{afp}} \tag{14}$$

2.1.6 The Heat Transfer Rate from the Heat Sources in the Cold Room (Q_{41}, Q_{42}, Q_{43}, Q_{44})

The duration of the cooling process was planned to be 20 h a day. The human working time, in other words, the illumination time was assumed to be 2 h a day for two individuals working in the cold room. The illumination was performed by four pieces of 100 W fluorescents. Each of four electric engines had 780 W of power in the case study. The heat transfers rates from the workers (Q_{41}), illumination (Q_{42}), electric engines (Q_{43}) and electric heater with defrost (Q_{44}) in the cold room were determined respectively as:

$$Q_{41} = n_{\mathrm{p}}\, t_{41}\, Q_{\mathrm{i}} \tag{15}$$

$$Q_{42} = W_1\, t_{42} \tag{16}$$

$$Q_{43} = n_{\mathrm{em}}\, W_2\, Q_{\mathrm{em}}\, t_{43} \tag{17}$$

$$Q_{44} = n_{\mathrm{eh}}\, W_3\, \mathrm{Ft}_{44} \tag{18}$$

2.2 Calculation Procedure for Energy Analysis

The state-point properties and results of energy equations below are presented in Table 4 as a case study. The heat transfer rate of the evaporator (Q_{evap}) and refrigerant charge rate, respectively, were calculated as follows:

$$Q_{\mathrm{CL}} = Q_{\mathrm{evap}} = m(h_1 - h_4) \tag{19}$$

$$m = \frac{Q_{\mathrm{CL}}}{h_1 - h_4} \tag{20}$$

The condenser capacity (Q_{cond}) and isentropic compression work of the compressor (W_{comp}), respectively, were expressed as follows:

$$Q_{\mathrm{cond}} = m(h_2 - h_3) \tag{21}$$

$$W_{\mathrm{comp}} = m(h_2 - h_1) \tag{22}$$

The efficiency of a refrigerator is expressed in terms of the COP. It is the ratio of the heat removed from the space to be refrigerated to the work to be consumed to accomplish this task. As the COP value rises, power consumption decreases. It is obvious that this situation will help to reduce the environmental pollution caused by power production systems. The COP of the refrigeration system's cycle can be determined by the following equation:

$$\mathrm{COP} = \frac{Q_{\mathrm{evap}}}{W_{\mathrm{comp}}} \tag{23}$$

2.3 Calculation Procedure for Exergy Analysis

Energy and exergy analyses were used in this subsection to conduct thermodynamic performance comparisons. Many researchers have proposed that the thermodynamic performance of a process is best evaluated using exergy analysis [18,19]. Exergy is the maximum amount of work that can be produced by a stream or a system as it is brought into equilibrium with a reference environment. It can be thought of as a measure of the usefulness or quality of energy. Exergy is consumed during real processes and conserved during ideal

Author's personal copy

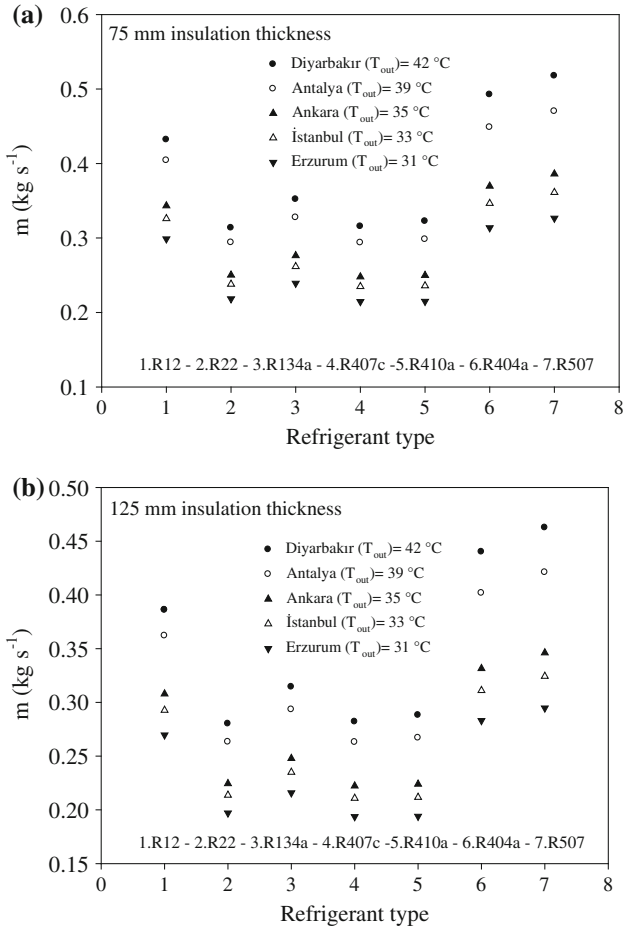

Fig. 2 Alteration of the refrigerant charge rate obtained by Eq. (20) according to the investigated cities of Turkey and refrigerant types

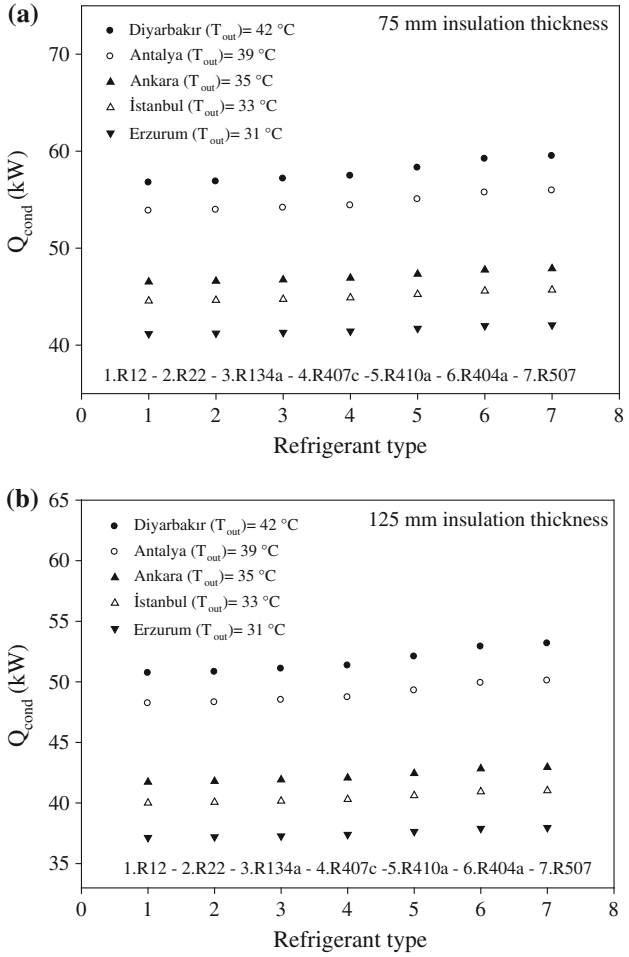

Fig. 3 Alteration of the condenser capacity obtained by Eq. (21) according to the investigated cities of Turkey and refrigerant types

processes. In general, energy and exergy efficiencies are calculated as the ratio of the energy (or exergy) of the product(s) to the energy (or exergy) of the input(s). The exergy balance of the refrigeration system was calculated in a steady state. Neglecting the kinetic, chemical and potential energies and the balances of mass, energy and exergy were used for the determination of heat input, rate of exergy loss and efficiency of exergy in this study. The mass balance and exergy balance equations are shown in the following equations:

$$\sum_{\text{in}} m - \sum_{\text{out}} m = 0 \tag{24}$$

$$E_{\text{Q}} - E_{\text{W}} = \sum_{\text{out}} \text{me} + \sum_{\text{in}} \text{me} + I \tag{25}$$

where I is the rate of irreversibility (or the rate of exergy destruction, $I = T_{\text{os}}$), m_{e} is the exergy flow rate of working fluid, E_{Q} is the rate of exergy of heat input, E_{W} is the rate of exergy of power output and s_{gen} is the rate of entropy generation. The rate of heat exergy and the power exergy, respectively, were defined in the following equations:

$$E_{\text{Q}} = Q\left(1 - \frac{T_0}{T}\right) \tag{26}$$

$$E_{\text{W}} = W \tag{27}$$

The exergy rate at the state points in Fig. 1 was calculated as:

$$E_{\text{i}} = m\left[(h_{\text{i}} - T_0 s_{\text{i}}) - (h_0 - T_0 s_0)\right] \tag{28}$$

The exergy analysis for each component of the refrigeration cycle in Fig. 1 was summarized from Eqs. (29) to (40). The exergy rate balance, irreversibility and exergy efficiency for the compressor (i.e., processes 1–2) are shown in Eqs. (29), (30), and (31), respectively.

$$\text{me}_1 = E_{\text{W}} + \text{me}_2 + I_{\text{comp}} \tag{29}$$

$$I_{\text{comp}} = mT_0(s_2 - s_1) \tag{30}$$

$$\eta_{\text{comp}} = \frac{E_2 - E_1}{W_{\text{comp}}} \tag{31}$$

The exergy rate balance, irreversibility and exergy efficiency for the condenser (i.e., processes 2–3) are shown in Eqs. (32), (33), and (34), respectively:

Author's personal copy

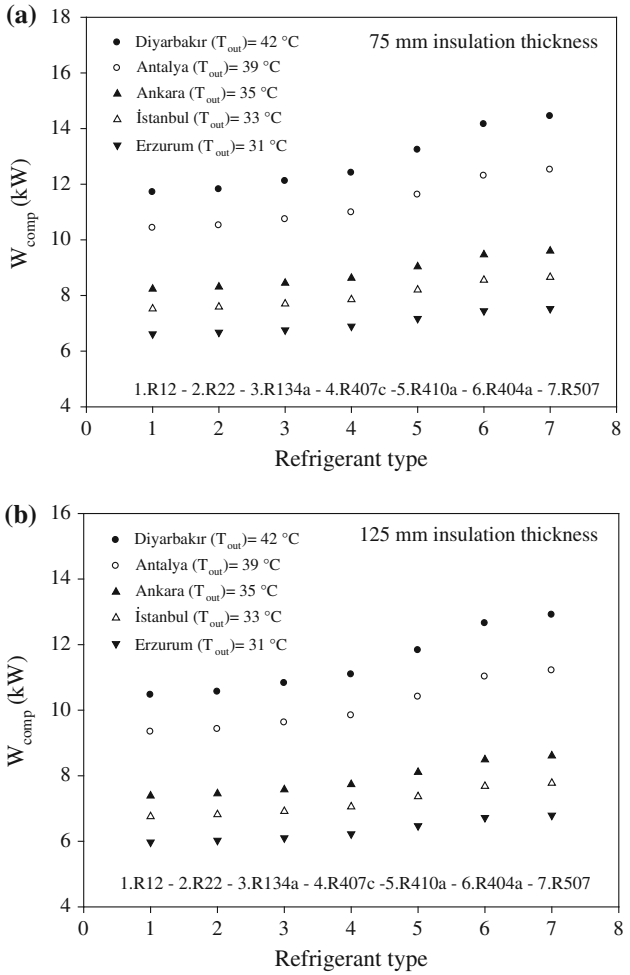

Fig. 4 Alteration of the compressor work obtained by Eq. (22) according to the investigated cities of Turkey and refrigerant types

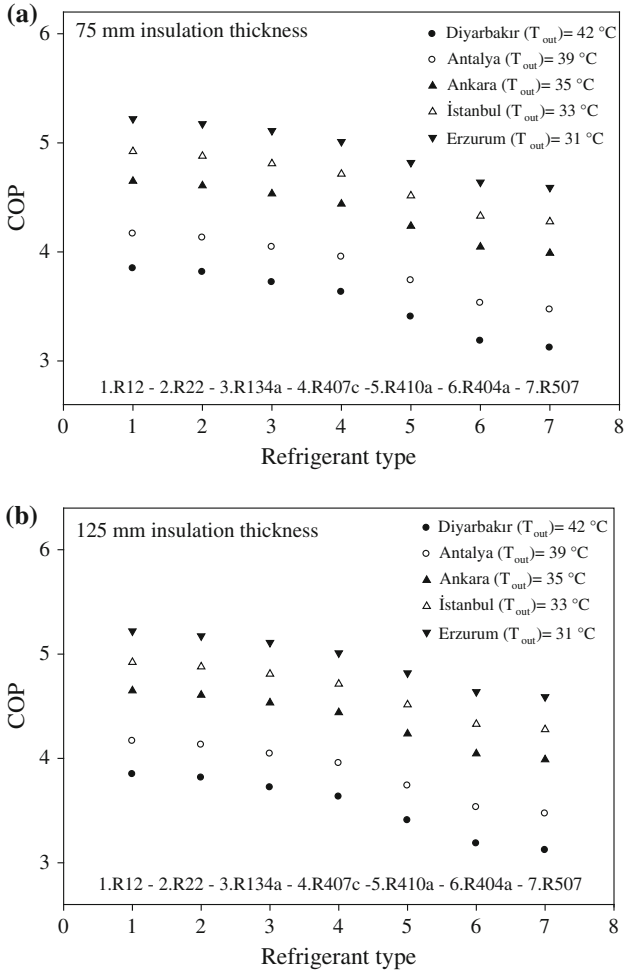

Fig. 5 Alteration of the COP obtained by Eq. (23) according to the investigated cities of Turkey and refrigerant types

$$\mathrm{me}_2 = E_{\mathrm{Q,cond}} + \mathrm{me}_3 + I_{\mathrm{cond}} \tag{32}$$

$$I_{\mathrm{cond}} = m\left[(h_2 - h_3) - T_0(s_2 - s_3)\right] \tag{33}$$

$$\eta_{\mathrm{cond}} = \frac{E_3}{E_2} \tag{34}$$

The exergy rate balance, irreversibility and exergy efficiency for the throttling valve (i.e., processes 3–4) are shown in Eqs. (35), (36), and (37), respectively:

$$\mathrm{me}_3 = \mathrm{me}_4 + I_{\mathrm{tv}} \tag{35}$$

$$I_{\mathrm{tv}} = mT_0(s_4 - s_3) \tag{36}$$

$$\eta_{\mathrm{tv}} = \frac{E_4}{E_3} \tag{37}$$

The exergy rate balance, irreversibility and exergy efficiency for the evaporator (i.e., processes 4–1) are shown in Eqs. (38), (39), and (40), respectively:

$$\mathrm{me}_4 + E_{\mathrm{Q,evap}} = \mathrm{me}_1 + I_{\mathrm{evap}} \tag{38}$$

$$I_{\mathrm{evap}} = m\left[(h_4 - h_1) - T_0(s_4 - s_1)\right] \tag{39}$$

$$\eta_{\mathrm{tv}} = \frac{E_1}{E_4} \tag{40}$$

The total refrigeration cycle's irreversibility rate can be expressed as:

$$I_{\mathrm{TOTAL}} = I_{\mathrm{comp}} + I_{\mathrm{cond}} + I_{\mathrm{tv}} + I_{\mathrm{evap}} \tag{41}$$

Efficiency defect is a significant parameter in analyses of multicomponent thermal systems. Fractions of input are lost through irreversibilities. They can be calculated as efficiency defects [20] in Eq. (42):

$$\delta_i = \frac{I_i}{W_{\mathrm{comp}}} \tag{42}$$

Detailed information on the subject of thermodynamics of exergy analysis can be found in Bejan's works [21,22].

Author's personal copy

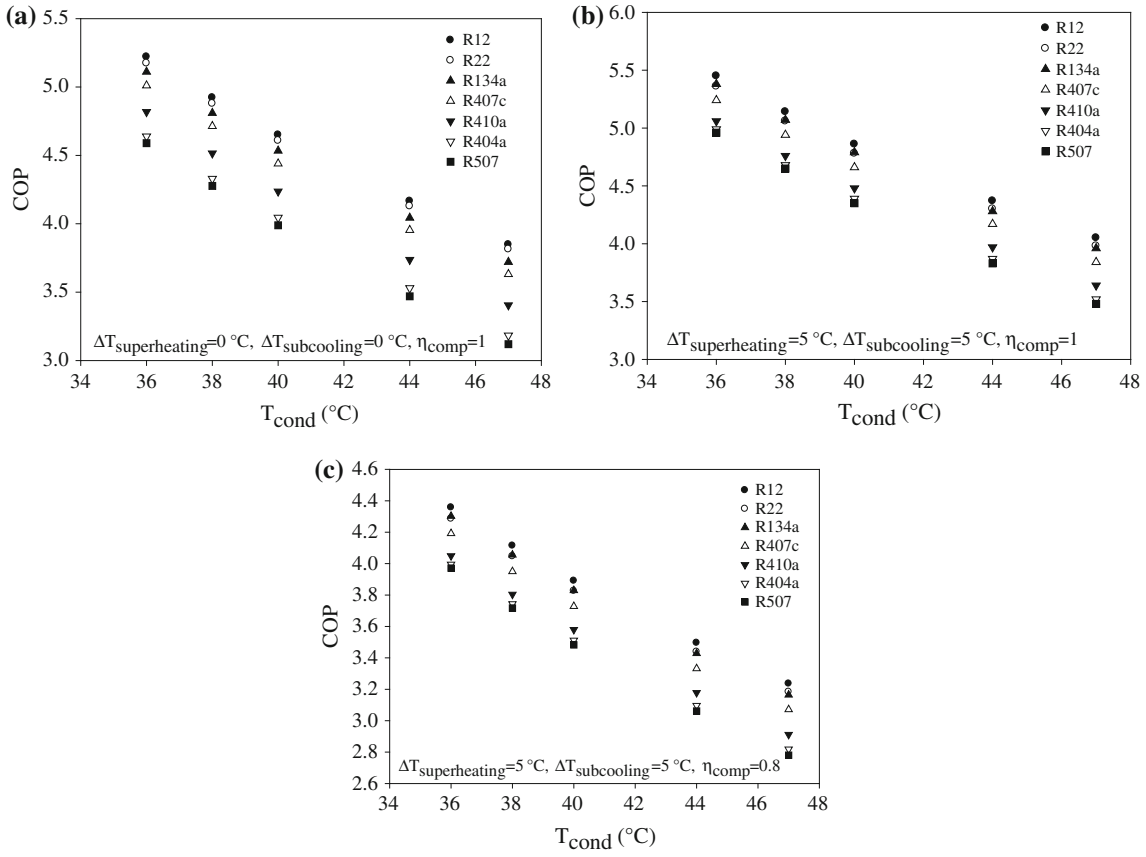

Fig. 6 Coefficient of performance (**a**–**c**) versus condensing temperature

3 Results and Discussion

This paper included a description of a theoretical model and its application on the design of a cold room using Turkey as a case study. The investigated model can be used to assess the completeness and effectiveness of cold-room systems with regard to heat transfer and thermodynamics analyses for the basic components of the single-stage vapor-compression refrigeration cycle. The effective cooling of approximately −40 °C can be obtained with the use of a single-stage vapor compression refrigeration system. Efficiency begins to decrease at temperatures below −35 °C due to a large difference between the evaporator and the condenser temperatures. The evaporating temperature was held constant at −6 °C due to the preserved products. For that reason, the single-stage vapor compression system was supposed to correspond to the necessary performance issues. A cascade refrigeration system should be utilized to work with a lower temperature than −40 °C.

Thermodynamic efficiency is determined by first-law energy analysis, which can be used to compare alternative cycles. The determination of COP is performed for this purpose. Irreversibilities cause reductions in the cycle's COP, and the minimization of irreversibilities increases the cycle's efficiency. These irreversibilities' places as components in the refrigeration cycle and their magnitudes cannot be detected by first-law energy analysis. Second-law exergy analysis can handle this problem. Stegou-Sagia and Paignigiannia [23] emphasized that exergy analysis was a dominant method in the design, optimization and performance estimation of the refrigeration cycle.

The general characteristics of energy analyses are listed in Figs. 2, 3, 4, 5, which show either the effect of alterations of outside temperatures in different cities or the effect of the use of various refrigerants and alterations of insulation thickness of the cold room on the refrigerant charge rate, condenser capacity, compressor work and COP. Figure 2 shows that the refrigeration charge rate decreases with increases in the insulation thickness. The highest use of refrigerant charge rate was in the city of Diyarbakır, which has a higher outside temperature than the other cities examined. Further, R410A and R407C have the lowest refrigerant charge rate values together with R22. Figures 3 and 4 show that the condenser capacity and the compressor work have a similar pattern. That is, they decrease with increasing insulation thickness from 75 to 125 mm and increase with increasing outside temperatures of the cold room from 36 to 47 °C or condenser temperatures from 36 to 47 °C. Figure 5 shows the alteration of COP values

Author's personal copy

Table 5 Sample case study for the comparison of various refrigerants according to the components of refrigeration cycle for Istanbul ($T_{out} = 33\,^{\circ}C$, $T_{cond} = 38\,^{\circ}C$, $Q_{evap} = 33.25\,kW$) at the fixed temperature of $T_{CR} = -1\,^{\circ}C$, $T_{evap} = -6\,^{\circ}C$, $\Delta T_{subcooling} = 5\,^{\circ}C$, $\Delta T_{superheating} = 5\,^{\circ}C$ and $\eta_{comp} = 0.8$, $T_o = T_{out} = 33\,^{\circ}C$

Compressor								Condenser							
Refrigerant	e_1 (kJ kg^{-1})	e_2 (kJ kg^{-1})	E_1 (kW)	E_2 (kW)	I (kW)	δ	η_E (%)	Refrigerant	e_2 (kJ kg^{-1})	e_3 (kJ kg^{-1})	E_2 (kW)	E_3 (kW)	I (kW)	δ	η_E (%)
R12	98.21	122.24	1.37	1.7	0.07683	0.186	81.35	R12	122.25	119.22	1.71	1.66	0.04223	0.102	97.52
R22	90.46	124.08	0.925	1.26	0.07484	0.178	82.13	R22	124.09	118.99	1.27	1.22	0.05218	0.124	95.89
R134a	91.54	122.19	1.013	1.35	0.07861	0.188	81.19	R134a	122.19	118.78	1.35	1.32	0.03782	0.09	97.21
R407c	86.66	121.77	0.864	1.21	0.07877	0.183	81.64	R407c	121.78	119.00	1.22	1.19	0.02774	0.064	97.72
R410A	87.77	124.62	0.869	1.23	0.08036	0.18	81.96	R410A	124.62	118.78	1.24	1.18	0.05797	0.13	95.31
R404a	95.96	121.88	1.36	1.72	0.08545	0.188	81.12	R404a	121.88	119.07	1.73	1.69	0.03989	0.088	97.69
R507	96.73	121.89	1.42	1.79	0.08633	0.189	81.06	R507	121.89	118.87	1.79	1.75	0.04451	0.097	97.52
Throttling valve								Evaporator							
Refrigerant	e_3 (kJ kg^{-1})	e_4 (kJ kg^{-1})	E_3 (kW)	E_4 (kW)	I (kW)	δ	η_E (%)	Refrigerant	e_4 (kJ kg^{-1})	e_1 (kJ kg^{-1})	E_4 (kW)	E_1 (kW)	I (kW)	δ	η_E (%)
R12	119.22	115.85	1.66	1.62	0.04695	0.113	97.18	R12	115.85	98.22	1.62	1.37	0.24605	0.597	84.78
R22	118.99	114.52	1.22	1.17	0.04572	0.109	96.25	R22	114.52	90.46	1.17	0.93	0.24622	0.588	78.99
R134a	118.78	113.76	1.32	1.26	0.05557	0.132	95.77	R134a	113.76	91.54	1.26	1.01	0.24603	0.589	80.47
R407c	119.00	113.55	1.19	1.13	0.05435	0.126	95.42	R407c	113.55	86.66	1.13	0.86	0.26830	0.625	76.32
R410A	118.78	112.63	1.18	1.12	0.06096	0.136	94.82	R410A	112.63	87.77	1.12	0.87	0.24630	0.553	77.93
R404a	119.07	113.41	1.69	1.61	0.08025	0.177	95.25	R404a	113.41	95.97	1.61	1.36	0.24718	0.546	84.62
R507	118.87	113.42	1.75	1.67	0.08004	0.175	95.42	R507	113.42	96.74	1.67	1.42	0.24511	0.538	85.29

Author's personal copy

Table 6 Sample case study for the comparison of various refrigerants according to the components of refrigeration cycle for Istanbul ($T_{out} = 33\,^{\circ}C$, $T_{cond} = 38\,^{\circ}C$, $Q_{evap} = 33.25\,kW$) at the fixed temperature of $T_{CR} = -1\,^{\circ}C$, $T_{evap} = -6\,^{\circ}C$, $\Delta T_{subcooling} = 5\,^{\circ}C$, $\Delta T_{superheating} = 5\,^{\circ}C$ and $\eta_{comp} = 0.8$, $T_0 = 25\,^{\circ}C$

Compressor								Condenser							
Refrigerant	e_1 (kJ kg^{-1})	e_2 (kJ kg^{-1})	E_1 (kW)	E_2 (kW)	I (kW)	δ	η_E (%)	Refrigerant	e_2 (kJ kg^{-1})	e_3 (kJ kg^{-1})	E_2 (kW)	E_3 (kW)	I (kW)	δ	η_E (%)
R12	83.14	107.32	1.16	1.50	0.07482	0.182	81.84	R12	107.32	100.42	1.50	1.40	0.09622	0.234	93.57
R22	76.96	110.78	0.79	1.13	0.07288	0.174	82.60	R22	110.78	100.42	1.13	1.03	0.10609	0.253	90.64
R134a	77.83	108.67	0.86	1.20	0.07656	0.183	81.69	R134a	108.67	100.35	1.20	1.11	0.09208	0.220	92.35
R407c	73.39	108.71	0.73	1.08	0.07672	0.179	82.12	R407c	108.71	100.44	1.08	1.00	0.08255	0.192	92.39
R410A	74.82	111.88	0.74	1.11	0.07827	0.176	82.44	R410A	111.88	100.54	1.11	1.00	0.11243	0.252	89.86
R404a	81.32	107.39	1.15	1.52	0.08322	0.184	81.62	R404a	107.39	100.68	1.52	1.43	0.09501	0.210	93.76
R507	81.97	107.27	1.20	1.58	0.08408	0.184	81.56	R507	107.27	100.50	1.58	1.48	0.09959	0.218	93.68
Throttling valve								Evaporator							
Refrigerant	e_3 (kJ kg^{-1})	e_4 (kJ kg^{-1})	E_3 (kW)	E_4 (kW)	I (kW)	δ	η_E (%)	Refrigerant	e_4 (kJ kg^{-1})	e_1 (kJ kg^{-1})	E_4 (kW)	E_1 (kW)	I (kW)	δ	η_E (%)
R12	100.42	97.14	1.40	1.36	0.04572	0.111	96.74	R12	97.14	83.14	1.36	1.16	0.24605	0.597	85.59
R22	100.42	96.06	1.03	0.98	0.04452	0.106	95.67	R22	96.06	76.96	0.98	0.79	0.24622	0.588	80.12
R134a	100.35	95.47	1.11	1.06	0.05412	0.129	95.13	R134a	95.47	77.83	1.06	0.86	0.24603	0.589	81.53
R407c	100.44	95.13	1.00	0.95	0.05292	0.123	94.72	R407c	95.13	73.39	0.95	0.73	0.26830	0.625	77.14
R410A	100.54	94.55	1.00	0.94	0.05936	0.133	94.04	R410A	94.55	74.82	0.94	0.74	0.24630	0.553	79.13
R404a	100.68	95.17	1.43	1.35	0.07815	0.173	94.52	R404a	95.17	81.32	1.35	1.15	0.24718	0.546	85.44
R507	100.50	95.19	1.48	1.40	0.07795	0.171	94.72	R507	95.19	81.97	1.40	1.20	0.24511	0.538	86.11

Author's personal copy

Table 7 Irreversibility rates for the stated values of T_{cond} for the comparison of investigated refrigerants at the fixed temperature of $T_{CR} = -1\,^{\circ}C$, $T_{evap} = -6\,^{\circ}C$, $\Delta T_{subcooling} = 5\,^{\circ}C$, $\Delta T_{superheating} = 5\,^{\circ}C$ and $\eta_{comp} = 0.8$

Investigated cities of Turkey	T_{cond} (°C)	Q_{evap} (kW)	Total irreversibility rates (kW)						
			R12	R22	R134a	R407c	R410a	R404a	R507
$T_o = T_{out}$									
Diyarbakır	47	40.25	0.52389	0.53257	0.53575	0.55199	0.5822	0.60144	0.60970
Antalya	44	38.88	0.48495	0.49298	0.49445	0.50884	0.53341	0.54746	0.55369
Ankara	40	34.34	0.43573	0.44302	0.44272	0.45473	0.47359	0.48268	0.48680
İstanbul	38	33.25	0.41206	0.41895	0.41803	0.42915	0.44559	0.45277	0.456
Erzurum	36	31.18	0.38903	0.39557	0.39406	0.40437	0.41867	0.4243	0.42689
$T_0 = 25\,^{\circ}C$									
Diyarbakır	47	40.25	0.63177	0.64045	0.64359	0.66109	0.69008	0.70934	0.71751
Antalya	44	38.88	0.573778	0.581812	0.583263	0.598689	0.62224	0.63632	0.642473
Ankara	40	34.34	0.49918	0.50647	0.50617	0.51890	0.53705	0.54616	0.55022
İstanbul	38	33.25	0.46282	0.46972	0.46879	0.48049	0.49636	0.50356	0.50673
Erzurum	36	31.18	0.42711	0.43364	0.43213	0.44288	0.45675	0.46240	0.46495

with the investigated refrigerants. COP was found to increase with decreasing outside temperatures or condenser temperature. In addition, the insulation thickness of the cold room has no significant effect on the COP of the refrigerant cycle. R12 and R22 have the highest COP values, whereas R404A and R507 have the lowest values.

Cycle performance can be improved by the subcooling and superheating application. In this paper, the effects of the degree of subcooling and superheating were calculated respectively. A comparison was made between the superheating/subcoolingcase in Fig. 1b with the non-superheating/subcooling case in Fig. 1a. It is illustrated from Fig. 6a–c for the investigated refrigerants. Figure 6 shows the effect of assumed values of superheating, subcooling and compressor efficiency cases on the COP step by step. The ideal situation for the single-stage refrigeration cycle is presented for comparison in Fig. 6a. The case of subcooling and superheating, assuming that compressor isentropic efficiency was 100 %, caused increase in COP (see Fig. 6b). The improvement was due to the increase in the compressor inlet temperature, which increased the compressor power (W_{comp}) and performance coefficient. The cycle performance was affected by the subcooling more than the superheating. On the other hand, Fig. 6c shows that compressor isentropic efficiency was more dominant than the subcooling and superheating cases on COP. In a real system, compressor isentropic efficiency is a function of the evaporator and condenser pressures. The real refrigerating capacity and COP can be calculated if the efficiency of the compressor is known. The refrigerating capacity is influenced by the volumetric efficiency and COP by the isentropic efficiency. Despite the increase in COP by means of the subcooling and superheating cases in Fig. 6b, the assumed compressor isentropic efficiency caused decrease in COP values lower than those in Fig. 6a, b.

From Tables 4, 5, 6, 7, significant parameters of cycle performance under different conditions are calculated as case studies of the investigated refrigerants for the same evaporation temperature related to the preserved products. In addition, the evaluation of cycle performance results under different working conditions was consistent with those under real working conditions.

Table 4 shows a case study to determine the characteristic parameters of the energy analyses for the specific conditions of selected Turkish cities. Diyarbakır had the highest outside temperature and condenser temperatures (42 and 47 °C, respectively). Erzurum had the lowest outside temperature and condenser temperatures (31 and 36 °C, respectively). Ideal conditions for the components of the refrigeration system were used to show the effect of the use of various refrigerants on the required refrigerant charge rate, capacity of the condenser, required compressor work and COP for a constant insulation thickness of 100 mm and a constant cooling load (i.e., a constant evaporating temperature). As a result, the high performance refrigerants were put in order according to their COP values. As seen in Table 4, traditional refrigerants have higher COP values than alternative refrigerants. The refrigerant charge rates of R134A, R407C, R410A and R404A are similar to that of R22, whereas R507 has the lowest COP value and highest refrigerant charge rate. The comparison of the refrigeration systems in the cities of Erzurum and Diyarbakır demonstrates the effect of the outside temperature on the preservation of the same product in a cold room. The low outside temperature condition (Erzurum) has

Author's personal copy

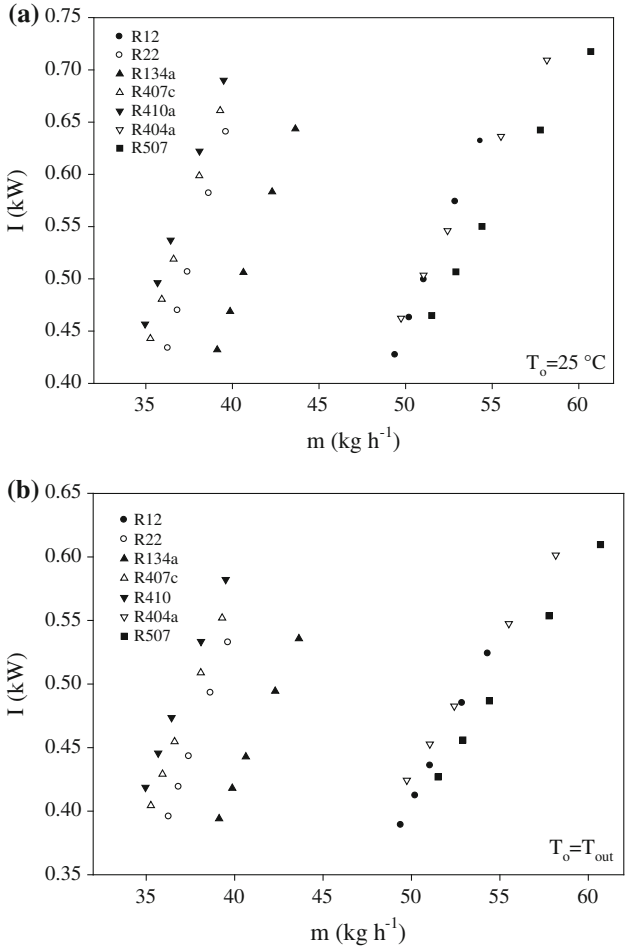

Fig. 7 Total irreversibilities versus refrigerant charge rate for all investigated cities at the fixed temperature of $T_{CR} = -1\,^{\circ}C$, $T_{evap} = -6\,^{\circ}C$, $\Delta T_{subcooling} = 5\,^{\circ}C$, $\Delta T_{superheating} = 5\,^{\circ}C$ and $\eta_{comp} = 0.8$, $T_0 = 25\,^{\circ}C$

higher COP values and lower refrigerant charge rate values than the high outside temperature condition (Diyarbakır) in the case study.

Tables 5 and 6 illustrate the difference in the use of reference temperature and its effect on each component of the refrigeration cycle. First, the reference temperature was equal to the outside temperature of the cold room (see Table 5) and assumed to be 25 °C, which is commonly done in the literature. As a result, the losses in the evaporator seemed important with their large and constant values apart from the others. In addition, exergetic efficiencies of the condenser and throttling valve were found to be higher than those of other components. Tables 5 and 6 also show the exergy performance of the investigated refrigerants for each component of the refrigeration cycle.

The irreversibility rates of all the investigated refrigerants were plotted against the refrigerant charge rates in Fig. 7, according to the alteration of the reference temperature. The largest irreversibility rate and refrigerant charge rate were seen in R507 and R404A. As shown in Fig. 7, the refrigerant charge rate increased with the irreversibility rate. Moreover, when the reference temperature was assumed to be 25 °C, as shown in Fig. 7a, the irreversibility values were found to be higher than of those in Fig. 7b, which shows the reference temperature as the outside temperature of the cold room. This situation regarding the increase in irreversibility values can also be clearly seen in Table 7. That is, the total irreversibility rates increased with increasing condenser temperatures.

The efficiency defects in the components of the refrigerating cycle in Fig. 1 are shown in Fig. 8 for all of the investigated refrigerants. The maximum efficiency defect was found in the evaporator in comparison to other components, followed by the condenser, compressor and refrigerant expansion valve. The efficiency defects for R407C and R410A were also the maximum values in the evaporator. These findings associated with the efficiency defects indicate that design improvements of components are needed to enhance the exergetic efficiency of the single-stage refrigeration system.

The thermodynamic analysis of CFC-12, HCFC-22 and their alternatives, such as HFC-134A, HFC-404A, HFC-407C, HFC-410A and HFC-507 was studied by both the first and the second laws of thermodynamics using the single-stage vapor-compression refrigeration cycle. The analysis was performed on each of the system components to determine their individual roles in the overall system of irreversible losses. Most of the losses were found to be due to the evaporator. The irreversibility of the condenser was also significant.

4 Conclusion

A thermodynamic energy and exergy analysis to optimize a single-stage vapor-compression refrigeration system to be used for a cold-storage application was presented in this paper. Its fundamental issues were discussed in detail. Many case studies with different theoretical conditions were described to determine the optimum operating conditions for the preservation of pears.

The proposed model provided a useful procedure for the cold-room project design. It is expected that it will be a beneficial source for researchers interested in the topic of refrigeration and air conditioning. The results of this study are of technological importance for efficient design when cold-room systems are assigned to utilize various alternative refrigerants in different regions of Turkey.

An ideal vapor compression refrigeration system was used for the performance analysis of alternative new refrigerants as substitutes for CFC-12, HFC134A and CFC-22. Considering the comparison of COP and refrigerant charge rates of the tested refrigerants, refrigerants of R407C and

Author's personal copy

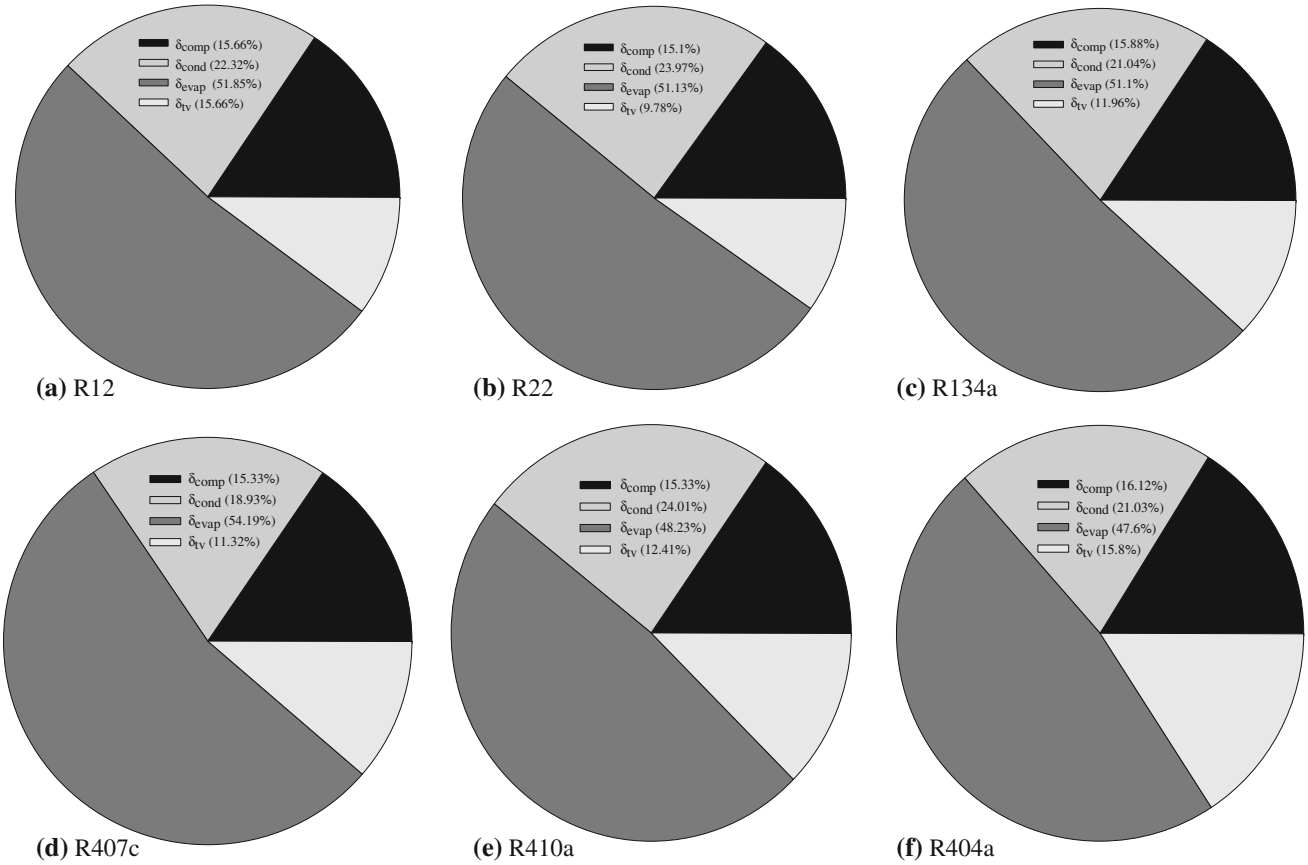

Fig. 8 Pie chart of efficiency defects of the investigated refrigerants belong to Ankara city for a condenser temperature of 40 °C and the fixed temperature of $T_{CR} = -1\,^{\circ}C$, $T_{evap} = -6\,^{\circ}C$, $\Delta T_{subcooling} = 5\,^{\circ}C$, $\Delta T_{superheating} = 5\,^{\circ}C$ and $\eta_{comp} = 0.8$, $T_o = 25\,^{\circ}C$

R410A were found to be the most suitable alternatives among refrigerants tested for R12 and R22, respectively. The COP of the system decreased with increasing condensing temperature for a constant evaporating temperature in the analysis. All systems were improved by analyzing the effect of the superheating/subcooling case. Further, the effect of compressor efficiency on COP was also discussed in various case studies.

The analysis of the single-stage vapor-compression refrigeration cycle's performance by the exergy method illustrates the utility of this method. Employing the concept of efficiency defect enabled the ratios of input lost through irreversibilities and demonstrated the components of the refrigeration system needed to optimize the specified preservation conditions of the product. A large amount of exergy is wasted during the working of the system, which decreases the exergy efficiency of the refrigeration system.

There is not any refrigerant that meets all of the necessary requirements due to the changes in the thermodynamic physical properties of the refrigerant. The thermo-physical properties, such as performance and efficiency, limitations and restrictions related to safety, environmental impact and associated legislation, are the most significant factors in choosing a new refrigerant. Low viscosities of liquid and vapor phases, high liquid specific heat, high thermal conductivities of liquid and vapor phases, high latent heat, and limited temperature glide are the desired thermo-physical properties of refrigerant/refrigerant mixtures.

Acknowledgments The authors are indebted to the Departments of Mechanical Engineering, Yildiz Technical University (YTU) and King Mongkut's University of Technology Thonburi (KMUTT) for supporting this study. The first author wishes to thank King Mongkut's University of Technology Thonburi (KMUTT) for providing him with a postdoctoral fellowship. The fourth author would like to thank the Thailand Research Fund for the support.

References

1. Lee, Y.S.; Su, C.C.: Experimental studies of isobutane (R600a) as the refrigerant in domestic refrigeration system. Appl. Thermal Eng. **22**, 507–519 (2002)
2. Devotta, S.; Gopichand, S.; Pendyola, V.R.: Assessment of HFCs, fluorinated ethers and amine as alternatives to CFC 12. Int. J. Refrig. **16**, 84–89 (1993)
3. Wongwises, S.; Kamboon, A.; Orachon, B.: Experimental investigation of hydrocarbon mixtures to replace HFC-134a in an automotive air conditioning system. Energy Convers. Manag. **47**, 1644–1659 (2006)

Author's personal copy

4. Wongwises, S.; Chimres, N.: Experimental study of hydrocarbon mixtures to replace HFC-134a in a domestic refrigerator. Energy Convers. Manag. **46**, 85–100 (2005)
5. Wongwises, S.; Pirompak, W.: Flow characteristics of pure refrigerants and refrigerant mixtures in adiabatic capillary tubes. Appl. Thermal Eng. **21**, 845–861 (2001)
6. Wongwiscs, S.; Songnetichaovalit, T.; Lokathada, N.; Kritsadathikarn, P.; Suchatawat, M.; Pirompak, W.: A comparison of the flow characteristics of refrigerants flowing through adiabatic capillary tubes. Int. Commun. Heat Mass Transf. **27**, 611–621 (2000)
7. Dalkilic, A.S.; Wongwises, S.: A performance comparison of vapour-compression refrigeration system using various alternative refrigerants. Int. Commun. Heat Mass Transf. **37**(9), 1340–1349 (2010)
8. Dalkilic, A.S.; Wongwises, S.: Comparison of various alternative refrigerants for vapour compression refrigeration systems. In: Proceedings of the ASME/JSME 8th Thermal Engineering Joint Conference, March 13–17, USA (2011)
9. Dalkilic, A.S.: Theoretical analysis on the prediction of performance coefficient of two-stage cascade refrigeration system using various alternative refrigerants. Isi BilimiveTeknigiDergisi/J. Thermal Sci. Technol. (2012) (in Press)
10. Dopazo, J.A.; Fernández-Seara, J.; Sieres, J.; Uhía, F.J.: Theoretical analysis of a CO_2–NH_3 cascade refrigeration system for cooling applications at low temperatures. Appl. Thermal Eng. **29**, 1577–1583 (2009)
11. Lee, Y.S.; Su, C.C.: Experimental studies of isobutane (R600a) as the refrigerant in domestic refrigeration system. Appl. Thermal Eng. **22**, 507–519 (2002)
12. Kanoğlu, M.: Exergy analysis of multistage cascade refrigeration cycle used for natural gas liquefaction. Int. J. Energy Res. **26**, 763–774 (2002)
13. Cengel, Y.; Boles, M.A.: Thermodynamics—An Engineering Approach. McGraw-Hill, New York (2010)
14. REFPROP, Thermodynamic properties of refrigerants and refrigerant mixtures, version 7, Gaithersburg, M.D. National Institute of Standards and Technology (2001)
15. SOLKANE Refrigerant software, version 7, Hannover, Solvay Fluor Gmbh (2010)
16. Duruk, A.M.; Sarıbatı, Ş.: Soğutmatesisatı, TMMOB, publication number MMO/295-2 (2002)
17. Özkol, N.: Uygulamalısoğutmatekniği, TMMOB, publication number MMO/115-7 (1999)
18. Stegou-Sagia, A.; Paignigiannis, N.: Evaluation of mixtures efficiency in refrigerating systems. Energy Convers. Manag. **46**, 2787–2802 (2005)
19. Arcaklıoglu, E.; Cavusoglu, A.; Erisen, A.: Thermodynamic analysis of refrigerant mixtures for possible replacements for CFCs by an algorithm compiling property data. Appl. Thermal Eng. **26**, 430–439 (2006)
20. Kopac, M.; Zehmer, B.: Effect of saturation-temperature on the performance of a vapour-compression refrigeration-cycle working on different refrigerants using exergy method. Int. J. Energy Res. **30**, 729–740 (2006)
21. Bejan, A.: Advanced Engineering Thermodynamics, 3rd edn. Wiley, Hoboken, New York (2006)
22. Bejan, A.: Entropy Generation Minimization. CRC Press, Boca Raton (1996)
23. Stegou-Sagia, A.; Paignigiannia, N.: Exergy losses in refrigerating systems. A study for performance comparisons in compressor and condenser. Int. J. Energy Res. **27**, 1067–1078 (2003)

International Communications in Heat and Mass Transfer 44 (2013) 87–92

Contents lists available at SciVerse ScienceDirect

International Communications in Heat and Mass Transfer

journal homepage: www.elsevier.com/locate/ichmt

Entropy generation between two vertical cylinders in the presence of MHD flow subjected to constant wall temperature ☆

Omid Mahian [a,*], Hakan Oztop [b], Ioan Pop [c,*], Shohel Mahmud [d], Somchai Wongwises [e]

[a] Young Researchers Club and Elites, Mashhad Branch, Islamic Azad University, Mashhad, Iran
[b] Department of Mechanical Engineering, Technology Faculty, Fırat University, Elazig, Turkey
[c] Department of Mathematics, Babeş-Bolyai University, R-400084 Cluj-Napoca, Romania
[d] School of Engineering, University of Guelph, Guelph, Ontario, Canada
[e] Fluid Mechanics, Thermal Engineering and Multiphase Flow Research Lab. (FUTURE), Department of Mechanical Engineering, Faculty of Engineering, King Mongkut's University of Technology Thonburi, Bangmod, Bangkok 10140, Thailand

ARTICLE INFO

Available online 3 April 2013

Keywords:
Entropy generation
MHD flow
Isothermal annulus
Mixed convection

ABSTRACT

An analytical solution is presented on the entropy generation due to mixed convection between two isothermal cylinders where a transverse magnetic field is applied to the system. The governing equations in cylindrical coordinates are simplified and solved to obtain the distribution of entropy generation and the effects of MHD flow on it. The results for the entropy generation number (N_S), the Bejan number (Be) and average entropy generation number ($N_{S,ave}$) are presented for different values of the Hartmann numbers, radius ratios and a flow parameter, Gr/Re. The results show that the entropy generation decreases with increases in the magnetic field. In addition, it is found that with decreases in the radius ratio, the effects of MHD flow on the entropy generation are reduced.
© 2013 Elsevier Ltd. All rights reserved.

1. Introduction

There is a great deal of information available about the convective flow over bodies of various shapes and relevant literature can be found, for example, in the books by Bejan [1], and Martynenko and Khramtsov [2]. Entropy generation minimization is a well-known approach to optimize the performance of a thermal device. Entropy generation occurs in all of the thermal engineering systems. Bejan [3,4] investigated the different factors which are effective in the entropy generation in applied thermal engineering where available work (exergy) of a system is lost and destructed through the entropy production. Later on, many researchers focused on the entropy generation in different geometric arrangements, flow states, and thermal boundary conditions. Recently, Oztop and Al-Salem [5] presented a review of natural and mixed convection heat transfer for energy systems. The flow and heat transfer between two vertical cylinders in the presence of magnetic field has many important engineering applications. Some applications are found in industrial heat exchangers, microelectronic devices, cooling of nuclear reactors, petroleum equipment, and so forth. Therefore, before manufacturing such systems the analysis of the second law of thermodynamics (entropy generation) is necessary to have the best system design. For this purpose, an analysis of such systems using the simplified governing equations of a process, where reasonable assumptions are made, could be helpful to discover the important features of the complex process.

Due to non-linearity nature of entropy generation problems, there are relatively few analytical works in this field. Here, some analytical works related to entropy generation between two cylinders in different situations (i.e., both cylinders are stationary, or one of them rotates) in which MHD flow has not considered, are mentioned in brief. Yilbas [6] by neglecting the irreversibility due to fluid friction and assuming a linear velocity profile presented an entropy generation analysis for a rotating outer cylinder and differentially heated isothermal boundary condition. Mahmud and Fraser [7,8] performed an entropy generation analysis within an annulus with isoflux and isothermal boundary conditions. They solved the simplified governing equations in cylindrical coordinates to obtain the dimensionless entropy generation and the Bejan number as a function of the parameters involved in the analysis. Tasnim and Mahmud [9,10] investigated the entropy production in a vertical annulus with a circular cross-section by considering the fully developed laminar flow and mixed convection heat transfer, analytically. Mirzazadeh et al. [11] studied the entropy generation between concentric rotating cylinders where the working fluid is a non-linear viscoelastic fluid. Mahian et al. [12] investigated analytically the entropy generation between two rotating cylinders using nanofluids with different volume fractions and isoflux boundary conditions. Mahian et al. [13] also studied the effects of uncertainties in the models presented for thermophysical properties of nanofluids on entropy generation. Making use of an external magnetic field is of considerable importance in many industrial applications, particularly as a control mechanism in material manufacturing [14]. In addition, the study of flow and heat transfer in

☆ Communicated by O.G. Martynenko.
* Corresponding authors.
E-mail addresses: popm.ioan@yahoo.co.uk (I. Pop), omid.mahian@gmail.com (O. Mahian).

0735-1933/$ – see front matter © 2013 Elsevier Ltd. All rights reserved.
http://dx.doi.org/10.1016/j.icheatmasstransfer.2013.03.005

Nomenclature

Be	Bejan number
Br	Brinkman number
B_0	constant magnetic flux density
E	electric field
g	gravitation acceleration
k	thermal conductivity
N_F	entropy generation number, fluid friction
N_H	entropy generation number, heat transfer
N_m	entropy generation number, MHD flow
N_S	entropy generation number, total
P	pressure
P^*	dimensionless pressure
T	temperature
T_0	inlet temperature
U	dimensionless velocity
U_0	inlet velocity
Q	electric charge density
r	radius
R	dimensionless radius
λ	radius ratio (r_i/r_0)
β	thermal expansion coefficient
μ	dynamic viscosity
S_G	entropy generation rate

Greek symbols

J	electric current
M	Hartmann number
Γn	constants, n = 1,2,....
ρ	density
Π	radius ratio (r_0/r_i)
θ	dimensionless temperature
Ω	dimensionless temperature difference
$\forall$	volume

Subscripts

I	value at the inner cylinder
O	value at the outer cylinder

a closed cavity or a channel in the presence of the magnetic field is important because of engineering applications such as cooling of nuclear reactors, MHD marine propulsion, MHD micropumps, microelectronic devices, electronic packages, and so on. In the last decade, the study of MHD flow and its effect on entropy generation, in the related systems, received considerable attention because of its importance in industries, as mentioned above. Here, some works that investigated the effect of MHD flow on entropy generation for various flows and geometries have been reviewed. Salas et al. [15] analyzed the second law for MHD induction devices, such as electromagnetic pumps and electrical generators. Ibanez et al. [16] optimized the operation conditions of an alternate MHD generator based on the global entropy generation rate. Mahmud et al. [17] conducted an analysis to study the effects of transverse magnetic field on entropy generation inside a vertical channel made of two parallel plates by considering mixed convection inside the channel. Later on, Tasnim et al. [18] examined the same problem for porous media. Mahmud and Fraser [19] investigated analytically, the second law for mixed convection–radiation interaction in a vertical porous channel in the presence of MHD flow. In another work, Mahmud and Fraser [20] studied the problem of entropy generation in a fluid saturated porous cavity for laminar natural convection with MHD flow. Al-Odat et al. [21] investigated numerically the effect of magnetic field on local entropy generation caused by steady two-dimensional laminar forced convection flow past a horizontal plate. Ibanez et al. [22] applied the entropy generation minimization method to optimize MHD flow between two infinite parallel walls with limited electrical conductivity. Mahmud and Fraser [23] presented a general relation for entropy generation for a single-plate thermoacoustic system that is exposed to a transverse magnetic field. Ibanez and Cuevas [24] considered a stationary buoyant MHD flow of a liquid metal immersed in a magnetic field through a vertical rectangular duct with thin conducting or insulating walls. Arikoglu et al. [25] investigated the effects of slip and Joule dissipation on the entropy generation in a single rotating disk in the presence of MHD flow. Aiboud and Saouli [26] applied the second law to analysis of the viscoelastic MHD flow over a stretching surface. Kolsi et al. [27] studied numerically the effect of MHD flow on the entropy generation of liquid metal laminar natural convection in a cubic cavity that is differentially heated. The effect of the magnetic field on entropy generation in a microchannel is investigated by Ibanez and Cuevas [28]. Recently, Mahian et al. [29] investigated the entropy generation between two isothermal rotating cylinders in the presence of MHD flow. They concluded that MHD flow increases the entropy generation. In the last work, Mahian et al. [30] studied the effects of nanofluids on entropy generation between two cylinders in the presence of a magnetic field.

A review of the literature shows that there is no analytical work on entropy generation due to mixed convection in an annulus subjected to constant wall temperature and under magnetic field. The main aim of this work is to investigate the effects of magnetic field on the entropy generation in the annulus. The results for the entropy generation at different Hartmann numbers, radius ratios and the flow parameter Gr/Re are presented.

2. Problem formulation

2.1. Analysis according to the first law of thermodynamics

Consider a steady laminar and fully developed flow where a Newtonian incompressible fluid enters a vertical annulus with an inlet velocity U_0 and an inlet temperature T_0. A constant magnetic field with strength of B_0 is applied normally to the fluid flow direction. The schematic of the present problem is displayed in Fig. 1. Neglecting the velocity in r-direction, the heating due to magnetic field, and the use of Boussinesq approximation the momentum and energy equations become as follows (see Refs. [9, 10] for similar analysis):

$$-\frac{1}{\rho}\frac{\partial P}{\partial z}+\frac{\mu}{\rho}\left[\frac{\partial^2 V_z}{\partial r^2}+\frac{1}{r}\frac{\partial V_z}{\partial r}\right]+g\beta(T-T_0)-\frac{\sigma B_0^2 V_z}{\rho}=0 \tag{1}$$

$$\frac{\partial^2 T}{\partial r^2}+\frac{1}{r}\frac{\partial T}{\partial r}=0 \tag{2}$$

in the above relations ρ, μ, and σ are density, viscosity and fluid electrical conductivity of the working fluid, respectively. With the assumption of no slip between the walls of the cylinders, the velocity boundary conditions are given as follows:

$$\begin{aligned} V_z &= 0 \quad \text{at} \quad r = r_i \\ V_z &= 0 \quad \text{at} \quad r = r_0 . \end{aligned} \tag{3}$$

The thermal boundary conditions are:

$$\begin{aligned} T &= T_i \quad \text{at} \quad r = r_i \\ T &= T_0 \quad \text{at} \quad r = r_0 . \end{aligned} \tag{4}$$

The following parameters are used for scaling the governing equations:

$$R=\frac{r}{r_0}, U=\frac{V_z}{U_0}, \mathrm{Re}=\frac{U_0 r_0}{\nu}, \lambda=\frac{r_i}{r_0}, P^*=\frac{\mathrm{Pr}_0}{U_0\mu}, Z=\frac{z}{r_0}, M=B_0 r_0\sqrt{\frac{\sigma}{\mu}} \quad (5)$$

where M is the Hartmann number. In addition, the Grashof number and dimensionless temperature are as follows:

$$\theta=\frac{T-T_0}{\Delta T}, \mathrm{Gr}=\frac{g\beta\Delta T r_0^3}{k\nu^2}, \Delta T=T_i-T_0. \quad (6)$$

Therefore, the dimensionless equations can be written as:

$$\frac{\partial^2 U}{\partial R^2}+\frac{1}{R}\frac{\partial U}{\partial R}=-\frac{\mathrm{Gr}}{\mathrm{Re}}\theta+M^2U+\frac{\partial P^*}{\partial Z} \quad (7)$$

$$\frac{\partial^2\theta}{\partial R^2}+\frac{1}{R}\frac{\partial\theta}{\partial R}=0. \quad (8)$$

The boundary conditions in dimensional form become:velocity boundary conditions:

$$\begin{array}{l} U=0 \quad \text{at} \quad R=\lambda \\ U=0 \quad \text{at} \quad R=1. \end{array} \quad (9)$$

Thermal boundary conditions:

$$\begin{array}{l} \theta=\theta_i \quad \text{at} \quad R=\lambda \\ \theta=\theta_0 \quad \text{at} \quad R=1. \end{array} \quad (10)$$

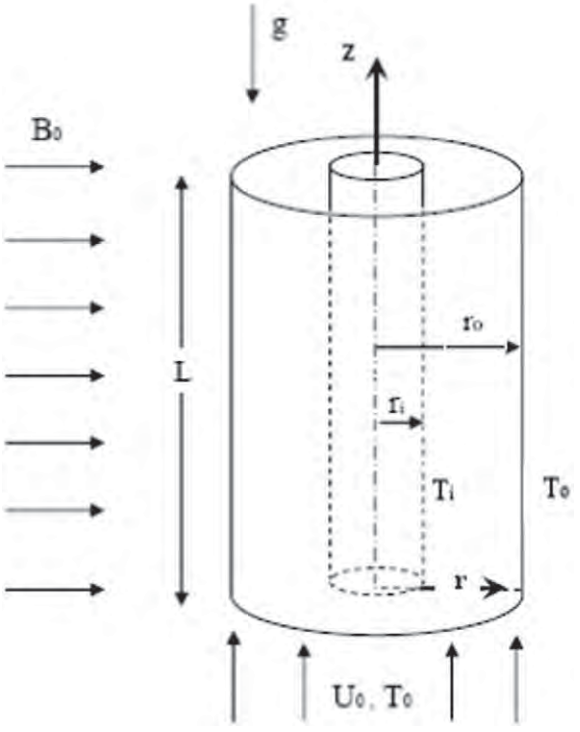

Fig. 1. Schematic of the present problem.

2.2. Analysis according to the second law of thermodynamics

The entropy generation rate in the presence of MHD flow can be written as follows:

$$\dot{S}'''_{gen}=\frac{k}{T_0^2}[\nabla T]^2+\frac{\mu}{T_0}\varphi+\frac{1}{T_0}[(J-QV)\cdot(E+V\times B)] \quad (11)$$

where:

$$J=\sigma(E+V\times B). \quad (12)$$

In the above relations, ϕ represents viscous dissipation, J is electric current, Q is electric charge density, V is velocity vector, E is the electric field, and B is the magnetic induction. Neglecting QV compared to J and disregarding E in comparison with $V\times B$, the entropy generation rate, Eq. (11), is reduced in this case as:

$$\dot{S}'''_{gen}=\frac{k}{T_0^2}\left(\frac{\partial T}{\partial r}\right)^2+\frac{\mu}{T_0}\left(\frac{\partial V_z}{\partial r}\right)^2+\frac{\sigma B_0^2}{T_0}V_z^2. \quad (13)$$

The entropy generation number that is the dimensionless entropy generation rate becomes:

$$N_S=\frac{\dot{S}'''_{gen}}{\frac{\mu U_0^2}{T_0 r_0^2}}=\left(\frac{\Omega}{\mathrm{Br}}\right)\left(\frac{\partial\theta}{\partial R}\right)^2+\left(\frac{\partial U}{\partial R}\right)^2+M^2U^2=N_H+N_F+N_M \quad (14)$$

where N_H, N_F, and N_M on the right hand of the equation are the irreversibilities due to heat transfer, fluid friction, and magnetic field. Also, the Brinkman number (Br) and the parameter Ω are defined as follows:

$$\mathrm{Br}=\frac{U_0^2\mu}{k\Delta T}, \Omega=\frac{\Delta T}{T_0}. \quad (15)$$

To determine the irreversibility distribution, Bejan number (Be) that is the ratio of entropy generation due to heat transfer to the overall entropy generation [31], is defined as:

$$\mathrm{Be}=\frac{N_H}{N_H+N_F+N_M}. \quad (16)$$

The average (overall) entropy generation number is given as:

$$N_{S,ave}=\frac{1}{\forall}\int_{\forall}N_S d\forall. \quad (17)$$

3. Solution of the problem

3.1. Velocity and temperature distributions

Eqs. (7) and (8) are coupled via the buoyancy term in the momentum equation. Therefore, firstly the energy equation should be solved. The solution of the energy equation after applying the boundary conditions is as:

$$\theta(R)=\frac{\theta_i-\theta_o}{\ln(\lambda)}\ln(R)+\theta_o. \quad (18)$$

Now, the velocity distribution is obtained easily as:

$$U(R)=\Gamma_1 I_0(MR)+\Gamma_2 K_0(MR)+\Gamma_3\ln(R)+\Gamma_4 \quad (19)$$

where $I_1(MR)$ is the modified Bessel function of the first kind, of order 1, and $K_1(MR)$ as the modified Bessel function of the second kind, of order 1.

The constants $\Gamma_1 - \Gamma_4$ are as follows:

$$\begin{aligned}
\Gamma_1 &= \frac{(\mathrm{Gr}/\mathrm{Re})[\theta_o K_0(M\lambda) - \theta_i K_0(M)] + (\partial P^*/\partial Z)[K_0(M) - K_0(M\lambda)]}{M^2[K_0(M)I_0(M\lambda) - K_0(M\lambda)I_0(M)]} \\
\Gamma_2 &= -\frac{(\mathrm{Gr}/\mathrm{Re})[\theta_o I_0(M\lambda) - \theta_i I_0(M)] + (\partial P^*/\partial Z)[I_0(M) - I_0(M\lambda)]}{M^2[K_0(M)I_0(M\lambda) - K_0(M\lambda)I_0(M)]} \\
\Gamma_3 &= \frac{(\mathrm{Gr}/\mathrm{Re})(\theta_i - \theta_o)}{M^2 \ln(\lambda)} \\
\Gamma_4 &= \frac{[(\mathrm{Gr}/\mathrm{Re})\theta_o - \partial P^*/\partial Z]}{M^2}
\end{aligned} \tag{20}$$

3.2. Local entropy generation

The local entropy generation can be obtained based on Eq. (14) and the velocity and temperature distributions. Therefore, the entropy generation number can be determined by the following relation:

$$N_S = \left(\frac{\Omega}{\mathrm{Br}}\right)\left(\frac{\theta_i - \theta_o}{\ln(\lambda)R}\right)^2 + \left(\Gamma_1 M I_1(MR) - \Gamma_2 M K_1(MR) + \frac{\Gamma_3}{R}\right)^2 + M^2(\Gamma_1 I_0(MR) + \Gamma_2 K_0(MR) + \Gamma_3 \ln(R) + \Gamma_4)^2 = N_H + N_F + N_M. \tag{21}$$

3.3. Average entropy generation number

The average entropy generation number is calculated based on Eq. (17):

$$N_{S,ave} = \frac{2}{(1-\lambda^2)}\int_{\lambda}^{1} N_S R dR. \tag{22}$$

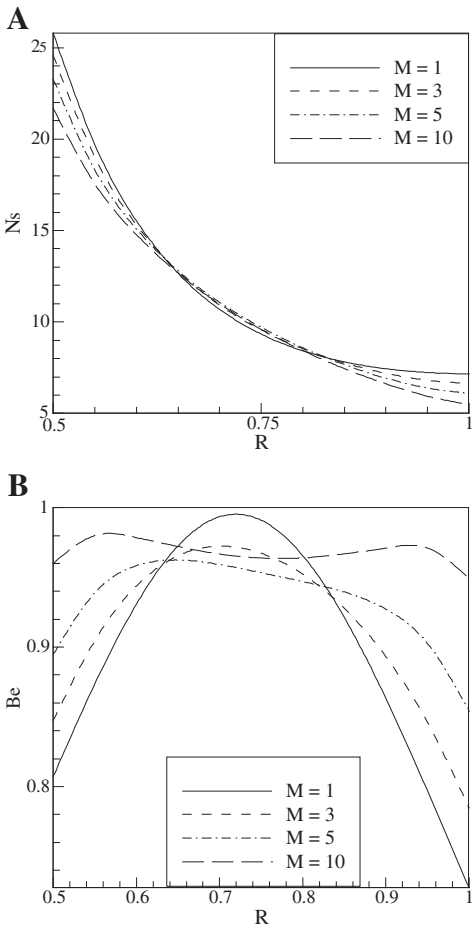

Fig. 2. Effects of MHD flow on (a) entropy generation number and (b) Bejan number.

4. Results and discussions

Before presenting the results, it should be noted that in this work only the effects of flow parameters including, Gr/Re, M and the geometric parameter of radius ratio on entropy generation are investigated. Fig. 2 shows the effects of MHD flow on the entropy generation number and Bejan number for $\theta_i = 1$, $\theta_0 = 0.5$, $\Omega/\mathrm{Br} = 10$, $dP^*/dZ = -0.1$ and $\mathrm{Gr}/\mathrm{Re} = 10$. As seen, an increase in the Hartmann number leads to a decrease in the entropy generation number near the walls of the cylinders whereas the value of N_S increases in the middle of the two cylinders. In this case, although the contribution of the magnetic field to entropy generation is increased a little, the magnetic field reduces the contribution of fluid friction to entropy generation with the lowering of the shear stresses and hence the velocity gradients near the walls. In the middle of the annulus where the effects of walls on the flow diminish, the entropy generation increases with an increase in the Hartmann number. The distribution of the Bejan number Be shows that the contribution of viscous dissipations (N_F) near the walls decreases with an increase in the Hartmann number. It should be noted that based on Eq. (14), the magnetic field has no effect on the temperature field and hence N_H remains constant. Therefore, according to the definition of the Bejan number (see Eq. (16)), with the reduction of N_F, the Bejan number will increase. Fig. 3 shows the variation of the entropy generation and the Bejan number in the annulus at different values of Gr/Re. The parameter of Gr/Re represents the ratio of free convection to forced convection. When $\mathrm{Gr}/\mathrm{Re} = 0.1$, the forced convection is dominant on free convection. Therefore, because of the enhancement of heat transfer in forced convection rather than free convection, the irreversibilities are decreased in this case. The distribution of the Bejan number shows that the irreversibility due to heat transfer is the highest in the middle of annulus for any value of Gr/Re. Fig. 4 shows the effects of MHD flow on the average entropy generation number at different values of Gr/Re. It is observed that with an increase in the magnetic field the average entropy generation number remains nearly constant for $\mathrm{Gr}/\mathrm{Re} = 0.1$. However, in high values of Gr/Re, the entropy generation decreases with increases in the Hartmann number. The rate of this decrease is greater for higher amounts of Gr/Re. An important issue in the design of such type of heat exchanger is the selection of optimum radius ratios. The effects of MHD flow on average entropy generation for different values of radius ratios ($\Pi = 1/\lambda = r_0/r_i$) are presented in Fig. 5 for $1.5 \le \Pi \le 6$ and $\mathrm{Gr}/\mathrm{Re} = 10$. It is observed that by increasing the radius ratio the entropy generation is decreased due to decreases of gradients in the gap. As shown, for smaller radius ratios the MHD flow effects on the average entropy generation are not visible. In other words, the decrease in the entropy generation is higher in magnitude for greater radius ratios.

5. Conclusion

An entropy generation analysis is conducted to find the effects of MHD flow on the entropy generation due to a mixed convection between two vertical cylinders. The equations of momentum and energy in cylindrical coordinates are simplified and solved analytically. The results show that an increase in the magnetic field results in a decrease in the entropy generation. It is also found that the decrease in the entropy generation is higher for greater radius ratios.

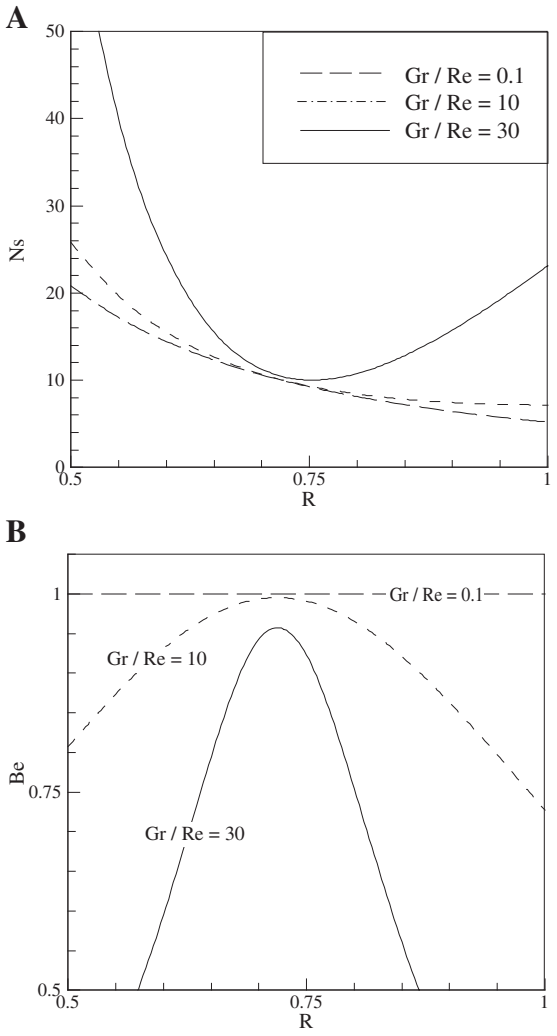

Fig. 3. Effects of Gr/Re on (a) entropy generation number and (b) Bejan number.

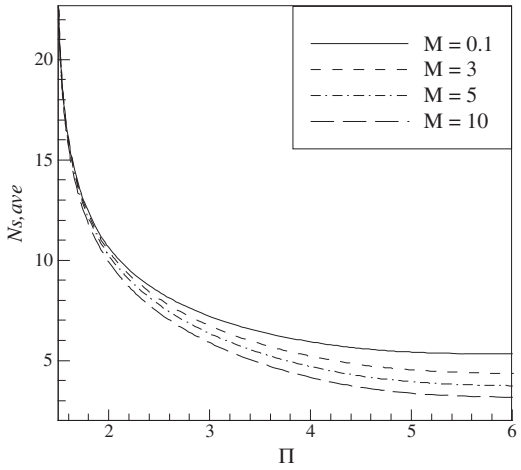

Fig. 5. Effects MHD flow on the average entropy generation at different radius ratios ($\Pi = 1/\lambda$).

Acknowledgment

The first and fifth authors would like to thank the Thailand Research Fund and the National Research University Project for supporting this study.

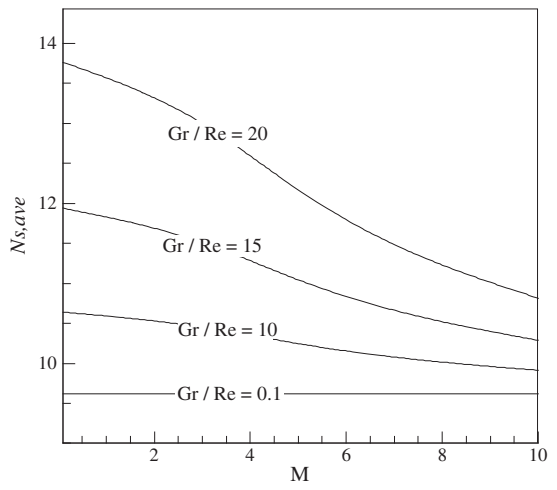

Fig. 4. Effects of MHD flow on average entropy generation number at different Gr/Re.

References

[1] A. Bejan, Convection Heat Transfer, 2nd edition Wiley, New York, 1995.
[2] O.G. Martynenko, P.P. Khramtsov, Free-convective Heat Transfer, Springer, New York, 2005.
[3] A. Bejan, Second-law analysis in heat transfer and thermal design, Advances in Heat Transfer 15 (1982) 1–58.
[4] A. Bejan, Entropy Generation Minimization, CRC Press, Boca Raton, NY, 1996.
[5] H.F. Oztop, K. Al-Salem, A review on entropy generation in natural and mixed convection heat transfer for energy systems, Renewable and Sustainable Energy Reviews 16 (2012) 911–920.
[6] B.S. Yilbas, Entropy analysis of concentric annuli with rotating outer cylinder, International Journal of Exergy 1 (2001) 60–66.
[7] S. Mahmud, R.A. Fraser, Second law analysis of heat transfer and fluid flow inside a cylindrical annular space, International Journal of Exergy 2 (2002) 322–329.
[8] S. Mahmud, R.A. Fraser, Analysis of entropy generation inside concentric cylindrical annuli with relative rotation, International Journal of Thermal Sciences 42 (2003) 513–521.
[9] S.H. Tasnim, S. Mahmud, Mixed convection and entropy generation in a vertical annular space, International Journal of Exergy 2 (2002) 373–379.
[10] S.H. Tasnim, S. Mahmud, Entropy generation in a vertical concentric channel with temperature dependent viscosity, International Communications in Heat and Mass Transfer 29 (2002) 907–918.
[11] M. Mirzazadeh, A. Shafaei, F. Rashidi, Entropy analysis for non-linear viscoelastic fluid in concentric rotating cylinders, International Journal of Thermal Sciences 47 (2008) 1701–1711.
[12] O. Mahian, S. Mahmud, S. Zeinali Heris, Analysis of entropy generation between co-rotating cylinders using nanofluids, Energy 44 (2012) 438–446.
[13] O. Mahian, S. Mahmud, S. Zeinali Heris, Effect of uncertainties in physical properties on entropy generation between two rotating cylinders with nanofluids, ASME Journal of Heat Transfer 134 (10) (2012), [art. no. 101704].
[14] A.E. Jery, N. Hidouri, M. Magherbi, A.B. Brahim, Effect of an external oriented magnetic field on entropy generation in natural convection, Entropy 12 (2010) 1391–1417.
[15] H. Salas, S. Cuevas, M.L. Haro, Entropy generation analysis of magnetohydrodynamic induction devices, Journal of Physics D: Applied Physics 32 (1999) 2605.
[16] G. Ibanez, S. Cuevas, M.L. Haro, Optimization analysis of an alternate magnetohydrodynamic generator, Energy Conversion and Management 43 (2002) 1757–1771.
[17] S. Mahmud, S.H. Tasnim, M.A.H. Mamun, Thermodynamic analysis of mixed convection in a channel with transverse hydromagnetic effect, International Journal of Thermal Sciences 42 (2003) 731–740.
[18] S.H. Tasnim, M. Shohel, M.A.H. Mamun, Entropy generation in a porous channel with hydromagnetic effect, Energy 2 (2002) 300–308.
[19] S. Mahmud, R.A. Fraser, Mixed convection–radiation interaction in a vertical porous channel: entropy generation, Energy 28 (2003) 1557–1577.
[20] S. Mahmud, R.A. Fraser, Magnetohydrodynamic free convection and entropy generation in a square porous cavity, International Journal of Heat and Mass Transfer 47 (2004) 3245–3256.
[21] M. Odat, R.A. Damseh, M. Nimr, Effect of magnetic field on entropy generation due to laminar forced convection past a horizontal flat plate, Entropy 4 (2004) 293–303.
[22] G. Ibanez, S. Cuevas, M.L. Haro, Optimization of a magnetohydrodynamic flow based on the entropy generation minimization method, International Communications in Heat and Mass Transfer 33 (2006) 295–301.
[23] S. Mahmud, R.A. Fraser, The thermagoustic irreversibility for a single-plate thermoacoustic system, International Journal of Heat and Mass Transfer 49 (2006) 3448–3461.
[24] G. Ibanez, S. Cuevas, Optimum wall conductance ratio in magnetoconvective flow in a long vertical rectangular duct, International Journal of Thermal Sciences 47 (2008) 1012–1019.

[25] A. Arikoglu, I. Ozkol, G. Komurgoz, Effect of slip on entropy generation in a single rotating disk in MHD flow, Applied Energy 85 (2008) 1225–1236.
[26] S. Alboud, S. Saouli, Entropy analysis for viscoelastic magnetohydrodynamic flow over a stretching surface, International Journal of Non-Linear Mechanics 45 (2010) 482–489.
[27] L. Kolsi, A. Abidi, M.N. Borjini, H.B. Aissia, The effect of an external magnetic field on the entropy generation in three dimensional natural convection, Thermal Science 14 (2010) 341–352.
[28] G. Ibanez, S. Cuevas, Entropy generation minimization of a MHD (magnetohydrodynamic) flow in a microchannel, Energy 35 (2010) 4149–4155.
[29] O. Mahian, S. Mahmud, I. Pop, Analysis of first and second laws of thermodynamics between two isothermal cylinders with relative rotation in the presence of MHD flow, International Journal of Heat and Mass Transfer 55 (2012) 4808–4816.
[30] O. Mahian, S. Mahmud, S. Wongwises, Entropy generation between two rotating cylinders with magnetohydrodynamic flow using nanofluids, Journal of Thermophysics and Heat Transfer 27 (1) (2013) 161–169.
[31] S. Paoletti, F. Rispoli, E. Sciubba, Calculation of exergetic losses in compact heat exchanger passages, ASME AES 10 (1980) 21–29.

Provided for non-commercial research and education use.
Not for reproduction, distribution or commercial use.

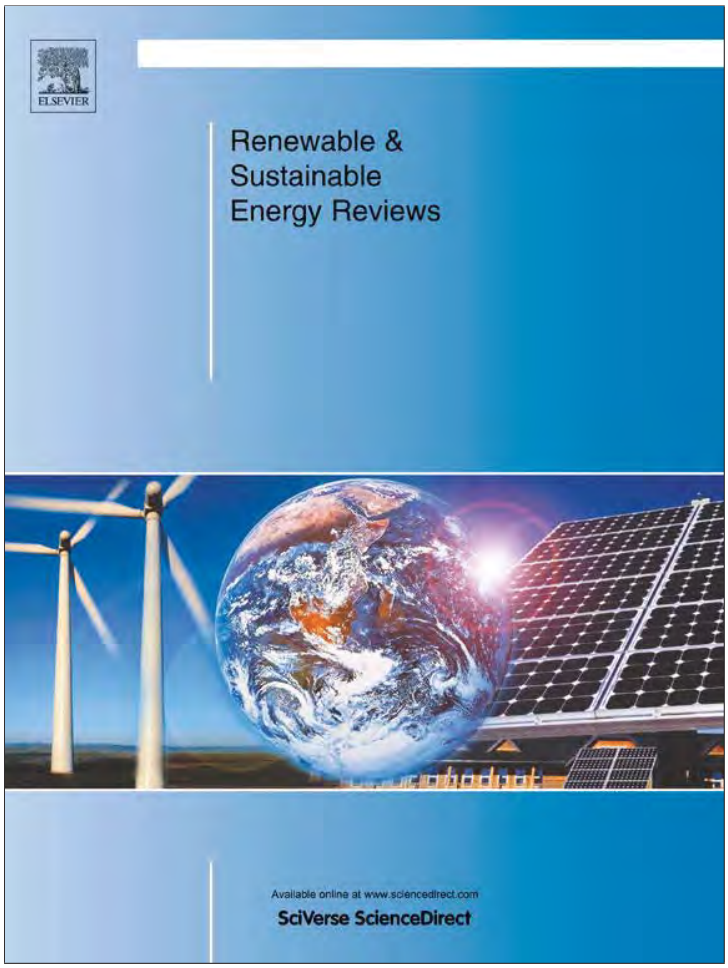

This article appeared in a journal published by Elsevier. The attached copy is furnished to the author for internal non-commercial research and education use, including for instruction at the authors institution and sharing with colleagues.

Other uses, including reproduction and distribution, or selling or licensing copies, or posting to personal, institutional or third party websites are prohibited.

In most cases authors are permitted to post their version of the article (e.g. in Word or Tex form) to their personal website or institutional repository. Authors requiring further information regarding Elsevier's archiving and manuscript policies are encouraged to visit:

http://www.elsevier.com/authorsrights

Author's personal copy

Renewable and Sustainable Energy Reviews 24 (2013) 586–592

Contents lists available at SciVerse ScienceDirect

Renewable and Sustainable Energy Reviews

journal homepage: www.elsevier.com/locate/rser

A review on nuclear power plant scenario in Thailand

Parinya Pongsoi [a], Somchai Wongwises [a,b,*]

[a] Fluid Mechanics, Thermal Engineering and Multiphase Flow Research Lab. (FUTURE), Department of Mechanical Engineering, Faculty of Engineering, King Mongkut's University of Technology Thonburi, Bangmod, Bangkok 10140, Thailand
[b] The Academy of Science, The Royal Institute of Thailand, Sanam Suea Pa, Dusit, Bangkok 10300, Thailand

ARTICLE INFO

Article history:
Received 8 October 2012
Received in revised form
12 March 2013
Accepted 15 March 2013

Keywords:
Nuclear energy
Nuclear power plant
Thailand

ABSTRACT

Since early civilization, humans have required energy. Energy grows increasingly important with globalization. The search for energy sets nuclear power as the highest priority for generating electricity. The need to delay global warming initiated a nuclear power plant using a nuclear reactor as its source of thermal energy to generate pollution-free electrical currents. Many countries see the important advantages of nuclear power plants, and Thailand plans nuclear power plant projects (NPP) to be built by the Electricity Generating Authority of Thailand (EGAT). These projects have improved, and the latest Power Development Plan 2010–2030 (PDP 2010) states that by 2023, Thailand will build nuclear power plants with electrical productivity of about 4000 MW. The plants will generate commercial electricity for domestic consumption with plans to increase productivity in preparation for Thailand's economic growth and its participation in the ASEAN Economic Community (AEC). These efforts stem from investments in domestic and international industrial businesses in order to impress foreign countries with Thailand's energy security policy. However, the Thai people are concerned with the impacts of nuclear power plants. The people of Thailand require societal awareness in the construction of these plants.

© 2013 Elsevier Ltd. All rights reserved.

Contents

1. Introduction . . . 586
1.1. Status and prospects of nuclear power plants in the world . . . 587
1.2. Nuclear power plant potential in Thailand . . . 589
1.3. History and background of nuclear energy in Thailand . . . 590
2. Conclusion . . . 591
Acknowledgements . . . 592
References . . . 592

1. Introduction

Based on the reports of the world primary energy consumption between 1985 and 2011 as shown in Fig. 1 [1], the considerable growth of electrical consumption in the world requires the massive use of nuclear energy. In 2010, demands for nuclear energy and renewable energy increased due to the limitations of fossil fuels such as oil, natural gas and coal [2–6]. As shown in Fig. 2 [7,8], a considerable portion of the electricity in the world in 2010 was generated from the fossil fuels-natural gas and coal-while nuclear energy supplied only 14 percent of the electricity demands [9].

World War II introduced the world to nuclear power. This power can be manipulated in order to solve high energy consumption with a growing world population and greater economic growth. Many countries, including Thailand, initiated the Nuclear Power Research and Development Institution with the expectation of making an effective use of this power in accordance with global warming reduction measures. Scientists have studied constructive purposes for nuclear reactions since 1951 [10]. A nuclear reactor generated electricity for the first time at the Idaho Engineering Laboratory in the United States [10]. Since then, several countries have shown increased interested in nuclear power for peace, including Thailand.

* Corresponding author at: King Mongkut's University of Technology Thonburi, Department of Mechanical Engineering, Fluid Mechanics, Thermal Engineering and Multiphase Flow Research Lab. (FUTURE), Prachauthit, Bangkok 10140, Thailand. Tel.: +662 470 9115; fax: +662 470 9111.
E-mail address: somchai.won@kmutt.ac.th (S. Wongwises).

1364-0321/$ - see front matter © 2013 Elsevier Ltd. All rights reserved.
http://dx.doi.org/10.1016/j.rser.2013.03.038

Author's personal copy

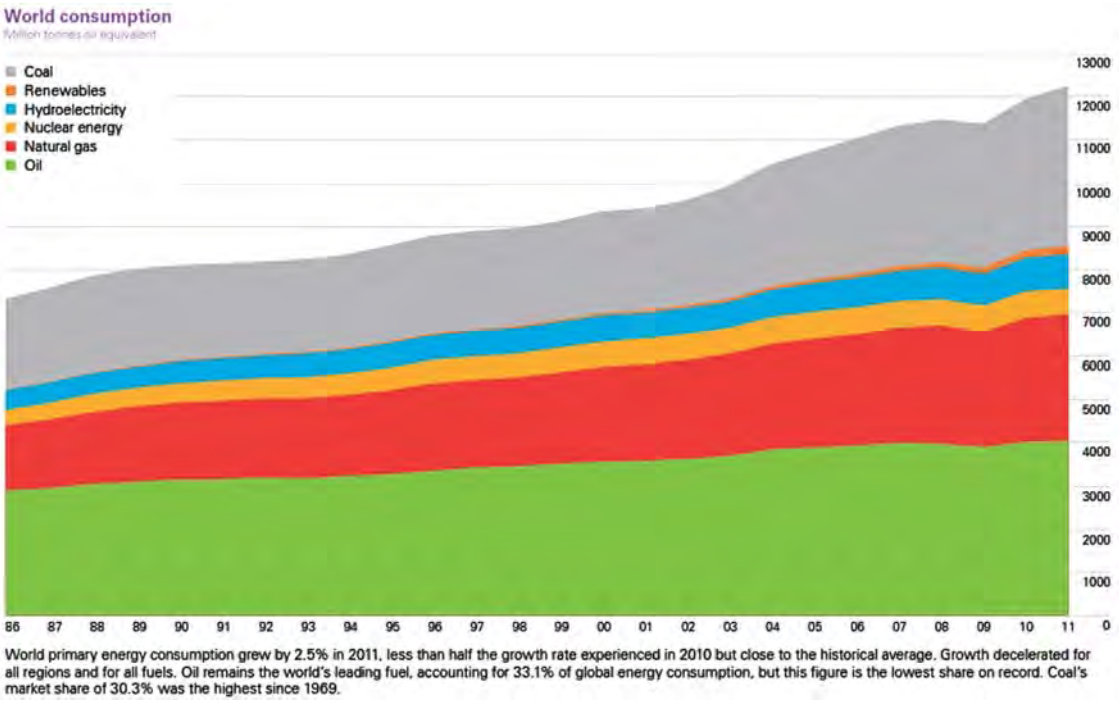

Fig. 1. World primary energy consumption 1985-2011 [from [1], with permission from BP].

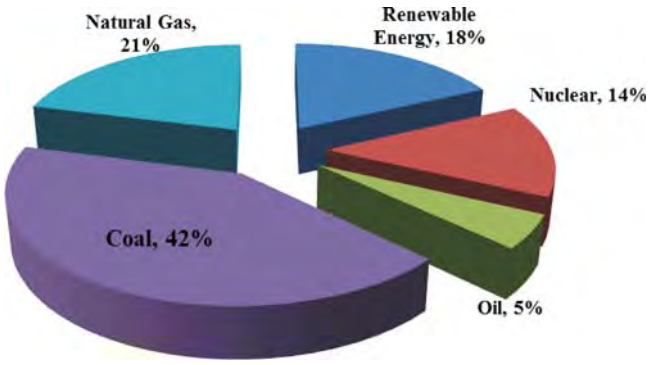

Fig. 2. World net electricity generation by energy source [data from [7,8]].

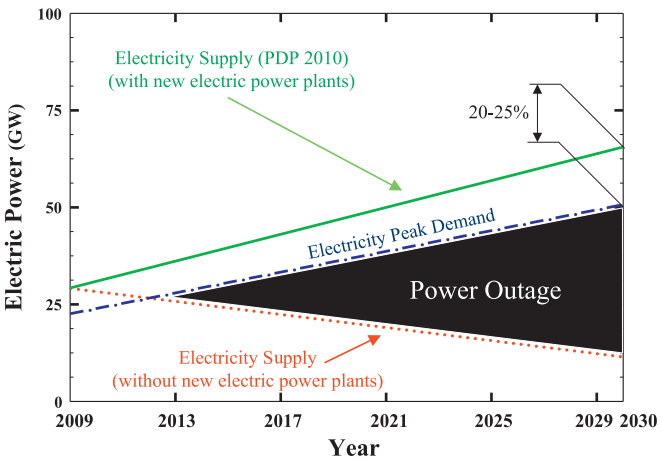

Fig. 3. Forecast of demand for electricity and electrical productivity of Thailand in 2010–2030 from PDP 2010 [data from [11]].

Thailand considers a plan to use nuclear power plants as an alternative source of energy. The Ministry of Energy of Thailand and its team of experts have devised and improved Thailand's Power Development Plan. Recently, the National Power Policy committee approved Thailand's Power Development Plan 2010–2030 (PDP 2010) with its strategies of creating confidence in the investment of electrical power development and reduction of greenhouse gas emissions from power plants in accordance with global warming measures [11]. The creation of secure energy reserves improved the strategy for electrical power production. For Thai people, energy is an important source that supports the country's development in agriculture, local economies, and public facilities. Energy must be cheap and adequate to meet demand.

Thailand plans for high energy consumption no less than 15 percent as the country continues to develop [11]. However, the retrieval of natural gas from the west coast may raise the increase in electrical production by more than 20 percent, according to Thailand's Energy Security hypothesis in the Power Development Plan 2010–2030 (PDP 2010). According to this plan, the addition of nuclear power plants to meet the increasing annual demand for electricity raises productivity rates 20 to 25 percent higher than actual demand. If additional power plants are not built, Thailand may encounter inadequate electricity beginning in 2013, which will negatively affect the public facilities and economy, as seen in Fig. 3.

With the implementation of an alternative energy development strategy, urgent strides are necessary to find sources of alternative energy. The generation of electricity from nuclear power plants with their lower-cost, greenhouse-gas-free clean energy and solid security should be an alternative in Thailand's national agenda. Advantages gained from nuclear power plants include: adequate electricity supply for future demand, a reduction of greenhouse gas emissions from carbon and natural gas power plants, and a reduction of dependence on natural gas, one-third of which is imported from Myanmar. All of these changes are significant for Thailand's energy security.

1.1. Status and prospects of nuclear power plants in the world

With the cost of fuel and the global warming directing the globe towards environmentally friendly alternative sources,

Author's personal copy

countries are choosing nuclear energy. Nuclear technology has progressed extensively in terms of work efficiency and safety. According to the report by the International Atomic Energy Agency (IAEA) in 2012 [12], the use of nuclear power plants is higher, particularly from 1954 to 1990. However, from 1990 to 2011, the number of nuclear power plants increased slightly, due to similar numbers for new and decommissioned nuclear power plants (Fig. 4(a)). In 2011, there were 435 nuclear power plants worldwide [12]. Examined by country (Fig. 4(b)), thirty countries had high numbers of nuclear power plants in 2011. With this rise in nuclear energy, countries compete in developing high-efficiency plants. When comparing the quantity of electricity output to the number of plants each year from 1954 to 2011 in terms of performance, current plants have a higher performance (Fig. 4(c)).

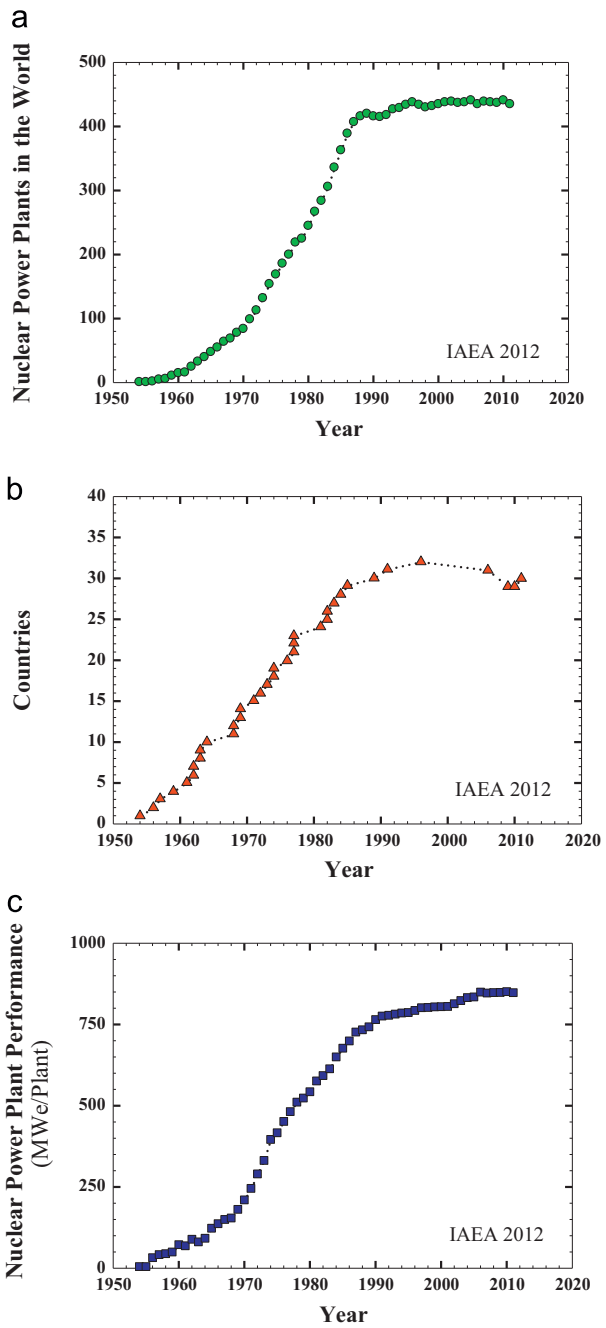

Fig. 4. From past to present (1954 to 2011) of (a) total number of nuclear power plants in the world, (b) number of countries with nuclear power plants, (c) average performance of nuclear power plants in the world [data from [12]].

The most widely used nuclear power plant is the pressurized-water reactor (PWR) [12]. The circuit-heat ventilating substance is highly controlled, so water has a higher temperature level than its boiling point without vaporization. The fast breeder reactor (FBR) can generate approximately 50 times more energy than the existing thermal reactors. Besides energy, this type of reactor, already used in China and Russia, can produce more plutonium fuel than the fuel breeder without a neutron moderator. This analysis clearly shows that nuclear power plants tend to have higher performance. However, Fig. 4(c) shows that the nuclear power plant performance from 2005 to 2011 remained constant or changed slightly due to various countries using lower performance. When compared with the number of all nuclear power plants worldwide, the electrical production scale in the future will increase, due to the improved performance of new nuclear power plants.

The International Atomic Energy Agency's meeting (IAEA) in 2012 shows that France has the highest rate of electrical production from nuclear power plants, 77.7 percent of total production [12]. The United States has the highest number of nuclear production plants, 104 with one reactor under construction. Asia, shown in Fig. 5 [12,13], has comparable numbers with: Japan's 50 plants including two under construction and 10 reactors planned, South Korea with 21 plants including five under construction and two planned, India with 20 plants including seven under construction, China with 16 plants including 26 under construction and 42 reactors planned, Pakistan with three plants including two under construction, Iran with one plant including three planned, and Armenia with one plant.

In the Association of Southeast Asian Nations (ASEAN), Vietnam has planned the construction of two nuclear power plants in the Ninh Thuan Province. Vietnam plans to construct the first plant in the Vinh Truong Village, Phuoc Dinh estate, and the second in the Thai An Village, Vinh Hai estate. Both plants will produce 4000 MW. Russia will provide support in budget, construction, staff preparation, security measures, and R&D in nuclear use for peace. The closest nuclear power plant accessible to Thailand is in Vietnam. Within six years, if the plan succeeds, Vietnam will be the first ASEAN country that will use nuclear power plants [14].

Neighboring countries to Thailand not on the list of the International Atomic Energy Agency (IAEA) but who might develop nuclear-powered electric power plant projects are detailed in the following paragraphs [15–20].

In the 30th ASEAN Ministers of Energy Meeting (AMEM) in September 2012, the government of Cambodia expressed an interest in launching a nuclear-powered electric power plant in Koh Kong province, which is closed to the border of Thailand. Their related agencies were assigned to study, and foreign experts were hired to conduct a feasibility study [15]. This study prepared for the economic expansion of the country's fuel use with higher cost of production. However, in October of the same year, Cambodia announced that it was not ready to construct the planned nuclear-powered electric power plant [16].

With the need for electricity in Indonesia, its government initiated several electric plant development projects. Additionally, it proceeded with the construction of nuclear-powered electric plants on Bangka Island, located on the southern coast of Sumatra Island, which had earthquakes due to volcano fault lines [17,18]. The nuclear-powered electric plants would be able to operate with a capacity of 6 GWe in 2025 [18].

Malaysia is concerned about the safety and danger of nuclear-powered electric plants postponing the planned launch of the first and second 2 GW-capacity nuclear-powered plants expected to operate in 2021 and 2022, respectively [19].

Myanmar's army announced its plan to develop peaceful nuclear projects, such as nuclear energy in cancer treatment. The

Author's personal copy

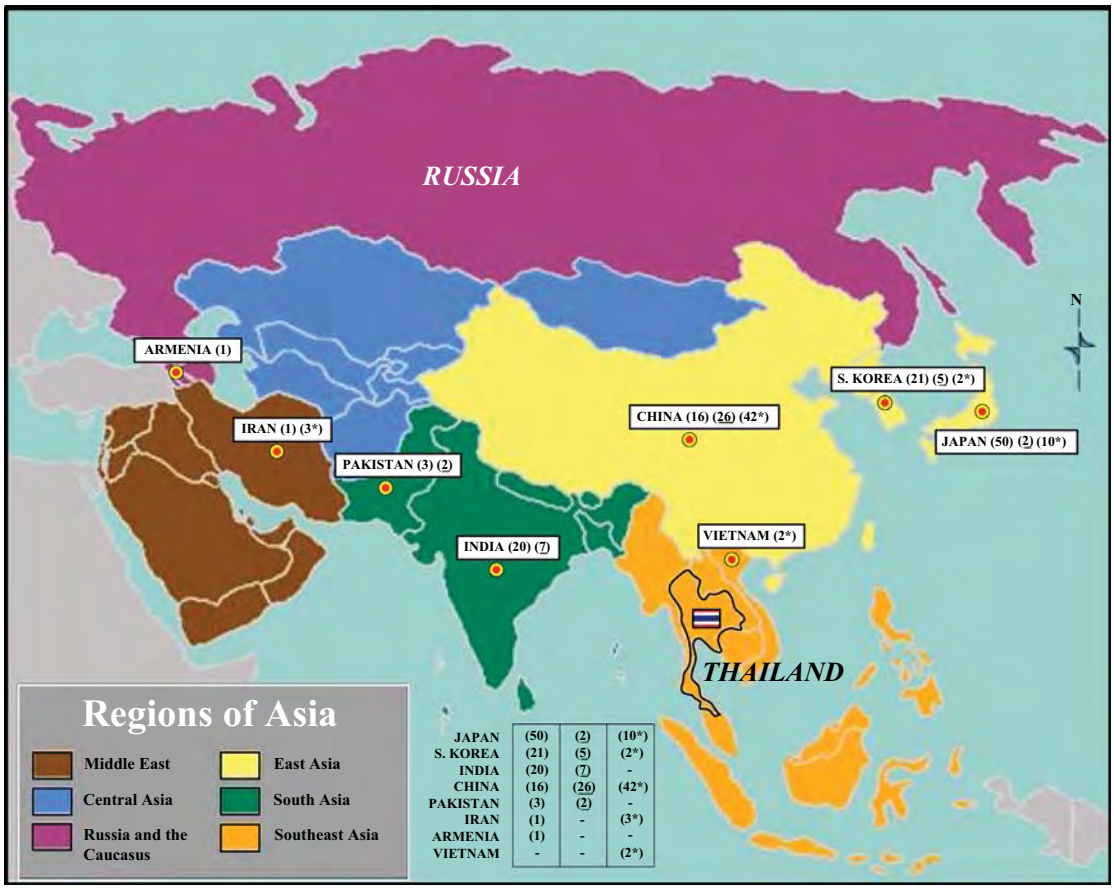

Notes :
X = Number
(X) = Reactors in Operation,
(X) = Reactors under Construction,
(X*) = Reactors Planned for Construction"

Fig. 5. Asian countries with building-in-progress nuclear power plants and future plans for nuclear power plants [data from [12] and map of Asia from [13]].

army did not consider nuclear development in creating a lethal weapon. The army will study nuclear energy for societal prosperity according to international standards, such as nuclear energy for medical use, energy, and the country's scientific development [20].

Many countries did not announce any policies in the construction of nuclear-powered electric plants, but these countries will learn of the importance of these projects and follow suit.

1.2. Nuclear power plant potential in Thailand

A modern lifestyle using science and technology requires an extensive amount of energy. Consequently, energy consumption rises, and countries such as Thailand depend on the help of outside sources for energy. Alternative energy sources help in reducing the amount of imported fuel. One energy source that scientists and academics see as having an important role in replacing oil, coal, and natural gas is nuclear power via nuclear power plants. The 7th National Economic and Social Development Plan (1992–1996) requested a feasibility study for nuclear power use in generating electricity in the economy, technology, and safety [21], as well as improving public relations.

Nuclear power plants in Thailand present two problems. First, energy is scarce. The supplies of fuel, natural gas, and coal are inadequate for the newly built power plants. Thailand depends on imported fuels from other countries. Thailand's electrical generation is increasingly tied to natural gas and coal imports.

The use of coal power plants in Thailand leads to high emissions of poisonous gases, CO_2, SO_X, and NO_X, into the atmosphere. These emissions cause air pollution, acid rain, and greenhouse gas. A nuclear power plant does not produce any of these gases. Nuclear power has less residual-spent fuel, which can remain in a plant for thirty years without any environmental problems.

Thailand's Power Development Plan utilizes nuclear power in order to reduce the dependency on fuels such as natural gas requiring imports from other countries for electric generation. In order to achieve security in electric generation, Thailand should retain at least 20 percent of reserved productivity due to the risk of finding natural gas supplies. With environment conservation through reduction in greenhouse gas emissions from new power plants and reserved productivity, Thailand exemplifies its Power Development Plan 2010–2030 (PDP 2010). High demand for household electricity and industrial growth requires the construction of more power plants. Diversity in electric generation would lower the dependency on natural gas and allow for successful electrical imports.

According to the Thailand Energy Statistics 2011 reported by the Ministry of Energy [22], as shown Fig. 6, Thailand depends on natural gas for 67.7 percent of its energy needs, compared to other fuels. Fig. 7 shows electricity by type of fuel in the PDP for 2010.

Author's personal copy

From 2015 to 2030, natural gas usage for electric generation declines while electric generation from nuclear power increases to 11 percent of total productivity in 2030. This strategic plan addresses the importance of using diversified types of fuels for electric generation. As a result, this generation requires five 1000-MW nuclear power plants [11]. Currently, the Power Development Plan 2010–2030 (PDP2010) is being revised to postpone the installation of four 1000-MW nuclear power plants, with a total productivity of 4000 MW [23].

This scientific reasoning, nuclear power plant licensing, site selection, plant construction, staff preparation, and management of radioactive waste to prevent radioactive leakage, and approximately ten years in advance full operation will lead Thailand to continue its construction in nuclear power plants. The plan for nuclear power plants in Thailand is shown in Table 1. The five technically viable sites are [24]: (1) Tha Tako District, Nakhon Sawan Province; (2) Sirindhorn District, Ubon Ratchathani Province; (3) Khlong Yai District, Trat Province; (4) Lamae District, Chumphon Province; and (5) Tha Chana District, Suratthani Province (Fig. 8). Selection of a technically viable site consists of four phases, and Thailand is in the third phase, the identification of candidate sites.

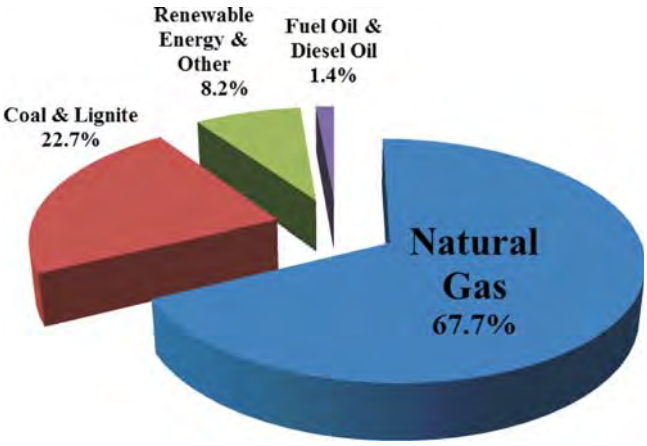

Fig. 6. Ratio of fuel used for generating electricity in Thailand in 2011 [data from [22]].

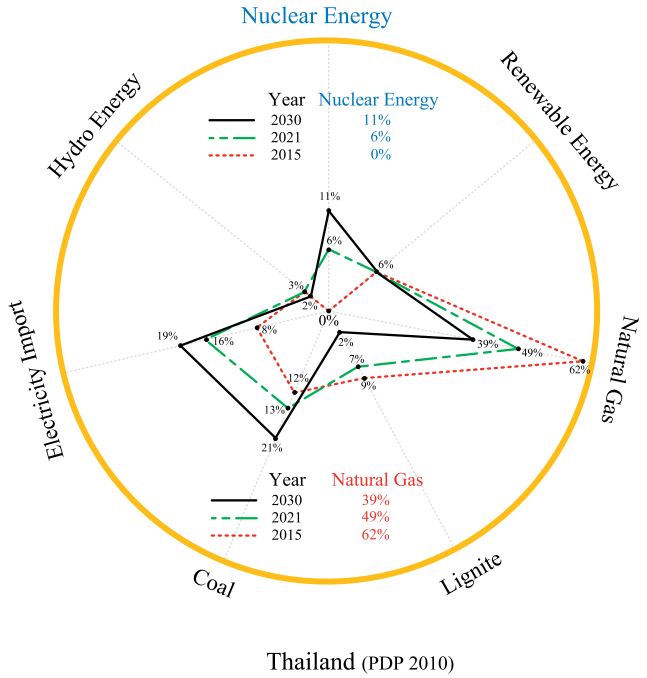

Fig. 7. Proportion of electrical power by types of fuel in the electrical Power Development Plan of Thailand for 2010–2030 [data from [11]].

1.3. History and background of nuclear energy in Thailand

The nuclear power plant officially began in Thailand with the founding of the Office of Atoms for Peace (OAP) [25]. According to the Atoms for Peace Act of 1960, the mission of the OAP is the issuance of policies, guidelines, and strategies in order to monitor and ensure the safety of the concerned parties according to international guidelines and standards [25]. The office has an obligation to support economic and social development through the safe utilization of nuclear power.

Thailand utilizes nuclear energy in medicine, agriculture, material industries, and power plant construction plans. The Nuclear Power Project (NPP) is important [26]. This project began when the Electricity Generating Authority of Thailand (EGAT) proposed the construction of nuclear power plants to a permissive government in 1966.

- In 1967, the government appointed the Nuclear Sub-Committee to consider the suitability of the NPP and to select sites.
- In 1969, the government approved sites selected for the construction of a nuclear power plant at Ban Aow Phai Subdistrict, Sri Racha District, and Chonburi Province.
- In 1970, the International Atomic Energy Agency (IAEA) approved the sites selected for nuclear power plant construction in Thailand.
- In 1972, the government gave its approval for 600-MWe boiling water reactor (BWR) in the Ban Aow Phai Subdistrict, Sri Racha District, and Chonburi Province.
- In 1974, Energy Research and Development Administration (ERDA) reserved uranium fuel in the United States.
- In 1976, a bid for nuclear power plant construction was submitted for approval with a scheduled operation in 1985.
- In 1978, the Thai government postponed the NPP projects indefinitely because it found a source of natural gas in the Thai Gulf in 1977.
- From 1982 to 1995, the Electricity Generating Authority of Thailand surveyed and studied various sites for the construction of nuclear power plants.
- In 1996–1998, the government permitted a committee appointed by the Ministry of Science and Technology to conduct a feasibility study for constructing nuclear power plants in Thailand, with a purpose to solve economic and infrastructure issues.
- In 1997, an economic crisis hit Thailand.
- In 2006, the Electricity Generating Authority of Thailand began to consider the nuclear power plan.
- In 2007, the National Energy Policy Commission (NEPC) gave its approval for the Power Development Plan 2007–2021 (PDP2007), which includes a plan for nuclear power use from two 1000-MW nuclear power plants in 2020 and two more plants in 2021.
- In 2008, the commission coordinated preparations for the construction of nuclear power infrastructure and selected the Burns and Roe Asia, Company Ltd. (B&R) as the consultant for the feasibility study of nuclear power plants. The committee of the Electricity Generating Authority of Thailand hired Burns and Roe and issued a Letter of Intent.
- In 2009, the Power Development Plan 2007–2021 (PDP2007^{rev}) was improved to reduce the electricity productivity of nuclear power plants to 1000 MW per year between 2020 and 2021.
- In 2010, the National Energy Policy Commission (NEPC) approved the Power Development Plan 2010–2020 (PDP2010) including a 5000-MW nuclear power plant starting in 2020.

Author's personal copy

Table 1
Nuclear power plant planning (Milestones for Nuclear Power Utility Planning, NPP).

Phase of project	Duration of project	Activities
Phase 0.1 Preliminary Phase	2007 (1 year)	– Placing project in Power Development Plan (PDP) – Appointing a committee to study suitability of electric generation in order to consider important issues and the procedure of the project – Prepare a Nuclear Power Infrastructure Establishment Plan (NPIEP)
Phase 1 Pre-Project Activity Phase	2008–2010 (3 years)	– Survey potential sites for plant construction – Conduct a feasibility study of the project and create understanding with public participation
Phase 2 Program Implementation Phase	2011–2013 (3 years)	– Set up an organization to monitor the project – Conduct a feasibility study of the project and create understanding with public participation – Enforcement of law and international obligations – Select suitable sites for plant construction, as well as appropriate technology and constructor, and start bidding
Phase 3 Construction Phase	2014–2019 (6 years)	– Complete the bidding process – Design and bid of engineering work – Construct and install equipment – Conduct system tests and inspection – Apply for permission to start the operation of the plant
Phase 4 Operation Phase	Start at 2023	– Start operation for commercial – Operate and maintain the plant – Plan for future increase of productivity – Plan for related industrial and technological development

- In 2011, the National Energy Policy Commission (NEPC) permitted the adjustment of the Power Development Plan 2010–2030 (PDP2010^{rev}) to defer the schedule of the 4000-MW nuclear power plant by three years. This decision came from concerns with a nuclear power plant accident after the earthquake and tsunami in Fukushima, Japan. The event was a natural disaster with no reactor malfunctions or human error. However, this incident led to its reconsideration and deferral of the project until 2023.

The MPP project needs to take the results from a survey of public opinion into consideration concerning the construction of nuclear power plants [27]. 3807 people, ages eighteen through sixty, were surveyed in various provinces, including Bangkok. The ABAC Poll Research Institute, a highly regarded research organization in Thailand, conducted the survey. Results of the survey indicate that about 83.4 percent of people do not agree with the plan for constructing nuclear power plants in Thailand. Only 16.6 percent agree with the project [27]. This evidence proves that, despite the many advantages of nuclear power plants, people still worry about nuclear explosions. In addition, people are concerned with radioactive waste management or spent fuel. Environmental agencies should boost the public's confidence in safety. Thailand fortunately has multiple organizations and has produced engineers with the knowledge and capability in controlling the operations of nuclear power plants, which could help increase public confidence. Furthermore, there are globally approved organizations such as the (International Atomic Energy Agency [IAEA]) to oversee operations and promote international cooperation concerning the use of nuclear energy for peace. Laboratories and research centers are promoting the construction of nuclear power plants in countries. For example, the Sandia National Research Institute in the United States provides strength tests for reactor-building wall. These tests examine their resistance for collision and unplanned accidents. Similar efforts would increase the confidence among Thai people surrounding nuclear power plants.

Over the years, the Electricity Generating Authority of Thailand (EGAT) has prepared potential sites, surveyed locations, conducted geological inspection, prepared water resource for use in the nuclear plants, and found suitable areas for the construction of the nuclear-powered electric plants [24]. However, there is resistance from local communities. People ask for a public hearing to discuss pros and cons, particularly, the safety promised in case of an accident similar to the nuclear plant in Japan. However, when nuclear-powered plants are compared with electric power plants, it is found that nuclear-powered plants have lower cost of fuel and are a reliable source of electric production. Due to its ability to run continuously for two years without closing, the plant has a lower cost of electric production and emits less carbon dioxide. Therefore, the nuclear-powered plant project (NPP) is a sufficient solution for Thailand in solving the energy crisis. However, the first nuclear power plant of Thailand should be a small plant of 100-200 MW capacity, which will take at least 10 years for preparation and operation. The large-scale one with 1000 MW capacity will require up to 20 years for preparation and operation [28].

2. Conclusion

This paper provides an overview of a plan to use nuclear power plants as an alternative source of energy in Thailand. This analysis assesses successful plans to promote nuclear energy within the country.

The Thai government deferred the nuclear power plant construction plan of the Electricity Generating Authority of Thailand (EGAT) in order to study public opinion concerning natural disasters and their effects. The Thai people are worried about the dangers of nuclear power plants. Education about nuclear power plants is very important. Public relation campaigns and community involvement in the nuclear power plant construction projects will help reduce these concerns and increase the country's confidence.

To ensure energy security, Thailand should construct nuclear power plants that, in economic aspects, have the lowest unit cost.

Author's personal copy

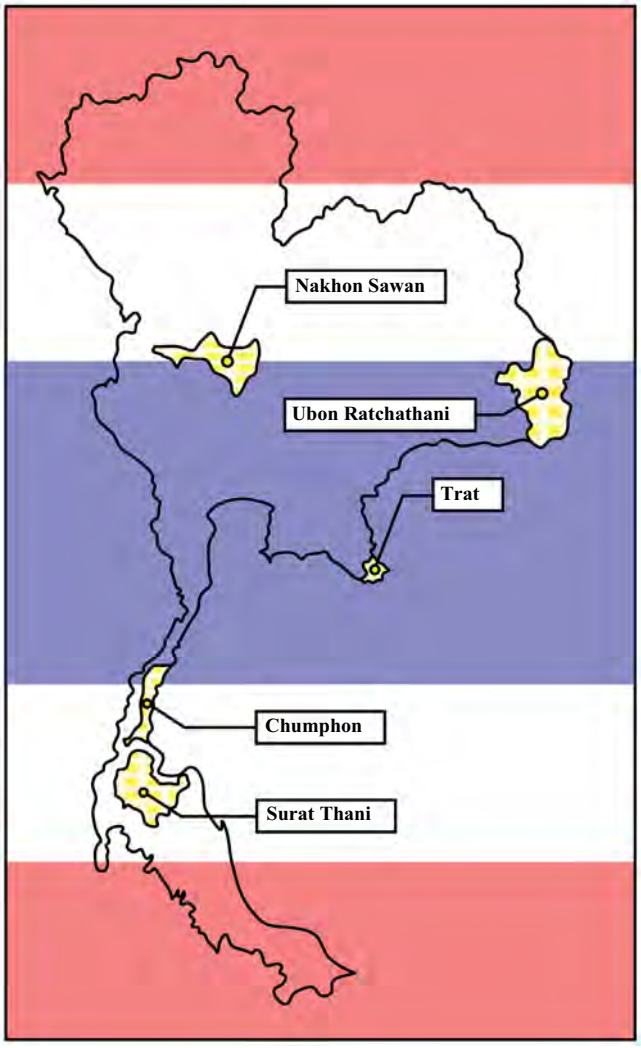

Fig. 8. Suitable locations for nuclear power plants in Thailand [data from [24]].

Thailand should pressure large-scale nuclear power plants to be cost-effective. Since Thailand is a developing country, increased needs of domestic and foreign investors require great demand.

Thailand should have nuclear power plants in order to prepare for secure energy consumption. Thailand will be prepared with energy policies with the Asean Economic Community, which will affect business and society in Thailand in the near future. However, Thailand should maintain secure areas near nuclear power plants for community and global safety.

Acknowledgements

The study was supported financially by the Thailand Research Fund, the Office of the Higher Education Commission, and the National Research University Project, whose guidance and assistance are gratefully acknowledged.

References

[1] British Petroleum. Statistical review of world energy; June 2012. Available from: 〈http://www.bp.com/assets/bp_internet/globalbp/globalbp_uk_english/reports_and_publications/statistical_energy_review_2011/STAGING/local_assets/pdf/statistical_review_of_world_energy_full_report_2012.pdf〉.
[2] De Almeida P, Silva Pedro D. The peak of oil production-timings and market recognition. Energy Policy 2009;37(4):1267–76.
[3] Mohr SH, Evans GM. Forecasting coal production until 2100. Fuel 2009;88(11):2059–67.
[4] Campbell C, Heapes S. An atlas of oil and gas depletion. Lindley. Huddersfield. UK: Jeremy Mills Publishing; 2008.
[5] Campbell C, Laherrere J. The end of cheap oil. Scientific American 1998;287(3):78–83.
[6] Campbell CJ. The depletion of oil. Marine and Petroleum Geology 1992;9(6):666–71.
[7] IEA-International Energy Agency. Key World Energy Statistics; 2012.
[8] Karakosta C, Pappas C, Marinakis V, Psarras J. Renewable energy and nuclear power towards sustainable development: characteristics and prospects. Renewable and Sustainable Energy Reviews 2013;22:187–97.
[9] IEA-International Energy Agency. Energy technology perspectives 2012. Pathways to a clean energy system; 2012.
[10] Office of the atoms for peace. Nuclear vocabulary; 2009:109.
[11] Energy Policy and Planning Office, Ministry of Energy. Summary of the Power Development Plan 2010–2030 (PDP2010); 2010.
[12] International Atomic Energy Agency IAEA. Nuclear power reactors in the world. Reference data series no. 2. 2012 edition. Vienna; 2012.
[13] Earth picture, Map of Asia. Available from: 〈http://www.earthpic.info/tag/map-of-asia/〉.
[14] Chaikan C. Vietnam with Asean Nuclear Energy Leadership. The National Policy and Transnational Relations. The Thailand Research Fund (TRF);2012. Available from: 〈http://pr.trf.or.th/index.php?option=com_content&view=article&id=1228:-asean-insight-&catid=76:asean-insight-&Itemid=100〉.
[15] The Matichon/News; October 6 2012. Available from: 〈http://www.matichon.co.th/news_detail.php?newsid=1349501869&grpid=03&catid=03〉.
[16] The global times, Cambodia has no plan to build nuclear power plant for now; October 29 2012. Available from: 〈http://www.globaltimes.cn/content/741035.shtml〉.
[17] The Nuclear Society of Thailand (NST). Asia's nuclear energy growth; October 6 2012. Available from: 〈http://www.nst.or.th/article/article5001/article5001j.htm〉.
[18] The world nuclear association. Asia's nuclear energy growth; October 6 2012. Available from: 〈http://www.world-nuclear.org/info/inf47.html〉.
[19] The Ryt9/News; January 15 2013. Available from: 〈http://www.ryt9.com/s/iq01/1568921〉.
[20] The MThai/News; January 12 2013. Available from: 〈http://talk.mthai.com/topic/363864〉.
[21] Office of the National Economic and Social Development Board, Summary of the Eleventh National Economic and Social Development Plan; 1992–1996. Available from: 〈http://www.nesdb.go.th/Default.aspx?tabid=89〉.
[22] Department of Alternative Energy Development and Efficiency, Ministry of Energy. Thailand Energy Statistics; 2011(Preliminary). Available from: 〈http://www.dede.go.th/dede/index.php?option=com_content&view=article&id=1841&Itemid=318&lang=th〉.
[23] Energy Policy and Planning Office, Ministry of Energy. Thailand Power Development Plan 2010–2030 (PDP2010: Revision);2011.
[24] Siriudomrat T. Nuclear energy technology, lecture note, division of energy technology, school of energy, environment and materials. King Mongkut's University of Technology Thonburi; 2012.
[25] Office of the atoms for peace. The history of office of the atoms for peace. Available from: 〈http://www.oaep.go.th/about_us.php〉.
[26] Electricity Generating Authority of Thailand (EGAT), Nuclear Power Program Development, The explanation report on the sub-committee of community rights and resource-based and national human rights commission of Thailand; 2011.
[27] The Nation/Asia News Network, 80% of Thai people oppose nuclear power plants; March 27 2011. Available from: 〈http://news.asiaone.com/News/Latest%2BNews/Asia/Story/A1Story20110327-270371.html〉.
[28] Wibulswas P. Thailand's potential for electricity production from alternative energy sources Presented at the Academy of Science, The Royal Institute of Thailand; April 27, 2011.

Available online at www.sciencedirect.com

SciVerse ScienceDirect

Procedia IUTAM 8 (2013) 144 – 152

Procedia IUTAM

www.elsevier.com/locate/procedia

IUTAM Symposium on Waves in Fluids: Effects of Nonlinearity, Rotation, Stratification and Dissipation

The Effect of Viscoelasticity on Breaking Standing Waves

Vladimir A. Kalinichenko [a]*, Somchai Wongwises [b]

[a] *A.Ishlinsky Institute for Problems in Mechanics RAS, Moscow Russia*
[b] *King Mongkut's University of Technology Thonburi, Bangkok Thailand*

Abstract

Here we present novel experimental evidence that the presence of polymer in water dramatically affects the transition to breaking standing gravity surface waves excited under Faraday resonance. Our measurements showed that by adding of a small amount of polymers to the distilled water the transition into wave breaking state was delayed, and the elongational viscosity of the polymer solution accounts for this behavior.

© 2013 The Authors. Published by Elsevier B.V.
Selection and/or peer-review under responsibility of Yuli Chashechkin and David Dritschel

Keywords: gravity surface Faraday waves; parametric resonance, wave breaking; polymer solution; elongational viscosity.

1. Inroduction

Relating to the class of free surface problems the steep and breaking water waves are of interest to fundamental hydrodynamics [1 – 3] as well as engineering applications [4, 5]. The formation of vertical jets, splashes and plumes of water frequently accompany the impact of progressive waves against a vertical wall. Other examples of such behavior are known to occur in standing gravity waves in cylindrical [6] and rectangular [7] tanks when a jet arises out of a wave antinode. The formation of these jets can be referred to a class of nonstationary problems of the cavity collapse on a free surface of a liquid; these problems were always of great interest to researchers because of high-speed cumulative jet generation and of its subsequent fragmentation. As theoretical modeling of the given phenomenon is completed by localized surface singularities, the laboratory experiment on the dynamics of collapsing cavity takes on special significance.

The object of our experimental study is breaking standing gravity waves excited by the parametric resonance. Since Faraday's founding work [8], much is already known about the excitation of these Faraday waves and their limit characteristics. So far, the breaking waves have been mostly studied in simple Newtonian viscous fluids [7, 9, 10]. Recently, interest has grown in the effect of vertical vibrations on a layer of complex non-Newtonian

* Corresponding author. Tel.: +7-495-434-1487; fax: +7-499-739-9531.
E-mail address: kalin@ipmnet.ru

2210-9838 © 2013 The Authors. Published by Elsevier B.V.
Selection and/or peer-review under responsibility of Yuli Chashechkin and David Dritschel
doi:10.1016/j.piutam.2013.04.018

fluids, e.g. [11 – 13]. Due to their microstructure, complex fluids display viscoelastic properties, which may affect classical hydrodynamic instabilities. Previous experiments showed the significant effect of diluted flexible polymers on a parametrically driven, disordered capillary waves [12, 13].

In this paper, we report novel experimental evidence that polymers affect the transition to breaking standing gravity surface waves excited under Faraday resonance.

2. Experimental procedure

Experiments were performed with an electromechanical shaking table (Fig. 1(a)) with a frequency range of 0.3 - 10 Hz. The second wave mode ($n = 2$) was excited under the conditions of main Faraday resonance ($\Omega \sim 2\omega$) in a rectangular acrylic tank ($50 \times 4 \times 40$ cm) which was filled with liquid to a depth of $h = 15$cm and oscillated vertically with amplitude s =0.75 cm and frequency Ω . At the fixed value of s the variation of Ω provided change of a wave steepness $\Gamma = H / \lambda$ (H is the wave height, λ = 50cm is the wavelength, $\omega^2 = gk \operatorname{th} kh$, $k = 2\pi / \lambda$). Waves produced in this way could be precisely controlled under experimental conditions [14]. The wave profiles were obtained by the use of regular (DIMAGE Z2, 30 fps) and high-speed (VS FAST, 200-500 fps) video cameras oscillating with the tank, and image processing by the software ImageJ 1.43u[†]. The behavior of surface waves was examined by slowly increasing or decreasing Ω , with s fixed. In order to exclude transient effects, we made the observation and recording of surface waves after waiting for at least 200 - 300 forcing periods, keeping Ω fixed.

Aqueous solutions of polyacrilamide (PAM) with molecular mass $M = 11 \times 10^6$ g/mol at concentrations $C = 10, 100, 500, 1000$ ppm were used in this work. The wave breaking processes in pure water ($C = 0$) is treated as a “reference point”. Most of our experiments were conducted with water and PAM solutions, but to estimate the viscous effect we also used aqueous solution of sugar (density: 1.236 g/cm^3; kinematic viscosity: 13.43 cSt).

3. Breaking Faraday waves

3.1. The collapsing cavity

Since the linear stability of Faraday waves [15] is described by the dimensionless detuning parameter $p = \left(2\omega / \Omega\right)^2$ and the forcing parameter $q = 2\kappa s \tanh \kappa h$, the parametric excitation of waves can be interpreted in the (p, q)-plane. The neutral stability chart (Fig. 1(b), the plot in the upper right corner) determines the (p, q)-values corresponding to the condition of subharmonic resonance from quiescent initial fluid states, i.e. the unstable region in (p, q)-plane. Consequently, each regime of fluid oscillations in our experiments can be quantitatively represented by pair values of (p, q). This approach has special value in case of irregular and breaking waves since their height H can be estimated only in statistical sense.

The observable Faraday waves can be separated into three classes – regular, irregular and breaking waves. Locations of these waveforms in (p, q) parameter space are shown in Fig. 1(b). Regular waves (region 1) are periodic and symmetric in time and space. It was determined [9] that they have a limit steepness of 0.255, and a limiting angle at a crest less than 80°. For irregular waves (region 2), the temporal and space symmetry is broken. Observe that in regular and irregular waves, the volume of the oscillating liquid keeps its connectivity. Breaking Faraday waves (region 3) occupying the most part of (p, q)-plane are characterized by the broken free liquid surface with ejected drops and jets.

[†] Freely distributed on the Internet: http://rsbweb.nih.gov/ij/. No license is required

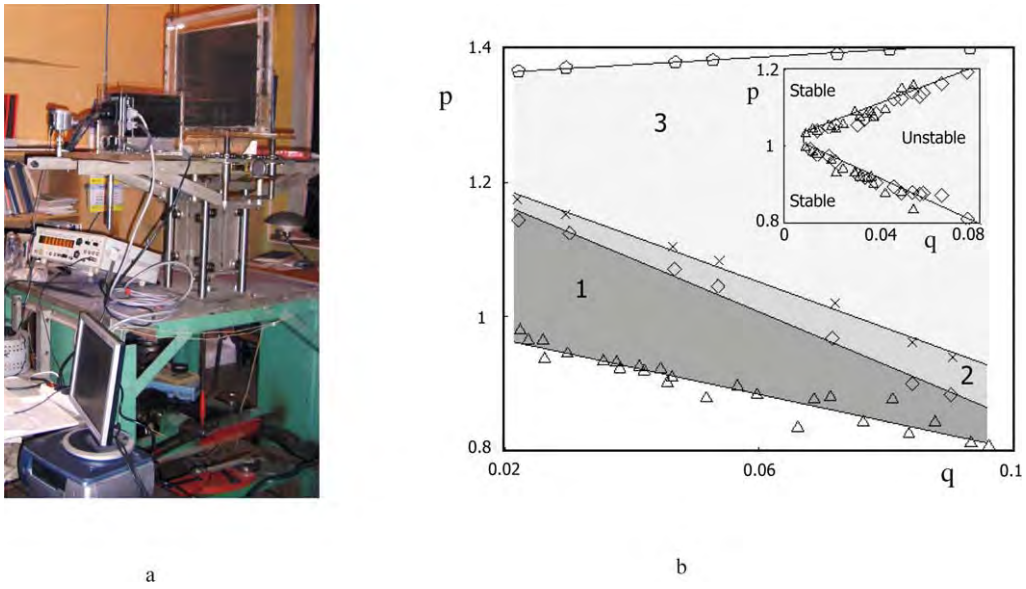

Fig. 1. (a) The experimental setup. (b) Locations of the various waveforms in parametric space (p, q): 1 – regular; 2 – irregular; 3 – breaking waves. Shaded areas determine the approximate boundaries of waveforms. The plot in the upper right corner of this figure is the stability chart of the free surface of the liquid for second and third wave modes (n =2, 3)

Careful analysis of the high-speed video data shows that the wave breaking process occurs in the following scenario of jet generation in sharp-crested wave mode. The origin of the jet is due to the cavity collapsing at the crest formation stage when the central part of the fluid moves upward - Fig. 2(a). When a cavity on the wave crest collapses, it generally produces a well-defined high velocity jet.

As shown in Fig. 2(a), during the crest formation from the initial “horizontal” free surface position, the first observable cavity is a shallow depression with an almost flat bottom (frame 2); the length of this deepening (from edge to edge) is about 8 cm. For the description of the cavity dynamics, we use its length l and depth d measured with respect to the free surface of the liquid. The length of the first observable cavity is considered as the initial value of l_0. From the moment of cavity occurrence, its length monotonously decreases (frames 2-9). However the cavity depth first reaches the maximum, d_0~1.1 cm (frame 4), and then decreases to zero at the moment of cavity closure. Hence, from the moment of the maximal depth d_0, the cavity stops growing downward and the process of its collapse begins. This means that the vertical velocity of the liquid around the cavity bottom has reached a zero value and has changed its sign. Taking into account the monotone length change, this is evidence of complex flow pattern near the cavity boundaries. Note that at the maximal depth d_0, the cavity takes the shape of a semicylinder. After cavity closure has occurred (frame 10, time t_0 = 0.1 s), a jet of liquid forms at the point of closure and moves together with the growing wave crest (frames 11-14). Finally, the jet breaks down into liquid fragments (frames 15-21). Hence, the entire collapsing process taking place within about 40 - 70 ms can be divided into two stages: 1) the cavity is initiated and grows on the forming crest above the still water level, and 2) it collapses.

The detailed analysis of the process of the cavity collapsing in Fig. 2(b) shows that in 0.01 s after the moment when d_0 = 1.3 cm (frame 1), the cavity takes the dihedral form (frame 3) with a linear angle of about 112°. Then the bottom of the dihedral surface is rounded (frame 4), and until the cavity closure (frames 5 and 6), any jets are absent. The initial indication of jet ejection can be only noted in frames 7 – 8.

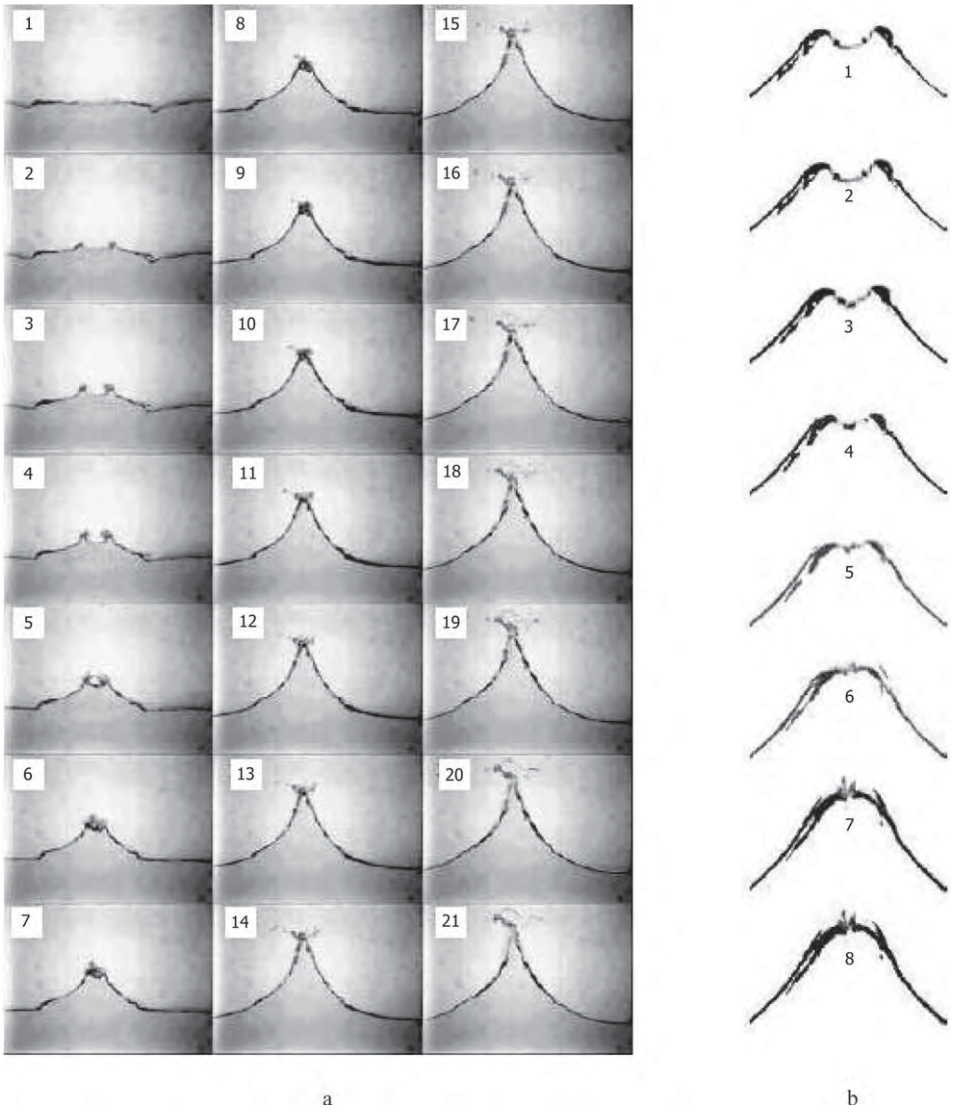

Fig. 2. Sequence of video frames showing details of breaking Faraday waves. The numbers superposed on the images determine their sequence order. (a) Initiation, development and collapse of the cavity during crest formation; $p = 1.109$, $q = 0.180$. (b) Cavity collapse on forming crest; $p = 0.941$, $q = 0.180$; the maximal depth of a cavity is $d_0 = 1.3$ cm; the field of view is 5×5 cm. The images are taken at time intervals 0.01s (a), and 0.005s (b), respectively

The sequence of events presented in Fig. 2 and described above is general for breaking Faraday waves on a free surface of water, aqueous solutions of sugar and PAM in a rectangular tank. The initiation, development and collapsing of the cavity takes place during wave crest forming after the free surface has passed the still water level. It is necessary to note basic difference of this our conclusion from all previous experiments, e.g. [16], in which the jet eruption in axisymmetric standing waves on the free surface of liquids in cylindrical tanks was considered. All authors observed the translation of the rising trough (below the still water level) to a narrow jet. Numerical model [17] also considered formation of a jet from a trough of a standing wave in a rectangular tank.

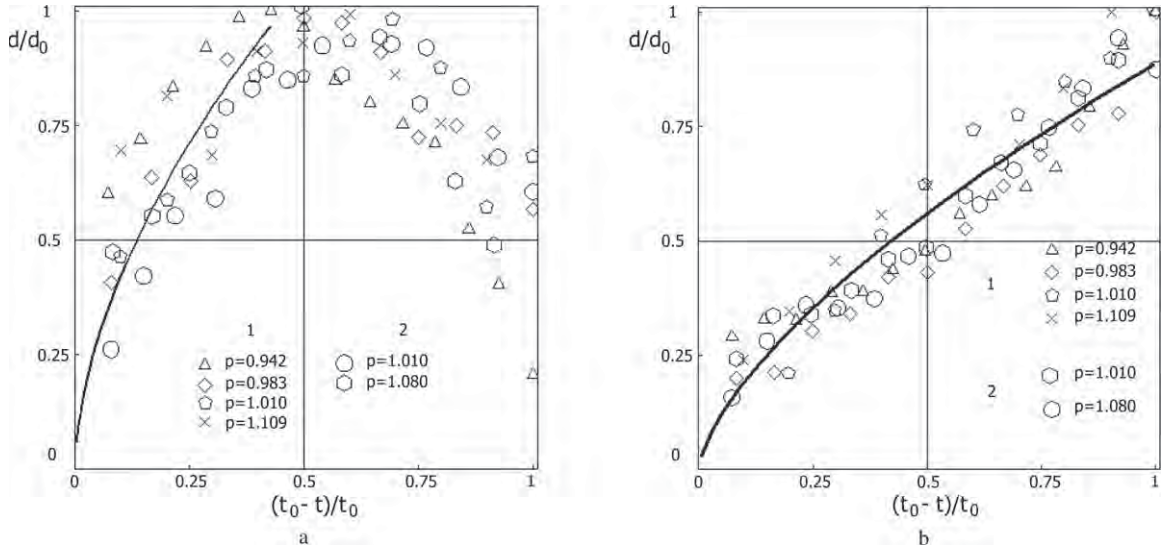

Fig. 3. Cavity depth (a) and length (b) at various times after cavity formation $(t_0 - t) / t_0 = 1$ and before cavity collapse $(t_0 - t) / t_0 = 0$; q = 0.090, p = 0.942, 0.983, 1.010, 1.109 and 1.080. Experimental points 1 and 2 correspond to water and aqueous solution of sugar (density: 1.236 g/cm^3; kinematic viscosity: 13.43 cSt), respectively. The solid line is the functional dependency $(1 - t / t_0)^{-2/3}$ for dimensionless geometrics of collapsing cavity

Dimensionless dependencies of cavity depth d / d_0 and length l / l_0 from time $(t_0 - t) / t_0$ are presented in Fig. 3, where t_0 is the time of cavity closure. All the data for water and aqueous solution of sugar collapse reasonably well into a single curve at the stage of cavity collapse:

$$(l / l_0; d / d_0) \sim \left(1 - t / t_o\right)^{2/3}$$

This relationship reflects a monotonic decrease in cavity length and depth with increasing time. Solid lines on Fig. 3 correspond to functional dependency $\left(1 - t / t_o\right)^{2/3}$. It is significant that the $2/3$ - exponent reflects the general laws inherent in problems [18,19] with a conic deepening on a free surface of a liquid and most likely corresponds to a balance between inertia and surface tension. It seems that the viscosity effects are small in our case (*see* Fig. 3, data for water and aqueous sugar solution) and do not exert influence on process of a cavity collapse.

Using the data on cavity dynamics, we estimate the velocities of the fluid particles in pure wave motion and in the collapsing cavity. The maximum wave velocity (horizontal or vertical) of the free surface particles is about 90 cm/s. The average horizontal and vertical closure velocities have the same order of value (~ 50 – 150 cm/s). However, at the moment of cavity closure, there was a velocity jump (~ 400 cm/s), and the corresponding estimation for vertical acceleration gives a value of about 30 – 40g.

3.2. Ejected jets and the effect of viscoelasticity

Experiments showed almost no difference between Newtonian and non-Newtonian fluids for regular and irregular Faraday waves. Resonance curves $H(\Omega)$ in Fig. 4 show that with decrease in the tank frequency Ω the height of regular and irregular waves monotonically increases without significant differences between water and polymer solutions.

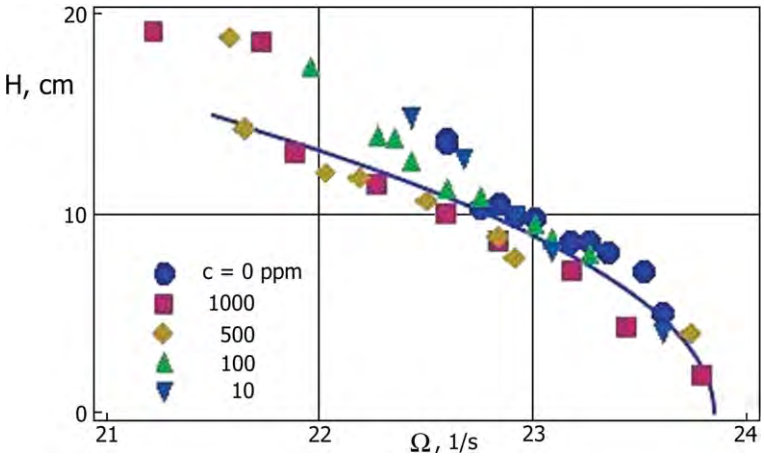

Fig. 4. Resonance curves of non-breaking waves on free surface of water and polymer solutions

The transition to wave-breaking state occurs at a further frequency decreasing. For water, this state means a change from a simply connected surface to a free surface connected in multiple ways. At close examination the formation of the ejected jet is associated with the collapsing cavity during crest formation when the central part of fluid moves upward. When a cavity of the developing wave crest collapses, it generally produces a well-defined high velocity jet.

Figure 5 shows two typical images of the jet evolution for pure water (a), and for PAM aqueous solution, $C = 10^3$ ppm (b). In these pictures, the images were obtained using the same driving frequency $\Omega = 20.81$ s^{-1}. It can be seen that the presence of a small polymer concentration fundamentally changes the structures of the ejected jet.

In both cases, the ejected jet is stretched due to the difference of the growing crest velocity and cumulative velocity of the jet tip. This difference is estimated to be about 150 – 200 cm/s.

A water stretched jet on the growing crest breaks into droplets, which can be clearly seen from 35 ms and on - Fig. 5(a).

The picture changes drastically in the case of polymer solutions – Fig. 5(b). The stretched jet keeps its integrity practically for the entire time interval (320 ms). One can see only a single drop when the wave surface moves to the undisturbed horizontal level (downward motion of the free surface).

The main morphological differences between the stretched jets of water and PAM solution are explained from a molecular standpoint. The presence of PAM molecules increases the elongational viscosity of the fluid [20]. The retardation of breakup of polymeric liquids may be attributable to the fact that in the process of disintegration the liquid is subjected to strong local tensile deformation along the jet. At the same time, one of the most unusual properties of polymeric liquids is the ability to accumulate giant reversible strains and develop high elastic stresses in strong elongational flows. Formally, this corresponds to multiple increase in the longitudinal (elongational) viscosity. In liquid disintegration the elastic stresses impede the separation of the liquid continuum into isolated fragments

The effect of polymer additives is particularly evident in the construction of the free surface envelope built upon overlapping of wave profiles for several wave periods – Fig. 6.

To quantify the effect of polymer additives we used the steepness of waves without droplet detachments. The corresponding dependence $\Gamma(C)$ is shown in Fig. 7.

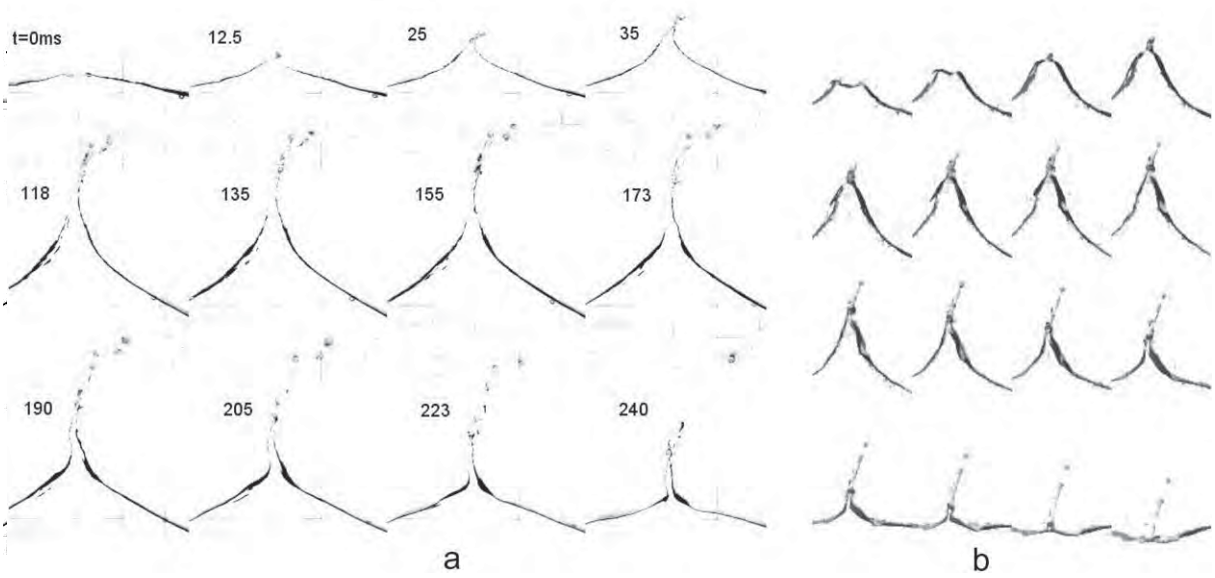

Fig. 5. Comparative evolution of the ejected jets for: a – a pure water; b – PAM ($C = 10^3$ ppm; time step between frames Δt =20 ms). Driving frequency Ω = 20.81 s^{-1}

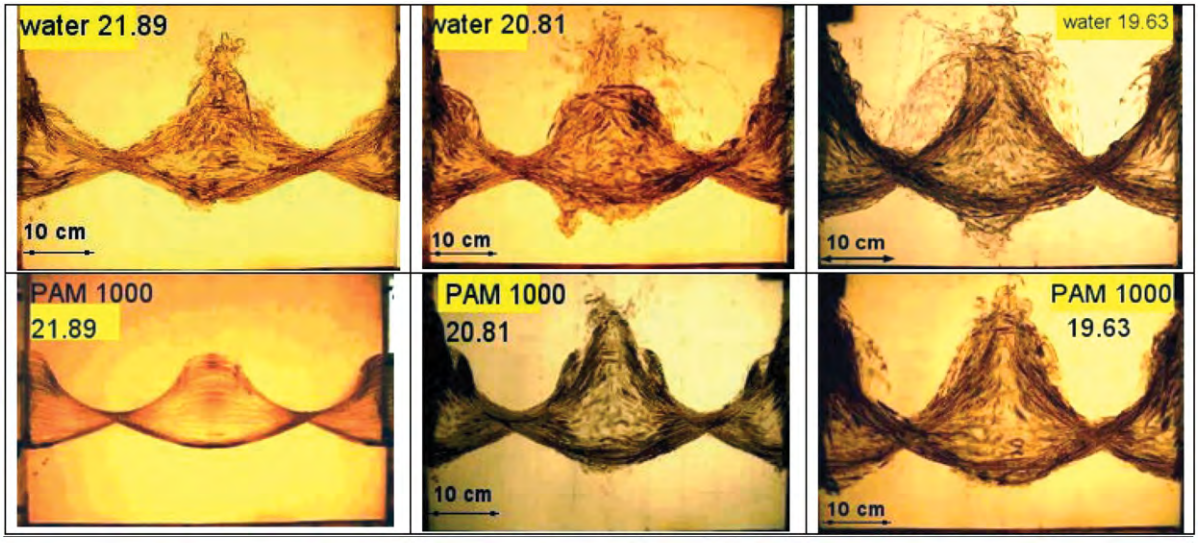

Fig. 6. . Development (water – top row of pictures) and suppression (PAM, $C = 10^3$ ppm – bottom row of pictures) of liquid spray formation over the upper wave envelopes at Ω = 21.89, 20.81 and 19.63 s^{-1}. The envelopes have obtained by overlapping the wave profiles for 15 wave periods with a time step of 1/30 s

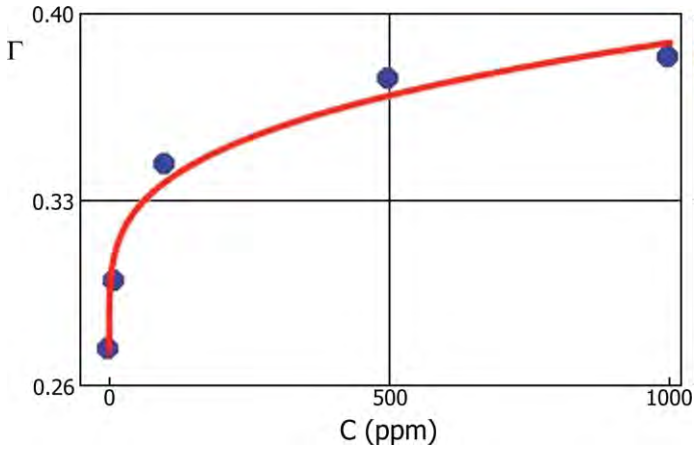

Fig. 7. The dependence of the steepness of waves without liquid fragmentation on the concentration of polymer

Thus, in pure water the ejected jets break up into droplets due to Rayleigh instability – there is a tendency towards the development of beadlike swellings and contractions along the jet. These swellings and contractions (initially small in size) grow until ultimately the jet is broken into drops (Fig. 5(b)). In the polymer solution the long and stable filament-like peak is visible (Fig. 5(b)). In fact, such peaks prevent from liquid spray formation over upper wave envelopes (Fig. 6). As a result, the steepness of Faraday waves in non-Newtonian liquids increases significantly (Fig. 7).

4. Concluding remarks

We have presented novel experimental results on breaking standing gravity waves in viscoelastic liquids. We obtain a significant strengthening effect of the oscillating liquid at polymer (PAM) concentrations of about 10 - 1000 ppm.

Without PAM additives we observed a rapid development of Rayleigh instability along the jet ejected from the growing wave crest and the subsequent fragmentation of this jet into drops.

The addition of the polymer possessing elastic properties suppress the jet breakup which significantly increases of the steepness of non-breaking Faraday waves.

Acknowledgements

Experiments were performed at the “PR-2M” USU setup “HPC IPMech RAS” (State contract 16.518.11.7059) with the partial support of the Thai Research Fund and the Commission on Higher Education of Thailand, and the Russian Foundation for Basic Research (Pr. No. 12-08-00067).

References

[1] Whitham GB. *Linear and nonlinear waves.* New York: Wiley-Interscience; 1974.
[2] Penney WG, Price AT. Finite periodic stationary gravity waves in a perfect fluid. *Phil. Trans. Roy. Soc. Lond.* 1952;**A224**:254 – 84.
[3] Taylor GI. An experimental study of standing waves. *Proc. Roy. Soc. Lond.* 1953;**A218**:44 – 59.
[4] Ibrahim RA. *Liquid sloshing dynamics: theory and applications.* Cambridge: University Press; 2005.
[5] Peregrine DH. Water-wave impact on walls. *Ann. Rev. Fluid Mech.* 2003;**35**:23 – 43.

[6] Longuet-Higgins MS. Bubbles, breaking waves and hyperbolic jets at a free surface. *J. Fluid Mech.* 1983;**127**:103 – 21.
[7] Jiang L, Ting CL, Perlin M, Schultz WW. Moderate and steep Faraday waves: instabilities, modulation and temporal asymmetries. *J. Fluid Mech.* 1996;**329:**215 – 307.
[8] Faraday M. On a peculiar class of acoustical figures, and on certain forms assumed by groups of particles upon vibrating elastic surfaces. *Phil. Trans. Roy. Soc. Lond.* 1831;**121**:299 – 340.
[9] Kalinichenko VA, Sekerzh-Zenkovich SYa. An experimental study on maximal height Faraday waves. *Fluid Dynamics* 2007;**42**:959 – 65.
[10] Kalinichenko VA. Breaking Faraday waves and jet launch formation. *Fluid Dynamics* 2009;**44**:577 – 86.
[11] Ballesta P, Manneville S. Signature of elasticity in the Faraday waves. *Phys.Rev.E* 2005;**71**:026308.
[12] Kityk AV, Wagner C. Delay of disorder by diluted polymers. *EPL* 2006;**75**(3):441 – 7.
[13] Shats M, Xia H, Punzmann H. Parametrically excited water surface ripples as ensembles of oscillons. *PRL* 2012;**108**:034502.
[14]. Kalinichenko VA, Nesterov SV, Sekerzh-Zen'kovich SYa, Chaykovskii AA. Experimental study of surface waves with Faraday resonance excitation. *Fluid Dynamics* 1995;**30**:101 – 6.
[15] Benjamin TB, Ursell F. The stability of the plane free surface of a liquid in vertical periodic motion. *Proc.R.Soc.Lond.* 1954;**A225**:505 – 15.
[16] Zeff BW, Kleber B, Fineberg J, Lathrop DP. Singularity dynamics in curvature collapse and jet eruption on a fluid surface. *Nature* 2000;**403**:401 – 4.
[17] Longuet-Higgins MS, Dommermuth DG. Vertical jets from standing waves. II *Proc.R.Soc.Lond.* 2001;**A457**:2137 – 49.
[18] Duchemin L, Popinet S, Josserand C, Zaleski S. Jet formation in bubbles bursting at a free surface. *Phys. Fluids* 2002;**14**:3000 – 8.
[19] Eggers J, Fontelos M, Leppinen AD, Snoeijer JH. Theory of the collapsing axisymmetric cavity. *Phys. Rev. Lett.* 2007;**98**:094502.
[20] Rozhkov AN. Dynamics and breaking of viscoelastic liquids (a review). *Fluid Dynamics* 2005;**40**:835 – 53.

Provided for non-commercial research and education use.
Not for reproduction, distribution or commercial use.

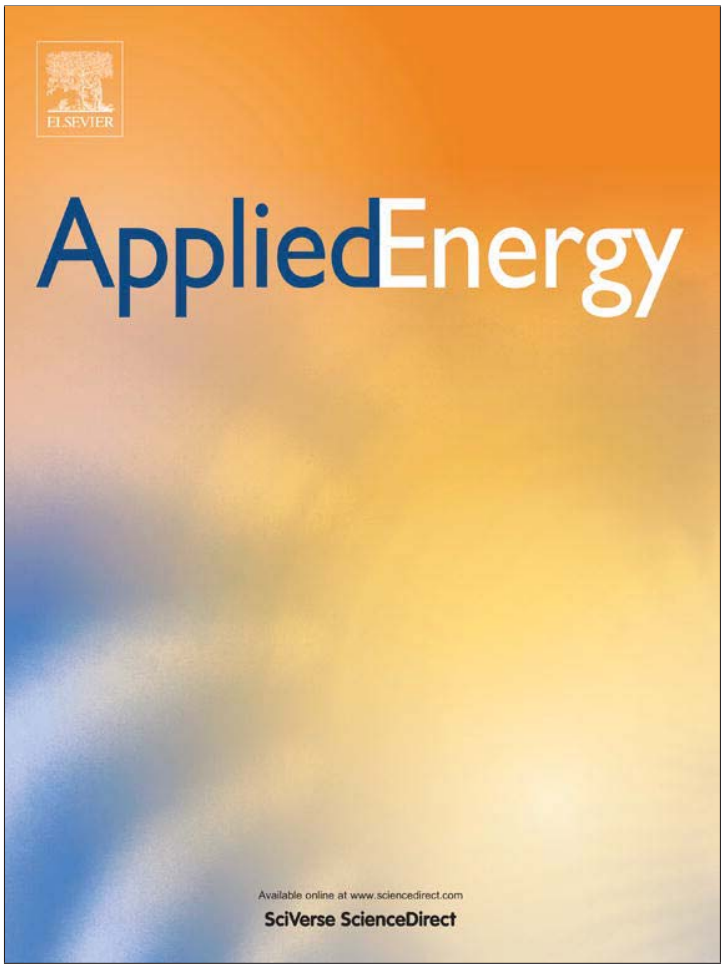

This article appeared in a journal published by Elsevier. The attached copy is furnished to the author for internal non-commercial research and education use, including for instruction at the authors institution and sharing with colleagues.

Other uses, including reproduction and distribution, or selling or licensing copies, or posting to personal, institutional or third party websites are prohibited.

In most cases authors are permitted to post their version of the article (e.g. in Word or Tex form) to their personal website or institutional repository. Authors requiring further information regarding Elsevier's archiving and manuscript policies are encouraged to visit:

http://www.elsevier.com/authorsrights

Author's personal copy

Applied Energy 111 (2013) 40–45

Contents lists available at SciVerse ScienceDirect

Applied Energy

journal homepage: www.elsevier.com/locate/apenergy

Experimental studies on the viscosity of TiO_2 and Al_2O_3 nanoparticles suspended in a mixture of ethylene glycol and water for high temperature applications

Thaklaew Yiamsawas [a], Omid Mahian [b], Ahmet Selim Dalkilic [c], Suthep Kaewnai [a], Somchai Wongwises [a,d,*]

[a] Fluid Mechanics, Thermal Engineering and Multiphase Flow Research Lab. (FUTURE), Department of Mechanical Engineering, Faculty of Engineering, King Mongkut's University of Technology Thonburi, Bangmod, Bangkok 10140, Thailand
[b] Young Researchers Club and Elites, Mashhad Branch, Islamic Azad University, Mashhad, Iran
[c] Heat and Thermodynamics Division, Department of Mechanical Engineering, Yildiz Technical University, Yildiz, Besiktas, Istanbul 34349, Turkey
[d] The Academy of Science, The Royal Institute of Thailand, Sanam Suea Pa, Dusit, Bangkok 10300, Thailand

HIGHLIGHTS

- Measuring the viscosity of Al_2O_3 and TiO_2 nanoparticles suspended in EG/water.
- Theoretical models fail to predict the viscosity of nanofluids.
- A correlation is presented to use in practical applications and high temperatures.

ARTICLE INFO

Article history:
Received 24 November 2012
Received in revised form 27 February 2013
Accepted 23 April 2013

Keywords:
Viscosity
Nanofluids
Experimental study
Theoretical models
High temperature

ABSTRACT

Experimental investigations are performed to determine the viscosity of TiO_2 and Al_2O_3 nanoparticles suspended in a mixture of ethylene glycol/water (EG–water, 20/80 wt%). The experiments are conducted at various volume fractions between 0% and 4% and a temperature range of 15–60 °C. Some comparisons are made between the experimental results and the theoretical models and correlations presented for viscosity in the literature. The results indicate that the theoretical models are not suitable to predict the viscosity of nanofluids. Finally, using the experimental data, a useful correlation is presented to predict the viscosity. To estimate the required pumping power in an energy device, in the first, the viscosity should be determined. Therefore, the results of the present work may be helpful in the design of energy devices.

© 2013 Elsevier Ltd. All rights reserved.

1. Introduction

The world in recent years has observed a rapid progress in applications of nanofluids in different fields of thermal engineering. A nanofluid is an advanced kind of working fluids containing very small particles with the size of about 1–100 nm suspended in common fluids such as water and ethylene glycol [1]. Nanofluids can be used in many systems such as solar energy systems [2], cooling of electronics, medical applications, fuel cells, nuclear reactors [3], heating of buildings and the reduction of pollution [4], air conditioning systems [5], and enhancement of the performance and efficiency of the thermal systems [6].

Measurement of the properties of nanofluids such as viscosity is very important, especially at high temperatures, in the design of energy engineering systems such as heat exchangers and cooling systems [7], because the required pumping power for the system is estimated by using the amount of viscosity. Many researches have been conducted to determine the viscosity of nanofluids, both experimentally and theoretically. Here, some of the recent experimental works are briefly reviewed.

Pak and Cho [8] measured the viscosity of Al_2O_3 and TiO_2 water based nanofluids at room temperature. They concluded that at a volume fraction of 10%, the relative viscosities of TiO_2/water and Al_2O_3/water compared to water increase by 3 and 100 times, respectively.

* Corresponding author at: Fluid Mechanics, Thermal Engineering and Multiphase Flow Research Lab. (FUTURE), Department of Mechanical Engineering, Faculty of Engineering, King Mongkut's University of Technology Thonburi, Bangmod, Bangkok 10140, Thailand. Tel.: +66 2 470 9115; fax: +66 2 470 9111.
E-mail address: somchai.won@kmutt.ac.th (S. Wongwises).

0306-2619/$ - see front matter © 2013 Elsevier Ltd. All rights reserved.
http://dx.doi.org/10.1016/j.apenergy.2013.04.068

Author's personal copy

He et al. [9] investigated the effects of concentration and particle size on the viscosity of TiO_2/water nanofluid where the volume fraction is between 1 and 5 wt%, and the sizes of nanoparticles are 95, 145, 210 nm. They found that the viscosity ratio increases nonlinearly with an increase in concentration of nanofluid. They also perceived that an increase in particle size leads to the increase in viscosity ratio.

Nguyen et al. [10] studied the effects of temperature, concentration, and particle size on the viscosity of Al_2O_3/water and CuO/water nanofluids. They used Al_2O_3 nanoparticles in the sizes of 36 and 47 nm, and CuO nanoparticles of 36 nm diameter. The experiments are conducted at a temperature range between 22 and 75 °C with a concentration range of 1–12 vol%. They found that in high concentrations, the viscosity decreases with an increase in temperature, but in small concentrations, the temperature has no considerable effect on the viscosity.

Murshed et al. [11] measured the viscosity of TiO_2 and Al_2O_3 water based nanofluids where the sizes of TiO_2 and Al_2O_3 particles are 15 and 80 nm, respectively. The experiments are conducted at a concentration range of 1–5 vol%. Their results showed that the viscosity of nanofluids is greater than the base fluid. Duangthongsuk and Wongwises [12] studied the effects of temperature on the viscosity of TiO_2/water nanofluid where the particle size of TiO_2 is 21 nm. They performed the experiments at a temperature range of 15–35 °C and the volume fraction between 0.2% and 2%. Their results indicated that the viscosity decreases with increasing temperature, while the viscosity ratio increases with an increase in temperature (especially at large concentrations).

Turgut et al. [13] measured the viscosity of TiO_2/water nanofluid with volume fraction at the range of 0.2–3% and the temperature range of 13–55 °C. They found that the viscosity decreases with an increase in temperature. They concluded that the classic equations of Einstein [14], Nielsen [15], and Krieger and Dougherty [16] underestimate the viscosity compared to the experimental models.

Chandrasekar et al. [17] conducted an experimental study of the effects of concentration on the viscosity of Al_2O_3/water nanofluid with particle size of 43 nm and volume fraction less than 5%, at room temperature.

Xie et al. [18] compared the viscosity of five different nanofluids including MgO, TiO_2, ZnO, Al_2O_3 and SiO_2 ethylene glycol based nanofluids. They concluded that where temperature is between 10 and 60 °C, the viscosity of MgO/EG nanofluid is the lowest.

In another work, Fedele et al. [19] presented some results for the viscosity of TiO_2 water based nanofluid at the temperature range of 10–70 °C. Recently, Aladag et al. [20] and Mare et al. [21] measured the viscosities of Al_2O_3/water and CNT/water based nanofluids at low concentrations and temperatures (between 2 and 10 °C).

Pastoriza-Gallego et al. [22] found that the effect of particle size in the viscosity of Al_2O_3/water nanofluids is considerable. A helpful review of the latest results on the viscosity of nanofluids is presented by Mahbubul et al. [23].

A review of the literature shows that there is no study on the viscosity of Al_2O_3 and TiO_2 nanoparticles where the base fluid is a mixture of EG–water (20:80). In comparison with water, the mixture of EG and water is more helpful because the mixture has higher boiling and freezing point. On the other hand, in comparison with EG, the viscosity of mixture is less than EG, hence, the required pumping power decreases. In this study, the viscosity of nanofluids is measured for temperatures between15 and 60 °C. The results can be useful in the design of energy devices which work under high temperatures. The results are also compared with the theoretical models and some correlations available in the literature. Finally, a useful correlation is presented to predict the viscosity of the nanofluids.

2. Experimental set up

In this study, TiO_2–EG/water and Al_2O_3–EG/water nanofluids with volume fractions of 1%, 2%, 3%, and 4% are prepared and tested.

To prepare the nanofluids, two types of TiO_2 (diameter of 21 nm) and Al_2O_3 (diameter of 120 nm) nanoparticles suspended in water, respectively with weight fractions of 40% and 30% are used which provided by DEGUSSA, a German Company (DEGUSSA, VP Disp. W740x and W630). In order to prepare the required concentrations of nanofluids, the dilution is mixed with a mixture of water and EG so that finally 20% of the base fluid is EG, and 80% is water. An ultrasonic vibrator with power of 600 W is also used to sonicate the solution continuously for 2 h to break down agglomeration of the nanoparticles. As a result, the suspension stability of nanoparticles within the base fluid is found to be very good for months. TEM images are taken to confirm the results. Fig. 1 shows a sample of the TEM image that is taken from TiO2–EG/water nanofluid. To measure the viscosities of nanofluids a capillary tube viscometer (Cannon Instrument, USA) is utilized. The schematic of the experimental set up is shown in Fig. 2. The system is composed of a 0.75 mm viscometer tube with a measurement range of 1.6–8 cSt. Fig. 3 shows a schematic view of the viscometer presented in the catalogue provided by the company. The tube is

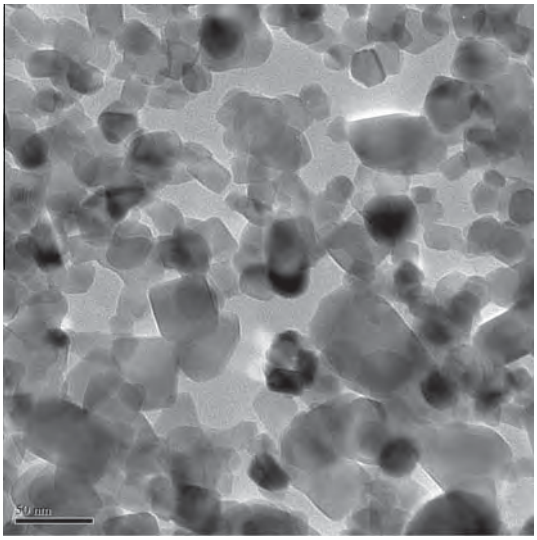

Fig. 1. TEM image of the TiO_2–EG/water nanofluid.

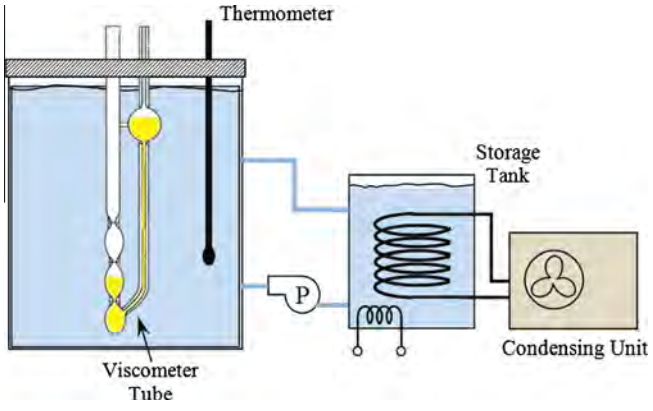

Fig. 2. Schematic of the experimental set up.

Author's personal copy

Fig. 3. A schematic view of the viscometer manufactored by Cannon Instrument company.

immersed in a transparent temperature-controlled basin connected to a temperature-controlled water tank. A stopwatch with an accuracy of 0.01 s is used to record the time of passing the fluid from a specified section of the viscometer, and a thermometer with the accuracy of 0.1 °C is used to measure the temperature. For any volume fraction, the tests are repeated three times. Using the viscometer, one can find that the nanofluid is Newtonian or not. By referring to Fig. 3, if the efflux time in bulbs *C* and *J* are approximately the same, the sample is Newtonian. It is observed that for volume fractions less than 4%, the nanofluids have a Newtonian behaviour. In this work, maximum uncertainty is 1.62%, and average uncertainty is 0.82% for viscosity.

3. Data reduction

The following relation is used to obtain the viscosity:

$$\mu_{nf} = C \cdot \rho_{nf} t \tag{1}$$

where μ is the viscosity (kg/ms), *C* is a constant for the viscometer tube that is obtained from calibration with reference substance supplied by the company (=0.008 cSt/s), ρ is the density (kg/m^3), and t is the flowing time of the nanofluid during each test (s). The density of Al_2O_3 and TiO_2 nanoparticles are 3600 kg/m^3 and 4170 kg/m^3, respectively. The density of nanofluid (ρ_{nf}) is obtained as follows [24]:

$$\rho_{nf} = \phi\rho_p + (1-\phi)\rho_f \tag{2}$$

In this study, some comparisons are made with the most used theoretical models and some correlations. In the following the models are presented.

Einstein's model [14]: This model is defined as:

$$\mu_{nf} = (1 + 2.5\phi)\mu_f \tag{3}$$

This equation is based on phenomenological hydrodynamic equations and considers a suspension containing solute particles in a total volume. In the above relation μ_{nf} is the viscosity of nanofluid, μ_f is the viscosity of base fluid, and ϕ is the volume fraction (vol.%).

Brinkman [25] improved the Einstein's model as follows:

$$\mu_{nf} = \frac{1}{(1-\phi)^{2.5}}\mu_f \tag{4}$$

Another classic model that is based on the reciprocal theorem in Stokes flow problem is Batchelor's equation [26]. The equation is as follows:

$$\mu_{nf} = (1 + 2.5\phi + 6.2\phi^2)\mu_f \tag{5}$$

Einstein's model [14] and Brinkman model [25] are applicable typically for 1% and 4% of volume fraction of nanoparticles, respectively (see Ref. [20]). Although, it is seen that in some studies for comparison purposes, Eqs. (3)–(5) are used for volume fractions up to 5% (see Ref. [27]).

Nguyen et al. [10] measured viscosity of Al_2O_3–water nanofluids and presented correlations both in concentration and temperature functions as follows:

$$\mu_{nf} = \mu_b \times 0.904e^{0.148\phi} \quad dp = 47\ \text{nm} \tag{6}$$

$$\mu_{nf} = (2.1275 - 0.0215T + 0.0002T^2)\mu_b \quad \phi = 4\ \text{vol}\% \tag{7}$$

The results of the present work are compared with the above models.

Khanafer and Vafai [24] presented the following correlation to predict the nanofluid viscosity of Al_2O_3/water nanofluids from curve fitting of experimental data obtained from many studies as follows:

$$\mu_{nf} = -0.4491 + \tfrac{28.837}{T} + 0.574\phi - 0.1634\phi^2 + 23.053\tfrac{\phi^2}{T^2} + 0.0132\phi^3 - 2354.735\tfrac{\phi}{T^3} + 23.498\tfrac{\phi^2}{d_p^2} \tag{8}$$

Also, they presented the following correlation to estimate the TiO_2/water nanofluid from curve fitting of experimental data of Duangthongsuk and Wongwises [12]:

$$\tfrac{\mu_{nf}}{\mu_b} = -1.0538 + 0.1448\phi - 3.363\times10^{-3}T - 0.0147\phi + 6.735\times10^{-5}T^2 - 1.337\tfrac{\varphi}{T} \tag{9}$$

Author's personal copy

4. Results and discussions

To examine the accuracy of the results which is obtained by the experimental set up, a comparison between the present results and the presented results in ASHRAE [28] for the viscosity of the EG/water mixture (See Fig. 4) is made. It is found that the average difference does not exceed 7%. Fig. 5 shows the variations of viscosity in TiO_2–EG/water nanofluid as a function of the volume fraction of nanoparticles and temperature. The results indicate that the viscosity of nanofluid increases with an increase in volume fraction, and a decrease in temperature, as expected. It can be seen that with an increase in temperature, the differences among the amounts of viscosity at various concentrations are decreased. This implies that at higher temperatures, the particle loading is more reasonable for practical applications, because with an increase in temperature, the difference between the viscosities of nanofluids at different concentrations is decreased.

Fig. 6 provides the viscosity variations of Al_2O_3–EG/water nanofluid with temperature at different concentrations. By comparing Fig. 5 and Fig. 6, it is observed that at given values of temperature and concentration the viscosities of Al_2O_3–EG/water nanofluids are higher than TiO_2–EG/water nanofluids. This may be because of the larger size of Al_2O_3 nanoparticles compared to TiO_2. As known, there are a number of system parameters to consider, such as nanoparticle characteristics (size, shape, surface charge, etc.), particle loading (or concentration) and measurement technique (realism, accuracy, consistency, isothermal), when comparing the reported results for viscosity values of certain nanofluids.

However, in general, nanoparticles with the size bigger than 100 nm may display inertia and more complex (nano-scale) flow pattern, both effects contributing to elevated hydraulic resistance, i.e., higher apparent viscosities. As mentioned, one has to examine the phenomena on a case-by-case basis.

In the literature, different reports are presented on the effect of particle size. Some of them indicate that with increasing the particle size the viscosity increases, while some other researchers reported opposite results (for instance see the review paper by Mahbubul et al. [23] and the paper by Nield and Kuznetsov [29]).

The difference between the viscosity of the two nanofluids is more considerable at high concentrations, so that at volume fraction of 4% (at a given value of temperature), the viscosity of Al_2O_3–EG/water is more than twice the TiO_2–EG/water nanofluid. Therefore, the classic models fail to give a good estimation of the nanofluid viscosity, because in these models the effects of particle size and agglomeration are not considered. Of course, it should be noted that in this work it is tried to avoid agglomeration using sonication.

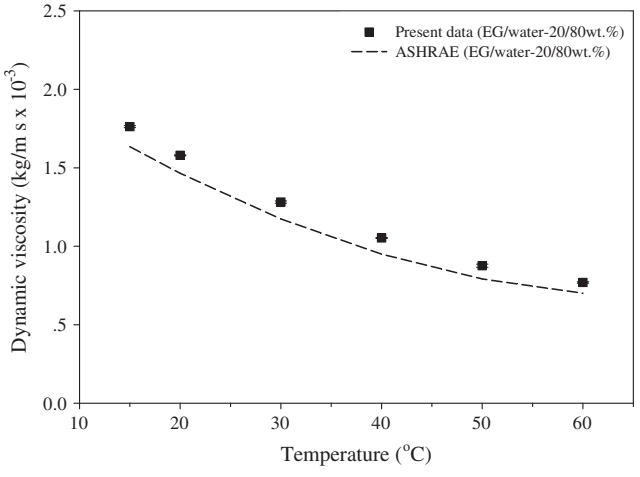

Fig. 4. Comparison of the measured viscosity with reference data.

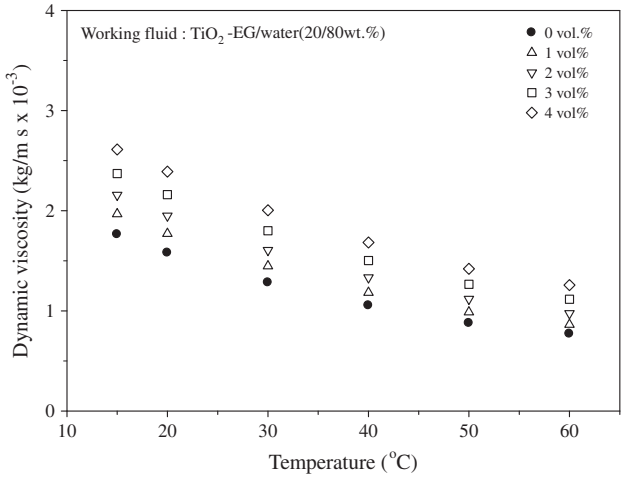

Fig. 5. Comparison of experimental viscosity ratios of TiO_2–EG/water nanofluid with those obtained from various model equations as a function of concentration.

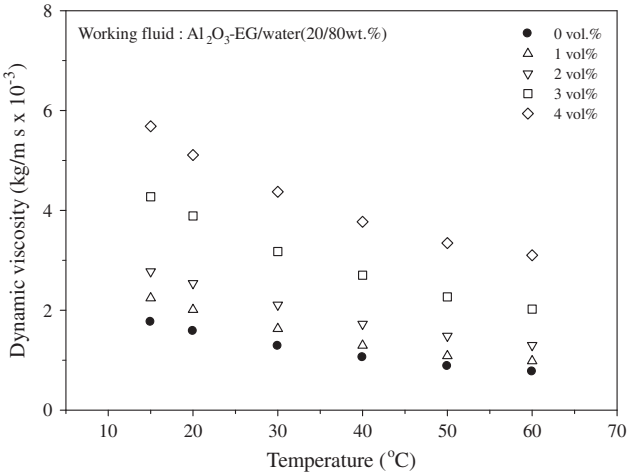

Fig. 6. Comparison of experimental viscosity ratios of TiO_2–EG/water nanofluid with those obtained from various model equations as a function of temperature.

Figs. 7 and 8 show comparisons between the viscosity ratios at various concentrations and various temperatures of TiO_2–EG/water nanofluid obtained from the experiment and those obtained from several equations reported in open literature. As shown in both figures, the correlation of Khanafer and Vafai [24] gives slightly corresponding trend. It should be noted that the base fluid in the present work is the mixture of water/EG whereas the correlation of Khanafer and Vafai is for base fluid of water. The viscosity ratios obtained from the classic models are almost the same at various concentrations and temperatures as shown in Figs. 7 and 8 respectively.

The variations of the viscosity ratios versus concentrations and temperatures of Al_2O_3–EG/water nanofluid are shown in Figs. 9 and 10 respectively. It can be clearly seen that all equations fail to predict the viscosity. It should be stressed that the base fluid in papers of Nguyen [10] and Khanafer and Vafai [24] is only water. But, in the present work, the base fluid (mixture of water and EG) has higher viscosity than water.

The main reason of the difference between our measured data and the classic models is that the models are developed based on the low concentrations. In addition to this, because the particle sizes, configurations of particle were not included in the model, this may affect the accuracy of the application of the model.

Author's personal copy

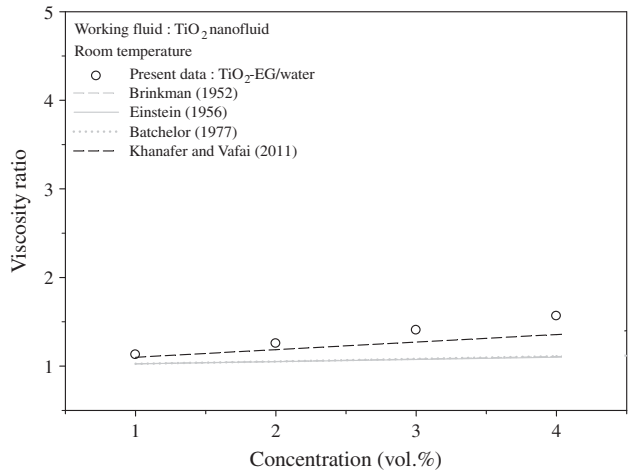

Fig. 7. Comparison of experimental viscosity ratio of Al_2O_3–EG/water nanofluid with those obtained from various model equations as a function of concentration.

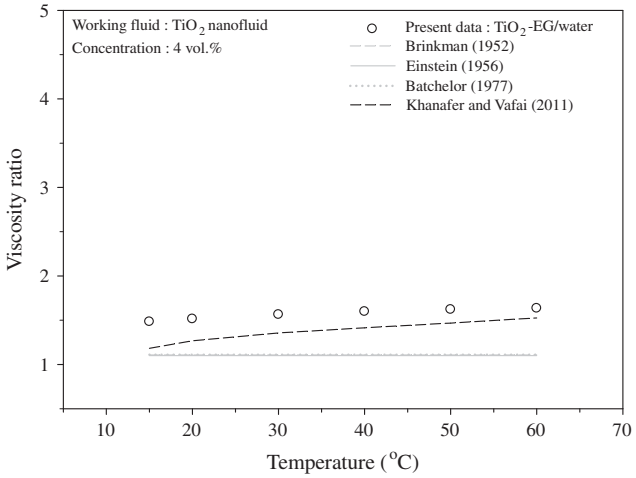

Fig. 8. Comparison of experimental viscosity ratios of Al_2O_3–EG/water nanofluid with those obtained from various model equations as a function of temperature.

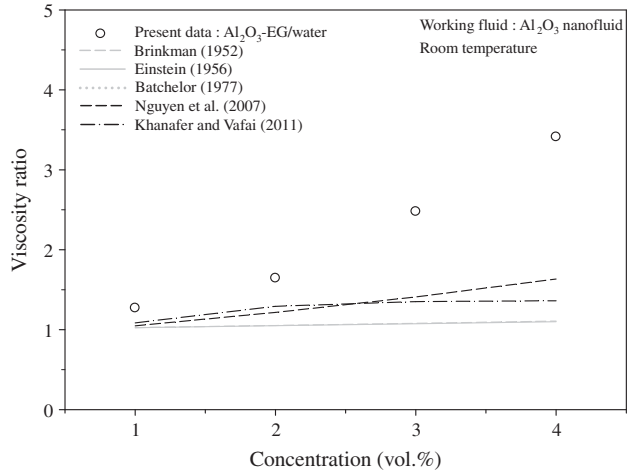

Fig. 9. Comparison of the experimental viscosity ratio of Al_2O_3–EG/water nanofluid with theoretical models at different concentrations.

As a suggestion for future works, different factors including the shape and size of the nanoparticles, the size of the molecules of

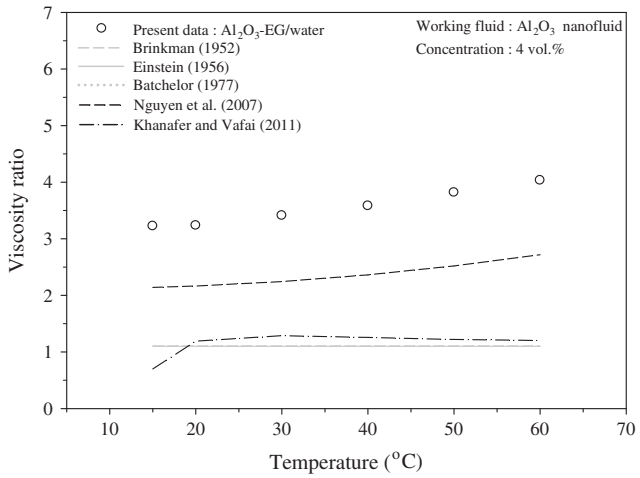

Fig. 10. Comparison of the experimental viscosity ratio of Al_2O_3–EG/water nanofluid with theoretical models at different temperatures.

Table 1
Coefficients for correlations predicting viscosity.

Nanoparticle	Coefficient			
	A	*B*	*C*	*D*
TiO_2	0.837931	0.188264	0.089069	1.100945
Al_2O_3	0.891842	0.739192	0.099205	0.9844

base fluid, temperature, pH of the nanofluid may be considered in the theoretical models to obtain more exact predictions for viscosity.

Now, a helpful correlation is presented to predict he viscosity of TiO_2 and Al_2O_3 nanoparticles suspended in the mixture of EG/water (20:80) for practical applications. Because of different physical properties such as density, etc., two separate correlations (with different coefficients) are obtained for both nanofluids of Al_2O_3 and TiO_2. In the correlation, the viscosity is a function of temperature, volume fraction of nanoparticles and the viscosity of base fluid as follows:

$$\mu_{nf} = A\phi^B T^C \mu_f^D \tag{10}$$

where the coefficients of *A*, *B*, *C*, and *D* are listed for the two types of nanoparticles in Table 1. In the above relation, although the power of temperature (coefficient of *C*) is positive, however, it should be noted that the viscosity of base fluid decreases with an increase in temperature, hence, totally the viscosity of nanofluid decreases. The viscosity of the EG/water mixture (base fluid) is obtained by the following relation:

$$\mu_f = 0.0003T^2 - 0.0461T + 2.3775 \tag{11}$$

Fig. 11 compares the results obtained from correlation and experimental data. The average error for TiO_2–EG/water nanofluid is about 5%, and for Al_2O_3–EG/water nanofluid is about 7%.

5. Conclusion

The viscosity of TiO_2 and Al_2O_3 nanoparticles suspended in a mixture of EG/water (20:80) is measured at high temperatures up to 60 °C. The sizes of TiO_2 and Al_2O_3 nanoparticles are respectively 21 and 120 nm where the maximum volume fraction used in the tests is 4%. Some comparisons with the most well-known theoretical models are made. It is found that the differences between the results obtained from theoretical models and

Author's personal copy

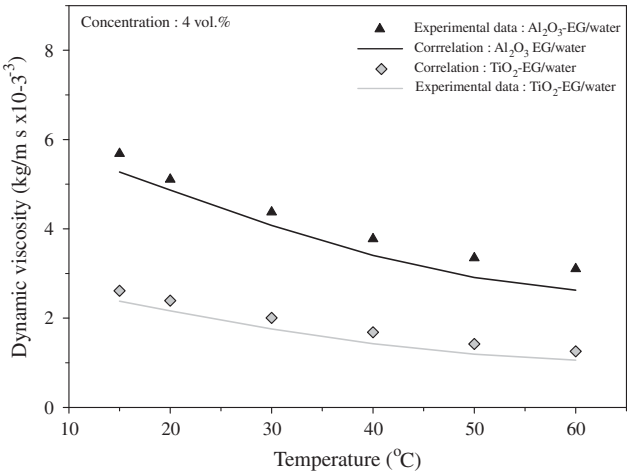

Fig. 11. Comparison of measured viscosity with proposed correlation.

experimental data are considerable. It is suggested that for future works, different factors including the shape and size of the nanoparticles, the size of the molecules of base fluid, temperature, pH of the nanofluid could be considered to obtain a better estimation of viscosity.

Finally, a helpful correlation is presented to calculate the viscosity of nanofluids in which the viscosity of nanofluid is a function of temperature, volume fraction of nanoparticles, and the viscosity of base fluid. This relation can be useful in the design of energy devices.

Acknowledgments

The present study is supported by the Thailand Research Fund, the Office of the Higher Education Commission and the National Research University Project whose guidance and assistance are gratefully acknowledged. The authors wish to thank Department of Mechanical Engineering, King Mongkut's University of Technology Thonburi for providing them fellowships for doing their research in Thailand. The authors would like to thank Professor Clement Kleinstreuer from North Carolina State University, USA for valuable comments.

References

[1] Mahian O, Mahmud S, Heris SZ. Effect of uncertainties in physical properties on entropy generation between two rotating cylinders with nanofluids. J Heat Transfer-ASME 2012;134:101704.
[2] Mahian O, Kianifar A, Kalogirou SA, Pop I, Wongwises S. A review of the applications of nanofluids in solar energy. Int J Heat Mass Transfer 2013;57(2):582–94.
[3] Saidur R, Leong KY, Mohammad HA. A review on applications and challenges of nanofluids. Renew Sustain Energy Rev 2011;15:1646–68.
[4] Kulkarni DP, Das DK, Vajjha RS. Application of nanofluids in heating buildings and reducing pollution. Appl Energy 2009;86:2566–73.
[5] Mo S, Chen Y, Jia L, Luo X. Investigation on crystallization of TiO_2-water nanofluids and deionized water. Appl Energy 2012;93:65–70.
[6] Colangelo G, Favale E, de Risi A, Laforgia D. Results of experimental investigations on the heat conductivity of nanofluids based on diathermic oil for high temperature applications. Appl Energy 2012;97:828–33.
[7] Lin CY, Wang JC, Chen TC. Analysis of suspension and heat transfer characteristics of Al_2O_3 nanofluids prepared through ultrasonic vibration. Appl Energy 2011;88(12):4527–33.
[8] Pak BC, Cho YI. Hydrodynamic and heat transfer study of dispersed fluids with submicron metallic oxide particles. Exp Heat Transfer 1998;11:151–70.
[9] He Y, Jin Y, Chen H, Ding Y, Cang D, Lu H. Heat transfer and flow behavior of aqueous suspensions of TiO_2 nanoparticles (Nanofluids) flowing upward through a vertical pipe. Int J Heat Mass Transfer 2007;50:2272–81.
[10] Nguyen CT, Desgranges F, Roy G, Galanis N, Mare T, Boucher S, et al. Temperature and particle-size dependent viscosity data for water-based nanofluids – Hysteresis phenomenon. Int J Heat Fluid Flow 2007;28:1492–506.
[11] Murshed SMS, Leong KC, Yang C. Investigations of thermal conductivity and viscosity of nanofluids. Int J Therm Sci 2008;47:560–8.
[12] Duangthongsuk W, Wongwises S. Measurement of temperature-dependent thermal conductivity and viscosity of TiO_2-water nanofluids. Exp Therm Fluid Sci 2009;33:706–14.
[13] Turgut A, Tavman I, Chirtoc M, Schuchmann HP, Sauter C, Tavman S. Thermal conductivity and viscosity measurements of water-based TiO_2-nanofluids. Int J Thermophys 2009;30:1213–26.
[14] Einstein A. Investigations on the theory of the Brownian movement. New York: Dover; 1956.
[15] Nielsen E. Generalised equation for the elastic moduli for composite materials. J. Appl. Phys. 1970;41:4626–7.
[16] Krieger M, Dougherty TJ. A mechanism for non- Newtonien flow in suspensions of rigid spheres. Trans. Soc. Rheol. 1959;3:137.
[17] Chandrasekar M, Suresh S, Bose AC. Experimental investigations and theoretical determination of thermal conductivity and viscosity of Al_2O_3/water nanofluid. Exp Therm Fluid Sci 2010;34:210–6.
[18] Xie H, Yu W, Chen W. MgO nanofluids: higher thermal conductivity and lower viscosity among ethylene glycol-based nanofluids containing oxide nanoparticles. J Exp Nanosci 2010;5:463–72.
[19] Fedele L, Colla L, Bobbo S. Viscosity and thermal conductivity measurements of water-based nanofluids containing titanium oxide nanoparticles. Int J Ref 2012;35:1359–66.
[20] Aladag B, Halelfadl S, Doner N, Maré T, Duret S, Estellé P. Experimental investigations of the viscosity of nanofluids at low temperatures. Appl Energy 2012;97:876–80.
[21] Maré T, Halelfadl S, Sow O, Estellé P, Duret S, Bazantay F. Comparison of the thermal performances of two nanofluids at low temperature in a plate heat exchanger. Exp Therm Fluid Sci 2011;35:1535–43.
[22] Pastoriza-Gallego MJ, Casanova C, Páramo R, Barbés B, Legido JL, Piñeiro MM. A study on stability and thermophysical properties (density and viscosity) of Al_2O_3 in water nanofluid. J Appl Phys 2009;106(6):064301.
[23] Mahbubul IM, Saidur R, Amalina MA. Latest developments on the viscosity of nanofluids. Int J Heat Mass Transfer 2012;55:874–85.
[24] Khanafer K, Vafai K. A critical synthesis of thermophysical characteristics of nanofluids. Int J Heat Mass Transfer 2011;54:4410–28.
[25] Brinkman HC. The viscosity of concentrated suspensions and solutions. J Chem Phys 1952;20:571.
[26] Batchelor G. The effect of Brownian motion on the bulk stress in a suspension of spherical particles. J Fluid Mech 1977;83:97–117.
[27] Duan F, Kwek D, Crivoi A. Viscosity affected by nanoparticle aggregation in Al_2O_3–water nanofluids. Nanoscale Res Lett 2011;6:248.
[28] ASHRAE. ASHRAE handbook: fundamentals. American Society of Heating, Refrigerating and air-conditioning engineers Inc., Atlanta, GA; 2005.
[29] Nield DA, Kuznetsov AV. A note on the variation of nanofluid viscosity with temperature. Int Commun Heat Mass Transfer 2013;41:17–8.

Provided for non-commercial research and education use.
Not for reproduction, distribution or commercial use.

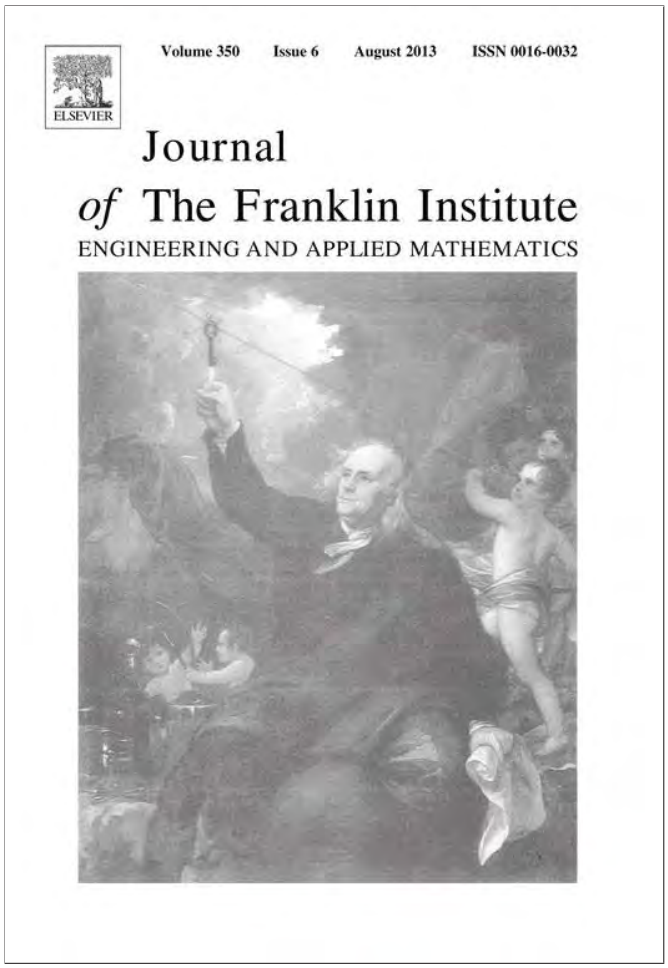

This article appeared in a journal published by Elsevier. The attached copy is furnished to the author for internal non-commercial research and education use, including for instruction at the authors institution and sharing with colleagues.

Other uses, including reproduction and distribution, or selling or licensing copies, or posting to personal, institutional or third party websites are prohibited.

In most cases authors are permitted to post their version of the article (e.g. in Word or Tex form) to their personal website or institutional repository. Authors requiring further information regarding Elsevier's archiving and manuscript policies are encouraged to visit:

http://www.elsevier.com/authorsrights

Author's personal copy

Available online at www.sciencedirect.com

SciVerse ScienceDirect

Journal of the Franklin Institute 350 (2013) 1424–1442

Journal of The Franklin Institute

www.elsevier.com/locate/jfranklin

Partially wet fin efficiency for the longitudinal fins of rectangular, triangular, concave parabolic, and convex parabolic profiles

Worachest Pirompugd[a], Somchai Wongwises[b,c,*]

[a]*Department of Mechanical Engineering, Faculty of Engineering, Burapha University, Saensook, Muang, Chonburi 20131, Thailand*

[b]*Fluid Mechanics, Thermal Engineering and Multiphase Flow Research Lab.(FUTURE), Department of Mechanical Engineering, Faculty of Engineering, King Mongkut's University of Technology Thonburi, Bangmod, Bangkok 10140, Thailand*

[c]*The Academy of Science, The Royal Institute of Thailand, SanamSueaPa, Dusit, Bangkok 10300, Thailand*

Received 12 January 2012; received in revised form 17 February 2013; accepted 19 February 2013
Available online 6 March 2013

Abstract

Fins are used in many extended heat exchangers. Occasionally, they are used in fully dry or fully wet surface conditions. However, if the dew point temperature is in the range of the fin base and fin tip temperatures, a partially wet surface condition is present. In this study, the partially wet fin efficiencies for the longitudinal fin of rectangular, triangular, concave parabolic, and convex parabolic profiles are presented. However, for each profile, there are two methods to derive the partially wet fin efficiency that depend on a set of boundary conditions. In addition, eight equations of fin efficiencies are investigated. According to the derivation, the fin efficiencies are the function of the length of the dry portion. Thus, the equations for calculating the length of the dry portion must also be presented. The results indicate that the fin with larger cross-section has a higher conduction heat transfer rate and more fin efficiency. Moreover, the partially wet fin efficiencies decrease with an increase in relative humidity. The equation for predicting the partially wet fin efficiency from fully wet and fully dry fin efficiencies is also presented.
© 2013 The Franklin Institute. Published by Elsevier Ltd. All rights reserved.

*Corresponding author at: Fluid Mechanics, Thermal Engineering and Multiphase Flow Research Lab. (FUTURE), Department of Mechanical Engineering, Faculty of Engineering, King Mongkut's University of Technology Thonburi, Bangmod, Bangkok 10140, Thailand. Tel.: +662 470 9115; fax: +662 470 9111.
E-mail address: somchai.won@kmutt.ac.th (S. Wongwises).

0016-0032/$32.00 © 2013 The Franklin Institute. Published by Elsevier Ltd. All rights reserved.
http://dx.doi.org/10.1016/j.jfranklin.2013.02.019

Author's personal copy

Nomenclature

b	distance from fin tip to fin base, m
$b'_{w,dp}$	slope of the saturated air enthalpy curve at the dew point temperature, J kg^{-1} K^{-1}
$b'_{w,f}$	slope of the saturated air enthalpy curve at the mean fin surface temperature, J kg^{-1} K^{-1}
$b'_{w,0}$	slope of the saturated air enthalpy curve at the fin base temperature, J kg^{-1} K^{-1}
$C_{p,a}$	air specific heat capacity, J kg^{-1} °C^{-1}
h_c	convection heat transfer coefficient, kg m^{-2} s^{-1}
i	air enthalpy, J kg^{-1}
$I_{-2/3}$	modified Bessel function solution of the first kind, order $-2/3$.
$I_{-1/3}$	modified Bessel function solution of the first kind, order $-1/3$.
I_0	modified Bessel function solution of the first kind, order 0.
$I_{1/3}$	modified Bessel function solution of the first kind, order 1/3.
$I_{2/3}$	modified Bessel function solution of the first kind, order 2/3.
I_1	modified Bessel function solution of the first kind, order 1.
k_f	thermal conductivity of the fin, W m^{-1} K^{-1}
k_w	thermal conductivity of the water film, W m^{-1} K^{-1}
K_0	modified Bessel function solution of the second kind, order 0
K_1	modified Bessel function solution of the second kind, order 1
RH	relative humidity
T	air temperature, °C
x	distance from fin tip, m
x_{dry}	distance from fin tip to saturation point, m
y_w	thickness of the water film, m
δ_0	thickness of fin base, m
γ	air enthalpy difference, J kg^{-1}
η	fin efficiency
θ	air temperature difference, °C

1. Introduction

Extended surfaces are routinely used in many heat exchangers. Fins can enhance the heat transfer rate because of the surface area increment and increased turbulence. To obtain better surface effectiveness, fin efficiency must be evaluated. Schmidt [1] and Kraus et al. [2] derived dry fin efficiency years ago. Subsequently, Arslanturk [3], Joneidi et al. [4], Kulkarni and Joglekar [5] presented methods for evaluating dry fin efficiency and studied the influence of fin thermal conductivity on fin efficiency. However, Arslanturk [3] used the Adomian decomposition method (ADM), which is different from the differential transformation method (DTM) used by Joneidi et al. [4] and the residue minimization technique (RMT) used by Kulkarni and Joglekar [5]. Moreover, Ganji [6], Jalaal et al. [7] and Jalaal and Ganji [8,9] studied He's homotopy perturbation method for nonlinear heat

Author's personal copy

transfer. From their results, it can be noted that variation of thermal conductivity with temperature has a strong influence on fin efficiency. By the analytical method, Torabi and Aziz [10] investigated the thermal performance of convective–radiative T-shaped fin with simultaneous variation of thermal conductivity, heat transfer coefficient and surface emissivity with temperature. Different from other fin studies, the sink temperatures for convection and radiation were assumed to be non-zero. Kundu and Barman [11] proposed

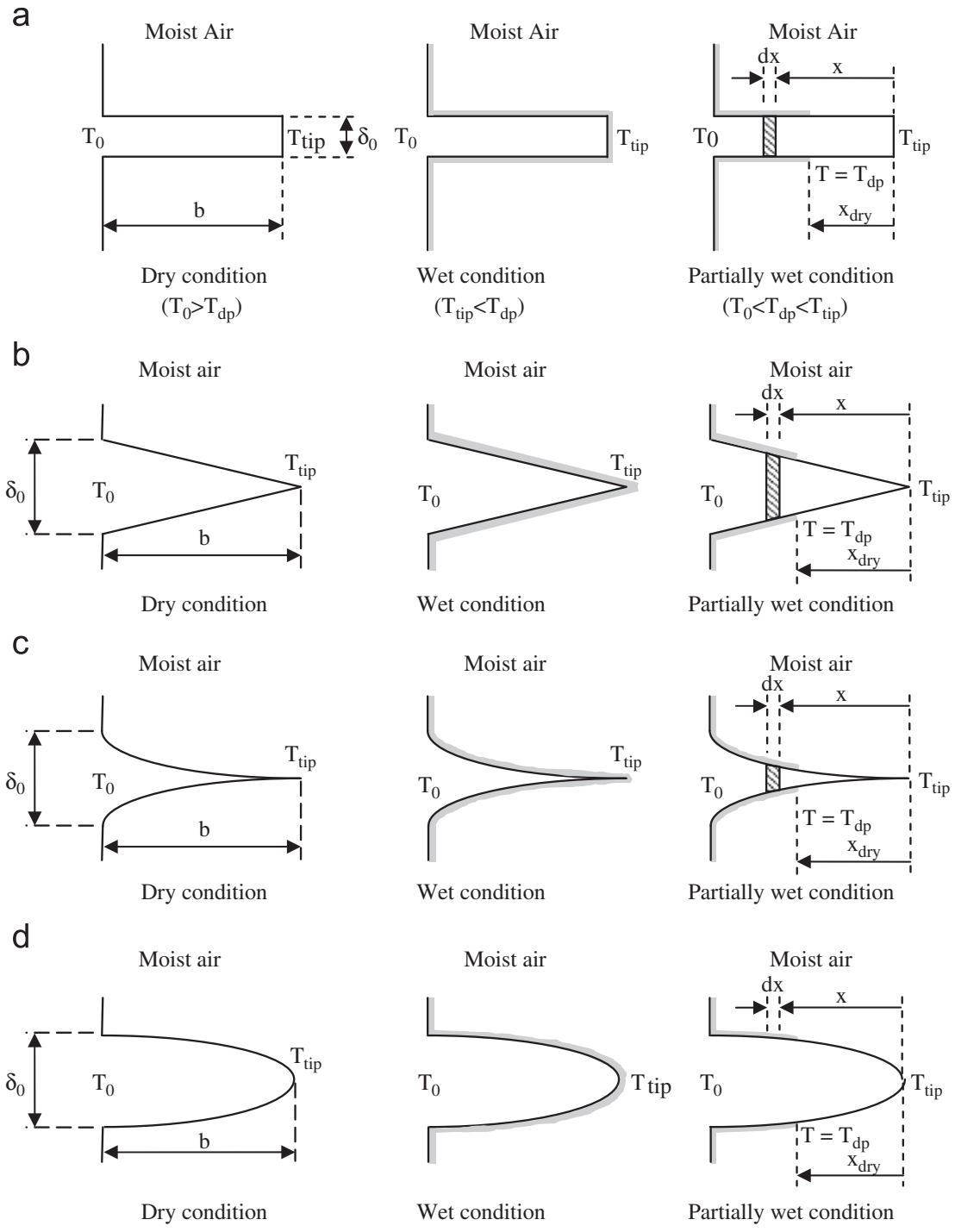

Fig. 1. Longitudinal fins of 4 profiles in full dry, fully wet and partially wet surface conditions. (a) Longitudinal fin of rectangular profile, (b) Longitudinal fin of triangular profile, (c) Longitudinal fin of concave parabolic profile and (d) Longitudinal fin of convex parabolic profile.

Author's personal copy

an analytical prediction to determine the performances and optimization of an annular fin assembly of trapezoidal profile under dehumidifying conditions.

However, in many applications of refrigeration, all fin surface temperatures are lower than the dew point temperatures. Then, the water vapor in air will condense on the fin surface. As a consequence, the fins are in wet conditions as shown in Fig. 1(a.2), (b.2), (c.2), and (d.2). In 1970, Threlkeld [12] presented the longitudinal fin efficiency in wet conditions based on the enthalpy potential method. Thus, using Threlkeld's method, wet fin efficiencies can be obtained; their forms are similar to dry fin efficiencies. Moreover, many researchers have studied extended heat exchangers in dehumidifying conditions and applied the wet fin efficiency in the reduction method. In 2000, Liang et al. [13] investigated the wet fin efficiency of a plate fin-and-tube heat exchanger. Using an equivalent circular area method, the fins were considered as circular fin. The researchers then studied three models: a one-dimensional analytical model, a one-dimensional numerical model, and a two-dimensional numerical model.

For many applications of refrigeration, the fin temperature generally decreases from the fin tip to fin base. The surface near fin tip is in dry condition but the other region may be wet due to condensation of the water vapor. Thus, the fins are in the partially wet surface conditions as shown in Fig. 1(a.3), (b.3), (c.3), and (d.3). Liang et al. [13] presented the method to determine the partially wet circular fin efficiency. However, according to their derivation, it is not the exact partially wet fin efficiency, it is an approximate value obtained from the dry fin efficiency weighted by area of dry surface and the wet fin efficiency weighted by area of wet surface. Pirompugd et al. [14] presented the circular fin efficiency in partially wet surface conditions using an analytical method. Moreover, they applied the fin efficiency to reduce the experimental data of plate fin-and-tube heat exchangers. Nevertheless, the extended surfaces in some applications are in partially wet surface conditions. The overall surface effectiveness must be a function of the partially wet fin efficiency. However, the available literature concerning fin efficiency is related to either fully dry conditions or completely wet surfaces. Thus, this research presents the partially wet fin efficiency for the longitudinal fin of rectangular, triangular, concave parabolic, and convex parabolic profiles.

2. Mathematical modeling

2.1. Dry and wet fin efficiency

In the past, the differential equations for heat transfer and their solutions for four longitudinal fins in dry conditions as shown in Fig. 1(a.1), (b.1), (c.1), and (d.1) were proposed by Schmidt [1] and Kraus et al. [2]:

$$\text{Rectangular profile: } \eta_{rect,dry} = \frac{\tanh mb}{mb} \tag{1}$$

$$\text{Triangular profile: } \eta_{tri,dry} = \frac{I_1(2mb)}{mbI_0(2mb)} \tag{2}$$

$$\text{Concave profile: } \eta_{ccave,dry} = \frac{2}{1+\sqrt{1+(2mb)^2}} \tag{3}$$

Author's personal copy

$$\text{Convex profile: } \eta_{cvex,dry} = \frac{I_{2/3}(4/3mb)}{mbI_{-1/3}(4/3mb)} \tag{4}$$

where

$$m = \sqrt{\frac{2h_c}{k_f\delta_0}} \tag{5}$$

However, Eqs. (1)–(4) are generally used for fins in dry conditions. For dehumidifying conditions, shown in Fig. 1(a.2), Threlkeld [12] presented the differential equation for temperature excess as shown in Eq. (6) and the wet fin efficiency as shown in Eq. (11) that accounts for the sensible and latent heat for the longitudinal fin of a rectangular profile. However, for the triangular, concave, and convex profiles shown in Fig. 1(b.2), (c.2), and (d.2), the differential equation of enthalpy excess can be shown as

$$\text{Rectangular profile: } \frac{d^2\gamma}{dx^2} - M_T\gamma = 0 \tag{6}$$

$$\text{Triangular profile: } \frac{d^2\gamma}{dx^2} + \frac{1}{x}\frac{d\gamma}{dx} - {M_T}^2\frac{b}{x}\gamma = 0 \tag{7}$$

$$\text{Concave profile: } \frac{d^2\gamma}{dv^2} + \frac{d\gamma}{dv} - {M_T}^2b^2\gamma = 0 \tag{8}$$

$$\text{Convex profile: } \frac{d^2\gamma}{dx^2} + \frac{1}{2x}\frac{d\gamma}{dx} - {M_T}^2\sqrt{\frac{b}{x}}\gamma = 0 \tag{9}$$

Subject to the boundary conditions of $d\gamma/dx|_{x=0} = 0$ and $\gamma|_{x=b} = \gamma_0$, where $\gamma_0 = i_0 - i_a$. Then, the enthalpy excess profiles and wet fin efficiency can be obtained as follows:

$$\text{Rectangular profile: } \gamma_{rect,wet} = \frac{\gamma_0 \cosh M_T x}{\cosh M_T b} \tag{10}$$

$$\eta_{rect,wet} = \frac{\tanh M_T b}{M_T b} \tag{11}$$

$$\text{Triangular profile: } \gamma_{tri,wet} = \frac{\gamma_0 I_0(2M_T\sqrt{bx})}{I_0(2M_T b)} \tag{12}$$

$$\eta_{tri,wet} = \frac{I_1(2M_T b)}{M_T b I_0(2M_T b)} \tag{13}$$

$$\text{Concave profile: } \gamma_{ccave,wet} = \gamma_0\left(\frac{x}{b}\right)^{-0.5+0.5(1+4{M_T}^2b^2)^{0.5}} \tag{14}$$

$$\eta_{ccave,wet} = \frac{2}{1+\sqrt{1+(2M_T b)^2}} \tag{15}$$

$$\text{Convex profile : } \gamma_{cvex,wet} = \gamma_0\left(\frac{x}{b}\right)^{0.25}\frac{I_{-1/3}(4/3M_T b^{0.25}x^{0.75})}{I_{-1/3}(4/3M_T b)} \tag{16}$$

Author's personal copy

$$\eta_{cvex,wet} = \frac{I_{2/3}(4/3M_T b)}{M_T b I_{-1/3}(4/3M_T b)} \tag{17}$$

where

$$M_T = \sqrt{\frac{2h_0}{k_f \delta_0}} \tag{18}$$

$$h_0 = \frac{1}{(C_{p,a}/b'_{w,f}h_c) + (y_w/k_w)} \tag{19}$$

2.2. Partially wet fin efficiency

However, the fin surface may not be in the fully dry or fully wet conditions. If the dew point temperature is higher than the fin base temperature but lower than the fin tip temperature, the water vapor in moist air condenses only onto the fin surface near the fin base region. There are two regions in a longitudinal fin: (1) the wet region between the fin base and the saturation point, and (2) the dry region between the saturation point and the fin tip, as shown in Fig. 1(a.3), (b.3), (c.3), and (d.3).The fin is in partially wet surface conditions.

Fig. 2 shows the heat transfer for the rectangular fin. The air with the dry bulb temperature of T_a, the dew point temperature of T_{dp}, and the convection heat transfer coefficient of h_c flows across the fin. The h_c depends on the air flow characteristics which the details can be found in many published literature. The fin thickness of δ_0 compared with fin length of b is very tiny. The base temperature of T_0 is lower than the dew point temperature of T_{dp} but the tip temperature is higher. The temperature increases from fin base to fin tip. Then, there are two conditions on the fin surface such as: the wet region near the base and the dry region near the tip. When the air flows across the fin, there is convection heat transfer on the fin surface. Only sensible heat transfer takes place on the

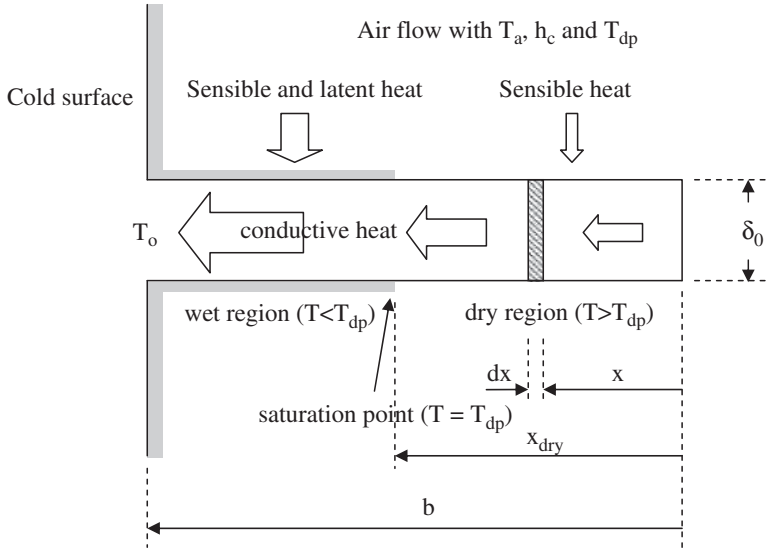

Fig. 2. Schematic diagram for heat transfer in partially wet fin.

Author's personal copy

dry surface. The heat conducts and increases from the fin tip to the saturation point. After this point, the surface temperature is lower than the dew point temperature. Then, the water vapor in air condenses on the fin surface. There is simultaneous sensible and latent heat transfer on the wet surface. The heat conducts and increases from the saturation point to the fin base. Thus, the heat transferred through the fin base is the total heat. From this phenomenon, the derivation of partially wet fin efficiency can be shown as follows.

For the dry fin portion ($0 \le x < x_{dry}$), neglecting the heat transfer through the fin tip and side surface, the differential equation in terms of temperature excess $\theta = T - T_a$ can be developed as follows:

$$\text{Rectangular profile: } \frac{d^2\theta}{dx^2} - m\theta = 0 \tag{20}$$

$$\text{Triangular profile: } \frac{d^2\theta}{dx^2} + \frac{1}{x}\frac{d\theta}{dx} - m^2\frac{b}{x}\theta = 0 \tag{21}$$

$$\text{Concave profile: } \frac{d^2\theta}{dv^2} + \frac{d\theta}{dv} - m^2b^2\theta = 0 \tag{22}$$

where $v = \ln x$

$$\text{Convex profile: } \frac{d^2\theta}{dx^2} + \frac{1}{2x}\frac{d\theta}{dx} - m^2\sqrt{\frac{b}{x}}\theta = 0 \tag{23}$$

For the derivation of general solutions, Eqs. (16)–(19) must be subjected to the following two boundary conditions:

The 1st boundary condition, for Eq. (20),

$$d\theta/dx|_{x=0} = 0 \tag{24}$$

for Eqs. (21)–(23), with unbounded condition at $x=0$, Kraus et al. [2] showed that a constant in solution must equal zero.

The 2nd boundary condition

$$\theta|_{x=x_{dry}} = \theta_{dp} \tag{25}$$

where $\theta_{dp} = T_{dp} - T_a$

The first boundary condition of Eq. (24) indicates that heat transfer rate through the fin tip is zero. This is exactly true for the tiny fin. The second boundary condition of Eq. (25) indicates that, at the saturation point ($x=x_{dry}$), the fin surface temperature is equal to the dew point temperature.

The solutions of Eqs. (20)–(23)in response to Eqs. (24) and (25) are

$$\text{Rectangular profile: } \theta_{rect,part} = \frac{\theta_{dp}\cosh mx}{\cosh mx_{dry}} \tag{26}$$

$$\text{Triangular profile: } \theta_{tri,part} = \frac{\theta_{dp}I_0(2m\sqrt{bx})}{I_0(2m\sqrt{bx_{dry}})} \tag{27}$$

$$\text{Concave profile: } \theta_{ccave,part} = \theta_{dp}\left(\frac{x}{x_{dry}}\right)^{-0.5+0.5(1+4m^2b^2)^{0.5}} \tag{28}$$

Author's personal copy

$$\text{Convex profile: } \theta_{cvex,part} = \theta_{dp}\left(\frac{x}{x_{dry}}\right)^{0.25}\frac{I_{-1/3}(4/3mb^{0.25}x^{0.75})}{I_{-1/3}(4/3mb^{0.25}x_{dry}^{0.75})} \tag{29}$$

For the wet portion ($x_{dry} \le x \le b$), the differential heat equations in terms of enthalpy excess ($\gamma = i - i_a$) for rectangular, triangular, concave, and convex profiles can be written as same as Eqs. (6), (7), (8) and (9), respectively. However, the boundary conditions are different. There are three boundary conditions

$$\left.\frac{d\gamma}{dx}\right|_{x=x_{dry}} = b'_{w,dp}\left.\frac{d\theta}{dx}\right|_{x=x_{dry}} \tag{30}$$

$$\gamma|_{x=x_{dry}} = \gamma_{dp} \tag{31}$$

$$\gamma|_{x=b} = \gamma_0 \tag{32}$$

where $\gamma_{dp} = i_{dp} - i_a$ and $\gamma_0 = i_0 - i_a$

The first boundary condition of Eq. (30) is given by considering the conduction heat transfer from the dry portion to the wet portion. The secondary condition of Eq. (31) is similar to that of Eq. (25). The enthalpy excess of saturated air at the saturation point equals that at the dew point. The last boundary condition of Eq. (32) describes the enthalpy excess at the fin base.

The general solutions of Eqs. (6)–(9) can be shown as follows:

$$\text{Rectangular profile: } \gamma_{rect,part} = C_1 e^{M_T x} + C_2 e^{-M_T x} \tag{33}$$

$$\text{Triangular profile: } \gamma_{tri,part} = C_1 I_0(2M_T\sqrt{bx}) + C_2 K_0(2M_T\sqrt{bx}) \tag{34}$$

$$\text{Concave profile: } \gamma_{ccave,part} = C_1 x^{-0.5+0.5(1+4M_T{}^2b^2)^{0.5}} + C_2 x^{-0.5-0.5(1+4M_T{}^2b^2)^{0.5}} \tag{35}$$

$$\text{Convex profile: } \gamma_{cvex,part} = x^{0.25}[C_1 I_{1/3}(4/3M_T b^{0.25}x^{0.75}) + C_2 I_{-1/3}(4/3M_T b^{0.25}x^{0.75})] \tag{36}$$

The constants of C_1 and C_2 in Eqs. (33)–(36) can be solved by two boundary conditions. There are two methods for finding the solutions. The first method can be performed using Eqs. (31) and (32) and the second method can be done using Eqs. (30) and (32).The fin efficiency can then be obtained. However, fin efficiency is still a function of x_{dry} and it is difficult to substitute the x_{dry} obtained from the remaining boundary condition in the fin efficiency equation. Thus, fin efficiency will be presented in terms of x_{dry} and x_{dry} can be obtained from the remaining boundary condition.

The 1st method with the first set of boundary conditions of Eqs. (31) and (32), and Eqs. (33)–(36) can be solved as follows:

$$\text{Rectangular profile: } \gamma_{rect1,part} = \frac{\gamma_0 e^{M_T b} - \gamma_{dp} e^{M_T x_{dry}}}{e^{2M_T b} - e^{2M_T x_{dry}}} e^{M_T x} + \frac{\gamma_{dp} e^{(M_T x_{dry} + 2M_T b)} - \gamma_0 e^{(2M_T x_{dry} + M_T b)}}{e^{2M_T b} - e^{2M_T x_{dry}}} e^{-M_T x} \tag{37}$$

Author's personal copy

Triangular profile: $\gamma_{tri1,part}$

$$=\frac{\gamma_0 K_0(2M_T\sqrt{bx_{dry}})-\gamma_{dp}K_0(2M_Tb)}{I_0(2M_Tb)K_0(2M_T\sqrt{bx_{dry}})-I_0(2M_T\sqrt{bx_{dry}})K_0(2M_Tb)}I_0(2M_T\sqrt{bx})$$
$$+\frac{\gamma_{dp}I_0(2M_Tb)-\gamma_0 I_0(2M_T\sqrt{bx_{dry}})}{I_0(2M_Tb)K_0(2M_T\sqrt{bx_{dry}})-I_0(2M_T\sqrt{bx_{dry}})K_0(2M_Tb)}K_0(2M_T\sqrt{bx}) \tag{38}$$

Concave profile: $\gamma_{ccave1,part}$

$$=\frac{\gamma_0 x_{dry}^{-0.5-0.5(1+4M_T{}^2b^2)^{0.5}}-\gamma_{dp}b^{-0.5-0.5(1+4M_T{}^2b^2)^{0.5}}}{x_{dry}^{-0.5-0.5(1+4M_T{}^2b^2)^{0.5}}b^{-0.5+0.5(1+4M_T{}^2b^2)^{0.5}}-x_{dry}^{-0.5+0.5(1+4M_T{}^2b^2)^{0.5}}b^{-0.5-0.5(1+4M_T{}^2b^2)^{0.5}}}x^{-0.5+0.5(1+4M_T{}^2b^2)^{0.5}}$$
$$+\frac{\gamma_{dp}b^{-0.5+0.5(1+4M_T{}^2b^2)^{0.5}}-\gamma_0 x_{dry}^{-0.5+0.5(1+4M_T{}^2b^2)^{0.5}}}{x_{dry}^{-0.5-0.5(1+4M_T{}^2b^2)^{0.5}}b^{-0.5+0.5(1+4M_T{}^2b^2)^{0.5}}-x_{dry}^{-0.5+0.5(1+4M_T{}^2b^2)^{0.5}}b^{-0.5-0.5(1+4M_T{}^2b^2)^{0.5}}}x^{-0.5-0.5(1+4M_T{}^2b^2)^{0.5}} \tag{39}$$

Convex profile: $\gamma_{cvex1,part}$

$$=\frac{\gamma_{dp}x_{dry}^{-0.25}I_{-1/3}(4/3M_Tb)-\gamma_0 b^{-0.25}I_{-1/3}(4/3M_Tb^{0.25}x_{dry}^{0.75})}{I_{-1/3}(4/3M_Tb)I_{1/3}(4/3M_Tb^{0.25}x_{dry}^{0.75})-I_{1/3}(4/3M_Tb)I_{-1/3}(4/3M_Tb^{0.25}x_{dry}^{0.75})}x^{0.25}I_{1/3}(4/3M_Tb^{0.25}x^{0.75})$$
$$+\frac{\gamma_0 b^{-0.25}I_{1/3}(4/3M_Tb^{0.25}x_{dry}^{0.75})-\gamma_{dp}x_{dry}^{-0.25}I_{1/3}(4/3M_Tb)}{I_{-1/3}(4/3M_Tb)I_{1/3}(4/3M_Tb^{0.25}x_{dry}^{0.75})-I_{1/3}(4/3M_Tb)I_{-1/3}(4/3M_Tb^{0.25}x_{dry}^{0.75})}x^{0.25}I_{-1/3}(4/3M_Tb^{0.25}x^{0.75}) \tag{40}$$

Then the fin efficiency can be evaluated by dividing the conduction heat transfer rate through the fin base by the convection heat transfer rate with the assumption that all fin surface temperatures and fin base temperatures are equal. Then

$$\eta_{part}=\frac{-(k_f\delta_0/b'_{w,0})d\gamma/dx|_{x=b}}{-2(h_c/C_{p,a})b\gamma_0} \tag{41}$$

By substituting Eqs. (37)–(40) into Eq.(41), the fin efficiency can be rewritten as follows:

Rectangular profile: $\eta_{rect1,part}=\dfrac{\gamma_0(e^{2M_Tx_{dry}}+e^{2M_Tb})-2\gamma_{dp}e^{M_T(x_{dry}+b)}}{M_Tb\gamma_0(e^{2M_Tb}-e^{2M_Tx_{dry}})}$ (42)

Triangular profile: $\eta_{tri1,part}$

$$=\frac{I_1(2M_Tb)\left[K_0(2M_T\sqrt{bx_{dry}})-\frac{\gamma_{dp}}{\gamma_0}K_0(2M_Tb)\right]+K_1(2M_Tb)\left[I_0(2M_T\sqrt{bx_{dry}})-\frac{\gamma_{dp}}{\gamma_0}I_0(2M_Tb)\right]}{M_Tb[I_0(2M_Tb)K_0(2M_T\sqrt{bx_{dry}})-I_0(2M_T\sqrt{bx_{dry}})K_0(2M_Tb)]} \tag{43}$$

Concave profile: $\eta_{ccave1,part}$

$$=\frac{(-0.5+0.5(1+4M_T{}^2b^2)^{0.5})b^{-1.5+0.5(1+4M_T{}^2b^2)^{0.5}}[\gamma_0 x_{dry}^{-0.5-0.5(1+4M_T{}^2b^2)^{0.5}}-\gamma_{dp}b^{-0.5-0.5(1+4M_T{}^2b^2)^{0.5}}]}{M_T{}^2b\gamma_0[x_{dry}^{-0.5-0.5(1+4M_T{}^2b^2)^{0.5}}b^{-0.5+0.5(1+4M_T{}^2b^2)^{0.5}}-x_{dry}^{-0.5+0.5(1+4M_T{}^2b^2)^{0.5}}b^{-0.5-0.5(1+4M_T{}^2b^2)^{0.5}}]}$$

Author's personal copy

$$+\frac{(-0.5-0.5(1+4M_T{}^2b^2)^{0.5})b^{-1.5-0.5(1+4M_T{}^2b^2)^{0.5}}[\gamma_{dp}b^{-0.5+0.5(1+4M_T{}^2b^2)^{0.5}}-\gamma_0 x_{dry}^{-0.5+0.5(1+4M_T{}^2b^2)^{0.5}}]}{M_T{}^2b\gamma_0[x_{dry}^{-0.5-0.5(1+4M_T{}^2b^2)^{0.5}}b^{-0.5+0.5(1+4M_T{}^2b^2)^{0.5}}-x_{dry}^{-0.5+0.5(1+4M_T{}^2b^2)^{0.5}}b^{-0.5-0.5(1+4M_T{}^2b^2)^{0.5}}]} \tag{44}$$

Convex profile:

$$\eta_{cvex1,part}=\frac{\left(\frac{x_{dry}}{b}\right)^{-0.25}\frac{\gamma_{dp}}{\gamma_0}\left[I_{-1/3}(\frac{4}{3}M_Tb)I_{-2/3}(\frac{4}{3}M_Tb)-I_{1/3}(\frac{4}{3}M_Tb)I_{2/3}(\frac{4}{3}M_Tb)\right]}{M_Tb\left[I_{-1/3}(\frac{4}{3}M_Tb)I_{1/3}(\frac{4}{3}M_Tb^{0.25}x_{dry}^{0.75})-I_{1/3}(\frac{4}{3}M_Tb)I_{-1/3}(\frac{4}{3}M_Tb^{0.25}x_{dry}^{0.75})\right]}$$
$$+\frac{\left[I_{1/3}(\frac{4}{3}M_Tb^{0.25}x_{dry}^{0.75})I_{2/3}(\frac{4}{3}M_Tb)-I_{-1/3}(\frac{4}{3}M_Tb^{0.25}x_{dry}^{0.75})I_{-2/3}(\frac{4}{3}M_Tb)\right]}{M_Tb\left[I_{-1/3}(\frac{4}{3}M_Tb)I_{1/3}(\frac{4}{3}M_Tb^{0.25}x_{dry}^{0.75})-I_{1/3}(\frac{4}{3}M_Tb)I_{-1/3}(\frac{4}{3}M_Tb^{0.25}x_{dry}^{0.75})\right]} \tag{45}$$

x_{dry} can be derived from the first boundary condition of Eq. (30). By substituting Eqs. (26)–(29) and (37)–(40) into Eq. (30), the relations can be shown in Eqs. (46)–(49) as follows:

$$\text{Rectangular profile: }\frac{2M_T\gamma_0e^{M_T(x_{dry}+b)}-M_T\gamma_{dp}(e^{2M_Tx_{dry}}+e^{2M_Tb})}{e^{2M_Tb}-e^{2M_Tx_{dry}}}$$
$$=mb'_{w,dp}\theta_{dp}\tanh(mx_{dry}) \tag{46}$$

$$\text{Triangular profile: }\frac{I_1(2M_T\sqrt{bx_{dry}})[\gamma_0K_0(2M_T\sqrt{bx_{dry}})-\gamma_{dp}K_0(2M_Tb)]+K_1(2M_T\sqrt{bx_{dry}})[\gamma_0I_0(2M_T\sqrt{bx_{dry}})-\gamma_{dp}I_0(2M_Tb)]}{I_0(2M_Tb)K_0(2M_T\sqrt{bx_{dry}})-I_0(2M_T\sqrt{bx_{dry}})K_0(2M_Tb)}$$
$$=m\frac{\sqrt{b}}{M_T\sqrt{x_{dry}}}b'_{w,dp}\theta_{dp}\frac{I_1(2m\sqrt{bx_{dry}})}{I_0(2m\sqrt{bx_{dry}})} \tag{47}$$

$$\text{Concave profile: }\frac{(-0.5+0.5(1+4M_T{}^2b^2)^{0.5})x_{dry}^{-1.5+0.5(1+4M_T{}^2b^2)^{0.5}}[\gamma_0x_{dry}^{-0.5-0.5(1+4M_T{}^2b^2)^{0.5}}-\gamma_{dp}b^{-0.5-0.5(1+4M_T{}^2b^2)^{0.5}}]}{x_{dry}^{-0.5-0.5(1+4M_T{}^2b^2)^{0.5}}b^{-0.5+0.5(1+4M_T{}^2b^2)^{0.5}}-x_{dry}^{-0.5+0.5(1+4M_T{}^2b^2)^{0.5}}b^{-0.5-0.5(1+4M_T{}^2b^2)^{0.5}}}$$
$$+\frac{(-0.5-0.5(1+4M_T{}^2b^2)^{0.5})x_{dry}^{-1.5-0.5(1+4M_T{}^2b^2)^{0.5}}[\gamma_{dp}b^{-0.5+0.5(1+4M_T{}^2b^2)^{0.5}}-\gamma_0x_{dry}^{-0.5+0.5(1+4M_T{}^2b^2)^{0.5}}]}{x_{dry}^{-0.5-0.5(1+4M_T{}^2b^2)^{0.5}}b^{-0.5+0.5(1+4M_T{}^2b^2)^{0.5}}-x_{dry}^{-0.5+0.5(1+4M_T{}^2b^2)^{0.5}}b^{-0.5-0.5(1+4M_T{}^2b^2)^{0.5}}}$$
$$=b'_{w,dp}\theta_{dp}\frac{-0.5+0.5(1+4m^2b^2)^{0.5}}{x_{dry}} \tag{48}$$

$$\text{Convex profile: }\frac{M_Tb^{0.25}[\gamma_{dp}x_{dry}^{-0.25}I_{-1/3}(4/3M_Tb)-\gamma_0b^{-0.25}I_{-1/3}(4/3M_Tb^{0.25}x_{dry}^{0.75})]I_{-2/3}(4/3M_Tb^{0.25}x_{dry}^{0.75})}{I_{-1/3}(4/3M_Tb)I_{1/3}(4/3M_Tb^{0.25}x_{dry}^{0.75})-I_{1/3}(4/3M_Tb)I_{-1/3}(4/3M_Tb^{0.25}x_{dry}^{0.75})}$$
$$+\frac{M_Tb^{0.25}[\gamma_0b^{-0.25}I_{1/3}(4/3M_Tb^{0.25}x_{dry}^{0.75})-\gamma_{dp}x_{dry}^{-0.25}I_{1/3}(4/3M_Tb)]I_{2/3}(4/3M_Tb^{0.25}x_{dry}^{0.75})}{I_{-1/3}(4/3M_Tb)I_{1/3}(4/3M_Tb^{0.25}x_{dry}^{0.75})-I_{1/3}(4/3M_Tb)I_{-1/3}(4/3M_Tb^{0.25}x_{dry}^{0.75})}$$
$$=mb'_{w,dp}\theta_{dp}\left(\frac{b}{x_{dry}}\right)^{0.25}\frac{I_{2/3}(4/3mb^{0.25}x_{dry}^{0.75}))}{I_{-1/3}(4/3mb^{0.25}x_{dry}^{0.75})} \tag{49}$$

However, the iterative calculation is needed to solve x_{dry}.

The 2nd method with the other set of boundary conditions of Eqs. (30) and (32), and Eqs. (33)–(36) can be solved as follows:

$$\text{Rectangular profile: }\gamma_{rect2,part}=\frac{M_T\gamma_0e^{-M_T(2x_{dry}+b)}+mb'_{w,dp}\theta_{dp}e^{-M_T(x_{dry}+2b)}\tanh(mx_{dry})}{M_T(e^{-2M_Tx_{dry}}+e^{-2M_Tb})}e^{M_Tx}$$
$$+\frac{M_T\gamma_0e^{-M_Tb}-mb'_{w,dp}\theta_{dp}e^{-M_Tx_{dry}}\tanh(mx_{dry})}{M_T(e^{-2M_Tx_{dry}}+e^{-2M_Tb})}e^{-M_Tx} \tag{50}$$

Author's personal copy

Triangular profile : $\gamma_{tri2,part}$

$$=\frac{b'_{w,dp}\theta_{dp}\frac{m}{M_T}(I_1(2m\sqrt{bx_{dry}})/I_0(2m\sqrt{bx_{dry}}))K_0(2M_Tb)+\gamma_0K_1(2M_T\sqrt{bx_{dry}})}{I_1(2M_T\sqrt{bx_{dry}})K_0(2M_Tb)+I_0(2M_Tb)K_1(2M_T\sqrt{bx_{dry}})}I_0(2M_T\sqrt{bx})$$

$$+\frac{\gamma_0I_1(2M_T\sqrt{bx_{dry}})-b'_{w,dp}\theta_{dp}\frac{m}{M_T}(I_1(2m\sqrt{bx_{dry}})/I_0(2m\sqrt{bx_{dry}}))I_0(2M_Tb)}{I_1(2M_T\sqrt{bx_{dry}})K_0(2M_Tb)+I_0(2M_Tb)K_1(2M_T\sqrt{bx_{dry}})}K_0(2M_T\sqrt{bx}) \tag{51}$$

Concave profile: $\gamma_{ccave2,part}=C_{1,ccave2}x^{-0.5+0.5(1+4M_T{}^2b^2)^{0.5}}+\dfrac{C_{2,ccave2}}{x^{0.5+0.5(1+4M_T{}^2b^2)^{0.5}}}$ (52)

where

$$C_{1,ccave2}=\frac{\gamma_0\left[(-0.5-0.5(1+4M_T{}^2b^2)^{0.5})x_{dry}^{-(1+4M_T{}^2b^2)^{0.5}}-(-0.5+0.5(1+4M_T{}^2b^2)^{0.5})b^{-(1+4M_T{}^2b^2)^{0.5}}\right]}{b^{-0.5+0.5(1+4M_T{}^2b^2)^{0.5}}\left[(-0.5-0.5(1+4M_T{}^2b^2)^{0.5})x_{dry}^{-(1+4M_T{}^2b^2)^{0.5}}-(-0.5+0.5(1+4M_T{}^2b^2)^{0.5})b^{-(1+4M_T{}^2b^2)^{0.5}}\right]}$$

$$-\frac{(-0.5+0.5(1+4M_T{}^2b^2)^{0.5})b^{-0.5-0.5(1+4M_T{}^2b^2)^{0.5}}\left[b'_{w,dp}\theta_{dp}\left(\frac{-0.5+0.5(1+4m^2b^2)^{0.5}}{-0.5+0.5(1+4M_T{}^2b^2)^{0.5}}\right)x_{dry}^{0.5-0.5(1+4M_T{}^2b^2)^{0.5}}-\gamma_0b^{0.5-0.5(1+4M_T{}^2b^2)^{0.5}}\right]}{b^{-0.5+0.5(1+4M_T{}^2b^2)^{0.5}}\left[(-0.5-0.5(1+4M_T{}^2b^2)^{0.5})x_{dry}^{-(1+4M_T{}^2b^2)^{0.5}}-(-0.5+0.5(1+4M_T{}^2b^2)^{0.5})b^{-(1+4M_T{}^2b^2)^{0.5}}\right]} \tag{53}$$

$$C_{2,ccave2}=\left[\frac{(-0.5+0.5(1+4M_T{}^2b^2)^{0.5})\left[b'_{w,dp}\theta_{dp}\left(\frac{-0.5+0.5(1+4m^2b^2)^{0.5}}{-0.5+0.5(1+4M_T{}^2b^2)^{0.5}}\right)x_{dry}^{0.5-0.5(1+4M_T{}^2b^2)^{0.5}}-\gamma_0b^{0.5-0.5(1+4M_T{}^2b^2)^{0.5}}\right]}{(-0.5-0.5(1+4M_T{}^2b^2)^{0.5})x_{dry}^{-(1+4M_T{}^2b^2)^{0.5}}-(-0.5+0.5(1+4M_T{}^2b^2)^{0.5})b^{-(1+4M_T{}^2b^2)^{0.5}}}\right] \tag{54}$$

Convex profile: $\gamma_{cvex2,part}=\dfrac{\gamma_0b^{-0.25}I_{2/3}(4/3M_Tb^{0.25}x_{dry}^{0.75})-b'_{w,dp}\theta_{dp}x_{dry}^{-0.25}m/M_T(I_{-1/3}(4/3M_Tb)/I_{-1/3}(4/3mb^{0.25}x_{dry}^{0.75}))I_{2/3}(4/3mb^{0.25}x_{dry}^{0.75})}{I_{1/3}(4/3M_Tb)I_{2/3}(4/3M_Tb^{0.25}x_{dry}^{0.75})-I_{-1/3}(4/3M_Tb)I_{-2/3}(4/3M_Tb^{0.25}x_{dry}^{0.75})}x^{0.25}I_{1/3}(4/3M_Tb^{0.25}x^{0.75})$

$$+\frac{b'_{w,dp}\theta_{dp}x_{dry}^{-0.25}m/M_T(I_{1/3}(4/3M_Tb)/I_{-1/3}(4/3mb^{0.25}x_{dry}^{0.75}))I_{2/3}(4/3mb^{0.25}x_{dry}^{0.75})-\gamma_0b^{-0.25}I_{-2/3}(4/3M_Tb^{0.25}x_{dry}^{0.75})}{I_{1/3}(4/3M_Tb)I_{2/3}(4/3M_Tb^{0.25}x_{dry}^{0.75})-I_{-1/3}(4/3M_Tb)I_{-2/3}(4/3M_Tb^{0.25}x_{dry}^{0.75})}x^{0.25}I_{-1/3}(4/3M_Tb^{0.25}x^{0.75}) \tag{55}$$

Then, the fin efficiency can be evaluated as in Eq. (41) as follows:

Rectangular profile: $\eta_{rect2,part}=\dfrac{M_T\gamma_0(e^{-2M_Tx_{dry}}-e^{-2M_Tb})+2mb'_{w,dp}\theta_{dp}\tanh(mx_{dry})e^{-M_T(x_{dry}+b)}}{M_T{}^2b\gamma_0(e^{-2M_Tx_{dry}}+e^{-2M_Tb})}$ (56)

Author's personal copy

$$\text{Triangular profile: } \eta_{tri2,part} = b'_{w,dp}\theta_{dp}\frac{m}{M_T}\frac{\left[I_1(2M_Tb)K_0(2M_Tb)\frac{I_1\left(2m\sqrt{bx_{dry}}\right)}{I_0\left(2m\sqrt{bx_{dry}}\right)} + I_0(2M_Tb)K_1(2M_Tb)\frac{I_1\left(2m\sqrt{bx_{dry}}\right)}{I_0\left(2m\sqrt{bx_{dry}}\right)}\right]}{M_Tb\gamma_0\left[I_1\left(2M_T\sqrt{bx_{dry}}\right)K_0(2M_Tb) + I_0(2M_Tb)K_1\left(2M_T\sqrt{bx_{dry}}\right)\right]}$$

$$+\frac{\gamma_0\left[I_1(2M_Tb)K_1(2M_T\sqrt{bx_{dry}}) - I_1(2M_T\sqrt{bx_{dry}})K_1(2M_Tb)\right]}{M_Tb\gamma_0\left[I_1(2M_T\sqrt{bx_{dry}})K_0(2M_Tb) + I_0(2M_Tb)K_1(2M_T\sqrt{bx_{dry}})\right]} \tag{57}$$

$$\text{Concaveprofile: } \eta_{ccave2,part} = \frac{(-0.5+0.5(1+4{M_T}^2b^2)^{0.5})C_{1,cave2}b^{-1.5+0.5(1+4{M_T}^2b^2)^{0.5}} + (-0.5-0.5(1+4{M_T}^2b^2)^{0.5})C_{2,cave2}b^{-1.5-0.5(1+4{M_T}^2b^2)^{0.5}}}{{M_T}^2b\gamma_0} \tag{58}$$

$$\text{Convexprofile: } \eta_{ccvex2,part} = \frac{[I_{-2/3}(\frac{4}{3}M_Tb)I_{2/3}(\frac{4}{3}M_Tb^{0.25}x_{dry}^{0.75}) - I_{2/3}(\frac{4}{3}M_Tb)I_{-2/3}(\frac{4}{3}M_Tb^{0.25}x_{dry}^{0.75})]}{\mathrm{M_T b}\left[I_{1/3}(\frac{4}{3}M_Tb)I_{2/3}(\frac{4}{3}M_Tb^{0.25}x_{dry}^{0.75}) - I_{-1/3}(\frac{4}{3}M_Tb)I_{-2/3}(\frac{4}{3}M_Tb^{0.25}x_{dry}^{0.75})\right]}$$

$$+\frac{b'_{w,dp}\frac{m}{M_T}\left(\frac{b}{x_{dry}}\right)^{0.25}\frac{\theta_{dp}}{\gamma_0}\times\left[\frac{I_{1/3}(\frac{4}{3}M_Tb)}{I_{-1/3}(\frac{4}{3}mb^{0.25}x_{dry}^{0.75})}I_{2/3}(\frac{4}{3}mb^{0.25}x_{dry}^{0.75})I_{2/3}(\frac{4}{3}M_Tb) - \frac{I_{-1/3}(\frac{4}{3}M_Tb)}{I_{-1/3}(\frac{4}{3}mb^{0.25}x_{dry}^{0.75})}I_{2/3}(\frac{4}{3}mb^{0.25}x_{dry}^{0.75})I_{-2/3}(\frac{4}{3}M_Tb)\right]}{\mathrm{M_T b}\left[I_{1/3}(\frac{4}{3}M_Tb)I_{2/3}(\frac{4}{3}M_Tb^{0.25}x_{dry}^{0.75}) - I_{-1/3}(\frac{4}{3}M_Tb)I_{-2/3}(\frac{4}{3}M_Tb^{0.25}x_{dry}^{0.75})\right]} \tag{59}$$

Author's personal copy

To evaluate x_{dry}, the second boundary condition of Eq. (31) is continued. $\gamma|_{x=x_{dry}}$ can be calculated from Eqs. (50)–(52) and (55) and γ_{dp} is known. Using the iteration procedure, x_{dry} can then be calculated.

3. Results and discussion

The proposed partially wet fin efficiency is solved by the analytical method. Then, its solution is exacted. However, the verification is done by comparing with the fully dry fin efficiency and fully wet fin efficiency. For dry conditions, as shown in Eqs. (1)–(4), the fin efficiencies for 4 longitudinal fins are dependent on the variable of *mb*. Schmidt [1] and Kraus et al. [2] showed the graphs of η plotted against *mb* for dry conditions; they are also shown in Fig. 3. According to the results, the fin efficiencies decrease with the increase of *mb*. According to the results, the fin efficiencies decrease with the increase of *mb*. This can be explained that high M_T gives high velocity or high turbulence or low conduction rate. Then, at high M_T, the convection performance increases (or constant) but the conduction performance does not increase (or decrease). Thus, the fin efficiency (rate of actual conduction per rate of ideal convection) decreases. At the same *mb*, the fin efficiency can be sorted from highest value to lowest value into the following categories: rectangular profile, convex parabolic, triangular, and concave parabolic. This can be described that the fin with large cross sectional area gives high conduction heat transfer rate and high fin efficiency. However, it is noted that the surface area for convection heat transfer also affects the fin efficiency. This effect is conspicuous for the spine fin. In case of longitudinal fin (constant cross sectional area in the *z*-direction), it is dominated by the conduction effect. For fully wet conditions, as shown in Eqs. (11), (13), (15), and (17), the fin efficiencies are dependent only on M_Tb. Fig. 3 shows that the trends of results are similar in dry conditions, but all values are lower. This is because the ratio of latent heat transfer in wet condition affects the decrease of fin efficiency. For the wet condition, the ideal rate of latent heat in wet condition is higher than the actual latent heat rate. Then, the fin efficiency (actual rate per ideal rate) decreases with increasing latent heat transfer. However, while the fully wet fin efficiency obtained from the Threlkeld method [12] is

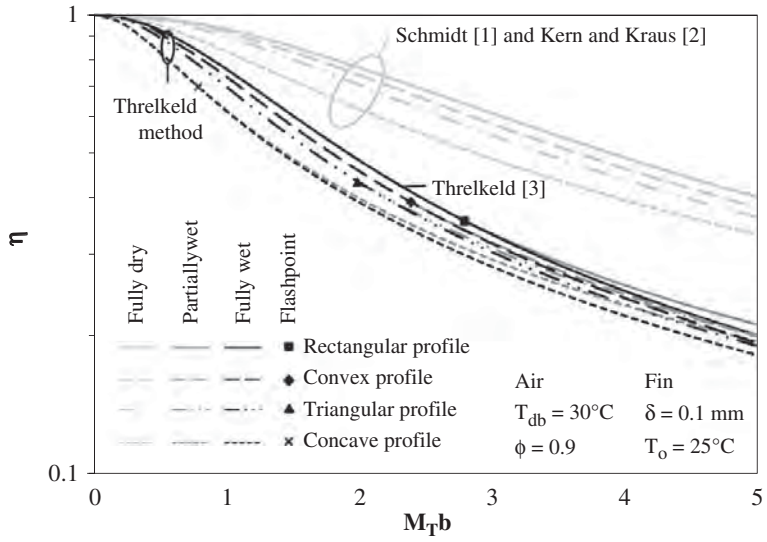

Fig. 3. Fin efficiency plotted against M_Tb.

Author's personal copy

based on enthalpy potential, McQuiston [15] presented the wet fin efficiency based on temperature difference. There are some ambiguities in the determination of wet fin efficiency. Webb and Kim [16] believed that McQuiston's approach was incorrect. A detailed discussion about this difference can be found by Lin et al. [17]. For partially wet conditions as shown in Fig. 3, the fin efficiencies (also constants of C_1 and C_2) determined by Eqs. (42)–(45) for the first method are equal to the fin efficiencies determined by Eqs. (56)–(59) for the second method, respectively. The fin efficiencies are not dependent only on $M_T b$, but they are more complicated than those that exist in dry and wet conditions. However, Fig. 3 shows the partially wet fin efficiencies plotted against $M_T b$ at 90% RH. According to the graphs, at low $M_T b$, the vanished lines before the saturation point occur because of fully wet conditions. Moreover, one can see that the partially wet fin efficiencies are between the dry and wet fin efficiencies. With higher RH, the partially wet fin efficiency and fully wet fin efficiency lines are proximate. Contrarily, the proximity of partially wet fin efficiency and fully dry fin efficiency lines occurs at low RH. This can be described by the latent heat transfer that depends on the relative humidity. However, the partially wet fin efficiency still decreases with the increase of $M_T b$, and the results of sorting are the same as those in dry and wet conditions.

Fig. 4 shows the fin efficiency for the rectangular profile. The modified fin efficiency in dry conditions is calculated by dividing the actual heat transfer rate in dry conditions by the ideal heat transfer rate in wet conditions. The divisors in fully wet and fully dry fin efficiencies are the same. Moreover, assuming that all wet surface temperatures are equal to the fin base temperature, the partially wet fin efficiency line (case 1) will continue from the fully wet fin efficiency line at the saturation point to the modified fully dry fin efficiency line. On the contrary, with distinguishing the ideal heat transfer rate into two regions (dry and wet regions), the partially wet fin efficiency (case 2) will continue from the saturation point to the fully dry fin efficiency line. It must be noted that Cases 1 and 2 are the ideal cases for studying but it does not mean the first and second methods. These lines are not useful in application, but some phenomena of heat transfer can be clearly described. The temperature distribution along the distance from the fin base is plotted in Fig. 5. According to the graph, the slope at the fin base and the position of the saturation point can be

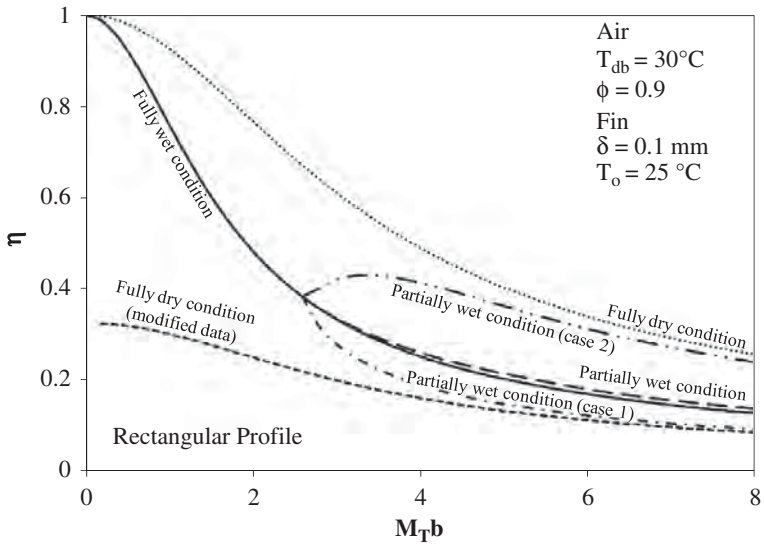

Fig. 4. Fin efficiency for rectangular profile plotted against $M_T b$.

Author's personal copy

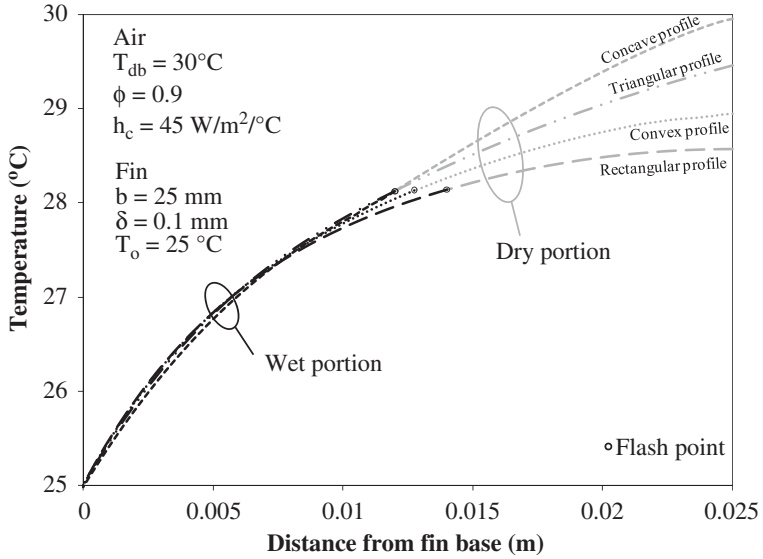

Fig. 5. Temperature distribution for 4 longitudinal fins.

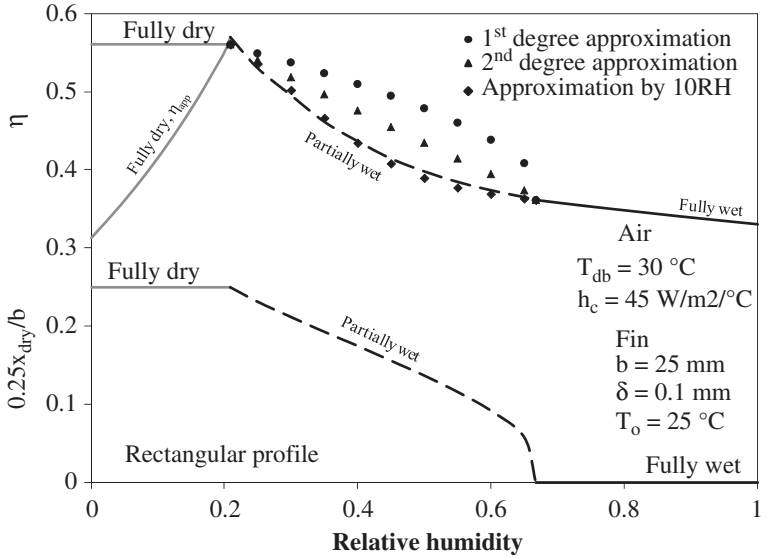

Fig. 6. Rectangular fin efficiency plotted against relative humidity.

considered for the performance of heat transfer. In the same condition, the steep line at the fin base with the saturation point near the fin tip promotes good heat transfer. This can be described by the conduction of heat transfer at the fin base as shown in Eq. (41). Moreover, with the saturation point near the fin tip, more condensation takes place, which allows for more heat transfer. However, one can see that the heat transfer phenomena in the dry portion are opposite to those in wet portion. Considering the heat transfer from fin tip to fin base, it can be described that although the heat transfer rate in dry region for fin with high cross sectional area is higher, the temperature distribution is not steep due to the effect of variation on cross sectional area along the fin. The increase of cross sectional area of fin causes the heat dispersion to increase and temperature to decrease. It should be noted that the fin with rectangular profile gives the least slope. Figs. 6–9 show η and $0.25x_{dry}/b$ plotted against the relative humidity. The lines of partially wet and fully wet conditions are continuous, but there is a break between the lines of fully dry and partially

Author's personal copy

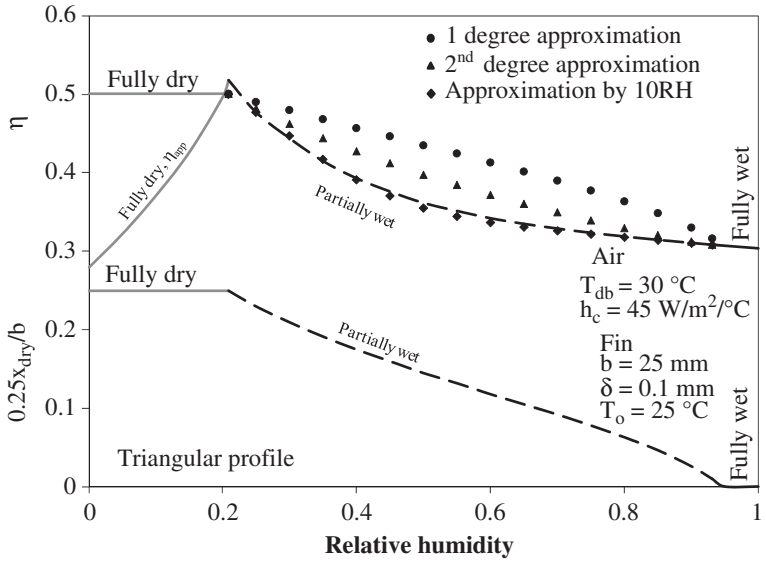

Fig. 7. Triangular fin efficiency plotted against relative humidity.

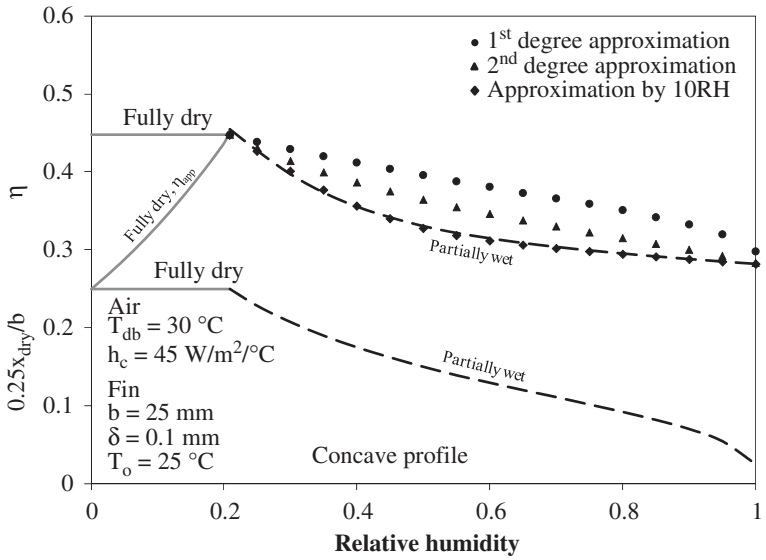

Fig. 8. Concave fin efficiency plotted against relative humidity.

wet conditions. This can be described by saying that the divisor in the fin efficiency in fully dry conditions is different from those in partially wet and fully wet conditions. The η_{app} for fully dry conditions is calculated by dividing the actual heat transfer rate at the fin base by the heat transfer rate obtained by assuming that all fin surface temperatures are equal to the dew point temperature. One can see that the η_{app} increases with an increase in relative humidity. This is different from the real fin efficiency in dry conditions that is independent of relative humidity. For partially wet and fully wet conditions, the fin efficiencies decrease with increasing relative humidity because the increase in the ideal or maximum heat transfer rate is higher than the increase in the actual heat transfer rate. These results agree with the results of a circular fin in partially wet and fully wet conditions determined by Pirompugd et al. [14]. Rosario and Rahman [18] presented an equation to determine the partially wet fin efficiency for a circular fin. That equation is the 2nd degree polynomial and is a function of dry portion length per total length of fin. However, for the longitudinal

Author's personal copy

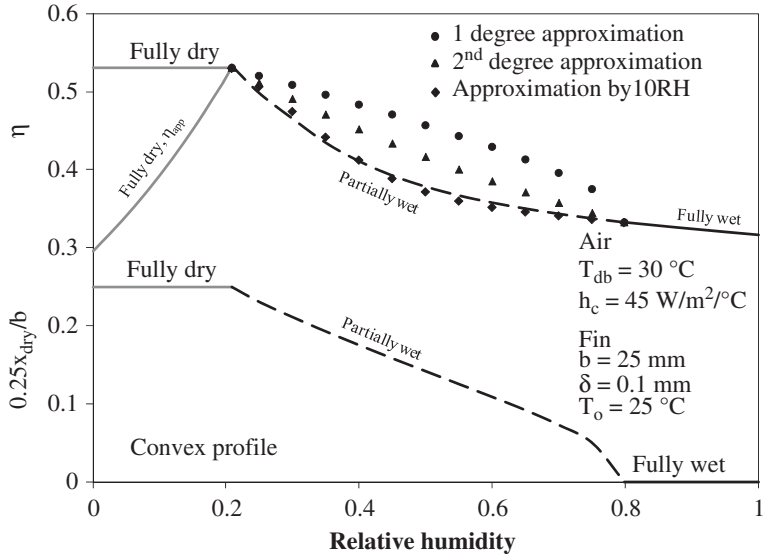

Fig. 9. Convex fin efficiency plotted against relative humidity.

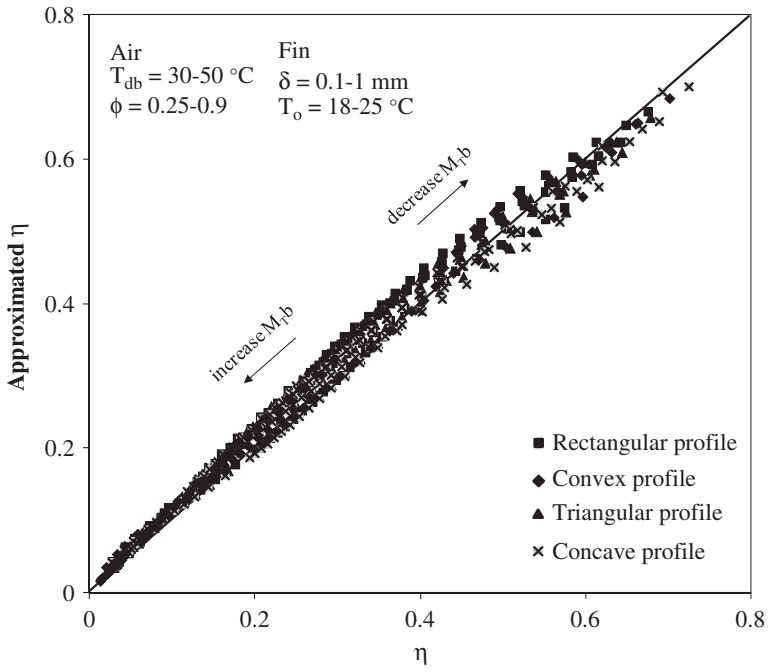

Fig. 10. Comparison of approximate η and η at many $M_T b$.

fin as shown in Figs. 5–8, the 1st or 2nd degree polynomial approximation cannot precisely predict the partially wet fin efficiency. Although some polynomials can provide a good prediction in some conditions, poor results will occur in the other conditions of $M_T b$. The new approximation for the longitudinal fin in partially wet conditions is presented as follows:

$$\eta_{part} = \left(\frac{x_{dry}}{b}\right)^{10\ \mathrm{RH}} \eta_{dry} + \left[1-(x_{dry}/b)^{10\ \mathrm{RH}}\right]\eta_{wet} \tag{60}$$

As seen in Figs. 6–9, the results from Eq. (60) agree with the theoretical data. Moreover, Fig. 10 shows a comparison with the other conditions. According to the figure, at $\eta \geq 0.3$,

Author's personal copy

and at $0.1 \leq \eta \leq 0.3$, almost all the measured data fall within $\pm 10\%$ and $\pm 20\%$ of those obtained from Eq. (60), respectively. However, the error over $\pm 50\%$ may take place with $\eta \leq 0.1$.Therefore, Eq. (60) can be applied only to the extended surface of $\eta \geq 0.3$. The methods for evaluating x_{dry} have been described in the 1st and 2nd method for partially wet surface conditions. However, Eq. (60) is not necessary because this study has proposed the theoretically partially wet fin efficiency.

4. Conclusions

Using 2 methods of grouping boundary conditions, the partially wet fin efficiencies for the longitudinal fin of rectangular, triangular, concave, and convex profiles are presented. Equations for evaluating the length of the dry portion are also proposed.

The order of high fin efficiency can be sorted as follows: (1) rectangular fin, (2) convex fin, (3) triangular fin, and (4) concave fin. The fin with the larger cross-section area has a higher heat transfer rate.

The dry fin efficiencies are independent of the relative humidity. Contrarily, with an increase of relative humidity, the partially wet fin efficiencies decrease rapidly, but the decrease of fully wet fin efficiencies is slower.

Conveniently, the equation for predicting the partially wet fin efficiency from the fully wet and fully dry fin efficiencies is also presented. The methods for obtaining the length of the dry portion are also described.

Acknowledgments

The authors are indebted to the Thailand Research Fund, the Office of the Higher Education Commission and the National Research University Project for supporting this study. The authors would like to thank Mr. Pornthep Panya, Mr. Pichayapol Khandee, and Mr. Sirichai Pakare for the result verification of 1st method of rectangular and triangular profiles.

References

[1] T.E. Schmidt, Heat transfer calculations for extended surfaces, Refrigeration Engineering 49 (1949) 351–357.
[2] A.D. Kraus, A. Aziz, J.R. Welty, Extended Surface Heat Transfer, John Wiley, New York, 2001.
[3] C. Arslanturk, A decomposition method for fin efficiency of convective straight fins with temperature-dependent thermal conductivity, International Journal of Heat and Mass Transfer 32 (2005) 831–841.
[4] A.A. Joneidi, D.D. Ganji, M. Babaelahi, Differential transformation method to determine fin efficiency of convective straight fins with temperature dependent thermal conductivity, International Communications in Heat and Mass Transfer 36 (2009) 757–762.
[5] D.B. Kulkarni, M.M. Joglekar, Residue minimization technique to analyze the efficiency of convective straight fins having temperature-dependent thermal conductivity, Applied Mathematics and Computation 215 (2009) 2184–2191.
[6] D.D. Ganji, The application of He's homotopy perturbation method to nonlinear equations arising in heat transfer, Physics Letters A 355 (2006) 337–341.
[7] M. Jalaal, D.D. Ganji, G. Ahmadi, Analytical investigation on acceleration motion of a vertically fallingspherical particle in incompressible Newtonian media, Advanced Powder Technology 21 (2010) 298–304.

Author's personal copy

[8] M. Jalaal, D.D. Ganji, On unsteady rolling motion of spheres in inclined tubes filled withincompressible Newtonian fluids, Advanced Powder Technology 22 (2011) 58–67.
[9] M. Jalaal, D.D. Ganji, An analytical study on motion of a sphere rolling down an inclined plane submergedin a Newtonian fluid, Powder Technology 198 (2010) 82–92.
[10] M. Torabi, A. Aziz, Thermal performance and efficiency of convective–radiative T-shaped fins with temperature dependent thermal conductivity, heat transfer coefficient and surface emissivity, International Communications in Heat and Mass Transfer 39 (2012) 1018–1029.
[11] B. Kundu, D. Barman, An analytical prediction for performance and optimization of an annular fin assembly of trapezoidal profile under dehumidifying conditions, Energy 36 (2011) 2572–2588.
[12] J.L. Threlkeld, Thermal Environmental Engineering, Prentice-Hall, Inc., New York, NY, 1970.
[13] S.Y. Liang, T.N. Wong, G.K. Nathan, Comparison of one-dimensional and two-dimensional models for wet-surface fin efficiency of a plate-fin-tube heat exchanger, Applied Thermal Engineering 20 (2000) 941–962.
[14] W. Pirompugd, C.C. Wang, S. Wongwises, Finite circular fin method for heat and mass transfer characteristics for plain fin-and-tube heat exchangers under fully and partially wet surface conditions, International Journal Heat Mass Transfer 50 (3–4) (2007) 552–565.
[15] F.C. McQuiston, Fin efficiency with combined heat and masstransfer, ASHRAE Transactions Part 1 81 (1975) 350–355.
[16] R.L. Webb, N.H. Kim, Principles of Enhanced Heat Transfer, second edition, Taylor & Francis, New York, 2005, p. 197.
[17] Y.T. Lin, K.C. Hsu, Y.J. Chang, C.C. Wang, Performance of rectangular fin in wet conditions: visualization and wet fin efficiency, ASME Journal of Heat Transfer 123 (2001) 836–927.
[18] L. Rosario, M.M. Rahman, Analysis of heat transfer in a partially wet radial fin assembly during dehumidification, International Journal of Heat and Fluid Flow 20 (1999) 642–648.

International Journal of Heat and Mass Transfer 64 (2013) 671–679

Contents lists available at SciVerse ScienceDirect

International Journal of Heat and Mass Transfer

journal homepage: www.elsevier.com/locate/ijhmt

Technical Note

Irreversibility analysis of a vertical annulus using TiO_2/water nanofluid with MHD flow effects

Omid Mahian [a,*], Ioan Pop [b], Ahmet Z. Sahin [c], Hakan F. Oztop [d], Somchai Wongwises [e]

[a] Young Researchers Club and elites, Mashhad Branch, Islamic Azad University, Mashhad, Iran
[b] Department of Mathematics, Babeş-Bolyai University, 400084 Cluj-Napoca, Romania
[c] Mechanical Engineering Department, King Fahd University of Petroleum & Minerals, Dhahran, Saudi Arabia
[d] Department of Mechanical Engineering, Technology Faculty, Fırat University, Elazig, Turkey
[e] Fluid Mechanics, Thermal Engineering and Multiphase Flow Research Lab (FUTURE), Department of Mechanical Engineering, Faculty of Engineering, King Mongkut's University of Technology Thonburi, Bangmod, Bangkok 10140, Thailand

ARTICLE INFO

Article history:
Received 15 March 2013
Received in revised form 30 April 2013
Accepted 2 May 2013

Keywords:
Nanofluid
Entropy generation
Vertical annulus
MHD flow
Analytical solution

ABSTRACT

In this paper, an analytical study of the second law of thermodynamics is performed for the flow and heat transfer of TiO_2/water nanofluid in a vertical annulus with isoflux walls and under the influence of magnetohydrodynamic (MHD) field. The governing equations in cylindrical coordinates are written and then simplified with reasonable assumptions. The simplified equations are solved analytically to obtain expressions for the velocity, temperature, and entropy generation distributions. The results are presented for different values of nanofluid volume fractions $\phi(0\% \leqslant \phi \leqslant 2\%)$, Hartmann number M and the flow parameter Gr/Re. To calculate the thermal conductivity and viscosity of TiO_2/water nanofluid, relations based on experimental data are used. Finally, using the well-known theoretical models for the thermal conductivity and viscosity, the effects of Hartmann number on the results are investigated.

© 2013 Elsevier Ltd. All rights reserved.

1. Introduction

Thermal conductivity enhancement of common base fluids such as water, oil, and ethylene glycol could be helpful to have a higher thermal efficiency and more compact thermal systems. Adding solid particles with very small sizes (in the order of a nanometer) to the base fluid is one of the solutions to enhance the thermal conductivity. Choi [1] is the first person that used the term "nanofluid" to refer to a fluid in which very fine particles (1–100 nm) are suspended. During recent years, many researches have been made on the applications of nanofluids. For instance, the readers can refer to some research and review articles, and textbooks [2–11].

Using the first law of thermodynamics for nanofluids the rate of enhancement of heat transfer is determined. However, for optimizing the performance of a system where a nanofluid is the working fluid, the second law of thermodynamics (entropy generation analysis) should be applied. Entropy generation can be used to establish criteria for the performance of thermal engineering systems [12]. Lower entropy generation in a thermal system means lower energy dissipation. Bejan [13,14] is the most famous researcher in this field that focused on the different factors behind the entropy generation in thermal engineering systems. Next, many researchers investigated the entropy generation in different systems.

Recently, Oztop and Al-Salem [15] reviewed the entropy generation for natural and mixed convection heat transfer for energy systems and Herwig [16] investigated the role of entropy generation in momentum and heat transfer.

A review of the literature shows that little has been reported on the entropy generation in the thermal systems where the working fluid is a nanofluid. Here, the former works regarding the entropy generation due to flow and heat transfer of nanofluids are briefly mentioned.

Singh et al. [17] theoretically studied the entropy generation in different regimes within channels (with different sizes) including microchannels, minichannels and conventional channels using water–alumina nanofluids. They concluded that, using the water–alumina nanofluid with high viscosity in microchannels with laminar flow as well as in minichannels and conventional channels with turbulent flow is not beneficial.

Li and Kleinstreuer [18] found that, using nanofluids (water–CuO nanofluids) with very low particle loading in trapezoidal microchannels, reduces the entropy generation at low Reynolds numbers.

Feng and Kleinstreuer [19] also studied the flow of an alumina–water nanofluid with heat transfer in a parallel disk system. They revealed that, the total entropy generation rate decreases with increases of volume fraction of nanofluids.

Moghaddami et al. [20] analytically investigated the entropy production due to water–Al_2O_3 and ethylene glycol–Al_2O_3

* Corresponding author.
E-mail address: Omid.mahian@gmail.com (O. Mahian).

0017-9310/$ - see front matter © 2013 Elsevier Ltd. All rights reserved.
http://dx.doi.org/10.1016/j.ijheatmasstransfer.2013.05.001

Nomenclature

Be	Bejan number
Br	Brinkman number
B_0	constant magnetic flux density (Wb)
C	constant of integration in energy equation
D_m	difference between theoretical and experimental results (%)
E	electric field (V/m)
g	constant of gravity (m^2/s)
Gr	Grashof number
$H^2 = (\frac{\mu_f}{\mu_{nf}})M^2J$	electric current (A)
k	thermal conductivity (W/m k)
N_F	entropy generation number, fluid friction
N_H	entropy generation number, heat transfer
N_m	entropy generation number, MHD flow
N_S	entropy generation number, total
M	Hartmann number
P	pressure (Pa)
P^*	dimensionless pressure
q	heat flux (W/m^2)
Q	electric charge density (Coulomb)
r	radius (m)
R	dimensionless radius
U	dimensionless velocity
U_0	velocity inlet (m/s)
$\dot{S}'''_{gen}$	entropy generation rate (W/m^3 K)
T	temperature (C)
T_0	intel temperature (C)
z	axial distance (m)
Z	dimensionless axial distance

Greek symbols

Γ_n	constants, $n = 1, 2, \ldots$
μ	dynamic viscosity (Pa S)
ρ	density (kg/m^3)
υ	kinematic viscosity (m^2/s)
β_f	thermal expansion coefficient of base fluid (1/K)
λ	radius ratio (r_i/r_o)
γ	the ratio of the nanolayer thickness to the original particle radius (=0.1)
Π	radius ratio, (r_o/r_i)
θ	dimensionless temperature
Ω	dimensionless temperature difference
Φ	viscous dissipation
ϕ	volume fraction of nanoparticles
$\forall$	volume (m^3)

Subscripts

ave	average value
i	value at the inner cylinder
o	value at the outer cylinder
f	base fluid
nf	nanofluid
p	nanoparticles
r	ratio of nanofluid property to base fluid property
0	value at the inlet

nanofluids flow inside a pipe under constant heat flux for both laminar and turbulent regimes. They found that an increase in the volume fraction of nanofluids is effective only when the irreversibility caused by heat transfer is dominant. Shahi et al. [21] investigated the effects of Rayleigh number, nanoparticles concentration, and the position of heat source on entropy generation in a cavity filled with water–Cu nanofluid.

Esmaeilpour and Abdollahzadeh [22] investigated the entropy generation due to natural convection in a two-dimensional wavy enclosure using Cu–water nanofluids.

Bianco et al. [23] provided an analysis of turbulent forced convection flow of water–Al_2O_3 nanofluids inside a square tube with constant and uniform wall heat flux. They determined the optimum Reynolds number by using an analytical method at which the entropy generation is the smallest.

Mah et al. [24] reported the viscous dissipation effects on the entropy generation in laminar fully developed forced convection of water–alumina nanofluid in circular microchannels.

Shalchi-Tabrizi and Seyf [25] investigated numerically the effects of Al_2O_3–water nanofluids with different volume fractions and particle diameters on the entropy generation for a tangential micro-heat sink (TMHS).

Mahian et al. [26] analytically investigated the entropy generation between two isoflux rotating cylinders using nanofluids with different volume fractions. Mahian et al. [27], studied the effects of uncertainties in the thermophysical models presented for nanofluids on entropy generation. Later on, Mahian et al. [28] investigated the effects of MHD flow on entropy generation due to nanofluid forced convection flow between two rotating cylinders. Recently, Sarkar et al. [29] studied the entropy generation due to mixed convection flow of a nanofluid past a square barrier in a vertical channel.

A review of the literature shows that there is no analytical study on the effects of nanofluids and MHD flow on entropy generation in a vertical annulus with mixed convection. Mixed convection inside a vertical annulus (with or without MHD flow) has many practical applications. Some applications are found in industrial heat exchangers, microelectronic devices, cooling of nuclear reactors, petroleum equipment, and so forth [30,31]. On the other hand, the study of the effect of an external magnetic field on the flow and heat transfer in a channel or a closed cavity is significant because of engineering applications such as cooling of nuclear reactors, MHD micropumps, electronic packages, microelectronic devices, and so on [32].

The main aim of this work is to present an analytical solution for calculating the entropy generation in a vertical annulus with isoflux boundary conditions subjected to MHD flow where the working fluid is TiO_2/water nanofluid.

2. Problem formulation

To obtain the entropy generation rate in the system, firstly, the velocity and temperature fields should be obtained using the first law of thermodynamics.

2.1. First law of thermodynamics

Consider a laminar mixed convection flow of a Newtonian nanofluid between two isoflux cylinders with the inner and outer radii r_i and r_o, respectively. The nanofluid enters the annulus with an inlet velocity of U_0 and an inlet temperature of T_0, while a magnetic field with a constant intensity of B_0 is applied normal to the flow direction. For such a system, a differential pressure transmitter can be installed in the experimental studies to measure the

pressure drop along the heat exchanger. The schematic of the problem is indicated in Fig. 1.

It is assumed that the fluid and nanoparticles are in thermal equilibrium and no slip occurs between the particles and water. It should be stated that, in a practical situation, most nanofluids used for augmentation of heat transfer are made up of extremely fine particles, usually under 40 nm diameter. As a result, the nanofluids can be considered to act similar to a conventional homogeneous single-phase fluid [33]. It is also assumed that the thermal properties of nanofluids are temperature-independent. The recent assumption is taken into account in many studies in the field of nanofluids, for instance in mixed convection flows [29,34] and natural convection problems [35].

Hence, the continuity, momentum, and energy equations can be written as follows

Continuity Equation

$$\frac{\partial V_r}{\partial r}+\frac{V_r}{r}+\frac{\partial V_z}{\partial z}=0 \tag{1}$$

Momentum r-direction

$$\rho_{nf}\left[V_r\frac{\partial V_r}{\partial r}+V_z\frac{\partial V_r}{\partial z}\right]=-\frac{\partial P}{\partial r}+\mu_{nf}\left[\frac{\partial^2 V_r}{\partial r^2}+\frac{1}{r}\frac{\partial V_r}{\partial r}-\frac{V_r}{r^2}+\frac{\partial^2 V_r}{\partial z^2}\right] \tag{2}$$

Momentum z-direction

$$\rho_{nf}\left[V_r\frac{\partial V_z}{\partial r}+V_z\frac{\partial V_z}{\partial z}\right]=-\frac{\partial P}{\partial z}+\mu_{nf}\left[\frac{\partial^2 V_z}{\partial r^2}+\frac{1}{r}\frac{\partial V_z}{\partial r}+\frac{\partial^2 V_z}{\partial z^2}\right]-\rho_{nf}g-\sigma B_0^2 V_z \tag{3}$$

Energy

$$(\rho C_p)_{nf}\left[V_r\frac{\partial T}{\partial r}+V_z\frac{\partial T}{\partial z}\right]=k_{nf}\left[\frac{1}{r}\frac{\partial}{\partial r}\left(r\frac{\partial T}{\partial r}\right)+\frac{\partial^2 T}{\partial z^2}\right]+\sigma B_0^2 V_z^2 \tag{4}$$

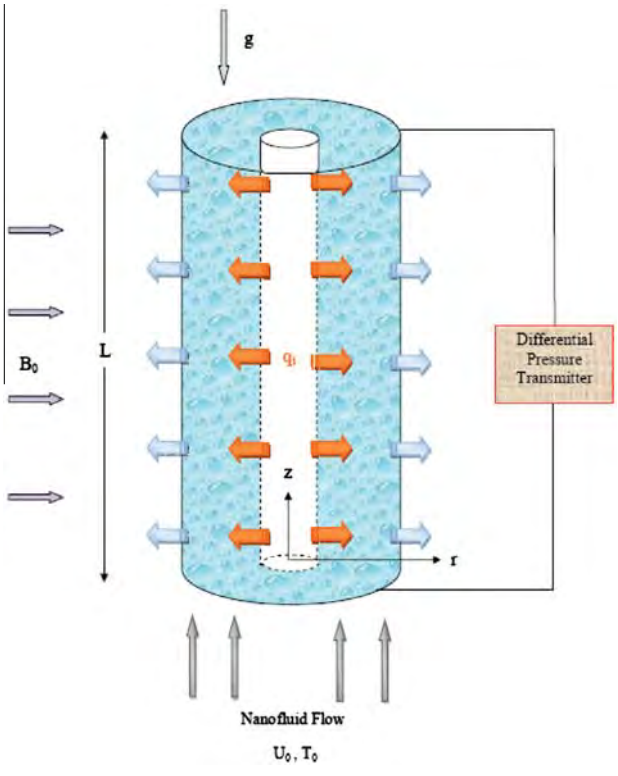

Fig. 1. Schematic view of the present problem.

By considering a hydrodynamically and thermally fully developed flow, neglecting the magnetic heating, using the Boussinesq approximation, and a small variation of temperature in z-direction (see Refs. [30,31,36]) the momentum and energy equations are simplified. These assumptions are made to have an analytical solution of the problem. The simplified equations are as follows:

$$-\frac{1}{\rho_{nf}}\frac{\partial P}{\partial z}+\frac{\mu_{nf}}{\rho_{nf}}\left[\frac{\partial^2 V_z}{\partial r^2}+\frac{1}{r}\frac{\partial V_z}{\partial r}\right]+g\beta_{nf}(T-T_0)-\frac{\sigma B_0^2 V_z}{\rho_{nf}}=0 \tag{5}$$

$$\frac{\partial^2 T}{\partial r^2}+\frac{1}{r}\frac{\partial T}{\partial r}=0 \tag{6}$$

It should be noted that because the working fluid is a nanofluid based on water (no viscous fluids such oil), hence, the viscous dissipation term can be ignored in the energy equation.

By assuming no slip between the nanofluid and the walls of the cylinders, the boundary conditions for velocity can be written as:

$$\begin{aligned} r=r_i \quad &\Rightarrow \quad V_z=0\\ r=r_o \quad &\Rightarrow \quad V_z=0 \end{aligned} \tag{7}$$

The thermal boundary conditions are as

$$\begin{aligned} r=r_i \quad &\Rightarrow \quad -k_{nf}\frac{\partial T}{\partial r}=q_i\\ r=r_o \quad &\Rightarrow \quad -k_{nf}\frac{\partial T}{\partial r}=f(q_i) \end{aligned} \tag{8}$$

where q_i is the heat flux at inner cylinder. It should be noted that $f(q_i)$ could be obtained using energy balance in the annulus. In fact, $f(q_i)$ is the heat dissipated from the outer wall, but it has no role in the solution of the present paper.

The dimensionless momentum and energy equations can be expressed as

$$\left(\frac{\mu_{nf}}{\mu_f}\right)\left[\frac{1}{R}\frac{\partial}{\partial R}\left(R\frac{\partial U}{\partial R}\right)\right]=-\frac{\mathrm{Gr}}{\mathrm{Re}}\left(\frac{\rho_{nf}}{\rho_f}\right)\left(\frac{\beta_{nf}}{\beta_f}\right)\theta+M^2U+\frac{\partial P^*}{\partial Z} \tag{9}$$

$$\frac{\partial^2\theta}{\partial R^2}+\frac{1}{R}\frac{\partial\theta}{\partial R}=0 \tag{10}$$

in which the dimensionless parameters are defined as follows

$$\theta=\frac{T-T_0}{q_i r_o/k_f},\quad U=\frac{V_z}{U_0},\quad R=\frac{r}{r_o},\quad \mathrm{Gr}=\frac{g\beta_f q_i r_o^4}{k_f\upsilon_f^2},$$
$$\mathrm{Re}=\frac{U_0 r_o}{\upsilon_f}\quad P^*=\frac{P}{U_0\mu_f}r_o,\quad Z=\frac{z}{r_o},\quad M^2=\frac{\sigma B_0^2}{\mu_f}r_o^2,\quad \lambda=\frac{r_i}{r_o} \tag{11}$$

In the above relations M is the Hartmann number, σ is the electrical conductivity of fluid. Gr and Re are Grashof and Reynolds numbers, respectively. Also, it should be noted that the subscripts of nf and f represent the characteristics of nanofluid and the base fluid, respectively. The dimensionless boundary conditions of velocity become

$$\begin{aligned} R=\lambda \quad &\Rightarrow \quad U=0\\ R=1 \quad &\Rightarrow \quad U=0 \end{aligned} \tag{12}$$

In addition, the thermal boundary conditions are as follows

$$\begin{aligned} R=\lambda \quad &\Rightarrow \frac{\partial\theta}{\partial R}=-\frac{k_f}{k_{nf}}\\ R=1 \quad &\Rightarrow \frac{\partial\theta}{\partial R}=F(q_i) \end{aligned} \tag{13}$$

The following relations are used to calculate the quantities of thermal expansion coefficient and the density of the nanofluid, respectively [11]:

$$\frac{\beta_{nf}}{\beta_f} = (1-\phi) + \frac{\phi\beta_p}{\beta_f} \tag{14}$$

$$\frac{\rho_{nf}}{\rho_f} = (1-\phi) + \frac{\phi\rho_p}{\rho_f} \tag{15}$$

where ϕ is the volume fraction of nanofluid.

Here, to calculate the thermal conductivity and viscosity of TiO_2/water nanofluid, two sets of relations are used. The first set, which is based on experimental data and is presented by Duangthongsuk and Wongwises [37] can be written as:

Viscosity

$$\frac{\mu_{nf}}{\mu_f} = 1.013 + 0.092\phi - 0.015\phi^2 \tag{16}$$

Thermal conductivity

$$\frac{k_{nf}}{k_f} = 1.0204 + 0.0249\phi \tag{17}$$

It should be noted that the above equations for thermal conductivity and viscosity are presented for 25 °C and are valid for 0.2–2%. For water ($\phi = 0$), there is no need to the above equations and the ratio of k_{nf}/k_f and μ_{nf}/μ_f is equal to 1.

The second set is including the Brinkman [38] model for viscosity, and Yu and Choi [39] model for thermal conductivity, which are the famous available theoretical models in the literature.

Viscosity

$$\mu_{nf} = \frac{\mu_f}{(1-\phi)^{2.5}} \tag{18}$$

Thermal conductivity

$$k_{nf} = \frac{k_P + 2k_f + 2(k_p - k_f)(1+\gamma)^3\phi}{k_p + 2k_f - 2(k_p - k_f)(1+\gamma)^3\phi}k_p \tag{19}$$

k_p is the thermal conductivity of TiO_2 nanoparticles that is approximately 9 W/m K, also k_f is the thermal conductivity of water that is 0.613 W/m K. In Eq. (19), γ is a dimensionless number and is defined as the ratio of the nanolayer thickness to the original particle radius. The value of γ is considered usually equal to 0.1 [33,40]. In the literature, the relations (18) and (19) are used to calculate the thermal conductivity and viscosity of nanofluids for 5% and even higher than 5% of volume fraction of nanoparticles, hence, certainly those are valid for the smaller range of volume fraction that is selected in this work (up to 2%).

It should be noted that all calculations are made by the experimental models, and only for the comparison purpose, the theoretical models are used.

2.2. Second law of thermodynamics

In the present work, the vertical annulus considered is under a constant magnetic field. Generally, in the presence of magnetic field, the local volumetric entropy generation, $\dot{S}'''_{gen}$(W/m^{3}k) rate becomes (see Ref. [33]),

$$\dot{S}'''_{gen} = \frac{k_{nf}}{T_0^2}[\nabla T]^2 + \frac{\mu_{nf}}{T_0}\Phi + \frac{1}{T_0}[(J - QV).(E + V \times B)]$$

where

$$J = \sigma(E + V \times B) \tag{20}$$

In the above equations, Φ is viscous dissipation, J is electric current, Q is electric charge density, V is velocity vector, E is the electric field, and B is the magnetic induction. Assuming that QV is negligible compared to J and disregarding E in comparison with $V \times B$, the volumetric entropy generation rate, Eq. (18), reduces in this case to the following relation:

$$\dot{S}'''_{gen} = \frac{k_{nf}}{T_0^2}\left(\frac{\partial T}{\partial r}\right)^2 + \frac{\mu_{nf}}{T_0}\left(\frac{\partial V_z}{\partial r}\right)^2 + \frac{\sigma B_0^2}{T_0}V_z^2 \tag{21}$$

The volumetric entropy generation number is defined as

$$N_S = \frac{\dot{S}'''_{gen}}{\frac{\mu_{nf}U_0^2}{T_0 r_o^2}} = \left(\frac{k_{nf}}{k_f}\right)\left(\frac{\mu_f}{\mu_{nf}}\right)\left(\frac{\Omega}{Br_f}\right)\left(\frac{\partial\theta}{\partial R}\right)^2 + \left(\frac{\partial U}{\partial R}\right)^2 + H^2U^2$$
$$= N_H + N_F + N_M \tag{22}$$

where Brinkman number (Br_f) and parameters of Ω and H^2 are defined as:

$$Br_f = \frac{U_0^2\mu_f}{q_i r_o}, \quad \Omega = \frac{q_i r_o}{k_f T_0}, \quad H^2 = \left(\frac{\mu_f}{\mu_{nf}}\right)M^2$$

On the right hand side of Eq. (21), N_H represents the entropy generation due to heat transfer, N_F is the entropy generation caused by viscous dissipation, and N_M is the entropy generation induced by MHD flow.

The distribution of irreversibility can be evaluated by using the Bejan number definition (Be) that is the ratio of entropy generation due to heat transfer to the overall entropy generation as [41].

$$Be = \frac{N_H}{N_S} \tag{23}$$

3. Problem solution

The momentum and the energy equations are coupled via buoyancy term. Therefore, firstly, the energy equation should be solved to obtain the temperature distribution.

The solution of the energy equation is obtained by using the boundary conditions as follows

$$\theta(R) = -\frac{k_f}{k_{nf}}\lambda\ln(R) + C \tag{24}$$

where C is the integration constant. The constant C cannot be determined in this step because of the isoflux boundary conditions. Using the temperature distribution, the solution of momentum equation (Eq. (9)) becomes

$$U(R) = \Gamma_1 K_0(HR) + \Gamma_2 I_0(HR) - \frac{(\partial P^*/\partial Z) + (\mathrm{Gr}/\mathrm{Re})\rho_r\beta_r\lambda\ln(R)}{\mu_r H^2} + \frac{(\mathrm{Gr}/\mathrm{Re})\rho_r\beta_r}{\mu_r H^2}C \tag{25}$$

where $I_0(HR)$ is the modified Bessel function of the first kind, of order 0, and $K_0(HR)$ is the modified Bessel function of the second kind, of order 0.

The constants Γ_1 and Γ_2 are the integration constants. The constants are determined by the following relations:

$$\Gamma_1 = -\frac{\{(\mathrm{Gr}/\mathrm{Re})\rho_r\beta_r C[I_0(H\lambda) - I_0(H)] - (\partial P^*/\partial Z)[I_0(H\lambda) - I_0(H)] + (\mathrm{Gr}/\mathrm{Re})\rho_r\beta_r\lambda\ln(\lambda)I_0(H)\}}{\mu_r H^2[K_0(H)I_0(H\lambda) - K_0(H\lambda)I_0(H)]}$$
$$\Gamma_2 = \frac{\{(\mathrm{Gr}/\mathrm{Re})\rho_r\beta_r C[K_0(H\lambda) - K_0(H)] - (\partial P^*/\partial Z)[K_0(H\lambda) - K_0(H)] + (\mathrm{Gr}/\mathrm{Re})\rho_r\beta_r\lambda\ln(\lambda)K_0(H)\}}{\mu_r H^2[K_0(H)I_0(H\lambda) - K_0(H\lambda)I_0(H)]} \tag{26}$$

In the above relations $\beta_r, \rho_r \mu_r k_r$ represent $\frac{\beta_{nf}}{\beta_f}, \frac{\rho_{nf}}{\rho_f}, \frac{\mu_{nf}}{\mu_f}, \frac{k_{nf}}{k_f}$, respectively.

Now, the constant C should be determined from the continuity equation as follows:

$$\int_{r_i}^{r_o} \rho_{nf} V_z(r) 2\pi r dr = \rho_{nf} U_0 \left[\pi\left(r_o^2 - r_i^2\right)\right] \tag{27}$$

The above relation in the dimensionless form is

$$\int_{\lambda}^{1} U(R) R dR = \frac{(1-\lambda^2)}{2} \tag{28}$$

Using Eqs. (23) and (27), one can obtain the constant C easily. The expression for constant C is presented in the appendix. The constant C is in a function of the involving parameters in the problem including geometric parameter (λ), flow parameters $\left(M, \frac{\mathrm{Gr}}{\mathrm{Re}}, \frac{\partial P^*}{\partial Z}\right)$, and nanofluid properties $\mu_r, k_r, \beta_r, \rho_r$ as:

$$C = g\left(M, \lambda, \frac{\mathrm{Gr}}{\mathrm{Re}}, \frac{\partial P^*}{\partial Z}, \mu_r, k_r, \beta_r, \rho_r\right) \tag{29}$$

Here, by substituting the temperature field and the velocity distribution and its first derivative in Eq. (21), the volumetric entropy generation number can be obtained as

$$N_S = \left(\frac{k_r}{\mu_r}\right)\left(\frac{\Omega}{Br_f}\right)\left(\frac{-\lambda}{k_r R}\right)^2 + \left(-\Gamma_1 H K_1(HR) + \Gamma_2 H I_1(HR) - \frac{\lambda \rho_r \beta_r (\mathrm{Gr}/\mathrm{Re})}{\mu_r H^2 R}\right)^2 + H^2\left(\Gamma_1 K_0(HR) + \Gamma_2 I_0(HR) - \frac{(\partial P^*/\partial Z) + (\mathrm{Gr}/\mathrm{Re})\rho_r \beta_r \lambda \ln(R)}{\mu_r H^2} + \frac{(\mathrm{Gr}/\mathrm{Re})\rho_r \beta_r}{\mu_r H^2} C\right)^2 \tag{30}$$

The average volumetric entropy generation number is determined by:

$$N_{S,ave} = \frac{2}{(1-\lambda^2)} \int_{\lambda}^{1} N_S R dR \tag{31}$$

4. Results and discussion

An analytical study has been performed for TiO_2/water nanofluid on the entropy generation in an isoflux vertical annulus under MHD flow effects. Before presenting the results it is helpful to discuss about the variables and flow parameters considered in the problem. The first parameter is the dimensionless pressure drop (dP^*/dZ) through the tube. This parameter is assumed to be -0.1 in all of the calculations. Of course, it should be mentioned that the magnitude of this parameter has no considerable effect on the results. The second important variable is Gr/Re. This parameter indicates the importance of the buoyancy term in the momentum equation (Eq. (9)). In this work the range of this parameter is considered between 0.1 and 100. If the value of Gr/Re being 0.1, this means that the role of free convection in the heat transfer is negligible, while for Gr/Re = 100 the contribution of free convection to heat transfer becomes maximum. The third variable is the Hartmann number. This variable shows the magnitude of magnetic field applied to the system. In practical applications, considering the Hartmann number from order 10^0 to 10^1 may be reasonable (see Ref. [42]). The last parameter in this problem is Ω/Br. This dimensionless parameter indicates the contribution of heat transfer to entropy generation. It should be noted that the main aim of solving a problem with dimensionless parameters, is to study the effects of different variable on the objective parameter as qualitative and not quantitative. Fig. 2 shows the effects of MHD flow on the entropy generation number (a) and the Bejan number (b) at different volume fractions of nanoparticles for $\frac{dP^*}{dZ} = -0.1, \frac{\mathrm{Gr}}{\mathrm{Re}} = 10, \frac{\Omega}{Br} = 50$where$\lambda = \frac{r_i}{r_o} = 0.5$. It is observed that the entropy generation number is minimized approximately at the center of the annulus for all conditions. This happens because at the center of the annulus, the effects of shear stress induced by the walls and, hence, viscous dissipations are diminished so that in the center the entropy generation is minimized. Although the entropy generation due to heat transfer (N_H) is minimized at the outer cylinder (not the centre of annulus) because based on Eq. (29) it is proportional inversely to radius (R) and the entropy generation due to magnetic field (N_M) is minimized at inner and outer cylinders (not the centre of annulus) because of zero velocity on the walls (see Eq. (21)). However, the contribution of viscous effects is dominant and hence the total entropy generation is reduced. It should be stated that the distribution of entropy generation number is not symmetric with respect to the central line because of buoyancy effects. As shown, the entropy generation is increased by the increases in the magnetic field (Hartmann number). For isoflux boundary conditions, when the intensity of magnetic field increases, the entropy generation induced by viscous effects is increased on the walls, because the Lorentz force produced by the magnetic field act as a drag force and presses the fluid layers near the walls together, hence, the contribution of viscous effects to entropy generation on the walls increases. On the other hand, the entropy generation number increases in the whole of annulus by increasing the contribution of MHD flow to entropy generation. It is also found that the entropy generation decreases with increases in the volume fraction of nanofluids. This decrease is most visible where ϕ increases from 0% to 1% in comparison with the case in which ϕ increases from 1% to 2%. This happens because with increases in the volume fraction of nanoparticles, the effective viscosity of nanofluid increases remarkably. This decreases the rate of entropy generation reduction. As seen, the entropy generation is higher in the vicinity of inner cylinder compared to the outer cylinder because of higher gradients of velocity and temperature in this region.

From the Bejan number distribution, one can observe that the Bejan number decreases with increases in volume fraction of nanoparticles. This is due to the decreases in the heat transfer contribution to entropy generation. The thermal conductance in the nanofluid is higher than the base fluid due to higher thermal conductivity of nanofluid, hence, the irreversibility due to heat transfer decreases with increasing the particle loadings. It is also perceived that the Bejan number decreases with increases in the Hartmann number, due to the increasing of MHD flow contribution to entropy generation (see Eq. (22)).

The effects of the flow parameter Gr/Re and volume fraction of nanoparticles on the entropy generation number is displayed in Fig. 3, for $M = 1$. As seen, the entropy generation number has an unpredictable behavior in the annulus where the parameter Gr/Re increases from 0.1 to 100, for a given value of ϕ, so that it cannot be found easily that the entropy generation decreases or increases with an increase in Gr/Re. This behavior is caused by the

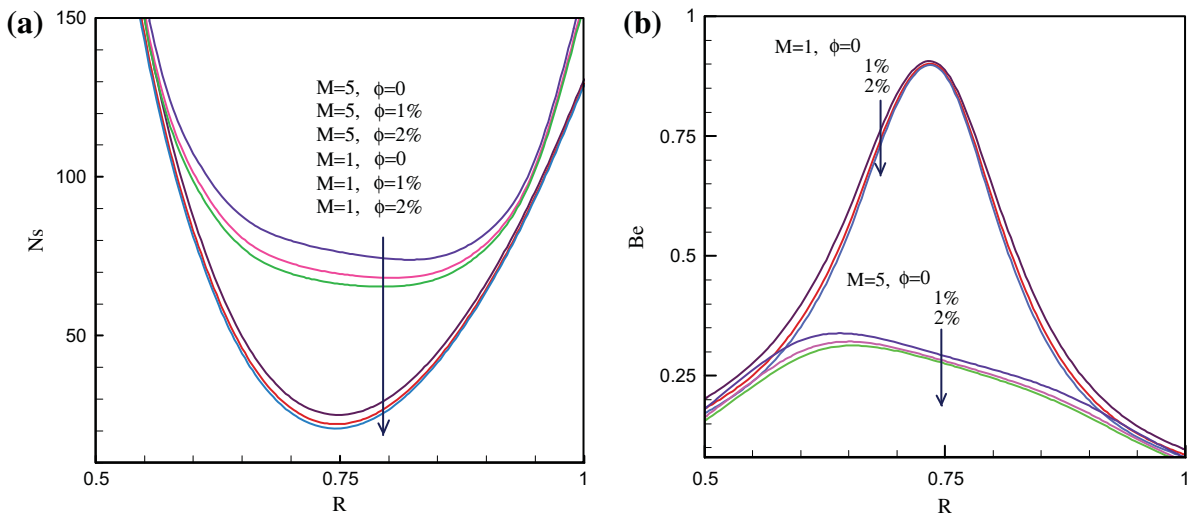

Fig. 2. Effects of MHD flow and volume fraction on (a) entropy generation and (b) Bejan numbers.

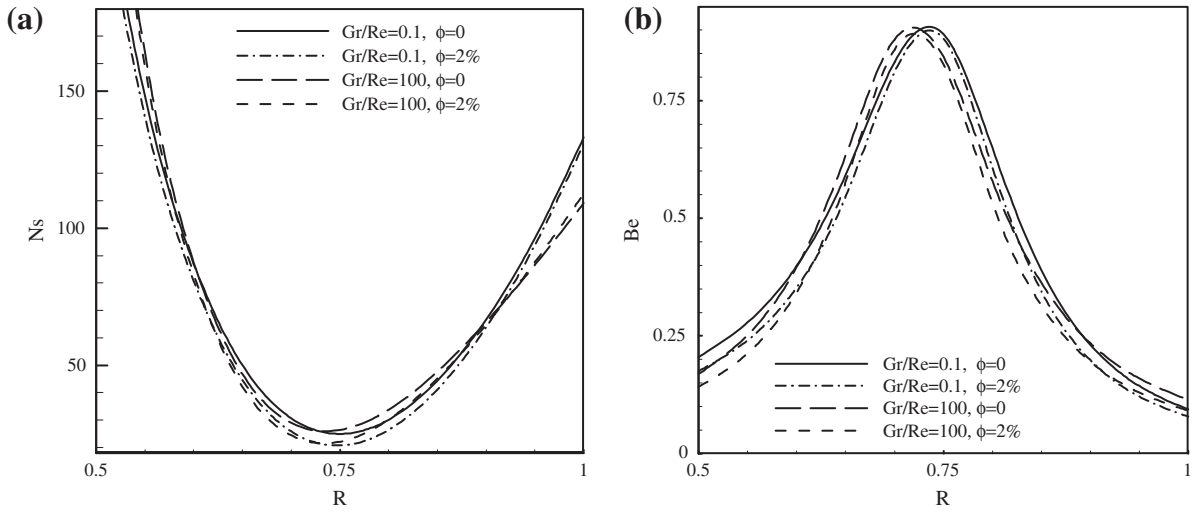

Fig. 3. Effects of Gr/Re and volume fraction on (a) entropy generation and (b) Bejan numbers.

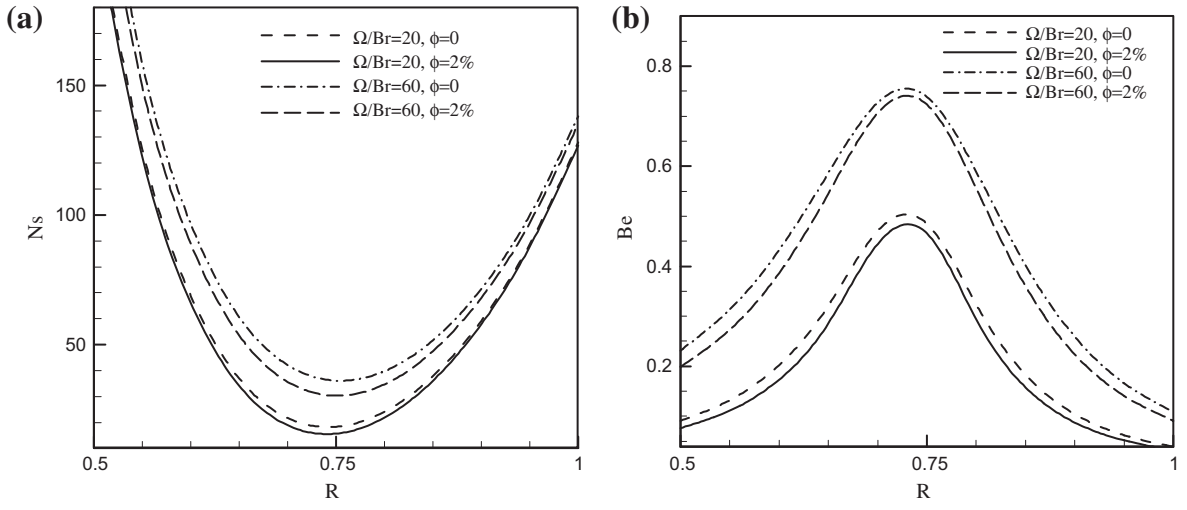

Fig. 4. Effects of Ω/*Br* and volume fraction on (a) entropy generation and (b) Bejan numbers.

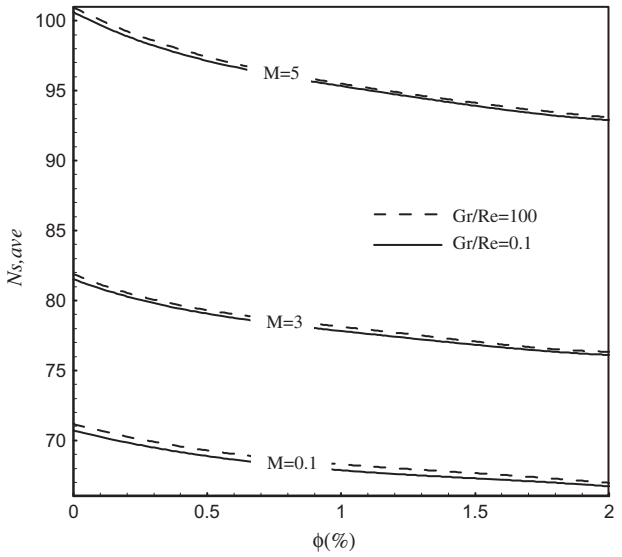

Fig. 5. Effects of MHD flow and Gr/Re on the average entropy generation number in different volume fractions.

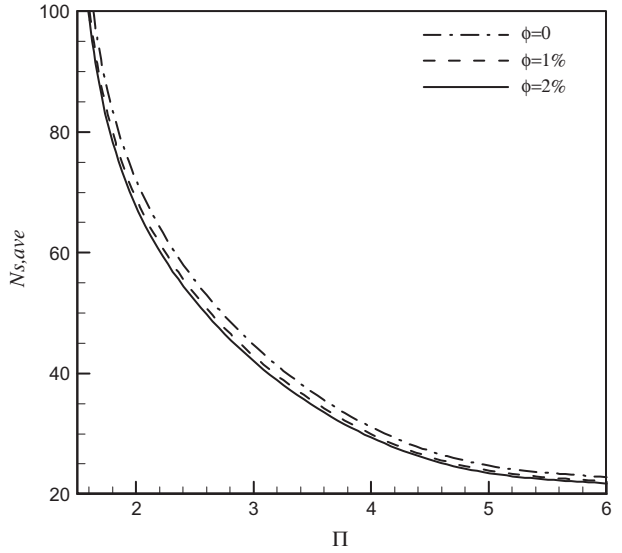

Fig. 6. Effects of volume fractions on average entropy generation at different radius ratios.

interactions among buoyancy forces, shear stresses near the walls and the heat flux at the inner cylinder. The Fig. 3(a) also reveals that the entropy generation number is reduced in the whole of annuli for Gr/Re = 0.1, with increasing the volume fraction of nanoparticles. However, it is seen that for Gr/Re = 100, the entropy generation number is decreased near the outer cylinder with an increase in volume fraction. It should be stated that the free convection is dominant on the forced convection where the flow parameter of Gr/Re is 100. Therefore, near the outer cylinder that the heat flux is smallest, a flow in which free convection is dominant leads to the increase of the fluid friction contribution to entropy with increases in volume fraction.

From the Fig. 3(b), it is observed that the Bejan number is maximized nearly in the centerline of the annulus. With an increase in $\frac{Gr}{Re}$, this maximum point moves towards inner cylinder. Like the Bejan number distribution in Fig. 2(a), the Bejan number decreases with increases in volume fraction of nanoparticles.

Fig. 4 shows the effects of volume fraction and the parameter of Ω/Br on the entropy generation number. As seen from the figure,

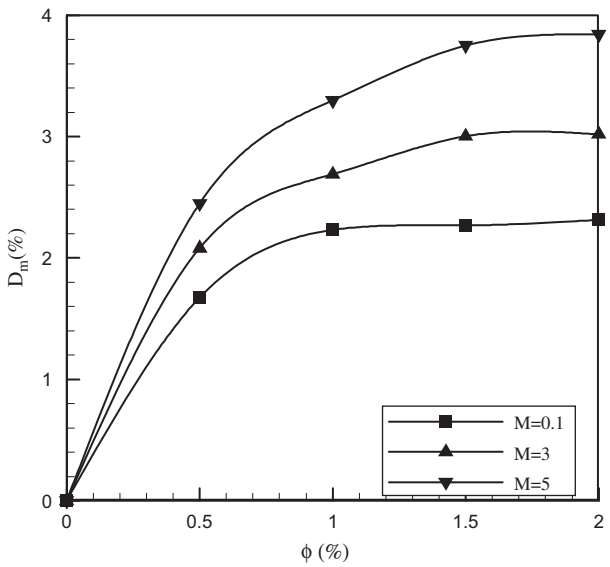

Fig. 7. Difference between the results obtained by theoretical models and experimental models at different Hartmann numbers.

the decreases in entropy generation due to adding TiO_2 nanoparticles into the base fluid is more visible for higher values of Ω/Br. For these values of Ω/Br the contribution of heat transfer to entropy generation is greater. Hence, increasing of the effective thermal conductivity of working fluid can be more helpful to reduce of entropy generation number. The Bejan number increases with increases in Ω/Br, as expected.

Fig. 5 presents the effects of Hartmann number and Gr/Re on average entropy generation number with respect to ϕ. It is found that the average entropy generation number decreases with increasing of ϕ for all values of M. The gradients are bigger for higher Hartmann numbers. This reveals that adding of nanoparticles is more advantageous in higher Hartmann numbers than lower Hartmann numbers. It is also concluded that the average entropy generation number increases a little as Gr/Re increases from 0.1 to 100. Meanwhile, the average entropy generation increases with an increase of magnetic field.

Fig. 6 displays the effects of volume fractions on the average entropy generation at different radius ratios. It is seen from the figure, the average entropy generation decreases with the increase in the radius ratio because of the reductions in velocity and temperature gradients. It is found that the radius ratio increases from 2 to 6 and the average entropy generation is reduced more than a third. The average entropy generation number is decreased in any radius ratio with increases in the volume fraction of nanoparticles.

Finally, a comparison has been made between the results obtained from experimental and theoretical models used to calculate the thermal conductivity and viscosity. The difference between the results, $D_m(\%)$, can be calculated as follows:

$$D_m(\%) = \frac{(N_{S,\mathrm{ave}})_{\mathrm{theo}} - (N_{S,\mathrm{ave}})_{\mathrm{exp}}}{(N_{S,\mathrm{ave}})_{\mathrm{theo}}} \times 100 \tag{32}$$

It should be noted that the theoretical models give higher values for average entropy generation number. Fig. 7 shows the results of the comparison for Gr/Re = 0.1 at different Hartmann numbers. It is found that the difference between the theoretical and experimental models is lower where the Hartmann number is smaller. It is also observed that the difference between the results obtained by the two sets models is nearly 4% at $M = 5$. This reveals that using theoretical models rather than experimental models has no significant effect on the prediction of entropy generation. Of course, it should

be considered that a small volume fraction of the nanoparticles is examined in this study (by 2%), whereas for higher values of volume fraction the difference between the results may be considerable.

5. Conclusion

An analytical study is performed to examine the effects of using TiO_2/water nanofluid ($0 \leqslant \phi \leqslant 2\%$) on the entropy generation in an isoflux vertical annulus under MHD flow effects. The flow is assumed as laminar, steady and fully developed inside the heat exchanger. The governing equations are simplified and solved to obtain analytical expressions for the distribution of velocity, temperature and entropy generation in the annulus. The effects of various flow parameters including Gr/Re, Hartmann number, and Ω/Br on entropy generation are investigated qualitatively. The flow parameter Gr/Re indicates the contribution of free convection in the problem. Hartmann number indicates the strength of the magnetic field and the parameter of Ω/Br shows the contribution of heat transfer to entropy generation. The results show that using TiO_2/water nanofluid reduces the entropy generation in the annulus while an increase in the Hartmann number increases the entropy generation number. Two sets of models including the relations obtained based on experiments and the theoretical relations are used to find the effects of using different models on the results. The results show that theoretical models predict the average entropy generation nearly 4% higher than the experimental models for $M = 5$. It is also concluded that the difference between the results obtained by the two sets of models is greater for higher Hartmann numbers.

Acknowledgments

The first and fifth author would like to thank the Thailand Research Fund and the National Research University Project for the support. The third author acknowledges the support of King Fahd University of Petroleum and Minerals (KFUPM), Dhahran, Saudi Arabia, for this work.

Appendix A.

In the following, the value of constant C is presented as:

$$C = \frac{N}{D}$$

where the numerator of the fraction is given as

$$N = \frac{1}{2}\left\{\left[-4\lambda k_r \frac{\partial P^*}{\partial Z} K_1(H\lambda)\right] - 2HK_0(H)\left[\rho_r\beta_r\lambda^3\frac{\mathrm{Gr}}{\mathrm{Re}}\ln(\lambda) + (\lambda^2-1)\left(-\frac{1}{2}\rho_r\beta_r\lambda\frac{\mathrm{Gr}}{\mathrm{Re}} + k_r\left(H^2\mu_r + \frac{\partial P^*}{\partial Z}\right)\right) + 4k_r\frac{\partial P^*}{\partial Z}K_1(H)\right]I_0(H\lambda)\right.$$
$$+K_0(H\lambda)\left[-4\frac{\partial P^*}{\partial Z}\lambda k_r I_1(H\lambda) + 2HI_0(H)\left(\rho_r\beta_r\frac{\mathrm{Gr}}{\mathrm{Re}}\lambda^3\ln(\lambda) + (\lambda^2-1)\left(-\frac{1}{2}\rho_r\beta_r\lambda\frac{\mathrm{Gr}}{\mathrm{Re}} + k_r\left(H^2\mu_r + \frac{\partial P^*}{\partial Z}\right)\right)\right) + 4k_r\frac{\partial P^*}{\partial Z}I_1(H)\right]$$
$$\left.+4\left(\rho_r\beta_r\frac{\mathrm{Gr}}{\mathrm{Re}}\lambda\ln(\lambda) + k_r\frac{\partial P^*}{\partial Z}\right)(\lambda K_1(H\lambda)I_0(H) - K_1(H)I_0(H) - K_0(H)I_1(H) + \lambda I_1(H\lambda)K_0(H))\right\}$$

and the denominator of the fraction is

$$D = \left[k_r\rho_r\beta_r\frac{\mathrm{Gr}}{\mathrm{Re}}((-2\lambda K_1(H\lambda) + K_0(H)(H - H\lambda^2) + 2K_1(H))I_0(H\lambda) + (-2\lambda I_1(H\lambda) + (-H + H\lambda^2)I_0(H)\right.$$
$$\left.+2I_1(H))K_0(H\lambda) - 2K_1(H)I_0(H) + 2\lambda K_1(H\lambda)I_0(H) + 2\lambda I_1(H\lambda)K_0(H) - 2K_0(H)I_1(H))\right]$$

References

[1] S.U.S. Choi, Enhancing thermal conductivity of fluids with nanoparticles, in: D.A. Siginer, H.P. Wang (Eds.), ASME International Mechanical Engineering Congress and Exposition Proceedings, vol. 231, 1995, pp. 99–105.
[2] H.R. Seyf, B. Nikaaein, Analysis of Brownian motion and particle size effects on the thermal behavior and cooling performance of microchannel heat sinks, Int. J. Therm. Sci. 58 (2012) 36–44.
[3] H.R. Seyf, S. Keshavarz Mohammadian, Thermal and hydraulic performance of counterflow microchannel heat exchangers with and without nanofluids, J. Heat Transfer 133 (8) (2011). art. no. 081801..
[4] W. Duangthongsuk, S. Wongwises, A critical review of convective heat transfer of nanofluids, Renew. Sustain. Energy Rev. 11 (5) (2007) 797–817.
[5] W. Duangthongsuk, S. Wongwises, A dispersion model for predicting the heat transfer performance of TiO_2–water nanofluids under a laminar flow regime, Int. J. Heat Mass Transfer 55 (11–12) (2012) 3138–3146.
[6] L.G. Asirvatham, R. Nimmagadda, S. Wongwises, Heat transfer performance of screen mesh wick heat pipes using silver–water nanofluid, Int. J. Heat Mass Transfer 60 (1) (2013) 201–209.
[7] L. Godson, B. Raja, D. Mohan Lal, S. Wongwises, Enhancement of heat transfer using nanofluids – an overview, Renew. Sustain. Energy Rev. 14 (2) (2010) 629–641.
[8] W.J. Minkowycz, E.M. Sparrow, J.P. Abraham, Nanoparticle Heat Transfer and Fluid Flow, CRC Press, 2012.
[9] O. Mahian, A. Kianifar, S.A. Kalogirou, I. Pop, S. Wongwises, A review of the applications of nanofluids in solar energy, Int. J. Heat Mass Transfer 57 (2013) 582–594.
[10] R. Saidur, K.Y. Leong, H.A. Mohammad, A review on applications and challenges of nanofluids, Renew. Sustain. Energy Rev. 15 (2011) 1646–1668.
[11] K. Khanafer, K. Vafai, A critical synthesis of thermophysical characteristics of nanofluids, Int. J. Heat Mass Transfer 54 (2011) 4410–4428.
[12] Y.A. Cengel, M.A. Boles, Thermodynamics an Engineering Approach, fifth ed., McGraw-Hill, 2006.
[13] A. Bejan, Second-law analysis in heat transfer and thermal design, Adv. Heat Transfer 15 (1982) 1–58.
[14] A. Bejan, Entropy Generation Minimization, CRC Press, Boca Raton, NY, 1996.
[15] H.F. Oztop, K. Al-Salem, A review on entropy generation in natural and mixed convection heat transfer for energy systems, Renew. Sustain. Energy Rev. 16 (2012) 911–920.
[16] H. Herwig, The role of entropy generation in momentum and heat transfer, ASME J. Heat Transfer 134 (2012) 031003–31012.
[17] P.K. Singh, K.B. Anoop, T. Sundararajan, S.K. Das, Entropy generation due to flow and heat transfer in nanofluids, Int. J. Heat Mass Transfer 53 (2010) 4757–4767.
[18] J. Li, C. Kleinstreuer, Entropy generation analysis for nanofluid flow in microchannels, ASME J. Heat Transfer 132 (2010) 122401.
[19] Y. Feng, C. Kleinstreuer, Nanofluid convective heat transfer in a parallel-disk system, Int. J. Heat Mass Transfer 53 (2010) 4619–4628.
[20] M. Moghaddami, A. Mohammadzade, S.A. Varzane Esfehani, Second law analysis of nanofluid flow, Energy Convers. Manage. 52 (2011) 1397–1405.
[21] M. Shahi, A.H. Mahmoudi, A.H. Raouf, Entropy generation due to natural convection cooling of a nanofluid, Int. Commun. Heat Mass Transfer 38 (2011) 972–983.
[22] M. Esmaeilpour, M. Abdollahzadeh, Free convection and entropy generation of nanofluid inside an enclosure with different patterns of vertical wavy walls, Int. J. Therm. Sci. 57 (2012) 127–136.

[23] V. Bianco, S. Nardini, O. Manca, Enhancement of heat transfer and entropy generation analysis of nanofluids turbulent convection flow in square section tubes, Nanoscale Res. Lett. 6 (2011) 252.
[24] W.H. Mah, Y.M. Hung, N. Guo, Entropy generation of viscous dissipative nanofluid flow in microchannels, Int. J. Heat Mass Transfer 55 (2012) 4169–4182.
[25] A. Shalchi-Tabrizi, H.R. Seyf, Analysis of entropy generation and convective heat transfer of Al_2O_3 nanofluid flow in a tangential micro heat sink, Int. J. Heat Mass Transfer 55 (2012) 4366–4375.
[26] O. Mahian, S. Mahmud, S. Zeinali Heris, Analysis of entropy generation between co-rotating cylinders using nanofluids, Energy 44 (2012) 438–446.
[27] O. Mahian, S. Mahmud, S. Zeinali Heris, Effect of uncertainties in physical properties on entropy generation between two rotating cylinders with nanofluids, ASME J. Heat Transfer 134 (2012) 101704.
[28] O. Mahian, S. Mahmud, S. Wongwises, Entropy generation between two rotating cylinders in the presence of magnetohydrodynamic flow using nanofluids, J. Thermophys. Heat Transfer 27 (1) (2013) 161–169.
[29] S. Sarkar, S. Ganguly, A. Dalal, Analysis of entropy generation during mixed convection heat transfer of nanofluids past a square cylinder in vertically upward flow, ASME J. Heat Transfer 134 (2012) 122501.
[30] S.H. Tasnim, S. Mahmud, Mixed convection and entropy generation in a vertical annular space, Int. J. Exergy 2 (2002) 373–379.
[31] S.H. Tasnim, S. Mahmud, Entropy generation in a vertical concentric channel with temperature dependent viscosity, Int. Commun. Heat Mass Transfer 29 (2002) 907–918.
[32] O. Mahian, S. Mahmud, I. Pop, Analysis of first and second laws of thermodynamics between two isothermal cylinders with relative rotation in the presence of MHD flow, Int. J. Heat Mass Transfer 55 (2012) 4808–4816.
[33] R.B. Mansour, N. Galanis, C.T. Nguyen, Effect of uncertainties in physical properties on forced convection heat transfer with nanofluids, Appl. Therm. Eng. 27 (2007) 240–249.
[34] T. Grosan, I. Pop, Axisymmetric mixed convection boundary layer flow past a vertical cylinder in a nanofluid, Int. J. Heat Mass Transfer 54 (2011) 3139–3145.
[35] K. Khanafer, K. Vafai, M. Lightstone, Buoyancy-driven heat transfer enhancement in a two-dimensional enclosure utilizing nanofluids, Int. J. Heat Mass Transfer 46 (2003) 3639–3653.
[36] O. Mahian, H.F. Oztop, I. Pop, S. Mahmud, S. Wongwises, Entropy generation between two vertical cylinders in the presence of MHD flow subjected to constant wall temperature, Int. Commun. Heat Mass Transfer 44 (2013) 87–92.
[37] W.S. Daungthongsuk, S. Wongwises, Measurement of temperature-dependent thermal conductivity and viscosity of TiO_2–water nanofluids, Exp. Therm. Fluid Sci. 33 (2009) 706–714.
[38] H.C. Brinkman, The viscosity of concentrated suspensions and solutions, J. Chem. Phys. 20 (1952) 571–581.
[39] W. Yu, S.U.S. Choi, The role of interfacial layers in the enhanced thermal conductivity of nanofluids: a renovated Maxwell model, J. Nanopart. Res. 5 (2003) 167–171.
[40] W.S. Daungthongsuk, S. Wongwises, Comparison of the effects of measured and computed thermophysical properties of nanofluids on heat transfer performance, Exp. Therm. Fluid Sci. 34 (2010) 706–714.
[41] S. Paoletti, F. Rispoli, E. Sciubba, Calculation of exergetic losses in compact heat exchanger passages, ASME AES 10 (1980) 21–29.
[42] M.A.A. Hamad, Analytical solution of natural convection flow of a nanofluid over a linearly stretching sheet in the presence of magnetic field, Int. Commun. Heat Mass Transfer 38 (2011) 487–492.

International Journal of Heat and Mass Transfer 64 (2013) 976–985

Contents lists available at SciVerse ScienceDirect

International Journal of Heat and Mass Transfer

journal homepage: www.elsevier.com/locate/ijhmt

Condensation heat transfer characteristics of R-134a flowing inside the multiport minichannels

Kittipong Sakamatapan [a], Jatuporn Kaew-On [a,b], Ahmet Selim Dalkilic [c], Omid Mahian [d], Somchai Wongwises [a,e,*]

[a] Fluid Mechanics, Thermal Engineering and Multiphase Flow Research Lab. (FUTURE), Department of Mechanical Engineering, Faculty of Engineering, King Mongkut's University of Technology Thonburi, Bangmod, Bangkok 10140, Thailand
[b] Department of Physics, Faculty of Science, Taksin University, Phattalung 93110, Thailand
[c] Heat and Thermodynamics Division, Department of Mechanical Engineering, Yildiz Technical University, Yildiz, Besiktas, Istanbul 34349, Turkey
[d] Young Researchers Club and Elites, Mashhad Branch, Islamic Azad University, Mashhad, Iran
[e] The Academy of Science, The Royal Institute of Thailand, Sanam Suea Pa, Dusit, Bangkok 10300, Thailand

ARTICLE INFO

Article history:
Received 19 January 2013
Received in revised form 9 April 2013
Accepted 10 April 2013

Keywords:
Condensation
Heat transfer characteristics
R-134a
Multiport minichannels

ABSTRACT

In this study, the condensation heat transfer characteristics of R-134a flowing inside multiport minichannels were investigated. The multiport minichannel-tested tubes have 14 channels with a 1.1 mm hydraulic diameter, and eight channels with a 1.2 mm hydraulic diameter were designed as a counterflow tube-in-tube heat exchanger. The experiment was performed with mass fluxes of refrigerant between 340 and 680 kg/m^{2}s, with 15, 20, and 25 kW/m^2 heat fluxes, and saturation temperatures of 35–45 °C. The flow pattern for the experimental data was initially predicted using existing flow pattern maps. It could be noted that the annular flow pattern existed for most of the experimental data. Results showed that the average heat transfer coefficient increased with the increase of vapor quality, mass flux, and heat flux, but decreased as saturation temperature rose. When compared with two correlations obtained from condensation inside the multiport minichannels, the heat transfer coefficient could be predicted within an acceptable range.

© 2013 Elsevier Ltd. All rights reserved.

1. Introduction

In compact condensers for automotive air conditioning systems, multiport minichannels with hydraulic diameters ranging from 0.2 mm to 3 mm have been widely used for many years. Multiport minichannels provide some advantages over conventional tubes, such as more compact size, lower refrigerant charge, lighter weight, and reduced air-side pressure drop. However, sound understanding about condensation heat transfer in multiport minichannels needs more attention.

The few available studies on condensation heat transfer in minichannels are summarized as follows: An experimental study of R-12 in small hydraulic diameter, flat extruded aluminum tubes was done by Yang and Webb [1]. Two internal geometries were tested; one set of tubes had a plain inner surface, and the other had microfin and a 0.2 mm. height. The heat transfer coefficient for water-side flow in the annulus was determined by the modified Wilson plot method. It was determined that the condensation heat transfer coefficient rises when heat flux is increased to the 0.2 power. This result showed agreement with the Aker [2] correlation, except at high mass flux. In addition, the authors proposed that for vapor quality greater than 0.5, surface tension force affects the condensation heat transfer coefficient at low mass flux.

The condensation of R12 and R134a in extruded microchannels having a respective hydraulic diameter of 1.41 and 1.56 mm, with 0.2 and 0.3 mm depth of microfin, was also studied by Yang and Webb [3]. In their study, the condensation heat transfer model was developed through their contribution regarding vapor shear and surface tension.

Yan and Lin [4] determined the condensation heat transfer coefficient of R134a in a small pipe with an inner diameter of 2 mm arranged parallelly. Two copper plates were soldered to the upper and lower ends of the pipe bundle, and coolant tubes were in turn attached to the copper plate, which acted as a heat sink. The result showed a corresponding increase in the condensation heat transfer coefficient with increases to the mass flux in the high vapor quality region, but only slight influence in the low vapor quality region. The condensation heat transfer coefficient was lower when a higher heat flux was swapped for the given mass flux except in the low vapor quality region, and it also decreased as the saturation tem-

* Corresponding author at: Fluid Mechanics, Thermal Engineering and Multiphase Flow Research Lab. (FUTURE), Department of Mechanical Engineering, Faculty of Engineering, King Mongkut's University of Technology Thonburi, Bangmod, Bangkok 10140, Thailand. Tel.: +66 2 470 9115; fax: +66 2 470 9111.
E-mail address: somchai.won@kmutt.ac.th (S. Wongwises).

0017-9310/$ - see front matter © 2013 Elsevier Ltd. All rights reserved.
http://dx.doi.org/10.1016/j.ijheatmasstransfer.2013.04.020

Nomenclature

A	surface area (m^2)
A_c	cross section area (m^2)
C_p	specific heat at constant pressure (kJ kg^{-1} K^{-1})
d_h	hydraulic diameter (m)
G	mass flux (kg m^{-2} s^{-1})
h	heat transfer coefficient (W m^{-2} K^{-1})
i	enthalpy (kJ kg^{-1})
k	thermal conductivity (W m^{-1} K^{-1})
LMTD	Log mean temperature difference (°C)
$\dot{m}$	mass flow rate (kg s^{-1})
N	number of channels
P	pressure (kPa)
Q	heat transfer (kJ)
$\dot{Q}$	heat transfer rate (kW)
Q''	heat flux (kW m^{-2})
Re	Reynolds number, $\mathrm{Re} = \frac{Gd}{\mu}$
T	temperature (°C)
U	overall heat transfer coefficient (Wm^{-2} K^{-1})
x	vapor quality

Greek letters

ΔP	pressure drop (kPa m^{-1})
β	aspect ratio
μ	dynamic viscosity (Pa-s)
α	void fraction
ρ	density (kg m^{-3})
σ	surface tension (N m^{-1})
δ	wall thickness (m)

Subscripts

avg	average
c	cross section
cir	circular
i	inner
in	inlet
l	liquid
m	mean
v	vapour
o	outter
out	outlet
rec	rectangular
ref	refrigerant
sat	saturation
t	tube
TS	test section
W	water
Wall	wall

perature was increased. Their results also indicated that the condensation heat transfer coefficient for conventional tubes was about 10% lower than that for small tubes. Finally, the correlations for predicting stratified and annular flow were also developed from this work.

Apart from that, Wang et al. [5] also investigated the condensation of R134a in a rectangular multiport with a hydraulic diameter of 1.46 mm, 10 channels at 61.5–66 °C over a mass flux range of 75–750 kg/m^2s. Flow visualization also was conducted. Results showed that the stratified or wavy flow occurred, and the heat transfer coefficient was independent of vapor quality at low mass flux. At the same time, the flow pattern was annular, and vapor quality and mass flux had strong effects on the heat transfer coefficient at high mass flux. Their annular flow data was found to agree most with the Aker [2] correlation, while their stratified data agreed best with the correlation from Jaster and Kosky [6].

Koyama et al. [7] studied the condensation of pure refrigerant R134a in two multiport extruded tubes having eight channels in 1.1 hydraulic diameter and 19 channels in 0.8 hydraulic diameter. They used heat flux sensors to measure the local heat transfer coefficient for greater accuracy, then used the temperature rising within the coolant for the Wilson plot method. Their tests were conducted over the range of $100 < G < 700$ kg/m^2s at 60 °C. The researchers also proposed combining convective and film condensation terms. While the individual annular and stratified terms were obtained from Haraguchi's [8] correlation, their two-phase multiplier was estimated using the correlation from Mishima and Hibiki [9].

Kim et al. [10] compared the results of R410A and R22 for mass flux between 200 and 600 kg/m^2s, as well as heat flux between 5 and 15 kW/m^2, at 45 °C. Their work was conducted similarly to that of Yang and Webb [1]. The heat transfer coefficient of R410A is slightly higher than that of R22 for the smooth tube, but the reverse occurs in the case of microfin. They mentioned that the greater surface tension drainage and heat transfer were caused by the 2.7 times lower Webber number of R22 compared to R410A. The use of Webb et al. [11] correlation for smooth tubes and the modified Yan and Webb [1] correlation for microfin were referenced in this work.

The investigation of heat transfer coefficients and pressure drops during condensation of R134a and R410A in a multiport minichannel with a hydraulic diameter of 1.4 mm was done by Cavallini et al.[12]. For heat transfer coefficients, they compared their data with correlations from Aker [2], Moser et al. [13], Zhang and Webb [14], Cavallini et al. [15], Wang et al. [5]., and Koyama et al. [7]. Based on this, their data under-predicted correlations at high mass flux. They attributed this to the flow patterns in their experiment, since they involved mist flow at high mass flux, whereas the compared results were for annular flow in conventional tubes.

Additionally, comparison of the new refrigerant R1234ze (E) in vertical multiport minichannels of 1.45 mm hydraulic diameter with R1134a and 236fa was presented by Park et al. [16]. For mass flux of 50–260 kg/m^2s, heat flux of 1–62 kW/m^2, and saturation temperature of 25–70 °C, the condensation heat transfer coefficient showed the expected increase as the vapor quality and mass flux increased, and as saturation temperature decreased. The heat flux had no effect on the heat transfer coefficient, and the heat transfer coefficient of R1234ze (E) appeared relatively similar to R236fa but was lower than R134a's by about 15–25%. The agreement was poor when compared to available horizontal correlations. Finally, a developed heat transfer correlation, in terms of force convection and gravity, resulted from this work.

Information on the condensation heat transfer in multiport minichannels is still limited, and there remains room for further research. Especially, most of the researchers have studied only very specific parameters. Moreover, some results in the literature have shown different effects. The present study's main objective is to investigate the effects of all of the involved parameters for condensing flow, including mass fluxes, heat fluxes, saturation temperature, and vapor quality. The resulting data, which have never before appeared in open literature, are presented here.

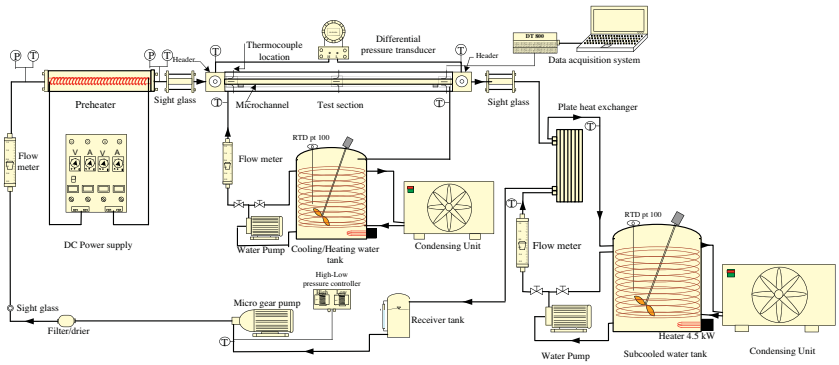

Fig. 1. Schematic diagrams of the experimental apparatus.

2. Apparatus and method

The schematic diagram of the experimental apparatus is presented in Fig. 1. It should be noted that this apparatus was also used for flow boiling heat transfer study in the multiport minichannel [17,18]. The main components of the system consisted of a test section, refrigerant loop, cooling water loop, sub-cooling loop, and data acquisition system.

For the refrigerant circulating loop, as shown in Fig. 1, a gear pump sends liquid refrigerant, with its flow rate regulated by an inverter, through a filter and dryer, refrigerant flow meter, preheater, sight glass tube, test section, and plate heat exchanger. From there, it is then re-circulated, collected in a receiver tank, and returned to the refrigerant gear pump to complete the cycle. The quality at the inlet of the test section is controlled by the pre-heater. A DC power supply is used to power the pre-heater, which can be controlled by adjusting the supply voltage and current. The desired inlet quality is controlled to about 0.1–0.9 before the refrigerant enters the test section. After leaving this area, the vapor refrigerant then condenses in the plate heat exchanger by transferring its heat to the sub-cooling water loop. Instruments are installed at various positions, as clearly shown in Fig. 1, to monitor the refrigerant's state. All of the signals from the thermocouples and pressure transducer are collected by a data acquisition.

Fig. 2 presents a schematic of the test section for this study. The test section is designed as a counter flow tube-in-tube heat exchanger. The refrigerant side is an aluminium rectangular multiport minichannels having 14 channels in 1.11 mm hydraulic diameter and 8 channels in 1.2 mm hydraulic diameter. The cooling water side is made from transparent acrylic, 12 mm thick, and designed as a rectangular channel. It is used to supply heat flux to the tested tubes. The photographs and details of these test sections are presented in Fig. 3 and Table 1, respectively. In addition, the inlet and outlet saturation temperatures are measured by T-type thermocouples installed at the inlet and outlet points of the test section header. For measuring the pressure drop across the section, a differential pressure transducer is installed at the other side of header. The length between the pressure taps is 250 mm. The accuracy of differential pressure drop is ±0.25% of full scale, or ±0.125 kPa. Sixteen well-calibrated thermocouples are installed at four points along the multiport minichannels, both top and bottom, to measure the wall temperature. The thermocouples are also installed at inlet and outlet of the water channel to measure the inlet and outlet cooling water temperatures. Rubber foam with 0.04 W/m K of thermal conductivity provides thermal insulation for this section. The refrigerant flow meter is a variable-area type. The flow meter is specially calibrated in the range of 0.2–1.8 LPM for R134a by the manufacturer. Details of the test conditions are presented in Table 2. The uncertainties of measured quantities and calculated parameters calculated from the root mean sum square method are shown in Table 3.

3. Data reduction

Data reduction for the measured results was done using the methods outlined below.

The vapor quality of the refrigerant R134a at the inlet of test section is calculated as follows

$$x_{TS,in} = \frac{i_{TS,in} - i_{l@TS,in}}{i_{lv@TS,in}} \tag{1}$$

where $i_{l@TS,in}$ is the enthalpy of saturated liquid refrigerant based on the temperature at the test section inlet, and $i_{lv@TS,in}$ is the enthalpy of vaporization based on the temperature at the test section inlet, and $i_{TS,in}$ is the refrigerant enthalpy at the test section inlet which is given by

$$i_{TS,in} = i_{ph,in} + \frac{\dot{Q}_{lat}}{\dot{m}_{ref}} \tag{2}$$

where $i_{ph,in}$ is the enthalpy of the liquid refrigerant at the preheater inlet, $\dot{m}_{ref}$ is the mass flow rate of the refrigerant, $\dot{Q}_{lat}$ is the latent heat transfer rate in the pre-heater

$$\dot{Q}_{lat} = \dot{Q}_{ph} + \dot{Q}_{sen} \tag{3}$$

where $\dot{Q}_{ph}$ is the electrical power from a heater to the refrigerant flowing through the pre-heater, $\dot{Q}_{Sen}$ is the sensible heat transfer rate in the pre-heater which is defined as

$$\dot{Q}_{ph} = (VI)_{@ph} \tag{4}$$

and

$$\dot{Q}_{sen} = \dot{m}_{ref} c_{ref} (T_{ph,out} - T_{ph,in}) \tag{5}$$

The vapor quality at the test section outlet is determined from

$$x_{TS,out} = \frac{i_{TS,out} - i_{l@TS,out}}{i_{lv@TS,out}} \tag{6}$$

where $i_{TS,out}$ is the refrigerant enthalpy at the test section outlet, $i_{l@TS,out}$ is the enthalpy of saturated liquid refrigerant based on the temperature of the test section outlet, and $i_{lv@TS,out}$ is the enthalpy of vaporization. As a consequence, the enthalpy of the refrigerant flow at the test section outlet can be determined from

$$i_{TS,out} = i_{TS,in} + \frac{\dot{Q}_{TS}}{\dot{m}_{ref}} \tag{7}$$

where $\dot{Q}_{TS}$ is obtained from the heat transferring from the refrigerant to the cooling water

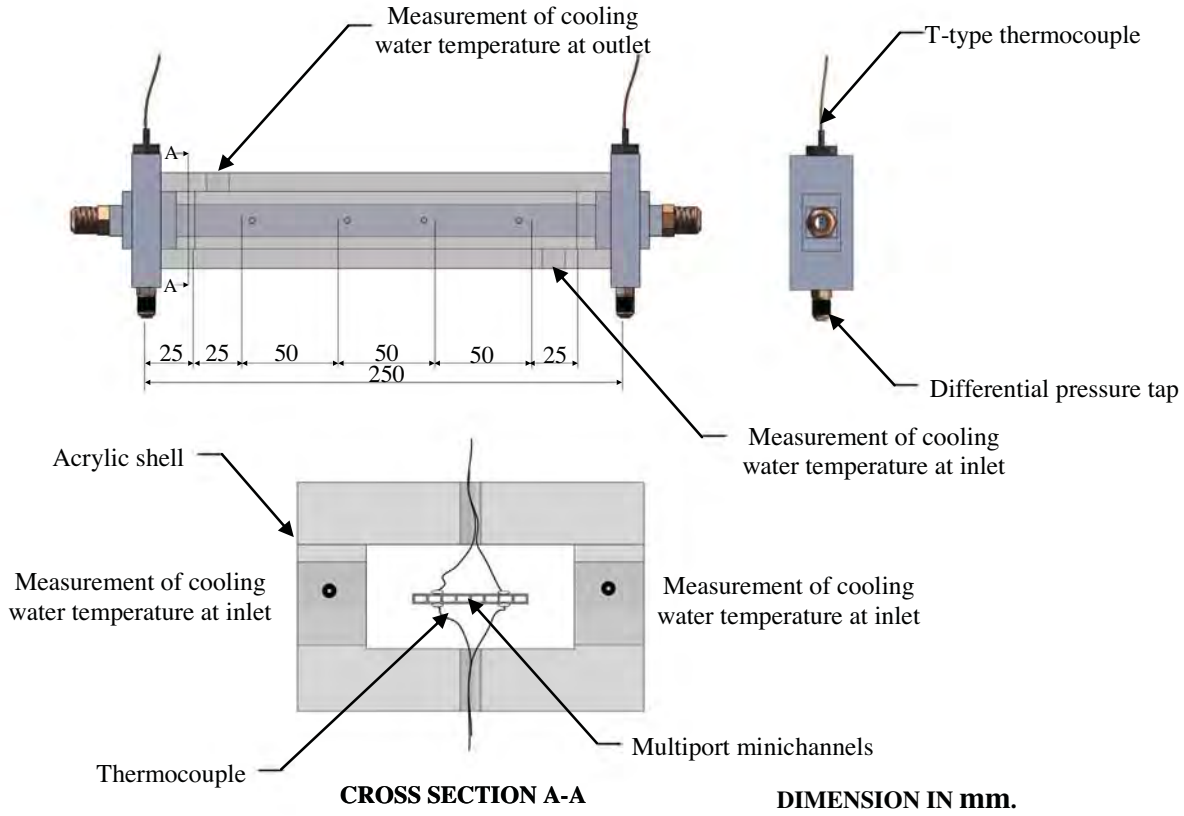

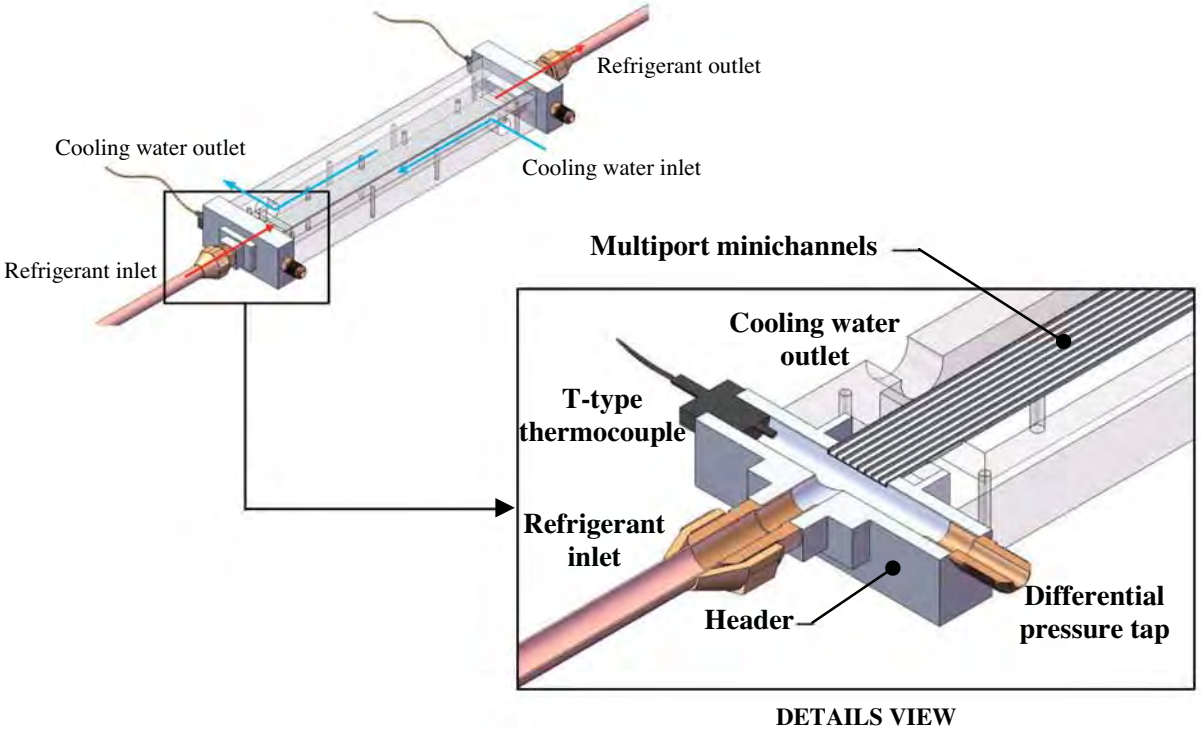

Fig. 2. Schematic diagram of the test section.

Fig. 3. Photographs of cross section of the multiport minichannels: (a) d_h = 1.1 mm, n = 14, (b) d_h = 1.2 mm, n = 8.

The log mean temperature difference (LMTD) method is used to calculate the overall heat transfer rate as follows:

$$\dot{Q} = UA \cdot LMTD \tag{8}$$

Here, U is the overall heat transfer coefficient, A is the surface area base on the outside surface of multiport minichannel, and LMTD is the log mean temperature difference. LMTD is defined this way:

$$LMTD = \frac{(T_{ref,in} - T_{w,out}) - (T_{ref,out} - T_{w,in})}{\ln\left(\frac{T_{ref,in} - T_{w,out}}{T_{ref,out} - T_{w,in}}\right)} \tag{9}$$

T_{ref} and T_w are the refrigerant and water temperatures, respectively.

Considering the test section as present in Fig. 2, and assuming no heat loss from surroundings, the heat transfer rate from refrigerant to cooling water as it passes the wall of the multiport minichannels can be calculated as follows:

$$\dot{Q} = \dot{m}_w Cp_w (T_{w,out} - T_{w,in}) = \dot{m}_{ref} (i_{ref,in} - i_{ref,out}) \tag{10}$$

Here, $\dot{Q}$ is the heat transfer rate, $\dot{m}_w$ and $\dot{m}_{ref}$ are the mass flow rate of the coolant water and refrigerant, respectively, and $i_{ref,in}$ and $i_{ref,out}$ represent the enthalpy at the respective inlet and outlet points of the test section. Finally, the total resistance of the multiport minichanels can be expressed this way:

$$\frac{1}{UA} = \frac{1}{h_o A_o} + \frac{\delta_t}{k_t A_m} + \frac{1}{h_i A_i} \tag{11}$$

The outside heat transfer coefficient, h_o, can be calculated from the following equation:

$$h_o = \frac{\dot{Q}}{A_o (T_{wall,avg} - T_{w,avg})} \tag{12}$$

where A_o is the outer surface area of the multiport minichannels, $T_{w,avg}$ is the average water temperature measured at the inlet and outlet of the water side, and $T_{wall,avg}$ refers to the average wall temperatures. $T_{wall,avg}$ can be calculated by the following equation:

$$T_{wall,avg} = \frac{1}{N}\sum_{i=1}^{N} T_{wall,i} \tag{13}$$

$T_{wall,i}$ as expressed above is the local wall temperature at each section of the multiport minichannels.

From Eq. (4), the inside heat transfer coefficient can be calculated by:

$$\frac{1}{h_i A_i} = \frac{1}{UA} - \frac{1}{h_o A_o} - \frac{\delta_t}{k_t A_m} \tag{14}$$

The inside heat transfer coefficient or the refrigerant side heat transfer coefficient is h_i. A_i is the inside surface area and can be calculated by:

Table 2
Experimental conditions.

Refrigerant	R134a
Hydraulic diameter (mm)	1.1 and 1.2
Number of channels, N	14 and 8
Mass flux (kg/m^{2}s)	340–680
Heat flux (kW/m^2)	15–25
Saturation temperature (°C)	35–45

Table 3
Uncertainties of measured quantities and calculated parameters.

Parameter	Uncertainty
Temperature	±0.1
Mass flow rate of refrigerant	±0.5%
Heat transfer rate of test section	±14%
Average heat transfer coefficient	±19%
Average quality	±8%

$$A_i = [2n_{rec}(a+b) + n_{cir}(a+\pi b)]L \tag{15}$$

In this equation, a is height of the channel, b is the width of the channel, n_{rec} is the number of rectangular channel, n_{cir} is the number of the half-circular channel, and L is the length of the test section.

4. Results and discussion

4.1. Flow pattern

It was expected that the refrigerant's channel flow pattern will influence the mechanism of heat transfer during the condensation process. Therefore, the flow patterns for the present experimental data were identified using the existing flow pattern map proposed by Soliman [19]. The annular-wavy and the mist-annular transition criterion based on experimental data from many different sources were also proposed by Soliman [19]. The data include steam, R12, and R113 flowing inside tubes with hydraulic diameter of 4.8–15.9 mm at the saturation temperature of 28–110 °C during condensation process. This flow pattern map has often been used in the condensation study. The flow pattern plotted on the Soliman flow pattern map [19] is shown in Fig. 4. Most of the data points lie between the wavy and the intermittent/annular transition and annular/annular mist transition lines, while very few data points fall into the wavy flow region.

The mini-scale flow pattern map was developed by Coleman and Garimella [20,21] and Garimella [22]. They conducted the condensation flow visualization of R134a in nine tubes with different cross-sections for hydraulic diameters between 1 and 4.91 mm under the mass flux ranging between 150 and 750 kg/m^{2}s. In their study, four major flow regimes including annular, intermittent, wavy, and dispersed flow patterns were found. The present results are plotted on this flow pattern map, as show in Fig. 5. Most of current experimental data fall in the annular film and mist flow pattern regions, except the results obtained at low vapor quality, which fall into the plug/slug and annular film flow regions.

Table 1
The details of multiport tested channels.

Test No.	Hydraulic diameter (mm)	Number of channel	Channel width (mm)	Channel height (mm)	Aspect ratio	Outer surface (mm^2)
1	1.1	14	1	1.25	1.25	5797.5
2	1.2	8	1.8	0.9	0.5	6171

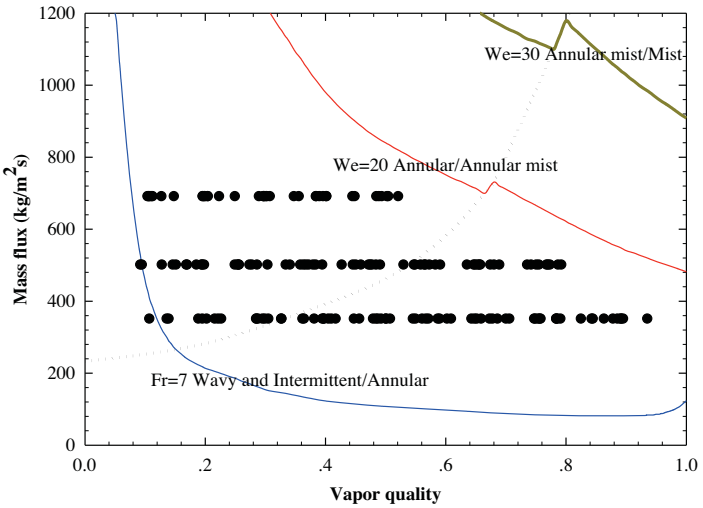

Fig. 4. Flow pattern prediction by Soliman flow pattern map [19].

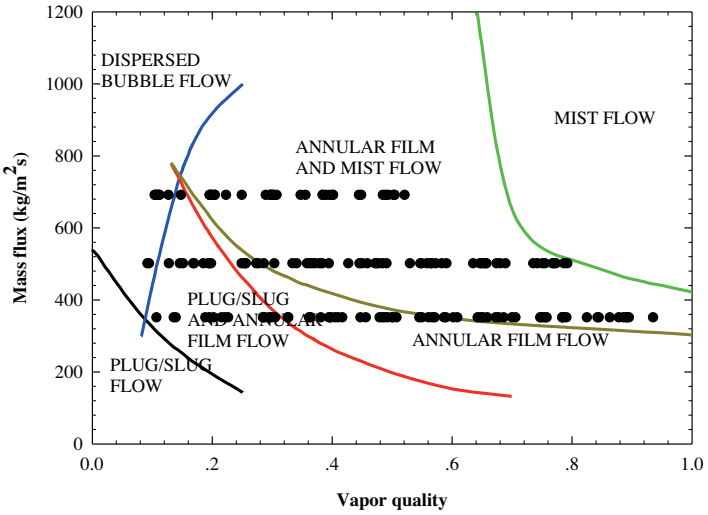

Fig. 5. Flow pattern prediction by Coleman and Garimella [20,21] and Garimella [22].

From two existing flow pattern maps of this study, it can be concluded that most of the presently available experimental data are for annular flow, and this can be considered as a flow mechanism for heat transfer during the condensation flow process.

4.2. Average heat transfer coefficient

The effects of mass flux, heat flux, saturation temperature, and vapor quality on the average heat transfer coefficients of R134a during condensation in multiport minichannels were examined and discussed in this study. Results were obtained for three different mass fluxes in the range of 340–680 kg/m^{2}s, heat fluxes from 15 to 25 kW/m^2, and saturation temperatures of 35, 40, and 45 °C over the vapor quality range.

Fig. 6 depicts the variation in the average heat transfer coefficient, with the vapor quality of R134a in multiport minichannels at a saturation temperature of 40 °C and heat flux of 20 kW/m^2 for different mass fluxes from 340 to 680 kg/m^{2}s. We found that the average heat transfer coefficient decreased as condensation proceeded, meaning, it corresponded to a decrease in vapor quality. At high vapor quality, the velocity of the vapor and liquid phases is high; shear stress at the interface between the vapor and liquid film is higher than that at low vapor quality. More turbulence is caused by increases in shear stress, which lead to a corresponding increase in the heat transfer coefficient. Furthermore, Fig. 6 also demonstrates that the average heat transfer coefficients increase according to the increases in mass flux. The dependence of mass flux on heat transfer coefficient suggests that the contribution of forced convective heat transfer is dominant.

The effects of heat flux on average heat transfer coefficient at heat fluxes of 15, 20, and 25 kW/m^2 at mass flux of 340 kg/m^{2}s and saturation temperature of 40 °C are presented in Fig. 7. Increasing the heat flux means the average heat transfer coefficient also increase. The authors suggest that the increase in heat flux also changes the momentum of the liquid and vapor phase, which causes the observed increase in the heat transfer coefficient. These trends are quite similar to that found by Yang and Webb [1].

By changing the system saturation temperature and keeping mass flux and heat flux constant, the effect of saturation temperature on the average heat transfer coefficient can be investigated. Fig. 8 shows the effect of saturation temperature at mass flux of 340 kg/m^{2}s and heat flux of 25 kW/m^2. The experiment indicates that the average heat transfer coefficient at a saturation temperature of 35 °C is higher than that of 40 or 45 °C. This is related to

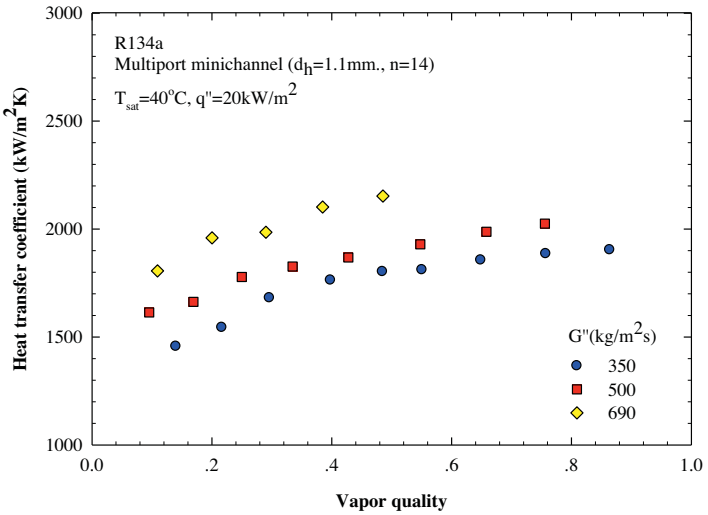

Fig. 6. The effect of mass flux on average heat transfer coefficient.

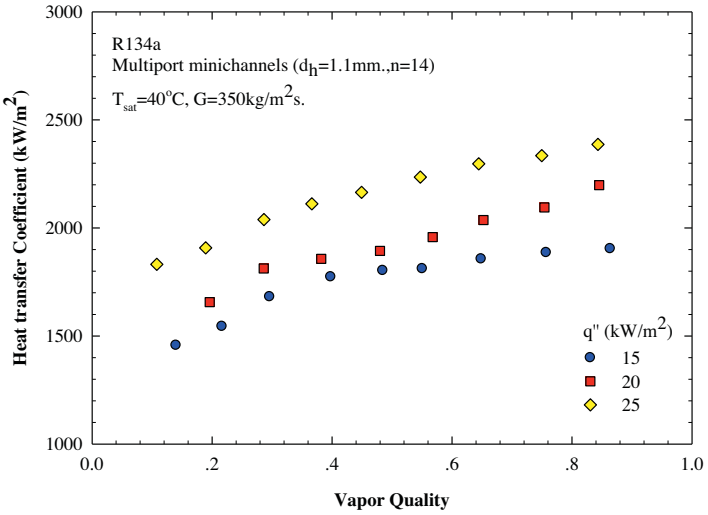

Fig. 7. The effect of heat flux on average heat transfer coefficient.

the properties of R134a, since the thermal conductivities of liquid film for R134a at 35 °C are higher than those of R134a at 40 °C and at 45 °C, respectively.

In addition, the measured average heat transfer coefficients of two different numbers of channels, as tested with multiport mini-channels in similar experimental conditions, are compared in this study. The results of two are presented in Fig. 9, shows that the heat transfer coefficients for the multiport mini-channels No. 1 are higher than those for the multiport mini-channels No. 2 about 5–15%. The higher velocity of refrigerant in the multiport mini-channels No. 1, which has smaller hydraulic diameter, causes the liquid film to become thinner which results in higher heat transfer coefficient.

4.3. Comparison with existing correlations

The experimental data were compared against existing correlations to predict the condensation heat transfer coefficient. Two condensation heat transfer coefficient correlations obtained from the data taken from multiport mini-microchannels as shown in Table 4 were proposed by Webb et al. [11] and Koyama et al. [23].

The first comparison, depicted in Fig. 10, shows the experimental data was predicted by Webb et al. correlation[11]. This was developed for a copper round tube and multiport minichannel with a hydraulic diameter of 2.13 mm. We found that the agreement between the experimental results and our prediction was quite clear; about 90% of the data points fell within a ±25% error margin.

Comparison of the heat transfer coefficient obtained from the present experiment with those calculated by the Koyama et al. [23] correlation which was modeled by the combination of convective and film condensation term of R134a in two multiport minichanels, is shown in Fig. 11. It can be seen from this figure that 72% of the data fall within ±40% of the correlation.

5. Conclusion

This study mainly examined the heat transfer characteristics of R134a as it flowed inside multiport minichannels. Tests covering several conditions were conducted; mass fluxes ranged from 340 to 680 kg/m^{2}s, heat fluxes, 15 to 25 kW/m^2, and saturation temperature, 35 to 45 °C. From these experiments, we can make the following conclusions.

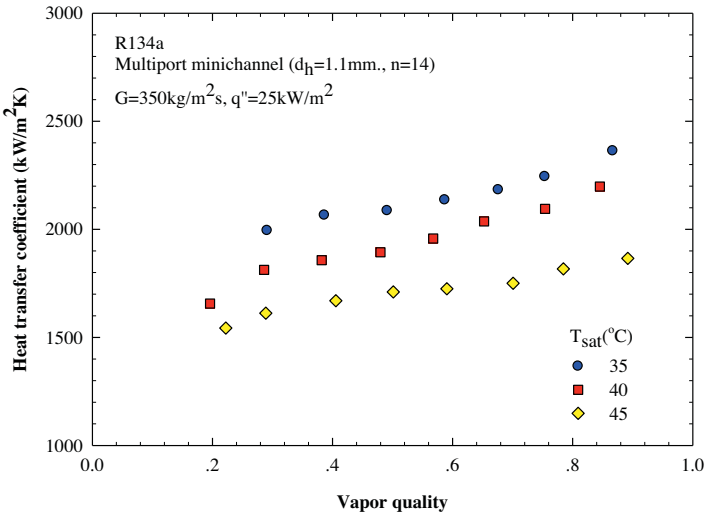

Fig. 8. The effect of saturation temperature on average heat transfer coefficient.

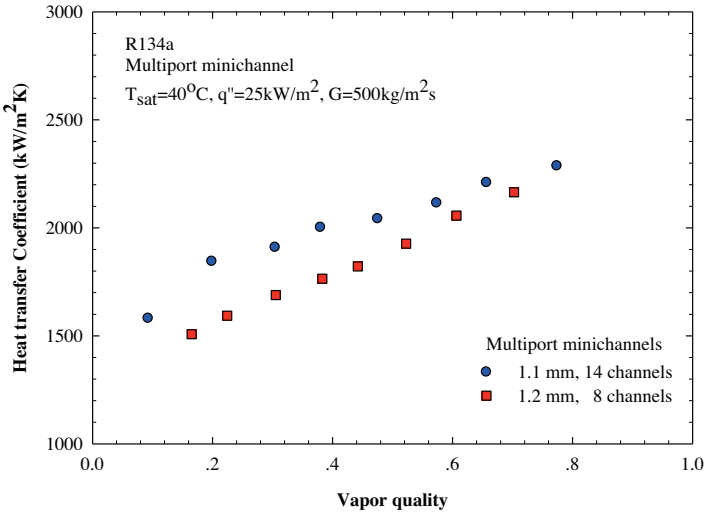

Fig. 9. Comparison of heat transfer coefficient between multiport minichannels No. 1 and multiport minichannels No. 2.

Table 4
Correlations from literature.

No	Author(s)	Correlation	Conditions
1	Webb et al. [11]	$h = h_f(1.31\mathrm{Pr}_f^{-0.815}(R^+)^A\mathrm{Re}_f^B$ where $R^+ = 0.994\mathrm{Re}_{eq}^{7/8}, A = 0.126Pr_f^{-0.448}, B = -0.113Pr_f^{-0.563}$ $\mathrm{Re}_{eq} = \left[0.5\frac{d_h^3}{f_{f,eq}}\frac{\rho_l}{\mu_l^2}\left(\frac{dP}{dz}\right)_f\right]^{0.5}$ and $f_{l,eq} = 0.079\mathrm{Re}_{eq}^{-0.25}$	Circular tube, d_h = 3.25 mm. and Multiport minichannels, d_h = 2.13 mm., R134a
2	Koyama et al. [23]	$h = \frac{k_f}{d_h}(Nu_F^2 + Nu_B^2)^{1/2}$ Where $Nu_F = 0.0112\mathrm{Pr}_f^{1.37}(\frac{\phi_g}{X_{tt}})\mathrm{Re}_f^{0.7}$ with $\mathrm{Re}_f = \frac{G(1-x)d_h}{\mu_f}$ $Nu_B = 0.725(1 - e^{-0.85\sqrt{Bo}})H(\varepsilon)\left(\frac{Ga_f\mathrm{Pr}_f}{Ph_f}\right)^{1/4}$ With $H(\varepsilon) = \varepsilon + [10(1-\varepsilon)^{0.1} - 8.9]\sqrt{\varepsilon}(1-\sqrt{\varepsilon})$ $Ga = \frac{g\rho_f^2 d_h^3}{\mu_f^2}$, $Ph_f = \frac{c_{pf}(T_r - T_w)}{h_{fg}}$ and $Bo = \frac{d^2 g(\rho_f - \rho_g)}{\sigma}$	Local heat transfer coefficient, Two multiport minichannel d_h = 0.8 and 1.1 mm, R134a

There were two flow pattern maps used for experimental data plotting. The first is a well-known flow pattern map for condensation research by Soliman [19]; the other is maps flow in minichannels and was designed by Coleman and Garimella [20,21] and Garimella [22]. Most of the plotted data points were located in the region of annular flow regime. When we consider the trend of these plotted results, the average heat transfer tends to increase along with average vapor quality, mass flux, and heat flux. On the other hand, the average heat transfer tends to decrease with increases in saturation temperature. Apart from that, when the hydraulic diameter is decreased from 1.2 mm to 1.1 mm under the same testing conditions, the average heat transfer coefficients

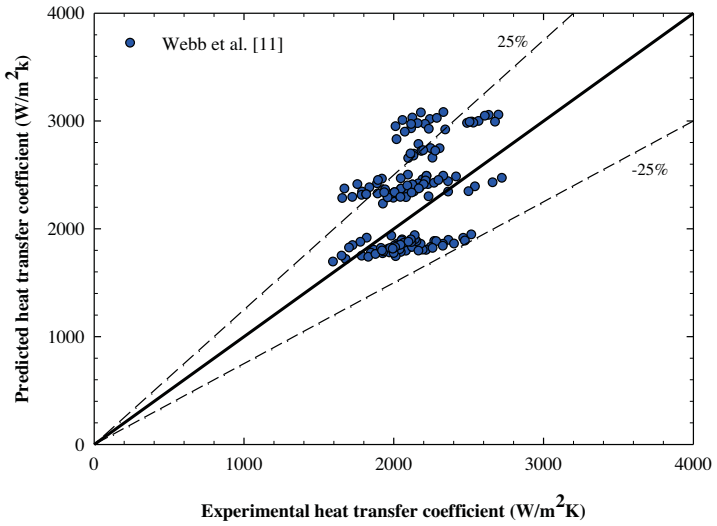

Fig. 10. Comparison of experimental average heat transfer coefficient with Webb et al. [11] correlation.

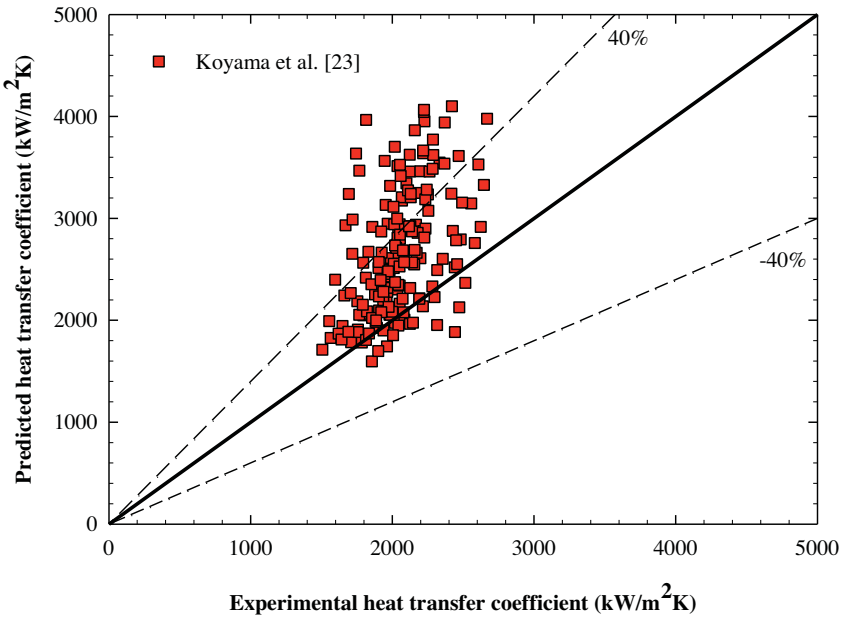

Fig. 11. Comparison of experimental average heat transfer coefficient with Koyama et al. [23] correlation.

increase by about 5–15%. Using existing correlations by Webb et al. [11] and Koyama et al. [23] the experimental data can be predicted with a deviation of less than 40%.

Acknowledgements

The authors would like to express their appreciation to the Thailand Research Fund, the Office of the Higher Education Commission and the National Research University Project for providing financial support for this study. The third and fourth authors would like to thank the fifth author for the supporting during their research at King Mongkut's University of Technology Thonburi.

References

[1] C.Y. Yang, R.L. Webb, Condensation of R-12 in small hydraulic diameter extruded aluminium tubes with and without micro-fins, Int. J. Heat Mass Transfer 39 (1996) 791–800.
[2] W.W. Akers, H.A. Deans, O.K. Crosser, Condensation heat transfer within horizontal tubes, Chem. Eng. Process Symp. Ser. 55 (1959) 171–176.
[3] C.Y. Yang, R.L. Webb, A predicted model for condensation in small hydraulic diameter tubes having axial micro-fins, J. Heat Transfer 119 (1997) 776–782.
[4] Y.Y. Yan, T.F. Lin, Condensation heat transfer and pressure drop of refrigerant R-134a in a small pipe, Int. J. Heat Mass Transfer 42 (1999) 697–708.
[5] W.W. Wang, T.D. Radcliff, R.N. Christensen, A condensation heat transfer correlation for millimetre-scale tubing with flow regime transition, Exp. Therm. Fluid Sci. 26 (2002) 473–485.
[6] H. Jaster, P.G. Kosky, Condensation in mixed flow regime, Int. J. Heat Mass Transfer 19 (1976) 96–99.
[7] S. Koyama, K. Kuwahara, K. Nakashita, K. Yamamoto, An experimental study on condensation of refrigerant R134a in multi-port extruded tube, Int. J. Refrigerant 24 (2003) 425–432.
[8] H. Haraguchi, S. Koyama, T. Fujii, Condensation of refrigerants HFC22, HFC134a, and HCFC123 in horizontal smooth tube (2nd Report, Proposal of Empirical Expressions for the Local Heat Transfer Coefficient), Trans. JSME (B) 60 (1994) 245–252.
[9] K. Mishima, T. Hibiki, Effect of inner diameter on some characteristics of air–water two-phase flows in capillary tubes, Trans. JSME (B) 61 (1995) 99–106.
[10] N.H. Kim, J.P. Cho, J.O. Kim, B. Youn, Condensation heat transfer of R-22 and R-410A in flat aluminium multi-channel tubes with or without micro-fin, International Journal of Refrigeration 26 (2003) 830–839.
[11] R.L. Webb, M. Zhang, R. Narayanamurthy, Condensation heat transfer in small diameter tubes, in: Proceedings of the 11th International Heat Transfer Conference, Kyongju, Korea 6 (1998) 403–408.

[12] A. Cavallini, D. Del Col, L. Doretti, M. Matkovic, L. Rossetto, C. Zilio, Two-phase frictional gradient of R236ea, R134a, and R410A inside multi-port mini-channels, Exp. Therm. Fluid Sci. 29 (2005) 861–870.
[13] K.W. Moser, R.L. Webb, B. Na, A new equivalent Renolds number model for condensation in smooth tubes, J. Heat Transfer 119 (1997) 776–782.
[14] M. Zhang, R.L. Webb, Correlation of two-phase friction for refrigerants in small-diameter tubes, Exp. Therm. Fluid Sci. 25 (2001) 131–139.
[15] A. Cavallini, G. Censi, D. Del Col, L. Doretti, G.A. Longo, L. Rossetto, Condensation of halogenated refrigerant in side smooth tubes, HVAC R Res. 8 (2002) 429–451.
[16] J.E. Park, F. Vakill-Farahani, J.R. Thome, Experimental study on condensation heat transfer in vertical minichannels for new refrigerant R123ze(E) versus R134a and R236fa, Exp. Therm. Fluid Sci. 35 (2011) 442–454.
[17] J. Kaew-On, K. Sakamatapan, S. Wongwises, Flow boiling heat transfer of R134a in the multiport minichannel heat exchangers, Exp. Therm. Fluid Sci. 35 (2011) 364–374.
[18] J. Kaew-On, K. Sakamatapan, S. Wongwises, Flow boiling pressure drop of R134a in the counter flow multiport minichannel heat exchangers, Exp. Therm. Fluid Sci. 36 (2012) 107–117.
[19] H.M. Soliman, Mist-annular transition during condensation and its influence on the heat transfer mechanism, Int. Multiphase Flow 12 (1986) 277–288.
[20] J.W. Coleman, S. Garimella, Characterization of two-phase flow patterns in small diameter round and rectangular tubes, Int. J. Heat Mass Transfer 42 (1999) 2869–2881.
[21] J.W. Coleman, S. Garimella, Two-phase flow regime transition in microchannel tubes: the effect of hydraulic diameter, ASME HTD 366 (4) (2000) 71–83.
[22] S. Garimella, Condensation flow mechanisms in microchannels: basis for pressure for pressure drop and heat transfer models, Heat Transfer Eng. 25 (2004) 104–116.
[23] S. Koyama, K. Kuwahara, K. Nakashita, Condensation of Refrigerant in multi-port channel, in: Proceedings of the 1st International Conference on Microchannels and Minichannels, Rochester, New York, 193–205.

ANALYSIS OF FLOW THROUGH A DOUBLE-ACTING IMPELLER WITH A STRAIGHT RADIAL BLADES USING CFD

SUTHEP. KAEWNAI[1], SOMCHAI WONGWISES[2]

[1,2]Fluid Mechanics, Thermal Engineering and Multiphase Flow Research Lab. (FUTURE), Department of Mechanical Engineering, Faculty of Engineering, King Mongkut's University of Technology Thonburi, Bangmod, Bangkok 10140, Thailand
Corresponding author: E-mail: Suthep.kae@kmutt.ac.th[1], somchai.won@kmutt.ac.th[2]

Abstract- This study aims to analyze water flow through a centrifugal pump with straight radial blades double-acting impeller using computational fluid dynamics (CFD). The impeller analyzed was designed with the following conditions: a volume flow rate of 33.5 m^3/h, head of 100 m, rotational speed of 2,950 rpm, and specific speed of 9. The first stage began with calculations for various dimensions of double-acting isolated impeller and impeller-collector assembly, followed by three-dimensional drawing and domain specification. In the second stage, grids for the isolated impeller and impeller-collector assembly were generated. In the third stage, the initial conditions and boundary conditions were specified. Finally, the water flow through the isolated impeller and impeller-collector assembly was analyzed using the CFX 13 code to predict the water flow state. A fluid dynamic analysis of the isolated impeller and impeller-collector assembly reveals that the Q-H curve rises continuously toward shutoff as the flow rate is reduced. The results indicate that the total head rise of the isolated impeller is approximately 98.8 m for a 65 mm impeller inlet width and 99.89 m for a 70 mm impeller inlet width. This may be due to reduced circulation between blade passages of impeller. Similar to the isolated impeller, the Q-H curve of the impeller-collector assembly also rises continuously toward shutoff as the flow rate is reduced. The total head rise is reduced to approximately 98 m because of losses in the collector. Concerning the flow in the impeller-collector assembly when Q/Q_{design} is or less than 1.0, the pressure distribution is high at the tongue of collector. Concerning the velocity distribution when Q/Q_{design} is more or less than 1.0, there is circulation or a vortex at the top of the collector.

Keyword- *Double acting, blade, impeller, specific speed*

I. INTRODUCTION

The potential of computational fluid dynamics (CFD) for the design of centrifugal pumps has not been extensively exploited in the pump industry. Many types of pumps continue to be designed using empirical principles and techniques by means of one-dimensional flow analysis or simple tests. These have a limitation in accurate performance prediction and cannot contribute to improvement by considering three-dimensional flow. The key advantage of CFD analysis is that it can be used as a numerical test bed that can minimize the required testing and costs for the development of new products and also offers the support for the design optimization of existing configurations. The applications of CFD in pumps have been studied by a number of researchers [1],[2], [5-8]. M. Asujie et al. [1] performed a 3D-CFD simulation of the impeller and volute of a centrifugal pump with a specific speed of 32 (metric units) using CFX code. A 3D flow simulation for an impeller with structured grids was presented. Muggli et al. [2] showed good agreement between simulation and experimental results.

Although some information is currently available on applying CFD for the prediction of radial flow type impellers, but no researchers have applied it in predicting stability and other features in double-acting impeller with straight radial blades for a centrifugal pump.

A. Overview of double-acting impeller with straight radial blades

According to Croper et al. [3], many processes in the hydrocarbon processing industry require pumps that deliver high heads at low flows. To reach high heads, either the pump has to operate above synchronous speed or the impellers need to have large diameters and very small flow passages. The former solution usually requires gear-driven pumps with inducer-type hydraulics to manage the suction requirements. The latter solution leads to large impellers with narrow passages, which require special casting techniques to reliably reach performance goals. A centrifugal pump with double-acting impeller geometry can avoid these disadvantages.

A double-acting impeller with straight radial blades is shown in Fig. 1. The impeller is used in a single-stage, single-entry centrifugal pump. The head achieved is above 300 m [3], [4]. Nearly identical blades are arranged on both sides of the center rib. The large opening in the center rib near the hub allows half of the fluid to flow to the blades in the rear. The impeller is used for pumps in the range of about $1 < n_q < 10$. The shape of the head capacity, or the Q-H curve, of a centrifugal pump has a major

impact on reliable operation of the pump. A Q-H curve rising continuously toward shutoff as the flow rate is reduced is considered stable. An unstable Q-H curve can be drooping toward shutoff or have a saddle. In a double-acting impeller with straight blades for centrifugal pumps, Q-H curves are stable because of the high head coefficient. Due to the low blade loading, vibrations are very low.

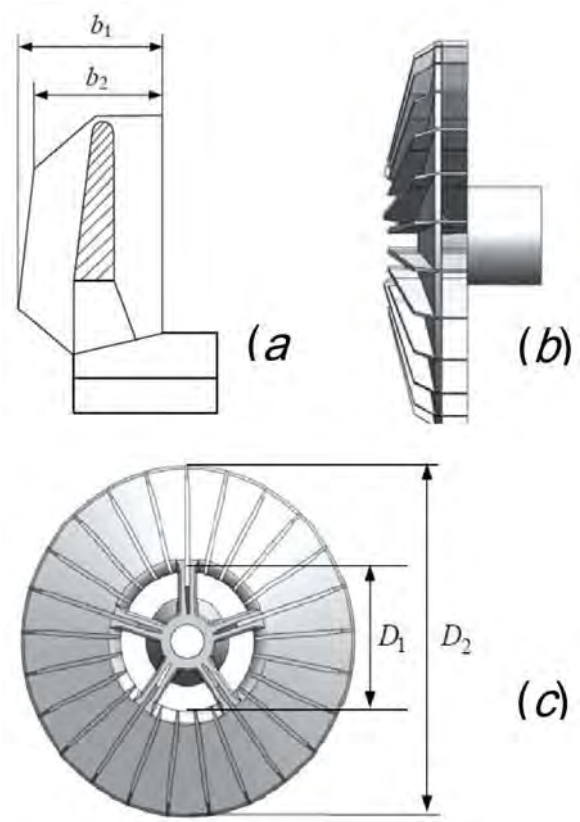

Fig.1. Double-acting impeller with straight radial blades

II. ONE-DIMENSIONAL DESIGN OF THE IMPELLER

Initially, the specifications of the impeller were established. The volume flow rate (Q), total head (H), and rotational speed (n) were defined. The one-dimensional preliminary was focused on the BEP (best efficiency point).

A. Basic equation for impeller design and performance

Specific speed: $$n_q = \frac{n\sqrt{Q}}{H^{3/4}} \quad (1)$$

Head coefficient: $$\psi = \frac{2gH}{u_2^2} \quad (2)$$

Flow coefficient : $$\phi = \frac{C_{2m}}{u_2} \quad (3)$$

Circumferential impeller velocity: $$u = \frac{\pi nD}{60} \quad (4)$$

Impeller width: $$b = \frac{Q}{\pi DC_m} \quad (5)$$

Circumferential component of absolute velocity:

$$C_u = u - \frac{C_m}{tan\,\beta} \quad (6)$$

Simulated total head rise:

$$H_{rise} = \frac{\overline{P_{2total}} - \overline{P_{1total}}}{\rho g} \quad (7)$$

B. Collector design

For this study, the collector is built as a concentric casing followed by a partial volute that discharges into a diffuser. The combined casing is started by designing an annular collector over 180° followed by a volute leading the fluid into the discharge diffuser. Shape of collector is shown in Fig. 2.

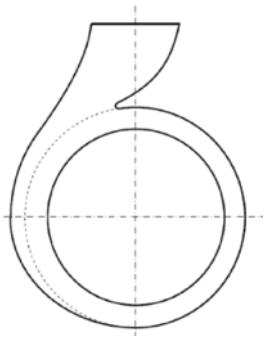

Fig. 2. Shape of collector

III. BASIC MATHEMATICAL EQUATION OF THE MODEL

For three-dimensional incompressible and unsteady flow, the continuity and momentum equations in the rotating coordinate system are as follows:

Continuity equation: $$\frac{\partial \rho}{\partial t} = \vec{\nabla} \cdot \rho \vec{V} \quad (8)$$

Momentum equation:

$$\rho \frac{d\vec{V}}{dt} + \vec{\nabla} P = \rho \vec{g} + \mu\left(\nabla^2 \cdot \vec{V}\right) - 2\rho\vec{\omega} \times \vec{V} - \rho\vec{\omega} \times \left(\vec{\omega} \times \vec{r}\right) \quad (9)$$

IV. ANALYSIS OF 3D IN THE IMPELLER

The analysis for the double-acting impeller with straight radial blades was based on the following design details: a volume flow rate of 33.5 m^3/h, head of 100 m, rotational speed of 2950 1/min, and specific speed of 9. A head coefficient of 1.4 and a flow coefficient of 5.9 x 10^{-3} were established. The analysis starts with grid generation and refinement on a single channel domain of Fig 3. All the grids generated were hexahedral structured grids with approximately 29,870 nodes as shown in Fig.4. The inlet and outlet flow of a single channel of simulation domain were shown in Fig.5. The numerical flow

field calculation was performed using CFX 13 code. The main parameters are presented in Table 1 and the analyzed parameters were shown in Table 2.

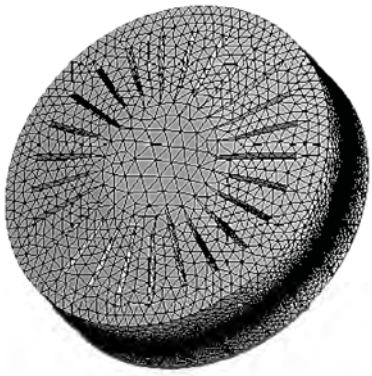

Fig. 3. Domain of impeller

Fig.4. Computational grids for a single channel of the impeller

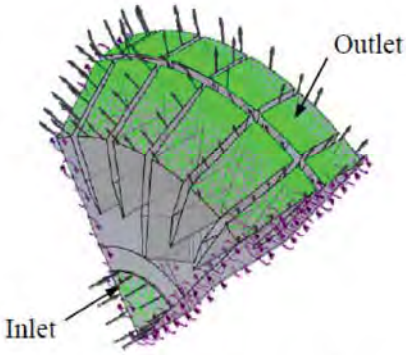

Fig.5. Inlet and outlet flow of a single channel of simulation domain

Table 1: Geometrical parameters of double acting impeller with straight radial blades and collector: $n_q = 9$

Parameter	Value	Description
Impeller		
b_2	60 mm	Impeller outlet width
b_1	65 mm	Impeller inlet width
D_2	230 mm	Impeller outlet Diameter
$\beta_1 = \beta_2$	90 deg	Angle of blade at inlet and outlet
Ns	20	Short blade number
Nl	5	Long blade number
Collector		
D_3	244 mm	Base collector diameter
b_3	75 mm	Collector width

Table 2: Simulation parameters

Parameters	CFX 13
Flow simulation domain	One impeller flow channel
Grid	Structured
Fluid	Water at 25 °C
Inlet	Total pressure = 101325 Pa
Outlet	Mass flow rate
Wall	No slip
Turbulence model	$k-\varepsilon$
Turbulence intensity	5%
Maximum residual convergence	10^{-4} (RMS)

V. RESULTS AND DISCUSSION

Based on this study, the Q-H curve of an impeller can be determined as shown in Fig. 6. The head value determined at the design point is 100 m. Hence, Fig. 6 shows that the total head rise value of 98.80 m is close to the designed head. Fig. 6 shows that the Q-H curve rises continuously toward shutoff as the flow rate is reduced.

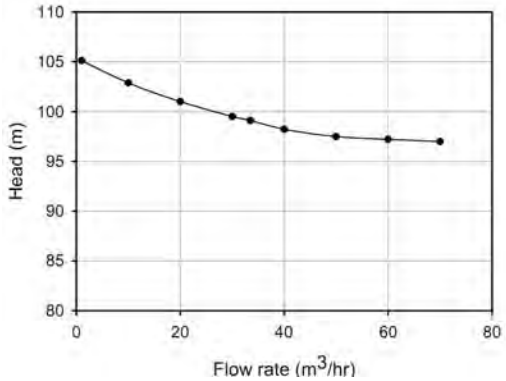

Fig.6. Q-H curve of impeller obtained from simulation

A. Variation of the impeller inlet width

Considering the streamline occured in blade passages of a single channel of impeller with the impeller inlet width of $b_1 = 65$ mm, there is a lot of circulation close to the surface of blades in every blade passages. This circulation causes losses, which leads to reduced the performance of the impeller.

The impeller was re-designed by fixing the values of every parameters and adjusting only the impeller inlet width (b_1). It was found that, when the impeller inlet width (b_1) changes from 65 mm to 70 mm, there is still circulation in every blade passages, but it becomes smaller. The circulation can be observed from streamline occured in a single channel of impeller as shown in Fig. 7 and Fig. 8. It was also found that water does not flow fully in the blade passages. Calculations show that the head at the design point is 99.89 meters.

Figure 9 shows a comparison of the Q-H curves before and after adjusting the impeller inlet width. It can be seen that the adjustment of the impeller inlet width causes reduced circulation in the blade passages and water can flow more fully in the blade passages. Hence, the performance of impeller much better.

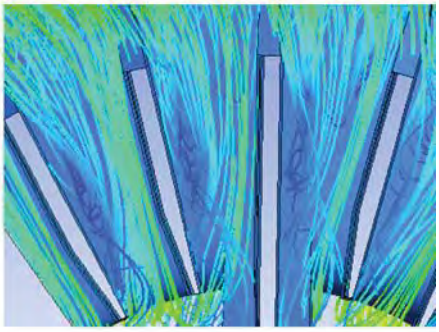

Fig. 7. Streamline at impeller inlet width, b^1=65 mm before refinement

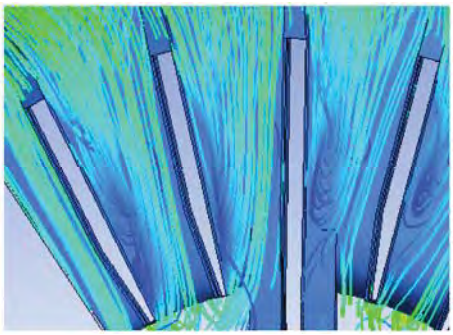

Fig. 8. Streamline at impeller inlet width, b^1=70 mm after refinement

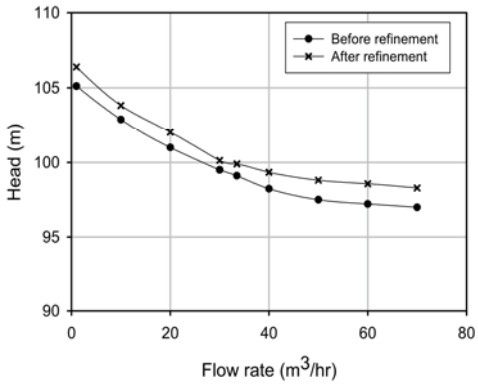

Fig. 9. Q-H Curve before and after impeller refinement

B. Effect of velocity distribution on the blade passages of the impeller

Considering the meridian velocity distribution of the absolute velocity from the hub to the shroud at the impeller inlet (C_{1m}) and outlet (C_{2m}), it was found that the meridian velocity at the impeller inlet and outlet are uniform at both the front side and the rear side as shown in Fig 10 and Fig. 11. However, the meridian velocity at the rear side is less than that at the front side. It is noticeable that the meridian velocity distribution of the absolute velocity at the out let (C_{2m}) at the front side overlaid that at the rear side.

The circumferential component of the absolute velocity from the hub to the shroud at the impeller inlet (C_{1u}) and outlet (C_{2u}) can be observed from Fig. 12 and Fig. 13. It was found that in case of the circumferential component of the absolute velocity at the impeller inlet (C_{1u}) is not equal to zero, this suggests that there is swirl or pre-rotation in the flow at the impeller inlet.

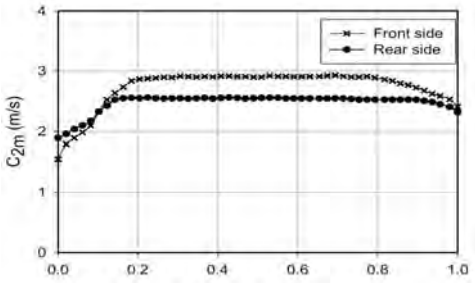

Fig. 10. Meridian component of absolute velocity distribution at the impeller outlet

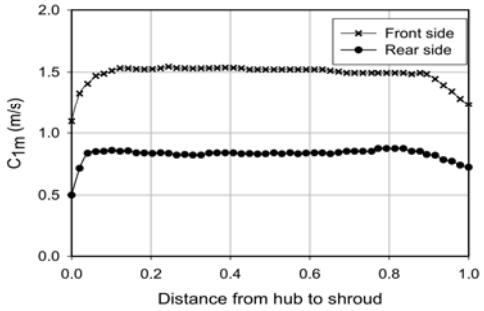

Fig. 11. Meridian component of absolute velocity distribution at the impeller inlet

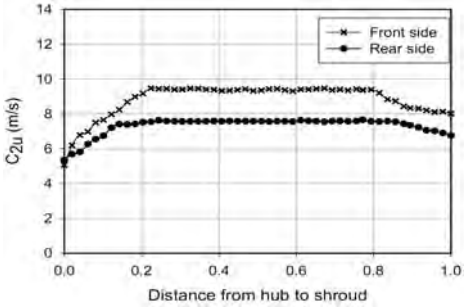

Fig. 12. Circumferential component of absolute velocity distribution at the impeller outlet

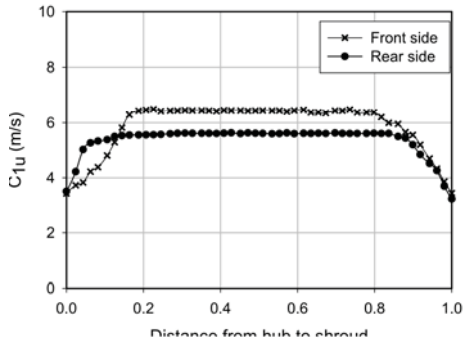

Fig. 13. Circumferential component of absolute velocity distribution at the impeller inlet

C. Impeller-collector 3D flow simulation

A 3D view of the collector is shown in Fig. 14. All the grids of the collector were hexahedral structured grids with approximately 121,848 nodes. The original configuration of the outlet collector was essentially extended for numerical reasons since convergence problems and related flow instabilities are prevented. Swirling flow appeared in the impeller inlet. Therefore, it was necessary to extend the impeller inlet upstream as shown in Fig. 15. Due to the change between the reference frame of the rotating impeller and the static collector, the interaction of the impeller-collector was simulated using the frozen-rotor interface model. The interface between impeller domain and collector domain is shown in Fig. 16.

The simulation parameters for the impeller-collector assembly can be summarized as shown in Table 3. An image of the internal flow inside the impeller-collector assembly given by the simulation enables us to analyze and understand this complex phenomenon. The fluid dynamics calculations for the impeller-collector assembly using CFX 13 code gives the total head rise, which can be used to calculate heads at various flow rates using equation 7 . The Q-H curve can be plotted as shown in Fig. 17. The total head rise at the design flow rate is 98.0 m, which is lower than the head at the design point of 100 m. The Q-H curve rises continuously toward shutoff as the flow rate is reduced, as in the case of the isolated impeller. A change in the Q-H curve cannot be dropping toward shutoff or does not have a saddle characteristic. A comparison of the graphs reveals that the Q-H curve of the impeller-collector assembly is slightly lower than that of the isolated impeller. It should be noted that the flow at both the front side and the rear side of the blades causes the axial thrust to drop.

Figures 18, 19, and 20 show the velocity field and pressure distribution at various Q/Q_{design} values. Figure 18 shows the pressure field at the design point of $Q/Q_{design}=1.0$. It can be seen that the pressure distribution and velocity field around the impeller periphery is uniform. Considering the pressure distribution at a lower point than the design point of $Q/Q_{design}=0.6$ and higher than the design point of $Q/Q_{design}=1.5$, it was found that the pressure near the tongue was slightly higher than the pressure at the design point. The velocity field outside the design point causes a vortex or circulation at the rear side of the diffuser. This could be improved by re-designing the diffuser.

Fig. 14. Domain of collector

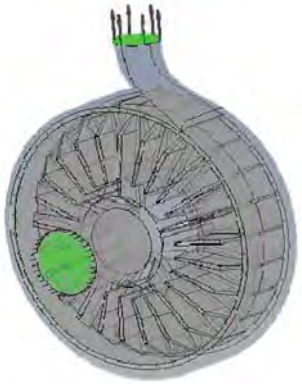

Fig. 15. Extension impeller inlet and collector outlet

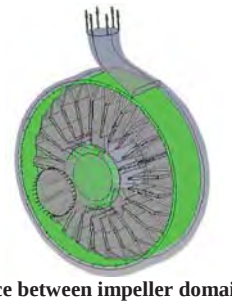

Fig. 16. Interface between impeller domain and collector domain

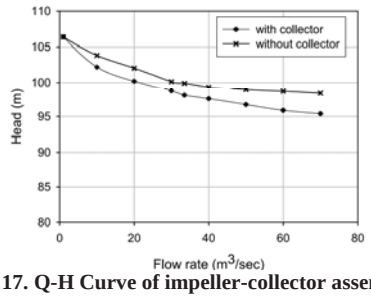

Fig. 17. Q-H Curve of impeller-collector assembly

VI. CONCLUSION

This study analyzed the flow simulation in a double-acting isolated impeller and in an impeller-collector

assembly using CFX 13 code. The study begins with an isolated impeller. The mathematical model used is the $k-\varepsilon$ model with 29,870 nodes on the blade passage. The resulting Q-H has stable characteristics. In the case of the impeller-collector assembly, more computational domains are needed at the impeller inlet and the collector outlet. The interface between the impeller and the extended duct at inlet and between the impeller and the collector is a frozen-rotor model. The Q-H curve has similar stable characteristics as the isolated impeller, with a slightly lower graph due to losses in the collector. The circumferential component of the absolute velocity at the inlet (C_{1u}) is not equal to zero due to the occurrence of pre-rotation or swirl. The analysis of flow in the blade passage shows circulation in nearly every blade passages or channels. However, widening the impeller inlet width reduces the circulation. In the impeller-collector assembly, there is circulation at the rear side of the diffuser when Q/Q_{design} is both lower and higher than 1.0. This study experiments with a double-acting impeller with straight radial blades centrifugal pump that could be manufactured for commercial use as mentioned in references [3] and [4].

ACKNOWLEDGMENT

The present study was supported financially by the Thailand Research Fund, whose guidance and assistance are gratefully acknowledged.

NOMENCLATURE

b_1 : Width of impeller inlet (mm)

b_2 : Width of impeller outlet (mm)

b_3 : Width of collector (mm)

C_{1u} : Circumferential component of absolute velocity at inlet (m/s)

C_{2u} : Circumferential component of absolute velocity at outlet (m/s)

C_{1m} : Meridian component of absolute velocity at inlet (m/s)

C_{2m} : Meridian component of absolute velocity at outlet (m/s)

D_1 : Diameter of impeller at inlet (mm)

D_2 : Diameter of impeller at exit (mm)

D_3 : Base collector diameter

g : Gravitational acceleration (m/s^2)

H : Design head (m)

$H_{rise:}$: Simulated total head rise (m)

Ns : Short blade number

Nl : Long blade number

k : Turbulence kinetics energy

n : Speed (rpm)

n_q : Specific speed (1/min)

-

P_{1total} : Total pressure at impeller inlet (N/m^2)

P_{2total} : Total pressure at impeller outlet (N/m^2)

Q : Volume flow rate (m^3/s)

u : Circumferential impeller velocity (m/s)

β_1 : Angle of blade at inlet (deg)

β_2 : Angle of blade at outlet (deg)

ε : Turbulence eddy Dissipation

-

ρ : Density (kg/m^3)

ω : Angular velocity (rad/s)

ϕ : Flow Coefficient

ψ : Head Coefficient

REFERENCES

[1] M.Asujie, F. Bakir, S. Kouidri, F.Kenyery and R. Rey, Numerical Modelization of the Flow in Centrifugal Pump: Volute Influence in Velocity and Pressure Fields, International Journal of Rotating Machinery, 3, 2005, 244-255.

[2] F. Muggli, P. Holbein, and P. Dupont, CFD calculation of a mixed flow pump Characteristic from shutoff to maximum flow Proceedings of the ASME Fluids Engineering Division Summer Meeting (FED01), New Orleans, La, USA, June, 2001, Paper FEDSM01-18072.

[3] Cropper M, Dupont P, Parker J: Low flow – high pressure, Sulzer Technical Review, 2005.

[4] J.F. Guelich, Centrifugal Pumps, 2nd Edition, Springer, Berlin, (2010).

[5] E. Blanco-Marigorta, J. Fernandez-francos, J.L. Parrondo-Gayo and C. Santoria-Marros, umerical simulation of centrifugal pumps, Proceedings of the ASME Fluids Engineering Division Summer Meeting (FED00), Boston, Mass USA, June, 2000, Paper FEDSM00- 11162.

[6] J. Gonzalez, J. Fernandez-Francos, E Blanco and C. Santolaria-Marros, Numerical Simulation of the dynamic effects due to impeller-volute interaction in a centrifugal pump, Transactions of the ASME, Journal of Fluids Engineering, 124, 2002, 348-355.

[7] J.L. Parrondo-Gayo, J. Gonzalez-Perez and J. Fernandez-Francos, The effect of operating point on the pressure fluctuations at the blade passage frequency in the volute of a centrifugal pump, Transactions of the ASME, Journal of Fluids Engineering, 124, 2002, 784-794.

[8] F.Gu, A. Engeda, M Cave and J.L. Di Liberti, A Numerical investigation on the volute/diffuser interaction due to the axial distortion at the impeller exit, Transactions of the ASME, Journal of Fluids Engineering, 123, 2001, 475-483.

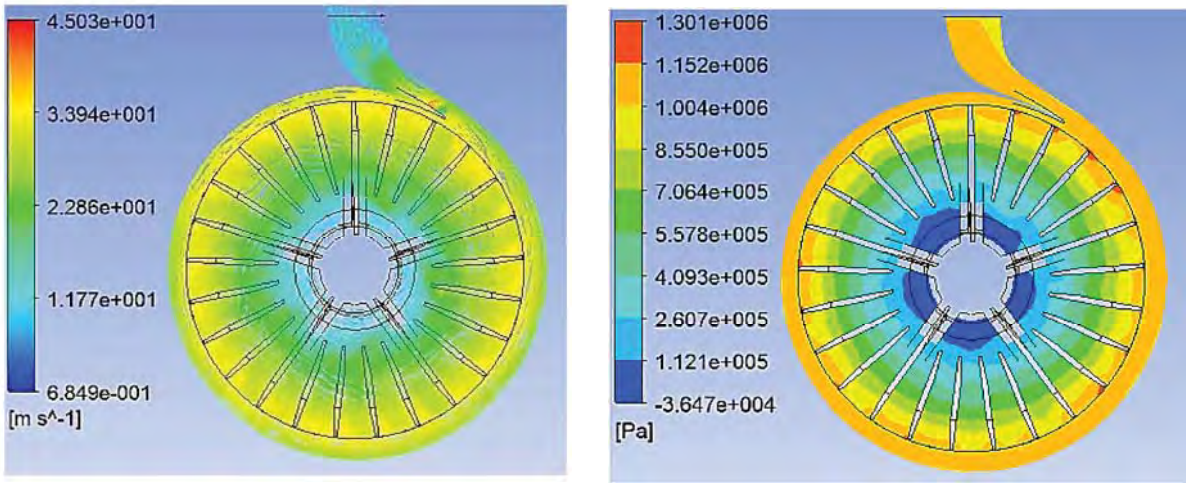

Fig. 18. Velocity field and pressure field at $Q / Q_{design} = 1.0$

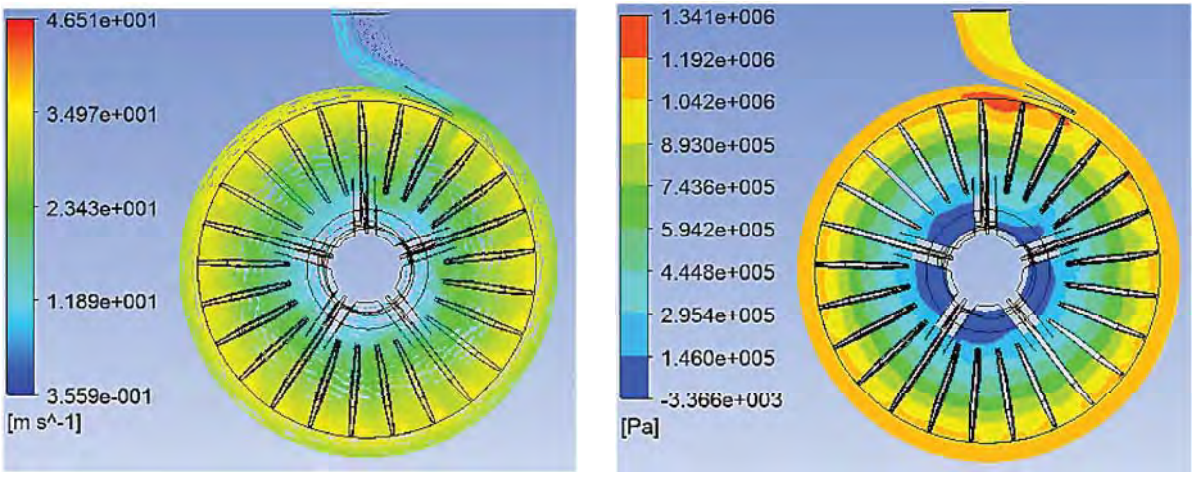

Fig. 19. Velocity field and pressure field at $Q / Q_{design} = 0.6$

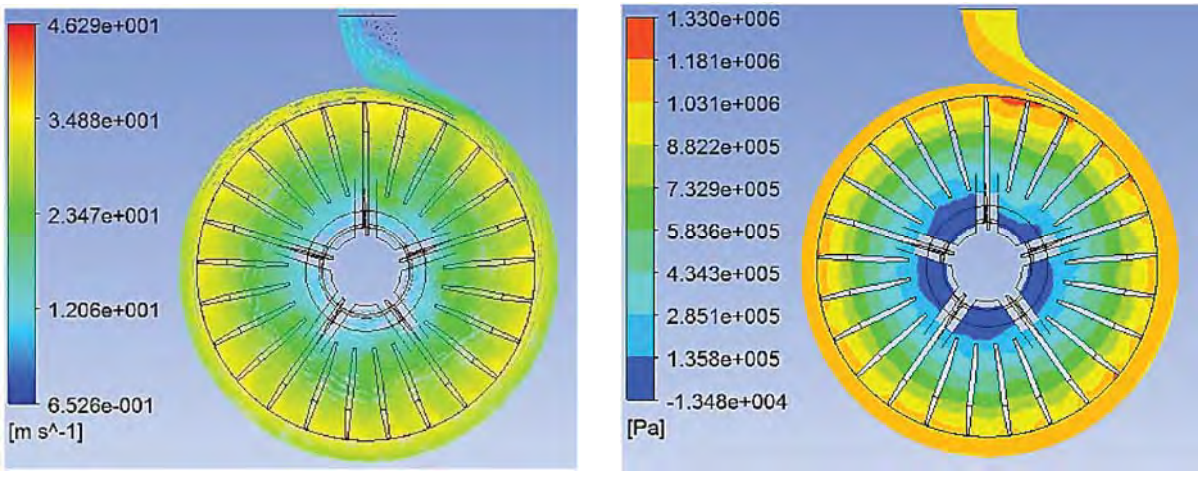

Fig. 20. Velocity field and pressure field at $Q / Q_{design} = 1.5$

◈◈◈

An Experimental Investigation of the Reynolds Analogy and its Modifications Applied to Annular Condensation Laminar Flow of R134a in a Vertical Tube

A. S. Dalkilic, B. Kundu & S. Wongwises

Arabian Journal for Science and Engineering

ISSN 1319-8025
Volume 38
Number A

a rJ b c Si Eng( )2013: 38DO93-150.
7 / l 10s100. 64133A9-013-0595-0

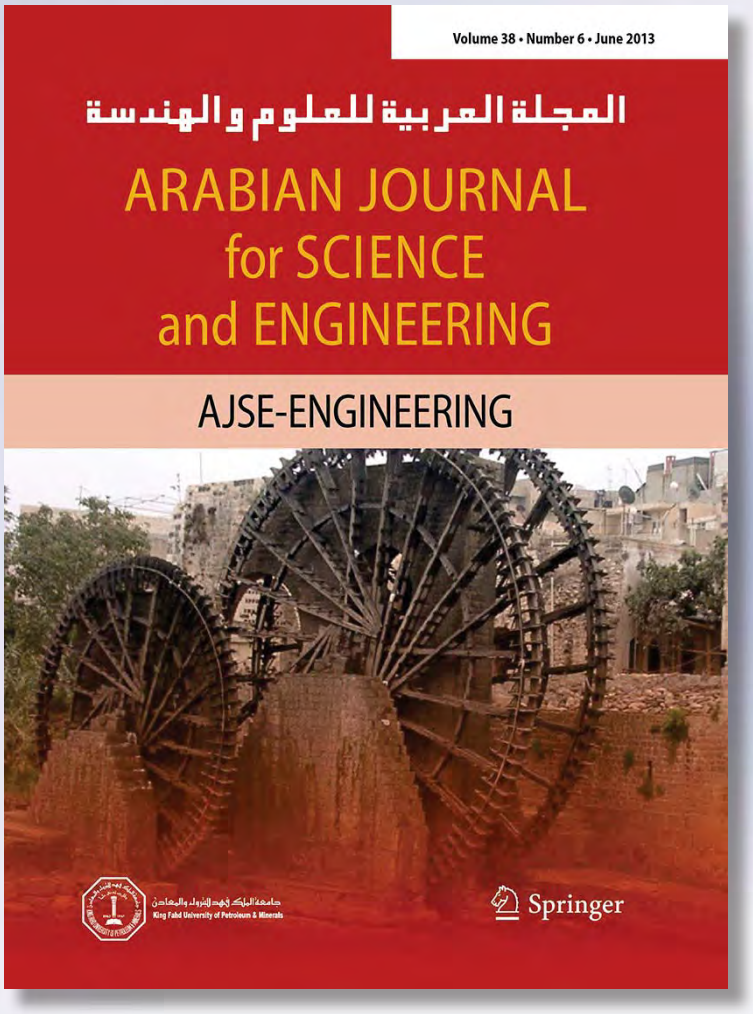

Springer

Your article is protected by copyright and all rights are held exclusively by King Fahd University of Petroleum and Minerals. This e-offprint is for personal use only and shall not be self-archived in electronic repositories. If you wish to self-archive your article, please use the accepted manuscript version for posting on your own website. You may further deposit the accepted manuscript version in any repository, provided it is only made publicly available 12 months after official publication or later and provided acknowledgement is given to the original source of publication and a link is inserted to the published article on Springer's website. The link must be accompanied by the following text: "The final publication is available at link.springer.com".

Author's personal copy

Arab J Sci Eng (2013) 38:1493–1507
DOI 10.1007/s13369-013-0595-0

RESEARCH ARTICLE - MECHANICAL ENGINEERING

An Experimental Investigation of the Reynolds Analogy and its Modifications Applied to Annular Condensation Laminar Flow of R134a in a Vertical Tube

A. S. Dalkilic · B. Kundu · S. Wongwises

Received: 27 May 2011 / Accepted: 24 July 2011 / Published online: 27 February 2013
© King Fahd University of Petroleum and Minerals 2013

Abstract The Reynolds analogy and its modifications are applied to forced convection laminar in-tube condensation to predict the heat transfer coefficient of R134a by means of well-known two-phase friction factors and agreed void fraction models and correlations explained in the authors' previous works. The vertical test section is a 0.5 m long countercurrent flow double tube heat exchanger with refrigerant flowing in the inner smooth copper tube (8.1 mm i.d.) and cooling water flowing in the annulus (26 mm i.d.). The test runs are performed at average saturated condensing temperatures of 40 °C ($Pr = 0.92$) and 50 °C ($Pr = 0.97$). The heat fluxes are between 10.16 and 66.61 kW m^{-2} while the mass fluxes are between 260 and 515 kg m^{-2} s^{-1} for the vertical test sections. The Reynolds' model is modified by various two-phase flow models and correlations to account for the partial condensation inside the tube. The refrigerant side heat transfer coefficients are determined within ±30 % using the two-phase friction factors of Wallis, Moeck, Fore et al., while all the proposed friction factor correlations for the Reynolds analogy, Prandtl and Taylor analogy, and Colburn analogy predict the experimental friction factor within a ±20 % deviation band. The importance of altering the Prandtl number to the Reynolds analogy ($Pr = 1$) is also shown in the paper.

Keywords Colburn analogy · Condensation · Film thickness · Friction factor · Prandtl and Taylor analogy · Reynolds analogy · R134a · Void fraction

الخلاصة

تم - في هذه الورقة - تطبيق تناظر رينولدز وتعديلاته على الحمل الحراري الرقائقي القسري في أنبوب التكثيف للتنبؤ بمعامل الانتقال الحراري ل- R134a عن طريق عوامل الاحتكاك ذات المرحلتين المعروفة جيدا ووافقت نماذج الجزء الباطل والارتباطات الموضحة في أعمال المؤلفين السابقة. ومقطع الاختبار العمودي هو أنبوب مبادل حراري بطول 0.5 متر وبتدفق تيار معاكس طويل مزدوج مع تدفق غاز التبريد في أنابيب النحاس السلس الداخلية (8.1 ملم قطر داخلي) وتدفق مياه التبريد في الحلقة (26 ملم قطر داخلي).

وقد تم تنفيذ تجارب التشغيل في متوسط درجات حرارة التكثيف المشبعة من 40 مئوية (Pr = 0.92) و 50 مئوية (Pr = 0.97)، في حين أن تدفقات الحرارة هي ما بين 10.16 و 66.61 كيلوواط\م^2 في حين أن تدفقات الكتلة هي بين 260 و 515 كجم\(م^2. ثانية) لمقاطع الاختبار العمودي. وتم تعديل أنموذج رينولدز من قبل نماذج تدفق ذات المرحلتين المختلفة والارتباطات لحساب التكثيف الجزئي داخل الأنبوب. وتم أيضاً تحديد معاملات نقل حرارة المبرد الجانبي ضمن ± 30٪ باستخدام عوامل الاحتكاك ذات المرحلتين لواليس وميك وفور وآخرين، في حين أن جميع ارتباطات معامل الاحتكاك المقترحة لتناظر رينولدز، وتناظر تايلور وبراندتل، وتناظر كولبرن تنبأت بعامل الاحتكاك التجريبي ضمن حزمة انحراف ± 20٪. إن أهمية تغيير عدد براندتل إلى تناظر رينولدز (Pr = 1) قد أظهر أيضا في هذه الورقة العلمية.

A. S. Dalkilic (✉)
Heat and Thermodynamics Division, Department of Mechanical Engineering, Yildiz Technical University (YTU), Yildiz, Besiktas, Istanbul 34349, Turkey
e-mail: dalkilic@yildiz.edu.tr

B. Kundu
Department of Mechanical Engineering,
Jadavpur University, Kolkata 700032, India
e-mail: bkundu123@rediffmail.com

S. Wongwises
Fluid Mechanics, Thermal Engineering and Multiphase Flow Research Lab. (FUTURE), Department of Mechanical Engineering, Faculty of Engineering, King Mongkut's University of Technology Thonburi, Bangmod, Bangkok 10140, Thailand
e-mail: somchai.won@kmutt.ac.th

S. Wongwises
Academy of Science, The Royal Institute of Thailand,
SanamSuea Pa, Dusit, Bangkok 10300, Thailand

Author's personal copy

List of Symbols

A	Inside surface area, m^{-2}
C_p	Specific heat, J kg^{-1} K^{-1}
d	Internal tube diameter, m
f	Friction factor
G	Mass flux, kg m^{-2} s^{-1}
h	Heat transfer coefficient, W m^{-2} K^{-1}
i	Enthalpy, J kg^{-1}
i_{fg}	Latent heat of condensation, J kg^{-1}
L	Length of test tube, m
k	Thermal conductivity, W m^{-1} K^{-1}
m	Mass flow rate, kg s^{-1}
P	Pressure, MPa
Pr	Prandtl number
r	Internal tube radius, m
Re	Reynolds number
S	Slip ratio
T	Temperature, °C
u	Velocity, m s^{-1}
Q	Heat transfer rate, W
q	Mean heat flux, kW m^{-2}
x	Mean vapor quality
y	Wall coordinate
ΔP	Pressure drop, Pa
ΔT	Vapor side temperature difference, $T_{sat} - T_{wi}$, K

Greek Symbols

ε_c	Conductive diffusivity/viscosity, m^2 s^{-1}
ε_m	Eddy momentum diffusivity/viscosity, m^2 s^{-1}
ε_q	Eddy heat diffusivity/viscosity, m^2 s^{-1}
ρ	Density, kg m^{-3}
μ	Dynamic viscosity, kg m^{-1} s^{-1}
δ	Film thickness, m
δ^+	Dimensionless film thickness
α	Void fraction
τ	Shear stress, N m^{-2}
ν	Kinematic viscosity, m^2 s^{-1}

Subscripts

corr	Correlation
exp	Measured
f	Fluid
g	Gas/vapor
H	Homogeneous
i	Inlet
l	Liquid
o	Outlet
ph	Preheater
ref	Refrigerant
sat	Saturation
SG	Superficial
TS	Test section
w	Water
wi	Inner wall

1 Introduction

Adaptation of forced convection condensation inside tubes is extensively performed in process industries including nuclear power plants, refrigeration, and air-conditioning equipment due to the advantage of high heat transfer coefficients. The design of condensers in such applications is strongly dependent on the heat transfer analysis of film condensation. The determination of film heat transfer coefficients appeals to most designers' interest in specified flow conditions. Owing to the fact that pure theoretical solutions are very difficult for two-phase flows, empirical or semi-empirical models or correlations based on experimental studies are usually used in the analysis. A good understanding of the two-phase flow characteristic should be included in the studies of the two-phase flow regimes, void fraction, and pressure drop.

It is known from the literature that the most dominant flow regime is the annular flow, especially for high vapor qualities during condensation inside tubes. It is reported in the literature that annular flow inside tubes can exist until the vapor quality reaches a value of 0.25. Therefore, there are many theoretical and experimental two-phase flow studies focused on the annular flow. This situation makes it easier for the in-tube condensation phenomenon to be solved by designers. There are many void fraction models and correlations specified as local, chordal, cross-sectional, and volumetric for different flow regimes in the literature. The heat transfer resistance of the condensate strongly affects the heat transfer characteristics of the flow in condenser tubes. Hence, film thickness is one of the most significant parameters for the prediction of local heat flux.

Two principal types of flow models were used in developing frictional pressure drop: the homogeneous model and the separated flow model. Most of the two-phase frictional pressure drop models are related to the separated flow analysis. It is essential to apply a properly defined single-phase friction factor to a two-phase friction factor according to the homogeneous model. The homogeneous model is also known as the friction factor model.

Interfacial shear stress in annular two-phase flow is one of the main parameters governing transport phenomena and is required for modeling the flow. There are many proposed friction factors in the literature. Wallis's [1] interfacial friction factor is used for the condensation in the vertical annular flow in the literature, such as Carey [2] and Maheshawari et al. [3]. Fukano and Furukawa [4] investigated the effects of liquid viscosity on the mean liquid film thickness, wave heights, and gas–liquid interfacial stresses in the vertical upward co-current annular flow in a 26 mm inner diameter tube using

Author's personal copy

water and glycerol solutions as working fluids. Moeck [5] performed experiments on the diameter of entrained liquid droplets for air–water annular flow. Fore et al. [6] obtained the film thickness and pressure gradient data for co-current upward flow of nitrogen and water under high pressure in a rectangular duct.

The Fanning [7], Darcy [8], and Weisbach [9] friction factors are widely used in the literature for laminar and turbulent single phase flow in round and square tubes. The Darcy [8] and Weisbach [9] friction factor is four times larger than the Fanning friction factor [7]. The Darcy and Weisbach equation, valid for fully developed, steady state, and incompressible flow, with the Moody Diagram, is considered to be the most accurate model for estimating frictional head loss in steady pipe flow. Wongwises and Kongkiatwanitch [10] presented new data on the gas–liquid interfacial friction factor in annular two-phase upward co-current flow in a vertical circular pipe. Their study has been performed at relatively high film thickness, taking into consideration the effect of the entrained droplets, which occur from the breakup of the disturbance waves. Soliman and Feingold [11] performed an analytical solution for the fully developed laminar flow in internally finned tubes assuming a fin shape very close to the real fin configuration. Al-Sarkhi and Hanratty [12] examined the influence of a drag-reducing polymer on air–water annular flows in 9.53 and 2.54 cm pipelines. They reported that the annular flow has different characteristics for which the friction factors assume larger values in air–water systems. Choi et al. [13] presented a pressure drop correlation and friction factor for evaporation and condensation in smooth and micro-fin tubes for lubricant-free refrigerants and refrigerant/lubricant mixtures. The form of the generalized correlation was taken from the Pierre pressure drop model [14]. Carey [2] developed Blasius's [15] friction factor and reported that the vapor flow in the tube can be treated as a single phase flow.

Although the Reynolds analogy [16] and its modifications of Prandtl [17], Taylor [18], and Colburn [19] analogies have been used extensively in numerous studies in the technical literature, there is a lack of research on its application to the prediction of the convective condensation heat transfer coefficient in vertical tubes, apart from Ambrosini et al. [20] for the steam condensation on a flat plate in the presence of non-condensable gases, Chitti and Anand [21] for the R22 condensation inside a smooth horizontal tube, and Kim and Corradini [22] for the steam condensation inside vertical tubes and on the plates. Apart from the authors' previous publications [23–39] there are few studies in the literature using the experimental parameters of this study related to the heat transfer and pressure drop characteristics for condensation in a small diameter vertical tube during co-current down flow of R134a. As a result, the main concern of this study is to show the application of the Reynolds analogy [16] and its modifications to the annular flow condensation in a vertical tube by means of certain agreeable void fraction models and correlations reported in the authors' previous studies. The results also apply selected well-known two-phase friction factors from the literature using a large number of experimental heat transfer and pressure drops to determine the convective condensation heat transfer coefficient. A comparison of convective heat transfer coefficients belonging to the model and experiment is performed, and its results are also in agreement with the valid operating range of the Reynolds analogy [16] and its modifications in terms of the Prandtl number. The independence of void fraction, pressure drop, and heat transfer annular flow models from tube orientation [40] is also shown by means of the results. The content of this study is expected to fill this gap in the literature.

2 Experimental Apparatus and Method

A schematic diagram of the test apparatus is shown in Fig. 1. The refrigerant loop consists of a pre-heating loop, test section, cooling loop, and chilling loop. The refrigerant is circulated by a gear pump controlled by an inverter. The refrigerant flows in series through a filter/dryer, a sight glass tube, a refrigerant flow meter, and a pre-heater, and then enters the test section. A spiral counter-flow double tube heat exchanger is designed to supply heat to control the inlet quality of the refrigerant before entering the test section. After exiting the test section, the chilling loop condenses and sub-cools the refrigerant, removes the heat input from the pre-heater and test section, and ejects it into the surroundings. After leaving the chilling loop, the refrigerant changes from the two-phase refrigerant to a sub-cooled state. Eventually, the refrigerant returns to the refrigerant pump to complete the cycle.

The test section, well insulated with a proper material to minimize the heat loss, is a vertical counter-flow tube-in-tube heat exchanger with refrigerant flowing downward (co-current liquid and vapor of R134a's down flow) in the inner tube and cooling water flowing upward in the annulus. The inner and outer tubes are made from smooth vertical copper having inner diameters of 8.1 and 26 mm, respectively. The length of the heat exchanger is 0.5 m. Figure 2 shows the detailed dimensions of the heat exchanger and the location of the thermocouples.

T-type thermocouples are used to measure refrigerant temperature and the tube wall temperatures in the test section. A total of ten thermocouples are located on the sidewall at five points along the test tube. A thermostat is used to control the inlet temperature of the water. All the temperature

Author's personal copy

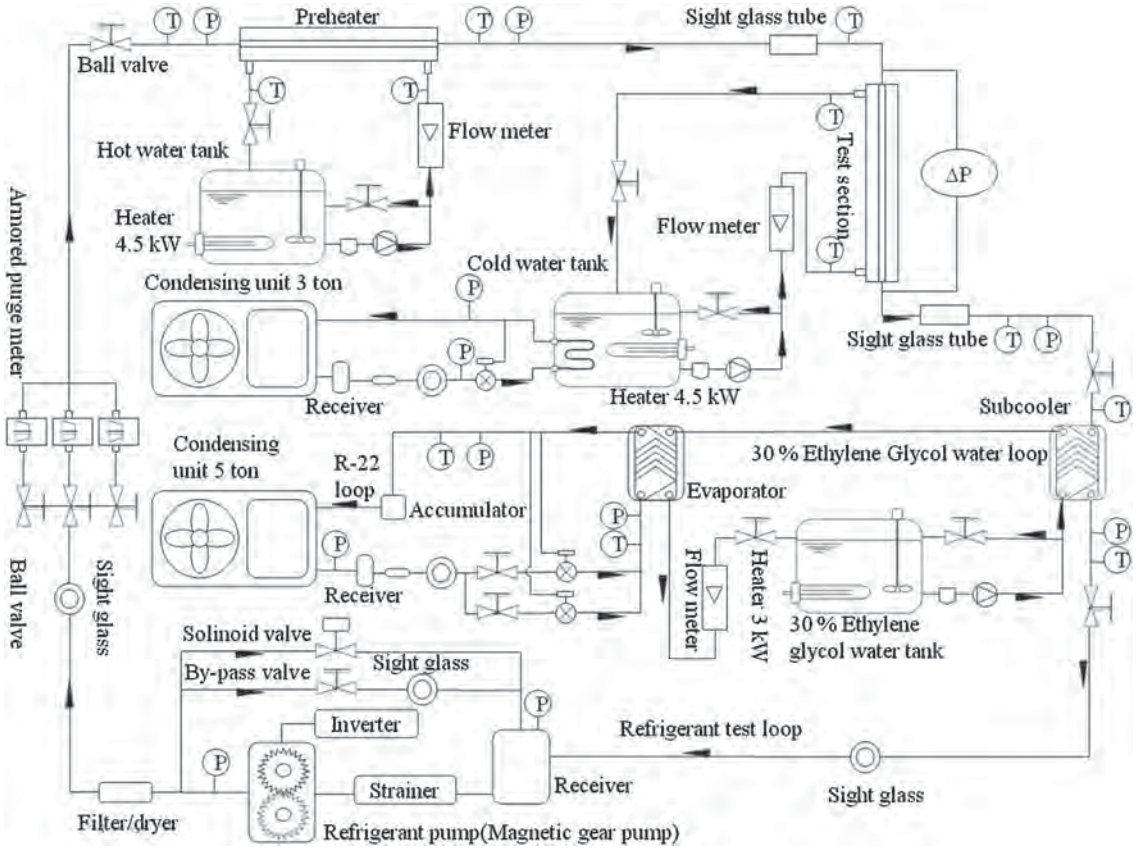

Fig. 1 Schematic diagram of experimental apparatus [from Dalkilic et al. [23], with permission from Elsevier]

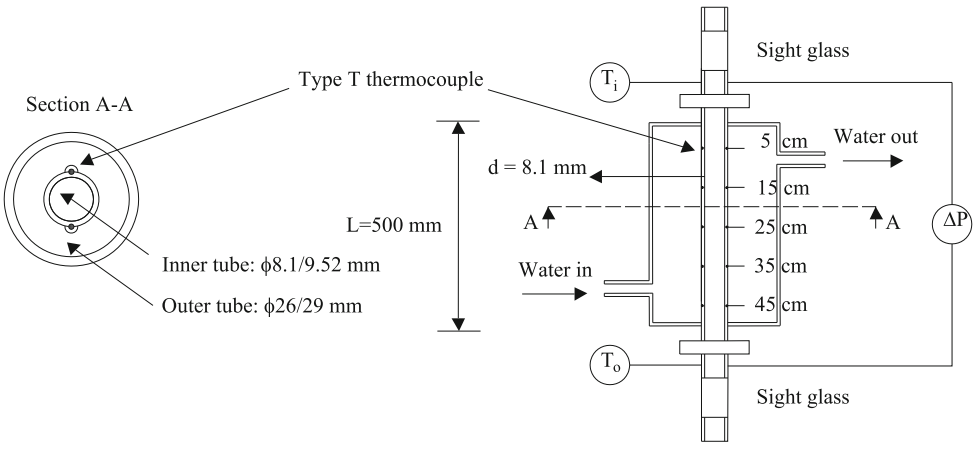

Fig. 2 Schematic diagram of test section [from Dalkilic et al. [25], with permission from Elsevier]

measuring devices are calibrated in a controlled temperature bath using standard precision mercury glass thermometers. The uncertainty of the temperature measurements is ±0.1 °C. All static pressure taps are mounted on the tube wall. The refrigerant flow meter is a variable area type. The flow meter was calibrated in the range of 0–2.2 gal min^{-1} for HFC-134a by the manufacturer. Pressure drop is measured by a differential pressure transducer installed between the inlet and outlet of the test section. The length between pressure taps is 0.7 m. A low temperature thermostat is used to control the system pressure of the refrigerant flow. The differential pressure transducer and pressure gauges are calibrated against a primary standard, the dead weight tester. All signals from thermocouples and pressure transducers are recorded by a data logger. Tests are performed in the steady state.

Author's personal copy

3 Data Reduction and Experimental Uncertainty

The following equations are used to prepare the system for experiments. The system has saturated vapor of R134a at the inlet of the test section during steady-state regime conditions. Energy balances are written for the evaporator and test section separately. Data reduction of measured results is summarized in the following procedures:

3.1 The Inlet Vapor Quality of the Test Section ($x_{TS,i}$)

$$x_{TS,i} = \frac{i_{TS,i} - i_{l@T_{TS,i}}}{i_{fg@T_{TS,i}}} \tag{1}$$

where $i_{l@T_{TS,i}}$ is the enthalpy of the saturated liquid based on the inlet temperature of the test section, $i_{fg@T_{TS,i}}$ is the enthalpy of vaporization based on the inlet temperature of the test section, and $i_{TS,i}$ is the refrigerant enthalpy at the test section inlet, given by:

$$i_{TS,i} = i_{ph,i} + \frac{Q_{ph}}{m_{ref}} \tag{2}$$

where $i_{ph,i}$ is the inlet enthalpy of the liquid refrigerant before entering the pre-heater, m_{ref} is the mass flow rate of the refrigerant, and Q_{ph} is the heat transfer rate in the pre-heater. The heat transfer rate is determined by:

$$Q_{ph} = m_{w,ph} c_{p,w} (T_{w,i} - T_{w,o})_{ph} \tag{3}$$

where $m_{w,ph}$ is the mass flow rate of the water entering the pre-heater, $c_{p,w}$ is the specific heat of water, and $(T_{w,i} - T_{w,o})_{ph}$ is the temperature difference between inlet and outlet positions of the pre-heater.

3.2 The Outlet Vapor Quality of the Test Section ($x_{TS,o}$)

$$x_{TS,o} = \frac{i_{TS,o} - i_{l@T_{TS,o}}}{i_{fg@T_{TS,o}}} \tag{4}$$

where $i_{TS,o}$ is the refrigerant enthalpy at the test section outlet, $i_{l@T_{TS,o}}$ is the enthalpy of the saturated liquid based on the outlet temperature of the test section, and $i_{fg@T_{TS,o}}$ is the enthalpy of vaporization. The outlet enthalpy of the refrigerant flow is calculated as follows:

$$i_{TS,o} = i_{TS,i} - \frac{Q_{TS}}{m_{ref}} \tag{5}$$

where the heat transfer rate, Q_{TS}, in the test section is obtained from:

$$Q_{TS} = m_{w,TS} c_{p,w} (T_{w,o} - T_{w,i})_{TS} \tag{6}$$

where $m_{w,TS}$ is the mass flow rate of the water entering the test section and $(T_{w,o} - T_{w,i})_{TS}$ is the temperature difference between the outlet and inlet positions of the test section.

3.3 The Average Heat Transfer Coefficient (h_{exp})

$$h_{exp} = \frac{Q_{TS}}{A_i (T_{ref,sat} - T_{wi})} \tag{7}$$

where h_{exp} is the experimental average heat transfer coefficient, Q_{TS} is the heat transfer rate in the test section, T_{wi} is the average temperature of the inner wall, $T_{ref,sat}$ is the average saturation temperature of the refrigerant at the test section inlet and outlet, and A_i is the inside surface area of the test section:

$$A_i = \pi d L \tag{8}$$

where d is the inside diameter of the test tube and L is the length of the test tube.

3.4 Void Fraction Models and Correlations

Void fraction is commonly used for two-phase flow and is defined as:

$$\alpha = \frac{A_g}{A} = \left(1 - \frac{\delta}{r}\right)^2 \tag{9}$$

where δ is the liquid film thickness for annular flow, assuming $\delta \ll d$,

$$\alpha = 1 - \frac{4\delta}{d} \tag{10}$$

$$\alpha = \frac{1}{1 + \left(\frac{1-x}{x}\right)\left(\frac{\rho_g}{\rho_l}\right) S} \tag{11}$$

where the slip factor, S, is defined as:

$$S = \frac{u_g}{u_l} \tag{12}$$

Several agreeable void fraction models and correlations [41–45]are shown in Table 1 and are also reported in the authors' previous publications [23,26,31,33]. It should be noted that the film thickness values are calculated indirectly from the agreed void fractions in Table 1 by means of Eq. (10) and the calculation of film thickness in this manner was also discussed in the authors' previous publication [26] in detail.

3.5 Two-Phase Friction Factor Models and Correlations

Some well-known two-phase friction factors [1,2,4–7,10–13] in the literature are summarized in Table 2 to be used in the model based on Reynolds' analogy and its modifications.

Author's personal copy

Table 1 Void fraction models and correlations

Number	Void fraction model/correlation	Model/correlation
1	Homogeneous model	$\alpha_{\mathrm{H}} = \frac{1}{1+\left(\frac{1-x}{x}\right)\left(\frac{\rho_{\mathrm{g}}}{\rho_{\mathrm{l}}}\right)S} \quad S = 1$
2	Chisholm [41]	$\alpha = \frac{1}{\alpha_{\mathrm{H}}+(1-\alpha_{\mathrm{H}})^{0.5}}\alpha_{\mathrm{H}}$
3	Soliman [42]	$G(1-x) = 4\rho_{\mathrm{l}}u_{\mathrm{l}}\left(\frac{\delta}{d}\right) \quad \alpha = 1 - \frac{4\delta}{d}$
4	Smith [43]	$\alpha = \left\{1 + \left(\frac{\rho_{\mathrm{g}}}{\rho_{\mathrm{l}}}\right)K\left(\frac{1}{x}-1\right) + \left(\frac{\rho_{\mathrm{g}}}{\rho_{\mathrm{l}}}\right)(1-K)\left(\frac{1}{x}-1\right)\left[\frac{\left(\frac{\rho_{\mathrm{l}}}{\rho_{\mathrm{g}}}\right)+K\left(\frac{1}{x}-1\right)}{1+K\left(\frac{1}{x}-1\right)}\right]\right\}^{-1}$ $K = 0.4$
5	Turner and Wallis [44]	$\frac{1-\alpha}{\alpha} = A\left(\frac{1-x}{x}\right)^{\mathrm{p}}\left(\frac{\rho_{\mathrm{g}}}{\rho_{\mathrm{l}}}\right)^{\mathrm{q}}\left(\frac{\mu_{\mathrm{l}}}{\mu_{\mathrm{g}}}\right)^{\mathrm{r}}$
6	Spedding and Spence [45]	$\alpha = \left(1 + 2.22\left(\frac{1-x}{x}\right)^{0.65}\left(\frac{\rho_{\mathrm{g}}}{\rho_{\mathrm{l}}}\right)^{0.65}\right)^{-1}$

Correlation or model	A	p	q	r
Homogeneous	1	1	1	0
Zivi	1	1	0.67	0
Turner-Wallis	1	0.72	0.4	0.08
Lockhart-Martinelli	0.28	0.64	0.36	0.07
Thom	1	1	0.89	0.18
Baroczy	1	0.74	0.65	0.13

Table 2 Friction factor models and correlations

Number	Friction factor model/correlation	Model/correlation
1	Wallis [1]	$f_{\mathrm{g}} = f_{\mathrm{i}} = 0.005\left[1 + 300\left(\frac{\delta}{d}\right)\right]$
2	Fukano and Furukawa [4]	$f_{\mathrm{i}} = 0.425\left[12 + \left(\frac{\nu_{\mathrm{l}}}{\nu_{\mathrm{w}}}\right)\right]^{-1.33}\left(1 + 12\left(\frac{\delta}{d}\right)\right)$
3	Moeck [5]	$f_{\mathrm{i}} = 0.005\left[1 + 1458\left(\frac{\delta}{d}\right)^{1.42}\right]$
4	Fore et al. [6]	$f_{\mathrm{i}} = 0.005\left[1 + 300\left(\frac{\delta}{d} - 0.0015\right)\right]$
5	Fanning [7]	$f = \frac{16}{Re}\ Re < 2{,}000\ f = 0.079(Re)^{-0.25}\ Re > 2{,}000\ Re = \frac{Gd}{\mu_{\mathrm{g}}}$
6	Wongwises and Kongkiatwanitch [10]	$f_{\mathrm{i}} = 17.172 Re_{\mathrm{SG}}^{-0.768}\left(\frac{\delta}{d}\right)^{-0.253} \quad Re_{\mathrm{SG}} = \frac{u_{\mathrm{SG}}\rho_{\mathrm{g}}d}{\mu_{\mathrm{g}}}$ $u_{\mathrm{SG}} = \frac{u_{\mathrm{g}}(1-4\delta^{+}+4\delta^{+^2})}{\mu_{\mathrm{g}}}\ \delta^{+} = \frac{\delta}{d}$
7	Soliman and Feingold [11]	$f = \frac{\pi^2\rho r^5}{m^2}\left(\frac{\mathrm{d}P}{\mathrm{d}x}\right)$
8	Al-Sarkhi and Hanratty [12]	$f = \frac{d}{2\rho_{\mathrm{g}}u_{\mathrm{SG}}^2}\left(\frac{\Delta P}{L}\right)$
9	Choi et al. [13]	$f = 0.00506 Re_{\mathrm{fo}}^{-0.0951} K_{\mathrm{f}}^{0.1554}\ Re = \frac{Gd}{\mu_{\mathrm{l}}}\ K_{\mathrm{f}} = \frac{\Delta x i_{\mathrm{fg}}}{L_{\mathrm{g}}}$
10	Carey [2]	$f_{\mathrm{g}} = 0.079\left[\frac{Gx(D-\delta)}{\mu_{\mathrm{g}}(1-4\delta/\mathrm{D})}\right]^{-0.25}$

3.6 Calculation Procedure for the Model Based on Reynolds' Analogy [16] and its Modifications

The analogies between momentum, heat, and mass transfer are used for correlating friction factors or heat transfer coefficients by means of experimental data in the literature [20]. The Reynolds analogy [16] between heat and momentum transfer is one of the most well-known proposals on this subject, and Colburn's proposal [19] is its extension to more general conditions. The analogy has been applied with success in the prediction of many other phenomena involving laminar or turbulent conditions. Reynolds [16] observed the similarity between momentum and heat flux and proposed a new analogy to predict heat transfer coefficients by

Author's personal copy

Table 3 Uncertainty of experimental parameters

Parameters	Uncertainty
$T_{ref,sat}$ (°C)	0.19
x_i	±6.96–8.24 %
ΔT (K)	±0.191
$(T_{w,o} - T_{w,i})_{TS}$ (K)	±0.045
$(T_{w,i} - T_{w,o})_{ph}$ (K)	±0.13
m_{ref} (g s^{-1})	±0.023
$m_{w,TS}$ (g s^{-1})	±0.35
$m_{w,ph}$ (g s^{-1})	±0.38
q_{TS} (kW m^{-2})	±6.55–8.93 %
q_{ph} (kW m^{-2})	±12–14.81 %
h_{ref} (W m^{-2} K^{-1})	±7.64–10.71 %
ΔP (kPa)	±0.15

means of measured pressure drops caused by the friction in flow.

3.6.1 Shear Stress in the Boundary Layer

Shear stress in the boundary layer in laminar (Eq. 13) and turbulent flow (Eq. 14) can be expressed as shown below. It should be noted that there is an additional shear stress caused by eddies in turbulent flow.

$$\tau = \mu \frac{du}{dy} = \rho \nu \frac{du}{dy} \tag{13}$$

$$\tau = \rho \varepsilon_m \frac{du}{dy} \tag{14}$$

Total shear stress is obtained from Eqs. (13) and (14) as:

$$\tau = \rho(\nu + \varepsilon_m)\frac{du}{dy} \tag{15}$$

3.6.2 Heat Transfer in the Boundary Layer

The heat transfer in laminar (Eq. 16) and turbulent flow (Eq. 17) can be defined as follows. As above, it should be noted that there is an additional heat transfer caused by eddies in turbulent flow:

$$q = -k\frac{dT}{dy} \tag{16}$$

$$q = -\rho C_p \varepsilon_q \frac{dT}{dy} \tag{17}$$

The conductive diffusivity is given as:

$$\varepsilon_c = \frac{k}{\rho C_p} \tag{18}$$

Total heat transfer is obtained from Eqs. (16), (17) and (18) as:

$$q = -\rho C_p \left(\frac{k}{\rho C_p} + \varepsilon_q\right)\frac{dT}{dy} \tag{19}$$

$$q = -\rho C_p (\varepsilon_c + \varepsilon_q)\frac{dT}{dy} \tag{20}$$

Reynolds [16] performed an experimental study. The following assumptions were made in his analysis as a result of the experiments: equal heat and momentum eddies ($\varepsilon_m = \varepsilon_q$), similar velocity and temperature profile ($du/dy = dT/dy$), the values of eddy momentum and heat diffusivity are much greater than the kinematic ($\varepsilon_m \gg \nu$) and conductive ($\varepsilon_q \gg \varepsilon_c$) viscosities, respectively, equal conductive and kinematic viscosities ($\varepsilon_c = \nu$). Under these assumptions, Eq. (20) is divided by Eq. (15) and the basic equation of the analogy is derived as follows:

$$\frac{q}{\tau C_p} = \frac{dT}{du} = \text{constant} \tag{21}$$

Integration of Eq. (21) gives Eq. (22) at the wall, as:

$$\frac{q_w}{\tau_w C_p} = \frac{T - T_w}{u - u_w} \tag{22}$$

where temperature difference is shown ($T - T_w$) as ΔT and velocity at the wall is zero ($u_w = 0$), thus the Reynolds analogy's well-known equation is obtained as follows:

$$\frac{q_w}{\tau_w} = \frac{C_p \Delta T}{u} \tag{23}$$

It is valid for laminar and turbulent flow when the Prandtl number equals 1 ($Pr = 1$). When it is applied to the flow in

Table 4 Operating conditions of the study

Refrigerant	HFC-134a
Test tube material, inner diameter d, length L	Copper, ϕ 8.1 mm, 500 mm
Range of condensing pressure, P_{sat} (bar)	10–12
Range of condensing temperature, T_{sat} (°C)	40–50
Range of mass flux, G (kg m^{-2} s^{-1})	260–515
Range of heat flux, q (kW m^{-2})	10.16–66.61
Range of temperature difference, $\Delta T = T_{sat} - T_{wi}$, K	1.25–8.98
Range of average vapor quality, x	0.87–0.96

Author's personal copy

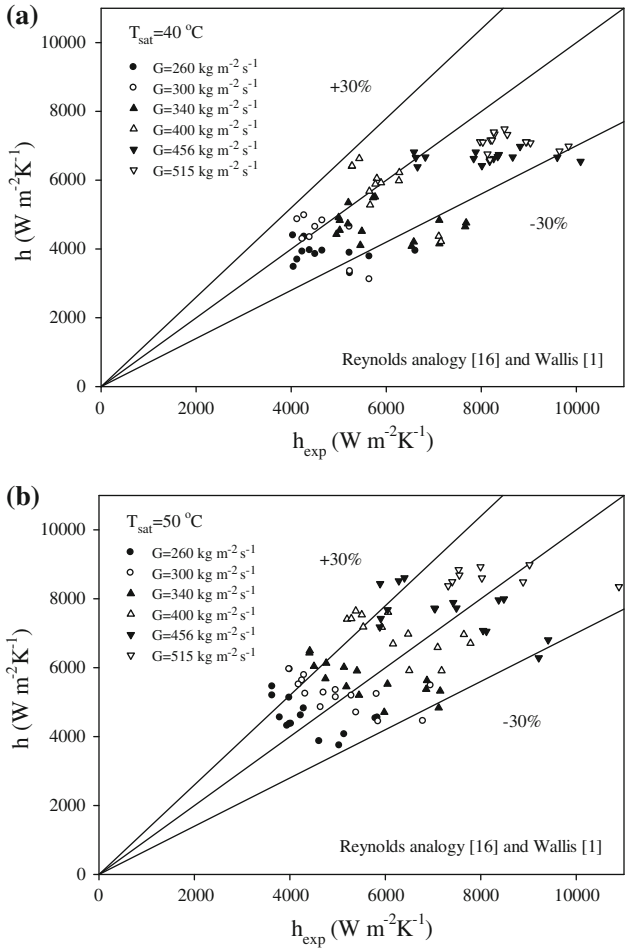

Fig. 3 Comparison of experimental and calculated condensation heat transfer coefficients from the model of Wallis [1] and Reynolds [16] for $G = 260{-}515$ kg m^{-2} s^{-1} **a** $T_{sat} = 40$ °C and **b** $T_{sat} = 50$ °C

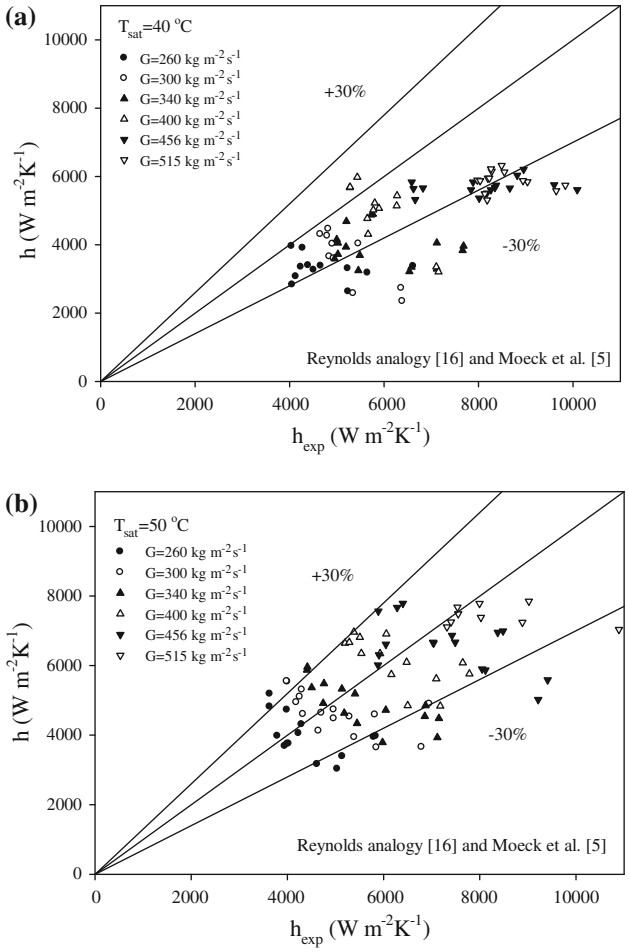

Fig. 4 Comparison of experimental and calculated condensation heat transfer coefficients from the model of Moeck [5] and Reynolds [16] for $G = 260{-}515$ kg m^{-2} s^{-1} **a** $T_{sat} = 40$ °C and **b** $T_{sat} = 50$ °C

tubes, flow pattern should be considered in the analysis. In this case, the temperature difference and velocity in Eq. (23) should be taken as T_f and u_f, respectively. Its latest form in Eq. (26) is obtained from Eqs. (24) and (25) and friction factors in Table 2 are used in Eq. (26) to compute convective heat transfer coefficient as follows:

$$q = h\Delta T \tag{24}$$

$$\tau_w = \frac{1}{2}\rho u^2 f \tag{25}$$

$$\frac{h}{\rho u C_p} = \frac{f}{2} \tag{26}$$

It should be noted that there are some basic studies on the improvement of the Reynolds model [16], using the Stanton number in Eq. (27), such as Prandtl [17] and Taylor [18] in Eq. (28), and Colburn [19] in Eq. (31).

$$St = \frac{h}{\rho u C_p} \tag{27}$$

The Prandtl [17] and Taylor [18] modification of the Reynolds analogy ($Pr \neq 1$) is given as follows:

$$St = \frac{f}{2}\left[\frac{1}{1 + r_v(Pr - 1)}\right] \tag{28}$$

where the coefficient of the equation is given for smooth surfaces of tubes in Eq. (29) and plates in Eq. (30), respectively:

$$r_v = 1.99Re^{-1/8} \tag{29}$$

$$r_v = 2.11Re^{-1/10} \tag{30}$$

The Colburn [19] modification of Reynolds analogy ($0.6 < Pr < 50$) is expressed as follows:

$$St\ Pr^{2/5} = \frac{f}{2} \tag{31}$$

It should be also noted that heat transfer coefficient values obtained from Eq. (7) are assumed as comparative values for the error analysis. Film thickness values are calculated using Eq. (10) in the analysis. Equation (32) gives the mass flow rate of gas flow; hence, vapor velocity can be derived from

Author's personal copy

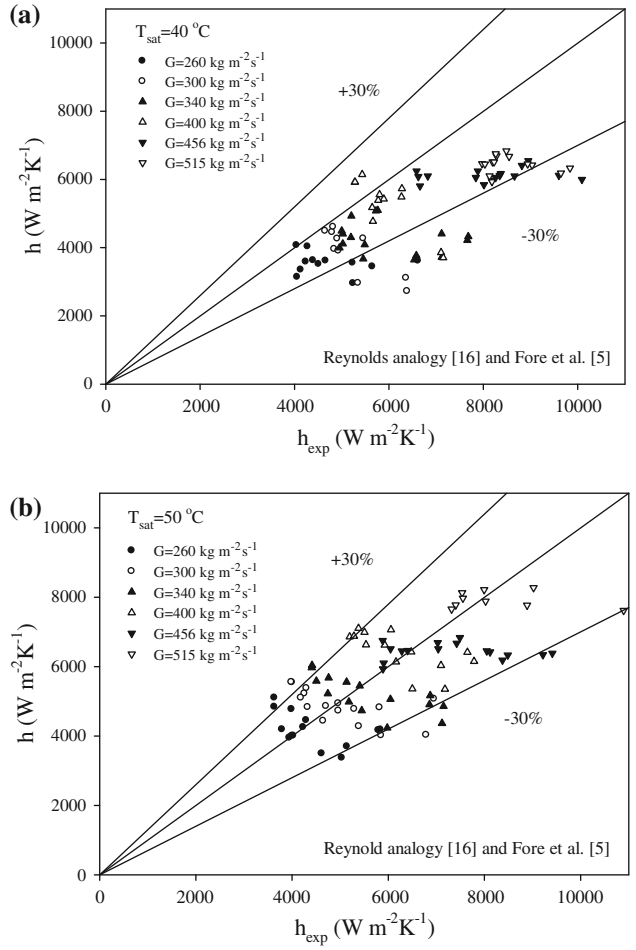

Fig. 5 Comparison of experimental and calculated condensation heat transfer coefficients from the model of Fore et al. [6] and Reynolds [16] for $G = 260{-}515$ kg m^{-2} s^{-1} **a** $T_{sat} = 40$ °C and **b** $T_{sat} = 50$ °C

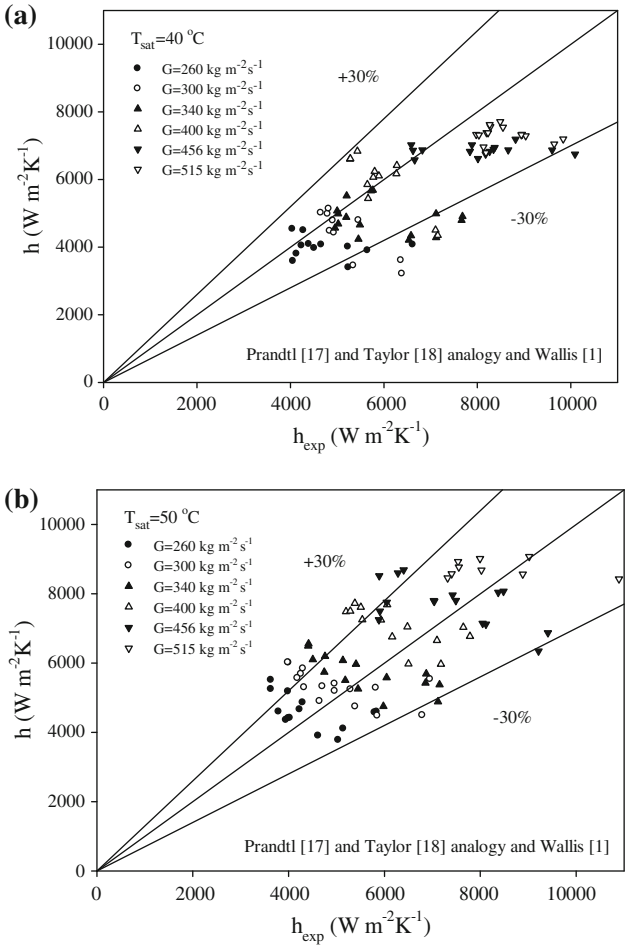

Fig. 6 Comparison of experimental and calculated condensation heat transfer coefficients from the model of Wallis [1], Prandtl [17], and Taylor [18] for $G = 260{-}515$ kg m^{-2} s^{-1} **a** $T_{sat} = 40$ °C and **b** $T_{sat} = 50$ °C

Eq. (33) as follows:

$$m_g = GxA \tag{32}$$

$$u_g = \frac{m_g}{\rho_g A_g} \tag{33}$$

where gas flow area is calculated considering film thickness in Eq. (34):

$$A_g = \frac{\pi(d - 2\delta)^2}{4} \tag{34}$$

Mean errors between predicted and experimental heat transfer coefficient values are shown in Table 5 and are calculated as follows:

$$\text{Error} = \left(\frac{\alpha_{corr} - \alpha_{model}}{\alpha_{model}}\right) 100 \tag{35}$$

$$\text{Mean Error} = \frac{\Sigma \text{Error}}{\text{data}} \tag{36}$$

With an approximation by Carey [2], the vapor flow in the tube can be treated as a single phase flow. Because the film is thin, the mean velocity of vapor is much larger than the liquid velocity at the interface due to the high viscosity of the liquid phase compared to the vapor phase. The test tube is large in diameter, compared with the film thickness. Hence, physical properties in Eq. (26) and other related equations belong to the gas phase of the flow in the test tube. The friction factor is investigated as a two-phase friction factor to account for the effect of condensation in the test tube.

3.7 Correlation Development

The correlation of the friction coefficient with boundary layer thickness for flow through the smooth tube was modified by Reynolds [16], Prandtl [17], Taylor [18], and Colburn [19] to improve the accuracy of the calculations for practical applications. The experimental heat transfer coefficient presented in Eq. (7) is used to calculate experimental friction factors for the Reynolds analogy, Prandtl and Taylor analogy, and Colburn analogy. In this paper, a new correlation between

Author's personal copy

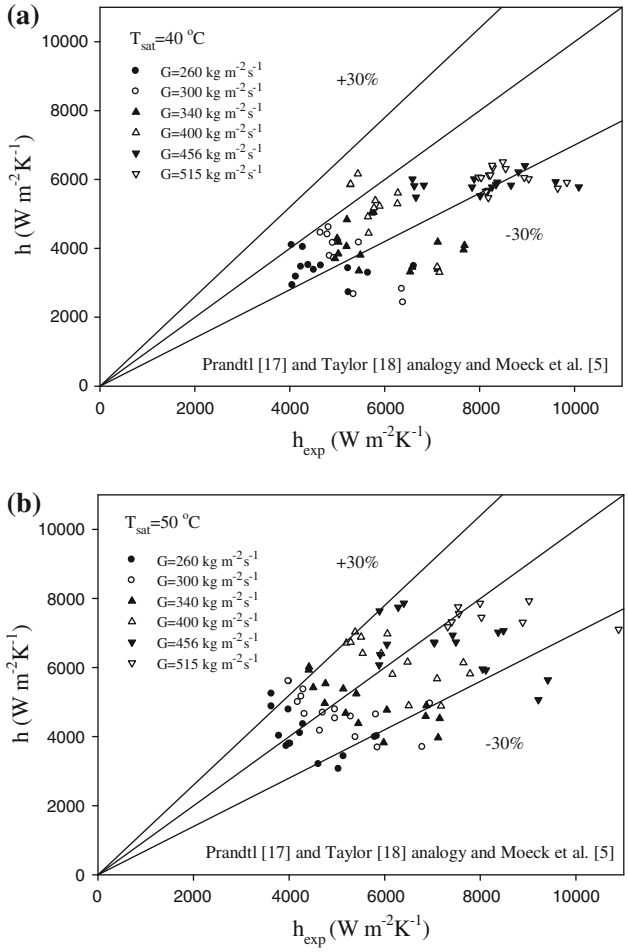

Fig. 7 Comparison of experimental and calculated condensation heat transfer coefficients from the model of Moeck [5], Prandtl [17], and Taylor [18] for $G = 260-515$ kg m^{-2} s^{-1} **a** $T_{sat} = 40$ °C and **b** $T_{sat} = 50$ °C

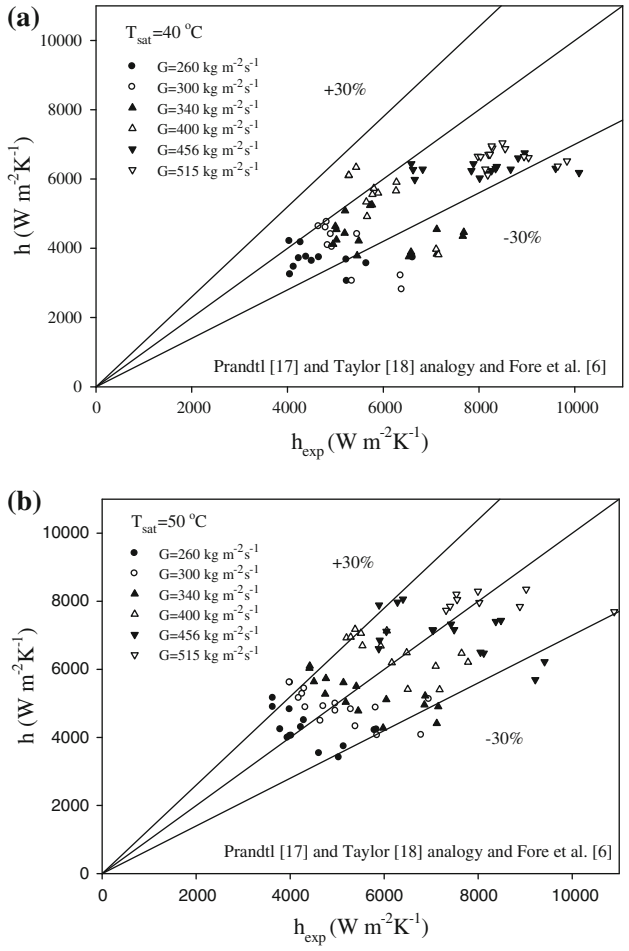

Fig. 8 Comparison of experimental and calculated condensation heat transfer coefficients from the model of Fore et al. [6], Prandtl [17], and Taylor [18] for $G = 260-515$ kg m^{-2} s^{-1} **a** $T_{sat} = 40$ °C and **b** $T_{sat} = 50$ °C

friction factor and boundary layer thickness for the aforementioned analogies is derived using a least-squares technique [48], which can be expressed in the following:

$$f = 0.0449375\left[1 - 26.3453\left(\frac{\delta}{d}\right)\right] \tag{37}$$

$$f = 0.045552\left[1 - 25.89509\left(\frac{\delta}{d}\right)\right] \tag{38}$$

$$f = 0.045554\left[1 - 25.87277\left(\frac{\delta}{d}\right)\right] \tag{39}$$

From Eqs. (37), (38), and (39), these correlations are developed based on their linear relationship. However, a quadratic relationship is also possible using the same methodology. It is suggested, however, that the error of predictions using a quadratic relationship instead of a linear one does not improve significantly.

3.8 Uncertainties

The uncertainties of the Nusselt number and condensation heat transfer coefficient in the test tube varied from ±7.64 to ±10.71 %. It should be noted that similar ranges of uncertainty with minimum and maximum values exist in the literature. The procedures of Kline and McClintock [46] were used for the calculation of all uncertainties. Various uncertainty values of the study can be seen from the authors' previous work. The details are given in Table 3.

4 Results and Discussion

The following paragraphs present the indirectly determined void fraction and film thickness and the friction factor and convective heat transfer coefficient using relevant measured data. For example, there were 80 data points for 40 °C data and 86 data points for 50 °C during the downward laminar

Author's personal copy

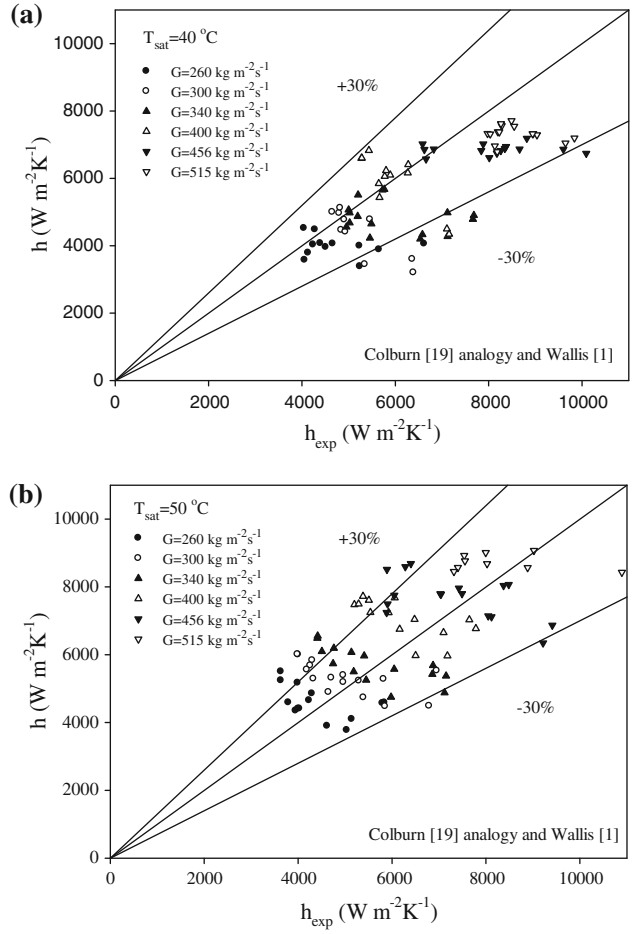

Fig. 9 Comparison of experimental and calculated condensation heat transfer coefficients from the model of Wallis [1] and Colburn [19] for $G = 260-515$ kg m^{-2} s^{-1} **a** $T_{sat} = 40$ °C and **b** $T_{sat} = 50$ °C

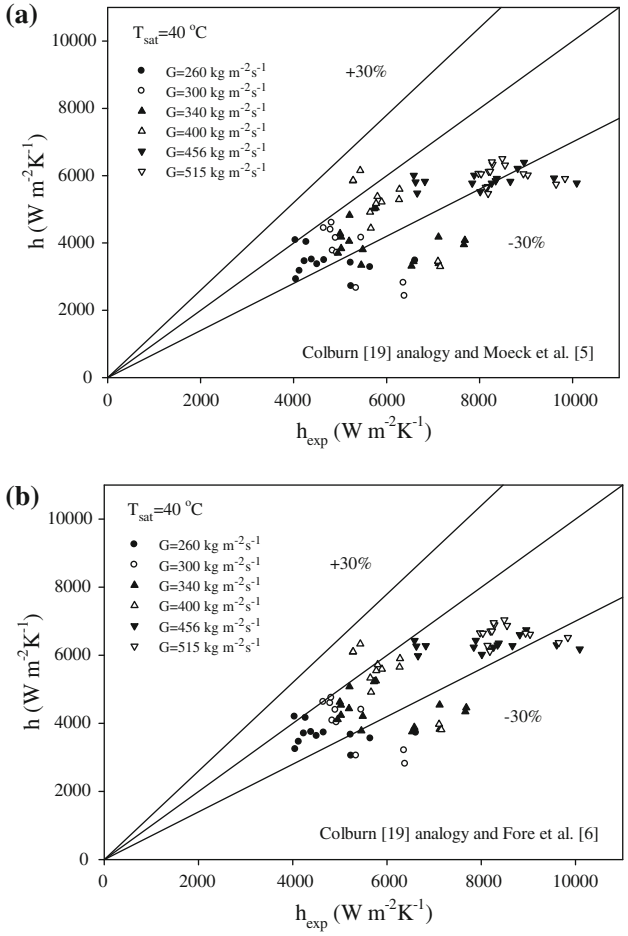

Fig. 10 Comparison of experimental and calculated condensation heat transfer coefficients from the model of Moeck [5] and Colburn [19] for $G = 260-515$ kg m^{-2} s^{-1} **a** $T_{sat} = 40$ °C and **b** $T_{sat} = 50$ °C

condensation of R134a at a high mass flux in a vertical smooth tube over a range of experimental conditions, as shown in Table 4. It should be noted that detailed explanations and some additional figures and tables with different experimental parameters related to this study on the void fraction models and correlations in Table 1, film thickness models, friction factor and frictional pressure drop models, and heat transfer and pressure drop characteristics of data belonging to the experimental apparatuses can be seen in the authors' previous publications [23–39].

In order to develop the empirical convective condensation heat transfer coefficient correlation and investigate the well-known two-phase friction factor models and correlations for the downward two-phase flow of R134a in a vertical round tube with an inner diameter of 8.1 mm, the present study was performed at the Fluid Mechanics, Thermal Engineering and Multiphase Flow Research Laboratory (FUTURE) in KMUTT. Pure HFC-134a was used in the experiments. The discussion of the results follows.

According to the authors' investigation of flow identification studies [30,31] using various flow pattern maps and correlations, the data shown in all tables and figures for the study of R134a condensation in a vertical tube were found in the annular flow section and also checked by sight glass at the inlet and outlet of the test section.

The pressure drop is obtained by dividing the measured pressure drop by the length between pressure taps. In the vertical test section, the length between pressure taps is 0.7 m while the length of the heat exchanger is 0.5 m.

During condensation, the liquid film thickness gradually increases and the thermal resistance is therefore increased, resulting in a decrease in the heat transfer rate. Comparison of the heat transfer coefficient at higher and lower inlet qualities shows that a smaller liquid film thickness, together with a higher vapor velocity at the vapor–liquid interface, results in an increase in the heat transfer coefficient when the inlet quality is higher. The result is that the average heat transfer coefficient increases with increasing inlet quality. In addition to this, the film heat transfer coefficients at low saturation

Author's personal copy

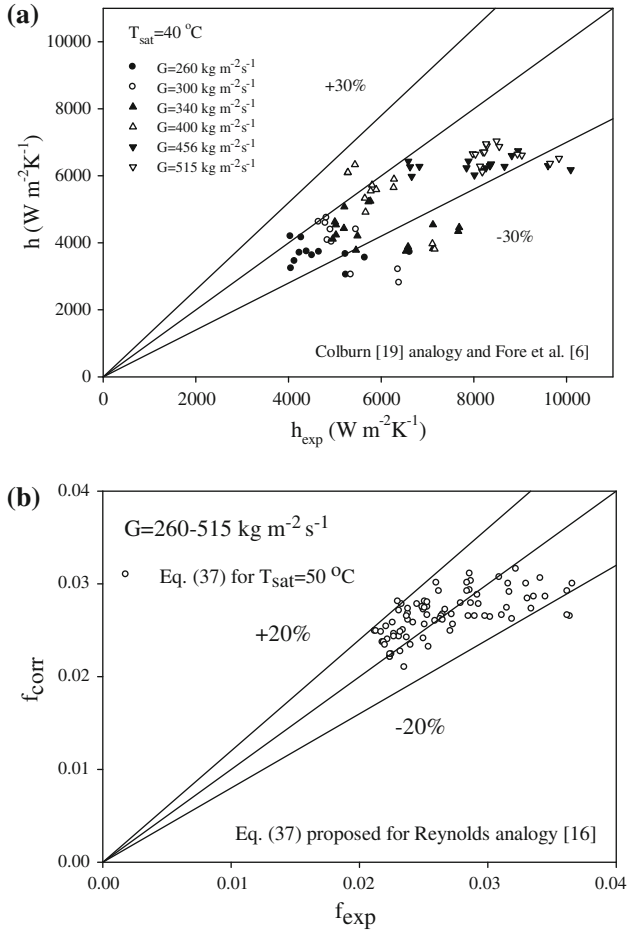

Fig. 11 Comparison of experimental and calculated condensation heat transfer coefficients from the model of Fore et al. [6] and Colburn [19] for $G = 260{-}515$ kg m^{-2} s^{-1} **a** $T_{sat} = 40$ °C and **b** $T_{sat} = 50$ °C

temperature are higher than those at high saturation temperature. This is due to alteration of the physical properties of the refrigerant by condensation temperature or pressure. For that reason, film thickness at low saturation temperature is thinner than at high saturation temperature. As expected, all models show that void fraction values decrease with increasing saturation temperature during the analysis. It is also known that decreasing the vapor quality decreased the void fraction; increasing the gas Reynolds number increased the friction factor in the tube.

According to the authors' investigation of void fraction studies [23,26,31,33] the void fraction models and correlations that agree with the experimental database are shown in Table 1. As a result of the analysis, these void fraction models and correlations give quite similar convective condensation heat transfer coefficients. For that reason, the Chisholm correlation [41] is used as a constant void fraction correlation in the analysis. The effect of the film thickness values from Eq. (10) in the gas flow area in Eq. (34) on the prediction of the convective heat transfer coefficient is found to be negligible due to the film thickness values being much lower than the tube diameter.

Plots of the variation in convective condensation heat transfer coefficients belonging to most predictive friction factors introduced by researchers such as Wallis [1], Moeck [5], and Fore et al. [6] are included in Figs. 3, 4, 5, 6, 7, 8, 9, 10 and 11. It should be noted that the friction models and correlations of Fukano and Furukawa [4], Fanning [7], Wongwises and Kongkiatwanitch [10], Soliman and Feingold [11], Al-Sarkhi and Hanratty [12], Choi et al. [13], and Carey [2] in Table 2 have considerably large deviations from the experimental data due to their incompatible operating conditions; they are not presented in the figures. It should be noted that Carey's [2] friction factor was found to be agreeable with the laminar flow data during low mass flux of R134a in a vertical tube in the authors' previous publication [24]. Comparisons of heat transfer coefficients are shown in Figs. 3, 4 and 5 for the Reynolds analogy [16], Figs. 6, 7 and 8 for the Prandtl [17] and Taylor [18] analogy, and Figs. 9, 10 and 11 for the Colburn analogy [19]. All analyses were performed for the laminar condensation of R134a inside a vertical tube at mean mass fluxes from 260 to 515 kg m^{-2} s^{-1}, saturation temperatures of 40–50 °C, and average vapor qualities of 0.87 and 0.96.

It is clear from the figures for 50°C (Figs. 3b, 4b, 5b) in comparison to those for 40 °C (Figs. 3a, 4a, 5a) that the distribution of the data between the error bands of ±30 % seems quite balanced, as expected, because the Prandtl number of the data is for 50 °C ($Pr = 0.97$). This situation is evident from the mean errors shown in Table 5. As explained in this paper, the Reynolds analogy [16] is valid for the Prandtl number of 1. Hence, these results support the validity of the analysis in the paper. In spite of the different Prandtl number ($Pr = 0.92$) of the 40 °C data, the majority of the data fall within the ±30 % deviation band. In spite of the wide ranges of validity of the Prandtl numbers belonging to the modifications of Prandtl [17], Taylor [18], and Colburn [19], the distribution of the 50 °C data in comparison to the 40 °C ($Pr = 0.92$) data within the error band of ±30 % seems quite balanced, similar to the results of the Reynolds analogy [24]. It can be seen from Table 5 that these modifications of the Reynolds analogy [16] give slightly better lower error rates than the Reynolds analogy [16] for 40 °C ($Pr = 0.92$) data, as expected.

Comparisons of the proposed two-phase friction factors and experimental friction factor are shown in Fig. 12. The majority of the data fall within ± 20 % of the proposed correlations in Eq. (37) for the Reynolds analogy [16], Eq. (38) for the Prandtl [17] and Taylor [18] analogy, and Eq. (39) for the Colburn analogy [19]. Regression analysis was performed and gave convincing correlations as shown in Table 5, especially for the 40 °C ($Pr = 0.92$) data. From the experimental results, the two-phase friction factor of R134a in a copper smooth tube having an inner diameter of 8.1 mm and

Author's personal copy

Table 5 Standard deviation and mean error of analogies between successfully predicted convective heat transfer coefficients and friction factors for T_{sat} = 40 and 50 °C and $G = 260-515$ kg m^{-2} s^{-1}

Convective condensation heat transfer coefficients (h, W m^{-2} K^{-1})/ friction factors (f)	$T_{sat} = 40$ °C		$T_{sat} = 50$ °C	
	Mean error (%)	Standard deviation	Mean error (%)	Standard deviation
Reynolds analogy [16]				
Wallis [1] (h)	−14.84	1,292.33	7.49	2,482.35
Moeck [5] (h)	−28.04	4,631.57	−6.05	1,227.33
Fore et al. [6] (h)	−22.31	1,192.84	−2.69	1,131.75
Eq. (37) (f)	–	–	1.67	0.0022
Prandtl [17] and Taylor [18] analogy				
Wallis [1] (h)	−12.18	1,328.09	8.56	2,489.9
Moeck [5] (h)	−25.79	1,163.69	−5.11	1,238.36
Fore et al. [6] (h)	−19.89	1,225.99	−0.1	1,271.57
Eq. (38) (f)	−1.16	0.0023	5.36	0.0273
Colburn [19] analogy				
Wallis [1] (h)	−12.29	1,330.96	8.49	2,505.57
Moeck [5] (h)	−25.88	1,165.73	−5.17	1,238.81
Fore et al. [6] (h)	−19.99	1,228.5	2.69	1,131.75
Eq. (39) (f)	−1.16	0.0023	5.35	0.0022

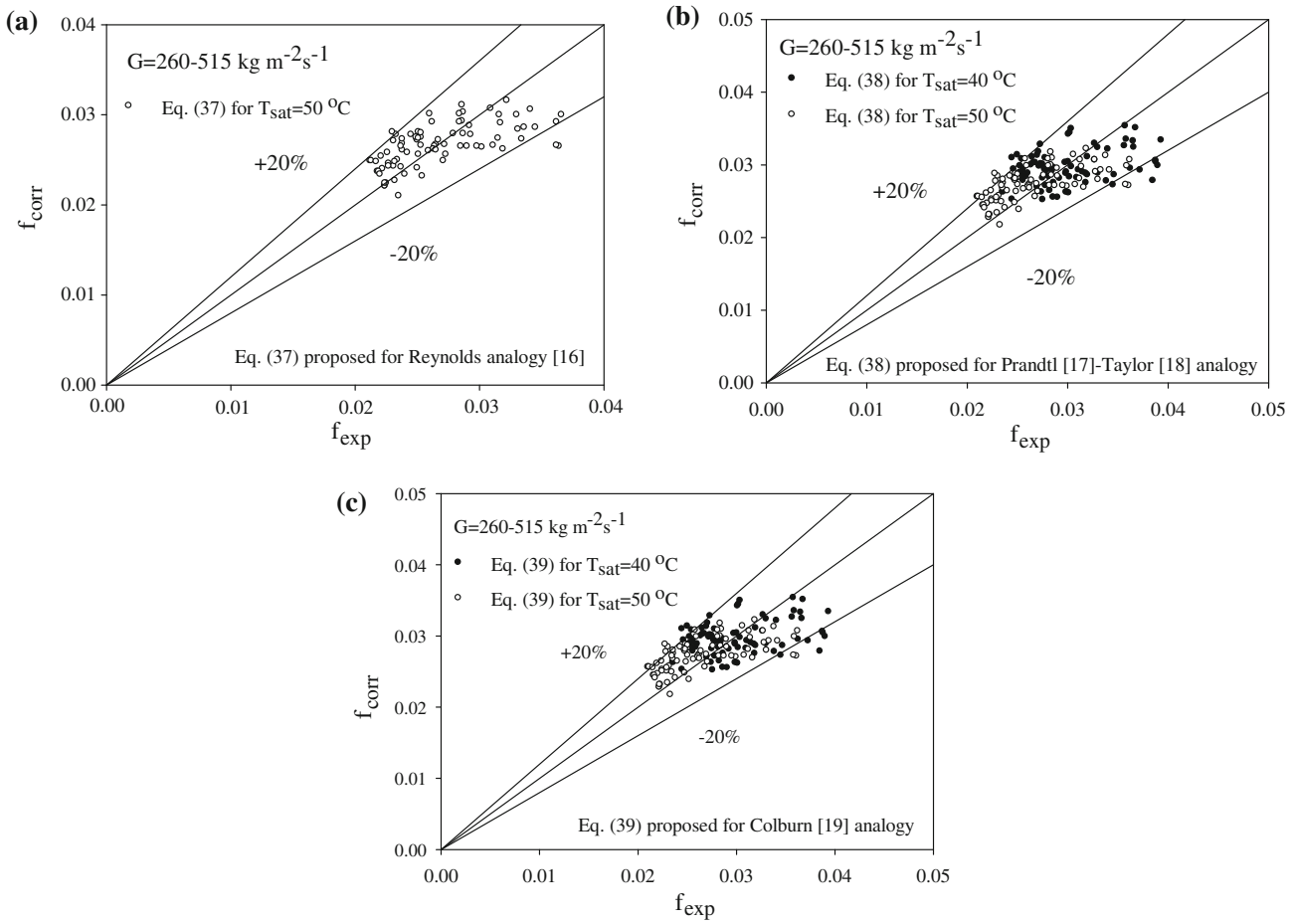

Fig. 12 Comparison of the experimental friction factor with the present friction factors in Eqs. (37), (38), and (39) for the smooth tube

Author's personal copy

length of 0.5 m during downward condensation is correlated based on 186 laminar flow data points for two different condensing temperatures (40 and 50 °C) and six different mass fluxes (260, 300, 340, 400, 456, and 515 kg m^{-2} s^{-1}). It should be noted that their mean error rates are valid for the convective heat transfer coefficients, which are calculated using these equations due to the equations' linear relationship. The friction factors at low saturation temperature are higher than those at high saturation temperature, similar to the situation for the convective heat transfer coefficient and pressure drop, as explained in the above paragraphs. Dalkilic et al. [25] showed that the two-phase friction factors obtained from the equivalent Reynolds number model [47] at the condensing temperature of 50 °C are lower than those obtained at the condensing temperature of 40 °C.

5 Conclusion

Experiments were performed to predict the convective condensation heat transfer coefficient by means of the proper two-phase friction factors and void fraction models and correlations. There is little research on the parameters used in this study. Accurate experiments were performed for annular flow heat transfer data in a vertical tube for the condensation of R134a at high mass flux.

The calculated heat transfer coefficients by means of all film thickness values from the void fraction models and correlations considering the friction factors of Wallis [1], Moeck [5], and Fore et al. [6] are found to be quite near to each other and also to be in agreement with the 186 numbers of laminar flow experimental data within the ±30 % deviation band. In this way, the accuracy of the agreeing void fraction models and correlations of Chisholm [41], Soliman [42], Smith [43], Turner and Wallis [44], and Spedding and Spence [46] is again validated by means of a different model from the authors' previous publications on this subject [23,26,31,33]. New correlations of the two-phase friction factors for the investigated analogies were determined separately from the same dataset within the ±20 % deviation band using the least-squares technique [48], similar to other friction factors in the paper.

Acknowledgments The present study was financially supported by King Mongkut's University of Technology Thonburi (KMUTT). The first and second authors wish to thank KMUTT for providing them with Post-doctoral fellowships, while the third author wish to acknowledge the financial support provided by the Thailand Research Fund and the National Research University Project.

References

1. Wallis, G.B.: One-Dimensional Two-Phase Flow. McGraw-Hill, New York (1969)
2. Carey, V.P.: Liquid-Vapor Phase Change Phenomena. Hemisphere Publishing, New York (1992)
3. Maheshwari, N.K.; Sinha, R.K.; Saha, D.; Aritomi, M.: Inverstigation on condensation in presence of a noncondensible gas for a wide range of Reynolds number. Nucl. Eng. Des. **227**, 219–238 (2004)
4. Fukano, T.; Furukawa, T.: Prediction of the effects of liquid viscosity on interfacial shear and frictional pressure drop in vertical upward gas–liquid annular flow. Int. J. Multiph. Flow **24**, 587–603 (1998)
5. Moeck, E.O.: Annular-dispersed two-phase flow and critical heat flux. AECL **3656**, 337–346 (1970)
6. Fore, L.B.; Beus, S.G.; Bauer, R.C.: Interfacial friction in gas–liquid annular flow: analogies to full and transition roughness. Int. J. Multiph. Flow **26**, 1755–1769 (2000)
7. Fanning, J.T.: A Practical Treatise on Hydraulic and Water Supply Engineering. Van Nostrand, New York (1877) [Revised ed. 1886]
8. Darcy, H.: Recherches experimentales relatives au mouvement de l'Eau dans les Tuyaux. Mallet-Bachelier, Paris (1857)
9. Weisbach, J.: Lehrbuch der Ingenieur und Maschinen-Mechanik, Braunschwieg (1845)
10. Wongwises, S.; Kongkiatwanitch, W.: Interfacial friction factor in vertical upward gas–liquid annular two-phase flow. Int. Commun. Heat Mass Transf. **28**, 323–336 (2001)
11. Soliman, H.M.; Feingold, A.: Analysis of fully developed laminar flow in longitudinal internally finned tubes. Chem. Eng. J. **14**, 119–128 (1977)
12. Al-Sarkhi, A.; Hanratty, T.J.: Effect of pipe diameter on the performance of drag-reducing polymers in annular gas–liquid flows. Inst. Chem. Eng. **79**, 402–408 (2001)
13. Choi, J.Y.; Kedzierski, M.A.; Domanski, P.A.: Generalized pressure drop correlation for evaporation and condensation in smooth and microfin tubes. In: Proceedings of IIF-IIR Commision B1, vol. B4, Paderborn, Germany, pp. 1–9 (2001)
14. Pierre, B.: Flow resistance with boiling refrigerants-part l. ASHRAE J. **6**, 58–65 (1964)
15. Blasius, H.: Grenzschichten in Flüssigkeiten mit kleiner Reibung. Z. Math. u. Phys. **56**, 1–37 (1908)
16. Reynolds, O.: On the extent and action of the heating surface of steam boilers. Proc. Manch. Lit. Phil. Soc. **8**, 7–12 (1874)
17. Prandtl, L.: Eine Beziehung zwischen WS.rmeaustausch und. Str6mungswiderstand bei Fliissigkeiten. Zeitschrift far Physik **11**, 1072–1078 (1910)
18. Taylor, G.I.: British Advisory Committee for Aeronautics. Reports and Memoranda, No. 272 (1916)
19. Colburn, A.P.: A method of correlating forced convection heat transfer data and a comparison with fluid friction. Trans. Am. Inst. Chem. Eng. **29**, 174–210 (1933)
20. Ambrosini, W.; Forgione, N.; Manfredini, A.; Oriolo, F.: On various forms of the heat and mass transfer analogy: Discussion and application to condensation experiments. Nucl. Eng. Des. **236**, 1013–1027 (2006)
21. Chitti, M.S.; Anand, N.K.: An analytical model for local heat transfer coefficients for forced convective condensation inside smooth horizontal tubes. Int. J. Heat Mass Transf. **38**, 615–627 (1995)
22. Kim, M.H.; Corradini, M.L.: Modelling of condensation heat transfer in a reactor containment. Nucl. Eng. Des. **118**, 193–212 (1990)
23. Dalkilic, A.S.; Laohalertdecha, S.; Wongwises, S.: Effect of void fraction models on the two-phase friction factor of R134a during condensation in vertical downward flow in a smooth tube. Int. Commun. Heat Mass Transf. **35**, 921–927 (2008)
24. Dalkilic, A.S.; Yildiz, S.; Wongwises, S.: Experimental investigation of convective heat transfer coefficient during downward laminar flow condensation of R134a in a vertical smooth tube. Int. J. Heat Mass Transf. **52**, 142–150 (2009)

Author's personal copy

25. Dalkilic, A.S.; Laohalertdecha, S.; Wongwises, S.: Two-phase friction factor in vertical downward flow in high mass flux region of refrigerant HFC-134a during condensation. Int. Commun. Heat Mass Transf. **35**, 1147–1152 (2008)
26. Dalkilic, A.S.; Laohalertdecha, S.; Wongwises, S.: Effect of void fraction models on the film thickness of R134a during downward condensation in a vertical smooth tube. Int. Commun. Heat Mass Transf. **36**, 172–179 (2009)
27. Dalkilic, A.S.; Wongwises, S.: Intensive literature review of condensation inside smooth and enhanced tubes. Int. J. Heat Mass Transf. **52**, 3409–3426 (2009)
28. Dalkilic, A.S.; Laohalertdecha, S.; Wongwises, S.: Experimental investigation on heat transfer coefficient of R134a during condensation in vertical downward flow at high mass flux in a smooth tube. Int. Commun. Heat Mass Transf. **36**, 1036–1043 (2009)
29. Dalkilic, A.S.; Agra, O.; Teke, I.; Wongwises, S.: Comparison of frictional pressure drop models during annular flow condensation of R600a in a horizontal tube at low mass flux and of R134a in a vertical tube at high mass flux. Int. J. Heat Mass Transf. **53**, 2052–2064 (2010)
30. Dalkilic, A.S.; Wongwises, S.: An investigation of a model of the flow pattern transition mechanism in relation to the identification of annular flow of R134a in a vertical tube using various void fraction models and flow regime maps. Exp. Therm. Fluid Sci. **34**, 692–705 (2010)
31. Dalkilic, A.S.; Laohalertdecha, S.; Wongwises, S.: Validation of void fraction models and correlations using a flow pattern transition mechanism model in relation to the identification of annular vertical downflow in-tube condensation of R134a. Int. Commun. Heat Mass Transf. **37**, 827–837 (2010)
32. Dalkilic, A.S.; Laohalertdecha, S.; Wongwises, S.: Experimental study of the condensation heat transfer coefficients in high mass flux region in annular flow regime of HFC-134a inside the vertical smooth tube. Heat Transf. Eng. **32**, 33–44 (2011)
33. Dalkilic, A.S.; Laohalertdecha, S.; Wongwises, S.: New experimental approach on the determination of condensation heat transfer coefficient using frictional pressure drop and void fraction models in a vertical tube. Energy Convers. Manag. **51**, 2535–2547 (2010)
34. Dalkilic, A.S.; Wongwises, S.P: A performance comparison of vapour compression refrigeration system using various alternative refrigerants. Int. Commun. Heat Mass Transf. **37**, 1340–1349 (2010)
35. Dalkilic, A.S.; Teke, I.; Wongwises, S.: Experimental analysis for the determination of the convective heat transfer coefficient by measuring pressure drop directly during annular condensation flow of R134a in a vertical smooth tube. Int. J. Heat Mass Transf. **54**, 1008–1014 (2011)
36. Balcilar, M.; Dalkilic, A.S.; Wongwises, S.: Artificial neural network (ANN) techniques for the determination of condensation heat transfer characteristics during downward annular flow of R134a inside a vertical smooth tube. Int. Commun. Heat Mass Transf. **38**, 75–84 (2011)
37. Dalkilic, A.S.: Condensation pressure drop characteristics of various refrigerants in a horizontal smooth tube. Int. Commun. Heat Mass Transf. **38**, 504–512 (2011)
38. Balcılar, M.; Dalkilic, A.S.; Bolat, B.; Wongwises, S.: Investigation of empirical correlations on the determination of condensation heat transfer characteristics using computational numerical methods during downward annular flow of R134a inside a vertical smooth tube. J. Mech. Sci. Technol. **25**, 2683–2701 (2011)
39. Dalkilic, A.S.; Kurekci, N.A.; Wongwises, S.: Effect of void fraction and friction factor models on the prediction of pressure drop of R134a during downward condensation in a vertical tube. Heat Mass Transf. **48**, 123–139 (2012)
40. Chen, S.L.; Gerner, F.M.; Tien, C.L.: General film condensation correlations. Exp. Heat Transf. **1**, 93–107 (1987)
41. Chisholm, D.: Two phase flow in pipelines and heat exchangers. George Godwin in association with The Institution of Chemical Engineers, London (1983)
42. Soliman, H.M.: On the annular-to-wavy flow pattern transition during condensation inside horizontal tubes. Can. J. Chem. Eng. **60**, 475–481 (1982)
43. Smith, S.L.: Void fractions in two-phase flow: a correlation based upon an equal velocity head model. Proc. Inst. Mech. Eng. **36**, 647–664 (1969)
44. Turner, J.M.; Wallis, G.B.: The separate-cylinders model of two-phase flow, paper no. NYO-3114-6, Thayer's School of Engineering, Dartmouth College, Hanover, NH, USA (1965)
45. Spedding, P.L.; Spence, D.R.: Prediction of holdup in two phase flow. Int. J. Eng. Fluid Mech. **2**, 109–118 (1989)
46. Kline, S.J.; McClintock, F.A.: Describing uncertainties in single sample experiments. Mech. Eng. **75**, 3–8 (1953)
47. Moser, K.; Webb, R.L.; Na, B.: A new equivalent Reynolds number model for condensation in smooth tubes. Int. J. Heat Transf. **120**, 410–417 (1998)
48. Scarborough, J.B.: Numerical Mathematical Analysis. Oxford & IBH, New Delhi (1966)

International Journal of Heat and Mass Transfer 65 (2013) 514–532

Contents lists available at SciVerse ScienceDirect

International Journal of Heat and Mass Transfer

journal homepage: www.elsevier.com/locate/ijhmt

A review of entropy generation in nanofluid flow

Omid Mahian [a,*], Ali Kianifar [a], Clement Kleinstreuer [b], Moh'd A. Al-Nimr [c], Ioan Pop [d,*], Ahmet Z. Sahin [e], Somchai Wongwises [f]

[a] Department of Mechanical Engineering, Faculty of Engineering, Ferdowsi University of Mashhad, Mashhad, Iran
[b] Department of Mechanical and Aerospace Engineering, North Carolina State University, Raleigh, NC 27695-7910, USA
[c] Mechanical Engineering Department, Jordan University of Science and Technology, Irbid 22110, Jordan
[d] Department of Mathematics, Babes_-Bolyai University, CP 325, 400084 Cluj-Napoca, Romania
[e] Mechanical Engineering Department, King Fahd University of Petroleum & Minerals, Dhahran, Saudi Arabia
[f] Fluid Mechanics, Thermal Engineering and Multiphase Flow Research Lab. (FUTURE), Department of Mechanical Engineering, Faculty of Engineering, King Mongkut's University of Technology Thonburi, Bangmod, Bangkok 10140, Thailand

ARTICLE INFO

Article history:
Received 9 January 2013
Received in revised form 1 June 2013
Accepted 6 June 2013

Keywords:
Nanofluid flow
Thermophysical property
Entropy generation

ABSTRACT

The development and use of nanofluids, i.e., dilute suspensions of nanoparticles in liquids, have found a wide range of applications in consumer products, nanomedicine, energy conversion, and microsystem cooling. Of special interest is the use of nanofluid flow for enhanced convection heat transfer to achieve rapid cooling of high heat-flux devices. However, for proper optimization of such thermal engineering systems in terms of design and operation, not only the heat transfer has to be maximized but the entropy generation has to be minimized as well. In this paper, theoretical and computational contributions on entropy generation due to flow and heat transfer of nanofluids in different geometries and flow regimes are reviewed. First, a variety of models used to calculate the thermophysical properties of nanofluids are presented. Then, the effects of thermal nanofluid flow on the rate of entropy generation for different applications are discussed. Finally, some suggestions for future work are presented. The aim of this review paper is to motivate the researchers to pay more attention to the entropy generation analysis of heat and fluid flow of nanofluids to improve the system performance.

© 2013 Elsevier Ltd. All rights reserved.

Contents

1. Introduction . . . 515
2. Thermophysical properties of nanofluids . . . 515
   2.1. Density . . . 516
   2.2. Specific heat . . . 516
   2.3. Thermal expansion coefficient . . . 516
   2.4. Viscosity . . . 516
   2.5. Thermal conductivity . . . 517
3. Entropy generation due to nanofluid flow and heat transfer . . . 520
   3.1. Entropy generation in microchannels . . . 521
   3.2. Entropy generation in square, circular, and coiled conduits . . . 522
      3.2.1. Square conduits . . . 522
      3.2.2. Circular tubes . . . 522
      3.2.3. Coiled tubes . . . 523
   3.3. Entropy generation between two rotating cylinders . . . 524
   3.4. Entropy generation in cavities with natural or mixed convection . . . 524
   3.5. Entropy generation in nanofluid flow past a barrier . . . 528
   3.6. Entropy generation in a parallel disk system . . . 528
   3.7. Entropy generation in heat exchangers . . . 530
   3.8. Entropy generation of flow over stretching sheets . . . 530

* Corresponding authors. Tel.: +40 264405300; fax: +40 264591906.
E-mail addresses: omid.mahian@gmail.com (O. Mahian), popm.ioan@yahoo.co.uk (I. .

0017-9310/$ - see front matter © 2013 Elsevier Ltd. All rights reserved.
http://dx.doi.org/10.1016/j.ijheatmasstransfer.2013.06.010

4. Conclusions and future work. 530
Acknowledgments 531
References 531

Nomenclature

A	surface area (m^2)
B_0	magnetic field intensity
C_{nf}	specific heat of nanofluid
D	inner diameter of microchannel
d_f	molecule diameter of base fluid (nm)
d_p	nanoparticle size (nm)
f	friction factor
g	constant of gravity (m/s^2)
Gr	Grashof number
k	thermal conductivity (W/m K)
M	molecular weight of base fluid
$\dot{m}$	mass flow rate (kg/s)
m_p	particle mass
N	Avogadro number
Nu	Nusselt number
P	pressure (Pa)
Pe	Peclet number
Pr	Prandtl Number
R_b	thermal interface resistance
$\dot{S}'_{gen}$	entropy generation rate in length unit (W/m K)
$\dot{S}'''_{gen}$	entropy generation rate in volume unit (W/m^3 K)
T	temperature (K)
u	velocity component in x direction
v	velocity component in y direction

Greek symbols

α	nanoparticle Biot number
α_f	thermal diffusivity of fluid (m^2/s)
δ_r	ratio of coil-to-tube radii
ε	empirical constant in Eq. (18)
η	empirical constant in Eq. (18)
κ_B	Boltzmann constant
μ	dynamic viscosity (kg m/s)
ρ	density (kg/m^3)
ϕ	volume fraction of nanoparticles
υ	kinematics viscosity (m^2/s)
β	thermal expansion coefficient
Γ	constant in Eq. (39)
σ_{nf}	electrical conductivity of nanofluid
γ	ratio of the nano-layer thickness to the original particle radius
ζ	damping coefficient
τ_p	characteristic time interval
ω_n	natural frequency

Subscript

f	base fluid
nf	nanofluid
p	nanoparticles

1. Introduction

In 1995 Choi [1] termed the dilute suspensions of ultrafine particles in common liquids "nanofluids", where the nanoparticles can be metals, metal-oxides, polymers, silica or even carbon nanotubes with at least one length-scale being less than 100 nm. The base fluid is typically water, oil, or ethylene glycol (EG). Such nanofluids exhibit higher thermal conductivities when compared to their base fluids, resulting in enhanced heat transfer rates. Currently the use of nanofluids in thermal engineering systems to augment the thermal efficiency and hence improve performance and reduce thermal device size is an ongoing research area. Examples include different types of heat exchangers [2,3], microchannels [4–6], thermosyphons and heat pipes [7–12], car radiators [13], chillers, cooling of electronics, cooling and heating in buildings, medical applications [14], and solar collectors [15–17]. A number of previous reviews have been devoted to this topic. For example, Saidur et al. [14] discussed the various applications of nanofluids. They also listed the challenges of using nanofluids in thermal engineering systems. Daungthongsuk and Wongwises [18] reviewed both experimental and numerical studies on forced convection heat transfer in nanofluid flow.

Haddad et al. [19] considered both numerical and experimental studies on natural convection of nanofluids in different types of cavities. Ahn and Kim [20] evaluated applications of nanofluids in pool boiling with focusing on the critical heat flux of nanofluid. Khanafer and Vafai [21] analysed published models for calculating thermophysical properties of nanofluids, including thermal conductivity, viscosity, specific heat, and density. Kleinstreuer and Feng [22] conducted a review of various theories and computer simulation models to obtain thermal conductivity values for different nanofluids. Kamyar et al. [23] discussed applications of computational fluid dynamics in nanofluid problems. They summarized the studies done on both conventional numerical and the lattice Boltzmann methods. Mahbubul et al. [24] compared different models presented for the viscosity of nanofluids in the literature. Yu and Xie [25] outlined the methods of preparation, stability and some applications of nanofluids in the fields of energy, mechanical, and biomedical. A review on heat conduction in nanofluids was performed by Fan and Wang [26] where the authors focused on thermal conductivity of nanofluids. Mahian et al. [27] focused on the application of nanofluids for solar energy conversion. Recently, a collection has been provided about flow and heat transfer of nanoparticles and their suspensions in various fields [28].

In recent years the second law of thermodynamics has been applied for the minimization of entropy generation to find optimal engineering system designs [29]. Entropy generation determines the level of irreversibilities accumulating during a process. Consequently, entropy production can be employed as a criterion to assess the performance of engineering devices [30]. For instance, Oztop and Al-Salem [31] conducted a review of entropy generation in natural and mixed convection heat transfer for energy systems. Generally, in a system entropy is generated due to thermal conductivity and viscous effects. In thermal systems where a working fluid is used both of the two effects are considered to calculate the

entropy generation while in solids entropy generation occurs only due to pure conduction (see Refs. [32–34] that discuss entropy generation due to conduction effects).

This paper reviews recent studies performed on entropy generation due to flow and heat transfer of nanofluids. The first part deals with methods to calculate the thermophysical properties of nanofluids. Then, the results are presented regarding the effects of nanofluids on entropy generation rates. Finally, some suggestions are made for future work.

2. Thermophysical properties of nanofluids

In this section, the models used in entropy generation problems to calculate the thermophysical properties of nanofluids, i.e., density, specific heat, thermal expansion coefficient, viscosity and thermal conductivity, are presented.

2.1. Density

The density of a nanofluid (ρ_{nf}) may be calculated from the following relation:

$$\rho_{nf} = \rho_f(1-\phi) - \rho_p\phi \tag{1}$$

where ρ_f is the density of base fluid, ρ_p is the density of nanoparticles, and ϕ is the volume fraction of nanoparticles. This popular correlation is temperature-independent. Thus, Khanafer and Vafai [21], based on the experimental results obtained by Ho et al. [35], presented an expression to calculate the density of Al_2O_3–water nanofluid as follows:

$$\rho_{nf} = 1001.064 - 2738.6191\phi - 0.2095T \tag{2}$$

where $0 \leqslant \phi \leqslant 4\%$ and $5 \leqslant T(^\circ C) \leqslant 40$. Clearly, when the working fluid is Al_2O_3–water, the use of Eq. (2) is more suitable than Eq. (1).

2.2. Specific heat

There are two expressions to calculate the specific heat (C_{nf}) of nanofluids. The first relation reads:

$$C_{nf} = \frac{\rho_f C_f(1-\phi) - \rho_p C_p\phi}{\rho_{nf}} \tag{3}$$

where C_f and C_p are the specific heats of base fluid and nanoparticles, respectively.

Alternatively:

$$C_{nf} = (1-\phi)C_f - \phi C_p \tag{4}$$

Khanafer and Vafai [21] showed that compared to the relation (4), Eq. (3) is in better agreement with experimental data. The review of the literature shows that most of the authors used the Eq. (3) to estimate the specific heat of nanofluids in entropy generation problems.

2.3. Thermal expansion coefficient

The model to calculate the thermal expansion coefficient (β_{nf}) of nanofluids is required in the solution of mixed and free convection problems. The following relation is frequently used to calculate the thermal expansion coefficient [21,36]:

$$\beta_{nf} = \frac{(1-\phi)(\rho\beta)_f - \phi(\rho\beta)_p}{\rho_{nf}} \tag{5}$$

Alternatively, a simpler model reads:

$$\beta_{nf} = (1-\phi)\beta_f - \phi\beta_p \tag{6}$$

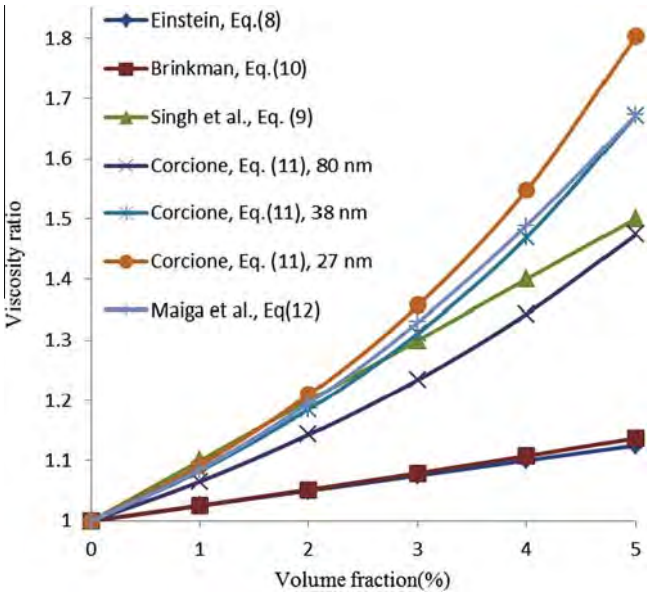

Fig. 1. A comparison of viscosity ratios for different models.

Based on experimental data [35], Khanafer and Vafai [21] presented the following correlation which is valid for Al_2O_3–water nanofluids:

$$\beta_{nf} = \left(-0.479\phi + 9.3158\times10^{-3}T - \frac{4.7211}{T^2}\right)\times10^{-3} \tag{7}$$

where $0 \leqslant \phi \leqslant 4\%$ and $10 \leqslant T(^\circ C) \leqslant 40$.

2.4. Viscosity

Einstein's model, based on kinetic theory, is the oldest one that is used to determine the nanofluid viscosity (μ_{nf}) [37]:

$$\mu_{nf} = \mu_f(1+2.5\phi) \tag{8}$$

where μ_f is the viscosity of base fluid and this relationship is useful for $\phi \leqslant 2\%$. Singh et al. [38] modified the above relation based on various experimental data in the literature for Al_2O_3–water nanofluids. They suggested the following relation:

$$\mu_{nf} = \mu_f(1+10\phi) \tag{9}$$

However, the most common relation that has been used to calculate the viscosity in the entropy generation problems is the Brinkman model [39]:

$$\mu_{nf} = \frac{\mu_f}{(1-\phi)^{2.5}} \tag{10}$$

The Brinkman model is applicable for spherical solid particles and valid for high moderate particle loadings.

As can be seen, in the above relations the temperature of nanofluid as well as the size of nanoparticles are not considered.

Corcione [40] presented an empirical correlation by using regression analysis of experimental data available in the literature as follows:

$$\frac{\mu_{nf}}{\mu_f} = \frac{1}{1-34.87(d_p/d_f)^{-0.3}\phi^{1.03}} \tag{11}$$

where d_p is nanoparticle size, and d_f is the molecule diameter of base fluid which can be calculated by:

$$d_f = \left[\frac{6M}{N\pi\rho_{f,0}}\right]^{1/3} \tag{11a}$$

Table 1
Summary of models used to calculate the viscosity of nanofluids in entropy generation problems.

Model	Nanofluid viscosity formula	Remarks
Einstein's model [37]	$\mu_{nf}=\mu_f(1+2.5\phi)$	– Valid for volume fractions less than 2%
Brinkman model [39]	$\mu_{nf}=\frac{\mu_f}{(1-\phi)^{2.5}}$	– For high volume fractions of nanoparticles with spherical shape
Singh et al. [38]	$\mu_{nf}=\mu_f(1+10\phi)$	– Modification of Einstein's model based on experimental data and valid for Al_2O_3–water nanofluids
Corcione [40]	$\frac{\mu_{nf}}{\mu_f}\frac{1}{1-34.87(d_p/d_f)^{-0.3}\phi^{1.03}}$ where $d_f\left[\frac{6M}{N\pi\rho_{f,0}}\right]$	– Correlation based on experimental data – This correlation considers the diameters of nanoparticle and base fluid molecules
Maiga et al.[41]	Al_2O_3–water:$\mu_{nf}=(123\phi^2+7.3\phi+1)\mu_f$ Al_2O_3–EG:$\mu_{nf}=(306\phi^2-0.19\phi+1)\mu_f$	– Correlations based on experimental data for 28 nm particles of Al_2O_3
Duangthongsuk and Wongwises [42]	$\frac{\mu_{nf}}{\mu_f}=1.0226+0.0477\phi-0.0112\phi^2;\quad T=15\,^\circ C$ $\frac{\mu_{nf}}{\mu_f}=1.013+0.092\phi-0.015\phi^2;\quad T=25\,^\circ C$ $\frac{\mu_{nf}}{\mu_f}=1.018+0.112\phi-0.0177\phi^2;\quad T=35\,^\circ C$	– Correlations based on experimental data, for TiO_2–water nanofluids – Valid for 0.2–2% of concentration
Khanafer and Vafai [21]	$\frac{\mu_{nf}}{\mu_f}=1.0538+0.1448\phi-3.363\times10^{-3}T-0.0147\phi+6.735\times10^{-5}T^2-1.337\frac{\phi}{T}$	– Modified relation of Duangthongsuk and Wongwises's correlations [40] – Valid for $15\leqslant T(^\circ C)\leqslant 35$ and $0.2\leqslant\phi(\%)\leqslant 2$
Rea et al. [43]	$\mu_{nf}(\phi,T)=\mu_f(T)\exp[4.91\phi(0.2092-\phi)]$	– Curve fitting of experimental data [42] for Al_2O_3–water nanofluids – Valid for $\phi(\%)\leqslant 6$ and $20\leqslant T(^\circ C)\leqslant 80$
Jang et al. [46]	$\mu_{nf}=(1+2.5\phi)[1+\eta(\frac{d_p}{D})^{-2\varepsilon}\phi^{2/3(\varepsilon+1)}]$	– Modified relation of Einstein's model [33] to calculate the viscosity of a nanofluid flowing in micro and mini tubes

where M is the molecular weight of base fluid, N is the Avogadro number, and $\rho_{f,0}$ is the density of base fluid calculated at the temperature of 293 K. As it is seen, in this relation the viscosity is a function of the size of nanoparticles and the molecular diameter of base fluid.

Based on curve-fitting of experimental results, Maiga et al. [41] presented for 28 nm-particles two relations for the viscosity of Al_2O_3–water and Al_2O_3–EG nanofluids, respectively:

$$\mu_{nf}=(123\phi^2+7.3\phi+1)\mu_f \tag{12}$$

$$\mu_{nf}=(306\phi^2-0.19\phi+1)\mu_f \tag{13}$$

Fig. 1 shows a comparison of the five relations for Al_2O_3–water nanofluids with volume fractions less than 5%. For the Corcione correlation, three nanoparticle sizes, including 27, 38, and 80 nm were considered. The Einstein and Brinkman models give approximately the same results for all volume fractions. It is seen that the Einstein and Brinkman models underestimate the viscosity ratio with respect to experimental correlations. Corcione's correlation [40] underestimates the viscosity ratio for the nanoparticle size of 80 nm compared to the correlation of Singh et al. [38], while for the size of 27 nm the results are the opposite. An increase in particle size decreases the viscosity ratio of the nanofluid based on Corcione's correlation [40]. It should be pointed out that, even for volume fractions of 2%, the difference between the models and the experimental correlations is about 10% and increases as the volume fraction is increased. It is also seen that the results obtained by correlation of Maiga et al. [41] which is for Al_2O_3 nanoparticles with size of 28 nm is very close to the results of Corcione's correlation [40] where the size is 38 nm. Since viscosity has an important contribution in the entropy generation, this difference can be important and discussion on this subject is needed. Particle size is one of the parameters that should be considered in the new models.

Duangthongsuk and Wongwises [42] based on their experimental data, presented the following correlations to calculate the viscosity of TiO2–water nanofluids:

$$\begin{aligned}\frac{\mu_{nf}}{\mu_f}&=1.0226+0.0477\phi-0.0112\phi^2;\quad T=15^\circ C\\ \frac{\mu_{nf}}{\mu_f}&=1.013+0.092\phi-0.015\phi^2;\quad T=25^\circ C\\ \frac{\mu_{nf}}{\mu_f}&=1.018+0.112\phi-0.0177\phi^2;\quad T=35^\circ C\end{aligned} \tag{14}$$

The above relations are valid for volume fractions between 0.2% and 2%, by considering the size of 21 nm for nanoparticles. Khanafer and Vafai [21] gave another correlation of the experimental data by Duangthongsuk and Wongwises [42] as follows:

$$\frac{\mu_{nf}}{\mu_f}=1.0538+0.1448\phi-3.363\times10^{-3}T-0.0147\phi+6.735\times10^{-5}T^2-1.337\frac{\phi}{T} \tag{15}$$

where $15\leqslant T(^\circ C)\leqslant 35$ and $0.2\leqslant\phi(\%)\leqslant 2$.

Rea et al. [43] using curve fitting of experimental data [44] presented the following correlation for Al_2O_3–water nanofluids:

$$\mu_{nf}(\phi,T)=\mu_f(T)\exp[4.91\phi(0.2092-\phi)] \tag{16}$$

For water as the base fluid, the viscosity (μ_f) can be obtained by the following relation [45]:

$$\mu_f=\mu_{ref}\left(\frac{T}{T_{ref}}\right)^n\exp\left[B\left(\frac{1}{T}-\frac{1}{T_{ref}}\right)\right] \tag{17}$$

where $B=4700$, $n=8.9$, $T_{ref}=295$ K and $\mu_{ref}=959\times10^{-6}\frac{N.S}{m^2}$.

The correlation given by Rea et al. [43] is valid for Al_2O_3–water nanofluid where the volume fraction is less than 6% and the range of temperature is between 20 °C and 80 °C. Jang et al. [46] modified the Einstein model by considering the slip velocity of nanoparticles to calculate the viscosity of a nanofluid flowing in micro and mini tubes.

$$\mu_{nf}=(1+2.5\phi)\left[1+\eta\left(\frac{d_p}{D}\right)^{-2\varepsilon}\phi^{2/3(\varepsilon+1)}\right] \tag{18}$$

in which D is the inner diameter of microchannel, and ε and η are empirical constants which are for Al_2O_3 nanoparticles $-1/4$ and 280, respectively. It should be noted that in more than 50% of the papers on entropy generation, the Brinkman model has been used to calculate the viscosity of nanofluid. Table 1 summarizes different models used to estimate the viscosity of nanofluids.

2.5. Thermal conductivity

The Maxwell model [47] is the oldest approach to calculate the thermal conductivity of solid-liquid mixtures, where

$$k_{nf}=\frac{k_p+2k_f+2\phi(k_p-k_f)}{k_p+2k_f-\phi(k_p-k_f)}k_f \tag{19}$$

In the above relation k_f, k_p and k_{nf} are thermal conductivities of the base fluid, nanoparticles, and nanofluid, respectively. This model is useable where $\phi \ll 1$ or the magnitude of $\left|\frac{k_p}{k_f}-1\right|$ is very smaller than one [21].

Bruggeman [48], considering interactions among the spherical particles, presented the following model:

$$\frac{k_{nf}}{k_f}=\frac{(3\phi-1)\frac{k_p}{k_f}+\{3(1-\phi)-1\}+\sqrt{\Delta}}{4};$$
$$\text{where}:\Delta=\left[(3\phi-1)\frac{k_p}{k_f}+\{3(1-\phi)-1\}\right]^2+8\frac{k_p}{k_f} \tag{20}$$

This relation can be used for high quantities of particle loadings of nanoparticles with a spherical shape.

Hamilton and Crosser [49] modified the Maxwell model by considering the shape of nanoparticles as:

$$k_{nf}=\frac{k_p+(n-1)k_f+(n-1)\phi(k_p-k_f)}{k_p+(n-1)k_f-\phi(k_p-k_f)}k_f \tag{21}$$

in which n is the empirical shape factor, given by $n=\frac{3}{\psi}$ and ψ is the particle sphericity. The sphericity is 1 and 0.5 for the spherical and cylindrical particles, respectively. Yu and Choi [50] considered the effect of the liquid nanolayer on the surface of the spherical nanoparticles, proposing:

$$k_{nf}=\frac{k_p+2k_f+2(k_p-k_f)(1+\gamma)^3\phi}{k_p+2k_f-2(k_p-k_f)(1+\gamma)^3\phi}k_p \tag{22}$$

where γ is the ratio of the nano-layer thickness to the original particle radius, which is considered to be equal to 0.1.

Singh et al. [38] postulated a simple correlation for Al_2O_3–water nanofluids as:

$$k_{nf}=k_f(1+4\phi) \tag{23}$$

Based on experimental data, Maiga et al. [41] presented two correlations for the thermal conductivity of Al_2O_3–water and Al_2O_3–EG nanofluids with 28 nm particle size as follows:

Al_2O_3–water:

$$k_{nf}=(4.97\phi^2+2.72\phi+1)k_f \tag{24}$$

Al_2O_3–ethylene glycol:

$$k_{nf}=(28.905\phi^2+2.8273\phi+1)k_f \tag{25}$$

Duangthongsuk and Wongwises [42] provided correlations for thermal conductivity of TiO_2 nanoparticles with diameters of 21 nm suspended in water where volume fractions are between 0.2% and 2% and at three different temperatures:

$$\begin{aligned}\frac{k_{nf}}{k_f}&=1.0225+0.0272\phi;\quad T=15^\circ\text{C}\\ \frac{k_{nf}}{k_f}&=1.0204+0.0249\phi;\quad T=25^\circ\text{C}\\ \frac{k_{nf}}{k_f}&=1.0139+0.0250\phi;\quad T=35^\circ\text{C}\end{aligned} \tag{26}$$

Considering the effect of Brownian motion on nanoparticles, Koo and Kleinstreuer [51] presented the following relation for the thermal conductivity of nanofluids (K–K model):

$$k_{nf}=k_{static}+k_{Brownian} \tag{27}$$

where the static part (k_{static}) is:

$$k_{static}=\left(1+\frac{3(k_p/k_f-1)\phi}{(k_p/k_f+2)-(k_p/k_f-1)\phi}\right)k_f \tag{27-a}$$

The thermal conductivity of nanofluid due to Brownian motion ($k_{Brownian}$) is obtained by:

$$k_{Brownian}=5\times10^4\sigma\phi(\rho c_p)_f\sqrt{\frac{\kappa_B T}{\rho_p d_p}}f(T,\phi) \tag{27-b}$$

where σ and f are two empirical functions and κ_B is the Boltzmann constant. Li [52] developed the K-K model further and replaced the functions σ and f by a single function g. The KKL model reads:

$$k_{Brownian}=5\times10^4\phi(\rho c_p)_f\sqrt{\frac{\kappa_B T}{\rho_p d_p}}g(T,\phi,d_p) \tag{27-c}$$

where:

$$\begin{aligned}g(T,\phi,d_p)=&(a_1+a_2\ln(d_p)+a_3\ln(\phi)+a_4\ln(\phi)\ln(d_p)\\&+a_5\ln(d_p)^2)\ln(T)+(a_6+a_7\ln(d_p)+a_8\ln(\phi)\\&+a_9\ln(\phi)\ln(d_p)+a_{10}\ln(d_p)^2)\end{aligned} \tag{28-a}$$

The constants a_1–a_{10} are determined based on the type of pairing of nanoparticle and carrier liquid [52]. A more advanced theory which is free of any matching function or coefficent, called the F–K model, has been proposed by Feng and Kleinstreuer [53]. This model is based on an analogy between the random nanoparticle fluctuations generated by the Brownian motion effect and turbulent fluctuations. The experimentally validated F–K model has served numerous nanofluid flow applications consisting of mixtures of water and metal-oxide nanoparticles with particle-diameters in the range $30 < d_p < 50$ nm, volume fractions up to 5%, and mixture temperatures below 350 K. The thermal conductivity model is given as:

$$k_{nf}=k_{static}+k_{mm} \tag{29}$$

in which k_{static} is given by Eq. (27-a), and k_{mm} which is the micro-mixing part induced by the Brownian motion of nanoparticles is defined as:

$$\begin{aligned}k_{mm}=&49500\frac{\kappa_B\tau_P}{2m_p}\cdot C_c\cdot(\rho c_p)_{nf}\cdot\phi^2\cdot(T\ln T-T)\\&\cdot\frac{\exp(-\zeta\omega_n\tau_p)Sinh\left(\sqrt{\frac{(3\pi\mu_f d_p)^2}{4m_p^2}-\frac{K_{p-p}}{m_p}}\frac{m_p}{3\pi\mu_f d_p}\right)}{\tau_p\sqrt{\frac{(3\pi\mu_f d_p)^2}{4m_p^2}-\frac{K_{p-p}}{m_p}}}\end{aligned} \tag{30}$$

Here, m_p is the particle mass and d_p is the particle diameter. The derived value of C_c is equal to 38 for nanofluids with metal-oxide nanoparticles. Also, the damping coefficient ζ, natural frequency ω_n, and characteristic time interval τ_p are defined as:

$$\zeta=\frac{3\pi d_p\mu_f}{2m_p\omega_n},\quad \omega_n=\sqrt{\frac{K_{P-P}}{m_p}},\quad \tau_p=\frac{m_p}{3\pi\mu_f d_p} \tag{31}$$

The parameter K_{P-P} indicates the magnitude of particle–particle interaction intensity and is determined as:

$$K_{P-P}=\rho_p\cdot\sqrt{d_p}\cdot\left(\frac{32.1724\times273K}{T}-19.4849\right) \tag{32}$$

Fig. 2 shows comparisons between the different models which are discussed above where Al_2O_3–water nanofluid is selected as the case study. The following can be noted from the figure:

1. The nanoparticles with cylindrical shape have higher thermal conductivity than particles with a spherical shape.
2. At low volume fractions, based on F–K model where the particle size is assumed to be 47 nm, the temperature has no significant effect on thermal conductivity, while for higher volume fractions (4%), the thermal conductivity at 60 °C is about 12% more than the thermal conductivity at 20 °C. Therefore, because of the strong role of thermal conductivity in entropy generation, the variations of thermal conductivity with temperature should be considered especially for high volume fractions.

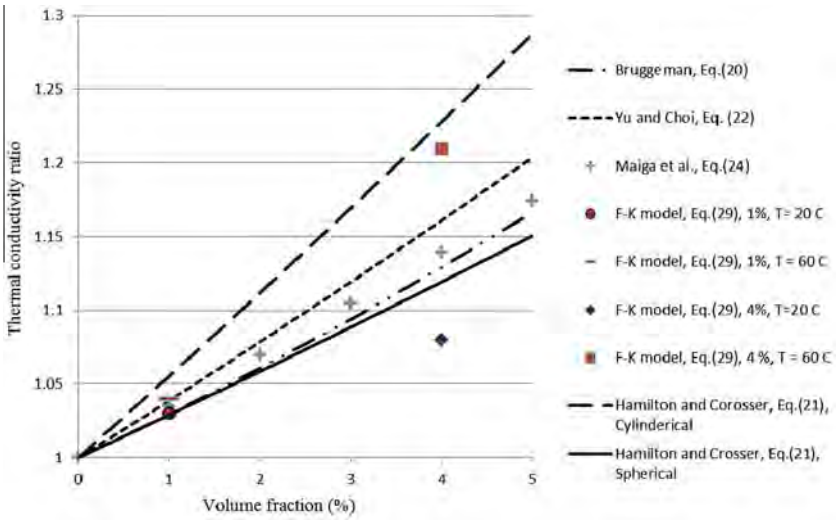

Fig. 2. A comparison of thermal conductivity ratios for different models.

3. At low volume fractions (i.e. less than 1%), the various models give close values for thermal conductivity for spherical particles, also the temperature effect is not considerable.

It should be noted that the thermal conductivity obtained by Eq. (23) is fitted exactly on the values of thermal conductivity calculated by Eq. (22) which is Yu and Choi model, therefore, it is not presented in Fig. 2.

Table 2
Summary of models used to calculate the thermal conductivity of nanofluids in entropy generation problems.

Model	Nanofluid thermal conductivity formula	Remarks
Maxwell [47]	$k_{nf}=\frac{k_p+2k_f+2\phi(k_p-k_f)}{k_p+2k_f-\phi(k_p-k_f)}k_f$	For spherical particles.
Bruggeman [48]	$\frac{k_{nf}}{k_f}=\frac{(3\phi-1)\frac{k_p}{k_f}+\{3(1-\phi)-1\}+\sqrt{\Delta}}{4}$; $where:\ \Delta=[(3\phi-1)\frac{k_p}{k_f}+\{3(1-\phi)-1\}]^2+8\frac{k_p}{k_f}$	For high volume fractions of nanoparticles with spherical shape.
Hamilton and Crosser [49]	$k_{nf}=\frac{k_p+(n-1)k_f+(n-1)\phi(k_p-k_f)}{k_p+(n-1)k_f-\phi(k_p-k_f)}$ where $n=\frac{3}{\psi}$ For spherical particles $\psi=1$ For cylindrical particles $\psi=0.5$	For spherical and non-spherical nanoparticles.
Yu and Choi [50]	$k_{nf}=\frac{k_p+2k_f+2(k_p-k_f)(1+\gamma)^3\phi}{k_p+2k_f-2(k_p-k_f)(1+\gamma)^3\phi}k_p$ where γ is the ratio of the nano-layer thickness to the original particle radius, which is considered to be equal to 0.1	– Modified Maxwell model [47] – Spherical particles.
Singh et al. [38]	$k_{nf}=k_f(1+4\phi)$	– Modified Maxwell model [47] based on experimental data for Al_2O_3–water nanofluids
Maiga et al. [40]	Al_2O_3–water: $k_{nf}=(4.97\phi^2+2.72\phi+1)k_f$ Al_2O_3–EG: $k_{nf}=(28.905\phi^2+2.8273\phi+1)k_f$	– Correlations based on experimental data for 28 nm nanoparticle size
Duangthongsuk and Wongwises [42]	$\frac{k_{nf}}{k_f}=1.0225+0.0272\phi \quad T=15\ ^\circ C$ $\frac{k_{nf}}{k_f}=1.0204+0.0249\phi; \quad T=25\ ^\circ C$ $\frac{k_{nf}}{k_f}=1.0139+0.0250\phi; \quad T=35\ ^\circ C$	– Correlations based on experimental data; for TiO_2–water nanofluids. – Valid for 0.2–2% of concentration.
Koo and Kleinstreuer (K-K model) [51]	$k_{nf}=k_{static}+k_{Brownian}$ where: $k_{static}=(1+\frac{3(k_p/k_f-1)\phi}{(k_p/k_f+2)-(k_p/k_f-1)\phi})k_f$ $k_{Brownian}=5\times10^4\sigma\phi(\rho c_p)_f\sqrt{\frac{\kappa_B T}{\rho_p d_p}}f(T,\phi)$	– Extension of the Maxwell model [47], considering the effect of Brownian motion on nanoparticles. – σ and f are two empirical functions.
Li [52] (KKL model)	$k_{nf}=k_{static}+k_{Brownian}$ where: $k_{static}=(1+\frac{3(k_p/k_f-1)\phi}{(k_p/k_f+2)-(k_p/k_f-1)\phi})k_f$ $k_{Brownian}=5\times10^4\phi(\rho c_p)_f\sqrt{\frac{\kappa_B T}{\rho_p d_p}}g(T,\phi,d_p)$	– Modified K-K model [51] by replacing the β and f functions with a g-function.
Feng and Kleinstreuer [53] (F–K model)	$k_{nf}=k_{static}+k_{mm}$ where: $k_{mm}=49500\frac{\kappa_B\tau_p}{2m_p}.C_c.(\rho c_p)_{nf}.\phi^2.(T\ln T-T)$. $k_{static}=(1+\frac{3(k_p/k_f-1)\phi}{(k_p/k_f+2)-(k_p/k_f-1)\phi})k_f\ \frac{\exp(-\zeta\omega_n\tau_p)Sinh(\sqrt{\frac{(3\pi\mu_f d_p)^2}{4m_p^2}-\frac{\kappa_{p-p}}{m_p}}\ \frac{m_p}{3\pi\mu_f d_p})}{\tau_p\sqrt{\frac{(3\pi\mu_f d_p)^2}{4m_p^2}-\frac{\kappa_{p-p}}{m_p}}}$	– Based on an analogy between the random nanoparticle fluctuations generated by Brownian motion effect and turbulent fluctuations. – For particle-diameters in the range of 30 < dp < 50 nm, volume fractions up to 5%, and mixture temperatures below 350 K – The model considers particle-particle interaction, and it is free of empirical constants or matching functions.
Patel et al. [54]	$\frac{k_{nf}}{k_f}=1+\frac{k_p A_p}{k_f A_f}+C_e k_p Pe\frac{A_p}{k_f A_f}$ where: $\frac{A_p}{A_f}=\frac{d_f}{d_p}\frac{\phi}{(1-\phi)}$ and $Pe=\frac{u_p d_p}{\alpha_f}u_p=\frac{2\kappa_B T}{\pi\mu_f d_p^2}$	– This model considers size and velocity of particles.
Rea et al. [43]	$k_{nf}=k_f(1+4.5503\phi)$	– Correlation for Al_2O_3–water nanofluids, based on experimental data [44]
Prasher et al.[57]	$\frac{k_{nf}}{k_f}=(1+\Gamma Re_b^m Pr^{0.333}\phi)\times(\frac{[k_p(1+2\alpha)+2k_f]+2varphi[k_p(1-2\alpha)-k_f]}{[k_p(1+2\alpha)+2k_f]-\phi[k_p(1-2\alpha)-k_f]})$	– Considers the random motion-induced convection
Khanafer and Vafai [21]	$\frac{k_{nf}}{k_f}=1+1.0112\phi+2.4375\phi\left(\frac{47}{d_p(\mathrm{nm})}\right)-0.0248\phi_p(\frac{k_p}{0.613})$	– Correlation based on different experimental works. – Valid for Al_2O_3–water and CuO–water nanofluids, volume fractions up to 15% and particle size between 13 nm and 80 nm

Patel et al. [54] presented the following model to calculate the thermal conductivity of nanofluids.

$$\frac{k_{nf}}{k_f} = 1 + \frac{k_p A_p}{k_f A_f} + C_e k_p Pe \frac{A_p}{k_f A_f} \tag{33}$$

where C_e is a constant and is obtained based on the experiments. Also, A_p/A_f and Pe are determined as:

$$\frac{A_p}{A_f} = \frac{d_f}{d_p}\frac{\phi}{(1-\phi)} \quad \text{and} \quad Pe = \frac{u_p d_p}{\alpha_f} \tag{34-a, -b}$$

where u_p is the Brownian motion velocity of the nanoparticles, given by:

$$u_p = \frac{2\kappa_B T}{\pi \mu_f d_p^2} \tag{35}$$

In another model [55,56], it is assumed that the thermal conductivity of nanofluid consists of two parts including the thermal conductivity of stagnant as well as thermal conductivity due to thermal dispersion as follows:

$$k_{nf} = k_{nf0} + k_d \tag{36}$$

The static thermal conductivity is obtained based on Maxwell's model [47], and the thermal conductivity due to thermal dispersion (k_d) is calculated as:

$$k_d = C_e (\rho C_p)_{nf} \sqrt{u^2 + v^2}\, \phi d_p \tag{37}$$

where C_e is the constant obtained from experiments, and u and v are the x- and y-components of the fluid velocity. Rea et al. [43] gave the following correlation for Al_2O_3–water nanofluids, based on experimental data [44]:

$$k_{nf} = k_f(1 + 4.5503\phi) \tag{38}$$

Prasher et al. [57] provided a correlation by considering the random motion-induced convection as follows:

$$\frac{k_{nf}}{k_f} = (1 + \Gamma \mathrm{Re}_b^m \mathrm{Pr}^{0.333}\phi) \times \left(\frac{[k_p(1+2\alpha)+2k_f] + 2\phi[k_p(1-2\alpha)-k_f]}{[k_p(1+2\alpha)+2k_f] - \phi[k_p(1-2\alpha)-k_f]}\right) \tag{39}$$

in which the Reynols number due to Brownian motion is $\mathrm{Re}_b = \sqrt{18\kappa_b T/\pi\rho_p d_p}/\upsilon_f$, and α is the nanoparticle Biot number which is defined as $\alpha = 2R_b k_f/d_p$. Also, R_b is the thermal interface resistance, where for water-based nanofluids $R_b = 0.77 \times 10^{-8}$ K m^2/W, while $\Gamma$and m are empirical constants. For Al_2O_3 nanoparticles suspended in water, it was observed that $m = 2.5$ and $\Gamma = 40{,}000$. Khanafer and Vafai [21], based on different works published in the literature, presented a general correlation for the thermal conductivity of Al_2O_3–water and CuO–water nanofluids as a function of particle size, volume fraction, and thermal conductivity of nanoparticles as follows:

$$\frac{k_{nf}}{k_f} = 1 + 1.0112\phi + 2.4375\phi\left(\frac{47}{d_p(\mathrm{nm})}\right) - 0.0248\phi_p\left(\frac{k_p}{0.613}\right) \tag{40}$$

This relation is valid for volume fractions up to 15% and particle size between 13 nm and 80 nm. Table 2 provides a summary of the different models used to estimate the thermal conductivity of nanofluids.

3. Entropy generation due to nanofluid flow and heat transfer

Before presenting the works done about the entropy generation due to naofluids flow in different geometries and regimes, it is useful to give some information about the methods used to calculate the entropy generation. The entropy generation can be calculated through two different approaches. In the first approach, the local entropy generation can be obtained at every point of the system under consideration. Then, if it is needed, the total entropy generation can be calculated easily by integrating the local entropy generation distribution over the volume. The local entropy generation in different coordinate systems can be obtained by using the following relations [58]:

in Cartesian coordinates (x,y,z):

$$\dot{S}'''_{gen} = \frac{k}{T^2}\left[\left(\frac{\partial T}{\partial x}\right)^2 + \left(\frac{\partial T}{\partial y}\right)^2 + \left(\frac{\partial T}{\partial z}\right)^2\right] + \frac{\mu}{T}\left\{2\left[\left(\frac{\partial v_x}{\partial x}\right)^2 + \left(\frac{\partial v_y}{\partial y}\right)^2 + \left(\frac{\partial v_z}{\partial z}\right)^2\right] + \left(\frac{\partial v_x}{\partial y} + \frac{\partial v_y}{\partial x}\right)^2 + \left(\frac{\partial v_x}{\partial z} + \frac{\partial v_z}{\partial x}\right)^2 + \left(\frac{\partial v_x}{\partial z} + \frac{\partial v_z}{\partial y}\right)^2\right\} \tag{41}$$

in Cylinderical coordinates (r,θ,z)

$$\dot{S}'''_{gen} = \frac{k}{T^2}\left[\left(\frac{\partial T}{\partial r}\right)^2 + \left(\frac{1}{r}\frac{\partial T}{\partial \theta}\right)^2 + \left(\frac{\partial T}{\partial z}\right)^2\right] + \frac{\mu}{T}\left\{2\left[\left(\frac{\partial v_r}{\partial r}\right)^2 + \frac{1}{r^2}\left(\frac{\partial v_\theta}{\partial \theta} + v_r\right)^2 + \left(\frac{\partial v_z}{\partial z}\right)^2\right] + \left(\frac{\partial v_\theta}{\partial z} + \frac{1}{r}\frac{\partial v_z}{\partial \theta}\right)^2 + \left(\frac{\partial v_z}{\partial r} + \frac{\partial v_r}{\partial z}\right)^2 + \left(\frac{1}{r}\frac{\partial v_r}{\partial \theta} + r\frac{\partial}{\partial r}\left(\frac{v_\theta}{r}\right)\right)^2\right\} \tag{42}$$

in Spherical coordinates (r,θ,ϕ)

$$\dot{S}'''_{gen} = \frac{k}{T^2}\left[\left(\frac{\partial T}{\partial r}\right)^2 + \left(\frac{1}{r}\frac{\partial T}{\partial \theta}\right)^2 + \left(\frac{1}{r\sin\theta}\frac{\partial T}{\partial \phi}\right)^2\right] + \frac{\mu}{T}\left\{2\left[\left(\frac{\partial v_r}{\partial r}\right)^2 + \left(\frac{1}{r}\frac{\partial v_\theta}{\partial \theta} + \frac{v_r}{r}\right)^2 + \left(\frac{1}{r\sin\theta}\frac{\partial v_\phi}{\partial \phi} + \frac{v_r}{r} + \frac{v_\theta \cot\theta}{r}\right)^2\right] + \left[r\frac{\partial}{\partial r}\left(\frac{v_\theta}{r}\right) + \frac{1}{r}\frac{\partial v_r}{\partial \theta}\right]^2 + \left[\frac{1}{r\sin\theta}\frac{\partial v_r}{\partial \phi} + r\frac{\partial}{\partial r}\left(\frac{v_\phi}{r}\right)\right]^2 + \left[\frac{\sin\theta}{r}\frac{\partial}{\partial \theta}\left(\frac{v_\phi}{\sin\theta}\right) + \frac{1}{r\sin\theta}\frac{\partial v_\phi}{\partial \phi}\right]^2\right\} \tag{43}$$

The above equations show clearly the important contributions of thermal conductivity and viscosity on the entropy generation. It is obvious that in the case of nanofluids, the properties of nanofluids (k_{nf}; μ_{nf}) should be used. The above equations indicate that, to calculate the local entropy generation, the gradients of velocity and temperature must be known at the relevant point in the domain.

In the second approach, correlations for friction factor and Nusselt number, if available, can be used to evaluate the total entropy generation. In this case, there is no need to solve the momentum and energy equations, because the values of Nusselt number and friction factor are assumed to be known.The entropy generation per unit of length for a duct with arbitrary cross section is derived by Bejan and is available in his book [58], here only the final form of the equation is presented. For a flow with the mass flow rate of $\dot{m}$ and the density of ρ in a channel of diameter D, and subject to a wall heat flux of q'', the rate of entropy generation per unit length $\dot{S}'_{gen}$ is given by:

Table 3
Classification of channels based on the hydraulic diameter [59].

Type of channel	Range of hydraulic diameter (D_h)
Microchannel	10–200 μm
Minichannel	200–3 mm
Conventional	$D_h \geqslant 3$ mm

$$\dot{S}'_{gen} = \frac{q''^2 \pi D^2}{kT^2 Nu((\mathrm{Re})_D, \mathrm{Pr})} + \frac{8\dot{m}^3}{\pi^2 \rho^2 T} \frac{f((\mathrm{Re})_D)}{D^5} = (\dot{S}'_{gen})_{heat\ transfer} + (\dot{S}'_{gen})_{fluid\ friction} \quad (44)$$

where f is the so called Darcy friction factor. Clearly, the Nusselt number (Nu) and friction factor (f) are functions of the flow regime and thermal properties of the working fluid. It should be noted that this equation is valid for internal flows where there are no external forces such as magnetic or electric forces. The right hand of Eq. (44) shows that two factors affect entropy generation, i.e., heat transfer and fluid friction, respectively.

Considering q' as the heat transfer to the tube per unit length, another form of Eq. (44) becomes:

$$\dot{S}'_{gen} = \frac{q'^2}{kT^2 Nu((\mathrm{Re})_D, \mathrm{Pr})} + \frac{8\dot{m}^3}{\pi^2 \rho^2 T} \frac{f((\mathrm{Re})_D)}{D^5} \quad (44\text{-a})$$

It should be noted that in some works, in relations (44) and (44), (44-a), (45-a,-b), (46-a,-b), (47), (48), (49), (50), (51), (52), (53), (54), (55), (56), (57), (58), (59), (60), (61), (62) f is multiplied by 32 instead of 8. In this case, the definition of fanning friction factor which is 1/4 of Darcy friction factor is used.

Now, the published works on the entropy generation using nanofluids are discussed where the entropy generation is obtained using one of the two approaches presented above.

3.1. Entropy generation in microchannels

Channels based on the magnitude of hydraulic diameter can be classified into three groups, i.e., conventional channels, minichannels, and microchannels. The range of hydraulic diameter for the three groups is given in Table 3 [59]. First, the entropy generation of nanofluids in microchannels is reviewed. One of the earliest papers on this topic was that of Singh et al. [38]. They performed an analytical analysis of entropy generation due to Al_2O_3–water nanofluid for three different sizes of tubes, including a microchannel (D_h = 0.1 mm), a minichannel (D_h = 1 mm), and a conventional channel (D_h = 10 mm), where the hydraulic diameter is $D_h = 4A/P$. They considered both laminar and turbulent flow regimes and predicted the entropy generation rate by using an order of magnitude approach. In this work, the relation (44) is used to obtain the entropy generation.

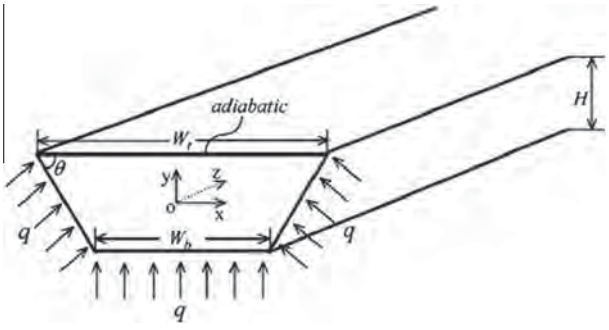

Fig. 3. Schematic of trapezoidal microchannel considered by Li and Kleinstreuer [60]. Reprinted with permission from ASME.

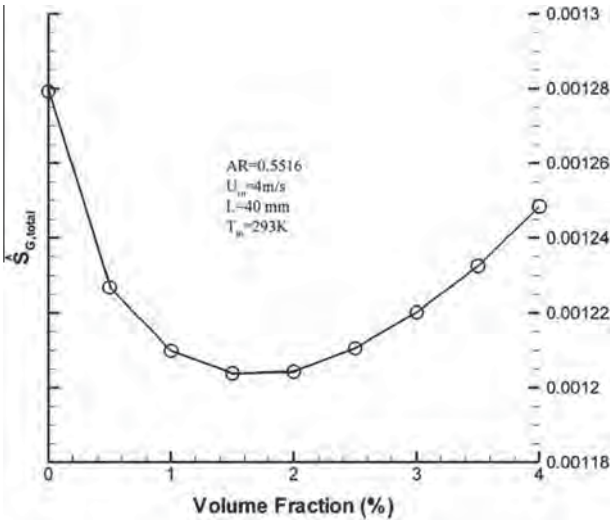

Fig. 4. Variation of entropy generation with volume fraction for trapezoidal microchannel [60]. Reprinted with permission from ASME.

Singh et al. [38] used the following well-known relations to estimate the Nusselt number and friction factor, assuming laminar fully-developed flow.

$$Nu = \frac{48}{11} \quad \text{and} \quad f = \frac{64}{\mathrm{Re}} \quad (45\text{-a, -b})$$

For turbulent flow, they calculated the Nusselt number and friction factor from the Dittus–Boelter and Blasius equations, respectively:

$$Nu = 0.023\mathrm{Re}^{0.8}\mathrm{Pr}^{0.4}, \quad f = 0.316\mathrm{Re}^{-1/4} \quad (46\text{-a, -b})$$

For laminar flow, the ratio of entropy generation due to nanofluid flow to the base fluid by substituting the definitions of Nu and f in Eq. (44) becomes:

$$\frac{\dot{S}'_{genNF}}{\dot{S}'_{gen}} = \frac{1}{k_r \rho_r^2} \frac{T_f^2}{T_{nf}^2} \left(\frac{C_{1lNF} \rho_{nf}^2 + C_{2lNF} \mu_{nf} k_{nf} T_{nf}}{C_{1l} \rho_f^2 + C_{2l} \mu_f k_f T_f} \right) \quad (47)$$

where $k_r = \frac{k_{nf}}{k_f}$ and $\rho_r = \frac{\rho_{nf}}{\rho_f}$. Also, for a constant wall heat flux and mixture-mass flow rate the constants C_{1l} and C_{2l} are defined as:

$$C_{1l} = C_{1lNF} = \frac{11}{48} q''^2 \pi D^2, \quad C_{2l} = C_{2lNF} = \frac{128\dot{m}^2}{\pi D^4} \quad (48)$$

Singh et al. [38] simplified Eq. (47) by using an order of magnitude analysis for the three tubes and both flow regimes. To study the effects of using both theoretical and experimental relations to estimate the viscosity and thermal conductivity, they introduced two models. The first model is a combination of Einstein's model for viscosity and the Hamilton–Crosser model for thermal conductivity, while the second model includes Eqs. (9) and (23). The results showed that for laminar flow the use of Al_2O_3–water nanofluid in the microchannel increases the entropy generation ratio, while in turbulent flow, the use of conventional channels increases the entropy generation ratio. They also concluded that the two models used to calculate the thermophysical properties may give opposite predictions. They obtained a general relation for an optimal diameter for which entropy generation is minimized.

Li and Kleinstreuer [60] investigated numerically entropy generation of CuO–water nanofluid flow with volume fractions less than 4% in trapezoidal microchannels, assuming steady laminar developing flow. Fig. 3 shows a schematic of the system. The authors concluded that adding nanoparticles to the base fluid reduces entropy generation while there is an optimum volume fraction for which entropy generation is minimized. For instance, as shown in Fig. 4, the

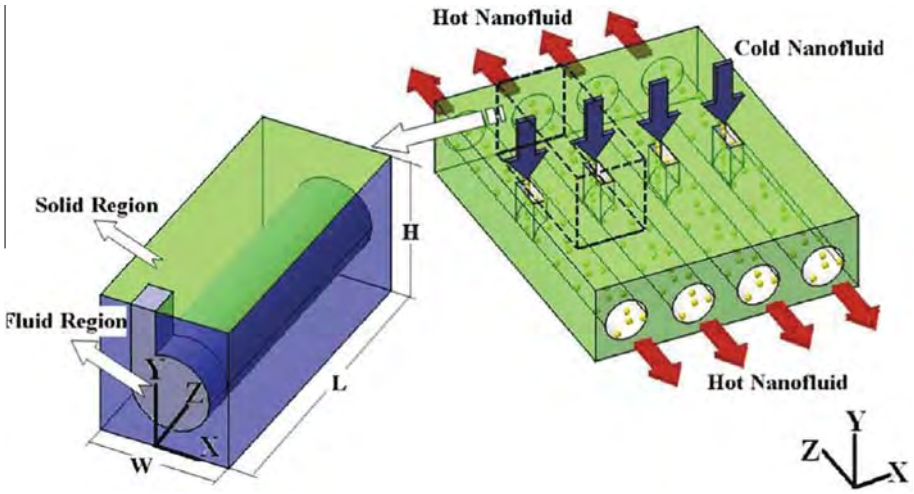

Fig. 5. Schematic of the tangential micro-heat sink assembly and coordinate system considered by Tabrizi and Seyf [61]. Reprinted with permission from Elsevier.

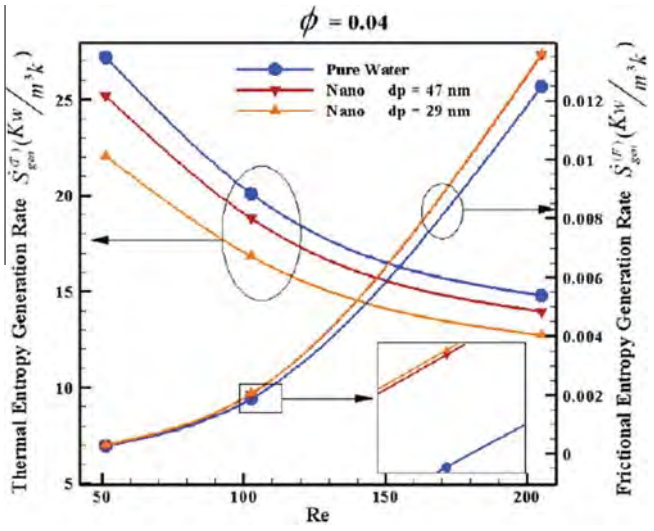

Fig. 6. Thermal and frictional entropy generation rate as a function of Reynolds number for different particle sizes and with a volume fraction of 4% [61]. Reprinted with permission from Elsevier.

entropy generation is the lowest at a volume fraction of 1.5%. The authors used the relations (10) and (28) to calculate the viscosity and thermal conductivity. Tabrizi and Seyf [61] investigated numerically entropy generation in Al_2O_3-nanofluid flow in a tangential micro heat sink (TMHS). The schematic of the problem is shown in Fig. 5. The cold nanofluid enters the TMHS and after cooling the system exits it. The Brinkman (Eq. (10)) and KKL (Eq. (28)) models were used to calculate the viscosity and thermal conductivity of the nanofluids, respectively. By using the KKL model, the authors investigated the effect of particle size on the mixture's thermal conductivity and then the entropy generation. In addition to particle size, the effects of Reynolds number and volume fraction on the entropy generation rate were examined. Fig. 6 shows the effects of particle size and Reynolds number on thermal and frictional entropy generation rates for a volume fraction of 4%. It can be seen that the contribution of viscous effects to entropy generation is negligible when compared to the heat transfer contribution. Thus, overall changes in total entropy generation is greatly determined by thermal effects. It is found that with a decrease in nanoparticle size from 47 nm to 29 nm, the entropy generation is reduced, while with the increase of Reynolds number the entropy generation decreases. The reasons are that decreasing the particle size and increasing the Reynolds number lead to higher Nusselt numbers within the TMHS, and hence entropy generation decreases (see Eq. (44) and Fig. 6). They also concluded that with an increase in volume fraction of nanoparticles, the entropy generation is decreased. May et al. [62] studied analytically the effects of viscous dissipation on entropy generation induced by Al_2O_3–water nanofluids in a circular microchannel. They concluded that when the viscous effects are considered in the entropy generation analysis, the entropy generation increases with an increase in volume fraction of nanoparticles. In their work, the relations of (19)and (39) were used to calculate the viscosity and thermal conductivity, respectively.

3.2. Entropy generation in square, circular, and coiled conduits

3.2.1. Square conduits

Bianco et al. [63] studied entropy generation for Al_2O_3–water nanofluid flow in a conduit with square cross section, subject to a constant heat flux and turbulent flow. They applied Eq. (44) in a somewhat different form; however, they used the following relations to calculate the Nusselt number and the friction factor for turbulent flow:

$$Nu = 0.021\mathrm{Re}^{0.8}\mathrm{Pr}^{0.5} \tag{49}$$

$$f = 0.184\mathrm{Re}^{-0.2} \tag{50}$$

They obtained an optimal Reynolds number for which the entropy generation is minimized. They found that with an increase in volume fraction, the Reynolds number decreases for the minimum entropy generation to occur. Equations (12) and (24) were used to calculate the viscosity and thermal conductivity.

3.2.2. Circular tubes

Moghaddami et al. [64] used Eq. (44-a) to estimate entropy generation for Al_2O_3–water and Al_2O_3–EG flows in a circular tube, subject to a constant heat flux and both laminar and turbulent flows. They found that adding nanoparticles decreases entropy generation for any Reynolds number in laminar flow, while in turbulent flow there is an optimum Reynolds number for which entropy generation is minimized. To analyse the impact of parameter variations, they defined an augmentation entropy generation number ($N_{S,a}$) as follows:

$$N_{S,a} = \frac{\dot{S}'_{gen,nf}}{\dot{S}'_{gen,f}} \tag{51}$$

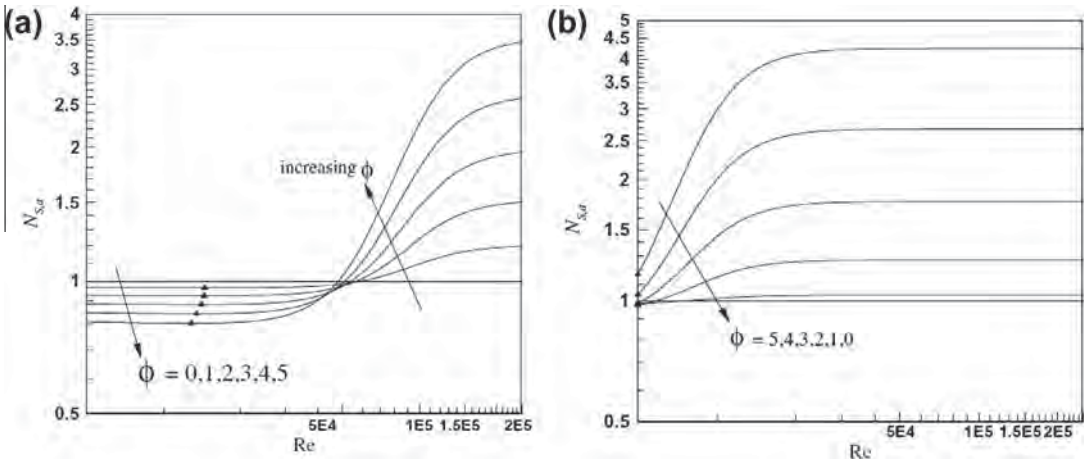

Fig. 7. Augmentation entropy generation number in turbulent flow for (a) Al_2O_3–water and (b) Al_2O_3–EG [64]. Reprinted with permission from Elsevier.

where $\dot{S}'_{gen.nf}$ and $\dot{S}'_{gen.f}$ are the entropy generation rates for the nanofluid and base fluid, respectively. The authors found that for laminar flow of Al_2O_3–water nanofluids entropy generation for any volume fraction ($0 \leqslant \phi \leqslant 5\%$) is minimized at Re = 853. They also perceived that entropy generation decreases with an increase in volume fraction. For turbulent flow of Al_2O_3–water nanofluids, particle loading is helpful when the Reynolds number is less than 40,000, where the optimal point is Re = 13,500. For Al_2O_3–EG, it was found that adding nanoparticles is only advantageous at Reynolds numbers less than 11. Fig. 7(a) and (b) show the augmentation entropy generation number in turbulent flow for Al_2O_3–water (Fig. 7(a)) and Al_2O_3–EG (Fig. 7(b)). Clearly, adding nanoparticles to EG mixture flow at any Reynolds number increases entropy generation because the viscous effects are dominant for this base fluid. In conclusion, adding nanoparticles is useful where the fluid friction contribution to entropy generation is adequately less than the contribution of heat transfer to entropy generation. The authors used the correlations presented by Maiga et al. [41] to calculate the thermal conductivity and viscosity. Moghaddami et al. [65] investigated entropy generation for tubular flow under constant heat flux using Al_2O_3–water nanofluids in both laminar and turbulent flow regimes. The difference between this work [64] and Ref. [65] is the method to obtain entropy generation results. In [65] the velocity and temperature fields were obtained, and then the entropy generation distribution was obtained locally. However, in Ref. [64] the Bejan equation was used. Moghaddami et al. [65] concluded that with an increase in the Reynolds number and volume fraction of nanoparticles the contribution of heat transfer to entropy generation decreases while the viscous dissipation contribution increases. The reason is that at higher Reynolds numbers and volume fractions, nanofluids are very effective in distributing the heat within the whole fluid and hence decreasing the local temperature gradients. As a result, the entropy generation due to heat transfer decreases. On the other hand, viscous dissipation becomes more significant at higher Reynolds numbers and volume fractions because of the increase in velocity gradients and generated fluctuations and disturbances due to the addition of the nanoparticles. Consequently, the fluid friction contribution to entropy generation increases. They also found that using nanofluids is advantageous for laminar flow whereas for turbulent flow there is an optimal Reynolds number for which entropy generation can be minimized. The optimal Reynold number value decreases with an increase in the volume fraction of nanoparticles. In their work, Eqs. (16) and (27) were used to calculate the viscosity and conductivity. Leong et al. [66] examined the entropy generation due to flow of titanium dioxide (TiO_2) and alumina (Al_2O_3) suspended in water within a circular tube where the wall of the tube was of constant temperature. They considered both laminar and turbulent flows. They found that the use of TiO_2 is more beneficial than Al_2O_3 nanoparticles. They also showed that entropy generation is reduced in both laminar and turbulent regimes by adding nanoparticles. Whereas it was observed that for the constant heat flux condition (see Refs. [64,65]), adding nanoparticles in turbulent flow does not always reduce the entropy generation. They used the relations (10) and (40) to calculate the viscosity and thermal conductivity. Karami et al. [45] investigated numerically the effects of Al_2O_3–water nanofluids in a circular tube under constant heat flux on entropy generation, pumping power, and wall temperature. They found that nanoparticle loadings decrease the generated entropy and the temperature of the wall, while they increase the required pumping power. In light of these findings, they concluded that using nanofluids at high concentrations is not beneficial. They used the relations (16) and (38) to calculate the viscosity and thermal conductivity.

3.2.3. Coiled tubes

Falahat and Vosough [68] computed entropy generation in a coiled tube under constant heat flux for both laminar and turbulent regimes using Al_2O_3–water nanofluids. They used Eq. (44) to obtain entropy generation values. Assuming laminar flow, they used the following relation for the friction factor [69]:

$$f = 0.37\left(\frac{64}{\mathrm{Re}}\right)(\mathrm{Re}\delta_r)^{0.36} \tag{52}$$

And for the Nusselt number [70]:

$$Nu = 0.7\mathrm{Re}^{0.43}\mathrm{Pr}^{1/6}\delta_r^{0.07} \tag{53}$$

For turbulent flow, the friction factor was obtained from [71]:

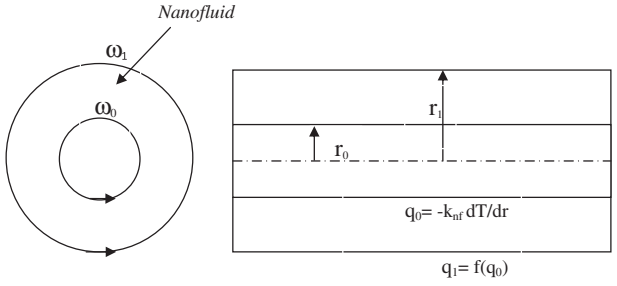

Fig. 8. Schematic of the flow between two rotating cylinders [73]. Reprinted with permission from Elsevier.

Table 4
Different models considered by Mahian et al. [74].

Models	Thermal conductivity	Dynamic viscosity
Model 1	Bruggeman	Brinkman
Model 2	Hamilton–Crosser	Brinkman
Model 3	Yu–Choi	Brinkman
Model 4	Bruggeman	Maiga et al.
Model 5	Hamilton–Crosser	Maiga et al.
Model 6	Yu–Choi	Maiga et al.

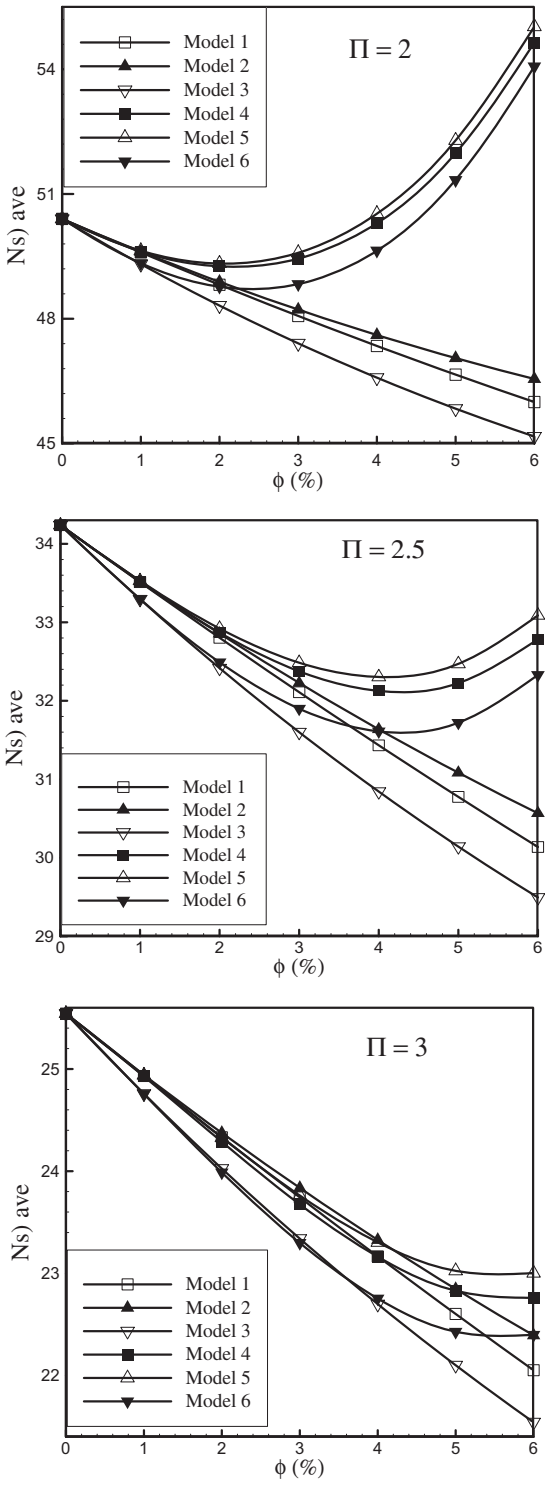

Fig. 9. Effects of uncertainties on entropy generation between two rotating cylinders [74]. Reprinted with permission from ASME.

$$f = \frac{64}{\mathrm{Re}}(\mathrm{Re}\delta_r^2)^{1/20} \tag{54}$$

And for the Nusselt number [72]:

$$Nu = 0.00619\mathrm{Re}^{0.92}\mathrm{Pr}^{0.4}(1 + 3.455\delta_r) \tag{55}$$

where in all equations δ_r is the ratio of coil-to-tube radii. Their results showed that by adding 1% volume fraction of nanoparticles to the base fluid, entropy generation decreases about 3% in laminar flow. For turbulent flow, they concluded that adding nanoparticles for Reynolds numbers greater than 140,000 is disadvantageous, while for Reynolds numbers lower than 40,000 adding nanoparticles reduces the entropy generation. Also, they obtained an optimal Reynolds number for the turbulent flow (≈41,500) for which the entropy generation was minimized. The relations (12) and (24) were used to calculate the viscosity and thermal conductivity, respectively.

3.3. Entropy generation between two rotating cylinders

In this section, contributions related to the entropy generation between two rotating cylinders are reviewed. This type of flow is important in electrical motors, turbojet turbines, rotating heat pipes, swirl nozzles, rotating disks, and standard commercial rheometers. Main et al. [73] investigated the entropy generation due to nanofluid flow between two isoflux rotating cylinders. They considered two nanofluids, i.e., Al_2O_3–EG, and TiO_2–water in their analytical analysis. The schematic of the problem is shown in Fig. 8. They solved the problem analytically by neglecting the radial velocity in the momentum equation, while for the energy equation they considered viscous dissipation but disregarded convection. It was found that the entropy generation is reduced with an increase in concentration of nanofluids where the heat transfer contribution to entropy generation is dominant in the annulus, when compared to the fluid friction contribution. They also concluded that TiO_2–water nanofluid is more suitable than Al_2O_3–EG nanofluid as the working fluid at low Brinkman numbers. To calculate the thermophysical properties of Al_2O_3–EG nanofluids, the correlations presented by Maiga et al. [41] were used while for TiO_2–water nanofluids the relations of Duangthongsuk and Wongwises [42] were utilized by considering temperature-independent properties. Mahian et al. [74] studied the effects of uncertainties in thermophysical models for Al_2O_3–EG nanofluids ($0 \leqslant \phi \leqslant 6\%$) when predicting the entropy generation between two rotating cylinders. The inner cylinder was subjected to a constant heat flux while the outer cylinder was at a constant temperature. They compared the amount of entropy generation, using six models as presented in Table 4. They found that there is a critical radius ratio for the annulus in which the entropy generation based on all models decreases with the increase of volume fraction of nanoparticles. The variation of average entropy generation number with the volume fraction of nanoparticles for the six models is shown in Fig. 9 for three different ratios, i.e., 2, 2.5, and 3. As can be seen, for the ratio of 3, the average entropy generation is reduced for all models. They also noted that the critical radii ratio reduces with increasing the Brinkman number. This work shows the importance of using suitable models to determine thermophysical properties of nanofluids accurately. Later on, Mahian et al. [75] considered the effect of MHD flow on the entropy generation between two cylinders using TiO_2–water nanofluids. In that study, beside the heat transfer and fluid friction effects, the contribution of the magnetic field was considered in the entropy generation equation. They suggested using nanofluids between two cylinders in the presence of MHD flow only for low values of the Brinkman number.

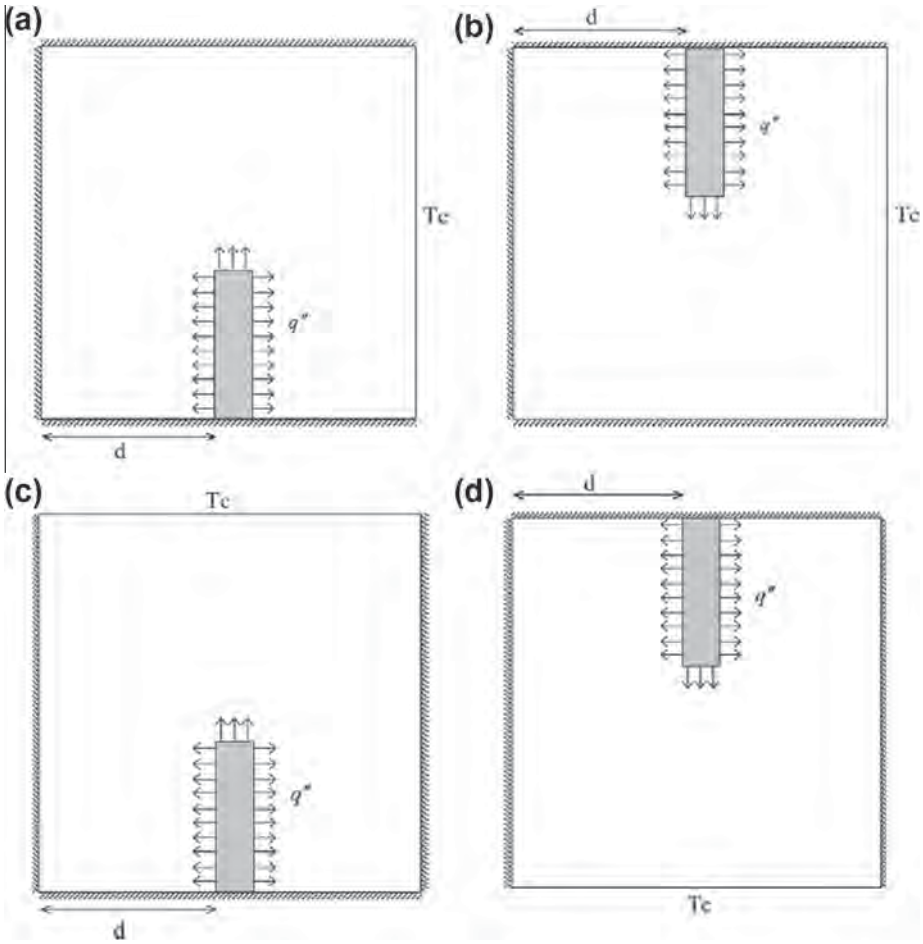

Fig. 10. Schematic flow configuration considered by Shahi et al. [76], (a) Case 1 (b) Case 2 (c) Case 3 and (d) Case 4. (Reprinted with permission from Elsevier).

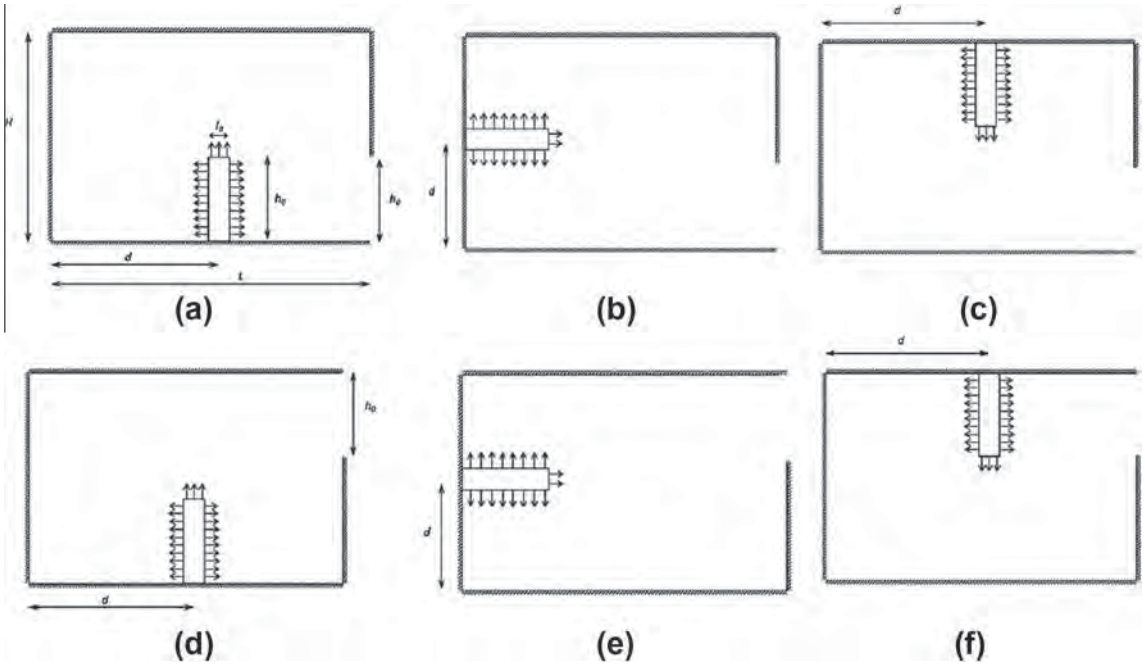

Fig. 11. Schematic flow configuration considered by Mahmoudi et al. [77], (a) Case 1 (b) Case 2, (c) Case 3, (d) Case 4, (e) Case 5, (f) Case 6. (Reprinted with permission from Taylor & Francis).

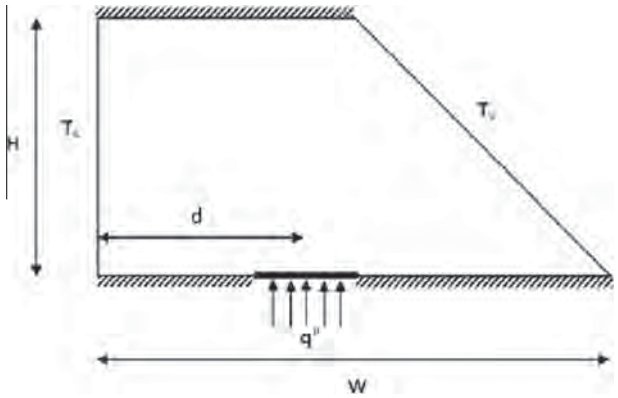

Fig. 12. Schematic of the trapezoidal cavity considered by Mahmoudi et al. [79]. Reprinted with permission from Elsevier.

3.4. Entropy generation in cavities with natural or mixed convection

Extensive studies on natural and mixed convection in cavities of different geometries have been performed. Such problems are important in the design of nuclear reactors, solar collectors, storage tanks, electronic cooling, and so on. In the following, studies conducted on the entropy generation due to nanofluid flow in cavities are reviewed. Shahi et al. [76] examined numerically the entropy generation due to Cu–water nanofluids in a square cavity with a heat source mounted inside it, and with four different designs as shown in Fig. 10. The distance of the heat source from the side walls was changed as well. The dimensionless distances were 0.2, 0.4, 0.6 and 0.8, where the distance 0.2 was near the left wall. The continuity, momentum and energy equations for this problem are:

$$\frac{\partial u}{\partial x}+\frac{\partial v}{\partial y}=0 \tag{56}$$

$$u\frac{\partial u}{\partial x}+v\frac{\partial u}{\partial y}=-\frac{1}{\rho_{nf}}\frac{\partial P}{\partial x}+\frac{\mu_{nf}}{\rho_{nf}}\left(\frac{\partial^2 u}{\partial x^2}+\frac{\partial^2 u}{\partial y^2}\right) \tag{57}$$

$$u\frac{\partial v}{\partial x}+v\frac{\partial v}{\partial y}=-\frac{1}{\rho_{nf}}\frac{\partial P}{\partial y}+\frac{\mu_{nf}}{\rho_{nf}}\left(\frac{\partial^2 v}{\partial x^2}+\frac{\partial^2 v}{\partial y^2}\right)+g\beta_{nf}(T-T_C) \tag{58}$$

$$u\frac{\partial T}{\partial x}+v\frac{\partial T}{\partial y}=\frac{k_{nf}}{(\rho C_p)_{nf}}\left(\frac{\partial^2 T}{\partial x^2}+\frac{\partial^2 T}{\partial y^2}\right) \tag{59}$$

After obtaining the velocity and temperature fields, the entropy generation was obtained via:

$$\dot{S}'''_{gen}=\frac{k_{nf}}{T^2}\left[\left(\frac{\partial T}{\partial x}\right)^2+\left(\frac{\partial T}{\partial y}\right)^2\right]+\frac{\mu_{nf}}{T}\left[2\left\{\left(\frac{\partial u}{\partial x}\right)^2+\left(\frac{\partial v}{\partial y}\right)^2\right\}+\left(\frac{\partial u}{\partial y}+\frac{\partial v}{\partial x}\right)^2\right] \tag{60}$$

The authors concluded that the use of configuration of Case 4, where the heat source was mounted at the dimensionless distance of 0.2, led to the maximum entropy generation. Thus, they suggested installing the heat source on the bottom wall to achieve the maximum heat transfer rate and minimum entropy generation rate. Mahmoudi et al. [77] considered natural convection of Cu–water nanofluids in a partially open cavity, where a heater was mounted at six different configurations, as shown in Fig. 11. They used the first law of thermodynamics and entropy generation analysis to select the best configuration. The governing equations were similar to the previous work [76], and only the boundary conditions were changed. The authors concluded that for Case 4, where the dimensionless distance was 0.95 (the dimensionless distance is 1.5 on the right wall) the entropy generation is minimized. However, by considering the ratio of the Nusselt number to entropy generation as an index performance, Case 5 with a dimensionless distance of 0.4 is the best selection, while Case 3 with dimensionless distance 1.25 is the worst selection. Later on, Shahi et al. [78] considered entropy generation due to natural convection of Cu–water in a cavity where three walls were adiabatic and the right wall was at a constant temperature. They investigated the effects of different heat sources on entropy generation. They considered five cases, i.e., heat source on the left wall (Case 1), heat source on the bottom wall (Case 2), heat source at the top wall (Case 3), heat source in the middle of the cavity as vertical (Case 4), and heat source in the middle of the cavity as horizontal (Case 5). They proposed to design the system based on Case 4 where the heat source is very close to the cold wall, so that the ratio of the Nusselt number to entropy generation could be minimized. Mahmoudi et al. [79] considered the effect of MHD flow on entropy generation in a trapezoidal cavity using Cu–water nanofluids (see Fig. 12). Because of MHD flow, the Lorentz force term should be added to the momentum equation, while the magnetic field term should be added to the entropy equation. Hence, the Eqs. (57) and (60) in this case convert to:

$$u\frac{\partial u}{\partial x}+v\frac{\partial u}{\partial y}=-\frac{1}{\rho_{nf}}\frac{\partial P}{\partial x}+\frac{\mu_{nf}}{\rho_{nf}}\left(\frac{\partial^2 u}{\partial x^2}+\frac{\partial^2 u}{\partial y^2}\right)-\frac{\sigma_{nf}B_0^2}{\rho_{nf}}u \tag{61}$$

$$\dot{S}'''_{gen}=\frac{k_{nf}}{T^2}\left[\left(\frac{\partial T}{\partial x}\right)^2+\left(\frac{\partial T}{\partial y}\right)^2\right]+\frac{\mu_{nf}}{T}\left[2\left\{\left(\frac{\partial u}{\partial x}\right)^2+\left(\frac{\partial v}{\partial y}\right)^2\right\}+\left(\frac{\partial u}{\partial y}+\frac{\partial v}{\partial x}\right)^2\right]+\frac{\sigma_{nf}B_0^2}{T}u^2 \tag{62}$$

where B_0 is the magnetic field intensity, and σ_{nf} is the electrical conductivity of the nanofluid. They concluded that the entropy generation decreases with increasing nanoparticles, whereas in the general entropy generation increases with the magnetic field. Recently, Mahmoudi and Houman [80] studied the effects of different locations of a heat source in a square cavity (bottom, left and right walls) where a flow enters from the bottom of the left wall, and exits from the top of the right wall. They found that the entropy generation is minimized when the heat source is located on the wall from which the flow exits. Khorasanizadeh et al. [81] studied the entropy generation of Cu–water nanofluids in a square cavity where the top wall moves with constant velocity from left to right and the bottom wall is insulated, while the left wall has a higher temperature than the right wall. Fig. 13 shows the variations of entropy generation due to heat transfer (Fig. 13(a)), due to viscous effects (Fig. 13(b)), total entropy generation (Fig. 13(c)), and the Bejan number (Fig. 13(d)) for different values of Rayleigh number, Reynolds number and two volume fraction of 0 and 5%. As can be observed, the entropy generation due to heat transfer increases with an increase in the volume fraction of nanoparticles, Reynolds number, and Rayleigh number. As shown in Fig. 13(b), adding nanoparticles increases entropy generation only considerably due to viscous effects at low values of the Rayleigh number and high values of the Reynolds number. Therefore, as shown in Fig. 13(c), the total entropy generation increases with an increase in volume fraction. They also found that the Bejan number remains nearly constant (Fig. 13(d)) because the entropy generation increases due to heat transfer and nanofluid friction at the same time. Khorasanizadeh et al. [82] also investigated the entropy generation inside a cavity where a baffle is mounted on the bottom hot wall for Rayleigh

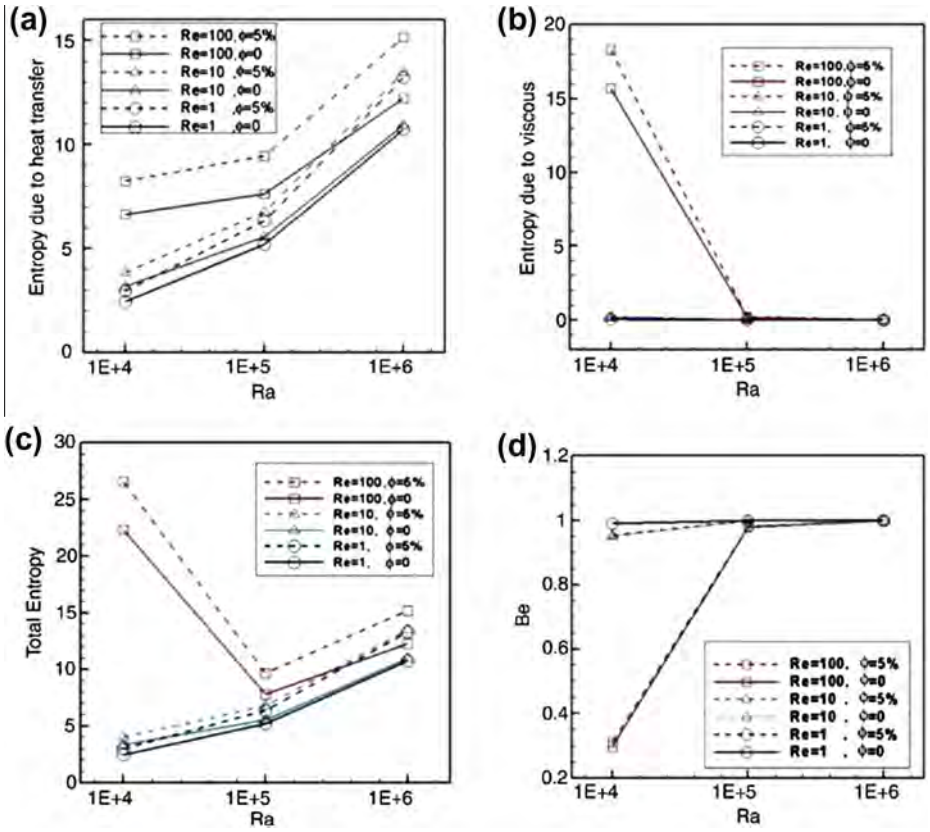

Fig. 13. (a) Entropy generation due to heat transfer effects, (b) entropy generation due to viscous effects, (c) total entropy generation and (d) Bejan number [81]. Reprinted with permission from Elsevier.

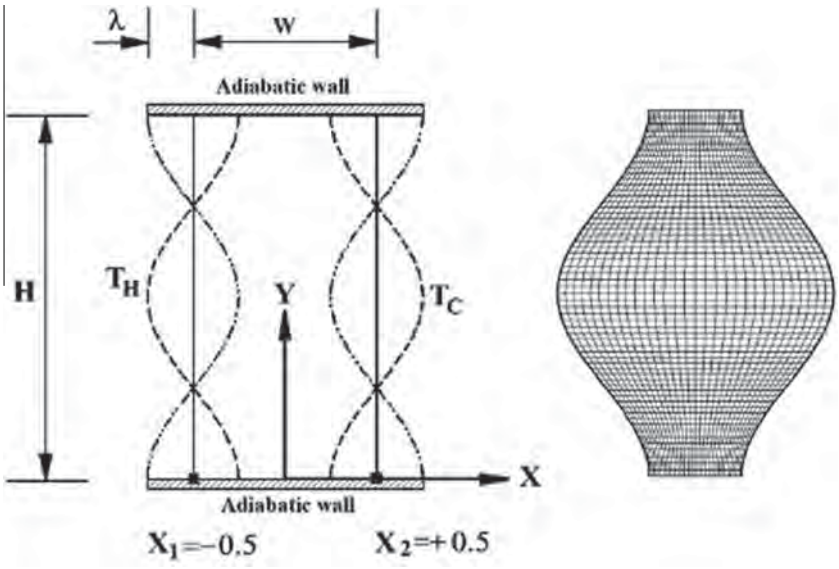

Fig. 14. Schematic of the cavity with wavy walls [83]. Reprinted with permission from Elsevier.

number between 10^4 and 10^6 and volume fractions less than 8%. The side walls had the same temperature and were cold while the top wall was insulated. The authors concluded that, without considering the position of the baffle, the entropy generation is minimized at the lowest value of the Rayleigh number (Ra = 10^4) where the volume fraction is maximal. They concluded that if convection heat transfer role is more important than conduction heat transfer the entropy generation is minimal at the minimum particle loadings, however, where the conduction is dominant the particle volume fraction should be maximum to have the minimum entropy generation.

Esmaeilpour and Abdollahzadeh [83] investigated entropy generation due to natural convection of Cu–water nanofluids in a cavity with wavy walls as shown in Fig. 14. They concluded that the entropy generation at a specified Grashof number decreases with an increase in the volume fraction of nanoparticles (see Fig. 15). As can be observed, with an increase in Grashof number the gradients of entropy generation increase. Relations (11) and

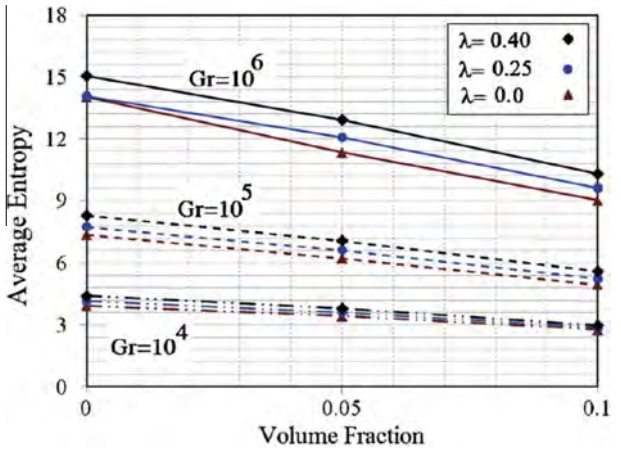

Fig. 15. Effects of volume fraction and Grashof number on average entropy generation [83]. Reprinted with permission from Elsevier.

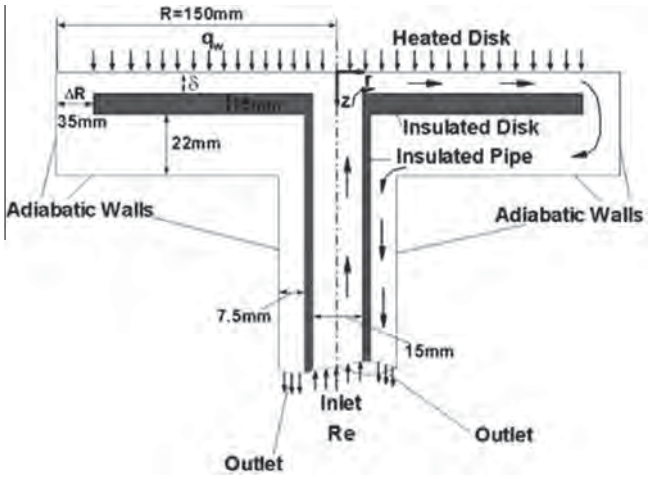

Fig. 16. Schematic of the parallel disks considered by Feng and Kleinstreuer [53]. Reprinted with permission from Elsevier.

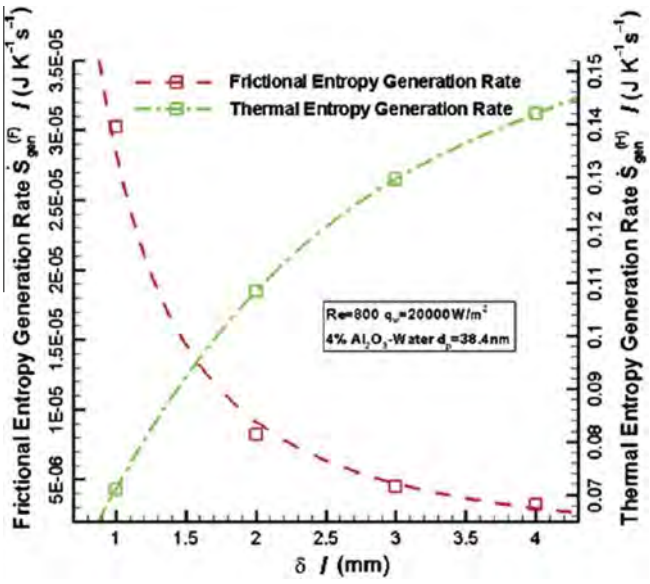

Fig. 17. Thermal and frictional entropy generation rates as a function of space between disks(δ) for Re = 800, and heat flux of 20 k W/m^2 [53]. Reprinted with permission from Elsevier.

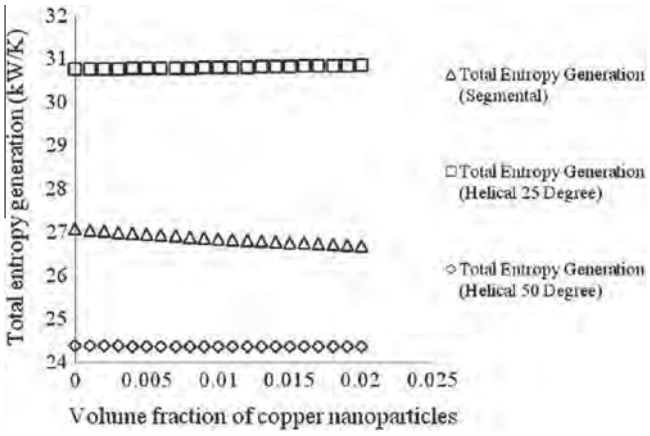

Fig. 18. Entropy generation of shell and tube heat exchanger [89]. Reprinted with permission from Elsevier.

(36) were selected to predict the properties. Cho et al. [84] investigated natural convection of three different nanoparticles including Cu, Al_2O_3 and TiO_2 suspended in water in an enclosure with wavy walls. They concluded that for Rayleigh numbers between 10^4 and 10^6, the total entropy generation decreases with increasing the particle loadings. Also, they showed that using Cu nanoparticles which its thermal conductivity is higher than Al_2O_3 and TiO_2 particles gives the highest heat transfer rate and the lowest entropy generation.

3.5. Entropy generation in nanofluid flow past a barrier

Boghrati et al. [85] examined numerically entropy generation due to the flow of Al_2O_3 and carbon nanotubes suspended in water through two horizontal parallel plates. A rectangular barrier was mounted between the two plates so that the nanofluid can flow up and down the barrier. They found that entropy generation increases by adding nanoparticles. They also observed that the entropy generation due to carbon nanotubes is more than 5 times than when using Al_2O_3 nanoparticles. To estimate the thermal conductivity and viscosity of the nanofluids, they used experimental data of Refs. [86,87]. Sarkar et al. [88] investigated the entropy generation due to mixed convection flow of water-based Al_2O_3 and Cu nanofluids flowing past a square barrier installed in the middle of two vertical parallel plates. They employed the finite element method for the transient analysis of the problem, considering the high value of volume fraction of nanoparticles to be equal to 20%. Their results show that the total entropy generation decreases by about 25% when the volume fraction increases from 0 to 20%. They also found that the entropy generation due to fluid friction is negligible compared to the irreversibilities due to heat transfer. There is no considerable difference between the total entropy generation for both nanoparticles (Al_2O_3 and CuO) when the volume fraction increases from 0 to 20%, except for negative values of the buoyancy parameter Gr/Re^2. It should be noted that Gr/Re^2 is negative when the inlet temperature of nanofluid to the channel is higher than the temperature of the channel walls. The Brinkman and Maxwell models were used to determine the viscosity and thermal conductivity of the nanofluids.

3.6. Entropy generation in a parallel disk system

Feng and Kleinstreuer [53] studied numerically entropy generation in Al_2O_3–water nanofluid flow between parallel disks. The schematic of the problem is shown in Fig. 16. They assumed steady, laminar, axisymmetric, developing dilute suspension flow. Equations (10) and (30) were considered to calculate the viscosity and thermal conductivity of the nanofluid. The authors [53] concluded that the total entropy generation rate in the system reduces by

Table 5
Summary of works done on entropy generation in nanofluid flow.

No.	Authors	Problem description, geometry and solution method	Nanofluid type, range of volume fraction	Thermophysical Properties		Solution method and remarks
				Viscosity	Thermal conductivity	
1	Singh et al. [38]	Analytical study of nanofluid flow in microchannels, minichannels and conventional channels for both laminar and turbulent regimes.	Al_2O_3–water ($\varphi \leqslant 5\%$)	Eqs. (8) and (9)	Eqs. (19) and (23)	– Use of the nanofluid in the microchannel increases the entropy generation ratio for laminar flow, while for turbulent flow the use of conventional channels increases the entropy generation ratio. – Use of different thermophysical models may give opposite predictions.
2	Li and Kleinstreuer [60]	Study of Steady laminar developing nanofluid flow in a trapezoidal microchannel using finite volume method (CFX software).	CuO–water nanofluid ($\varphi \leqslant 4$)	Eq. (10)	Eq. (28)	– Adding nanoparticles to the base fluid reduces entropy generation while there is an optimum concentration for which entropy generation can be minimized.
3	Tabrizi and Seyf [61]	Numerical study of laminar nanofluid flow in a tangential micro heat sink using finite volume method and SIMPLE approach.	Al_2O_3–water ($\varphi \leqslant 4$)	Eq. (10)	Eq. (28)	– With an increase in volume fraction of nanoparticles, the entropy generation decreases – With decrease in nanoparticle size from 47 nm to 29 nm, the entropy generation is reduced. – Viscous effects contribution is negligible in comparison with the heat transfer contribution
4	Mah et al. [62]	Analytical study of nanofluid flow in a circular microchannel by considering viscous effects.	Al_2O_3–water ($\varphi \leqslant 8\%$)	Eq. (18)	Eq. (39)	– Considering viscous effects, entropy generation increases with the increase of volume fraction.
5	Bianco et al. [63]	Study of turbulent flow in a square conduit under constant heat flux using control volume method (Fleunt software).	Al_2O_3-water ($\varphi \leqslant 6\%$)	Eq. (12)	Eq. (24)	– With an increase in volume fraction, the Reynolds number decreases for the minimum entropy generation to occur.
6	Moghaddami et al. [64]	Analytical study of laminar and turbulent flows in a circular tube under constant heat flux.	Al_2O_3–water and Al_2O_3–EG ($\varphi \leqslant 5\%$)	Al_2O_3–water: Eq. (12) Al_2O_3–EG Eq. (13)	Al_2O_3–water Eq. (24) Al_2O_3–EG Eq. (25)	– Adding nanoparticles decreases entropy generation in laminar flow, while in turbulent flow there is an optimum Reynolds number for which entropy generation is minimized.
7	Moghaddami et al. [65]	Laminar and turbulent flow regimes in a circular tube under constant heat flux. The equations are solved using finite volume method and SIMPLE algorithm.	Al_2O_3–water ($\varphi \leqslant 4\%$)	Eq. (16)	Eq. (27)	– Entropy generation is obtained locally (unlike Moghaddami et al. [63]). – For turbulent flow there is an optimal Reynolds number for which entropy generation is minimized. – The optimal Reynold number value decreases with an increase in the concentration.
8	Leong et al. [66]	Analytical study of laminar and turbulent flow regimes in a circular tube with wall constant wall temperature.	TiO_2–water ($\varphi \leqslant 4\%$)and Al_2O_3-water ($\varphi \leqslant 7$)	Eq. (10)	Eq. (40)	– Adding nanoparticles reduces the entropy generation in both flow regimes.
9	Karami et al. [67]	Numerical investigation of laminar flow in a circular tube under constant heat flux using finite volume and SIMPLE method.	Al_2O_3–water ($\varphi \leqslant 1.6\%$)	Eq. (16)	Eq. (38)	– By considering the entropy generation and pumping power, using nanofluids at high concentrations is not beneficial
10	Falahat and Vosough [68]	Analytical study of laminar and turbulent flow in a coiled tube.	Al_2O_3–water ($\varphi \leqslant 4\%$)	Eq. (12)	Eq. (24)	– In laminar flow Adding 1% volume fraction of nanoparticles to water, entropy generation decreases about 3%. – The optimal Reynolds number for turbulent flow is 41500.
11	Mahian et al. [73]	Analytical study of laminar flow between two rotating cylinders by neglecting the convection term.	Al_2O_3–EG ($\varphi \leqslant 5\%$) TiO_2–water ($\varphi \leqslant 2\%$)	Al_2O_3–EG Eq. (13) TiO_2–water Eq. (14)	Al_2O_3–EG Eq. (25) TiO_2–water Eq. (26)	– Entropy generation is reduced with an increase in concentration of nanofluids where the heat transfer contribution to entropy generation is dominant in the annulus – TiO_2-water nanofluid is more suitable than Al_2O_3-EG nanofluid as the working fluid at low Brinkman numbers
12	Mahian et al. [74]	Analytical study of laminar flow between two rotating cylinders by neglecting the convection term.	Al_2O_3–EG ($\varphi \leqslant 6\%$)	Eq. (10) and (13)	Eqs. ()()()(20)–(22)	– The authors investigated the effects of six different sets of thermophysical properties on entropy generation. – There is a critical radius ratio for the annulus in which the entropy generation based on all models decreases with the increase of concentration.
13	Mahian et al. [75]	Analytical study of laminar flow between two rotating cylinders with MHD flow effects	TiO_2–water ($\varphi \leqslant 2\%$)	Eq. (14)	Eq. (26)	– Using nanofluids only in low values of the Brinkman number is beneficial.
14	Shahi et al. [76]	Natural convection in a square cavity with a heat source mounted inside it using finite volume and SIMPLE method.	Cu–water ($\varphi \leqslant 5\%$)	Eq. (10)	Eq. (33)	– Selecting the best configuration based on heat transfer and entropy generation results.
15	Mahmoudi et al. [77]	Natural convection in a partially open square cavity with a heat source mounted inside it using finite volume and SIMPLE method.	Cu–water($\varphi \leqslant 5\%$)	Eq. (10)	Eq. (33)	– Selecting the best configuration based on heat transfer and entropy generation results.
16	Shahi et al. [78]	Natural convection in a cavity with three adiabatic walls and a heat source mounted inside it using finite volume and SIMPLE method.	Cu–water ($\varphi \leqslant 5\%$)	Eq. (10)	Eq. (33)	– Selecting the best configuration based on heat transfer and entropy generation results.

(*continued on next page*)

Table 5 (*continued*)

No.	Authors	Problem description, geometry and solution method	Nanofluid type, range of volume fraction	Thermophysical Properties		Solution method and remarks
				Viscosity	Thermal conductivity	
17	Mahmoudi et al. [79]	Natural convection in a trapezoidal cavity with MHD flow effects using finite volume and SIMPLE method. .	Cu-water ($\varphi \leqslant 5\%$)	Eq. (10)	Eq. (33)	- Entropy generation decreases with increasing nanoparticles, whereas in general entropy generation increases with the magnetic field
18	Mahmoudi and Hooman [80]	Effect of location a heat source in a cavity with enter and exit flows using finite volume and SIMPLE method.	Cu–water ($\varphi \leqslant 5\%$)	Eq. (10)	Eq. (33)	- Entropy generation is minimal where the heat source is on the wall from which the flow exits.
19	Khorasanizadeh et al. [81]	Mixed convection in a square cavity using finite volume and SIMPLE method.	Cu–water ($\varphi \leqslant 5\%$)	Eq. (10)	Eq. (33)	- Entropy generation due to heat transfer increases with an increase in the volume fraction of nanoparticles
20	Khorasanizadeh et al. [82]	Study of natural convection in a square cavity with a baffle mounted on bottom hot wall using finite volume and SIMPLE method.	Cu–water ($\varphi \leqslant 8\%$)	Eq. (10)	Eq. (19)	- Where the conduction is dominant the particle volume fraction should be maximum to have the minimum entropy generation
21	Esmaeilpour and Abdollahzadeh [83]	Natural convection in a wavy cavity using finite volume and SIMPLE method..	Cu–water ($\varphi \leqslant 10\%$)	Eq. (11)	Eq. (36)	- Entropy generation at a specified Grashof number decreases with an increase in the volume fraction of nanoparticles
22	Cho et al. [84]	Numerical study of natural convection heat transfer and entropy generation in wavy-wall enclosure containing water-based nanofluid.	Cu–water, Al_2O_3–water and TiO_2–water ($\varphi \leqslant 10\%$)	Eq. (10)	Eq. (19)	- Entropy generation for Cu nanoparticles is minimum.
23	Boghrati et al. [85]	Laminar forced convection between two horizontal plates with a rectangular barrier mounted in the middle of plates using finite volume and SIMPLE method.	Al_2O_3–water ($\varphi \leqslant 4\%$) and carbon nanotubes($\varphi \leqslant 1\%$)	Experimental data [86,87]	Experimental data [86,87]	- Entropy generation increases by adding nanoparticles. - Entropy generation due to carbon nanotubes is more than 5 times than when using Al_2O_3 nanoparticles
24	Sarkar et al. [88]	Laminar mixed convection between two vertical plates with a square barrier mounted in the middle of plates. Streamline Upwinding Petrov-Galerkin Method is used to solve the equations.	Al_2O_3–water and Cu–water ($\varphi \leqslant 20\%$)	Eq. (10)	Eq. (19)	- Total entropy generation decreases by about 25% when the volume fraction increases from 0 to 20%.

adding nanoparticles. Specifically, while adding nanoparticles increases entropy generation due to fluid friction as the mixture viscosity increases, particle loading reduces entropy generation induced by heat transfer because of smaller temperature gradients (see Fig. 17).

3.7. Entropy generation in heat exchangers

Leong et al. [89] investigated the performance of three types of shell-and-tube heat exchangers, including helical baffles of 25, 50 degree and segmental, using Cu–water nanofluids with volume fractions below 2%. Fig. 18 shows the variation of total entropy generation for the three types of heat exchangers. Apparently, nanofluids at this low amount have no considerable effect on the total entropy generation. It was also found that, in the presence of nanofluids, the entropy generation for the helical heat exchanger of 50° was the lowest. The Brinkman and Maxwell models were used to calculate the mixture properties.

3.8. Entropy generation of flow over stretching sheets

Matin et al. [90] presented a numerical study of MHD mixed convection flow of SiO_2–water nanofluids (with volume fractions up to 30%) over a non-linear stretching sheet. They concluded that the entropy generation decreases with the increase of volume fraction of nanoparticels. The Brinkman and Maxwell models were selected to calculate the thermal nanofluid properties; although, at nanoparticle concentrations as high as 30% non-Newtonian fluid flow effects should be considered.

An assessment of published work dealing with entropy generation due to nanofluid flow is given in Table 5.

4. Conclusions and future work

A review of entropy generation due to flow and heat transfer of different nanofluids in various geometries and with different boundary conditions is provided. In most studies, water was used as the base fluid, and in some cases EG was utilized. Also, Al_2O_3 and Cu were the most common nanoparticles which are used in the studies. To obtain the entropy generation in nanofluid flow, two methods are outlined. In the first approach, the total entropy generation is obtained for the entire system, and hence there is no need to solve locally for the momentum and energy equations. This method is applicable for internal flows, relying on the Bejan equation to calculate the entropy generation. In this method the Nusselt number and friction factor are calculated based on the correlations in the literature. In the second method, the momentum and energy equations are solved first, and then, by using the velocity and temperature fields, the local and total entropy generations can be obtained. After the problem formulation, it is necessary to use suitable relations to calculate the thermophysical properties of nanofluids, including the thermal conductivity, viscosity, specific heat, density, and thermal expansion coefficient.

In summary, based on the entropy generation studies reviewed, the following can be stated:

- Depending on the nanoparticle volume fraction, channel size and type of flow regime (i.e., laminar or turbulent), employing nanofluids can be very beneficial in decreasing entropy generation and hence system optimization.
- Different sets of models to calculate the thermophysical properties of nanofluids may generate opposite predictions for entropy generation.
- When just considering the viscous effects in microchannels, it can be observed that adding nanoparticles increases entropy generation.

- In general, it is expected that by using nanofluids in common flow systems the contribution of heat transfer to entropy generation is dominant, resulting in a measurable decrease in the entropy generation because of more uniform temperature fields.

It should be noted that the limit of the volume fractions is selected based on experimental data so that the nanofluids behave as Newtonian. In cases where high volume fractions are used (for example 10% or even 20%) nanofluids may show non-Newtonian behaviour, hence the governing equations considered in the present study are not applicable. As a note, in general, care must be taken when talking about entropy generation minimization and optimization of heat transfer in heat exchnagers. In some cases, entropy generation minimization leads to very slow processes that are not suited for heat exchanging devices.

Entropy generation in nanofluid flow has been investigated for different configurations, including flow in microchannels, flows in square, circular and coiled conduits, natural convection and mixed convection flows in cavities, flow between two rotating cylinders, flow between parallel disks, flow in heat exchangers, flow past barriers, and flow on stretching sheets. For future work, the following studies should be considered:

- Effect of thermal radiation on entropy generation within nanofluids.
- Entropy generation due to nanofluid flow in porous media, where the papers by Nield and Kuznetsov [91–93] may serve as examples.
- Entropy generation by considering mass transfer contributions.
- Entropy generation due to non-Newtonian nanofluids.
- Local entropy generation, using the two-phase model for nanofluids.
- Different types of thermal and hydrodynamics boundary conditions and geometries. For instance, there is almost no work about nanofluid flow in spherical geometries, therefore there is a need to study heat transfer and consequently entropy generation in spherical containers.
- Thermo-economics examination of nanofluid flows in thermal systems.
- Estimate entropy generation based on experimental studies.

Acknowledgments

The first and seventh authors wish to thank the Thailand Research Fund, and the National Research University Project for support for their study. Also, the sixth author would like to acknowledge the support provided by King Fahd University of Petroleum and Minerals (KFUPM), Dhahran, Saudi Arabia for this work. The valuable help of Prof. Kambiz Vafai from University of California, Riverside, USA is appreciated. The authors would like also to express their sincere thanks to the reviewers for their valuable comments and suggestions.

References

[1] U.S. Choi, Enhancing thermal conductivity of fluids with nanoparticles, ASME FED 231 (1995) 99–103.
[2] W. Duangthongsuk, S. Wongwises, Heat transfer enhancement and pressure drop characteristics of TiO_2–water nanofluid in a double-tube counter flow heat exchanger, Int. J. Heat Mass Transfer 52 (7–8) (2009) 2059–2067.
[3] G. Huminic, A. Huminic, Heat transfer characteristics in double tube helical heat exchangers using nanofluids, Int. J. Heat Mass Transfer 54 (19–20) (2011) 4280–4287.
[4] W. Duangthongsuk, A.S. Dalkilic, S. Wongwises, Convective heat transfer of Al_2O_3–water nanofluids in a microchannel heat sink, Curr. Nanosci. 8 (3) (2012) 317–322.
[5] J. Li, C. Kleinstreuer, Thermal performance of nanofluid flow in microchannels, Int. J. Heat Fluid Flow 29 (4) (2008) 1221–1232.
[6] J. Li, C. Kleinstreuer, Microfluidics analysis of nanoparticle mixing in a microchannel system, Microfluid. Nanofluid. 6 (2009) 661–668.
[7] Y.J. Chen, P.Y. Wang, Z.H. Liu, Application of water-based SiO_2 functionalized nanofluid in a loop thermosyphon, Int. J. Heat Mass Transfer 56 (1) (2013) 59–68.
[8] Z.H. Liu, Y.Y. Li, A new frontier of nanofluid research – application of nanofluids in heat pipes, Int. J. Heat Mass Transfer 55 (23–24) (2012) 6786–6797.
[9] M. Mohammadi, M. Mohammadi, M.B. Shafii, Experimental investigation of a pulsating heat pipe using ferrofluid (magnetic nanofluid), J. Heat Transfer 134 (1) (2012). art. no. 014504.
[10] K. Alizad, K. Vafai, M. Shafahi, Thermal performance and operational attributes of the startup characteristics of flat-shaped heat pipes using nanofluids, Int. J. Heat Mass Transfer 55 (1–3) (2012) 140–155.
[11] M. Shafahi, V. Bianco, K. Vafai, O. Manca, An investigation of the thermal performance of cylindrical heat pipes using nanofluids, Int. J. Heat Mass Transfer 53 (1–3) (2010) 376–383.
[12] M. Shafahi, V. Bianco, K. Vafai, O. Manca, Thermal performance of flat-shaped heat pipes using nanofluids, Int. J. Heat Mass Transfer 53 (7–8) (2010) 1438–1445.
[13] K.Y. Leong, R. Saidur, S.N. Kazi, A.H. Mamun, Performance investigation of an automotive car radiator operated with nanofluid-based coolants (nanofluid as a coolant in a radiator), Appl. Therm. Eng. 30 (17–18) (2010) 2685–2692.
[14] R. Saidur, K.Y. Leong, H.A. Mohammad, A review on applications and challenges of nanofluids, Renewable Sustainable Energy Rev. 15 (3) (2011) 1646–1668.
[15] T. Yousefi, F. Veysi, E. Shojaeizadeh, S. Zinadini, An experimental investigation on the effect of Al_2O_3–H_2O nanofluid on the efficiency of flat-plate solar collectors, Renewable Energy 39 (2012) 293–298.
[16] T. Yousefi, F. Veysi, E. Shojaeizadeh, S. Zinadini, An experimental investigation on the effect of MWCNT–H2O nanofluid on the efficiency of flat-plate solar collector, Exp. Therm. Fluid Sci. 39 (2012) 207–212.
[17] T. Yousefi, F. Veysi, E. Shojaeizadeh, S. Zinadini, An experimental investigation on the effect of pH variation of MWCNT–H2O nanofluid on the efficiency of a flat-plate solar collector, Sol. Energy 86 (2012) 771–779.
[18] W. Daungthongsuk, S. Wongwises, A critical review of convective heat transfer of nanofluids, Renewable Sustainable Energy Rev. 11 (5) (2007) 797–817.
[19] Z. Hadad, H.F. Oztop, E. Abu-Nada, A. Mataoui, A review on natural convective heat transfer of nanofluids, Renewable Sustainable Energy Rev. 16 (7) (2012) 5363–5378.
[20] H.S. Ahn, M.H. Kim, A review on critical heat flux enhancement with nanofluids and surface modification, J. Heat Transfer 134 (2) (2012). art. no. 024001.
[21] K. Khanafer, K. Vafai, A critical synthesis of thermophysical characteristics of nanofluids, Int. J. Heat Mass Transfer 54 (2011) 4410–4428.
[22] C. Kleinstreuer, Y. Feng, Experimental and theoretical studies of nanofluid thermal conductivity enhancement: a review, Nanoscale Res. Lett. 6 (2011) 229.
[23] A. Kamyar, R. Saidur, Hasanuzzaman, M. Application of Computational Fluid Dynamics (CFD) for nanofluids, Int. J. Heat Mass Transfer 55 (15–16) (2012) 4104–4115.
[24] I.M. Mahbubul, R. Saidur, M.A. Amalina, Latest developments on the viscosity of nanofluids, Int. J. Heat Mass Transfer 55 (4) (2012) 874–885.
[25] W.Yu, H. Xie, A review on nanofluids: preparation, stability, mechanisms, and applications, J. Nanomater. (2012). art. no. 435873.
[26] J. Fan, L.Wang, Review of heat conduction in nanofluids, J. Heat Transfer 133 (4) (2011). art. no. 040801.
[27] O. Mahian, A. Kianifar, S.A. Kalogirou, I. Pop, S. Wongwises, A review of the applications of nanofluids in solar energy, Int. J. Heat Mass Transfer 57 (2013) 582–594.
[28] W.J. Minkowycz, E.M. Sparrow, J.P. Abraham, Nanoparticle Heat Transfer and Fluid Flow, CRC Press, 2012.
[29] O. Mahian, S. Mahmud, I. Pop, Analysis of first and second laws of thermodynamics between two isothermal cylinders with relative rotation in the presence of MHD flow, Int. J. Heat Mass Transfer 55 (17–18) (2012) 4808–4816.
[30] Y.A. Cengel, M.A. Boles, Thermodynamics an Engineering Approach, fifth ed., McGraw-Hill, 2006.
[31] H.F. Oztop, K. Al-Salem, A review on entropy generation in natural and mixed convection heat transfer for energy systems, Renewable Sustainable Energy Rev. 16 (1) (2012) 911–920.
[32] M. Torabi, A. Aziz, Entropy generation in a hollow cylinder with temperature dependent thermal conductivity and internal heat generation with convective–radiative surface cooling, Int. Commun. Heat Mass Transfer 39 (10) (2012) 1487–1495.
[33] A. Aziz, W.A. Khan, Classical and minimum entropy generation analyses for steady state conduction with temperature dependent thermal conductivity and asymmetric thermal boundary conditions: regular and functionally graded materials, Energy 36 (2011) 6195–6207.
[34] A. Aziz, W.A. Khan, Entropy generation in an asymmetrically cooled slab with temperature-dependent internal heat generation, Heat Transfer Asian Res. 41 (3) (2012) 260–271.
[35] C.J. Ho, W.K. Liu, Y.S. Chang, C.C. Lin, Natural convection heat transfer of alumina–water nanofluid in vertical square enclosures: an experimental study, Int. J. Therm. Sci. 49 (2010) 1345–1353.

[36] J. Sarkar, A critical review on convective heat transfer correlations of nanofluids, Renew. Sust. Energ. Rev. 15 (2011) 3271–3277.
[37] A. Einstein, Eine neue bestimmung der molekuldimensionen, Ann. Phys. Leipzig 19 (1906) 289–306.
[38] P.K. Singh, K.B. Anoop, T. Sundararajan, S.K. Das, Entropy generation due to flow and heat transfer in nanofluids, Int. J. Heat Mass Transfer 53 (2010) 4757–4767.
[39] H.C. Brinkman, The viscosity of concentrated suspensions and solutions, J. Chem. Phys. 20 (1952) 571.
[40] M. Corcione, Heat transfer features of buoyancy-driven nanofluids inside rectangular enclosures differentially heated at the sidewalls, Int. J. Therm. Sci. 49 (2010) 1536–1546.
[41] S. Maiga, S.J. Palm, C.T. Nguyen, G. Roy, N. Galanis, Heat transfer enhancement by using nanofluids in forced convection flows, Int. J. Heat Fluid Flow 26 (2005) 530–546.
[42] W. Duangthongsuk, S. Wongwises, Measurement of temperature-dependent thermal conductivity and viscosity of TiO2–water nanofluids, Exp. Therm. Fluid Sci. 33 (2009) 706–714.
[43] U. Rea, T. Mckrell, L. Hu, J. Buongiorno, Laminar convective heat transfer and viscous pressure loss of alumina–water and zirconia–water nanofluids, Int. J. Heat Mass Transfer 52 (7–8) (2009) 2042–2048.
[44] W.C. Williams, J. Buongiorno, L.W. Hu, Experimental investigation of turbulent convective heat transfer and pressure loss of alumina/water and zirconia/water nanoparticle colloids (nanofluids) in horizontal tubes, J. Heat Transfer 130 (2008) 042412.
[45] M. Karami, E. Shirani, A. Avara, Analysis of entropy generation, pumping power, and tube wall temperature in aqueous suspensions of alumina particles, Heat Transfer Res. 43 (4) (2012) 327–342.
[46] S.P. Jang, J.H. Lee, K.S. Hwang, Particle concentration and tube size dependence of viscosities of Al_2O_3–water nanofluids flowing through micro- and minitubes, Appl. Phys. Lett. 91 (2007) 243112.
[47] J.C.A. Maxwell, Treatise Electricity Magn., second ed., Clarendon Press, Oxford, UK, 1881.
[48] D.A.G. Bruggeman, Berechnung verschiedener physikalischer konstanten von heterogenen substanzen, I. Dielektrizitatskonstanten und leitfahigkeiten dermischkorper aus isotropen substanzen, Ann. Phys. Leipzig 24 (1935) 636–679.
[49] R.L. Hamilton, O.K. Crosser, Thermal conductivity of heterogeneous two component systems, I&EC Fundam. 1 (1962) 182–191.
[50] W. Yu, S.U.S. Choi, The role of interfacial layers in the enhanced thermal of nanofluids: a renovated Maxwell model, J. Nanopart. Res. 5 (1–2) (2003) 167–171.
[51] J. Koo, C. Kleinstreuer, A new thermal conductivity model for nanofluids, J. Nanopart. Res. 6 (2004) 577–588.
[52] J. Li, Computational analysis of nanofluid flow in microchannels with applications to micro-heat sinks and bio-MEMS, Ph.D Thesis NC State University, Raleigh, NC, USA; 2008.
[53] Y. Feng, C. Kleinstreuer, Nanofluid convective heat transfer in a paralleldisk system, Int. J. Heat Mass Transfer 53 (2010) 4619–4628.
[54] H.E. Patel, T. Pradeep, T. Sundararajan, A. Dasgupta, N. Dasgupta, S.K. Das, A microconvection model for thermal conductivity of nanofluid, Pramana J. Phys. 65 (2005) 863–869.
[55] A. Amiri, K. Vafai, Analysis of dispersion effects and nonthermal equilibrium, non-Darcian, variable porosity, incompressible flow through porous media, Int. J. Heat Mass Transfer 37 (1994) 939–954.
[56] K. Khanafer, K. Vafai, M. Lightstone, Buoyancy-driven heat transfer enhancement in a two-dimensional enclosure utilizing nanofluids, Int. J. Heat Mass Transfer 46 (2003) 3639–3653.
[57] R. Prasher, P. Bhattacharya, P.E. Phelan, Thermal conductivity of nanoscale colloidal solutions (nanofluids), Phys. Rev. Lett. 94 (2005) 025901.
[58] A. Bejan, Entropy Generation Through Heat and Fluid Flow, Wiley, New York, 1982.
[59] Grande. Kandlikar, Evolution of microchannel flow passages – thermohydraulic performance and fabrication technology, Heat Transfer Eng. 24 (1) (2003) 3–17.
[60] J. Li, C. Kleinstreuer, Entropy generation analysis for nanofluid flow in microchannels, J. Heat Transfer 132 (2010) 122401.1–122401.8.
[61] A.S. Tabrizi, H.R. Seyf, Analysis of entropy generation and convective heat transfer of Al_2O_3 nanofluid flow in a tangential micro heat sink, Int. J. Heat Mass Transfer 55 (2012) 4366–4375.
[62] W.H. Mah, Y.M. Hung, N. Guo, Entropy generation of viscous dissipative nanofluid flow in microchannels, Int. J. Heat Mass Transfer 55 (2012) 4169–4182.
[63] V. Bianco, S. Nardini, O. Manca, Enhancement of heat transfer and entropy generation analysis of nanofluids turbulent convection flow in square section tubes, Nanoscale Res. Lett. 6 (2011) 252.
[64] M. Moghaddami, A. Mohammadzade, S.A. Varzane Esfehani, Second law analysis of nanofluid flow, Energy Convers. Manage. 52 (2011) 1397–1405.
[65] M. Moghaddami, S.E. Shahidi, M. Siavashi, Entropy generation analysis of nanofluid flow in turbulent and laminar regimes, J. Comput. Theor. Nanosci. 9 (2012) 1–10.
[66] K.Y. Leong, R. Saidur, T.M.I. Mahlia, Y.H. Yau, Entropy generation analysis of nanofluid flow in a circular tube subjected to constant wall temperature, Int. Commun. Heat Mass Transfer 39 (2012) 1169–1175.
[67] M. Karami, E. Shirani, A. Avara, Analysis of entropy generation, pumping power, and tube wall temperature in aqueous suspensions of alumina particles, Heat Transfer Res. 43 (4) (2012) 327–342.
[68] A. Falahat, A. Vosough, Effect of nanofluid on entropy generation and pumping power in coiled tube, J. Thermophys. Heat Transfer 26 (1) (2012) 141–146.
[69] H. Ito, Friction factors for turbulent flow in curved pipes, J. Basic Eng. 81 (1959) 123–134.
[70] L.A.M. Janssen, C.J. Hoogendoorn, Laminar convective heat transfer in helical coiled tubes, Int. J. Heat Mass Transfer 21 (1978) 1197–1206.
[71] Y. Mori, W. Nakayama, Study on forced convective heat transfer in curved pipes, Int. J. Heat Mass Transfer 10 (1967) 681–695.
[72] R.C. Xin, M.A. Ebadin, The effects of Prandtl numbers on local and average convective heat transfer characteristics in helical pipes, J. Heat Transfer 19 (1997) 467–473.
[73] O. Mahian, S. Mahmud, S. Zeinali Heris, Analysis of entropy generation between co-rotating cylinders using nanofluids, Energy 44 (2012) 438–446.
[74] O. Mahian, S. Mahmud, S. Zeinali Heris, Effect of uncertainties in physical properties on entropy generation between two rotating cylinders with nanofluids, J. Heat Transfer 134 (2012) 101704.
[75] O. Mahian, S. Mahmud, S. Wongwises, Entropy generation between two rotating cylinders in the presence of magnetohydrodynamic flow using nanofluids, Jounral of thermophysics and heat transfer 27 (2013) 161–169.
[76] M. Shahi, A.H. Mahmoudi, A.H. Raouf, Entropy generation due to natural convection cooling of a nanofluid, Int. Commun. Heat Mass Transfer 38 (2011) 972–983.
[77] A.H. Mahmoudi, M. Shahi, F. Talebi, Entropy generation due to natural convection in a partially open cavity with a thin heat source subjected to a nanofluid, Numer. Heat Transfer Part A 61 (2012) 283–305.
[78] A.H. Mahmoudi, F. Talebi, M. Shahi, Entropy generation due to natural convection cooling of a horizontal heat source mounted inside a square cavity filled with nanofluid, Heat Transfer Res. 43 (1) (2012) 19–46.
[79] A.H. Mahmoudi, M. Shahi, I. Pop, F. Talebi, MHD natural convection and entropy generation in a trapezoidal enclosure using Cu–water nanofluid, Comput. Fluids 72 (2013) 46–62.
[80] A. H. Mahmoudi, K. Hooman, Effect of a discrete heat source location on Entropy generation in mixed convective cooling of a nanofluid inside the ventilated cavity, Int. J. Exergy, in press.
[81] H. Khorasanizadeh, M. Nikfar, J. Amani, Entropy generation of Cu–water nanofluid mixed convection in a cavity, Eur. J. Mech. B Fluids 37 (2013) 143–152.
[82] H. Khorasanizadeh, M. Nikfar, J. Amani, Numerical investigation of Cu–water nanofluid natural convection and entropy generation within a cavity with an embedded conductive baffle, Sci. Iran. 19 (2012) 1996–2003.
[83] M. Esmaeilpoura, M. Abdollahzadeh, Free convection and entropy generation of nanofluid inside an enclosure with different patterns of vertical wavy walls, Int. J. Therm. Sci. 52 (2012) 127–136.
[84] C.C. Cho, C.L. Chen, C.K. Chen, Natural convection heat transfer and entropy generation in wavy-wall enclosure containing water-based nanofluid, Int. J. Heat Mass Transfer 61 (2013) 749–758.
[85] M. Boghrati, E. Ebrahim nia Bajestan, V. Etminan, Entropy generation minimization of confined nanofluids laminar flow around a block, in: Proceedings of the 10th Biennial Conference on Engineering Systems and Analysis ESDA2010, Istanbul, Turkey, July 12–14, 2010.
[86] S.E.B. Maiga, S.J. Palm, C.T. Nguyen, G. Roy, N. Galanis, Heat transfer enhancement by using nanofluids in forced convection flows, Int. J. Heat Fluid Flow 26 (2005) 530–546.
[87] L. Chen, H. Xie, Y. Li, W. Yu, Nanofluids containing carbon nanotubes treated by mechanochemical reaction, Thermochim. Acta 477 (2008) 21–24.
[88] S. Sarkar, S. Ganguly, A. Dalal, Analysis of entropy generation during mixed convection heat transfer of nanofluids past a square cylinder in vertically upward flow, J. Heat Transfer 134 (2012) 122501.
[89] K.Y. Leong, R. Saidur, M. Khairulmaini, Z. Michael, A. Kamyar, Heat transfer and entropy analysis of three different types of heat exchangers operated with nanofluids, Int. Commun. Heat Mass Transfer 39 (2012) 838–843.
[90] M.H. Matin, M.R.H. Nobari, P. Jahangiri, Entropy analysis in mixed convection MHDflow of nanofluid over a non-linear stretching sheet, J. Therm. Sci. Technol. 7 (1) (2012).
[91] D.A. Nield, A.V. Kuznetsov, Thermal instability in a porous medium layer saturated by a nanofluid, Int. J. Heat Mass Transfer 52 (25–26) (2009) 5796–5801.
[92] D.A. Nield, A.V. Kuznetsov, The Cheng–Minkowycz problem for natural convective boundary-layer flow in a porous medium saturated by a nanofluid, Int. J. Heat Mass Transfer 52 (25-26) (2009) 5792–5795.
[93] D.A. Nield, A.V. Kuznetsov, The Cheng–Minkowycz problem for the double-diffusive natural convective boundary layer flow in a porous medium saturated by a nanofluid, Int. J. Heat Mass Transfer 54 (1–3) (2011) 374–378.

International Communications in Heat and Mass Transfer 46 (2013) 58–66

Contents lists available at SciVerse ScienceDirect

International Communications in Heat and Mass Transfer

journal homepage: www.elsevier.com/locate/ichmt

Experimental analysis of the single phase pressure drop characteristics of smooth and microfin tubes ☆

Ali Celen [a], Ahmet Selim Dalkilic [a,*], Somchai Wongwises [b]

[a] Heat and Thermodynamics Division, Department of Mechanical Engineering, Yildiz Technical University (YTU), Yildiz, Besiktas, Istanbul 34349, Turkey
[b] Fluid Mechanics, Thermal Engineering and Multiphase Flow Research Lab. (FUTURE), Department of Mechanical Engineering, Faculty of Engineering, King Mongkut's University of Technology Thonburi, Bangmod, Bangkok 10140, Thailand

ARTICLE INFO

Available online 6 June 2013

Keywords:
Microfin tube
Pressure drop
Friction factor
Single-phase flow

ABSTRACT

In this study, the single phase pressure drop characteristics of smooth and microfin tubes are investigated experimentally. The horizontal test section is a counter flow double tube heat exchanger with water flowing in the inner tube and cooling water flowing in the annulus. By means of experimental setup, required temperature and pressure measurements are recorded and friction factor coefficient and pressure drop of smooth and microfin tubes are determined. Experiments are conducted for mass flow rates in the range between 0.023 kg/s and 0.100 kg/s and effect of Reynolds number on pressure drop is investigated. By using experimental results, Blasius type friction factor equations are developed for both smooth and microfin tubes. Experimental results for both smooth and microfin tubes are compared with correlations given in the literature.

© 2013 Elsevier Ltd. All rights reserved.

1. Introduction

In today's world, heat transfer enhancement has become a very important issue. Heat transfer enhancement in heat exchangers results in reduced size, low cost and improved heat transfer performance. There are two techniques for heat transfer enhancement: Active and passive techniques. First one is not popular technique because it requires the addition of external power. Passive heat transfer enhancement consists of alteration to the heat transfer surface such as extended surfaces, treated surface etc. Among the passive heat transfer enhancement techniques, the usage of microfin tubes is very popular because of their high heat enhancement and low increase in pressure drop when they are compared with smooth tube. Fuji et al. [1] invented the microfin tube. Geometric parameters which characterize microfin tubes are outside diameter, inside diameter, number of fins (ranges between 50 and 70), helix angle (ranges between 10° and 35°) and fin height (ranges between 0.1 and 0.4 mm). If the ratio of height and inside diameter of a microfin tube is between 0.02 and 0.04, this tube is classified as microfinned tube. If the ratio of height and inside diameter of a microfin tube is higher than 0.04, this tube is classified as finned tube. Microfin tubes are commonly used in HVAC applications (condensers and evaporators for cooling systems). The literature review on this subject is given in the following paragraphs and shown in Table 1.

Wang et al. [2] performed an experimental study related to single phase heat transfer and pressure drop characteristics of micro-fin tubes. In their study, they used double-pipe heat exchanger with water as test fluid and tested a smooth tube and seven micro-fin tubes each having different geometrical parameters. Wilson plot technique [3] is used in order to determine inside and outside heat transfer coefficients of test tubes. Their study showed that critical Reynolds number is an important parameter for enhanced heat transfer. They suggested that heat transfer data can be correlated by using heat-momentum transfer analogy instead of Dittus–Boelter type equation. As a result of their study, they produced heat transfer and pressure drop correlations in the range of $2500 < Re < 4000$ which can predict micro-fin data with high accuracy.

Copetti et al. [4] compared experimentally heat transfer performance of smooth and micro-fin tubes at different flow rates. In the experimental setup, water is used as test fluid and tubes having 9.52 mm diameter is used. They compared measured friction factor data with Blasius [5] and Petukhov [6] equations and heat transfer coefficient data with Dittus–Boelter [7] and Gnielinski [8] equations. They developed correlations for prediction of micro-fin heat transfer data and compared them with experimental results. The experimental study showed that heat transfer coefficient of micro-fin tube was 2.9 times higher than smooth tube in turbulent flow. Although pressure drop of micro-fin tube was 1.7 times higher than smooth tube, heat transfer increase was approximately 80%.

Wei et al. [9] presented an experimental study in order to determine single phase heat transfer and pressure drop in micro-fin tubes by using water and oil as working fluids. In the study, experiments were conducted for Reynolds number ranging between 2500 and 90,000 and Prandtl number varying between 3.2 and 220. Their study showed that critical Reynolds number is an important parameter for heat transfer enhancement. In the case of Reynolds number that is below critical

☆ Communicated by W.J. Minkowycz.

* Corresponding author.
E-mail address: dalkilic@yildiz.edu.tr (A.S. Dalkilic).

0735-1933/$ – see front matter © 2013 Elsevier Ltd. All rights reserved.
http://dx.doi.org/10.1016/j.icheatmasstransfer.2013.05.010

Nomenclature

A	actual flow area of tube [m^2]
A_n	nominal flow area of tube [m^2]
D	inside tube diameter [m]
D_h	hydraulic diameter [m]
D_o	outside tube diameter [m]
D_e	equivalent tube diameter [m]
e	height of fin [m]
f	friction factor
G	mass flux [kg/m^2s]
L	length of test tube [m]
l_c	characteristic length [m]
m	mass flow rate [kg/s]
n	number of fins
N	number of experiments
p	fin pitch [m]
s	average fin thickness [m]
ΔP	pressure drop [mbar]
Re	Reynolds number
t	fin tip thickness [m]
V_m	average fluid velocity [$m\ s^{-1}$]
μ	dynamic viscosity [Pa·s]
α	helix angle (°)
ρ	density of fluid [$kg\ m^{-3}$]

Reynolds number micro-fin tubes behave as smooth tube. For Reynolds numbers higher than critical Reynolds number, heat transfer enhancement can be observed. Their studies showed that heat transfer performance of micro-fin tube for Reynolds number greater than 30,000 with water as working fluid is two times higher than smooth tube. Friction factors of smooth and micro-fin tubes are just about equal for Reynolds number less than 10,000 but friction factor of micro-fin tube is 40–50% higher when it is compared with smooth tube for Reynolds number higher than 30,000.

Siddique and Alhazmy [10] studied heat transfer and pressure drop characteristics inside microfin tube for single phase flow. Double pipe heat exchanger and micro-fin tubes having 7.94 mm outside diameter were used in the experimental setup. They correlated a Dittus–Boelter type correlation for prediction Nusselt number and a Blasius type correlation for prediction of friction factor. These correlations were compared with both experimental results and studies in the literature. Their study showed that friction factor and Nusselt number of micro-finned tube in the range of $3300 < Re < 22{,}500$ can predict by means of developed correlations.

Carvanos [11] investigated heat transfer performance of internal spiral and longitudinal finned tubes in turbulent flow in the range of $10{,}000 < Re < 100{,}000$, $0.7 < Pr < 30$ and $0° <$ helix angle $< 30°$. The author used Wilson plot technique [3] in order to determine heat transfer performance and fin tube efficiency. According to fin tube efficiency results, tubes having higher helix angle and heat transfer surface area have the best heat transfer performance among 11 test tubes. As another result of the study, the pressure drop correlation is proposed which includes the effect of helix angle.

Jensen and Vlakancic [12] proposed new correlations for prediction of Nusselt number and friction factor of both high and microfin tubes. They investigated effect of fin geometry to the performance of finned tubes by means of these correlations and compared friction factor and Nusselt number results with Filonenko [13] and Gnielinski [8] correlations for smooth tube, respectively. The correlations are applied to a smooth and 15 finned tubes having different outside diameter, inside diameter fin height, fin thickness and fin helix angle. Their study showed that friction factor and Nusselt number increased with increasing number of fins. As another result of their study, friction factor and Nusselt number increased with increasing fin height under the same conditions.

Zdaniuk et al. [14] experimentally studied single phase heat transfer characteristic of one smooth tube and eight helically finned tubes having the helix angle of 25°–28°, e/D ratios of 0.0199–0.0327, and number of fin between 10 and 45. They conducted experiments in order to determine fanning friction and Colburn j-factors in the range of between $12{,}000 < Re < 60{,}000$ by using water as test fluid. They evaluated the performance of the correlations with data of other researchers and showed average prediction errors between 30% and 40%.

Al Fahed et al. [15] performed an experimental study in order to determine heat transfer coefficients and friction factors of microfinned tube under turbulent flow conditions. Inside and outside heat transfer coefficients were determined by using Wilson's method [16] in the study. They produced empirical correlations for prediction of heat transfer and friction factor data. They stated that micro-finned tube heat transfer performance enhancement varied from 1.2 to 1.8 times higher than smooth tube and pressure drop increase changed between 1.3 and 1.8.

Han and Lee [17] conducted experiments related to single phase heat transfer and flow characteristics of micro-fin tubes. They tested four different tubes in order to indicate experimental friction factor and heat transfer coefficients in the Reynolds number range between 3000 and 40,000. Heat transfer coefficients and friction factor correlations were produced by means of experimental data in the study. Their performance was evaluated with mean square deviation and root mean square deviation which were lower than 6.4%. Their study revealed that performance of tube having smaller spiral angle and higher relative roughness showed better than tube having larger spiral angle and lower relative roughness among the tested tubes. They also stated that heat transfer area increase was an important parameter for efficiency index.

Table 1
Summary of studies about single-phase flow in micro-fin tube.

Researcher	Year	Fluid	Reynolds number	Number of tested tubes
Wang et al. [2]	1996	Water	$2500 < Re < 40{,}000$	8
Copetti et al. [4]	2004	Water	$2000 < Re < 20{,}000$	2
Wei et al. [9]	2007	Water & oil	$2500 < Re < 90{,}000$	1
Siddique and Alhazmy [10]	2008	Water	$3300 < Re < 22{,}500$	1
Carvanos [11]	1980	Water	$10{,}000 < Re < 100{,}000$	14
Jensen and Vlakancic [12]	1999	Water & EG	$10{,}000 < Re < 100{,}000$	16
Zdaniuk et al. [14]	2008	Water	$12{,}000 < Re < 60{,}000$	9
Al Fahedet al. [15]	1993	Water	$10{,}000 < Re < 30{,}000$	2
Han and Lee [17]	2005	Water	$3000 < Re < 40{,}000$	4
Wang and Rose [18]	2004	Water & R11 & EG	$2000 < Re < 163{,}000$	21
Naphon and Sriromruln [22]	2006	Water	$8000 < Re < 25{,}000$	2
Brognaux et al. [23]	1997	Water	$2500 < Re < 50{,}000$	3

Wang and Rose [18] set up an experimental data for prediction of effective friction factor for single phase flow in horizontal micro-fin tubes. They used six correlations belonging to experimental studies given in the literature (Wang et al. [2], Carvanos [11], Jensen and Vlakancic [12], Webb et al. [19], Ravigururajan and Bergles [20] and Cavallini et al. [21]) containing a wide range of tube and fin geometric variables (inside diameter at the fin root between 6.46 and 24.13 mm, fin height between 0.13 and 0.47 mm, fin pitch between 0.32 and 1.15 mm and helix angle between 17 and 45°) and Reynolds number. They calculated mean square deviation and root mean

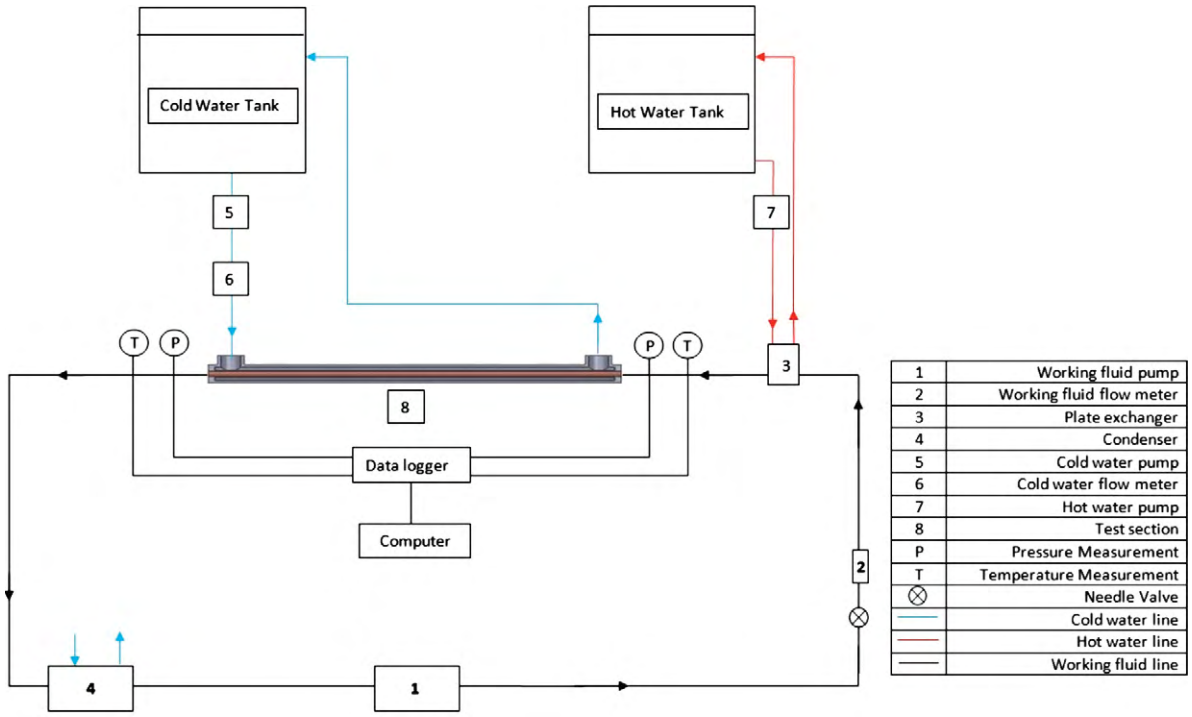

a) Schematic diagram of experimental setup

b) Picture of experimental setup

Fig. 1. Photograph of experimental setup.

square deviation of each correlation for different Reynolds number. They stated that correlation of Jensen and Vlakancic [12] presents the database the best.

Naphon and Sriromruln [22] investigated pressure drop and heat transfer characteristics of micro-fin tube both with and without coiled wire insert. They used smooth tube, micro-fin tube with coiled insert and micro-fin tube without coiled insert in the experiments and studied the effect of inlet hot water temperature, inlet cold water temperature, hot water mass flow rate, and cold water mass flow rate to the performance of double pipe heat exchanger performance. According to experimental results, they found that the coiled wire has a significant effect on the enhancement of heat transfer but the tube with coiled wire insert had higher friction factor results.

Brognaux et al. [23] studied single-phase heat transfer and friction factor of single and cross-grooved micro-fin tubes experimentally. They aimed to define Prandtl number dependency and the effect of surface geometry on the Prandtl number dependence. They stated that cross-grooved tube had higher performance than the best single grooved tube. Their study showed that usage of micro-fin tubes instead of smooth one provided enhancement ratio up to 95%. However, micro-fin tubes had higher friction factors between 35% and 80% when they compared with smooth tube.

It is well known that usage of microfin tubes improves heat transfer but increases pressure drop. This study is aimed to determine single phase pressure drop characteristics of smooth and microfin tubes in a double pipe heat exchanger for different working conditions experimentally. In order to determine pressure drop characteristic of smooth and microfin tubes, pressure drop and friction factor are calculated by using pure water as test fluid. Blasius type friction factor equations are proposed using experimental results. Comparisons with the empirical correlations in the literature are also performed in the study.

2. Experimental apparatus

The experimental setup which allows conducting pressure drop measurement of tube was installed and its schematic representation is given Fig. 1. By means of experiment setup, single phase pressure drop characteristics of smooth and micro-fin tubes were determined for different flow conditions. In the experimental study, as inner tube of double pipe heat exchanger smooth and microfin were used.

Basic working principle of experimental set up can be summarized as follows:

- Water (working fluid) is circulated by means of frequency controlled pump.
- Hot water is heated in the hot water tank and sent to plate heat exchanger in order to transfer its heat to working fluid.
- In the plate exchanger, water is heated until required temperature.
- Cold water is cooled in the cold water tank and sent to test section in order heat reject from working fluid.
- Experiments are conducted for 10 different mass flow rate of working fluid in the range between 0.02 and 0.1 kg/s.
- In the steady state conditions, temperature, pressure and flow rate parameters are recorded.

In the experiments two test sections (double pipe heat exchangers) are used. One of them is test section (double pipe heat exchangers) which is comprised of a copper inside smooth tube and plastic shell tube. Other one is a test section (double pipe heat exchangers) which is comprised of an internally microfinned copper inside tube and plastic shell tube. Internally microfinned tube is provided from Wieland Copper Products Company [24] and its details are shown in Table 2a. Test sections are isolated in order to avoid heat loss.

In this study, experiments are conducted in order to determine single phase pressure drop characteristic of smooth and microfin tubes and details of operating conditions are given Table 2b.

3. Data reduction

In a tube, there are three types of fluid flow depending on the flow conditions. They are laminar, transient and turbulent flows. In laminar flow, fluid particles have the same direction and velocity of fluid is small but flow turns turbulent when the velocity is increased. It should be noted that boundary layer is thick in this type flow. Transition from laminar to turbulent flows does not happen sharply, it can be defined as a mixture of laminar and turbulent flows. Fluid velocity in transient flow is higher than critical value. Turbulent flow can be seen in high flow rates and flow particles behave randomly. Contrary to laminar flow, boundary layer is thin in turbulent flow. Generally flow in pipes is turbulent in most engineering applications.

For flow in a circular tube, the Reynolds number is defined as follows:

$$\mathrm{Re} = \frac{\rho \cdot V_m \cdot D}{\mu}. \tag{3.1}$$

In application it is difficult to define precise values of Reynolds number for laminar, transitional and turbulent flows because the transition from laminar to turbulent flows depends on the degree of disturbance of the flow by surface roughness, pipe vibrations and the fluctuations in the flow. Under most practical conditions, flow in a tube is laminar for $\mathrm{Re} < 2300$, turbulent for $\mathrm{Re} > 10{,}000$ and transitional between this numbers [25].

Pressure drop is the one of important parameter in the analysis of tube flow because it affects required power of pump used in the system. When inlet and outlet pressures of a fluid are considered as P_1 and P_2 respectively, change in the pressure in the length of L can be expressed as follows:

$$\frac{dP}{dx} = \frac{P_2 - P_1}{L} = -\frac{\Delta P}{L}. \tag{3.2}$$

It should be noted that the pressure drop is a positive quantity in fluid mechanics and it is defined as $\Delta P = P_1 - P_2$.

For laminar flow, pressure drop can be expressed as follows:

$$\Delta P = \frac{8.\mu.L.V_m}{R^2} = \frac{32 \cdot \mu \cdot L \cdot V_m}{D^2}. \tag{3.3}$$

In applications, for all types of internal flows such as laminar or turbulent flows, circular or noncircular tubes, and smooth or rough surfaces, an equation can be used in order to calculate pressure drop and it is given below:

$$\Delta P = f \cdot \frac{L}{D} \cdot \frac{\rho V_m^{\,2}}{2} \tag{3.4}$$

where the dimensionless quantity f is the friction factor which is also called the Darcy friction factor.

Eq. (3.4) expresses the pressure drop for a flow section of length as long as (a) there aren't any effects of hydrostatic or gravity in other words there is a horizontal flow section, (b) the flow section does not include any work device such as a pump or turbine due to their effect on the alteration of the fluid pressure and (c) there is an assumption of the constant cross sectional area of the flow section and hence the average flow velocity is constant [25].

The friction factor for fully developed laminar flow in a circular tube is obtained by setting Eqs. (3.3) and (3.4) equal to each other as follows:

$$f = \frac{64 \cdot \mu}{\rho \cdot D \cdot V_m} = \frac{64}{\mathrm{Re}}. \tag{3.5}$$

Table 2
Geometrical parameters of tubes used in the experiments (a) and details of operating conditions (b).

a)

Parameter	Unit	Smooth tube 1	Smooth tube 2	Micro-fin tube
Length (L)	mm	1100	1100	1100
Outside diameter (D_o)	mm	8	10	8
Inside diameter (D_i)	mm	6	8	7.48
Thickness (t)	mm	1	1	0.26
Fin height (e)	mm	–	–	0.22
Fin pitch (p)	mm			0.34
Helix angle (α)	°	–	–	35
Number of fins (n)	–	–	–	65
e/D	–	–	–	0.027

b)

Experiment	Inside diameter (m)	Mass flow rate range (kg/s)	Reynolds number range	Hot water inlet temperature (°C)	Cold water inlet temperature (°C)
Smooth tube 1	0.006	0.023–0.100	7175–31,775	40–60	15
Smooth tube 2	0.008	0.023–0.100	5446–23,831	40	15
Simulated smooth tube 3	0.00748	0.023–0.100	5825–25,488	40	15
Microfin tube	0.00748	0.023–0.100	5725–25,353	40–60	15

This equation shows that in laminar flow, friction factor is function of the Reynolds number only and is independent of the roughness of the tube surface [25]. For smooth and microfin tubes, the friction factor in turbulent flow can be determined from the correlations given in the Table 3a and b respectively.

4. Correlation development

New friction factor correlation is developed by using experimental data and graphical program. Curve Expert program [29] is used in order to get new friction factor correlations. The R^2 value of fit data

Table 3
Friction factor correlations for smooth tube (a) and microfin tubes (b).

Researcher	Correlation
a)	
Blasius [5]	$f = 0.316Re^{-1/4}$
Petukhov [6]	$f = (0.79 \ln Re - 1.64)^{-2}$
Moody [26]	$f = 0.184Re^{-1/5}$
Colebrook [27]	$f = \left(1.8 \log \frac{Re}{6.9}\right)^{-2}$
b)	
Wang et al. [2]	$e^+ = \left(\frac{e}{D}\right) Re \sqrt{\frac{f}{2}}$ for $e^+ < 23$
	$e^+ = 0.1407 + 0.093675X_f + 0.58464/\ln(X_f)$
	for $e^+ > 23 e^+ = 0.07313 + 0.09511X_f$ $X_f = Re\left(\frac{e}{D+\lambda}\right)\frac{n^{0.25}}{(\cos\alpha)^{0.5}}$
Siddique and Alhazmy [10]	$f = 0.907Re^{-0.286}$
Carvanos [11]	$f = 0.046Re^{-0.2}\left(\frac{D}{D_h}\right)^{1.2}\left(\frac{A}{A_n}\right)^{0.5}(\sec\alpha)^{0.75}$
Jensen and Vlakancic [12]	$\frac{f}{f_{FI}} = \left(\frac{l_c}{D}\right)^{-1.25}\left(\frac{A_n}{A}\right)^{1.75} - \left(\frac{0.0151}{f_{FI}}\right)*$
	$\left\{\left(\frac{l_c}{D}\right)^{-1.25}\left(\frac{A_n}{A}\right)^{1.75} - 1\right\}\exp\left(-\frac{Re}{6780}\right)$
	$\frac{l_c}{D} = 1 - 1.577\left(\frac{n\sin\alpha}{\pi}\right)^{0.64}\left(\frac{2e}{D}\right)^{0.53}\left\{\left(\frac{\pi}{n} - \frac{s}{D}\right)\cos\alpha\right\}^{0.28}$
	$f_{FI} = (1.58 \ln Re - 3.28)^{-2}$ $s = \frac{p}{\cos\gamma} - \frac{\pi}{4}\left(D^2 - D_e{}^2\right)/(ne)$
Zdaniuk et al. [14]	$f = 0.128Re^{-0.305}n^{0.235}(e/D)^{0.319}\alpha^{0.397}$
Al Fahed et al. [15]	$f = 0.9978Re^{-0.2943}$
Webb et al. [19]	$\sqrt{\frac{2}{f}} = B(e^+) - 2.5\ln(2e/d) - 3.75$ $B(e^+) = 4.762(e^+)^{0.2138}n^{-0.1096}\alpha^{-0.297}$
	$e^+ = \left(\frac{e}{d}\right) Re \sqrt{\frac{f}{2}}$ or $f = 0.128Re^{-0.305}n^{0.235}(e/D)^{0.319}\alpha^{0.397}$
Ravigururajan and Bergles [20]	$\frac{f}{f_{FI}} = \left\{1 + \left[29.1Re^{a1}(e/D)^{a2}(p/D)^{a3}(\alpha/90)^{a4}(1 + 1.47\cos\alpha\right]^{15/16}\right\}^{16/15}$
	where $f_{FI} = (1.58 \ln Re - 3.28)^{-2}$
	$a1 = 0.67 - 0.06p/D - 0.49\alpha/90$ $a2 = 1.37 - 0.157p/D$
	$a3 = -1.66 \cdot 10^{-6}Re - 0.33\alpha/90$ $a4 = 4.59 + 4.11 \cdot 10^{-6}Re - 0.15p/D$
Haaland [28]	$f = \frac{0.3086}{\left\{\log\left[\frac{6.9}{Re} + \left(\frac{e}{3.7D}\right)^{1.11}\right]\right\}^2}$

Table 4
Friction factor data and proportional errors of smooth tube 2.

Mass flow rate	Re	Mass flux	Friction factor results			
			Blasius [5]	Petukhov [6]	Experiment	Correlation 2
kg/s	–	kg/m^{2}s	–	–	–	
0.0233	5446	464	0.0368	0.0376	0.0583	0.0549
0.0312	7274	620	0.0342	0.0345	0.0473	0.0481
0.0408	9532	812	0.0320	0.0319	0.0416	0.0425
0.0475	11,139	945	0.0308	0.0305	0.0380	0.0396
0.0575	13,296	1127	0.0294	0.0291	0.0360	0.0365
0.0675	15,636	1326	0.0283	0.0279	0.0333	0.0339
0.0742	17,467	1475	0.0275	0.0271	0.0325	0.0322
0.0833	19,640	1658	0.0267	0.0263	0.0319	0.0305
0.0917	21,646	1824	0.0261	0.0256	0.0304	0.0292
0.1008	23,831	2006	0.0254	0.0250	0.0292	0.0279
Proportional errors			%	%	%	%
			19.92	20.54	–	3.04

of correlation for power model is in the program 0.992 showing that the correlation model explains 99.292% of variability in the data.

Developed correlation according to Power model as a result of curve fitting process is given below:

Developed correlation of friction factor for 6/8 mm smooth tube 1 is obtained as:

$$f_{correlation1} = 0.269 \cdot Re^{-0.217}. \tag{4.1}$$

Pressure drop is obtained for the developed correlation of smooth tube 1 as:

$$\Delta P_{correlation2} = f_{correlation1} \cdot \frac{L}{D} \cdot \frac{\rho \cdot V_m{}^2}{2}. \tag{4.2}$$

Developed correlation of friction factor for 8/10 mm smooth tube 2 is determined as:

$$f_{correlation2} = 2.793 \cdot Re^{-0.456}. \tag{4.3}$$

Pressure drop is obtained for the developed correlation of smooth tube 2 as:

$$\Delta P_{correlation2} = f_{correlation2} \cdot \frac{L}{D} \cdot \frac{\rho \cdot V_m{}^2}{2}. \tag{4.4}$$

Proposed correlation 3 for the simulated smooth tube 3 is developed by using 6/8 mm and 8/10 mm tube data in order to predict smooth tube 3 having 7.48 mm inside diameter. Developed correlation according to Saturation Growth-Rate Model as a result of curve fitting process is given below:

Developed correlation of friction factor for smooth tube 3 is calculated as:

$$f_{correlation3} = \frac{0.026 \cdot Re}{-2915 + Re}. \tag{4.5}$$

Pressure drop is obtained for the developed correlation of smooth tube 3 as:

$$\Delta P_{correlation3} = f_{correlation3} \cdot \frac{L}{D} \cdot \frac{\rho \cdot V_m{}^2}{2}. \tag{4.6}$$

Developed correlation according to Power model as a result of curve fitting process is given below:

Result of curve fitting process produced correlations for microfin tube is given below:

$$f_{correlation4} = 0.605 \cdot Re^{-0.226} \tag{4.7}$$

$$\Delta P_{correlation4} = f_{correlation4} \cdot \frac{L}{D_e} \cdot \frac{\rho \cdot V_m{}^2}{2}. \tag{4.8}$$

Error for obtained results is calculated by means of equation below:

$$Error = \frac{1}{N}\sum_{i=1}^{N}\left|\left(\frac{Predicted\,value - Measured\,value}{Measured\,value}\right)\cdot 100.\right| \tag{4.9}$$

5. Results and discussion

In order to develop the empirical friction factor correlation and investigate the characteristics of pressure drop during single phase flow of pure water in horizontal smooth and microfin tubes with inner diameters of 6, 7.48 and 8 mm, the present study were performed at the Heat and Thermodynamics Division lab. in YTU. Calculated and experimental friction factors and their proportional errors of smooth tube 2 having 8 mm i.d. and microfin tube having 7.48 mm i.d. are shown in Tables 4 and 5, respectively. Comparison of pressure drop results for investigated smooth and microfin tubes using well-known equations and proposed ones in the literature and their alteration with Reynolds number and mass flux are shown from Figs. 2 to 4. Comparison of measured experimental pressure drop data for simulated smooth tube and microfin tube having equivalent inner diameter are

Table 5
Friction factor data and proportional errors of microfin tube.

Mass flow rate	Re	Mass flux	Friction factor results								
			Wang et al. [2]	Siddique and Alhazmy [10]	Jensen and Vlakancic [12]	Zdaniuk et al. [14]	Al Fahed et al. [15]	Webb et al. [19]	Haaland [28]	Experiment	Correlation 4
kg/s	–	kg/m^{2}s	–	–	–	–	–	–	–	–	–
0.0233	5725	526	0.050	0.076	0.085	0.032	0.078	0.023	0.062	0.086	0.085
0.0312	7657	695	0.050	0.070	0.079	0.029	0.071	0.021	0.060	0.080	0.079
0.0408	10,140	920	0.049	0.064	0.073	0.027	0.066	0.020	0.059	0.074	0.074
0.0475	11,850	1070	0.049	0.061	0.070	0.026	0.063	0.019	0.059	0.071	0.072
0.0575	14,353	1295	0.049	0.058	0.067	0.024	0.059	0.018	0.058	0.066	0.069
0.0675	16,842	1521	0.049	0.056	0.064	0.023	0.056	0.017	0.058	0.065	0.066
0.0742	18,582	1671	0.0495	0.0544	0.0633	0.0226	0.0552	0.0169	0.0585	0.0666	0.0653
0.0833	20,894	1877	0.0494	0.0527	0.0615	0.0218	0.0533	0.0163	0.0583	0.0638	0.0636
0.0917	23,027	2065	0.0493	0.0512	0.0600	0.0212	0.0518	0.0159	0.0581	0.0638	0.0622
0.1008	25,353	2271	0.0493	0.0498	0.0586	0.0206	0.0504	0.0155	0.0580	0.0604	0.0609
Proportional errors			%	%	%	%	%	%	%	%	%
			30.0	17.0	2,36	65.3	15.7	74.4	16.6	–	2,5

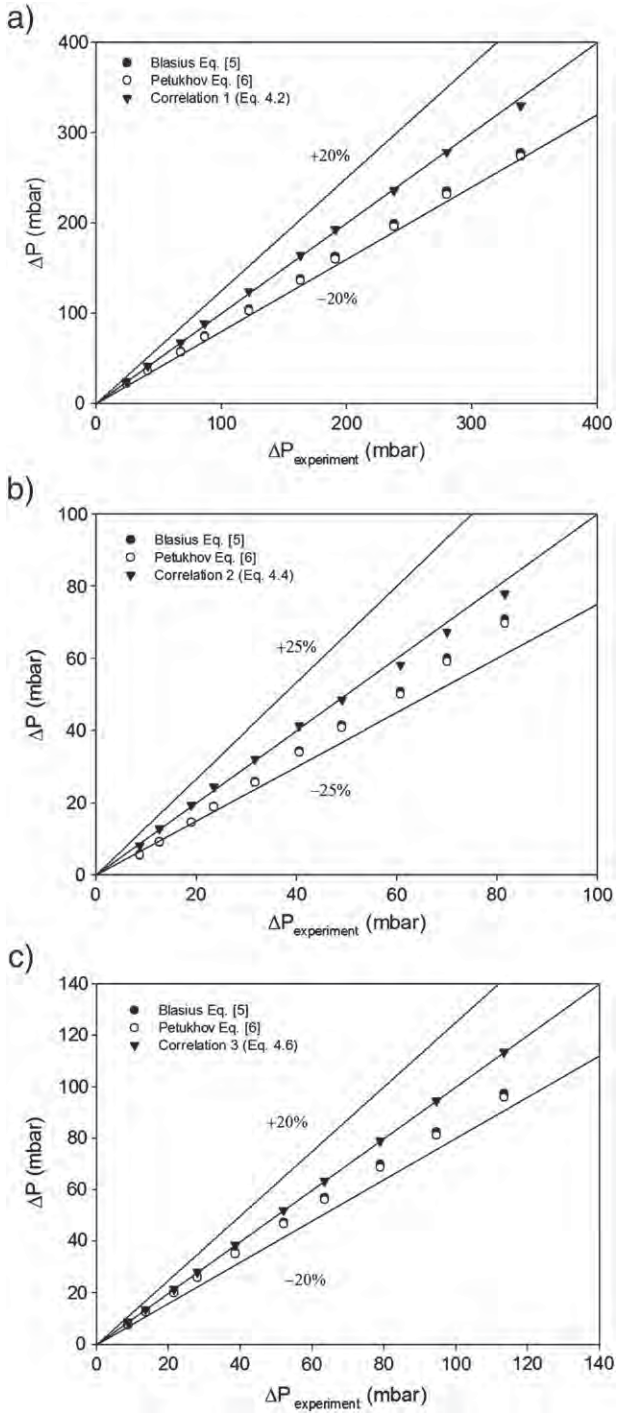

Fig. 2. Comparison of pressure drop results for the smooth tubes 1 (a), 2 (b) and 3 (c).

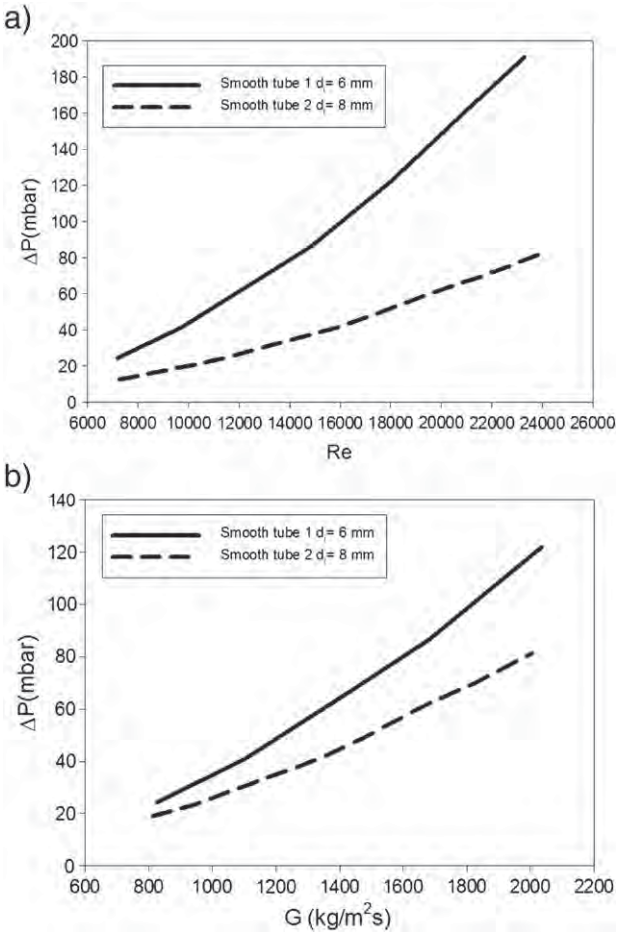

Fig. 3. Pressure drop comparison of smooth tubes according to Reynolds number (a) and mass flux (b).

illustrated in Table 6 and Fig. 5. The following paragraphs present the indirectly determined friction factor and measured pressure drops using relevant measured data. Discussion of the results will be given in turn as follows:

In Table 4, friction factor results of smooth tube 2 calculated according to Blasius equation [5], Petukhov equation [6], developed correlation of Eq. (4.3) and experimental friction factor and their proportional errors are shown. It should be noted that proportional errors of developed correlation 2 was calculated as 3.04% as shown in Table 4.

Friction factor data and proportional errors of microfin tube can be seen Table 5. It was observed that the friction factor decreased gradually as the Reynolds number increased. Decrease in the friction factor is related to sublayer thickness. When Reynolds number is increased, the thickness of sublayer decreases and it resulted in lower friction factor results.

Comparison of pressure drop results for the smooth tubes 1, 2 and 3 can be seen in Fig. 2(a), (b) and (c), respectively. It was observed that the experimental result were in good agreement with Blasius [5] and Petukhov [6] equations for all smooth tubes. It means that these equations can be used for prediction of the pressure drop of smooth tubes.

Fig. 3(a) and (b) illustrates pressure drop comparison of smooth tubes having different inside diameter according to Reynolds number and mass flux, respectively. As seen in Fig. 3, tube having lower inside diameter showed higher pressure drop when it is compared with higher one.

Fig. 4(a) and (b) shows variation of pressure drop with Reynolds number and mass flux for microfin tube, respectively. It was shown that the pressure drop increased gradually as the Reynolds number and mass flux increased. Fig. 4(c) compares experimental results with equations of other researchers given in Table 5. The experimental results were found in good agreement in the range of ±20% except Zdaniuk et al. [14] and Webb et al. [19] equations.

Fig. 5(a) and (b) represents pressure drop comparison of smooth tube 3 and microfin tubes according to Reynolds number and mass flux, respectively. Experimental pressure drop data for smooth and microfin tubes can be seen in Table 6. As it expected, the pressure drop for microfin tube was higher than the smooth tube. It means that the microfin tube produced more flow disturbance by the occurrence of the swirl flow and flow recirculation produced by the fins, which led to higher frictional pressure drop.

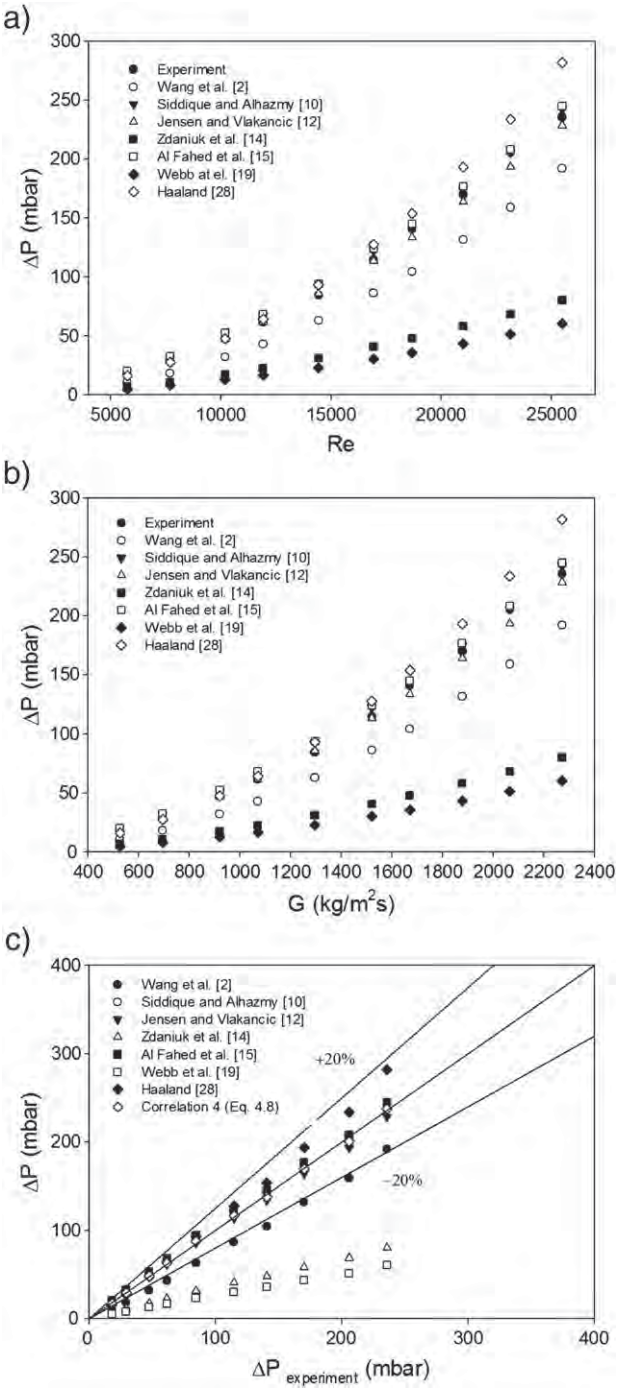

Fig. 4. Predicted and measured pressure drop results for microfin tube according to Reynolds number (a), mass flux (b) and comparison of them (c).

A large number of graphics could be generated from the output of the calculations, however, due to space limitation, only typical results are shown for limited data. It should be also noted that detailed information on the explanations above and some additional figures with different experimental parameters related to this study can be seen from the authors' previous publications [30–34].

6. Conclusion

Heat transfer enhancement has become a more important issue over the years. Microfin tubes play an important role in heat transfer enhancement applications. Many researchers have focused on two phase heat transfer characteristic of microfin tubes but single phase heat transfer characteristic of enhanced tubes are not well studied due to the new technological developments. In the present paper, pressure drop by means of microfin tube in single phase flow was discussed. Following results were obtained.

Table 6
Experimental pressure drop data for smooth and microfin tubes.

Smooth tube			Microfin tube			Pressure drop augmentation
Re	G	ΔP	Re	G	ΔP	
–	kg/m²s	mbar	–	kg/m²s	mbar	$P_{microfin}/P_{smooth}$
5809	528	8.70	5725	526	18.00	2.07
7759	705	13.60	7657	695	29.20	2.15
10,167	924	21.47	10,140	920	47.40	2.21
11,881	1075	28.02	11,850	1070	61.50	2.19
14,183	1283	38.54	14,353	1295	84.40	2.19
16,678	1509	52.01	16,842	1521	114.40	2.20
18,631	1679	63.42	18,582	1671	140.60	2.22
20,949	1886	78.97	20,894	1877	170.00	2.15
23,089	2075	94.58	23,027	2065	205.70	2.17
25,420	2282	113.41	25,353	2271	235.70	2.08

- It was found that the friction factor decreased gradually as the Reynolds number increased for both smooth and microfin tubes. With increase in Reynolds number, the thickness of sublayer decreases and hence in tube turbulent flow becomes more uniform.
- It was found that the pressure drop increased gradually as the Reynolds number increased for both smooth and microfin tubes.
- The pressure drop in smooth tube having lower inside diameter was higher than in the smooth tube having higher inside diameter.

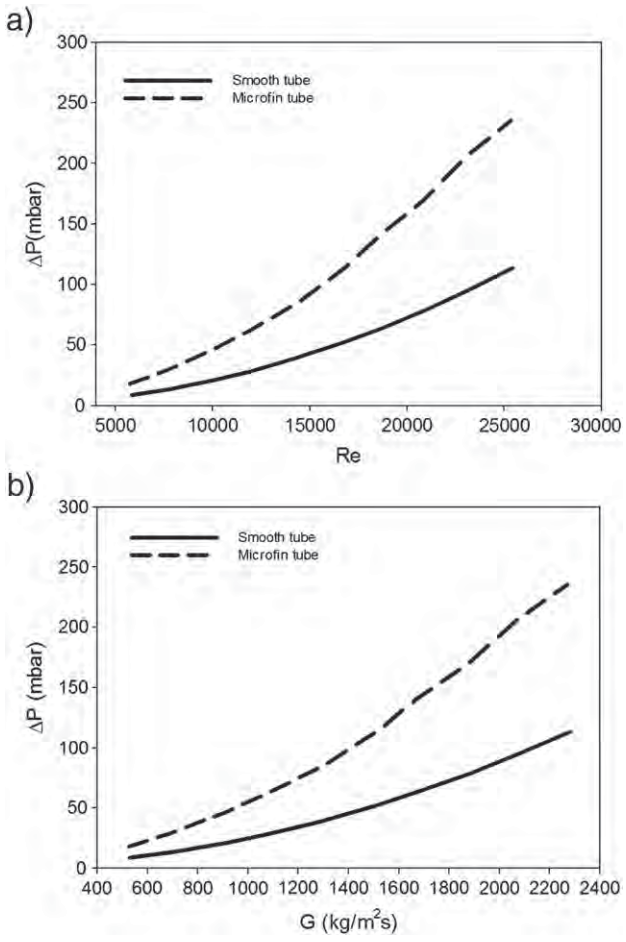

Fig. 5. Pressure drop comparison of smooth tube 3 and microfin tubes according to Reynolds number (a) and mass flux (b).

- The friction factor and pressure drop values for the microfin tube were higher than those for the smooth tube. This implies that the microfin tube produced more flow disturbance by the occurrence of the swirl flow and flow recirculation produced by the fins, which led to higher frictional pressure drop.
- Experimental results for smooth tubes compared with equations given in the literature. It is shown that there was good agreement for smooth tube results.
- Experimental results for microfin tube compared with equations given in the literature. It is shown that there was conflict about predict of microfin tube pressure drop characteristic prediction. By the means of experimental data, new correlation was developed in order to predict the friction factor for investigated microfin tube.

Acknowledgments

The present study was financially supported by Yildiz Technical University. The second author wishes to thank KMUTT for providing him with a Post-doctoral fellowship, while the third author wish to acknowledge the support provided by the Thailand Research Fund. The authors also wish to thank Wieland-Wilke AG (Ulm, Germany) for valuable donation of the micro-fin tube used in the present study.

References

[1] K. Fuji, N. Itoh, T. Innami, H. Kimura, N. Nakayama and T. Yanugidi, Heat transfer pipe, US Patent 4044797, assigned to Hitachi Ltd. 1977.
[2] C.C. Wang, C.B. Chiou, D.C. Lu, Single-phase heat transfer and flow friction correlations for micro-fin tubes, International Journal of Heat and Fluid Flow 17 (1996) 5–8.
[3] R.K. Shah, Assessment of modified Wilson plot techniques for obtaining heat exchanger design data, Proc. 9th Int. Heat Transfer Conf., 5, 1990, pp. 51–56.
[4] J.B. Copetti, M.H. Macagnan, D. De Souza, R.D. Oliveski, Experiments with micro-fin tube in single phase, International Journal of Refrigeration 27 (2004) 876–883.
[5] P.R.H. Blasius, Das AehnlichkeitsgesetzbeiReibungsvorgangen in Flüssigkeiten, Forschungsheft 131 (1913) 1–41.
[6] B.S. Petukhov, "Heat Transfer and Friction in Turbulent Referred to in Handbook of Single-Phase Convective Pipe Flow with Variable Physical Properties", In Heat Transferred. T. F. Irvine and J. P. New York: Wiley Interscience, 1987. Hartnett, 6. New York: Academic Press 1970.
[7] F.W. Dittus, L.M.K. Boelter, "Heat transfer in automobile radiators of the tubular type", University of California, Berkeley, Publications in Engineering 2 (1930) 443–461.
[8] V. Gnielinski, New equations for heat and mass transfer in turbulent pipe and channel flow, International Chemical Engineering 16 (1976) 359–368.
[9] L. Xiao-Wei, M. Ji-An, L. Zhi-Xin, Experimental study of single phase pressure drop and heat transfer in a micro-fin tube, Experimeantal Thermal and Fluid Science 32 (2007) 641–648.
[10] M. Siddique, M. Alhazmy, Experimental study of turbulent single-phase flow and heat transfer inside a micro-finned tube, International Journal of Refrigeration 31 (2008) 234–241.
[11] T.C. Carnavos, Heat transfer performance of internally finned tubes in turbulent flow', Heat Transfer Engineering 1 (1980) 32–37.
[12] M.K. Jensen, A. Vlakancic, Experimental investigation of turbulent heat transfer and fluid flow in internally finned tubes, International Journal of Heat and Mass Transfer 42 (1999) 1343–1351.
[13] S. Kakac, The effect of temperature dependent fluid properties on convective heat transfer, Handbook of Single-Phase Convective Heat Transfer, New York, John Wiley, 1987.
[14] G.J. Zdaniuk, L.M. Chamra, P.J. Mago, Experimental determination of heat transfer and friction in helically-finned tubes, Experimental Thermal and Fluid Science 32 (2008) 761–775.
[15] S.F. Al-Fahed, Z.H. Ayub, A.M. Al-Marsfie, B.M. Soliman, Heat transfer and pressure drop in a tube with internal microfins under turbulent water flow conditions, Experimental Thermal and Fluid Science 7 (1993) 249–253.
[16] E.E. Wilson, A basis for rational design of heat transfer apparatus, Transactions of ASME 37 (1915) 47–70.
[17] D.H. Han, K. Lee, Single phase heat transfer and flow characteristics of micro-fin tubes, Applied Thermal Engineering 25 (2005) 1657–1669.
[18] H.S. Wang, J.W. Rose, Prediction of effective friction factors for single-phase flow in horizontal microfin tubes, International Journal of Refrigeration 27 (2004) 904–913.
[19] R.L. Webb, R. Narayanamurthy, P. Thors, Heat transfer and friction characteristics of internal helical-rib roughness, Transaction of the ASME Journal of Heat Transfer 12 (2000) 301–318.
[20] T.S. Ravigururajan, A.E. Bergles, General correlations for pressure drop and heat transfer for single-phase turbulent flow in internally ribbed tubes, Augmentation of Heat Transfer in Energy Systems, ASME-HTD 52 (1985) 9–20.
[21] A. Cavallini, D. Del Col, L. Doretti, G.A. Longo, L. Rossetto, Pressure drop during condensation and vaporisation of refrigerants inside enhanced tubes, Heat Technology 15 (1) (1997) 3–10.
[22] P. Naphon, P. Sriromruln, Single-phase heat transfer and pressure drop in the micro-fin tubes with coiled wire insert, International Communications in Heat and Mass Transfer 33 (2006) 176–183.
[23] L.B. Brognaux, R.L. Webb, L.M. Chamra, Single phase heat transfer in micro-fin tubes, International Journal of Heat and Mass Transfer 40 (18) (1997) 4345–4357.
[24] Wieland Group Company, http://www.wieland.de/internet/en/produkte/Produits.jsp,01.10.2012.
[25] Y.A. Çengel, Heat Transfer: A Practical Approach, 3rd ed. McGraw Hill, 2006.
[26] L.F. Moody, Friction factors for pipe flows, Transactions of the ASME 66 (1944) 671–684.
[27] C.F. Colebrook, Turbulent flow in pipes, with particular reference to the transition region between smooth and rough pipe laws, Journal of the Institution of Civil Engineers 11 (1939) 133–156.
[28] S.E. Haaland, Simple and explicit formulas for the friction factor in turbulent pipe flow, Journal of Fluids Engineering 89–90 (1983).
[29] Curve Expert 1.3, http://www.curveexpert.net/,21.11.2012.
[30] N. Kayaci, M. Balcilar, M. Tabatabaei, A. Celen, O. Yıldız, A.S. Dalkilic, S. Wongwises, Determination of the single-phase forced convection heat transfer characteristics of TiO_2 nanofluids flowing in smooth and micro-fin tubes by means of CFD and ANN analyses, Current Nanoscience 9 (2013) 61–80.
[31] Ö. Ağra, H. Demir, Ş.Ö. Atayılmaz, F. Kantaş, A.S. Dalkılıç, Numerical investigation of heat transfer and pressure drop in enhanced tubes, International Communications in Heat and Mass Transfer 38 (2011) 1384–1391.
[32] H. Demir, A.S. Dalkilic, N.A. Kurekci, W. Duangthongsuk, S. Wongwises, Numerical investigation on the single phase forced convection heat transfer characteristics of TiO_2 nanofluids in a double-tube counter flow heat exchanger, International Communications in Heat and Mass Transfer 38 (2011) 218–228.
[33] K. Aroonrat, C. Jumpholkul, R. Leelaprachakul, A.S. Dalkilic, O. Mahian, S. Wongwises, Heat transfer and single phase flow in internally grooved tubes, International Communications in Heat and Mass Transfer 42 (2013) 62–68.
[34] N. Kayaci, A. Celen, M. Tabatabei, O. Yıldız, A.S. Dalkılıç, S. Wongwises, Numerical investigation of heat transfer enhancement using water based nanofluids flowing in enhanced tubes, ASME 2012 International Mechanical Engineering Congress & Exposition, November 9–15 2012, ASME, USA.

Efficiencies for Partially Wetted Spine Fins: Uniform Cross Section, Conical, Concave Parabolic, and Convex Parabolic Spines

Worachest Pirompugd
Department of Mechanical Engineering,
Faculty of Engineering,
Burapha University, Saensook,
Muang, Chonburi 20131, Thailand

Somchai Wongwises[1]
Fluid Mechanics, Thermal Engineering and
Multiphase Flow Research Lab. (FUTURE),
Department of Mechanical Engineering,
Faculty of Engineering,
King Mongkut's University of
Technology Thonburi,
Bangmod, Bangkok 10140, Thailand
e-mail: somchai.won@kmutt.ac.th

In this study, efficiencies for partially wetted fins for the uniform cross section spine, conical spine, concave parabolic spine, and convex parabolic spine are presented using an analytical method. Depending on the set of boundary conditions, there are two methods for deriving the efficiencies of partially wet fins for each spine. The eight equations for fin efficiencies were investigated. Fin efficiency is a function of the length of the dry portion. Thus, the equations for calculating the length of the dry portion are also presented. The findings indicate that a larger cross-sectional fin results in a higher conduction heat transfer rate. Contrarily, the fin efficiency is lower. This is different from the longitudinal fin, for which the trend lines of heat transfer rate and fin efficiency are the same. This converse relationship is due to the effect of the ratio of the cross-sectional area to the surface area. Moreover, partially wet fin efficiencies decrease with increased relative humidity. For convenience, the approximate equation for efficiencies for partially wet fins, which is derived from the equations for fully wet and fully dry fin efficiencies, is also presented. [DOI: 10.1115/1.4024017]

Keywords: concave parabolic spine, conical spine, uniform cross section spine, convex parabolic spine, partially wet fin efficiency

1 Introduction

A passive technique for heat transfer enhancement is to extend surfaces. By increasing surface and turbulence, fins can enhance heat transfer rate. For heat transfer evaluation, fin efficiency is necessarily known. Schmidt [1] and Kern and Kraus [2] derived dry fin efficiencies for longitudinal fins, spines, and circular fins. Subsequently, Arslanturk [3], Heggs and Somasundram [4], Joneidi et al. [5], Kulkarni and Joglekar [6], and Sharqawy et al. [7] presented methods for evaluating heat transfer rate and dry fin efficiency, and studied the influence of fin thermal conductivity on fin efficiency. Cortes et al. [8] presented a numerical method for evaluating dry fin efficiencies for fins of composite materials of variable thickness.

However, the fins used in many applications are in fully wet or partially wet surface conditions. Exemplarily, in evaporators, which typically use aluminum fins with the surface temperature generally being below the dew point temperature. As a result, simultaneous heat and mass transfer occurs along the fin surfaces. Moreover, if the dew point temperature is higher than the outside tube temperature but it is lower than the fin tip temperature, the condition the partially wet surface is seen. In 1970, Threlkeld [9] presented a method to obtain fin efficiency in fully wet conditions based on the enthalpy potential. Thus, fully wet fin efficiencies can be obtained using the Threlkeld method. Moreover, many researchers have studied extended heat exchangers in fully wet surface conditions and applied wet fin efficiency in the reduction method. In 2000, Liang et al. [10] investigated the fully wet and partially wet fin efficiencies of a plate fin-and-tube heat exchanger. However, Liang et al. [10] did not present the exact partially wet fin efficiency. They only note that the partially wet fin efficiency was obtained by multiplying the fully wet fin efficiency by some variable. In 2007, using an analytical method, Pirompugd et al. [11] presented circular fin efficiency in partially wet surface conditions. In 2012, using an analytical method, Pirompugd and Wongwises [12] presented partially wet fin efficiencies for longitudinal fins of rectangular, triangular, concave parabolic, and convex parabolic profiles. Moreover, using their results, they presented the approximation method for evaluating partially wet fin efficiencies from dry and wet fin efficiencies. Nevertheless, the extended surfaces in some applications are in partially wet surface conditions and may not be of longitudinal geometry. However, there is little literature concerning fin efficiency related to partially wet surface conditions. Thus, the objective of this present study is to derive partially wet fin efficiencies for fins of uniform cross section, conical, concave parabolic, and convex parabolic spines.

2 Mathematical Modeling

2.1 Dry and Wet Fin Efficiency. Differential equations for heat transfer and their solutions for the four types of spines in dry conditions were proposed by Kern and Kraus [2]. Then, the fin efficiency that is the ratio of the actual heat transfer rate of fin to the ideal heat transfer rate by assuming base temperature to entire fin ($\eta = (q_{\text{actual}}/q_{\text{ideal}})$) can be shown as

$$\text{Uniform cross section spine} : \eta_{\text{const,dry}} = \frac{\tanh mb}{mb} \tag{1}$$

$$\text{Conical spine} : \eta_{\text{cone,dry}} = \frac{\sqrt{2}I_2(2\sqrt{2}mb)}{mbI_1(2\sqrt{2}mb)} \tag{2}$$

[1]Corresponding author.

Contributed by the Heat Transfer Division of ASME for publication in the JOURNAL OF HEAT TRANSFER. Manuscript received September 21, 2012; final manuscript received March 11, 2013; published online July 18, 2013. Assoc. Editor: Giulio Lorenzini.

 Copyright © 2013 by ASME

Downloaded From: http://heattransfer.asmedigitalcollection.asme.org/ on 07/22/2013 Terms of Use: http://asme.org/terms

$$\text{Concave spine}: \eta_{\text{ccave,dry}} = \frac{2}{1+\sqrt{1+\frac{8}{9}(mb)^2}} \tag{3}$$

$$\text{Convex spine}: \eta_{\text{cvex,dry}} = \frac{3I_1\left(\frac{4}{3}\sqrt{2}mb\right)}{2\sqrt{2}mbI_0\left(\frac{4}{3}\sqrt{2}mb\right)} \tag{4}$$

where $m = \sqrt{(h_c P/k_f A)}$ for uniform cross section spines, P is the fin perimeter, and $m = \sqrt{(2h_c/k_f\delta_0)}$ for conical, concave parabolic, and convex parabolic spines. The subscript of "const", "cone", "ccave", and "cvex" means the uniform cross section spine, conical spine, concave parabolic spine, and convex parabolic spine. Moreover, the subscript of "part", "dry", and "wet" mean partially wet, fully dry, and fully wet conditions.

Moreover, Eqs. (1)–(4) are generally used for fins in dry conditions. For fully wet surface conditions, Threlkeld [9] presented a wet fin efficiency that accounts for the sensible and latent heat for the longitudinal fin of a rectangular profile. With the Threlkeld method, for uniform cross section, conical, concave parabolic, and convex parabolic pines, the enthalpy excess profiles and wet fin efficiencies can be developed as follows:

$$\text{Uniform cross section spine}: \gamma_{\text{const,wet}} = \frac{\gamma_0 \cosh m_T x}{\cosh m_T b} \tag{5}$$

$$\eta_{\text{const,wet}} = \frac{\tanh m_T b}{m_T b} \tag{6}$$

$$\text{Conical spine}: \gamma_{\text{cone,wet}} = \gamma_0\left(\frac{b}{x}\right)^{0.5}\frac{I_1(2\sqrt{2}m_T\sqrt{bx})}{I_1(2\sqrt{2}m_T b)} \tag{7}$$

$$\eta_{\text{cone,wet}} = \frac{\sqrt{2}I_2(2\sqrt{2}m_T b)}{m_T b I_1(2\sqrt{2}m_T b)} \tag{8}$$

$$\text{Concave spine}: \gamma_{\text{ccave,wet}} = \gamma_0\left(\frac{x}{b}\right)^{-1.5+0.5(9+8m_T^2 b^2)^{0.5}} \tag{9}$$

$$\eta_{\text{ccave,wet}} = \frac{2}{1+\sqrt{1+\frac{8}{9}(m_T b)^2}} \tag{10}$$

$$\text{Convex spine}: \gamma_{\text{cvex,wet}} = \frac{\gamma_0 I_0\left(\frac{4}{3}\sqrt{2}m_T b^{0.25}x^{0.75}\right)}{I_0\left(\frac{4}{3}\sqrt{2}m_T b\right)} \tag{11}$$

$$\eta_{\text{cvex,wet}} = \frac{3I_1\left(\frac{4}{3}\sqrt{2}m_T b\right)}{2\sqrt{2}m_T bI_0\left(\frac{4}{3}\sqrt{2}m_T b\right)} \tag{12}$$

where $m_T = \sqrt{(h_o P/k_f A)}$ for uniform cross section spines and $m_T = \sqrt{(2h_o/k_f\delta_0)}$ for conical, concave parabolic, and convex parabolic spines and

$$h_o = \frac{1}{\frac{C_{p,a}}{b'_{w,f}h_c} + \frac{y_w}{k_w}} \tag{13}$$

The definition and derivation of h_o can be found in Threlkeld [9].

2.2 Partially Wet Fin Efficiency. As mentioned above, if the dew point temperature is higher than the fin base temperature (T_0) but lower than the fin tip temperature (T_{tip}), the water vapor in moist air condenses onto the fin surface only near the fin base region. There are two regions in a spine: (1) the wet region between the fin base and the saturation point and (2) the dry region between the saturation point and the fin tip, as shown in Figs. 1(*a*), 1(*b*), 1(*c*), and 1(*d*). The fin is in partially wet surface conditions.

For the dry fin portion ($0 \le x < x_{\text{dry}}$), neglecting heat transfer through the fin tip, the differential equation in terms of temperature excess $\theta = T - T_a$ can be developed as follows:

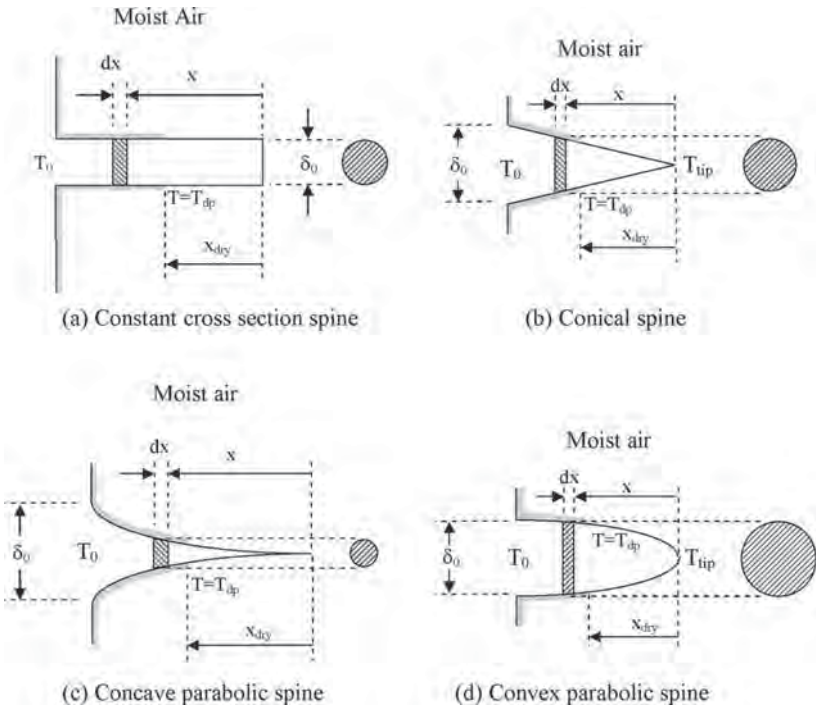

Fig. 1 Four spines in partially wet surface conditions

Downloaded From: http://heattransfer.asmedigitalcollection.asme.org/ on 07/22/2013 Terms of Use: http://asme.org/terms

$$\text{Uniform cross section spine}: \frac{d^2\theta}{dx^2} - m\theta = 0 \tag{14}$$

$$\text{Conical spine}: \frac{d^2\theta}{dx^2} + \frac{2}{x}\frac{d\theta}{dx} - 2m^2\frac{b}{x}\theta = 0 \tag{15}$$

$$\text{Concave spine}: \frac{d^2\theta}{dv^2} + 3\frac{d\theta}{dv} - 2m^2b^2\theta = 0 \tag{16}$$

where $v = \ln x$

$$\text{Convex spine}: \frac{d^2\theta}{dx^2} + \frac{1}{x}\frac{d\theta}{dx} - 2m^2\sqrt{\frac{b}{x}}\theta = 0 \tag{17}$$

For the derivation of general solutions, Eqs. (14)–(17) must be subjected to the following two boundary conditions:

$$\left.\frac{d\theta}{dx}\right|_{x=0} = 0 \tag{18}$$

$$\theta|_{x=x_{\text{dry}}} = \theta_{dp} \tag{19}$$

where $\theta_{dp} = T_{dp} - T_a$

The first boundary condition (Eq. (18)) indicates that the heat transfer rate through the fin tip is zero. This is exactly true for the tiny fin that the fin thickness compared with length is very small. ($\delta_0 \ll b$). The second boundary condition (Eq. (19)) indicates that, at the saturation point ($x = x_{\text{dry}}$), the fin surface temperature is equal to the dew point temperature.

The solutions for Eqs. (14)–(17), with boundary conditions, i.e., Eqs. (18) and (19) are

$$\text{Uniform cross section spine}: \theta_{\text{const,part}} = \frac{\theta_{dp}\cosh mx}{\cosh mx_{\text{dry}}} \tag{20}$$

$$\text{Conical spine}: \theta_{\text{cone,part}} = \theta_{dp}\left(\frac{x}{x_{\text{dry}}}\right)^{-0.5}\frac{I_1(2\sqrt{2}m\sqrt{bx})}{I_1(2\sqrt{2}m\sqrt{bx_{\text{dry}}})} \tag{21}$$

$$\text{Concave spine}: \theta_{\text{ccave,part}} = \theta_{dp}\left(\frac{x}{x_{\text{dry}}}\right)^{-1.5+0.5(9+8m^2b^2)^{0.5}} \tag{22}$$

$$\text{Convex spine}: \theta_{\text{cvex,part}} = \theta_{dp}\frac{I_0\left(\frac{4\sqrt{2}}{3}mb^{0.25}x^{0.75}\right)}{I_0\left(\frac{4\sqrt{2}}{3}mb^{0.25}x_{\text{dry}}^{0.75}\right)} \tag{23}$$

For the wet portion ($x_{\text{dry}} \le x \le b$), the differential heat equations in terms of enthalpy excess ($\gamma = i - i_a$) can be written as follows:

$$\text{Uniform cross section spine}: \frac{d^2\gamma}{dx^2} - m_T\gamma = 0 \tag{24}$$

$$\text{Conical spine}: \frac{d^2\gamma}{dx^2} + \frac{2}{x}\frac{d\gamma}{dx} - 2m_T^2\frac{b}{x}\gamma = 0 \tag{25}$$

$$\text{Concave spine}: \frac{d^2\gamma}{dv^2} + 3\frac{d\gamma}{dv} - 2m_T^2b^2\gamma = 0 \tag{26}$$

$$\text{Convex spine}: \frac{d^2\gamma}{dx^2} + \frac{1}{x}\frac{d\gamma}{dx} - 2m_T^2\sqrt{\frac{b}{x}}\gamma = 0 \tag{27}$$

subject to three boundary conditions:

$$\left.\frac{d\gamma}{dx}\right|_{x=x_{\text{dry}}} = b'_{w,dp}\left.\frac{d\theta}{dx}\right|_{x=x_{\text{dry}}} \tag{28}$$

$$\gamma|_{x=x_{\text{dry}}} = \gamma_{dp} \tag{29}$$

$$\gamma|_{x=b} = \gamma_0 \tag{30}$$

where $\gamma_{dp} = i_{dp} - i_a$ and $\gamma_0 = i_0 - i_a$.

The first boundary condition in Eq. (28) is given by considering the conduction heat transfer from the dry portion to the wet portion. The secondary condition in Eq. (29) is similar to that of Eq. (19). The enthalpy excess of saturated air at the saturation point equals that at the dew point. The last boundary condition in Eq. (30) describes the enthalpy excess at the fin base.

The general solutions of Eqs. (24)–(27) can be shown as follows:

$$\text{Uniform cross section spine}: \gamma_{\text{const,part}} = C_1e^{m_Tx} + C_2e^{-m_Tx} \tag{31}$$

$$\text{Conical spine}: \gamma_{\text{tcone,part}} = x^{-0.5}\left[C_1I_1(2m_T\sqrt{2bx}) + C_2K_1(2m_T\sqrt{2bx})\right] \tag{32}$$

$$\text{Concave spine}: \gamma_{\text{ccave,part}} = C_1x^{-1.5+0.5(9+8m_T^2b^2)^{0.5}} + C_2x^{-1.5-0.5(9+8m_T^2b^2)^{0.5}} \tag{33}$$

$$\text{Convex spine}: \gamma_{\text{cvex,part}} = C_1I_0\left(\frac{4\sqrt{2}}{3}m_Tb^{0.25}x^{0.75}\right) + C_2K_0\left(\frac{4\sqrt{2}}{3}m_Tb^{0.25}x^{0.75}\right) \tag{34}$$

The constants C_1 and C_2 in Eqs. (31)–(34) can be solved by two boundary conditions. There are two methods for finding the solutions. The first method can be performed using Eqs. (29) and (30) and the second method can be done using Eqs. (28) and (30). The fin efficiency can then be obtained. However, fin efficiency is still a function of x_{dry} and it is difficult to substitute the x_{dry} obtained from the remaining boundary condition in the fin efficiency equation. Thus, fin efficiency will be presented in terms of x_{dry}, and x_{dry} can be obtained from the remaining boundary condition.

The first method, with the first set of boundary conditions represented by Eqs. (29) and (30), and Eqs. (31)–(34), can be solved as follows:

Uniform cross section spine:

$$\gamma_{\text{const1,part}} = \frac{\gamma_0e^{m_Tb} - \gamma_{dp}e^{m_Tx_{\text{dry}}}}{e^{2m_Tb} - e^{2m_Tx_{\text{dry}}}}e^{m_Tx} + \frac{\gamma_{dp}e^{(m_Tx_{\text{dry}}+2m_Tb)} - \gamma_0e^{(2m_Tx_{\text{dry}}+m_Tb)}}{e^{2m_Tb} - e^{2m_Tx_{\text{dry}}}}e^{-m_Tx} \tag{35}$$

Conical spine:

$$\gamma_{\text{cone1,part}} = \frac{b^{0.5}\gamma_0K_1(2\sqrt{2}m_T\sqrt{bx_{\text{dry}}}) - x_{\text{dry}}^{0.5}\gamma_{dp}K_1(2\sqrt{2}m_Tb)}{I_1(2\sqrt{2}m_Tb)K_1(2\sqrt{2}m_T\sqrt{bx_{\text{dry}}}) - I_1(2\sqrt{2}m_T\sqrt{bx_{\text{dry}}})K_1(2\sqrt{2}m_Tb)}x^{-0.5}I_1(2\sqrt{2}m_T\sqrt{bx}) + \frac{x_{\text{dry}}^{0.5}\gamma_{dp}I_1(2\sqrt{2}m_Tb) - b^{0.5}\gamma_0I_1(2\sqrt{2}m_T\sqrt{bx_{\text{dry}}})}{I_1(2\sqrt{2}m_Tb)K_1(2\sqrt{2}m_T\sqrt{bx_{\text{dry}}}) - I_1(2\sqrt{2}m_T\sqrt{bx_{\text{dry}}})K_1(2\sqrt{2}m_Tb)}x^{-0.5}K_1(2\sqrt{2}m_T\sqrt{bx}) \tag{36}$$

Downloaded From: http://heattransfer.asmedigitalcollection.asme.org/ on 07/22/2013 Terms of Use: http://asme.org/terms

Concave parabolic spine:

$$\gamma_{\text{ccave1,part}} = \frac{\gamma_0 x_{\text{dry}}^{-1.5-0.5(9+8m_T^2b^2)^{0.5}} - \gamma_{dp} b^{-1.5-0.5(9+8m_T^2b^2)^{0.5}}}{x_{\text{dry}}^{-1.5-0.5(9+8m_T^2b^2)^{0.5}} b^{-1.5+0.5(9+8m_T^2b^2)^{0.5}} - x_{\text{dry}}^{-1.5+0.5(9+8m_T^2b^2)^{0.5}} b^{-1.5-0.5(9+8m_T^2b^2)^{0.5}}} x^{-1.5+0.5(9+8m_T^2b^2)^{0.5}}$$
$$+ \frac{\gamma_{dp} b^{-1.5+0.5(9+8m_T^2b^2)^{0.5}} - \gamma_0 x_{\text{dry}}^{-1.5+0.5(9+8m_T^2b^2)^{0.5}}}{x_{\text{dry}}^{-1.5-0.5(9+8m_T^2b^2)^{0.5}} b^{-1.5+0.5(9+8m_T^2b^2)^{0.5}} - x_{\text{dry}}^{-1.5+0.5(9+8m_T^2b^2)^{0.5}} b^{-1.5-0.5(9+8m_T^2b^2)^{0.5}}} x^{-1.5-0.5(9+8m_T^2b^2)^{0.5}} \tag{37}$$

Convex parabolic spine:

$$\gamma_{\text{cvex1,part}} = \frac{\gamma_0 K_0\left(\frac{4\sqrt{2}}{3} m_T b^{0.25} x_{\text{dry}}^{0.75}\right) - \gamma_{dp} K_0\left(\frac{4\sqrt{2}}{3} m_T b\right)}{I_0\left(\frac{4\sqrt{2}}{3} m_T b\right) K_0\left(\frac{4\sqrt{2}}{3} m_T b^{0.25} x_{\text{dry}}^{0.75}\right) - I_0\left(\frac{4\sqrt{2}}{3} m_T b^{0.25} x_{\text{dry}}^{0.75}\right) K_0\left(\frac{4\sqrt{2}}{3} m_T b\right)} I_0\left(\frac{4\sqrt{2}}{3} m_T b^{0.25} x^{0.75}\right)$$
$$+ \frac{\gamma_{dp} I_0\left(\frac{4\sqrt{2}}{3} m_T b\right) - \gamma_0 I_0\left(\frac{4\sqrt{2}}{3} m_T b^{0.25} x_{\text{dry}}^{0.75}\right)}{I_0\left(\frac{4\sqrt{2}}{3} m_T b\right) K_0\left(\frac{4\sqrt{2}}{3} m_T b^{0.25} x_{\text{dry}}^{0.75}\right) - I_0\left(\frac{4\sqrt{2}}{3} m_T b^{0.25} x_{\text{dry}}^{0.75}\right) K_0\left(\frac{4\sqrt{2}}{3} m_T b\right)} K_0\left(\frac{4\sqrt{2}}{3} m_T b^{0.25} x^{0.75}\right) \tag{38}$$

It must be noted that the subscript of 1 mean the 1st method, and subscript of 2 mean the 2nd method.

Then the fin efficiency can be evaluated by dividing the conduction heat transfer rate through the fin base by the convection heat transfer rate, with the assumption that all fin surface temperatures and fin base temperatures are equal. Then,

$$\eta_{\text{part}} = \frac{-\frac{k_f}{b'_{w,0}} A \frac{d\gamma}{dx}\Big|_{x=b}}{-\frac{h_c}{C_{p,a}} A' \gamma_0} \tag{39}$$

By substituting Eqs. (35)–(38) into Eq. (39), the fin efficiency can be rewritten as follows:

Uniform cross section spine:

$$\eta_{\text{const1,part}} = \frac{\gamma_0 (e^{2m_T x_{\text{dry}}} + e^{2m_T b}) - 2\gamma_{dp} e^{m_T (x_{\text{dry}} + b)}}{m_T b \gamma_0 (e^{2m_T b} - e^{2m_T x_{\text{dry}}})} \tag{40}$$

Conical spine:

$$\eta_{\text{cone1,part}} = \frac{\sqrt{2} b \gamma_0 [K_1(2\sqrt{2} m_T \sqrt{b x_{\text{dry}}}) I_2(2\sqrt{2} m_T b) + I_1(2\sqrt{2} m_T \sqrt{b x_{\text{dry}}}) K_2(2\sqrt{2} m_T b)]}{\mathrm{m}_T b^2 \gamma_0 [I_1(2\sqrt{2} m_T b) K_1(2\sqrt{2} m_T \sqrt{b x_{\text{dry}}}) - I_1(2\sqrt{2} m_T \sqrt{b x_{\text{dry}}}) K_1(2\sqrt{2} m_T b)]}$$
$$- \frac{\sqrt{2} \mathrm{b}^{0.5} x_{\text{dry}}^{0.5} \gamma_{dp} [I_1(2\sqrt{2} m_T b) K_2(2\sqrt{2} m_T b) + K_1(2\sqrt{2} m_T b) I_2(2\sqrt{2} m_T b)]}{\mathrm{m}_T b^2 \gamma_0 [I_1(2\sqrt{2} m_T b) K_1(2\sqrt{2} m_T \sqrt{b x_{\text{dry}}}) - I_1(2\sqrt{2} m_T \sqrt{b x_{\text{dry}}}) K_1(2\sqrt{2} m_T b)]} \tag{41}$$

Concave parabolic spine:

$$\eta_{\text{ccave1,part}} = \frac{1.5\gamma_0 [(-1.5 + 0.5(9 + 8m_T^2 b^2)^{0.5}) x_{\text{dry}}^{-1.5-0.5(9+8m_T^2b^2)^{0.5}} b^{-2.5+0.5(9+8m_T^2b^2)^{0.5}}}{m_T^2 b \gamma_0 \left[x_{\text{dry}}^{-1.5-0.5(9+8m_T^2b^2)^{0.5}} b^{-1.5+0.5(9+8m_T^2b^2)^{0.5}} - x_{\text{dry}}^{-1.5+0.5(9+8m_T^2b^2)^{0.5}} b^{-1.5-0.5(9+8m_T^2b^2)^{0.5}}\right]}$$
$$\times \frac{-(-1.5 - 0.5(9 + 8m_T^2 b^2)^{0.5}) x_{\text{dry}}^{-1.5+0.5(9+8m_T^2b^2)^{0.5}} b^{-2.5-0.5(9+8m_T^2b^2)^{0.5}}] - 1.5\gamma_{dp}(9 + 8m_T^2 b^2)^{0.5} b^{-4}}{m_T^2 b \gamma_0 \left[x_{\text{dry}}^{-1.5-0.5(9+8m_T^2b^2)^{0.5}} b^{-1.5+0.5(9+8m_T^2b^2)^{0.5}} - x_{\text{dry}}^{-1.5+0.5(9+8m_T^2b^2)^{0.5}} b^{-1.5-0.5(9+8m_T^2b^2)^{0.5}}\right]} \tag{42}$$

Convex parabolic spine:

$$\eta_{\text{cvex1,part}} = \frac{0.75\sqrt{2}\gamma_0 \left[K_0\left(\frac{4}{3}\sqrt{2} m_T x_{\text{dry}}^{0.75} b^{0.25}\right) I_1\left(\frac{4}{3}\sqrt{2} m_T b\right) + I_0\left(\frac{4}{3}\sqrt{2} m_T x_{\text{dry}}^{0.75} b^{0.25}\right) K_1\left(\frac{4}{3}\sqrt{2} m_T b\right)\right]}{m_T b \gamma_0 \left[I_0\left(\frac{4}{3}\sqrt{2} m_T b\right) K_0\left(\frac{4}{3}\sqrt{2} m_T x_{\text{dry}}^{0.75} b^{0.25}\right) - I_0\left(\frac{4}{3}\sqrt{2} m_T x_{\text{dry}}^{0.75} b^{0.25}\right) K_0\left(\frac{4}{3}\sqrt{2} m_T b\right)\right]}$$
$$- \frac{0.75\sqrt{2}\gamma_{dp} \left[I_0\left(\frac{4}{3}\sqrt{2} m_T b\right) K_1\left(\frac{4}{3}\sqrt{2} m_T b\right) + K_0\left(\frac{4}{3}\sqrt{2} m_T b\right) I_1\left(\frac{4}{3}\sqrt{2} m_T b\right)\right]}{m_T b \gamma_0 \left[I_0\left(\frac{4}{3}\sqrt{2} m_T b\right) K_0\left(\frac{4}{3}\sqrt{2} m_T x_{\text{dry}}^{0.75} b^{0.25}\right) - I_0\left(\frac{4}{3}\sqrt{2} m_T x_{\text{dry}}^{0.75} b^{0.25}\right) K_0\left(\frac{4}{3}\sqrt{2} m_T b\right)\right]} \tag{43}$$

Downloaded From: http://heattransfer.asmedigitalcollection.asme.org/ on 07/22/2013 Terms of Use: http://asme.org/terms

x_{dry} can be derived from the first boundary condition of Eq. (28). By substituting Eqs. (20)–(23) and (35)–(38) into Eq. (28), the relations can be shown in Eqs. (44)–(47) as follows:

Uniform cross section spine:

$$\frac{2m_T\gamma_0 e^{m_T(x_{\mathrm{dry}}+b)} - m_T\gamma_{dp}(e^{2m_T x_{\mathrm{dry}}} + e^{2m_T b})}{e^{2m_T b} - e^{2m_T x_{\mathrm{dry}}}} = mb'_{w,dp}\theta_{dp}\tanh(mx_{\mathrm{dry}}) \tag{44}$$

Conical spine:

$$\begin{aligned}&\frac{b^{0.5}\gamma_0\left[K_1(2\sqrt{2}m_T\sqrt{bx_{\mathrm{dry}}})I_2(2\sqrt{2}m_T\sqrt{bx_{\mathrm{dry}}}) + I_1(2\sqrt{2}m_T\sqrt{bx_{\mathrm{dry}}})K_2(2\sqrt{2}m_T\sqrt{bx_{\mathrm{dry}}})\right]}{I_1(2\sqrt{2}m_T b)K_1(2\sqrt{2}m_T\sqrt{bx_{\mathrm{dry}}}) - I_1(2\sqrt{2}m_T\sqrt{bx_{\mathrm{dry}}})K_1(2\sqrt{2}m_T b)}\\ &-\frac{x_{\mathrm{dry}}^{0.5}\gamma_{dp}\left[I_1(2\sqrt{2}m_T b)K_2(2\sqrt{2}m_T\sqrt{bx_{\mathrm{dry}}}) + K_1(2\sqrt{2}m_T b)I_2(2\sqrt{2}m_T\sqrt{bx_{\mathrm{dry}}})\right]}{I_1(2\sqrt{2}m_T b)K_1(2\sqrt{2}m_T\sqrt{bx_{\mathrm{dry}}}) - I_1(2\sqrt{2}m_T\sqrt{bx_{\mathrm{dry}}})K_1(2\sqrt{2}m_T b)} = \frac{x_{\mathrm{dry}}b'_{w,dp}\theta_{dp}}{\sqrt{2}m_T\sqrt{b}}\cdot\frac{I_2(2\sqrt{2}m\sqrt{bx_{\mathrm{dry}}})}{I_1(2\sqrt{2}m\sqrt{bx_{\mathrm{dry}}})}\end{aligned} \tag{45}$$

Concave parabolic profile:

$$\begin{aligned}&\frac{\gamma_{dp}[(-1.5-0.5(9+8m_T^2b^2)^{0.5})b^{-1.5+0.5(9+8m_T^2b^2)^{0.5}}x_{\mathrm{dry}}^{-2.5-0.5(9+8m_T^2b^2)^{0.5}}}{x_{\mathrm{dry}}^{-1.5-0.5(9+8m_T^2b^2)^{0.5}}b^{-1.5+0.5(9+8m_T^2b^2)^{0.5}} - x_{\mathrm{dry}}^{-1.5+0.5(9+8m_T^2b^2)^{0.5}}b^{-1.5-0.5(9+8m_T^2b^2)^{0.5}}}\\ &-\frac{(-1.5+0.5(9+8m_T^2b^2)^{0.5})b^{-1.5-0.5(9+8m_T^2b^2)^{0.5}}x_{\mathrm{dry}}^{-2.5+0.5(9+8m_T^2b^2)^{0.5}}] + \gamma_0(9+8m_T^2b^2)^{0.5}x_{\mathrm{dry}}^{-4}}{x_{\mathrm{dry}}^{-1.5-0.5(9+8m_T^2b^2)^{0.5}}b^{-1.5+0.5(9+8m_T^2b^2)^{0.5}} - x_{\mathrm{dry}}^{-1.5+0.5(9+8m_T^2b^2)^{0.5}}b^{-1.5-0.5(9+8m_T^2b^2)^{0.5}}} = b'_{w,dp}\theta_{dp}\frac{-1.5+0.5(9+8m^2b^2)^{0.5}}{x_{\mathrm{dry}}}\end{aligned} \tag{46}$$

Convex parabolic profile:

$$\begin{aligned}&\frac{m_T\gamma_0\left[K_0\left(\frac{4}{3}\sqrt{2}m_T x_{\mathrm{dry}}^{0.75}b^{0.25}\right)I_1\left(\frac{4}{3}\sqrt{2}m_T x_{\mathrm{dry}}^{0.75}b^{0.25}\right) + I_0\left(\frac{4}{3}\sqrt{2}m_T x_{\mathrm{dry}}^{0.75}b^{0.25}\right)K_1\left(\frac{4}{3}\sqrt{2}m_T x_{\mathrm{dry}}^{0.75}b^{0.25}\right)\right]}{I_0\left(\frac{4}{3}\sqrt{2}m_T b\right)K_0\left(\frac{4}{3}\sqrt{2}m_T x_{\mathrm{dry}}^{0.75}b^{0.25}\right) - I_0\left(\frac{4}{3}\sqrt{2}m_T x_{\mathrm{dry}}^{0.75}b^{0.25}\right)K_0\left(\frac{4}{3}\sqrt{2}m_T b\right)}\\ &-\frac{m_T\gamma_{dp}\left[I_0\left(\frac{4}{3}\sqrt{2}m_T b\right)K_1\left(\frac{4}{3}\sqrt{2}m_T x_{\mathrm{dry}}^{0.75}b^{0.25}\right) + K_0\left(\frac{4}{3}\sqrt{2}m_T b\right)I_1\left(\frac{4}{3}\sqrt{2}m_T x_{\mathrm{dry}}^{0.75}b^{0.25}\right)\right]}{I_0\left(\frac{4}{3}\sqrt{2}m_T b\right)K_0\left(\frac{4}{3}\sqrt{2}m_T x_{\mathrm{dry}}^{0.75}b^{0.25}\right) - I_0\left(\frac{4}{3}\sqrt{2}m_T x_{\mathrm{dry}}^{0.75}b^{0.25}\right)K_0\left(\frac{4}{3}\sqrt{2}m_T b\right)} = mb'_{w,dp}\theta_{dp}\frac{I_1\left(\frac{4}{3}\sqrt{2}mx_{\mathrm{dry}}^{0.75}b^{0.25}\right)}{I_0\left(\frac{4}{3}\sqrt{2}mx_{\mathrm{dry}}^{0.75}b^{0.25}\right)}\end{aligned} \tag{47}$$

However, the iterative calculation is needed to solve x_{dry}

The second method, with the other set of boundary conditions represented by Eqs. (28) and (30), and Eqs. (31)–(34), can be solved as follows:

Uniform cross section spine:

$$\gamma_{\mathrm{const2,part}} = \frac{m_T\gamma_0 e^{-m_T(2x_{\mathrm{dry}}+b)} + mb'_{w,dp}\theta_{dp}e^{-m_T(x_{\mathrm{dry}}+2b)}\tanh(mx_{\mathrm{dry}})}{m_T(e^{-2m_T x_{\mathrm{dry}}} + e^{-2m_T b})}e^{m_T x} + \frac{m_T\gamma_0 e^{-m_T b} - mb'_{w,dp}\theta_{dp}e^{-m_T x_{\mathrm{dry}}}\tanh(mx_{\mathrm{dry}})}{m_T(e^{-2m_T x_{\mathrm{dry}}} + e^{-2m_T b})}e^{-m_T x} \tag{48}$$

Conical spine:

$$\begin{aligned}\gamma_{\mathrm{cone2,part}} =& \frac{\sqrt{2}m_T b\gamma_0 I_1(2\sqrt{2}m\sqrt{bx_{\mathrm{dry}}})K_2(2\sqrt{2}m_T\sqrt{bx_{\mathrm{dry}}}) + \sqrt{2}mb^{0.5}x_{\mathrm{dry}}^{0.5}b'_{w,dp}\theta_{dp}K_1(2\sqrt{2}m_T b)I_2(2\sqrt{2}m\sqrt{bx_{\mathrm{dry}}})}{\sqrt{2}m_T b^{0.5}x^{0.5}I_1(2\sqrt{2}m\sqrt{bx_{\mathrm{dry}}})\left[I_1(2\sqrt{2}m_T b)K_2(2\sqrt{2}m_T\sqrt{bx_{\mathrm{dry}}}) + K_1(2\sqrt{2}m_T b)I_2(2\sqrt{2}m_T\sqrt{bx_{\mathrm{dry}}})\right]}I_1(2\sqrt{2}m_T\sqrt{bx})\\ &+\frac{\sqrt{2}m_T b\gamma_0 I_1(2\sqrt{2}m\sqrt{bx_{\mathrm{dry}}})I_2(2\sqrt{2}m_T\sqrt{bx_{\mathrm{dry}}}) - \sqrt{2}mb^{0.5}x_{\mathrm{dry}}^{0.5}b'_{w,dp}\theta_{dp}I_1(2\sqrt{2}m_T b)I_2(2\sqrt{2}m\sqrt{bx_{\mathrm{dry}}})}{\sqrt{2}m_T b^{0.5}x^{0.5}I_1(2\sqrt{2}m\sqrt{bx_{\mathrm{dry}}})\left[I_1(2\sqrt{2}m_T b)K_2(2\sqrt{2}m_T\sqrt{bx_{\mathrm{dry}}}) + K_1(2\sqrt{2}m_T b)I_2(2\sqrt{2}m_T\sqrt{bx_{\mathrm{dry}}})\right]}K_1(2\sqrt{2}m_T\sqrt{bx})\end{aligned} \tag{49}$$

Concave parabolic spine:

$$\gamma_{\mathrm{ccave2,part}} = C_{1,\mathrm{ccave2}}x^{-1.5+0.5(9+8m_T^2b^2)^{0.5}} + \frac{C_{2,\mathrm{ccave2}}}{x^{1.5+0.5(9+8m_T^2b^2)^{0.5}}} \tag{50}$$

where

Downloaded From: http://heattransfer.asmedigitalcollection.asme.org/ on 07/22/2013 Terms of Use: http://asme.org/terms

$$C_{1,\mathrm{ccave2}}=\frac{(-1.5-0.5\sqrt{9+8m_T^2b^2})\gamma_0 x_{\mathrm{dry}}^{-\sqrt{9+8m_T^2b^2}}b^{1.5-0.5\sqrt{9+8m_T^2b^2}}+(1.5-0.5\sqrt{9+8m^2b^2})b'_{w,dp}\theta_{dp}x_{\mathrm{dry}}^{1.5-0.5\sqrt{9+8m_T^2b^2}}b^{-\sqrt{9+8m_T^2b^2}}}{(-1.5-0.5\sqrt{9+8m_T^2b^2})x_{\mathrm{dry}}^{-\sqrt{9+8m_T^2b^2}}+(1.5-0.5\sqrt{9+8m_T^2b^2})b^{-\sqrt{9+8m_T^2b^2}}} \tag{51}$$

$$C_{2,\mathrm{ccave2}}=\frac{(1.5-0.5\sqrt{9+8m_T^2b^2})\gamma_0 b^{1.5-0.5\sqrt{9+8m_T^2b^2}}-(1.5-0.5\sqrt{9+8m^2b^2})b'_{w,dp}\theta_{dp}x_{\mathrm{dry}}^{1.5-0.5\sqrt{9+8m_T^2b^2}}}{(-1.5-0.5\sqrt{9+8m_T^2b^2})x_{\mathrm{dry}}^{-\sqrt{9+8m_T^2b^2}}+(1.5-0.5\sqrt{9+8m_T^2b^2})b^{-\sqrt{9+8m_T^2b^2}}} \tag{52}$$

Convex parabolic:

$$\gamma_{\mathrm{cvex2,part}}=\frac{\gamma_0 I_0\left(\frac{4}{3}\sqrt{2}mb^{0.25}x_{\mathrm{dry}}^{0.75}\right)K_1\left(\frac{4}{3}\sqrt{2}m_Tb^{0.25}x_{\mathrm{dry}}^{0.75}\right)+\frac{m}{m_T}b'_{w,dp}\theta_{dp}K_0\left(\frac{4}{3}\sqrt{2}m_Tb\right)I_1\left(\frac{4}{3}\sqrt{2}mb^{0.25}x_{\mathrm{dry}}^{0.75}\right)}{I_0\left(\frac{4}{3}\sqrt{2}mb^{0.25}x_{\mathrm{dry}}^{0.75}\right)\left[I_0\left(\frac{4}{3}\sqrt{2}m_Tb\right)K_1\left(\frac{4}{3}\sqrt{2}m_Tb^{0.25}x_{\mathrm{dry}}^{0.75}\right)+K_0\left(\frac{4}{3}\sqrt{2}m_Tb\right)I_1\left(\frac{4}{3}\sqrt{2}m_Tb^{0.25}x_{\mathrm{dry}}^{0.75}\right)\right]}I_0\left(\frac{4}{3}\sqrt{2}m_Tb^{0.25}x^{0.75}\right)$$
$$+\frac{\gamma_0 I_0\left(\frac{4}{3}\sqrt{2}mb^{0.25}x_{\mathrm{dry}}^{0.75}\right)I_1\left(\frac{4}{3}\sqrt{2}m_Tb^{0.25}x_{\mathrm{dry}}^{0.75}\right)-\frac{m}{m_T}b'_{w,dp}\theta_{dp}I_0\left(\frac{4}{3}\sqrt{2}m_Tb\right)I_1\left(\frac{4}{3}\sqrt{2}mb^{0.25}x_{\mathrm{dry}}^{0.75}\right)}{I_0\left(\frac{4}{3}\sqrt{2}mb^{0.25}x_{\mathrm{dry}}^{0.75}\right)\left[I_0\left(\frac{4}{3}\sqrt{2}m_Tb\right)K_1\left(\frac{4}{3}\sqrt{2}m_Tb^{0.25}x_{\mathrm{dry}}^{0.75}\right)+K_0\left(\frac{4}{3}\sqrt{2}m_Tb\right)I_1\left(\frac{4}{3}\sqrt{2}m_Tb^{0.25}x_{\mathrm{dry}}^{0.75}\right)\right]}K_0\left(\frac{4}{3}\sqrt{2}m_Tb^{0.25}x^{0.75}\right) \tag{53}$$

Then, the fin efficiency can be evaluated as in Eq. (39) as follows:

Uniform cross sections pine:

$$\eta_{\mathrm{const2,part}}=\frac{m_T\gamma_0(e^{-2m_Tx_{\mathrm{dry}}}-e^{-2m_Tb})+2mb'_{w,dp}\theta_{dp}\tanh(mx_{\mathrm{dry}})e^{-m_T(x_{\mathrm{dry}}+b)}}{m_T^2b\gamma_0(e^{-2m_Tx_{\mathrm{dry}}}+e^{-2m_Tb})} \tag{54}$$

Conical spine:

$$\eta_{\mathrm{cone2,part}}=\frac{\sqrt{2}m_Tb\gamma_0 I_1(2\sqrt{2bx_{\mathrm{dry}}}m)\left[I_2(2\sqrt{2}m_Tb)K_2(2\sqrt{2bx_{\mathrm{dry}}}m_T)-I_2(2\sqrt{2bx_{\mathrm{dry}}}m_T)K_2(2\sqrt{2}m_Tb)\right]}{m_T^2b^2\gamma_0 I_1(2\sqrt{2}m\sqrt{bx_{\mathrm{dry}}})\left[I_1(2\sqrt{2}m_Tb)K_2(2\sqrt{2}m_T\sqrt{bx_{\mathrm{dry}}})+K_1(2\sqrt{2}m_Tb)I_2(2\sqrt{2}m_T\sqrt{bx_{\mathrm{dry}}})\right]}$$
$$+\frac{\sqrt{2}mb^{0.5}x_{\mathrm{dry}}^{0.5}b'_{w,dp}\theta_{dp}I_2(2\sqrt{2bx_{\mathrm{dry}}}m_T)\left[I_1(2\sqrt{2}m_Tb)K_2(2\sqrt{2}m_Tb)+K_1(2\sqrt{2}m_Tb)I_2(2\sqrt{2}m_Tb)\right]}{m_T^2b^2\gamma_0 I_1(2\sqrt{2}m\sqrt{bx_{\mathrm{dry}}})\left[I_1(2\sqrt{2}m_Tb)K_2(2\sqrt{2}m_T\sqrt{bx_{\mathrm{dry}}})+K_1(2\sqrt{2}m_Tb)I_2(2\sqrt{2}m_T\sqrt{bx_{\mathrm{dry}}})\right]} \tag{55}$$

Concave parabolic spine:

$$\eta_{\mathrm{ccave2,part}}=\frac{\sqrt{9+8m_T^2b^2}(4.5-1.5\sqrt{9+8m^2b^2})b'_{w,dp}\theta_{dp}x_{\mathrm{dry}}^{1.5-0.5\sqrt{9+8m_T^2b^2}}b^{-2.5-0.5\sqrt{9+8m_T^2b^2}}+6m_T^2b^2\gamma_0\left(b^{-1-\sqrt{9+8m_T^2b^2}}-x_{\mathrm{dry}}^{-\sqrt{9+8m_T^2b^2}}\right)}{2m_T^2b\gamma_0\left[\left(-1.5-0.5\sqrt{9+8m_T^2b^2}\right)x_{\mathrm{dry}}^{-\sqrt{9+8m_T^2b^2}}+\left(1.5-0.5\sqrt{9+8m_T^2b^2}\right)b^{-\sqrt{9+8m_T^2b^2}}\right]} \tag{56}$$

Convex profile:

$$\eta_{\mathrm{cvex2,part}}=\frac{3\sqrt{2}\gamma_0 I_0\left(\frac{4}{3}\sqrt{2}mx_{\mathrm{dry}}^{0.75}b^{0.25}\right)\left[I_1\left(\frac{4}{3}\sqrt{2}m_Tb\right)K_1\left(\frac{4}{3}\sqrt{2}m_Tx_{\mathrm{dry}}^{0.75}b^{0.25}\right)-I_1\left(\frac{4}{3}\sqrt{2}m_Tx_{\mathrm{dry}}^{0.75}b^{0.25}\right)K_1\left(\frac{4}{3}\sqrt{2}m_Tb\right)\right]}{4m_Tb\gamma_0 I_0\left(\frac{4}{3}\sqrt{2}mb^{0.25}x_{\mathrm{dry}}^{0.75}\right)\left[I_0\left(\frac{4}{3}\sqrt{2}m_Tb\right)K_1\left(\frac{4}{3}\sqrt{2}m_Tb^{0.25}x_{\mathrm{dry}}^{0.75}\right)+K_0\left(\frac{4}{3}\sqrt{2}m_Tb\right)I_1\left(\frac{4}{3}\sqrt{2}m_Tb^{0.25}x_{\mathrm{dry}}^{0.75}\right)\right]}$$
$$+\frac{3\sqrt{2}b'_{w,dp}\theta_{dp}\frac{m}{m_T}\left[I_0\left(\frac{4}{3}\sqrt{2}m_Tb\right)K_1\left(\frac{4}{3}\sqrt{2}m_Tb\right)I_1\left(\frac{4}{3}\sqrt{2}mx_{\mathrm{dry}}^{0.75}b^{0.25}\right)+I_1\left(\frac{4}{3}\sqrt{2}m_Tb\right)K_0\left(\frac{4}{3}\sqrt{2}m_Tb\right)I_1\left(\frac{4}{3}\sqrt{2}mx_{\mathrm{dry}}^{0.75}b^{0.25}\right)\right]}{4m_Tb\gamma_0 I_0\left(\frac{4}{3}\sqrt{2}mb^{0.25}x_{\mathrm{dry}}^{0.75}\right)\left[I_0\left(\frac{4}{3}\sqrt{2}m_Tb\right)K_1\left(\frac{4}{3}\sqrt{2}m_Tb^{0.25}x_{\mathrm{dry}}^{0.75}\right)+K_0\left(\frac{4}{3}\sqrt{2}m_Tb\right)I_1\left(\frac{4}{3}\sqrt{2}m_Tb^{0.25}x_{\mathrm{dry}}^{0.75}\right)\right]} \tag{57}$$

To evaluate x_{dry}, the second boundary condition in Eq. (29) is continued. Then, $\gamma|_{x=x_{\mathrm{dry}}}$ can be calculated from Eqs. (48)–(50) and (53), and γ_{dp} is known. Using the iteration procedure, x_{dry} can then be calculated.

3 Results and Discussion

Like the results of Kern and Kraus [2] in fully dry conditions, the four very faint lines of η plotted against m_Tb are shown in Fig. 2.

Downloaded From: http://heattransfer.asmedigitalcollection.asme.org/ on 07/22/2013 Terms of Use: http://asme.org/terms

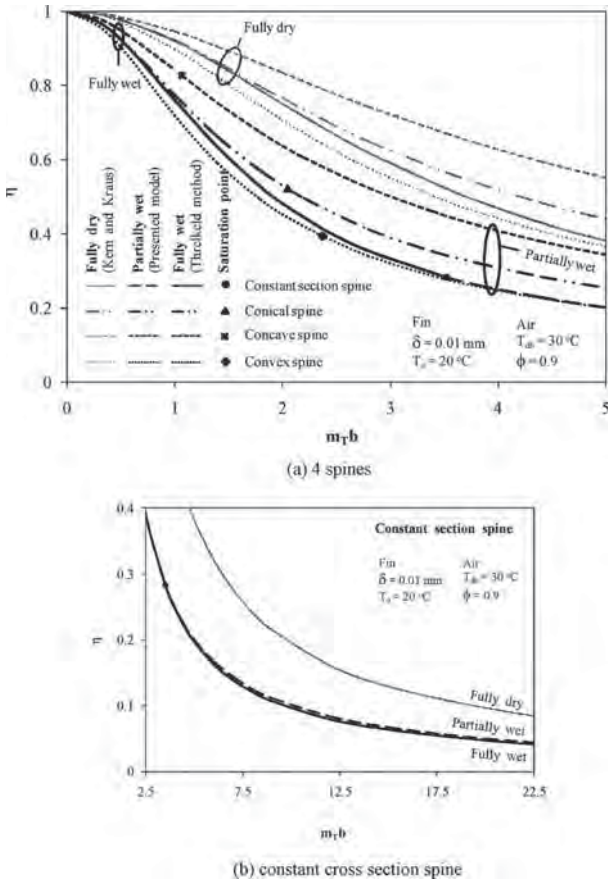

Fig. 2 Fin efficiency plotted against $m_T b$

It can be observed that the fin efficiencies decrease with increases of mb. At the same mb, the fin efficiency can be sorted from highest value to lowest value in the following order: concave parabolic spine, conical spine, uniform cross section spine, and convex parabolic spine. For fully wet conditions, as shown in Eqs. (6), (8), (10), and (12), the fin efficiencies are dependent only on $m_T b$. Figure 2 shows that the trends of the results are similar to those for dry conditions, but all values are lower. For partially wet surface conditions, as shown in Fig. 2, the fin efficiencies determined by Eqs. (40)–(43) and those determined by Eqs. (54)–(57) are not different. The fin efficiencies are not dependent only on $m_T b$, but they are more complicated than those in dry and wet conditions. Figure 2 shows the partially wet fin efficiencies plotted against $m_T b$ at 90% RH. Accordingly, at low $m_T b$, it can be found that the four gray lines representing the partially wet fin efficiencies have vanished. This is because the fins are in fully wet surface conditions. Moreover, one can see that the partially wet fin efficiencies are between the dry and wet fin efficiencies. The partially wet fin efficiencies are proximate to the fully wet fin efficiency at high RH, and are approximate to equal the fully dry fin efficiency at low RH. The partially wet fin efficiency still decreases with the increases of $m_T b$, and the order of the sorted results is the same as the order in dry and wet conditions. It must be noted that the m_T for the uniform cross section spine is $\sqrt{(h_o P/k_f A)}$ but m_T for the other spines is $\sqrt{(2h_o/k_f \delta_0)}$.

Figure 3 shows the temperature distribution along the distance from the fin base. According to the trend line, the slope at the fin base and the position of the saturation point can be evaluated for heat transfer performance. In the same conditions, the steep line at the fin base promotes good heat transfer. This can be described by the conductive heat transfer rate at the fin base as shown in Eq. (39). Moreover, more condensation, which promotes the heat transfer rate, takes place when the saturation point nears the fin tip. However, one can see that the trend lines in the dry portion are opposite those in the wet portion. Essentially, with the exception of the uniform cross section spine, it can be found that the sorting order of slope in Fig. 3 is opposite the sorting order of fin efficiency in Fig. 2. This can be described with the actual and ideal heat transfer rates as plotted in Fig. 4. From Fig. 4, with the exception of the uniform cross section spine, the order of actual and ideal heat transfer rates calculated from the part of the fraction over and below the line of Eq. (39) is convex parabolic spine, conical spine, and concave parabolic spine. The actual heat transfer rate can be described by the ordering in surface area because more surface area produces a higher heat transfer rate. However, for considering fin efficiency, the actual heat transfer rate must be

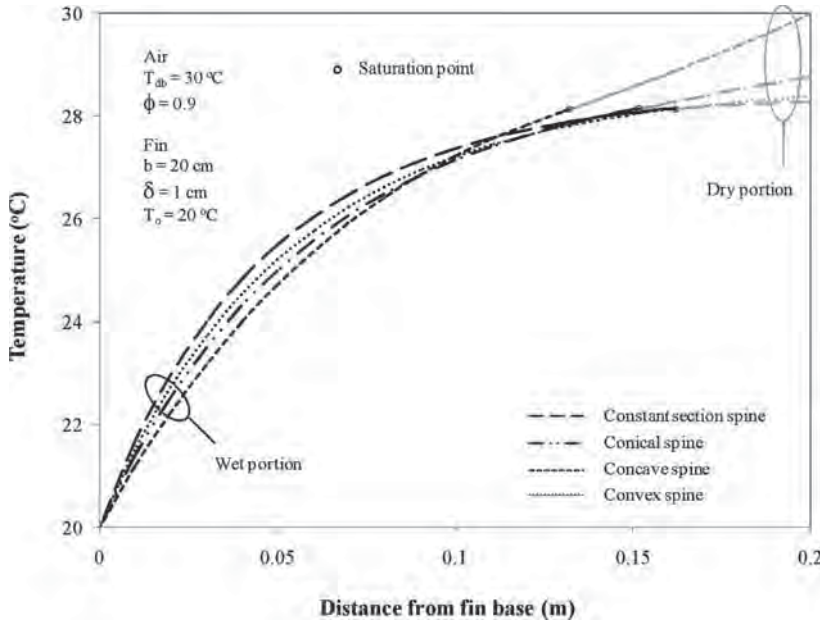

Fig. 3 Temperature distribution for four spines

Downloaded From: http://heattransfer.asmedigitalcollection.asme.org/ on 07/22/2013 Terms of Use: http://asme.org/terms

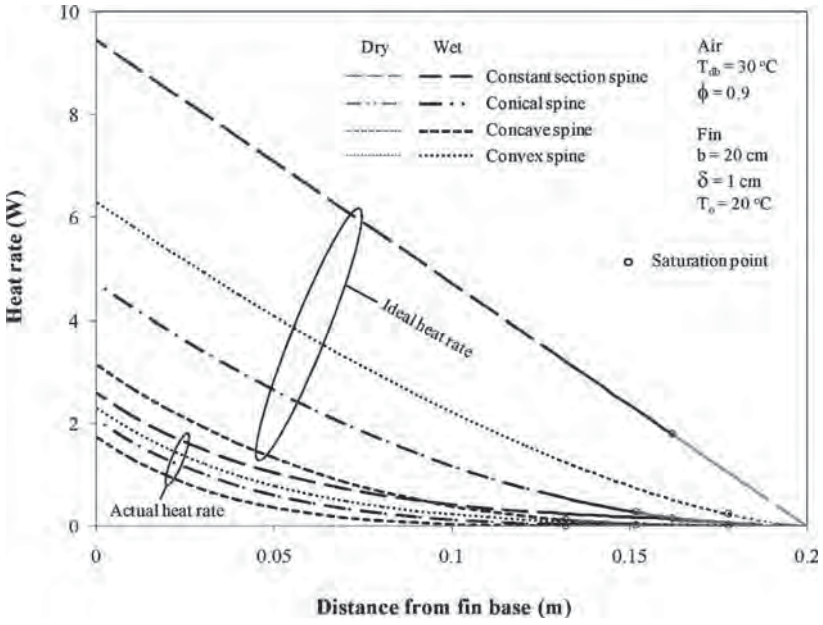

Fig. 4 Heat transfer through four spines

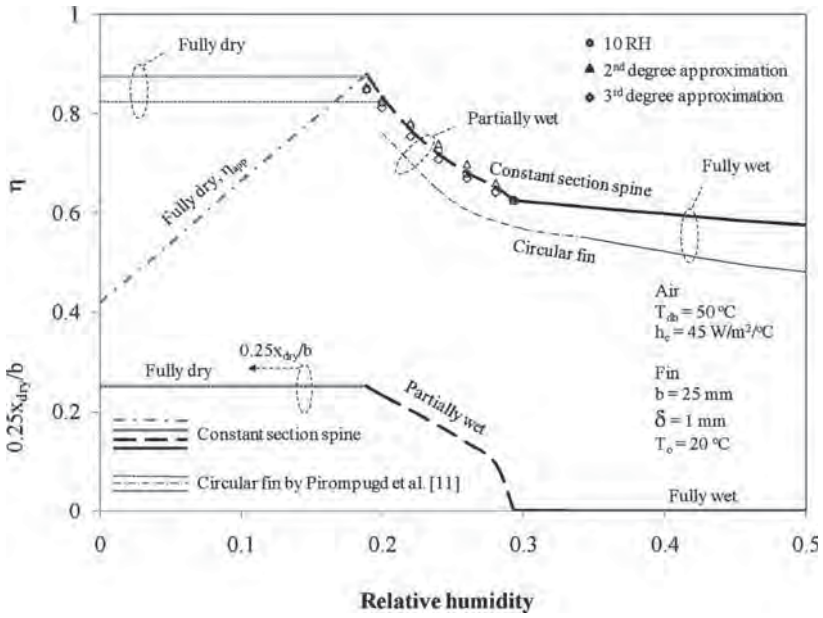

Fig. 5 Constant section spine efficiency plotted against relative humidity

compared with the ideal heat transfer rate. Figure 4 demonstrates that, with the exception of the uniform cross section spine, both the actual and ideal heat transfer rates of the convex parabolic spine are highest. Moreover, it can be observed that the increase in actual heat transfer rate is lower than the increase in ideal heat transfer rate. Thus, the fin efficiency of convex parabolic spine is lowest. This is the effect of the ratio of cross section area to surface area. This effect is not distinct in longitudinal fins.

Figures 5–8 show η and $0.25(x_{dry}/b)$ plotted against the relative humidity. The lines for partially wet and fully wet conditions are continuous, but there is a break between the lines of fully dry and partially wet conditions. The η_{app} for fully dry conditions calculated by dividing the actual heat transfer rate by the ideal heat transfer rate in fully wet conditions $(\eta = (q_{actual,dry}/q_{ideal,wet}))$ is presented in Figs. 5–8. For partially wet and fully wet conditions, the fin efficiencies decrease with increased relative humidity because the increase in the ideal or maximum heat transfer rate is higher than the increase in the actual heat transfer rate. These results are consistent with the results for a circular fin in partially wet and fully wet conditions as determined by Pirompugd et al. [11]. In 1999, Rosario and Rahman [13] presented an equation to determine the partially wet fin efficiency for a circular fin. That equation is a 2nd degree polynomial and is a function of dry portion length per total length of fin. Pirompugd and Wongwises [12] showed that, for longitudinal fins, the 1st or 2nd degree polynomial approximations cannot precisely predict partially wet fin efficiency. They derived the approximation by using ten times the relative humidity. Accordingly, the approximation for the spine in partially wet conditions is presented as follows:

$$\eta_{part} = \left(\frac{x_{dry}}{b}\right)^{10\times RH}\eta_{dry} + \left[1 - \left(\frac{x_{dry}}{b}\right)^{10\times RH}\right]\eta_{wet} \qquad (58)$$

Downloaded From: http://heattransfer.asmedigitalcollection.asme.org/ on 07/22/2013 Terms of Use: http://asme.org/terms

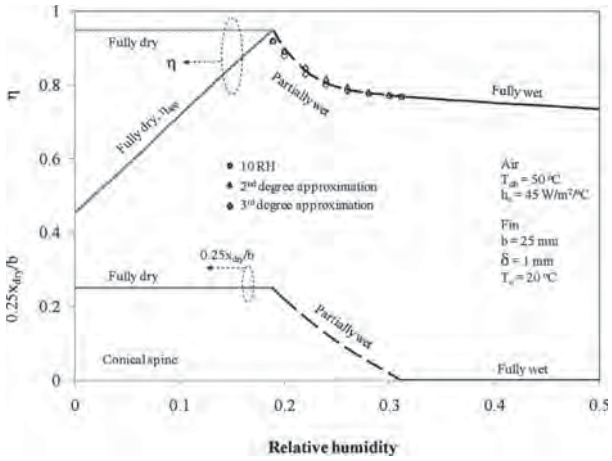

Fig. 6 Conical spine efficiency plotted against relative humidity

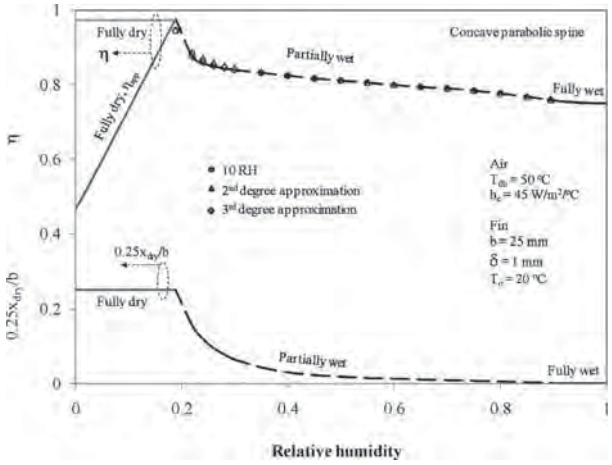

Fig. 7 Concave parabolic spine efficiency plotted against relative humidity

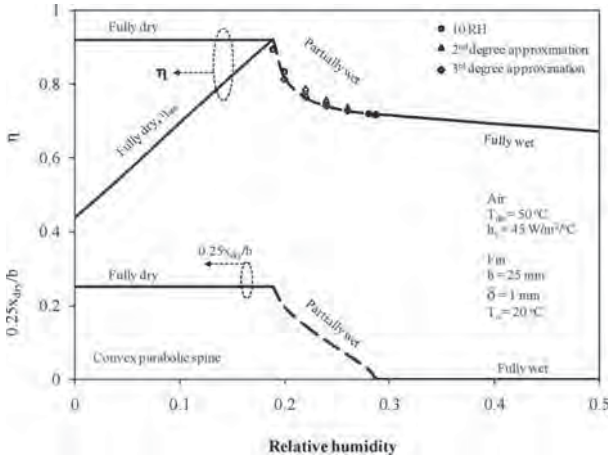

Fig. 8 Convex parabolic spine efficiency plotted against relative humidity

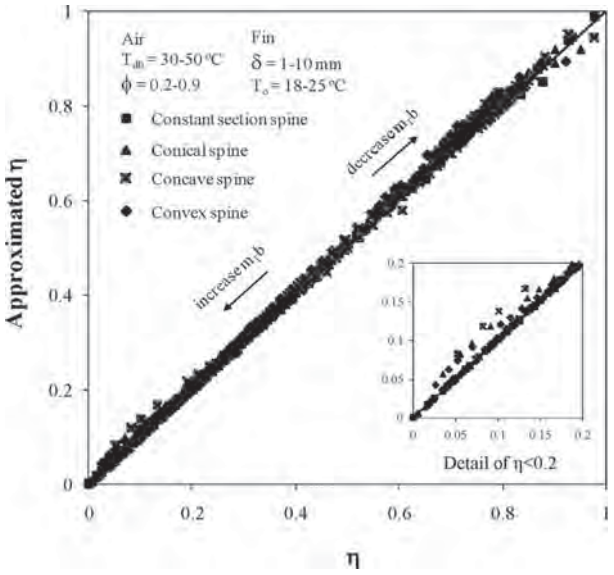

Fig. 9 Comparison of approximate η and η at many $M_T b$

As seen in Figs. 5–8, the results from Eq. (58) are consistent with the theoretical data. Moreover, Fig. 9 shows a comparison with the other conditions. According to the figure, at $\eta \geq 0.2$, almost all the measured data fall within $\pm$ 10%. However, error over $\pm$50% may occur when $\eta \leq 0.2$. Therefore, Eq. (58) can be applied only to extended surfaces of $\eta \geq 0.2$. The methods for evaluating x_{dry} have been described in the first method and second method for partially wet surface conditions. However, Eq. (58) is not necessary because this study has proposed a theoretical partially wet fin efficiency.

4 Conclusions

(1) The partially wet fin efficiencies for spines of uniform cross section area, conical, concave parabolic, and convex parabolic profiles are presented. Equations for evaluating the length of the dry portion are also proposed.
(2) The order of fin efficiency can be sorted, from highest to lowest, as follows: (1) concave parabolic spine, (2) conical spine, (3) uniform cross section spine, and (4) convex parabolic spine.
(3) The order of fin heat transfer rate can be sorted, from highest to lowest, as follows: (1) uniform cross section spine, (2) convex parabolic spine, (3) conical spine, (4) concave parabolic spine.
(4) With an increase in relative humidity, partially wet fin efficiencies decrease rapidly, but the decrease of fully wet fin efficiencies is slower. Contrarily, the dry fin efficiencies are independent of the relative humidity.
(5) Conveniently, the equation for predicting partially wet fin efficiency from fully wet and fully dry fin efficiencies is also presented. The methods for obtaining the length of the dry portion are also described.

Acknowledgment

The authors are indebted to the Thailand Research Fund, the Office of the Higher Education Commission, Burapha University and the National Research University Project for supporting this study.

Nomenclature

A = cross section area of fin, m^2
A' = fin surface area, m^2

Downloaded From: http://heattransfer.asmedigitalcollection.asme.org/ on 07/22/2013 Terms of Use: http://asme.org/terms

b = distance from fin tip to fin base, m
$b'_{w,dp}$ = slope of the saturated air enthalpy curved at the dew point temperature, J kg^{-1} K^{-1}
$b'_{w,f}$ = slope of the saturated air enthalpy curved at the mean fin surface temperature, J kg^{-1} K^{-1}
$b'_{w,o}$ = slope of the saturated air enthalpy curved at the fin base temperature, J kg^{-1} K^{-1}
$C_{p,a}$ = air specific heat capacity, J kg^{-1} °C^{-1}
h_c = convection heat transfer coefficient, kg m^{-2} s^{-1}
i = saturated air enthalpy at fin surface, J kg^{-1}
i_a = air enthalpy at free stream, J kg^{-1}
I_0 = modified Bessel function solution of the first kind, order 0
I_1 = modified Bessel function solution of the first kind, order 1
I_2 = modified Bessel function solution of the first kind, order 2
k_f = thermal conductivity of the fin, W m^{-1} K^{-1}
k_w = thermal conductivity of the water film, W m^{-1} K^{-1}
K_0 = modified Bessel function solution of the second kind, order 0
K_1 = modified Bessel function solution of the second kind, order 1
K_2 = modified Bessel function solution of the second kind, order 2
m = $\sqrt{(h_c P/k_f A)}$ for uniform cross section spines, and $m = \sqrt{(2h_c/k_f\delta_0)}$ for conical, concave parabolic, and convex parabolic spines.
m_T = $\sqrt{(h_o P/k_f A)}$ for uniform cross section spines, and $m = \sqrt{(2h_o/k_f\delta_0)}$ for conical, concave parabolic, and convex parabolic spines.
P = the fin perimeter, m
RH = relative humidity
T = air temperature, °C
x = distance from fin tip, m
x_{dry} = distance from fin tip to saturation point, m
y_w = thickness of the water film, m
δ_0 = thickness of fin base, m
γ = air enthalpy difference between fin surface and air, J kg^{-1}
η = fin efficiency
θ = air temperature difference, °C

Appendix

The section shows the 1st method for derivation of efficiency of partially wet conical fin. From Fig. 10, the fin is in the partially wet condition. The fin base is cold and the surface temperature is generally lower than the dew point temperature. Then, the condensation of water vapor in the moist air takes place. There is simultaneous heat and mass transfer from moist air to the fin surface and both sensible and latent heat transfer takes place. The surface temperature increases with a decrease of x until it is equal to the dew point temperature. After this point, the surface temperature is higher than the dew point temperature. Then, there is only sensible heat transfer takes place in this region.

For the dry portion:

By Kern and Kraus [2], the differential equation for the dry portion can be written as

$$x^2\frac{d^2\theta}{dx^2} + 2x\frac{d\theta}{dx} - M^2x\theta = 0 \tag{A1}$$

with the boundary condition of

$$\text{at } x = 0, \frac{d\theta}{dx} = 0 \tag{A2}$$

$$\text{at } x = x_{\text{dry}}, \theta = \theta_{dp} \tag{A3}$$

where $M = \sqrt{2m^2b}$.

By Frobenius method, the solution of differential equation can be found in many mathematical handbook and can be shown as

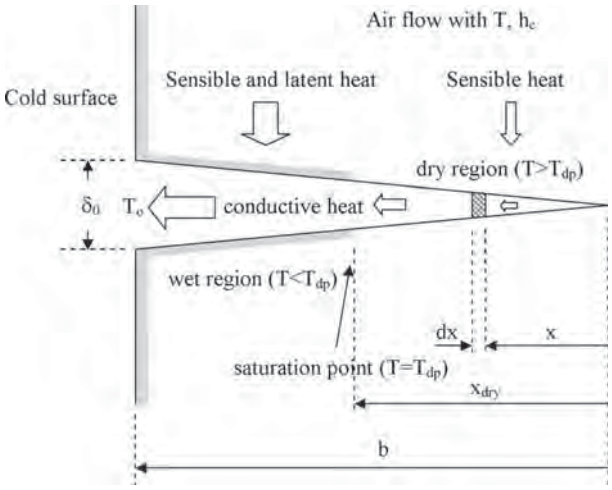

Fig. 10 Heat transfer along the conical spine

$$\theta = x^{-0.5}[C_1I_1(2M\sqrt{x}) + C_2K_1(2M\sqrt{x})] \tag{A4}$$

By the first boundary condition of Eq. (A2), $C_2 = 0$ and by the other boundary condition of Eq. (A3), the constant of C_1 can be obtained as

$$\theta_{dp} = x_{\text{dry}}^{-0.5}C_1I_1(2M\sqrt{x_{\text{dry}}}) \tag{A5}$$

$$C_1 = \frac{\theta_{dp}}{x_{\text{dry}}^{-0.5}I_1(2M\sqrt{x_{\text{dry}}})} \tag{A6}$$

$$\theta = \theta_{dp}\left(\frac{x}{x_{\text{dry}}}\right)^{-0.5}\frac{I_1(2M\sqrt{x})}{I_1(2M\sqrt{x_{\text{dry}}})} \tag{A7}$$

For the wet portion:

By method of Threlkeld [9], the differential equation for the wet portion can be written as

$$x^2\frac{d^2\gamma}{dx^2} + 2x\frac{d\gamma}{dx} - M_T^2x\gamma = 0 \tag{A8}$$

with the boundary condition of

$$\text{at } x = x_{\text{dry}}, \gamma = \gamma_{dp} \tag{A9}$$

$$\text{at } x = b, \gamma = \gamma_0 \tag{A10}$$

where $M_T = \sqrt{2m_T^2b}$.

By Frobenius method, the solution of differential equation can be found in many mathematical handbook and can be shown as

$$\gamma = x^{-0.5}[C_1I_1(2M_T\sqrt{x}) + C_2K_1(2M_T\sqrt{x})] \tag{A11}$$

By substituting Eqs. (A9) and (A10) into Eq. (A11),

$$\gamma_{dp} = x_{\text{dry}}^{-0.5}[C_1I_1(2M_T\sqrt{x_{\text{dry}}}) + C_2K_1(2M_T\sqrt{x_{\text{dry}}})] \tag{A12}$$

$$\gamma_0 = b^{0.5}[C_1I_1(2M_T\sqrt{b}) + C_2K_1(2M_T\sqrt{b})] \tag{A13}$$

Then, C_1 and C_2 can be obtained as

$$C_1 = \frac{b^{0.5}\gamma_0K_1(2M_T\sqrt{x_{\text{dry}}}) - x_{\text{dry}}^{0.5}\gamma_{dp}K_1(2M_T\sqrt{b})}{I_1(2M_T\sqrt{b})K_1(2M_T\sqrt{x_{\text{dry}}}) - I_1(2M_T\sqrt{x_{\text{dry}}})K_1(2M_T\sqrt{b})} \tag{A14}$$

$$C_2 = \frac{x_{\text{dry}}^{0.5}\gamma_{dp}I_1(2M_T\sqrt{b}) - b^{0.5}\gamma_0I_1(2M_T\sqrt{x_{\text{dry}}})}{I_1(2M_T\sqrt{b})K_1(2M_T\sqrt{x_{\text{dry}}}) - I_1(2M_T\sqrt{x_{\text{dry}}})K_1(2M_T\sqrt{b})} \tag{A15}$$

Then, Eq. (A11) can be rewritten as shown in Eq. (36) or

Downloaded From: http://heattransfer.asmedigitalcollection.asme.org/ on 07/22/2013 Terms of Use: http://asme.org/terms

$$\gamma = \frac{b^{0.5}\gamma_0 K_1(2\sqrt{2}m_T\sqrt{bx_{\text{dry}}}) - x_{\text{dry}}^{0.5}\gamma_{dp}K_1(2\sqrt{2}m_T b)}{I_1(2\sqrt{2}m_T b)K_1(2\sqrt{2}m_T\sqrt{bx_{\text{dry}}}) - I_1(2\sqrt{2}m_T\sqrt{bx_{\text{dry}}})K_1(2\sqrt{2}m_T b)} x^{-0.5} I_1(2\sqrt{2}m_T\sqrt{bx}) + \frac{x_{\text{dry}}^{0.5}\gamma_{dp}I_1(2\sqrt{2}m_T b) - b^{0.5}\gamma_0 I_1(2\sqrt{2}m_T\sqrt{bx_{\text{dry}}})}{I_1(2\sqrt{2}m_T b)K_1(2\sqrt{2}m_T\sqrt{bx_{\text{dry}}}) - I_1(2\sqrt{2}m_T\sqrt{bx_{\text{dry}}})K_1(2\sqrt{2}m_T b)} x^{-0.5} K_1(2\sqrt{2}m_T\sqrt{bx}) \tag{A16}$$

For the heat transfer rate and fin efficiency:

When C_1 and C_2 are obtained, the heat transfer rate can be evaluate by the conductive heat transfer through the fin base and can be shown as

$$q_0 = \frac{k\pi\delta_0^2}{4b'_{w,o}}\left.\frac{d\gamma}{dx}\right|_{x=b} \tag{A17}$$

For differentiating $d\gamma/dx$, the by-pass technique is applied as

$$q_0 = \frac{k\pi\delta_0^2}{4b'_{w,o}}\left.\frac{d\gamma}{du}\frac{du}{dx}\right|_{x=b} \tag{A18}$$

where $u = 2M_T\sqrt{x}$

Then,

$$q_0 = \frac{k\pi\delta_0^2}{4b'_{w,o}}\frac{M_T}{b}[C_1 I_2(2M_T\sqrt{b}) - C_2 K_2(2M_T\sqrt{b})] \tag{A19}$$

The ideal heat transfer rate with assumption of entire fin surface temperature equal to fin base temperature can be written as

$$q_{\text{ideal}} = \frac{h_o}{C_{p,a}}\frac{\pi}{2}\delta_0 b\gamma_0 \tag{A20}$$

Then, the fin efficiency can be shown as Eq. (41) or

$$\eta = \frac{q_{\text{actual}}(\text{or } q_0)}{q_{\text{ideal}}} \tag{A21}$$

$$\eta = \frac{k\pi\delta_0^2}{4b'_{w,o}}\frac{M_T}{b}\frac{2C_{p,a}}{h_o\pi\delta_0 b\gamma_0}[C_1 I_2(2M_T\sqrt{b}) - C_2 K_2(2M_T\sqrt{b})] \tag{A22}$$

$$\eta = \frac{\sqrt{2}b\gamma_0[K_1(2\sqrt{2}m_T\sqrt{bx_{\text{dry}}})I_2(2\sqrt{2}m_T b) + I_1(2\sqrt{2}m_T\sqrt{bx_{\text{dry}}})K_2(2\sqrt{2}m_T b)]}{m_T b^2\gamma_0[I_1(2\sqrt{2}m_T b)K_1(2\sqrt{2}m_T\sqrt{bx_{\text{dry}}}) - I_1(2\sqrt{2}m_T\sqrt{bx_{\text{dry}}})K_1(2\sqrt{2}m_T b)]} - \frac{\sqrt{2}b^{0.5}x_{\text{dry}}^{0.5}\gamma_{dp}[I_1(2\sqrt{2}m_T b)K_2(2\sqrt{2}m_T b) + K_1(2\sqrt{2}m_T b)I_2(2\sqrt{2}m_T b)]}{m_T b^2\gamma_0[I_1(2\sqrt{2}m_T b)K_1(2\sqrt{2}m_T\sqrt{bx_{\text{dry}}}) - I_1(2\sqrt{2}m_T\sqrt{bx_{\text{dry}}})K_1(2\sqrt{2}m_T b)]} \tag{A23}$$

References

[1] Schmidt, T. E., 1949, "Heat Transfer Calculations for Extended Surfaces," Refrig. Eng., **57**, pp. 351–357.

[2] Kern, D. Q., and Kraus, A. D., 1972, *Extended Surface Heat Transfer*, McGraw-Hill, New-York.

[3] Arslanturk, C., 2005, "A Decomposition Method for Fin Efficiency of Convective Straight Fins With Temperature-Dependent Thermal Conductivity," Int. J. Heat Mass Transfer, **32**, pp. 831–841.

[4] Heggs, P. J., and Somasundram, I.M., 2007, "Fin Performance Ratios Greater Than Unity: Not Just a Theoretical Aspiration," Appl. Therm. Eng., **27**, pp. 951–961.

[5] Joneidi, A. A., Ganji, D. D., and Babaelahi, M., 2009, "Differential Transformation Method to Determine Fin Efficiency of Convective Straight Fins With Temperature Dependent Thermal Conductivity," Int. Commun. Heat Mass Transfer, **36**, pp. 757–762.

[6] Kulkarni, D. B., and Joglekar, M. M., 2009, "Residue Minimization Technique to Analyze the Efficiency of Convective Straight Fins Having Temperature-Dependent Thermal Conductivity," Appl. Math. Comput., **215**, pp. 2184–2191.

[7] Sharqawy, M. H., Moinuddin, A., and Zubair, S. M., 2012, "Heat and Mass Transfer From Annular Fins of Different Cross-Sectional Area. Part I. Temperature Distribution and Fin Efficiency," Int. J. Refrig., **35**, pp. 365–376.

[8] Cortes, C., Diez, L. I., and Campo, A., 2008, "Efficiency of Composite Fins of Variable Thickness," Int. J. Heat Mass Transfer **51**, pp. 2153–2166.

[9] Threlkeld, J. L., 1970, *Thermal Environmental Engineering*, Prentice-Hall, Englewood Cliffs, NJ.

[10] Liang, S. Y., Wong, T. N., and Nathan, G. K., 2000, "Comparison of One-Dimensional and Two-Dimensional Models for Wet-Surface Fin Efficiency of a Plate-Fin-Tube Heat Exchanger," Appl. Therm. Eng., **20**, pp. 941–962.

[11] Pirompugd, W., Wang, C. C., and Wongwises, S., 2007, "Finite Circular Fin Method for Heat and Mass Transfer Characteristics for Plain Fin-and-Tube Heat Exchangers Under Fully and Partially Wet Surface Conditions," Int. J. Heat Mass Transfer, **50**(3–4), pp. 552–565.

[12] Pirompugd, W., and Wongwises, S., 2013, "Partially Wet Fin Efficiency for Longitudinal Fin of Rectangular, Triangular, Concave, and Convex Profiles," Journal of Franklin Institute, http://dx.doi.org/10.1016/j.jfranklin.2013.02.019

[13] Rosario, L., and Rahman, M. M., 1999, "Analysis of Heat Transfer in a Partially Wet Radial Fin Assembly During Dehumidification," Int. J. Heat Fluid Flow, **20**, pp. 642–648.

Downloaded From: http://heattransfer.asmedigitalcollection.asme.org/ on 07/22/2013 Terms of Use: http://asme.org/terms

Springer

KSME

Journal of Mechanical Science and Technology 27 (7) (2013) 2043~2052
www.springerlink.com/content/1738-494x
DOI 10.1007/s12206-013-0519-7

Parametric study and optimization of a food can corrugation design using a response surface method †

Pattaramon Jongpradist*, Rattharong Rojbunsongsri, Thoatsanope Kamnerdtong and Somchai Wongwises

Department of Mechanical Engineering, Faculty of Engineering, King Mongkut's University of Technology Thonburi, Bangkok, 10140, Thailand

(Manuscript Received March 2, 2012; Revised December 4, 2012; Accepted January 24, 2013)

Abstract

This paper presents the parametric design and functional optimization of a thin-walled food container with a corrugated surface. The configuration of the can corrugation should be designed to minimize the use of raw material subject to the constraints of the targeted structural performance. In the present study, the failure behaviors and the buckling strengths of a commercial food can under paneling pressure and axial loading are investigated with a series of experiments and finite element analyses. Full factorial design is implemented to study the effects of the geometric parameters of the corrugation (e.g., depth, radius, spacing and number of beadings) on its strength. Parameter optimization using a rotatable central composite design is employed to identify an optimal corrugation design by approximating the response surfaces of the can strength in terms of the significant design variables. The obtained surfaces are derived through the analysis of variance, and the suitability of the response is justified. A light- weight can body is then achieved by reduction of the can body thickness according to the required strength characteristics. Finite element analysis of the optimal model is also performed to confirm the predicted results. By using the proposed procedure, the can-body weight can be reduced by up to 12% compared with the original design.

Keywords: Buckling analysis; Corrugation design; Finite element analysis; Response surface method; Structural optimization

1. Introduction

The annual production of metal food and beverage containers in the United States has recently reached 100 billion cans per year [1]. Because of this large production volume, the can industry is actively pursuing new technologies to reduce costs. An appropriate container design is expected to minimize the can thickness and avoid compromising the structural performance requirements under the applicable manufacturing and transportation loads.

The three main loading conditions applied to the cans during the manufacturing processes are as follows: the vacuum pressure in the packaging procedure, the internal pressure during sterilization, and the compressive axial load during transportation and stacking. The can body of a cylindrical-shell shape possesses a high axial loading resistance but only a moderate resistance against paneling and internal pressure. To increase the can strength under a high out-of-plane pressure, most can structures are designed with a corrugated surface. However, the corrugation decreases the axial load resistance. Failure of the can structures from paneling pressure and axial load occur mostly due to shell instability. Calculations of the loading capability and the post-buckling behaviors of the shell are complicated due to the existence of several bifurcation points [2-4]. The analytical and the experimental results often vary significantly (e.g., Refs. [5, 6]) because the deformation behaviors depend on the imperfections of the geometry and the material properties [7].

Research on the container design using various tools has focused on analyses of the containers in use for different loading conditions. Sodiek and Sauer [8] studied the mechanical behaviors of food cans during the sterilization process and proposed a method for prediction of the loading capacity. Siad [9] suggested analytical formulae to predict the buckling of thin-walled orthotropic cylindrical shells under a uniform external pressure. The results were shown to be in agreement with experiments performed by Ref. [10]. Finite element analysis (FEA) has been employed to study the behaviors of food containers subject to different types of loading [11-13]. Certain optimization techniques for the lightest container design have also been widely proposed [14-16]. Yamazaki et al. [17] and Han et al. [18] studied the shape of the end of the can to minimize the weight of a beverage bottle. Ugail [19] demonstrated method for design of a light-weight food container shape with a required volume. Han et al. [20] applied a multi-objective optimization approach to obtain the proper rib design for a screw top bottle with a temperate touch surface for vending of

*Corresponding author. Tel.: +66 24709123, Fax.: +66 24709111
E-mail address: pattaramon.tan@kmutt.ac.th
† Recommended by Associate Editor Gang-Won Jang
© KSME & Springer 2013

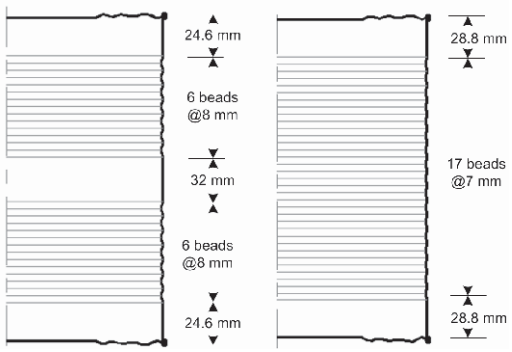

(a) mosel A (b) model B

Fig. 1. Beading configurations of the cans studied in the current work.

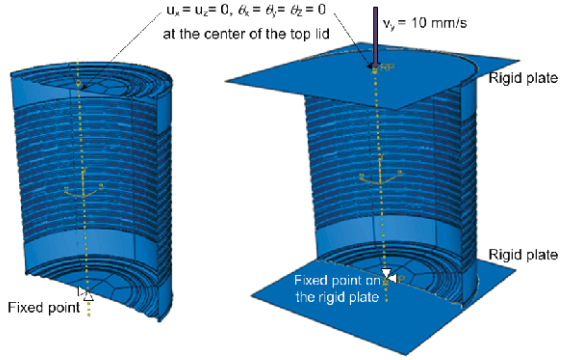

(a) (b)

Fig. 2. Boundary conditions for finite element analyses of the can under: (a) internal and vacuum pressures; (b) axial compressive load.

hot items. However, no application of an optimization technique for the study and design of the can-body corrugation have yet been performed, particularly, with consideration of the can structural performance, including the effects of a nonlinear structural response.

In the current work, finite element analysis using Abaqus software [21] is carried out to study the failure behavior and the strength of corrugated food containers under paneling pressure and axial load. Experiments performed on physical models are used to compare and validate the results from the FE models. The significant corrugation geometric parameters that affect the can structural performance are specified via a full factorial design based on the FEA results. The design parameters include the thickness of the can body, the beading depth, the spacing, the radius and the number of beadings.

The response surface methodology (RSM) [22], a statistical technique that uses quantitative data obtained from appropriately designed experiments to determine the regression model and operating conditions, is then applied to determine the optimal corrugation design. With the purpose of minimizing the can thickness, a numerical example is used to design the optimized corrugation for the given loading requirements.

2. Structural performance of a food container

In the cannery industry, the can sizes are categorized to avoid confusion from conflicting local names of cans. The can used in the current research is designated as 603 × 700, which would measure approximately 6-3/16 inches (157.2 mm) in the outside diameter of the double seam and 7 inches (177.8 mm) in the overall height. Both the lids and the body are produced from single-reduced continuous-annealed tinplate. The material properties of the tinplate are tested using five samples, and the average values are as follows: the elastic modulus of the tinplate is 219.86 GPa, the yield stress is 476.74 MPa, and the Poisson's ratio is 0.3. Two different models of beading configuration are considered, as illustrated in Fig. 1. Model A (or the 'half' beading configuration) consists of two sets of six beadings with a 32-mm spacing between. The thickness of the can body and the can lids is 0.28 mm. Model B (the so-called 'full' beading configuration) has a full corrugated surface of 17 beadings over the can body. The can-body and can-lid thicknesses are 0.25 mm and 0.28 mm, respectively. Both models display the same corrugation pattern at the can lids. The can structural performances are considered under three types of loadings, i.e., internal pressure, vacuum pressure, and compressive axial load. Three samples are tested for each model in the experiments for all load cases. The boundary conditions for analyses of the can under different loadings are shown in Fig. 2.

2.1 Internal pressure

The can deformation under internal pressure is studied by applying continuously increasing air pressure to the inside of the can. After a certain amount of pressure is applied, the can lids begin to bulge before a noticeable deformation of the can body occurs. The internal pressure requirement is such that the paneling growth (the maximum bulging of the can lid) does not exceed the reference level at the top of the seam. The average allowable amount of paneling growth (measured by using a dial gauge from three samples) is 4.496 mm, and the average internal pressure obtained from the test is 20.6 kPa.

To simulate the can lid deformation from internal pressure, a three-dimensional (geometrically and materially) nonlinear FEA is performed. The can body of a thin-walled cylindrical shell shape and the corrugated plate lids are modeled using 8-node reduced-integration quadrilateral shell (S8R) elements. The double seams along the rims of the can lids are stiffer than the other parts and are thus modeled by 20-node quadratic brick (C3D20) elements. The quadratic elements are preferred because of the curved boundaries of the can structure. An example of the finite element model including the type and the element size for each part is displayed in Fig. 3. The can material properties are assumed as elastic-perfectly plastic. The results from the FEA show that when the paneling growth is controlled to the measured value, the static internal pressure is 20.61 kPa. The radial displacement of the can-body shell remains minimal, which is in agreement with the experimental result.

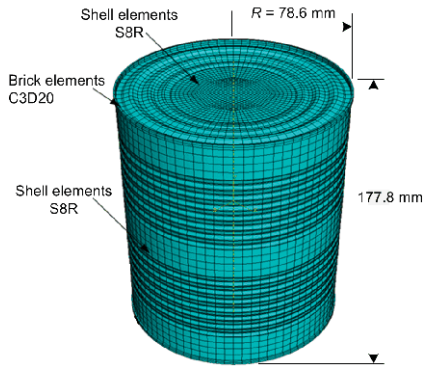

Fig. 3. Meshing and element types of the finite element model.

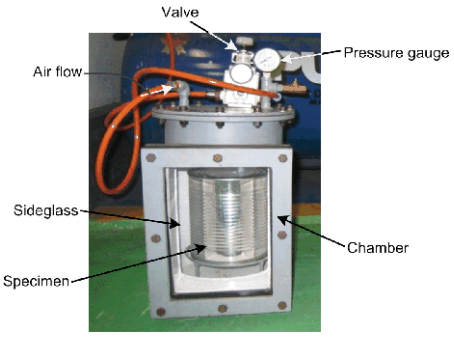

Fig. 4. Pressurized chamber for internal and vacuum load experiments.

Table 1. Comparisons of the plastic deformation of the can lid from FEA and experiments.

Method of analysis	Average deformation (mm)				
	O	*A*	*B*	*C*	*D*
Experiment	1.958	2.130	2.078	1.887	1.238
FEA	2.186	2.044	1.996	1.797	1.277
Difference (%)	+11.6	-4.0	-4.0	-4.8	+3.2

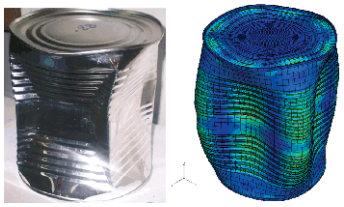

(a) model A

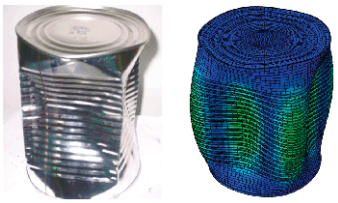

(b) model B

Fig. 5. Comparisons of buckling mode shape due to vacuum pressure in experiments and FEA.

2.2 Vacuum pressure

The deformation behavior and the can structural resistance under vacuum pressure are studied by placing the specimens in a closed chamber as shown in Fig. 4, where increasing external air pressure is applied. Similar to the previous case, when the pressure in the chamber is increased, the container lids first start to cave in while no visible deformation is observed in the can body.

Static and buckling tests are performed to study the can behaviors under vacuum pressure. First, an external pressure of 80 kPa is applied to the can, and the plastic deformations of the can are measured after the pressure is released. The measuring points are located along the radial direction of the can lid at the peaks of each lid corrugation, namely, at locations *A* to *D* and at the center *O*. The experimental deformation for each peak is obtained from an average of four measuring points located 90 degrees apart on the circumference.

The finite element simulation for this case is executed via a two-step analysis: in step one, a static pressure of 80 kPa is applied to the can, and in step two, the pressure is released. The plastic deformations of the can lids at locations *A* to *D* are recorded and compared in Table 1. The results from the experiments and the FEA are shown to be similar at all locations with less than 5% difference. A slightly larger yet acceptable difference is detected at the center of the can lid.

The next experiment examined the can structural strength and failure behavior under vacuum pressure. When the pressure in the chamber is increased although the high plastic deformation initially occurs at the can lids in both models, the eventual failure is due to the instability of the can body. The modes of failure for models A and B consist of four apexes located around the can body as shown in Figs. 5(a) and 5(b), respectively. The buckling strengths, read as the maximum value before the pressure inside the chamber drops, are 142 kPa and 126 kPa, respectively.

In the FEA simulations, this load case is simulated in a large-deformation static buckling analysis under a uniform vacuum pressure inside the can. The modes of failure obtained from the FEA for both models are analogous with those from the experiments (Fig. 5). The buckling paneling pressures of model A and B from the analysis are both comparable with their experimental results at 143 kPa and 129 kPa, respectively.

2.3 Compressive axial load

To evaluate the compressive axial resistance of the can structure, the specimens were tested under compression using a universal testing machine. As shown in Fig. 6, a linear-guide device is used to ensure movement in the vertical direction and a uniform load around the can axis. The crosshead speed is set to 10 mm/s. Failure from the compressive load occurs as buckling of the can, and the load drops rapidly. For both models, the can bodies buckle such that seven waves are formed around the can-body circumferences. In model A, the circum-

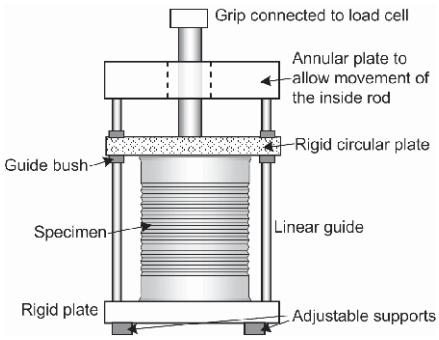

Fig. 6. Testing devices for axial load capacity.

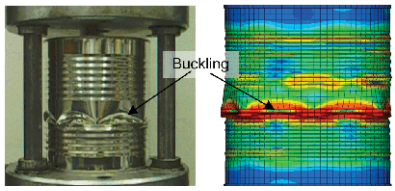

(a) model A

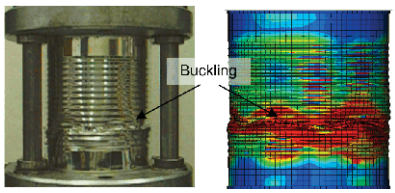

(b) model B

Fig. 7. Buckling of the can structure under axial compression.

ferential waves occur between the two sets of beadings (Fig. 7(a)) at an average compression of 10450 N with a maximum displacement of 1.89 mm. For model B, the buckling waves arise at locations around the first to the third corrugation from either side of the can ends. The average compressive load is 9884 N and the maximum displacement is 1.32 mm (Fig. 7(b)).

In the simulations, the can models are modified by the attachment of rigid plates to the top and the bottom of the can. The buckling mode shapes are first determined by static buckling analysis to measure the eigenfrequencies, followed by Riks analysis to study the buckling strength and the post-buckling behaviors.

The load-displacement response of a thin-walled structure under axial load usually produces a negative stiffness. To remain in equilibrium, the strain energy must be released. The Riks method is able to find the static equilibrium during the unstable phases of the model response.

To use the Riks procedure for solving a post-buckling problem, it is necessary to introduce an initial imperfection into the perfect geometry of the model. The definition of the geometric imperfection is created by a superposition of buckling eigenmodes obtained from a previous buckling analysis. The normalized displacement of the eigenmode shape and the imperfection scaling factor are multiplied and result in the imperfection amplitude. The imperfection amplitude alters the perfect structure to that of geometry with a deformation before the load is applied on the model.

Table 2. Normalized axial buckling resistances for various eigenmodes and imperfection sizes.

Eigenmode	Buckling load (N) for imperfection scaling factor			
	0.01t	**0.1t**	**0.2t**	**0.5t**
1	0.999	0.988	0.987	0.984
5	0.999	0.997	0.994	0.988
17	0.999	0.996	0.993	0.962

The imperfections used in the model were chosen in terms of percent of the shell thickness, *t*. An appropriate perturbation pattern in the initial condition corresponding to the eigenmodes obtained from the static buckling analysis is applied to trigger the buckling process. The top plate is assigned to move downward at the speed of the crosshead. The buckling resistance under the axial load is read from the maximum reaction force at the reference point on the top plate before the force drops. The stiffness of the structure and the maximum load are observed to decrease with increasing imperfection values. The respective buckling resistances of the perfect shell for model A and B are 11,584 N and 10,588 N. The buckling mode shapes from the FEA resemble those from the experiments. Table 2 shows an example of the normalized buckling resistance (as a ratio to the perfect shell buckling load) of model B for different eigenmodes and imperfection scaling factors. The sensitivity of the structure to the eigenmodes and imperfections appears to be marginal. The reduction of the buckling load in the models with imperfections of up to 50% of the shell thickness is less than 4%. Therefore, this study employs the first eigenmode shape with an imperfection scaling factor of 0.1 *t* to the axial buckling load analyses for all calculated models in the optimization design. Local imperfections are not introduced into the mode.

3. Effects of beading configuration and design parameters

As illustrated in the previous section, two beading configurations and five geometric parameters are investigated in the current work, as shown in Fig. 8. The parameters of interest include the thickness of the can body (*t*), the beading depth (*d*), the beading spacing (*s*), the beading radius (*r*) and the number of beadings (*n*).

3.1 Beading configuration

Model A and model B with the same material thickness of 0.28 mm, are examined to study the effects of the beading configuration. Because the thicknesses of the container are approximately uniform, the material volumes for models A and B can be computed by the multiplication of the can sur-

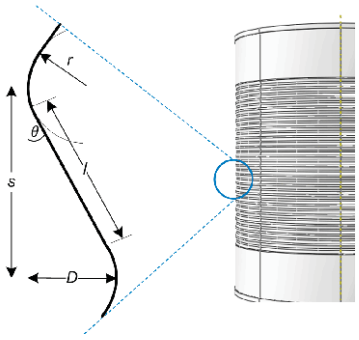

Fig. 8. Corrugation parameters.

face area and the can thickness.

The amount of tin-plate in the can body V (in mm^3) can be expressed in terms of the number of beadings n, the angle θ (in radians) and the length l (in mm) of the line shown in Fig. 8, as

$$V = \pi Dt[2n(2r\theta + l) + (H - 2ns)] \quad (1)$$

where D and H are the diameter and the height of the can body, respectively. The values of θ and l can be determined from their relationships to the beading spacing, s, and the beading depth, d:

$$s = l\cos\theta + 2r\sin\theta \quad (2)$$

$$d = l\sin\theta + 2r(1-\cos\theta)\,. \quad (3)$$

Eqs. (2) and (3) can be solved simultaneously to obtain θ as a function of other geometric parameters as

$$\theta = \sin^{-1}\left(\frac{4rs \pm \sqrt{16r^2s^2 - 4d(4r-d)((2r-d)^2 + s^2)}}{2((2r-d)^2 + s^2)}\right). \quad (4)$$

The length l can be calculated by substituting θ from Eq. (4) into either Eq. (2) or Eq. (3). Note that the two values of θ yield one positive and one negative value of l with the same magnitude. Thus, only the positive value of l is realistic.

The can model used in the current study has diameter D of 157.16 mm and height H of 177.8 mm. For the beading configuration of model A, there are two sets of six beadings (n = 12) with a spacing of 8 mm (s = 4 mm). The beading radius r is 2.8 mm, and the depth d is 0.7 mm. Substitution of all variables into Eq. (4) gives the angle θ of 0.201 radians. The length l is found from Eq. (2) or Eq. (3) as 2.94 mm. Therefore, the model A material volume, V_A, is calculated from Eq. (1) as 24,798 mm^3.

Model B has 17 beadings (n = 17) of radius r = 2.8 mm, depth d = 0.7 mm and spacing = 7 mm (s = 3.5 mm). Thus, we achieve a θ and l of 0.244 radians and 2.21 mm, respectively. Therefore, the model B material volume of the can body, V_B, is 24,939 mm^3. Thus, the material volumes for the two models are almost identical.

Table 3. Comparisons of structural performances for the two models.

Model	Material volume (mm^3)	Paneling strength (kPa)	Axial strength (N)
A	24,798	142	11584
B	24,939	158	11513
Difference (%)	+0.57%	+10.1%	-0.62%

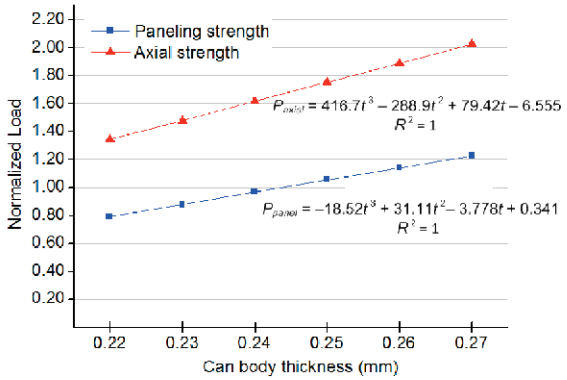

Fig. 9. Effects of changes the can-body thickness on the container strength.

The performances of models A and B with the same can body thickness of 0.28 mm under vacuum pressure and axial load as determined by FEA are shown in Table 3. Model B's pressure capacity is higher than that of model A by 10.1% while its axial strength is smaller by 0.62%. Because the beadings are designed to stiffen the unsupported wall section and to increase the paneling pressure, their influence on the axial load is smaller. The use of either design depends on the manufacturer's requirements and the intended usages. In the current study, the full beading configuration in model B is chosen as the prototype for optimization.

3.2 Design parameters

The design variables that affect the can strengths are the can-body thickness, the corrugation depth, the spacing, the radius and the number of beadings. Because the surface areas for the different corrugation designs quite similar, the key parameter that directly affects the amount of raw material used is the can thickness. Fig. 9 shows the FEA results for the paneling and axial strengths of the chosen model (Model B) for various can-body thicknesses. The ordinate is the normalized loading for the axial and paneling pressure resistances calculated by the ratio of the buckling strengths and the required loads. It can be observed that a decrease in the material thickness results in lower structural performance. The effects of the can thickness on both strengths are proportional to the magnitude of the bending stiffness and cubic relations are observed between the thickness and buckling strengths. Moreover, it was found that although can body thickness is one of the sig-

nificant parameters, its interactions with the other parameters are negligible. Therefore, the can-body thickness is excluded from the design of the optimization process. The corrugation shape needed to maximize the can performance should be first determined, and the can-body thickness is then adjusted according to the required safety factor.

The significance of the other design parameters (corrugation depth, spacing, radius and number of beadings) to the can structural strengths under paneling (vacuum) pressure and axial load are investigated using a two-level full factorial design. Two values (high and low) are used for each parameter. Note that the internal pressure condition does not affect the can body strength since failure under this condition is observed at the can lids. The normal probability plot shows that the most significant main effects on the paneling pressure are the spacing, the radius and the depth of corrugation. The spacing is found in the negative field while the radius and depth are found in the positive field. In addition, a subset of the factor interactions are found to be significant, which implies that the linear surface of the factors and the response is not suitable, and higher-order terms are required to achieve an adequate fit.

The corrugation spacing is a significant effect only for the paneling strength, in which a smaller spacing is more desirable. However, when the spacing is too small, the corrugation forming process is problematic or impossible in certain cases, especially when the corrugation radius is large. The corrugation formability can also be assessed mathematically using Eq. (4). When the designed corrugation shape can be formed efficiently, the value of the term inside the square roots in Eq. (4) will be large. When the obtained corrugation parameters are geometrically impossible, this term becomes negative.

Moreover, it can be observed that the main and interaction effects of the number of corrugations on both strengths are insignificant. Because the simultaneous optimization of many factors can cause a reduction in the changeable ranges of the design variables due to interactions between the parameters, the insignificant effects should be excluded from the response surface optimization. To avoid unrealistic geometrical connectivity problems, only the depth, radius and spacing are applied to the weight minimization problem under the structural performance constraints. The model with 17 beadings is therefore used in the optimization.

4. Optimal design of corrugation parameters

4.1 Formulation of weight minimization problem for the can body

The objective of the optimization is to minimize the can weight while ensuring that the container's strengths still meet the manufacturer's requirements. The axial strength A and the paneling pressure requirement P are restricted to be larger than the allowable minimum values A_{min} and P_{min}, respectively. The geometrical dimensions of the corrugation are selected as the design variables. For a given can size, the weight minimization of the can body is then posed as:

$$\text{Find design variables: } X = \{x_i\},\ i = 1, \ldots, n \tag{5}$$

where n is the number of design variables.

$$\text{Minimize} \quad f = V(X) \tag{6}$$

$$\text{subject to} \quad g_1 = 1\text{-}A(X)/A_{min} \le 0, \tag{7}$$

$$g_2 = 1\text{-}P(X)/P_{min} \le 0, \tag{8}$$

$$x_i^L \le x_i \le x_i^U \tag{9}$$

where x_i^L and x_i^U are the lower and upper bounds of the ith design variable, respectively.

The optimization via response surface methodology is performed based on the results from the finite element analyses. First, the path of steepest ascent is determined to evaluate a set of adjustments to the process variables that will move the process toward the optimum. Next, the response surface modeling procedure is applied to generate the approximated functions of the axial strength $A(X)$ and paneling pressure $P(X)$ in terms of the design variables.

A low-order polynomial in a selected relatively small region of the independent variable space is often appropriate. When the size of the region in which the response surface must be accurate enough to describe and approximate the real function is increased, a higher order polynomial or other response surface functions must be applied [23]. Often, the curvature in the true response surface is severe enough that a second-order model will likely be required. Central composite design (CCD) is the complete design which allows for efficient estimation of the terms in the second-order response surface model

$$y = \beta_0 + \Sigma_{i=1}^{n}\beta_i x_i + \Sigma_{i=1}^{n}\beta_{ii} x_i^2 + \Sigma\Sigma_{i<j=2}^{n}\beta_{ij} x_i x_j \tag{10}$$

where β_0, β_i, β_{ii} and β_{ij} are the constant, linear, quadratic and cross product coefficient, respectively. The variables x_i and x_j are the coded variables. The second-order model is widely used because it is flexible and works well in solving practical problems. In addition, in this type of model, the main effects and the interactions among the variables may be estimated by performing a minimum number of experiments and the parameters can be easily estimated using the least squares method [24]. For a two-level study, the total number of experiments to be performed is generally given as a sum of the $2n$ factorial runs, $2n$ axial runs, and n_c center runs, where n is the number of independent variables.

The adequacy of the selected model and the statistical significance of the regression coefficients are tested using analysis of variance (ANOVA). The measured and the model-predicted values of the response variables are used to compute the correlation coefficient R^2 and the relative standard error of prediction RSEP. The correlation between the measured and the predicted values indicates the goodness of fit of the model, whereas, the RSEP values are used to evaluate the predictive

Table 4. Effects of corrugation spacing, radius, and depth on the paneling and axial strengths.

Run	Independent variables						Dependent variables			
	Coded variables			Natural variables			Paneling strength (kPa)	Axial strength (N)	SF for paneling strength	SF for axial strength
	x_1	x_2	x_3	Spacing (mm)	Radius (mm)	Depth (mm)				
1	-1	-1	-1	6.15	2.5	0.51	104.1	12,361	1.301	1.482
2	1	-1	-1	7	2.5	0.51	100.7	12,352	1.259	1.481
3	-1	1	-1	6.15	3.47	0.51	109.5	12,299	1.369	1.475
4	1	1	-1	7	3.47	0.51	104.4	12,264	1.305	1.470
5	-1	-1	1	6.15	2.5	0.63	123.1	10,581	1.539	1.269
6	1	-1	1	7	2.5	0.63	118.9	10,661	1.486	1.279
7	-1	1	1	6.15	3.47	0.63	126.8	10,496	1.585	1.259
8	1	1	1	7	3.47	0.63	120.7	10,479	1.509	1.257
9	-1.682	0	0	5.86	2.985	0.57	121.9	11,333	1.524	1.359
10	1.682	0	0	7.29	2.985	0.57	116.2	11,409	1.453	1.368
11	0	-1.682	0	6.575	2.169	0.57	116.7	11,486	1.459	1.377
12	0	1.682	0	6.575	3.8	0.57	119.3	11,345	1.491	1.361
13	0	0	-1.682	6.575	2.985	0.47	95.2	13,015	1.19	1.561
14	0	0	1.682	6.575	2.985	0.67	127.2	10,050	1.59	1.205
15	0	0	0	6.575	2.985	0.57	118.8	11,416	1.485	1.369
16	0	0	0	6.575	2.985	0.57	118.8	11,416	1.485	1.369
17	0	0	0	6.575	2.985	0.57	118.8	11,416	1.485	1.369
18	0	0	0	6.575	2.985	0.57	118.8	11,416	1.485	1.369
19	0	0	0	6.575	2.985	0.57	118.8	11,416	1.485	1.369
20	0	0	0	6.575	2.985	0.57	118.8	11,416	1.485	1.369

ability of the selected model. The RSEP is computed as:

$$RSEP = \sqrt{\frac{\sum_{i=1}^{N}(y_{pred,i} - y_{meas,i})^2}{\sum_{i=1}^{N}(y_{meas,i})^2}} \times 100 \quad (11)$$

where $y_{pred,i}$ and $y_{meas,i}$ are the ith predicted and measured values, respectively.

4.2 Numerical example of optimal design

A design example for a food container of dimensions 603 × 700 with full beading corrugation is explained and discussed in this section. The paneling pressure and the axial load requirements are set as 80 kPa and 11,500 N, respectively.

To study the combined effect of the three significant variables of corrugation depth, radius and spacing, CCD is employed with an axial distance α of 1.682, which allows the design to possess the property of rotatability. After the method of steepest ascent, it was found that although the minimum spacing is preferable for the paneling strength, spacing lower than 6.15 mm may cause difficulties in the formation of the corrugation. Therefore, spacing between 6.15 and 7.00 mm are recommended. The appropriate minimum and maximum depths are obtained as 0.51 and 0.63 mm, while a radius between 2.50 and 3.47 mm is recommended.

The variables in the defined range of each parameter are coded to fall at ±1 for the factorial points, 0 for the center points and ±1.682 for the axial points. The complete designs consist of 20 combinations (including six replicates of the center point). All designs are carried out using finite element models as discussed in the earlier section. Because FEA gives the same responses for all replicates, only 15 necessary runs are performed. The combinations of the three independent variables together with the responses are shown in Table 4. The safety factor (SF) is computed by the ratio of the can strength and its required load.

Analyses of variance results of the two response variables for the prediction of paneling and axial strengths are shown in Tables 5 and 6. The suitability of the regression is justified by the fact that the Fisher's F-test statistic of the model is much higher than the critical F value ($F_{0.05,4,15} = 3.056$) for the considered probability ($P = 0.05$) and degrees of freedom, and the p-value approaches zero in both cases.

Based on the analysis of variance, the response surfaces of the paneling and axial strengths are approximated using a quadratic model. The model equations for the paneling strength (Y_{paneling}) and that of the axial strength (Y_{axial}) are obtained as:

Table 5. Analysis of variance of the response surface model for the prediction of paneling strength.

Source	DF	Seq. SS	Adj. SS	Adj. MS	F-test	p-value
Regression	9	1376.25	1376.25	152.916	61.53	0.000
Linear	3	1222.48	1222.48	407.493	163.9	0.000
Square	3	150.12	150.12	50.040	20.14	0.000
Interaction	3	3.64	3.64	1.215	0.49	0.698
Total	19	1401.1				

Table 6. Analysis of variance of the response surface model for the prediction of axial strength.

Source	DF	Seq. SS	Adj. SS	Adj. MS	F-test	p-value
Regression	9	10692060	10692060	1188007	4987.0	0.000
Linear	3	10657205	10657205	3552402	14823	0.000
Square	3	29822	29822	9941	41.48	0.000
Interaction	3	5033	5033	1678	7.00	0.008
Total	19	10694457				

$$Y_{paneling} = 118.877 - 2.079x_1 + 1.389x_2 + 9.125x_3 - 0.417x_1^2 - 0.788x_2^2 - 3.192x_3^2 - 0.45x_1x_2 - 0.225x_1x_3 - 0.45x_2x_3 \quad (12)$$

and

$$Y_{axial} = 11416.1 + 10.8x_1 - 47.9x_2 - 882x_3 - 16.9x_1^2 - 1.1x_2^2 + 40.2x_3^2 - 15.4x_1x_2 + 13.4x_1x_3 - 14.6x_2x_3 \quad (13)$$

where x_1, x_2 and x_3 are the coded variables for corrugation spacing, radius and depth, respectively. The regression coefficients are shown in Table 6.

The R^2 values for these response variables are greater than 0.98 indicating that the developed response surface models explain the response well. A particularly high value of the adjusted correlation coefficient R_{adj} also shows the high significance of the model. Additionally, considerably low RSEPs (0.91 and 0.10) underscore the adequacy of the fitted quadratic model.

The response surface plots of the paneling strength are illustrated in Fig. 10. For the specified ranges of the corrugation parameters, the maximum paneling strength is achieved when the corrugation spacing is less than 6 mm, the radius is between 3.20 and 3.50 mm and the corrugation depth ranges from 0.62 to 0.65 mm. Fig. 11 shows the surface plots for axial strength. From the steep surface plot along the depth axis, it is obvious that the effect driven by the corrugation depth is much more significant than that of the radius and the spacing. Moreover, the low-curvature surface located between the corrugation depth and the radius implies that the interaction of these two variables is not substantial. It can be observed from the plots that the maximum axial strength is obtained when the depth is lower than 0.50 mm.

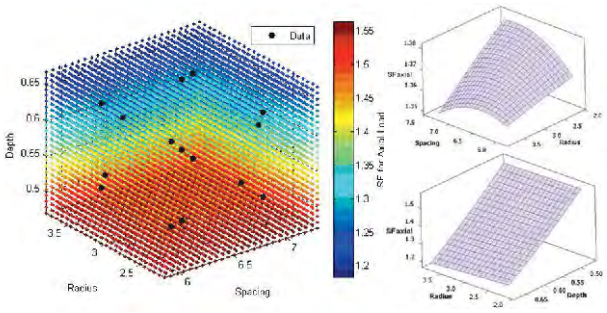

Fig. 10. Response surface plot of the safety factor for paneling pressure calculated from Eq. (12).

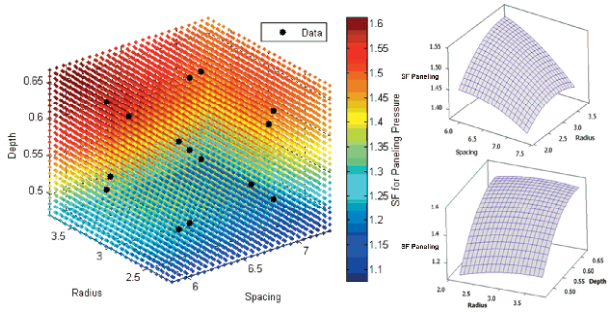

Fig. 11. Response surface plot of the safety factor for axial load calculated from Eq. (13).

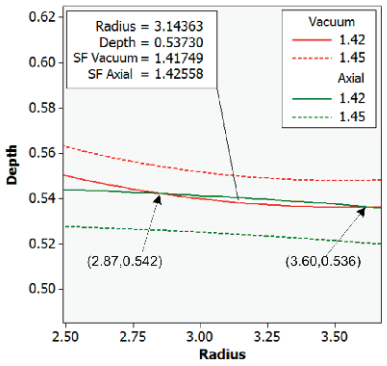

Fig. 12. Optimal region found by overlaying the paneling and axial safety factors for a spacing of 6.5 mm.

The optimal condition is determined using the desirability functions. In this study, the objective is to maximize the responses while emphasis is placed on remaining close to the target value. Thus, the weight of the desirability function is chosen to be greater than unity. The lower and upper bounds for the SFs are specified as 1.3 and 1.5, respectively, and the importance for both responses is set to 1. By using the optimizer, the highest desirability is attained at a value of 0.692 when the corrugation spacing, depth and radius are 5.86 mm, 0.54 mm and 3.65 mm, respectively. For this case, the SF for the paneling strength is 1.46 and that of the axial strength is 1.42.

Another approach for determining the optimal condition is to superimpose the contour plots of the two responses, as shown in Fig. 12. The final product is considered as optimal

Table 7. Safety factors and weight of the optimal design.

Can thickness (mm)	SF Paneling		SF Axial		Weight (g)
	Predicted	FE	Predicted	FE	
0.25	1.417	1.416	1.425	1.425	174.17
0.24	1.336	1.329	1.296	1.316	167.20
0.23	1.258	1.245	1.170	1.202	160.24
0.22	1.184	1.145	1.043	1.103	153.27

when the safety factors for both the paneling and axial strengths are highest. Therefore, the criteria for the optimization are targeted as higher than 1.3. By overlaying the responses, the optimal combined condition is found at a corrugation spacing of 6.5 mm, a depth between 0.536 and 0.542 mm and a radius between 2.87 and 3.60 mm. For this case, the SFs for both the paneling and axial strengths are approximately 1.42. Thus, the optimal configuration from the overlay plots is similar to that obtained from the optimizer. However, this method is not advised if several parameters are considered and the optimizer may be more convenient.

At the current stage, the optimal design gives the structure a higher safety factor but the can weight remains relatively unchanged (decreased by only 0.46%). The designed corrugation shape can be used with a reduced can-body thickness for the required safety factor such that the container weight is minimized. Because the can strengths are dependent on the can thickness, the slopes of the normalized loads from Fig. 9 are then used to estimate the safety factors and possible thickness reductions as listed in Table 7. The minimum can body thickness is found to be 0.22 mm, and the can body weight calculated from Eq. (1) is reduced by 12.4% compared with the original design. The predicted safety factors of the optimal model are also confirmed as comparable with the results from the FEA of the final model. The differences in the predicted and the FE strengths are less than 5.5% although the discrepancies are slightly larger for the axial load.

5. Conclusion

In this paper, parameter optimization using the response surface method has been applied to identify an optimal corrugation design for a food container that minimizes the container weight subject to predefined constraints on the paneling and axial strengths. Finite element analysis is applied to simulate the failure behaviors and calculate the can structural performances under loading in the manufacturing process. Full factorial design is used to define the key factors that affect the can strength. A central composite design is employed to approximate the response surfaces of the paneling and axial strengths in terms of the three significant design variables: corrugation depth, radius and spacing. A numerical optimal design example leads to the can-body weight minimization that reduces the container weight by up to 12.4%. A better understanding of the optimization of the corrugation design is achieved. It is clear from these results that using a RSM based on the design-of-experiments technique is able to reduce the computational costs of constructing approximate response surfaces and save time in designing the shape of the can corrugation to meet different levels of strength requirements.

Acknowledgment

The financial support from Thailand research fund (TRF) under grant MRG5380005 is gratefully acknowledged.

Nomenclature

d : Corrugation depth
D : Diameter of the can body
l, s : Corrugation parameters
r : Corrugation radius
n : Number of beadings
t : Thickness of the can body
V : Material volume
x_i : Coded variables
Y_{axial} : Axial strength
$Y_{paneling}$: Paneling strength
β_i : Response surface coefficients
θ : Corrugation angle

References

[1] J. Wang, Design optimization of rigid metal containers, *Finite Elem. Anal. Des*., 37 (2001) 273-286.
[2] F. Fujii, H. Noguchi and E. Ramm, Static path jumping to attain postbuckling equilibria of a compressed circular cylinder, *Computational Mech.*, 26 (2000) 259-266.
[3] A. N. Aljawi, Numerical simulation of axial crushing of circular tubes, *J. of King AbdulAziz University: Eng. Sci*., 14 (2002) 3-17.
[4] A. G. Arani, S. Golabi, A. Loghman and H. Daneshi, Investigating elastic stability of cylindrical shell with an elastic core under axial compression by energy method, *Journal of Mechanical Science and Technology*, 21 (2007) 983-996.
[5] N. Yamaki, *Elastic stability of circular cylindrical shells*, Amsterdam-New York-Oxford, North Holland (1984).
[6] D. Bushnell, *Computerized buckling analysis of shells*, Kluwer Academic Publishers, Dordrecht (1989).
[7] V. Papadopoutos and P. Iglesis, The effect of non-uniformity of axial loading on the buckling behavior of shells with random imperfections, *Int. J. of Solids and Struc*., 44 (2007) 6299-6317.
[8] M. Sodiek and R. Sauer, Mechanical behaviour of food cans under radial and axial load, *Third International Tin Plate Conference* (1984).
[9] L. Siad, Buckling of thin-walled orthotropic cylindrical shells under uniform external pressure: Application to corrugated tin cans, *Thin-Walled Structures*, 35 (1999) 101-115.
[10] C. T. F. Ross and M. Humphries, The buckling of corrugated circular cylinders under uniform external pressure,

Thin-Walled Structures, 17 (1993) 259-271.
[11] J. D. Reid, R. W. Bielenberg and B. A. Coon, Indenting, buckling and piercing of aluminum beverage cans, *Finite Elem. Anal. Des*., 37 (2001) 131-144.
[12] P. Teppunkulngam, P. Tantichattanont and T. Kamnertong, Study of loading capacity of corrugated food cans using finite element method, *Proc. of Mechanical Engineering Network Thailand 22nd Conference* 2008, October 15-17, 2008, Rungsit, Thailand.
[13] R. Rotbunsongsri, P. Jongpradist and T. Kamnerdtong, Parametric study of food can corrugation geometry by using finite element method, *Proc. of the Second TSME International Conference on Mechanical Engineering*, October 19-21, 2011, Krabi, Thailand.
[14] D. H. Chen and S. Ozaki, Numerical study of axially crushed cylindrical tubes with corrugated surface, *Thin-Walled Structures*, 47 (2009) 1387-1396.
[15] K. K. Choong and E. Ramm, Simulation of buckling process of shells by using finite element method, *Thin-Walled Structures*, 31 (1998) 39-72.
[16] C. T. F. Ross, A redesign of the corrugated tin can, *Thin-Walled Structures*, 26 (1996) 179-193.
[17] K. Yamazaki, R. Itoh, M. Watanabe, J. Han and S. Nishiyama, Applications of structural optimization techniques in light weighting of aluminum beverage can ends, *J. of Food Engineering*, 81 (2007) 341-346.
[18] J. Han, R. Itoh, S. Nishiyama and K. Yamazaki, Application of structure optimization technique to aluminum beverage bottle design, *Struct. Multidis Optim.*, 29 (2005) 304-311.
[19] H. Ugail, Parametric design and optimization of thin-walled structures for food packaging, *Optimization and Engineering*, 4 (2003) 291-307.
[20] J. Han, K. Yamazaki, R. Itoh and S. Nishiyama, Multiobjective optimization of a two-piece aluminum beverage bottle considering tactile sensation of heat and embossing formability, *Struct. Multidis. Optim.*, 32 (2006) 141-151.
[21] Simulia, *Abaqus Analysis User's Manual* (2011).
[22] R. H. Myers, D. C. Montgomery and C. M. Anderson-Cook, *Response surface methodology*, John Wiley & Sons, Inc., New Jersey (2009).
[23] G. Steenackers, F. Presezniak and P. Guillaume, Development of an adaptive response surface method for optimization of computation-intensive models, *Computers and Industrial Engineering*, 57 (2009) 847-855.
[24] N. Muhammad, Y. H. P. Manurung, M. Hafidzi, S. K. Abas, G. Tham and E. Haruman, Optimization and modeling of spot welding parameters with simultaneous multiple response consideration using multi-objective Taguchi method and RSM, *Journal of Mechanical Science and Technology*, 26 (8) (2012) 2365-2370.

Pattaramon Jongpradist is currently an Assistant Professor at Department of Mechanical Engineering, Faculty of Engineering, King Mongkut's university of Technology Thonburi. She received her B.Eng. degree from Chulalongkorn University, Thailand, her M.Eng. from Asian Institute of Technology, Thailand, and her Ph.D. in Mechanical Engineering from Memorial University, Canada, in 2006. Her current interest includes computational mechanics, such as techniques in finite element analysis and meshless methods, and behaviors of plate and shell structures.

Rattharong Rotbunsongsri is a graduate student in the Department of Mechanical Engineering at King Mongkut's university of Technology Thonburi. He also received his B.Eng. in Mechanical Engineering from King Mongkut's university of Technology Thonburi in 2009.

Thoatsanope Kamnerdtong is an Assistant Professor in the Department of Mechanical Engineering at King Mongkut's University of Technology Thonburi. His M.S. and Ph.D. degrees in Mechanical Engineering from Vanderbilt University, Nashville, Tennessee, USA. His research interests are in finite element analysis, failure analysis, micro-position and ultra-precision mechanisms, computer aided design and engineering (CAD/CAE), design and application in automotive and hard disk drive industries.

Somchai Wongwises is currently a Professor of Mechanical Engineering, Faculty of Engineering at King Mongkut's University of Technology Thonburi, Bangmod, Thailand. He received his Doktor Ingenieur (Dr.-Ing.) in Mechanical Engineering from the University of Hannover, Germany, in 1994. His research interests include Gas-Liquid Two-Phase Flow, Heat Transfer Enhancement, and Thermal System Design. Professor Wongwises is the head of the Fluid Mechanics, Thermal Engineering and Multiphase Flow Research Laboratory (Future).

Provided for non-commercial research and education use.
Not for reproduction, distribution or commercial use.

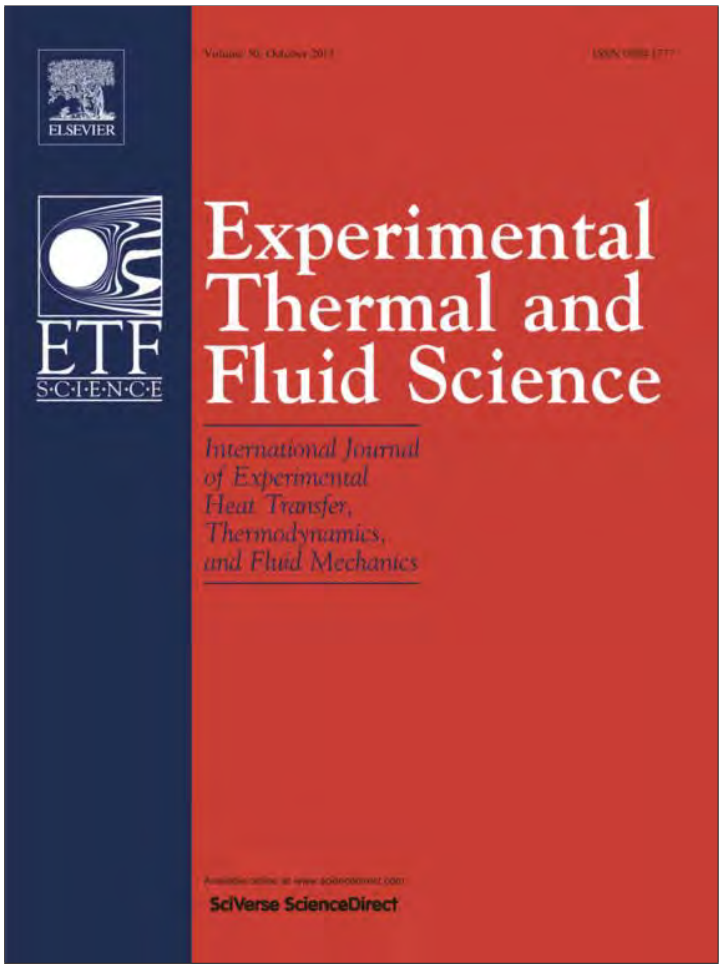

This article appeared in a journal published by Elsevier. The attached copy is furnished to the author for internal non-commercial research and education use, including for instruction at the authors institution and sharing with colleagues.

Other uses, including reproduction and distribution, or selling or licensing copies, or posting to personal, institutional or third party websites are prohibited.

In most cases authors are permitted to post their version of the article (e.g. in Word or Tex form) to their personal website or institutional repository. Authors requiring further information regarding Elsevier's archiving and manuscript policies are encouraged to visit:

http://www.elsevier.com/authorsrights

Author's personal copy

Experimental Thermal and Fluid Science 50 (2013) 222–228

Contents lists available at SciVerse ScienceDirect

Experimental Thermal and Fluid Science

journal homepage: www.elsevier.com/locate/etfs

Comparison of the heat transfer performance and friction characteristics between fixed and rotating turbine-type swirl generators fitted in a small circular tube

Weerapun Duangthongsuk [a,b], Somchai Wongwises [b,c,*]

[a] Department of Mechanical Engineering, South-East Asia University, Bangkok, Thailand
[b] Fluid Mechanics, Thermal Engineering and Multiphase Flow Research Lab. (FUTURE), Department of Mechanical Engineering, Faculty of Engineering, King Mongkut's University of Technology Thonburi, Bangmod, Bangkok 10140, Thailand
[c] The Academy of Science, The Royal Institute of Thailand, Sanam Suea Pa, Dusit, Bangkok 10300, Thailand

ARTICLE INFO

Article history:
Received 30 December 2012
Received in revised form 10 April 2013
Accepted 10 April 2013
Available online 30 April 2013

Keywords:
Nusselt number
Pressure drop
Swirl generator inserts
Passive technique

ABSTRACT

This paper is a continuation of the authors' previous work [W. Duangthongsuk, S. Wongwises, An experimental investigation of the heat transfer and pressure drop characteristics of a circular tube fitted with rotating turbine-type swirl generators, Exp. Therm. Fluid Sci. 45, (2013), 8–15.]. Swirl generators inserted into a conventional smooth tube is an innovative way to increase the thermal performance of the heat exchangers. The effect of the free rotation of a swirl device on the thermal performances and friction behaviors are investigated experimentally. Five turbine-type swirl generators with and without free rotation are inserted and installed equally distant along the test section. In the present study, DI water is used as a testing fluid and flows under a turbulent flow regime. A common stainless steel tube with an OD of 10 mm, ID of 9.2 mm, and length of 2.3 m is used as the test tube. A DC power supply is used to supply the heat load to the test section in order to meet the constant heat flux boundary condition. The data for a common smooth tube are compared with the data for fixed (FTSG) and freely rotating turbine type swirl generator (RTSG). The measured data illustrate that the heat transfer performance of the tube with RTSG inserts is 6.3% and 56% higher than that of the FTSG insert and the conventional smooth tube, respectively. Moreover, the heat transfer coefficient significantly increases when the fluid flows pass the RTSG and FTSG inserts. However, inserting the RTSG and FTSG into the common smooth tube results in an increase of the pressure drop. The tube with RTSG inserts gives the lowest pressure drop.

© 2013 Elsevier Inc. All rights reserved.

1. Introduction

In order to increase the thermal performance of the heat exchanger, two conventional heat transfer enhancement techniques are used. The first is the active technique and the other is the passive technique. For the active technique, external force such as jet impingement, stirring of the fluid, fluid and surface vibration, and electric field are required. Equally, the passive technique requires special surface geometries such as extended surface, displaced inserts, swirl flow inserts, and surface roughening. Focusing on the passive technique, swirl generator devices can be fitted both inside and outside of the tubes to create swirl flow, which leads to a decrease in the thermal boundary layer thickness for enhancing the thermal performance. At the same time, the tube being fitted with some devices can cause an increase in the pressure drop. The ratio of the heat transfer performance to the pressure drop should be maximized in order to improve the heat exchanger performance. As previously mentioned, many researchers have studied and have tried to develop the new type of swirl flow devices for increasing the thermal performance and reducing the pressure drop inside the common plain tube to be as low as possible. Several articles describing these attempts are depicted in the previous work of the authors [1]. However, the recent articles are in addition to those described [2–8].

From the above mentioned studies, many researchers illustrated that the use of swirl flow devices implanted in the common smooth tube gave higher thermal performances than the plain tube. However, this enhancement was supplemented by an increase in the penalty drop of pressure. Except the research wok of Zhang et al. [6], most of their works mentioned the swirl flow devices which are the fixed type swirl inserts. The effect of free rotation on the heat transfer performance and pressure drop characteristics which has never been seen before in the open literature is presented. The fixed and freely rotating turbine-type swirl

* Corresponding author at: Fluid Mechanics, Thermal Engineering and Multiphase Flow Research Lab. (FUTURE), Department of Mechanical Engineering, Faculty of Engineering, King Mongkut's University of Technology Thonburi, Bangmod, Bangkok 10140, Thailand.
E-mail address: somchai.won@kmutt.ac.th (S. Wongwises).

0894-1777/$ - see front matter © 2013 Elsevier Inc. All rights reserved.
http://dx.doi.org/10.1016/j.expthermflusci.2013.04.007

Author's personal copy

Nomenclature

A	area ($m^{2)}$
C_p	specific heat (J/kg K)
D	diameter (m)
f	friction factor
h	heat transfer coefficient (W/m^2 K)
I	electric current (A)
k	thermal conductivity (W/m K)
L	length of the test tube (m)
$\dot{m}$	mass flow rate (kg/s)
Nu	Nusselt number
Pr	Prandtl number
ΔP	pressure drop (Pa)
Q	heat transfer rate, W
Re	Reynolds number
T	temperature (°C)
u	velocity (m/s)
V	electric voltage (V)

Greek symbols

ε	roughness (m)
ρ	density (kg/m^3)
μ	viscosity (kg/ms)

Subscript

ave	average
elec	electric
f	fluid
in	inlet
m	average
out	outlet
s	surface
w	tube wall
x	local distance

generators (FTSG and RTSG) used in the present study are new designs. Both FTSG and RTSG are fitted inside the test section separately and tested in order to compare them with the data of a common plain tube.

2. Experimental apparatus and procedures

The experimental setup used in the present study is shown schematically in Fig. 1. It mainly consisted of two test sections: the first was conducted to test the conventional smooth tube, and the other was conducted to investigate the tube fitted with FTSG and RTSG. Moreover, the test loop consisted of a pump with a speed controller, two cooling tanks, and a rotameter. In this research, De-ionized (DI) water was used as the testing fluid, and it flowed through the test tubes under turbulent flow regimes and uniform wall heat flux boundary conditions. Straight stainless steel tubes with an inner diameter of 9.2 mm, 0.4 mm thickness, and 2,300 mm in length were used as the test sections. For the test section with both types of swirl generator inserts (FTSG and RTSG), RTSG was first installed and tested. Then, FTSG were mounted instead of FTSG for comparison. Both FTSG and RTSG used in the present study having 5 pieces and were located at x/L of 0.0, 0.2, 0.4, 0.6, and 0.8, respectively. FTSG and RTSG used in this research were made from aluminum material with twist angles of 60°, blade thickness of 0.5 mm, 2 cm in length, and 6.6 mm in outer diameter, and each FTSG or RTSG had four blades. Each FTSG and RTSG was installed inside the transparency tube to observe the flow fluid behavior after the flow passed the swirl devices. When the fluid was forced through the FTSG, swirl flow was created. Similarly, after fluid flowed through RTSG, continuously free rotation was obtained and swirl flow was produced simultaneously. Fig. 2 shows the detail of the FTSG and RTSG inserts used in the present work.

For measuring the available data, a differential pressure transmitter and the T-type thermocouples were installed at both ends of the section to measure the pressure drop and the bulk temperature of the working fluid, respectively. Likewise, in order to measure the wall temperature along the test section, 10 T-type thermocouples were placed at different longitudinal positions on the outer surface. For the thermocouple fixations at the outer wall of the test section, the thermal insulation tape was used to bind the thermocouple end around the tube. The positions of the wall temperature measurements and the FTSG and RTSG locations are described in Fig. 3. In order to meet the wall heat flux boundary condition, a DC power supply was used to adjust the heat load to the test section. Cooling tank No. 1, with a 4000 W electric heater, a 3.52 kW cooling capacity, and an RTD with a temperature controller, was used to keep the water temperature constant at a desired value. Also, cooling tank No. 2, with an 5.28 kW cooling capacity, and an RTD with a temperature controller, was used to cool the working fluid temperature leaving from the test section to the setting temperature. A rotameter was used to measure the flow rate of the working fluid. An inverter was used to control the water flow rate. In order to prevent the heat loss along the test section, the elastomer type insulator with thermal conductivity of 0.04 W/mK, 20 mm of thickness was used to shield the outer surface of the tube. The test section configurations and operating conditions are summarized in Table 1.

For instrument calibration, all of the thermocouples were well-calibrated in a controlled temperature bath, using standard precision mercury glass thermometers. The uncertainty of the temperature measurements as recorded by the data acquisition system was ±0.1 °C. An air-operated dead weight tester was used to calibrate the differential pressure transmitter. The uncertainty of the pressure measurement was ±0.030 kPa. The rotameter was specially calibrated by the manufacturer, and its accuracy was ±7% of full scale. Finally, in order to estimate the uncertainty of the measured data, the root mean sum square method was applied. The uncertainty of the measured heat transfer was approximately 5%.

The experiments were tested with different water flow rates. A Reynolds number ranged from 4500 to 9500 was conducted. The wall heat flux was kept constant at 15 kW/m^2 by adjusting the voltage regulator. The inlet water temperature was kept at 15 °C. During each experiment, the system was certified to approach a steady state before any data were recorded. After a steady state was reached, the wall temperatures and the inlet and outlet temperatures of the water and the pressure drop across the test section and the flow rates of water were recorded.

3. Data reduction

To determine the heat transfer performance and flow characteristics of the common plain tube with FTSG and RTSG inserts, the experimental system calibration is necessarily done. Thus, a conventional round tube is verified. The measured data of the heat transfer coefficient and friction are compared with the calculated

Author's personal copy

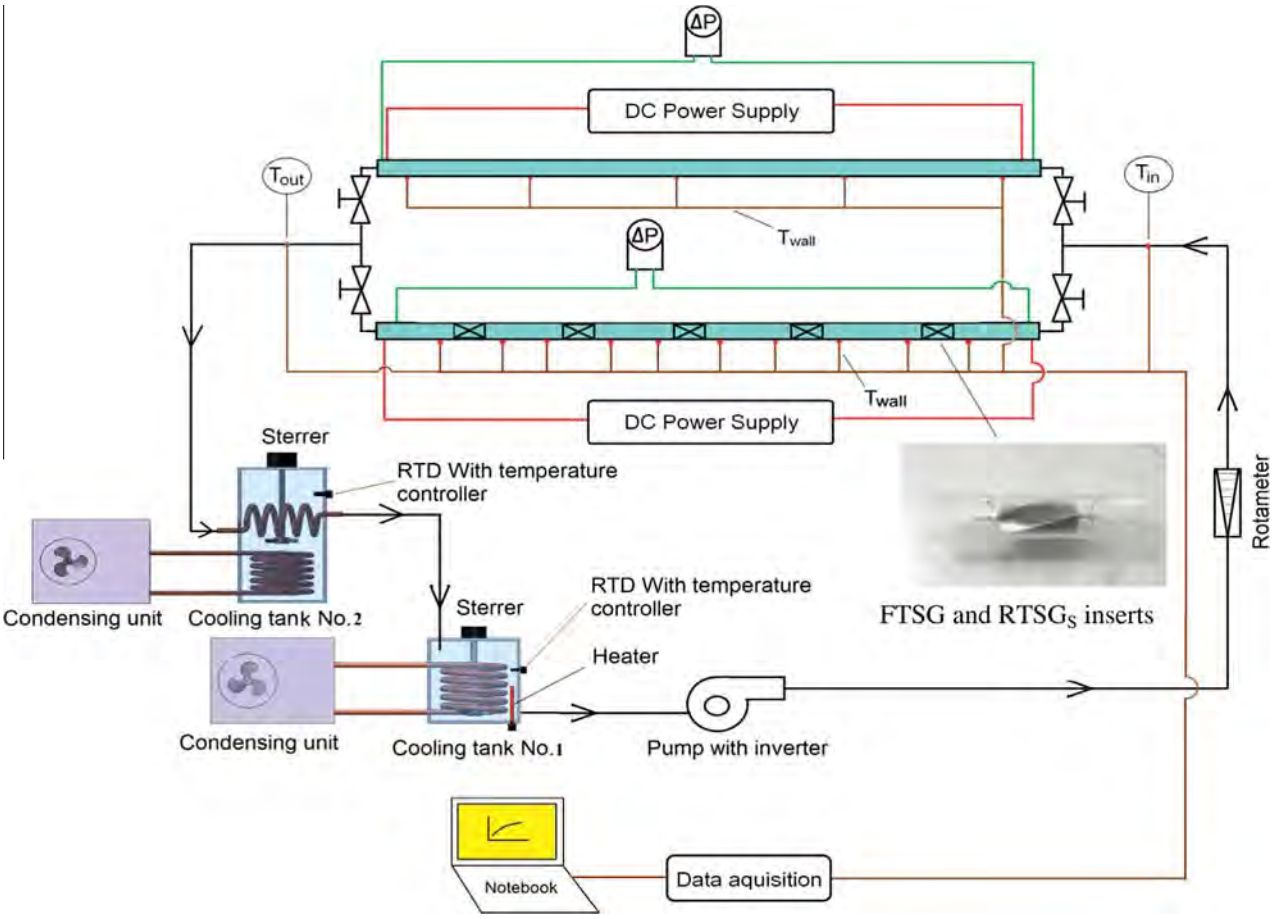

Fig. 1. Schematic diagram of the experimental apparatus [Duangthongsuk and Wongwises [1], with permission from Elsevier].

values obtained from Gnielinski's equation and Colebrook's equation, respectively.

The Gnielinski equation [9]:

$$Nu = \frac{(f/8)(\mathrm{Re} - 1000)\mathrm{Pr}}{1 + 12.7(f/8)^{0.5}(\mathrm{Pr}^{2/3} - 1)}, \tag{1}$$

where Nu is the Nusselt number, Re is the Reynolds number, Pr is the Prandtl number, and f is the friction factor.

The Colebrook equation [10]:

$$\frac{1}{\sqrt{f}} = -2.0\log\left(\frac{\varepsilon/D}{3.7} + \frac{2.51}{\mathrm{Re}\sqrt{f}}\right), \tag{2}$$

The pressure drop of working fluid can be calculated from:

$$\Delta P = f\frac{L}{D}\frac{u_m^2}{2}\rho, \tag{3}$$

where ΔP is the measured pressure drop, L is the length of the tube, D is the inner diameter of the tube, u_m is the average velocity of fluid, and ρ is the density of fluid.

Then, the heat transfer performance of plain tube with FTSG and RTSG inserts can be calculated from the following equation.

The heat load to the test section can be calculated from:

$$Q_{elec} = VI, \tag{4}$$

where V is the electric voltage, and I is the electric current.

The heat transferring into the fluid is computed from:

$$Q_f = \dot{m}Cp(T_{out} - T_{in}), \tag{5}$$

where $\dot{m}$ is the mass flow rate, Cp is the specific heat, and T_{in} and T_{out} are the temperatures of the fluid at the inlet and exit of the test section.

The average heat transfer rate is determined from:

$$Q_{ave} = \frac{Q_{elec} + Q_f}{2}, \tag{6}$$

where Q_{ave} is the average heat transfer rate. In the present study, the energy balance between heat supplied and working fluid are roughly less than 2.0%.

The local Nusselt number is calculated as follows:

$$h_x = \frac{q}{(T_w - T_f)_x}, \tag{7}$$

$$Nu_x = \frac{h_x D}{k}, \tag{8}$$

where h_x is the local heat transfer coefficient, Nu_x is the local Nusselt number, q is the wall heat flux, T_w is the wall temperature of the tube, T_f is the bulk temperature of the fluid at each section, and k is the thermal conductivity of the fluid.

The bulk fluid temperature at any position can be computed from:

$$T_{f,2} = T_{f,1} + \frac{q\pi Dx}{\dot{m}C_P}, \tag{9}$$

where q is the wall heat flux, T_f is the bulk temperature of the fluid at each section, and x is the length of the each section of test tube.

Finally, the average Nusselt number (h_{ave}) is also presented and can be calculated from.

Author's personal copy

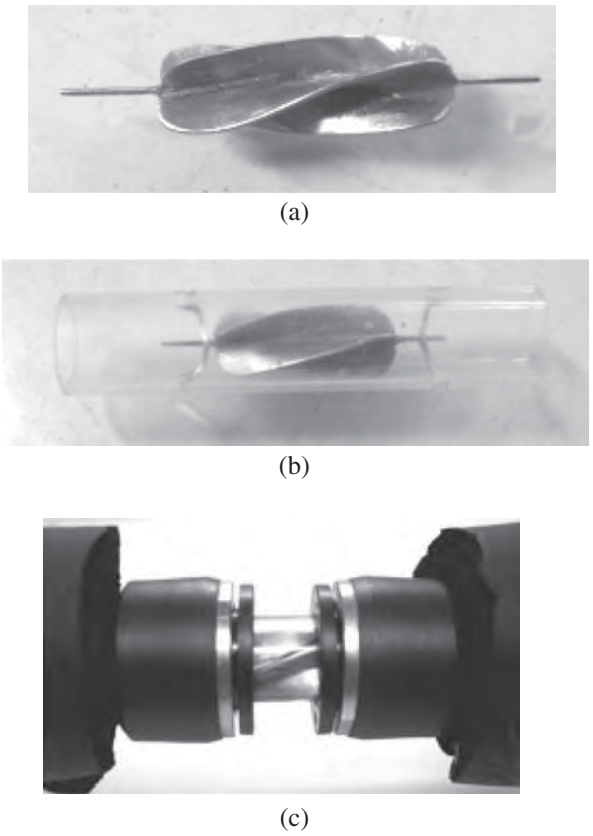

Fig. 2. Configuration of the swirl generator inserts used in the present study: (a) bare FTSG and RTSG, (b) fitted in an acrylic tube and (c) after fitting in the experimental system [Duangthongsuk and Wongwises [1], with permission from Elsevier].

$$Nu_{ave} = \frac{1}{L}\int_{x_1}^{x_2} Nu_x dx, \tag{10}$$

The Reynolds number is defined as follows:

$$\mathrm{Re} = \frac{\rho u_m D}{\mu}, \tag{11}$$

where L is the tube length, ρ is the density, and μ is the fluid viscosity.

Finally, the Prandtl number can be calculated from:

$$\mathrm{Pr} = \frac{\mu Cp}{k}. \tag{12}$$

In order to evaluate the flow characteristic of the common plain tube implanted with FTSG and RTSG, the data from the measured pressure drops of the common plain tubes are compared.

Table 1
Test section configurations and testing conditions.

Parameter	Quantity
1. Tube length (mm)	2300
2. Tube inside diameter (mm)	9.2
3. Tube thickness (mm)	0.4
4. Inlet fluid temperature (°C)	15
5. Wall heat flux (kW/m^2)	15
6. Reynolds number	4500–9500
7. Volume flow rate (LPM)	2–4

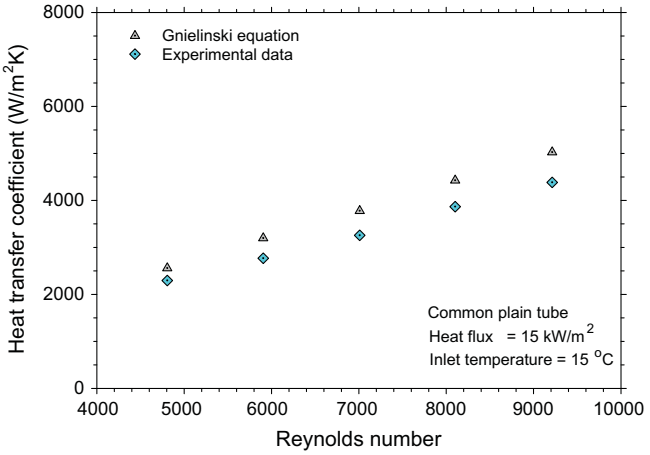

Fig. 4. Comparison between the Gnielinski equation and experimental data for heat transfer coefficient of common plain tube.

4. Results and discussion

In the present study, the experimental data can be categorized into two aspects: the first is the data for convective heat transfer performance, and the other is the pressure drop data. The results are described as follows:

4.1. Heat transfer performance

The heat transfer performance of the common plain tube is first measured for validating the experimental system. As a sequence, the measured data are compared with the predicted values from the Gnielinski equation [9]. As shown in Fig. 4, the results show good agreement between the measured values for the common plain tube and the calculated values.

The wall temperature variation along the test section for the conventional smooth tube and the FTSG and RTSG inserts is shown in Fig. 5a–c, respectively. For the conventional smooth tube, the measured data illustrate that the wall temperature increases with

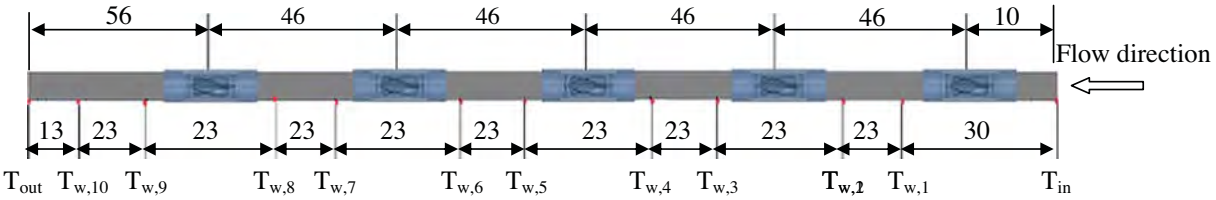

Fig. 3. The wall temperature measurement locations and the position of FTSG and RTFG inserts (unit: cm) [Duangthongsuk and Wongwises [1], with permission from Elsevier].

Author's personal copy

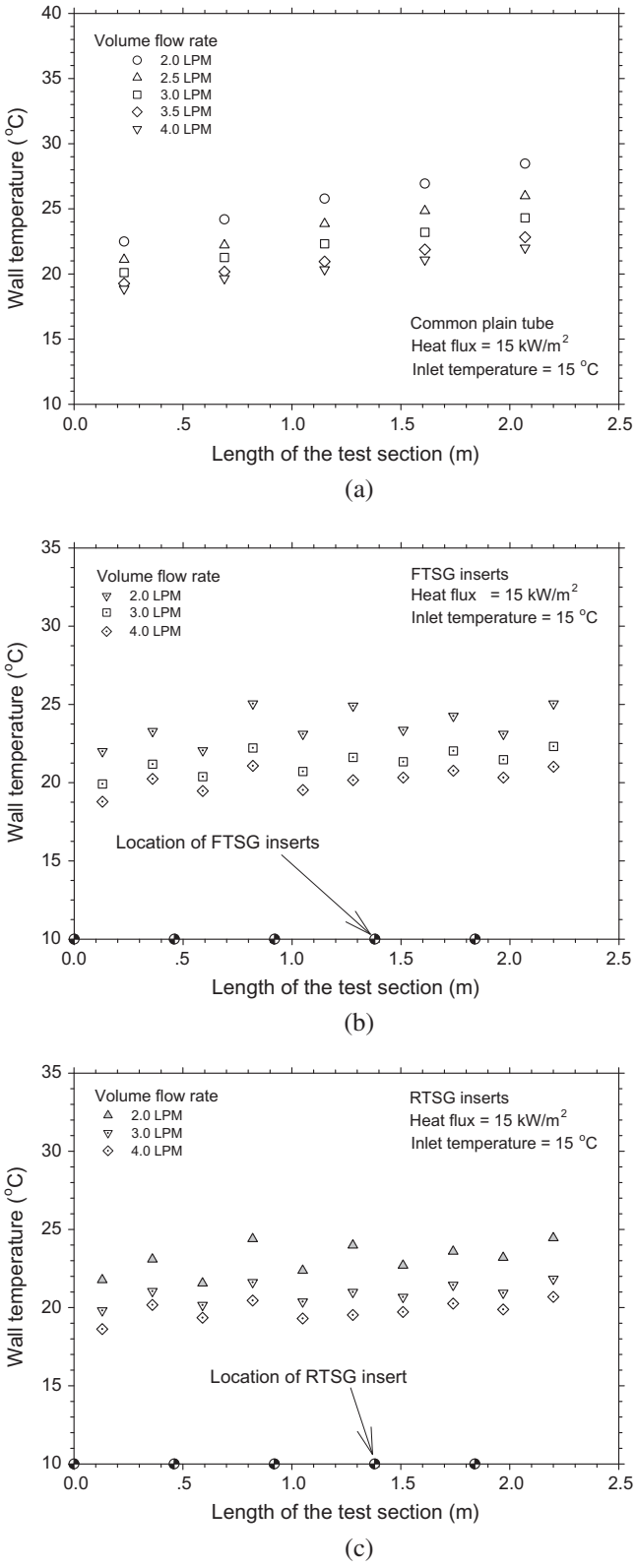

Fig. 5. The wall temperatures as function of tube length and volume flow rate: (a) for the common plain tube, (b) for FTSG inserts and (c) for RTSG inserts.

the tube length. This is due to the heat load continuously supplied to the test section. Thus an increase of the wall temperature is achieved. However, for the common tube fitted with the FTSG, unusual behavior is observed. As shown in Fig. 5b, it is clearly seen that the tube wall temperature is dropped behind the position of the FTSG. As shown in Fig. 5c, a similar tendency is obtained from the data of the RTSG inserts. A higher heat transfer rate is obtained due to swirling flow after each FTSG and RTSG, which leads to a reduction in the wall temperature.

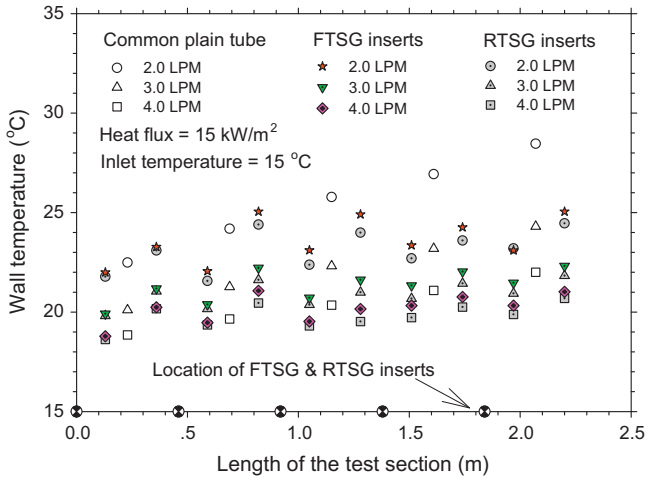

Fig. 6. Comparison between the wall temperatures obtained from the common plain tube and the tube with FTSG and RTSG inserts.

Comparison of the local wall temperature between plain tube, FTSG, and RTSG inserts is shown in Fig. 6. The measured data demonstrate that the wall temperature of the tube fitted with RTSG is slightly lower than that of the FTSG inserts. This may be because the swirling flows caused from continuous free rotation of the RTSG is more intensive than the FTSG inserts, which leads to high heat dissipation. Compared with the common plain tube, smaller tube wall temperature can be seen, especially at high x/L ratio. This behavior implies that the tubes implanted with swirl flow devices provide higher heat transfer performances than the common plain tube and the use of RTSG inserts provides a higher heat transfer performance than the FTSG inserts.

Variations of the local Nusselt number as a function of the flow rates and tube length for the common plain tube, FTSG, and the RTSG inserts are shown in Fig. 7a–c, respectively. For the common plain tube, the experimental data show that the local Nusselt number varies with the volume flow rate and remains constant along the test section. However, for both cases of the FTSG and RTSG inserts, abnormal behavior is observed. The local Nusselt number of the FTSG and RTSG inserts increases with increasing tube length. Moreover, focusing on the point after the FTSG and RTSG, a dramatically higher local Nusselt number is obtained. This result is due to the swirling flow after the FTSG and RTSG inserts, promoting greater heat transfer performance.

Comparison of the local Nusselt number between FTSG and RTSG inserts is shown in Fig. 8. The results show that the tube with RTSG inserts provides a slightly higher Nusselt number than that for the FTSG inserts. This behavior may be caused from the effect of the free rotation of the RTSG inserts can create a high disturbance of the fluid flow, which leads to an increase in the Nusselt number. This means that the use of RTSG inserts provides a higher heat transfer performance than the FTSG inserts.

Similarly, a comparison between the average Nusselt number obtained from the tube fitted with FTSG and that obtained from the RTSG inserts is shown in Fig. 9. The measured results show that the average Nusselt number of the RTSG inserts is approximately an average of 6.3% and 56% higher than that of the FTSG insert and the plain tube, respectively, and varied with Reynolds number. This result is due to more intensive swirling flow after the RTSG than the FTSG, which leads to enhancing the heat transfer performance.

Author's personal copy

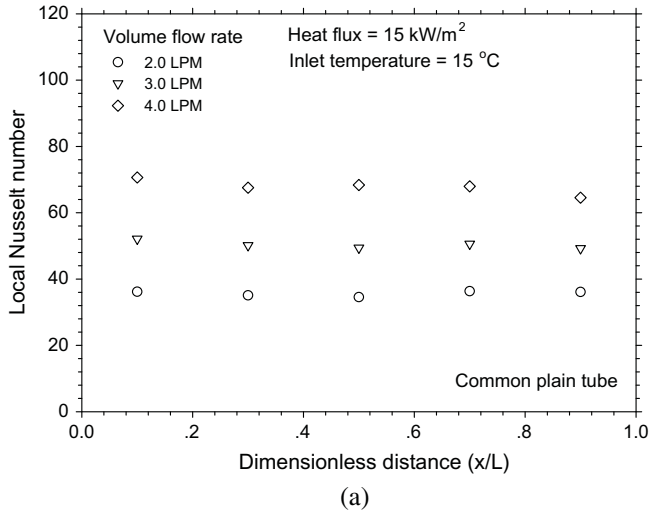

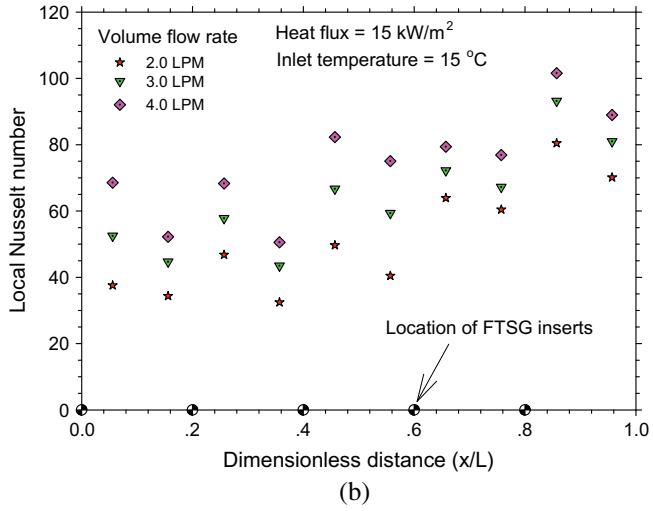

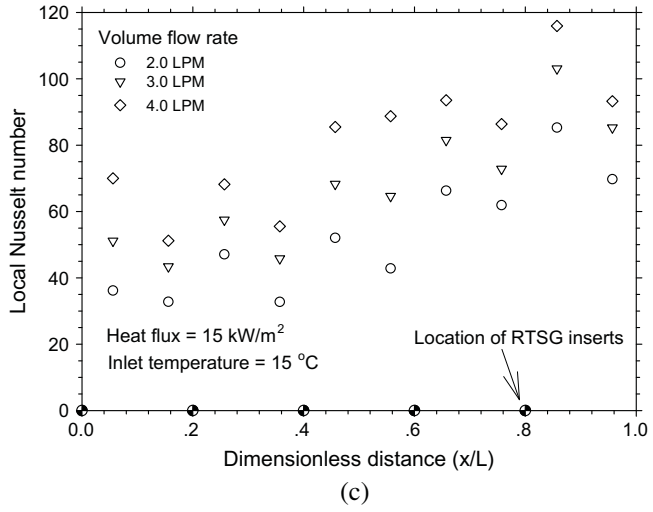

Fig. 7. Local Nusselt number as function of volume flow rate and dimensionless distance: (a) for the common plain tube, (b) for FTSG inserts and (c) for RTSG inserts.

4.2. Pressure drop

Similar to the heat transfer performance, the reliability and accuracy of the pressure drop data should first be verified. The data

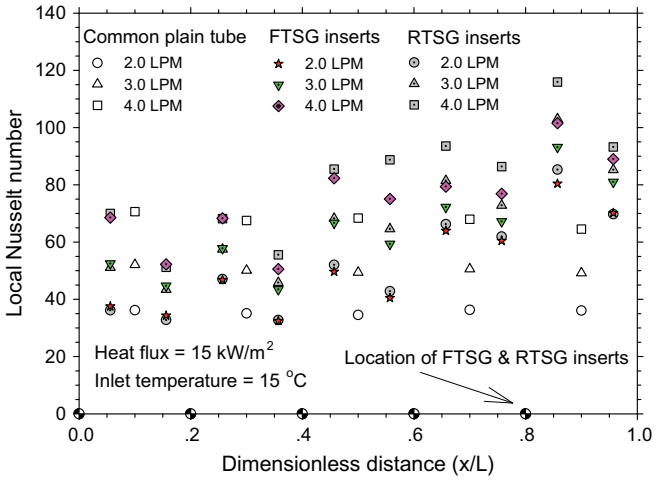

Fig. 8. Comparison between local Nusselt number obtained from the common plain tube and those obtained from FTSG and RTSG inserts.

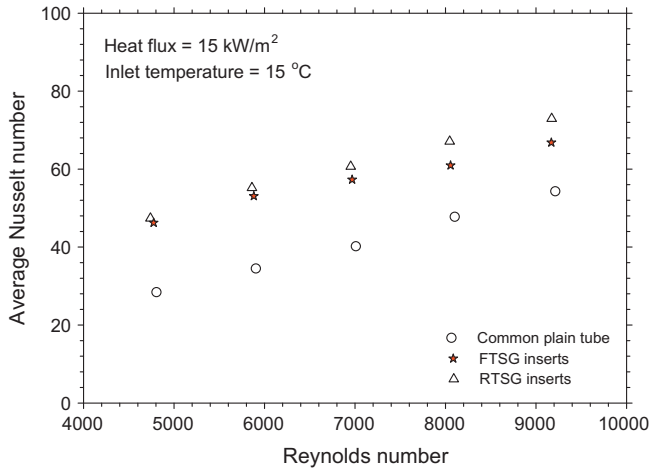

Fig. 9. Comparison of the average Nusselt number between the common plain tube, FTSG and RTSG inserts.

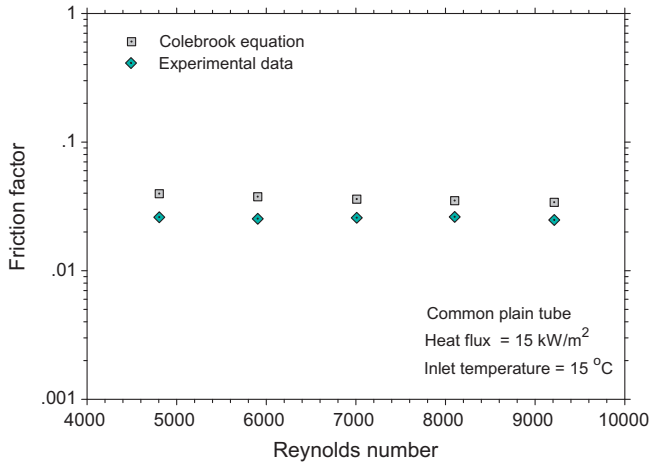

Fig. 10. Comparison between the Colebrook equation and the measured data for friction factor of common plain tube.

of the measured friction factors are compared with those obtained from the Colebrook equation [10]. As shown in Fig. 10, the exper-

Author's personal copy

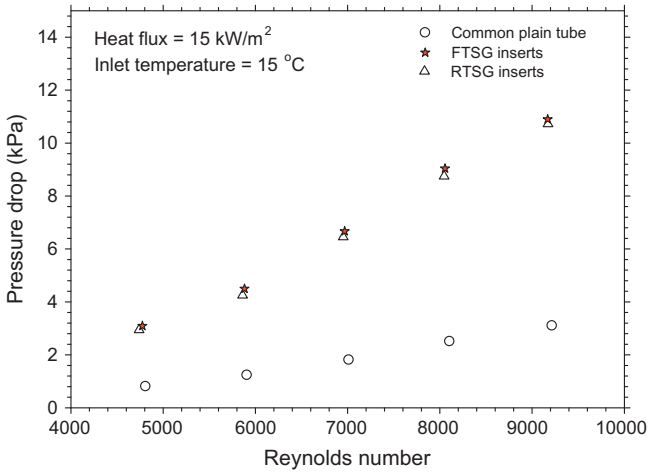

Fig. 11. Comparison of the pressure drop obtained from the common plain tube, FTSG and RTSG inserts.

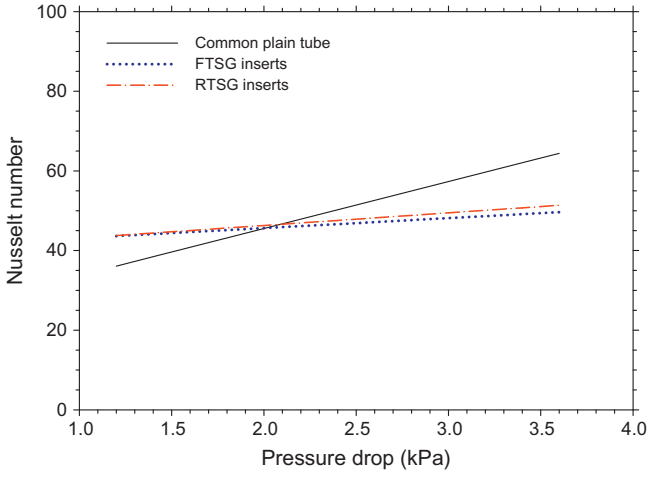

Fig. 12. Relationship between Nusselt number and pressure drop for all tubes.

imental friction factor agrees well with those of calculated values for the common plain tube.

In general, the addition of some swirl flow devices into the main flow will provide a higher penalty drop in the pressure. The value of a pressure drop should be minimized as well as possible. As shown in Fig. 11, the measured data indicate that the pressure drop of the tube with RTSG inserts is smaller than that of the tube with FTSG inserts by a few percent. It is caused from the effect of free rotation of the RTSG, which can not resist the flow as a case of FTSG inserts.

Fig. 12 shows the variation of the Nusselt number with pressure drop in the plain tube, FTSG and RTSG inserts. At pressure drop less than 2.0 kPa (lower flow rate), it can be seen that the average Nusselt number of RTSG and FTSG inserts are significantly higher than that of the common plain tube at the same pressure drop (or the same pumping power). However, opposite behaviors is obtained for the pressure drop greater than 2.0 kPa (higher flow rate). As shown above, the use of swirl flow device inserts can create higher heat transfer performance and pressure drop than the common plain tube simultaneously. This means that the tubes with swirl generator inserts consume much more pumping power than the plain tube and also give lower heat transfer performance, especially at high pressure drop (higher flow rate). Thus, an attempt to minimize the pressure drop in the case of swirl device inserts is the challenge task in order to meet the highest performance of the heat transfer apparatus.

5. Conclusions

This paper presents an experimental investigation on the heat transfer and pressure drop behaviors of a common circular tube with fixed (FTSG) and freely rotating turbine-type swirl generator (RTSG) inserts. Both types of the swirl devices are new designs. The measured data for the common circular tube are used for comparison. Major findings have been given as follows:

- The tube fitted with RTSG gives a larger heat transfer performance than that of the FTSG inserts. For both cases, unusual local heat transfer behaviors are observed.
- The tube with RTSG inserts promotes higher heat transfer performance than the FTSG and common plain tube by about 6.3% and 56%, respectively.
- The tube fitted with RTSG gives a smaller pressure drop than the FTSG and the common plain tube by approximately a few percent.
- Use of the RTSG insert instead of FTSG insert gives a higher heat transfer performance and lower pressure drop.

Acknowledgments

The authors would like to express their appreciation to the Thailand Research Fund, the Office of the Higher Education Commission and the National Research University Project for providing financial support.

References

[1] W. Duangthongsuk, S. Wongwises, An experimental investigation of the heat transfer and pressure drop characteristics of a circular tube fitted with rotating turbine-type swirl generators, Experimental Thermal and Fluid Science 45 (2013) 8–15.
[2] G. Pathipakka, P. Sivashanmugam, Heat transfer behaviour of nanofluids in a uniformly heated circular tube fitted with helical inserts in laminar flow, Supperlattices and Microstructures 47 (2010) 349–360.
[3] M. Chandrasekar, S. Suresh, A. Chandra Bose, Experimental studies on heat transfer and friction factor characteristics of Al_2O_3/water nanofluid in a circular pipe under laminar flow with wire coil inserts, Experimental Thermal and Fluid Science 34 (2010) 122–130.
[4] S. Suresh, P. Selvakumar, M. Chandra Bose, V.S. Raman, Experimental studies on heat transfer and friction factor characteristics of Al_2O_3/water nanofluid under turbulent flow with spiraled rod inserts, Chemical Engineering and Processing: Process Intensification 53 (2012) 24–30.
[5] M. Saeedinia, M.A. Akhavan-Behabadi, M. Nasr, Experimental study on heat transfer and pressure drop of nanofluid flow in a horizontal coiled wire inserted tube under constant heat flux, Experimental Thermal and Fluid Science 36 (2012) 158–168.
[6] Z. Zhang, Y. Ding, C. Guan, H. Yan, W. Yang, Heat transfer enhancement in double-pipe heat exchanger by means of rotor-assembled strands, Chemical Engineering and Processing: Process Intensification 60 (2012) 26–33.
[7] H. Bas, V. Ozceyhan, Heat transfer enhancement in a tube with twisted tape inserts placed separately from the tube wall, Experimental Thermal and Fluid Science 41 (2012) 51–58.
[8] S. Bhattacharyya, S.K. Saha, Thermohydraulics of laminar flow through a circular tube having integral helical rib roughness and fitted with centre-cleared twisted-tape, Experimental Thermal and Fluid Science 42 (2012) 154–162.
[9] V. Gnielinski, New equations for heat and mass transfer in turbulent pipe and channel flow, International Journal of Chemical Engineering 16 (1976) 359–368.
[10] C.F. Colebrook, Turbulent flow in pipes with particular reference to the transition between the smooth and rough pipe laws, Journal- Institution of Civil Engineers 11 (1939) 133.

International Communications in Heat and Mass Transfer 47 (2013) 98–104

Contents lists available at ScienceDirect

International Communications in Heat and Mass Transfer

journal homepage: www.elsevier.com/locate/ichmt

Performance characteristics of a microchannel heat sink using TiO_2/water nanofluid and different thermophysical models ☆

Piyanut Nitiapiruk [a], Omid Mahian [b,*], Ahmet Selim Dalkilic [c], Somchai Wongwises [a,d,**]

[a] Fluid Mechanics, Thermal Engineering and Multiphase Flow Research Lab. (FUTURE), Department of Mechanical Engineering, Faculty of Engineering, King Mongkut's University of Technology Thonburi, Bangmod, Bangkok 10140, Thailand
[b] Young Researchers Club and Elites, Mashhad Branch, Islamic Azad University, Mashhad, Iran
[c] Heat and Thermodynamics Division, Department of Mechanical Engineering, Yildiz Technical University, Yildiz, Besiktas, Istanbul 34349, Turkey
[d] The Academy of Science, The Royal Institute of Thailand, Sanam Suea Pa, Dusit, Bangkok 10300, Thailand

ARTICLE INFO

Available online 13 July 2013

Keywords:
Microchannel
Nanofluids
Thermophysical properties
Performance characteristics

ABSTRACT

In this paper, the performance of a microchannel heat sink using TiO_2/water nanofluid is experimentally investigated. The dimensions of the microchannel are 500 μm width, 800 μm height, and 40 mm length, where the number of flowing channels is 40.The effects of uncertainties in thermophysical properties on the Nusselt number and friction factor are investigated by using three different sets of thermophysical models, which are based on experimental and theoretical relations. It is concluded that the use of the model which is based on experimental data is very important to estimate the friction factor, while the use of different models to calculate of thermal conductivity has no considerable effect on the prediction of Nusselt number.

© 2013 Elsevier Ltd. All rights reserved.

1. Introduction

The use of nanofluids in various fields of thermal engineering has been developed. The nanofluids are used to enhance the efficiency and performance of thermal systems. For instance, the nanofluids could be utilized in cooling of electronics, combustion, fuel cell, medicine, heat exchangers [1,2] and renewable energy systems [3] while some review papers have been reported on the enhancement of heat transfer using nanofluids [4–6].

It is over than two decades that microchannel heat sinks have attracted special attention because of their ability to generate high heat transfer rate, small size, and small coolant requirements [7]. Many studies both experimentally and theoretically have been done on the performance of microchannels using common fluids. However, relatively there are few reports on the performance of microchannels where the working fluid is a nanofluid. Also, the number of experimental studies is less than the theoretical ones because of difficulties to perform experiments with microchannels and nanofluids. Here, the former experimental works on the flow of nanofluids in microchannels are reviewed briefly. Chein and Chuang [8] tested a microchannel heat sink using CuO/water nanofluid with volume fractions of 0.2% to 0.4%. They concluded that using nanofluids in high volume flow rates is not beneficial, but at low flow rates, the use of nanofluids is more helpful than water to absorb the heat from microchannel. Jung et al. [9] measured the convective heat transfer coefficient and friction factor of Al_2O_3/water nanofluid through a rectangular microchannel. They found that the convective heat transfer coefficient of the nanofluid with volume fraction of 1.8% is higher than water by 32% while the authors revealed that using the nanofluid has no considerable effect on the magnitude of friction factor. Ho et al. [10] tested the effects of Al_2O_3/water nanofluid on the heat transfer rate and friction factor in a microchannel heat sink with 25 flowing channels. For each channel, the length, width, and height are 50 mm, 283 μm and 800 μm, respectively. They indicated that the use of nanofluid is more beneficial than water. Also, it is found that the use of nanofluids results in a slight increase of friction factor. Wang et al. [11] investigated the performance of a microchannel heat sink using ZnO/water. They concluded that at a low Reynolds number (i.e. 3.8), the heat transfer coefficient of the nanofluid is higher than water by 13%. Vafaei and Wen [12] studied the subcooled flow boiling of Al_2O_3/water nanofluid in a microchannel. They found that the critical heat flux increases up to 51%, by using only 0.1% volume fraction of nanoparticles. Xu et al. [13] compared the effects of two different working fluids including water and Al_2O_3/water nanofluid (mass fraction = 0.2%) on the boiling thermal performance of a rectangular microchannel. They concluded that using the nanofluid enhances heat transfer rate and avoids boiling instability. Byrne et al. [14] used CuO/water nanofluids with and without surfactantin a parallel microchannel flow configuration.

☆ Communicated by W.J. Minkowycz.

* Corresponding author.
** Correspondence to: S. Wongwises, Fluid Mechanics, Thermal Engineering and Multiphase Flow Research Lab. (FUTURE), Department of Mechanical Engineering, Faculty of Engineering, King Mongkut's University of Technology Thonburi, Bangmod, Bangkok 10140, Thailand.
E-mail addresses: omid.mahian@gmail.com (O. Mahian), somchai.won@kmutt.ac.th (S. Wongwises).

0735-1933/$ – see front matter © 2013 Elsevier Ltd. All rights reserved.
http://dx.doi.org/10.1016/j.icheatmasstransfer.2013.07.001

Nomenclature

A	area, m^2
d_f	diameter of molecule of base fluid (m)
d_p	diameter of nanoparticle (m)
D_h	hydraulic diameter (m)
f	friction factor
h	heat transfer coefficient (W/m^2 K)
I	electric current (A)
k	thermal conductivity (W/mK)
L	length (m)
M	molecular weight of water (g/mol)
$\dot{m}$	mass flow rate (kg/s)
N	number of microchannel
Nu	Nusselt number
ΔP	pressure drop (Pa)
q	heat flux (W/m^2)
Q	heat transfer rate (W)
Re	Reynolds number
T	temperature (K)
u_m	mean velocity (m/s)
V	electric voltage (V)
W	width, m

Greek symbols

φ	volume fraction
μ	dynamic viscosity (kg/m s)
ρ	density (kg/m^3)

Subscript

ave	average
ch	channel
f	base fluid
in	inlet
out	outlet
w	wall

They observed that the heat transfer rate increases by 17% for low concentration of nanofluid that is 0.01%. Kalteh et al. [15] estimated the heat transfer rate for a wide rectangular microchannel heat sink (94.3 mm, 28.1 mm and 580 μm; length, width and height, respectively) where the working fluid is Al_2O_3/water nanofluid. They found that the Nusselt number increases with an increase in the Reynolds number and volume fraction of nanoparticles. They also concluded that a decrease in particle's size enhances the heat transfer rate. Duangthongsuk et al. [16] examined the heat transfer and pressure drop due to flow of Al_2O_3/water nanofluid (concentrations up to 3 wt.%) in a microchannel heat sink. They perceived that heat transfer increases by 15% where as using the nanofluid has no significant effect on pressure drop compared to water. Ning and Luo [17] experimented three microchannels with different hydraulic diameters using Al_2O_3/water nanofluid. They observed that with increasing the particle loading the Nusselt number increases while pressure drop decreases a little. In another work, the flow boiling heat transfer in a single microchannel with a size of 7500 × 100 × 250 μm is investigated using water and Al_2O_3/water nanofluid with weight concentration of 0.2% [18]. Recently, Anoop et al. [19] investigated the forced convection heat transfer of silica/water nanofluids in a microchannel with the size of 8 mm × 12 mm × 100 μm (width × length × height) where the wall temperature is kept as constant. Regarding the effects of uncertainties in thermophysical properties on the flow and heat transfer characteristics of nanofluids, Duangthongsuk and Wongwises [20] in study of turbulent flow of TiO_2 nanofluid in a heat exchanger concluded that the different models have no significant effect on the results. In another work, Mahian et al. [21] studied the effects of uncertainties in thermophysical models on prediction of entropy generation due to nanofluid flow between two rotating cylinders. They considered six different models and showed that the use of different models may give opposite results, so that one model predicts that using nanofluids increases the entropy generation, while another model predicts the decrease of entropy generation.

In this study, the heat transfer and pressure drop ofTiO_2/Water nanofluid flowing in a microchannel heat sink are experimentally investigated. The effects of uncertainties in thermophysical properties(Thermal conductivity and viscosity) on the prediction of Nusselt number and friction factor in a microchannel are investigated. Three sets of models are used to predict the viscosity and thermal conductivity. The size of the microchannel, the amounts of heat flux applied to the microchannel are completely in accordance with real situations observed in the personal computers.

2. Nanofluids preparation

In the present study, TiO_2/water nanofluid solution with a concentration of40 wt.% is provided from Degussa Company, Germany. The original solution is diluted before the beginning of experiments through adding water to prepare nanofluids with volume fractions of 0.5%, 1%, and 2%. In the preparation of nanofluids, the most important issue is the prevention of sedimentation of nanoparticles. An ultrasonic vibrator is used for 4 hours to sonicate the mixture to avoid the sedimentation.No sedimentation of nanoparticles has been observedduring the experiments

3. Experimental apparatus and procedure

The schematic of the experimental set up is shown in Fig. 1. The system consists of a temperature-controlled inlet tank, a temperature-controlled outlet tank, and a test section. The temperature of nanofluid is adjusted before entering the test section with cooling coils and a heater. Then, the nanofluid is pumped to the test section. The temperature of nanofluid is measured at four points in the inlet of the test section and at four points in the outlet of it, using T-type thermocouples with an accuracy of 0.1 °C. To measure the wall temperature of the microchannel, six T-type thermocouples are used, and to measure the pressure drop within the microchannel a differential pressure transmitter with accuracy of 0.01 kPa is used. The pressures are measured at three positions in the inlet and three positions in the outlet of the microchannel. The microchannel is heated using a power supply with the power of 90 W, where the output current is between 0 and 3 A and the output voltage is between 0 and 30 V. Three different values of heat flux including 50.6, 60.7, and 69.1 W are applied to the microchannel at each test. After heating, the nanofluid enters the temperature-controlled outlet tank to circulate. The range of flow rate is between 344 and 2363 cm^3/min with Reynolds numbers of250–1700. The time required to reach steady state conditions for each test is about 20–60 min. Fig. 2 illustrates two perspectives of the test section. The positions of the eight thermocouples in the inlet and outlet of the microchannel, data logger, pressure transmitter, and power supply are shown in Fig. 2(a). Fig. 2(b) displays the flow pattern of the nanofluid where the nanofluid passes through the microchannels. The width and height of microchannel are 500 μm, and 800 μm respectively. The 500 μm thick fins run throughout the total length of 40 mm, with a total width of40.5 mm and thickness of4 mm.

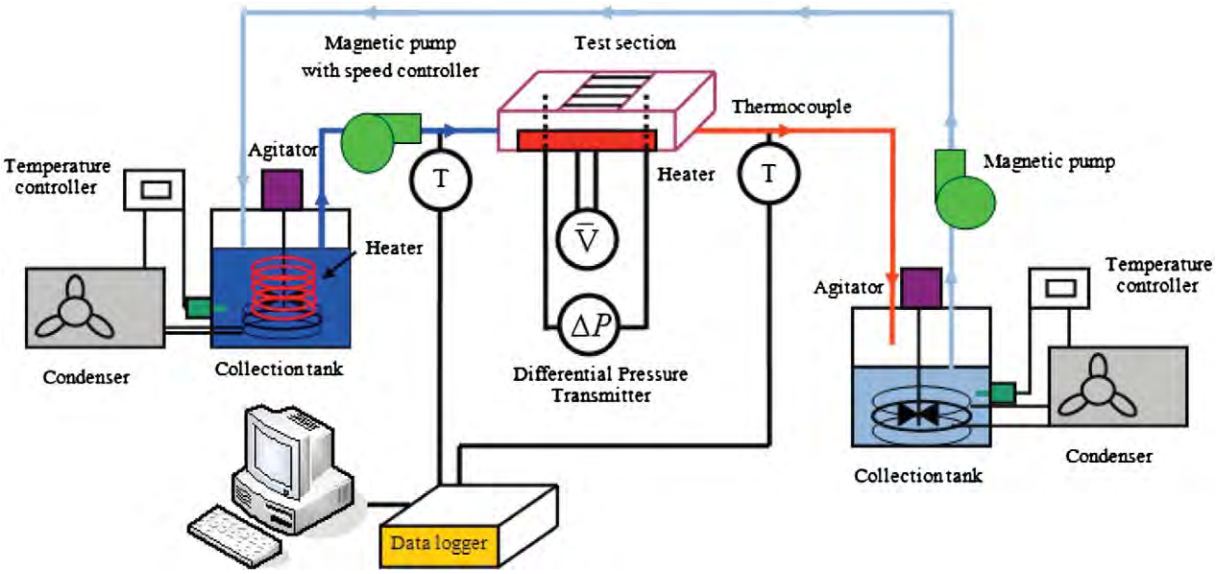

Fig. 1. Schematic diagram of experimental apparatus.

4. Data reduction

First, the relations that are used to calculate the thermophysical properties of nanofluid are presented. The density of nanofluids is calculated by using the following relation [22]:

$$\rho_{nf} = \phi \cdot \rho_p + (1-\phi) \cdot \rho_w \quad (1)$$

where ρ_{nf},ρ_p, and ρ_w are densities of the nanofluid, nanoparticle, and water, respectively.To study the effects of uncertainties in thermophysical properties (thermal conductivity and viscosity)on the performance characteristics of the microchannel three sets of models are used in as follows:

Model # 1 This model is the combination of the most used theoretical equations. The viscosity in model #1 is calculated by the

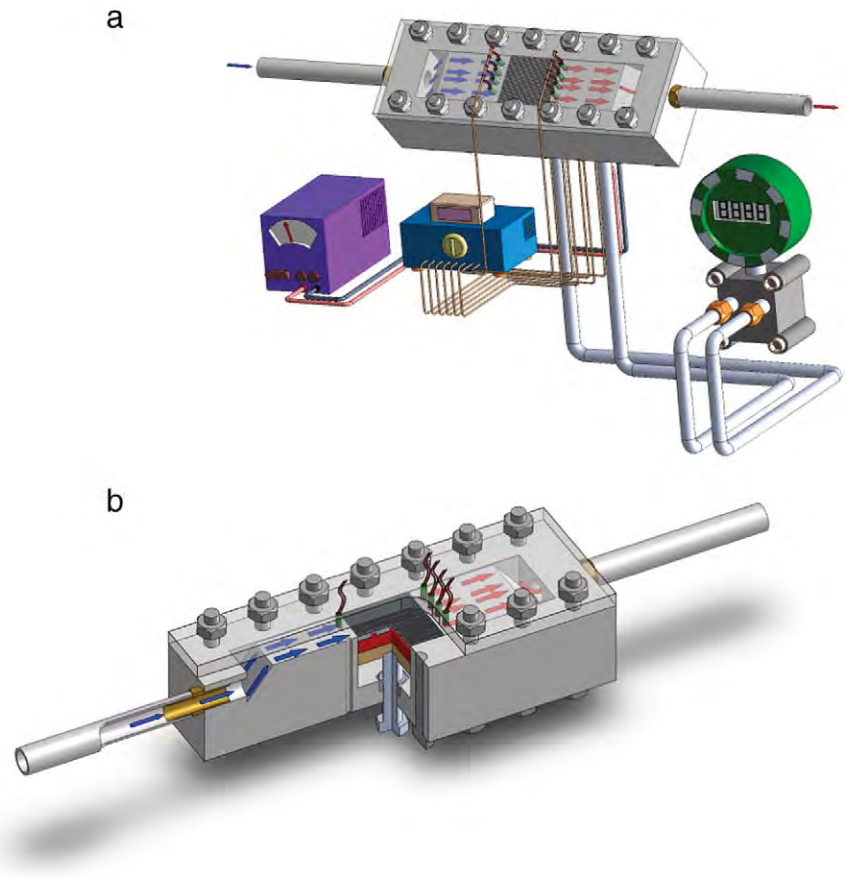

Fig. 2. Prospectives of the microchannel: (a) overview of the microchannel and measurement devices and (b) cross-sectional view of microchannel test section.

Brinkman relation [22]:

$$\frac{\mu_{nf}}{\mu_f} = \frac{1}{(1-\phi)^{2.5}} \tag{2}$$

For the thermal conductivity of model#1, the Maxwell equation [22] is utilized:

$$\frac{k_{nf}}{k_f} = \frac{k_p + 2k_f + 2\phi\left(k_p - k_f\right)}{k_p + 2k_f - \phi\left(k_p - k_f\right)} \tag{3}$$

Model # 2 In this model that is the combination of the newer relations, the viscosity is calculated as [23]:

$$\frac{\mu_{nf}}{\mu_f} = \frac{1}{1-34.87\left(d_p/d_f\right)^{-0.3}\phi^{1.03}} \tag{4}$$

where d_p is nanoparticle size, and d_f is the molecule diameter of base fluid which can be calculated by:

$$d_f = \left[\frac{6M}{N\pi\rho_{f,0}}\right]^{1/3} \tag{5}$$

where M is the molecular weight of base fluid, N is the Avogadro number, and $\rho_{f,0}$ is the density of base fluid calculated at the temperature of 293 K.To obtain the thermal conductivity, the Yu and Choi relation is used [24]:

$$\frac{k_{nf}}{k_f} = \frac{k_p + 2k_f + 2\left(k_p - k_f\right)(1+\beta)^3\phi}{k_p + 2k_f - \left(k_p - k_f\right)(1+\beta)^3\phi} \tag{6}$$

where $\beta = 0.1$.

Model # 3 This model is based on experimental data. Duangthongsuk and Wongwises [25] based on their experimental data on TiO_2/water nanofluid, presented following models to calculate the viscosity and thermal conductivity as: Viscosity:

$$\frac{\mu_{nf}}{\mu_f} = \left(a + b\phi + c\phi^2\right) \tag{7}$$

Thermal conductivity:

$$\frac{k_{nf}}{k_f} = d + e\phi \tag{8}$$

where a, b, c, d and e are functions of temperature.

Using the above models the Nusselt number and friction factor are calculated and the results are compared.

The amount of heat transfer to the nanofluid in the microchannel is determined as:

$$Q_{nf} = VI \tag{9}$$

where Q_{nf} is heat transferred to nanofluid, V is electrical voltage, and I is electrical current.The average convective heat transfer coefficient for the nanofluid is obtained as:

$$\overline{h}_{nf} = \frac{Q_{nf}}{A \cdot \left(T_{wall} - T_{nf}\right)} \tag{10}$$

where $\overline{h}_{nf}$ is the average convective heat transfer coefficient of the nanofluid, T_{wall} is the wall temperature of microchannel, T_{nf} is the temperature of nanofluid, and A is the surface area of the channels.Nusselt number is obtained based on the following relation:

$$\overline{N}u_{nf} = \frac{\overline{h}_{nf} \cdot D_h}{k_{nf}} \tag{11}$$

where $\overline{N}u_{nf}$ is the Nusselt number of nanofluids and D_h is the hydraulic diameter of the channel.To calculate the friction factor in the channel, following relation is used:

$$f_{nf} = \frac{2D_h\Delta P}{L\rho_{nf}u_m^2} \tag{12}$$

where ΔP is he pressure drop and it is obtained based on the experiments. Also, L is the length of the microchannel and u_m is the average velocity of the nanofluid in the microchannel. It should be noted that the friction factor will be depended to viscosity where the right hand side of Eq. (12), is defined based on the Reynolds number.

It is helpful to define the augmentation Nusselt number, which is the ratio between the Nusselt number of nanofluid to the Nusselt number of base fluid, as follows:

$$Nu_a = \frac{\overline{N}u_{nf}}{\overline{N}u_f} \tag{13}$$

This relation helps to find that using a nanofluid at a specified volume fraction how much is beneficial compared to the base fluid. A greater augmentation Nusselt number implies that using the nanofluid is more beneficial than the base fluid from the heat transfer point of view.

It should be noted that the uncertainty in Nusselt number and heat transfer coefficient does not exceed 4%.

5. Results and discussions

In this section, first, the results related to heat transfer coefficient are presented. Next, the effects of uncertainties in viscosity and thermal conductivity on the Nusselt number are discussed. Fig. 3 shows the variations of heat transfer coefficient with the Reynolds number for different volume fractions at heat fluxof69.1 W.

It is observed that the convective heat transfer coefficient increases with increasing the volume fraction of nanoparticles. This happens because of some factors such as Brownian motion of nanoparticles, higher thermal conductivity of nanoparticles. However, it is unknown that how much the heat transfer coefficient increases with increasing the volume fraction. For instance, it is seen from Fig. 3 that at low Reynolds

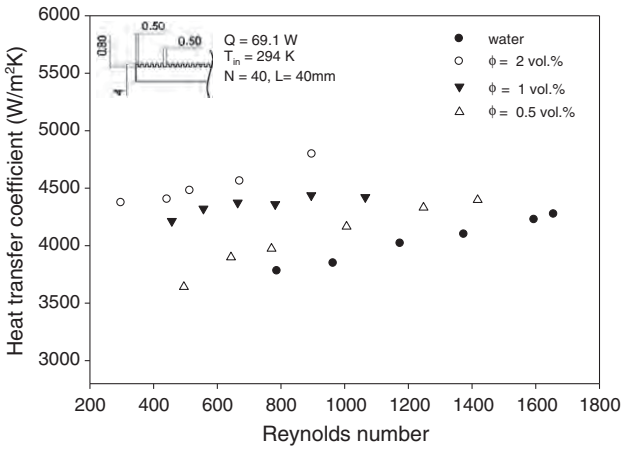

Fig. 3. Heat transfer coefficient at different volume fractions for Q = 69.1 W.

numbers (Re ≈ 400), with increasing the volume fraction from 0.5% to 1% the heat transfer coefficient increases more than 500 W/m^{2}K, while the amount of increase in the heat transfer coefficient is not more than 200 W/m^{2}K where the volume fraction increases from 1.5% to 2%. It is also perceived that with increasing the Reynolds number the heat transfer coefficient increases especially at the volume fraction of 0.5%. The gradient of heat transfer coefficient at concentration of 0.5% is greater than other concentrations because the unfavorable effects of viscous forces for $\phi = 0.5\%$ are lowest compared to other concentrations.

Figs. 4–6 show the variations of the Nusselt number with the volume fraction for the three sets of models, two amounts of Reynolds number including 400 and 1200 and three values of heat flux. From the figures it is found that the difference between the Nusselt numbers predicted by the three models is approximately 2%, and occurs at the concentration of 2%. In other concentrations (i.e. 0.5% and 1%), the difference is lower. Therefore, it is concluded that even using the Maxwell model which is a temperature-independent model may be reasonable for calculating the Nusselt number in the microchannels. From Figs. 4–6, it is also observed that the Nusselt number increases between 13% and 20% with increasing the volume fraction from 0 to 2%.

Table 1 provides the augmentation Nusselt numbers at different volume fractions for model 3 and for the three heat fluxes applied to the microchannel. It can be seen that the augmentation Nusselt number has the maximum amount at the maximum volume fraction

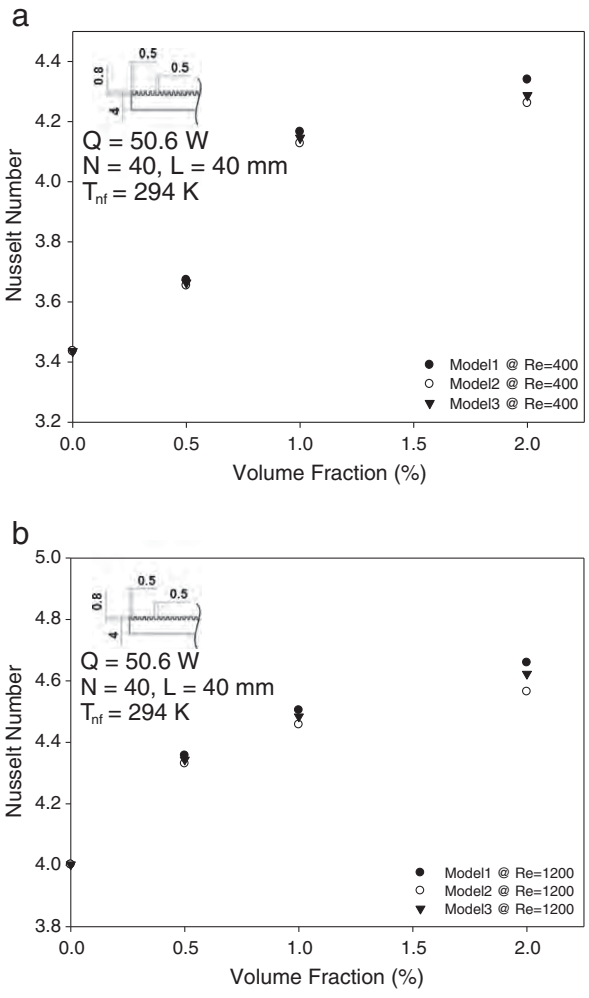

Fig. 4. Effects of uncertainties on the Nusselt number for Q = 50.6 W for (a) Re = 400 and (b) Re = 1200.

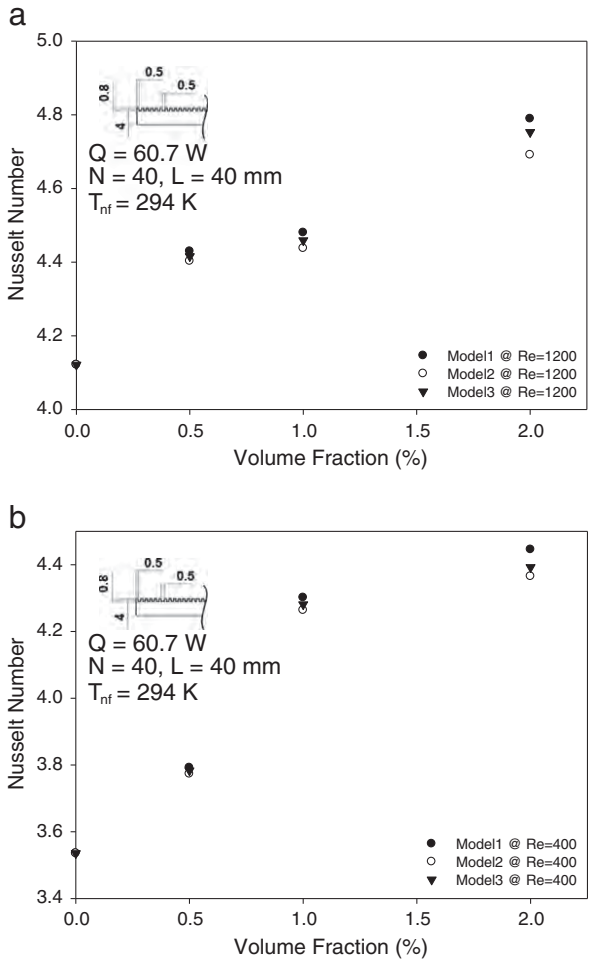

Fig. 5. Effects of uncertainties on the Nusselt number for Q = 60.7 W for (a) Re = 400 and (b) Re = 1200.

(2%) and minimum values of the Reynolds number (Re = 400) and heat flux (Q = 50.6 W). In other words, for Re = 400, and Q = 50.6 W, adding nanoparticles by 2% gives the best results from the heat transfer point of view compared other values of heat flux and the Reynolds number. On the other hand, the augmentation Nusselt number is minimized at Re = 400, Q = 69.1 W for concentration of 0.5.

Fig. 7 shows the effects of different models on the friction factor for Re = 400 and Re = 1200, and various volume fractions of nanoparticles. It can be observed that the difference between the results predicted by the models increases with increasing the volume fraction as expected. As shown in Fig. 7(a), for Re = 400, based on model #2 the friction factor increases with increasing the volume fraction while the models 1 and 3 predict that with increasing the volume fraction from 1.5% to 2%, the friction factor decreases. It is concluded that model # 2 fails to predict the trend of variations of friction factor. The increase of concentration from 1.5 to 2%, leads to a decrease in friction factor because of increasing the nanofluid density. In this case, the density of nanofluid increases with a higher rate compared to the pressure drop increase, and hence the friction factor decreases (see Eq. (12)). It can be seen also that model #3 gives the smallest amount of friction factor. At $\phi = 2\%$, the difference between the friction factors predicted by models 1 and 3 is about 14%, while the difference between the friction factors predicted by models 1 and 2 is about 21%. This shows that using model#3 which is based on experimental data is necessary to have an accurate estimation of friction factor. For Re = 1200 (Fig. 7(b)), it is found that all models predict the same trend for the friction factor where the volume

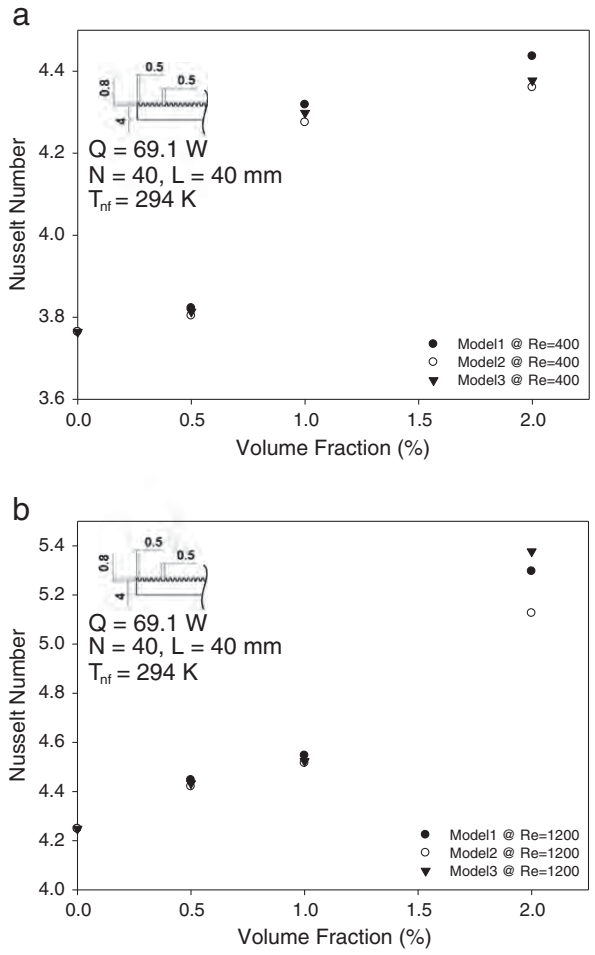

Fig. 6. Effects of uncertainties on the Nusselt number for Q = 69.1 W for (a) Re = 400 and (b) Re = 1200.

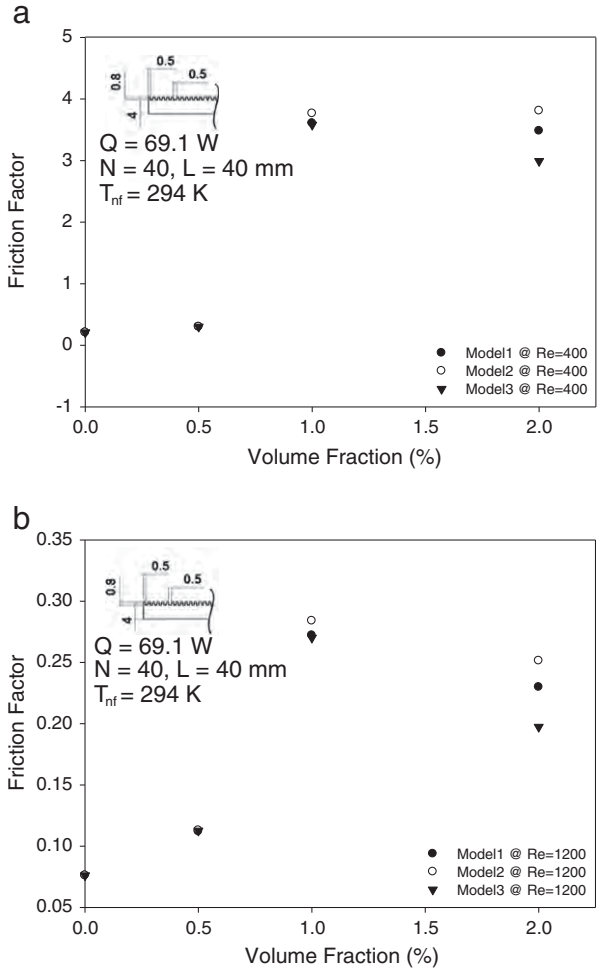

Fig. 7. Effects of uncertainties on the friction factor for Q = 69.1 W and (a) Re = 400, (b) Re = 1200.

fraction increases from 1.5% to 2%. However, the differences among the models are large, similar to the case of Re = 400.

6. Conclusion

An experimental study is performed on the flow and heat transfer of TiO_2/water nanofluid (with volume fractions between 0.5% and 2%) in a microchannel with a focus on the effects of uncertainties in thermal conductivity and viscosity models on the prediction of Nusselt number and friction factor. The size of microchannel and heat fluxes applied to the microchannels, are selected based on practical applications. To do this, three sets of models are used to calculate the thermal conductivity and viscosity of nanofluids. The results show that even the use of a very old model such as Maxwell model to calculate the thermal conductivity gives very good estimation of the Nusselt number. It is found that the difference among the Nusselt numbers predicted by the various models is about 2% (at ϕ = 2%), which is not considerable. However, for the friction factor, it is observed that the differences between the friction factors predicted by the three models at ϕ = 2% are great, so that using the viscosity obtained based on the experimental data is necessary to estimate the friction factor. From the values obtained for the augmentation Nusselt number, it is concluded that the use of nanofluid with volume fraction of 2% in the minimum amounts of heat flux and Reynolds number is more advantageous compared other situations.

Table 1
Augmentation Nusselt number at different heat fluxes and volume fractions.

	Nu_a at Q = 50.6 W		Nu_a at Q = 60.7 W		Nu_a at Q = 69.1 W	
Volume fraction (%)	Re = 400	Re = 1200	Re = 400	Re = 1200	Re = 400	Re = 1200
0	1	1	1	1	1	1
0.5	1.066332	1.085192	1.070055	1.071436	1.013103	1.043571
1	1.206521	1.120315	1.210766	1.081913	1.165728	1.086858
2	1.24769	1.154983	1.242311	1.15319	1.163649	1.170568

Acknowledgements

The present study was supported financially by the Thailand Research Fund and the National Research University Project, whose guidance and assistance are gratefully acknowledged. The second and third authors would like to thank Professor Somchai Wongwises for providing them for support during their research in the Department of Mechanical Engineering, King Mongkut's University of Technology Thonburi.

References

[1] R. Saidur, K.Y. Leong, H.A. Mohammad, A review on applications and challenges of nanofluids, Renewable and Sustainable Energy Reviews 15 (3) (2011) 1646–1668.
[2] W. Duangthongsuk, S. Wongwises, An experimental study on the heat transfer performance and pressure drop of TiO2-water nanofluids flowing under a turbulent flow regime, International Journal of Heat and Mass Transfer 53 (1–3) (2010) 334–344.
[3] O. Mahian, A. Kianifar, S.A. Kalogirou, I. Pop, S. Wongwises, A review of the applications of nanofluids in solar energy, International Journal of Heat and Mass Transfer 57 (2) (2013) 582–594.

[4] W. Daungthongsuk, S. Wongwises, A critical review of convective heat transfer of nanofluids, Renewable and Sustainable Energy Reviews 11 (5) (2007) 797–817.
[5] V. Trisaksri, S. Wongwises, Critical review of heat transfer characteristics of nanofluids, Renewable and Sustainable Energy Reviews 11 (3) (2007) 512–523.
[6] L. Godson, B. Raja, D. Mohan Lal, S. Wongwises, Enhancement of heat transfer using nanofluids—an overview, Renewable and Sustainable Energy Reviews 14 (2) (2010) 629–641.
[7] R. Chein, G. Huang, Analysis of microchannel heat sink performance using nanofluid, Applied Thermal Engineering 25 (17–18) (2005) 3104–3114.
[8] R. Chein, J. Chuang, Experimental microchannel heat sink performance studies using nanofluids, International Journal of Thermal Sciences 46 (1) (2007) 57–66.
[9] J.Y. Jung, H.-S. Oh, H.-Y. Kwak, Forced convective heat transfer of nanofluids in microchannels, International Journal of Heat and Mass Transfer 52 (1–2) (2009) 466–472.
[10] C.J. Ho, L.C. Wei, Z.W. Li, An experimental investigation of forced convective cooling performance of a microchannel heat sink with Al2O3/water nanofluid, Applied Thermal Engineering 30 (2–3) (2010) 96–103.
[11] Y. Wang, S.J. Chung, J.P. Leonard, S.K. Cho, T. Phuoc, Y. Soong, M.K. Chyu, Cooling performance of nanofluids in a microchannel heat sink, Proceedings of the ASME Micro/Nanoscale Heat and Mass Transfer International Conference 2009, MNHMT2009, 1, 2009, pp. 617–623.
[12] S. Vafaei, D. Wen, Critical heat flux (CHF) of subcooled flow boiling of alumina nanofluids in a horizontal microchannel, Journal of Heat Transfer 132 (10) (2010) 1–7.
[13] L. Xu, Y.-X. Li, J.-L. Xu, G.-H. Liu, Flow boiling heat transfer performance of nanofluids in a microchannel, Journal of Chemical Engineering of Chinese Universities 25 (4) (2011) 559–564.
[14] M.D. Byrne, R.A. Hart, A.K. Da Silva, Experimental thermal-hydraulic evaluation of CuO nanofluids in microchannels at various concentrations with and without suspension enhancers, International Journal of Heat and Mass Transfer 55 (9–10) (2012) 2684–2691.
[15] M. Kalteh, A. Abbassi, M. Saffar-Avval, A. Frijns, A. Darhuber, J. Harting, Experimental and numerical investigation of nanofluid forced convection inside a wide microchannel heat sink, Applied Thermal Engineering 36 (1) (2012) 260–268.
[16] W. Duangthongsuk, A.S. Dalkilic, S. Wongwises, Convective heat transfer of Al_2O_3-water nanofluids in a microchannel heat sink, Current Nanoscience 8 (3) (2012) 317–322.
[17] C.-J. Ning, X.-P. Luo, Heat transfer and pressure drop of Al 2O3 nanofluids in microchannels, Journal of Central South University (Science and Technology) 43 (8) (2012) 3000–3006.
[18] L. Xu, J. Xu, Nanofluid stabilizes and enhances convective boiling heat transfer in a single microchannel, International Journal of Heat and Mass Transfer 55 (21–22) (2012) 5673–5686.
[19] K. Anoop, R. Sadr, J. Yu, S. Kang, S. Jeon, D. Banerjee, Experimental study of forced convective heat transfer of nanofluids in a microchannel, International Communications in Heat and Mass Transfer 39 (9) (2012) 1325–1330.
[20] W. Duangthongsuk, S. Wongwises, Effect of thermophysical properties models on the predicting of the convective heat transfer coefficient for low concentration nanofluid, International Communications in Heat and Mass Transfer 35 (2008) 1320–1326.
[21] O. Mahian, S. Mahmud, S. Zeinali Heris, Effect of uncertainties in physical properties on entropy generation between two rotating cylinders with nanofluids, Journal of Heat Transfer 134 (10) (2012) 101704.
[22] K. Khanafer, K. Vafai, A critical synthesis of thermophysical characteristics of nanofluids, International Journal of Heat and Mass Transfer 54 (2011) 4410–4428.
[23] M. Corcione, Heat transfer features of buoyancy-driven nanofluids inside rectangular enclosures differentially heated at the sidewalls, International Journal of Thermal Sciences 49 (2010) 1536–1546.
[24] W. Yu, S.U.S. Choi, The role of interfacial layers in the enhanced thermal conductivity of nanofluids: a renovated Maxwell model, Journal of Nanoparticle Research 5 (2003) 167–171.
[25] W. Duangthongsuk, S. Wongwises, Measurement of temperature-dependent thermal conductivity and viscosity of TiO_2 water nanofluids, Experimental Thermal and Fluid Science 33 (2009) 706–714.

Lazarus Godson Asirvatham[1]
e-mail: godson@karunya.edu;
godasir@yahoo.co.in

Rajesh Nimmagadda
e-mail: rajesh.mech335@gmail.com

Department of Mechanical Engineering,
Karunya University,
Coimbatore 641 114, Tamil Nadu, India

Somchai Wongwises
Fluid Mechanics,
Thermal Engineering and Multiphase Flow
Research Lab (FUTURE),
Department of Mechanical Engineering,
Faculty of Engineering,
King Mongkut's University of Technology,
Thonburi, 126 Bangmod,
Tongkru, Bangkok 10140, Thailand;
The Academy of Science,
The Royal Institute of Thailand,
Sanam Suea Pa, Dusit,
Bangkok 10300, Thailand
e-mail: somchai.won@kmutt.ac.th

Operational Limitations of Heat Pipes With Silver-Water Nanofluids

The paper presents the enhancement in the operational limits (boiling, entrainment, sonic, viscous and capillary limits) of heat pipes using silver nanoparticles dispersed in de-ionized (DI) water. The tested nanoparticles concentration ranged from 0.003 vol. % to 0.009 vol. % with particle diameter of <100 nm. The nanofluid as working fluid enhances the effective thermal conductivity of heat pipe by 40%, 58%, and 70%, respectively, for volume concentrations of 0.003%, 0.006%, and 0.009%. For an input heat load of 60 W, the adiabatic vapor temperatures of nanofluid based heat pipes are reduced by 9 °C, 18 °C, and 20 °C, when compared with DI water. This reduction in the operating temperature enhances the thermophysical properties of working fluid and gives a change in the various operational limits of heat pipes. The use of silver nanoparticles with 0.009 vol. % concentration increases the capillary limit value of heat pipe by 54% when compared with DI water. This in turn improves the performance and operating range of the heat pipe. [DOI: 10.1115/1.4024616]

Keywords: silver, heat pipe, boiling limit, entrainment limit, capillary limit, sonic limit, viscous limit, nanofluid

1 Introduction

Heat pipes are widely used in thermal management of microelectronic devices. The heat transport capability of heat pipe is limited by the working fluid transport properties. The excessive heat transport capacity of the working fluid can be obtained by suspending nanoparticles in base fluids. Choi and Eastman [1] first applied these nanofluids in thermal engineering for efficient heat transfer due to its enhanced thermal conductivity. Many researchers like Shafai et al. [2] and Liu et al. [3] studied the effects of nanofluids on the performance of cylindrical heat pipes and cylindrical microgrooved heat pipes and found that nanofluids as working fluids enhance the performance of heat pipes. Nemec et al. [4] proposed a mathematical model to verify the heat transfer limitations of heat pipe. The modeling was done for ethanol heat pipe operating in the temperature varying from −30 °C to 140 °C with sintered wick and grooved capillary structure. The effect of these limitations on the cooling performance of heat pipes was evaluated. Finally, the study concluded that the increased permeability and increased pore dimensions decreases the capillary pressure. Since, the capillary limit is the primary heat transport limitation of the heat pipe. It was also observed that the capillary limit had the highest influence regarding circulation of the working fluid.

Nemec and Huzvar [5] presented a mathematical analysis of total heat power of the sodium heat pipe on the basis of heat transport limitation equations. The heat pipe was made up of steel with sodium as working fluid and operating temperature ranging from 500 K to 1000 K. It was found that the viscous and sonic limits reach very high values and are not important for influencing the total performance of the heat pipe. The results reported that the capillary limit was the maximum heat transport limitation and subsequently the other limits, such as the entrainment and boiling limits, also influence the heat pipe performance. Naik et al. [6] designed, fabricated, and tested the heat pipe with axially grooved wick for horizontal and gravity assisted conditions. The design was based on five primary heat transport limits which include viscous, sonic, capillary, entrainment, and boiling limits. Three different working fluids, such as methanol, acetone, and distilled water were used and the maximum heat transfer coefficient was found to be 3550 W/m^2 °C, 1700 W/m^2 °C, and 2400 W/m^2 °C, respectively, in horizontal and vertical orientation. Faghri [7] and Peterson [8] explained the modelling of heat pipes based on the various operational limits and suggested that these operational limits mainly depend on the operating temperature and thermophysical properties of working fluids. Thuchayapong et al. [9] presented a numerical approach with finite element method (FEM) to study the effect of capillary pressure on the performance of heat pipe. The two-dimensional heat transfer and fluid flow in a heat pipe at steady-state condition was numerically simulated using FEM. The numerical results indicated that the capillary pressure gradient inside the copper mesh wick at the end of the evaporator section was found to be very high. The finding of the numerical analysis suggested that the capillary pressure was one of the key parameters in the design and efficiency of the heat pipe. Riehl and Santos [10] investigated the operational behaviour of loop heat pipes and pulsating heat pipes (PHPs) with copper-water nanofluids with nanoparticles sizes (diameter) below 40 nm. Results have demonstrated that the liquid's thermal conductivity is enhanced by 20% for a nanoparticles concentration of 5% by mass. Further it is noted that the improvements on the overall device's operation have been observed when using the nanofluid with lower temperatures, as well as a direct influence on the thermal conductance throughout the PHP.

Chiang et al. [11] developed a magnetic-nanofluid (MNF) heat pipe (MNFHP) with magnetically enhanced thermal properties. The results showed that an optimal thermal conductivity exists in the applied field of 200 Oe. Furthermore, the minor thermal performance of MNF at the condenser limited the thermal conductivity of the entire MNFHP, which was 1.6 times greater than that

[1]Corresponding author.

Contributed by the Heat Transfer Division of ASME for publication in the Journal of Heat Transfer. Manuscript received May 28, 2012; final manuscript received March 9, 2013; published online September 23, 2013. Assoc. Editor: Sujoy Kumar Saha.

 Copyright © 2013 by ASME

Downloaded From: http://heattransfer.asmedigitalcollection.asme.org/ on 10/09/2013 Terms of Use: http://asme.org/terms

filled with water for the input power of 60 W. Liu and Li [12] reviewed the research done on heat pipes using nanofluids as working fluids in recent years. The effect of characteristics and mass concentrations of nanoparticles on the thermal performance, the mechanism of enhancement, or degradation of heat transfer and the relative reduction of the total heat resistance for various heat pipes with nanofluids are summarized in comparison with the existing ones and also presented a perspective on possible future research applications. Putra et al. [13] investigated the thermal performance and the effect of coatings on the structure of screen mesh wick heat pipes with Al_2O_3–water, Al_2O_3–ethylene glycol, TiO_2–water, TiO_2–ethylene glycol, and ZnO–ethylene glycol nanofluids with the concentration of the nanoparticles varied from 1% to 5% of the volume of the base fluid. It is observed that the screen mesh wick heat pipe with Al_2O_3–water nanofluid with 5% volume concentration yielded the best performance. Further it is noted that the use of nanofluids resulted in the formation of a thin coating on the screen mesh surface from the element of the nanoparticles which enhanced the thermal performance in the heat pipes. Hajian et al. [14] experimentally studied the thermal performance of silver-DI water nanofluids with concentrations of 50, 200, and 600 ppm in a medium-sized cylindrical meshed heat pipe, under both transient and steady-state conditions. The results showed that the thermal resistance and response time of the heat pipe decreased up to 30% and 20%, respectively, compared with DI water.

Alizad et al. [15] analyzed the thermal performance, transient behavior, and operational start-up characteristics of flat-shaped heat pipes using CuO, Al_2O_3, and TiO_2 nanofluids. The results showed an enhancement in the heat pipe performance while achieving a reduction in the thermal resistance for both flat-plate and disk-shaped heat pipes throughout the transient process.

Tsai et al. [16] investigated the thermal performance of disk-shaped miniature heat pipe (DMHP) with gold and carbon nanoparticles suspended in DI water as nanofluids. The measured results showed that the significant reduction in thermal resistance of DMHP for nanofluid when compared with that of DI water. Putra et al. [17] investigated the application of nanofluids to a heat pipe liquid-block and the thermoelectric cooling of electronic equipment. The results showed higher thermal performance in the heat pipe liquid-block and thermoelectric cooled system with nanofluids as a working fluid. Jamshidi et al. [18] experimentally investigated the thermal characteristics of closed loop pulsating heat pipe with nanofluids for (30%, 40%, 50%, 70%, 80%) volumetric filling ratio with an input heat power of (5–70 W). The results showed that the best thermal performance for water and ethanol as working fluids when the corresponding filling ratios are 40% and 50%, respectively.

Ji et al. [19] experimentally studied the effect of four different sizes of Al_2O_3 particles with average diameters of 50 nm, 80 nm, 2.2 μm, and 20 μm on the heat transfer performance of an oscillating heat pipe (OHP). Experimental results showed that the Al_2O_3 particles added in the OHP significantly enhances the heat transfer performance and it depends on the particle size. It has been found that the OHP charged with water and 80 nm Al_2O_3 particles, gave the best heat transfer performance among four particles investigated. Li et al. [20] experimentally investigated the two-phase flows in an OHP charged with DI water and a nanofluid. It is observed that the nanofluid OHP had a much lower thermal resistance than the DI water OHP with the most effective heat transfer in the nanofluid OHP occurring in the slug flow regime. Huminic et al. [21] presented an experimental investigation on the thermal performance of thermosyphon heat pipe using iron oxide nanoparticles suspended in DI water as a working fluid with 0%, 2%, and 5.3% concentration of nanoparticles. Results showed that the addition of 5.3% (by volume) of iron oxide nanoparticles in water presented improved thermal performance compared with the operation with DI water.

Liu and Zhu [22] analyzed the application of aqueous nanofluids in a horizontal mesh heat pipe adopting the fuzzy theory to control the frequency of compressor of water chilling unit, secondary pump, and ventilator of air conditioner box, so as to realize the thermal comfort of room and fixed outlet temperature. The experimental results reported that when the outlet temperature of chilling water is set as 12 °C, the thermal comfort of room is maintained at 0.5 and the energy is saved effectively. Wang et al. [23] performed an experimental study and investigated the operational characteristics of a cylindrical miniature grooved heat pipe using aqueous CuO nanofluid as the working fluid. The experiment results showed that the heat pipe with nanofluid apparently improved the thermal performance under steady operation. The total heat resistance and the maximum heat removal capacity of the heat pipe using nanofluids reduced by 50% and increased by 40% compared with that of the heat pipe using water, respectively. Li et al. [24] investigated the influence of the water-based CuO nanofluid with an average diameter of 50 nm on both steady and transient operation characteristics of a small capillary pumped loop (CPL) with mesh wicked construction. The experiment results of the transient operation indicated that both the start-up time and evaporator wall temperature were reduced and the operation characteristics of the CPL were improved after substituting the nanofluid for water as the working fluid. Liu et al. [25] experimentally studied the thermal performance of an inclined miniature grooved heat pipe using water-based CuO nanofluid as the working fluid. The inclination angle and the operating pressure on the heat transfer of the heat pipe using the nanofluid with the mass concentration of CuO nanoparticles of 1.0 wt. % were investigated. Experimental results showed that an inclination angle of 45 deg indicated the best heat transfer performance of heat pipes using both water and the nanofluid.

Shafahi et al. [26] analyzed the thermal performance of flat-shaped heat pipes using nanofluids. The presence of nanoparticles within the working fluid resulted in a decrease in the thermal resistance and an increase in the maximum heat load capacity of the flat-shaped heat pipe. Qu et al. [27] investigated the thermal performance of an oscillating heat pipe charged with water and spherical Al_2O_3 particles of 56 nm in diameter. Experimental results showed that the alumina nanofluids significantly improved the thermal performance of the oscillating heat pipe (OHP), with an optimal mass fraction of 0.9 wt. % for maximum heat transfer enhancement. The thermal resistance was decreased by 0.14 °C/W when compared with pure water. Kang et al. [28] experimentally studied the thermal performance of silver nanoparticles having the size of 10 nm and 35 nm in diameter suspended in pure water in sintered circular heat pipe with concentrations ranged from 1, 10, and 100 mg/l. The results indicated that at a same charge volume, the nanofluids filled heat pipe temperature distribution demonstrated that the temperature difference decreased 0.56–0.65 °C compared with DI water at an input power of 30–50 W. Yang et al. [29] carried out an experiment to study the heat transfer performance of a horizontal microgrooved heat pipe using CuO nanofluid as the working fluid. The Mass concentration of CuO nanoparticles varied from 0.5 wt. % to 2.0 wt. % with an average diameter 50 nm. Experimental results showed that the CuO nanofluid improved the thermal performance of the heat pipe.

Liu et al. [30] experimentally studied the nucleate boiling heat transfer of water-CuO nanoparticles suspension (nanofluids) at different operating pressures and different nanoparticle mass concentrations in a miniature flat heat pipe (MFHP) with microgrooved heat transfer surface of its evaporator. The experimental results indicated that the operating pressure has great influence on the nucleate boiling characteristics in the MFHP evaporator. The heat transfer coefficient and the critical heat flux (CHF) of nanofluids increased by about 25% and 50%, respectively, at atmospheric pressure, whereas about 100% and 150%, respectively, at the pressure of 7.4 kPa. Ma et al. [31] studied the effect of nanofluid on the heat transport capability in an OHP by combining nanofluids with thermally excited oscillating motion in an oscillating heat pipe. The results showed an increase in the heat transport capability of the OHP when charged with nanofluid. Tsai et al.

Downloaded From: http://heattransfer.asmedigitalcollection.asme.org/ on 10/09/2013 Terms of Use: http://asme.org/terms

[32] studied the effect of structural character of gold nanoparticles in nanofluid on heat pipe thermal performance. Results showed a reduction on thermal resistance of heat pipe with nanofluid as compared with DI water at the same charge volume. The measured results also indicated that the thermal resistance of a vertical meshed heat pipe varied with the size of gold nanoparticles.

From the above mentioned literature, it is observed that all the researchers have stated that the heat transport limitations, such as viscous, sonic, capillary, entrainment, and boiling limits are the key design parameters on the heat pipe performance. Peterson [8] has reported that the operational limits of the heat pipe mainly depend on the thermophysical properties of working fluids and significantly varies with the change in the operating temperature. Surprisingly, the amount of literature available with regard to the heat pipe limitations is quite small. Moreover, no published work has been reported in the open literature that deals with the various operational limitations of the heat pipe using the low volume concentration of pure metal nanoparticles. Hence in the present work, the silver nanoparticles with 0.003%, 0.006%, and 0.009% volume concentrations are dispersed in DI water and used as the working fluid in the heat pipe. The heat pipe is tested for a maximum heat load of up to 100 W. The effect of heat load and volume concentration on the various limitations of the heat pipe are experimentally investigated and presented.

2 Experimentation

2.1 Nanofluid Preparation. Silver-water nanofluid is prepared using a two step method. The silver nanoparticles (manufactured by Sigma Aldrich; the product number is 576,832, Silver nanopowder, <100 nm, 99.5% metals) is mixed with de-ionized water without any additive. The nanofluid is then sonicated using the ultrasonic processor, UP400S (Hielscher) ultra sound technology, with rated voltage, Nennspannung 200–240 and rated current, Nennstrom 4 A and rated frequency, Nennfrequenz 50/60 Hz) for about 45 min for stable suspension of the nanoparticles. After preparation of nanofluids, a stability test was conducted by taking some small sample of nanofluid for the maximum concentration (0.009 vol. %) and physically observed if there is any settling occurs. The photo was taken after 24 and 48 h as shown in Fig. 1. It is clearly seen from Fig. 1 that the settling does not occur in 48 h. Hence, the prepared nanofluid is considered to be stable throughout the experiment. Furthermore, the scanning electron microscopic (SEM) analysis is done on silver nanoparticles to characterize the average particle diameter. Figure 2(*a*) shows the SEM image of 0.009% volume concentration of silver nanoparticles. It is clearly seen from the image that the size of the nanoparticles is found to be less than 100 nm. It is also found that in some places, the size exceeds 100 nm due to the agglomeration of the nanoparticles. Figure 2(*b*) shows the histogram of the size distribution in percentage against the particle size of the silver nanoparticles. The SEM micrographs confirmed the spherical shape of the silver nanoparticles and revealed a single modal particle size distribution with average diameters of 160 nm estimated by measuring the diameter of randomly selected particles in enlarged SEM image.

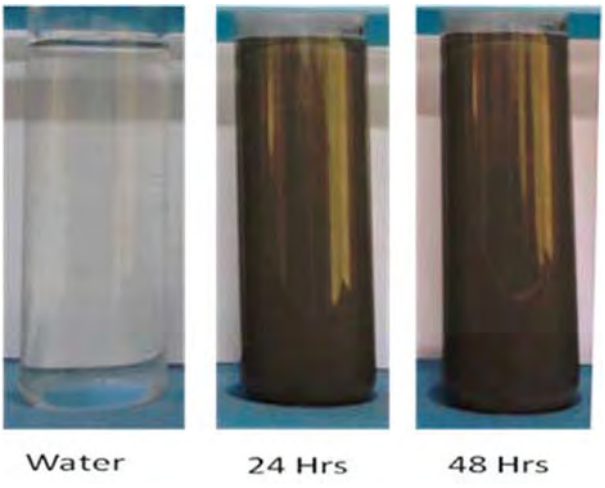

Fig. 1 Stability test for 0.009 vol. % silver/water nanofluid

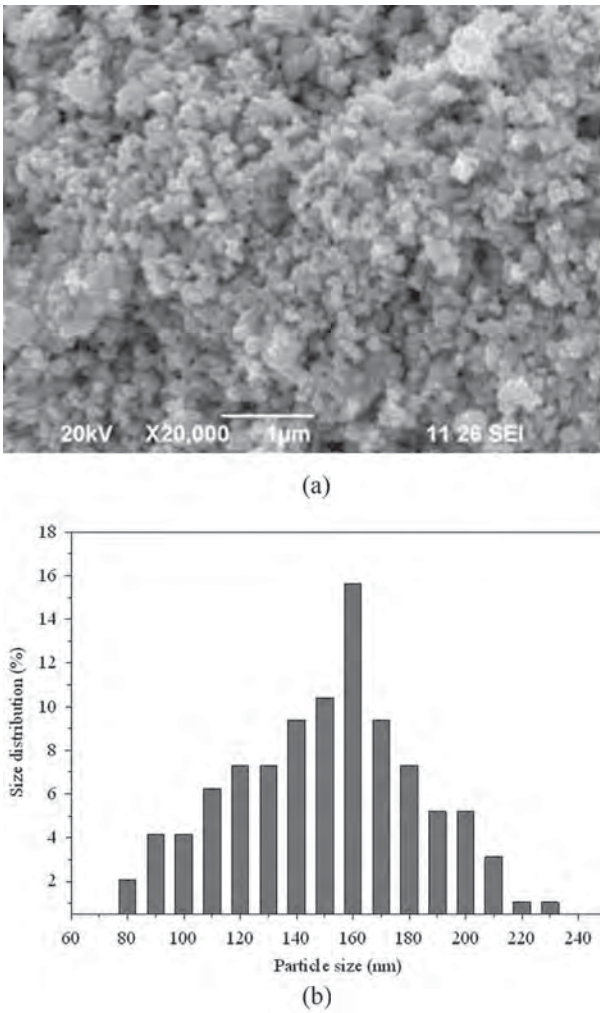

Fig. 2 (*a*) SEM image of 0.009% volume concentration of silver nanoparticles and (*b*) particle distribution percentage against size of silver nanoparticles

2.2 Experimental Setup and Procedure. The schematic layout of test facility to measure the effect of nanoparticles concentration on the operational limitations of heat pipe is shown in Fig. 3.The heat pipe is made up of copper material with a length of 180 mm and outer diameter of 10 mm, respectively. The inner diameter of the heat pipe is 9 mm and lengths of evaporator section, adiabatic section, and condenser section of the heat pipes are, 50 mm, 50 mm and 80 mm, respectively, with wall thickness of 0.5 mm. The screen mesh wick wrapped inside the heat pipe is made up of copper with a wire diameter of 0.105 mm and mesh number 100/in. The condenser section of the heat pipe is made up of acrylic material with Teflon end closures. The test set up is equipped with a pump and flow meter (with an uncertainty of $0.17 \pm 10 \times 10^{-6}$ m^3/s) to circulate cooling water at a constant flow rate of 4.33×10^{-6} m^3/s through the condenser section. The

Downloaded From: http://heattransfer.asmedigitalcollection.asme.org/ on 10/09/2013 Terms of Use: http://asme.org/terms

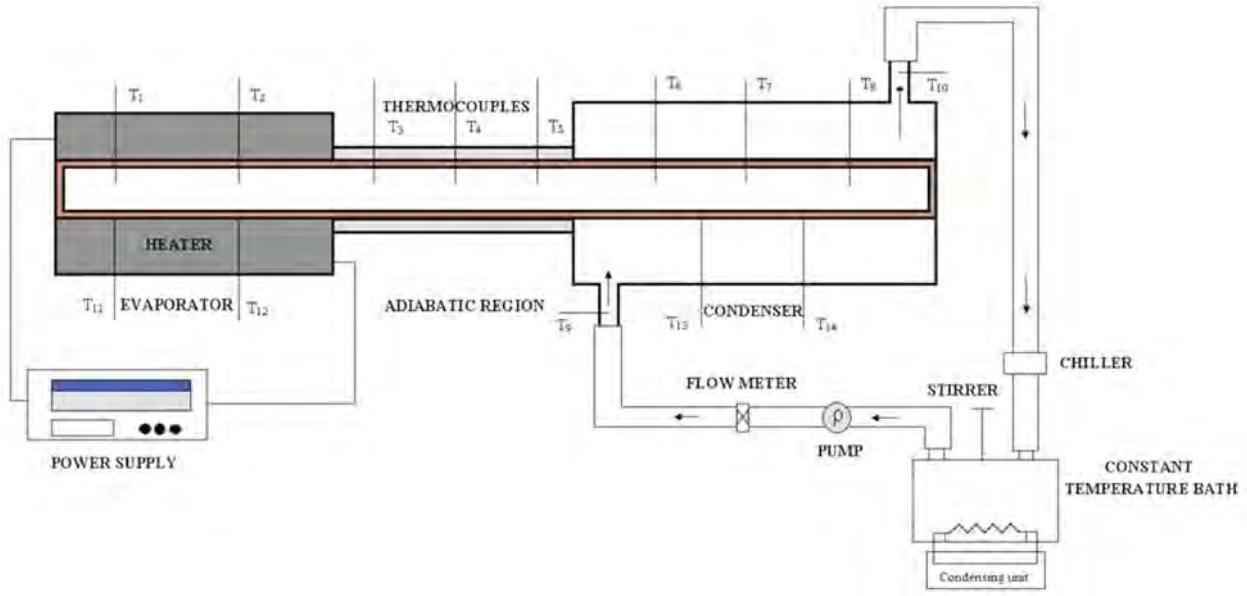

Fig. 3 Schematic diagram of the experimental setup

inlet temperature of the circulating water is maintained at 24 °C for all the test conditions by using a constant temperature chilled water bath. Two T-type thermocouples are fixed between the inlet and outlet of the condenser to measure the inlet and outlet temperatures of the circulating cooling water. Eight T-type thermocouples (uncertainty ±0.5 °C), are inserted in to the heat pipe (two in evaporator, three in adiabatic and three in condenser section, respectively) to measure the inside vapor temperatures. The surface temperatures in the evaporator and condenser are also measured by fixing four T-type thermocouples two on each section. The thermocouples are calibrated separately under the experimental heat loads before the experiments are being conducted. A data logger (Model-(DA 100-13-1 F), Yokogawa-N 200) is used to measure the fluctuation in the measured temperatures of the thermocouples for a sample of 40 readings for each applied heat load. It is observed from this uncertainty study that the temperature reading measured by each of the thermocouple is ±0.5 °C. However, the operational limitations calculated in the present study depend up on the mean adiabatic vapor temperature (operating temperature) of the heat pipe. The thermocouples used in the adiabatic section are calibrated twice and no maximum deviation in the measured temperature is observed more than ±0.5 °C. The input heat load is applied by using a digital wattmeter with an uncertainty of ±0.5 W (Make MECO). An electric heater made up of nichrome wire is wounded on the evaporator section. The heater coil is energized by using a 220 V ac supply. Glass wool is used to insulate the evaporator and adiabatic sections to minimize the heat loss to the surroundings. The experiments are conducted on four identical heat pipes fabricated as per the above mentioned dimensions. One of the four heat pipes is filled with DI water and the remaining three are filled with 0.003%, 0.006%, and 0.009% volume concentrations of silver nanoparticles. The amount of working fluid charged in all the four heat pipes remains constant. The testing conditions, such as condenser coolant circulation rate and inlet temperature, are identical to obtain the performance accuracy. The initial heat load of 20 W is applied on the heat pipe by switching on the power supply and energizing the heater. The input heat load is gradually increased from 20 W to 100 W in five steps. During the experimental test, the vapor and surface temperature readings of the heat pipe are measured using a data logger (Model-(DA 100-13-1 F), Yokogawa-N 200). The entire data acquisition system is monitored and controlled by using a personal computer.

2.3 Thermophysical Properties of Nanofluid. The thermophysical properties of silver-water nanofluid are calculated based on the following equations.

The density is calculated from Pak and Cho [33] using the following equation:

$$\rho_{nf} = \varphi\rho_p + (1-\varphi)\rho_b \tag{1}$$

The specific heat is calculated from Xuan and Roetzel [34] as follows:

$$(\rho C_p)_{nf} = \varphi(\rho C_p)_p + (1-\varphi)(\rho C_p)_b \tag{2}$$

where $(\rho C_p)_{nf}$ is the heat capacity of the nanofluid, $(\rho C_p)_p$ is the heat capacity of the nanoparticles, and $(\rho C_p)_b$ is the heat capacity of the base fluid. The other properties, such as viscosity and thermal conductivity, are measured using the following equations proposed by the present authors. The detailed measurement techniques and procedure are given elsewhere [35] in a published literature by the present authors for reference.

$$\frac{\mu_{nf}}{\mu_b} = (1.005 + 0.497\varphi - 0.1149\varphi^2) \tag{3}$$

$$\frac{k_{nf}}{k_b} = (0.9692\varphi + 0.9508) \tag{4}$$

2.4 Data Reduction. The maximum heat transport capability of heat pipe is governed by various operational limits. The present study deals with the five primary heat transport limitations, including boiling, entrainment, capillary, sonic, and viscous limits. All the equations for calculating the operating limits of heat pipes are taken from Peterson [8].

2.4.1 Capillary Limit. The pumping ability of the capillary structure to provide the circulation of the working fluid is limited for a given working fluid and wick structure. This limit is termed as capillary or hydrodynamic limit. The wick structure will develop a pressure head and this will cause stable circulation of working fluid in the heat pipe. For an effective operation of the heat pipe, the net capillary pressure difference or capillary head should be greater than or equal to all the pressure losses occurring throughout the liquid and vapor flow paths of the heat pipe.

Downloaded From: http://heattransfer.asmedigitalcollection.asme.org/ on 10/09/2013 Terms of Use: http://asme.org/terms

$$\Delta P_{cm} \geq \Delta P_l + \Delta P_v + \Delta P_{ph,e} + \Delta P_{ph,c} + \Delta P_g \quad (5)$$

where ΔP_l is the sum of inertial and viscous pressure drops occurring in liquid phase, ΔP_v is the sum of inertial and viscous pressure drops occurring in vapor phase, $\Delta P_{ph,e}$ is the pressure gradient across phase transition in evaporator, $\Delta P_{ph,c}$ is the pressure gradient across phase transition in condenser, and ΔP_g is the pressure drop in the liquid due to the effect of the gravitational force in the direction of the heat pipe axis.

$$\Delta P_{cm} \text{ maximum capillary pressure} = \frac{2\sigma\cos\theta}{r_c}$$

$$\Delta P_l = [\mu_l/(KA_w\lambda\rho_l)]L_{eff}Q \quad (6)$$

$$\Delta P_v = \left[(C(f_v\mathrm{Re}_v)\mu_v)/\left(2(r_{h,v})^2A_v\rho_v\lambda\right)\right] \quad (7)$$

$$\Delta P_g = \rho_l g d_v \cos\varphi \quad (8)$$

If the above expression is satisfied, then the capillary structure is capable of returning an adequate amount of working fluid to the evaporator in order to prevent the dry-out.

2.4.2 Capillary Pressure. The main phenomenon that governs the operation of the heat pipe is capillary pressure difference developed across liquid–vapor interfaces in evaporator and condenser regions. The pumping ability depends on the capillary pressure. Vaporization in the evaporator region and condensation in the condenser region causes a difference in the local capillary radius. Vaporization causes the meniscus to recede in to the wicking structure, reducing the radius of curvature in the evaporator portion. Similarly, condensation causes a greater radius of curvature in condenser region at liquid interface. This resulting difference in the two radii will provide the capillary pumping pressure necessary for operation of heat pipe. The capillary pressure is calculated based on the following equation:

$$\Delta P_{cm} = \text{maximum capillary pressure} = \frac{2\sigma\cos\theta}{r_c} \quad (9)$$

for perfectly wetting system, contact angle between fluid and wick $\theta = 0$ deg.

2.4.3 Boiling Limit. The boiling limit also called as heat flux limit is comprised two separate phenomena: (1) bubble formation and (2) growth or collapse of bubble.

The bubble formation is governed by the size and number of nucleation sites on the solid surface and the difference between heat pipe wall temperature and working fluid temperature. The growth or collapse of bubbles formed on plane flat surface depends on liquid temperature and corresponding pressure difference across the liquid–vapor interface caused by the vapor pressure and surface tension of the liquid. The boiling limit depends on radial heat flux or circumferential heat flux applied to the evaporator. If the heat pipe wall temperature becomes excessively high, nucleate boiling phenomena of the working fluid will take place in the wick. This causes the vapor bubbles to block the return of the working fluid back to evaporator and results in evaporator dry-out. The heat pipe should be operated within this limit to avoid nucleate boiling phenomena. The boiling limit is calculated based on the following equation:

$$\text{Boiling limit, } Q_{bo} = Q_{bo} = 2\pi\frac{L_{eff}k_{eff}T_v}{h_{fg}\rho_v \ln\left(\frac{r_i}{r_v}\right)}\left[\frac{2\sigma}{r_n} - \Delta P_{cm}\right] \quad (10)$$

where L_{eff} is the effective length of heat pipe that is equal to 0.5 $L_e + L_a + 0.5\,L_c$

k_{eff} is the effective thermal conductivity of the liquid–wick combination

$$k_{eff} = \frac{(k_l(k_l + k_w - (1-\in)(k_l - k_w)))}{k_l + k_w + (1-\in)(k_l - k_w)}$$

$\longrightarrow$For wrapped screen wick

k_l is the liquid thermal conductivity and k_w is the wick thermal conductivity, $\in$ is the wick porosity that is equal to $1-1.05\pi\mathrm{N}d_w/4$, d_w is the wire diameter of the wick, and N is the screen mesh number, 1.05 is the wick crimping factor, ΔP_{cm} is the mMaximum capillary pressure $= 2\sigma\cos\theta/r_c$ where r_c is the effective capillary radius that is equal to $1/2N$ for wire screen wick, $\cos\theta$ is the wetting angle, and r_n is the nucleation site radius.

2.4.4 Entrainment Limit. This limit depends on vapor velocities, when the vapor velocity in the heat pipe is sufficiently high, the shear forces between liquid–vapor interfaces may become greater than the liquid surface tension forces in the wick. This may cause the liquid droplets being picked up or entrained in the vapor flow and will be carried back to condenser. This entrainment of liquid droplets will limit the axial heat transport capability of heat pipe. The entrainment limit is calculated based on the following equation:

$$\text{Entrainment limit } Q_{en} = A_v h_{fg}\left[\frac{\sigma\rho_v}{2r_{hw}}\right]^{1/2} \quad (11)$$

where A_v is the cross-sectional area of the vapor core $= \pi d_v^2/4$ and r_{hw} is the wick surface pore hydraulic radius $= 1/2N - d_w/2$.

2.4.5 Sonic Limit. In a converging–diverging nozzle, the mass flow rate is constant but the vapor velocity varies due to varying cross-sectional area. Whereas in the case of heat pipes, the area is constant and the vapor velocity varies because of evaporation and condensation along the heat pipe. Decreased condenser temperature results in a decrement in the evaporator temperature; however, the vapor velocity may reach sonic or supersonic values at a particular condenser temperature. Any further reduction in the condenser temperature will not reduce evaporator temperature. This mainly arises during start-up or steady-state operation. The sonic limit is calculated based on the following equation:

$$Q_s = A_v\rho_v h_{fg}[(\gamma_v R_v T_v)/(2(\gamma_v + 1))]^{1/2} \quad (12)$$

where γ_v = specific heat ratio of vapor, $R_v = \overline{R}/\mathrm{M} = 8.314 \times 10^3/18 = 462$ J/Kg k, M is molecular weight of vapor = 18 moles, and $\overline{R}$ is the universal gas constant.

2.4.6 Viscous Limit. The vapor pressure difference between evaporator and condenser will be low at low operating temperatures. This will cause the viscous forces to dominate the pressure gradient. When this happens, the pressure gradients will not be sufficient to generate vapor flow and the vapor will be stagnating. This no-flow or low-flow condition refers to viscous limitation. The viscous limit is calculated based on the following equation:

$$Q_{vi} = d_v^2 h_{fg} A_v\left(\frac{P_v\rho_v}{4(f_v\mathrm{Re}_v)L_e\mu_v}\right) \quad (13)$$

where Re_v = local axial Reynolds number in the vapor.

2.4.7 Uncertainty Analysis of the Measured Parameters.

2.4.7.1 Uncertainty in evaporator and adiabatic section. The uncertainty in the calculated operational limitations depends on the corresponding measured temperature at which they are calculated. This in turn will depend on the accuracy of the thermocouples and the uncertainty in the wattmeter ($\pm 0.5\%$) used to supply the corresponding heat load. It is found from thermocouple calibration that the eight T-type thermocouples used in the present

Downloaded From: http://heattransfer.asmedigitalcollection.asme.org/ on 10/09/2013 Terms of Use: http://asme.org/terms

study has an uncertainty of ±0.5 °C. The uncertainty in heat load is calculated using Eq. (14). It is calculated based on the uncertainties in the applied voltage ∂V and the applied current ∂I to the heater coil. It also includes the uncertainties in the measured length ∂L_E and diameter ∂d_E of the evaporator region over which heater coil is wrapped. The least count of the vernier calipers used to measure this length and diameter is taken as the uncertainty value.

$$\frac{\partial Q}{Q} = \left[\left(\frac{\partial V}{V}\right)^2 + \left(\frac{\partial I}{I}\right)^2 + \left(\frac{\partial L_E}{L_E}\right)^2 + \left(\frac{\partial d_E}{d_E}\right)^2\right]^{1/2}$$

$$\frac{\partial Q}{60} = \left[\left(\frac{0.5}{20}\right)^2 + \left(\frac{0.1}{3}\right)^2 + \left(\frac{0.02}{50}\right)^2 + \left(\frac{0.02}{10}\right)^2\right]^{1/2} \quad (14)$$

$$\partial Q = 2.53 \text{ W}$$

$$\frac{\partial Q}{Q} = \left(\frac{2.53}{60} \times 100\right) = 4.2\%$$

2.4.7.2 Uncertainty in condenser section. The uncertainty in the condenser section based on energy balance principle between the heat absorbed in the evaporator and heat rejected in the condenser. The uncertainty in the coolant flow rate maintained in the condenser is $\pm 0.17 \times 10^{-6}$ m^3/s. The uncertainty in the heat rejected from the condenser is calculated using Eq. (15):

$$\omega = \left[\left(\frac{\partial Q}{\partial m}\omega_m\right)^2 + \left(\frac{\partial Q}{\partial C_p}\omega_{C_p}\right)^2 + \left(\frac{\partial Q}{\partial \Delta T}\omega_{\Delta T}\right)^2\right]^{1/2} \quad (15)$$

The maximum uncertainty in the heat absorbed in the evaporator and heat rejected in the condenser is found to be 3.16%. The average values of uncertainties in the heat load applied in evaporator, adiabatic, and condenser sections based on the applied voltage, current, temperature, and mass flow rate are 3.68%. Therefore, it is found that an uncertainty data of the calculated limitations in the evaporator, adiabatic, and condenser sections are around 4%.

3 Results and Discussion

The experiments are conducted with test section kept in horizontal orientation as shown in Fig. 3. Table 1 shows the mean adiabatic vapor temperatures for which all the limit values are calculated and plotted. The experimental results are compared between water and nanofluid for all the concentrations and the enhancement in various operational limits with respect to water and nanofluid are discussed and presented.

The capillary limit as a function of adiabatic vapor temperature is shown in Fig. 4. It is noted that as the nanoparticle's volume concentration and adiabatic vapor temperature increases, the capillary limit also increases and the maximum increment is found to be 54.20% for 0.009 vol. % concentration when compared with DI water. The surface tension of the working fluid and effective capillary radius of the wick influences the maximum capillary pressure head and acts as the pumping force for the operation of the heat pipe. High surface tension values of working fluid are observed as shown in Table 2 at high nanoparticle concentrations. This increment is directly proportional to the increase in the capillary pressure. Moreover, the increase in the liquid density, latent heat of vaporization, and the surface tension of the working fluid are accountable for the increase in the capillary limit.

Table 1 Operating temperatures of heat pipe test section

Q (W)	Adiabatic vapor temperature (°C) Water	0.003 Vol. %	0.006 Vol. %	0.009 Vol. %	Mean adiabatic vapor temperature (°C)
20	68	53	50	50	55.25
40	76	67	60	57	65
60	87	78	69	67	75.25
80	94	91	79	76	85
100	103	99	91	87	95

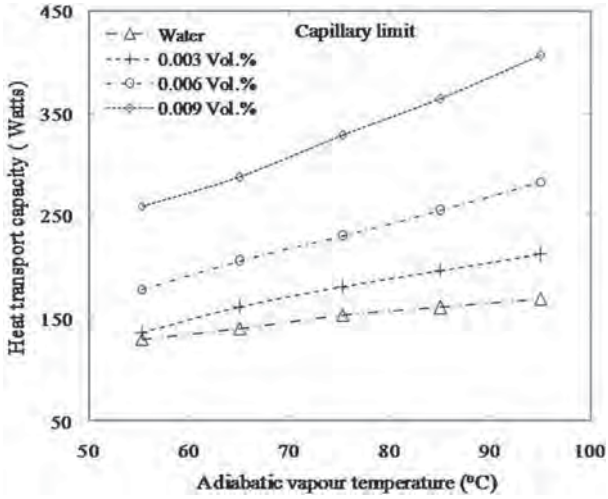

Fig. 4 Capillary limit with respect to adiabatic vapor temperature

The boiling limit as a function of adiabatic vapor temperature is shown in Fig. 5. It is observed that the boiling limit increases with the increase in the volume concentration of the nanoparticles and decreases with the increase in the adiabatic vapor temperature. An enhancement of 87.34% in boiling limit is observed for 0.009 vol. % concentration based heat pipe when compared with DI water. Similarly, for 0.003 vol. % and 0.006 vol. %, a significant enhancement of 53.48% and 77.66% is observed when compared with DI water. The increment in the nanoparticle volume concentration increases the effective thermal conductivity of working fluid, this leads to an enhancement in the effective thermal conductivity of liquid–wick combination (K_{eff}) Also, the surface tension of the nanofluid increases with respect to volume concentration. The other properties, such as vapor density and latent heat of vaporization also influence the boiling limit. The increment in heat load causes an increment in the adiabatic vapor temperature and raises the vapor density. This combined enhancement effect leads to an increment in the boiling limit when using nanofluids and the same decreases with respect to increase in adiabatic vapor temperature. The physical phenomena that lies behind the boiling limit enhancement is that during heat pipe operation the nanoparticles gets deposited on the wall and forms a layer on the heating surface in the evaporator. This layer improves the boiling performance of the working fluid by creating more number of localized spots for bubble formation leading to effective heat transfer by reducing the wall temperature.

The entrainment limit as a function of adiabatic vapor temperature is shown in Fig. 6. It is clearly seen that the entrainment limit increases with the increase in the adiabatic vapor temperature and volume concentration of the nanoparticles. An enhancement of 10.73% in the entrainment limit is observed for 0.009 vol. % concentration of the nanoparticles. The properties that significantly affect the entrainment limit are surface tension of the working fluid, vapor density, and latent heat of vaporization. It is observed that the surface tension values significantly increases by 11.35%, 28.48%, and 52.74% with respect to volume concentration as shown in Table 2 when compared with DI water. This change in the thermophysical properties as a function of operating temperature and concentration enhances the entrainment limit value. The underlying phenomena in the enhancement of entrainment limit is

Downloaded From: http://heattransfer.asmedigitalcollection.asme.org/ on 10/09/2013 Terms of Use: http://asme.org/terms

Table 2 Thermophysical properties of working fluids

	T_v (°C)	P_v (Kg · m^3)	h_{fg} (J/Kg)	σ (N/m)	P_v (Pa)	μ_v (Pa s)	μ_1 (Pa s)	ρ_1 (Kg m^3)
	68	0.18288	2,338,000	0.064838	28599	0.000011195	0.0004152	978.86
	76	0.25184	2,318,100	0.063402	40239	0.000011456	0.0003728	974.22
DI water	87	0.38064	2,290,200	0.061378	62556	0.000011828	0.0003255	967.29
	94	0.48777	2,272,100	0.06006	81541	0.000012065	0.0003006	962.57
	103	0.66056	2,248,500	0.058332	112770	0.000012372	0.0002731	956.18
	53	0.095494	2,374,700	0.081138	14312	0.000010711	0.0005238	1015.12
	67	0.17549	2,340,500	0.079013	27368	0.000011162	0.0004238	1007.95
0.003 Vol. %	78	0.27209	2,313,000	0.077038	43703	0.000011526	0.0003657	1001.53
	91	0.43918	2,279,900	0.074628	72890	0.000011963	0.0003201	993.15
	99	0.57847	2,259,000	0.073104	97852	0.000012235	0.0002866	987.59
	50	0.083147	2,381,900	0.107944	12352	0.000010616	0.0005512	1045.012
	60	0.13043	2,357,700	0.106238	19946	0.000010935	0.0004701	1040.2
0.006 Vol. %	69	0.19052	2,335,500	0.104659	29876	0.000011228	0.0004128	1035.37
	79	0.28271	2,310,500	0.102856	45527	0.000011559	0.0003617	1029.4957
	91	0.43918	2,279,900	0.100628	72890	0.000011963	0.0003133	1021.7723
	50	0.083147	2,381,900	0.150944	12352	0.000010616	0.000552	1073.52
	57	0.11433	2,365,000	0.149755	17336	0.000010838	0.000493	1070.23
0.009 Vol. %	67	0.17549	2,340,500	0.148013	27368	0.000011162	0.0004251	1065.02
	76	0.25184	2,318,100	0.146402	40239	0.000011459	0.0003764	1059.86
	87	0.38064	2,290,200	0.144378	62556	0.000011828	0.0003286	1052.99

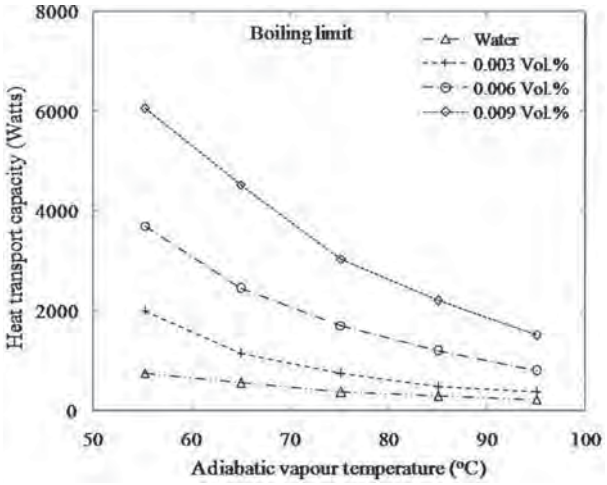

Fig. 5 Boiling limit with respect to adiabatic vapor temperature

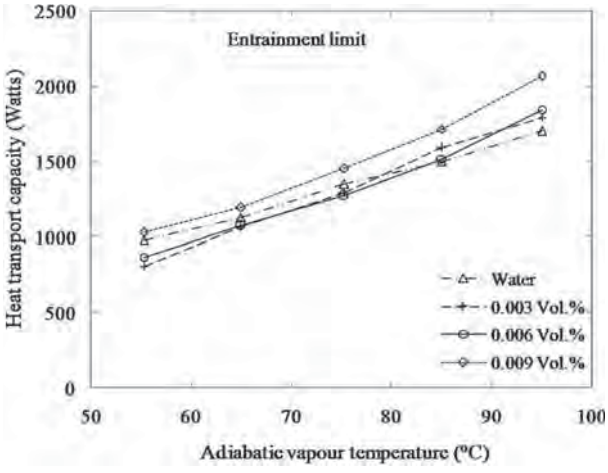

Fig. 6 Entrainment limit with respect to adiabatic vapor temperature

that, as the surface tension of the working fluid increases with respect to concentration the adhesive property between the working fluid and wick also increases and obviously resulting in high velocity vapors at high operating temperatures which cannot entrain or tear the liquid from the wick surface and carry back to the condenser.

The sonic limit with respect to the adiabatic vapor temperature is shown in Fig. 7. The rate of cooling maintained in the condenser is constant for all the heat pipes under various heat loads. Hence, the condenser pressure remains constant. It is observed that the sonic limit is directly proportional to the adiabatic vapor temperature and inversely proportional to the nanoparticle volume concentration in the base fluid. A reduction in sonic limit value by 20.6%, 42.88%, and 49% is observed for 0.003%, 0.006%, and 0.009% volume concentrations of nanofluids when compared with DI water. An increase in the heat load of heat pipe causes a raise in the vapor pressure, vapor density, and adiabatic vapor temperature. As mentioned before, the properties, such as vapor density, adiabatic vapor temperature, and latent heat of vaporization significantly influences the sonic limit. The operating temperatures of heat pipes with nanofluid are less when compared with DI water. This reduction in adiabatic vapor temperature reduces the vapor density by 9%, 19%, and 26%, respectively, for 0.003%,

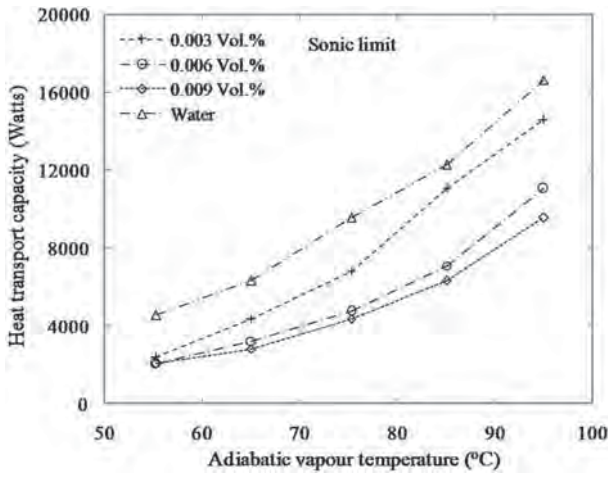

Fig. 7 Sonic limit with respect to adiabatic vapor temperature

Downloaded From: http://heattransfer.asmedigitalcollection.asme.org/ on 10/09/2013 Terms of Use: http://asme.org/terms

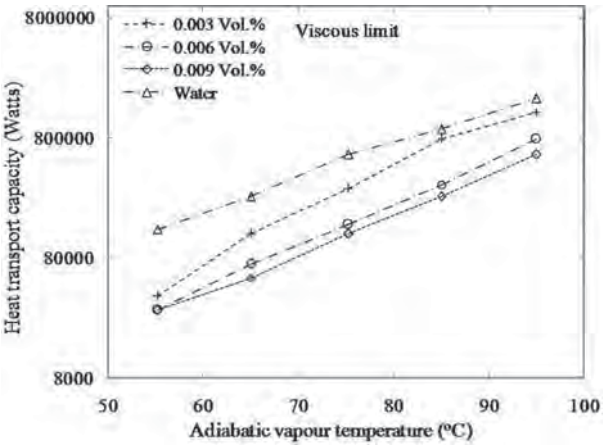

Fig. 8 The logarithmic plot of viscous limits with respect to adiabatic vapor temperature

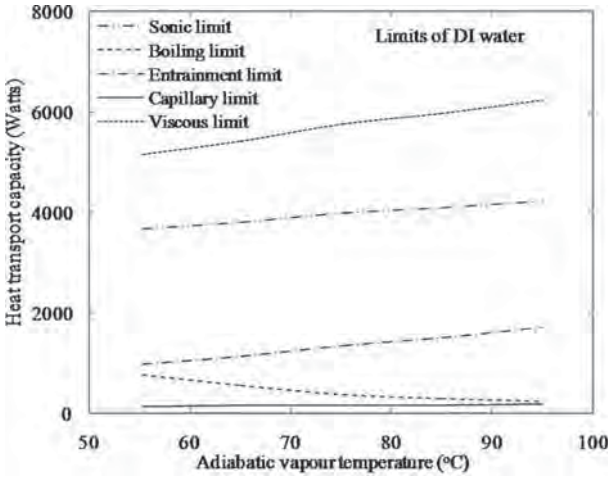

Fig. 10 Operating limits of DI water-based heat pipe against adiabatic vapor temperature

0.006%, and 0.009% volume concentrations when compared with DI water which lead to the reduction in the sonic limit. The influence of latent heat of vaporization on sonic limit is less when compared with vapor density and operating temperature.

The logarithmic plot of viscous limit as a function of adiabatic vapor temperature is shown in Fig. 8. It is observed that the viscous limit gradually increases with respect to adiabatic vapor temperature and reduces as concentration level of nanoparticles in base fluid increases. The key properties that influence the viscous limit are vapor pressure, vapor density, latent heat of vaporization, and dynamic viscosity of vapor. As mentioned earlier, the use of nanofluids reduces the adiabatic vapor temperature of heat pipe which in turn drastically reduces the vapor pressure and vapor density and conversely increases the latent heat of vaporization of working fluid. However, this increase in latent heat is very small when compared with the influence of vapor pressure and vapor density on viscous limit. Hence, viscous limit decreases with the use of nanofluids when compared with DI water. It is noted that the viscous limit decreases by 29.65%, 63%, and 71.05%, respectively, for 0.003%, 0.006%, and 0.009% volume concentration of nanoparticles in base fluid when compared with DI water. The present values of viscous limit are very high when compared with other operational limits for constant adiabatic vapor temperature. A similar trend and high values in the viscous limits have also been observed by other researchers [4,5] which state that the viscous limit will not influence the performance of heat pipes.

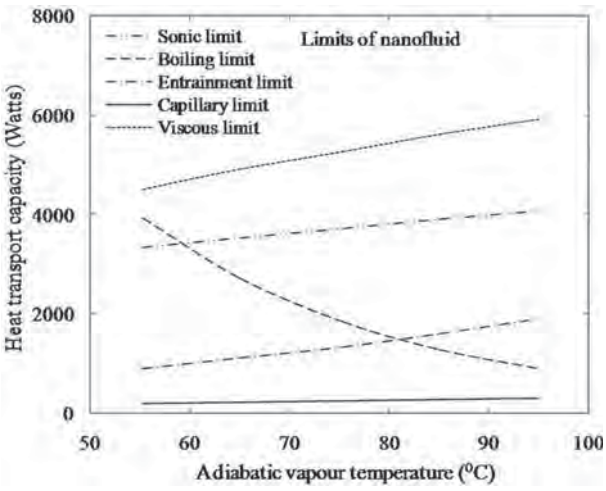

Fig. 9 Operating limits of nanofluid based heat pipes against adiabatic vapor temperature

The various operational limits as a function of mean adiabatic vapor temperature for nanofluid (by taking the average values of all the concentrations of silver nanoparticles) and for DI water are plotted and shown in Figs. 9 and 10. The plot represents the logarithmic values of sonic and viscous limits along with other operating limits with respect to the experimentally recorded mean adiabatic vapor temperatures. It is observed that the viscous and sonic limit values obtained are found to be very high when compared with that of the other limits. To incorporate all the operating limits in a single plot, the very high values of viscous and sonic limits are taken as the logarithmic values multiplied with 1000 as common multiplier. Bejan and Kraus [36] and Ahmad and Rajab [37] reported that the heat input to the heat pipe can be limited to a certain value beyond which heat pipe fails to operate or works with very low performance. It is suggested that the capillary, boiling, and entrainment limits are the failure limitations of heat pipes which are characterized by insufficient liquid flow to the evaporator for a given heat input and resulting in dry-out of the evaporator wick structure. The other two limits, such as sonic and viscous limits are termed as the nonfailure limits of heat pipe. It is observed from the present study that the failure limits (boiling, entrainment and capillary limits) of heat pipe are found to be higher and the nonfailure limits (sonic and viscous limits) are lower for nanofluids when compared with that of DI water. It is also seen that the capillary limit is an essential parameter that primarily influences the heat pipes performance. It is also reported that the higher values of nonfailure limits do not affect the heat pipe performance and the same trend is also observed by researchers [4,5]. The main phenomenon that deals with the enhancement in heat pipe performance with the use of nanofluids is the increase in the number of localized spots by the deposited nanoparticles layer in the evaporator surface. This localized spots effectively increase the boiling of the working fluid by increasing the bubble formation and growth. It is also observed that the boiling limit values of nanofluid gradually decreases with increment in adiabatic vapor temperature, since gradual increase in heat loads causes the boiling phenomena to come closer to nucleate boiling. Addition of nanoparticles to the base fluid also increases the adhesiveness of working fluid toward wick structure due to increased surface tension. This prevents the liquid droplets to be carried back to condenser by the high velocity vapors and hence an increment in the entrainment limit is recorded. This high surface tension values and adhesiveness also increases the capillary pressure head and results in an increment in the capillary limit. It is observed that the average capillary limit value of all the

Downloaded From: http://heattransfer.asmedigitalcollection.asme.org/ on 10/09/2013 Terms of Use: http://asme.org/terms

concentrations increases by 38.63% when compared with DI water and this increases the operating range of heat pipes employed with nanofluids.

4 Conclusion

The present study shows the variation in the operational limitations of heat pipes using silver-water nanofluid. It is observed that the use of silver nanoparticles with volume concentrations of 0.003%, 0.006%, and 0.009% gives the reduction in the adiabatic vapor temperature for a given input heat load of 60 W. This reduction in operating temperatures enhances the failure limitations (capillary, boiling, and entrainment limits) of heat pipes by 54%, 87.34%, and 10.73% when compared with DI water. The enhancement in terms of failure limits of heat pipes with the use of nanofluids improves the heat pipes performance and operating range by providing sufficient amount of working fluid to the evaporator region and preventing the evaporator dry-out even beyond the optimum heat transport capability observed in the case of DI water-based heat pipe. It is also observed that the capillary limit is the lowest value among the failure and nonfailure limitations of heat pipe. The heat pipe fails to operate beyond this limit due to the incapability of the wick structure in providing sufficient amount of working fluid to the evaporator. The use of silver nanoparticles with 0.009 vol. % concentration increases the capillary limit value of heat pipe by 54% when compared with DI water.

Acknowledgment

The authors would like to thank Mr. Seelan, Mr. P. Augustine, and Mr. Jeyakumar of Karunya University for helping in the fabrication of the experimental test facility. The third author thanks the Thailand Research Fund for the support.

Nomenclature

A = cross-sectional area (m^2)
C = constant depending on Mach number (value taken as 1)
c_p = specific heat capacity (J kg K)
d = diameter (m)
f = drag coefficient
g = acceleration due to gravity (m/s^2)
h = latent heat (J/kg)
k = thermal conductivity (W/m K)
K = wick permeability (m^2)
L = length (m)
M = molecular weight of vapor (moles)
N = wick screen mesh number (m^{-1})
P = pressure (Pa)
Q = heat load (W)
r = radius (m)
Re = Reynolds number
R = specific gas constant (J/kg K)
$\overline{R}$ = universal gas constant (J/kg mol K)
S = wick crimping factor
T = temperature (K)

Greek Symbols

Δ = difference
γ = specific heat ratio of vapors
σ = surface tension (N/m)
$\in$ = wick porosity
φ = volume fraction
μ = dynamic viscosity (kg/m s)
ρ = density (kg/m^3)
θ = inclination angle (deg)
λ = latent heat of vaporization (J/kg K)
ω = uncertainty

Subscripts

a = adiabatic
b = basefluid
bo = boiling
c = condenser, capillary
cm = maximum capillary
e = evaporator
en = entrainment
eff = effective
fg = vaporization
g = gravity
hw = wick surface pore hydraulic
i = inner
l = liquid
n = nucleation
nf = nanofluid
p = particle
ph = phase transition
so = sonic
v = vapor
vi = viscous
w = wick, wire

References

[1] Choi, S. U. S., and Eastman, J. A., 1995, "Enhancing Thermal Conductivity of Fluids With Nanoparticles," Proceedings of the ASME International Mechanical Engineering Congress and Exhibition, San Francisco, CA, pp. 99–105.
[2] Shafai, M., Bianco, V., Vafai, K., and Manca, O., 2010, "An Investigation of the Thermal Performance of Cylindrical Heat Pipes Using Nanofluids," Int. J. Heat Mass Transfer, **53**, pp. 376–383.
[3] Liu, Z. H., Li, Y., and Bao, R., 2011, "Compositive Effect of Nanoparticle Parameter on Thermal Performance of Cylindrical Micro-Grooved Heat Pipe Using Nanofluids," Int. J. Therm. Sci., **50**, pp. 558–568.
[4] Nemec, P., Caja, A., and Malcho, M., 2011, "Mathematical Model for Heat Transfer Limitations of Heat Pipe," Math. Comput. Modell., 57, pp. 126–136.
[5] Nemec, P., and Huzvar, J., 2007, "Mathematical Calculation of Total Heat Power of the Sodium Heat Pipe," Institute of Inorganic Chemistry, Slovak Academy of Science, Article for Solution to Project APVV-0517-07.
[6] Naik, R., Varadarajan, V., and Pundarika, G., 2011, "Design, Fabrication and Performance Evaluation of Axially Grooved Wick Assisted Heat Pipe," Int. J. Emerg. Trends Eng. Dev., **2**(1), pp. 25–39.
[7] Faghri, A., 1995, *Heat Pipe Science and Technology*, Taylor and Francis Publication, Washington, DC.
[8] Peterson, G. P., 1994, *An Introduction to Heat Pipes, Modeling, Testing and Applications*, Wiley-Interscience Publication, John Wiley and Sons, New York.
[9] Thuchayapong, N., Nakanob, A., Sakulchangsatjataia, P., and Terdtoona, P., 2012, "Effect of Capillary Pressure on Performance of a Heat Pipe: Numerical Approach With FEM," Appl. Therm. Eng., 32, pp. 93–99.
[10] Riehl, R. R., and Santos, N. D., 2012, "Water-Copper Nanofluid Application in an Open Loop Pulsating Heat Pipe," Appl. Therm. Eng., **42**, pp. 6–10.
[11] Chiang, Y. C., Chieh, J.-J., and Ho, C. C., 2012, "The Magnetic-Nanofluid Heat Pipe With Superior Thermal Properties Through Magnetic Enhancement," Nanoscale Res. Lett., **7**, pp. 322–328.
[12] Liu, Z. H., and Li, Y. Y., 2012, "A New Frontier of Nanofluid Research—Application of Nanofluids in Heat Pipes," Int. J. Heat Mass Transfer, **55**, pp. 6786–6797.
[13] Putra, N., Septiadi, W. N., Rahman, H., and Irwansyah, R., 2012, "Thermal Performance of Screen Mesh Wick Heat Pipes With Nanofluids," Exp. Therm. Fluid Sci., **40**, pp. 10–17.
[14] Hajian, R., Layeghi, M., and Abbaspour Sani, K., 2012, "Experimental Study of Nanofluid Effects on the Thermal Performance With Response Time of Heat Pipe," Energy Convers. Manage., **56**, pp. 63–68.
[15] Alizad, K., Vafai, K., and Shafahi, M., 2012, "Thermal Performance and Operational Attributes of the Startup Characteristics of Flat-Shaped Heat Pipes Using Nanofluids," Int. J. Heat Mass Transfer, **55**(1–3), pp. 140–155.
[16] Tsai, T. H., Chien, H. T., and Chen, P. H., 2011, "Improvement on Thermal Performance of a Disk-Shaped Miniature Heat Pipe With Nanofluid," Nanoscale Res. Lett., **6**, pp. 590–596.
[17] Putra, N., Yanuar, Iskandar, F. N., 2011, "Application of Nanofluids to a Heat Pipe Liquid-Block and the Thermoelectric Cooling of Electronic Equipment," Exp. Therm. Fluid Sci., **35**(7), pp. 1274–1281.
[18] Jamshidi, H., Arabnejad, S., Shafii, M. B., Saboohi, Y., 2011, "Thermal Characteristics of Closed Loop Pulsating Heat Pipe With Nanofluids," J. Enhanced Heat Transfer, **18**(3), pp. 221–237.
[19] Ji, Y., Ma, H., Su, F., and Wang, G., 2011, "Particle Size Effect on Heat Transfer Performance in an Oscillating Heat Pipe," Exp. Therm. Fluid Sci., **35**(4), pp. 724–727.
[20] Li, Q. M., Zou, J., Yang, Z., Duan, Y.-Y., and Wang, B.-X., 2011, "Visualization of Two-Phase Flows in Nanofluid Oscillating Heat Pipes," ASME J. Heat Transfer, **133**(5), p. 052901.

Downloaded From: http://heattransfer.asmedigitalcollection.asme.org/ on 10/09/2013 Terms of Use: http://asme.org/terms

[21] Huminic, G., Huminic, A., Morjan, I., and Dumitrache, F., 2011, "Experimental Study of the Thermal Performance of Thermosyphon Heat Pipe Using Iron Oxide Nanoparticles," Int. J. Heat Mass Transfer, **54**(1–3), pp. 656–661.
[22] Liu, Z., and Zhu, Q., 2011, "Application of Aqueous Nanofluids in a Horizontal Mesh Heat Pipe," Energy Convers. Manage., **52**(1), pp. 292–300.
[23] Wang, G. S., Song, B., and Liu, Z. H., 2012, "Operation Characteristics of Cylindrical Miniature Grooved Heat Pipe Using Aqueous CuO Nanofluids," Exp. Therm. Fluid Sci., **34**(8), pp. 1415–1421.
[24] Li, Y., Lv, L., and Liu, Z., 2010, "Influence of Nanofluids on the Operation Characteristics of Small Capillary Pumped Loop," Energy Convers. Manage., **51**(11), pp. 2312–2320.
[25] Liu, Z. H., Li, Y. Y., and Bao, R., 2010, "Thermal Performance of Inclined Grooved Heat Pipes Using Nanofluids," Int. J. Therm. Sci., **49**(9), pp. 1680–1687.
[26] Shafahi, M., Bianco, V., Vafai, K., and Manca, O., 2010, "Thermal Performance of Flat-Shaped Heat Pipes Using Nanofluids," Int. J. Heat Mass Transfer, **53**(7–8), pp. 1438–1445.
[27] Qu, J., Wu, H. Y., and Cheng, P., 2010, "Thermal Performance of an Oscillating Heat Pipe With Al_2O_3-Water Nanofluids," Int. Commun. Heat Mass Transfer, **37**(2), pp. 111–115.
[28] Kang, S. W., Wei, W. C., Tsai, S. H., and Huang, C. C., 2009, "Experimental Investigation of Nanofluids on Sintered Heat Pipe Thermal Performance," Appl. Therm. Eng., **29**(5–6), pp. 973–979.
[29] Yang, X. F., Liu, Z. H., and Zhao, J., 2008, "Heat Transfer Performance of a Horizontal Micro-Grooved Heat Pipe Using CuO Nanofluid," J. Micromech. Microeng. **18**(3), p. 035038.
[30] Liu, Z. H., Xiong, J. G., and Bao, R., 2007, "Boiling Heat Transfer Characteristics of Nanofluids in a Flat Heat Pipe Evaporator With Micro-Grooved Heating Surface," Int. J. Multiphase Flow, **33**(12), pp. 1284–1295.
[31] Ma, H. B., Wilson, C., Borgmeyer, B., Park, K., Yu, Q., Choi, S. U. S., and Tirumala, M., 2006, "Effect of Nanofluid on the Heat Transport Capability in an Oscillating Heat Pipe," Appl. Phys. Lett., **88**(14), p. 143116.
[32] Tsai, C. Y., Chien, H. T., Ding, P. P., Chan, B., Luh, T. Y., and Chen, P. H., 2004, "Effect of Structural Character of Gold Nanoparticles in Nanofluid on Heat Pipe Thermal Performance," Mater. Lett., **58**(9), pp. 1461–1465.
[33] Pak, B. C., and Cho, I. Y., 1998, "Hydrodynamic and Heat Transfer Study of Dispersed Fluids With Sub-Micron Metallic Oxide Particles," Exp. Heat Transfer, **11**, pp. 151–170.
[34] Xuan, Y., and Roetzel, W., 2000, "Conceptions for Heat Transfer Correlation of Nanofluids," Int. J. Heat Mass Transfer, **43**, pp. 3701–3707.
[35] Godson, L., Raja, B., Lal, M. D., Wongwises, S., 2010, "Experimental Investigation of Thermal Conductivity and Viscosity of Silver-Deionized Water Nanofluid," Exp. Heat Transfer, **23**(4), pp. 317–332.
[36] Bejan, A., and Kraus, A. D., 2003, *Heat Transfer Handbook*, John Wiley & Sons, Inc., Hoboken, NJ.
[37] Ahmad, H., and Rajab, H., 2010, "An Experimental Study of Parameters Affecting a Heat Pipe Performance," Al-Rafidain Eng. J., **18**(3), pp. 97–116.

Downloaded From: http://heattransfer.asmedigitalcollection.asme.org/ on 10/09/2013 Terms of Use: http://asme.org/terms

JOURNAL OF THERMOPHYSICS AND HEAT TRANSFER
Vol. 27, No. 4, October–December 2013

Nanofluids Flow Between Two Rotating Cylinders: Effects of Thermophoresis and Brownian Motion

Meisam Habibi Matin*
Kermanshah University of Technology, 67178-63766 Kermanshah, Iran
Omid Mahian†
Islamic Azad University, 91735 Mashhad, Iran
and
Somchai Wongwises‡
King Mongkut's University of Technology Thonburi, Bangkok 10140, Thailand

DOI: 10.2514/1.T4122

In this paper, the effects of thermophoresis and Brownian motion on the heat transfer of nanofluids between two rotating cylinders are investigated. The flow between the cylinders is considered laminar and steady, whereas the walls of the cylinders are kept at different constant temperatures. The governing equations, including momentum, energy, and volume fraction in cylindrical coordinates, are simplified and solved. An exact solution for the velocity distribution is presented and the homotopy perturbation method is employed to obtain the temperature field. The results obtained from the homotopy perturbation method are validated with the results of a numerical solution. The effects of various quantities of the Eckert and Prandtl numbers, the rotational velocity ratio of the cylinders, Brownian motion, and thermophoresis parameters on the temperature field, and Nusselt number in the annulus are examined.

I. Introduction

FLUID flow and heat transfer between two concentric rotating cylinders is a classical problem in fluids engineering. It has significant applications such as electrical motors and generators, mixing equipment, journal bearings, and swirl nozzles [1,2].

Water, ethylene glycol, and oil as the traditional fluids in thermal engineering systems have low thermal conductivity and hence, the heat transfer enhancement is limited. An innovative technique to enhance the heat transfer is the use of a nanofluid, which is a mixture of common liquids and very fine particles (1–100 nm), introduced by Choi [3].

Currently, nanofluids are applied in various thermal systems to enhance the heat transfer rate and thermal efficiency. Nanofluids can be used in different fields of thermal engineering such as solar energy [4], heat exchangers, nuclear reactors, and cooling of electronic devices [5]. In addition, the readers can refer to the most recent theoretical and experimental works that have been done on nanofluids in different geometries and conditions [6–22].

Different factors, such as the thermal conductivity increase, particle migration, dispersion and chaotic movement of nanoparticles, Brownian motion, and thermophoresis, could be effective in the enhancement of the heat transfer rate where the nanofluid is used as a working fluid. The most obvious factor is the increase of thermal conductivity of base fluid due to adding nanoparticles that have higher thermal conductivity in comparison with the base fluid. Two other main factors are Brownian motion and thermophoresis effects.

Here, a brief review of the former works related to the nanofluid flow in a cylindrical annulus in both natural and forced convection cases is performed. Abu-Nada et al. [23] investigated the natural convection due to four different nanoparticles including Cu, Ag, Al_2O_3 and TiO_2 suspended in pure water in a horizontal annulus. They presented the results for different values of Rayleigh number, gap magnitude, and volume fraction. Abu-Nada [24] studied the effects of uncertainties in thermophysics models on the predicting of heat transfer rate due to free convection of Al_2O_3/water nanofluid in an annulus. He used four sets of models to calculate the thermal conductivity and viscosity. These models include temperature-dependent and temperature-independent relations. His results show that opposite predictions of average Nusselt number trend may be obtained by using different models. Later on, Abu-Nada [25] developed his former work [24] for CuO/water nanofluid. Abouali and Falahatpisheh [26] presented a numerical study of natural convection of Al_2O_3/water nanofluid between two vertical cylinders where the bottom and top ends are insulated. Izadi et al. [27] investigated the forced convection of Al_2O_3/water nanofluid between two cylindrical tubes where the flow is developing. Shahi et al. [28] numerically studied the natural convection of Cu/water nanofluid in an annulus at different angles with respect to the horizontal surface where the ends of the annulus are adiabatic. Moghari et al. [29] examined the mixed convection of Al_2O_3/water nanofluid in a horizontal iso-flux annulus by considering the effects of Brownian motion of nanoparticles. Cianfrini et al. [30] theoretically investigated the natural convection heat transfer due to a nanofluid between two long horizontal cylinders where the wall of the annulus is subject to a constant wall temperature. They found that there is an optimal volume fraction of nanoparticles for which the heat transfer rate is maximized. Soleimani et al. [31] numerically solved the natural convection in a semi-annulus enclosure where the working fluid is Cu/water nanofluid. They obtained the optimal angle of the arc in which the heat transfer reaches maximum. Sheikhzadeh et al. [32] performed a numerical study of natural convection of Cu/water nanofluid between two concentric cylinders where four fins are mounted on the wall of the inner cylinder. Later on, Sheikhzadeh et al. [33] investigated the effects of different parameters including the number of fins installed on the inner cylinder, fin length, and the volume fraction of nanoparticles. Nasrin et al. [34] investigated the effects of viscosity variation of Al_2O_3/water nanofluid on natural convection in an annulus. They assumed that the nanofluid confined in the annulus produces heat internally. In another work, Parvin et al. [35] focused on natural convection of Al_2O_3/water nanofluid in the annulus where two models are used to calculate the thermal conductivity. They assumed that the inner cylinder is under constant heat flux while the outer one is kept at constant temperature. Ashorynejad et al. [36] used the Lattice Boltzmann method to study

Received 31 January 2013; revision received 7 April 2013; accepted for publication 25 April 2013; published online 24 June 2013. Copyright © 2013 by the American Institute of Aeronautics and Astronautics, Inc. All rights reserved. Copies of this paper may be made for personal or internal use, on condition that the copier pay the $10.00 per-copy fee to the Copyright Clearance Center, Inc., 222 Rosewood Drive, Danvers, MA 01923; include the code 1533-6808/13 and $10.00 in correspondence with the CCC.

*Department of Mechanical Engineering; m.habibi@aut.ac.ir (Corresponding Author).
†Ph.D. Student, Young Researchers Club and Elites.
‡Faculty of Engineering, Department of Mechanical Engineering, Bangmod; currently Professor, Fluid Mechanics, Thermal Engineering and Multiphase Flow Research Laboratory (FUTURE).

the effects of magnetic field on natural convection of Ag/water nanofluid between two horizontal cylinders. The previously mentioned works were concerning the first law of thermodynamics analysis. Some works performed by Mahian et al. [37–39] on the entropy generation between two rotating cylinders used nanofluids in different conditions.

A review of the literature shows that there is no reported research on Brownian motion and thermophoresis effects of a nanofluid on heat transfer between two rotating cylinders. Buongiorno [40] proposed a mathematical nanofluid model by taking into account the Brownian motion and thermophoresis effects on flow and heat transfer fields. In this model, an additional equation for nanoparticle volume fraction is introduced so that the volume fraction distribution could be obtained.

This paper aims to present analytical and numerical studies of the Brownian motion and thermophoresis effects of a nanofluid on heat transfer between two isothermal cylinders. The mathematical model proposed by Buongiorno [40] is used to take into consideration the Brownian motion and thermophoresis effects. An exact solution for the velocity distribution is presented. Energy and volume fraction equations are naturally coupled. These equations are decoupled after some manipulations and it leads to convert the energy equation to an ordinary differential equation. The homotopy perturbation method (HPM) is used to solve the energy equation and consequently the temperature field is obtained. The results obtained from the HPM are validated with the results of a numerical solution.

II. Problem Formulation

Consider the steady, laminar, and fully developed flow and heat transfer of a nanofluid between two rotating cylinders. The schematic of the problem is shown in Fig. 1. The inner and outer cylinders have radii of r_i and r_o, respectively, whereas the inner and outer walls of the annulus are kept at temperatures of T_i and T_o. The inner and outer cylinders can rotate with constant angular velocities ω_i and ω_o, respectively. Assuming a two-dimensional problem that corresponds to no relative axial motion between the cylinders and ignoring the radial velocity component compared to the tangential u_θ, the momentum equation reads

$$\frac{\partial^2 u_\theta}{\partial r^2}+\frac{1}{r}\frac{\partial u_\theta}{\partial r}-\frac{1}{r^2}u_\theta=0 \tag{1}$$

Also, by neglecting the convection term and taking into account the viscous dissipation term, the energy equation becomes

$$\begin{aligned}&\frac{\alpha}{r}\frac{\partial}{\partial r}\left(r\frac{\partial T}{\partial r}\right)+\frac{(\rho C_P)_S}{(\rho C_P)_f}\\&\quad\times\left[D_B\left(\frac{\partial\phi}{\partial r}+\frac{\phi}{r}\right)\left(\frac{\partial T}{\partial r}+\frac{T}{r}\right)+\frac{D_T}{T_C}\left(\frac{\partial T}{\partial r}+\frac{T}{r}\right)^2\right]\\&\quad+\mu\left(\frac{\partial u_\theta}{\partial r}-\frac{u_\theta}{r}\right)^2=0\end{aligned} \tag{2}$$

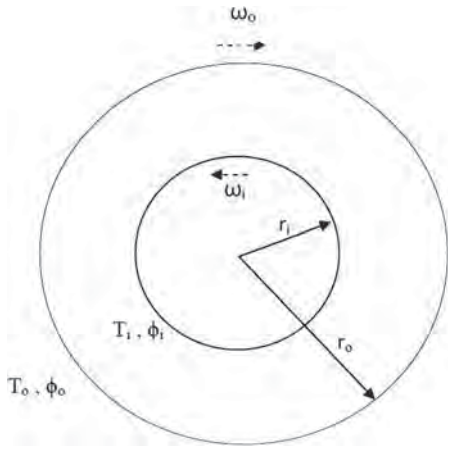

Fig. 1 Schematic of the problem and boundary conditions.

The equation of nanoparticle volume fraction can be written as

$$D_B\left(\frac{\partial\phi}{\partial r}+\frac{\phi}{r}\right)+\frac{D_T}{T_C}\left(\frac{\partial T}{\partial r}+\frac{T}{r}\right)=\xi \tag{3}$$

In the preceding relations, T and ϕ are the temperature and nanoparticles volume fraction. μ, α, and k are the dynamic viscosity, thermal diffusion coefficient, and the thermal conductivity of the base fluid, respectively. Here, D_B and D_T are Brownian diffusion coefficient and thermophoresis diffusion coefficient, respectively. Here, ρ and C_p are the density and heat capacity where the subscripts of S and f represents the solid and fluid. In the volume fraction equation, ξ is a constant. The following boundary conditions are used for the inner and outer cylinders

$$\begin{aligned}&r=r_i\rightarrow u_\theta=r_i\omega_i, \qquad T=T_i=T_h, \qquad \phi=\phi_i\\&r=r_O\rightarrow u_\theta=r_O\omega_O, \qquad T=T_O=T_C, \qquad \phi=\phi_O\end{aligned} \tag{4}$$

The following dimensionless parameters are defined

$$\begin{aligned}&\lambda=\frac{\omega_i}{\omega_o}, \quad \Pi=\frac{r_i}{r_o}, \quad Pr=\frac{\nu_f}{\alpha_f}, \quad Ec=\frac{r_o^2\omega_o^2}{C_P\Delta T}, \quad R=\frac{r}{r_o},\\&U=\frac{u_\theta}{r_o\omega_o}, \quad \theta=\frac{T-T_C}{T_h-T_C}, \Phi=\frac{\phi-\phi_o}{\phi_i-\phi_o}, \quad \theta_r=\frac{T_o}{\Delta T},\\&\phi_r=\frac{\phi_o}{\Delta\phi}, \quad Nb=\frac{(\rho C_P)_S}{(\rho C_P)_f}\frac{D_B\Delta\phi}{\nu_f}, \quad Nt=\frac{(\rho C_P)_S}{(\rho C_P)_f}\frac{D_T\Delta T}{\nu_f T_C}\end{aligned} \tag{5}$$

In the preceding relations Pr, Nb, Nt, and Ec are the Prandtl number, the Brownian motion parameter, the thermophoresis parameter, and the Eckert number, respectively. Also, U, Φ, θ, θ_r, and ϕ_r are dimensionless velocity, dimensionless volume fraction, dimensionless temperature, temperature ratio, and volume fraction ratio, respectively. Using the dimensionless parameters defined in Eq. (5), the dimensionless forms of governing equations can be written as

$$\frac{\partial^2 U}{\partial R^2}+\frac{1}{R}\frac{\partial U}{\partial R}-\frac{U}{R^2}=0 \tag{6}$$

$$\begin{aligned}&\frac{1}{R}\frac{\partial}{\partial R}\left(R\frac{\partial\theta}{\partial R}\right)+NbPr\left(\frac{\partial\Phi}{\partial R}+\frac{\Phi+\Phi_r}{R}\right)\left(\frac{\partial\theta}{\partial R}+\frac{\theta+\theta_r}{R}\right)\\&\quad+NtPr\left(\frac{\partial\theta}{\partial R}+\frac{\theta+\theta_r}{R}\right)^2+EcPr\left(\frac{\partial U}{\partial R}-\frac{U}{R}\right)^2=0\end{aligned} \tag{7}$$

$$Nb\left(\frac{\partial\Phi}{\partial R}+\frac{\Phi+\Phi_r}{R}\right)+Nt\left(\frac{\partial\theta}{\partial R}+\frac{\theta+\theta_r}{R}\right)=\beta_1 \tag{8}$$

Subject to the following dimensionless boundary conditions

$$\begin{aligned}&R=\Pi\rightarrow U=\Pi\lambda, \qquad \theta=1, \qquad \Phi=1\\&R=1\rightarrow U=1, \qquad \theta=0, \qquad \Phi=0\end{aligned} \tag{9}$$

III. Solution to the Problem

A. Velocity Distribution

The exact solution of the momentum equation, Eq. (6), is obtained as

$$U=C_1R+\frac{C_2}{R} \tag{10}$$

where

$$C_1=\frac{1-\Pi^2\lambda}{1-\Pi^2}, \qquad C_2=\frac{\Pi^2(\lambda-1)}{1-\Pi^2} \tag{11}$$

By using the solution of the velocity, the skin friction coefficient on the inner cylinder can be expressed as

$$f_i = \frac{1}{Re}\frac{\partial U}{\partial R}\bigg|_{R=\Pi}$$

in which

$$Re = \frac{\rho_f r_0^2 \omega_0}{\mu_f}$$

is the rotational Reynolds number.

The energy and volume fraction equations, Eqs. (7) and (8), are nonlinearly coupled. Integrating from the volume fraction equation, Eq. (8), and substituting the boundary conditions for dimensionless temperature and volume fraction gives

$$Nb(\Phi + \Phi_r) + Nt(\theta + \theta_r) = \frac{\beta_1}{2}R + \frac{\beta_2}{R} \tag{12}$$

where

$$\beta_1 = 2\frac{Nb + Nt + Nb\Phi_r + Nt\theta_r - \frac{1}{\Pi}(Nb\Phi_r + Nt\theta_r)}{\Pi - \frac{1}{\Pi}}$$
$$\beta_2 = Nb\Phi_r + Nt\theta_r - \frac{\beta_1}{2} \tag{13}$$

The approximation for the dimensionless temperature θ in terms of the power series parameter p is written as

$$\theta = \theta_0 + p\theta_1 + p^2\theta_2 + p^3\theta_3 + \ldots = \sum_{i=0}^{n} p^i\theta_i \tag{15}$$

Substituting Eq. (15) into Eq. (14a) and after manipulations, a set of recursive ordinary differential equations, along with their boundary conditions, are obtained and solved. To save space, only three terms of the homotopy series are presented. The calculations are made by the MAPLE software for the dimensionless temperature (for $\Pi = 0.5$)

$$\theta_0 = -2R + 2 \tag{16}$$

$$\theta_1 = 2bR^2 + (2\ln R - 2b\ln R - 3b - e\ln R - d - 2\ln 2 + 2b\ln 2 + e\ln 2)R - e\ln 2 + \frac{7}{6}d + 2\ln 2 - 2b\ln 2 + b - \frac{1}{6}\frac{d}{R^2} \tag{17}$$

$$\theta_2 = -R^3b^2 + (eb\ln R + b^2 - eb\ln 2 + bd - 2b^2\ln 2 + 2b\ln 2 - 2b\ln R - be + 2b^2\ln R)R^2 + \begin{pmatrix} -\frac{\mathrm{d}}{3} - 5b\ln 2 + 5(\ln 2)^2 b + \frac{3}{2}(\ln 2)^2 e + 3b^2\ln 2 - \mathrm{d}\ln 2 + \frac{3}{2}be - \frac{5}{3}bd + \frac{1}{4}b^2 + \frac{7}{6}bd\ln 2 \\ -(\ln 2)^2 eb - 2(\ln 2)^2 b^2 - 3(\ln 2)^2 + eb\ln 2\ln R + eb\ln 2 - (\ln R)^2 - e\ln 2\ln R + 2b^2\ln 2\ln R \\ -4b\ln 2\ln R - \frac{7}{6}bd\ln R - b^2\ln R + 3b\ln R + \mathrm{d}\ln R + b(\ln R)^2 + \frac{1}{2}e(\ln R)^2 + 2\ln 2\ln R \end{pmatrix} R - b^2\ln 2 + 2b^2(\ln 2)^2 + \frac{7}{18}\mathrm{d} - \frac{1}{4}b^2 - \frac{1}{2}be + \frac{3}{4}bd + d\ln 2 - 5b(\ln 2)^2 + 3b\ln 2 + 3(\ln 2)^2 + eb(\ln 2)^2 - \frac{3}{2}e(\ln 2)^2 - \frac{7}{6}bd\ln 2 - \frac{1}{12}\frac{bd}{R} - \frac{1}{18}\frac{d}{R^2} \tag{18}$$

Eliminating the dimensionless volume fraction parameter Φ from the energy equation by using Eq. (12), one reaches the following ordinary differential equation

$$\frac{\partial^2\theta}{\partial R^2} + \left(\frac{1}{R} + \beta_1 Pr\right)\frac{\partial\theta}{\partial R} + \frac{\beta_1 Pr}{R}(\theta + \theta_r) + \frac{4EcPr\Lambda^2}{R^4} = 0 \tag{14}$$

The preceding equation should be solved to obtain the temperature field and consequently the Nusselt number. Here, Eq. (14) is solved both analytically and numerically, and the results of both solutions are compared. A semi-analytical solution is carried out to obtain a parametric correlation for temperature distribution. In the present study, HPM is used as a semi-analytic method.

B. Thermal Field

1. *Homotopy Perturbation Solution*

We are now ready to apply the HPM to solve the ordinary differential equation (14) with its boundary conditions, as defined in Eq. (9). First, we construct a homotopy for Eq. (14) as follows

$$(1-p)\left(\frac{\mathrm{d}^2\theta}{\mathrm{d}R^2} - \frac{\mathrm{d}^2\theta_0}{\mathrm{d}R^2}\right) + p\left[\frac{\mathrm{d}^2\theta}{\mathrm{d}R^2} + \left(\frac{1}{R} + \beta_1 Pr\right)\frac{\mathrm{d}\theta}{\mathrm{d}R} + \frac{\beta_1 Pr}{R}(\theta + \theta_r) + \frac{4EcPr\Lambda^2}{R^4}\right] = 0 \tag{14a}$$

In the preceding relations parameters b, e, d, and Λ are

$$b = -\frac{4}{3}Pr(Nb + Nt - Nb\Phi_r - Nt\Theta_r)$$
$$e = b\theta_r$$
$$d = 4EcPr\Lambda^2$$
$$\Lambda = \frac{\lambda}{3} - \frac{1}{3} \tag{19}$$

For more details on the homotopy perturbation method, the readers can refer to [41–44].

2. *Numerical Solution*

Equation (14) is solved using the finite difference method, and the obtained results are compared with the results of HPM. It should be mentioned that the HPM solution is valid in a limited range of the key parameters of the problem, but this method is presented here to give a parametric relation that can be useful. The range of parameters for which the HPM provides acceptable results is as follows

$$Nb < 6, \qquad Nt < 2, \qquad \theta_r < 10, \qquad \Phi_r < 3,$$
$$Ec < 0.5, \qquad Pr < 10, \qquad -20 < \lambda < 20$$

A comparison between the results obtained from the HPM (up to four terms) and numerical solutions is presented in Table 1. It is seen that for the third and fourth terms of the series, the numerical and analytical results are in good agreement.

Table 1 Comparison between numerical and analytical results for $Nb = 3$, $Nt = 0.5$, $\theta_r = 4$, $\Phi_r = 0.5$, $Ec = 0.1$, $Pr = 2$, $\lambda = 7$, and $\Pi = 0.5$

R	Numerical	HPM (4 terms)	HPM (3 terms)	HPM (2 terms)	HPM (1 term)
0.5	1.0	1.0	1.0	1.0	1.0
0.6	1.083442	1.083638	1.085524	1.073379	0.8
0.7	0.916858	0.91692	0.920113	0.921441	0.6
0.8	0.644526	0.64441	0.646892	0.660229	0.4
0.9	0.329146	0.329011	0.329903	0.343878	0.2
1.0	0.0	0.0	0.0	0.0	0.0

The quantity of physical interest is the local Nusselt number Nu_L. From the fundamental heat transfer concepts, by writing energy balance on the inner cylinder, we can derive the relation for the Nusselt local number

$$k_f \left.\frac{\partial T}{\partial r}\right|_{r_i} = h_{nf}(T_h - T_C) \Rightarrow -k_f \frac{\Delta T}{r_o}\left.\frac{\partial \Theta}{\partial R}\right|_{R=\Pi} = h_{nf}\Delta T \Rightarrow Nu_i = \frac{h_{nf} r_o}{k_f} = \left.\frac{\partial \theta}{\partial R}\right|_{R=\Pi} \tag{20}$$

This definition also implies the mean Nusselt number because the temperature is independent of tangential coordinate.

C. Volume Fraction Distribution

It is clear from Eq. (12) that by obtaining the temperature, the nanoparticle volume fraction could be obtained as

$$\Phi = \frac{1}{Nb}\left[\frac{\beta_1}{2}R + \frac{\beta_2}{R} - Nt(\theta + \theta_r)\right] - \Phi_r \tag{21}$$

Also, the relation for the Sherwood number on the inner cylinder is presented below:

$$Sh_i = \left.\frac{\partial \Phi}{\partial R}\right|_{R=\Pi} \tag{22}$$

IV. Results and Discussion

Figure 2 displays the velocity distribution in the annulus as a function of radial distance for various values of velocity ratio where the radius ratio is 0.2. As seen, increasing the magnitude of λ, the velocity reaches a minimum point in the vicinity of the inner cylinder. This minimum point can be obtained by taking the velocity gradient equal to zero at the inner cylinders. Generally, the velocity ratio for which the minimum velocity occurs on the inner cylinder is obtained by

$$\lambda = \frac{2}{\Pi^2 + 1}\left(\text{obtained from} \left.\frac{\partial U}{\partial R}\right|_{R=\Pi} = 0\right)$$

Here, in radius ratio of 0.2, the minimum point can be found in the velocity profile for $\lambda \geq 1.92$. As the velocity ratio increases, this minimum point moves toward the outer cylinder. The velocity distribution is linear where the cylinders rotate with the same velocity but in opposite directions ($\lambda = -1$).

The effects of the Brownian motion parameter on the dimensionless temperature are presented in Fig. 3. As shown, with an increase in the Brownian motion parameter, the absolute dimensionless temperature decreases in the whole of the annulus, so that for high values of N_b (say 5 and 6) the temperature reaches a minimum point near the outer cylinder. With increasing the Brownian

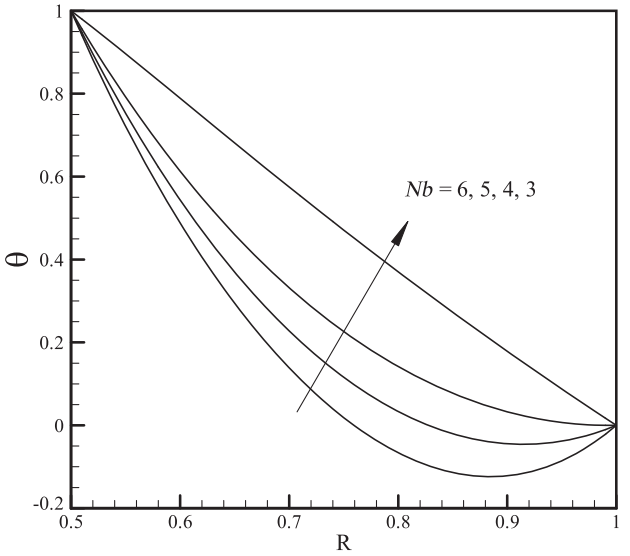

Fig. 3 Dimensionless temperature distribution for different values of Brownian motion parameter at $Nt = 0.5$, $\theta_r = 4$, $\Phi_r = 0.5$, $Ec = 0.01$, $Pr = 3$, and $\lambda = 7$.

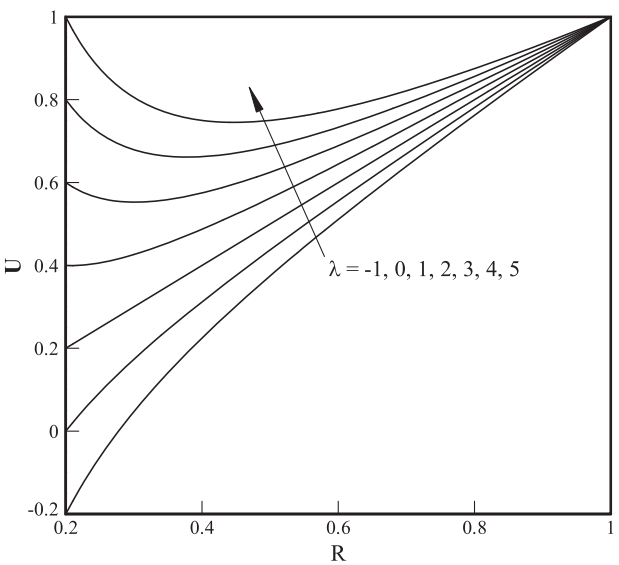

Fig. 2 Dimensionless velocity distribution for different values of velocity ratio.

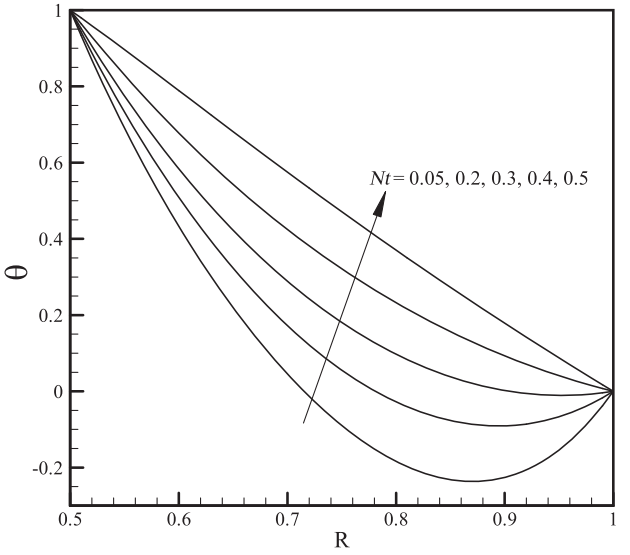

Fig. 4 Dimensionless temperature distribution for different values of thermophoresis parameter at $Nb = 3$, $\theta_r = 4$, $\Phi_r = 0.5$, $Ec = 0.01$, $Pr = 3$, and $\lambda = 7$.

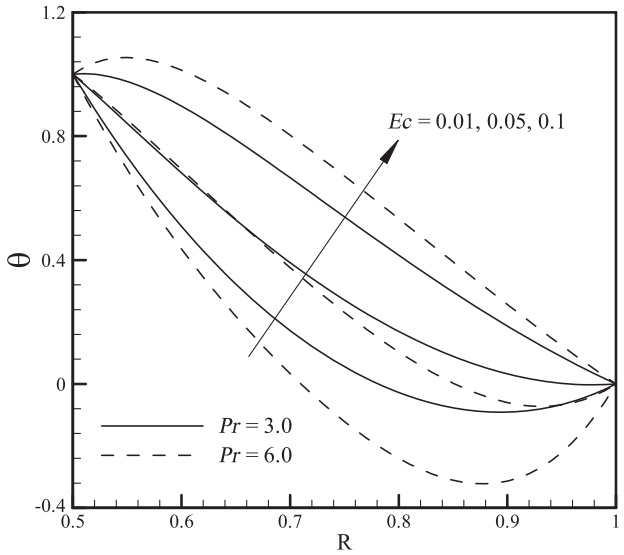

Fig. 5 Dimensionless temperature distribution for different values of Prandtl and Eckert numbers at $Nt = 0.2$, $Nb = 3$, $\theta_r = 4$, $\Phi_r = 0.5$, and $\lambda = 7$.

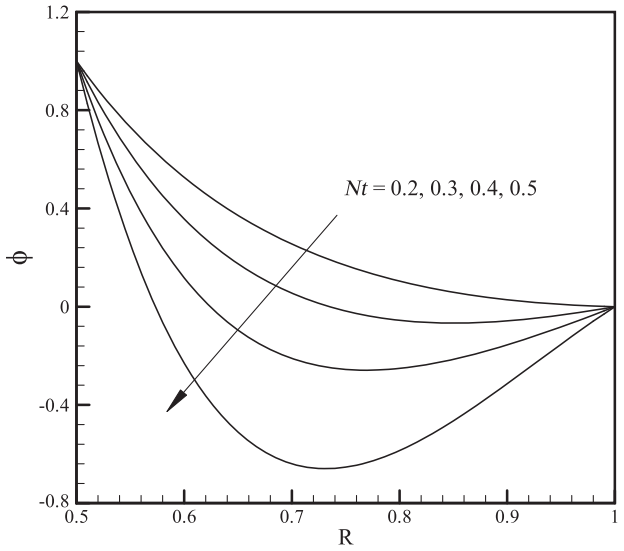

Fig. 7 Dimensionless nanoparticles volume fraction for different values of thermophoresis parameter at $Nb = 3$, $\theta_r = 4$, $\Phi_r = 0.5$, $Ec = 0.01$, $Pr = 3$, and $\lambda = 7$.

motion of nanoparticles, the thickness of thermal boundary layer increases, and hence, the temperature gradients in the annulus fall down. The variation of dimensionless temperature in the annulus is plotted in Fig. 4 for different thermophoresis parameters. It is found that an increase in the thermophoresis parameter leads to the increase in the dimensionless temperature. This shows the opposite effects of the thermophoresis parameter on the temperature field, compared to the Brownian motion parameter. The effects of both Prandtl and Eckert numbers on the dimensionless temperature are presented in Fig. 5. The Eckert number indicates the magnitude of viscous dissipation effects due to nanofluid flow in the annulus. As expected, with an increase in Eckert number the fluid temperature in the annulus increases because the kinetic energy due to fluid flow converts to heat, and consequently the temperature in the annulus increases. It is also observed that the fluid temperature increases with increasing Pr. From the physical point of view, as the Prandtl number increases, the thermal diffusivity in the annuli decreases so that the diffusion of heat generated by the viscous dissipation decreases. Consequently, because of the accumulation of heat between the cylinders, the fluid temperature increases. The effects of Brownian motion on the nanoparticles volume fraction are presented in Fig. 6. It is observed that as the Brownian motion increases, the dimensionless volume fraction increases. Returning to Eq. (12), it is reasonable that for fixed values of the other parameters at a certain position R, with a decrease in the dimensionless temperature resulted from increasing Nb (see Fig. 3), the dimensionless volume fraction increases.

Figure 7 shows the dimensionless nanoparticle volume fraction for different values of the thermophoresis parameter. As the thermophoresis increases, the nanoparticles volume fraction decreases. Returning to Eq. (12), it is reasonable that for fixed values of the other parameters at a certain position R, with an increase in the dimensionless temperature resulted from increasing Nt (see Fig. 4), the dimensionless volume fraction decreases.

Figures 8 and 9 present the dimensionless nanoparticles volume fraction for different values of Eckert number and velocity ratio, respectively. It is seen that when the Eckert number and the velocity ratio increase, the volume fraction profiles fall down in the annuli. This is due to this fact that as the Eckert number increases, the temperature inside the annulus rises because of the viscous effects and as a result, the concentration of the nanofluid (nanoparticles volume fraction) is reduced. In addition, a higher velocity ratio means a higher relative velocity between the layers of the nanofluid, which

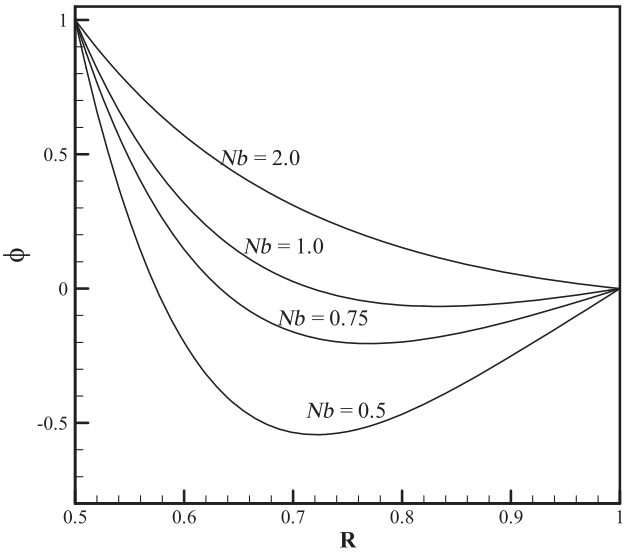

Fig. 6 Dimensionless nanoparticles volume fraction for different values of Brownian motion parameter at $Nt = 0.5$, $\theta_r = 4$, $\Phi_r = 0.5$, $Ec = 0.01$, $Pr = 3$, and $\lambda = 7$.

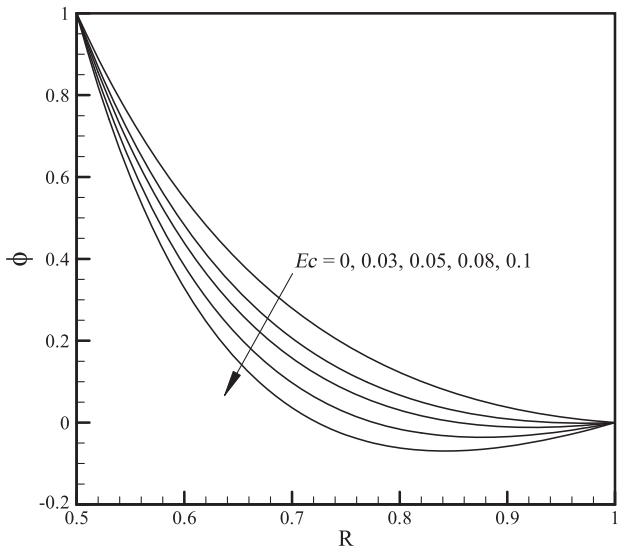

Fig. 8 Dimensionless nanoparticles volume fraction for different values of Eckert number at $Nt = 0.2$, $Nb = 0.5$, $\theta_r = 4$, $\Phi_r = 0.5$, $Pr = 3$, and $\lambda = 7$.

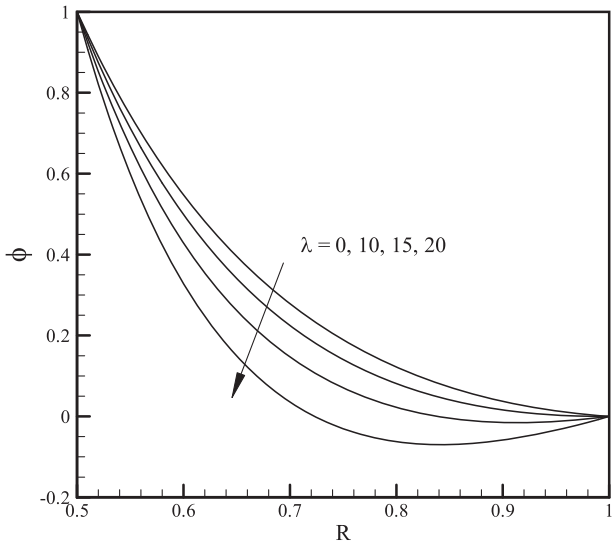

Fig. 9 Dimensionless nanoparticles volume fraction for different values of velocity ratio at $Nt = 0.2$, $Nb = 0.5$, $\theta_r = 4$, $\Phi_r = 0.5$, $Ec = 0.01$, and $Pr = 3$.

leads to higher viscous force between the cylinders and causes a higher temperature and as a result, the concentration of nanofluid decreases.

The variation of Nusselt number in the inner cylinder is plotted as a function of the Brownian motion parameter in Fig. 10 for different values of thermophoresis parameter. It is perceived that the Nusselt number decreases with an increase in the Brownian motion. On the other hand, Nusselt number increases with the increase of thermophoresis parameter. The changes in the Nusselt number are higher for smaller values of the parameter *Nb*. These results can be explained by the fact that as the Brownian motion decreases, or thermophoresis effect increases, the temperature gradients increase and finally lead to an increase in the heat transfer rate (as seen in Figs. 3 and 4).

The Nusselt number vs the velocity ratio at different values of the temperature ratio θ_r is plotted in Fig. 11. The lower temperature ratio results in the increase in Nusselt number. It is interesting to note that as the velocity ratio increases, first the Nusselt number decreases and reaches a minimum value, and then increases. The Nusselt number is minimum at $\lambda = 1.0$ regardless the temperature ratio. From the physical point of view, at $\lambda = 1.0$, there is no relative motion between

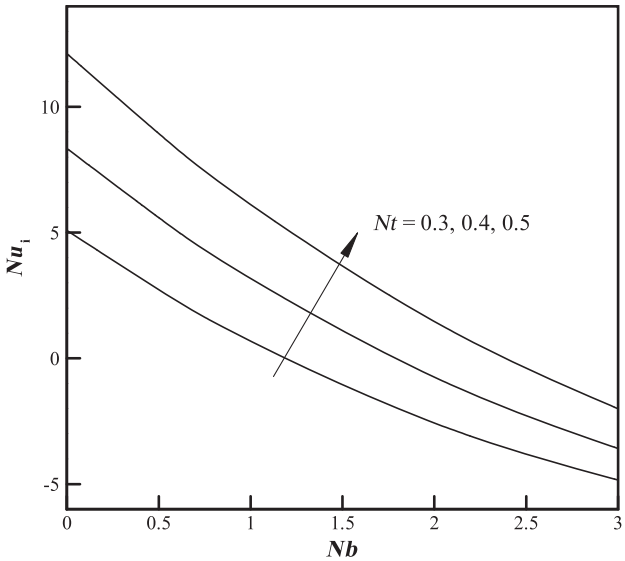

Fig. 10 Nusselt number (inner cylinder) vs Brownian motion parameter for different values of thermophoresis parameter at $\theta_r = 4$, $\Phi_r = 0.5$, $Ec = 0.01$, $Pr = 3$, and $\lambda = 7$.

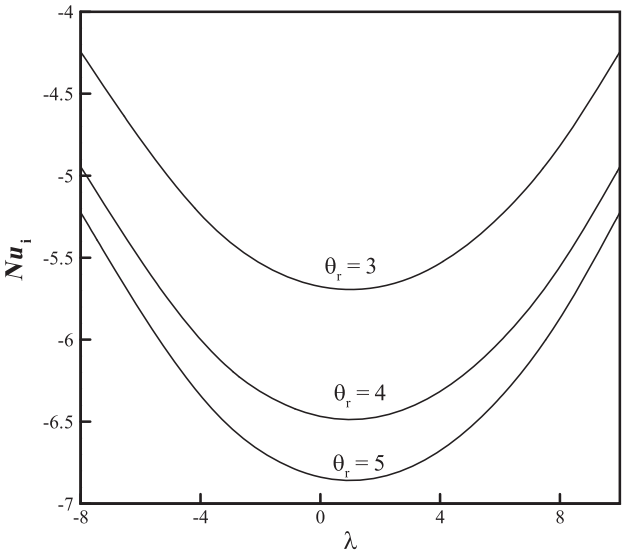

Fig. 11 Nusselt number (inner cylinder) vs velocity ratio for different values of Eckert temperature ratio at $Nt = 0.2$, $Nb = 3$, $\Phi_r = 0.5$, $Ec = 0.01$, and $Pr = 3$.

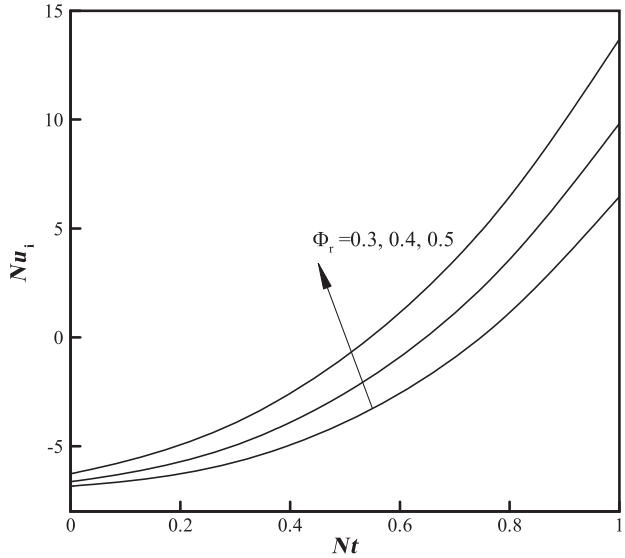

Fig. 12 Nusselt number (inner cylinder) vs thermophoresis parameter for different values of volume fraction ratio at $Nb = 3$, $\theta_r = 4$, $Ec = 0.01$, $\lambda = 10$, and $Pr = 3$.

the two cylinders so it is similar to the case in which the nanofluid is stationary in the system. In such a case, the fluid layers have no relative motion and hence the viscous dissipation due to shear stresses is minimized. Figure 12 illustrates the Nusselt number vs thermophoresis parameter in the presence of volume fraction ratio. As seen, the higher volume fraction ratios lead to a higher Nusselt number. It is found that the change in the Nusselt number increases for higher values of the thermophoresis parameter.

V. Conclusions

Analytical and numerical solutions to the flow and heat transfer of a nanofluid between two rotating cylinders are presented, considering the effects of Brownian motion and thermophoresis. The momentum, energy, and volume fraction equations are simplified and solved in the cylindrical coordinate system. The homotopy perturbation method (HPM) is employed to solve the energy equation, whereas the results obtained from the HPM are compared to the results of a numerical solution. The following results are found from the study:

1) Temperature decreases in the whole of the annulus with increasing the Brownian motion parameter, whereas the increase of thermophoresis parameter has an opposite effect.

2) With an increase in the Brownian motion parameter, the Nusselt number of the inner cylinder decreases, while the Nusselt number increases with increases of the thermophoresis parameter.

3) With an increase in the angular velocity of outer cylinder (considering a constant velocity for the inner cylinder), the volume fraction in the annulus fall down.

Acknowledgment

The second and third authors would like to thank the Thailand Research Fund and the National Research University Project for supporting this study.

References

[1] Mahian, O., Mahmud, S., and Pop, I., "Analysis of First and Second Laws of Thermodynamics Between Two Isothermal Cylinders with Relative Rotation in the Presence of MHD Flow," *International Journal of Heat and Mass Transfer*, Vol. 55, Nos. 17–18, 2012, pp. 4808–4816. doi:10.1016/j.ijheatmasstransfer.2012.04.048

[2] Fénot, M., Bertin, Y., Dorignac, E., and Lalizel, G., "A Review of Heat Transfer Between Concentric Rotating Cylinders with or Without Axial Flow," *International Journal of Thermal Sciences*, Vol. 50, No. 7, 2011, pp. 1138–1155. doi:10.1016/j.ijthermalsci.2011.02.013

[3] Choi, S. U. S., "Enhancing Thermal Conductivity of Fluids with Nanoparticles," *The Proceedings of the ASME International Mechanical Engineering Congress and Exposition*, ASME, San Francisco, CA, FED 231/MD 66, 1995, pp. 99–105.

[4] Mahian, O., Kianifar, A., Kalogirou, S. A., Pop, I., and Wongwises, S., "A Review of the Applications of Nanofluids in Solar Energy," *International Journal of Heat and Mass Transfer*, Vol. 57, No. 2, 2013, pp. 582–594. doi:10.1016/j.ijheatmasstransfer.2012.10.037

[5] Saidur, R., Leong, K. Y., and Mohammad, H. A., "A Review on Applications and Challenges of Nanofluids," *Renewable and Sustainable Energy Reviews*, Vol. 15, No. 3, 2011, pp. 1646–1668. doi:10.1016/j.rser.2010.11.035

[6] Makinde, O. D., and Aziz, A., "Boundary Layer Flow of a Nanofluid Past a Stretching Sheet with a Convective Boundary Condition," *International Journal of Thermal Sciences*, Vol. 50, No. 7, 2011, pp. 1326–1332. doi:10.1016/j.ijthermalsci.2011.02.019

[7] Motsumi, T. G., and Makinde, O. D., "Effects of Thermal Radiation and Viscous Dissipation on Boundary Layer Flow of Nanofluids over a Permeable Moving Flat Plate," *Physica Scripta*, Vol. 86, No. 4, 2012, Paper 045003. doi:10.1088/0031-8949/86/04/045003

[8] Makinde, O. D., "Analysis of Sakiadis Flow of Nanofluids with Viscous Dissipation and Newtonian Heating," *Applied Mathematics and Mechanics*, Vol. 33, No. 12, 2012, pp. 1545–1554. doi:10.1007/s10483-012-1642-8

[9] Olanrewaju, M., and Makinde, O. D., "On Boundary Layer Stagnation Point Flow of a Nanofluid over a Permeable Flat Surface with Newtonian Heating," *Chemical Engineering Communications*, Vol. 200, No. 6, 2013, pp. 836–852. doi:10.1080/00986445.2012.721825

[10] Ji, Y., Ma, H. B., and Chen, H., "Volume Fraction Effect on Heat Transfer Performance of an Oscillating Heat Pipe," *Journal of Thermophysics and Heat Transfer*, Vol. 27, No. 1, 2013, pp. 111–115. doi:10.2514/1.T3867

[11] Farzin, F., Heris, S. Z., and Rahimi, S., "Laminar Convective Heat Transfer and Pressure Drop of TiO2/Turbine Oil Nanofluid," *Journal of Thermophysics and Heat Transfer*, Vol. 27, No. 1, 2013, pp. 127–133. doi:10.2514/1.T3935

[12] Khan, W. A., Aziz, A., and Uddin, N., "Buongiorno Model for Nanofluid Blasius Flow with Surface Heat and Mass Fluxes," *Journal of Thermophysics and Heat Transfer*, Vol. 27, No. 1, 2013, pp. 134–141. doi:10.2514/1.T3916

[13] Abdel-Rahman, G. M., "Thermal Radiation and Unsteady Magneto-hydrodynamic Flow of Nanofluid in Stretching Porous Medium," *Journal of Thermophysics and Heat Transfer*, Vol. 27, No. 1, 2013, pp. 142–150. doi:10.2514/1.T3889

[14] Mahmoud, M. A. A., and Waheed, S. E., "Hydromagnetic Hiemenz Slip Flow of Convective Micropolar Fluid Towards a Stretching Plate," *Journal of Thermophysics and Heat Transfer*, Vol. 27, No. 1, 2013, pp. 151–160. doi:10.2514/1.T4016

[15] Azari, A., Kalbasi, M., and Rahimi, M., "Numerical Study on the Laminar Convective Heat Transfer of Alumina/Water Nanofluids," *Journal of Thermophysics and Heat Transfer*, Vol. 27, No. 1, 2013, pp. 170–173. doi:10.2514/1.T3834

[16] Jin, J. S., and Lee, J. S., "Effects of Aggregated Sphere Distribution and Percolation on Thermal Conduction of Nanofluids," *Journal of Thermophysics and Heat Transfer*, Vol. 27, No. 1, 2013, pp. 173–178. doi:10.2514/1.T3915

[17] Vermahmoudi, Y., Peyghambarzadeh, S. M., Naraki, M., and Hashemabadi, S. H., "Statistical Analysis of Nanofluid Heat Transfer in a Heat Exchange System," *Journal of Thermophysics and Heat Transfer*, Vol. 27, No. 2, 2013, pp. 320–325. doi:10.2514/1.T4062

[18] Noghrehabadi, A., Behseresht, A., Ghalambaz, M., and Behseresht, J., "Natural-Convection Flow of Nanofluids over Vertical Cone Embedded in Non-Darcy Porous Media," *Journal of Thermophysics and Heat Transfer*, Vol. 27, No. 2, 2013, pp. 334–341. doi:10.2514/1.T3965

[19] Uddin, M. J., Khan, W. A., and Ismail, A. I. Md., "Free Convective Flow of Non-Newtonian Nanofluids in Porous Media with Gyrotactic Microorganism," *Journal of Thermophysics and Heat Transfer*, Vol. 27, No. 2, 2013, pp. 326–333. doi:10.2514/1.T3983

[20] Asirvatham, L. G., Nimmagadda, R., and Wongwises, S., "Heat Transfer Performance of Screen Mesh Wick Heat Pipes Using Silver-Water Nanofluid," *International Journal of Heat and Mass Transfer*, Vol. 60, No. 1, 2013, pp. 201–209. doi:10.1016/j.ijheatmasstransfer.2012.11.037

[21] Godson, L., Raja, B., Mohan Lal, D., and Wongwises, S., "Convective Heat Transfer Characteristics of Silver-Water Nanofluid Under Laminar and Turbulent Flow Conditions," *Journal of Thermal Science and Engineering Applications*, Vol. 4, No. 3, 2012, Paper 031001. doi:10.1115/1.4006027

[22] Duangthongsuk, W., Dalkilic, A. S., and Wongwises, S., "Convective Heat Transfer of Al_2O_3–Water Nanofluids in a Microchannel Heat Sink," *Current Nanoscience*, Vol. 8, No. 3, 2012, pp. 317–322. doi:10.2174/157341312800620368

[23] Abu-Nada, E., Masoud, Z., and Hijazi, A., "Natural Convection Heat Transfer Enhancement in Horizontal Concentric Annuli Using Nanofluids," *International Communications in Heat and Mass Transfer*, Vol. 35, No. 5, 2008, pp. 657–665. doi:10.1016/j.icheatmasstransfer.2007.11.004

[24] Abu-Nada, E., "Effects of Variable Viscosity and Thermal Conductivity of Al_2O_3–Water Nanofluid on Heat Transfer Enhancement in Natural Convection," *International Journal of Heat and Fluid Flow*, Vol. 30, No. 4, 2009, pp. 679–690. doi:10.1016/j.ijheatfluidflow.2009.02.003

[25] Abu-Nada, E., "Effects of Variable Viscosity and Thermal Conductivity of Cuo-Water Nanofluid on Heat Transfer Enhancement in Natural Convection: Mathematical Model and Simulation," *Journal of Heat Transfer*, Vol. 132, No. 5, 2010, pp. 1–9. doi:10.1115/1.4000440

[26] Abouali, O., and Falahatpisheh, A., "Numerical Investigation of Natural Convection of Al_2O_3 Nanofluid in Vertical Annuli," *Heat and Mass Transfer*, Vol. 46, No. 1, 2009, pp. 15–23. doi:10.1007/s00231-009-0540-7

[27] Izadi, M., Behzadmehr, A., and Jalali-Vahida, D., "Numerical Study of Developing Laminar Forced Convection of a Nanofluid in an Annulus," *International Journal of Thermal Sciences*, Vol. 48, No. 11, 2009, pp. 2119–2129. doi:10.1016/j.ijthermalsci.2009.04.003

[28] Shahi, M., Mahmoudi, A. H., and Talebi, F., "A Numerical Investigation of Conjugated-Natural Convection Heat Transfer Enhancement of a Nanofluid in an Annular Tube Driven by Inner Heat Generating Solid Cylinder," *International Communications in Heat and Mass Transfer*, Vol. 38, No. 4, 2011, pp. 533–542. doi:10.1016/j.icheatmasstransfer.2010.12.022

[29] Moghari, R. M., Akbarinia, A., Shariat, M., Talebi, F., and Laur, R., "Two Phase Mixed Convection Al_2O_3–Water Nanofluid Flow in an Annulus," *International Journal of Multiphase Flow*, Vol. 37, No. 6, 2011, pp. 585–595. doi:10.1016/j.ijmultiphaseflow.2011.03.008

[30] Cianfrini, M., Corcione, M., and Quintino, A., "Natural Convection Heat Transfer of Nanofluids in Annular Spaces Between Horizontal

Concentric Cylinders," *Applied Thermal Engineering*, Vol. 31, Nos. 17–18, 2011, pp. 4055–4063. doi:10.1016/j.applthermaleng.2011.08.010

[31] Soleimani, S., Sheikholeslami, M., Ganji, D. D., and Gorji-Bandpay, M., "Natural Convection Heat Transfer in a Nanofluid Filled Semi-Annulus Enclosure," *International Communications in Heat and Mass Transfer*, Vol. 39, No. 4, 2012, pp. 565–574. doi:10.1016/j.icheatmasstransfer.2012.01.016

[32] Sheikhzadeh, G. A., Arbaban, M., and Arefmanesh, A. "Effects of Radial Fins on the Laminar Natural Convection of a Nanofluid in Concentric Annuli," *Computational Thermal Sciences*, Vol. 4, No. 2, 2012, pp. 151–158. doi:10.1615/ComputThermalScien.2012004025

[33] Sheikhzadeh, G. A., Arbaban, M., and Mehrabian, M. A., "Laminar Natural Convection of Cu-Water Nanofluid in Concentric Annuli with Radial Fins Attached to the Inner Cylinder," *Heat and Mass Transfer*, Vol. 49, No. 3, 2013, pp. 391–403. doi:10.1007/s00231-012-1084-9

[34] Nasrin, R., Alim, M., and Chamkha, A. J., "Effect of Viscosity Variation on Natural Convection Flow of Water-Alumina Nanofluid in an Annulus with Internal Heat Generation," *Heat Transfer — Asian Research*, Vol. 41, No. 6, 2012, pp. 536–552. doi:10.1002/htj.21016

[35] Parvin, S., Nasrin, R., Alim, M. A., Hossain, N. F., and Chamkha, A. J., "Thermal Conductivity Variation on Natural Convection Flow of Water-Alumina Nanofluid in an Annulus," *International Journal of Heat and Mass Transfer*, Vol. 55, Nos. 19–20, 2012, pp. 5268–5274. doi:10.1016/j.ijheatmasstransfer.2012.05.035

[36] Ashorynejad, H. R., Mohamad, A. A., and Sheikholeslami, M., "Magnetic Field Effects on Natural Convection Flow of a Nanofluid in a Horizontal Cylindrical Annulus Using Lattice Boltzmann Method," *International Journal of Thermal Sciences*, Vol. 64, No. 2, 2013, pp. 240–250. doi:10.1016/j.ijthermalsci.2012.08.006

[37] Mahian, O., Mahmud, S., and Heris, S. Z., "Analysis of Entropy Generation Between Co-Rotating Cylinders Using Nanofluids," *Energy*, Vol. 44, No. 1, 2012, pp. 438–446. doi:10.1016/j.energy.2012.06.009

[38] Mahian, O., Mahmud, S., and Heris, S. Z., "Effect of Uncertainties in Physical Properties on Entropy Generation Between Two Rotating Cylinders with Nanofluids," *ASME Journal of Heat Transfer*, Vol. 134, No. 10, 2012, Paper 101704. doi:10.1115/1.4006662

[39] Mahian, O., Mahmud, S., and Wongwises, S., "Entropy Generation Between Two Rotating Cylinders with Magnetohydrodynamic Flow Using Nanofluids," *Journal of Thermophysics and Heat Transfer*, Vol. 27, No. 1, 2013, pp. 161–169. doi:10.2514/1.T3908

[40] Buongiorno, J., "Convective Transport in Nanofluids," *ASME Journal of Heat Transfer*, Vol. 128, Nos. 1–2, 2006, pp. 240–250. doi:10.1115/1.2150834

[41] He, J. H., "Homotopy Perturbation Method for Solving Boundary Value Problems," *Physical Letters A*, Vol. 350, Nos. 1–2, 2006, pp. 87–88. doi:10.1016/j.physleta.2005.10.005

[42] Ariel, P., Hayat, T., and Asghar, S., "Homotopy Perturbation Method and Axisymmetric Flow over a Stretching Sheet," *International Journal of Nonlinear Sciences and Numerical Simulation*, Vol. 7, No. 4, 2006, pp. 399–406. doi:10.1515/IJNSNS.2006.7.4.399

[43] Nourazar, S. S., Matin, M. H., and Simiari, M., "The HPM Applied to MHD Nanofluid Flow over a Horizontal Stretching Plate," *Journal of Applied Mathematics*, 2011. doi:10.1155/2011/876437

[44] Rashidi, M. M., Keimanesh, M., and Rajvanshi, S. C., "Study of Pulsatile Flow in a Porous Annulus with the Homotopy Analysis Method," *International Journal of Numerical Methods for Heat and Fluid Flow*, Vol. 22, No. 8, 2012, pp. 971–989. doi:10.1108/09615531211271817

International Communications in Heat and Mass Transfer 48 (2013) 141–148

Contents lists available at ScienceDirect

International Communications in Heat and Mass Transfer

journal homepage: www.elsevier.com/locate/ichmt

A numerical correlation development study for the determination of Nusselt numbers during boiling and condensation of R134a inside smooth and corrugated tubes ☆

M. Balcilar [a], K. Aroonrat [b], A.S. Dalkilic [c,*], S. Wongwises [b]

[a] Computer Engineering Department, Yildiz Technical University, Davutpasa, Esenler, Istanbul 34220, Turkey
[b] Fluid Mechanics, Thermal Engineering and Multiphase Flow Research Lab. (FUTURE), Department of Mechanical Engineering, King Mongkut's University of Technology Thonburi, Bangmod, Bangkok 10140, Thailand
[c] Heat and Thermodynamics Division, Department of Mechanical Engineering, Yildiz Technical University, Yildiz, Besiktas, Istanbul 34349, Turkey

ARTICLE INFO

Available online 9 September 2013

Keywords:
Condensation
Boling
Nusselt number
Heat transfer coefficient
Modeling
Neural network

ABSTRACT

In this study, the closed form of artificial neural network method is used to have a reliable empirical correlation to estimate the measured Nusselt numbers of R134a flowing downward and horizontally inside smooth and corrugated copper tubes by means of some dimensionless numbers. R134a and water are used as working fluids flowing in the tube side and annular side of a double tube heat exchanger, respectively. The training sets have the experimental data of in-tube condensation and in-tube boiling tests including various mass fluxes and saturation temperatures of R134a. Inputs of the formula are the dimensionless numbers obtained from measured values of test section such as Froude number, Weber number, Bond number, Lockhart and Martinelli number, void fraction, the ratio of density to dynamic viscosity, liquid, vapor and equivalent Reynolds numbers, surface tension parameter and liquid Prandtl number, while the output of the formula is the experimental Nusselt numbers in the analysis. Nusselt numbers of R134a are modeled using closed form of multi-layer perceptron (MLP) method of artificial neural network (ANN). Analyses of the ANN method are accomplished by means of 1177 data points. The performance of the closed form of multi-layer perceptron (MLP) with three inputs and one hidden neuron architecture was found to be in good agreement, predicting the experimental Nusselt numbers with their deviations being within the range of ± 30% for all tested conditions. Empirical correlations are proposed for both condensation and boiling flows separately. A single empirical correlation is found to be capable of predicting the experimental Nusselt numbers of both condensation and boiling flows together. Dependency of output of the ANNs from input values is also investigated in the paper. Vapor Reynolds number, equivalent Reynolds number, Weber number and Froude number are found to be the most affective parameters as a result of the dependency analyses.

© 2013 Elsevier Ltd. All rights reserved.

1. Introduction

Heat exchangers using in-tube condensation have great significance in the refrigeration, automotive and process industries. Effective heat exchangers have been rapidly developed due to the demand for more compact systems, higher energy efficiency, lower material costs and other economic incentives. The surface area of heat exchangers has a directly significant effect on their heat-transfer performance. Improvements to make heat transfer equipment more energy-efficient would need to focus on miniaturization on the one hand and an astronomical increase in heat flux on the other. Normally, heat-transfer enhancement techniques necessarily reduce the thermal resistance in a conventional heat exchanger by promoting a higher convection heat-transfer coefficient in order to minimize the size of the heat exchanger. Recent numerical studies of authors on these subjects regarding the two-phase flows in the literature are summarized in the following paragraphs.

Dalkilic and Wongwises [1,2], Laohalertdecha et al. [3], and Balcilar et al. [4] reviewed the studies on in-tube condensation using smooth and enhanced tubes intensively since two-phase flow in tubes is the most challenging phenomenon in the heat exchanger systems. All effective possible research subjects of in-tube condensation were classified generally according to the tube orientation (horizontal, vertical, and inclined tubes) and tube geometry (smooth and enhanced tubes). Detailed information on the in-tube condensation studies of heat transfer, pressure drop, flow pattern, void fraction, and refrigerants in the literature were given. Their papers not only mention the new enhancement techniques of heat transfer, but also include some information on the new refrigerants, theoretical, numerical and empirical models in the literature.

☆ Communicated by W.J. Minkowycz.

* Corresponding author.
E-mail address: dalkilic@yildiz.edu.tr (A.S. Dalkilic).

0735-1933/$ – see front matter © 2013 Elsevier Ltd. All rights reserved.
http://dx.doi.org/10.1016/j.icheatmasstransfer.2013.08.012

Nomenclature

Bo	Bond number
d	internal tube diameter, m
f	function
Fr	Froude number
G	mass flux, kg m^{-2} s^{-1}
j	superficial velocity
Pr	Prandtl number
R	ratio of density to dynamic viscosity
Re	Reynolds number
x	average vapor quality
We	Weber number
X_{tt}	Lockhart and Martinelli parameter

Greek Symbols

α	void fraction
ρ	density, kg m^{-3}
μ	dynamic viscosity, kg m^{-1} s^{-1}
σ	surface tension, N m^{-1}
Ψ	surface tension parameter

Subscripts

ANN	artificial neural network
eq	equivalent
exp	experiment
g	gas
h	hydraulic
l	liquid
TP	two-phase

Artificial intelligence methods such as genetic algorithms (GAs) and artificial neural networks (ANNs) modeling validated by the experimental work, have been gaining increased popularity in correlating two-phase flows in tubes. However, investigations into the prediction of in-tube condensation and evaporation's characteristics by means of artificial intelligence techniques are not sufficient in the literature. Authors of this paper have these publications on the determination of heat transfer characteristics of two-phase flows in-tubes numerically [5–10].

Improvements in condensation heat transfer in horizontal tubes have been the subject of significant concern in the design and operation of air conditioning and refrigeration systems. Performance of smooth tubes has been determined by many researchers with pure refrigerants as operating fluids. Generally, empirical methods have been offered to compute the condensation heat transfer coefficients in horizontal smooth-tubes. In the past, some researchers have studied several enhancement techniques, such as rough surfaces and twisted-tape inserts, while on the other hand, micro-fin and corrugated tubes have recently been used intensively because of their high condensation heat transfer performance and moderate pressure drop. Authors of this paper have these publications on the determination of two-phase heat transfer coefficient in smooth and enhanced tubes [11–22]. This paper is a continuation of the authors' previous works and includes all their previous works about condensation and boiling in tubes.

The leading aim of this study is to model the condensation and boiling in smooth and corrugated tubes in MATLAB with the methods of MLP and NLS, and then determine the most affected parameters and develop reliable correlations with several sets of basic heat transfer data [11,19–21] belonging to the condensation and boiling flow in smooth and corrugated tubes. The proposed correlations are believed to be useful in predicting the heat transfer characteristics of new smooth and corrugated tubes, without additional experiments, due to the use of reliable data from the authors' laboratory in King Mongkut's University of Technology Thonburi.

2. Experimental apparatus and method

Detailed descriptions of the experimental apparatuses and summary of test conditions in terms of flow type, refrigerant, mass flux, average pressure, inlet and outlet vapor qualities and number of data points belonging to the data for studying condensation and evaporation of R134a inside horizontal/vertical smooth and corrugated tubes can be found either in authors' previous publications and in Table 1 partly.

3. Calculation procedure for the analyses

3.1. Error analysis

The error analyses' calculation procedure for the average values of the experimental and calculated results of the two-phase pressure drops regarding with R square error, proportional error and mean square error (MSE) can be seen from authors' previous publications.

3.2. The generalized artificial neural networks (ANNs) model

The detailed information on the ANN analyses of the determination condensation heat transfer coefficient, pressure drop and correlation development can be seen from the authors' previous publications. It should be noted that the authors benefitted from either their own experimental database or their database of independent laboratories in these publications.

Table 1
Experimental parameters and operating conditions.

Data set / Specifications	Data set 1 [11]	Data set 2 [19]	Data set 3 [20]	Data set 4 [21]
Phase change type	Condensation	Condensation	Boiling	Boiling
Refrigerant type	R134a	R134a	R134a	R134a
Tube type	Smooth	Smooth and 5 different corrugated tubes	Smooth and 5 different corrugated tubes	Smooth and 5 different corrugated tubes
Tube orientation	Vertical	Horizontal	Vertical	Horizontal
Inner diameter (m)	0.0081	0.0081	0.0087	0.0081
Tube length (m)	0.5	2.5	0.85	2.5
Mass flux (kg m^{-2} s^{-1})	260, 300, 340, 400, 455, 515	200, 300, 400, 500, 600, 700	200, 300, 400	300, 400, 500
Saturation pressure (bar)	10, 12	10, 11.3, 12.7	4,5, 5.7	4,5, 5.7
x_{avg}	0.7–0.96	0.07–0.82	0.14–0.86	0.09–0.81
Number of data points	368	280	302	227

Table 2
Proposed correlations and their error rates.

Eq. number	Proposed correlation	Data set	MSE	RMSE	R^2	Data number
1	$Nu = \frac{b_1}{1+\exp\left[b_2\psi+b_3\frac{Re_{eq}}{10000}+b_4 Pr_l+b_5\right]}$ $b_1 = 2207.661, b_2 = 6.857,$ $b_3 = -0.171, b_4 = -0.37, b_5 = 3.213$	All data	6140	78.34	0.8	1177
2	$Nu = \frac{b_1}{1+\exp\left[b_2\psi+b_3\frac{Re_g}{10000}+b_4\frac{Re_g}{10000}+b_5\right]}+b_6$ $b_1 = -1385.293, b_2 = -17.339, b_3 = 0.641,$ $b_4 = 0.108, b_5 = -2.656, b_6 = 1614.92$	1–3	6063.5	77.9	0.84	670
3	$Nu = \frac{100000}{1+\exp\left[b_1\frac{Re_g}{10000}+b_2\frac{Re_g}{10000}+b_3\frac{Re_{eq}}{10000}+b_4\right]}$ $b_1 = -4.606, b_2 = -1.73, b_3 = 4.615,$ $b_4 = 5.827$	2–4	4374.6	66.14	0.71	507
4	$Nu = \frac{100000}{1+\exp\left[b_1 Bo+b_2\psi+b_3\frac{Re_{eq}}{10000}+b_4\right]}$ $b_1 = 0.014, b_2 = 3.958, b_3 = -0.118,$ $b_4 = 3.112$	1–2	7946.6	89.14	0.8	648
5	$Nu = \frac{22650}{1+\exp\left[b_1 Bo+b_2\frac{Re_g}{10000}+b_3\frac{Re_{eq}}{10000}+b_4\right]}+b_5$ $b_1 = -0.083, b_2 = -0.292, b_3 = -1.749,$ $b_4 = 7.774, b_5 = 228.98$	3–4	2322.2	48.19	0.77	529
6	$Nu = \frac{2286}{1+\exp\left[b_1 Bo+b_2\frac{Re_g}{10000}+b_3 Pr_l+b_4\right]}+263$ $b_1 = -6.23, b_2 = -7.91, b_3 = -138.177,$ $b_4 = 604.191$	1	11304	106.32	0.68	368
7	$Nu = \frac{-466}{1+\exp[b_1 Fr+b_2 X_{tt}+b_3]}+741$ $b_1 = 0.003, b_2 = -1.109, b_3 = -1.098$	2	4279	65.4	0.58	280
8	$Nu = \frac{b_1}{1+\exp\left[b_2 Bo+b_3\frac{Re_{eq}}{10000}+b_4\right]}$ $b_1 = 645.682, b_2 = -0.065, b_3 = -0.171,$ $b_4 = 1.667$	3	382	19.5	0.75	302
9	$Nu = \frac{b_1}{1+\exp\left[b_2 Bo+b_3\frac{Re_{eq}}{10000}+b_4 Pr_l\right]}$ $b_1 = 1790.746, b_2 = -0.056, b_3 = -0.212,$ $b_4 = 0.944$	4	2421	49.2	0.88	227

3.3. The closed form of MLP

The success of the modeling experimental data with MLP has been reported many times by the researchers. But the worst part of this method is the mathematical expression of the relationship between input and output grows by growing architecture of MLP. Because of the relationship between inputs and outputs is not showing as a simple equation, this method is called by the researchers as black box. The success of correlation decreases when the model architecture is quite small, but this time, the closed form of the model is too simplified, and it can be shown as a simple equation. For that reason, in this study, the closed form of MLP with 3-1-1 architecture is used. In this model the transfer function of hidden layer is considered to be tansig function. According to this consideration the output of hidden layer is written as Eq. (1).

$$O_h = \frac{1}{1+\exp\left[w_1^1 \cdot I_1 + w_2^1 I_2 + w_3^1 I_3 + b_1\right]} \quad (1)$$

Because of the transfer function of output layer is considered to be linear function, the output of the model, in other word, the closed form of model is written as Eq. (2).

$$O = \frac{w_1^2}{1+\exp\left[w_1^1 \cdot I_1 + w_2^1 I_2 + w_3^1 I_3 + b_1\right]} + b_2 \quad (2)$$

3.4. The non-linear least square (NLS) algorithm

The non-linear least square (NLS) method allows the user to determine the most optimal non-linear function coefficients in order to fit data collected from an experimental environment to a non-linear function (non-linear curve fitting). This method tries to minimize the mean square error, beginning from the first estimated values determined by the user. Since it advances step by step through optimizing this point, it finds the local minimum and not the global minimum by starting from this initial point. The method is tested by starting from different initial points, and thus the global minimum value of model is determined.

3.5. Correlation development for the two-phase pressure drop

There have been a number of studies on the in-tube condensation and evaporation pressure drops of smooth and enhanced tubes in the literature. Generally, empirical methods have been used to compute

Table 3
The most predictive input parameters according to the error rates.

Inputs											Input number	Data Set	Output
Fr	We	Bo	X_{tt}	α	ψ	Re_l	Re_g	Re_{eq}	R	Pr_l			R^2 – Nu (%)
0	0	0	0	0	0	0	1	0	0	0	1	All	0.891
0	0	1	0	0	0	0	1	0	0	0	2	All	0.896
0	0	0	0	0	1	0	0	1	0	1	3	All	0.897
0	0	0	0	0	0	0	1	0	0	0	1	1–3	0.914
0	0	0	0	0	0	0	1	0	1	0	2	1–3	0.916
0	0	0	0	0	1	1	1	0	0	0	3	1–3	0.917
1	0	0	0	0	0	0	0	0	0	0	1	2–4	0.765
1	0	0	0	0	0	0	0	0	10	0	2	2–4	0.806
0	0	0	0	0	0	1	1	1	0	0	3	2–4	0.843
0	0	0	0	0	0	0	1	0	0	0	1	1–2	0.883
0	0	0	0	0	1	0	0	1	0	0	2	1–2	0.89
0	0	1	0	0	1	0	0	1	0	0	3	1–2	0.894
0	0	0	0	0	0	0	0	1	0	0	1	3–4	0.855
0	0	1	0	0	0	0	0	1	0	0	2	3–4	0.879
0	0	1	0	0	0	0	1	1	0	0	3	3–4	0.881

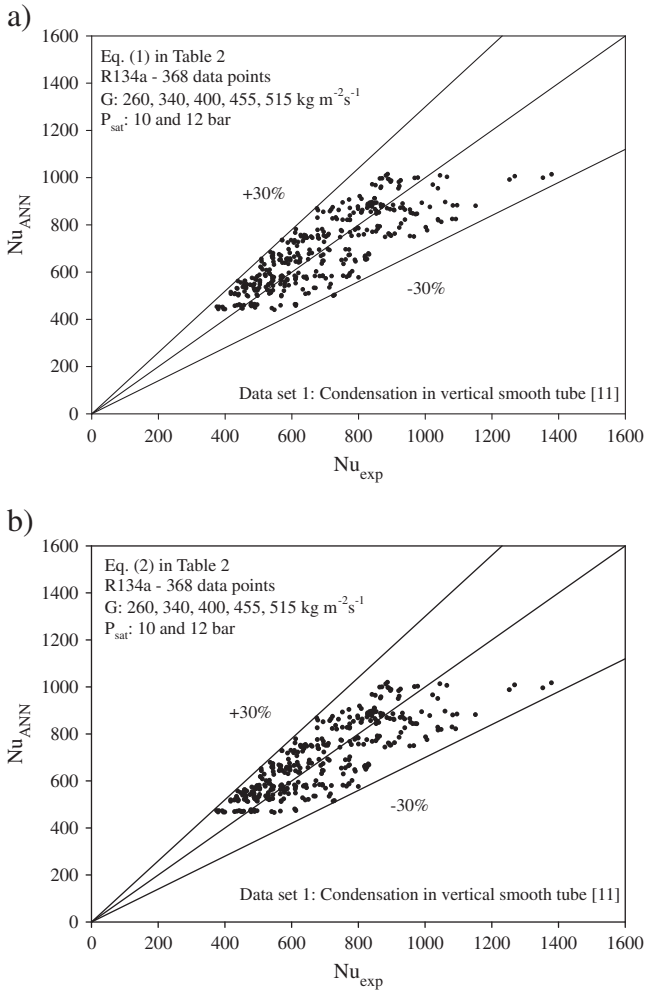

Fig. 1. Performance comparison of Eq. (1) (a) and Eq. (2) (b) for the data set 1.

the Nusselt numbers and convective heat transfer coefficients in tubes. As a result, Eq. (3) is formed to predict the Nusselt number of evaporation and condensation in terms of the above explanations as follows

$$Nu = \frac{b_1}{1 + \exp\left[b_2\psi + b_3\frac{Re_{eq}}{10000} + b_4 Pr_l + b_5\right]} \tag{3}$$

where the coefficients from b_1 to b_5 are the constants. It should be noted that detailed information on the developed correlations can be seen in Table 2.

The inputs of model have the following dimensionless numbers to determine their effects on the Nusselt number selected as the output of the analyses. Table 3 shows the significance of these input parameters below considering their error values of R^2.

The all liquid equivalent Re number is determined from:

$$Re_{eq} = \frac{G_{eq} d_h}{\mu_l} \tag{4}$$

and equivalent liquid mass flux and the ratio of density to dynamic viscosity are defined as:

$$G_{eq} = G\left((1-x) + x\left(\frac{\rho_l}{\rho_g}\right)^{0.5}\right) \tag{5}$$

$$R = \frac{\rho_l \mu_l}{\rho_g \mu_g} \tag{6}$$

and Bond number and the Froude number are defined respectively as:

$$Bo = g\left(\rho_l - \rho_g\right)\left(\frac{(d_h/2)^2}{\sigma}\right) \tag{7}$$

$$Fr = \frac{G^2}{g d_h {\rho_{TP}}^2} \tag{8}$$

where the two-phase density and the Lockhart and Martinelli parameter is determined from:

$$\rho_{TP} = \left(\frac{x}{\rho_g} + \frac{1-x}{\rho_l}\right)^{-1} \tag{9}$$

$$X_{tt} = \left(\frac{1-x}{x}\right)^{0.9}\left(\frac{\mu_g}{\mu_l}\right)^{0.1}\left(\frac{\rho_g}{\rho_l}\right)^{0.5} \tag{10}$$

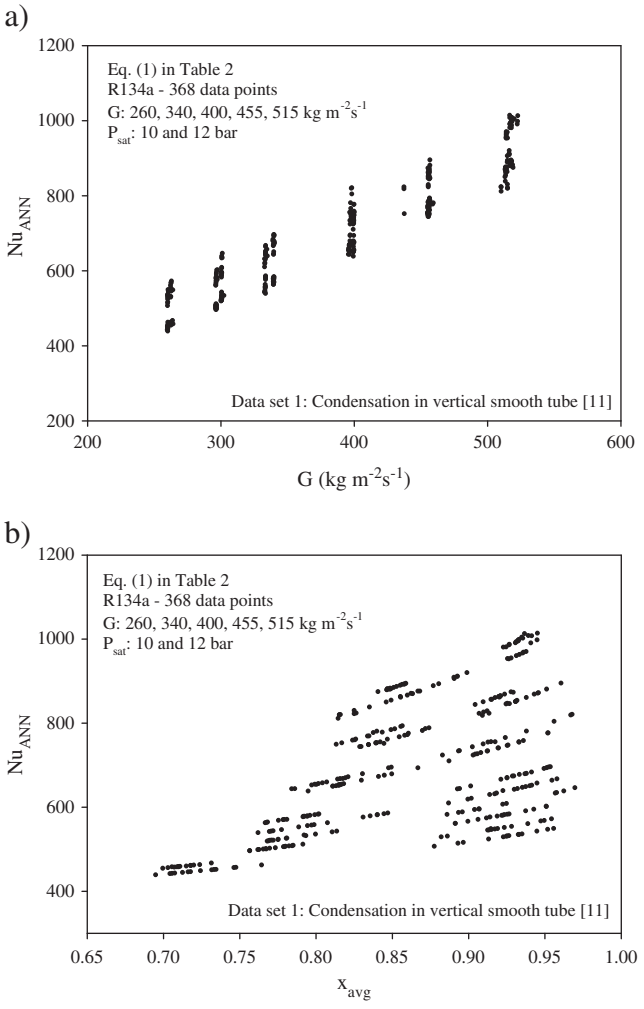

Fig. 2. Alteration of obtained Nusselt numbers with mass flux (a) and average vapor quality (b) for data set 1.

and the all liquid Reynolds number and all gas Reynolds number equations can be expressed as:

$$Re_l = \frac{Gd_h}{\mu_l} \tag{11}$$

$$Re_g = \frac{Gd_h}{\mu_g} \tag{12}$$

and the void fraction, α, can be determined from Butterworth's correlation as follows:

$$\alpha = \frac{1}{1 + 0.28\left(\frac{1-x}{x}\right)^{0.64}\left(\frac{\rho_g}{\rho_l}\right)^{0.36}\left(\frac{\mu_l}{\mu_g}\right)^{0.07}} \tag{13}$$

and Weber number, We, is used as:

$$We = \frac{G^2 d_h}{\sigma \rho_{TP}} \tag{14}$$

and surface tension parameter, ψ, and the liquid superficial velocity, j_l, are calculated respectively.

$$\psi = \frac{j_l \mu_l}{\sigma} \tag{15}$$

$$j_l = \frac{G(1-x)}{\rho_l(1-\alpha)} \tag{16}$$

4. Results and discussion

The following paragraphs numerically present the discussion of calculated Nusselt numbers of condensation and boiling flows of R134a using the database of authors' previous studies [11,19–21] in horizontal/vertical smooth and corrugated tubes. It should be noted that detailed explanations and some additional figures and tables containing different experimental parameters related to their studies on the heat transfer characteristics can be seen in the applied reference databases [11,19–21], which demonstrate the accuracy of the experiments. A discussion of the results follows.

There are one-type of closed form formula in the paper. It is developed for the calculation of the coefficients in correlations in Table 2 using the experimental databases in Table 1. The inputs of closed form are selected in the set of Froude number, Weber number, Bond number, Lockhart and Martinelli number, void fraction, the ratio of density to dynamic viscosity, liquid, vapor and equivalent Reynolds numbers, surface tension parameter and liquid Prandtl number, while the output of the closed form is the experimental Nusselt numbers in the analysis. Four-fold cross validation was used

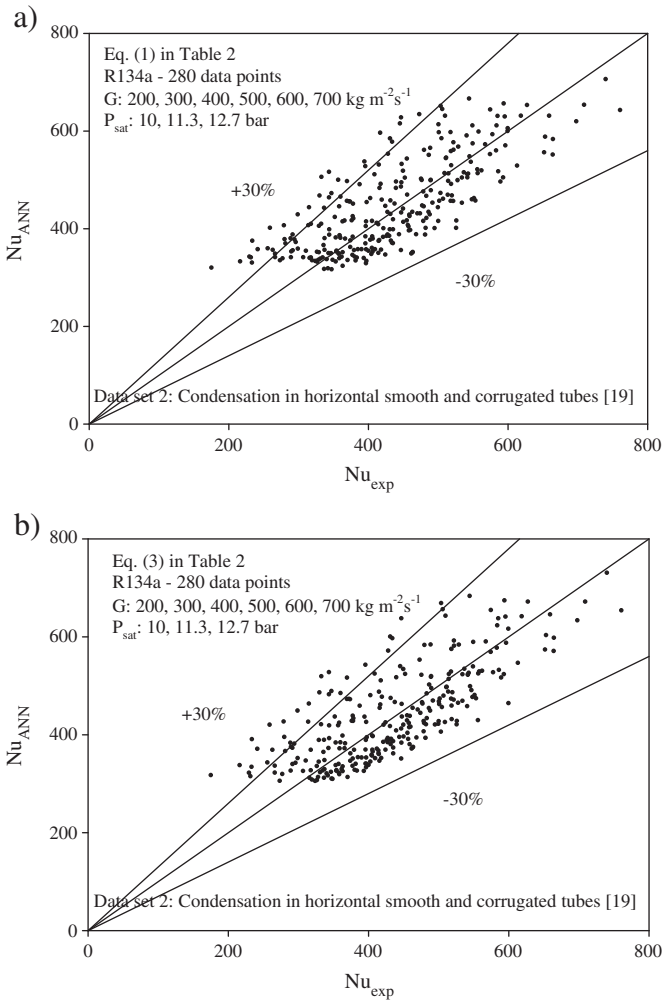

Fig. 3. Performance comparison of Eq. (1) (a) and Eq. (3) (b) for the data set 2.

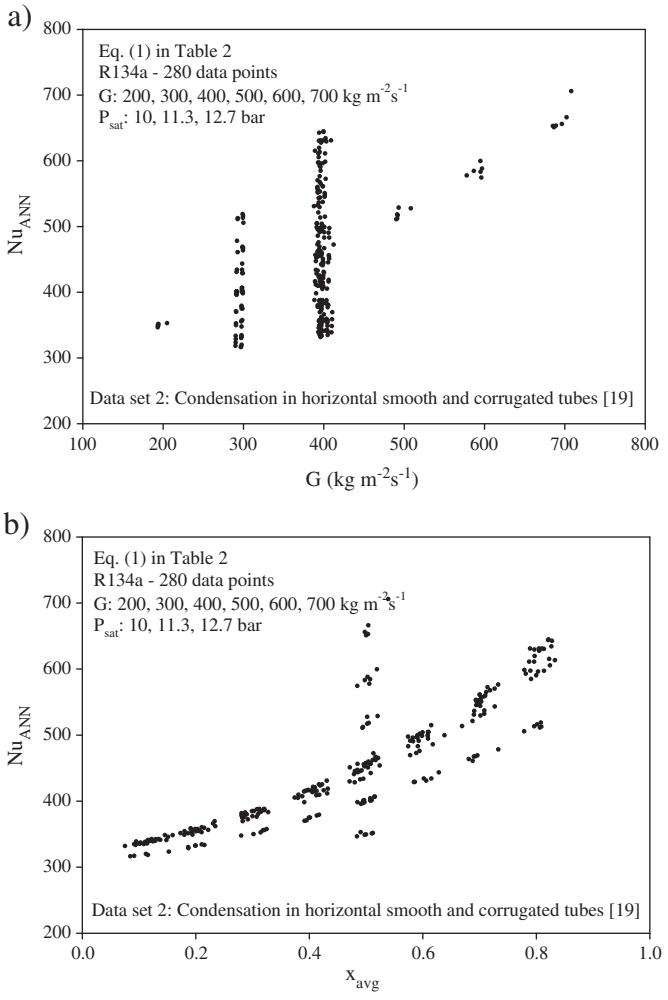

Fig. 4. Alteration of obtained Nusselt numbers with mass flux (a) and average vapor quality (b) for data set 2.

for regression analysis. It means that 1177 data points (all data of boiling and condensation in smooth and corrugated tubes) were divided by 4 sets randomly and one of the sets selected for the test process, and the rest of them (3 sets) were selected for the training process. These processes were continued until there were no untested data sets. Four different data sets of researchers [11,19–21] are defined in Table 1 and used for all analyses. It should be noted that although various architectures were tested for elimination, only the typical one was used in the paper due to limited space.

Table 1 shows the operating conditions of the database. 1177 data points were used in the analyses. 648 of them belong to in tube flow of condensation of vertical and horizontal orientations whereas 529 of them belong in tube flow of boiling of vertical and horizontal orientations. There were 5 different corrugated tubes and a smooth tube having 8 mm i.d. tested in the experiments. Mass fluxes and vapor qualities had a wide range for the accuracy of the developed correlations.

Table 2 includes 9 different developed correlations for each dataset or combination of them separately. Their R^2 values show their success and reliability. Eq. (1) in Table 2 has the most importance among others in the paper. It can predict all data including condensation/boiling in smooth/corrugated horizontal/vertical tubes at the same time with an acceptable accuracy as shown in all figures. The difference between the R^2 results is due to the hardness of generalization in the two-phase flow.

Table 3 illustrates the dependency of the output parameter from the input ones, in other words, these tables imply the most important affective dimensionless number on the prediction of the Nusselt number. It is possible from this table to determine the first 3 most affective parameters of databases separately. From this table, it is possible to reveal that vapor Reynolds number, equivalent Reynolds number and Weber number have the most influence on the Nusselt number considering all databases with their R^2 values over 0.8. Moreover, Froude number has also some importance apart from other input parameters. In this analysis, when the input parameter number is one in all databases, vapor Reynolds number seems to be dominant on the prediction of the Nusselt number with the R^2 value of 0.891. When there are 2 known input parameters, vapor Reynolds number and Bond number have the R^2 value of 0.896. When there are 3 known input parameters, vapor Reynolds number, Bond number and surface tension parameter have the R^2 value of 0.897. Datasets 1–3 refer to condensation and boiling datasets in vertical smooth and corrugated tubes, datasets 2–4 refer to condensation in horizontal tubes and boiling in vertical smooth and corrugated tubes, datasets 1–2 refer to condensation in horizontal and vertical smooth and corrugated tubes, datasets 3–4 refer to boiling in horizontal and vertical smooth and corrugated tubes as they can be realized from Table 1. These tables show that the accuracy of the estimated output value by means of input values increases along an increasing number of proper input parameters. In addition, they show the existence of less important input parameters on the prediction of the Nusselt number. It should be noted that it is possible to derive more results from these tables for each database specifically.

In this paper, an intensive concentration has been focused on the determination of the Nusselt numbers using all datasets by means of Eq. (1) in Table 2. The predictability (a) and performance comparison with other developed correlations (b) can be seen from Figs. 1, 3, 5 and 7. As it can be seen from these figures, majority of data points fall

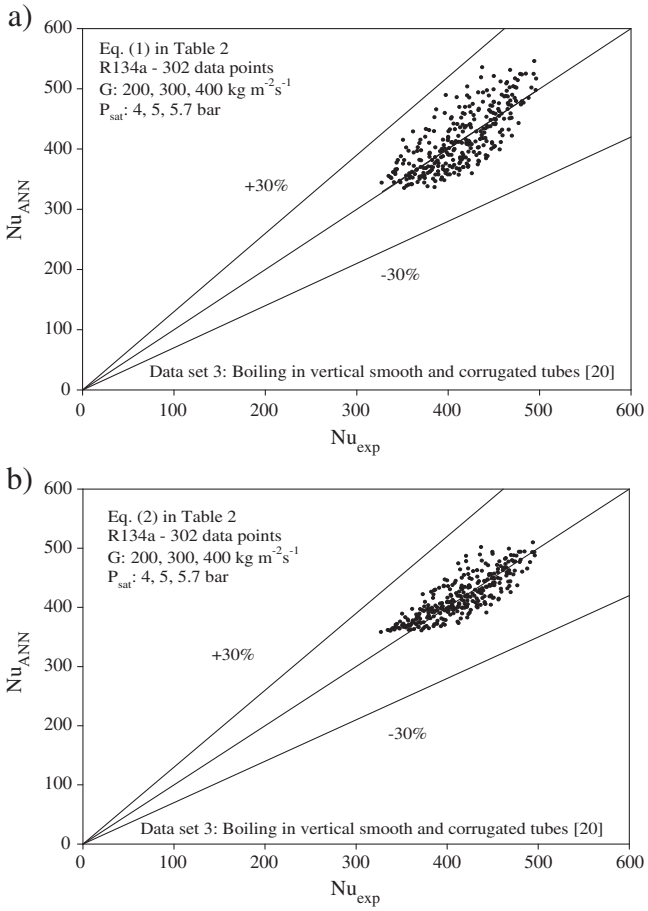

Fig. 5. Performance comparison of Eq. (1) (a) and Eq. (2) (b) for the data set 3.

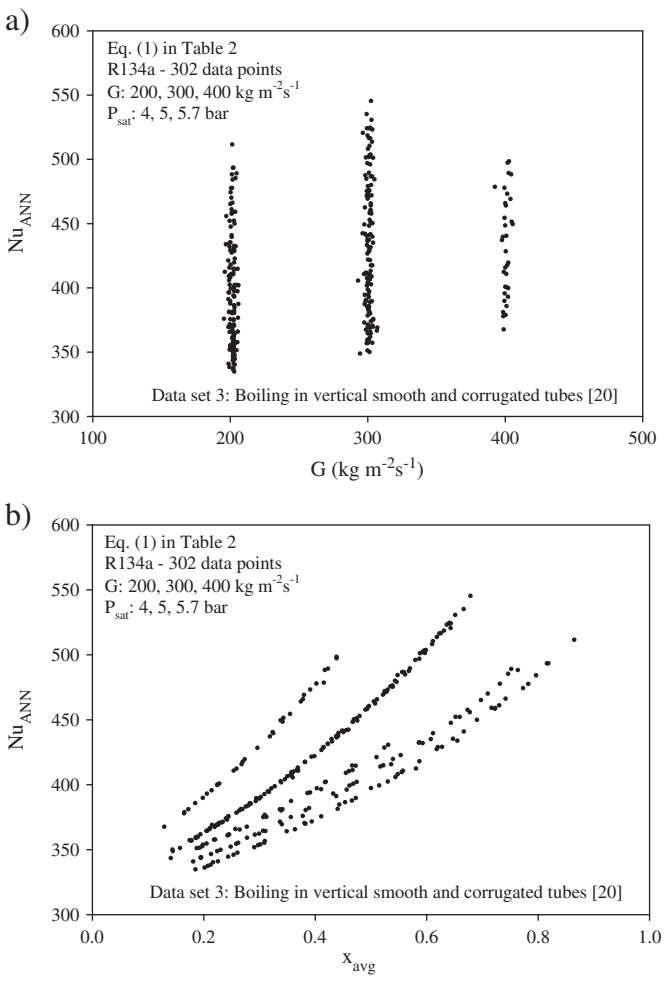

Fig. 6. Alteration of obtained Nusselt numbers with mass flux (a) and average vapor quality (b) for data set 3.

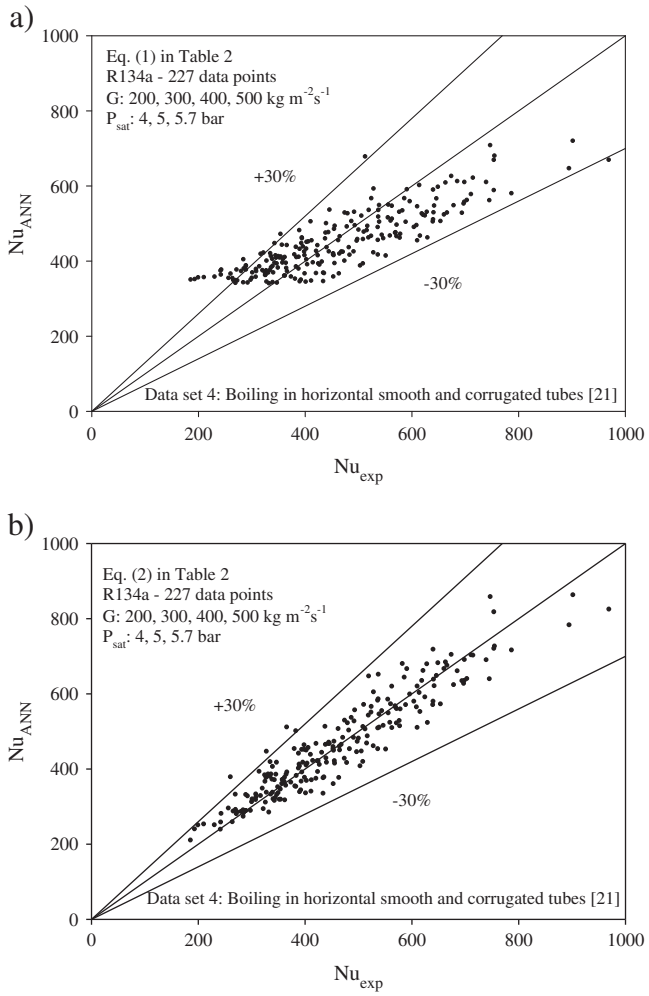

Fig. 7. Performance comparison of Eq. (1) (a) and Eq. (2) (b) for the data set 4.

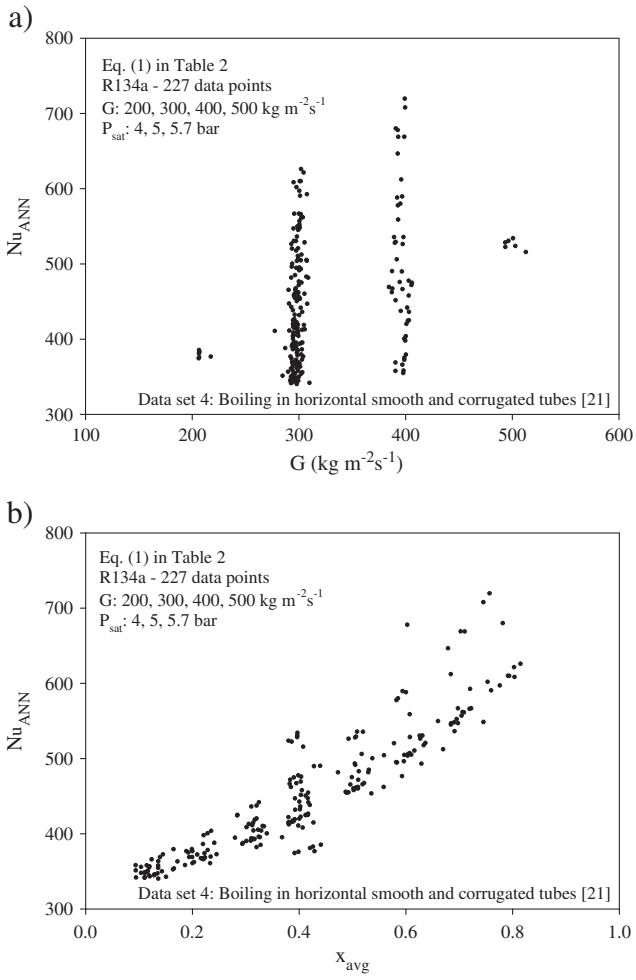

Fig. 8. Alteration of obtained Nusselt numbers with mass flux (a) and average vapor quality (b) for data set 4.

under the ±30% deviation bands for all proposed correlations. Figs. 2, 4, 6 and 8 show the proposed correlations' results meaningfulness considering the trends in the alterations of the obtained Nusselt numbers and mass fluxes (a) and average vapor qualities (b). As expectedly, Nusselt numbers increases with increasing mass fluxes and vapor qualities in all datasets.

5. Conclusion

Numerical analyses have been performed to determine the Nusselt numbers and to develop reliable correlations of condensation and boiling in smooth and corrugated tubes by means of computational numerical techniques. In order to derive reliable correlations, the authors' experimental databases in the literature [11, 19–21] are used in the analyses. This paper reports that although there are numerous studies on the determination of two-phase Nusselt numbers in tubes, application of artificial neural networks (ANN) together with non-linear least squares (NLS) to the in-tube boiling and condensation for the aim of correlation development does not exist in the literature. For that reason, the content of this study is expected to fill this gap in the literature.

Not only this paper proposes some correlations for boiling and condensation datasets but also it enables researchers to predict both condensation and boiling flows in smooth/corrugated horizontal/vertical tubes by means of a single correlation with a reasonable deviation.

Dependency of output of the ANNs closed form from input values is investigated in the paper. Vapor Reynolds number, equivalent Reynolds number, Weber number and Froude number are found to be the most affective parameters as a result of the dependency analyses.

Acknowledgments

The fourth author wishes to thank King Mongkut's University of Technology Thonburi (KMUTT) for providing him with a Post-doctoral fellowship. The fifth author is indebted to the Thailand Research Fund and the National Science and Technology Development Agency for their financial support.

References

[1] A.S. Dalkilic, S. Wongwises, Intensive literature review of condensation inside smooth and enhanced tubes, Int. J. Heat Mass Transfer 52 (2009) 3409–3426.
[2] A.S. Dalkilic, S. Wongwises, Book chapter, "Condensation heat transfer in smooth and enhanced geometries — A review of 2010 literature", in the book "Refrigeration Systems, Design Technologies and Developments", ISBN 978-1-62417-230-4, Nova Publishers, 2013.
[3] S. Laohalertdecha, A.S. Dalkilic, S. Wongwises, A review on the heat-transfer performance and pressure-drop characteristics of various enhanced tubes, Int. J. Air Cond. Refrig. 20 (2012) 1–20.
[4] M. Balcilar, A. Celen, N. Kayaci, A.S. Dalkilic, S. Wongwises, A critical review on the numerical methods of two-phase flows, ASME 2012 International Mechanical Engineering Congress & Exposition (2012) November 9–15, USA, 2012.
[5] M. Balcilar, A.S. Dalkilic, S. Wongwises, Artificial neural networks (ANNs) techniques for the determination of condensation heat transfer characteristics during downward annular flow of R134a inside a vertical smooth tube, Int. Commun. Heat Mass Transfer 38 (2011) 75–84.

[6] M. Balcilar, A.S. Dalkilic, B. Bolat, S. Wongwises, Investigation of empirical correlations on the determination of condensation heat transfer characteristics using computational numerical methods during downward annular flow of R134a inside a vertical smooth tube, J. Mech. Sci. Technol. 25 (10) (2011) 1–20.
[7] O. Agra, H. Demir, S. Ozgur Atayilmaz, F. Kantas, A.S. Dalkilic, Numerical investigation of heat transfer and pressure drop in enhanced tubes, Int. Commun. Heat Mass Transfer 38 (2011) 1384–1391.
[8] M. Balcilar, A.S. Dalkilic, K. Aroonrat, S. Wongwises, Neural network based analyses for the determination of evaporation heat transfer characteristics during downward flow of R134a inside a vertical smooth and corrugated tube, Arab. J. Sci. Eng. (2013), http://dx.doi.org/10.1007/s13369-013-0659-1(Accepted for Publication-Article in press).
[9] M. Balcilar, A.S. Dalkilic, O. Agra, S.O. Atayilmaz, S. Wongwises, A correlation development for predicting the pressure drop of various refrigerants during condensation and evaporation in horizontal smooth and micro-fin tubes, Int. Commun. Heat Mass Transfer 39 (2012) 937–944.
[10] A.S. Dalkilic, S. Laohalertdecha, S. Wongwises, Effect of void fraction models on the two-phase friction factor of R134a during condensation in vertical downward flow in a smooth tube, Int. Commun. Heat Mass Transfer 35 (2008) 921–927.
[11] A.S. Dalkilic, S. Laohalertdecha, S. Wongwises, New experimental approach on the determination of condensation heat transfer coefficient using frictional pressure drop and void fraction models in a vertical tube, Energy Convers. Manag. 51 (2010) 2535–2547.
[12] A.S. Dalkilic, S. Yildiz, S. Wongwises, Experimental investigation of convective heat transfer coefficient during downward laminar flow condensation of R134a in a vertical smooth tube, Int. J. Heat Mass Transfer 52 (2009) 142–150.
[13] A.S. Dalkilic, S. Laohalertdecha, S. Wongwises, Experimental investigation on heat transfer coefficient of R134a during condensation in vertical downward flow at high mass flux in a smooth tube, Int. Commun. Heat Mass Transfer 36 (2009) 1036–1043.
[14] A.S. Dalkilic, S. Wongwises, Experimental study on the condensation heat transfer coefficients in high mass flux region in annular flow regime of HFC-134a inside the vertical smooth tube, Heat Transfer Eng. 32 (2011) 33–44.
[15] A.S. Dalkilic, I. Teke, S. Wongwises, Experimental analysis for the determination of the convective heat transfer coefficient by measuring pressure drop directly during annular condensation flow of R134a in a vertical smooth tube, Int. J. Heat Mass Transfer 54 (2011) 1008–1014.
[16] S. Saisorn, J. Kaew-On, S. Wongwises, Flow pattern and heat transfer characteristics of R-134a refrigerant during flow boiling in a horizontal circular mini-channel, Int. J. Heat Mass Transfer 53 (2010) 4023–4038.
[17] A.S. Dalkılıç, İ. Teke, S. Wongwises, Heat transfer enhancement during downward laminar flow condensation of R134a in vertical smooth and micro-fin tubes, Isi Bilimi Ve Teknigi Dergisi/J. Therm. Sci. Technol. 32 (2012) 19–31.
[18] A.S. Dalkilic, B. Kundu, S. Wongwises, An experimental investigation of the Reynolds analogy and its modifications applied to annular condensation laminar flow of R134a in a vertical tube, Arab. J. Sci. Eng. 38 (2013) 1493–1507.
[19] S. Laohalertdecha, S. Wongwises, Condensation heat transfer and flow characteristics of R-134a flowing through corrugated tubes, Int. J. Heat Mass Transfer 54 (2011) 2673–2682.
[20] K. Aroonrat, S. Wongwises, Evaporation heat transfer and friction characteristics of R-134a flowing downward in a vertical corrugated tube, Exp. Therm. Fluid Sci. 35 (2011) 20–28.
[21] S. Laohalerdecha, A.S. Dalkilic, S. Wongwises, Correlations for evaporation heat transfer coefficient and two-phase friction factor for R134a flowing through corrugated tubes, Int. Commun. Heat Mass Transfer 38 (2011) 1406–1413.
[22] A.S. Dalkilic, S. Laohalertdecha, S. Wongwises, Experimental research on the similarity of annular flow models and correlations for the condensation of R134a at high mass flux inside vertical and horizontal tubes, International Mechanical Engineering Congress and Exposition, ASME (2009), November 13–19, USA, 2009.

DESIGN OF A VERTICAL ANNULUS WITH MHD FLOW USING ENTROPY GENERATION ANALYSIS

by

Omid MAHIAN [a], Hakan F. OZTOP [b*], Ioan POP [c], Shohel MAHMUD [d], and Somchai WONGWISES [e]

[a] Department of Mechanical Engineering, Ferdowsi University of Mashhad, Mashhad, Iran
[b] Department of Mechanical Engineering, Technology Faculty, Firat University, Elazig, Turkey
[c] Faculty of Mathematics, University of Cluj, Cluj, Romania
[d] School of Engineering, University of Guelph, Guelph, Ont., Canada
[e] Fluid Mechanics, Thermal Engineering and Multiphase Flow Research Lab. (FUTURE), Department of Mechanical Engineering, Faculty of Engineering, King Mongkut´s University of Technology Thonburi, Bangmod, Bangkok, Thailand

Original scientific paper
DOI: 10.2298/TSCI121017038M

Optimal design of a heat exchanger is one of the concerns of energy conversion engineers. In the present work, the mixed convection flow between two vertical concentric pipes with constant heat flux at the boundaries and MHD flow effects is considered. To determine the optimal design for such a heat exchanger, at first, the momentum and energy equations are simplified and solved analytically. Next, using entropy generation analysis and cost analysis, the operational costs due to entropy generation are estimated. It is concluded that with an increase in the Hartmann number, the energy costs increase. In addition, for two small deviations from the base radius ratio ($\Pi = 2$) including $\Pi = 19$ and $\Pi = 2.1$, the changes in the energy cost are calculated. It is found that for $\Pi = 1.9$ the energy cost increases by 17.5% while for $\Pi = 2.1$ the energy cost is reduced by 13.6%.

Key words: *vertical annulus, magnetic field, mixed convection, entropy generation, cost analysis.*

Introduction

Mixed convection inside a vertical annulus in the presence of magnetic field has many practical applications. Some applications are found in industrial heat exchangers, micro electronic devices, cooling of nuclear reactors, petroleum equipment, and so forth. The optimal design of such equipments is necessary before the manufacturing process to reduce the operating and energy costs. Bejan's entropy generation minimization (EGM) method is a recognized approach to optimize the performance of thermal-fluid devices. This method also can be used to determine the optimum heat exchanger dimensions [1].

Generally, the entropy generation problems are non-linear. Therefore, a helpful way to study of entropy generation through a process with complex equations is the simplification of the governing equations with reasonable assumptions to obtain analytical solutions. In this context, Yilbas [2] examined the entropy generation for a rotating outer cylinder and differentially heated isothermal boundary condition with neglecting the irreversibility induced by viscous dissipation. The author [2] assumed a linear velocity profile in his work. Mahmud and Fraser [3, 4]

* Corresponding author; e-mail: hfoztopl@gmail.com

solved analytically the dimensionless entropy generation equation for the flow and heat transfer between two rotating cylinders with isoflux and isothermal boundary conditions. Tasnim and Mahmud [5] considered the fully developed laminar and mixed convection flow in a vertical annulus with circular cross-section and obtained analytical expressions for entropy generation in the annulus. They obtained the optimum radius ratio, at which the entropy generation is minimized. Tasnim and Mahmud [6] considered a fluid with temperature-dependent viscosity and developed their previous work [5]. Mirzazadeh *et al.* [7] studied the entropy generation due to flow and heat conduction of a non-linear viscoelastic fluid between concentric rotating cylinders. Mahian *et al.* [8] investigated analytically the entropy generation between two rotating cylinders using nanofluids with different volume fractions and isoflux boundary conditions. In another work, Mahian *et al.* [9] presented an analytical solution of the second law analysis between two rotating cylinders using nanofluids. They studied the effects of uncertainties in the models presented for thermophysical properties of nanofluids on entropy generation.

The study of flow and heat transfer in a closed cavity or a channel in the presence of MHD flow is important because of engineering applications such as MHD micropumps, micro electronic devices, electronic packages, cooling of nuclear reactors, and MHD marine propulsion [10]. Here, several works in which the effects of MHD flow on entropy generation for various flows and geometries are investigated, briefly have been reviewed. Salas *et al.* [11] and Ibanez *et al.* [12] analysed the second law for MHD induction devices, such as electromagnetic pumps, and electrical generators. Mahmud *et al.* [13] examined the entropy generation due to mixed convection in a channel made of two parallel plates. Later on, Tasnim *et al*. [14] solved the same problem using porous media. Mahmud and Fraser [15] analytically investigated the entropy generation due to mixed convection-radiation interaction in a vertical porous channel in the presence of MHD flow. In another paper, Mahmud and Fraser [16] studied the problem of entropy generation in a porous cavity with laminar natural convection and MHD flow. Mahmud and Fraser [17] presented a general equation for entropy generation for a single-plate thermoacoustic system, which is subjected to a constant magnetic field. Ibanez and Cuevas [18] considered a stationary buoyant MHD flow of a liquid metal immersed in a MHD flow through a vertical rectangular duct. They obtained the optimum conductance ratio of the wall in which the entropy generation is minimized. The effects of slip and Joule dissipation on the entropy generation in a single rotating disk in the presence of MHD flow are investigated by Arikoglu *et al.* [19]. Aiboud and Saouli [20] applied the analysis of entropy generation for a viscoelastic MHD flow over a stretching surface. Recently, Mahian *et al.* [21] investigated the entropy generation between two isothermal rotating cylinders in the presence of magnetic field. They revealed that the entropy generation increases with an increase in MHD flow. Mahian *et al.* [22] studied the effects of nanofluids on entropy generation between two cylinders in the presence of MHD flow. They obtained the conditions in which using nanofluids results in a decrease in entropy generation.

In the present work, the energy costs of a vertical annulus heat exchanger with MHD flow and constant heat flux at the boundaries in different conditions are determined by using Bejan' EGM method.

Mathematical modelling

Analysis of the First law of thermodynamics

A steady, laminar and fully developed mixed convection flow of a Newtonian, incompressible fluid is considered where the fluid enters a vertical annulus with length of L and inlet

velocity U_0 and an inlet temperature T_0. In practical situations, a differential pressure transmitter can be installed to measure the pressure losses through the heat exchanger. A constant heat flux is imposed on the boundary of the inner pipe. The cooling fluid flows inside the annulus and cools the surface of the inner pipe and a portion of the heat is dissipated to the surrounding based on the energy balance. The heat exchanger is subjected to a transverse magnetic field with constant strength of B_0. The schematic of problem is indicated in fig. 1.

The governing equations for 2-D flow in the heat exchanger can be written in general as:

– continuity

$$\frac{\partial V_\mathrm{r}}{\partial r}+\frac{V_\mathrm{r}}{r}+\frac{\partial V_\mathrm{z}}{\partial z}=0 \tag{1}$$

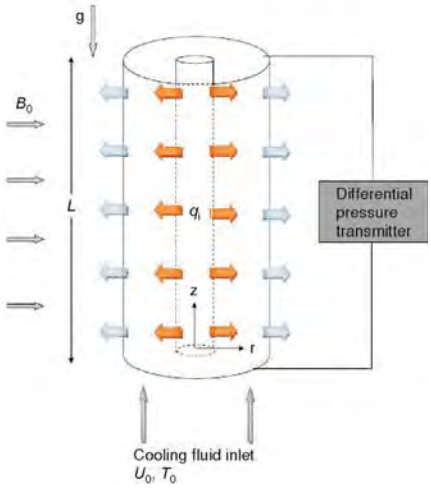

Figure 1. Schematic of heat exchanger considered in the study

– r-momentum

$$\rho\left(V_\mathrm{r}\frac{\partial V_\mathrm{r}}{\partial r}+V_z\frac{\partial V_\mathrm{r}}{\partial z}\right)=-\frac{\partial P}{\partial r}+\mu\left(\frac{\partial^2 V_\mathrm{r}}{\partial r^2}+\frac{1}{r}\frac{\partial V_\mathrm{r}}{\partial r}-\frac{V_\mathrm{r}}{r^2}+\frac{\partial^2 V_\mathrm{r}}{\partial z^2}\right) \tag{2}$$

– z-momentum

$$\rho\left(V_\mathrm{r}\frac{\partial V_\mathrm{z}}{\partial r}+V_z\frac{\partial V_\mathrm{z}}{\partial z}\right)=-\frac{\partial P}{\partial z}+\mu\left(\frac{\partial^2 V_\mathrm{z}}{\partial r^2}+\frac{1}{r}\frac{\partial V_\mathrm{z}}{\partial r}+\frac{\partial^2 V_\mathrm{z}}{\partial z^2}\right)-\rho\mathrm{g}-\sigma B_0^2 V_\mathrm{z} \tag{3}$$

– energy

$$\rho C_p\left(V_r\frac{\partial T}{\partial r}+V_z\frac{\partial T}{\partial z}\right)=k\left[\frac{1}{r}\frac{\partial}{\partial r}\left(r\frac{\partial T}{\partial r}\right)+\frac{\partial^2 T}{\partial z^2}\right]+\sigma B_0^2 V_z^2 \tag{4}$$

As mentioned before, the flow is assumed as hydrodynamically and thermally fully developed; hence, using the order of magnitude the radial velocity (V_r) can be neglected in comparison with the axial velocity (V_z). With this assumption, the continuity equation reduces to $\partial V_\mathrm{z}/\partial \mathrm{z} = 0$. Therefore, using the Boussinesq approximation in the buoyancy term, and neglecting the axial effects (see refs. [5, 6]), the simplified dimensionless equations can be expressed as:

$$\frac{\partial^2 U}{\partial R^2}+\frac{1}{R}\frac{\partial U}{\partial R}=-\frac{\mathrm{Gr}}{\mathrm{Re}}\theta+M^2U+\frac{\partial P^*}{\partial Z} \tag{5}$$

$$\frac{\partial^2 \theta}{\partial R^2}+\frac{1}{R}\frac{\partial \theta}{\partial R}=0 \tag{6}$$

where the dimensionless parameters are defined as:

$$R=\frac{r}{r_\mathrm{o}},\quad U=\frac{V_\mathrm{z}}{U_0},\quad \mathrm{Re}=\frac{U_0 r_\mathrm{o}}{\upsilon},\quad \lambda=\frac{r_\mathrm{i}}{r_\mathrm{o}},\quad P^*=\frac{P}{U_0\mu}r_\mathrm{o},\quad Z=\frac{z}{r_\mathrm{o}},\quad M=\sqrt{\frac{\sigma}{\mu}}B_0 r_0 \tag{7}$$

In the above relations M is the Hartmann number, and σ – the electrical conductivity of fluid. The subscripts of *i* and *o* indicate the characteristics of inner and outer pipes, respectively. The Grashof number and dimensionless temperature are defined as:

$$\mathrm{Gr} = \frac{g\beta q_\mathrm{i} r_o^4}{k\upsilon^2}, \quad \theta = \frac{T - T_0}{\frac{q_\mathrm{i} r_\mathrm{o}}{k}} \tag{8}$$

The velocity boundary conditions with no slip assumption are written as:

$$\begin{aligned} R = \lambda &\Rightarrow U = 0 \\ R = 1 &\Rightarrow U = 0 \end{aligned} \tag{9}$$

The thermal boundary conditions are given by:

$$\begin{aligned} R = \lambda &\Rightarrow \frac{\partial\theta}{\partial R} = -1 \\ R = 1 &\Rightarrow \frac{\partial\theta}{\partial R} = f(q_\mathrm{i}) \end{aligned} \tag{10}$$

Analysis of the Second law of thermodynamics

Entropy generation rate in the presence of MHD flow can be written as:

$$\dot{S}_{gen}^{m} = \frac{k}{T_0^2}[\nabla T]^2 + \frac{\mu}{T_0}\phi + \frac{1}{T_0}[(J - QV)(E + V \times B)] \tag{11}$$

where

$$J = \sigma(E + V \times B) \tag{12}$$

In the above equations, ϕ is viscous dissipation, J – the electric current, Q – the electric charge density, V – the velocity vector, E – the electric field, and B – the magnetic induction. Neglecting QV in comparison with J and disregarding E in comparison with $V \times B$, the relation (11) reduces to the:

$$\dot{S}_{gen}''' = \frac{k}{T_0^2}\left(\frac{\partial T}{\partial r}\right)^2 + \frac{\mu}{T_0}\left(\frac{\partial V_z}{\partial r}\right)^2 + \frac{\sigma B_0^2}{T_0}V_z^2 \tag{13}$$

The dimensionless entropy generation rate is determined as:

$$N_\mathrm{S} = \frac{\dot{S}_{gen}'''}{\frac{\mu U_0^2}{T_0 r_o^2}} = \frac{\Omega}{\mathrm{Br}}\left(\frac{\partial\theta}{\partial R}\right)^2 + \left(\frac{\partial U}{\partial R}\right)^2 + M^2U^2 = N_\mathrm{H} + N_\mathrm{F} + N_\mathrm{M} \tag{14}$$

where N_H, N_F, and N_M on the right hand of the equation are the irreversibilities due to heat transfer, fluid friction, and magnetic field, respectively. Also, the Brinkman number (Br) and the parameter Ω are defined as:

$$\mathrm{Br} = \frac{U_0^2\mu}{q_\mathrm{i} r_\mathrm{o}}, \quad \Omega = \frac{q_\mathrm{i} r_\mathrm{o}}{kT_0} \tag{15}$$

The irreversibility distribution can be obtained using the definition of Bejan number (Be) that is the ratio of entropy generation due to heat transfer to the overall entropy generation as [23]:

$$\mathrm{Be} = \frac{N_\mathrm{H}}{N_\mathrm{H} + N_\mathrm{F} + N_\mathrm{M}} \tag{16}$$

The average volumetric entropy generation number is given by:

$$N_{\mathrm{S,\,ave}} = \frac{1}{\forall}\int_{\forall} N_{\mathrm{S}}\mathrm{d}\forall \tag{17}$$

Solution of the problem

Velocity and temperature fields

The eqs. (5) and (6) are coupled *via* the buoyancy term in the momentum equation.

Therefore, first, the energy equation must be solved. The solution of the energy equation is:

$$\theta(R) = -\lambda \ln R + C \tag{18}$$

where C is the constant of integration. In this stage, the constant C cannot be obtained because of the isoflux boundary conditions. The velocity field is obtained using the temperature distribution and solving the related differential equation as:

$$U(R) = \Gamma_5 K_0(MR) + \Gamma_6 I_0(MR) - \frac{\left(\dfrac{\partial P^*}{\partial Z}\right) + \left(\dfrac{\mathrm{Gr}}{\mathrm{Re}}\right)\lambda \ln R}{M^2} + \frac{\left(\dfrac{\mathrm{Gr}}{\mathrm{Re}}\right)}{M^2} C \tag{19}$$

where the constants Γ_5 and Γ_6 are equal to:

$$\Gamma_5 = -\frac{\dfrac{\mathrm{Gr}}{\mathrm{Re}} C[I_0(M\lambda) - I_0(M)] - \dfrac{\partial P^*}{\partial Z}[I_0(M\lambda) - I_0(M)] + \dfrac{\mathrm{Gr}}{\mathrm{Re}}\lambda \ln \lambda I_0(M)}{M^2[K_0(M)I_0(M\lambda) - K_0(M\lambda)I_0(M)]}$$

$$\Gamma_6 = -\frac{\dfrac{\mathrm{Gr}}{\mathrm{Re}} C[K_0(M\lambda) - K_0(M)] - \dfrac{\partial P^*}{\partial Z}[K_0(M\lambda) - K_0(M)] + \dfrac{\mathrm{Gr}}{\mathrm{Re}}\lambda \ln K_0(M)}{M^2[K_0(M)I_0(M\lambda) - K_0(M\lambda)I_0(M)]} \tag{20}$$

The unknown constant C can be determined using the continuity equation that is:

$$\int_{r_i}^{r_o} \rho V_z(z) 2\pi r \mathrm{d}r = \rho U_0[\pi(r_0^2 - r_i^2)] \tag{21}$$

which in dimensionless form is:

$$2\int_{\lambda}^{1} U(R) R \mathrm{d}R = 1 - \lambda^2 \tag{22}$$

By substituting the velocity profile from eq. (19) into the above relation and solving the equation, the constant C is calculated. The expression obtained for C is long, therefore to save the space, the constant C is not presented here, but it is a function of involving parameters in the problem as:

$$C = h\left(M, \lambda, \frac{\mathrm{Gr}}{\mathrm{Re}}, \frac{\partial P^*}{\partial Z}\right) \tag{23}$$

Entropy generation

The local entropy generation is obtained using Eq. (14) and the velocity and temperature distributions as:

$$N_S = \frac{\Omega}{\mathrm{Br}}\left(\frac{-\lambda}{R}\right)^2 + \left(-\Gamma_5 MK_1(MR) + \Gamma_6 MI_1(MR) - \frac{\lambda\left(\frac{\mathrm{Gr}}{\mathrm{Re}}\right)^2}{M^2 R}\right) + \\ + M^2\left[\Gamma_5 K_0(MR) + \Gamma_6 I_0(MR) - \frac{\frac{\partial P^*}{\partial Z} + \frac{\mathrm{Gr}}{\mathrm{Re}}\lambda\ln(R)}{M^2} + \frac{\frac{\mathrm{Gr}}{\mathrm{Re}}}{M^2}C\right]^2 \tag{24}$$

The average volumetric entropy generation number is calculated based on eq. (17) as:

$$N_{\mathrm{S,\,ave}} = \frac{2}{1-\lambda^2}\int_{\lambda}^{1} N_{\mathrm{S}} R\,\mathrm{d}R \tag{25}$$

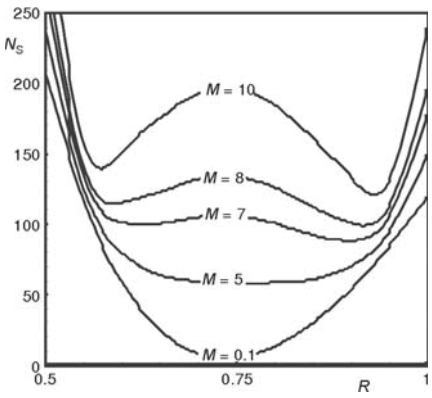

Figure 2. Effects of MHD flow on entropy generation number for Gr/Re = 10 and Ω/Br = 10

Results and discussion

Local entropy generation

The effects of Hartmann number on local entropy generation for Gr/Re =10, dP^*/dZ = 0.1 and Ω/Br = 10 are shown in fig. 2. It is seen that an increase in the Hartmann number leads to an increase in entropy generation number. The entropy generation number is greater near the walls (especially near the inner wall) due to higher gradients of temperature and velocity. The effects of parameter Gr/Re on the entropy generation and Bejan numbers for M = 1 and Ω/Br = 20 are displayed in fig. 3. It is observed that the entropy generation number has an un-

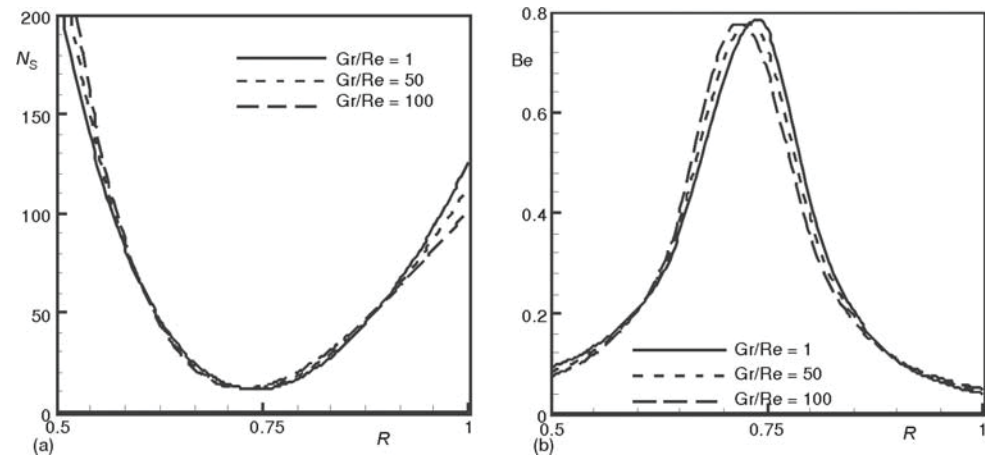

Figure 3. Effects of Gr/ Re on (a) entropy generation and (b) Bejan numbers for M =1 and Ω/Br = 20

predictable trend in the gap. The interactions among the viscous effects near the walls, the reduction of heat flux along the radial distance and buoyancy forces make this irregular behaviour. The effects of Gr/Re on the Bejan number are drawn in fig. 3(b). It is found that the Bejan number is approximately maximized in the middle of the annulus. At this point, the contribution of viscous effects to entropy generation is lowest. This maximum point moves towards the outer cylinder with a decrease in the force of natural convection and heat flux.

Design and cost analysis

In this section, by using the Bejan's EGM method and cost analysis the operational costs due to entropy generation in the heat exchanger at different conditions are determined. The operational cost due to entropy generation is reduced by optimal design and hence leads to the most saving in energy consumption cost.

Sahin *et al.* [24] calculated the total cost of irreversibility for the flow in a pipe in the absence of magnetic field as:

$$\dot{C} = C_{\mathrm{H}} T_0 (\dot{S}_{\mathrm{gen}})_{\mathrm{H}} + C_{\mathrm{F}} T_0 (\dot{S}_{\mathrm{gen}})_{\mathrm{F}} \tag{26}$$

In the above relation, $\dot{C}$ is the total cost of irreversibility (\$ per day), C_{H} – the unit cost of irreversibility due to heat transfer, C_{F} – the unit cost of irreversibility due to fluid friction, $\dot{S}_{\mathrm{gen}}$ – the entropy generation. In this work, eq. (26) is developed to the following relation in the presence of MHD flow:

$$\dot{C} = C_{\mathrm{H}} T_0 (\dot{S}_{\mathrm{gen}})_{\mathrm{H}} + C_{\mathrm{F}} T_0 (\dot{S}_{\mathrm{gen}})_{\mathrm{F}} + C_{\mathrm{M}} T_0 (\dot{S}_{\mathrm{gen}})_{\mathrm{M}} \tag{27}$$

Here, it is assumed that $C_{\mathrm{E}} = C_{\mathrm{H}} = C_{\mathrm{F}} = C_{\mathrm{M}} = 0.2$, where C_{E} is the unit cost of irreversibility in the system. Therefore, the above relation for the heat exchanger with length of 1 m can be rewritten as:

$$\dot{C} = C_{\mathrm{E}} T_0 \left(\frac{\mu U_0^2}{T_0 r_0^2} \right) \forall N_{\mathrm{S,\,ave}} = \pi C_{\mathrm{E}} \mu U_0^2 (1 - \lambda^2) N_{\mathrm{S,ave}} \tag{28}$$

The above relation in terms of mass flow rate and (inverse of λ) can be expressed as:

$$\dot{C} = \frac{C_{\mathrm{E}} \dot{m}^2 \upsilon \Pi^2}{\pi \rho r_o^4 (\Pi^2 - 1)} N_{\mathrm{S,\,ave}} \tag{29}$$

where ρ and υ are density viscosity and kinematic viscosity of the working fluid at the inlet temperature. If the base radius ratio is 2 ($\Pi = 2$), using the relation (30) one can calculate the amount of changes in energy cost, $\dot{C}_{\mathrm{r}}$, in comparison with another radius ratio:

$$\dot{C}_{\mathrm{r}} = \frac{\dot{C})_{\Pi=2} - \dot{C})_{\Pi}}{\dot{C})_{\Pi=2}} \cdot 100 \tag{30}$$

Now as a numerical example, the engine oil with mass flow rate of 0.85 kg/s is considered as the cooling fluid in the heat exchanger where the outer radius is 1. 5 cm.

The total cost due to irreversibility, $\dot{C}$ (\$/ day), is presented in fig. 4 for Gr/Re = 0.1 and Gr/Re = 50, three different Hartmann numbers and the radius ratio between 1.5 and 6, where it is assumed the system works 10 hours in a day. It is observed that the total cost of irreversibility for the system in one day is approximately 0.5-10 \$ depends on the radius ratio of the heat exchanger. The total cost of irreversibility increases with increases in the Hartmann number because the average volumetric entropy generation number increases with the increase of *M*. It is also seen that with an increase in the radius ratio, the total costs due to entropy generation de-

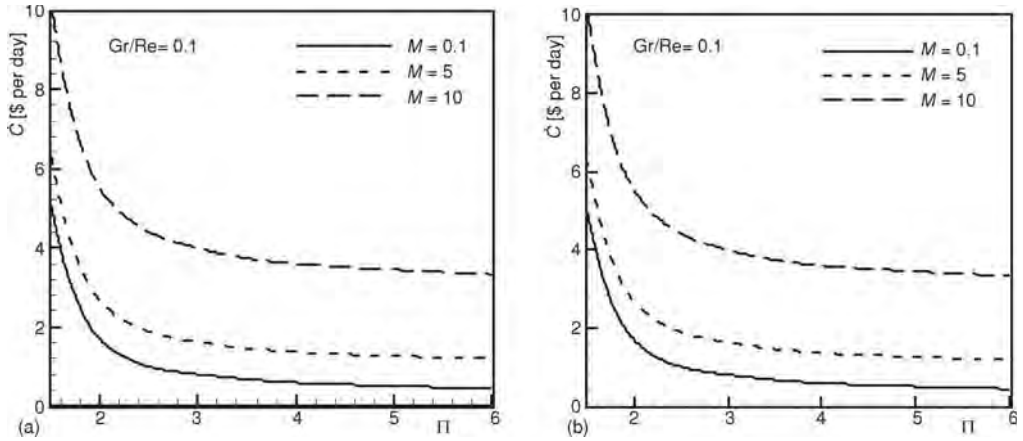

Figure 4. Effects of MHD flow and Gr/Re on total cost of irreversibility; (a) Gr/Re = 0.1, (b) Gr/Re = 50

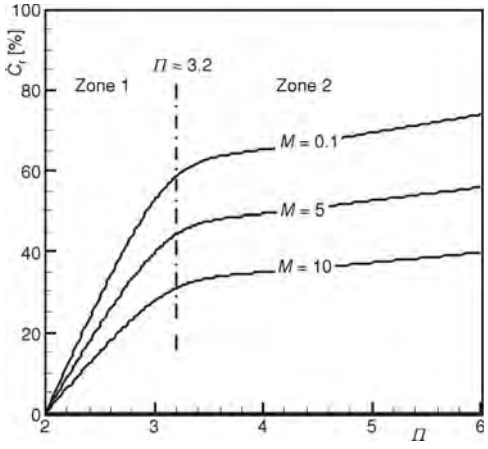

Figure 5. Effects of Hartmann number and Gr/Re on savings in operational costs

crease. This happens because the gradients of temperature and especially velocity with increasing the radius ratio are increased. From fig. 4, it is also observed that the parameter of Gr/Re has no visible effect on the total costs. Of course, with the increase of Gr/Re from 0.1 to 50, the total costs increase slightly.

Figure 5 shows the amount of changes in energy cost, $\dot{C}_r$, for different values of Hartmann number, $2 \le \Pi \le 6$ and Gr/Re = 50. The graph can be divided into two zones as indicated in the figure. In the first zone ($\Pi \le 3.2$), the amount of $\dot{C}_r$ increases rapidly, whereas for $\Pi > 3.2$ the rate of increases in $\dot{C}_r$ is reduced. As shown, $\dot{C}_r$ is higher in magnitude for smaller magnetic fields. It is also concluded that where the radius ratio increases from 2 to 6, the savings in energy cost are approximately 74%, 56%, and 40% for the Hartmann numbers of 0.1, 5, and 10, respectively.

Finally, the effects of a small deviation in the radius ratio are investigated. This deviation may be produced in the manufacturing process. If the base radius ratio is 2, the effects of a deviation of ±0.1 in the radius ratio on the amount of $\dot{C}_r$ are investigated. It is found, for $\Pi = 1.9$ and $M = 0.1$, the amount of $\dot{C}_r$ is –17.5%. The negative sign means that where the radius ratio decreases from 2 to 1.9, the total costs due to entropy generation increase by 17.5%. On the other hand, for $\Pi = 2.1$, it is found that the costs decrease between 6.3-13.6% depend on the Hartmann number. It should be noted that the costs required to produce the pipes in different sizes and the changes in costs due to heat transfer enhancements are not considered in this study.

Conclusions

An entropy generation analysis is performed for flow and heat transfer between two vertical cylinders subjected to constant heat flux and MHD flow. The equations of momentum

and energy in cylindrical co-ordinates are simplified and solved analytically. The results are presented for different values of Hartmann number and a flow parameter Gr/Re. The Bejan's EGM (entropy generation minimization) method and cost analysis are used to find the effects of different radius ratios on the total costs due to irreversibilities in the system where engine oil is considered as the working fluid. It is perceived that with an increase in the Hartmann number, the energy costs increase while the total cost does not change with increases in Gr/Re. In addition, for two small deviations from the base radius ratio ($\Pi = 2$) including $\Pi = 1.9$ and $\Pi = 2.1$, the changes in the energy cost are estimated. It is found that for $\Pi = 1.9$ the energy cost increases by 17.5% while for $\Pi = 2.1$the energy consumption cost reduces by 13.6%.

Acknowledgment

Omid Mahian, Hakan F. Oztop, Ioan Pop, Shohel Mahmud, and Somchai Wongwises would like to thank the Thailand Research Fund and the National Research University Project for the support.

Nomenclature

Be – Bejan number (= $N_H/N_H + N_F + N_M$), [–]
Br – Brinkman number (= $U_0^2\mu/q_i r_0$) , [–]
B_0 – constant magnetic flux density, [T]
C – constant of integration in energy equation, [–]
C_E – unit cost of irreversibility, [\$W^{-1}h^{-1}]
C_H – unit cost of irreversibility due to heat transfer, [\$W^{-1}h^{-1}]
C_F – unit cost of irreversibility due to fluid friction, [\$W^{-1}h^{-1}]
C_M – unit cost of irreversibility due to MHD flow, [\$W^{-1}h^{-1}]
$\dot{C}$ – total cost of irreversibility, [\$ per day]
$\dot{C}_r$ – amount of changes in energy cost, [%]
E – electric field , [Vm^{-1}]
g – constant of gravity, [m^{2}s^{-1}]
Gr – Grashof number, (= $g\beta q_i r_o^4/k\upsilon^2$), [–]
J – electric current , [A]
k – thermal conductivity, [Wm^{-1}K^{-1}]
M – Hartmann number, (= $(\sigma/\mu)^{1/2}B_0 r_0$), [–]
N_F – entropy generation number, fluid friction, [–]
N_H – entropy generation number, heat transfer, [–]
N_M – entropy generation number, MHD flow, [–]
N_S – entropy generation number, total, [–]
P – pressure [Pa]
P^* – dimensionless pressure (= $Pr_0/\mu U_0$), [–]
Q – electric charge density, [Asm^{-3}]
R – dimensionless radius (= r/r_0), [–]
r – radius,[m]
S_G – entropy generation rate, [Wm^{-3}K^{-1}]
T – temperature, [K]
T_0 – inlet temperature, [K]
U – dimensionless velocity, [ms^{-1}]
U_0 – velocity inlet, [ms^{-1}]
$\forall$ – volume, [m^3]

Greek symbols

β – thermal expansion coefficient,[K^{-1}]
Γn – constants, $n = 1, 2,\ldots$
θ – dimensionless temperature, [–]
λ – radius ratio (= r_i/r_o)
μ – dynamic viscosity, [kgm^{-1}s^{-1}]
υ – kinematic viscosity, [m^{2}s^{-1}]
Π – radius ratio, (= r_o/r_i)
ρ – density, [kgm^{-3}]
Ω – dimensionless temperature difference, [–]

Subscript

i – value at the inner cylinder
o – value at the outer cylinder

References

[1] Dagtekin, I., *et al*., An Analysis of Entropy Generation through a Circular Duct with Different Shaped Longitudinal Fins for Laminar Flow, *International Journal of Heat and Mass Transfer, 48* (2005), pp. 171-181
[2] Yilbas, B. S., Entropy Analysis of Concentric Annuli with Rotating outer Cylinder, *Int. J. Exergy, 1* (2001), pp. 60-66
[3] Mahmud, S., Fraser, R. A., Second Law Analysis of Heat Transfer and Fluid Flow Inside a Cylindrical Annular Space, *Int. J. Exergy, 2* (2002), pp. 322-329

[4] Mahmud, S., Fraser, R. A., Analysis of Entropy Generation Inside Concentric Cylindrical Annuli with Relative Rotation, *Int. J. Thermal Sciences, 42* (2003), pp. 513-521
[5] Tasnim, S. H., Mahmud, S., Mixed Convection and Entropy Generation in a Vertical Annular Space, *Int. J. Exergy, 2* (2002), pp. 373-379
[6] Tasnim, S. H., Mahmud, S., Entropy Generation in a Vertical Concentric Channel with Temperature Dependent Viscosity, *Int. Commun. Heat Mass Transfer, 29* (2002), pp. 907-918
[7] Mirzazadeh, M., *et al*., Entropy Analysis for Non-Linear Viscoelastic Fluid in Concentric Rotating Cylinders, *Int. J. Thermal Sciences, 47* (2008), pp. 1701-1711
[8] Mahian, O., *et al*., Analysis of Entropy Generation between Co-Rotating Cylinders Using Nanofluids, *Energy, 44* (2012), pp. 438-446
[9] Mahian , O., *et al.*, Effect of Uncertainties in Physical Properties on Entropy Generation between Two Rotating Cylinders with Nanofluids, *ASME J. Heat Transfer,134* (2012), 101704
[10] Jery, A. E., *et al*., Effect of an External Oriented Magnetic Field on Entropy Generation in Natural Convection, *Entropy, 12* (2010), pp. 1391-1417
[11] Salas, H., *et al*., Entropy Generation Analysis of Magnetohydrodynamic Induction Devices, *J. Phys D: Appl Phys., 32* (1999), pp. 2605-2608
[12] Ibanez, G., *et al*., Optimization Analysis of an Alternate Magnetohydrodynamic Generator, *Energy Conversion and Management, 43* (2002), pp. 1757-1771
[13] Mahmud, S., *et al*., Thermodynamic Analysis of Mixed Convection in a Channel with Transverse Hydromagnetic Effect, *Int. J. Thermal Sci., 42* (2003), pp. 731-740
[14] Tasnim, S. H., *et al*., Entropy Generation in a Porous Channel with Hydromagnetic Effect, *Energy, 2* (2002), pp. 300-308
[15] Mahmud, S., Fraser, R. A., Mixed Convection-Radiation Interaction in a Vertical Porous Channel: Entropy Generation, *Energy, 28* (2003), pp. 1557-1577
[16] Mahmud, S., Fraser, R. A., Magnetohydrodynamic Free Convection and Entropy Generation in a Square Porous Cavity, *Int. J. Heat Mass Transfer, 47* (2004), pp. 3245-3256
[17] Mahmud, S., Fraser, R. A., The Thermagoustic Irreversibility for a Single-Plate Thermoacoustic System, *Int. J. Heat Mass Transfer, 49* (2006), pp. 3448-3461
[18] Ibanez, G., Cuevas, S., Optimum Wall Conductance Ratio in Magnetoconvective Flow in a Long Vertical Rectangular Duct, *Int. J. Thermal Sci., 47* (2008), pp. 1012-1019
[19] Arikoglu, A., *et al*., Effect of Slip on Entropy Generation in a Single Rotating Disk in MHD Flow, *Appl Energy, 85* (2008), pp. 1225-1236
[20] AIboud, S., Saouli, S., Entropy Analysis for Viscoelastic Magnetohydrodynamic Flow over a Stretching Surface, *Int. J. Non-Linear Mech, 45* (2010), pp. 482-489
[21] Mahian, O., *et al*., Analysis of First and Second Laws of Thermodynamics between Two Isothermal Cylinders with Relative Rotation in the Presence of MHD Flow, *Int. J. Heat Mass Transfer, 55* (2012), pp. 4808-4816
[22] Mahian, O., *et al*., Entropy Generation between Two Rotating Cylinders in the Presence of MHD Flow Using Nanofluids, *Journal of Thermophysics and Heat Transfer, 27* (2013), pp. 161-169
[23] Paoletti, S., *et al*., Calculation of Exergetic Losses in Compact Heat Exchanger Passages, *ASME AES, 10* (1980), pp. 21-29
[24] Sahin, A. Z., *et al*., Effect of Fouling on Operational Cost in Pipe Flow Due to Entropy Generation, *Energy Conversion & Management, 41* (2000), pp. 1485-1496

Paper submitted: October 17, 2012
Paper revised: April 10, 2013
Paper accepted: April 10, 2013

Dispersion of ZnO Nanoparticles in a Mixture of Ethylene Glycol–Water, Exploration of Temperature-Dependent Density, and Sensitivity Analysis

Omid Mahian, Ali Kianifar & Somchai Wongwises

Journal of Cluster Science
Including Nanoclusters and Nanoparticles

ISSN 1040-7278
Volume 24
Number 4

J Clust Sci (2013) 24:1103-1114
DOI 10.1007/s10876-013-0601-4

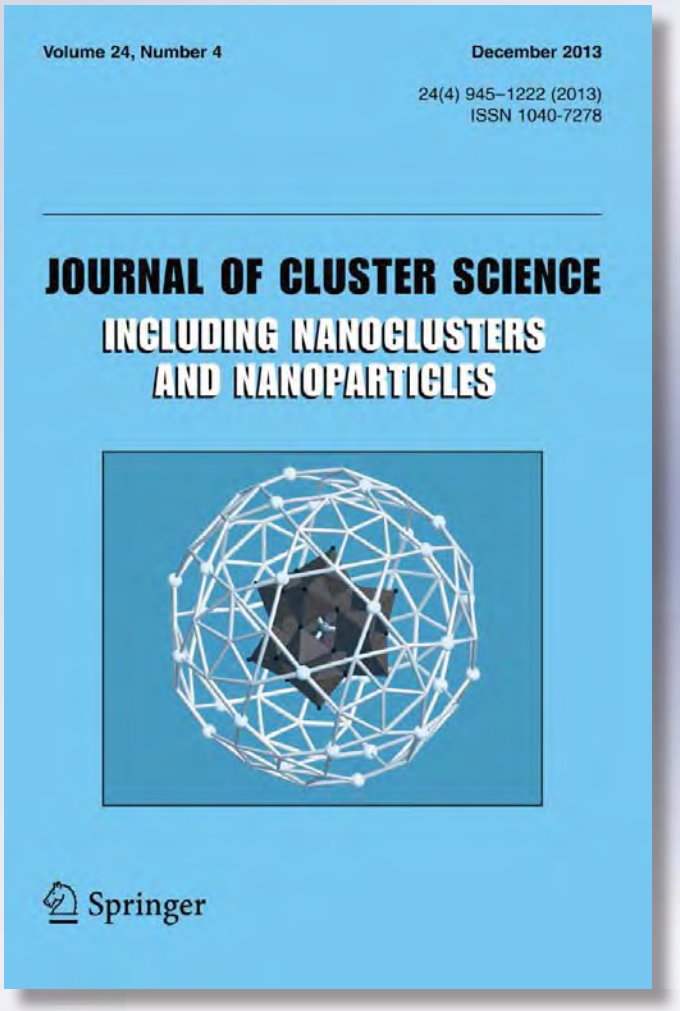

Springer

Your article is protected by copyright and all rights are held exclusively by Springer Science +Business Media New York. This e-offprint is for personal use only and shall not be self-archived in electronic repositories. If you wish to self-archive your article, please use the accepted manuscript version for posting on your own website. You may further deposit the accepted manuscript version in any repository, provided it is only made publicly available 12 months after official publication or later and provided acknowledgement is given to the original source of publication and a link is inserted to the published article on Springer's website. The link must be accompanied by the following text: "The final publication is available at link.springer.com".

Author's personal copy

J Clust Sci (2013) 24:1103–1114
DOI 10.1007/s10876-013-0601-4

ORIGINAL PAPER

Dispersion of ZnO Nanoparticles in a Mixture of Ethylene Glycol–Water, Exploration of Temperature-Dependent Density, and Sensitivity Analysis

Omid Mahian · Ali Kianifar · Somchai Wongwises

Received: 18 April 2013 / Published online: 11 June 2013
© Springer Science+Business Media New York 2013

Abstract Experimental studies are performed to evaluate the stability of zinc oxide (ZnO) nanoparticles suspended in a mixture of ethylene glycol and water with weight ratio of 40–60 as the base fluid. Different methods have been employed to disperse ZnO nanoparticles. It is found that using Gum Arabic leads to clustering and settle the nanoparticles. Also, the use of DI ammonium hydrogen citrate with weight ratio 1:1 (surfactant:nanoparticles) gives the acceptable stability. The density of nanofluids is measured and the results are compared with theoretical results. A helpful correlation for the measured densities of the stable nanofluids in a temperature range of 25–40 °C is presented which can used in practical applications. Finally based on the correlation a sensitivity analysis has been done. It is found that at higher temperatures the density is more sensitive to the increases in volume fraction.

Keywords Dispersion · Stability · ZnO nanoparticles · Surfactant · Density · Sensitivity analysis

Introduction

Nanometer-sized particles suspended in liquids such as water, glycol, ethylene glycol, and engine oil are called "Nanofluids" [1]. Nanofluids have attracted special attention in many fields of science and technology such as solar energy [2], medical

O. Mahian (✉) · A. Kianifar
Department of Mechanical Engineering, Ferdowsi University of Mashhad, Mashhad, Iran
e-mail: omid.mahian@gmail.com

S. Wongwises (✉)
Fluid Mechanics, Thermal Engineering and Multiphase Flow Research Laboratory (FUTURE), Department of Mechanical Engineering, Faculty of Engineering, King Mongkut's University of Technology Thonburi, Bangmod, Bangkok 10140, Thailand
e-mail: somchai.won@kmutt.ac.th

Author's personal copy

applications, chemical reactions [3], cooling of electronic devices, and thermal storage materials [4].

The first step in using nanofluids in various applications is the preparation of a stable nanofluid. The method of preparation of nanofluids has a significant effect on the properties of these suspensions [5]. Some of the techniques such as adding a suitable surfactant or sonication are used to increase the stability time of these suspensions. In this study, nanofluids containing ZnO nanoparticles have been investigated where the base fluid is a mixture of water and ethylene glycol. Here, the previous studies concerning the nanofluids containing ZnO nanoparticles are reviewed.

Vajjha et al. [6] measured the density of ZnO nanoparticles suspended in a mixture of EG/water (60:40) at a temperature range of 0–50 °C. They found that with an increase in the volume fraction, the difference between the measured data and the theoretical results increases. Yu et al. [7] prepared ZnO nanoparticles suspended in ethylene glycol without any surfactant. They measured the thermal conductivity and viscosity of the nanofluids for volume fractions up to 5 %. Neogy and Raychaudhuri [8] investigated the effects of temperature and volume fraction on the heat transport factor (that is the product of thermal conductivity and heat capacity) at different frequencies for ZnO suspensions.

Chung et al. [9] prepared ZnO/water nanofluids with different methods of sonication. They noted that ZnO nanoparticles could be dispersed in the water with a fragmentation process well.

Raykar and Singh [10] used Acetylacetone (acac) as a surfactant to obtain a stable suspension with volume fractions up to 0.5 % of water and ZnO nanoparticles. Next, they measured thermal conductivity and viscosity of the nanofluids.

Jalal et al. [11] after synthesizing of ZnO nanoparticles with the aid of microwave decomposition, dispersed the nanoparticles in glycerol using ammonium citrate as the surfactant. Then, the authors investigated the antibacterial properties of the nanofluids. In another work, Moosavi et al. [12] prepared suspensions of ZnO nanoparticles dispersed in two base fluids including glycerol and ethylene glycol using ammonium citrate as the surfactant. They measured thermal conductivity, viscosity and surface tension of the nanofluids for volume fractions by 3 %. In references of [11] and [12], the weight ratio of surfactant to nanoparticles is 1:1. Singh [13] synthesized ZnO nanoparticles and prepared nanofluids with volume fractions up to 0.5 % to study the thermal conductivity. Lee et al. [14] prepared ZnO/EG nanofluids by one step pulsed wire evaporation (PWE) approach without any surfactant. They measured the thermal conductivity of nanofluids with volume fraction up to 5.5 %.

Singh et al. [15] dispersed ZnO nanoparticles in polyvinyl alcohol and used sonication to have a stable nanofluid. Kole and Dey [16] prepared a solution of ZnO nanoparticles and ethylene glycol under 60 h sonication and without any surfactant. They measured the thermal conductivity of the nanofluids with volume fractions up to 3.75 %, while the nanofluids exhibit acceptable stability.

Later on, Kole and Dey [17] investigated the effects of sonication time (up to 100 h) on the effective thermal conductivity of ZnO/EG nanofluids. They showed

Author's personal copy

that there is an optimum sonication time in which the thermal conductivity is optimized. Lee et al. [18] prepared ZnO/EG nanofluids with volume fractions up to 5.5 % by the pulsed wire evaporation method. They concluded that all of the nanofluids show a Newtonian behaviour. Colangelo et al. [19] measured the thermal conductivity of ZnO nanoparticles suspended in Diathermic oil. They used no surfactant for stability of the nanofluids. The maximum particle loading for ZnO nanoparticles is 2 %. Zafarani-Moattar and Cegincara [20] measured the density and viscosity of ZnO nanoparticles suspended in poly ethylene glycol and water at a temperature range of 20–45 °C.

Cabaleiro et al. [21] measured the density, thermal conductivity, rheological behaviors of ZnO nanoparticles suspended in ethane-1,2-diol and a mixture of water and ethane-1,2-diol for a temperature range of 10–50 °C. Saleh et al. [22] measured the thermal conductivity of ZnO/EG nanofluids with volume fractions by 0.5 %. They did not use any surfactant to stable the nanofluids.

Suganthi et al. [23] measured thermal conductivity of ZnO–propylene glycol nanofluids for volume fractions less than 2 % and temperatures between 10–60 °C. The nanofluids are prepared by the aid of probe ultrasonication and without any surfactant.

Suganthi and Rajan [24] measured the viscosity of ZnO–water nanofluids at a volume fraction range of 0.25–2 %. They could prepare the nanofluids with a stable state using sonication (probe ultrasonication) without any additives. Recently in a comprehensive study, Witharana et al. [25] investigated the effects of different conditions on the stability of ZnO nanoparticles suspended in propylene glycol, ethylene glycol, and a mixture of PG and EG in water. Beside the above special studies, Ghadimi et al. [26] reviewed different methods for stability of different nanofluids.

The main aim of this study is to present some experiences obtained during the tests conducted to have stable ZnO suspensions where the base fluid is a mixture of EG and water (40:60 wt%). The mixture of EG and water has a higher boiling point compared to the water, which means that the mixture is more suitable for applications under high temperatures. On the other hand, the viscosity of the mixture is lower than the pure EG, hence, by using the mixture the pumping power required in industrial applications would be reduced. First, the methods which were not successful to prepare the stable nanofluids are presented. Afterwards, a successful method to obtain the stable nanofluids is suggested. Finally, the density of nanofluids at a temperature range of 25–40 °C is measured for volume fractions up to 4 %, and a helpful correlation is achieved for practical applications.

Nanofluid Preparation

ZnO nanoparticles with the average size of 20 nm were purchased from MKnano Company. The aim is to make a stable suspension with ZnO nanoparticles in the mixture of EG/water. Different approaches have tried to obtain a stable nanofluid. Two surfactants including Gum Arabic and DI ammonium hydrogen citrate were used in the study. Figure 1 shows a photograph of the nanoparticles, and the two

Author's personal copy

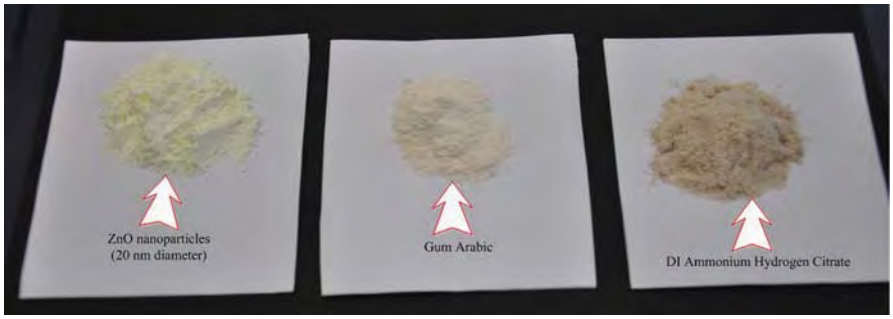

Fig. 1 Photo of the nanoparticles and two surfactants

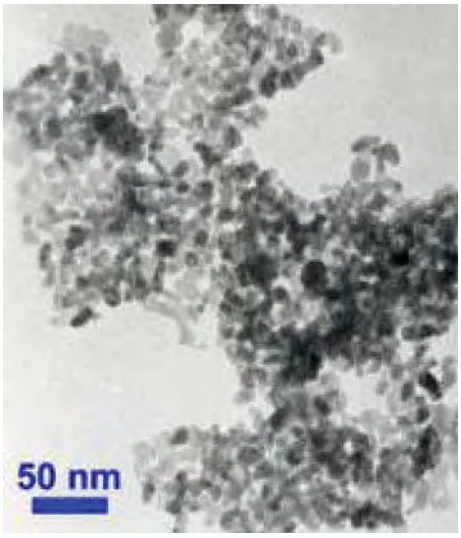

Fig. 2 TEM image of the nanoparticles

surfactants. Also, Fig. 2 shows the TEM image from the nanoparticles. It should be noted that the density of ZnO nanoparticles, DI Ammonium Hydrogen Citrate, and Gum Arabic are 5,610, 1,500, and 1,350 kg/m^3, respectively. The ultrasonic bath used in the experiments has a power of 600 W and frequency of 40 kHz.

First, the authors would like to mention the unsuccessful approaches to prepare stable ZnO–EG/water nanofluids so that other researchers avoid trying, then the successful method is presented. It should be noted that there is no a special way to have stable nanofluids. The companies that produce nanofluids do not give the details of dispersion of nanoparticles into base fluids to the costumers. Therefore, the researchers have to find the best surfactant by trial and error.

Experience No # 1: Nanofluid Preparation without Surfactant

First, it was attempted to get a stable suspension without using any surfactant. Because using any surfactant changes the properties of pure nanofluid. Also, for the

Author's personal copy

Fig. 3 Nanofluid without surfactant

beginning the low volume fraction of 0.5 % was tried. A weighing scale with an accuracy of 0.001 g is used to weigh the required amount of ZnO nanoparticles for concentration of 0.5 %. Also, to weigh the base fluid a weighing scale with an accuracy of 1 g is utilized. After weighing the base fluid (EG) and the nanoparticles, the nanoparticles were added to the base fluid in small doses at several steps, so that in each step the nanoparticles were well mixed with the base fluid well. The mixture of nanoparticles and the base fluid were stirred about 30 min. Next, the suspension was sonicated. After 2 h, the suspension was pulled out from the ultrasonic. The suspension was stirred for about 15–30 min and again was inserted inside the bath to sonicate for 2 h. In the first look, it was observed that the nanoparticles were settled in the glass container. Figure 3 shows a photograph of the suspension which is taken once the nanofluid was pulled out from the ultrasonic bath.

Experience No # 2: Adding DI Ammonium Hydrogen Citrate to the Base Fluid Before Nanoparticles

For this case, it was attempted to get a stable nanofluid with volume fraction of 1 % using the DI ammonium hydrogen citrate as the surfactant. The molecular formula of DI ammonium hydrogen citrate is $(NH_4)_2HC_6H_5O_7$. The mixture of EG/water (40:60) and the surfactant was stirred for about 30 min and then is inserted in the ultrasonic bath for about 1 h. Next, the nanoparticles were added bit by bit to the mixture and simultaneously were stirred for 15–30 min. The final suspension was inserted inside the ultrasonic bath for about 2 h. At first, it seems that the nanofluid is stable. However, the photographs that are taken after 1 and 6 days after preparing the nanofluids which show this approach has been failed (see Fig. 4). As seen, the

Author's personal copy

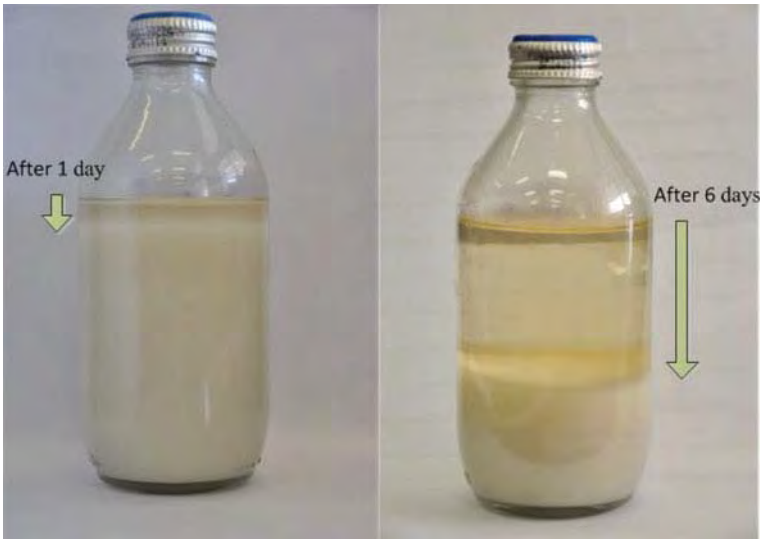

Fig. 4 Sedimentation of nanofluid due to adding DI Ammonium Hydrogen Citrate to the base fluid before nanoparticles

sedimentation rate of nanoparticles after 6 days is considerable. In this experiment, the weight ratio of surfactant to nanoparticles was 1:1. It should be noted that for lower volume fractions (i.e. 0.5 %), this method is repeated to be sure that the reason for the instability is not a high volume fraction, but the same results are obtained.

Experience No # 3: Adding Gum Arabic to the Base Fluid After Nanoparticles

In this experience, it was attempted to make a nanofluid with concentration of 0.5 % using Gum Arabic. First, the nanoparticles were added to the base fluid and the mixture was stirred for about 30 min and then was inserted into the ultrasonic bath for 1 h. After that, the Gum Arabic with weight ratio of 1:10 (Gum Arabic to nanoparticles) was added to the mixture of base fluid and nanoparticles. Next, the suspension was inserted for 4 h in the ultrasonic bath. After pulling out, it was observed that the Gum Arabic and nanoparticles are clustered at the bottom of the glass container. This shows that even with longer sonication, but not a suitable surfactant, the nanofluid is instable. Figure 5 displays this phenomenon.

Experience No # 4: Adding DI Ammonium Hydrogen Citrate to the Base Fluid After Nanoparticles

In this case, three weight ratios of surfactant to nanoparticles including 1:10, 1:2, and 1:1 were tested where the volume fraction of 0.5 % was considered. It should be noted that the thermal and chemical properties of nanofluids will be changed with the use of a surfactant, thus at first, low amounts of surfactant is tried (1:10). It was

Author's personal copy

Fig. 5 Clustering the Gum Arabic and nanoparticles in the bottom of the glass

observed that when the weight ratio of 1:10 is used, the sedimentation of nanoparticles in the glass container is visible so that the nanoparticles are adhered to the glass (see Fig. 6). With an increase in the surfactant (weight ratio of 1:2), the nanoparticles do not adhere to the bottom of the glass container, but separation occurs between the liquid and solid phase. With increasing the surfactant where the weight ratio is 1:1, a good stability and dispersion is observed in the nanofluid (see Fig. 7). The instability in low amounts of surfactant may due to the high density of nanoparticles which needs higher quantities of surfactant to avoid the sedimentation. The timing and sequence of sonication and mixing were the same in experiences 3 and 4.

From the above discussions, it is concluded that DI Ammonium Hydrogen Citrate should be used as the surfactant with a weight ratio of 1:1.

Density Measurement

Nanofluids with volume fractions of 0.25, 0.5, 1, 2, and 4 % were prepared and then their densities were measured with a 25 ml capillary type pycnometer. It should be stated that the stability time of nanofluids decreases with an increase in the volume fraction. To investigate the accuracy of the pycnometer, the density of the EG/water mixture was measured at different temperatures (25–40 °C). A small basin of hot water was used to increase and regulate the temperature of nanofluids. After filling the pycnometer with the nanofluid and adjusting the desired temperature, the mass of pycnometer is measured by the weighing scale with an accuracy of 0.001 g. The weight of pycnometer is 20.720 g while its accuracy in volume measurement is 2.887×10^{-7} m^3 (given by the company). To investigate the accuracy of the

Author's personal copy

Fig. 6 Nanofluid with DI Ammonium Hydrogen Citrate where weight ratio is 1:10

Fig. 7 Nanofluid with good stability

device, some comparisons are made between the data obtained in the present study and the data reported in the literature [27]. It is found that the maximum difference between the measured data and the data reported in the literature is 6 %. For example, at 30 °C the measured density is 1,115.4 kg/m^3, whereas for this condition in the literature the density is reported equal to 1,051.794 kg/m^3 which indicates a difference with a magnitude of 6 %. Table 1 shows the data obtained for density from the measurements for different nanofluids.

Author's personal copy

Table 1 Density in different temperatures and volume fractions

ϕ (%)	Density (kg/m^3)			
	T(C)			
	25	30	35	40
0	1122.41	1115.40	1112.85	1107.80
0.25	1142.20	1139.40	1138.24	1136.12
0.5	1155.48	1152.72	1149.72	1148.72
1	1183.08	1174.92	1170.8	1167.36
2	1235.76	1232.08	1228.92	1219.56
4	1328.72	1326.60	1323.76	1319.40

Figure 8 shows the variations of density at different volume fractions with temperature. It is seen that with increasing the particle loading of nanoparticles the density increases considerably, but the density decreases slightly with the temperature.

In the literature, the following relation is suggested to calculate the density of nanofluids [28]:

$$\rho_{nf} = \rho_f(1-\phi) + \rho_p\phi \tag{1}$$

where $\rho_{nf}$is the density of nanofluid, $\rho_f$is the fluid density, $\rho_p$is the particle density and ϕ is the volume fraction of nanoparticles. Figure 9 presents a comparison between the present data and the theoretical density. As it is seen, the theory relation underestimates the experimental data. The difference between the two data (experimental and theoretical) is about 7 % in all volume fractions. This happens because in the theory equation, the density of surfactant is not considered. The

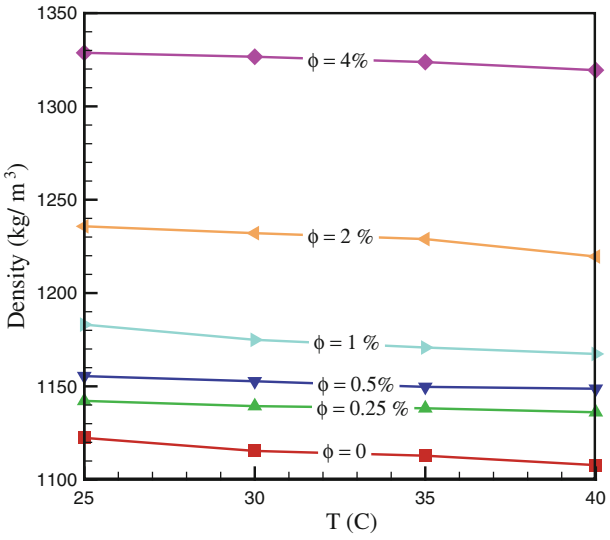

Fig. 8 Experimental results of density for ZnO/EG–water

Author's personal copy

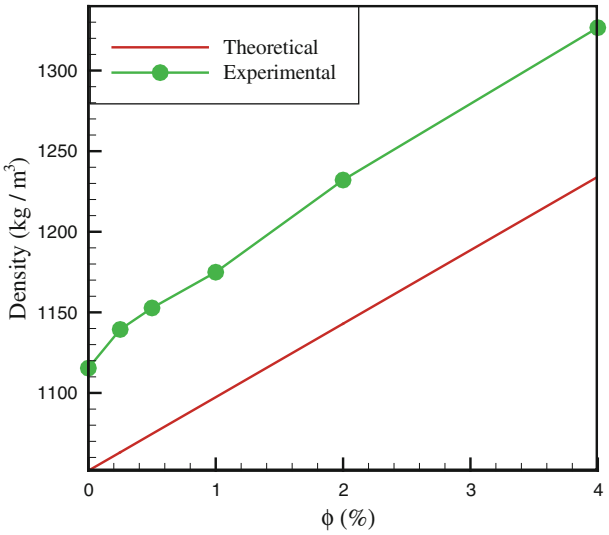

Fig. 9 Comparison between the measured data and theoretical equation

uncertainty analysis shows that the uncertainty does not exceed 2 %. In general, the following relation can be used to calculate the density of nanofluid in the presence of a surfactant:

$$\rho_{nf} = \left(\frac{m_f + m_s + m_p}{V_f + V_s + V_p}\right) = \left(\frac{\rho_f V_f + \rho_s V_s + \rho_p V_p}{V_f + V_s + V_p}\right) = \left(\frac{\rho_f V_f + \rho_s V_s}{V_f + V_s + V_p}\right) + \rho_p \phi \quad (2)$$

In the above relation, V is the volume, and the subscript "s" refers to the surfactant.

Correlation

In this section using the experimental data and regression analysis a correlation is obtained as follows:

$$\rho_{nf,c} = 1146.948 + 51.123\phi - 0.743\,T \quad (3)$$

where subscript "c" is the abbreviation of correlation word. The above correlation is valid for ZnO/EG–water nanofluid with volume fractions less than 4 %, and the temperature range of 25–40 °C. The value of R^2 for this correlation is 99.6 % which shows the high accuracy of it.

The differences do not exceed 0.8 % for all volume fractions and temperatures.

Sensitivity Analysis

In this section a sensitivity analysis is performed to show that how much the density is sensitive to the changes of volume fraction and temperature. For this purpose, first

Author's personal copy

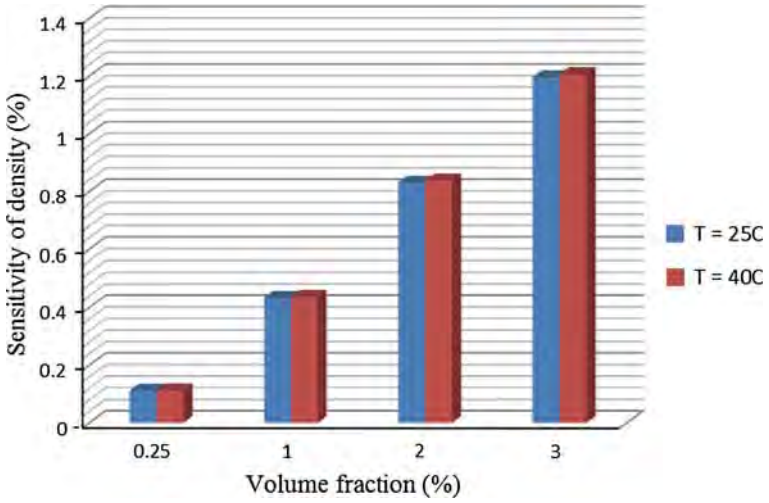

Fig. 10 Results of sensitivity analysis for density of ZnO nanofluids at different volume fractions as the base condition

a base condition should be defined. For example, the volume fraction of 1 % is assumed as the base condition. Now, it should be investigated that how much the density increases or decreases with specified changes in volume fraction. Here, the change of volume fraction is considered 10 %. Therefore, the sensitivity of density to volume fraction at different temperatures when the volume fraction changes 10 % (from 1 to 1.1 % where 1 % is base condition), can be calculated by dividing the difference between density after 10 % change and the density at the base condition to the density in the base condition.

Figure 10 shows the results of the sensitivity analysis at two temperatures of 25 and 40 °C where different volume fractions are selected as the base condition. As it is observed, the sensitivity of density of ZnO nanofluids to changes in temperature is very small. From the sensitivity analysis; it is found that at higher temperatures, density is more sensitive to the changes in volume fraction. As known, the changes of density are important in engineering systems. The sensitivity analysis reveals that under higher temperatures the engineers should be more careful to increase the volume fraction of a system because the sensitivity increases with increasing temperature. Also, it is seen that the sensitivity increases about 10 times when the volume fraction increases from 0.25 to 3. This shows the importance of adding nanoparticles in high volume fractions.

Conclusion

An experimental study was performed to prepare samples of ZnO–EG/water nanofluids with good stability. In this way, different approaches were tested. At first, it was attempted to reach a nanofluid with good stability without any surfactant, but

Author's personal copy

this effort was unsuccessful. After that, two surfactant including DI Ammonium Hydrogen Citrate and Gum Arabic were tried. Among different ways, it was found that when the DI Ammonium Hydrogen Citrate is added to the mixture of base fluid and nanoparticles, the nanofluids are stable. Also, it was experienced that the weight ratio of nanoparticle to surfactant should be equal. The density of nanofluids with volume fractions by 4 % and in a temperature range of 25–40 °C was measured and a helpful correlation was presented for practical applications. Finally, based on the correlation, a sensitivity analysis is performed. The sensitivity analysis showed that density is more sensitive to the addition of nanoparticles at higher temperatures.

Acknowledgments The first and third authors wish to thank the Thailand Research Fund, and the National Research University Project to support this study. The authors would like to thank from Mr. Raviwat Srisomba to take the photos, from Mr. Chaiwat Jumpholkul for his help and from Professor Elaheh K. Goharshadi from Ferdowsi university of Mashhad for her valuable guidance.

References

1. P. Estellé, S. Halelfadl, N. Doner, and T. Maré (2013). *Curr. Nanosci.* **9**, 225.
2. O. Mahian, A. Kianifar, S. A. Kalogirou, I. Pop, and S. Wongwises (2013). *Int. J. Heat Mass Transf.* **57**, 582.
3. R. Taylor, S. Coulombe, T. Otanicar, P. Phelan, A. Gunawan, W. Lv, G. Rosengarten, R. Prasher, and H. Tyagi (2013). *J. Appl. Phys.* **113**, 011301.
4. R. Saidur, K. Y. Leong, and H. A. Mohammad (2011). *Renew. Sustain. Energy Rev.* **15**, 1646.
5. B. Aladag, S. Halelfadl, N. Doner, T. Maré, S. Duret, and P. Estellé (2012). *Appl. Energy* **97**, 876.
6. R. S. Vajjha, D. K. Das, and B. M. Mahagaonkar (2009). *Petroleum Sci. Technol.* **27**, 612.
7. W. Yu, H. Xie, L. Chen, and Y. Li (2009). *Thermochim. Acta* **491**, 92.
8. R. K. Neogy and A. K. Raychaudhuri (2009). *Nanotechnology* **20**, 305706.
9. S. J. Chung, J. P. Leonard, I. Nettleship, J. K. Lee, Y. Soong, D. V. Martello, and M. K. Chyu (2009). *Powder Technol.* **194**, 75.
10. V. S. Raykar and A. K. Singh (2010). *Thermochim. Acta* **502**, 60.
11. R. Jalal, E. K. Goharshadi, M. Abareshi, M. Moosavi, A. Yousefi, and P. Nancarrow (2010). *Mater. Chem. Phys.* **121**, 198.
12. M. Moosavi, E. K. Goharshadi, and A. Youssefi (2010). *Int. J. Heat Fluid Flow* **31**, 599.
13. A. Singh (2010). *Adv. Powder Technol.* **21**, 609.
14. W. H. Lee, C. K. Rhee, J. Koo, J. Lee, S. P. Jang, S. U. Choi, K. W. Lee, H. Y. Bae, G. J. Lee, C. K. Kim, S. W. Hong, Y. Kwon, D. Kim, S. H. Kim, K. S. Hwang, H. Jin Kim, H. J. Ha, S. H. Lee, C. J. Choi, and J. H. Lee (2011). *Nanoscale Res. Lett.* **6**, 4.
15. D. K. Singh, D. K. Pandey, R. R. Yadav, and D. Pramana (2012). *J. Phys.* **78**, 759.
16. M. Kole and T. K. Dey (2012). *Appl. Therm. Eng.* **37**, 112.
17. M. Kole and T. K. Dey (2012). *Thermochim. Acta* **535**, 58.
18. G.-J. Lee, C. K. Kim, M. K. Lee, C. K. Rhee, S. Kim, and C. Kim (2012). *Thermochim. Acta* **542**, 24.
19. G. Colangelo, E. Favale, A. Risi, and D. Laforgia (2012). *Appl. Energy* **97**, 828.
20. M. T. Zafarani-Moattar and R. Majdan-Cegincara (2012). *J.Chem. Thermodyn.* **54**, 55.
21. D. Cabaleiro, M. J. Pastoriza-Gallego, M. M. Piñeiro, and L. Lugo (2013). *J. Chem. Thermodyn.* **58**, 405.
22. R. Saleh, N. Putra, S. P. Prakoso, and W. N. Septiadi (2013). *Int. J. Ther. Sci.* **63**, 125.
23. K. S. Suganthi, M. Parthasarathy, and K. S. Rajan (2013). *Chem. Phys. Lett.* **561**, 120.
24. K. S. Suganthi and K. S. Rajan (2012). *Int. J. Heat Mass Transf.* **55**, 7969.
25. S. Witharana, I. Palabiyik, Z. Musina, and Y. Ding (2013). *Powder Technol.* **239**, 72.
26. A. Ghadimi, R. Saidur, and H. S. C. Metselaar (2011). *Int. J. Heat Mass Transf.* **54**, 4051.
27. ASHRAE *ASHRAE handbook: fundamentals* (American Society of Heating, Refrigerating and Air-Conditioning Engineers Inc., Atlanta, 2005), p. 437.
28. K. Khanafer and K. Vafai (2011). *Int. J. Heat Mass Transf.* **54**, 4410.

International Communications in Heat and Mass Transfer 49 (2013) 78–85

Contents lists available at ScienceDirect

International Communications in Heat and Mass Transfer

journal homepage: www.elsevier.com/locate/ichmt

A generalized numerical correlation study for the determination of pressure drop during condensation and boiling of R134a inside smooth and corrugated tubes ☆

M. Balcilar [a], K. Aroonrat [b], A.S. Dalkilic [c,*], S. Wongwises [b]

[a] Computer Engineering Department, Yildiz Technical University, Davutpaşa, Istanbul 34349, Turkey
[b] Fluid Mechanics, Thermal Engineering and Multiphase Flow Research Lab. (FUTURE), Department of Mechanical Engineering, Faculty of Engineering, King Mongkut's University of Technology Thonburi, Bangmod, Bangkok 10140, Thailand
[c] Heat and Thermodynamics Division, Department of Mechanical Engineering, Faculty of Mechanical Engineering, Yildiz Technical University, Yildiz, Besiktas, Istanbul 34349, Turkey

ARTICLE INFO

Available online 7 September 2013

Keywords:
Condensation
Boling
Pressure drop
Modeling
Neural network
Corrugated tubes

ABSTRACT

The measured pressure drop of R134a, flowing downward and horizontally inside smooth and corrugated copper tubes, is estimated by the closed form of artificial neural network method to have a reliable empirical correlation using some dimensionless numbers. The working fluids are R134a and water flowing in the test tube and annular tube, respectively. This paper is a continuation of the authors' previous work and includes all their previous works about condensation and boiling in tubes. All data used in the present paper are obtained from the authors' previous studies. The training sets have the experimental data of convective condensation and boiling experiments including various mass fluxes and saturation temperatures of R134a. Froude number, Weber number, Bond number, Lockhart and Martinelli number, void fraction, the ratio of density to dynamic viscosity, liquid, vapor and equivalent Reynolds numbers, surface tension parameter and liquid Prandtl number are the inputs of the formula as the dimensionless numbers obtained from measured values of test section, while the output of the formula is the measured pressure drops in the analysis. A closed form of multi-layer perceptron (MLP) method of artificial neural network (ANN) is used to estimate the experimental pressure drop of R134a numerically. 1177 data points are used in the analyses of the ANN method to be able to have a single generalized empirical correlation for both condensation and boiling flows. The evaluation of the closed form of multi-layer perceptron (MLP) with two or three inputs and one hidden neuron architecture was successful predicting the measured pressure drops with their error bands being within the range of ±30% for all used data. The proposition of empirical correlations are performed for both condensation and boiling flows separately. A single empirical correlation is able to calculate the measured pressure drop of both condensation and boiling flows together. Moreover, the dependency of output of the proposed formula from input values is examined in the study. By means of the dependency analyses, liquid Prandtl number, Butterworth's void fraction and Lockhart and Martinelli parameter are found to be the most dominant parameters among other dimensionless numbers.

© 2013 Elsevier Ltd. All rights reserved.

1. Introduction

Some reviews on in-tube condensation having smooth and enhanced tubes were performed by Dalkilic and Wongwises [1,2] and Laohalertdecha et al. [3] to show that a two-phase flow in tubes is the hardest phenomenon in the system of heat exchangers. Classifications regarding the tubes' orientation geometry on in-tube condensation were prepared. Detailed information was given on the convective condensation investigations of heat transfer, pressure drop, flow pattern, void fraction and refrigerants in the available sources. Their papers not only mention the latest improvements on heat transfer but also include some useful knowledge on the alternative refrigerants, theoretical, numerical and empirical models in the literature.

A two-phase flow has the important characteristic regarding the orientation and interaction of the liquid and vapor phases inside the tubes regarding with flow regime and flow pattern. The geometry of the tube affects interfacial area of the phases, and due to this, mass, momentum and energy exchange between phases have great significance in the design. The tube position, the geometry of the tube, flow rates, superficial velocities and physical properties such as density, viscosity and surface tension of the two phases cause various flow regimes. Mostly, flow patterns are detected by visual ways and these include bubble flow, slug flow, churn flow, wispy-annular flow and annular flow for both vertical and horizontal flow. Authors of this paper have publications on determination of flow regimes [4,5].

Lately, two of the most important criteria are the ozone-depleting potential (ODP) and global-warming potential (GWP) in the progress of alternative refrigerants excepting the refrigerant CFCs and

☆ Communicated by: W.J. Minkowycz.
* Corresponding author. Tel.: +90 2123832821; fax: +90 2123833024.
E-mail address: dalkilic@yildiz.edu.tr (A.S. Dalkilic).

0735-1933/$ – see front matter © 2013 Elsevier Ltd. All rights reserved.
http://dx.doi.org/10.1016/j.icheatmasstransfer.2013.08.010

Nomenclature

Bo	Bond number
d	internal tube diameter, m
f	function
Fr	Froude number
G	mass flux, kg m^{-2} s^{-1}
j	superficial velocity
Pr	Prandtl number
R	ratio of density to dynamic viscosity
Re	Reynolds number
x	average vapor quality
We	Weber number
X_{tt}	Lockhart and Martinelli parameter

Greek Symbols

α	void fraction
ρ	density, kg m^{-3}
μ	dynamic viscosity, kg m^{-1} s^{-1}
σ	surface tension, N m^{-1}
Ψ	surface tension parameter
ΔP	pressure drop, kPa

Subscripts

eq	equivalent
exp	experiment
g	gas
h	hydraulic
l	liquid
TP	two-phase

HCFCs, both of which have high ODP and GWP by reason of the their contribution to ozone layer depletion and global warming. Despite their harmful GWP, substitutions to CFCs and HCFCs, such as hydro fluorocarbon (HFC) refrigerants, with their zero ODP, have been selected for use in various devices commonly. HFC refrigerants also have more proper specifications such as non-flammability, stability and similar vapor pressure than CFCs and HCFCs. All new land-based systems have usually Ammonia (R717), frequently in arrangement with other refrigerants such as water-based blends of propylene glycol or ethylene glycol and CO_2 in systems of cascade. The high-temperature sides of the systems have this fluid which has toxicity, zero ODP and zero GWP. Authors of this paper have publications on obtaining of the most proper refrigerants and their blends in the cycles of refrigeration [6,7].

To have a reliable correlation during two-phase flows in tubes, genetic algorithms (GAs) and artificial neural networks (ANNs) modeling as artificial intelligence methods confirmed by the experimental work have been having augmented status. On the other hand, there are rare research on the determination of the characteristics of in-tube condensation and evaporation using artificial intelligence techniques in the literature. Authors of this paper have publications on determination of heat transfer characteristics of two-phase flows in-tubes numerically [8–11].

The industrial processes and various applications have the two-phase pressure drop as an important design consideration. A large number of studies on this subject exist owing to its significance. The convective two-phase total pressure drop has the frictional, acceleration and gravitational parts. The acceleration and gravitational components are calculated using void fraction, and calculation of either the two-phase friction factor or the two-phase frictional multiplier is necessary for computing the frictional part of pressure drop similarly. Authors of this paper have publications on determination of pressure drop, friction factor and void fraction of two-phase flows in tubes [12–19].

The efficient plan and processing of air conditioning and refrigeration systems depend on the improvements in condensation heat transfer in horizontal tubes. Many researchers have tested smooth tubes' performance with pure refrigerants as working fluids. Condensation heat transfer coefficients have been calculated by empirical methods in horizontal smooth tubes in general. Formerly, various augmentation techniques, such as rough surfaces and twisted-tape inserts, have been investigated by some researchers, alternatively, micro-fin and corrugated tubes have lately been tested intensively as a result of their high heat transfer capability and moderate pressure drop. Authors of this paper have publications on determination of two-phase heat transfer coefficient in smooth and enhanced tubes [20–29].

The major aim of this study is to develop a model on the condensation and boiling in smooth and corrugated tubes using MATLAB with the non-linear least squares (NLS) and then conclude the dominant parameters and correlate better predictive correlations using them with reliable experimental database [16,27–29] belonging to the condensation and boiling flow in smooth and corrugated tubes. This paper is the one in a series of the authors' previous work. Only the data obtained from the authors' previous studies on condensation and boiling in tubes are used in the present study. The developed empirical correlations are supposed to be beneficial for the investigation of the heat transfer fundamentals for new smooth and corrugated tubes, without doing extra experiments, thanks to the availability of reliable data from the authors' laboratory in King Mongkut's University of Technology Thonburi.

2. Experimental setup and data reduction

Comprehensive presentations of the experimental setups and operating conditions regarding flow type, refrigerant, mass flux, average pressure, inlet and outlet vapor qualities and data point numbers belonging to the data for the subjects of condensation and evaporation of R134a inside horizontal/vertical smooth/corrugated tubes exist either in authors' previous publications or partially in all figures.

3. Calculation method for the analyses

Calculation method for the error analyses of the mean values of measured and determined results of the two-phase pressure drops regarding R^2 error, proportional error and mean square error (MSE), heat transfer coefficient determination, pressure drop's ANN studies and correlation development for convective condensation exist in authors' previous publications.

The achievement of the modeling experimental data with multilayer perceptron (MLP) has been stated numerous times by the researchers. However, the downside of this method is the mathematical expression of the relationship between inputs and outputs growing by increasing architectural size of MLP. Because of the relationship between inputs and outputs cannot be described with a simple equation, researchers call this as black box. The success of correlation decreases when the model architecture is quite small, however since the closed form of the model also simplifies, it can be shown as simple equation. For that reason, in this study, the closed form of MLP with 3–1–1 architecture (it was used 2–1–1 architecture in some formulas) is used. In this model, the transfer function of hidden layer is considered to be tansig function.

Table 1
Proposed correlations and their error rates.

Eq. number	Proposed correlation	Data set	MSE	RMSE	R^2	Data number
1	$\Delta P=\left(\frac{G^2}{\rho_g}\right)\left(\frac{b_1}{1+\exp\left(b_2\mathrm{Re_l}+b_3\mathrm{Re_g}+b_4\mathrm{Re_{eq}}+b_5\right)}+b_6\right)$ $b_1=-0.006002$, $b_2=0.003294$, $b_3=0.001297$, $b_4=-0.003532$, $b_5=4.064121$, $b_6=0.007255$	All data	4.233	2.057	0.88	1177
2	$\Delta P=\left(\frac{G^2}{\rho_g}\right)\left(\frac{b_1}{1+\exp(b_2Fr+b_3We+b_4\psi+b_5)}+b_6\right)$ $b_1=0.004888$, $b_2=-0.04286$, $b_3=0.016243$, $b_4=-747.278$, $b_5=11.15224$, $b_6=0.001272$	1–3	3.168	1.78	0.74	670
3	$\Delta P=\left(\frac{G^2}{\rho_g}\right)\left(\frac{b_1}{1+\exp(b_2Fr+b_3\alpha+b_4\mathrm{Pr_l}+b_5)}+b_6\right)$ $b_1=0.030521$, $b_2=0.00052$, $b_3=-3.91275$, $b_4=-1.4453$, $b_5=9.324669$, $b_6=-0.00113$	2–4	0.976	0.988	0.97	507
4	$\Delta P=\left(\frac{G^2}{\rho_g}\right)\left(\frac{b_1}{1+\exp(b_2Bo+b_3\mathrm{Re_l}+b_4R+b_5)}+b_6\right)$ $b_1=0.005538$, $b_2=-1.82695$, $b_3=0.000206$, $b_4=-0.09426$ $b_5=77.58698$, $b_6=0.00119$	1–2	0.324	0.57	0.98	648
5	$\Delta P=\left(\frac{G^2}{\rho_g}\right)\left(\frac{b_1}{1+\exp(b_2X_{tt}+b_3R+b_4\mathrm{Pr_l}+b_5)}+b_6\right)$ $b_1=0.004354$, $b_2=5.896766$, $b_3=0.048752$, $b_4=-165.881$, $b_5=548.7939$, $b_6=0.003914$	3–4	7.449	2.729	0.83	529
6	$\Delta P=\left(\frac{G^2}{\rho_g}\right)\left(\frac{b_1}{1+\exp(b_2Fr+b_3\mathrm{Pr_l}+b_4)}+b_5\right)$ $b_1=0.014646$, $b_2=0.000578$, $b_3=-3.92449$, $b_4=9.013503$ $b_5=-0.01274$	1	0.0154	0.1243	0.99	368
7	$\Delta P=\left(\frac{G^2}{\rho_g}\right)\left(\frac{b_1}{1+\exp(b_2\mathrm{Re_l}+b_3\mathrm{Pr_l}+b_4)}+b_5\right)$ $b_1=0.003822$, $b_2=0.000176$, $b_3=-12.4623$, $b_4=38.50283$ $b_5=0.003437$	2	0.4622	0.6799	0.98	280
8	$\Delta P=\left(\frac{G^2}{\rho_g}\right)\left(\frac{b_1}{1+\exp(b_2Fr+b_3X_{tt}+b_4)}+b_5\right)$ $b_1=0.041218$, $b_2=0.00018$, $b_3=1.04458$, $b_4=0.458855$ $b_5=-0.00818$	3	6.908	2.628	0.65	302
9	$\Delta P=\left(\frac{G^2}{\rho_g}\right)\left(\frac{b_1}{1+\exp(b_2Fr+b_3\mathrm{Re_l}+b_4)}+b_5\right)$ $b_1=0.006999$, $b_2=0.00172$, $b_3=0.000174$, $b_4=-2.727289$ $b_5=0.003662$	4	1.1577	1.0759	0.97	227

According to this consideration, the output of hidden layer is written as Eq. (1).

$$O_h=\frac{1}{1+\exp\left[w_1^1.I_1+w_2^1I_2+w_3^1I_3+b_1\right]} \tag{1}$$

Because the transfer function of output layer is considered to be a linear function, the output of the model, in other words, the closed form of model, is written as follows:

$$O=\frac{w_1^2}{1+\exp\left[w_1^1.I_1+w_2^1I_2+w_3^1I_3+b_1\right]}+b_2 \tag{2}$$

Many investigations on the convective condensation and evaporation pressure drop of plain and augmented tubes exist in the available sources. Commonly, researchers have benefitted from empirical methods to determine the pressure drop and its components in tubes. Finally, Eq. (3) is correlated to estimate the pressure drop of evaporation and condensation regarding with the below explanation as follows.

$$\Delta P=\left(\frac{G^2}{\rho_g}\right)\left(\frac{b_1}{1+\exp\left(b_2\mathrm{Re_l}+b_3\mathrm{Re_g}+b_4\mathrm{Re_{eq}}+b_5\right)}+b_6\right) \tag{3}$$

Table 2
Best input parameters of data sets.

Input	Data set	Input number	OUTPUT
			$R^2-\Delta P$ (%)
$\mathrm{Pr_l}$	All	1	0.782
A	All	1	0.642
X_{tt}	All	1	0.615
$\mathrm{Pr_l}$	1–3	1	0.72
R	1–3	1	0.72
$\mathrm{Re_{eq}}$	1–3	1	0.633
We	2–4	1	0.908
R	2–4	1	0.908
$\mathrm{Pr_l}$	2–4	1	0.908
Bo	1–2	1	0.961
$\mathrm{Pr_l}$	1–2	1	0.703
X_{tt}	1–2	1	0.844
We	3–4	1	0.804
Fr	3–4	1	0.846
$R-\mathrm{Pr_l}$	3–4	1	0.803

where the coefficients from b_1 to b_6 are the constants. The detailed information on the developed correlations can be seen in Table 1.

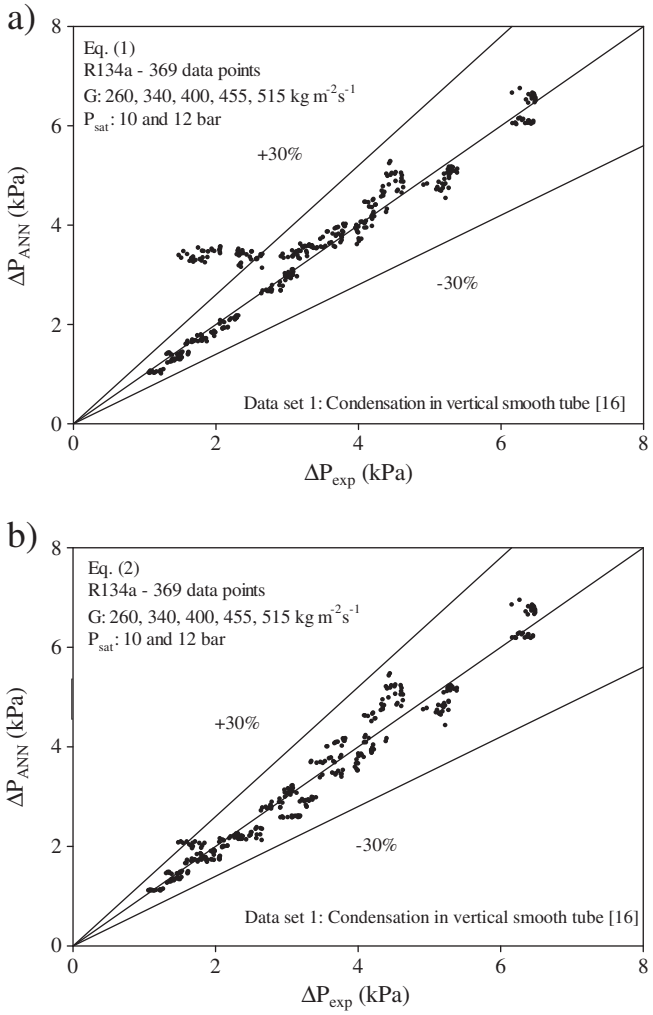

Fig. 1. Performance comparison of Eq. (1) (a) and Eq. (2) (b) for the data set 1.

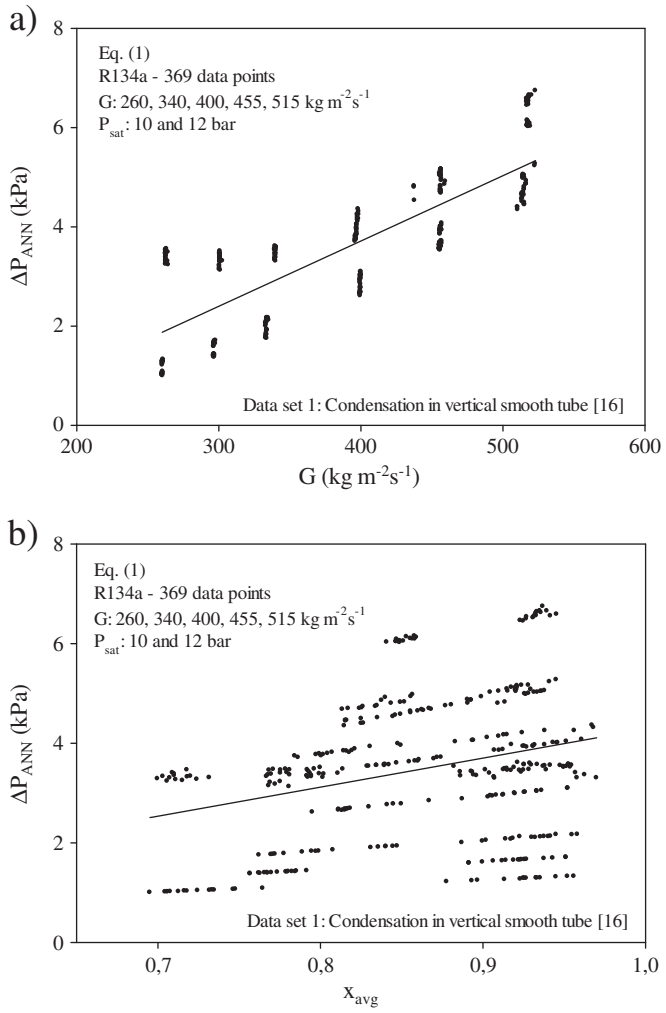

Fig. 2. Alteration of obtained pressure drops with mass flux (a) and average vapor quality (b) for data set 1.

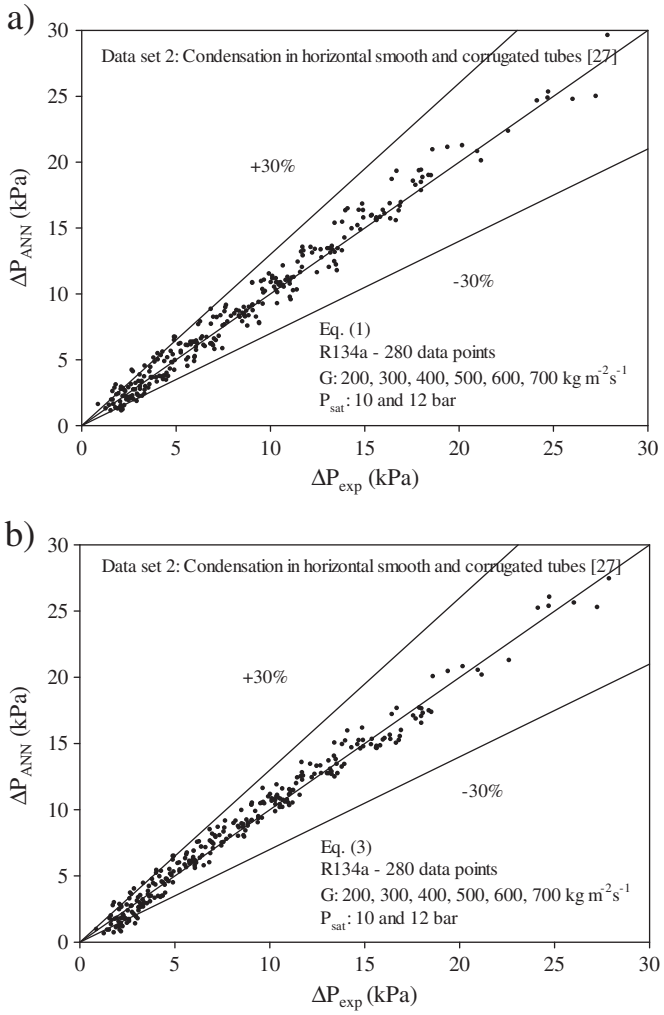

Fig. 3. Performance comparison of Eq. (1) (a) and Eq. (3) (b) for the data set 2.

The inputs of model have the following dimensionless numbers to determine their effects on the pressure drop selected as the output of the analyses. Table 2 shows the significance of these input parameters below, considering their error values of R^2.

All the liquid equivalent of Re number is calculated as

$$\mathrm{Re}_{eq} = \frac{G_{eq} d_E}{\mu_l} \tag{4}$$

and equivalent liquid mass flux is given as

$$G_{eq} = G\left((1-x) + x\left(\frac{\rho_l}{\rho_g}\right)^{0.5}\right) \tag{5}$$

and the ratio of density to dynamic viscosity is determined as

$$R = \frac{\rho_l \mu_l}{\rho_g \mu_g} \tag{6}$$

and Bond number is calculated as

$$\mathrm{Bo} = g\left(\rho_l - \rho_g\right)\left(\frac{(d_h/2)^2}{\sigma}\right) \tag{7}$$

and the Froude number is calculated as

$$Fr = \frac{G^2}{g d_h \rho_{TP}{}^2} \tag{8}$$

where the two-phase density is calculated from

$$\rho_{TP} = \left(\frac{x}{\rho_g} + \frac{1-x}{\rho_l}\right)^{-1} \tag{9}$$

and the Lockhart and Martinelli parameter is given as

$$X_{tt} = \left(\frac{1-x}{x}\right)^{0.9}\left(\frac{\mu_g}{\mu_l}\right)^{0.1}\left(\frac{\rho_g}{\rho_l}\right)^{0.5} \tag{10}$$

and the all liquid Reynolds number is defined as

$$\mathrm{Re}_l = \frac{G d_h}{\mu_l} \tag{11}$$

and all gas Reynolds number can be calculated as

$$\mathrm{Re}_g = \frac{G d_h}{\mu_g} \tag{12}$$

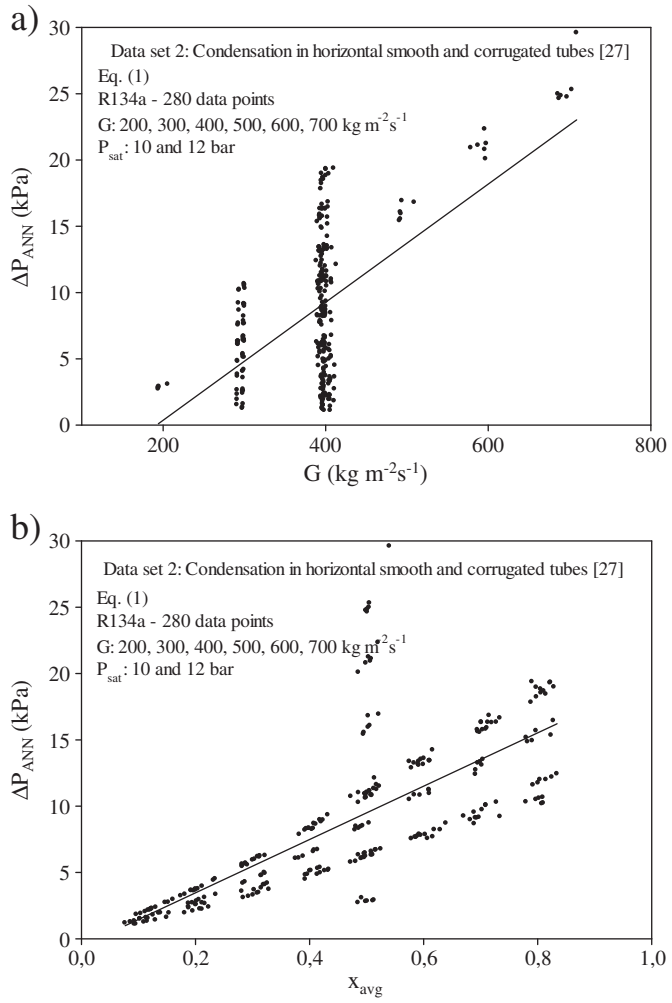

Fig. 4. Alteration of obtained pressure drops with mass flux (a) and average vapor quality (b) for data set 2.

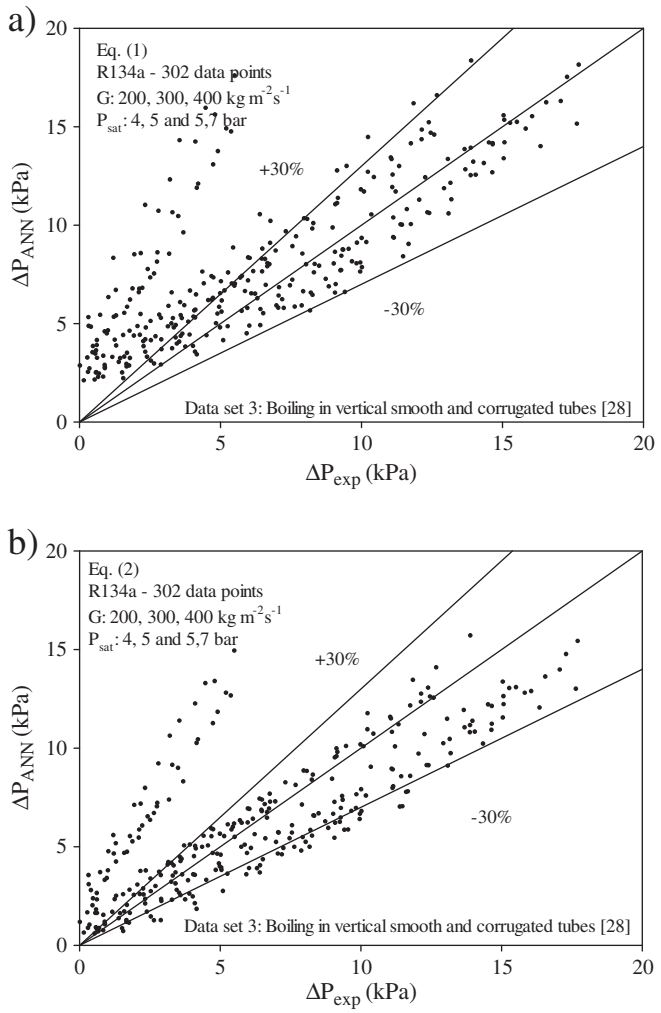

Fig. 5. Performance comparison of Eq. (1) (a) and Eq. (2) (b) for the data set 3.

and the void fraction, α, can be calculated from Butterworth's equation as follows:

$$\alpha = \frac{1}{1 + 0.28\left(\frac{1-x}{x}\right)^{0.64}\left(\frac{\rho_g}{\rho_l}\right)^{0.36}\left(\frac{\mu_l}{\mu_g}\right)^{0.07}} \tag{13}$$

and the Weber number, We, is defined as

$$We = \frac{G^2 d_h}{\sigma \rho_{TP}} \tag{14}$$

and surface tension parameter, ψ, is obtained as

$$\psi = \frac{j_l \mu_l}{\sigma} \tag{15}$$

where the liquid superficial velocity, j_l, is determined as

$$j_l = \frac{G(1-x)}{\rho_l(1-\alpha)} \tag{16}$$

4. Results and discussion

The next explanations illustrate the results and discussion of obtained total pressure drop of condensation and boiling flows of R134a using the database of authors previous studies [16,27–29] in horizontal/vertical smooth and corrugated tubes numerically. The comprehensive explanation and some extra figures and tables including dissimilar measured parameters in terms of their works on the heat transfer characteristics exist in the used references [16,27–29], which show the correctness of the measurements. A discussion of the conclusions can be found below.

In this research, two kind of closed form MLP was used. According to Table 1, the first 5 empirical correlations were modeled with 3–1–1 architecture, and the last 4 correlations were modeled with 2–1–1 architecture. The calculations of the coefficients in correlations in Table 1 are found by means of this developed formula using the experimental databases in [16,27–29]. Froude number, Weber number, Bond number, Lockhart and Martinelli number, void fraction, the ratio of density to dynamic viscosity, liquid, vapor and equivalent Reynolds numbers, surface tension parameter and liquid Prandtl number are the set of the inputs of closed form, while experimental pressure drop is the output of the closed form in the analyses. Regression analysis has the four-fold cross validation. For that reason, 1177 data points (all data of boiling and condensation in smooth and corrugated tubes) were divided by 4 sets unsystematically, where one of the sets was selected for the test process, and the rest of them (3 sets) were used for the training procedure. These procedures were lasted till there were no untested data sets. It should be considered that despite several architectures were eliminated by tests; just the characteristic one was used in the paper due to limited space.

Four different data sets were tested by the authors [16,27–29] and used for all analyses as the operating conditions of the database. There

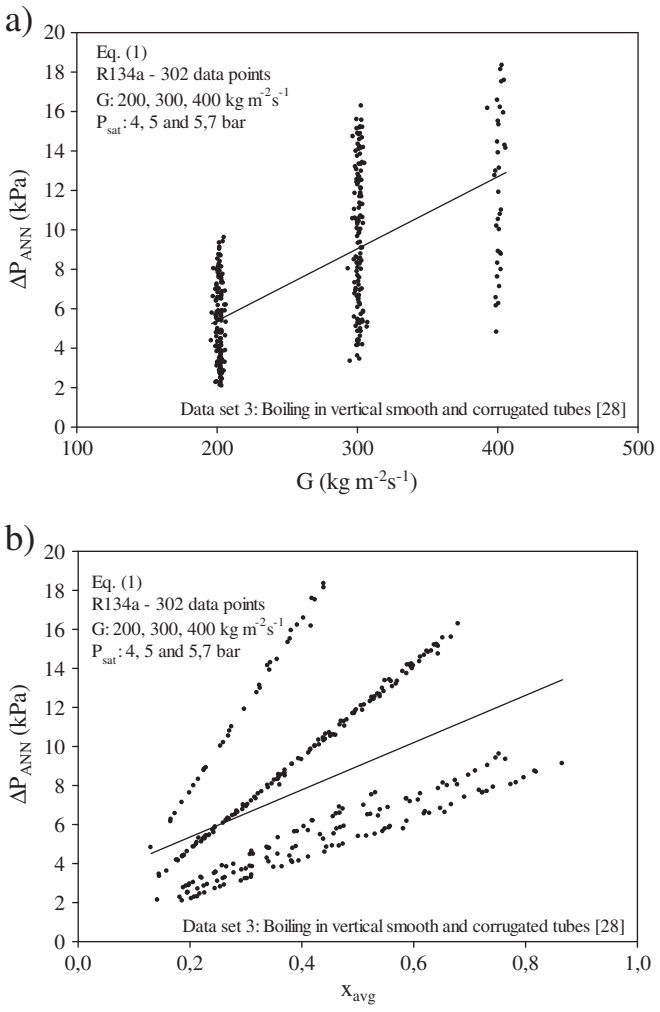

Fig. 6. Alteration of obtained pressure drops with mass flux (a) and average vapor quality (b) for data set 3.

were 1177 data points in the analyses. In-tube flow of condensation of vertical and horizontal orientations has 648 data points whereas in-tube flow of boiling of vertical and horizontal orientations has 529 data points. Five different corrugated tubes and a smooth tube were tested in the experiments. Mass fluxes and vapor qualities had a wide range for the accuracy of the proposed correlations.

Nine different developed empirical correlations for each data set or combination of them were proposed in Table 1 separately. Their success and reliability can be seen from their R^2 values. Eq. (1) in Table 1 has the most importance among the others included in the paper. It can predict all data including condensation/boiling in smooth/corrugated horizontal/vertical tubes at the same time with an acceptable accuracy as shown in all figures. The alteration between the R^2 outputs is by reason of the dificulty of generalization in the two-phase flow.

The dependency of the output parameters from the input ones was shown in Table 2; in other words, this table suggests the most significant dominant dimensionless number on the determination of the total pressure drop. The first 3 most dominant parameters of databases were shown in Table 2 separately. It is possible predict from this table that liquid Prandtl number, Butterworth's void fraction and Lockhart–Martinelli parameter having the biggest effect on the pressure drop, considering condensing and boiling databases with their R^2 values over 0.6. In the analyses, when the input parameter number is only one in all the databases, liquid Prandtl number are the dominant one on the estimation of the pressure drop with the R^2 value of 0.782. For the two known input parameters, liquid Prandtl number and Bond number have the R^2 value of 0.866. For the three known input parameters, liquid Prandtl number, Bond number and equivalent Reynolds number have the R^2 value of 0.88. This result also illustrates the effect of Bond number on the accuracy of the predictability. Data sets 1–3 include the condensation and boiling data sets in vertical smooth and corrugated tubes, data sets 2–4 include the condensation in horizontal tubes and boiling in vertical smooth and corrugated tubes, data sets 1–2 include the condensation in horizontal and vertical plain and corrugated tubes and data sets 3–4 include the boiling in horizontal and vertical smooth and corrugated tubes. Finally, the correctness of determined output value via input values increases along an increasing number of suitable input parameters. Furthermore, they depict less significant input parameters on the estimation of the pressure drop. It is clear that derivation of more results from these tables for each database is possible individually.

This paper focuses intensely on the determination of the pressure drop using all data sets by means of Eq. (1) in Table 1. Its predictability (a) and performance in comparison with other proposed correlations (b) can be seen in Figs. 1, 3, 5 and 7. Majority of data points fall under the ±30% deviation bands for all proposed correlations as it can be seen in these figures. Figs. 2, 4, 6 and 8 show meaningfulness of the proposed correlations' results, considering the trends in the change of the numerical pressure drops and mass fluxes (a) and average vapor qualities (b). As expected, obtained pressure drops from ANN analyses increase with increasing mass fluxes and vapor qualities in all data sets.

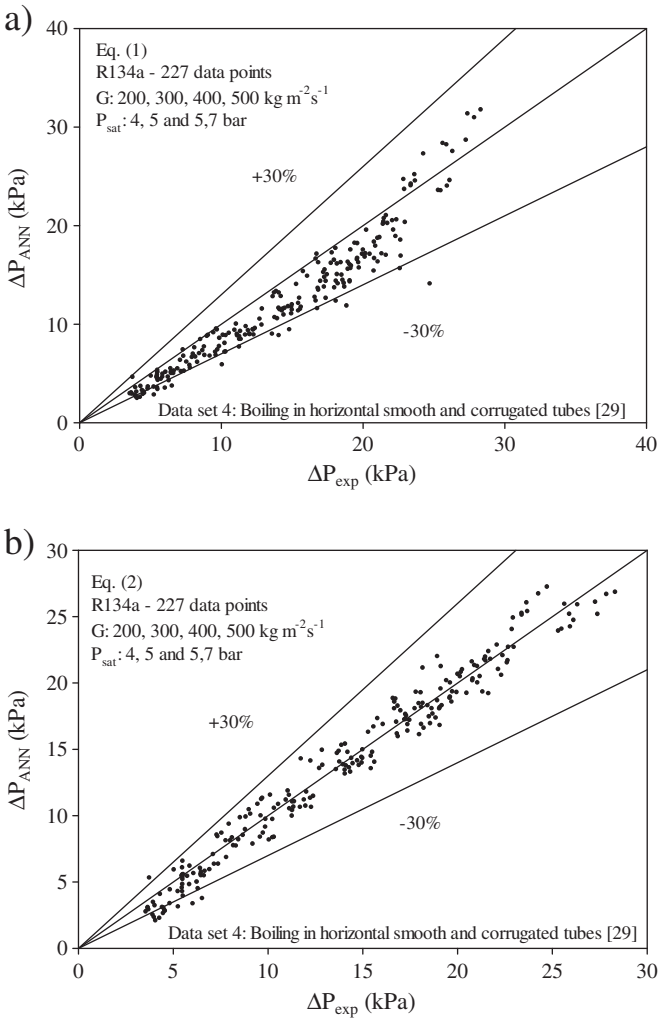

Fig. 7. Performance comparison of Eq. (1) (a) and Eq. (2) (b) for the data set 4.

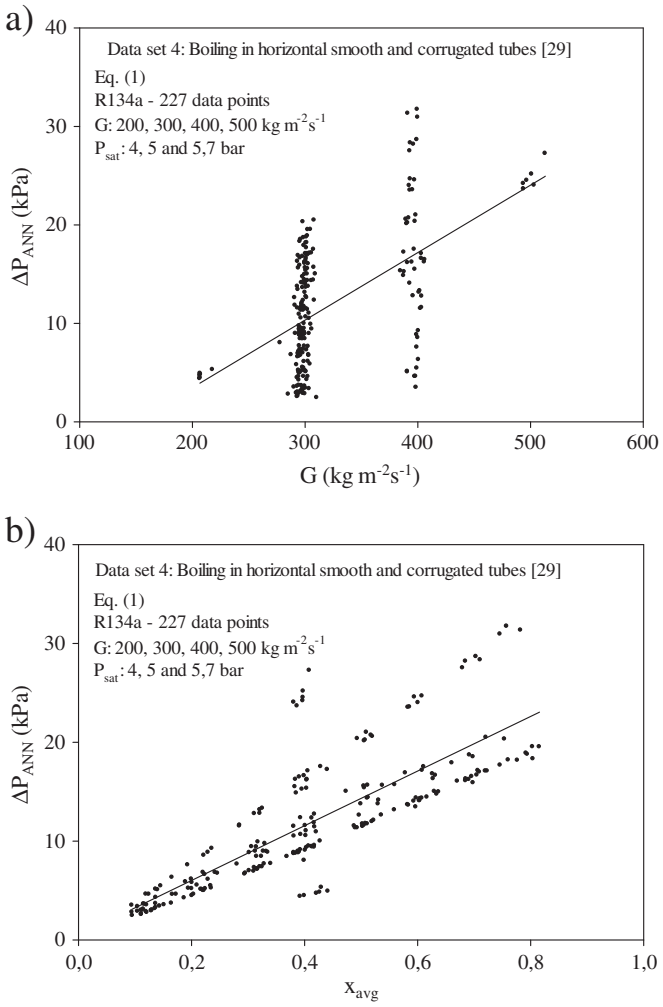

Fig. 8. Alteration of obtained pressure drops with mass flux (a) and average vapor quality (b) for data set 4.

5. Conclusion

Prediction of pressure drop is accomplished and dependable correlations of condensation and boiling in plain and corrugated tubes are developed using computational numerical techniques. The authors' experimental databases in the literature have been benefitted from in the analyses in order to have reliable empirical correlations. This paper reveals that although there are many works on the prediction of two-phase pressure drop in tubes, application of artificial neural networks (ANN) accompanied by non-linear least squares (NLS) to the in-tube boiling and condensation for the aim of correlation development does not appear in the previous papers. Therefore, this investigation's content is supposed to bring new insight to the subject of two-phase flow.

This paper not only proposes some pressure drop empirical correlations for boiling and condensation data sets but also enables researchers to predict both condensation and boiling flows in smooth/corrugated horizontal/vertical tubes by means of a single correlation with a reasonable deviation.

The dependency of output of the ANNs closed form from input values is investigated in the study. Dependency analyses show that liquid Prandtl number, Butterworth's void fraction and Lockhart–Martinelli parameter are the most effective parameters for the tested operating conditions.

Acknowledgements

The third author wishes to thank King Mongkut's University of Technology Thonburi (KMUTT) for providing him with a Post-doctoral fellowship. The fourth author is indebted to the Thailand Research Fund and National Science and Technology Development Agency for its financial support.

References

[1] A.S. Dalkilic, S. Wongwises, Intensive literature review of condensation inside smooth and enhanced tubes, Int. J. Heat Mass Transfer 52 (2009) 3409–3426.
[2] A.S. Dalkilic, S. Wongwises, Book chapter, "Condensation heat transfer in smooth and enhanced geometries - A review of 2010 literature", in the book "Refrigeration Systems, Design Technologies and Developments", Nova Publishers, 2013, ISBN 978-1-62417-230-4.
[3] S. Laohalertdecha, A.S. Dalkilic, S. Wongwises, A review on the heat-transfer performance and pressure-drop characteristics of various enhanced tubes, Int. J. Air Cond. Refrig. 20 (2012) 1–20.
[4] A.S. Dalkilic, S. Wongwises, An investigation of a model of the flow pattern transition mechanism in relation to the identification of annular flow of R134a in a vertical tube using various void fraction models and flow regime maps, Exp. Thermal Fluid Sci. 34 (2010) 692–705.
[5] A.S. Dalkilic, S. Wongwises, Validation of void fraction models and correlations using a flow pattern transition mechanism model in relation to the identification of annular vertical downflow in-tube condensation of R134a, Int. Commun. Heat Mass Transfer 37 (2010) 827–834.
[6] Ahmet Selim Dalkılıç, Theoretical analysis on the prediction of coefficient of performance (COP) of vapour compression refrigeration systems using various alternative refrigerants, J. Therm. Sci. Technol. 32 (2012) 67–79.
[7] A.S. Dalkilic, S. Wongwises, A performance comparison of vapour compression refrigeration system using various alternative refrigerants, Int. Commun. Heat Mass Transfer 37 (2010) 1340–1349.
[8] M. Balcilar, A.S. Dalkilic, S. Wongwises, Artificial neural networks (ANNs) techniques for the determination of condensation heat transfer characteristics during downward annular flow of R134a inside a vertical smooth tube, Int. Commun. Heat Mass Transfer 38 (2011) 75–84.
[9] M. Balcilar, A.S. Dalkilic, B. Bolat, S. Wongwises, Investigation of empirical correlations on the determination of condensation heat transfer characteristics using computational numerical methods during downward annular flow of R134a inside a vertical smooth tube, J. Mech. Sci. Technol. 25 (10) (2011) 1–20.
[10] O. Agra, H. Demir, S. Ozgur Atayilmaz, F. Kantas, A.S. Dalkilic, Numerical investigation of heat transfer and pressure drop in enhanced tubes, Int. Commun. Heat Mass Transfer 38 (2011) 1384–1391.
[11] M. Balcilar, A.S. Dalkilic, O. Agra, S.O. Atayilmaz, S. Wongwises, A correlation development for predicting the pressure drop of various refrigerants during condensation and evaporation in horizontal smooth and micro-fin tubes, Int. Commun. Heat Mass Transfer 39 (2012) 937–944.
[12] A.S. Dalkilic, S. Laohalertdecha, S. Wongwises, Effect of void fraction models on the two-phase friction factor of R134a during condensation in vertical downward flow in a smooth tube, Int. Commun. Heat Mass Transfer 35 (2008) 921–927.
[13] A.S. Dalkilic, S. Laohalertdecha, S. Wongwises, Two-phase friction factor in vertical downward flow in high mass flux region of refrigerant HFC-134a during condensation, Int. Commun. Heat Mass Transfer 35 (2008) 1147–1152.
[14] A.S. Dalkilic, S. Laohalertdecha, S. Wongwises, Effect of void fraction models on the film thickness of R134a during downward condensation in a vertical smooth tube, Int. Commun. Heat Mass Transfer 36 (2009) 172–179.
[15] A.S. Dalkilic, O. Agra, I. Teke, S. Wongwises, Comparison of frictional pressure drop models during annular flow condensation of R600a in a horizontal tube at low mass flux and of R134a in a vertical tube at high mass flux, Int. J. Heat Mass Transf. 53 (2010) 2052–2064.
[16] A.S. Dalkilic, S. Laohalertdecha, S. Wongwises, New experimental approach on the determination of condensation heat transfer coefficient using frictional pressure drop and void fraction models in a vertical tube, Energy Convers. Manag. 51 (2010) 2535–2547.
[17] A.S. Dalkilic, Condensation pressure drop characteristics of various refrigerants in a horizontal smooth tube, Int. Commun. Heat Mass Transfer 38 (2011) 504–512.
[18] A.S. Dalkilic, N.A. Kürekci, S. Wongwises, Effect of void fraction and friction factor models on the prediction of pressure drop of R134a during downward condensation in a vertical tube, Heat Mass Transfer 48 (2012) 123–139.
[19] K. Aroonrat, A.S. Dalkilic, S. Wongwises, Experimental study on evaporative heat transfer and pressure drop of R-134a flowing downward through vertical corrugated tubes with different corrugation pitches, Heat Mass Transfer 26 (2013) 41–63.
[20] A.S. Dalkilic, S. Yildiz, S. Wongwises, Experimental investigation of convective heat transfer coefficient during downward laminar flow condensation of R134a in a vertical smooth tube, Int. J. Heat Mass Transfer 52 (2009) 142–150.
[21] A.S. Dalkilic, S. Laohalertdecha, S. Wongwises, Experimental investigation on heat transfer coefficient of R134a during condensation in vertical downward flow at high mass flux in a smooth tube, Int. Commun. Heat Mass Transfer 36 (2009) 1036–1043.

[22] A.S. Dalkilic, S. Wongwises, Experimental study on the condensation heat transfer coefficients in high mass flux region in annular flow regime of HFC-134a inside the vertical smooth tube, Heat Transfer Eng. 32 (2011) 33–44.
[23] A.S. Dalkilic, I. Teke, S. Wongwises, Experimental analysis for the determination of the convective heat transfer coefficient by measuring pressure drop directly during annular condensation flow of R134a in a vertical smooth tube, Int. J. Heat Mass Transf. 54 (2011) 1008–1014.
[24] S. Saisorn, J. Kaew-On, S. Wongwises, Flow pattern and heat transfer characteristics of R-134a refrigerant during flow boiling in a horizontal circular mini-channel, Int. J. Heat Mass Transf. 53 (2010) 4023–4038.
[25] A.S. Dalkılıç, İ. Teke, S. Wongwises, Heat transfer enhancement during downward laminar flow condensation of R134a in vertical smooth and micro-fin tubes, J. Therm. Sci. Technol. 32 (2012) 19–31.
[26] A.S. Dalkilic, B. Kundu, S. Wongwises, An experimental investigation on the Reynolds analogy applied to annular condensation laminar flow of R134a in a vertical tube, Arab. J. Sci. Eng. 38 (2013) 1493–1507.
[27] S. Laohalertdecha, S. Wongwises, Condensation heat transfer and flow characteristics of R-134a flowing through corrugated tubes, Int. J. Heat Mass Transfer 54 (2011) 2673–2682.
[28] K. Aroonrat, S. Wongwises, Evaporation heat transfer and friction characteristics of R-134a flowing downward in a vertical corrugated tube, Exp. Therm. Fluid Sci. 35 (2011) 20–28.
[29] S. Laohalerdecha, A.S. Dalkilic, S. Wongwises, Correlations for evaporation heat transfer coefficient and two-phase friction factor for R134a flowing through corrugated tubes, Int. Commun. Heat Mass Transfer 38 (2011) 1406–1413.

This article was downloaded by: [Omid Mahian]
On: 15 November 2013, At: 06:28
Publisher: Taylor & Francis
Informa Ltd Registered in England and Wales Registered Number: 1072954 Registered office: Mortimer House, 37-41 Mortimer Street, London W1T 3JH, UK

Journal of Dispersion Science and Technology
Publication details, including instructions for authors and subscription information:
http://www.tandfonline.com/loi/ldis20

Measurement and Correlation of the Viscosity of Water-Based Al_2O_3 and TiO_2 Nanofluids in High Temperatures and Comparisons with Literature Reports

Thaklaew Yiamsawas [a] , Ahmet Selim Dalkilic [b] , Omid Mahian [c] & Somchai Wongwises [a d]
[a] Fluid Mechanics, Thermal Engineering and Multiphase Flow Research Lab. (FUTURE), Department of Mechanical Engineering , Faculty of Engineering, King Mongkut's University of Technology Thonburi , Bangmod , Bangkok , Thailand
[b] Heat and Thermodynamics Division, Department of Mechanical Engineering , Yildiz Technical University, Yildiz , Besiktas , Istanbul , Turkey
[c] Young Researchers and Elite Club, Mashhad Branch, Islamic Azad University , Mashhad , Iran
[d] The Academy of Science, The Royal Institute of Thailand, Sanam Suea Pa , Dusit , Bangkok , Thailand
Accepted author version posted online: 06 Mar 2013.Published online: 14 Nov 2013.

To cite this article: Thaklaew Yiamsawas , Ahmet Selim Dalkilic , Omid Mahian & Somchai Wongwises (2013) Measurement and Correlation of the Viscosity of Water-Based Al_2O_3 and TiO_2 Nanofluids in High Temperatures and Comparisons with Literature Reports, Journal of Dispersion Science and Technology, 34:12, 1697-1703, DOI: 10.1080/01932691.2013.764483

To link to this article: http://dx.doi.org/10.1080/01932691.2013.764483

PLEASE SCROLL DOWN FOR ARTICLE

Taylor & Francis makes every effort to ensure the accuracy of all the information (the “Content”) contained in the publications on our platform. However, Taylor & Francis, our agents, and our licensors make no representations or warranties whatsoever as to the accuracy, completeness, or suitability for any purpose of the Content. Any opinions and views expressed in this publication are the opinions and views of the authors, and are not the views of or endorsed by Taylor & Francis. The accuracy of the Content should not be relied upon and should be independently verified with primary sources of information. Taylor and Francis shall not be liable for any losses, actions, claims, proceedings, demands, costs, expenses, damages, and other liabilities whatsoever or howsoever caused arising directly or indirectly in connection with, in relation to or arising out of the use of the Content.

This article may be used for research, teaching, and private study purposes. Any substantial or systematic reproduction, redistribution, reselling, loan, sub-licensing, systematic supply, or distribution in any form to anyone is expressly forbidden. Terms & Conditions of access and use can be found at http://www.tandfonline.com/page/terms-and-conditions

Journal of Dispersion Science and Technology, 34:1697–1703, 2013
Copyright © Taylor & Francis Group, LLC
ISSN: 0193-2691 print/1532-2351 online
DOI: 10.1080/01932691.2013.764483

Taylor & Francis
Taylor & Francis Group

Measurement and Correlation of the Viscosity of Water-Based Al_2O_3 and TiO_2 Nanofluids in High Temperatures and Comparisons with Literature Reports

Thaklaew Yiamsawas,[1] Ahmet Selim Dalkilic,[2] Omid Mahian,[3] and Somchai Wongwises[1,4]

[1]*Fluid Mechanics, Thermal Engineering and Multiphase Flow Research Lab. (FUTURE), Department of Mechanical Engineering, Faculty of Engineering, King Mongkut's University of Technology Thonburi, Bangmod, Bangkok, Thailand*
[2]*Heat and Thermodynamics Division, Department of Mechanical Engineering, Yildiz Technical University, Yildiz, Besiktas, Istanbul, Turkey*
[3]*Young Researchers and Elite Club, Mashhad Branch, Islamic Azad University, Mashhad, Iran*
[4]*The Academy of Science, The Royal Institute of Thailand, Sanam Suea Pa, Dusit, Bangkok, Thailand*

Downloaded by [Omid Mahian] at 06:28 15 November 2013

GRAPHICAL ABSTRACT

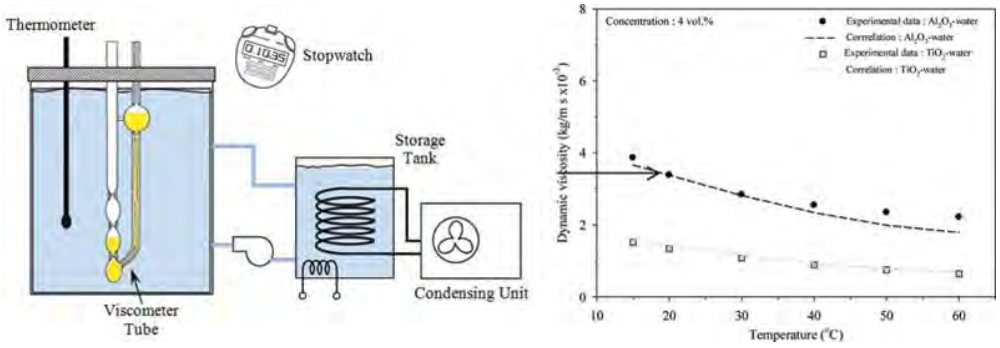

In this article, the viscosity of two common nanofluids including Al_2O_3/water and TiO_2/water is measured at high temperatures, and high concentrations of the nanofluids. The range of temperature is 15–60°C where the volume fraction of nanoparticles varies from 1 to 8%. Next, comparisons have been done with the most well-known theoretical and experimental reports in the literature. Finally, using the experimental data, a helpful correlation is presented.

Keywords Correlation, high temperature, nanofluid, viscosity

Received 13 November 2012; accepted 1 January 2013.

The present study was supported by the Thailand Research Fund (TRF), the National Science and Technology Development Agency, the Office of the Higher Education Commission, and the National Research University Project whose guidance and assistance are gratefully acknowledged. A. S. Dalkilic and O. Mahian thank the Department of Mechanical Engineering, King Mongkut's University of Technology Thonburi and Professor Somchai Wongwises for providing them fellowships for doing their research in Thailand.

Address correspondence to Somchai Wongwises, Fluid Mechanics, Thermal Engineering and Multiphase Flow Research Lab. (FUTURE), Department of Mechanical Engineering, Faculty of Engineering, King Mongkut's University of Technology Thonburi, Bangmod, Bangkok 10140, Thailand. E-mail: somchai.won@kmutt.ac.th

INTRODUCTION

Nanofluids as a new group of working fluids with a small volume fraction of nanometer-sized solid particles in suspension have attracted special attention.[1] Currently, the use of nanofluids to enhance the performance and thermal efficiency of engineering systems is in progress. During the last decades many researches have been done on the preparation, properties, and applications of nanofluids. The readers can refer to some of these studies that have been conducted recently.[2–11]

Up to now, extensive studies have been done on the viscosity of nanofluids. Estimation of the viscosity of nanofluids at different temperatures and concentrations is very important for the design of various thermal engineering systems such as heat exchangers; because the amount of

Downloaded by [Omid Mahian] at 06:28 15 November 2013

viscosity determines the pumping power, and consequently the performance costs of thermal systems. Here, the most important studies in the field are reviewed briefly.

Pak and Cho[12] measured the viscosity of Al_2O_3/water and TiO_2/water nanofluids at room temperature using a rotational viscometer. Particle sizes of alumina (Al_2O_3) and titanium dioxide (TiO_2) are 13 nm and 27 nm, respectively. Their results indicated that the viscosity of nanofluids is greater than that of the base fluid. For the volume fraction of 10%, they found that the relative viscosity of TiO_2/water increases by 3 times, whereas the relative viscosity of Al_2O_3/water increases by 200 times. They also showed that the classic model underestimates the viscosity.

Wang et al.[13] examined the viscosity of Al_2O_3 suspended in water and ethylene glycol (EG) solution. They investigated the effects of dispersion methods on the viscosity, which are mechanical blending (method 1), particles coated with polymers (method 2), and filtration (method 3). The authors found that the second and third methods are superior because of providing smaller viscosities than the first method. They also perceived that with increases of concentration, both viscosity quantity and viscosity ratio increase linearly.

He et al.[14] measured the viscosity of the TiO_2/water nanofluid. Particle sizes of TiO_2 are 95, 145, and 210 nm where the concentration range is 1 to 5 wt%. They found that the viscosity ratio increases nonlinearly with the concentration. They found that the increase of particle size leads to increases of the viscosity ratio.

Nguyen et al.[15] studied the effects of temperature, concentration, and particle size on the viscosity of Al_2O_3/water and CuO/water nanofluids. They utilized two dimensions of Al_2O_3 nanoparticles including 36 and 47 nm, and particle size of 36 nm for CuO nanoparticles. The experiments are conducted at a temperature range of 22 to 75°C with a concentration range of 1 to 12 vol%. A piston-type viscometer is used in this research. Results showed that with increasing the temperature, viscosity decreases. On the contrary, the increase of concentration results in an increase of viscosity. It is also found that particle size has no effect on the viscosity of Al_2O_3/water at small concentrations. However, at large concentrations, the increase of particle size increases the viscosity. They also found that CuO–water had greater viscosity than Al_2O_3–water nanofluid. The comparison between the experimental results and theoretical models shows that the theoretical models of Einstein, Brinkman, and Batchelor are not useful to predict the viscosity.

Murshed et al.[16] measured the viscosity of TiO_2 and Al_2O_3 nanofluids, both suspended in deionized water. Particle sizes of TiO_2 and Al_2O_3 are 15 and 80 nm, respectively. The experiments are conducted at a concentration range of 1–5 vol%, and a rotational viscometer is used for measurement.

Duangthongsuk and Wongwises[17] studied the effects of temperature on the viscosity of TiO_2/water nanofluid. A rotational rheometer (Malvern Instrument) is used to measure the viscosity. The particle size of TiO_2 is 21 nm, with a temperature range of 15 to 35°C and concentration range of 0.2 to 2 vol%. They found that with increasing of temperature the viscosity ratio increases, especially at the large volume fraction.

Turgut et al.[18] measured the viscosity of TiO_2 nanofluid mixed in a deionized water base fluid. A vibration viscometer (Vibro A&D) is used to measure the viscosity of nanofluid in a concentration range of 0.2 to 3 vol% and temperature range of 13 to 55°C. They found that the relative viscosity increases nonlinearly with concentration. They showed that classic models of Einstein, Nielsen, and Krieger and Dougherty underestimates the viscosity obtained by the experimental study.

Chandrasekar et al.[19] performed an experimental and theoretical study on the effects of concentration on the viscosity of Al_2O_3/water nanofluid where the particle size is 43 nm. The experiments are conducted at a concentration range of 1 to 5 vol% at room temperature. The Results showed that Al_2O_3/water nanofluid at the volume fractions mentioned is Newtonian.

In a comparative work, Xie et al.[20] compared the viscosity of five different nanofluids including ethylene glycol based MgO, TiO_2, ZnO, Al_2O_3 and SiO_2 nanofluids. They found that for the temperatures range of 10 to 60°C, the viscosity of MgO/EG nanofluid is the smallest. Fedele et al.[21] presented some results for the viscosity of water based TiO_2 nanofluid at a temperature range of 10 to 70°C. Recently, Aladag et al.[22] obtained the viscosity of Al_2O_3/water and CNT/water based nanofluids at low volume fractions and low temperatures (between 2 and 10°C). A review of the latest results on the viscosity of nanofluids is performed by Mahbubul et al.[23]

From the researches mentioned above and with a review of the literature, it is found that the viscosity of nanofluids is greater than that of the base fluid and it increases with concentration, and decreases with temperature. However, there are still many differences and deviations in the research. For instance, the results presented by Duangthongsuk and Wongwises[17] contradict the results reported by Nungyen et al.[15] indicated that the viscosity ratio decreases with temperature, but, Duangthongsuk and Wongwises[17] reached to an opposite result.

In this work, in the first, the viscosities of water based Al_2O_3 and TiO_2 nanofluids are measured at high temperatures (by 60°C) and volume fractions between 1–8%. Next, comparisons with the works reported in the literature are conducted. Finally, a helpful correlation to calculate the viscosity of nanofluids is presented for using in the design of thermal systems. Based on the best knowledge of the authors, the data presented in the present work, have not appeared never in the open literature.

Downloaded by [Omid Mahian] at 06:28 15 November 2013

NANOFLUID PREPARTION

In this study, TiO_2 (21 nm) and Al_2O_3 (120 nm) nanoparticles suspended in water, respectively, with weight fractions of 40% and 30% were provided by Degussa Company, Germany. To prepare the desired concentrations of nanofluids, the dilution is mixed with water. Next, using an ultrasonic vibration system the mixture is sonicated for 2 hours to avoid agglomeration.

No sedimentation of nanoparticles is observed after months. In this work, high concentrations of TiO_2/water nanofluid (by 8%) are used, while for Al_2O_3/water nanofluid, only the volume fractions up to 4% are used. It should be noted that Al_2O_3/water nanofluid is non-Newtonian for volume fractions higher than 4%, whereas the suspensions of TiO_2 are Newtonian for concentrations by 8%. This is because of the bigger size of Al_2O_3 nanoparticles (120 nm), which makes it non-Newtonian.

EXPERIMENTAL SETUP

A capillary tube viscometer (Cannon Instrument, USA) is used to measure the viscosity of nanofluids. This type of capillary tube viscometer has very good accuracy so that it is widely used in both industry and laboratory, and has been used by many researchers. The components of the viscometer, is shown in Figure 1. It is composed of a 0.75 mm viscometer tube with a measurement range of 1.6 to 8 cSt. The tube is immersed in a transparent temperature-controlled basin connected to a temperature-controlled water tank. A stopwatch with the accuracy of 0.01 s is used to record the time of passing the fluid from a specified section of the viscometer and a thermometer with the accuracy of 0.1°C is used to measure the temperature.

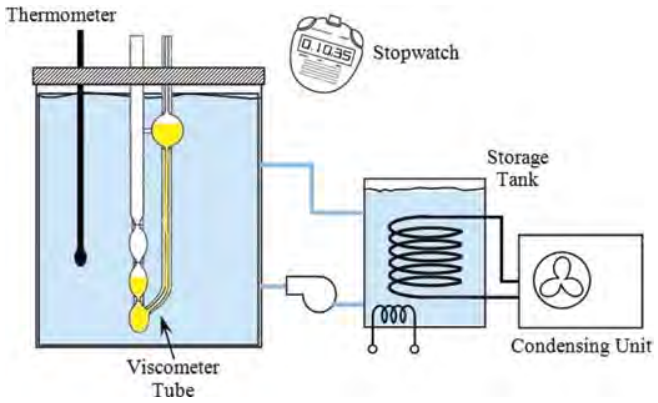

FIG. 1. Schematic diagram of the experimental setup. (Figure available in color online.)

DATA REDUCTION

The viscosity can be obtained by the following relation:

$$\mu = C \cdot \rho t. \quad [1]$$

Where μ is the viscosity (kg/ms), C is a constant fo the viscometer tube obtained from calibration with reference substance supplied by the manufacturer (=0.008 cSt/s), ρ is the density (kg/m^3), and t is the flowing time of the sample substance during each test (s). The density of nanofluid (ρ_{nf}) is obtained by the following well known relation [3]:

$$\rho_{nf} = \phi\rho_p + (1-\phi)\rho_f. \quad [2]$$

In this work, some comparisons have been done by the theoretical models and correlations which the relations are presented here.

Einstein's equation [3]: This model is based on phenomenological hydrodynamic equations and considers suspension containing solute particles in a total volume. This model is as follows:

$$\mu_{nf} = (1+2.5\phi)\mu_f, \quad [3]$$

where μ_{nf} is the viscosity of nanofluid, μ_f is the viscosity of base fluid, and ϕ is the volume fraction (vol%).

Brinkman[3] presented a model to predict the viscosity of mixtures by improving and developing the Einstein's model, which can be derived by considering the effect of the addition of one solute molecule to an existing solution. The model, which can be used in the cases of large concentrations, is as follows:

$$\mu_{nf} = \frac{1}{(1-\phi)^{2.5}}\mu_f \quad [4]$$

Another popular classic model is Batchelor's equation,[3] which is based on the reciprocal theorem in Stokes flow problem. It produces an expression of the bulk stress due to the thermodynamic forces and incorporates both hydrodynamic effects and Brownian motion. The equation is as follows:

$$\mu_{nf} = (1+2.5\phi+6.2\phi^2)\mu_f \quad [5]$$

The above relations are old. Recently, Conrcione[24] presented the following relation:

$$\frac{\mu_{nf}}{\mu_f} = \frac{1}{1-34.87(d_p/d_f)^{-0.3}\phi^{1.03}}, \quad [6]$$

where d_p is nanoparticle size, and d_f is the molecule diameter of base fluid which can be calculated by:

$$d_f = \left[\frac{6M}{N\pi\rho_{f,0}}\right]^{1/3}, \quad [7]$$

where M is the molecular weight of base fluid, N is the Avogadro number, and $\rho_{f,0}$ is the density of base fluid calculated at the temperature of 293 K.

The results of the present work are compared with the above models and the experimental data in the literature.

RESULTS AND DISCUSSIONS

Before performing the experiments with nanofluids, to examine the accuracy of the experimental set up, a comparison of the viscosity of water has been made between the results obtained by the present set up and the results presented in ASHRAE.[25] As it is seen from Figure 2, there is a little difference between the two results (average 7%).

Figure 3 shows the variations of TiO_2/water nanofluid as a function of particle concentration and temperature. The results show that the viscosity increases with increasing of volume fraction and decreasing temperature, as expected. It is seen that with an increase in the temperature, the differences among the values of viscosity at various concentrations are decreased. This means that at high temperatures where the distances among the molecules of base fluid increases, adding nanoparticles is more reasonable for practical applications, because with increasing the temperature, the difference between the viscosity of water and the concentration of 8% is reduced. It is also observed that with an increase in the volume fraction, the viscosity increases.

Figure 4 shows the variations of viscosity of Al_2O_3/water with temperature at different volume fractions. As it is mentioned, for Al_2O_3/water nanofluid, the viscosity only for volume fractions by 4% is measured. A comparison between Al_2O_3/water and TiO_2/water nanofluids at volume fraction of 4% shows that the viscosity of Al_2O_3/water is more than twice the nanofluid of TiO_2/water. This

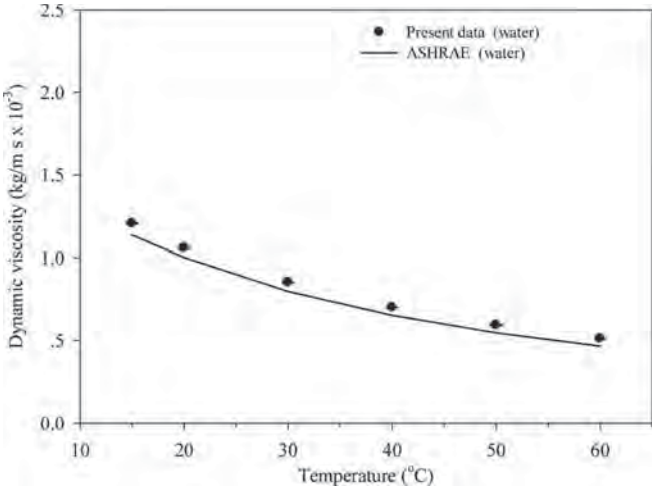

FIG. 2. Comparison of the measured viscosity with reference data.

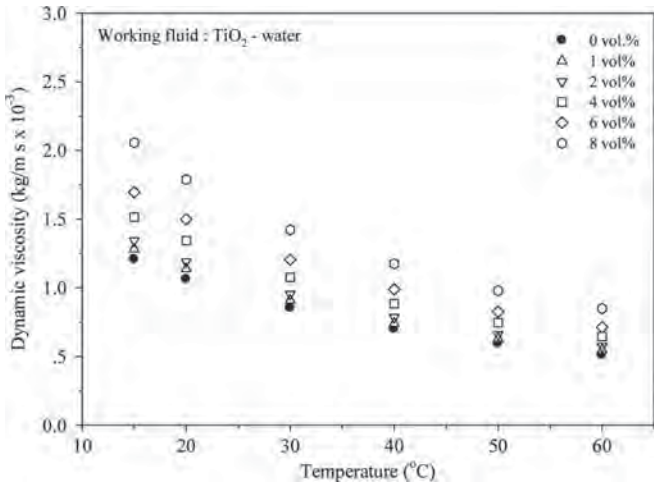

FIG. 3. Viscosity of TiO_2-water nanofluid as a function of temperature and concentration.

difference may be due to larger size of Al_2O_3 nanoparticles. This comparison shows that classic models such as Brinkman, and Batchelor are not suitable models, because the viscosity ratio in these models is only a function of volume fraction and the effect of is not considered.

Figure 5 provides a comparison between the present data and the former workers reported in the literature for TiO_2/water. Figure 5 is plotted to show the trend of variation of viscosity with volume fraction. It is seen that the trend is different for the works. For example, the present data show that the rate of increase in the viscosity ratio with concentration is nearly constant. Masuda et al.[26] and Pak and Cho[12] reached to a similar result. However, Murshed et al.[16] concluded that the rate of increase in the

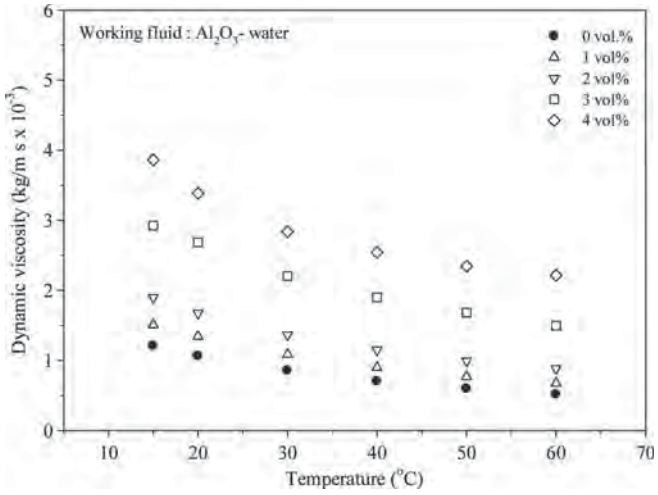

FIG. 4. Viscosity of Al_2O_3-water nanofluid as a function of temperature and concentration.

Downloaded by [Omid Mahian] at 06:28 15 November 2013

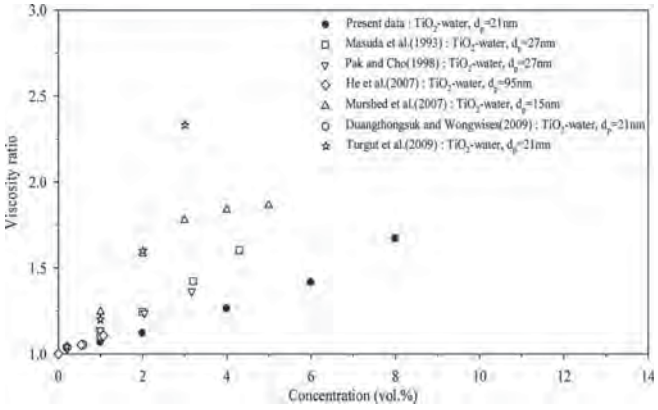

FIG. 5. Effect of concentration on the viscosity ratio of TiO_2/water nanofluid.

viscosity ratio decreases with increasing the concentration. Turgut et al.[18] perceived that the rate of increase in the viscosity ratio increases rapidly with increasing the concentration. As seen, three different trends are presented for TiO_2/water nanofluid.

In Figure 6. the comparisons between the viscosity ratios for Al_2O_3/water nanofluid performed by various researchers are presented. As it is observed, the trend of the present data is in accordance with the works conducted by Kulkalni et al.,[27] Chandrasekar et al.[19] However, other works show nearly a linear variation in the viscosity ratio with increasing the concentration. The differences between the studies for the two nanofluids may be due to various factors such as different shape and size of nanoparticles, different methods of preparation and functionalizing.

Figure 7 provides a comparison between the present data and the theoretical models presented in the literature for the viscosity ratio of TiO_2/water nanofluid. It is observed that the Corcione model overestimates the

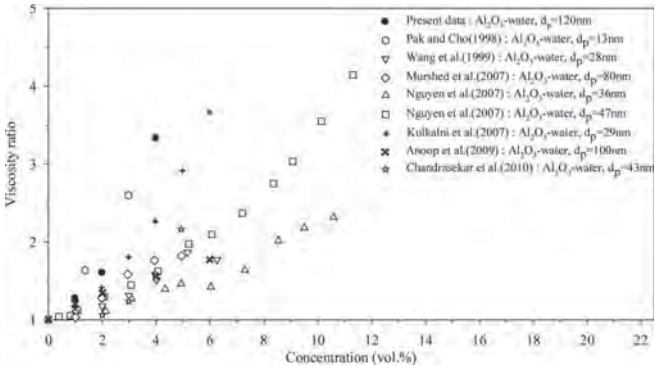

FIG. 6. Effect of concentration on the viscosity ratio of Al_2O_3 nanofluid.

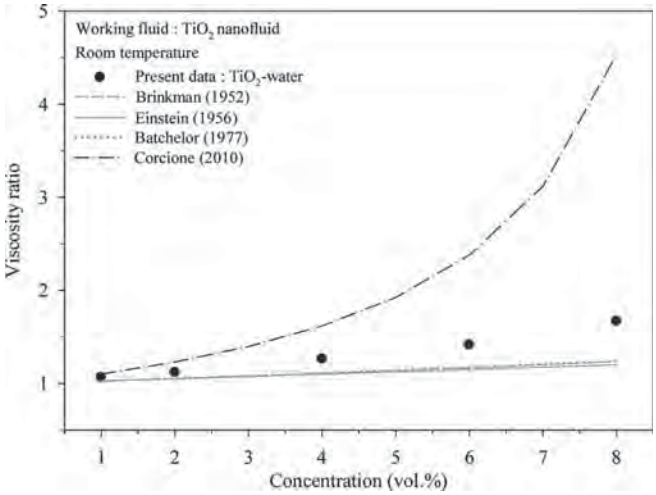

FIG. 7. Comparison of experimental viscosity ratio of TiO_2-water nanofluid with those obtained from various model equations as a function of concentration.

viscosity ratio, while other theoretical models underestimate the viscosity ratio.

Figure 8 gives a comparison between the present data and theoretical models for the viscosity ratio of Al_2O_3/water nanofluid. As shown, the difference between the present data and other models is very large especially at high concentrations

Figure 9 shows that at a given value of concentration (here 4%), the viscosity ratio obtained by the present work is approximately linear and constant with respect to temperature. In comparison with theoretical models, the viscosity ratio provided by this work is about 15% higher than the viscosity ratio calculated by the models.

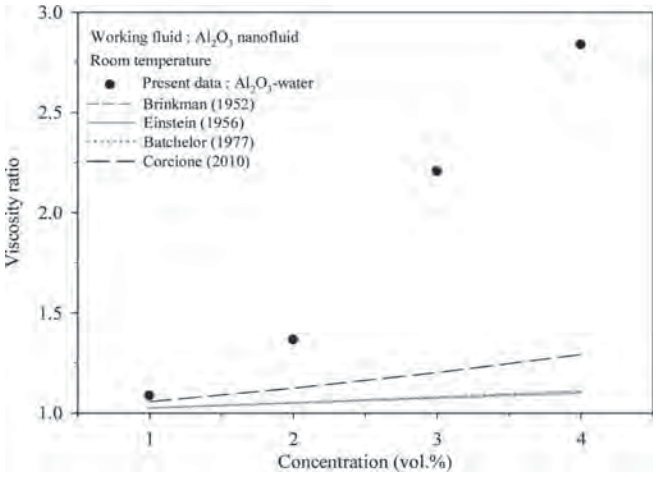

FIG. 8. Comparison of experimental viscosity ratio of Al_2O_3-water nanofluid with those obtained from various model equations as a function of concentration.

Downloaded by [Omid Mahian] at 06:28 15 November 2013

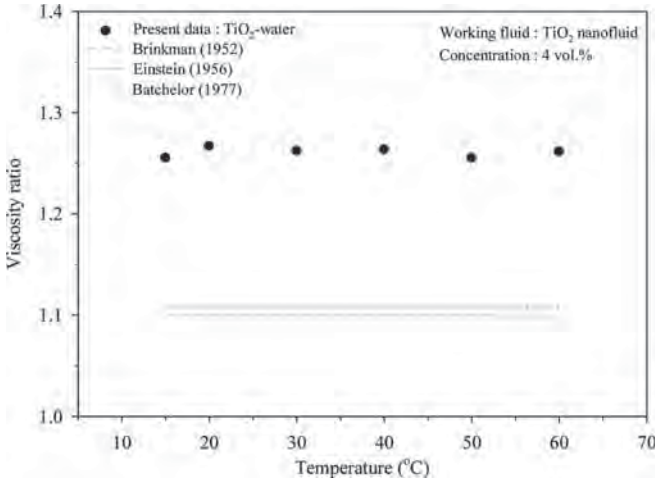

FIG. 9. Comparison of experimental viscosity ratio of TiO_2-water nanofluid with those obtained from various model equations as a function of temperature.

Figure 10 shows the variation of viscosity ratio with temperature for different models.

It is seen that theoretical models fail to predict the viscosity ratio. Also, it is observed that the viscosity ratio predicted by Nguyen et al.[15] is lower than the present data. It may be due to the bigger size of Al_2O_3 nanoparticles tested in this work compared Nguyen et al.[15]

Finally, a correlation is presented for using in the practical applications. In this correlation, the viscosity is a function of temperature, volume fraction and the viscosity of base fluid as:

$$\mu_{nf} = A\phi^B T^C \mu_f^D, \qquad [8]$$

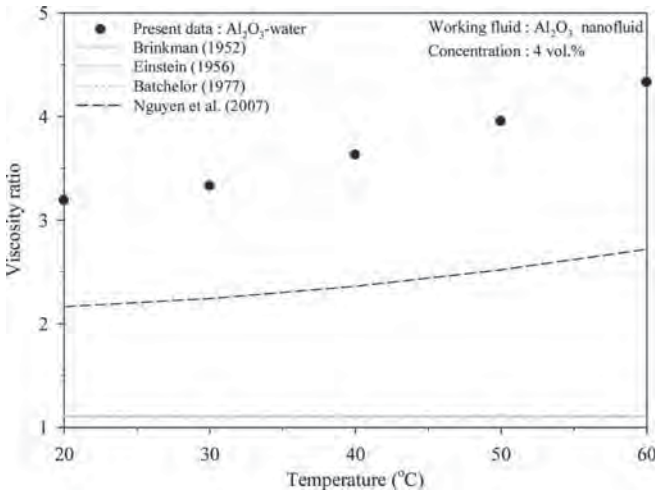

FIG. 10. Comparison of experimental viscosity ratio of Al_2O_3-water nanofluid with those obtained from various model equations as a function of temperature.

TABLE 1
Coefficients for correlations predicting viscosity

	Coefficient			
Nanoparticle	A	B	C	D
Al_2O_3	0.891842	0.739192	0.099205	0.9844
TiO_2	0.837931	0.188264	0.089069	1.100945

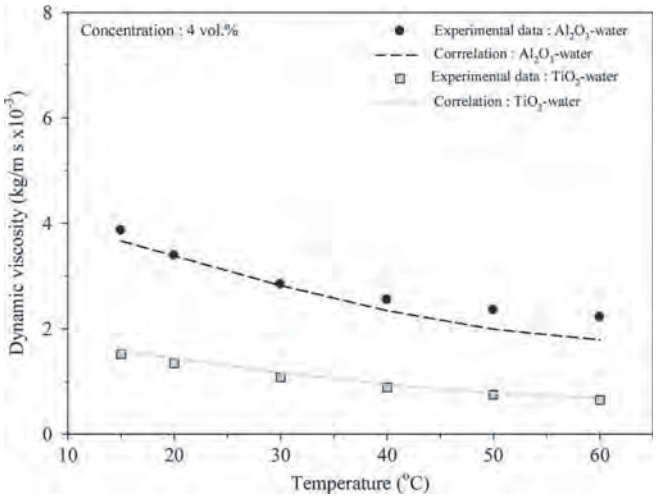

FIG. 11. Comparison of measured viscosity with proposed correlation.

where the coefficients of A, B, C, and D are provided for the two types of nanoparticles in Table 1.

In the above relation, although the coefficient of C (the power of temperature) is positive and one may claim the viscosity of nanofluid increases with increasing the temperature. However, it should be noted that the viscosity of base fluid decreases with increasing the temperature, hence, totally the viscosity of nanofluid decrease. The viscosity of water as the base fluid is obtained by the following relation:

$$\mu_f = 0.0002\,T^2 - 0.0335\,T + 1.6428. \qquad [9]$$

Figure 11 shows the comparison between the correlation and experimental data. The average error in the comparison for TiO2/water nanofluid is about 5%, and for Al_2O_3/water nanofluid is about 9%.

CONCLUSION

The viscosity of TiO_2 and Al_2O_3 nanoparticles suspended in water is measured at high temperatures (by 60°C). The sizes of TiO_2 and Al_2O_3 nanoparticles are respectively 21 and 120 nm where volume fractions 8% and 4% are used for TiO_2 and Al_2O_3 nanoparticles, respectively. Some

Downloaded by [Omid Mahian] at 06:28 15 November 2013

comparisons with the reported works in the literature have been done. From the comparison, it is found that the trend of variations of viscosity ratio with concentration is different in various works. In some of them the viscosity ratio increases linearly, and in some of them the viscosity ratio increases rapidly as parabolic. The differences among different studies may be due to various factors such as different shape and size of nanoparticles, different methods of preparation and functionalizing. This study reveals that in the theory models, besides of volume fraction, the size and shape of nanoparticles, and temperature should be considered. Finally, a helpful correlation to use in practical applications is presented in which the viscosity of nanofluid is a function of temperature, volume fraction, and viscosity of base fluid.

REFERENCES

[1] Mahian, O., Mahmud, S., and Heris, S.Z. (2012) *J. Heat Transfer*, 134: 101704.

[2] Saidur, R., Leong, K.Y., and Mohammad, H.A. (2011) *Renewable and Sustainable Energy Reviews*, 15: 1646.

[3] Khanafer, K. and Vafai, K. (2011) *Int. J. Heat Mass Transfer*, 54: 4410.

[4] Mahian, O., Kianifar, A., Kalogirou, S.A., Pop, I., and Wongwises, S. (in press) *International journal of Heat and Mass Transfer*, http://dx.doi.org/10.1016/j.ijheatmasstransfer.2012.10.037

[5] Yu, W., Xie, H., and Wang, X. (2011) *J. Dispersion Science and Technology*, 32: 948.

[6] Chen, L., Xie, H., Yu, W., and Li, Y. (2011) *J. Dispersion Science and Technology*, 32: 550.

[7] Solanki, J.N. and Murthy, Z.V.P. (2011) *J. Dispersion Science and Technology*, 32: 724.

[8] Park, E.J., Lee, J., Jung, D., and Shim, S.E. (2011) *J. Dispersion Science and Technology*, 32: 1485.

[9] Aminfar, H. and Motallebzadeh, R. (2011) *J. Dispersion Science and Technology*, 32: 1311.

[10] Aminfar, H. and Motallebzadeh, R. (2012) *J. Dispersion Science and Technology*, 33: 155.

[11] Hojjat, M., Etemad, S.Gh., Bagheri, R., and Thibault, J. (2012) *J. Dispersion Science and Technology*, 33: 1066.

[12] Pak, B.C. and Cho, Y.I. (1998) *Experimental Heat Transfer*, 11: 151.

[13] Wang, X.Q. and Mujumdar, A.S. (2007) *International Journal of Thermal Science*, 46: 1.

[14] He, Y., Jin, Y., Chen, H., Ding, Y., Cang, D., and Lu, H. (2007) *International Journal of Heat and Mass Transfer*, 50: 2272.

[15] Nguyen, C.T., Desgranges, F., Roy, G., Galanis, N., Mare, T., Boucher, S., and Mintsa, H.A. (2007) *International Journal of Heat and Fluid Flow*, 28: 1492.

[16] Murshed, S.M.S., Leong, K.C., and Yang, C. (2008) *International Journal of Thermal Science*, 47: 560.

[17] Duangthongsuk, W. and Wongwises, S. (2009) *Experimental Thermal and Fluid Science*, 33: 706.

[18] Turgut, A., Tavman, I., Chirtoc, M., Schuchmann H. P., Sauter, C., and Tavman, S. (2009) *Int. J. Thermophys*, 30: 1213.

[19] Chandrasekar, M., Suresh, S., and Bose, A.C. (2010) *Experimental Thermal and Fluid Science*, 34: 210.

[20] Xie, H., Yu, W., and Chen, W. (2010) *Journal of Experimental Nanoscience*, 5: 463–472.

[21] Fedele, L., Colla, L., and Sergio Bobbo. (2012) *International Journal of Refrigeration*, 35: 1359.

[22] Aladag, B., Halelfadl, S., Doner, N., Maré, T., Duret, S., and Estellé, P. (2012) *Applied Energy*, 97: 876.

[23] Mahbubul, I.M., Saidur, R., and Amalina, M.A. (2012) *International Journal of Heat and Mass Transfer*, 55: 874.

[24] Corcione, M. (2011) *Energy Conversion and Management*, 52: 789.

[25] ASHRAE. (2005) American Society of Heating, Refrigerating and Air-Conditioning Engineers Inc., Atlanta, GA.

[26] Masuda, H., Ebata, A., Teramae, K., and Hishinuma, N. (1993) *Netsu Bussei (Japan)*, 7: 227.

[27] Kulkarni, D.P., Das, D.K., and Patil, S.L. (2007) *J. Nanosci. Nanotechno.*, 7: 2318.

Downloaded by [Omid Mahian] at 06:28 15 November 2013

Estimation of operational costs due to entropy generation in a vertical annulus

Omid Mahian

Young Researchers and Elite Club,
Mashhad Branch, Islamic Azad University,
Mashhad, Iran
E-mail: omid.mahian@gmail.com

Hakan F. Oztop

Technology Faculty,
Department of Mechanical Engineering,
Fırat University,
Elazig 23119, Turkey
E-mail: hfoztop1@gmail.com

Ahmet Z. Sahin*

Mechanical Engineering Department,
King Fahd University of Petroleum and Minerals,
Dhahran 31261, Saudi Arabia
E-mail: azsahin@kfupm.edu.sa
*Corresponding author

Somchai Wongwises

Fluid Mechanics, Thermal Engineering
and Multiphase Flow Research Lab. (FUTURE),
Department of Mechanical Engineering,
Faculty of Engineering,
King Mongkut's University of Technology Thonburi,
Bangmod, Bangkok 10140, Thailand
E-mail: somchai.won@kmutt.ac.th

Abstract: The study of flow and heat transfer in a vertical annulus is important due to its applications in the cooling of reactors, industrial heat exchangers, microelectronic devices, and so forth. The aim of the present work is to estimate the operational costs due to entropy generation in an annulus with isoflux boundary conditions. For this purpose, the governing equations are simplified and solved analytically to obtain the entropy generation distribution in the annulus. Using the results obtained by the entropy generation analysis, the operational costs due to entropy generation are calculated for various radius

Copyright © 2013 Inderscience Enterprises Ltd.

ratios and different quantities of the flow parameters involved in the problem. The results of this study can be helpful in the design of such heat exchangers to reduce the operational costs caused by the irreversibilities.

Keywords: operational cost; isoflux heat exchanger; entropy generation; refrigerant flow; analytical solution.

Reference to this paper should be made as follows: Mahian, O., Oztop, H.F., Sahin, A.Z. and Wongwises, S. (2013) 'Estimation of operational costs due to entropy generation in a vertical annulus', *Int. J. Exergy*, Vol. 13, No. 4, pp.472–486.

Biographical notes: Omid Mahian is a PhD student in Mechanical Engineering (energy conversion) in Ferdowsi University of Mashahd, Iran. He is interested in some topics in heat transfer engineering include entropy generation and exergy analysis, heat and fluid flow of nanofluids, and solar stills. He has more than 13 ISI papers in high quality journals such as *International Journal of Heat and Mass Transfer*, *Journal of Heat Transfer (ASME)*, *Journal of Thermophysics and Heat transfer (AIAA)* and *Energy (Elsevier)*. He is selected as the best researcher student in the department of his university at 2012.

Hakan F. Oztop is an Associate Professor at Mechanical Education Department of Technical Education Faculty of Firat University. He received the BS from Firat University, Department of Mechanical Engineering in 1996, MS and PhD from the same university in 1998 and 2003, respectively. His main research area is numerical heat transfer and fluid flow in forced, mixed and natural convection through porous ducts and cavities and renewable energy sources. He has also experience on second law analysis of thermal and fluid systems. He has published 125 papers in SCI journals and 70 research articles in international or national conferences.

Ahmet Z. Sahin, PhD, is a Professor of Mechanical Engineering at King Fahd University of Petroleum and Minerals (KFUPM), Dhahran, Saudi Arabia. He received his PhD in Mechanical Engineering from the University of Michigan, Ann Arbor, MI, USA, in 1988. He has published over 200 technical journal/conference papers. He received the KFUPM Distinguished Researcher Award three times, in 2000, 2005 and 2010. His research interests include thermodynamic design optimisation, entropy generation minimisation, solar energy and wind energy applications.

Somchai Wongwises is currently a Professor of Mechanical Engineering at King Mongkut's University of Technology Thonburi, Bangmod, Thailand. He received his Doktor-Ingenieur (Dr.-Ing.) in Mechanical Engineering from the University of Hannover, Germany, in 1994. His research interests include two-phase flow, heat transfer enhancement, and thermal system design.

1 Introduction

The analysis of the second law of thermodynamics implies the use of availability to determine irreversibility, or lost work, during a process (Kumar et al., 1989). In the 1980s, Bejan (1982) applied the second law of thermodynamics to find the various effective factors in the loss of available work (exergy) of the thermal systems through entropy generation. During the recent years, many research studies have been carried out

on entropy generation and thermoeconomic analysis in different thermal systems. A number of the recent studies in the field of entropy generation, thermoeconomic analyses of different thermal systems could be found in Ghazi et al. (2012), Anandan and Bhaskaran (2012), Ahmadi et al. (2012), Aydin et al. (2012), Wu et al. (2012), Askar et al. (2012), Matawala and Prabhakaran (2012), Makinde (2012), Aziz and Khan (2012a, 2012b), Ramos-Alvarado et al. (2012) and Sahin (2012).

The entropy generation problems are usually non-linear and it is difficult to solve them. Therefore, a helpful way to determine the entropy generation rate in complex systems is by simplifying the governing equations with reasonable assumptions to obtain analytical expressions for entropy generation distribution in the system. Here, the entropy generation in an annulus has been investigated; hence, a brief review is presented, adapted from the former analytical works related to the entropy generation between two cylinders.

Yilbas (2001) performed an entropy generation analysis for a rotating outer cylinder by neglecting the irreversibility due to fluid friction and assuming a linear velocity profile. Mahmud and Fraser (2002a, 2002b, 2003a) presented an entropy generation analysis within an annulus under the different boundary conditions. They solved the simplified governing equations in cylindrical coordinates to obtain the distributions of entropy generation and Bejan number. Tasnim and Mahmud (2002a, 2002b) investigated that the generation of entropy in vertical annuli by considering the fully developed laminar flow and the mixed convection heat transfer. Mirzazadeh et al. (2008) studied that the entropy generation between the concentric rotating cylinders using a non-linear viscoelastic fluid as the working fluid. Mahian et al. (2012a) investigated that the entropy generation between two rotating cylinders using nanofluids with the different volume fractions and under different isoflux boundary conditions. In another work, Mahian et al. (2012b) examined that the effects of uncertainties in the models presented for thermophysical properties of nanofluids on entropy generation. Mahian et al. (2012c) recently investigated that the effects of MHD flow on the entropy generation between two isothermal rotating cylinders. In addition, Mahian et al. (2013) studied that the effects of nanofluids on entropy generation between two cylinders in the presence of a magnetic field.

A review of the literature shows that there is no work focusing on the estimation of operational costs due to entropy generation (thermoeconomic analysis) in an isoflux annulus with refrigerant, whereas in the former papers the isothermal boundary conditions are applied. Beside this point, in most of the published works, the economic aspects for such heat exchangers are not considered. Of course, for the flow in a pipe, Sahin et al. (2000) estimated that the operational costs due to the entropy generation by considering the fouling effects. Indeed, the main aim of this work is to estimate the operational costs due to irreversibilities for the vertical annulus under different conditions where the working fluid is engine oil.

2 Problem formulation

In the first, the formulation of the velocity and temperature fields is presented. Next, the formulation of entropy generation is given.

2.1 Velocity and temperature fields

Schematic of the problem is shown in Figure 1. Consider a laminar, steady, and incompressible flow of a viscous fluid with inlet velocity U_0 and inlet temperature T_0 entering an isoflux annulus with radii r_i and r_o. The properties of the working fluid are assumed temperature-independent.

Figure 1 Schematic view of the problem (see online version for colours)

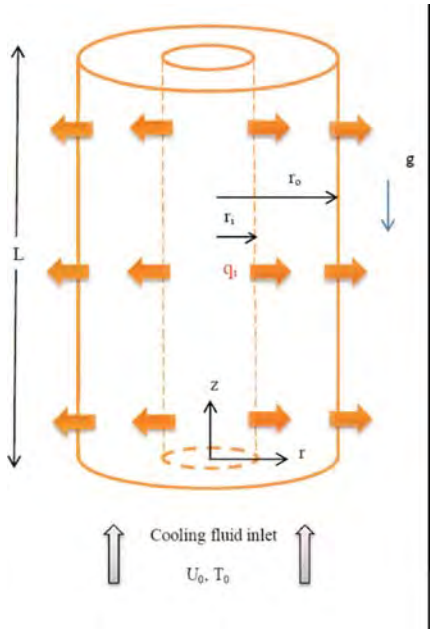

By considering a fully developed flow, the buoyancy effects, and a small variation of temperature in z-direction, the governing equations in dimensionless form can be written as (see Tasnim and Mahmud, 2002a, 2002b; Tasnim et al., 2002; Mahmud and Fraser, 2002c; Sahin et al., 2000):

$$\frac{\partial^2 U}{\partial R^2}+\frac{1}{R}\frac{\partial U}{\partial R}=-\frac{Gr}{\mathrm{Re}}\theta+\frac{\partial P^*}{\partial Z} \tag{1}$$

$$\frac{\partial^2 \theta}{\partial R^2}+\frac{1}{R}\frac{\partial \theta}{\partial R}=0 \tag{2}$$

with the following boundary conditions:

$$\begin{aligned} &U=0 \quad \text{and} \quad \frac{\partial \theta}{\partial R}=-1 \quad \text{at } R=\lambda \\ &U=0 \quad \text{and} \quad \frac{\partial \theta}{\partial R}=F(q_i) \quad \text{at } R=1 \end{aligned} \tag{3}$$

in which the value of $F(q_i)$ is obtained based on the heat flux in the inner cylinder so that the energy equation is satisfied. Of course, because of heat flux boundary conditions, there is no need to obtain the heat flux on outer cylinder. In the above, the dimensionless parameters are defined as follows:

$$U=\frac{V_z}{U_0},\ R=\frac{r}{r_o},\ \mathrm{Re}=\frac{U_0 r_o}{\upsilon},\ P^*=\frac{P}{U_0\mu}r_o,\ Z=\frac{z}{r_o},\ \lambda=\frac{r_i}{r_o}$$
$$\theta=\frac{T-T_0}{q_i r_o/k},\ \mathrm{Gr}=\frac{g\beta\Delta T\quad r_o^3}{\upsilon^2},\ \Delta T=\frac{q_i r_o}{k}. \tag{4}$$

2.2 Entropy generation

The entropy generation rate is obtained by the following relation (see Tasnim and Mahmud (2002a, 2002b) for more details):

$$\dot{S}'''_{\mathrm{gen}}=\frac{k}{T_0^2}\left(\frac{\partial T}{\partial r}\right)^2+\frac{\mu}{T_0}\left(\frac{\partial V_z}{\partial r}\right)^2. \tag{5}$$

The above relation indicates that entropy generation is due to two effects. The first is heat transfer, and the second is fluid friction. The above relation is as follows in dimensionless form:

$$N_S=\frac{\dot{S}'''_{\mathrm{gen}}}{\mu U_0^2/T_0 r_0^2}=\left(\frac{\Omega}{\mathrm{Br}}\right)\left(\frac{\partial\theta}{\partial R}\right)^2+\left(\frac{\partial U}{\partial R}\right)^2=N_H+N_F \tag{6}$$

where N_s is the entropy generation number and N_H, N_F represent the contribution of heat transfer and fluid friction to the entropy generation, respectively. In the above relation, Ω and Br (Brinkman number) are equal to $\Delta T/T_0$ and $U_0^2\mu/k\Delta T$, respectively.

The Bejan number can be defined as:

$$\mathrm{Be}=\frac{N_H}{N_S}. \tag{7}$$

3 Solution to the problem

3.1 Velocity and temperature fields

The governing equations are coupled via the buoyancy term. Therefore, in the first, the energy equation should be solved.

The solution of the energy equation is obtained by twice integrating from the relation with respect to *R*. The solution becomes:

$$\theta(R)=-\lambda\ln(R)+C \tag{8}$$

where *C* is the constant of integration and cannot be obtained in this step, due to isoflux boundary conditions. The velocity field is determined by substituting the temperature distribution in the momentum equation and the solution of the differential equation as follows:

$$U(R) = \Gamma_1 \ln(R) + \Gamma_2 (1 - R^2) + \frac{(-\lambda^3 + \lambda R^2)(\mathrm{Gr}/\mathrm{Re})}{4} \ln(R) \tag{9}$$

where Γ_1 and Γ_2 are constant and are obtained by:

$$\begin{aligned} \Gamma_1 &= \frac{[(C+\lambda)(\mathrm{Gr}/\mathrm{Re}) - (\partial P^*/\partial Z)](\lambda^2 - 1)}{4\ln(\lambda)} \\ \Gamma_2 &= \frac{[(C+\lambda)(\mathrm{Gr}/\mathrm{Re}) - (\partial P^*/\partial Z)]}{4}. \end{aligned} \tag{10}$$

Now, by substituting the velocity distribution in the dimensionless continuity equation, we see that:

$$2\int_{\lambda}^{1} U(R) R \, \mathrm{d}R = (1 - \lambda^2). \tag{11}$$

The constant C is obtained as:

$$C = \frac{1}{4(\mathrm{Gr}/\mathrm{Re})(\lambda^4(\ln(\lambda) - 1) + 2\lambda^2 - \ln(\lambda) - 1)} \left\{ \begin{array}{l} \lambda^5(\mathrm{Gr}/\mathrm{Re})(-7\ln(\lambda) + 4(\ln(\lambda))^2 + 4) \\ +4\lambda^4(\partial P^*/\partial Z)(\ln(\lambda) - 1) \\ +4\lambda^3(\mathrm{Gr}/\mathrm{Re})(\ln(\lambda) - 2) \\ +8\lambda^2(\partial P^*/\partial Z) + \lambda(Gr/\mathrm{Re})(4 + 3\ln(\lambda)) \\ -4(\partial P^*/\partial Z)(1 + \ln(\lambda)) + 32\ln(\lambda)(\lambda^2 - 1) \end{array} \right\}. \tag{12}$$

3.2 Entropy generation number

The entropy generation number distribution is determined based on equation (6) as follows:

$$\begin{aligned} N_S &= \left(\frac{\Omega}{\mathrm{Br}}\right)\left(\frac{-\lambda}{R}\right)^2 + \left(\frac{\Gamma_1}{R} - 2\Gamma_2 R + \frac{-\lambda^3(\mathrm{Gr}/\mathrm{Re})}{4R} + \frac{\lambda(\mathrm{Gr}/\mathrm{Re})(2R\ln(R) + R)}{4}\right)^2 \\ &= N_H + N_F. \end{aligned} \tag{13}$$

4 Estimation of operational costs due to irreversibilities

Total cost due to irreversibility is very important issue in engineering application from energy saving point of view. Sahin et al. (2000) estimated that the total cost due to irreversibility for the flow in a pipe as follows:

$$\dot{C} = C_H T_0 (\dot{S}_{\mathrm{gen}})_H + C_F T_0 (\dot{S}_{\mathrm{gen}})_F \tag{14}$$

where $\dot{C}$ is the total cost of irreversibility (\$/h), C_H is the unit cost of irreversibility due to heat transfer (\$/W h), C_F is the unit cost of irreversibility due to fluid friction (\$/W h), and $\dot{S}_{\mathrm{gen}}$ is the total rate of entropy generation (W/K).

In the current study, the above relation is modified as:

$$\dot{C} = \frac{2\dot{m}^2 \mu L}{\pi \rho^2 r_0^4 (1-\lambda^2)^2} \left[C_H \int_\lambda^1 N_H R \, \mathrm{d}R + C_F \int_\lambda^1 N_F R \, \mathrm{d}R \right]. \tag{15}$$

Another form of equation (15) where the length of the heat exchanger is 1 m is expressed as:

$$\dot{C} = \frac{2\dot{m}^2 \mu C_H}{\pi \rho^2 r_0^4 (1-\lambda^2)^2} \left[\int_\lambda^1 N_H R \, \mathrm{d}R + r_C \int_\lambda^1 N_F R \, \mathrm{d}R \right] \tag{16}$$

where r_c is the cost ratio and in practical situations is more than one (Mahmud and Fraser, 2003b) (a range of 1–20 is considered in this study). The unit cost of irreversibility due to heat transfer C_H may be considered equal to the cost of electricity. The price of electricity shows considerable variation (0.02–0.50 $/kW h) depending on the country (http://en.wikipedia.org/wiki/Electricity_pricing). Therefore a representative value of 0.2 ($/kW h) has been considered for the cost of irreversibility due to heat transfer in the present study, where the electricity price is selected based on the costs in Iran. For the numerical estimations, engine oil is considered as the working fluid in the heat exchanger. The properties of the particular engine oil, its geometry, and its flow characteristics are provided in Table 1.

Table 1 Fluid and flow properties considered for numerical estimations

Parameter	*Numerical value*
C_H ($/kW h)	0.2
$\dot{m}$ (kg/s)	1.0
ρ (kg/ m^3)	876.1
μ (kg/m s)	0.21
r_o (cm)	2.0

5 Results and discussion

Figure 2 shows the velocity distribution in the annulus for $\partial P^*/\partial Z = -0.1$ and two different values of Gr/Re including 5 and 50. The annulus can be divided into two zones based on the variations of velocity with Gr/Re. In the first zone with an increase in Gr/Re, the fluid velocity in the gap increases while in the second zone the velocity decreases. The velocities near the inner cylinder are greater due to higher heat flux in this region.

Figure 3 displays the temperature field for three different values of Gr/Re. It is seen that with an increase in the buoyancy parameter Gr/Re, the temperature decreases in the annulus. The parameter Gr/Re indicates the ratio of natural convection to forced convection. With an increase in Gr/Re, the effects of natural convection increase, and, consequently, the temperature decreases. It is observed from Figure 3 that the profiles of temperature for any value of Gr/Re changes as parallel. This means that the gradients

of temperature remain constant with the changes in the parameter Gr/Re. From the above discussions, one can conclude that, the parameter Gr/Re has considerable effects on the amounts of temperature. However, its effect on gradients of temperature, and, hence entropy generation is not considerable.

The variations of the entropy generation number and Bejan number with respect to radial distance are plotted in Figure 4 for $\partial P^*/\partial Z = -0.1$, $\Omega/\mathrm{Br} = 50$ and two values of Gr/Re, including Gr/Re = 0.1 and Gr/Re = 50. The distribution of the entropy generation number shows an irregular trend in the annulus, such that the annulus is divided into four zones as shown in the figure. In zones 1 and 3, with an increase in Gr/Re, the entropy generation number increases, while with an increase in Gr/Re, the entropy generation number decreases in zones 2 and 4.

Figure 2 Effects of Gr/Re on velocity distribution

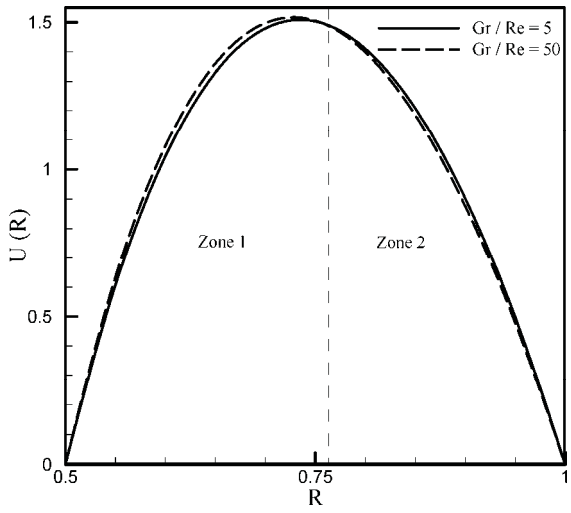

Figure 3 Effects of Gr/Re on temperature distribution

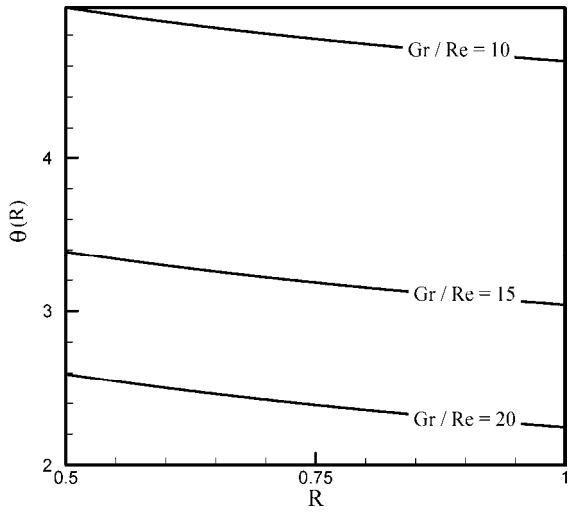

This unpredictable behaviour is due to the interactions of wall effects, heat flux at the inner cylinder, and buoyancy effects in the gap. It should be noted that the total entropy generation demonstrates no considerable change with increases in the flow parameter Gr/Re.

The effect of Gr/Re on the Bejan number is shown in Figure 4(b). It is observed that the Bejan number reaches its maximum near the centreline of the gap ($R = 0.75$), where the effects of the wall on the flow and, hence, the fluid friction effects are minimised. This maximum point moves towards the outer cylinder with decreases in Gr/Re.

Figure 4 Effects of Gr/Re on (a) entropy generation number and (b) Bejan number

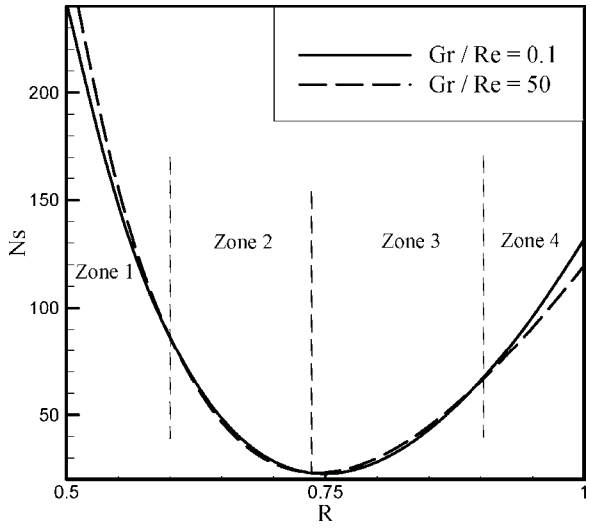

(a)

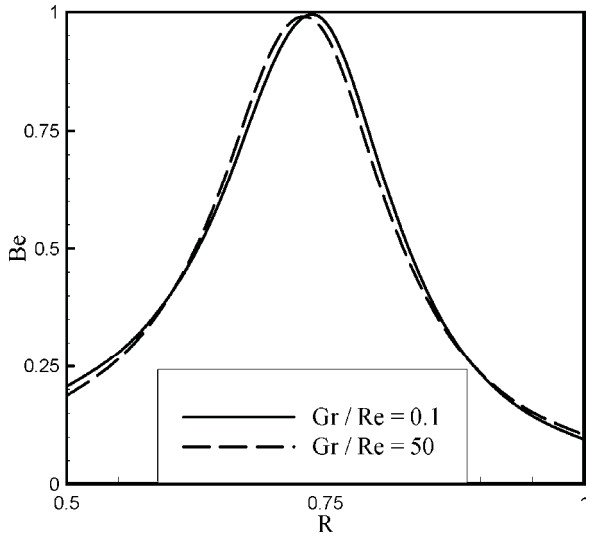

(b)

Figure 5 shows the variations of the entropy generation number and the Bejan number, with radius for $\partial P^*/\partial Z = -0.1$, Gr/Re = 1, and different values of Ω/Br. As expected, entropy generation increases with an increase in Ω/Br. As seen, the entropy generation is the highest on the inner cylinder because of the maximum gradients of velocity and temperature at this point. The profiles of N_s are not symmetric in the annulus due to buoyancy forces.

The effects of Ω/Br on the Bejan number are shown in Figure 5(b). It is seen that an increase in Ω/Br leads to considerable changes in the Bejan number near the walls, while it has no significant effect on the Bejan number in the centreline.

Figure 5 Effects of Ω/Br on the (a) entropy generation number and (b) Bejan number

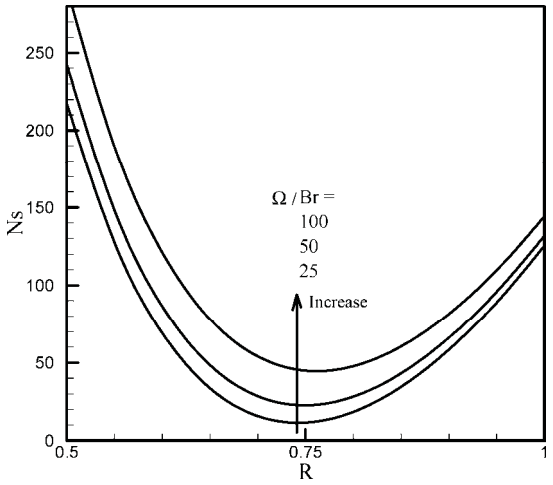

(a)

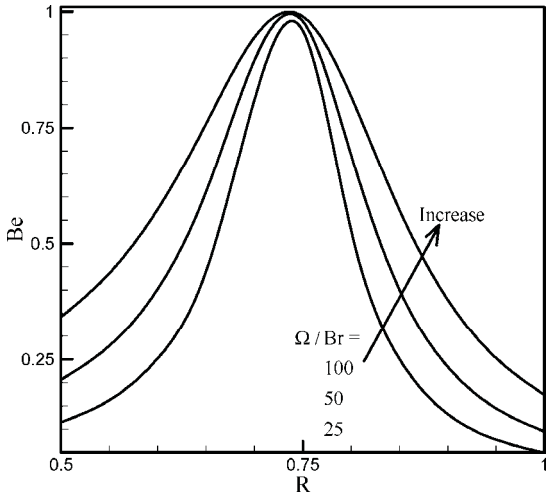

(b)

Figure 6 shows the total cost due to irreversibilities $\dot{C}(\$/\text{day})$, for $r_c = 1$, 10, and 20, $\partial P^*/\partial Z = -0.1$, Gr/Re = 1, and the radius ratio ($\Pi = 1/\lambda$) between 1.5 and 6. It is observed that for $\Pi < 2$, an increase in the parameter r_c results in a considerable change in the total cost. This happens because, in small radius ratios, the irreversibilities increase remarkably in the gap. It is found that for $\Pi = 1.5$ and $r_c = 20$, the total costs in one day exceeds \$10.

Figure 6 Total cost due to irreversibilities for different radius ratios and cost ratios

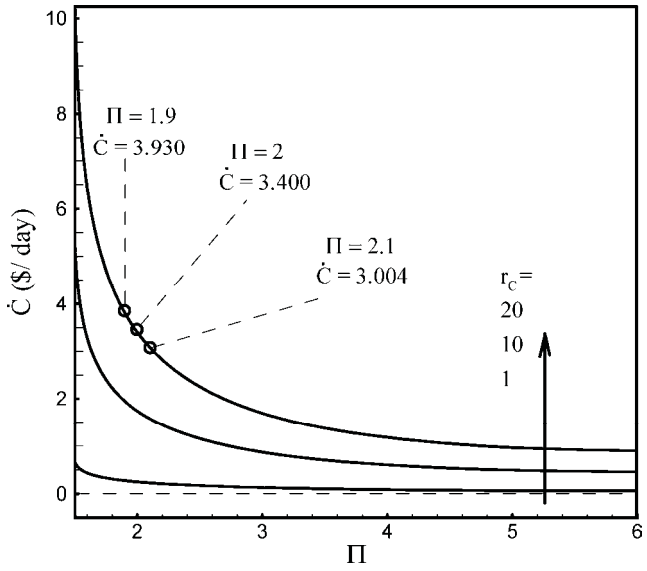

Now, consider a radius ratio of 2 as the base ratio in the design. The aim is to investigate the effect of a small deviation from the base radius ratio on the total costs.

For this purpose, two radius ratios, including $\Pi = 1.9$ and $\Pi = 2.1$, are considered. It is found that if the annulus is manufactured with a radius ratio of 2.1, the total cost drops by nearly 12%, while for $\Pi = 1.9$ the total cost increases by approximately 16%. This shows that the importance of producing an exact design for improving the savings in energy costs.

From another point of view, assume that the radius ratio is reduced from 2 to 1.9 due to fouling in the heat exchanger. By cleaning the heat exchanger and removing the fouling, one can realise a savings of 16% in energy costs.

Figure 7 shows the effects of Ω/Br on the total cost due to entropy generation for $r_c = 10$. The parameter of Ω/Br represents the ratio of the thermal effects to viscosity effects in the annulus. Indeed, by increasing the heat flux at the boundary of the inner cylinder, the parameter of Ω/Br increases. It is observed that when the radius ratio is nearly between 2 and 3, the effects of Ω/Br on the total cost is more visible than the effect of other radius ratios.

Figure 7 Total cost due to irreversibilities for different radius ratios and parameter Ω/Br

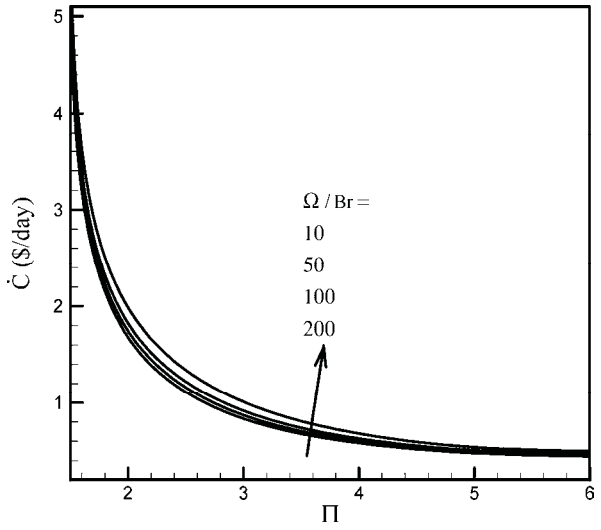

6 Conclusion

In this paper, a thermoeconomic analysis of a heat exchanger was performed to estimate the total costs due to entropy generation for the flow of a refrigerant inside the heat exchanger. The governing equations are simplified and solved analytically to find the distribution of velocity and temperature, and consequently to determine the entropy generation in the heat exchanger, where the walls of the annulus are subjected to a constant heat flux. From the distribution of entropy generation in the annulus, it was found that in the cases investigated the parameter Gr/Re has no considerable effect on entropy generation. Next, using the results of the entropy generation analysis, the total costs due to entropy generation were estimated for different values of the radius ratio. For a base radius ratio of 2, it was concluded that when the radius ratio decreases from 2 to 1.9 (e.g., due to fouling), the total costs increase by 16%. In this work, the aim is only the study of costs due to entropy generation. For the future works, the cost of pipe in different radius ratios can be considered.

Acknowledgements

The first author would like to thank the Thailand Research Fund and the National Research University Project for support. The support provided by the Deanship of Scientific Research at King Fahd University of Petroleum and Minerals (KFUPM) under Research Grant IN090031 is also acknowledged. The fourth author would like to thank the Thailand Research Fund, National Science And Technology Development Agency, and the National Research University Project for support.

References

Ahmadi, P., Enadi, N., Avval, H.B. and Dincer, I. (2012) 'Modelling and exergoeconomic optimisation of a gas turbine with absorption chiller using evolutionary algorithm', *Int. J. Exergy*, Vol. 11, pp.1–18.

Anandan, S.S. and Bhaskaran, A. (2012) 'Thermo-economic analysis of heat pipe heat exchanger for waste heat recovery in thermal systems', *Int. J. Exergy*, Vol. 11, pp.35–51.

Askar, S., Fartaj, A., Dasgupta, E.S. and Quayium, A. (2012) 'Second law analysis of a multiport serpentine micro-channel slab heat exchanger', *Int. J. Exergy*, Vol. 11, pp.379–399.

Aydin, H., Turan, O., Midilli, A. and Karakoc, T.H. (2012) 'Exergetic and exergo-economic analysis of a turboprop engine: a case study for CT7-9C', *Int. J. Exergy*, Vol. 11, pp.69–88.

Aziz, A. and Khan, W.A. (2012a) 'Entropy generation in an asymmetrically cooled hollow sphere with temperature dependent internal heat generation', *Int. J. Exergy*, Vol. 10, pp.110–123.

Aziz, A. and Khan, W.A. (2012b) 'Minimum entropy generation design of a convectively heated pin fin with tip heat loss', *Int. J. Exergy*, Vol. 10, pp.44–60.

Bejan, A. (1982) 'Second-law analysis in heat transfer and thermal design', *Adv. Heat Transfer*, Vol. 15, pp.1–58.

Ghazi, M., Sotoodeh, A.F. and Amidpour, M. (2012) 'Modelling and optimisation of a water-ethanol distillation column based on exergoeconomic analysis', *Int. J. Exergy*, Vol. 11, pp.173–190.

Kumar, S.V., Minkowycz, W.J. and Patel, K.S. (1989) 'Thermodynamic cycle simulation of the diesel cycle: exergy as a second law analysis parameter', *Int. Commun. Heat Mass Transfer*, Vol. 16, pp.335–346.

Mahian, O., Mahmud, S. and Pop, I. (2012c) 'Analysis of first and second laws of thermodynamics between two isothermal cylinders with relative rotation in the presence of MHD flow', *Int. J. Heat Mass Transfer*, Vol. 55, pp.4808–4816.

Mahian, O., Mahmud, S. and Wongwises, S. (2013) 'Entropy generation between two rotating cylinders with magnetohydrodynamic flow using nanofluids', *Journal of Thermophysics and Heat Transfer*, Vol. 27, No. 1, pp.161–169.

Mahian, O., Mahmud, S. and Zeinali Heris, S. (2012a) 'Analysis of entropy generation between co-rotating cylinders using nanofluids', *Energy*, Vol. 44, pp.438–446.

Mahian, O., Mahmud, S. and Zeinali Heris, S. (2012b) 'Effect of uncertainties in physical properties on entropy generation between two rotating cylinders with nanofluids', *ASME-Journal of Heat Transfer*, Vol. 134, p.101704.

Mahmud, S. and Fraser, R.A. (2002a) 'Irreversibility analysis of concentrically rotating annuli', *Int. Commun. Heat Mass Transfer*, Vol. 29, pp.697–706.

Mahmud, S. and Fraser, R.A. (2002b) 'Second law analysis of heat transfer and fluid flow inside a cylindrical annular space', *Int. J. Exergy*, Vol. 2, pp.322–329.

Mahmud, S. and Fraser, R.A. (2002c) 'Analysis of mixed convection – radiation interaction in a vertical channel: entropy generation', *Exergy, An International Journal*, Vol. 2, pp.330–339.

Mahmud, S. and Fraser, R.A. (2003a) 'Analysis of entropy generation inside concentric cylindrical annuli with relative rotation', *Int. J. Thermal Sci.*, Vol. 42, pp.513–521.

Mahmud, S. and Fraser, R.A. (2003b) 'Mixed convection–radiation interaction in a vertical porous channel: Entropy generation', *Energy*, Vol. 28, pp.1557–1577.

Makinde, O.D. (2102) 'Entropy analysis for MHD boundary layer flow and heat transfer over a flat plate with a convective surface boundary condition', *Int. J. Exergy*, Vol. 10, pp.142–154.

Matawala, V.K. and Prabhakaran, P. (2012) 'Exergoeconomic optimisation of steam power plant', *Int. J. Exergy*, Vol. 11, pp.209–227.

Mirzazadeh, M., Shafaei, A. and Rashidi, F. (2008) 'Entropy analysis for non-linear viscoelastic fluid in concentric rotating cylinders', *Int. J. Thermal Sci.*, Vol. 47, pp.1701–1711.

Ramos-Alvarado, B., Hernandez-Guerrero, A. and Rangel-Hernandez, V.H. (2012) 'Irreversibilities reduction of a flow distribution system by means of the EGM methodology', *Int. J. Exergy*, Vol. 10, pp.94–109.

Sahin, A.Z. (2012) 'Critical insulation thickness for maximum entropy generation', *Int. J. Exergy*, Vol. 10, pp.34–43.

Sahin, A.Z., Zubair, S.M., Al-Garni, A.Z. and Kahraman, R. (2000) 'Effect of fouling on operational cost in pipe flow due to entropy generation', *Energy Conversion & Management*, Vo. 41, pp.1485–1496.

Tasnim, S.H. and Mahmud, S. (2002a) 'Entropy generation in a vertical concentric channel with temperature dependent viscosity', *Int. Commun. Heat Mass Transfer*, Vol. 29, pp.907–918.

Tasnim, S.H. and Mahmud, S. (2002b) 'Mixed convection and entropy generation in a vertical annular space', *Int. J. Exergy*, Vol. 2, pp.373–379.

Tasnim, S.H., Mahmud, S. and Mamun, M.A.H. (2002) 'Entropy generation in a porous channel with hydromagnetic effect', *Exergy, An International Journal*, Vo. 2, pp.300–308.

Wu, S.Y., Chen, S.M., Xiao, L. and Li, Y.R. (2012) 'Extended exergo-economic performance evaluation criteria for enhanced heat transfer duct with constant wall heat flux', *Int. J. Exergy*, Vol. 11, pp.89–111.

Yilbas, B.S. (2001) 'Entropy analysis of concentric annuli with rotating outer cylinder', *Int. J. Exergy*, Vol. 1, pp.60–66.

Website

http://en.wikipedia.org/wiki/Electricity_pricing (Accessed 29 September, 2012).

Nomenclature

Be	Bejan number, Be = N_H/N_S
Br	Brinkman number, BR = $U_0^2\mu / k\Delta T$
C	Constant of integration in energy equation
C_H	Unit cost of irreversibility due to heat transfer ($/W h)
C_F	Unit cost of irreversibility due to fluid friction ($/W h)
$\dot{C}$	Total cost of irreversibility ($/hr)
g	gravity (m^2/s)
Gr	Grashof number, Gr = $g\beta\Delta T r_o^3 / \upsilon^2$
K	Thermal conductivity (W/ mK)
L	Axial length of annulus (m)
$\dot{m}$	Mass flow rate (kg/s)
N_F	Entropy generation number, fluid friction
N_H	Entropy generation number, heat transfer
N_S	Entropy generation number, $N_S = \dot{S}'''_{\text{gen}} /(\mu U_0^2 / T_0 r_0^2)$
P	Pressure (Pa)
P^*	Dimensionless Pressure, $P^* = (P/U_0\mu)r_o$
R	Radius (m)

r_c	Cost ratio, $r_c = C_F/C_H$
R	Dimensionless radius, $R = r/r_o$
Re	Reynolds number, $\mathrm{Re} = U_0 r_o/\nu$
$\dot{S}'''_{\mathrm{gen}}$	Volumetric entropy generation rate ($\mathrm{W/m^3K}$)
$\dot{S}_{\mathrm{gen}}$	Total entropy generation rate (W/K)
T	Temperature (K)
T_0	Inlet temperature (K)
U	Dimensionless velocity, $U = V_z/U_0$
U_0	Inlet velocity (m/s)
V_z	Axial velocity (m/s)
Z	Dimensionless axial distance, $Z = z/r_o$
Greek symbols	
Γn	Constants, $n = 1, 2, \ldots$
μ	Dynamic viscosity (kg/m s)
β	Thermal expansion coefficient (1/K)
λ	Radius ratio, $\lambda = r_i/r_o$
Π	Inverse radius ratio, $\Pi = 1/\lambda$
θ	Dimensionless temperature, $\theta = (T - T_0)/(q_i r_o/k)$
ρ	Density ($\mathrm{kg/m^3}$)
Ω	Dimensionless temperature difference, $\Delta T/T_0$
Subscript	
i	Value at the inner cylinder
o	Value at the outer cylinder
H	Heat transfer
F	Fluid friction

Hindawi Publishing Corporation
Advances in Mechanical Engineering
Volume 2013, Article ID 256839, 2 pages
http://dx.doi.org/10.1155/2013/256839

Hindawi

Editorial

Two-Phase Flow and Heat Transfer Enhancement

Somchai Wongwises,[1] Afshin J. Ghajar,[2] Kwok-wing Chau,[3] Octavio García Valladares,[4] Balaram Kundu,[5] Ahmet Selim Dalkılıç,[6] and Godson Asirvatham Lazarus[7]

[1] *Fluid Mechanics, Thermal Engineering and Multiphase Flow Research Lab. (FUTURE), Department of Mechanical Engineering, Faculty of Engineering, King Mongkut's University of Technology Thonburi, Bangmod, Bangkok 10140, Thailand*
[2] *School of Mechanical and Aerospace Engineering, Oklahoma State University, Stillwater, OK 74078, USA*
[3] *Department of Civil & Environmental Engineering, The Hong Kong Polytechnic University Hunghom, Kowloon, Hong Kong*
[4] *Department of Energy Systems, Centro de Investigación en Energía, CIE-UNAM, Privada Xochicalco S/N, 62580 Temixco, MOR, Mexico*
[5] *Department of Mechanical Engineering, Jadavpur University, Kolkata 700032, India*
[6] *Heat and Thermodynamics Division, Department of Mechanical Engineering, Yildiz Technical University, Yildiz, 34349 Istanbul, Turkey*
[7] *Department of Mechanical Engineering, Karunya University, Coimbatore, Tamil Nadu 641 114, India*

Correspondence should be addressed to Somchai Wongwises; somchai.won@kmutt.ac.th

Received 2 December 2013; Accepted 2 December 2013

Copyright © 2013 Somchai Wongwises et al. This is an open access article distributed under the Creative Commons Attribution License, which permits unrestricted use, distribution, and reproduction in any medium, provided the original work is properly cited.

Gas-liquid two-phase flow and heat transfer processes are commonly encountered in a wide variety of applications, for example, refrigeration and air-conditioning systems, power engineering, and other thermal processing plants. The advantage of high thermal performance in comparison to the single-phase applications leads to various engineering applications including the cooling systems of various types of equipment such as high performance microelectronics, supercomputers, high-powered lasers, medical devices, high heat-flux compact heat exchangers in spacecraft and satellites, and so forth. The aim of this special issue was to collect the original research and review papers on the recent developments in the field of two-phase flow and heat transfer enhancement. Potential topics included advanced heat pipe technologies, boiling and condensation heat transfer, CHF and post-CHF heat transfer, cooling of electronic system, Heat and mass transfer in phase change processes, instabilities of two-phase flow, measurements and modeling of two-phase flow in microchannel, microgravity in two-phase flow, nanofluids science and technology, nuclear reactor applications, passive and active heat transfer enhancement techniques, Refrigeration and air-conditioning technology, two-phase flow with heat and mass transfer, two-phase refrigerant flow, and special topics on the latest advances in two-phase flow and heat transfer. In this special issue, we have invited a few papers that address such issues.

First paper of special issue investigates the effect of convergence angle of microchannel on two-phase flow and heat transfer during steam condensation experimentally. The experimental results show that the condensation heat flux increases with an increase in the convergence angle and/or the steam mass flux at a given coolant flow rate but decreases with an increase in the coolant flow rate at a given steam mass flux. Second paper focuses on simulating mist impingement cooling under typical gas turbine operating conditions of high temperature and pressure in a double chamber model. The results of this paper can provide guidance for corresponding experiments and serve as the qualification reference for future more complicated studies with convex surface cooling. In third paper, economic analysis of rebuilding an aged pulverized coal-fired boiler with a new pulverized coal-fired boiler including flue gas desulfurization unit and a circulating fluidized bed boiler is investigated in existing old thermal power plants. The fourth paper presents the results of a CFD analysis and experimental tests of two identical miniature flat plate heat pipes using sintered and screen

mesh wicks and a comparative analysis and measurement of two solid copper base plates 1 mm and 3 mm thick. In fifth paper, a modeled room was numerically heated from a wall and cooled from the opposite wall in order to create a real-room simulation. The cooled wall simulated heat loss of the room, and the heated wall simulated the heat source of enclosure. The effects of heated and cooled wall temperatures on convective heat transfer coefficient and Nusselt number in the enclosure were investigated numerically for two- and three-dimensional (3D) modeling states.

In summary, this special issue reflects a variety of contemporary research in heat transfer and is expected to promote further research activities and development opportunities.

Acknowledgment

We thank the authors who prepared the paper within the stringent length and time requirements. We thank the reviewers who provided meaningful suggestions on short notice.

Somchai Wongwises
Afshin J. Ghajar
Kwok-wing Chau
Octavio García Valladares
Balaram Kundu
Ahmet Selim Dalkılıç
Godson Asirvatham Lazarus

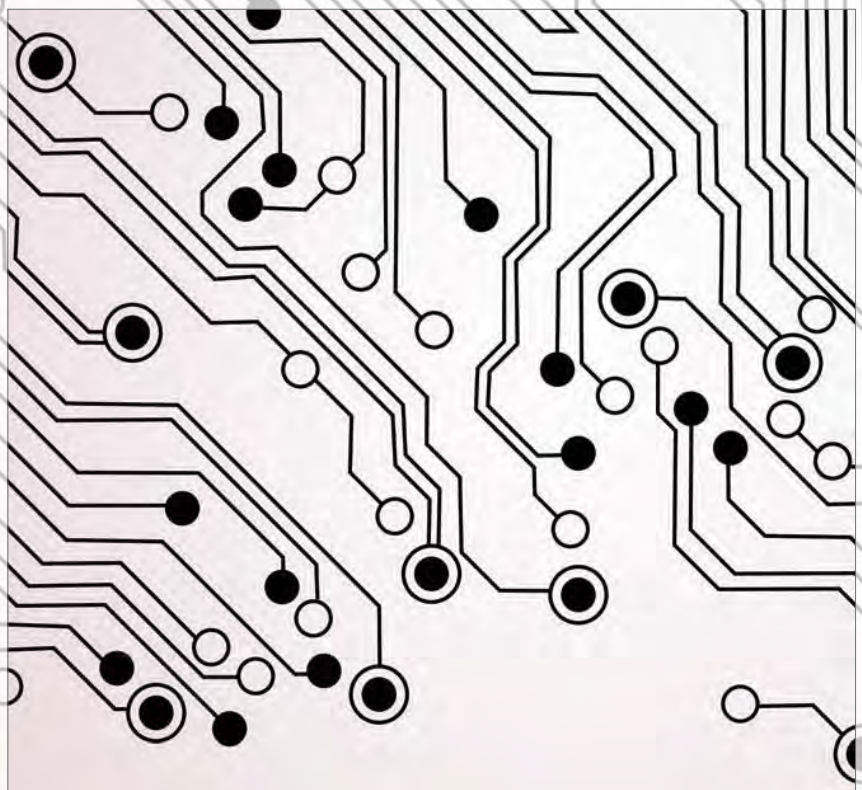

The Scientific World Journal

Hindawi Publishing Corporation
http://www.hindawi.com

Volume 2013

Hindawi

- Impact Factor **1.730**
- **28 Days** Fast Track Peer Review
- All Subject Areas of Science
- Submit at http://www.tswj.com

Renewable and Sustainable Energy Reviews 31 (2014) 312–318

Contents lists available at ScienceDirect

Renewable and Sustainable Energy Reviews

journal homepage: www.elsevier.com/locate/rser

Critical review of the current status of wind energy in Thailand

Sakkarin Chingulpitak, Somchai Wongwises *

Fluid Mechanics, Thermal Engineering and Multiphase Flow Research Lab. (FUTURE), Department of Mechanical Engineering, Faculty of Engineering, King Mongkut's University of Technology Thonburi, Bangmod, Bangkok 10140, Thailand

ARTICLE INFO

Article history:
Received 22 August 2012
Received in revised form
22 October 2013
Accepted 18 November 2013

Keywords:
Wind energy
Wind energy potential
Wind farm
Electricity
Renewable energy
Thailand

ABSTRACT

Thailand generates electricity from many sources, including natural gas, coal/lignite, fuel oil, diesel, and renewable energies, such as wind, hydroelectricity, and solar power. In 2012, the main electrical energy sources in Thailand were natural gas (63.8%) and coal/lignite (27.7%). Due to fuel price spikes and global warming, several countries are now more interested in studying and developing sources of renewable energy.

Wind energy – an unlimited and environmentally friendly form of natural energy – has attracted increasing levels of investment, particularly in China, which derives more of its electricity from wind energy generation than any other country in the world. Thailand has also developed and promoted the use of wind turbines to generate electricity. In 2012, Thailand generated about 111.7 MW of electricity from wind energy. By 2021, the Thai government's goals are to increase the use of alternative electric energy to about 25% of fossil fuel use and to achieve 1800 MW of electricity output from wind energy.

This article will present a critical review of the current status of wind energy in Thailand, including future plans for using wind energy in place of fossil fuels – oil, natural gas, and coal – to generate electricity.

© 2013 Elsevier Ltd. All rights reserved.

Contents

1. Background . . . 312
2. Energy and electricity situations in Thailand . . . 313
3. Wind energy potential in Thailand . . . 313
4. Current status of wind energy in Thailand. . . . 314
5. Thailand's wind energy policy . . . 316
6. Conclusions . . . 318
Acknowledgments . . . 318
References . . . 318

1. Background

For past several decades, energy has been an important, fundamental factor in daily life, business, and industry, including the transportation, manufacturing, and telecommunications sectors. For this reason, a reliable energy supply with sufficient quantity, good quality, and reasonable prices is vital. However, the unstable price of energy in the world market, especially the steadily increasing price of crude oil, has had a serious effect on the economies of several countries, particularly those that must import significant quantities of oil. Furthermore, the use of fossil fuels also contributes to the problem of global warming. As a result, several countries have supported the use of renewable energy to promote energy security and environmental conservation. In 2012, China increased its wind-powered electricity generation and had the highest rate of wind-powered energy generation in the world. Thailand has also developed and promoted wind turbines to generate electricity because it is clean, eco-friendly, and cost-effective.

Abbreviations: AEDP, alternative energy development plan; GWh, gigawatt hour; GRP, glass-reinforced plastic; DEDE, department of alternative energy development and efficiency; EGAT, electricity generating authority of Thailand; EIA, environmental impact assessment; EPPO, energy policy and planning office; ktoe, kilotons of oil equivalent; kWh, kilowatt hour; PDP, Thailand power development plan; PEA, provincial electricity authority; SPPs and VSPPs, small and very small power producers, respectively; US$, US dollar (31.245 baht/US dollar foreign exchange rate, as of 13 August 2013)

* Corresponding author. Tel.: +66 2470 9115; fax: +66 2470 9111.
E-mail address: somchai.won@kmutt.ac.th (S. Wongwises).

1364-0321/$ - see front matter © 2013 Elsevier Ltd. All rights reserved.
http://dx.doi.org/10.1016/j.rser.2013.11.038

This paper presents the current status of electricity generation and the proportion of electricity generated from renewable resources, especially wind energy. Wind energy potential is investigated and compared to other countries in Southeast Asia, including its obstacles to development and promotion, as well as future plans to use wind energy in Thailand.

2. Energy and electricity situations in Thailand

The final energy consumption of Thailand in 2012 was about 73,316 ktoe [1], an increase of 13% [2] from 2007. The total value of the final energy consumption was US$57,545.21 million. As shown in Fig. 1, petroleum products, renewable energy, electricity, coal/lignite, and natural gas represented 48.0%, 18.2%, 18.9%, 7.9%, and 7.0% of the total final energy consumption in 2012, respectively.

Considering the trends in primary energy supply (excluding energy exports) and final energy consumption from 2007 to 2012, as revealed in Fig. 2, it is observed that the primary energy supply

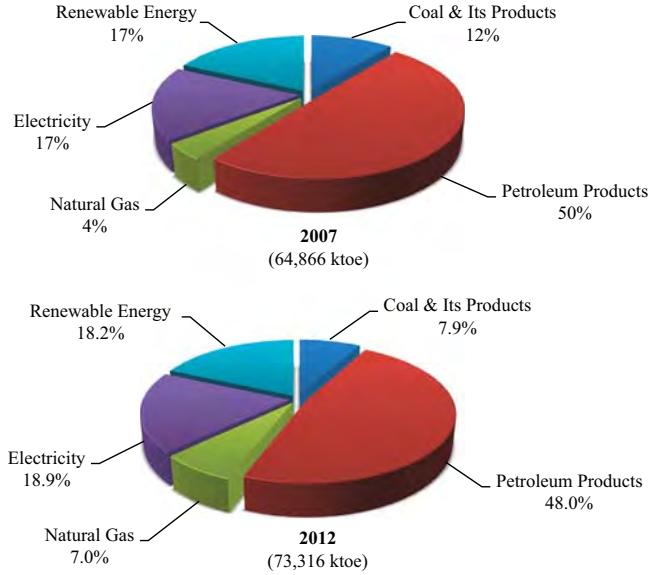

Fig. 1. Final energy consumption by types of Thailand for years 2007 [data from [2]] and 2012 [data from [1]].

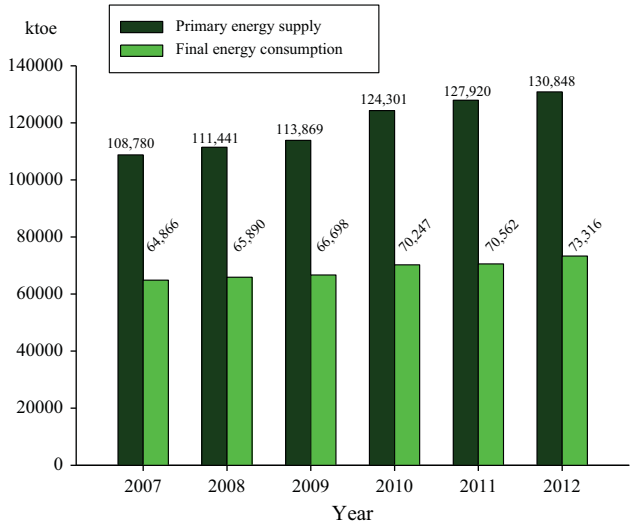

Fig. 2. Primary energy supply and final energy consumption from year 2007 until 2012 [data from [1] and [2]].

increases year-by-year. In 2012, the amount of primary energy supplies was 130,848 ktoe [1]. For primary energy supplies classified by energy type, the highest share, which contributed 82.8% of the total primary energy supply, was from commercial energy (crude oil, lignite, natural gas, and so on), followed by renewable energy, biofuels (ethanol and biodiesel), and other forms of energy (black liquor and residual gas), at 16.2%, 0.8%, and 0.2%, respectively.

Thailand's electricity consumption was 162,668 GWh [1] in 2012. Most of this electrical energy, equal to 82,068 GWh, was consumed by the industrial sector. The commercial sector (including government, non-profit organizations, and street lighting), residential sector, agricultural sector, transportation sector, and other sectors (temporary customers) used 47,210 GWh, 32,097 GWh, 70 GWh, and 930 GWh, respectively.

Table 1 shows electricity generation, installation capacity, consumption, and electricity generation by energy source from 2007 to 2012, according to Thailand Energy Statistics 2012 [1] and 2007 [3]. There is a trend towards increased electricity generation every year. Thailand's electricity consumption in 2010 increased 10.4% from that of 2009, whereas it decreased by 0.4% in 2011, due to severe flooding by that year end. In 2012, Thailand's total electricity generation was 168,471 GWh [1], of which 63.8% was generated by natural gas, followed by coal/lignite (27.7%), and fuel oil and diesel (1.6%), with the balance being renewable energy and other types of energy (6.9%). From Table 1, it is clear that use of natural gas and renewable energy are increasing slightly. On the other hand, use of fuel oil for electricity generation has decreased significantly, due to an unexpected increase in oil prices; thus, promoting alternative energy to replace oil is necessary, especially alternative energy that can be produced in Thailand, such as biomass, biogas, solar energy, hydro energy, wind energy, garbage reclamation, and natural gas.

According to the CIA World Factbook, which lists all countries by electricity consumption, China had the highest electricity consumption, of 4,693,000 GWh [4], followed by the United States, the European Union, Japan, and Russia. Thailand's electricity consumption is rated twenty-fifth in the world and is the highest in Southeast Asia.

3. Wind energy potential in Thailand

Thailand is located near the equator and has low to moderate wind speeds that average about 3–5 m/s. A study of wind energy potential in Thailand began in 1975, when the Department of Energy Affairs of the National Energy Policy Office made a map of wind speed for use in planning, design, and installation of wind turbines. Average wind-speed data were supplied by the Thai Meteorological Department. Field studies then surveyed, measured, collected, and analyzed the wind-speed data. However, since there were several restrictions in making a map of wind-speed potential, the data are only available for low elevations.

In 2001, the map of wind-speed potential in Thailand was improved to include higher-elevation wind data in the analysis. The suitable areas that were selected have average wind speeds of not less than Class 3: 6.4–7.0 m/s or 300–400 kW/m^2 at an elevation of 50 m [5]. The existing data indicate that the coastal area of the Thai Gulf has the best wind energy potential in Thailand, followed by the upper southern region around the western coast of the Thai Gulf, which has an average annual wind speed of 4.4 m/s at an elevation of 50 m, as shown in Table 2 and Fig. 3.

In the same year, the World Bank proposed a wind energy resource atlas report for four countries in Southeast Asia: Cambodia, Laos, Thailand, and Vietnam [6]. As shown in Tables 3 and 4, the report uses simulations based on global winds to demonstrate which areas are best for the development of wind energy. Table 3

Table 1
Electricity generation, installation and consumption, and electricity generation by energy sources [data from [1] and [3]].

	2007	2008	2009	2010	2011	2012
Electric generation (GWh)[a]	143,378	147,427	148,390	159,518	155,986	168,471
Installed capacity (MW)[a]	28,285	30,508	30,607	31,485	31,773	33,177
Electric consumption (GWh)[a]	133,178	135,449	135,209	149,320	148,700	162,668
National grid generation (GWh)[a,b]	128,819	132,781	133,458	144,362	138,247	–
Natural gas	88,166	94,549	97,595	109,454	98,128	–
Coal and lignite	28,716	29,480	28,020	28,207	29,642	–
Hydro	8114	7113	7148	5537	8163	–
Fuel oil	3646	1454	604	997	1986	–
Diesel oil	174	180	79	159	319	–
Other[c]	3	5	12	8	9	–

[a] Excluding private generation for own use.
[b] Excluding generation from small and very small power producers (SPPs and VSPPs) generated from renewable and conventional energy.
[c] Including geothermal, solar cell and wind turbine, etc.

Table 2
Good wind energy sites from a map of wind energy potential [data from [5]].

Area	Province	Wind power classes	Height of 50 m	
			Wind speed (m/s)	Wind power (W/m^2)
1 Tai Rom Yen national park	Nakhon Sri Thammarat	6–7	8.00–11.90	600–2000
2 Khao Luang national park	Nakhon Sri Thammarat	6–7	8.00–11.90	600–2000
3 Khao Pu – Khao Ya national park	Pattalung	6–7	8.00–11.90	600–2000
4 Wang Chao national park	Tak	6	8.00–8.80	600–800
5 Doi Intanon national park	Chiang Mai	4	7.00–7.50	400–500
6 Kaeng Krung national park	Surat Thani	4–5	7.00–7.50	400–600
7 Khao Phanom Bencha	Krabi	6	8.00–8.80	600–800
8 Ranod district	Songkhla	4	7.00–7.50	400–500
9 Songkhla Lake	Songkhla	5–6	7.50–8.00	500–700
10 Laem Tachee	Pattani	4	7.00–7.50	400–500
11 Hua Sai district	Nakhon Sri Thammarat	3	6.40–7.00	300–400

presents the percentages of rural population in the areas of each country where small wind turbines can be used at 30 m. This was estimated by determining the number of villages and towns located within each wind resource class. The data show that more than 30% of the rural population of Vietnam live in areas with good wind resources, whereas only 13%, 9%, and 5% of the rural populations of Laos, Thailand and Cambodia, respectively, live in favorable areas. For large wind turbines, Table 4 shows the land area in each country and total wind energy potential based on each wind speed class at 65 m. It is clear that Vietnam has the opportunity to develop large-scale wind turbines because of its large resource potential, followed by Thailand, due to its moderate resource potential and well-developed energy infrastructure.

In 2008, wind measurement stations were set up in six provinces along the coast of Southern Thailand: Surat thani, Nakhon Si Thammarat, Songkhla, Krabi, Trang, and Satun. Sensors for measuring wind speed and direction were installed at heights of 20, 30, and 40 m [7]. During 2008, the wind statistics that were recorded were used to estimate wind speed at heights of 80, 90, and 100 m. Moreover, the observed wind climate was analyzed for the prediction of 15 km wind resources around the wind station by using WAsP 9.0, the Wind Atlas Analysis and Application Program. The results showed that the average annual wind speeds at heights of 80, 90, and 100 m were between 3.4 and 9.5 m/s. From economic analysis based on very small power producers (VSPP), the study found that wind farm power plants installing wind turbine generators (WTGs) of 1.0, 1.5, and 2.0 MW can generate about 1018, 1038, and 1148 MW of electricity from wind energy, respectively, in the long term.

To measure the potential of wind energy in the upper northern region [8], the wind speed and direction were measured and recorded at heights of 20, 30, and 40 m at Rompothai, Phatung, Norlae, Nonghoi, Monlan, and Killom stations from April 2007 to June 2009. Over the same period, wind speed and direction were recorded at heights of 20, 30, and 80 m at the Maehae station. The wind data recorded were analyzed with WAsP 9.1 to evaluate the potential for electricity generation. In the case of a potential wind farm using a 1 MW wind turbine at a height of 80 m, the total installed capacity of the wind turbines is 68 MW, or around 160 GWh/yr. Moreover, the results of the site survey showed that the suitable areas – Killom, Monlan, and Maehae – were ready to install wind farms with capacities of 1 MW and 3 MW (total capacities of 9 MW and 27 MW), which can produce approximately 18.7 and 44.9 GWh/yr of electricity, respectively.

4. Current status of wind energy in Thailand

Wind-powered electricity generation around the world has increased every year since 1996. In 2012, the global production of wind energy totaled 282,587 MW [9], an increase of 44,799 MW, or 19%, over 2011. Most of the increase occurred in the United States, which accounted for 29.3% of the global increase in wind-powered energy generation. As a result, China had the highest wind-powered energy generation (75,324 MW), followed by the United States (60,007 MW) and Germany (31,308 MW).

Wind-powered energy generation in Thailand began in 1983, when the electricity generating authority of Thailand (EGAT) installed six sets of small turbines for a pilot project at Laem Phromthep in Phuket Province. In 1992, EGAT installed two more turbines with a total capacity of 10 kW. After that, both government and private agencies – particularly educational institutions –

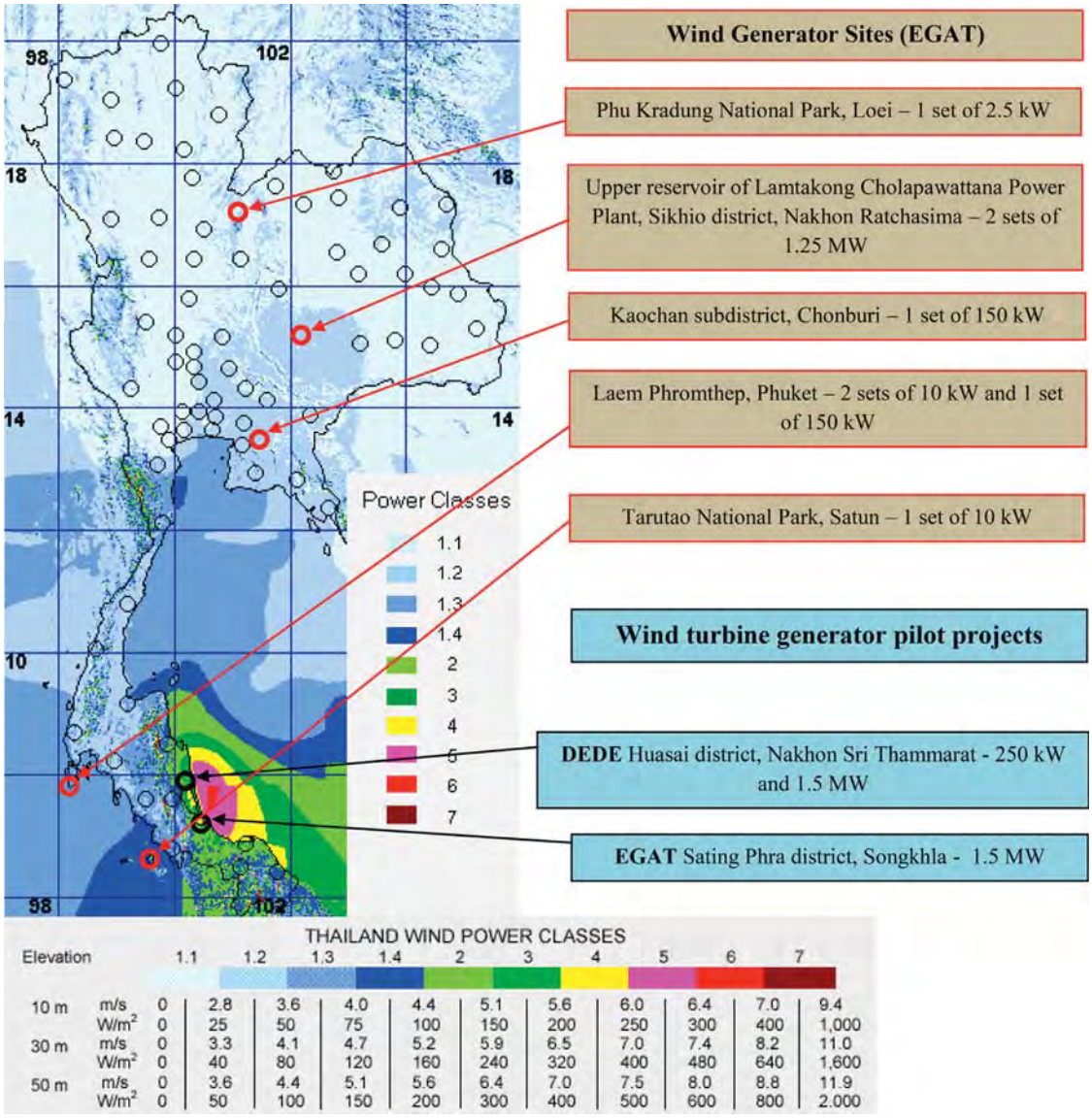

Fig. 3. Map of wind power potential in calm wind conditions – annual average [data and map from [5]].

Table 3
Proportion of rural population in each small wind turbine resource class[a] [data from [6]].

Country	*Poor (%) (< 4 m/s)*	*Fair (%) (4–5 m/s)*	*Good (%) (5–6 m/s)*	*Very good (%) (6–7 m/s)*	*Excellent (%) (> 7 m/s)*
Cambodia	15	79	5	1	0
Laos	55	32	13	0	0
Thailand	26	64	9	0	0
Vietnam	29	31	34	6	1

[a] Wind speeds are for cleared or open land with no obstructions at 30 m height. The proportion of rural population is estimated from the number of towns and villages in each wind resource class from the VMAP database (the US National Imagery and Mapping Agency Vector Map).

paid more attention to the study of wind energy for electricity generation. In 1996, King Mongkut's University of Technology/Thonburi was the first to install 2.5 kW and 10 kW wind turbines at Phu Kradueng National Park, in Loei Province, and Tarutao National Park, in Satun Province, respectively. In the same year, the Recycle Engineering Company Limited installed one 150 kW wind turbine at Koh Chan Sub-district in Chonburi Province to generate electricity for use in buildings. As for government agencies, under the aegis of the Ministry of Energy, the Department of alternative energy development and efficiency (DEDE) installed one 250 kW turbine and one 1.5 MW turbine for electricity generation at Hua Sai District in Nakhon Si Thammarat Province in 2007 and 2009 [10], respectively.

The wind turbines were installed in 2009 by EGAT and connected to the electricity distribution system of the Provincial Electricity Authority (PEA). Two sets of 1.25 MW wind turbines – with a total capacity of 2.5 MW, which became the first large, wind-powered generation plant in Thailand – were installed at the upper reservoir of Lamtakong Cholapawattana Power Plant in Khlongphai Sub-district, Sikhio District, Nakhon Ratchasima [11]. The wind turbines that were used are Chinese-made D6-1250 models, which are three-blade horizontal-axis wind turbines with a pole height of 68 m and a blade diameter of 64 m. The blades are made of glass-reinforced plastic (GRP). The wind turbines turn automatically at wind speeds of 2.8 m/s or greater. The highest wind speed for electricity generation is 12.5 m/s. The turbines stop working when the wind speed reaches 23 m/s and stop generating electricity when the wind speed reaches 50.5 m/s [12].

Later, the provincial electricity authority (PEA) conducted a project to demonstrate the electricity generation from one 1.5 MW

Table 4
Wind energy potential of Southeast Asia at 65 m[a] [data from [6]].

Country	*Characteristic*	*Poor* (< 6 *m/s*)	*Fair* (*6–7 m/s*)	*Good* (*7–8 m/s*)	*Very good* (*8–9 m/s*)	*Excellent* (> 9 *m/s*)
Cambodia	Land area (sq km)	175,468	6155	315	30	0
	% of Total land area	96.4	3.4	0.2	0.0	0.0
	MW potential	NA	24,620	1260	120	0
Laos	Land area (sq km)	184,511	38,787	6070	671	35
	% of Total land area	80.2	16.9	2.6	0.3	0.0
	MW Potential	NA	155,148	24,280	2684	140
Thailand	Land area (sq km)	477,157	37,337	748	13	0
	% of Total land area	92.6	7.2	0.2	0.0	0.0
	MW potential	NA	149,348	2992	52	0
Vietnam	Land area (sq km)	197,342	100,361	25,679	2187	113
	% of Total land area	60.6	30.8	7.9	0.7	0.0
	MW potential	NA	401444	102716	8748	452

[a] Wind speeds are for 65 m height in the predominant land cover with no obstructions. For large wind turbines only. Potential MW estimates an average wind turbine density of 4 MW/km^2 and no exclusions for parks, urban, or inaccessible areas.

turbine at Sating Phra District in Songkhla Province [11]. The wind turbine used was a Chinese-made YFKF01-500/4 model and has the highest productivity in Thailand. The turbine has a horizontal axis driven by an asynchronous generator gear box, with a pole height of 80 m and a blade diameter of 77 m. Its three blades are made of GRP, with a total weight of 160 t. The turbine begins generating electricity at a wind speed of 3 m/s and reaches its maximum productivity at a wind speed of 11.5 m/s. The turbine can resist a maximum wind speed of 21 m/s [13].

The locations of the wind power plants in Thailand described above are shown in Fig. 3. It includes private generation for personal use, educational institutions, and commercial operations. However, in 2013, an updated map for the locations of wind power plants in Thailand was proposed [14], as shown in Fig. 4. It only presents the locations of wind power plants that generate electricity and supply it to the grid system, with a total capacity of 186 MW. The information of wind power plants that are being added are shown below.

The wind power plant “Chang-Hua-Mun” is located in Chang-Hua-Mun Royal Initiative Project, at Khao Krapuk Sub-district, Tha Yang District in Phetchaburi Province. His Majesty the King graciously observed that the landscape of the project area was suitable for the installation of wind turbines [15]. He graciously granted funds for the installation of 205 kW wind turbines (with a total capacity of 100 kW). The electricity used for the project was distributed to residents in the project area. Moreover, it was fed into the grid system of the Provincial Electricity Authority in 2009, with a capacity of 50 kW [15].

Later, the provincial electricity authority (PEA) installed one 250 kW wind turbine at Ko Tao, Ko Pha-ngan District in Surat Thani Province. A data collection and analysis during 2003 that assessed the wind energy potential found average wind speeds of 5.53 m/s. The wind turbine used is a Pioneer Wincon P250/29 model with a total capacity of 250 kW, or 10% of Ko Tao Island's total power consumption. The turbine (three blades) has a horizontal axis with a hub height 50 m and a blade length of 13.4 m. The turbine begins generating electricity at a wind speed of 3 m/s and cuts out at a wind speed of 25 m/s [16].

The “First Korat Wind” and “K.R. Two” projects for wind power generation were established by Wind Energy Holding Co., Ltd. at Huay Bong Sub-district, Dan Khun Tod District, Nakorn Ratchasima province in 2012 and 2013, respectively. The average wind speeds for both projects' areas are 6.2 m/s. In each project, 45 2.3 MW wind turbines (with a total capacity 90 MW) were installed, with a height of 99.5 m and a blade diameter of 101 m. These projects are the first large-scale wind farms in Thailand and have the highest capacity in Southeast Asia. Moreover, they are supported by governmental adder subsidies of about US$0.11/kWh over 10 yr [17].

5. Thailand's wind energy policy

Regarding the promotion and support for the use of renewable energy to generate electricity, the energy policy and planning office (EPPO) specified adder subsidies for several types of renewable energy. Therefore, small and very small power producers (SPPs and VSPPs) can sell their electricity to the electricity generating authority of Thailand (EGAT) or the provincial electricity authority (PEA) at higher-than-normal prices. Wind energy received adder subsidies of about US$0.08–0.11/kWh. The three southern provinces (Yala, Pattani, and Narathiwat) have special adder subsidies of US$0.16/kWh. This adder support lasts 10 yr, starting from the effective date of the contract [18–20].

Regarding the long-term 10-yr alternative energy development plan (AEDP 2012–2021), the Ministry of Energy aims to increase the ratio of alternative energy use to 25% [21] by 2021. Under this policy, renewable energy development projects will be initiated under the Thailand power development plan 2012–2030 (PDP2010: Revision 3) by the Energy Policy and Planning Office (EPPO). Therefore, in 2030, electricity generation from renewable energy will be 20,546.3 MW, or 29% of total electricity generation. Renewable energy sources can be classified into domestic renewable energy and renewable energy from neighboring countries, at 13,688 MW and 6,858 MW [22], respectively. Wind-powered electricity generation will be increased to a productivity of over 1800 MW. In 2012, Thailand had a wind-powered electricity generation of around 111.7 MW [23], as shown in Table 5.

Obstacles to development and promotion of wind energy in Thailand are as follows:

(1) Areas with high wind-energy potential are often located in mountainous or reserved forest areas; thus, private organizations that intend to invest in wind turbines (of more than 1400 MW) often face problems in getting permission to use the area from related governmental agencies. However, this obstacle can be resolved between private organizations and governmental agencies by allowing the installation of wind

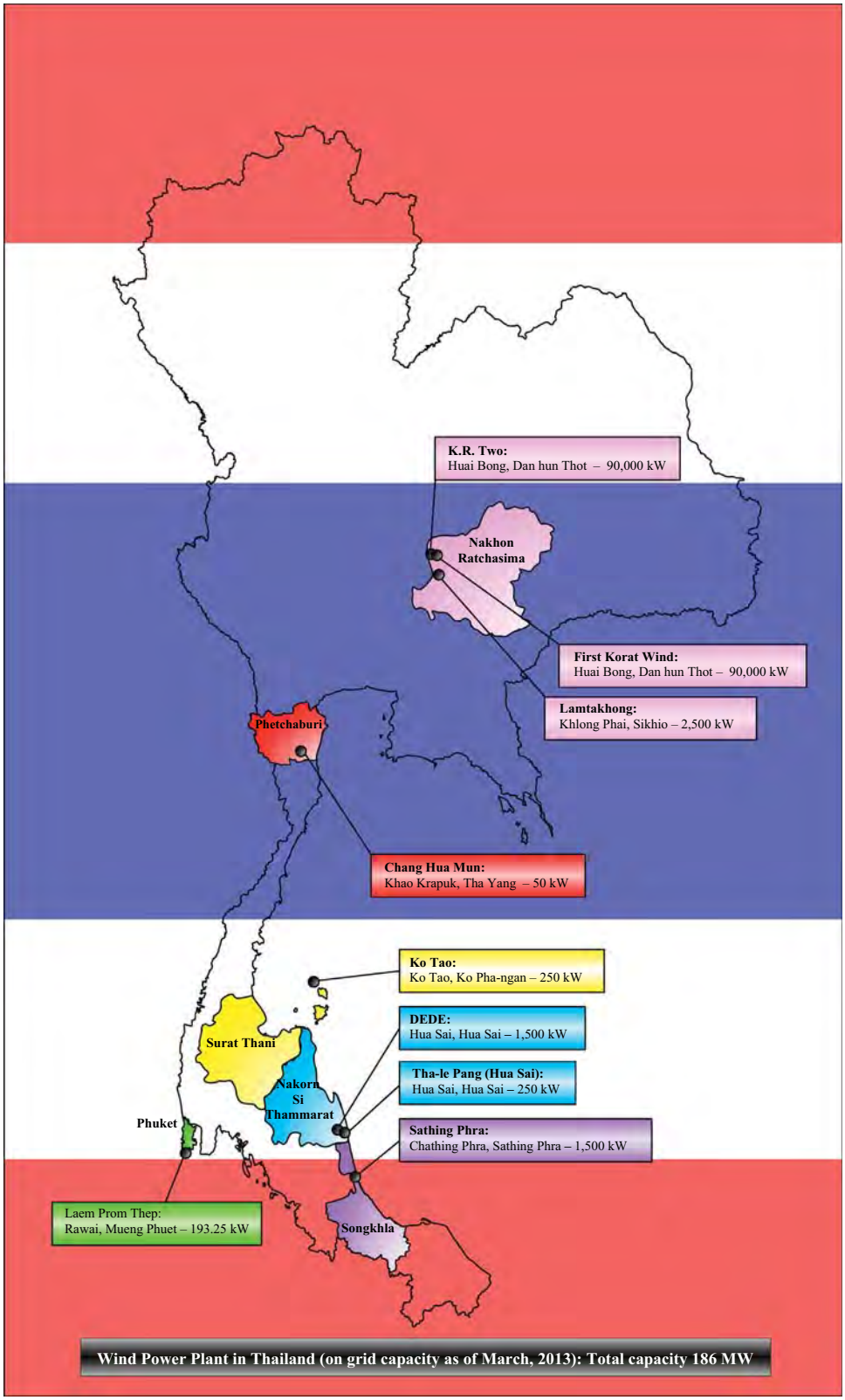

Fig. 4. Map of wind power plant in Thailand [data from [14]]

farms at rental rates of US$0.7/m^2/yr and project durations of no more than 27 yr [20].

(2) Some other problems are the cost of producing and installing wind turbines and the appropriateness of the site. There must be 22, 33, or 115 kV high-current electricity discharge systems within a 10 km radius of the area to connect with the electrical system of the provincial electricity authority (PEA). Because of this, the Thai government plans to improve its power

Table 5
Status and target for use of alternative energy in electricity generation [23].

Type of energy	Output in 2010 (MW)	Output in 2011 (MW)	Output in 2012 (MW)	Target in 2021 (MW)
Wind	*5.6*	*7.3*	*111.7*	*1800*
Solar	48.6	78.7	376.7	3000
Water	58.9	95.7	101.8	324
Biomass	1650.2	1790.2	1959.9	4800
Biogas	103.4	159.2	193.4	3600
Waste	13.1	25.5	42.7	400
New energy	–	–	–	3

infrastructure, including its grid and energy storage systems. In addition, the government has promoted the creation network of wind energy producers and users to facilitate wind energy connections in the future.

(3) There are also environmental problems, such as destruction of scenery, noise pollution, impact on creatures living within the installation area, and so on. To solve these problems, the environmental impact assessment (EIA) should be considered at the potentiality stage of a project.

6. Conclusions

Thailand's best wind-energy potential areas are around the coast of the Thai Gulf and higher-elevation lands, with average annual wind speeds of 6.4 m/s at an elevation of 50 m. Another potentially good area is around the western mountain ridgeline, from the lower northern to the upper southern part. The next-best potential areas, with average annual wind speeds of 4.4 m/s and higher at an elevation of 50 m, are the upper southern portion, the western coast of the Thai Gulf, the northern mountainous areas, the western coast of the south, and the eastern coast of the Thai Gulf.

Wind-powered electricity generation in Thailand has increased continuously in both the governmental and private sectors. In 2012, Thailand generated approximately 111.7 MW of electricity from wind energy. By 2021, Thailand aims to increase the ratio of wind energy use in electricity generation to a total productivity of 1800 MW, or 12.9% of all electricity generated from alternative energy in the country.

Acknowledgments

The authors are indebted to the Thailand Research Fund, the National Science and Technology Development Agency and the National Research University Project for supporting this study.

References

[1] Department of Alternative Energy Development and Efficiency. Ministry of energy, Thailand energy statistics (Preliminary), ⟨http://www.dede.go.th/dede/images/stories/stat_dede/report12/%202555_1.pdf⟩; 2012 [accessed 13.08.13].
[2] Department of Alternative Energy Development and Efficiency. Ministry of energy, Thailand energy statistics, ⟨http://www.dede.go.th/dede/images/stories/stat_dede/file_zip/Report%2011.rar⟩; 2011 [accessed 13.08.13].
[3] Department of Alternative Energy Development and Efficiency. Ministry of energy, electric power in Thailand: annual report, ⟨http://www.dede.go.th/dede/images/stories/stat_dede/electric54_1.pdf⟩; 2011 [accessed 13.08.13].
[4] Central Intelligence Agency (CIA). The World factbook, ⟨https://www.cia.gov/library/publications/the-world-factbook/rankorder/2042rank.html⟩ [accessed 18.04.12].
[5] Department of Energy Affairs. Wind resource assessment of Thailand, final report, central press, Thailand, ⟨http://www2.dede.go.th/dede/renew/Twm/MAIN.htm⟩; 2001 [accessed 19.08.13].
[6] The World Bank Asia Alternative Energy Program. Wind energy resource atlas of Southeast Asia; September 2001.
[7] Waewsak J, Kongruang C, Tirawanichakul Y, Tirawanichakul S, Matan N, Prompat C, et al. The potential of wind power along the coasts of southern Thailand. J Natl Res Counc Thail 2009:51–60 (Special Issue: 50th Anniversary).
[8] Dussadee N, Sasujit K, Suwannasit N, Kangvankij S, Suankamgong A, Kiatsiriroat T. Study on potential of power generation from wind energy in upper northern region. J Natl Res Counc Thail 2009:61–70 (Special Issue: 50th Anniversary).
[9] Global Wind Energy Council. Global wind report: annual market update, ⟨http://www.gwec.net/wp-content/uploads/2012/06/Annual_report_2012_LowRes.pdf⟩; 2012 [accessed 13.08.13].
[10] Ministry of Energy. Thai energy vision, public relations office; 2006. p. 214–31.
[11] Electricity Generating Authority of Thailand. EGAT and wind energy development for electricity generation, ⟨http://www3.egat.co.th/re/egat_wind/egat_wind.htm⟩ [accessed 17.08.13].
[12] Electricity Generating Authority of Thailand. Wind generator at Lamtakhong, Sikhio district, NakhonRatchasima, ⟨http://www3.egat.co.th/re/egat_wind/egat_windlamtakhong/wind_lamtakhong.htm⟩ [accessed 17.08.13].
[13] Sriwelaiwat T. The biggest wind turbine in Thailand, ⟨http://www.oknation.net/blog/nn1234/2010/06/04/entry-1⟩; September 28, 2009 [accessed 17.08.13].
[14] Department of Alternative Energy Development and Efficiency. Ministry of energy, map of wind power plant in Thailand, ⟨http://weben.dede.go.th/webmax/content/map-wind-power-plant-thailand⟩ [accessed 13.08.13].
[15] Provincial Electricity Authority. Electricity production from wind power project of "Chang-Hua-Mun" Royal Initiative Project, ⟨http://peas1.pea.co.th/bangsaphan/images/stories/PDF/wind%20power.pdf⟩ [accessed 23.08.13].
[16] Kitworawut P, Vathananukij H. Wind power: evolution Technology from the past to presence and futurity, ⟨http://gis.eng.ku.ac.th/Research/paper_wind%20energy.pdf⟩ [accessed 26.08.13].
[17] Wind Energy Holding Co., LTD. West Huay Bong 2 and West Huay Bong 3 Wind Farm projects, ⟨http://www.windenergyholding.co.th⟩ [accessed 23.08.13].
[18] Prapakdi S. Wind generator: environmental perspective. J Environ 2009;13:42–8.
[19] Energy Conservation Promotion Fund. Energy conservation plan and guidelines, criteria, conditions and priority of expense, ⟨http://www.eppo.go.th/encon/plan-2551-2554/encon-2551-2554.pdf⟩ [accessed 26.08.13].
[20] Ruangrong P. Thailand's approach to promoting clean energy in the electricity sector. Forum on clean energy, good governance and regulation: Singapore, ⟨http://electricitygovernance.wri.org/files/egi/Thailand.pdf⟩; 16–18 March 2008 [accessed 26.08.13].
[21] Department of Alternative Energy Development and Efficiency. Ministry of energy, the renewable and alternative energy plan for 25 percent in 10 years (AEDP 2012–2021), ⟨http://www.dede.go.th/dede/images/stories/dede_aedp_2012_2021.pdf⟩ [accessed 23.08.13].
[22] Energy Policy and Planning Office. Ministry of energy, summary of Thailand power development plan 2012–2030 (PDP2010: REVISION 3, June 2012), ⟨http://www.egat.co.th/en/images/about-egat/PDP2010-Rev3-Eng.pdf⟩ [accessed 20.08.13].
[23] Department of Alternative Energy Development and Efficiency. Ministry of energy, Thailand alternative energy situation, ⟨http://www.dede.go.th/dede/images/stories/stat_dede/Alternative_1012/thailand%20alternative%20energy%20situation%202012.pdf⟩; 2012 [accessed 20.08.13].

Selection of the most suitable refrigerant for a shell and tube condenser

A. S. Dalkilic, O. Mahian & S. Wongwises

Heat and Mass Transfer
Wärme- und Stoffübertragung

ISSN 0947-7411
Volume 50
Number 2

Heat Mass Transfer (2014) 50:183-197
DOI 10.1007/s00231-013-1235-7

Springer

Your article is protected by copyright and all rights are held exclusively by Springer-Verlag Berlin Heidelberg. This e-offprint is for personal use only and shall not be self-archived in electronic repositories. If you wish to self-archive your article, please use the accepted manuscript version for posting on your own website. You may further deposit the accepted manuscript version in any repository, provided it is only made publicly available 12 months after official publication or later and provided acknowledgement is given to the original source of publication and a link is inserted to the published article on Springer's website. The link must be accompanied by the following text: "The final publication is available at link.springer.com".

Author's personal copy

Heat Mass Transfer (2014) 50:183–197
DOI 10.1007/s00231-013-1235-7

ORIGINAL

Selection of the most suitable refrigerant for a shell and tube condenser

A. S. Dalkilic · O. Mahian · S. Wongwises

Received: 1 March 2012 / Accepted: 17 September 2013 / Published online: 6 October 2013
© Springer-Verlag Berlin Heidelberg 2013

Abstract A theoretical performance study on a shell and tube condenser with various refrigerant blends was conducted for various ratios proposed by other researchers in the literature. The theoretical results showed that all of the alternative refrigerants investigated in the analysis have a slightly lower convective heat transfer coefficient than their base refrigerants. The refrigerant mixture of R290/R600, R152a/R125/R32 and R32/R134a were found to be the most proper replacement refrigerant among the alternatives.

List of symbols

A	Inside surface area, m^2
CFC	Chlorofluorocarbon
d	Diameter, m
f	Friction factor
F	Correction factor
G	Mass flux, kg $m^{-2}s^{-1}$
GWP	Global warming potential
h	Convective heat transfer coefficient, W $m^{-2}K^{-1}$
HC	Hydrocarbon
HCFC	Hydrochlorofluorocarbon
L	Tube length, m
LMTD	Logarithmic mean temperature difference
m	Flow rate, kg s^{-1}
N	Number of tubes
ODP	Ozone depleting potential
R	Tube radius, m
P	Pitch, m
R	Resistance, $m^2K\ W^{-1}$
Q	Heat rejection duty, kW
U	Overall heat transfer coefficient, W $m^{-2}K^{-1}$
U_∞	Water flow velocity, m s^{-1}
Δh	Enthalpy of phase change, kJ kg^{-1}
ΔP	Pressure drop, Pa
ΔT_m	Mean temperature difference

Greek symbols

ρ	Density, kg m^{-3}
υ	Specific volume, $m^3\ kg^{-1}$
ν	Kinematic viscosity, $m^2\ s^{-1}$
η_p	Pump efficiency

Subscripts

c	Cold
c	Clean
cs	Cold surface
D	Dirty
F	Fouling
g	Gas
h	Hot
i	Inside
l	Liquid
o	Outside
m	Mean
p	Pass

A. S. Dalkilic (✉)
Heat and Thermodynamics Division, Department of Mechanical Engineering, Mechanical Engineering Faculty, Yildiz Technical University, Yildiz, Besiktas, 34349 Istanbul, Turkey
e-mail: dalkilic@yildiz.edu.tr

O. Mahian
Young Researchers and Elite Club, Mashhad Branch, Islamic Azad University, Mashhad, Iran

S. Wongwises
Fluid Mechanics, Thermal Engineering and Multiphase Flow Research Lab. (FUTURE), Department of Mechanical Engineering, Faculty of Engineering, King Mongkut's University of Technology Thonburi, Bangmod, Bangkok 10140, Thailand

Author's personal copy

r Return
s Shell
sat Saturation
T Total
t Tube
w Water

1 Introduction

Not only has the significance of heat exchangers increased from the perspective of energy recovery, conservation, conversion, and successful implementation of new energy sources in recent decades but its significance is also increasing from the angle of environmental issues such as the contamination of air, water, and waste removal. Heat exchangers are used in the process, power, transportation, air-conditioning and refrigeration, cryogenic, heat recovery, alternate fuels, and manufacturing industries, besides being main aspects of numerous industrial goods that are available in the marketplace. Many publications exist regarding the improvement of heat exchangers in the literature due to their importance in industry and our actual lives. On the contrary, this paper was motivated by the fact that few of the studies available seem to provide detailed analyses with respect to the use of alternative refrigerants in condensers and their selection in terms of cost and economy.

Heat exchangers can be classified according to their transfer processes, number of fluids, heat transfer mechanisms, construction types, flow arrangements, and heat transfer surface area/volume ratio. In this paper, the analyses include a useful sample design procedure for a shell and tube condenser, which is one of the indirect-contact heat exchangers used in the power industry (surface condenser and feed water heater) and the process industry [E, G, H, J, and X shells and total condensation applications (reflux and knockback)].

The latest agreements have reduced and will finally eliminate the production and usage of chlorofluorocarbons (CFCs) and hydrochlorofluorocarbons (HCFCs) in the market. At this stage, the discovery of new refrigerants is needed as a solution to the problems of global warming (GWP) and ozone depletion (ODP). The refrigerant mixtures are used as alternative replacements in the systems. These mixtures may be azeotropic, near-azeotropic, or zeotropic (non-azeotropic). Azeotropic refrigerants act similarly to a single component (pure fluid) under constant pressure and condense and evaporate at a constant temperature, and the composition of the blend will be identical in the vapor and liquid phases. Azeotropic blends have been commonly used in refrigeration, and some of their popular mixtures used in place of R22 are R502, a mixture of R22 and R152a; and R410A, a mixture of R32 and R125. Near-azeotropic blends have slight temperature variations during phase change and a small alteration in the composition in the liquid and vapor phases at equilibrium. The aim of their occurrence is to use a refrigerant alternative beyond pure fluids and azeotropic blends. The mixture of a small amount of R290 to R502 is a sample that was developed to enhance R502's solubility in lubricating oil. Zeotropic blends undergo an important variation in temperature during condensation and evaporation, and the compositions of the vapor and liquid phases are different at the equilibrium state. R407C, a mixture of R32, R125, and R134a, is a common example. Table 1 lists most of the well-known theoretical and experimental refrigerant mixture studies [1–48] in the literature from 1975 to 2011. The development of blends from the past to today and the prediction of new blends to be used in the near future can be evaluated clearly based on this table.

2 Calculations of the design procedure for the investigated shell and tube condenser

In the case studies, refrigerants were evaporated at −10 °C and condensed at various temperatures with the heat of condensation rejected to cooling water taken from a small cooling tower at 25 °C. A shell and tube construction with 1, 2, and 4 pass designs (N_p) on the water side was used in the simulation studies. Copper tubes with inside/outside diameters of 0.012573/0.01588 m (d_i/d_d) were selected due to their compatibility with the refrigerants. The design procedures of a condenser for a 91.92 kW (Q_c) refrigerating system are given in the following section.

2.1 Tube-side calculations

The bulk temperature of water is calculated from Eq. (1) to determine the physical properties:

$$T_{bulk} = \frac{(T_{c1} + T_{c2})}{2} \tag{1}$$

The cold-side flow area is determined as follows:

$$A_{cs} = \frac{\pi d_i^2}{2} \tag{2}$$

The flow velocity of water (U_∞) is varied from 1 to 3 m s^{-1}; thus, the mass flux is determined from Eq. (3):

$$G = \rho_w U_\infty = \frac{U_\infty}{\upsilon_w} \tag{3}$$

The cooling water flow rate per tube is calculated as follows:

Author's personal copy

Table 1 Literature review on the evaluation of refrigerant mixtures

Researcher	Proposed mixture refrigerant
Lorenz and Meutzner [1]	R22-R11 (50/50 by wt %)
Stoecker [2]	R12/R114 (70/30 by wt %)
Stoecker and Walukas [3]	R12-R114 (50/50 by wt %)
Mishra et al. [4]	R12/R22 (23/77 by wt %)
	R12/R22 (27/73 by wt %)
	R12/R22 (41/59 by wt %)
	R12/R22 (48/52 by wt %)
Singal et al. [5]	R13/R12 (5/95 by wt %)
	R13/R12 (10/90 by wt %)
	R13/R12 (15/80 by wt %)
	R13/R12 (20/85 by wt %)
Kruse and Hesse [6]	R22/R114 (60/40 by wt %)
Kuijpers et al. [7]	R600a/R290 (79/21 by wt %)
Jung et al. [8]	R22/Rl14 (23/71 by wt %)
	R22/R114 (48/52 by wt %)
	R22/R114 (77/23 by wt %)
	Rl2/R152a (21/79 by wt %)
	R12/R152a (88/12 by wt %)
Koyama et al. [9]	R22/R114 (52/48 by wt %)
Kedzierski and Didion [10]	R22/R114 (37.7/62.3 mol %)
Rivis and Bedone [11]	R290/R600a (50/50 and 60/40 by wt %)
Kim et al. [12]	R290/R134a (45/55 by wt %)
	R134a/R600a (80/20 by wt %)
Nozu et al. [13]	R114/R113 (23/36 by wt %)
Richardson and Butterworth [14]	R290/R600 (48/52 by wt %)
	R290/R600a (50/50 by wt %)
Sami and Song [15]	R-32/R-125/R-143a/R-l34a (40/25/25/10 by wt. %)
Doongso et al. [16]	R290/R600a (20/80 by wt %)
	R290/R600a (30/70 by wt %)
	R290/R600a (40/60 by wt %)
	R290/R600a (50/50 by wt %)
	R290/R600a (60/40 by wt %)
Shin et al. [17]	R32/R134a (25/75 by wt %)
	R32/R134a (50/50 by wt %)
	R32/R134a (75/25 by wt %)
	R290/R600a (25/75 by wt %)
	R290/R600a (50/50 by wt %)
	R290/R600a (75/25 by wt %)
	R32/R125 (50/50 by wt %).
Alsaad and Hammad [18]	R290/R600/R600a (24.4/56.4/17.2 by wt. %)
Shao and Granryd [19]	R32/R134a (26.5/73.5 by wt %)
Baskin [20]	R600a/R290 (60/40 by wt %)
	R600a/R290 (70/30 by wt %)

Table 1 continued

Researcher	Proposed mixture refrigerant
Hammad and Alsaad [21]	R290/R600/R600a (50/38.3/11.7 by wt %)
	R290/R600/R600a (75/19.1/5.9 by wt %)
	R290/R600/R600a (25/57/17.5 by wt %)
Jung et al. [22]	R290/R600a (60/40 by wt %)
Miyara et al. [23]	R134a/R123 (50/50 by wt %–R410A)
Chang et al. [24]	R290/R600a (50/50 by wt %)
Choi et al. [25]	R32/R125/R134a (23/25/52 by wt %–R407C)
Tashtoush et al. [26]	R600/R290/R134a (35.71/35.71/28.58 by wt %)
	R600/R290/R134a (31.25/31.25/37.5 by wt %)
	R600/R290/R134a (27.78/27.78/44.44 by wt %)
	R600/R290/R134a (25/25/50 by wt %)
	R600/R290/R134a (22.73/22.73/54.54 by wt %)
Akash and Said [27]	R290/R600/R600a (30/55/15 by wt %–LPG)
Wongwises and Chimres [28]	R290/R600 (60/40 by wt %)
	R290/R600/R600a (70/25/5 by wt %)
	R290/R600/R600a (50/40/10 by wt %)
	R290/R600a (60/40 by wt %)
	R290/R600/R134a (40/30/0/30 by wt %)
	R290/R600a/R134a (40/30/30 by wt %)
Wen and Ho [29]	R290/R600 (55/45 by wt %)
Koyoma et al. [30]	CO_2/RE170 (90/10 by wt %)
Wen et al. [31]	R600/R290 (50/50 by wt %)
Han et al. [32]	R32/R125/R134a (23/25/52 by wt %–R407C)
	R32/R125/R161 (15/34/51 by wt %)
Park et al. [33]	R1270/R290 (20/80 by wt %)
	R1270/R290 (50/50 by wt %)
	R1270/R290 (80/20 by wt %)
	R290/R152a (60/40 by wt %)
	R290/R152a (71/29 by wt %)
	R290/R152a (75/25 by wt %)
Afroz et al. [34]	CO_2/RE170 (39/61 by wt %)
	CO_2/RE170 (21/79 by wt %)
Xue et al. [35]	CO_2/RE170 (95/5 by wt %)
	CO_2/RE170 (90/10 by wt %)
Chen and Yu [36]	R32/R134a (30/70 by wt %)
Lee et al. [37]	R290/R600a (55/45 by wt %)

Author's personal copy

Table 1 continued

Researcher	Proposed mixture refrigerant
Mani and Selladurai [38]	R290/R600a (68/32 by wt %)
Kim et al. [39]	CO_2/R290 (75/25by wt %)
Wu et al. [40]	R152a/R125/R32 (48/18/34 by wt %)
Onaka et al. [41]	CO_2/RE170 (10/90 by wt %)
	CO_2/RE170 (25/75 by wt %)
Park and Jung [42]	R170/R290 (2/98 by wt %)
	R170/R290 (4/96 by wt %)
	R170/R290 (6/94 by wt %)
	R170/R290 (8/92 by wt %)
	R170/R290 (10/90 by wt %)
Cho et al. [43]	CO_2/R290 (75/25 by wt %)
	CO_2/R290 (50/50 by wt %)
	CO_2/R290 (25/75 by wt %)
Zou et al. [44]	R170/R290 (30/70 by wt %)
Dalkilic and Wongwises [45]	R290/R600 (50/50 by wt %)
	R290/R600 (60/40 by wt %)
	R290/R600 (70/30 by wt %)
	R290/R600 (80/20 by wt %)
	R290/R600a (40/60 by wt %)
Dalkilic and Wongwises [45] (cont.)	R290/R600a (50/50 by wt %)
	R290/R600a (60/40 by wt %)
	R290/R600a (70/30 by wt %)
	R290/R1270 (20/80 by wt %)
	R290/R1270 (50/50 by wt %)
	R290/R1270 (60/40 by wt %)
	R290/R1270 (80/20 by wt %)
	R290/R152a (60/40 by wt %)
	R290/R152a (70/30 by wt %)
	R290/R152a (80/20 by wt %)
	R32/R134a (30/70 by wt %)
Kabul et al. [46]	R125/R134a/R143a (44/4/52)
Yoon et al. [47]	R290/R600 (40/60 by wt %)
Grauso et al. [48]	CO_2/R290 (83.2/16.8 by wt %)
	CO_2/R290 (70/30 by wt %)

$$\dot{m}_t = GA_{cs} \tag{4}$$

The coolant flow rate ($\dot{m}_c$) is obtained from the heat rejection duty (Q_c) as follows:

$$Q_c = \dot{m}_c \, \Delta h_c \tag{5}$$

The number of tubes (N_t) is determined from Eq. (6). It should be noted that the rounding process may be applied to the number of tubes according to its calculated value.

$$\dot{m}_c = \dot{m}_t N_t / N_p \tag{6}$$

The Reynolds number of water inside the tubes is shown in Eq. (7). Its value was over 10,000 for all working conditions, so the flow is determined to be turbulent. Eq. (8) was proposed by Gnielinski's [49] correlation for turbulent flow conditions as the Nusselt number and used in the analyses.

$$Re_l = \frac{Gd_i}{\mu_w}. \tag{7}$$

$$Nu = \frac{(f/2)(Re_l - 1000)\,Pr_l}{1 + 12.7(f/2)^{1/2}(Pr_l^{2/3} - 1)} \tag{8}$$

where the Fanning friction factor is expressed as follows:

$$f = [1.58 \ln(Re_l) - 3.28]^{-2} \tag{9}$$

The heat transfer coefficient of water (h_i) is obtained from the Nusselt number:

$$Nu = \frac{h_i d_i}{k_l} \tag{10}$$

The Nusselt number increases with increasing Reynolds numbers, in other words, the convective heat transfer coefficient of water increases with the increasing in-tube fluid velocity due to the increase in heat transfer. The Fanning friction factor decreases with increasing mass flux. The increase in mass flux will increase the fluid velocity and flow turbulence. This will enable both high heat transfer performance and high pressure drop.

2.2 Shell-side condensing calculations

The bulk temperature of the refrigerant can be assumed to be equal to the refrigerant's condensing temperature to determine the physical properties.

The refrigerant flow rate (m_R) is determined from the heat balance for the coolant and refrigerant:

$$Q_c = Q_R \tag{11}$$

$$m_c \Delta h_c = m_R \Delta h_R \tag{12}$$

The shell-side condensing heat transfer coefficient was proposed by Dhir and Lienhard [50] and modified with the coefficient of N by Incropera and DeWitt [51] and calculated from Eq. (13) as follows:

$$h_o = 0.729 \left[\frac{g(\rho_l - \rho_g)\rho_l \Delta h_g k_l^3}{\mu_l \Delta T N d_o} \right]^{1/4} \tag{13}$$

where the number of tubes in the vertical direction (N) in Eq. (13) is determined by the arrangement as shown in Figs. 1 and 2 for the staggered (square) and line (triangular) pitches. The temperature difference (ΔT) is found from Eq. (14), and it should be noted that the wall temperature (T_{wall}) is assumed and tested during further calculations in this section.

Author's personal copy

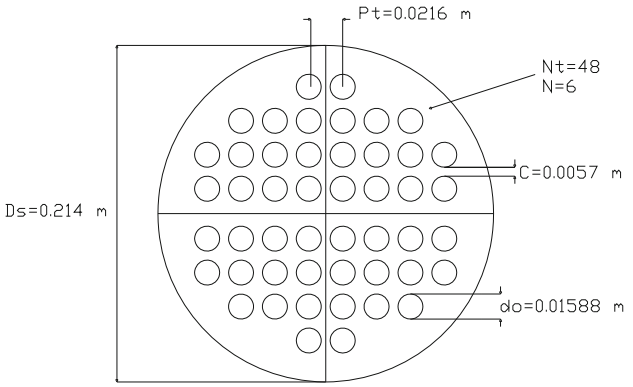

(a) Staggered pitch

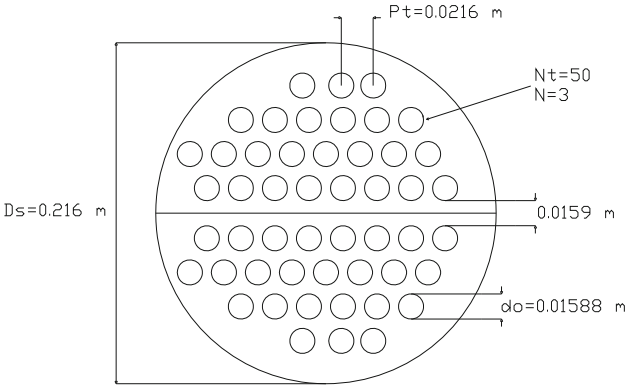

(b) Line pitch

Fig. 1 Tube configuration for two pass shell and tube condenser *plotted* with 1/25 scale in mm

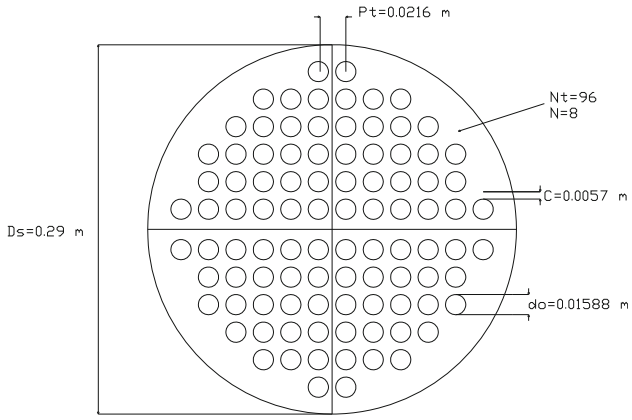

(a) Staggered pitch

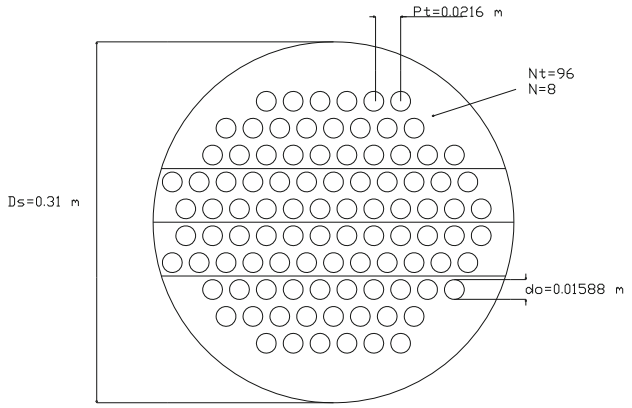

(b) Line pitch

Fig. 2 Tube configurations for four-pass shell and tube condenser *plotted* with 1/25 scale in mm

$$\Delta T = (T_{sat} - T_{wall}) \tag{14}$$

2.3 Dimensions of the condenser

The overall heat transfer coefficient is determined from Eq. (15) for the condition of being either clean or dirty. R_{fi} and R_{fo} should be omitted for clean tubes.

$$U_{oD} = \left[\frac{r_o}{h_i r_i} + \frac{r_o R_{fi}}{r_i} + \frac{r_o \ln(r_o/r_i)}{k_t} + R_{fo} + \frac{1}{h_o}\right]^{-1} \tag{15}$$

The logarithmic mean temperature difference (LMTD) and the mean temperature difference (ΔT_m) are calculated as follows:

$$LMTD = \frac{\Delta T_1 - \Delta T_2}{\ln \frac{\Delta T_1}{\Delta T_2}} = \frac{(T_h - T_{c1}) - (T_h - T_{c2})}{\ln \frac{(T_h - T_{c1})}{(T_h - T_{c2})}} \tag{16}$$

$$\Delta T_m = LMTDxF \tag{17}$$

where the correction factor (F) is 1 for a condenser.

The heat transfer surface area of the condenser (A_o) is calculated from the heat transfer rate in Eq. (18) as:

$$Q_c = U_o A_o \Delta T_m \tag{18}$$

where the tube length is obtained from Eq. (19). It should be calculated separately for either clean or dirty tubes or staggered or line pitches.

$$A_o = N_t \pi d_o L \tag{19}$$

The shell diameter (d_s) is estimated assuming $C_a = 1.1$, $C_L = 1$, and $PR = P_t/d_t$ in Eq. (20). It should be also checked by the tube arrangement figures as shown in Figs. 1 and 2.

$$d_s = C_a \sqrt{(C_L/2.5)(A/L)(PR)^2 d_t} \tag{20}$$

The temperature difference (ΔT) in Eq. (14) is also recalculated from Eq. (21). The same value of ΔT should be obtained for staggered or line pitches separately, including clean and dirty tubes, by means of a trial and error method using a computer program.

Author's personal copy

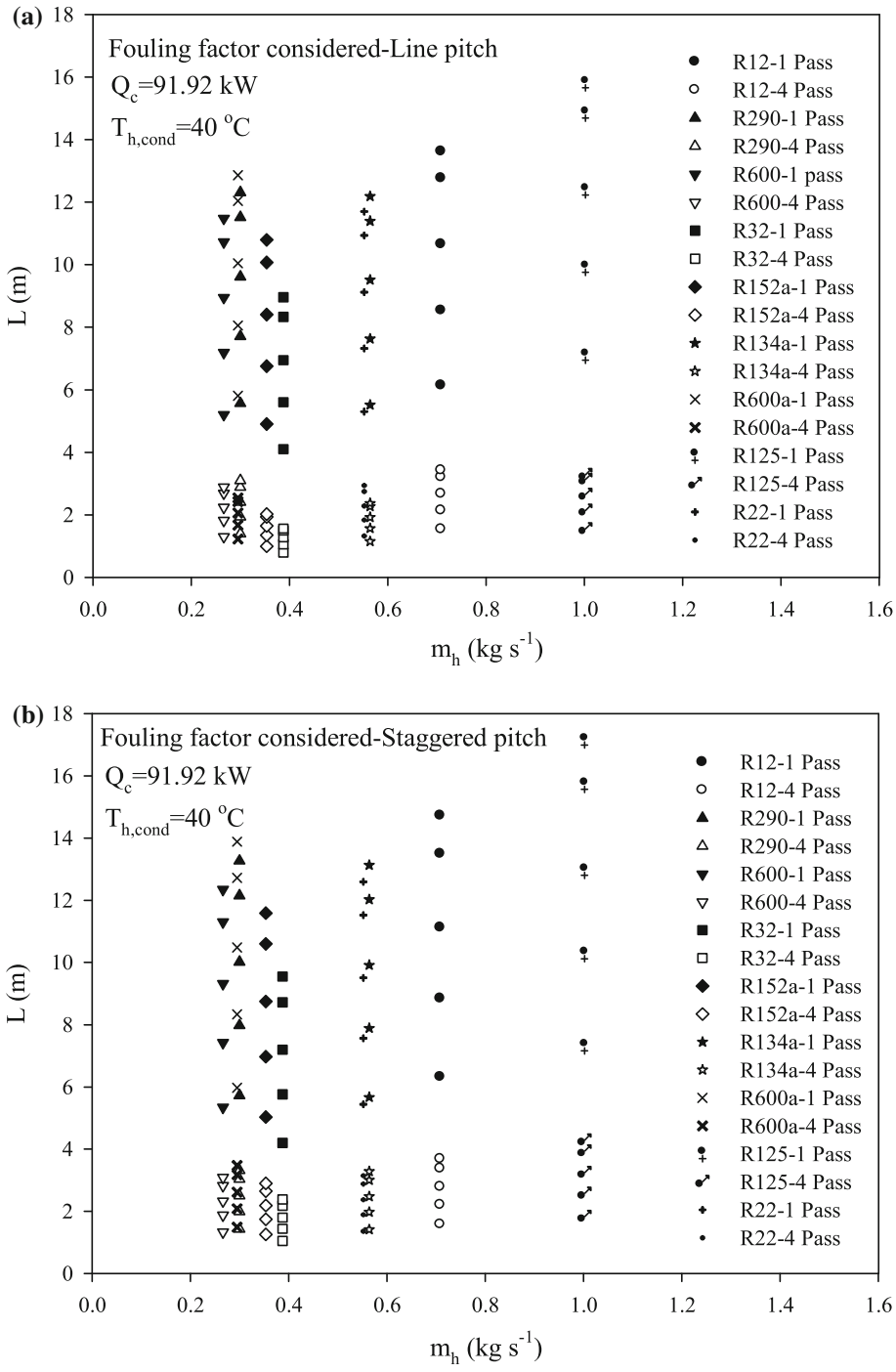

Fig. 3 Tube lengths versus refrigerant flow rates

$$q = \frac{Q_c}{A_o} = h_o(T_s - T_{w2}) = h_o \Delta T \tag{21}$$

2.4 Water-side pressure drop

The water-side pressure drop for all the tubes is determined from Eq. (22) as follows:

$$\Delta P_t = \frac{4fLN_pG^2 v_l}{2d_i} \tag{22}$$

where the friction factor is defined in Eq. (9) for the turbulent flow conditions in the tubes.

The fluid has an extra loss because of sudden expansions and contractions during a return [52].

Author's personal copy

Table 2 A case study for the conditions of $d_i = 12.57$ mm, $N_p = 2$, $T_{evap} = -10$ °C, $Q_c = 91.92$ kW (Line pitch with fouling factor)

Tube side						Shell side						
Refrigerant	$T_{c,i}$ (°C)	$T_{c,o}$ (°C)	u_c (m s^{-1})	N_t	h_i (W $m^{-2}K^{-1}$)	Refrigerant	$T_{h,cond}$ (°C)	m (kg s^{-1})	L (m)	h_o (W $m^{-2}K^{-1}$)	u_o (W $m^{-2}K^{-1}$)	W_p (kW)
Water	25	30	1	72	5,110.8	R290	40	0.299	2.78	1,156.71	744.29	49.16
Water	25	30	1.5	48	7,305.02	R290	40	0.299	3.86	1,196.4	806.03	126.92
Water	25	30	2	36	9,379.99	R290	40	0.299	4.81	1,259.47	861.67	249.94
Water	25	30	2.5	28	11,374.14	R290	40	0.299	5.77	1,352.21	923.81	429.55
Water	25	30	3	24	13,307.92	R290	40	0.299	6.19	1,499.53	1,006.35	638.56
Water	25	30	1	72	5,110.8	R600	40	0.266	2.6	1,286.87	967.29	47.29
Water	25	30	1.5	48	7,305.02	R600	40	0.266	3.6	1,330.02	1,070.24	121.4
Water	25	30	2	36	9,379.99	R600	40	0.266	4.48	1,399.5	1,164.42	238.3
Water	25	30	2.5	28	11,374.14	R600	40	0.266	5.384	1,502.51	1,271.93	408.58
Water	25	30	3	24	13,307.92	R600	40	0.266	5.77	1,666.31	1,419.16	607.19
Water	25	30	1	72	5,110.8	R600a	40	0.295	2.91	1,083.44	713.26	50.42
Water	25	30	1.5	48	7,305.02	R600a	40	0.295	4.03	1,121.23	771.2	130.6
Water	25	30	2	36	9,379.99	R600a	40	0.295	5.04	1,180.44	823.93	257.73
Water	25	30	2.5	28	11,374.14	R600a	40	0.295	6.04	1,267.38	883.41	443.59
Water	25	30	3	24	13,307.92	R600a	40	0.295	6.46	1,405.4	963.06	659.56
Water	25	30	1	72	5,110.8	R125	40	1.001	3.55	810.94	584.06	57.08
Water	25	30	1.5	48	7,305.02	R125	40	1.001	4.96	841.13	627.48	150.12
Water	25	30	2	36	9,379.99	R125	40	1.001	6.06	913.4	684.29	294.02
Water	25	30	2.5	28	11,374.14	R125	40	1.001	7.44	951.9	717.63	517.73
Water	25	30	3	24	13,307.92	R125	40	1.001	7.941	1,054.84	784.43	770.7

$$\Delta P_r = \frac{4N_p \rho U_{m^2}}{2} \tag{23}$$

The total pressure drop is the sum of the pressure in the tube (Eq. 22) and due to returns (Eq. 23).

$$\Delta P_T = \Delta P_t + \Delta P_r \tag{24}$$

The fluid pumping power (P) is proportional to the pressure drop in the fluid across a heat exchanger and shown in Eq. (26) as:

$$W_p = \frac{m\Delta P}{\rho \eta_p} \tag{25}$$

where η_p is the pump efficiency, assumed to be 0.85.

It should be noted that details of this procedure can be found in Kakac [53].

2.5 Cost analysis

According to Shah and Sekulic [54], the lifetime costs of a heat exchanger—in other words, the overall total cost—may be grouped as the capital, installation, operating, and disposal costs. The costs related to design, materials, manufacturing (machinery, labor, and overhead), testing, shipping, installation, and depreciation are included in the capital (total installed) cost. The installation cost of some shell-and-tube and plate heat exchangers may be considerable in comparison to the capital cost. The other costs of heat exchangers associated with fluid pumping power, a warranty, insurance, maintenance, repair, cleaning, lost production/downtime caused by failure, energy costs related with utilities (steam, fuel, and water) are included in the operating cost. The cost estimation sometimes may be hard to determine, so the best estimates are made at the design stage [54]. This information shows the importance of the design process for heat exchangers. The unit cost value of C_{UA} in Eq. (26) was obtained from Shah and Sekulic [54] according to the calculated UA values of the operating conditions in the case studies.

$$\text{Cost} = C_{UA}\left(\frac{q}{\Delta T_m}\right) \tag{26}$$

3 Results and discussion

The costs of evaporators, condensers, and other heat exchangers comprise approximately 30 % of the total cost of a thermal power plant. These costs are significant in applications where heat exchangers should have very large surface areas due to their low logarithmic mean temperature differences. Many techniques have been investigated in recent years to improve heat transfer to reduce the sizes

Author's personal copy

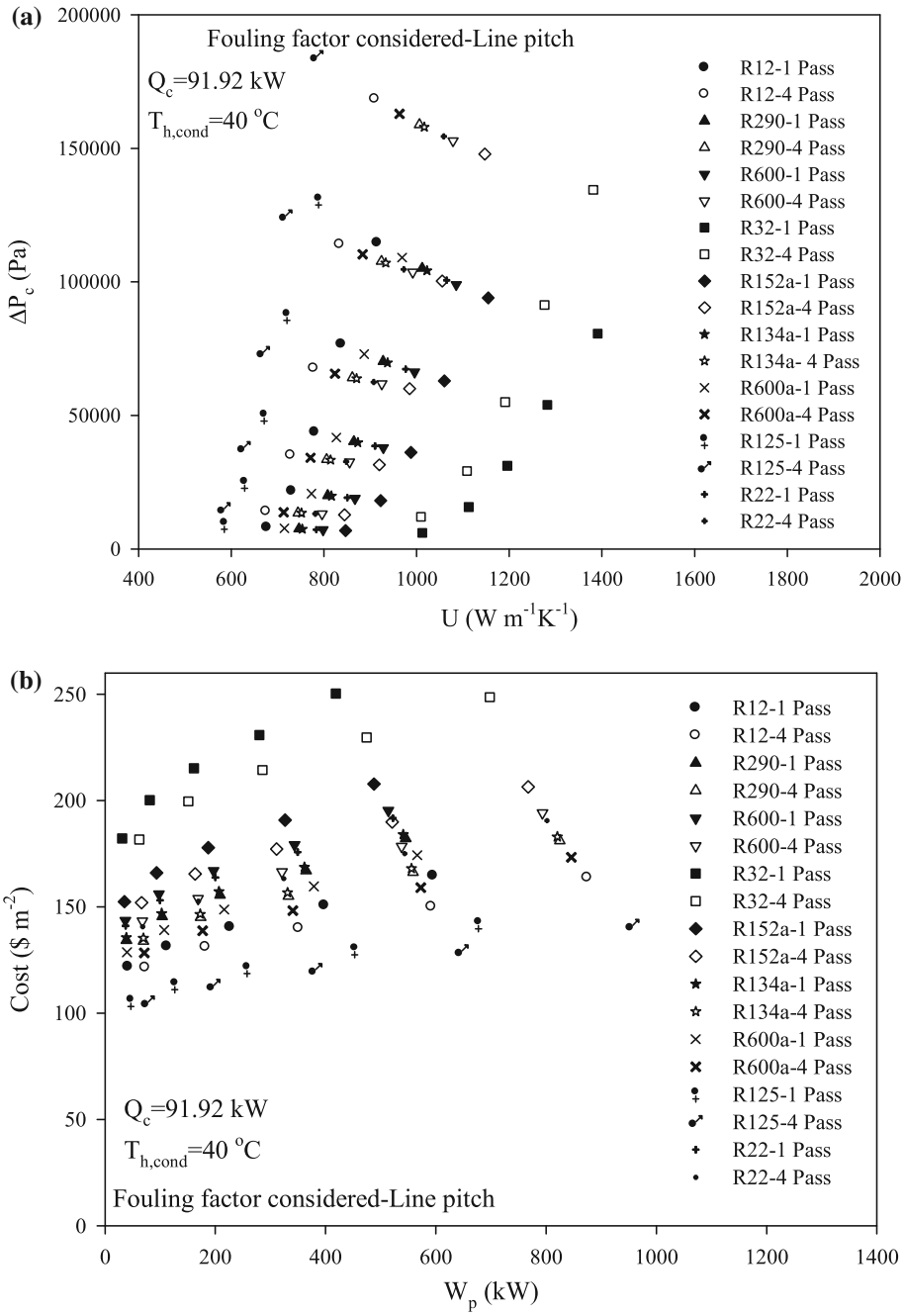

Fig. 4 **a** Pressure drop versus overall heat transfer coefficient **b** Cost versus pumping power

and costs of these heat exchangers as a solution to the cost problem. In this paper, a simple parametric analysis is given in terms of the use of alternative refrigerants. The thermodynamics and transport properties of the blend refrigerants were evaluated with the REFPROP computer program, version 6.01 [55]. It should be noted that this analysis is applied when condensate does not flood any tubes. In general, refrigerant is first determined based on system's operating conditions. And then, optimal design of each component is made. In this work, however, the order is reversed. A condenser design is made and then refrigerant is selected which can best fit to this condenser.

R12, R290, R600, R32, R152a, R134a, R600a, R125, and R22, and their mixtures of R290/R600 (40/60 by wt %); R125/R134a/R143a (44/4/52); R290/R600a (40/60 by wt %); R290/R1270 (20/80 by wt %); R170/R290 (30/70 by wt %); CO_2/R290 (50/50 by wt %); R152a/R125/R32 (48/18/34 by wt %); R32/R134a (30/70 by wt %); and R290/R152a (75/25 by wt %) are used as shell-side condensing hot refrigerants, while cooling water is used as the in-tube cold-side fluid in the investigated condenser. The evaporation temperature of the refrigerants was taken as constant at −10 °C, the condensing temperatures were varied from 35 to 55 °C, and the water-side conditions

Author's personal copy

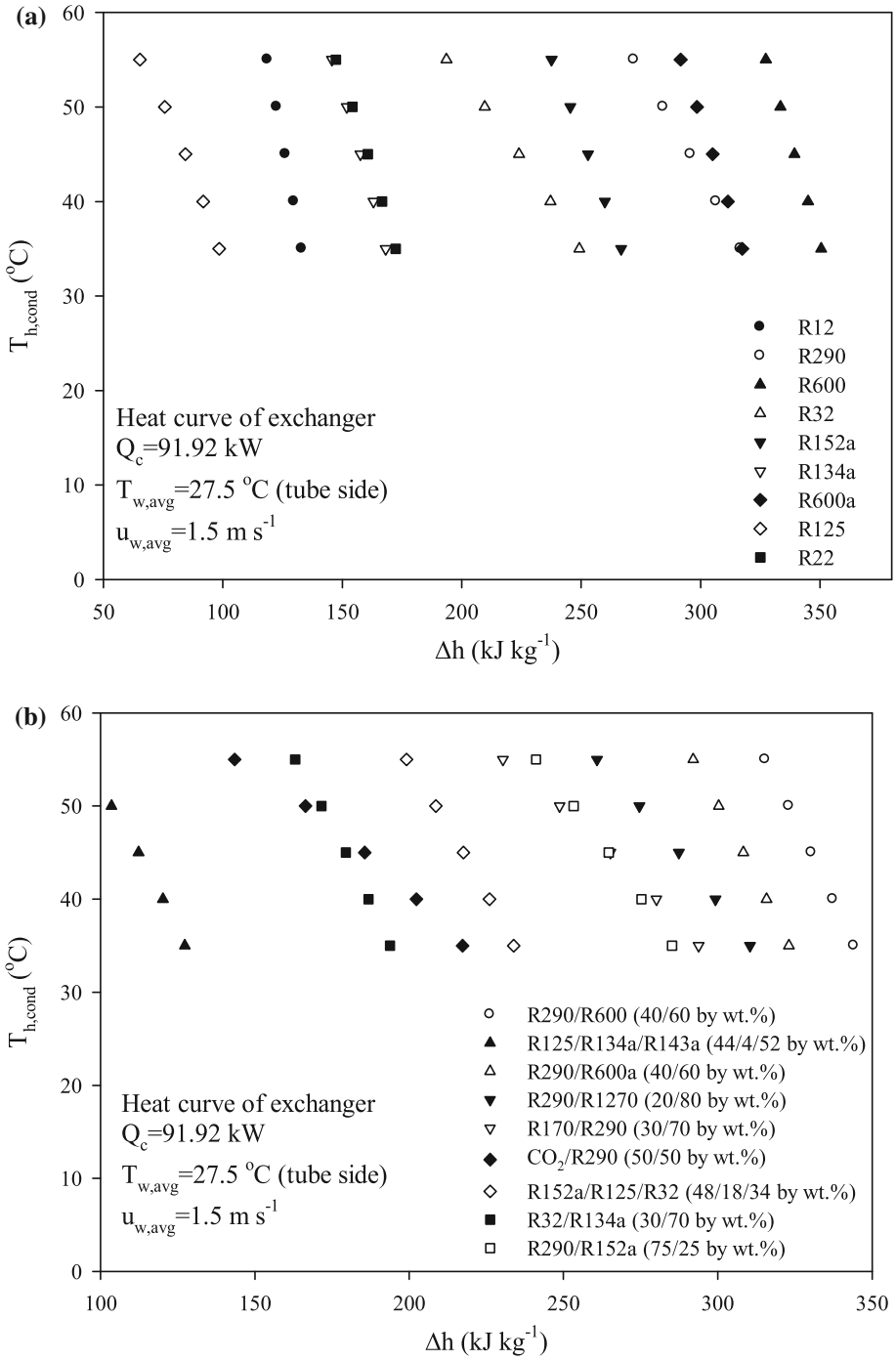

Fig. 5 Enthalpy change versus condensing temperatures for **a** pure refrigerants **b** refrigerant mixtures

were the same for all investigated conditions. Specifically, from Figs. 3 to 5, the operating conditions include in-tube water velocities ranging from 1 to 3 m s^{-1} with various tube numbers changing according to tube pass numbers for a constant condensing temperature of 40 °C in shell side, and from Figs. 6 to 9, it has a constant in-tube water velocity of 1.5 m s^{-1} with a constant tube numbers 24 for 1 pass design, 48 for 2 pass design and 96 for 4 pass design for different condensing temperatures varying from 35 to 55 °C. It should be noted that all calculations were performed for a constant cooling load of 91.92 kW.

The process of developing a new refrigerant started with the use of chlorofluorocarbons (CFCs) such as R12 (GWP = 8,500, ODP = 1) and R22 (GWP = 1,700, ODP = 0.05) in the 1980s, as shown in Table 1. In the 1990s, the mixtures were obtained using hydrochlorofluorocarbons (HCFCs) and hydrocarbons (HCs) such as R134a (GWP = 1,300, ODP = 0), R290 (GWP = 20,

Author's personal copy

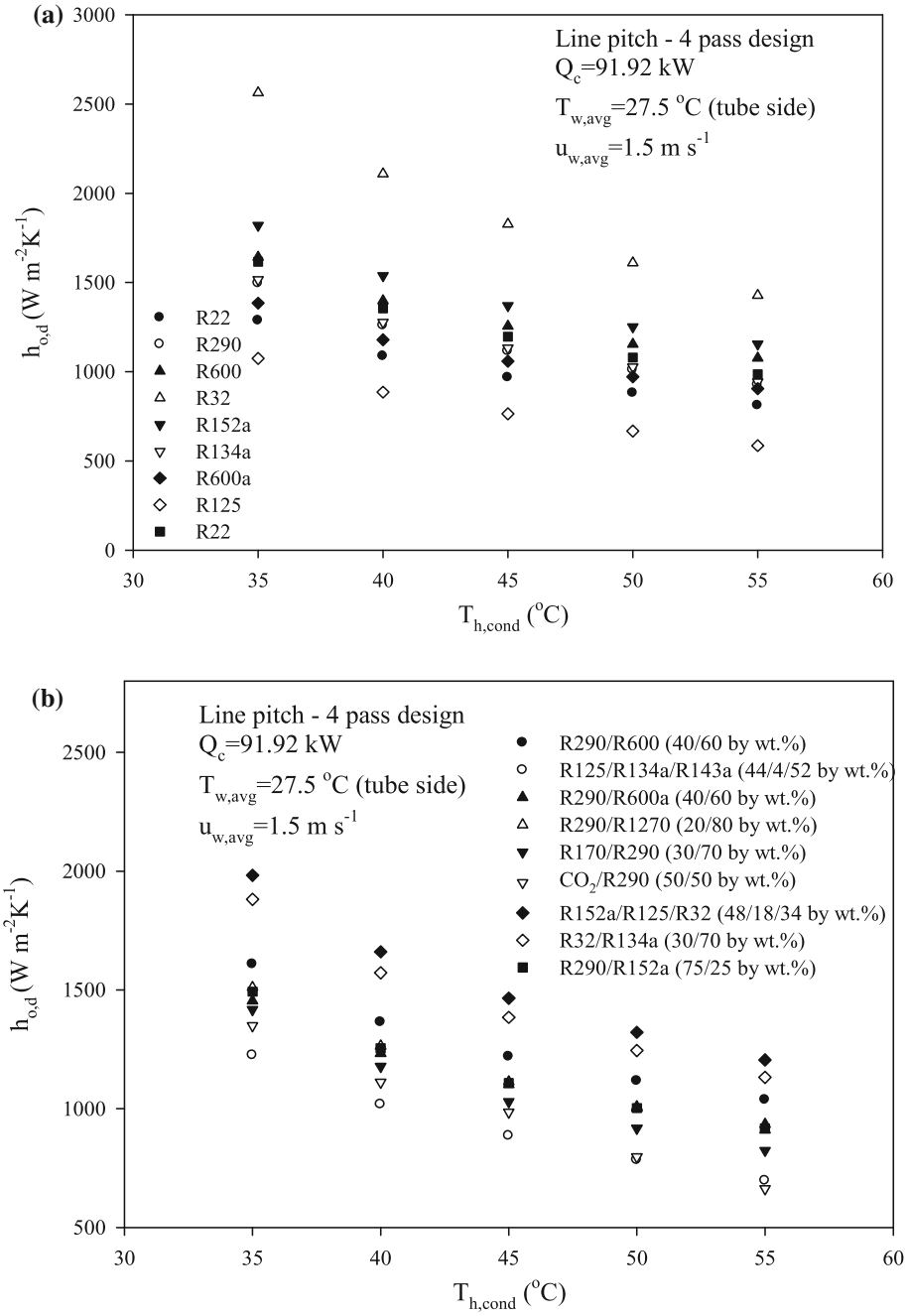

Fig. 6 Convective heat transfer coefficients versus condensing temperatures for **a** pure refrigerants **b** refrigerant mixtures

ODP = 0), and R600a (GWP = 20, ODP = 0). Since the 2000s, refrigerant blend studies have addressed mostly pairs of hydrocarbons (HCs) such as R290, R600 (GWP = 0.1, ODP = 0), R600a, R32 (GWP = 0.11, ODP = 0), and R1270 (GWP = 3, ODP = 0) due to their low global warming potential (GWPs) and ozone depleting potential (ODPs). In the near future, CO_2 (GWP = 1, ODP = 0) is expected to be employed in mixture studies. Ammonia (NH_3) (GWP = 0, ODP = 0) is also a refrigerant considered for enhancement by new compositions. It has far better heat transfer and pressure drop characteristics compared to HFCs. In this study, the selected refrigerant mixtures, listed Table 1, have been associated with the latest trends in the literature since 2007.

Table 2 describes a case study of pure refrigerants to determine the shell-side flow rates, tube lengths, shell-side convective heat transfer coefficients, overall heat transfer coefficients, and pumping powers for various in-tube fluid velocities ranging from 1 to 3 m s^{-1}, a constant cooling load of 91.92 kW, and 1 shell-2 tube pass design. R290,

Author's personal copy

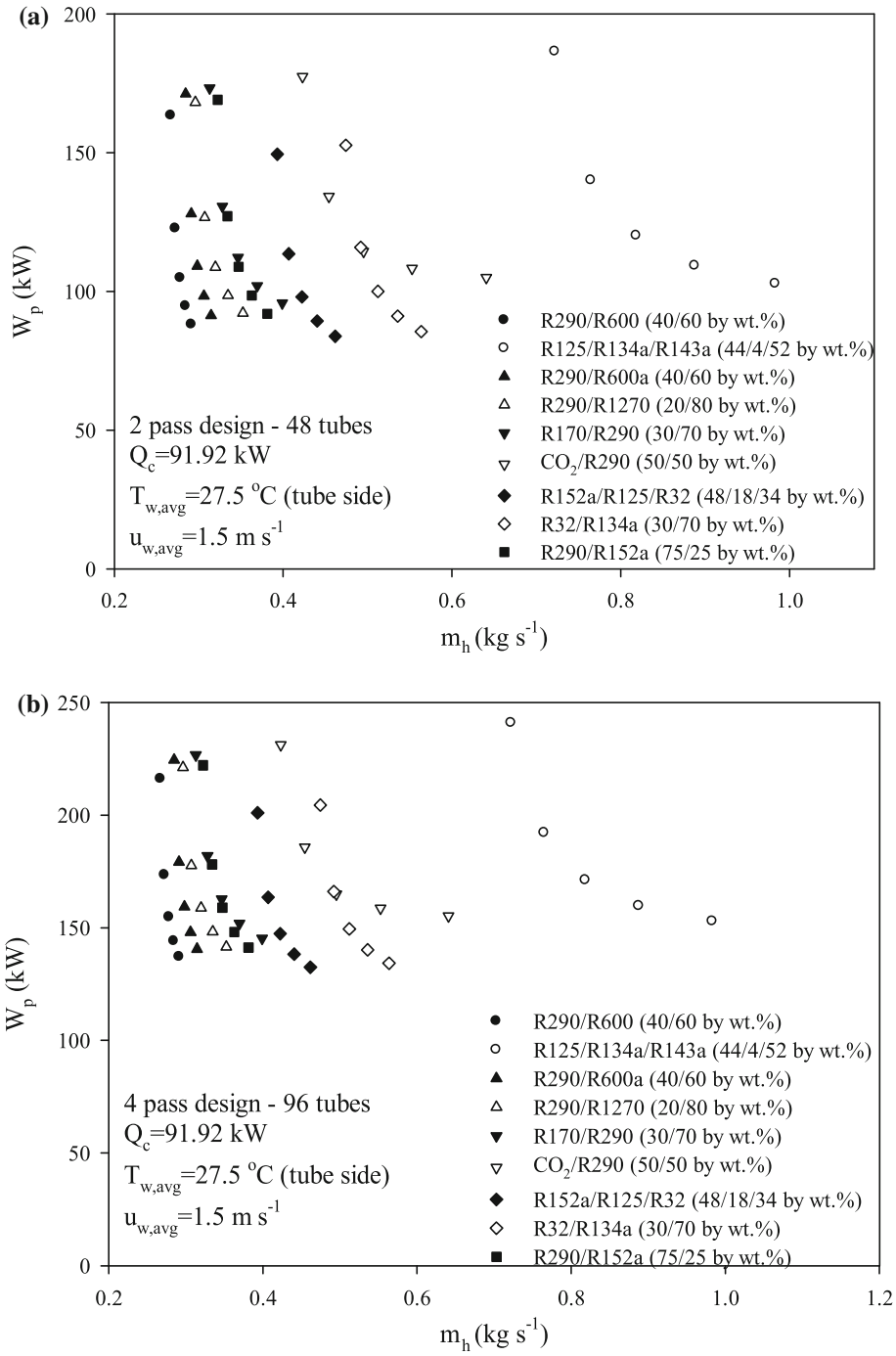

Fig. 7 Comparison of pumping powers of water in tube side according to various condensing temperatures of various refrigerant mixtures for **a** 2 pass and **b** 4 pass designs

R600, and R600a seem to have the shortest tube lengths and pumping powers, according to the table. These results prove their high efficiency and wide usage as optimum refrigerants.

Figure 3 shows the alteration of tube length and pure refrigerant flow rate in the shell side of the condenser according to the staggered or line tube arrangements and tube pass numbers 1 and 4. The desirable specification for the refrigerant is to have a short tube length and low flow rate in these figures. R32, R600, R600a, and R152a seem to fulfill this requirement, according to Fig. 3. A high tube pass number reduces the tube length as expected. This figure also shows the importance of the use of errors in the calculations. It should be also noted that the visual differences in the arrangements with tube pass numbers can be seen clearly in Figs. 1 and 2.

Figure 4 shows some of the important parameters of the condenser with respect to the selection of the optimum refrigerant. The differences in the physical properties of the investigated refrigerants affect the pressure drop of cooling

Author's personal copy

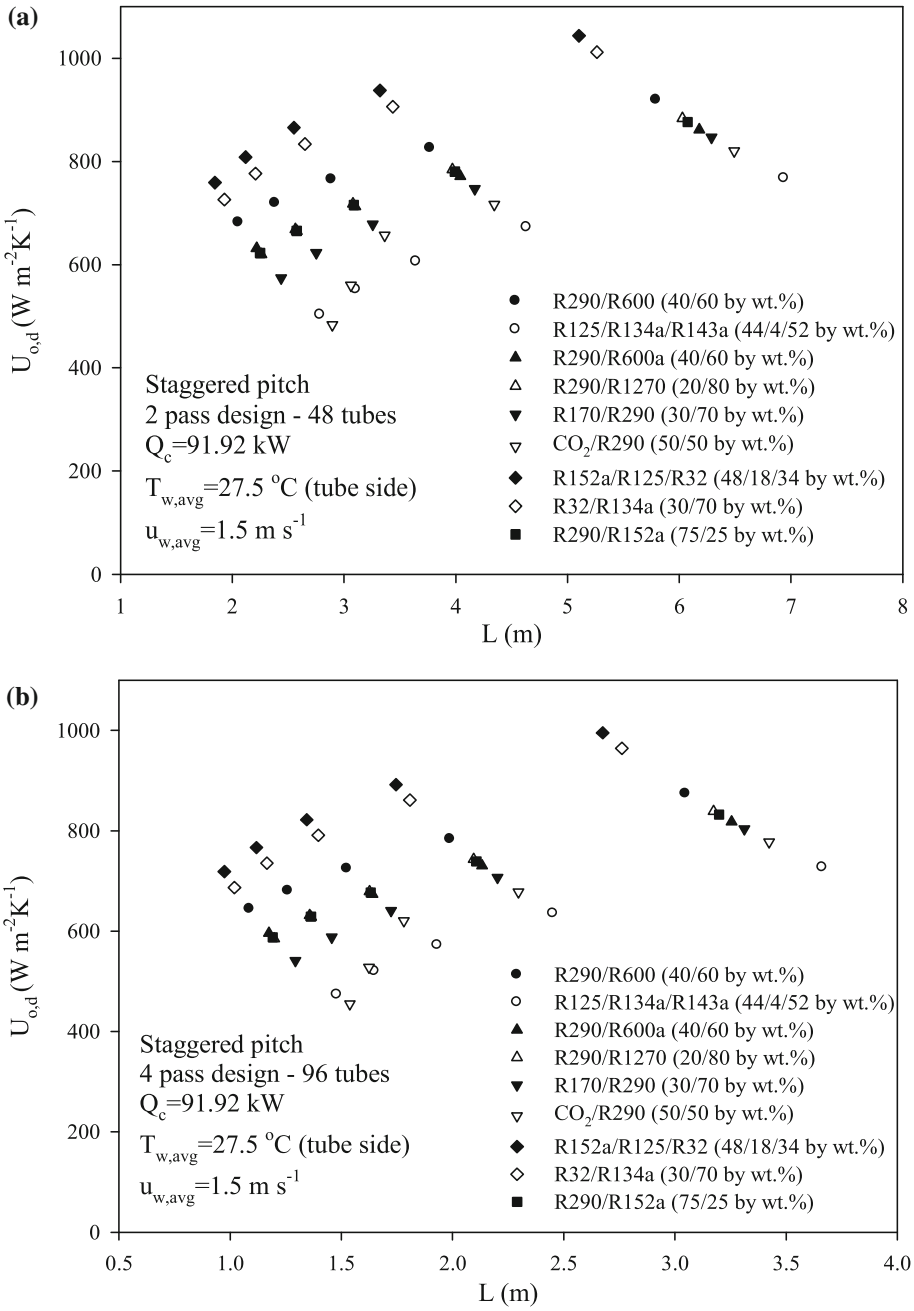

Fig. 8 Overall heat transfer coefficient versus tube length for **a** 2 pass and **b** 4 pass designs

water in-tube, and all of them have different total pressure drop values as a result, as shown in Fig. 4a. R32, R600, R600a, and R152a seem to have lower pressure drop values in comparison to the others for a constant cooling load. It is also seen that increasing tube pass numbers increase the pressure drop, as anticipated and shown in Fig. 4a. It can also be seen that total pressure drop of water increases with increasing overall heat transfer coefficient, in other words, decreasing condensing temperatures in shell side for constant in-tube water side conditions. The cost of the condenser increases with increasing pumping power, as shown in Fig. 4b. Hydrocarbon refrigerants (HCs) showed similar results.

Phase transitions are accompanied by changes in enthalpy and entropy. Because phase changes generally occur at constant pressure, the heat can be described by a change in enthalpy. Figure 5 shows the phase change enthalpies of the pure and blended refrigerants according to various condensing temperatures ranging from 35 to 55 °C. It can be seen from this figure that most of the refrigerant mixtures show improvement in the value of the phase change enthalpy compared to their base refrigerants. For instance, the mixture of R290/R600 (40/60 by wt.) has higher phase change enthalpy than R290 and slightly lower phase change enthalpy than R600 according to this figure.

Author's personal copy

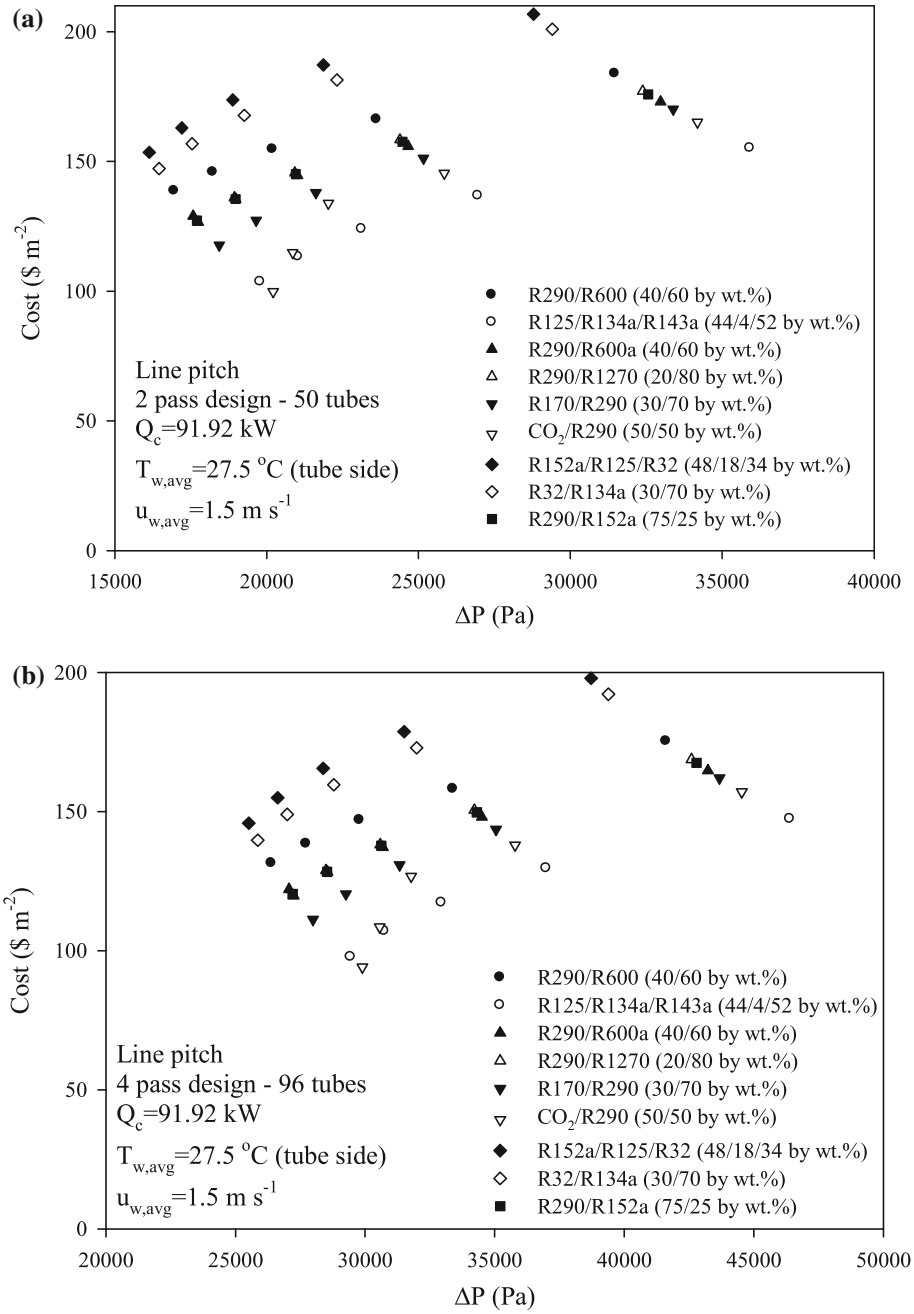

Fig. 9 Cost versus pressure drop for **a** 2 pass and **b** 4 pass designs

Figure 6 shows the alteration of the convective heat transfer coefficients of pure (a) and blended (b) refrigerants in the shell side of the condenser for a constant evaporation temperature of −10 °C and various condensing temperatures ranging from 35 to 55 °C. The figure shows that blended refrigerants did not have higher convective heat transfer coefficients than the pure refrigerants.

Figure 7 illustrates the difference in the pumping power results in terms of the tube arrangement (two or four pass design) and number or tubes (48 and 96) according to the flow rates of the blended refrigerants flowing in the shell side of the condenser. As expected, a four pass condenser has more tubes and requires more pumping power than a two pass condenser for a constant cooling load.

Figure 8 depicts the alterations of the overall heat transfer coefficients and the calculated tube lengths for different tube arrangements in the condenser. In spite of the fact that a four pass condenser has slightly lower overall heat transfer coefficients, they have a significant reduction in the tube length.

Figure 9 reveals the cost of the condensers designed as two and four pass systems according to the calculated total pressure drops in-tube. The two pass condenser has higher cost values than the four pass designed condenser and

Author's personal copy

lower pressure drops. The R125/R134a/R143a (44/4/52 by wt %) mixture has the minimum cost values regarding with the manufacturing of its condenser in spite of its high pressure drop values. Besides, the same refrigerant hasn't got the lowest required tube length and highest overall heat transfer coefficient in Fig. 8. These kinds of results can be obtained from previous figures, and this situation shows the necessity of finding the optimum refrigerant for efficient and effective condenser designs. Moreover, R290/R600 (40/60 by wt %) proposed by Yoon et al. [47], R152a/R125/R32 (48/18/34 by wt %) proposed by Wu et al. [40] and R32/R134a (30/70 by wt %) proposed by Dalkilic and Wongwises [45] can be considered as the optimum blend refrigerants with their high convective heat transfer coefficients in Fig. 6b, moderate pumping powers in Fig. 7 and low pressure drops in Fig. 9. It should be noted that the determination of the most proper refrigerant depends on the needing and aims of the systems.

4 Conclusion

The analyses include the important parameters of the condenser such as its basic geometry, flow rate, pressure drop, and pumping power to increase heat transfer, reduce pumping power, and reduce condenser size using alternative refrigerants in comparison to those required for their pure base refrigerants for a constant heat duty.

Hydrocarbon refrigerants and blended refrigerants are found to be reasonable alternatives to the older ones and optimum refrigerants, according to the analyses. Blends have the advantage of modifying the composition to meet various temperature demands. Their negative attributes, such as toxicity, flammability, and oil miscibility, can be reduced by influencing the composition. Therefore, they have greater use nowadays and investigation of them will not stop in the future due to the problems of global warming and ozone depletion. In particular, the use of zeotropic mixtures requires greater attention due to the change in their physical properties in case of leakage.

Acknowledgments The present study was supported financially by the Thailand Research Fund, the National Research University Project and National Science and Technology Development Agency, whose guidance and assistance are gratefully acknowledged. The first and second authors would like to thank Professor Somchai Wongwises for providing him fellowships during his research in the Department of Mechanical Engineering, King Mongkut's University of Technology Thonburi.

References

1. Lorenz A, Meutzner K (1975) On application of non-azeotropic two component refrigerants in domestic refrigerators and home freezers. XIV International Congress of Refrigeration, Moscow
2. Stoecker WF (1982) Energy Characteristics of a two-evaporater refrigerator using a refrigerant mixture, U.S. Department of Energy Office of Buildings and Community Systems, Phase II–Project X01 7762
3. Stoecker WF, Walukas DJ (1981) Conserving energy in domestic refrigerators through the use of refrigerant mixtures. ASHRAE Transactions 87:279–281
4. Mishra MP, Varma HK, Sharma CP (1981) Heat transfer coefficients in forced convection evaporation of refrigerants mixtures. Int J Heat Mass Transf 8:127–136
5. Singal LC, Sharma CP, Varma HK (1983) Experimental heat transfer coefficient for binary refrigerant mixtures of R13 and R12. ASHRAE Transact 2747:175–188
6. Kruse H, Hesse U (1988) Possible substitutes for fully halogenated clorofluorocarbons using fluids already marketed. Int J Refrig 11:276–283
7. Kuijpers LJM, de Wit JA, Janssen MJP (1988) Possibilities for the replacement of CFC12 in domestic equipment. Int J Refrig 11:284–291
8. Jung DS, McLinden M, Radermachert R, Didion D (1989) A study of flow boiling heat transfer with refrigerant mixtures. Int J Heat Mass Transf 32:1751–1764
9. Koyama S, Miyara A, Takamatsu H, Fujii T (1990) Condensation heat transfer of binary refrigerant mixtures of R22 and R114 inside a horizontal tube with internal spiral grooves. Int J Refrig 13:256–263
10. Kedzierski MA, Didion DA (1990) Visualization of nucleate flow boiling for an R22/R114 mixture and its components. Exp Heat Trans 3:447–463
11. Rivis E, Bidone A (1994) Isobutane/propane mixtures: comparison with traditional refrigerants. The Day After Conference. Padua, Italy
12. Kim MS, Mulroy WJ, Didion DA (1994) Performance evaluation of two azeotropic refrigerant mixtures of HFC-134a with R-290 (Propane) and R-600a (Isobutane). Trans ASME 148:148–154
13. Nozu S, Honda H, Nishida S (1995) Condensation of a zeotropic CFC114-CFC113 refrigerant mixture in the annulus of a double-tube coil with an enhanced inner tube. Exp Thermal Fluid Sci 11:364–371
14. Richardson R, Butterworth J (1995) The performance of propane/isobutane mixtures in vapor compression systems. Int J Refrig 18:58–62
15. Sami SM, Song B (1996) Heat transfer and pressure drop characteristics of hfc quaternary refrigerant mixtures inside horizontal enhanced surface tubing. Appl Therm Eng 16:461–473
16. Dongsoo J, Chong KB, Byoung LH, Hong LW (1996) Testing of a hydrocarbon mixture in domestic refrigerators, Symposia AT-96-19-3, ASHRAE Trans 1077–1084
17. Shin JY, Kim MS, Ro ST (1997) Experimental study on forced convective boiling heat transfer of pure refrigerants and refrigerant mixtures in a horizontal tube. Int J Refrig 20:267–275
18. Alsaad MA, Hammad MA (1998) The application of propane/butane mixture for domestic refrigerators. Appl Therm Eng 18:911–918
19. Shao DW, Granryd E (1998) Experimental and theoretical study on flow condensation with non-azeotropic refrigerant mixtures of R32/R134a. Int J Refrig 21:230–246
20. Baskin E (1998) Synopsis of residential refrigerator/freezer alternative refrigerants evaluation, ASHRAE Trans 266–273
21. Hammad MA, Alsaad MA (1999) The use of hydrocarbon mixtures as refrigerants in domestic refrigerators. Appl Therm Eng 19:1181–1189
22. Jung D, Kim CB, Song K, Park B (2000) Testing of propane/isobutane mixture in domestic refrigerators. Int J Refrig 23:517–527

Author's personal copy

23. Miyara A, Nonaka K, Taniguchi M (2000) Condensation heat transfer and flow pattern inside a herringbone-type micro-fin tube. Int J Refrig 23:141–152
24. Chang YS, Kim MS, Ro ST (2000) Performance and heat transfer characteristics of hydrocarbon refrigerants in a heat pump system. Int J Refrig 23:232–242
25. Choi TY, Kim YJ, Kim MS, Ro ST (2000) Evaporation heat transfer of R-32, R-134a, R-32/134a, and R-32/125/134a inside a horizontal smooth tube. Int J Heat Mass Transf 43:3651–3660
26. Tashtoush B, Tahat M, Shudeifat MA (2002) Experimental study of new refrigerant mixtures to replace R12 in domestic refrigerators. Appl Therm Eng 22:495–506
27. Akash BA, Said SA (2003) Assessment of LPG as a possible alternative to R-12 in domestic refrigerator. Energy Convers Manage 44:381–388
28. Wongwises S, Chimres N (2005) Experimental study of hydrocarbon mixtures to replace HFC-134a in a domestic refrigerator. Energy Convers Manage 46:85–100
29. Wen MY, Ho CY (2005) Evaporation heat transfer and pressure drop characteristics of R-290 (propane), R-600 (butane), and a mixture of R-290/R-600 in the three-lines serpentine small-tube bank. Appl Therm Eng 25:2921–2936
30. Koyama S, Takato N, Kuwahara K, Jin D, Xue J, Miyara A (2006) Experimental study on the performance of a refrigerant mixture CO2/DME system. Proceedings of JSRAE Annual Conference, JASRAE, pp 133–136
31. Wen MY, Ho CY, Hsieh JM (2006) Condensation heat transfer and pressure drop characteristics of R-290 (propane), R-600 (butane), and a mixture of R-290/R-600 in the serpentine small-tube bank. Appl Therm Eng 26:2045–2053
32. Han XH, Wang Q, Zhu ZW, Chen GM (2007) Cycle performance study on R32/R125/R161 as an alternative refrigerant to R407C. Appl Therm Eng 27:2559–2565
33. Park KJ, Seo T, Jung D (2007) Performance of alternative refrigerants for residential air-conditioning applications. Appl Energy 84:985–991
34. Afroz HMM, Miyara A, Tsubaki K (2008) Heat transfer coefficients and pressure drops during in-tube condensation of CO_2/DME mixture refrigerant. Int J Refrig 31:1458–1466
35. Xue J, Takata N, Ochiai A, Kuwahara K, Koyama S, Miyara A (2008) Experiments on performance evaluation of a heat pump system using CO2/DME mixture, Proceedings of JSRAE Annual Conference, JASRAE, E234-1–4
36. Chen J, Yu J (2008) Performance of a new refrigeration cycle using refrigerant mixture R32/R134a for residential air-conditioner applications. Energy Build 40:2022–2027
37. Lee MY, Lee DY, Kim Y (2008) Performance characteristics of a small-capacity directly cooled refrigerator using R290/R600a (55/45). Int J Refrig 31:734–741
38. Mani K, Selladurai V (2008) Experimental analysis of a new refrigerant mixture as drop-in replacement for CFC12 and HFC134a. Int J Therm Sci 47:1490–1495
39. Kim JH, Cho JM, Kim MS (2008) Cooling performance of several CO2/propane mixtures and glide matching with secondary heat transfer fluid. Int J Refrig 31:800–806
40. Wu J, Chu Y, Hu J, Liu Z (2009) Performance of mixture refrigerants R152a/125/R32 in domestic air-conditioner. Int J Refrig 32:1049–1057
41. Onaka Y, Miyara A, Tsubaki K (2010) Experimental study on evaporation heat transfer of CO_2/DME mixture refrigerant in a horizontal smooth tube. Int J Refrig 33:1277–1291
42. Park KJ, Jung D (2009) Performance of heat pumps charged with R170/R290 mixture. Appl Energy 86:2598–2603
43. Cho JM, Kim YJ, Kim MS (2010) Experimental studies on the characteristics of evaporative heat transfer and pressure drop of CO2/propane mixtures in horizontal and vertical smooth and micro-fin tubes. Int J Refrig 33:170–179
44. Zou X, Gong MQ, Chen GF, Sun ZH, Zhang Y, Wu JF (2010) Experimental study on saturated flow boiling heat transfer of R170/R290 mixtures in a horizontal tube. Int J Refrig 33:371–380
45. Dalkilic AS, Wongwises S (2010) A performance comparison of vapour compression refrigeration system using various alternative refrigerants. Int Commun Heat Mass Trans 37:1340–1349
46. Kabul A, Kızılkan Ö, Yakut AK (2010) Energy and exergy analysis of a refrigeration system with shell and tube heat exchanger using R404A Isı Bilimi ve Tekniği Dergisi. JThermal Sci Technol 30:85–93
47. Yoon WJ, HJ Chung KS, Lee EJ, Kim Y (2012) Performance optimization of a Lorenz-Meutzner cycle charged with hydrocarbon mixtures for a domestic refrigerator-freezer, International Journal of Refrigeration 35 36–46
48. Grauso S, Mastrullo R, Mauro AW, Vanoli GP (2011) CO_2 and propane blends Experiments and assessment of predictive methods for flow boiling in horizontal tubes. Intern J Refrig 34:1028–1039
49. Gnielinski V (1976) New equations for heat and mass transfer in turbulent pipe and channel flow. Intern Chem Eng 16:359–368
50. Dhir VK, Lienhard J (1971) Laminar film condensation on plan and axisymmetric bodies in non-uniform gravity. J Heat Transfer 93:97–100
51. Incropera FP, DeWitt DP (2002). Fundamentals of heat and mass transfer, John Wiley and Sons, 2002
52. Kern DQ (1950) Process heat transfer, McGraw-Hill
53. Kakac S (1996) Fundamentals and applications. Technical University of Istanbul, Heat exchanger design course
54. Shah RK (2003) D.P. Sekulic. Fundamentals of heat exchanger design, John Wiley & Sons
55. McLinden MO, Klein SA, Lemmon EW (1998) REFPROP, Thermodynamic and transport properties of refrigerants and refrigerant mixtures. NIST Standard Reference Database-version 6.01

Neural Network Based Analyses for the Determination of Evaporation Heat Transfer Characteristics During Downward Flow of R134a Inside a Vertical Smooth and Corrugated Tube

M. Balcilar, A. S. Dalkilic, K. Aroonrat & S. Wongwises

Arabian Journal for Science and Engineering

ISSN 1319-8025
Volume 39
Number 2

Arab J Sci Eng (2014) 39:1271-1290
DOI 10.1007/s13369-013-0659-1

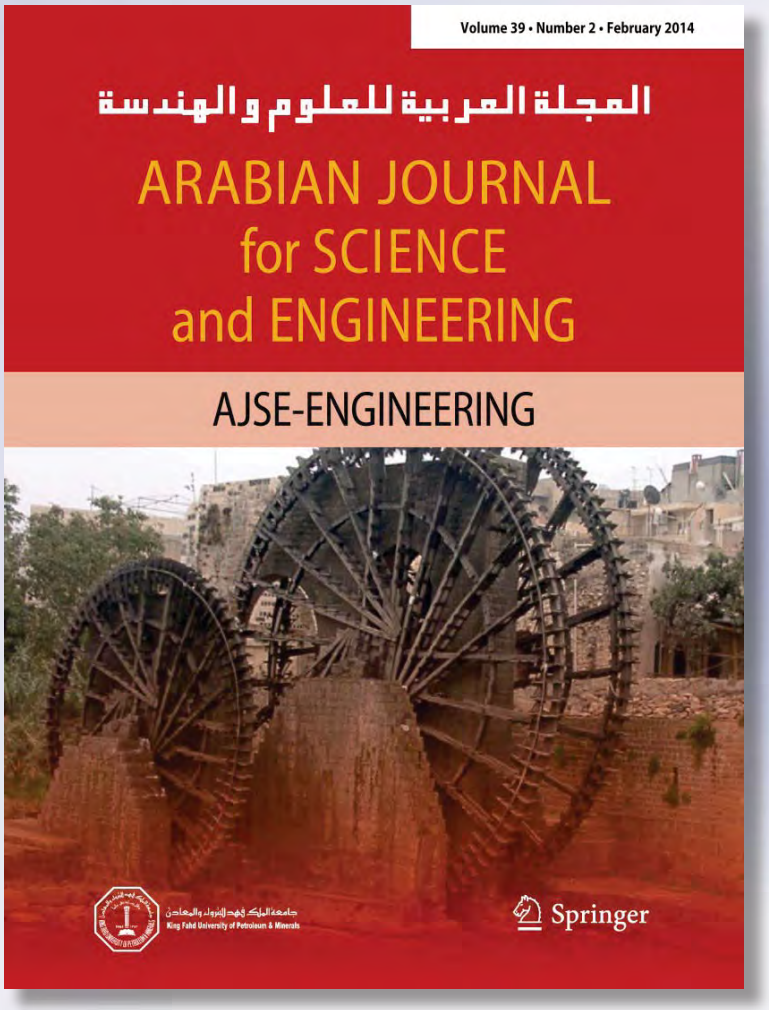

Springer

Your article is protected by copyright and all rights are held exclusively by King Fahd University of Petroleum and Minerals. This e-offprint is for personal use only and shall not be self-archived in electronic repositories. If you wish to self-archive your article, please use the accepted manuscript version for posting on your own website. You may further deposit the accepted manuscript version in any repository, provided it is only made publicly available 12 months after official publication or later and provided acknowledgement is given to the original source of publication and a link is inserted to the published article on Springer's website. The link must be accompanied by the following text: "The final publication is available at link.springer.com".

Author's personal copy

Arab J Sci Eng (2014) 39:1271–1290
DOI 10.1007/s13369-013-0659-1

RESEARCH ARTICLE - MECHANICAL ENGINEERING

Neural Network Based Analyses for the Determination of Evaporation Heat Transfer Characteristics During Downward Flow of R134a Inside a Vertical Smooth and Corrugated Tube

M. Balcilar · A. S. Dalkilic · K. Aroonrat · S. Wongwises

Received: 24 April 2011 / Accepted: 4 July 2013 / Published online: 5 September 2013
© King Fahd University of Petroleum and Minerals 2013

Abstract The heat transfer characteristics of the refrigerant HFC–134a are investigated, such as convective heat transfer coefficient and pressure drop during evaporation inside a vertical smooth and five pieces of corrugated tube, using experimental data with the aim of numerically determining the best artificial intelligence method. The double tube test sections are 0.5 m long with refrigerant flowing in the inner tube and heating water flowing in the annulus. Input of the ANNs are the 14 numbers of dimensional and dimensionless values of test section, such as mass flux, heat flux, temperature difference between the tube wall and saturation temperature, average vapour quality, evaporating temperature, two-phase friction factor, two-phase multiplier, liquid and vapour Reynolds numbers, Bond number, Froude number, Weber number, depth of corrugation and helix angle for the tested corrugated tubes, whereas the outputs of the ANNs are the experimental condensation heat transfer coefficient and measured pressure drop from the analysis. The evaporation heat transfer characteristics of R134a are modelled to decide the best approach, using several ANN methods such as multi layer perceptron (MLP) and radial basis networks (RBFN). The performance of the method of MLP with 10-5-1 architecture and RBFNs with the spread coefficient of 100,000 and a hidden layer neuron number of 200 were found to be in good agreement, predicting the evaporation heat transfer coefficient and pressure drop. Dependency of outputs of the ANNs from input values is investigated and new ANN-based heat transfer coefficient correlations are developed as a result of the analyses.

Keywords Evaporation · Boiling · Heat transfer coefficient · Pressure drop · Modeling · Neural network

M. Balcilar
Computer Engineering Department,
Yildiz Technical University, 34220 Davutpasa,
Esenler, Istanbul, Turkey

A. S. Dalkilic (✉)
Heat and Thermodynamics Division,
Department of Mechanical Engineering,
Yildiz Technical University, Yildiz,
Besiktas, Istanbul 34349, Turkey
e-mail: dalkilic@yildiz.edu.tr

K. Aroonrat · S. Wongwises (✉)
Fluid Mechanics, Thermal Engineering
and Multi phase Flow Research Lab. (FUTURE),
Department of Mechanical Engineering,
Faculty of Engineering, King Mongkut's
University of Technology Thonburi, Bangmod,
Bangkok 10140, Thailand
e-mail: somchai.won@kmutt.ac.th

الخلاصة

تم التحقيق في خصائص نقل الحرارة لمبرد HFC-134a، مثل معامل انتقال الحمل الحراري وانخفاض الضغط في أثناء التبخر داخل تمليس عمودي وخمس قطع من أنبوب مموج، وذلك باستخدام البيانات التجريبية بهدف تحديد ـ عدديا ـ أفضل طريقة ذكاء اصطناعي ، وكان طول أقسام أنبوب الاختبار المزدوج 0.5 م مع تدفق المبردات في الأنبوب الداخلي وتسخين المياه المتدفقة في الحلقة ، ومدخلات الشبكات العصبية الصناعية هي 14 رقما من قيم بعدية وغير بعدية لمقطع الاختبار للأنابيب المموجة التي تم اختبارها، مثل التدفق الشامل، والتدفق الحراري، والفرق في درجة الحرارة بين جدار الأنبوب ودرجة الحرارة التشبع، ومتوسط جودة البخار، ودرجة حرارة التبخير، ومعامل الاحتكاك ذي مرحلتين، والمضاعف ذي مرحلتين ، وأرقام رينولدز للسائل والبخار، وعدد بوند، وعدد فرويد، وعدد

Author's personal copy

وبير، وعمق التمويج وزاوية اللولب، في حين أن مخرجات الشبكات العصبية الصناعية هي معامل اننقال حرارة التكثيف التجريبي وهبوط الضغط المقاس من التحليل. وقد تمت نمذجة خصائص نقل حرارة التبخر ل R134a لتحديد أفضل نهج، وذلك باستخدام عدة أساليب ANN مثل مستقبلات الطبقة المتعددة (MLP) وشبكات القاعدة الشعاعية (RBFN)، ووجد أن أداء طريقة MLP مع هندسة معمارية 1-5-10 وRBFNs مع معامل انتشار خلايا عصبيه بمقدار 100،000 وعدد خلايا عصبية لطبقة مخفية مقداره 200 هو في اتفاق جيد، ويتوقع معامل انتقال حرارة التبخر وانخفاض الضغط ، وتم التحقيق في اعتمادية مخرجات الشبكات العصبية الصناعية على قيم الإدخال، وطورت معاملات ارتباط نقل حرارة جديدة على أساس ANN كنتيجة للتحليلات.

Abbreviations

A	Surface area, m^2
ANFIS	Adaptive neuro–fuzzy inference system
ANN	Artificial neural network
Bo	Bond number
CHF	Critical heat flux
c_p	Specific heat, J kg^{-1} K^{-1}
d	Internal tube diameter, m
E	Error
EHD	Electro hydrodynamic
f	Friction factor
Fr	Froude number
G	Mass flux, kg m^{-2} s^{-1}
GA	Genetic algorithm
GRNN	Generalized regression neural network
h	Heat transfer coefficient, W m^{-2} K^{-1}
HFC	Hydro fluorocarbons
I	Input
i	Enthalpy, J kg^{-1}
i_{fg}	Latent heat of condensation, J kg^{-1}
k	Thermal conductivity, W m^{-1} K^{-1}
L	Length of test tube, m
m	Mass flow rate, kg s^{-1}
MLP	Multi-layer perception
N	Element number
N_i^j	ith Neuron of jth hidden layer
O	Output
P	Pressure, N m^{-2}
ΔP	Pressure drop, N m^{-2}
R	Refrigerant
Re	Reynolds number
RBFN	Radial basis networks
S	Slip ratio
sp	Spread coefficient
Q	Heat transfer rate, W
q	Heat flux, kW m^{-2}
T	Temperature, °C
ΔT	Temperature difference, K
x	Average vapor quality
X_{tt}	Lockhart–Martinelli parameter
We	Weber number

Greek Symbols

φ_l^2	Two-phase multiplier
α	Void fraction
ρ	Density, kg m^{-3}
μ	Dynamic viscosity, kg m^{-1} s^{-1}
σ	Surface tension, N m^{-1}

Subscripts

avg	Average
calc	Calculated
eq	Equivalent
exp	Experimental
F	Frictional term
g	Gas/vapor
G	Gravitational term
i	Number of test data
in	Inlet
l	Liquid
M	Momentum term
ph	Preheater
o	Outlet
ref	Refrigerant
sat	Saturation
TS	Test section
tp	Two-phase
w	Water
wi	Wall inside

1 Introduction

The thermal performance of heat transfer equipment can be improved using heat transfer enhancement techniques. The rough surface technique is one of them that usually involves surface modification to promote turbulent flow and increases the heat transfer surface area. Normally, smooth tubes are replaced by corrugated tubes in many heat exchangers to increase the heat transfer rate by mixing and also limiting the fluid boundary layers close to the heat transfer surfaces. Moreover, they can promote two-phase heat transfer enhancement. Some of works regarding the heat transfer and flow characteristics of corrugated tubes are summarised below.

Nozu et al. [1,2] investigated local heat transfer and pressure gradients in pure R-114, R-113 and a zeotropic refrigerant mixture during condensation in a tube-in-tube heat exchanger. The results showed that the frictional pressure gradient data and measured heat transfer data were approximately 11 and 13 %, respectively. Dong et al. [3] investigated turbulent friction and heat transfer characteristics of four spirally corrugated tubes with various geometrical parameters. Water and oil were used as the working fluid. Their results

Author's personal copy

showed that the heat transfer coefficient enhancement varied from 30 to 120 %, while the friction factor increased from 60 to 160 % when compared with a smooth tube. One of most productive studies has been performed by Zimparov [4]. The heat transfer enhancement of a combination of three-start spirally corrugated tubes with a twisted tape was investigated. Two three-start spirally corrugated tubes combined with five twisted tape inserts with different relative pitches were employed as the test section. The results showed that the friction factor and heat transfer coefficients of three-start spirally corrugated tubes with a twisted tape were significantly higher than those of a smooth tube under the same operating conditions. Zimparov [5] presented the heat transfer enhancement using a combination of single-start spirally corrugated tubes with a twisted tape. The friction factors and inside heat transfer coefficients obtained from these tubes were higher than those obtained from the smooth tube under the same conditions. In addition, Zimparov [6,7] applied a simple mathematical model to predict the friction factors and heat transfer coefficients in a spirally corrugated configuration combined with twisted tape inserts flowing in the turbulent flow regime. The calculated friction factors and heat transfer coefficients were compared with the experimental data. The results showed that the agreement between the predicted and experimental data was fairly good.

Existing numerical studies on the subject of in-tube evaporation and boiling in the literature are summarised briefly in the following paragraphs.

Nafey [8] proposed a new method using artificial neural networks (ANN) to predict the critical heat flux (CHF) for a steam–water mixture flowing in pipes. The testing processes is performed by means of a large volume of experimental data. The algorithm of Levenberg–Marquardt was used in the analysis of ANN. Accuracy of the validation was good and a new correlation was proposed to determine the CHF. Wang et al. [9] developed a generalised neural network correlation for boiling heat transfer coefficient of R22 and its alternative refrigerants R134a, R407C and R410A, inside horizontal smooth tubes. The input of the neural network analysis was selected from four kinds of dimensionless parameter groups while the Nusselt number was used as the output. As a result of the analysis, the input parameter group based on the Gungor–Winterton correlation was found to be better than the other three groups. Scalabrin et al. [10] investigated the flow boiling inside horizontal smooth tubes for mixtures and proposed a new modelling method based on ANN for heat transfer. They extended their former study [11], which was about the same topic using pure fluids in smooth tubes, to mixtures. Their new numerical method was stated to be better than the conventional methods with regard to its accuracy. Wongwises and Disawas [12] experimentally investigated the two-phase heat transfer coefficient characteristics of HFC-134a evaporating under forced flow conditions inside a smooth horizontal tube. Different from most previous studies, the present experiments have been performed with lubricating oil in the refrigerant loop at high flow rate and high heat flux conditions. The effects of heat flux, mass flux, evaporation pressure and lubricating oil on the convection heat transfer coefficients were discussed. Sripattrapan and Wongwises [13] presented the results of simulations using a two-phase separated flow model to study the heat transfer and flow characteristics of refrigerants during evaporation in a horizontal tube. A one-dimensional annular flow model of the evaporation of refrigerants under constant heat flux was developed. Their proposed model is used to predict the variation of the temperature, heat transfer coefficient and pressure drop of various pure refrigerants flowing along a horizontal tube. Wongwises and Polsongkram [14] investigated the two-phase heat transfer coefficient and pressure drop of HFC-134a during evaporation inside a smooth, helically coiled concentric tube-in-tube heat exchanger. New correlations for the convection heat transfer coefficient and pressure drop were proposed for practical applications. Kaew-On and Wongwises [15] investigated the evaporation heat transfer coefficient and pressure drop of R-410A flowing through a horizontal aluminium rectangular multiport mini-channel of 3.48 mm hydraulic diameter. Their analysis showed that the average heat transfer coefficient of R-410A during evaporation tended to increase with increasing average quality, mass flux and heat flux, but tended to decrease with increasing saturation temperature. The pressure drop increased with increasing the mass flux, but decreased with increasing the saturation temperature, and the heat flux has no significant effect on the pressure drop. Posew et al. [16] investigated the heat transfer enhancement using the electrohydrodynamic (EHD) technique during evaporation inside horizontal smooth and micro-fin tubes. The test section was a counter-flow concentric tube-in-tube heat exchanger with R-134a flowing inside the inner tube and heating water flowing in the annulus. The maximum heat transfer enhancement ratios were 1.25 and 1.15 for smooth tube and micro-fin tube, respectively. Laohalertdecha and Wongwises [17] investigated the effects of corrugation pitch on the evaporation of R-134a flowing inside horizontal corrugated tubes. The effects of average vapour quality, equivalent Reynolds number and corrugation pitch were discussed. Differently from most previous studies, Aroonrat and Wongwises [18] studied the heat transfer and friction characteristics of the pure refrigerant HFC-134a during evaporation inside a vertical corrugated tube. The effects of heat flux, mass flux and evaporation temperature on the heat transfer coefficient and two-phase friction factor were also discussed. It is found that the percentage increases of the heat transfer coefficient and the two-phase friction factor of the corrugated tubes compared with those of the smooth tube were approximately 0–10 and 70–140 %, respectively. Balcilar et al. [19] investigated the best artificial intelligence method

Author's personal copy

to estimate the measured convective heat transfer coefficient and pressure drop of R134a flowing downward inside a vertical smooth copper tube using several ANN methods, such as multi layer perceptron (MLP), radial basis networks (RBFN), generalised regression neural network (GRNN) and adaptive neuro-fuzzy inference system (ANFIS). Colorado et al. [20] developed a physical–empirical model to investigate heat transfer of helical coil in oil and glycerol/water solution. They benefited from an artificial neural network (ANN) model working with equations of continuity, momentum and energy in each flow to have a reliable the natural convection heat transfer correlations. As a result of their analyses, it was found that saving time and improving general system performance were achieved using ANN.

Despite worthwhile experimental studies in the literature, relatively little information is currently available on numerical work such as ANN analysis on the evaporation heat transfer and flow characteristics in smooth and corrugated tubes. As mentioned previously, it is evident that the corrugated tubes have greater heat transfer potential than smooth tubes. As a consequence, in the present study the main concern is to fill this gap in the literature. The results for the solution of neural network analysis on the evaporation two-phase heat transfer coefficient and pressure drop, which have never before appeared in open literature, are presented. The large amount of measured data obtained from the experimental study regarding the convective heat transfer coefficient and pressure drop are compared with the results from ANN methods such as MLP and RBFN. In addition to this, the effect of input parameters (mass flux, heat flux, the temperature difference between the tube wall and saturation temperature, average vapour quality, evaporating temperature, two-phase friction factor, two-phase multiplier, liquid and vapour Reynolds numbers, Bond number, Froude number, Weber number, depth of corrugation and helix angle for the tested corrugated tubes) on the output parameters (convective heat transfer coefficient (h), pressure drop (ΔP)) is shown and discussed as a primary study on this subject in the literature. Moreover, correlation development study is performed to calculate the evaporation heat transfer coefficient using the most effective input parameters and the measured pressure drop values.

2 Experimental Apparatus and Method

A schematic diagram of the test apparatus is shown in Fig. 1. The refrigerant loop consists of a pre-heating loop, test sec-

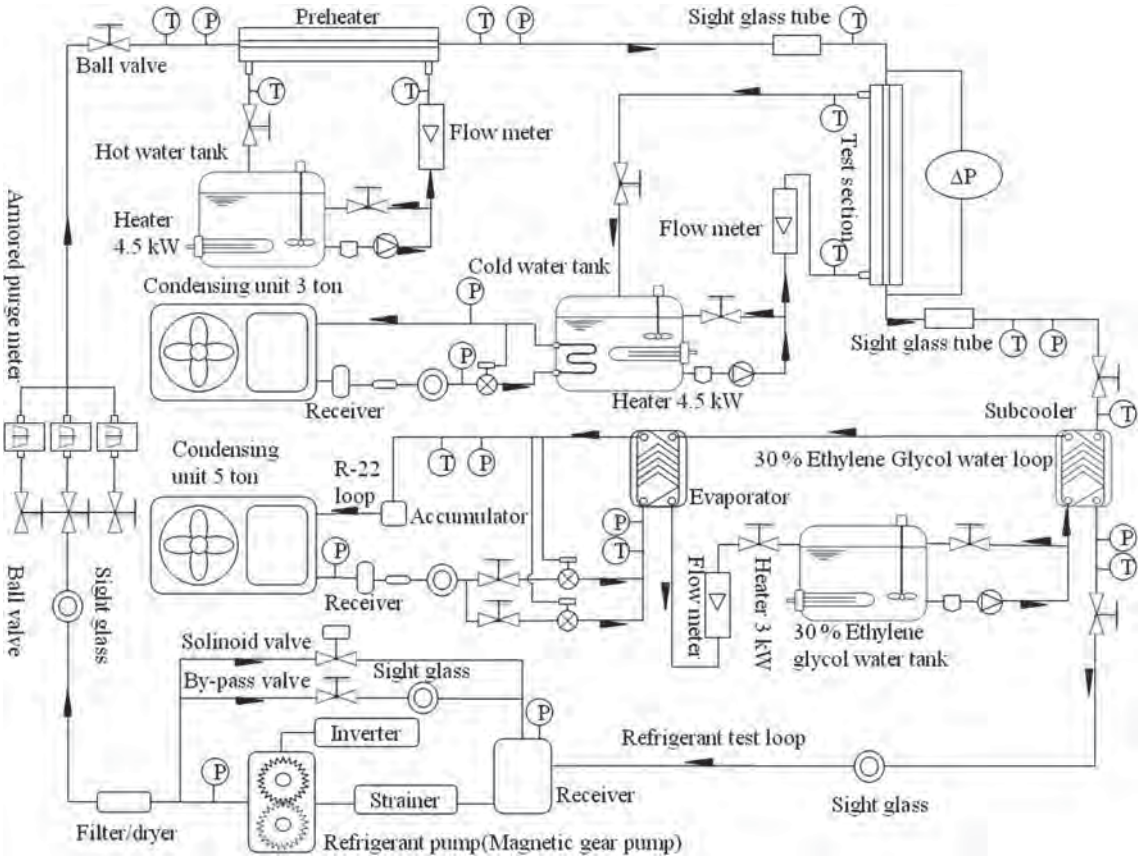

Fig. 1 Schematic diagram of experimental apparatus (from Aroonrat and Wongwises [18], with permission from Elsevier)

Author's personal copy

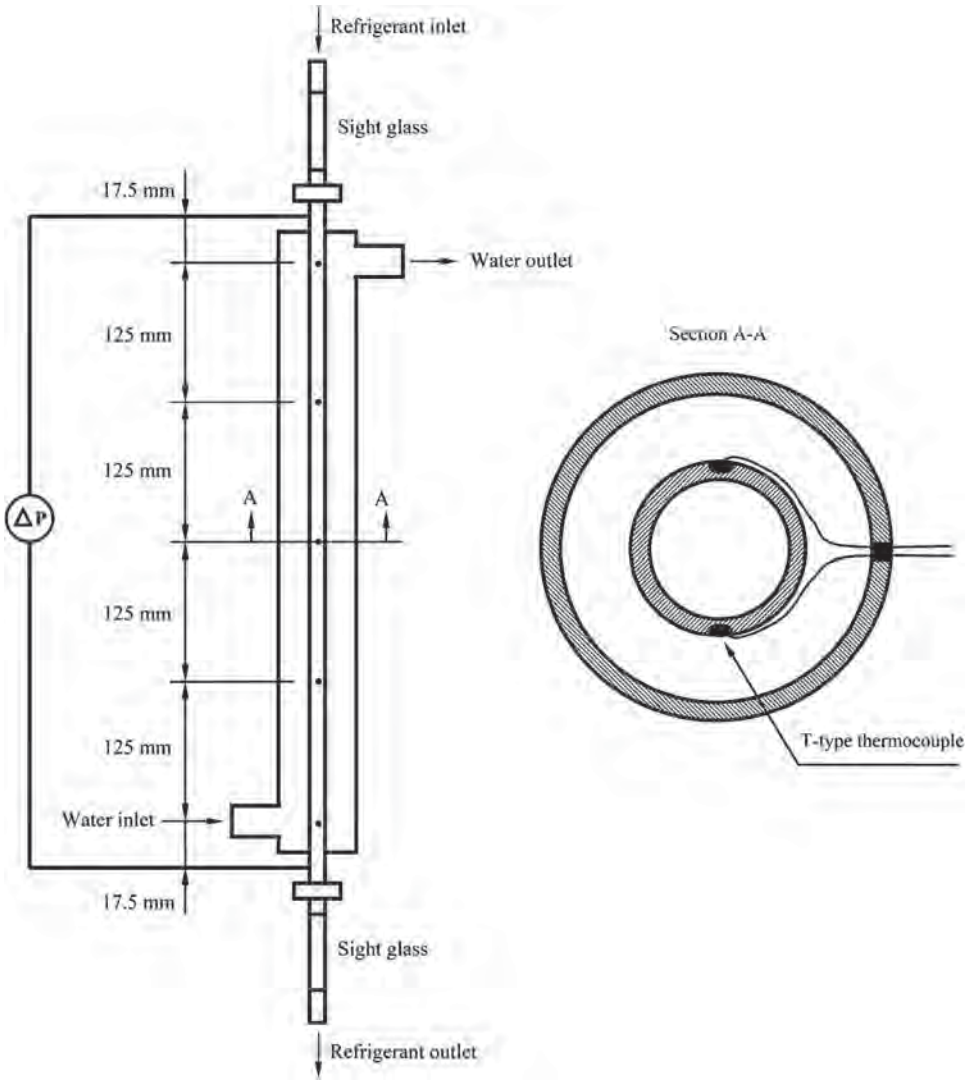

Fig. 2 Schematic diagram of the test section (from Aroonrat and Wongwises [18], with permission from Elsevier)

tion, heating loop and chilling loop. For the refrigerant circulating loop, liquid refrigerant is forced by a gear pump which can be adjusted to the flow rate using an inverter. The refrigerant then passes in series through a filter/dryer, a refrigerant flow meter, a pre-heater, and a sight glass and enters the test section. The pre-heater controls the inlet quality before entering the test section. It consists of a spiral counter-flow tube-in-tube heat exchanger which is designed to supply heat to prepare an inlet quality for the vaporization of the refrigerant. Leaving the test section, the refrigerant vapour then condenses inside a sub-cooler and is collected in a receiver. After leaving the chilling loop, the refrigerant returns from a two-phase refrigerant to a sub-cooled state. Eventually, the refrigerant returns to the refrigerant pump to complete the cycle.

Details of the test section are shown schematically in Fig. 2. The test section is a vertical counter-flow double tube heat exchanger with refrigerant flowing downward in the inner tube and heating water flowing upward in the annulus. The test sections are one smooth tube and five corrugated tubes, which are made from copper. The inner diameter and outer diameter of the inner tube are 8.7 and 9.52 mm, respectively. The length of the test section is 500 mm. Figure 3 shows a sketch and a photograph of a corrugated tube. The dimensions of the test section and the range of experimental conditions tested are listed in Tables 1 and 2, respectively. T-type thermocouples are installed at the inlet and outlet of the test section to measure the saturation temperature of the refrigerant. Similarly, the differential pressure transducer is installed to measure the pressure drop across the test section. The length between the pressure taps is 850 mm. There are 10 thermocouples located at five positions along the test section. All of the wall thermocouples are fixed with special glue having low thermal conductivity. The test section is insulated with rubber foam with a thermal conductivity of 0.04 W/mK. All of the thermocouples are well calibrated by standard thermometers with a precision of 0.1 °C. The refrigerant flow meter is a variable area type

Author's personal copy

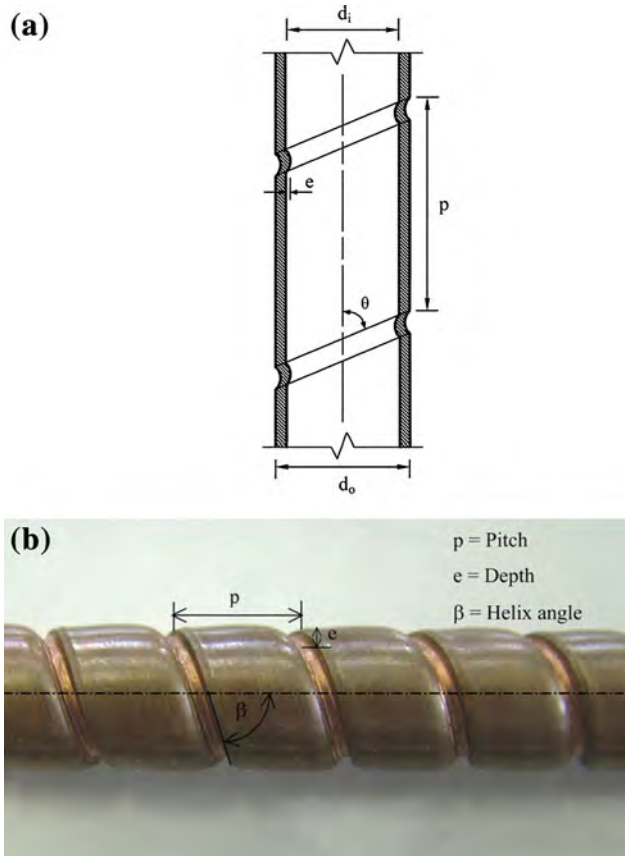

Fig. 3 Sketch (**a**) and photograph (**b**) of helically corrugated tube (from Aroonrat and Wongwises [18], with permission from Elsevier)

and is specially calibrated in the range of 0.2–3.4 LPM for R-134a by the manufacturer, as is the differential pressure transducer.

In the experiments, the inlet quality of the test section is varied by small increments. The imposed heat flux, mass flux and saturation temperature are kept constantly at the desired values. The system is allowed to approach a steady state before any data are recorded. During experiments, the temperature and pressure are continuously recorded along the test section by the data acquisition system. The uncertainties of measured quantities and calculated parameters, which are calculated from the root mean sum square method, are shown in Table 3.

3 Data Reduction and Experimental Uncertainty

The data reduction of the measured results can be analysed as follows:

3.1 The Inlet Vapour Quality of the Test Section ($X_{TS,in}$)

$$X_{TS,in} = \frac{i_{TS,in} - i_{l@T_{TS,in}}}{i_{fg@T_{TS,in}}}, \tag{1}$$

where $i_{l@T_{TS,in}}$ is the enthalpy of the saturated liquid based on the temperature of the test section inlet, $i_{fg@T_{TS,in}}$ is the enthalpy of vaporisation based on the temperature of the test section inlet, $i_{TS,in}$ is the refrigerant enthalpy at the test section inlet and is given by

$$i_{TS,in} = i_{ph,in} + \frac{Q_{ph}}{m_{ref}}, \tag{2}$$

where $i_{ph,in}$ is the inlet enthalpy of the liquid refrigerant before entering the pre-heater, m_{ref} is the mass flow rate of the refrigerant and Q_{ph} is the heat transfer rate in the pre-heater:

$$Q_{ph} = m_{w,ph} c_{p,w} (T_{w,in} - T_{w,o})_{ph}, \tag{3}$$

where $m_{w,ph}$ is the mass flow rate of the water entering the preheater, $c_{p,w}$ is the specific heat of water and $(T_{w,in} - T_{w,o})_{ph}$ is the temperature difference between inlet and outlet positions of the preheater.

3.2 The Outlet Vapour Quality of the Test Section ($X_{TS,o}$)

$$X_{TS,o} = \frac{i_{TS,o} - i_{l@T_{TS,o}}}{i_{fg@T_{TS,o}}}, \tag{4}$$

where $i_{TS,o}$ is the refrigerant enthalpy at the test section outlet, $i_{l@T_{TS,o}}$ is the enthalpy of the saturated liquid based on

Table 1 The dimensions of the test sections

Parameters	Smooth tube	Corrugated tube (A)	Corrugated tube (B)	Corrugated tube (C)	Corrugated tube (D)	Corrugated tube (E)
Outer diameter (mm)	9.52	9.52	9.52	9.52	9.52	9.52
Inner diameter (mm)	8.7	8.7	8.7	8.7	8.7	8.7
Length of test section (mm)	500	500	500	500	500	500
Inside tube area (mm^2)	13,665.9	14,514	14,938.1	15,362.1	15,951.4	16,582.8
Pitch of corrugation (mm)	–	12.7	12.7	12.7	8.46	6.35
Depth of corrugation (mm)	–	0.5	0.75	1	1	1
Helix angle (°)	–	53.875	53.875	53.875	64.07	69.95

Author's personal copy

Table 2 Experimental conditions

Controlled variable	Range
Refrigerant	R134a
Test tube material	Copper
Evaporating pressure, P_{sat}(bar)	4.14, 4.88, 5.71
Evaporating temperature, T_{sat} (°C)	10, 15, 20
Mass flux, G (kg m^{-2} s^{-1})	200, 300, 400
Heat flux, q (kW m^{-2})	19.91–30.64
Temperature difference, $\Delta T = T_{wi} - T_{sat}$, K	4.27–8.01
Average vapor quality, x	0.14–0.86

Table 3 Uncertainties of measured quantities and calculated parameters

Parameter	Uncertainty
Temperature, (T °C)	±0.1
Pressure drop, ΔP (kPa)	±0.37
Mass flow rate of refrigerant, m_{ref} (%)	±2 Full scale
Heat transfer rate of test section, Q_{TS} (%)	±15.01
Heat transfer rate of pre-heater, Q_{ph} (%)	±10.04
Average heat transfer coefficient, h_{exp} (%)	±15.01
Two-phase friction factor, f_{tp} (%)	±13.52
Average quality, x (%)	±7.63
Equivalent Reynolds number, Re_{eq} (%)	±6.03

the temperature of the test section outlet, and $i_{fg@T_{TS,o}}$ is the enthalpy of vaporisation. The outlet enthalpy of the refrigerant flow is calculated as follows:

$$i_{TS,o} = i_{TS,in} + \frac{Q_{TS}}{m_{ref}}, \tag{5}$$

where the heat transfer rate, Q_{TS}, in the test section is obtained from

$$Q_{TS} = m_{w,TS} c_{p,w} (T_{w,in} - T_{w,o})_{TS}, \tag{6}$$

where $m_{w,TS}$ is the mass flow rate of the water entering the test section, and $(T_{w,in} - T_{w,o})_{TS}$ is temperature difference between the outlet and inlet position of the test section.

3.3 The Average Heat Transfer Coefficient

$$h_{exp} = \frac{Q_{TS}}{A_{wi}(T_{wi} - T_{ref,sat})} \tag{7}$$

where h_{exp} is the experimental average heat transfer coefficient, Q_{TS} is the heat transfer rate in the test section, T_{wi} is the average temperature of the inner wall, $T_{ref,sat}$ is the average temperature of the refrigerant at the test section inlet and outlet, and A_{wi} is the inside surface area of the test section:

$$A_{wi} = \pi \mathrm{dL} \tag{8}$$

where d is the inside diameter of the test tube, and L is the length of the test tube.

3.4 Calculation Procedure for the Generalised Artificial Neural Networks (ANNs) Model

An ANN is an information-processing system that has certain performance characteristics in common with biological neural networks. ANNs have been developed as generalisations of mathematical models of human cognition or neural biology, based on the assumptions that (1) information processing occurs at many simple elements called neurons, (2) signals are passed between neurons over connection links, (3) each connection link has an associated weight, which, in a typical neural net multiplies the signal transmitted, and (4) each neuron applies an activation function (usually non-linear) to its net input (sum of weighted input signals) to determine its output signal [21].

ANNs are such factors that can utilize machine learning for the duty of considered necessary mapping of the inputs to the outputs. A dataset is divided into three parts such as training, testing and validation. ANNs determine a function between the inputs and outputs generalizing the training group. The success of this group is calculated using the test group. The training duration of ANNs is determined by the validation group. When the training group has over fitting as a result of long time training, ANNs memorize the training group and its success on the test group reduces. The optimum point for the stop of training is determined using validation group.

As the ANNs are one of the most commonly used and developed models to investigate the relationship between linear or non-linear input–output patterns, they try to generalise the training group and then estimate the test group. Performance of ANNs is measured by the success of the prediction. There are many described ANN types and their architectures (different size of layers, neuron numbers and spread coefficients) related to function approximation in the literature. The most known methods are multi layer perceptron (MLP), radial basis functions networks (RBFN), generalised regression neural networks (GRNN) and artificial neural fuzzy inference system (ANFIS) which is the combination of fuzzy logic decision systems and ANNs. Schematic diagrams of artificial intelligence models used in the analysis, obtained by Matlab software [22], are shown in Fig. 4.

3.4.1 Multi Layer Perceptron (MLP)

An artificial neuron performs the duty of taking weighted total of the inputs and evaluates it by an activation function. The single-layer perceptron is used for the linear problems and cannot be applied for the non-linear in nature. All perceptrons of MLP are arranged in an orderly manner of layers.

Author's personal copy

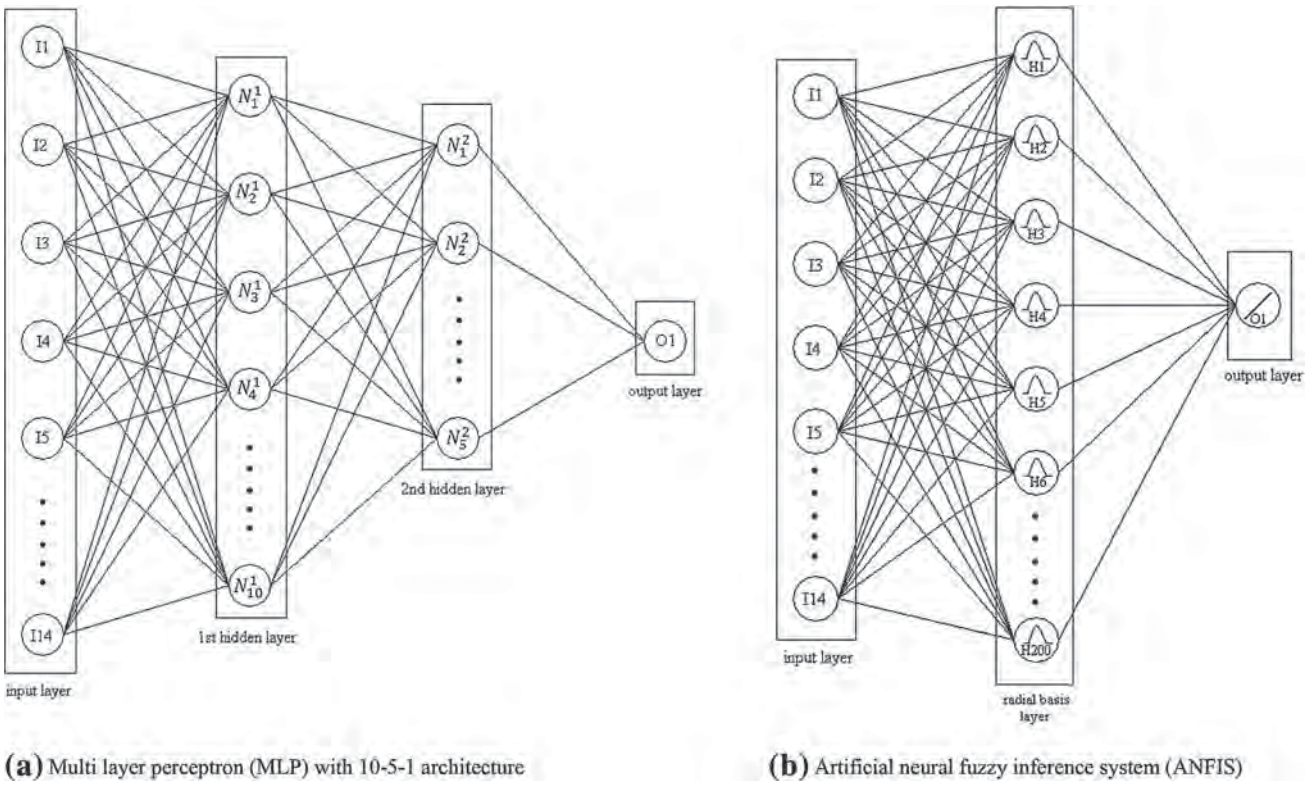

Fig. 4 Schematic diagrams of artificial intelligence models used in the analysis

The initial layer is the input layer and is called as passive layer. It should be noted that the inputs are passed to the next layer for processing after the first one. The output layer forms the last layer and is called as the active layer. These neurons take the inputs in the structure of neural connections among the neurons. Each connection has a weight connected with it. The computation of the weighted average of the input and its application to the activation function are performed by each neuron.

MLP is the member of the feed-forward network family. According to this method, the number of input and output neurons is equal to the number of input and output parameters, and there are some layers including neurons between them. Specification of non-linearity and calculation process increases with increasing numbers of hidden layers and neurons. Different architectures of MLP were used for the calculation of heat transfer coefficient and pressure drop. All neurons of MLP are connected with another neurons in the next layer making massive number of connections between the various connections and the direction of these connections are forward which means that the way of the connection among neurons is not recurrent. A Levenberg–Marquardt algorithm, based on the method of back propagation, was used for the training process to model the outputs using inputs of the problem.

3.4.2 Radial Basis Function Networks (RBFN)

This model has a simple 3-layer ANN architecture: input layer, hidden layer and output layer.

RBFN architecture has a single hidden layer and some similarities with the MLP method. On the other hand, it has a different calculation process for the determination of the neuron number, different activation function including Gaussian or exponential manner and difference in neuron number in the hidden layer. RBFN's single-layer architecture has equal neuron numbers with the element numbers in the training group. Bias numbers are the control parameters of RBFN architecture and should be determined by the user as trial and error method during calculations in Matlab Software [22]. Training of this architecture, in other words, values of neuron connections, are calculated using training group by means of least square method [22] as its training algorithm.

3.5 Correlation Development

Determination of heat transfer characteristics of compact systems such as heat transfer coefficient, frictional pressure drop, flow type between the fluids and heat transfer surface area in heat exchangers should be determined accurately for the optimum design. The two-phase heat trans-

Author's personal copy

fer systems have a higher thermal heat transfer performance than single-phase heat transfer systems in limited apparatus volumes. The advantage of high thermal performance in comparison with the single-phase applications includes smaller, more compact systems regarding tube length, tube diameter and internal tube geometry shape in a wide variety of applications, e.g. refrigeration and air conditioning systems, power engineering and other thermal processing plants. Before doing any numerical work on this subject, the validation process of the experimental setup and data is very significant with regard to the reliability of the study. The correctness of experimental data should be evaluated by either graphics regarding the characteristics of trend lines such as alteration of heat transfer coefficient versus quality, heat flux versus temperature difference between the vapour and inlet wall temperature, pressure drop versus vapour quality etc., or by widely accepted correlations in the literature, and desired working conditions should be agreeable with the heat balance correlations and flow type observations by means of sight glasses at the different points of the experimental apparatus.

There have been a number of studies on the in-tube evaporation heat transfer coefficient and pressure drop. The frictional, acceleration and gravitational components determine the two-phase total pressure drop in tubes. Determination of the void fraction is required to compute the acceleration and gravitational components, and in a similar way the determination of either the two-phase friction factor or the two-phase frictional multiplier is required to compute the frictional component of the pressure drop. Generally, empirical methods have been used to compute the evaporation heat transfer coefficients and pressure drops in tubes.

The correlation for the laminar and turbulent flow inside the test tube was developed as a form of Dittus and Boelter's [23] correlation in Eq. (9) by means of several dimensionless numbers which were defined in the following section. As a result, Eq. (9) is formed to predict the convective condensation heat transfer coefficient in terms of the above explanations as follows:

$$h = A\left(\frac{k_l}{d}\right)(\mathrm{Re}_g)^B(f_{\mathrm{tp}})^C(\mathrm{Fr})^D(x)^E(\mathrm{Bo})^F(\Delta \mathrm{T}_{\mathrm{sat}})^G(\phi_l^2)^H \times(\mathrm{We})^I\left(\Delta P\frac{L}{P}\right)^J(\mathrm{Re}_l)^K \quad (9)$$

3.6 Definition of Input Parameters of the Artificial Neural Network (ANN) Analysis

The total pressure gradient is the sum of three contributions: the gravitational pressure gradient, the momentum pressure gradient and the frictional pressure gradient as follows:

Table 4 Elimination of ANN methods belonging to all the tested tubes according to the error rates for pressure drop (a) and convective heat transfer coefficients (b) for the mass fluxes of 200, 300, 400 kg m^{-2} s^{-1} and T_{sat} = 10, 15 and 20 °C.

ΔP L^{-1} (kPa m^{-1})	Error analysis /ANN methods		Square law
	R square	Proportional (%)	
(a)			
MLP 10-5-1	0.999993	0.001677	0.043752
MLP 10-1	0.999988	0.012214	0.754229
MLP 5-1	0.999991	0.006793	0.22766
MLP 2-1	0.998872	0.054519	10.9036
RBF 1,000	0.029942	5.06416	66761.6
RBF 10,000	0.723309	3.712494	35227.66
RBF 100,000	0.980169	0.370425	502.1212
RBF 1,000,000	0.976075	0.462784	647.2979
RBF 1,000,000	0.905844	2.537781	14,664
(b)			
MLP 10-5-1	0.9999996	0.358	0.000198
MLP 10-1	0.999993	0.438	0.000316
MLP 5-1	0.999998	0.561	0.000259
MLP 2-1	0.999905	5.685	0.030739
RBF 1,000	0.447754	682.017	1,927.148
RBF 10,000	0.731676	59.682	8.71043
RBF 100,000	0.995606	18.519	0.538876
RBF 1,000,000	0.994327	22.937	0.649612
RBF 1,000,000	0.871393	98.393	2.556523

$$\frac{d\mathrm{P}}{dz} = \left(\frac{d\mathrm{P}}{dz}\right)_G + \left(\frac{d\mathrm{P}}{dz}\right)_M + \left(\frac{d\mathrm{P}}{dz}\right)_F \quad (10)$$

Pressure drop due to gravity can be determined from

$$(\Delta P)_G = -g\left(\alpha\rho_g + (1-\alpha)\rho_l\right)L \quad (11)$$

where the void fraction, a, can be determined from the Zivi correlation [24] stated below:

$$\alpha = \frac{1}{1+\left(\frac{1-x}{x}\right)\left(\frac{\rho_g}{\rho_l}\right)S} \quad (12)$$

$$S = \left(1 - x + x\frac{\rho_l}{\rho_g}\right)^{1/2} \quad (13)$$

The momentum pressure gradient can be defined as follows:

$$\left(\frac{d\mathrm{P}}{dz}\right)_M = -G^2\frac{d}{dz}\left[\frac{x^2}{\rho_g\alpha} + \frac{(1-x)^2}{\rho_l(1-\alpha)}\right] \quad (14)$$

The two-phase frictional pressure gradient can be obtained by subtracting the gravitational and momentum terms from the total measured pressure drop as follows:

Author's personal copy

Table 5 The most predictive input parameters according to the error rates for all tested tubes

Inputs														Input number	Outputs	
I	II	III	IV	V	VI	VII	VIII	IX	X	XI	XII	XIII	XIV		R^2–ΔP (%)	R^2–h (%)
0	0	0	0	0	0	0	0	0	0	0	0	1	0	1	0.614656	0.619369
0	0	0	0	0	0	0	0	0	1	0	0	0	0	1	0.606841	0.643204
0	0	0	0	0	0	0	0	0	0	0	1	0	0	1	0.561001	0.556516
1	0	0	0	0	0	0	0	0	0	0	0	0	0	1	0.271441	0.289444
0	0	0	0	1	0	0	0	0	0	0	0	0	0	1	0.219961	0.128164
0	0	0	0	0	1	0	0	0	0	0	0	0	0	1	0.215296	0.134689
0	1	0	0	0	0	0	0	0	0	0	0	0	0	1	0.178929	0.209764
0	0	0	0	0	0	0	0	0	0	1	0	0	0	1	0.124609	0.145161
0	0	1	0	0	0	0	0	0	0	0	0	0	0	1	0.080089	0.191844
0	0	0	1	0	0	0	0	0	0	0	0	0	0	1	0.038416	0.148225
0	0	0	0	0	0	1	0	0	0	0	0	0	0	1	0.000289	0.008649
0	0	0	0	0	0	0	0	1	0	0	0	0	0	1	0.0036	0.000961
0	0	0	0	0	0	0	0	0	0	0	0	0	1	1	0.088209	0.020736
0	0	0	0	0	0	0	1	0	0	0	0	0	0	1	0.093636	0.053824

Table 6 The most predictive combinations of input parameters according to the error rates for the two known input parameters

Inputs														Input number	Outputs	
I	II	III	IV	V	VI	VII	VIII	IX	X	XI	XII	XIII	XIV		R^2–ΔP (%)	R^2–h (%)
0	0	0	0	0	0	1	0	0	1	0	0	0	0	2	0.970225	0.863041
0	0	0	0	0	0	1	0	0	0	0	1	0	1	2	0.929296	0.748225
0	0	0	0	0	1	0	0	0	0	0	0	1	0	2	0.915849	0.8836
0	0	0	0	1	0	0	0	0	0	0	0	1	0	2	0.913936	0.799236
0	0	0	0	0	1	0	0	0	1	0	0	0	0	2	0.893025	0.876096
0	0	0	0	1	0	0	0	0	1	0	0	0	0	2	0.891136	0.776161
0	0	0	1	0	0	0	0	0	0	0	0	0	1	2	0.874225	0.9999
0	0	0	0	0	1	0	0	0	0	0	1	0	0	2	0.872356	0.801025
0	0	0	0	0	0	1	0	0	0	0	0	1	0	2	0.870489	0.802816
0	0	0	0	0	0	0	1	0	0	0	0	0	1	2	0.848241	0.986049
0	0	0	0	1	0	0	0	0	0	0	1	0	0	2	0.8464	0.710649
0	0	0	0	0	0	0	0	0	1	0	0	0	1	2	0.817216	0.933156
0	0	0	0	0	0	0	0	0	0	0	0	1	1	2	0.762129	0.948676
0	0	0	0	0	0	0	0	0	0	0	1	0	1	2	0.677329	0.877969
1	0	0	0	0	0	0	0	0	0	0	0	0	1	2	0.6724	0.7744
0	0	0	0	0	0	0	0	0	0	1	0	0	1	2	0.627264	0.727609
0	0	0	0	0	0	0	0	1	0	0	0	1	0	2	0.616225	0.664225
0	0	0	0	0	1	1	0	0	0	0	0	0	0	2	0.611524	0.64

$$\left(\frac{d\mathrm{P}}{dz}\right)_F = \left(\frac{d\mathrm{P}}{dz}\right)_{\mathrm{Exp}} - \left(\frac{d\mathrm{P}}{dz}\right)_G - \left(\frac{d\mathrm{P}}{dz}\right)_M \tag{15}$$

The two-phase friction factor is calculated by the following equation based on the equivalent Reynolds number:

$$f_{\mathrm{tp}} = \left(\frac{d\mathrm{P}}{dz}\right)\frac{\rho_l d^3}{2\mathrm{Re}_{\mathrm{eq}}^2 \mu_l^2}, \tag{16}$$

where the all liquid equivalent Re number is determined from

$$\mathrm{Re}_{\mathrm{eq}} = \frac{G_{\mathrm{eq}} d}{\mu_l} \tag{17}$$

and the equivalent liquid mass flux is defined as

$$G_{\mathrm{eq}} = G\left((1-x) + x\left(\frac{\rho_l}{\rho_g}\right)^{0,5}\right) \tag{18}$$

Author's personal copy

Table 7 The most predictive combinations of input parameters according to the error rates for the three known input parameters

Inputs														Input number	Outputs	
I	II	III	IV	V	VI	VII	VIII	IX	X	XI	XII	XIII	XIV		R^2–ΔP (%)	R^2–h (%)
0	0	0	0	0	0	1	0	1	0	0	0	1	0	3	0.998001	0.933156
0	1	0	0	0	0	1	0	0	0	0	0	1	0	3	0.998001	0.923521
0	0	0	0	0	0	1	0	0	1	0	0	1	0	3	0.998001	0.906304
1	0	0	0	0	0	1	0	0	0	0	0	1	0	3	0.998001	0.942841
0	0	0	0	0	0	1	0	0	0	0	1	1	0	3	0.998001	0.893025
0	0	0	0	0	0	1	0	0	0	1	0	1	0	3	0.996004	0.925444
0	0	0	0	0	0	1	0	1	0	0	1	0	0	3	0.994009	0.933156
1	0	0	0	0	0	1	0	1	0	0	0	0	0	3	0.994009	0.900601
1	0	0	0	0	0	1	0	0	1	0	0	0	0	3	0.994009	0.948676
0	0	0	0	0	0	1	0	1	1	0	0	0	0	3	0.992016	0.944784
0	0	0	0	0	0	1	0	0	0	1	1	0	0	3	0.992016	0.819025
0	0	0	0	0	0	1	0	1	0	1	0	0	0	3	0.990025	0.946729
0	1	0	0	0	0	1	0	1	0	0	0	0	0	3	0.990025	0.9409
0	1	0	0	0	0	1	0	0	1	0	0	0	0	3	0.990025	0.925444
0	0	0	0	0	0	1	1	0	1	0	0	0	0	3	0.988036	0.8836
1	1	0	0	0	0	1	0	0	0	0	0	0	0	3	0.986049	0.929296
1	0	0	0	0	0	1	0	0	0	0	1	0	0	3	0.984064	0.829921
0	0	0	0	0	0	1	0	0	1	1	0	0	0	3	0.984064	0.887364
0	0	0	0	0	0	1	0	0	1	0	1	0	0	3	0.984064	0.887364
0	0	0	0	0	0	1	1	0	0	0	1	0	0	3	0.982081	0.904401
0	0	1	0	0	0	1	0	0	0	0	1	0	0	3	0.976144	0.887364
0	1	0	0	0	0	1	0	0	0	1	0	0	0	3	0.972196	0.946729
0	0	0	0	1	0	1	0	0	1	0	0	0	0	3	0.972196	0.891136
0	0	1	0	0	0	1	0	0	1	0	0	0	0	3	0.972196	0.877969
0	0	0	0	0	1	1	0	0	1	0	0	0	0	3	0.972196	0.906304
1	0	0	0	1	0	0	0	0	0	0	0	1	0	3	0.970225	0.885481
0	0	0	0	1	0	0	0	0	0	0	1	1	0	3	0.970225	0.8836
0	0	0	0	1	0	0	0	0	1	0	0	1	0	3	0.964324	0.885481
0	1	0	0	0	1	0	0	0	0	0	1	0	0	3	0.964324	0.948676
0	0	0	0	0	0	1	0	0	1	0	0	0	1	3	0.964324	0.9801
0	1	0	0	0	0	1	0	0	0	0	0	0	1	3	0.964324	0.908209
0	0	0	0	1	0	0	0	1	1	0	0	0	0	3	0.962361	0.908209
0	0	0	0	0	1	0	0	0	0	0	1	1	0	3	0.962361	0.952576
0	0	0	0	1	0	0	0	0	0	0	0	1	0	3	0.962361	0.6724
0	1	0	0	0	1	0	0	0	0	0	0	1	0	3	0.962361	0.962361
0	0	0	0	0	1	0	0	1	0	0	0	1	0	3	0.962361	0.950625
1	0	0	0	1	0	0	0	0	1	0	0	0	0	3	0.962361	0.906304
0	0	0	0	0	1	0	0	1	1	0	0	0	0	3	0.9604	0.9409
0	1	0	0	0	1	0	0	1	0	0	0	0	0	3	0.9604	0.956484
1	1	0	0	1	0	0	0	0	0	0	0	0	0	3	0.9604	0.923521
0	0	0	0	0	1	0	0	1	0	0	1	0	0	3	0.9604	0.956484
0	0	0	0	1	0	0	1	0	0	0	0	1	0	3	0.9604	0.906304
1	0	0	0	0	1	0	0	0	0	0	1	0	0	3	0.958441	0.861184
1	0	0	0	0	1	0	0	1	0	0	0	0	0	3	0.956484	0.935089
0	1	0	0	0	1	0	0	0	1	0	0	0	0	3	0.956484	0.844561
0	0	0	0	0	1	0	0	0	1	0	0	1	0	3	0.956484	0.950625

Author's personal copy

Table 7 continued

Inputs														Input number	Outputs	
I	II	III	IV	V	VI	VII	VIII	IX	X	XI	XII	XIII	XIV		R^2–ΔP (%)	R^2–h (%)
1	0	0	0	0	1	0	0	0	1	0	0	0	0	3	0.956484	0.948676
0	1	0	0	1	0	0	0	0	0	1	0	0	0	3	0.954529	0.912025
0	1	0	0	1	0	0	0	0	0	0	0	1	0	3	0.954529	0.906304
0	0	0	0	0	0	1	1	0	0	0	0	1	0	3	0.954529	0.887364
0	0	0	0	1	0	0	0	0	1	1	0	0	0	3	0.954529	0.896809
0	0	0	0	1	0	0	0	1	0	0	0	1	0	3	0.952576	0.906304
0	0	0	0	0	0	1	0	0	0	0	0	1	1	3	0.952576	0.982081

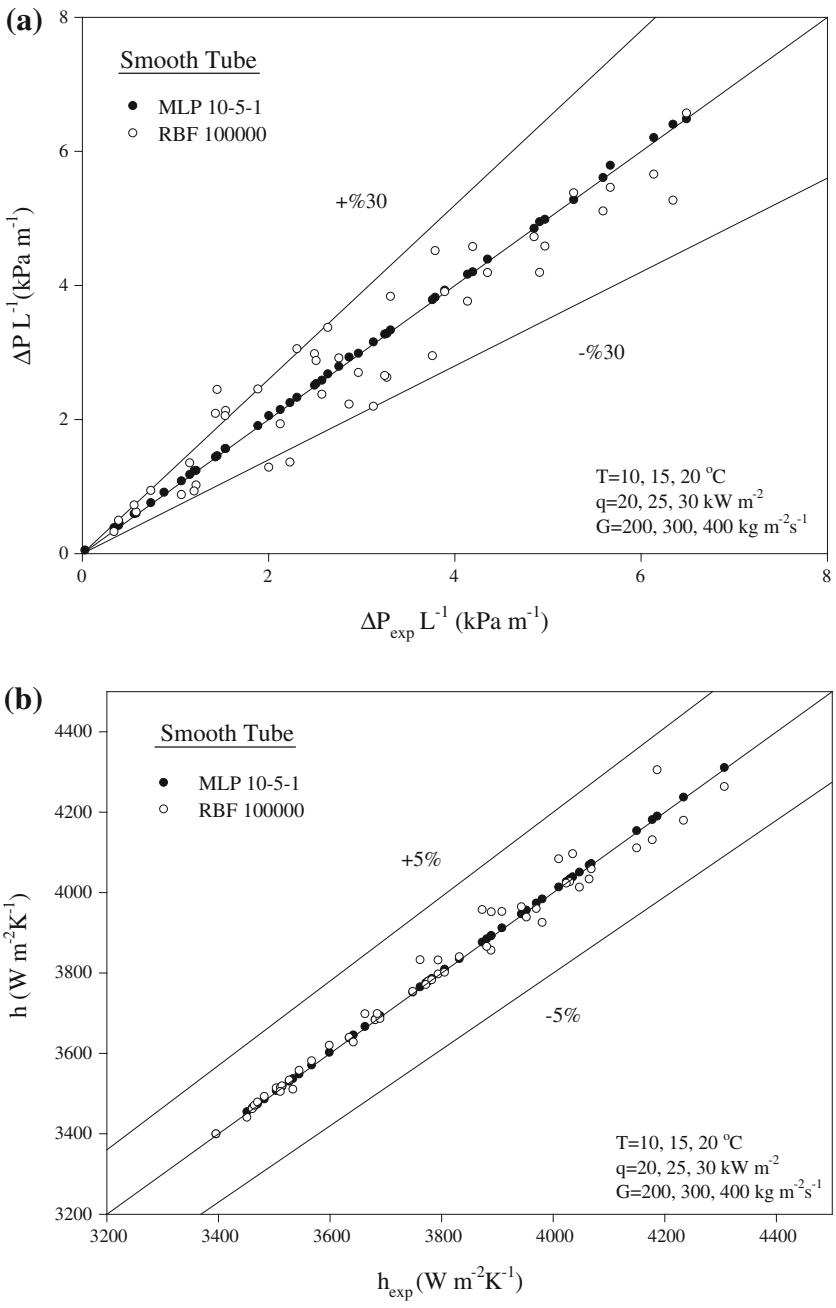

Fig. 5 Comparisons of experimental pressure drop (**a**) and convective heat transfer coefficients (**b**) with the artificial neural network methods for the smooth tube

Author's personal copy

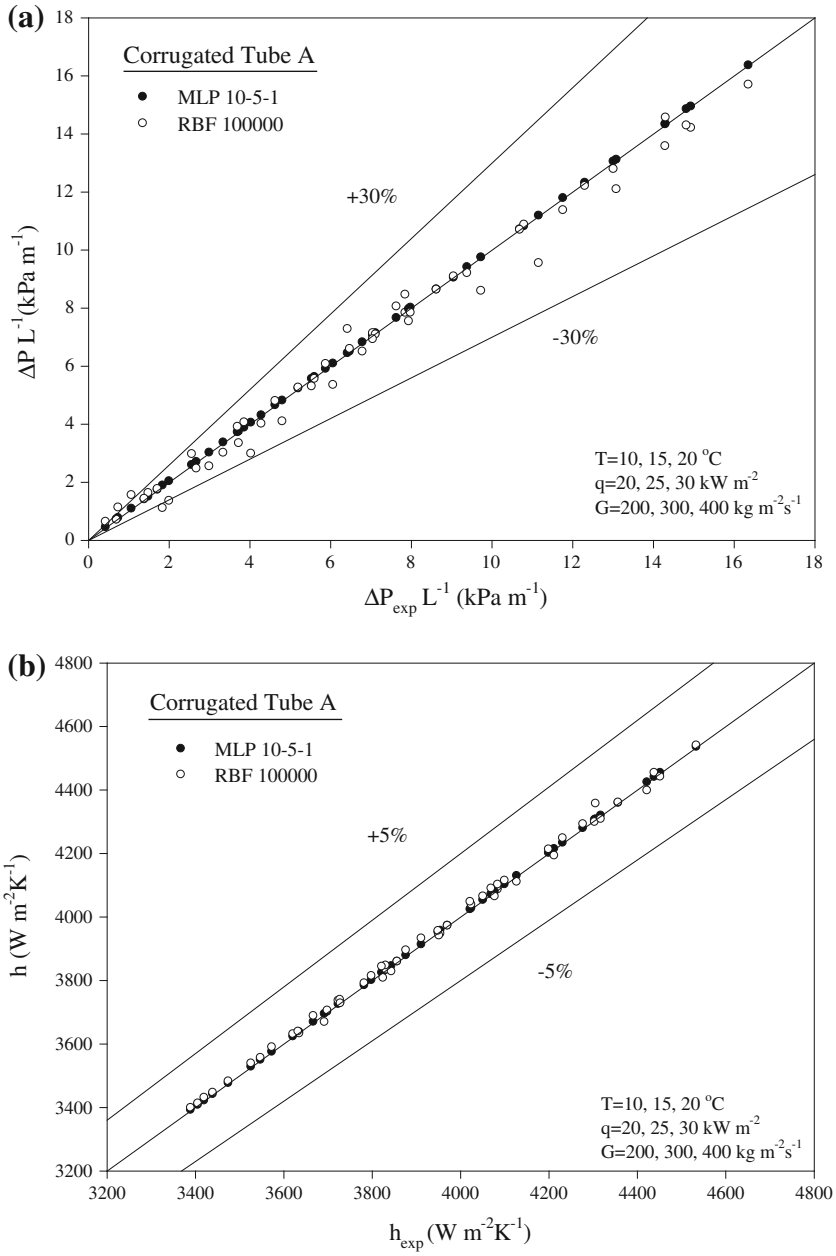

Fig. 6 Comparisons of experimental pressure drop (**a**) and convective heat transfer coefficients (**b**) with the artificial neural network methods for the corrugated tube A

Bond number (Bo), liquid and vapour Reynolds numbers ($\mathrm{Re_l}$, $\mathrm{Re_g}$), two-phase multiplier (ϕ_l^2), Froude number (Fr) and Weber number (We) are defined, respectively, as follows:

$$\mathrm{Bo} = \frac{q}{i_{\mathrm{fg}} G} \tag{19}$$

$$\mathrm{Re}_l = \frac{\mathrm{Gd}(1-x)}{\mu_l} \tag{20}$$

$$\mathrm{Re}_g = \frac{\mathrm{Gdx}}{\mu_g} \tag{21}$$

$$\phi_l^2 = 1 + \frac{C}{X} + \frac{1}{X^2} \tag{22}$$

where Martinelli parameter is defined as

$$X_{\mathrm{tt}} = \left(\frac{1-x}{x}\right)^{0.9} \left(\frac{\rho_g}{\rho_l}\right)^{0.5} \left(\frac{\mu_l}{\mu_g}\right)^{0.1} \tag{23}$$

The constant C in Eq. (22) is the parameter which indicates the two-phase flow condition. The value of this parameter, proposed by Chisholm [25] and varying from 5 to 20, depends on the flow condition of the vapour and liquid. For instance, the constant $C = 20$ when the vapour and liquid flow is in the turbulent region, and $C = 5$ if the two-phase flow is in the laminar region.

$$\mathrm{Fr} = \frac{G^2}{\mathrm{gd}\rho_{\mathrm{TP}}^2}, \tag{24}$$

Author's personal copy

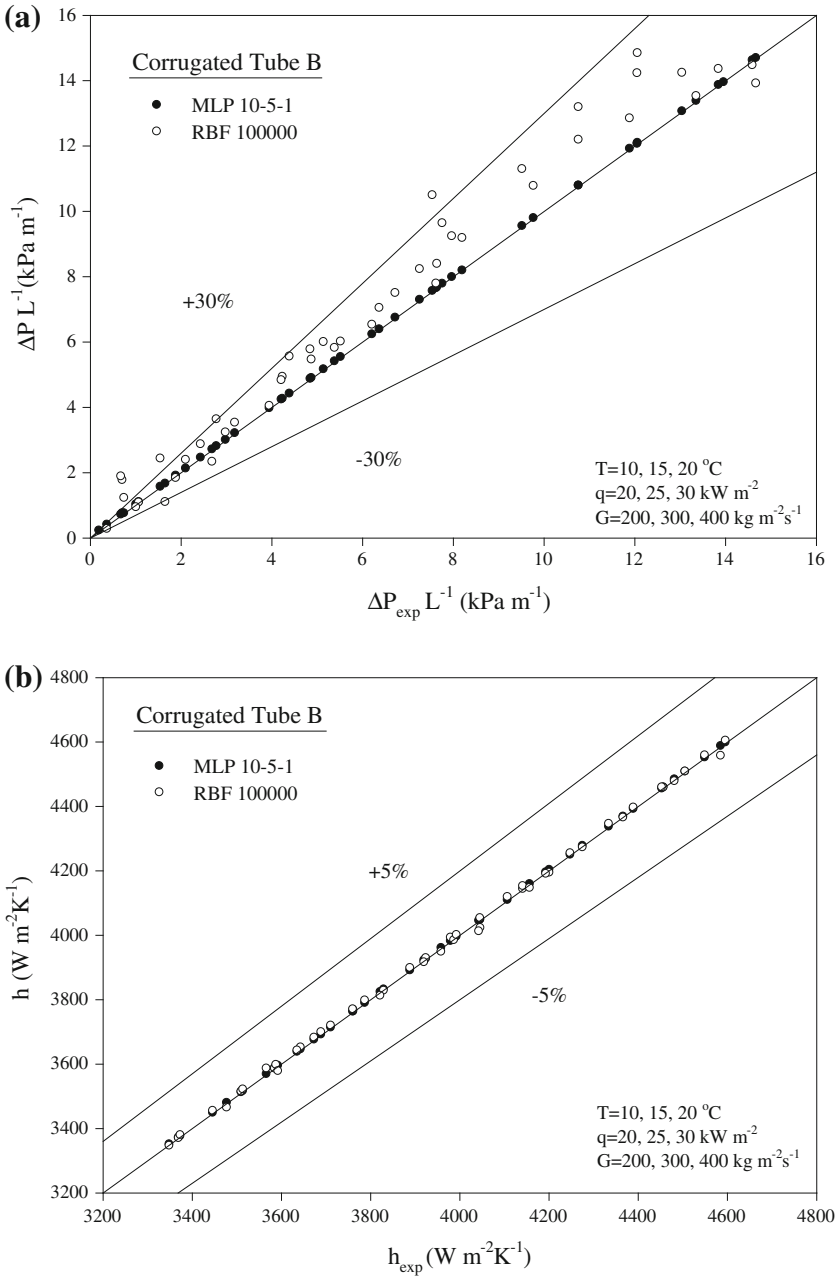

Fig. 7 Comparisons of experimental pressure drop (**a**) and convective heat transfer coefficients (**b**) with the artificial neural network methods for the corrugated tube B

where the two-phase density is determined from

$$\rho_{\mathrm{TP}} = \left(\frac{x}{\rho_g} + \frac{1-x}{\rho_l}\right)^{-1} \tag{25}$$

$$\mathrm{We} = \frac{G^{2\mathrm{d}}}{\rho_{\mathrm{TP}}\sigma} \tag{26}$$

Reynolds equivalent number, Lockhart and Martinelli parameter, Weber number, Bond and Froude numbers were used as the most significant variables in the proposed correlation. Reynolds number gives a measure of the ratio of inertial forces to viscous forces characterising different flow regimes such as laminar and turbulent flow. Lockhart and Martinelli parameter is used in internal two-phase flow calculations expressing the liquid fraction of a flowing fluid. Weber number is used for fluid flows where there is an interface between two different fluids, and it can be considered as a measure of the relative significance of the fluid's inertia compared with its surface tension. Bond number expresses the ratio of body forces to surface tension forces, low Bond numbers indicate the surface tension domination on the system and Froude number is used to compare inertial and gravitational forces. The effect of other important parameters belonging to the fluid properties such as liquid and vapour phases of

Author's personal copy

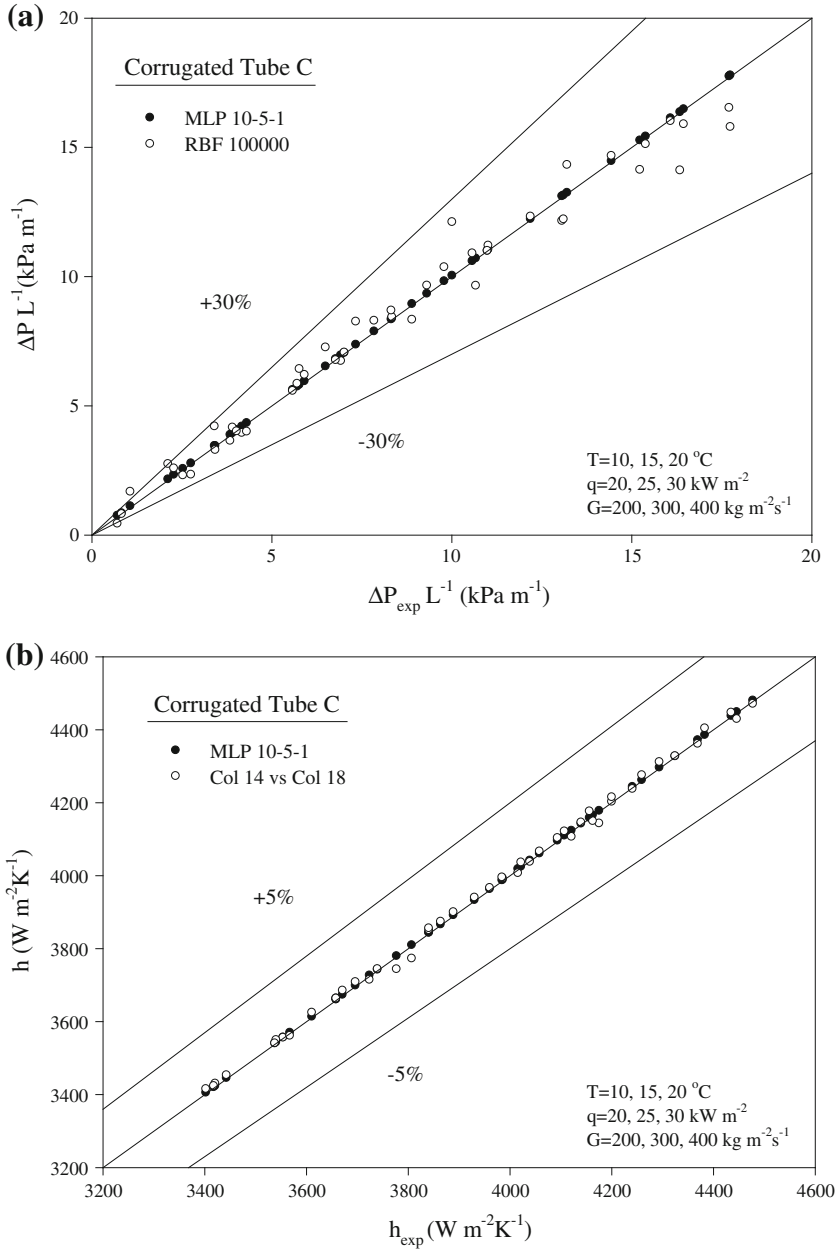

Fig. 8 Comparisons of experimental pressure drop (**a**) and convective heat transfer coefficients (**b**) with the artificial neural network methods for the corrugated tube C

density, dynamic viscosity, kinematic viscosity and thermal diffusivity exist in the Prandtl number and other dimensionless numbers.

3.7 Error Analysis

Error analysis of the study is performed by means of Eqs. (27), (28) and (29) and the results are given in Tables 4, 5, 6 and 7. In these equations, N is the element number of the test group, h^i_{exp} and h^i_{calc} are the experimental and calculated results of the heat transfer coefficient obtained from "i" number of test data, and $\overline{h}_{\text{exp}}$ and $\overline{h}_{\text{calc}}$ are the average values of experimental and calculated results of heat transfer coefficient obtained from the numerical analysis. It should be noted that error analysis of pressure drop was carried out similarly.

The R-square error is determined as follows:

$$E_{\text{Rsquare}} = \frac{\left(\sum_{i=1}^{N}(h^i_{\text{exp}} - \overline{h}_{\text{exp}})(h^i_{\text{calc}} - \overline{h}_{\text{calc}})\right)^2}{\left(\sum_{i=1}^{N}(h^i_{\text{exp}} - \overline{h}_{\text{exp}})^2\right)\left(\sum_{i=1}^{N}(h^i_{\text{calc}} - \overline{h}_{\text{calc}})^2\right)} \tag{27}$$

Proportional error is calculated as follows:

$$E_{\text{ratio}} = \frac{100}{N}\sum_{i=1}^{N}\frac{\left|h^i_{\text{exp}} - h^i_{\text{calc}}\right|}{h^i_{\text{exp}}} \tag{28}$$

Author's personal copy

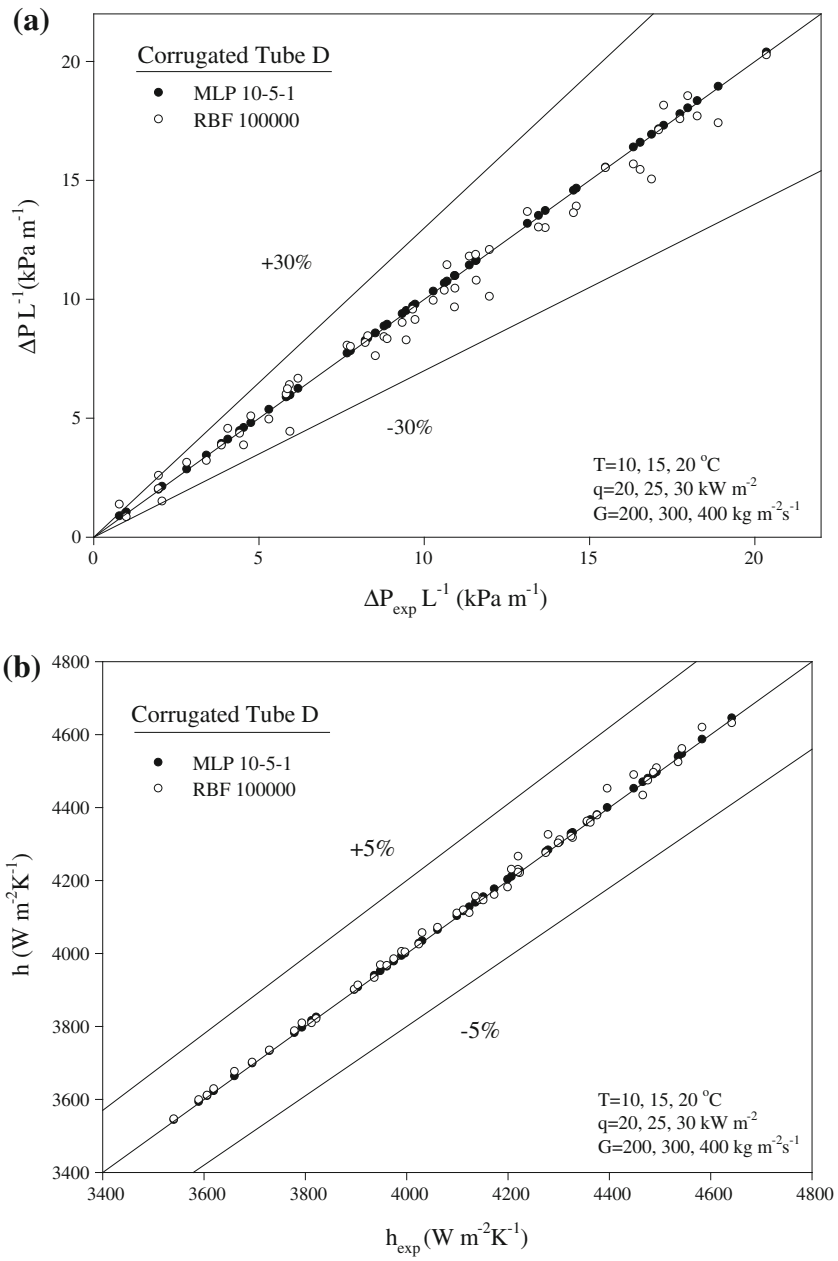

Fig. 9 Comparisons of experimental pressure drop (**a**) and convective heat transfer coefficients (**b**) with the artificial neural network methods for the corrugated tube D

Square law error is estimated as follows:

$$E_{\text{square}} = \sqrt{\frac{1}{N}.\sum_{i=1}^{N}(h^i_{\text{exp}} - h^i_{\text{calc}})^2} \tag{29}$$

4 Results and Discussion

The experiments of the present study were performed at the Fluid Mechanics, Thermal Engineering and Multiphase Flow Research Lab. (FUTURE) in KMUTT. Pure HFC-134a was used in the experiments. Special attention was paid to the accuracy of the measurements during the experiments as can be seen from authors' previous publications on in-tube evaporation processes.

Numerical analysis of artificial intelligence includes six-dimensional input parameters, such as mass flux (G, kg m^{-2} s^{-1}), heat flux (q, kW m^{-2}), saturation temperature (T_{sat}, °C), temperature difference between the tube wall and saturation temperature ($\Delta T_{\text{sat}} = T_{\text{wi}} - T_{\text{sat}}$), depth of corrugation (e, mm) and helix angle (β,°) for the tested corrugated tubes and eight-dimensionless input parameters, such as average vapour quality (x), two-phase friction factor (f_{tp}), two-phase multiplier (ϕ_l^2), liquid and vapour Reynolds numbers (Re_l, Re_g), Bond number (Bo), Froude number (Fr), Weber

Author's personal copy

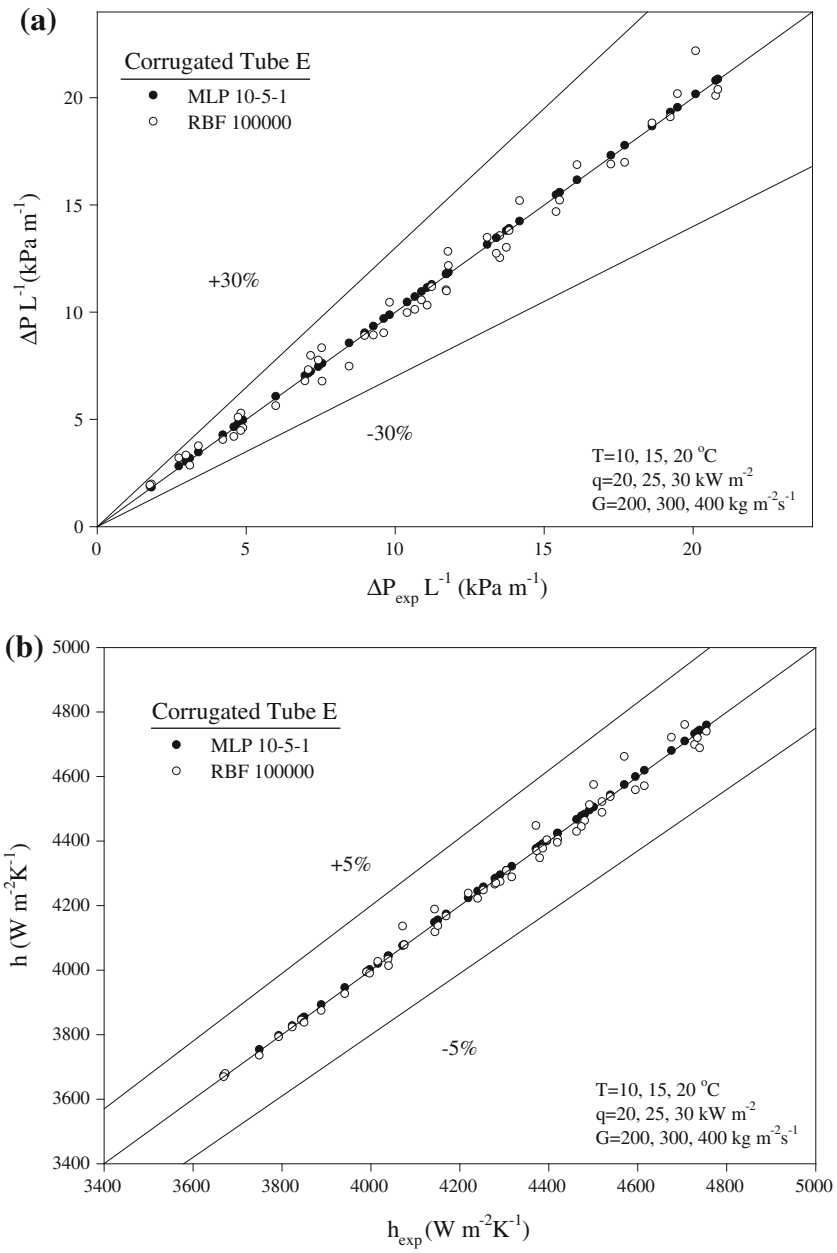

Fig. 10 Comparisons of experimental pressure drop (**a**) and convective heat transfer coefficients (**b**) with the artificial neural network methods for the corrugated tube E

number (We), two-dimensional output parameters such as convective heat transfer (h, W m^{-2} K^{-1}) and pressure drop (ΔP, Pa).

The K-fold cross validation algorithm is one of the best ways to measure the modelling success of the experimental data [26]. The coefficient of this algorithm (K) was chosen as 5. First, all data (300 data points) were divided into 5 equal sets according to this algorithm. Then, one of the 5 sets was assigned as test one, the other 4 sets became training one and the system was started to train. After that, the success rate was checked for the separated test set. At this stage, the systems' success had been measured for 1/5 data. This process was continued by changing the data sets which were used for test and training, and the success of the system was measured using the altered test set. As a result, the modelling performance of all data was measured at the end. There are several architectures tried in the analysis such as 10-5-1, 10-1 and 2-1. The random set for 20 % of the training sets was separated to prevent excess learning of the artificial intelligence during the application of the MLP algorithm. In this case, the sets of training, validation and test were determined with 192, 48 and 60 data points, respectively, during the training process of the MLP algorithm in a loop. The best architecture was investigated by changing the radial basis layer neuron number and spread coefficient as a parameter of Radial basis function (RBF). The tests were performed using the a

Author's personal copy

Table 8 Coefficients of the main proposed correlation (Eq. 9) obtained by ANN analyses

Eq. (9): $h = A(\frac{k_l}{d})(\mathrm{Re}_g)^B(f_{\mathrm{tp}})^C(\mathrm{Fr})^D(x)^E(\mathrm{Bo})^F(\Delta T_{\mathrm{sat}})^G(f_l^2)^H(\mathrm{We})^I(\Delta P\frac{L}{P})^J(\mathrm{Re}_l)^K$

Equations/ coefficients	Eq. (30)	Eq. (31)	Eq. (32)	Eq. (33)	Eq. (34)	Eq. (35)	Eq. (36)	Eq. (37)	Eq. (38)	Eq. (39)
A	60.19365	0.100143	−0.06397	3.327234	3.550174	6.20412	5.867284	21.73028	21.77796	21.70193
B	0.171773	0.516859	0.096179	−0.06397	−0.13991	−1.01466	−1.01955	−0.92148	8.05E-05	8.04E-05
C	0	−0.16681	0.511016	0.096179	0.095697	−0.00078	−0.00017	−0.00024	−0.92141	−0.92182
D	0	0	−0.13459	0.511016	0.090395	1.005651	1.001148	1.003015	−0.00036	−0.00036
E	0	0	0	−0.13459	0.55255	1.165526	1.164891	1.008696	1.003108	1.003111
F	0	0	0	0	−0.11753	−0.081	0.004695	0.002929	1.008488	−0.00047
G	0	0	0	0	0	−1.00624	−0.08187	−0.09576	0.002944	1.009437
H	0	0	0	0	0	0	−1.00106	0.092417	−0.09589	0.002547
I	0	0	0	0	0	0	0	−1.00344	0.092563	−0.09586
J	0	0	0	0	0	0	0	0	−1.00354	0.092303
K	0	0	0	0	0	0	0	0	0	−1.00353

spread coefficient of 100, 1,000, 10,000, 100,000, 1000,000, 10,000,000 and for the radial basis layer 50, 100, 150, 200, 250, 300, 350, 400, 450, 500.

The experimental data include the mass fluxes of 200, 300 and 400 kg m^{-2} s^{-1} belonging to the saturation temperatures of 10, 15 and 20 °C as shown in Table 3 and also in Figs. 5, 6, 7, 8, 9, 10, 11. Table 4 shows the best predictive method for the convective heat transfer coefficient (a) and pressure drop (b) regarding with the several error analysis such as R-square, proportional error and means square error (MSE). The performance of the method of multi-layer perception (MLP) with 10-5-1 architecture and radial basis function networks (RBFN) with the spread coefficient (sp) of 100,000 and hidden layer neuron number of 200, shown in Table 4, were found to be superior to other methods and architectures by means of satisfactory results with their deviations within the range of ±0.001677 % for the estimated pressure drop (Table 4a), and ±0.358 % for the estimated evaporation heat transfer coefficient (Table 4b). In addition to this, according to the evaporation temperatures of 10, 15 and 20 °C, comparison of the experimental heat transfer coefficients and pressure drops with those from various artificial neural network methods of test groups of all the tested tubes are shown in Figs. 5, 6, 7, 8, 9, 10 in a 30 % deviation line for the pressure drop and 5 % deviation line for the evaporation heat transfer coefficient. It can be clearly seen from these figures and tables that the radial basis function networks (RBFN) have poorer predictability of experimental data than the method of multi-layer perceptron (MLP).

In terms of the use of high data numbers for the accuracy and validation process of the experiments, numerical calculations are done by means of 300 experimental data points in all tables and figures. Tables 5, 6, 7 show the dependency of the input parameters on the outputs of the study according

Table 9 Evaluation of proposed correlations of convective heat transfer coefficient obtained from ANN analysis that belong to the all tested tubes according to the error rates for the mass fluxes of 200, 300, 400 kg m^{-2} s^{-1} and T_{sat} = 10, 15 and 20 °C

h (W m^{-2} K^{-1})	Error analysis/ANN methods		
	R square	Proportional (%)	Square law
Eq. (30)	0.536928	4.821048	53,059.02
Eq. (31)	0.766083	3.348161	26,881.77
Eq. (32)	0.852823	2.692073	16,573.89
Eq. (33)	0.8784	2.418055	13,687.29
Eq. (34)	0.901808	2.195584	11,052.15
Eq. (35)	0.999891	0.068428	12.22074
Eq. (36)	0.999952	0.040852	5.360154
Eq. (37)	0.99997	0.034258	3.372134
Eq. (38)	0.99997	0.034129	3.364506
Eq. (39)	0.99997	0.034181	3.361205

to the error rates of the test group of ANN, as a result of the most predictive ANN method of the MLP 10-5-1 architecture for the mass fluxes of 200, 300, 400 kg m^{-2} s^{-1} and evaporation temperatures of 10, 15 and 20 °C. They also show the most predictive combinations of input parameters, whose deviations are over 0.5 %, according to the error rates for the determination of evaporation heat transfer coefficient (h) and pressure drop (ΔP). The input parameters are shown with numbers in these tables as follows: average vapour quality (I), mass flux (II), evaporating temperature (III), heat flux (IV), depth of corrugation (V), helix angle of corrugation (VI), two-phase friction factor (VII), Bond number (VIII), liquid Reynolds number (IX), vapour Reynolds number (X), two–phase multiplier (XI), Froude number (XII),Weber number (XIII) and temperature difference between the tube wall and

Author's personal copy

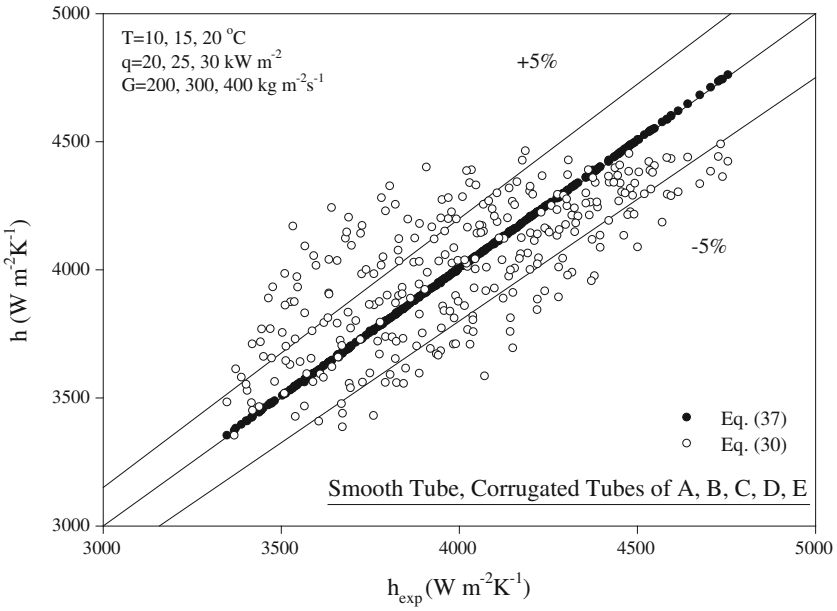

Fig. 11 Comparisons of experimental convective heat transfer coefficients (**b**) with the proposed empirical correlations by artificial neural network methods for all tubes

saturation temperature (XIV). Table 5 shows each input parameter's predictability of the outputs of experimental pressure drop and evaporating heat transfer coefficient separately. They are ordered from the best predictive to the worst predictive one in all tables considering the experimental pressure drop. For instance, artificial intelligence was able to determine the experimental pressure drop and evaporation heat transfer coefficient with an accuracy of over 74 % by means of the separate use of inputs of vapour Reynolds number (X), Froude number (XII) and Weber number (XIII) in Table 5. In Tables 6 and 7, neural network analyses tried to determine the outputs by means of two and three known input combinations. Prediction rates on these tables increase with increasing added input numbers due to the result of the learning process of the artificial intelligence. For example, when the helix angle of corrugation (VI) and two-phase friction factor (VII) are selected as known inputs in Table 6, their predictabilities are found as 78.2 and 80 % for the outputs of pressure drop and heat transfer coefficient, respectively. In Table 7, when the vapour Reynolds number (X) is added to the selected inputs of the helix angle of corrugation (VI) and two-phase friction factor (VII), the prediction rate increases to 98.6 % for the pressure drop and 95.2 % for the evaporating heat transfer coefficient in comparison with the former situation. As a result, it is possible to derive many results from these figures on the input combination performance. For another example, it should be noted that in spite of the rather low self-prediction rate of two-phase friction factor (IV) in Table 5, it produced a good combination with others and increased the predictability in these tables.

The correlation development study results are shown in Tables 8 and 9, and also in Fig. 11. The main frame of the proposed correlation is shown in Eq. (9) which has 12 possible dominant parameters on the evaporation heat transfer coefficient. Artificial intelligence decided the coefficients of these significant parameters step by step in Table 8 and their error rates can be seen in Table 9. It is possible to see the success of each term in Eq. (9) in this table. It also shows that the accuracy of the estimated output values by means of added input values increases with increasing added proper input parameters into Eq. (9). Equation (30) is found to have the lowest predictability, while Eq. (37) has the optimum predictability in Table 9 and their performance comparison is shown in Fig. 11. The majority of the data obtained from the ANN analysis of Eq. (30) fall between the deviations of ±5 % in this figure. It can be seen that Eq. (37) showed a great success with its accuracy in Fig. 11.

A large number of graphics could be generated from the output of the calculations; however, due to space limitation only the typical results are shown from the experimental database of the authors. It should also be noted that detailed information on the evaporation heat transfer characteristics of the study with some additional figures and different experimental parameters can be seen in the authors' previous publications.

5 Conclusion

Comparison of the numerical evaporation heat transfer coefficient and pressure drop values with the measured values by means of artificial intelligence methods was performed in this paper. There is no research on the content of this paper considering its parameters in current literature. The results of this study are expected to fill this gap in the literature.

Except for the different architectures of the artificial neural network (ANN) methods of multi-layer perceptron (MLP)

Author's personal copy

and radial basis networks (RBFN), the performance of the method of MLP with 10-5-1 architecture and RBFN with the spread coefficient of 100,000 are found to be capable of predicting the evaporation heat transfer coefficient and pressure drop of R134a in a vertical tube within the range of ±30 % and also within very small error rates.

Convective heat transfer coefficient and pressure drop of R134a in the paper are found to be dependent on mass flux, heat flux, the temperature difference between the tube wall and saturation temperature, average vapour quality, evaporating temperature, two-phase friction factor, two-phase multiplier, liquid and vapour Reynolds numbers, Bond number, Froude number, Weber number, depth of corrugation and helix angle for the tested corrugated tubes according to the results of the analysis.

The new empirical correlations, based on this simple architecture which have never appeared in the literature, for predicting the convective heat transfer coefficient valid for the evaporation process in a smooth tube and five different corrugated tubes, are proposed for practical applications.

Acknowledgments The first author wishes to thank King Mongkut's University of Technology Thonburi (KMUTT) for providing him with a Post-doctoral fellowship. The third and fourth authors wish to thank the Thailand Research Fund, the Office of the Higher Education Commission and the National Research University Project for financial support for this study.

References

1. Nozu, S.; Honda, H.; Nakata, H.: Condensation of refrigerants CFC11 and CFC113 in the annulus of a double-tube coil with an enhanced inner tube. Exp. Therm. Fluid Sci. **11**, 40–51 (1995)
2. Nozu, S.; Honda, H.; Nishida, S.: Condensation of a zeotropic CFC 114-CFC 113 refrigerant mixture in the annulus of a double-tube coil with an enhanced inner tube. Exp. Therm. Fluid Sci. **11**, 364–371 (1995)
3. Dong, Y.; Huixiong, L.; Tingkuan, C.: Pressure drop, heat transfer and performance of single-phase turbulent flow in spirally corrugated tubes. Exp. Therm. Fluid Sci. **24**, 131–138 (2001)
4. Zimparov, V.: Enhancement of heat transfer by a combination of three-start spirally corrugated tubes with a twisted tape. Intern. J. Heat Mass Transf. **44**, 551–574 (2001)
5. Zimparov, V.: Enhancement of heat transfer by a combination of a single-start spirally corrugated tubes with a twisted tape. Exp. Therm. Fluid Sci. **25**, 535–546 (2002)
6. Zimparov, V.: Prediction of friction factors and heat transfer coefficients for turbulent flow in corrugated tubes combined with twisted tape inserts. Part 1: friction factors. Intern. J. Heat Mass Transf. **47**, 589–599 (2004)
7. Zimparov, V.: Prediction of friction factors and heat transfer coefficients for turbulent flow in corrugated tubes combined with twisted tape inserts. Part 2: heat transfer coefficients. Intern. J. Heat Mass Transf. **47**, 385–393 (2004)
8. Nafey, A.S.: Neural network based correlation for critical heat flux in steam-water flows in pipes. Intern. J. Therm. Sci. **48**, 2264–2270 (2009)
9. Wang, W.J.; Zhao, L.X.; Chun-Lu, Z.: Generalized neural network correlation for flow boiling heat transfer of R22 and its alternative refrigerants inside horizontal smooth tubes. Intern. J. Heat Mass Transf. **49**, 2458–2465 (2006)
10. Scalabrin, G.; Condosta, M.; Marchi, P.: Mixtures flow boiling: modeling heat transfer through artificial neural networks. Intern. J. Therm. Sci. **45**, 664–680 (2006)
11. Scalabrin, G.; Condosta, M.; Marchi, P.: Modeling flow boiling heat transfer of pure fluids through artificial neural networks. Intern. J. Therm. Sci. **45**, 643–663 (2006)
12. Wongwises, S.; Disawas, S.: Two-phase evaporative heat transfer coefficients of refrigerant HFC-134a under forced flow conditions in a small horizontal smooth tube. Intern. Commun. Heat Mass Transf. **27**, 35–48 (2000)
13. Sripattrapan, W.; Wongwises, S.: Two-phase flow of refrigerants during evaporation under constant heat flux in a horizontal tube. Intern. Commun. Heat Mass Transf. **32**, 386–402 (2005)
14. Wongwises, S.; Polsongkram, M.: Evaporation heat transfer and pressure drop of HFC-134a in a helically coiled concentric tube-in-tube heat exchanger. Intern. J. Heat Mass Transf. **49**, 658–670 (2006)
15. Kaew–On, J.; Wongwises, S.: Experimental investigation of evaporation heat transfer coefficient and pressure drop of R-410A in a multiport mini-channel. Intern. J. Ref. **32**, 124–137 (2009)
16. Posew, K.; Laohalertdecha, S.; Wongwises, S.: Evaporation heat transfer enhancement of R-134a flowing inside smooth and microfin tubes using the electrohydrodynamic technique. Energy Conv. Manag. **50**, 1851–1861 (2009)
17. Laohalertdecha, S.; Wongwises, S.: An experimental study into the evaporation heat transfer and flow characteristics of R-134a refrigerant flowing through corrugated tubes. Intern. J. Ref. **34**, 280–291 (2011)
18. Aroonrat, K.; Wongwises, S.: Evaporation heat transfer and friction characteristics of R-134a flowing downward in a vertical corrugated tube. Exp. Therm. Fluid Sci. **35**, 20–28 (2011)
19. Balcilar, M.; Dalkilic, A.S.; Wongwises, S.: Artificial neural network techniques for the determination of condensation heat transfer characteristics during downward annular flow of R134a inside a vertical smooth tube. Intern. Commun. Heat Mass Transf. **38**, 75–84 (2011)
20. Colorado, D.; Ali, M.E.; Garcia-Valladares, O.; Hernandez, J.A.: Heat transfer using a correlation by neural network for natural convection from vertical helical coil in oil and glycerol/water solution. Energy **36**, 854–863 (2011)
21. Fausett, L.: Fundamentals of neural networks, architectures, algorithms, and applications, Prentice-Hall, Inc. Press, Prentice–Hall (1994)
22. Matlab, R2010a, 2010, http://mathworks.com/
23. Dittus, F.W.; Boelter, L.M.E.: Engineering publication, vol. 2, p. 443, University of California, California (1930)
24. Zivi, S.M.: Estimation of steady-state steam void-fraction by means of the principle of minimum entropy production. Trans. ASME J. Heat Transf. Ser. C **86**, 247–252 (1975)
25. Chisholm, D.: Pressure gradients due to friction during the flow of evaporating two-phase mixtures in smooth tubes and channels. Intern. J. Heat Mass Transf. **16**, 347–358 (1973)
26. Duda, R.O.; Hard, P.E.; Stork, D.G.: Pattern classification (2nd Edn). Wiley, New York (2002)

Heat Mass Transfer (2014) 50:469–482
DOI 10.1007/s00231-013-1252-6

ORIGINAL

Prediction of heat transfer coefficients and friction factors for evaporation of R-134a flowing inside corrugated tubes

S. Laohalertdecha · K. Aroonrat · A. S. Dalkilic · O. Mahian · S. Kaewnai · S. Wongwises

Received: 12 May 2012 / Accepted: 17 September 2013 / Published online: 27 October 2013
© Springer-Verlag Berlin Heidelberg 2013

Abstract In this study, experimental and simulation studies of the evaporation heat transfer coefficient and pressure drop of R-134a flowing through corrugated tubes are conducted. The test section is a horizontal counter-flow concentric tube-in-tube heat exchanger 2.0 m in length. A smooth tube and corrugated tubes with inner diameters of 8.7 mm are used as the inner tube. The outer tube is made from a smooth copper tube with an inner diameter of 21.2 mm. The corrugation pitches used in this study are 5.08, 6.35, and 8.46 mm. Similarly, the corrugation depths are 1, 1.25, and 1.5 mm, respectively. The results show that the maximum heat transfer coefficient and pressure drop obtained from the corrugated tube are up to 22 and 19 % higher than those obtained from the smooth tube, respectively. In addition, the average difference of the heat transfer coefficient and pressure drop between the simulation model and experimental data are about 10 and 15 %, respectively.

S. Laohalertdecha · K. Aroonrat · S. Kaewnai · S. Wongwises (✉)
Fluid Mechanics, Thermal Engineering and Multiphase Flow Research Lab. (FUTURE), Department of Mechanical Engineering, Faculty of Engineering, King Mongkut's University of Technology Thonburi, Bangmod, Bangkok 10140, Thailand
e-mail: somchai.won@kmutt.ac.th

A. S. Dalkilic
Heat and Thermodynamics Division, Department of Mechanical Engineering, Yildiz Technical University, Yildiz, Besiktas, 34349 Istanbul, Turkey

O. Mahian
Young Researchers and Elite Club, Mashhad Branch, Islamic Azad University, Mashhad, Iran

List of symbols

A	Surface area of the test section (m^2)
c_p	Specific heat at constant pressure (J/kg °C)
d	Inner diameter (m)
D	Outer diameter (m)
e	Corrugation depth (mm)
f	Friction factor
G	Mass flux (kg/m^2 s)
h	Heat transfer coefficient (W/m^2 °C)
i	Enthalpy (J/kg)
i_f	Enthalpy of the saturated liquid (J/kg)
i_{fg}	Enthalpy of vaporization (J/kg)
k	Thermal conductivity (W/m °C)
L	Length of the test tube (m)
LMTD	Logarithmic mean temperature difference
m	Mass flow rate (kg/s)
Nu	Nusselt number
p	Corrugation pitch (mm)
Pr	Prandtl number
Q	Heat transfer rate (W)
Re	Reynolds number
q''	Heat flux (W/m^2)
T	Temperature (°C)
U	Overall heat transfer coefficient (W/m^2 K)
x	Vapour quality
X	Martinelli parameter

Greek letters

α	Void fraction
β	Helix angle (degree)
ε	Relative roughness (m)
ρ	Density (kg/m^3)
ϕ_l^2	Two-phase multiplier
μ	Dynamic viscosity (Pa s)
ΔP	Pressure drop (Pa/m)

Subscripts

a	Acceleration
avg	Average
eq	Equivalent
f	Friction
g	Gravitation
i	Inside
in	Inlet
l	Liquid
o	Outside
out	Outlet
ph	Pre-heater
ref	Refrigerant
sat	Saturation
tp	Two-phase
$T_{TS,in}$	Based on temperature of the test section inlet
$T_{TS,out}$	Based on temperature of the test section outlet
TS	Test section
v	Vapor
w	Water

1 Introduction

Heat transfer enhancement techniques can be used to reduce the thermal resistance in a conventional heat exchanger by promoting a higher convection heat transfer coefficient and to minimize the size of the heat exchanger for a given heat duty. One of them is using a corrugated tube to replace the smooth tube. Typically, for the corrugated tube, the increase in heat transfer coefficient is higher than that in pressure drop. The corrugated tube can improve the performance of the heat exchanger by increasing fluid mixing, unsteadiness, turbulence flow, or limiting the growth of the fluid boundary layers close to the heat transfer surfaces. Corrugated tubes are sometimes chosen in the design of industrial shell-and-tube heat exchangers for heat transfer enhancement purpose. As a result, many researchers have investigated the heat transfer performance and flow characteristics of corrugated tubes. Several subsequently published articles involving the use of corrugated tubes are described in the following sections.

Nozu et al. [1, 2] investigated local heat transfer and pressure gradients in pure R-114, R-113, and a zeotropic refrigerant mixture during condensation in a tube-in-tube heat exchanger. A corrugated copper tube with an O.D. of 19.1 mm was used as the test section. Mass flows were tested in the range from 80 to 240 kg/m^{2}s. The results showed that the frictional pressure gradient and heat transfer data were correlated by the prediction method presented in this study with a mean absolute deviation of 11 and 13 %, respectively.

Dong et al. [3] investigated the turbulent friction and heat transfer characteristics of four spirally corrugated tubes with various geometrical parameters. Water and oil were used as the working fluids. The experimental conditions gave Reynolds numbers ranging from 6,000 to 93,000 for water and from 3,200 to 19,000 for oil. Their results showed that the heat transfer enhancement varied from 30 to 120 %, while the friction factor increased from 60 to 160 % when compared with a smooth tube.

Barba et al. [4] experimentally studied the heat transfer and pressure drop of single phase flows in a corrugated tube that could be used in the chemical and food industries. The Reynolds number ranged from 100 to 800. Ethylene glycol was used as the working fluid. The results gave a heat transfer enhancement of around 100 %, while the friction factor increased between 83 and 145 % compared to the smooth tube. Based on the experimental data, Nusselt number and friction factor correlations were proposed for the fully developed region.

Rainieri and Pagliarini [5] studied experimentally the thermal performance of corrugated tubes in an attempt to increase the convection heat transfer. Helical and transverse corrugated tubes with different pitch values were used as the test section. Ethylene glycol was employed as the working fluid. The test conditions were conducted at Reynolds numbers ranging from 90 to 800. A comparison of helical and transverse corrugated tubes to a smooth tube demonstrated that the transverse corrugated tubes give higher heat transfer enhancement than the helical corrugated tubes.

Among these previous studies, the most productive studies have been performed by Zimparov [6]. The heat transfer enhancement of a combination of three-start spirally corrugated tubes with a twisted tape was investigated. Two three-start spirally corrugated tubes combined with five twisted tape inserts with different relative pitches were employed as the test section. The experimental conditions were conducted at Reynolds numbers ranging from 3,000 to 60,000. There were two corrugated tubes with the height-to-diameter ratio (e/Di) of 0.0407 and 0.0569. Five twisted tapes with different relative pitch (H/Di) of 15.3, 12.2, 7.7, 5.8, and 4.7 were used in this study. The results showed that the friction factor and heat transfer coefficients of three-start spirally corrugated tubes with a twisted tape insert were significantly higher than those of a smooth tube under the same operating conditions.

Zimparov [7] presented the heat transfer enhancement using a combination of single-start spirally corrugated tubes with a twisted tape. The friction factors and inside heat transfer coefficients obtained from these tubes were higher than those obtained from the smooth tube under a given condition. In addition, Zimparov [8, 9] applied a simple mathematical model to predict the friction factors

and heat transfer coefficients in a spirally corrugated configuration combined with twisted tape inserts under the turbulent flow regime. The calculated friction factors and heat transfer coefficients were compared with the experimental data. The results showed that the agreement between the predicted and experimental data was fairly good.

Rousseau et al. [10] presented a mathematical formulation and numerical method to investigate the heat transfer and pressure drop characteristics of a fluted tube refrigerant-to-water condenser. In this model, the surface area was divided into three regions as follows: superheated, two-phase, and sub-cooled regions in which all properties of the refrigerant and water can be calculated. The proposed model was formulated based on the effectiveness-NTU method. For the water side, the existing empirical correlations for the friction factor and heat transfer coefficient were used. Unfortunately, for the refrigerant side, it was reported that there were no available correlations for calculating the friction factor and heat transfer coefficient of the fluted tube-in-tube condenser. Thus, the existing correlations for a smooth tube combined with an enhancement ratio based on the available correlations for helical coils as well as an enhancement factor based on empirical data for a fluted tube condenser were employed. Data for two commercial fluted tube heat exchangers were used to validate the proposed model. The average difference between the measured and the predicted pressure drop was 7.27 %. Similarly, the log mean temperature difference was 4.41 %.

Vicente et al. [11, 12] presented measurements of the mixed convection heat transfer and isothermal pressure drop in corrugated tubes for laminar, transition, and turbulent flow regions. Water and ethylene glycol were used as the working fluids. The results indicated that corrugated tubes gave a higher pressure drop and heat transfer coefficient than the smooth tube. The pressure drop obtained from the laminar to transition flow and turbulent flow increased by up to 25 and 300 %, respectively. Similarly, the Nusselt number obtained from laminar to transition flow and turbulent flow increased by up to 30 and 250 %, respectively.

Targanski and Cieslinski [13] experimentally studied the heat transfer coefficient and pressure drop of pure R407C and R407C/oil mixtures during evaporation inside a smooth stainless steel tube, smooth copper tubes, and two enhanced tubes. The inlet and outlet vapor quality were set at 0 and 0.7, respectively. The mass flow was varied from 250 to 500 kg/m^{2}s. The average saturation temperature was 0 °C. It was found that the heat transfer coefficient and pressure drop for the enhanced tubes were distinctly higher than those of the smooth tube. The maximum heat transfer enhancement factor and pressure drop penalty factor for the corrugated tube were 1.25 and 1.8, respectively.

Laohalertdecha and Wongwises [14–16] experimentally investigated the effect of pitch on the heat transfer coefficient and pressure drop of R134a flowing in corrugated tubes under condensation and evaporation conditions. The results indicated that the heat transfer coefficient and pressure drop obtained from the corrugated tube were higher than those of the smooth tube for all of the experimental conditions. Moreover, the results also showed that the corrugation surface promotes turbulent flow significantly. However, the effect of pitch on the heat transfer coefficient had absolute significance of high average quality. On the other hand, the effect of pitch on pressure drop was insignificant.

In addition, Laohalertdecha and Wongwises [17] formed heat transfer coefficient and two-phase friction factor correlations using approximately 200 data points for five different corrugated tube geometries and then proposed, in terms of Nusselt numbers, equivalent Reynolds numbers, Prandtl numbers, corrugation pitch and depth, and inside diameters. The results showed that 81 % of the Nusselt number data and 79 % of the two-phase friction factor data fell within a deviation of ±20 %.

As mentioned above, a number of researchers have studied mainly the effect of corrugated tubes on heat transfer and flow characteristics in a single phase. The results show that corrugated tubes have greater heat transfer potential than smooth tubes. However, very few studies have been conducted on the heat transfer and flow characteristics of the two-phase flow of the refrigerants through a corrugated copper tube. The effects of corrugation pitch and depth on the evaporation heat transfer coefficient and pressure drop of the refrigerant flowing inside horizontal corrugated tubes remain unstudied. Similarly, there is still no simulation model to determine the heat transfer and flow behaviour of a refrigerant flowing inside a corrugated tube. As a consequence, this study mainly presents the effect of pitch and depth on the evaporation heat transfer coefficient and pressure drop of R-134a flowing through corrugated copper tubes. In addition, a simulation model of the heat transfer coefficient and pressure drop during the evaporation of R-134a flowing through corrugated tubes is also investigated.

2 Experimental apparatus and procedure

A schematic diagram of the test apparatus is shown in Fig. 1. The experimental apparatus was designed to determine the heat transfer coefficient and pressure drop of pure R-134a over the length of the test tube. The test loop consists of a test section, refrigeration loop, cooling water flow loops, sub-cooling loop and relevant instrumentation. The objective of the water loop before the test section is to

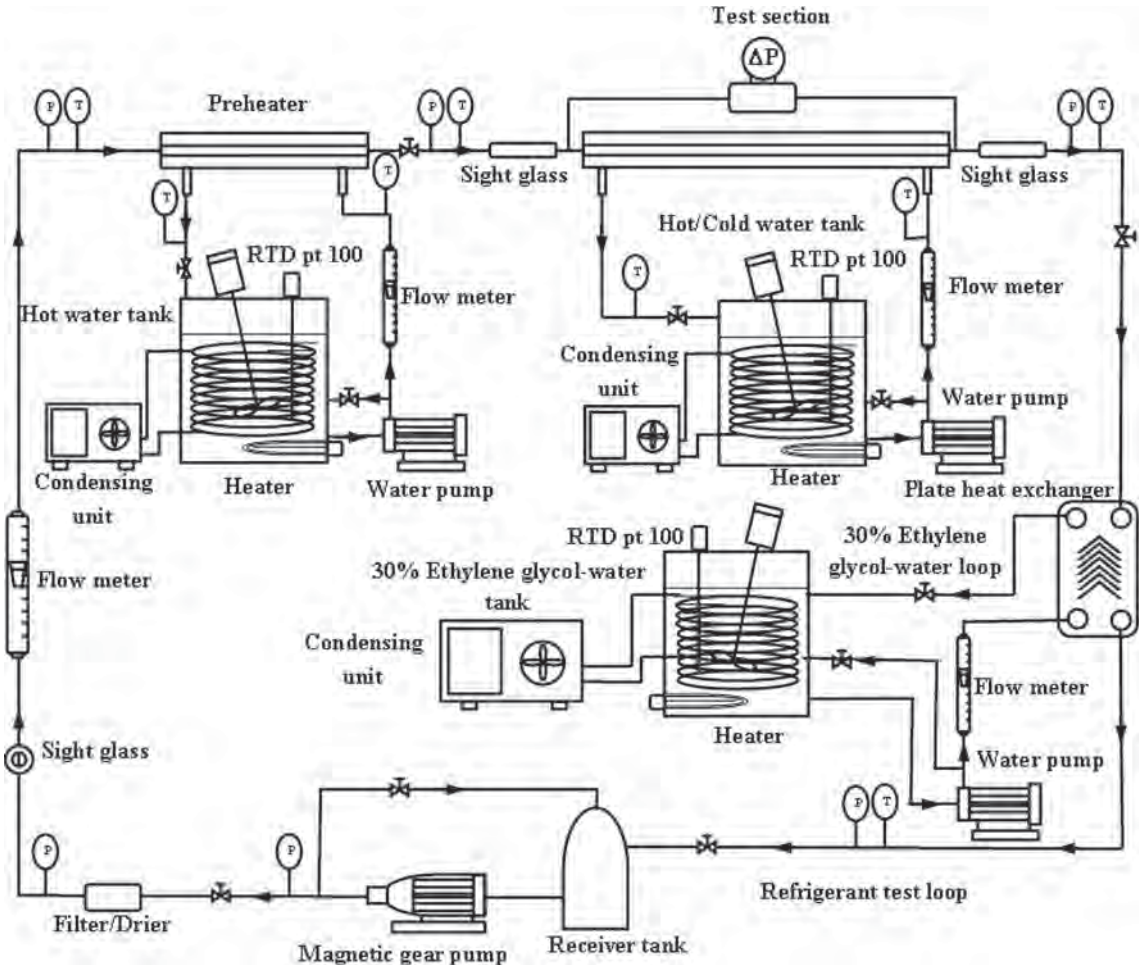

Fig. 1 Schematic diagram of the experimental apparatus (Laohalertdecha and Wongwises [14], with permission from Elsevier)

provide a controlled inlet vapour quality. The second water loop located in the test section provides a controlled heat output from the test section. The sub-cooling loop is used to prevent any two-phase flow condition of the refrigerant occurring before it enters the refrigerant pump.

For the refrigeration circulating loop, liquid refrigerant is discharged by a gear pump regulated by an inverter. The refrigerant passes in series through a filter/dryer, a sight glass tube, flow meter, pre-heater and enters the test section. The inlet vapour quality before entering the test section is controlled by the pre-heater. The pre-heater is a spiral counter flow heat exchanger that supplies energy to provide a controlled inlet vapour quality for vaporization of the refrigerant. On leaving the test section, the refrigerant is then condensed and sub-cooled by a chilling loop that removes the heat input from the pre-heater and test section and then it returns from the two-phase refrigerant to a sub-cooled state, which later collects in a receiver and eventually returns to the refrigerant pump to complete the cycle.

The test section is a horizontal counter-flow double tube heat exchanger. The length of the heat exchanger is 2,000 mm. The detailed dimensions of the heat exchanger and the location of the thermocouples are shown in Fig. 2. A photograph of a corrugated tube and nomenclature to describe the geometry is shown in Fig. 3. The dimensions of the test section are shown in Table 1.

The inlet temperature of the water is controlled by a thermostat. A differential pressure transducer and thermocouples are installed in the test section to measure the pressure drop and temperature across the test section. The length between pressure taps is 2,500 mm. In the present study, the pressure of the refrigerant is mainly controlled by a high-pressure limit switch. High-pressure limit switches (Danfoss Type KP 5) are devices for regulating the pressure of a system so that the pressure is maintained near a desired set point pressure in order to prevent the damage to the apparatus.

The refrigerant temperature and tube wall temperature in the test section are measured by T-Type thermocouples. A total of 15 thermocouples are soldered to the top, bottom and at five points along side of the tube as shown in Fig. 2. All the temperature measuring devices are well calibrated in

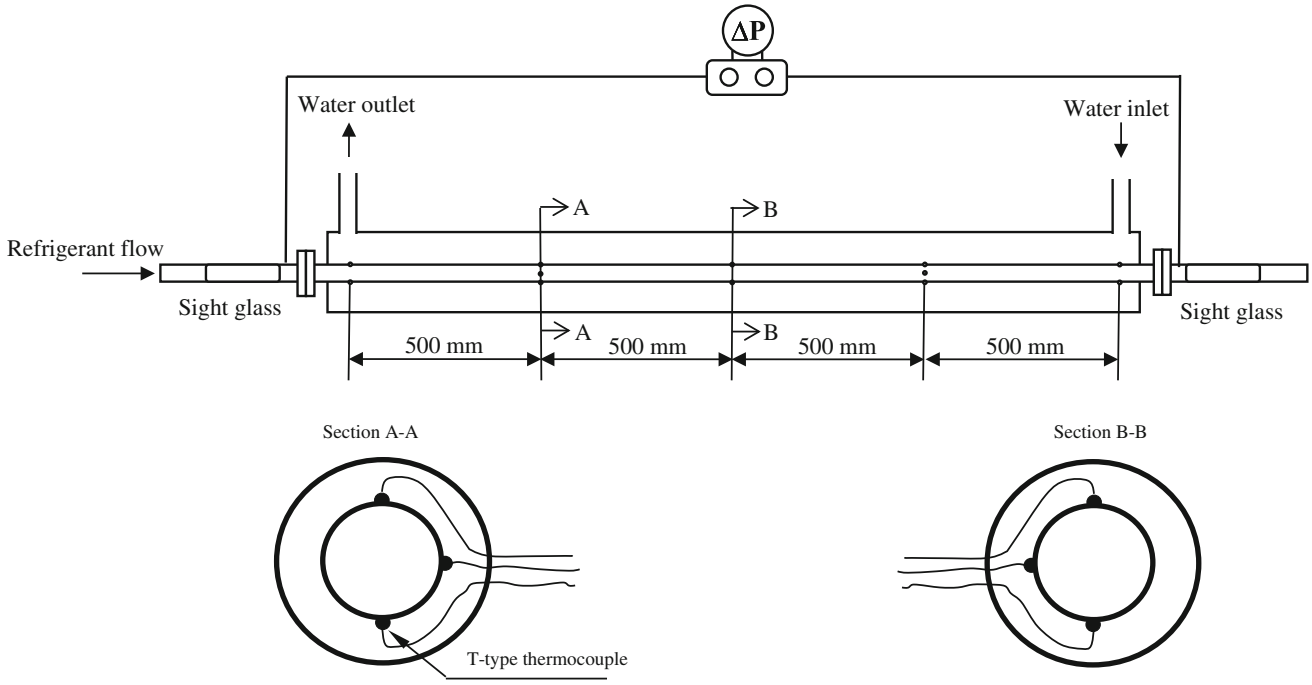

Fig. 2 Schematic diagram of the test section (Laohalertdecha and Wongwises [14], with permission from Elsevier)

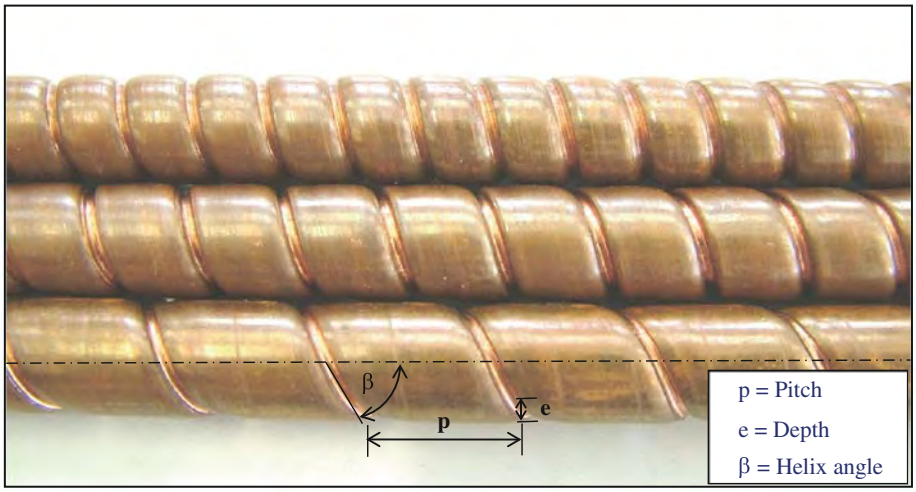

Fig. 3 Photograph of the corrugated tube (Laohalertdecha and Wongwises [16], with permission from Elsevier)

a controlled temperature bath using standard precision mercury glass thermometers. The uncertainty of the temperature measurements as recorded by the data acquisition system is ±0.1 °C. All static pressure taps are mounted on the tube wall. The refrigerant flow meter is a variable area type and specially calibrated in the range of 0.2–3.4 LPM for R-134a by the manufacturer. Also, the differential pressure transducer is calibrated by the manufacturer.

Experiments were conducted with various flow rates, average vapour qualities, heat fluxes and saturation temperatures. In the experiments, the refrigerant flow rate in the test section was controlled by adjusting the speed of the magnetic gear pump. To vary the vapour quality at the inlet of the test section, the heating water flow and the cooling water flow rates were varied by small increments while the refrigerant flow rate was kept constant. The hot water in the test section was re-circulated by a centrifugal pump to supply heat to the refrigerant. During each experiment, the heat transferred from the test section was kept at a desired value. This might be obtained by simultaneously adjusting and controlling the temperature and flow rate of the hot water entering the test section. The system was allowed to approach a steady state before any data was recorded. After stabilisation, the temperature on the tube wall, the

Table 1 The dimensions of the test section

Number	p (mm)	e (mm)	w (mm)	β (degree)	d_i (mm)	L (mm)
1	5.08	1	1	79.47	8.7	2,000
2	5.08	1.25	1	79.47	8.7	2,000
3	5.08	1.5	1	79.47	8.7	2,000
4	8.46	1.5	1	74.20	8.7	2,000
5	6.35	1.5	1	76.56	8.7	2,000
6	Smooth tube				8.7	2,000

Table 2 Uncertainties of measured quantities and calculated parameters

Parameter	Uncertainty
Temperature, T (°C)	±0.1
Pressure drop, ΔP (kPa)	±0.37
Mass flow rate of refrigerant, m_{ref}	±2 %
Mass flow rate of water, m_w	±2 %
Heat transfer rate at test section, Q_{TS}	±10 %
Heat transfer rate at pre-heater, Q_{ph}	±5 %
Evaporation heat transfer coefficient, h	±10 %
Average vapour quality, x	±5 %

temperature of the refrigerant at the locations mentioned above, the inlet and outlet temperatures of the heating water and flow rates of heating water and refrigerant were all recorded. The pressure drop was measured by a differential pressure transducer installed between the inlet and outlet of the test section. The experiments could be carried out by increasing the refrigerant flow rate while the saturation temperature in the test section was kept constant. The accuracy of the direct measurements and the uncertainties in the derived experimental values are shown in Table 2.

3 Data reduction

The data reduction for calculating the two-phase heat transfer coefficient and pressure drop of R-134a flowing in horizontal smooth and corrugated tubes under evaporation conditions can be summarized as follows:

3.1 The inlet vapour quality of the test section ($x_{TS,in}$)

The inlet vapour quality entering the test section can be calculated as follows:

$$x_{TS,in} = \frac{i_{TS,in} - i_{f,T_{TS,in}}}{i_{fg,T_{TS,in}}} \tag{1}$$

The refrigerant enthalpy at the test section inlet ($i_{TS,in}$) is given by:

$$i_{TS,in} = i_{ph,in} + \frac{Q_{ph}}{m_{ref}} \tag{2}$$

The heat transfer rate in the pre-heater (Q_{ph}) is calculated as follows:

$$Q_{ph} = m_{w,ph} c_{p,w} (T_{w,in} - T_{w,out})_{ph} \tag{3}$$

3.2 The outlet vapour quality of the test section ($x_{TS,out}$)

Similarly, Eq. (4) can be used to calculate the exit vapour quality of the test section:

$$x_{TS,out} = \frac{i_{TS,out} - i_{f,T_{TS,out}}}{i_{fg,T_{TS,out}}} \tag{4}$$

The outlet enthalpy of the refrigerant flow is calculated as:

$$i_{TS,out} = i_{TS,in} + \frac{Q_{TS}}{m_{ref}} \tag{5}$$

The heat transfer rate in the test section is obtained from:

$$Q_{TS} = m_{w,TS} c_{p,w} (T_{w,in} - T_{w,out})_{TS} \tag{6}$$

3.3 The inside heat transfer coefficient (h_i)

The inside heat transfer coefficient is calculated as follows:

$$h_i = \frac{1}{\left(\frac{1}{U_i}\right) - \left(\frac{1}{2k}\right) d_i \ln\left(\frac{d_o}{d_i}\right) - \left(\frac{d_i}{d_o}\right)\left(\frac{1}{h_o}\right)} \tag{7}$$

The overall heat transfer coefficient based on the inside surface area (U_i) can be determined by:

$$U_i = \frac{Q_{TS}}{A_i (LMTD)} \tag{8}$$

The logarithmic mean temperature difference is defined as follows:

$$LMTD = \frac{\Delta T_1 - \Delta T_2}{\ln\left(\frac{\Delta T_1}{\Delta T_2}\right)} \tag{9}$$

$$\Delta T_1 = T_{w,out} - T_{ref,in} \tag{10}$$

$$\Delta T_2 = T_{w,in} - T_{ref,out} \tag{11}$$

The outside heat transfer coefficient (h_o) is obtained from:

$$h_o A_o = \frac{Q_{TS}}{T_{w,avg} - T_{wall,avg}} \tag{12}$$

The Nusselt number is determined as:

$$Nu = \frac{hd}{k_l} \tag{13}$$

3.4 The frictional pressure drop (ΔP_f)

The total pressure drop, ΔP_{total}, is expressed as the sum of the three different components, as follows:

$$\Delta P_{total} = \Delta P_f + \Delta P_a + \Delta P_g \tag{14}$$

The gravitational pressure drop (ΔP_g) is zero in a horizontal tube. The acceleration pressure drop, ΔP_a, was proposed by Tran [18]:

$$\Delta P_a = G^2\left(\left(\frac{x_{out}^2}{\rho_v \alpha_{out}} + \frac{(1-x_{out})^2}{\rho_l(1-\alpha_{out})}\right) - \left(\frac{x_{in}^2}{\rho_v \alpha_{in}} + \frac{(1-x_{in})^2}{\rho_l(1-\alpha_{in})}\right)\right) \tag{15}$$

The void fraction, α, can be determined from Zivi's correlation [19] as follows:

$$\alpha = \left(1 + \frac{(1-x)}{x}\left(\frac{\rho_v}{\rho_l}\right)^{\frac{2}{3}}\right)^{-1} \tag{16}$$

The frictional pressure drop, ΔP_f, can be obtained by subtracting the acceleration pressure drop from the total measured pressure drop. The two-phase friction factor is defined in terms of the equivalent mass flux (G_{eq}) proposed by Akers et al. [20], as shown in Eq. (17).

$$f_{tp} = \frac{d_i \Delta P_f \rho_l}{2G_{eq}^2} \tag{17}$$

$$G_{eq} = G\left[(1-x) + x\left(\frac{\rho_l}{\rho_g}\right)^{0.5}\right] \tag{18}$$

3.5 Equivalent Reynolds number (Re_{eq})

The equivalent Reynolds number is defined as:

$$\text{Re}_{eq} = \text{Re}_l + \text{Re}_v\left(\frac{\mu_v}{\mu_l}\right)\left(\frac{\rho_l}{\rho_v}\right)^{0.5} \tag{19}$$

The liquid Reynolds number (Re_l) and vapour Reynolds number (Re_v) can be obtained from Eqs. (20) and (21) as follows:

$$\text{Re}_l = \frac{Gd_i(1-x)}{\mu_l} \tag{20}$$

$$\text{Re}_v = \frac{Gd_i x}{\mu_v} \tag{21}$$

4 Mathematical modeling

In this present simulation model, the test section is a horizontal counter-flow concentric double-tube heat exchanger with refrigerant flows in the inner tube, whereas hot water flows in the annulus. In addition, the outer tube surface is well-insulated. The following assumptions are employed.

1. Steady, one-dimensional flow of the refrigerant is analysed.
2. Heat loss along the test section is negligible.

4.1 Heat transfer coefficient

The concept of the overall heat transfer coefficient based on the inside surface is applied in the heat exchanger as shown below:

$$\frac{1}{U_i A_i} = \frac{1}{h_i A_i} + \frac{\ln(d_o/d_i)}{2\pi kL} + \frac{1}{h_o A_o} \tag{22}$$

The overall heat transfer coefficient (U_i) is determined from Eq. (8). The outside heat transfer coefficient (h_o) was proposed by Laohalertdecha and Wongwises' [17] correlation as follows:

$$Nu_o = 0.006\text{Re}_{eq}^{0.8}\,\text{Pr}_l^{\frac{1}{3}}\left(\frac{ep}{D_{eq}^2}\right)^{-0.1} \tag{23}$$

where Nu_o is determined by:

$$Nu_o = \frac{h_o D_{eq}}{k_w} \tag{24}$$

where D_{eq} is defined as follows:

$$D_{eq} = \frac{D_i^2 - d_o^2}{d_o} \tag{25}$$

Therefore, the inside heat transfer coefficient can be calculated as Eq. (7). The average heat transfer coefficient can be calculated by:

$$h_{avg} = \frac{1}{L}\int_0^z h_z dz \tag{26}$$

4.2 Pressure drop

The total pressure drop (ΔP_{total}) is expressed as the sum of the three different components, as shown in Eq. (14). The frictional pressure drop of the refrigerant flowing inside the corrugated tube is calculated as follows:

$$\Delta P_f = \frac{2f_{tp}G_{eq}^2 L}{d_i \rho_l} \tag{27}$$

Equivalent mass flux (G_{eq}) is determined from Eq. (18). The two-phase friction factor (f_{tp}) is determined by using the correlation proposed by Laohalertdecha and Wongwises [17] as follows:

$$f_{tp} = 33.368\text{Re}_{eq}^{-0.68}\left(\frac{ep}{d_i^2}\right)^{0.1} \tag{28}$$

The equivalent Reynolds number (Re_{eq}) is defined as Eq. (19). From Eq. (18), the average quality can be

determined by:

$$x = \frac{x_{ref,in} + x_{ref,out}}{2} \tag{29}$$

The accelerational pressure drop, ΔP_a, is defined by Eq. (15). For the horizontal tube, the gravitational pressure drop (ΔP_g) is zero.

5 Solution methodology

Figure 4 shows the details of the solution method in the types of flow diagrams. The selected input parameters used in the present simulation model are the corrugated tube geometries, inlet and outlet water temperatures, inlet temperature of the refrigerant, the water and refrigerant mass flow rates, and the inlet quality of the refrigerant.

The first step in the simulation model is intended to find the limited scope of calculation by guessing the values of the outlet refrigerant temperature ($T_{ref,out}$), as shown in Fig. 4. The outlet refrigerant temperature can be converted into the outlet pressure. The calculation is terminated when the error between the total pressure drop found using calculation Eq. (14) and that shown in the saturation table is smaller than 10^{-3}.

$$\text{if } \frac{(\Delta P_{total})_{cal} - (\Delta P_{total})_{sat.table}}{(\Delta P_{total})_{sat.table}} > 10^{-3}$$

then change value of T_{guess}

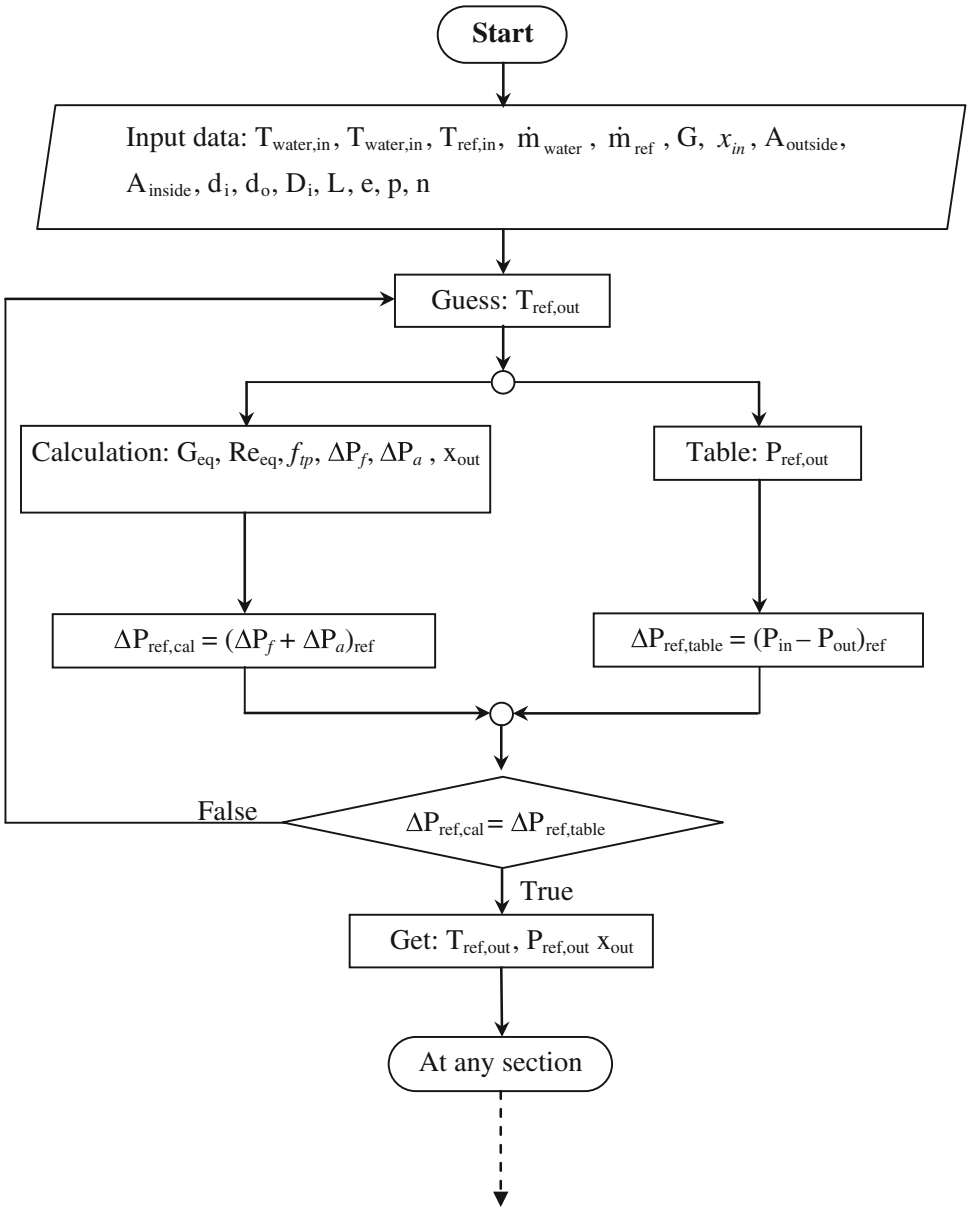

Fig. 4 Flow diagram of simulation method

Fig. 4 continued

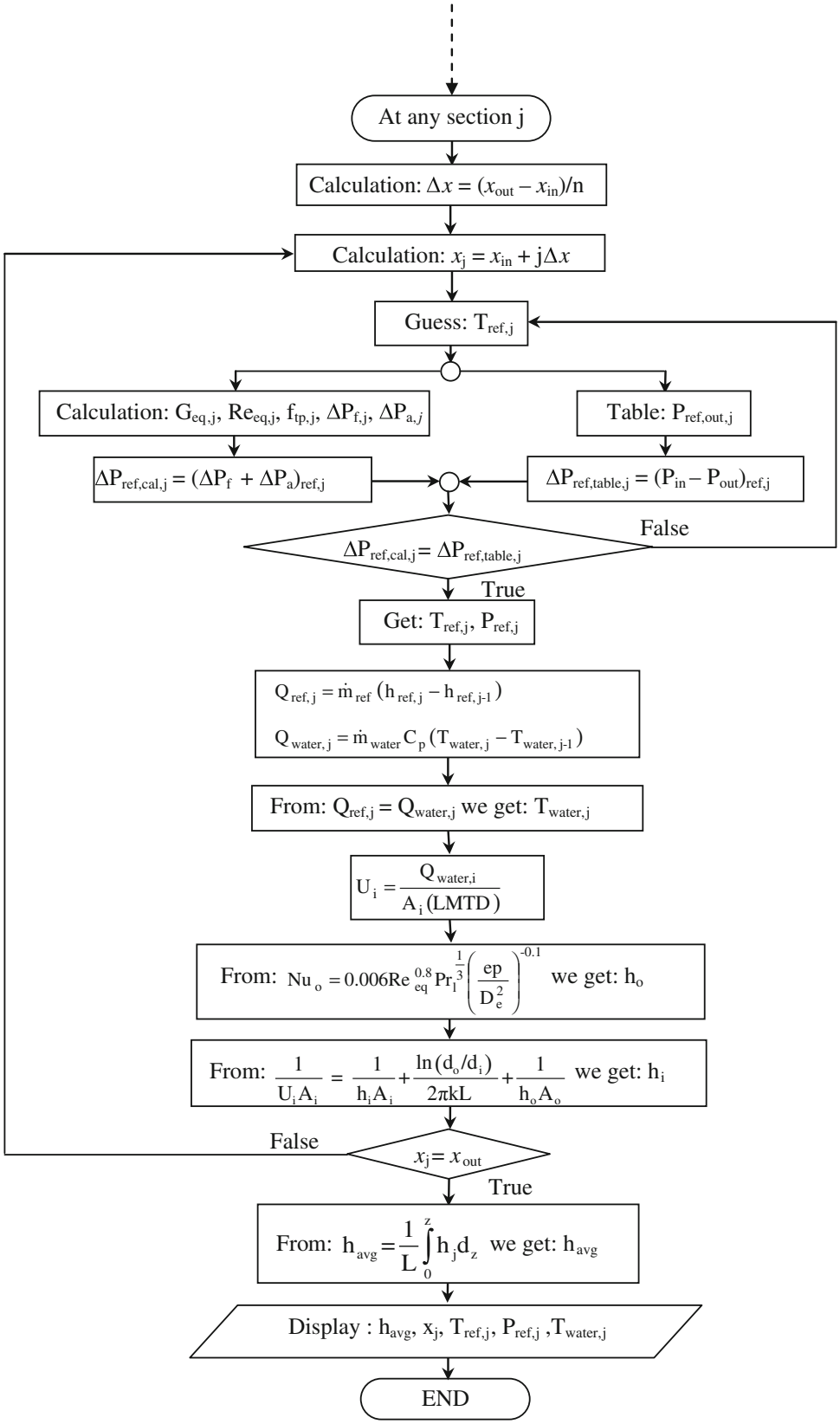

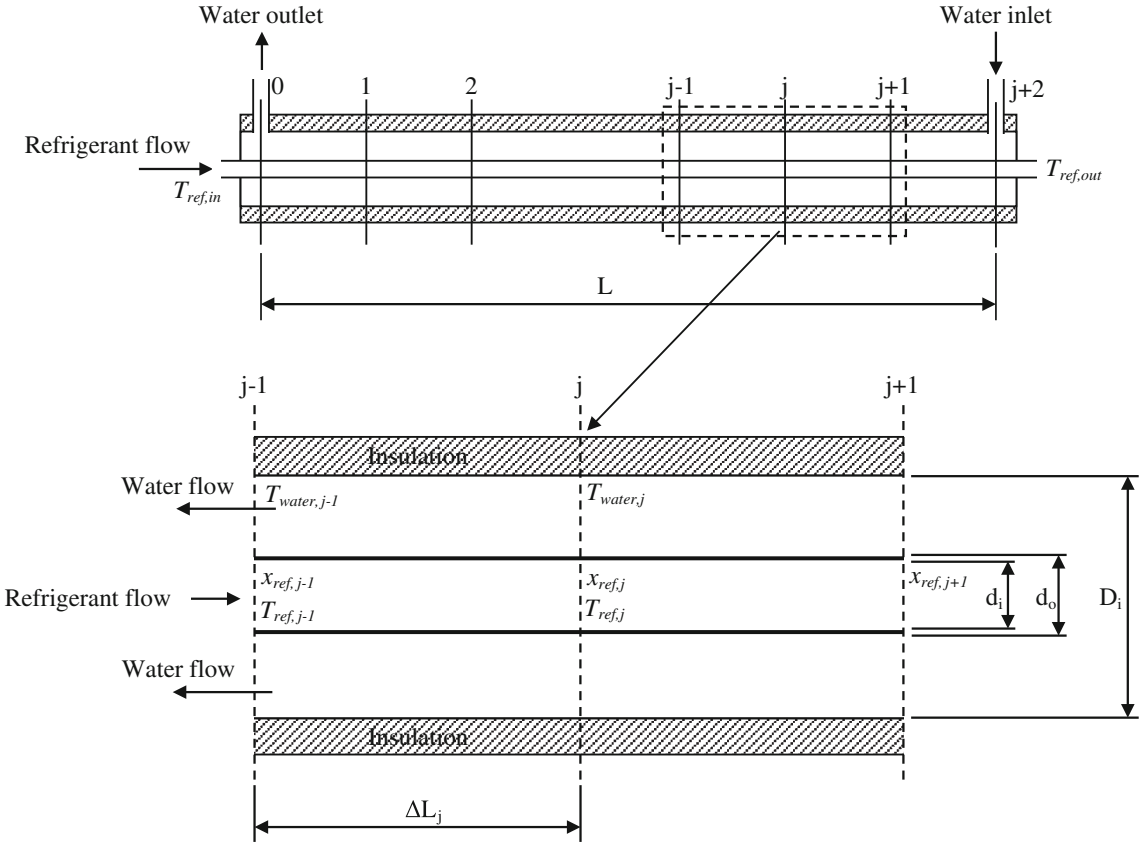

Fig. 5 Schematic diagram of simulation approach for a corrugated tube

if $\dfrac{(\Delta P_{total})_{cal}-(\Delta P_{total})_{sat.table}}{(\Delta P_{total})_{sat.table}} \leq 10^{-3}$

then $T_{guess} \cong T_{ref,out}$

The total pressure drop obtained from the saturation table is the pressure difference between the inlet pressure and outlet pressure of the test section. The REFPROP program, version 6.01 [21] is used to calculate the thermophysical properties of the refrigerant. Once the $T_{ref,out}$ is known, the outlet quality is obtained.

As shown in Fig. 5, the corrugated tube can be divided into 16 sections by constant quality increments. The quality of each section j is calculated by:

$$\Delta x = \frac{\left(x_{ref,out} - x_{ref,in}\right)}{n} \tag{30}$$

$$x_{ref,j} = x_{ref,in} + j\Delta x \tag{31}$$

where n is the number of sections.

$j = 1, 2 \ldots, 16$

The corrugated tube length of each section can be calculated by:

$$\Delta L_j = \frac{L}{n} \tag{32}$$

Thereafter, the temperature and pressure of the refrigerant at the outlet of each section can be calculated by a process similar to the one shown in Fig. 4. The outlet water temperature is determined by energy balance between the refrigerant side and the water side.

$$Q_{ref,j} = Q_{water,j} \tag{33}$$

$$\dot{m}_{ref}\left(h_{ref,j} - h_{ref,j-1}\right) = \dot{m}_{water} C_p \left(T_{water,j} - T_{water,j-1}\right) \tag{34}$$

Rearranging Eq. (34) yields:

$$T_{water,j} = \frac{\dot{m}_{ref}}{\dot{m}_{water} C_p}\left(h_{ref,j} - h_{ref,j-1}\right) + T_{water,j-1} \tag{35}$$

The inside and outside heat transfer coefficients are calculated by Eqs. (7) and (23), respectively. The whole process of section-by-section analysis is then repeated until $x_{ref,j} = x_{ref,out}$. Finally, the average heat transfer coefficient can be calculated by:

$$h_{avg} = \frac{1}{L}\int_0^z h_j dz \tag{36}$$

6 Results and discussion

The effects of the corrugation pitch and depth on the evaporation heat transfer coefficient and frictional pressure drop of R-134a flowing through horizontal corrugated tubes are studied experimentally. Moreover, this work presents the results of a simulation model used to describe the heat transfer coefficient and pressure drop of R-134a flowing through a corrugated tube. Before measuring the evaporation heat transfer coefficient and pressure drop, a single-phase liquid flowing through a smooth tube is first conducted to check the energy balance. The results indicate that the energy balance between the cold water and the refrigerant is within 10 % for all runs [14]. Moreover, the experimental Nusselt number and the frictional pressure drop are compared with well-known correlations. The results show that almost all correlations are in agreement with the present data [15].

6.1 Effects of depth and pitch on the heat transfer coefficient

Figure 6 displays the effect of depth on the evaporation heat transfer coefficient at $G = 300$ kg/m^2 s, $q'' = 10$ kW/m^2, and $T_{sat} = 20$ °C. The results show that the average heat transfer coefficient increases with increasing average vapor quality. This is because at higher vapor quality, the higher vapor velocity led to higher interfacial shear stress between the vapor core and liquid film. The increasing interfacial shear stress causes the liquid film thinner, resulting in lower thermal resistance. Therefore, the average heat transfer coefficient tends to increase as the average vapor quality increases. The average heat transfer coefficients at the same average quality obtained from the corrugated tubes are clearly higher than those obtained from the smooth tube across the range of the average quality because the corrugated surface has a simultaneous effect on the axial flow, secondary fluid motion, and swirl mixing. Moreover, the corrugation depth has a significant effect on the heat transfer coefficient because the tube with higher corrugation depth yields higher turbulence. The maximum heat transfer enhancement is obtained up to 22, 19 and 13 % for a depth of 1.5, 1.25, and 1 mm, respectively, in comparison with the smooth tube.

Figure 7 shows the effect of corrugation pitch on the average heat transfer coefficient at $G = 300$ kg/m^{2}s, $q'' = 5$ kW/m^2, and $T_{sat} = 15$ °C. The average heat transfer coefficient increases with decreasing corrugation pitch. The reason for this is similar to the explanation above. In other words, the tube with lower corrugation pitch promotes more turbulence by increasing the amount of the swirl flow induced by higher number of corrugation. As a consequence, the highest heat transfer coefficient can be obtained by the tube with the lowest corrugation pitch. The maximum value of heat transfer coefficient obtained from a pitch of 5.08 mm is 21 % in comparison with the smooth tube.

6.2 Effects of depth and pitch on frictional pressure drop

As shown in Figs. 8 and 9, the effects of depth and pitch on frictional pressure drop are plotted against the average vapor quality. In the smooth tube and corrugated tubes, the increasing pressure drop depends on increased average vapor quality. This is because the vapor velocity is increased at higher vapor quality, resulting in more shear

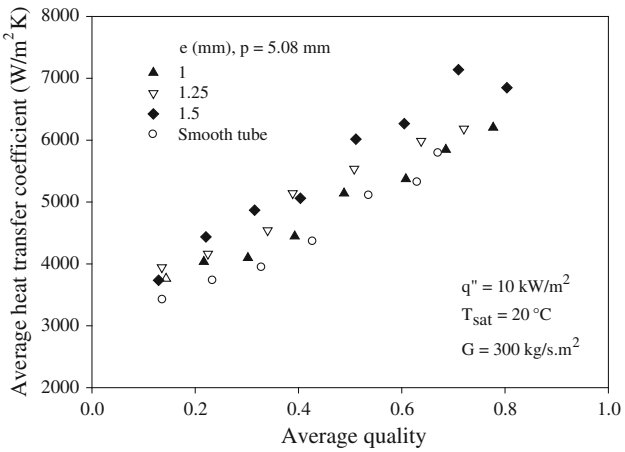

Fig. 6 Average heat transfer coefficient versus average quality at $T_{sat} = 20$ °C, $G = 300$ kg/m^{2}s and $q'' = 10$ kW/m^2 for different depths

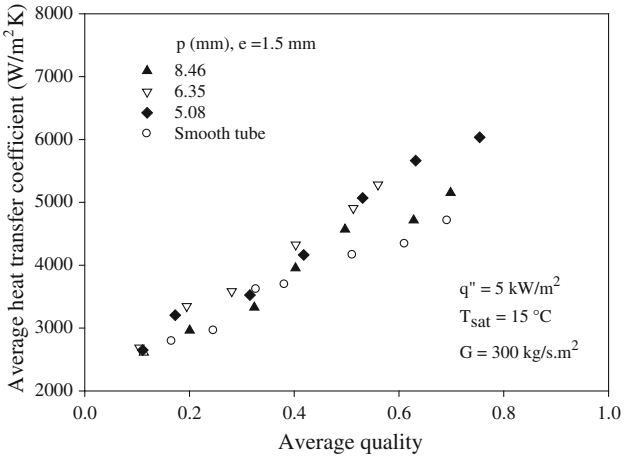

Fig. 7 Average heat transfer coefficient versus average quality at $T_{sat} = 15$ °C, $G = 300$ kg/m^{2}s and $q'' = 5$ kW/m^2 for different pitches

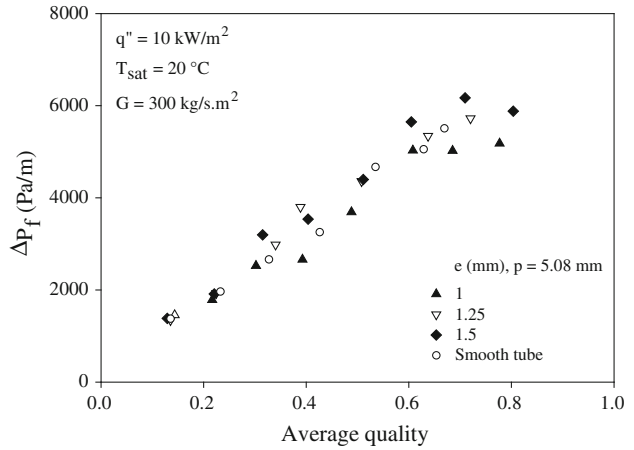

Fig. 8 Frictional pressure drop versus average quality at $T_{sat} = 20$ °C, $G = 300$ kg/m^{2}s and $q'' = 10$ kW/m^2 for different depths

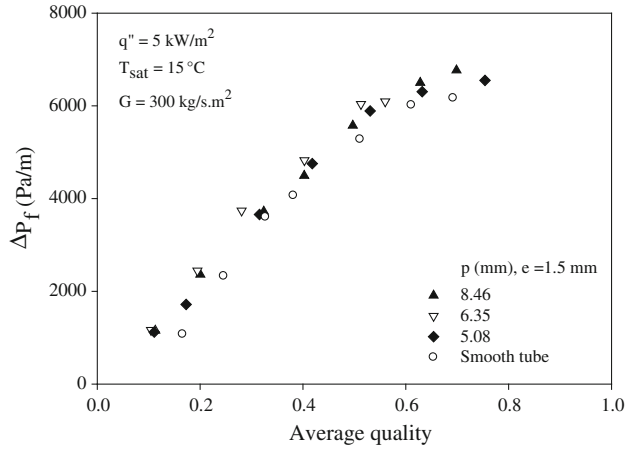

Fig. 9 Frictional pressure drop versus average quality at $T_{sat} = 15$ °C, $G = 300$ kg/m^{2}s and $q'' = 5$ kW/m^2 for different pitches

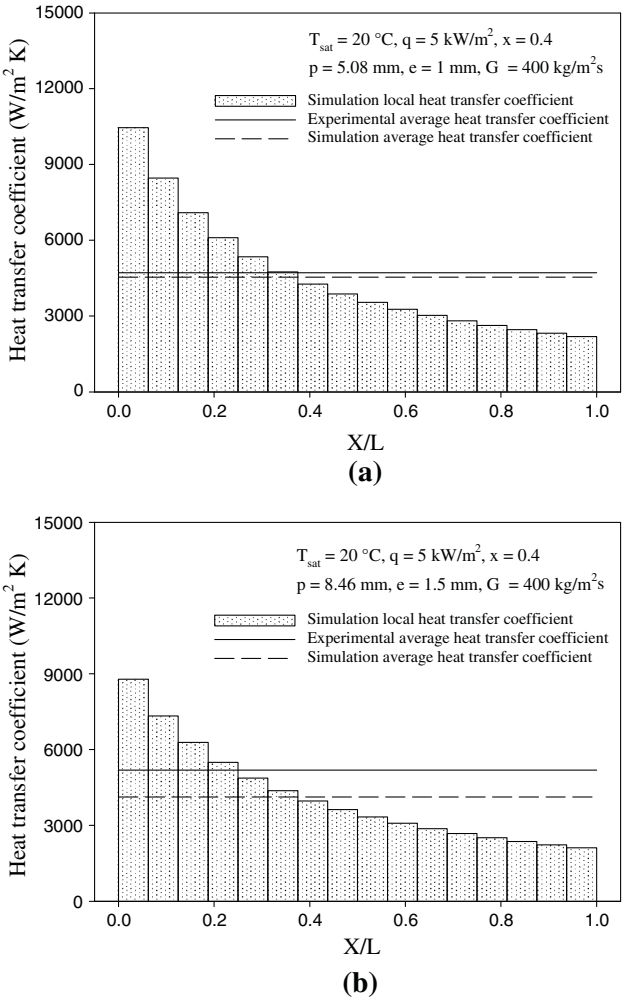

Fig. 10 Comparison of the heat transfer coefficient with those obtained from measured data and calculated values from the present model

stress at the interface of the vapor and liquid film, causing the increase of flow turbulence. At the same quality, the pressure drop obtained from the corrugated tube is higher than that from a smooth tube because the corrugation surface has an effect on the turbulent flow. In other words, the corrugation surface produces rotational flow, which led to more effect on turbulence of the fluid flow. However, the effects of the corrugation pitch and depth on the frictional pressure drop are not significant. This may be due to very small difference in variation of corrugation pitch and depth. The maximum value of frictional pressure drop obtained from a pitch of 5.08 mm and a depth of 1.5 mm is about 19 % in comparison with the smooth tube at the mass flux of 300 kg/m^{2}s, heat flux of 10 kW/m^2, and saturation temperature of 20 °C.

6.3 Simulation results

Figure 10 shows the distributions of the simulation local heat transfer coefficient, simulation average heat transfer coefficient, and experimental average heat transfer coefficient along the test section (X/L). The bar chart represents the predicted local heat transfer coefficient obtained from the proposed simulation. The solid line and the dashed line represent the average values for the heat transfer coefficient obtained from the measured data and the predicted value from the simulation, respectively. These figures show that the simulation local heat transfer coefficient decreases with increasing tube length. Compared with the experimental data, the results show that the simulation average heat transfer coefficient has good agreement with the measured data. In addition, the average difference of the heat transfer coefficient between the simulation and experimental data is about 10 %.

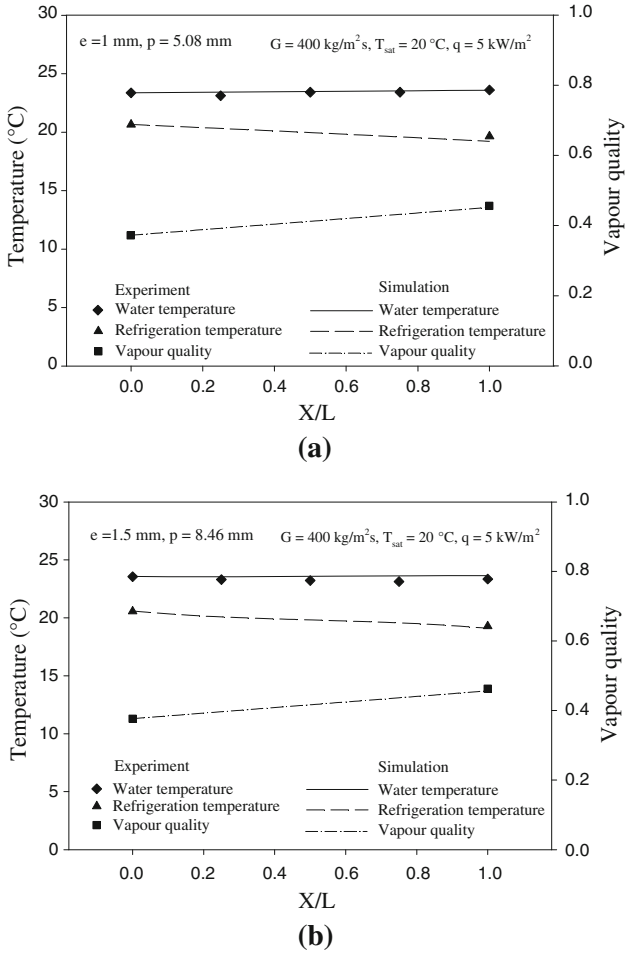

Fig. 11 Comparison of the water temperature, refrigerant temperature and vapor quality with those obtained from measured data and calculated values from the present model

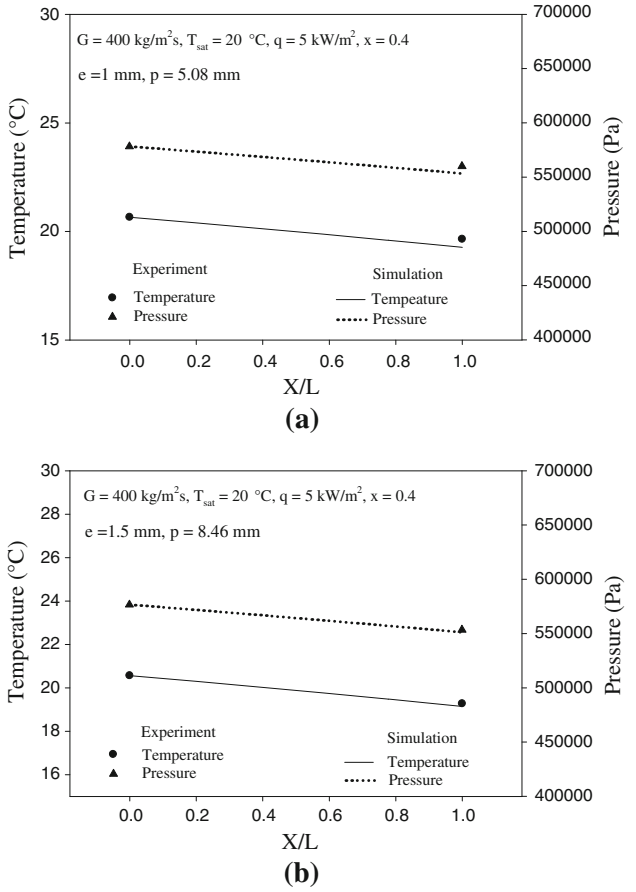

Fig. 12 Comparison of the refrigerant temperature and pressure with those obtained from measured data and calculated values from the present model

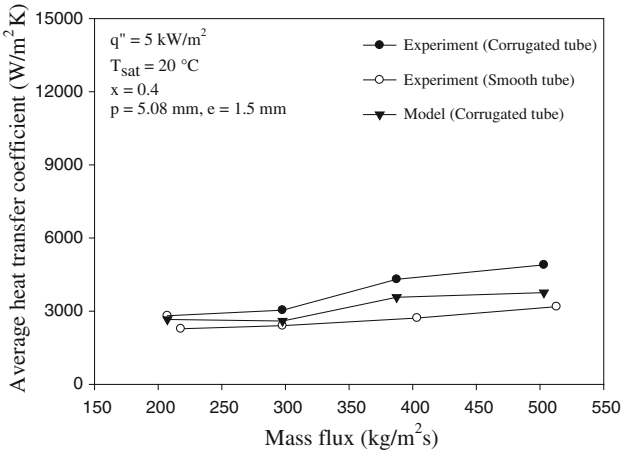

Fig. 13 Calculated values from the present model versus experimental data

Figure 11 displays the temperature and vapour quality distribution along the test tube obtained from the measured data and then compared with the simulation value. The lines and the symbols represent the simulation results and the experimental data, respectively. The results show that the refrigerant temperature decreases with the axial length of the tube, which corresponds with the saturation pressure. The vapour quality increases gradually along the tube because the energy from the water is supplied to the refrigerant. Moreover, the results also indicate that the inlet water temperatures are higher than the outlet water temperatures due to the evaporation condition. However, the simulation results have good agreement with the experimental data.

Figure 12 shows the saturation temperature and pressure distribution along the test tube obtained from the measured data and compared with the simulation values. The results show that the saturation temperature and pressure decrease along the tube due to friction. In addition, the average difference of the pressure drop between the simulation and experimental data are about 15 %.

Figure 13 illustrates the comparison between the average heat transfer coefficients obtained from the simulation

data and those obtained from experimental data. The results show that all of the simulation data are lower than the experimental data obtained from the corrugated tube within 2–10 %. However, all the simulation data are higher than the measured data obtained from the smooth tube.

7 Conclusion

Experimental and simulation studies of the evaporation heat transfer coefficient and pressure drop of R-134a flowing through corrugated tubes were conducted. A new simulation model was presented for predicting the heat transfer behavior of the refrigerant flowing through corrugated tubes. The 2.0 m test section is a tube-in-tube heat exchanger placed in the horizontal direction in which a refrigerant flows in the inner tube and hot water flows in the annulus. The corrugation pitches used in this study were 5.08, 6.35, and 8.46 mm. Similarly, the corrugation depths were 1, 1.25, and 1.5 mm, respectively. The measured heat transfer coefficient and pressure drop were presented. It was found that the heat transfer coefficient and pressure drop increased with increasing average vapour quality as well as mass flux. The heat transfer coefficient and pressure drop obtained from the corrugated tubes were higher than those of a conventional smooth tube under all test conditions. The corrugation pitches and depths had a significant effect on the heat transfer coefficient for all tested conditions. However, based on our test section, the effects of the corrugation pitch and depth on the frictional pressure drop were not significant. The maximum heat transfer coefficient and pressure drop obtained from the corrugated tube were up to 22 and 19 % higher than those obtained from the smooth tube, respectively. Moreover, the average difference of the heat transfer coefficient and pressure drop between the simulation model and the experimental data were about 10 and 15 %, respectively.

Acknowledgments The present study was supported financially by the Thailand Research Fund, the National Research University Project and National Science and Technology Development Agency, whose guidance and assistance are gratefully acknowledged. The third and fourth authors would like to thank Professor Somchai Wongwises for providing him fellowships during his research in the Department of Mechanical Engineering, King Mongkut's University of Technology Thonburi.

References

1. Nozu S, Honda H, Nakata H (1995) Condensation of refrigerants CFC11 and CFC113 in the annulus of a double-tube coil with an enhanced inner tube. Exp Therm FluidSci 11:40–51
2. Nozu S, Honda H, Nishida S (1995) Condensation of a zeotropic CFC 114-CFC 113 refrigerant mixture in the annulus of a double-tube coil with an enhanced inner tube. Exp Therm FluidSci 11:364–371
3. Dong Y, Huixiong L, Tingkuan C (2001) Pressure drop, heat transfer and performance of single-phase turbulent flow in spirally corrugated tubes. Exp Therm FluidSci 24:131–138
4. Barba A, Rainieri S, Spiga M (2002) Heat transfer enhancement in a corrugated tube. Int Commun Heat Mass Transfer 29:313–322
5. Rainieri S, Pagliarini G (2002) Convective heat transfer to temperature dependent property fluids in the entry region of corrugated tubes. Int J Heat Mass Transf 45:4525–4536
6. Zimparov V (2001) Enhancement of heat transfer by a combination of three-start spirally corrugated tubes with a twisted tape. Int J Heat Mass Transf 44:551–574
7. Zimparov V (2002) Enhancement of heat transfer by a combination of a single-start spirally corrugated tubes with a twisted tape. Exp Therm FluidSci 25:535–546
8. Zimparov V (2004) Prediction of friction factors and heat transfer coefficients for turbulent flow in corrugated tubes combined with twisted tape inserts. Part 1: friction factors. Int J Heat Mass Transf 47:589–599
9. Zimparov V (2004) Prediction of friction factors and heat transfer coefficients for turbulent flow in corrugated tubes combined with twisted tape inserts. Part 2: heat transfer coefficients. Int J Heat Mass Transf 47:385–393
10. Rousseau PG, Eldik MV, Greyvenstein GP (2003) Detailed simulation of fluted tube water heating condenser. Int J Refrig 26:232–239
11. Vicente PG, Garcia A, Viedma A (2004) Experimental investigation on heat transfer and friction factor characteristics of spirally corrugated tubes in turbulent flow at different Prandtl number. Int J Heat Mass Transf 47:671–681
12. Vicente PG, Garcia A, Viedma A (2004) Mixed convection heat transfer and isothermal pressure drop in corrugated tubes for laminar and transition flow. Int Commun Heat Mass Transf 31:651–662
13. Targanski T, Cieslinski JT (2007) Evaporation of R407C/oil mixtures inside corrugated and micro-fin tubes. Appl Therm Eng 27:2226–2232
14. Laohalertdecha S, Wongwises S (2010) The effects of corrugation pitch on the condensation heat transfer coefficient and pressure drop of R-134a inside horizontal corrugated tube. Int J Heat Mass Transf 53:2924–2931
15. Laohalertdecha S, Wongwises S (2011) An experimental study into the evaporation heat transfer and flow characteristics of R-134a refrigerant flowing through corrugated tubes. Int J Refrig 34:280–291
16. Laohalertdecha S, Wongwises S (2011) Condensation heat transfer and flow characteristics of R-134a flowing through corrugated tubes. Int J Heat Mass Transf 54:2673–2682
17. Laohalertdecha S, Wongwises S (2011) Correlations for evaporation heat transfer coefficient and two-phase friction factor for R-134a flowing through corrugated tubes. Int Commun Heat Mass Transf 38:1406–1413
18. Tran TN (1998) Pressure drop and heat transfer study of two-phase flow in small channels. Ph.D. Dissertation, Texas Tech University, Lubbock, Texas
19. Zivi SM (1964) Estimation of steady-state steam void-fraction by mean of the principle of minimum entropy production. Trans ASME J Heat Transf 86:247–252
20. Akers WW, Deans HA, Crasser OK (1959) Condensing heat transfer within horizontal tubes. Chem Eng Prog Symp 55:171–176
21. REFPROP (1998) Refrigerant properties database version 6.01. NIST, Gaithersburg

International Journal of Heat and Mass Transfer 73 (2014) 186–194

Contents lists available at ScienceDirect

International Journal of Heat and Mass Transfer

journal homepage: www.elsevier.com/locate/ijhmt

Heat transfer characteristics and pressure drop of COOH-functionalized DWCNTs/water nanofluid in turbulent flow at low concentrations

Mohammad Hemmat Esfe [a,*], Seyfolah Saedodin [a], Omid Mahian [b,c,*], Somchai Wongwises [c]

[a] Faculty of Mechanical Engineering, Semnan University, P.O. Box 3513119111, Semnan, Iran
[b] Young Researchers and Elite Club, Mashhad Branch, Islamic Azad University, Mashhad, Iran
[c] Fluid Mechanics, Thermal Engineering and Multiphase Flow Research Lab. (FUTURE), Department of Mechanical Engineering, Faculty of Engineering, King Mongkut's University of Technology Thonburi, Bangmod, Bangkok 10140, Thailand

ARTICLE INFO

Article history:
Received 28 September 2013
Received in revised form 31 January 2014
Accepted 31 January 2014

Keywords:
Heat transfer
Pressure drop
Functionalized carbon nanotube
Turbulent flow

ABSTRACT

In this paper, an experimental study is performed to assess the heat transfer characteristics and pressure drop of low concentrations of a new class of nanotubes, i.e. COOH-functionalized double-walled carbon nanotubes (DWCNTs) suspended in water under turbulent flow in a double tube heat exchanger. First, the thermal conductivity and viscosity of nanofluids at volume fractions of 0.01%, 0.02%, 0.05%, 0.1%, 0.2%, and 0.4% are measured and corresponding correlations are presented. Next, the heat transfer and pressure drop of the nanofluids through the double tube heat exchanger are evaluated. The results indicate that even the use of low concentration of the nanofluid, i.e. 0.4%, leads to a remarkable increase in heat transfer coefficient (by 32%) in comparison with the distilled water. On the other hand, the pressure drop due to using the volume fraction of 0.4% raised by 20%. Finally, analysis of the heat transfer and pressure drop data via thermal performance factor reveals that in spite of the pressure drop penalty, the COOH-functionalized DWCNTs/water nanofluid with volume fraction of 0.4% is a good option to use in the double tube heat exchanger.

© 2014 Elsevier Ltd. All rights reserved.

1. Introduction

In recent years, there has been an increasing interest in nanofluids and their applications in various thermal engineering devices. Application of nanofluids is established in many fields such as cooling of electronic devices, nuclear reactors, engine cooling, solar energy, cooling and heating of buildings, and so on [1,2].

The physical and chemical specifications of the nanoparticles and the base fluid will determine the thermal characteristics of nanofluids. Therefore, the use of a suitable type of nanoparticles is very important to have a nanofluid with a high efficiency. Some types of nanoparticles such as aluminium oxide, titanium dioxide, copper oxide, copper, zinc oxide, silicon dioxide, silver and carbon nanotubes are the most common particles used in the literature. In the present work, a new type of carbon nanotubes i.e. COOH-functionalized double-walled carbon nanotubes (DWCNTs) has been used. The heat transfer and pressure drop due to the suspension of very low volume fractions of this new type of nanoparticles in water are estimated under turbulent flow in a double tube heat exchanger.

Here, a brief review of the experimental studies on the nanofluid flow in the double tube heat exchangers under the turbulent regime is performed.

Yu et al. [3] performed the experiments on the silicon carbide/water nanofluid flow in a circular tube and a range of Reynolds number between 3000 and 13,000. They concluded that using nanofluid with volume fraction of 3.7% leads to heat transfer enhancement by 60%. Sundar et al. [4] investigated the turbulent flow and pressure drop of Al_2O_3/water nanofluid in a circular tube where the tube is equipped with twisted tapes. Their results showed that in the range of H/D tested, the heat transfer coefficient is enhanced by 23% for the case of the tube having tape insert compared to the plain tube.

Farajollahi et al. [5] studied the turbulent flow of γ-Al_2O_3/water and TiO_2/water nanofluids in a double tube heat exchanger for the Peclet numbers between 20,000 and 60,000. They found the optimum nanofluid concentration in which the heat transfer is maximized. Duangthongsuk and Wongwises [6–8] investigated the TiO_2/water nanofluid flow in a double tube heat exchanger under the turbulent regime. They investigated the effects of nanofluid

* Corresponding authors. Tel.: +98 9131680130.
E-mail addresses: M.hemmatesfe@gmail.com (M. Hemmat Esfe), omid.mahian@gmail.com (O. Mahian).

http://dx.doi.org/10.1016/j.ijheatmasstransfer.2014.01.069
0017-9310/© 2014 Elsevier Ltd. All rights reserved.

concentration, using different thermophysical models on the heat transfer characteristics and pressure drop of the nanofluid flow. Duangthongsuk and Wongwises [8] conducted the tests for volume fractions between 0.2% and 2% and found that the optimum particle loading is 1% in which the heat transfer is maximized. Sundar and Sharma [9] accomplished the experiments for Al_2O_3/water nanofluid flow through a plain tube where the Reynolds number changes in the range of 10,000 to 22,000. They studied the effects of inserting the tapes with different twist ratios inside the tube on the nanofluid flow and heat transfer. Based on the experimental results, they suggested suitable correlations to estimate the Nusselt number and friction factor. Zhang et al. [10] examined the effects of nanoparticle size (three different sizes i.e. 23, 51, 76 nm) on the heat transfer of CuO/water nanofluids in the turbulent flow. They perceived that using nanoparticles with a bigger size leads to higher heat transfer rate. Amrollahi et al. [11] measured the heat transfer rate of functionalized multi walled carbon nanotubes suspended in water as the base fluid under laminar and turbulent regimes. In their work, the nanofluid flows through a horizontal circular tube in entrance region. They reported the increases of 33–40% in heat transfer coefficient where the working fluid changes from pure water to the nanofluid with weight fraction of 0.25%.

Hojjat et al. [12,13] performed the tests on the turbulent flow of three types of nanoparticles including Al_2O_3, CuO, and TiO_2 suspended in an aqueous solution of carboxymethyl cellulose in a circular tube so that the nanofluids have a non-Newtonian behaviour.

Suresh et al. [14] studied the heat transfer and friction factor of CuO/water nanofluid in the Reynolds number range of 2500 to 6000 with the simple and helically dimpled tubes under constant heat flux boundary conditions. They revealed that using the nanofluid with concentration of 0.3% through the dimpled tube leads to 39% heat transfer enhancement in comparison with the case in which the pure water flows in the simple tube. Tumuluri et al. [15] investigated experimentally the turbulent flow of the nanofluids which are combined with multi-walled carbon nanotubes (MWCNT) and microencapsulated phase change materials (MPCMs) through a circular tube under constant heat flux. Suresh et al. [16] inserted spiral rods inside a circular tube and investigated the heat transfer and friction factor of Al_2O_3/water nanofluid with the maximum volume fraction of 0.5%. They reported a maximum heat transfer enhancement by 48%. Godson et al. [17] studied the heat transfer and pressure drop due to silver/water nanofluid in a counter flow heat exchanger under laminar and turbulent regimes. Their results indicated that using the nanofluid with the concentration of 0.9%, increases the heat transfer coefficient about 70%. Arani and Amani [18] performed their tests on the TiO_2/water nanofluid in a horizontal double tube counter flow heat exchanger where the Reynolds number changes between 8000–51,000. They concluded that using nanofluid at the Reynolds numbers lower than 30,000 is more advantageous by considering the heat transfer rate and pumping power. Darzi et al. [19] tested the heat transfer and pressure drop due to SiO_2/water nanofluid in corrugated tubes. Azmi et al. [20] investigated the turbulent flow of SiO_2/water nanofluid in a circular tube under constant heat flux where the nanofluid concentration does not exceed 4% and the Reynolds number is between 5000 and 27,000. They found the optimum volume fraction of nanoparticles in which the heat transfer rate is maximized. Recently, Esfe et al. [21] investigated the flow of MgO nanofluids with volume fractions less than 1% in a circular tube. The range of Reynolds number was between 3000 and 18,000. They reported remarkable heat transfer enhancement due to using nanofluids. To save the space, other papers in this field are not reviewed, but the readers can refer to the literature [22–26].

The aim of the present work is to investigate the turbulent flow of a new type of nanofluids i.e. COOH-functionalized double-walled carbon nanotubes suspended in water through a double tube heat exchanger. First, the thermal conductivity and viscosity of nanofluids are measured, then the tests are carried out in the range of Reynolds numbers between 4000–31,000 and low concentrations of the nanofluids (up to 0.4%). The results of heat transfer and pressure drop are reported for different volume fractions of nanoparticles.

2. Nanofluid preparation

In the most of studies on the flow and heat transfer of nanofluids, common nanoparticles such as Al_2O_3, TiO_2, and Cu are used as the additives to the base fluids. In this study, COOH-functionalized double-walled carbon nanotubes with purity of more than 60% (supplied by US research nanomaterials, Inc) are dispersed in water to prepare low volume fractions of nanofluids i.e. 0.01%, 0.02%, 0.05%, 0.1%, 0.2%, and 0.4%. A TEM image of COOH-functionalized DWCNTs is shown in Fig. 1 to display an approximation of the size and shape of the particles. It should be noted that by functionalizing the carbon nanotubes with COOH, the dispersion of nanotubes will be better in the base fluid. Therefore; there is no need to use a surfactant to have a stable suspension. In this way, the negative effects of surfactant on the thermophysical properties will not be observed. Properties of the nanotubes have been presented in Table 1.

For a given volume fraction of the nanofluid, a specific amount of COOH-functionalized DWCNTs is added to the distilled water and then a magnetic stirrer is used to mix the particles and water for 2 h. After mixing, the suspension is inserted inside an ultrasonic processor (Hielscher company, Germany) with the power of 400 W and frequency of 24 kHz for 5 h. This breaks down the agglomeration between the particles and avoids the sedimentation issue. The prepared samples are stable for a long time (at least 1 week) and no sedimentation is observed with naked eyes.

3. Thermophysical properties of nanofluids

Determination of thermophysical properties of nanofluids is important to estimate the heat transfer rate, pumping power, and efficiency of the thermal engineering systems. In this work, thermal conductivity and viscosity of COOH-functionalized DWCNTs/water nanofluids are measured and related correlations

Fig. 1. TEM image of the COOH-functionalized DWCNTs.

Table 1
Properties of COOH-functionalized DWCNT.

Outer diameter	2–4 nm
Inner diameter	1–3 nm
Length	50 um
SSA	>350 m^2/g
True density	2.1 g/cm^3
Electric conductivity	>100 S/cm
Color	black
Manufacturing method	CVD

are obtained by using regression analysis. The presented correlations are helpful to use in other studies in which the working fluid is the same.

3.1. Thermal conductivity

A transient hot-wire (THW) technique is used to measure the thermal conductivity which is a fast and reliable method. For this purpose, a KD2 Pro thermal properties Analyzer (Decagon devices, Inc., USA) is used where the maximum error of measurement is ±5%. Before measuring the thermal conductivity of nanofluids, the device is calibrated with distilled water. The tests for any volume fraction are repeated three times. The experimental data of thermal conductivity are compared with the following models:

Hamilton–Crosser (H–C) model [27] is a classic relation to estimate the effective thermal conductivity of solid–liquid mixtures. This model is applicable when the ratio of solid phase thermal conductivity to that of the liquid phase is bigger than 100. The H–C equation is:

$$K_{nf} = \frac{k_p + (n-1)k_f + (n-1)\phi(k_p - k_f)}{k_p + (n-1)k_f - \phi(k_p - k_f)} k_f \quad (1)$$

in which k_f, k_p, *and* k_{nf} are the thermal conductivities of the base fluid, nanoparticles, and nanofluid, respectively. Also, ϕ is the volume fraction of nanoparticles and n is the empirical shape factor, given by $n = \frac{3}{\psi}$ so that ψ is the particle sphericity. The sphericity for the spherical and cylindrical particles is 1 and 0.5, respectively.

Yu and Choi [28] considered the effect of the liquid nanolayer thickness on the surface of the nanoparticles, as:

$$k_{nf} = \frac{k_p + 2k_f + 2(k_p - k_f)(1+\gamma)^3\phi}{k_p + 2k_f - 2(k_p - k_f)(1+\gamma)^3\phi} k_p \quad (2)$$

The thermal conductivity of the samples is measured in the range of 300–340 °C.

3.2. Viscosity

The viscosity of nanofluids is measured using a Brookfield viscometer supplied by Brookfield engineering laboratories of USA. The accuracy of this device is ±5%. Before doing the tests, it is calibrated with distilled water at room temperature. For each concentration, the tests are repeated three times, and the average is recorded. It is found during the tests that for volume fractions less than 0.45% the nanofluids behave as a Newtonian fluid. The experimental data are compared with the following models for viscosity:

Einstein [29] presented a relation to calculate the viscosity of solid–liquid mixtures as a function of volume fraction (concentrations lower than 2%) as follows:

$$\mu_{nf} = \mu_f(1 + 2.5\phi) \quad (3)$$

Wang et al. [30,31] proposed the following equation for nanofluids:

$$\mu_{nf} = \mu_f(1 + 7.3\phi + 123\phi^2) \quad (4)$$

Although, it is known that CNTs are cylindrical (not spherical), but Eqs. (3), (4) only used for comparison purposes, and more studies are needed to present some relations to calculate the viscosity of nanofluids containing cylindrical particles.

4. Experimental set-up and procedure

The schematic of the experimental set-up is shown in Fig. 2. The set-up mainly consists of a test section, a pump, collection tanks for water and nanofluid, and a plate heat exchanger to cool down the working fluid. The test section consists of two concentric tubes made of copper. Hot water flows inside the annular with inner and outer diameters of 3.79 cm, and 3.82 cm, respectively. Nanofluid flows inside the inner tube with outer diameter of 8.1 mm and the inner diameter of 7.05 mm. Nanofluid absorbs the heat of the hot water that flows in the annulus. The annulus is insulated with glass wool with a thickness of 7 cm.

To avoid the axial heat conduction, two plastic fittings at the inlet and outlet of the test section are mounted.

In turbulent flow, the hydrodynamic and thermal entry can be obtained as ($L_e/D \approx 4.4 \times Re^{1/6}$) [32]. In the present work, the entrance length is about 17 cm, therefore all measurements are conducted after the length.

The length of the test section is about 1.1 m to have fully developed turbulent flow. To measure the bulk temperatures at the inlet and outlet of inner tube two calibrated RTD-PT100 thermometers with digital indicator and the accuracy of 0.1 °C are used. To determine the wall temperature of inner tube, eight K-type thermocouples (Chromel–Alumel) with a distance about 13 cm from each other and the accuracy of 0.5 °C are utilized. The inlet temperature of hot water is controlled with a PT100 sensor. Pressure drop due to nanofluid flow is measured using a differential pressure transmitter Rosemount 3051 cd (Rosemount, Inc., USA) with the accuracy of 0.1%. Also, two K-type thermocouples are used to measure the bulk temperature at the inlet and outlet of the annulus. A simple thermometer is used to record the ambient temperature. All the temperature measurement devices are calibrated before each test.

Nanofluid is pumped via a magnetic pump towards the test section. Before entering the test section, the flow rate of nanofluid is measured and controlled. At the same time, hot water is pumped to the annulus to heat up the nanofluid. The nanofluid after heating and exiting of the test section flows towards a plate heat exchanger to cool down. The tests for each concentration and flow rate are repeated several times (3 times) to be sure that the experiments are repeatable.

5. Data reduction and uncertainty analysis

Heat transfer coefficient (h) and Nusselt number (Nu) can be obtained by using the first law of thermodynamics (the conversation of energy) for the inner tube as follows:

$$\frac{dT_b}{dx} = \frac{S}{\dot{m}C_{nf}} h(T_s - T_b) \quad (5)$$

In which T_b is the bulk temperature, S is the periphery of the tube, $\dot{m}$ is mass flow rate, C_{nf} is the specific heat of nanofluid, and T_s is the surface (wall) temperature.

C_{nf} is calculated as [33]:

$$C_{nf} = \frac{\rho_f C_f(1-\phi) + \rho_p C_p \phi}{\rho_{nf}} \quad (6)$$

where ρ is the density and the density of nanofluid (ρ_{nf}) can be obtained according to [33]:

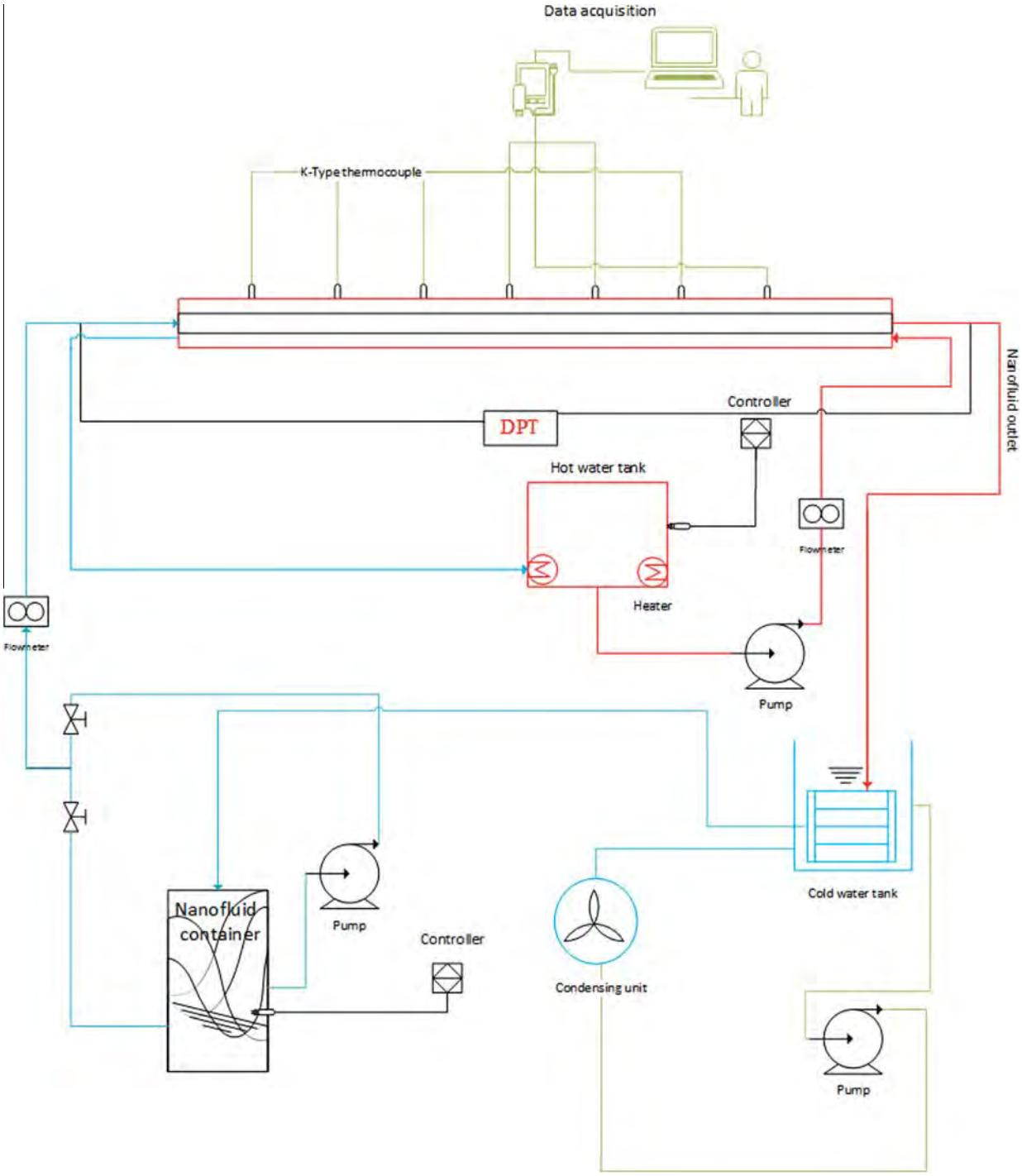

Fig. 2. A schematic view of the experimental set up.

$$\rho_{nf} = \rho_f(1-\phi) + \rho_p\phi \tag{7}$$

By integrating along the tube length (L), heat transfer coefficient can be determined as:

$$\bar{h} = \frac{\dot{m}C_{nf}}{SL} Ln\left(\frac{T_s - T_{b,i}}{T_s - T_{b,o}}\right) \tag{8}$$

where subscripts of i and o indicate the conditions are at the inlet and outlet, respectively.

Also, the Reynolds number and Nusselt number are defined as:

$$\mathrm{Re} = \frac{\rho_{nf}\overline{V}d}{\mu_{nf}}, \quad Nu = \frac{\bar{h}d}{k_{nf}} \tag{9}$$

where d is the diameter of the inner tube and $\overline{V}$ is the average velocity which can be calculated by dividing the flow rate to cross section area of the tube.

To estimate the costs of pumping, it is important to know the pressure drop (ΔP) and friction factor (f). Friction factor is determined as follows:

$$f = \frac{2\Delta P}{\rho_{nf}\overline{V}^2}\frac{d}{L} \tag{10}$$

The uncertainty in the reported data including heat transfer coefficient, Nusselt number, Reynolds number and friction factor

are computed based on the method of Kline and Mcclintock [34]. In general, to calculate the uncertainty of parameter R, the following relation is used:

$$U_R = \left[\sum_{i=1}^{n}\left(\frac{\partial R}{\partial V_i}U_{V_i}\right)^2\right]^{\frac{1}{2}} \tag{11}$$

in which U_R and U_{Vi} are the uncertainties associated with the parameter R and independent variable (V_i), respectively. In addition, n is the number of the independent variables. Using the above equation for the equations of heat transfer coefficient, Nusselt number, Reynolds number and friction factor, the uncertainty related to each parameter can be determined easily. The values of uncertainty for heat transfer coefficient, Nusselt number, Reynolds number and friction factor are ±4.3%, ±5.4%, ±3.2%, and ±6.1%, respectively.

6. Results and discussion

In the first, the results related to thermophysical properties are presented and then the data related to the tests on the double tube heat exchanger are exhibited. Fig. 3 shows the variations of dimensionless effective thermal conductivity with volume fraction in the experimental data and the results obtained based on the models. The comparison reveals that the models fail to estimate the experimental data so that at the maximum concentration of the nanofluid i.e. 0.4%, there is a remarkable difference, about 40%, between the experimental data and Yu-Choi model.

Fig. 4 displays the variations of dimensionless effective thermal conductivity with solid volume fraction for the temperature range of 300–340 K. It is observed that at low concentration of nanofluid, temperature has no significant effect on the dimensionless effective thermal conductivity, whereas with increasing the volume fraction of particles, the effects of temperature are more considerable. This phenomenon can be described as follows. At a given volume of the nanofluid (e.g. 1 lit), when the solid volume fraction increases, it means that the number of particles and consequently the number of collisions due to Brownian motion of particles increases. On the other hand, with an increase in the temperature, the kinetic energy of particles increases and hence the number of collisions among the particles increases. Therefore, increasing the temperature boosts the effects of volume fraction raising.

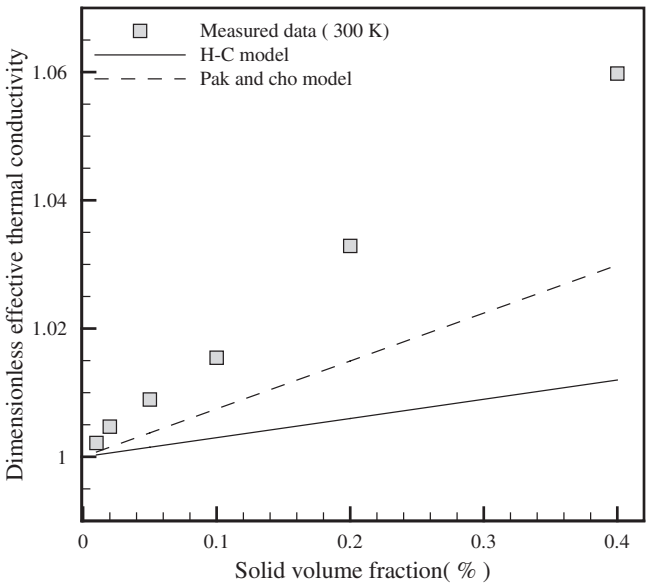

Fig. 3. Comparison between the experimental data and theoretical models for effective thermal conductivity.

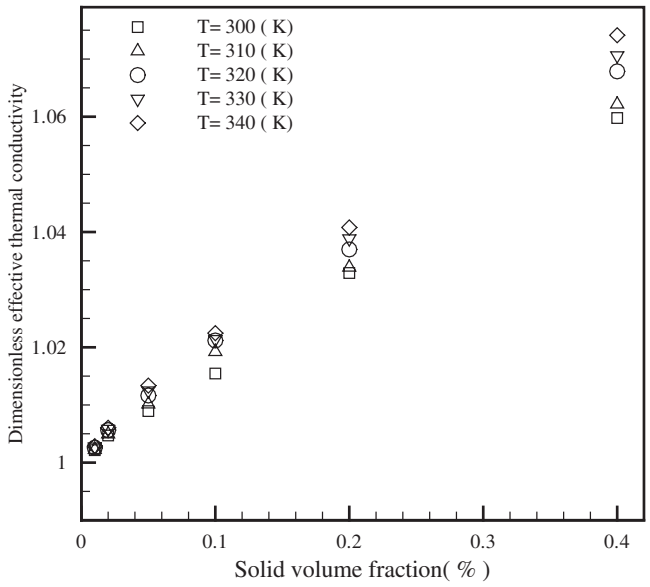

Fig. 4. Effective thermal conductivity at different temperatures.

Fig. 5 is plotted to show the fact that temperature has no significant effect on the effective thermal conductivity at low concentrations as mentioned in discussions of Fig. 4. As can be seen from Fig. 5, at volume fraction of 0.4%, the effective thermal conductivity increases up to 15% when increasing the temperature from 300 to 340 K.

Based on the experimental data a correlation can be presented using the regression analysis. This correlation is a function of the temperature and volume fraction of nanotubes as follows:

$$\frac{k_{nf}}{k_f} = \frac{\phi}{0.17981 - 0.000369T} + 1.0026 \tag{12}$$

Fig. 6 presents a comparison between the results obtained from experimental data and the two models of Einstein and Wang at T = 300 K and different quantities of solid volume fraction. As it is

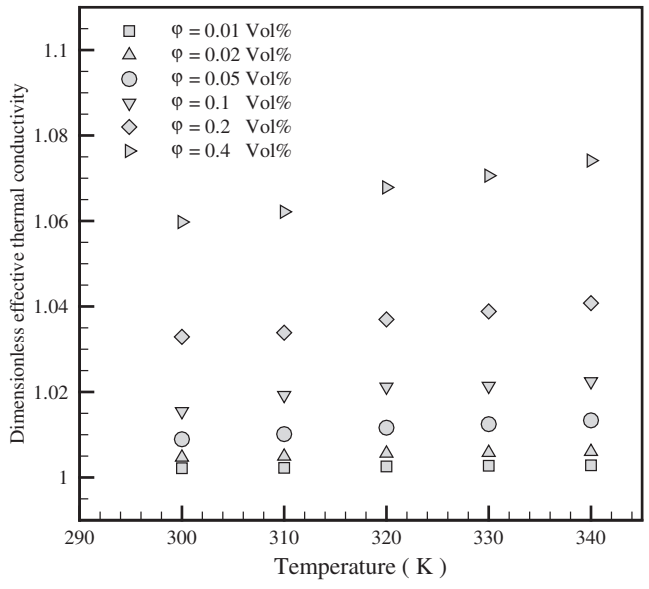

Fig. 5. Effective thermal conductivity at different volume fractions.

observed, the results predicted by Wang equation is close to the experimental data while Einstein model underestimates the viscosity of nanofluids.

Based on the experimental data, a correlation is presented to estimate the viscosity ratio as a function of volume fraction as follows:

$$\frac{\mu_{nf}}{\mu_f} = 1 + 3.575\phi + 6032.93\phi^2 - 1153669\phi^3 \quad (13)$$

Fig. 7 is plotted to verify the accuracy of the presented correlation.

Now, the results on the nanofluid flow in the heat exchanger are presented. First, to be sure about the accuracy of experiments, some tests have been done to evaluate the Nusselt number and friction factor where the working fluid is distilled water and the obtained results are compared with the most well-known correlations. The approximate range of Reynolds number is between 4000 and 31,000. The correlations used to estimate the Nusselt number are as follows:

Grielinski equation [35]:

$$Nu = \frac{f/8(\mathrm{Re}-1000)\mathrm{Pr}}{1+12.7\sqrt{\frac{f}{8}}\left(\mathrm{Pr}^{\frac{2}{3}}-1\right)}\left(\frac{\mathrm{Pr}}{\mathrm{Pr}_f}\right)^{0.11}\left[1+\left(\frac{d}{L}\right)^{\frac{2}{3}}\right] \quad (14)$$

This relation is valid for $0.5 < \mathrm{Pr} < 10^6$ and $2300 < \mathrm{Re} < 5 \times 10^6$. In this formulation, the Darcy coefficient is proposed as follows:

$$f = \frac{1}{(1.82log_{10}\mathrm{Re} - 1.64)^2} \quad (15)$$

where Re is the Reynolds number, Pr and $\mathrm{Pr_f}$ are the Prandtl numbers calculated at the water bulk temperature and at the inner wall temperature respectively; L is the tube length and d is the tube diameter. The bulk temperature is an average between the inlet and outlet fluid temperatures.

Dittues Bulter relation [36]:

$$Nu = 0.023\mathrm{Re}^{0.8}\mathrm{Pr}^{0.4} \quad (16)$$

Xuan and Li equation [37]:

$$Nu = 0.0059(1 + 7.62\varphi^{0.6886}Pe_d^{0.001})\mathrm{Re}^{0.9238}\mathrm{Pr}^{0.4} \quad (17)$$

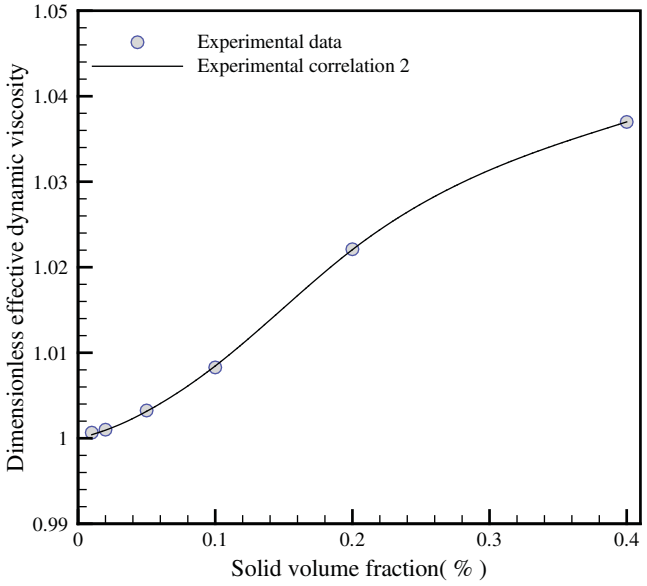

Fig. 7. Correlation for effective viscosity.

Petukhov correlation [38]:

$$Nu = \frac{(f/8)\mathrm{RePr}}{1.07 + 12.7(f/8)^{0.5}\left(\mathrm{Pr}^{\frac{2}{3}}-1\right)} \quad (18)$$

Which is applied in the range of $0.5 < \mathrm{Pr} < 200$ and $104 < \mathrm{Re} < 5 \times 10^6$.

Fig. 8 shows the comparison among different correlations and that one obtained from the tests on pure water. It is seen that the data are in good agreement with Xuan and Li correlation.

Fig. 9 gives a comparison between the friction factor obtained from the experiments and the values of friction factor obtained from Blasius equation($f = 0.25\mathrm{Re}^{-0.25}$).

As can be seen, the experimental data are very close to the results obtained from the equation.

After validating the results obtained by the set up, the experiments on the nanofluids at different volume fractions of

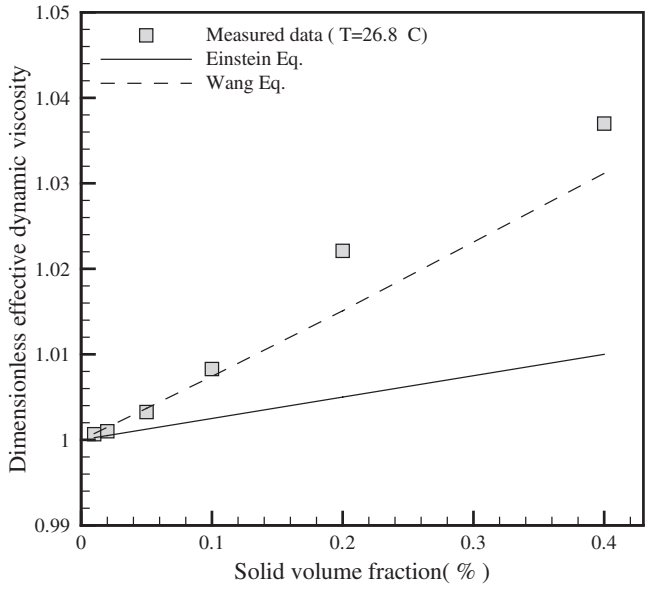

Fig. 6. Effective viscosity based on experimental data and the models.

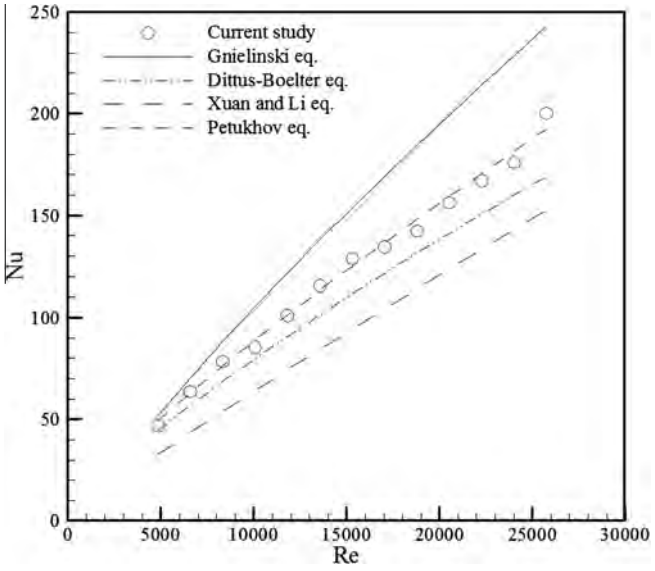

Fig. 8. Experimental Nusselt number and predictions correlations for pure water versus Reynolds number.

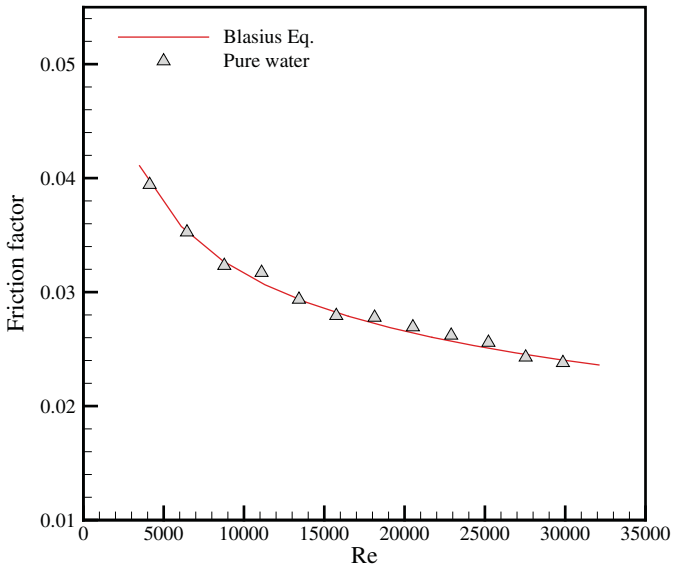

Fig. 9. Comparison of measured friction factor of water with Blasius theory.

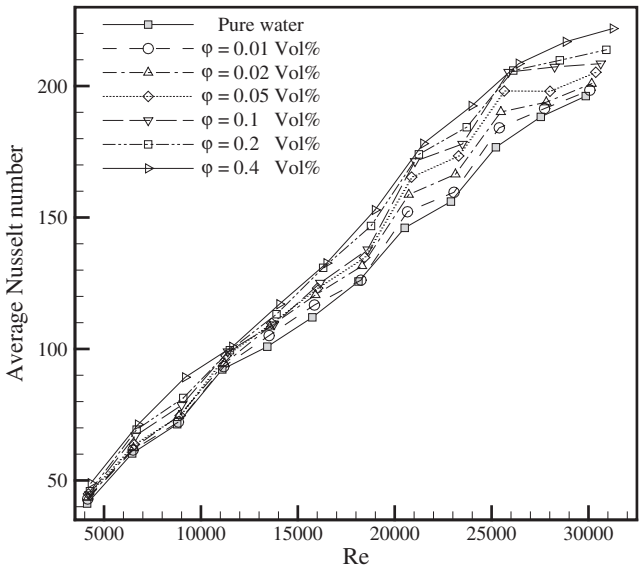

Fig. 11. Variations of average Nusselt number with the Reynolds number.

nanoparticles have been done. Fig. 10 shows the variation of heat transfer coefficient with the Reynolds number in different concentrations of nanofluids. As it is seen, with increasing the Reynolds number the effects of adding the nanoparticles to the pure water on the heat transfer enhancement is more visible. By increasing the Reynolds number, the turbulency of flow increases, on the other hand, with an increase in the particle loading the number of collisions among the particles increase, hence the effects of turbulency will be intensified. A higher number of collisions imply a greater thermal conductance, and hence heat transfer rate inside the tube. The data in the figure reveal that in the range of Reynolds numbers investigated on average the heat transfer coefficient is increased by 25% when the volume fraction of DWCNTs increases from 0 (pure water case) to 0.4%. This amount of enhancement (25%) which is obtained by adding a very low amount of particles to the pure water is so noticeable. The most likely reasons for this enhancement could be presented as follows. The first reason is the high thermal conductivity of DWCNTs that is about 3000 W/m K and enhances the effective thermal conductivity by 6% at 0.4% of

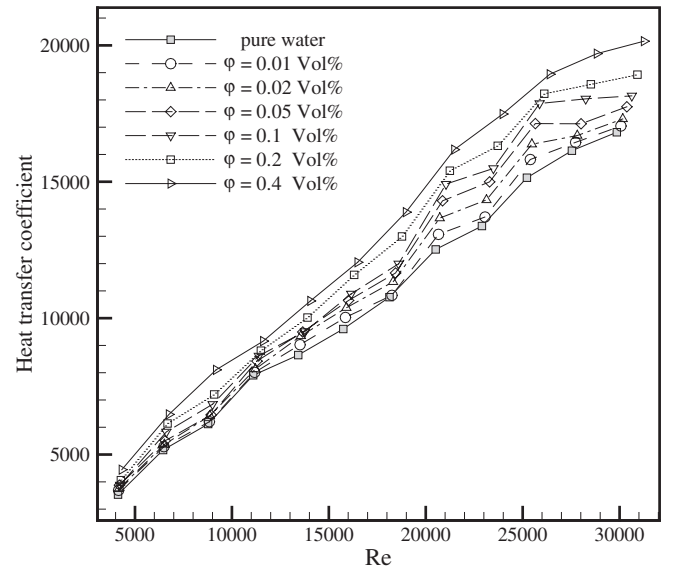

Fig. 10. Variations of heat transfer coefficient with the Reynolds number.

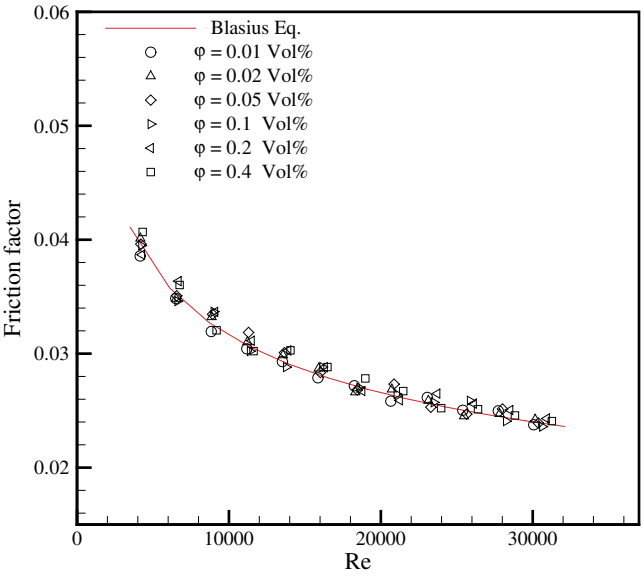

Fig. 12. Variations of friction factor with the Reynolds number.

particle loading (as shown in Fig. 3). Another reason is the cylindrical shape of nanotubes. The cylindrical shape of the particles causes greater contact area among the particles and hence a higher rate of heat transfer. Also, using the functionalized nanotubes due to better surface activity may be another reason for the heat transfer rate. It should be noted that the thermal conductivity of nanotubes is measured in stationary conditions, then the above mentioned reasons are more considerable when the nanofluid flows in turbulent conditions.

Using the data for heat transfer coefficient the average Nusselt number is demonstrated in Fig. 11, for the different concentrations of nanofluids. On average, the Nusselt number for 0.4% of the volume fraction of nanoparticles in comparison with the pure water increases by 18% .

The variations of friction factor with the Reynolds number is presented in Fig. 12 and the results are compared with Blasius equation. The effects of particle loading on the friction factor is more visible for low Reynolds numbers. At low Reynolds numbers,

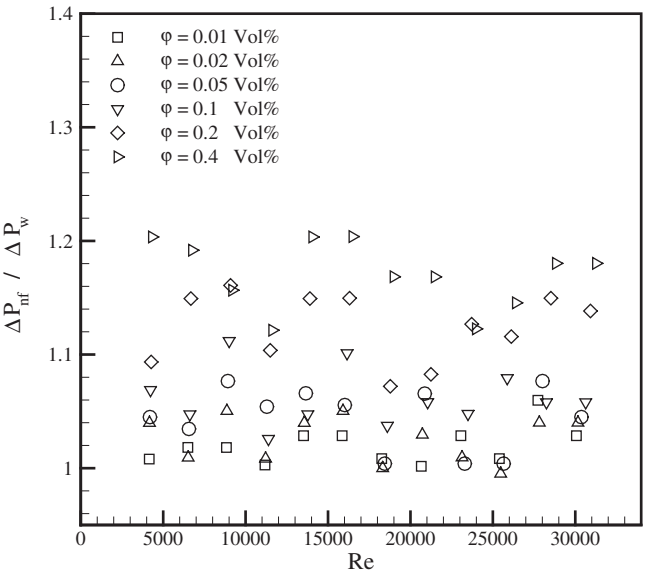

Fig. 13. Variations of pressure drop ratio with the Reynolds number.

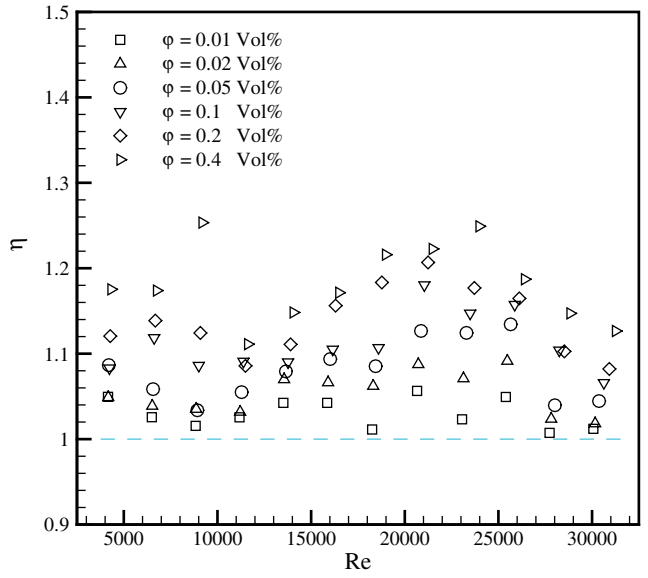

Fig. 14. Variations of thermal performance factor with the Reynolds number.

the friction factor increases with an increase in the volume fraction of nanoparticles. This happens because at low velocities of the flow, the ratio of the viscous forces to the inertia forces is greater, therefore; adding the cylindrical nanoparticles to pure water leads to more increase of shear stress among the fluid layers and hence the friction factor increases more considerable.

Fig. 13 is drawn to show the ratio of pressure drop due to the nanofluid flow to water flow. The findings indicate that for 0.4% of nanofluid concentration the pressure drop ratio is about 20%.

Now, using the thermal performance factor which is defined as:

$$\eta = (Nu_{nf}/Nu_f)/(f_{nf}/f_f)^{1/3} \quad (19)$$

one can evaluate the usefulness of nanofluids to apply in thermal systems. A higher thermal performance factor implies the greater usefulness. The thermal performance factor is shown in Fig. 14 for different Reynolds numbers and volume fractions. The results suggest that using the lowest quantities of volume fractions of nanotubes(i.e. 0.01%) is not so advantageous because the heat transfer enhancement effects are spoiled with the undesirable effects of pressure drop augmentation.

7. Conclusion

An experimental study is performed to evaluate the effects of adding low concentrations of a new class of nantubes i.e. COOH-functionalized double-walled carbon nanotubes (DWCNTs) to pure water on the heat transfer characteristics and pressure drop of nanofluid flow in a double tube heat exchanger. First, the thermal conductivity and viscosity of nanofluids are measured and it is found that the theoretical models for the two properties fail to predict the experimental data. After that, the tests are conducted under turbulent flow and the concentrations 0.01% to 0.4% of the nanofluid. The results indicate that even using a very low quantity of COOH-functionalized DWCNTs (0.4 vol.%) leads to remarkable enhancement in the heat transfer coefficient (on average 25%). Also, the average Nusselt number has increased on average by 18% while the pressure drop increases up to 20%. Finally, utilizing the definition of thermal performance factor, it was perceived that using 0.01% of nanotubes is not so advantageous due to the unfavourable effects of raising in pressure drop.

Acknowledgments

The authors sincerely would like to thank the Science and Technology Park of Semnan University for extending nano-reological laboratory facilities for this research work. The fourth author would like to thank the Thailand Research Fund, The National Science and Technology Development Agency, and the National Research University Project for the support.

References

[1] R. Saidur, K.Y. Leong, H.A. Mohammad, A review on applications and challenges of nanofluids, Renewable and Sustainable Energy Rev. 15 (3) (2011) 1646–1668.
[2] O. Mahian, A. Kianifar, S.A. Kalogirou, I. Pop, S. Wongwises, A review of the applications of nanofluids in solar energy, Int. J. Heat Mass Transfer 57 (2) (2013) 582–594.
[3] W. Yu, D.M. France, D.S. Smith, D. Singh, E.V. Timofeeva, J.L. Routbort, Heat transfer to a silicon carbide/water nanofluid, Int. J. Heat Mass Transfer 52 (2009) 3606–3612.
[4] L.S. Sundar, K.V. Sharma, Y.R. Sekhar, D.V. Rao, T. Subramanyam, J.V. Ramana Rao, Turbulent forced convection of Al_2O_3 nanofluid in a circular tube with tape inserts at low volume concentration, Int. J. Nano Biomater. 2 (1–5) (2009) 60–69.
[5] B. Farajollahi, S.Gh. Etemad, M. Hojjat, Heat transfer of nanofluids in a shell and tube heat exchanger, Int. J. Heat Mass Transfer 53 (1–3) (2010) 12–17.
[6] W. Duangthongsuk, S. Wongwises, Effect of thermophysical properties models on the prediction of the convective heat transfer coefficient for low concentration nanofluid, Int. Commun. Heat Mass Transfer 35 (2008) 1320–1326.
[7] W. Duangthongsuk, S. Wongwises, Heat transfer enhancement and pressure drop characteristics of TiO_2–water nanofluid in a double-tube counter flow heat exchanger, Int. J. Heat Mass Transfer 52 (2009) 2059–2067.
[8] W. Duangthongsuk, S. Wongwises, An experimental study on the heat transfer performance and pressure drop of TiO_2–water nanofluids flowing under a turbulent flow regime, Int. J. Heat Mass Transfer 53 (15) (2010) 334–344.
[9] L.S. Sundar, K.V. Sharma, Turbulent heat transfer and friction factor of Al_2O_3 nanofluid in circular tube with twisted tape inserts, Int. J. Heat Mass Transfer 53 (7–8) (2010) 1409–1416.
[10] S. Zhang, Z. Luo, T. Wang, C. Shou, M. Ni, K. Cen, Experimental study on the convective heat transfer of CuO–water nanofluid in a turbulent flow, J. Enhanced Heat Transfer 17 (2) (2010) 183–196.
[11] A. Amrollahi, A.M. Rashidi, R. Lotfi, Emami, M. Meibodi, K. Kashefi, Convection heat transfer of functionalized MWNT in aqueous fluids in laminar and turbulent flow at the entrance region, Int. Commun. Heat Mass Transfer 37 (6) (2010) 717–723.
[12] M. Hojjat, S.G. Etemad, R. Bagheri, J. Thibault, Convective heat transfer of non-Newtonian nanofluids through a uniformly heated circular tube, Int. J. Therm. Sci. 50 (4) (2011) 525–531.

[13] M. Hojjat, S.G. Etemad, R. Bagheri, J. Thibault, Turbulent forced convection heat transfer of non-Newtonian nanofluids, Exp. Therm. Fluid Sci. 35 (7) (2011) 1351–1356.
[14] S. Suresh, M. Chandrasekar, S. Chandra Sekhar, Experimental studies on heat transfer and friction factor characteristics of CuO/water nanofluid under turbulent flow in a helically dimpled tube, Exp. Therm. Fluid Sci. 35 (2011) 542–549.
[15] K. Tumuluri, J.L. Alvarado, H. Taherian, C. Marsh, Thermal performance of a novel heat transfer fluid containing multiwalled carbon nanotubes and microencapsulated phase change materials, Int. J. Heat Mass Transfer 54 (2011) 5554–5567.
[16] S. Suresh, P. Selvakumar, M. Chandrasekar, V.S. Raman, Experimental studies on heat transfer and friction factor characteristics of Al_2O_3/water nanofluid under turbulent flow with spiraled rod inserts, Chem. Eng. Process. 53 (2012) 24–30.
[17] L. Godson, B. Raja, D. Mohan Lal, S. Wongwises, Convective heat transfer characteristics of silver–water nanofluid under laminar and turbulent flow conditions, J. Therm. Sci. Eng. Appl. 4 (3) (2012) (art. no. 031001).
[18] A.A. Abbasian Arani, J. Amani, Experimental study on the effect of TiO2/water nanofluid on heat transfer and pressure drop, Exp. Therm. Fluid Sci. 42 (2012) 107–115.
[19] A.A.R. Darzi, M. Farhadi, K. Sedighi, R. Shafaghat, K. Zabihi, Experimental investigation of turbulent heat transfer and flow characteristics of SiO_2/water nanofluid within helically corrugated tubes, Int. Commun. Heat Mass Transfer 39 (9) (2012) 1425–1434.
[20] W.H. Azmi, K.V. Sharma, P.K. Sarma, R. Mamat, S. Anuar, V. D.Rao, Experimental determination of turbulent forced convection heat transfer and friction factor with SiO2 nanofluid, Exp. Therm. Fluid Sci., 2013, article in press.
[21] M. Hemmat Esfe, S. Saedodin, M. Mahmoodi, Experimental studies on the convective heat transfer performance and thermophysical properties of MgO–water nanofluid under turbulent flow, Exp. Therm. Fluid Sci., 2013, article in press.
[22] A.A.R. Darzi, M. Farhadi, K. Sedighi, Heat transfer and flow characteristics of AL_2O_3–water nanofluid in a double tube heat exchanger, Int. Commun. Heat Mass Transfer 47 (2013) 105–112.
[23] A.M. Hussein, K.V. Sharma, R.A. Bakar, K. Kadirgama, The effect of nanofluid volume concentration on heat transfer and friction factor inside a horizontal tube, J. Nanomater. (2013) (art. no. 859563).
[24] G.P. Celata, F. D'Annibale, A. Mariani, L. Saraceno, R. D'Amato, R. Bubbico, Heat transfer in water-based SiC and TiO_2 nanofluids, Heat Transfer Eng. 34 (13) (2013) 1060–1072.
[25] W. Yu, D.M. France, E.V. Timofeeva, D. Singh, J.L. Routbort, Comparative review of turbulent heat transfer of nanofluids, Int. J. Heat Mass Transfer 55 (2012) 5380–5396.
[26] R. Hamilton, O. Crosser, Thermal conductivity of heterogeneous two component systems, Ind. Eng. Chem. Fund. 1 (3) (1962) 187–191.
[27] W. Yu, S.U.S. Choi, The role of interfacial layers in the enhanced thermal conductivity of nanofluids: a renovated Maxwell model, J. Nanopart. Res. 5 (2003) 167–171.
[28] A. Einstein, Eine neue bestimmung der molekuldimensionen, Ann. Phys. Leipzig 19 (1906) 289–306.
[29] X. Wang, X. Xu, S.U.S. Choi, Thermal conductivity of nanoparticle–fluid mixture, J. Thermophys. Heat Transfer 13 (4) (1999) 474–480.
[30] I.M. Mahbubul, R. Saidur, M.A. Amalina, Latest developments on the viscosity of nanofluids, Int. J. Heat Mass Transfer 55 (2012) 874–885.
[31] F.M. White, Viscous Fluid Flow, second ed., McGraw Hill, New York, 2006.
[32] O. Mahian, A. Kianifar, C. Kleinstreuer, M.A. Nimr, I. Pop, A.Z. Sahin, S. Wongwises, A review of entropy generation in nanofluid flow, Int. J. Heat Mass Transfer 65 (2013) 514–532.
[33] S.J. Kline, F.A. Mcclintock, Describing uncertainties in single-sample experiments, Mech. Eng. 75 (1953) 3–8.
[34] V. Gnielinski, Int. Chem. Eng. 16 (1976) 359.
[35] F.P. Incropera, D.P. De Witt, Fundamentals of Heat and Mass Transfer, fourth ed., John Wiley, New York, 1996.
[36] Yimin. Xuan, Qiang. Li, Investigation on convective heat transfer and flow features of nanofluids, J. Heat Transfer 125 (2003) 151–155.
[37] B.S. Petukhov, Heat transfer and friction in turbulent pipe flow with variable physical properties, in: T.F. Irvine Jr., J.P. Hartnett (Eds.), Advances in Heat Transfer, vol. 6, Academic Press Inc., New York, 1970, pp. 504–564.

International Journal of Heat and Mass Transfer 73 (2014) 231–238

Contents lists available at ScienceDirect

International Journal of Heat and Mass Transfer

journal homepage: www.elsevier.com/locate/ijhmt

A comparative experimental study on the natural convection heat transfer of different metal oxide nanopowders suspended in turbine oil inside an inclined cavity

Saeed Zeinali Heris [a,*], Masoumeh Borhani Pour [a], Omid Mahian [b,c,*], Somchai Wongwises [c]

[a] Department of Chemical Engineering, Ferdowsi University of Mashhad, Mashhad, Iran
[b] Young Researchers and Elite Club, Mashhad Branch, Islamic Azad University, Mashhad, Iran
[c] Fluid Mechanics, Thermal Engineering and Multiphase Flow Research Lab. (FUTURE), Department of Mechanical Engineering, Faculty of Engineering, King Mongkut's University of Technology Thonburi, Bangmod, Bangkok 10140, Thailand

ARTICLE INFO

Article history:
Received 25 October 2013
Received in revised form 30 January 2014
Accepted 30 January 2014

Keywords:
Natural convection
Inclination angle
Nanofluids
Experimental study

ABSTRACT

An experimental study is conducted to investigate the effects of inclination angle on the natural convection of nanofluids inside a cubic cavity with the side size of 10 cm. One of the surfaces of the cavity is kept in cold temperature and another one (opposite side) in hot temperature while the other four surfaces are insulated. The mixtures of three different types of nanoparticles including Al_2O_3, TiO_2, and CuO within turbine oil (TO) are used as the heat transfer fluid. The heat transfer in the cavity is investigated in three inclination angles with respect to the horizontal position including 0°, 45° and 90° where the weight fractions of nanoparticles are 0.2%, 0.5%, and 0.8%. The Nusselt number results are presented for the three types of nanofluids, and different angles of inclination, Rayleigh number, and weight fraction of nanoparticles. The results reveal that the turbine oil has the highest Nusselt number in any inclination angle of the cavity compared to the nanofluids. Also, it is found that at the inclination angle of 90°, and the weight fraction 0.2%, the application of TiO_2 particles results in the maximum Nusselt number while for weight fraction of 0.8%, the maximum Nusselt number is associated with the CuO nanopowders.

© 2014 Elsevier Ltd. All rights reserved.

1. Introduction

Natural convection flow in enclosures is one of the classic problems that is important due to its application in many thermal engineering devices such as solar collectors, energy storage systems, electronic devices, and so on. Recent developments in the field of nanofluids as an advanced type of liquids with surprising properties have led to a renewed interest in the study of natural convection in enclosures where a nanofluid is the working fluid. The satisfactory effects of using nanofluids on the heat transfer enhancement are proven in many applications such as solar cells, solar collectors, nuclear reactors, automobiles, microchannels, electronic devices, phase change materials, and so on [1,2].

Here, some studies on the natural convection in cavities using nanofluids are reviewed briefly. First, the numerical works are reviewed. Ho et al. [3] in a numerical work investigated the effects of using different models to calculate the viscosity and thermal conductivity on the natural convection heat transfer inside a square cavity. The bottom and top walls were insulated while one of the side walls was assumed cold and another one hot. They used alumina/water nanofluids as the working fluid where the volume concentrations do not exceed 4%. They concluded that using different thermophysical models may lead to the estimations in an opposite trend for the Nusselt number especially in high solid volume fractions. Abu-Nada and Oztop [4] examined numerically the effects of inclination angle (between 0° and 120°) of a square cavity filled with Cu/water nanofluid (volume fractions upto 10%) on the heat transfer. The boundary conditions in this work were similar to the boundary conditions considered by Ho et al. [3]. Öğüt [5] simulated the natural convection of five different water based nanofluids (volume fractions upto 20%) containing Cu, Ag, CuO, Al_2O_3, and TiO_2 nanoparticles in a cavity where one of the side walls was heated using a heater mounted on the wall. The cavity angle was varied between 0° and 90°. They indicated that with increasing the concentration, the heat transfer rate increases. This increase was more considerable for the particles with higher thermal conductivity (i.e. Ag and Cu). In a similar work to the study of

* Corresponding authors. Tel./fax: +98 511 8816840.
E-mail addresses: zeinali@ferdowsi.um.ac.ir (S.Z. Heris), omid.mahian@gmail.com (O. Mahian).

http://dx.doi.org/10.1016/j.ijheatmasstransfer.2014.01.071
0017-9310/© 2014 Elsevier Ltd. All rights reserved.

Nomenclature

A	heat transfer area
c_p	specific heat (kJ/kg K)
d_p	diameter of the alumina particles (nm)
g	gravitational acceleration (m/s^2)
h	surface-averaged heat transfer coefficient (W/m^2 K)
k	thermal conductivity (W/m K)
l	length of cavity (m)
Nu_{nf}	average Nusselt number
q''	surface-averaged heat flux from the hot wall (W/m^2)
Pr_{nf}	Prandtl number
Ra_{nf}	Rayleigh number
T	temperature (C)

Greek symbols

α	thermal diffusivity (m^2/s)
β	volumetric thermal expansion coefficient (1/K)
μ	dynamic viscosity (kg/m s)
ρ	density (g/cm^3)

Subscripts

bf	base fluid
c	cold wall
h	hot wall
m	mean value
nf	nanofluid
p	nanoparticles

Ho et al. [3], Abu-Nada et al. [6] investigated the effects of uncertainties in thermophysical properties on the heat transfer of Al_2O_3–water and CuO–water nanofluids (volume fractions upto 9%) in the cavity. They concluded that the average Nusselt number has a higher sensitivity to viscosity compared to thermal conductivity at high Rayleigh numbers, hence, a suitable viscosity model should be selected for such conditions.

Ghasemi and Aminossadati [7] analysed numerically the flow of Cu, Al_2O_3 and TiO_2 nanoparticles suspended in water in a cavity where the top and bottom walls are insulated, right wall is kept cold and the left wall is subjected to a periodic heat flux. They found that using Cu and TiO_2 (volume fractions upto 20%) leads to the maximum and minimum heat removal from the heat source, respectively. Shahi et al. [8] considered the flow of Cu/water nanofluid (volume fractions upto 5%) in a square cavity where the bottom wall is subjected a constant heat flux, while the cooling of the cavity is conducted by entering a nanofluid flow from the left wall and exiting from the right wall. They concluded that an increase in the volume fraction increases the average Nusselt number in the cavity. Lin and Violi [9] simulated the effects of particle size on the natural convection flow of Al_2O_3/water nanofluid (volume fraction upto 5%) in a cavity. Their results indicated that by decreasing the nanoparticle size from 250 nm to 5 nm, the heat transfer rate increases.

Kahveci [10] conducted a work similar to Ref. [5], with this difference that the cavity can rotate from 0° to 90°. The author revealed that with the increase of the Rayleigh number, the inclination angle in which the maximum heat transfer rate occurs, changes from 45° to 30°. He also found that using Ag nanopartilces results in the maximum heat transfer rate, while the heat transfer rate is minimum for TiO_2 nanoparticles. Corcione [11] obtained the optimum particle loading for the nanofluid flow in a cavity with different aspect ratios. The author concluded that with the decrease of nanoparticle size, the level of optimal volume fraction increases. Mahmoudi et al. [12] studied the mixed convection flow of Cu/water nanofluid in a cavity where four different configurations were considered based on the inlet and outlet flow. In another work, Mahmoudi et al. [13] solved the natural convection problem where the thickness of the left wall is considered.

The interested readers can refer to other numerical works are as follows. The effects of temperature dependent models on the natural convection were considered by Abu-Nada [14], the natural convection of nanofluids in a cavity using the lattice Boltzmann method was studied by Lee and Yang [15], investigation of thermophoresis and Brownian motion effects on natural convection by Haddad et al. [16], double-diffusive natural convection of nanofluid was studied by Parvin et al. [17], heatline analysis of nanofluid flow in natural convection has been conducted by Basak and Chamkhah [18], the effect of nanoparticle shape was investigated by Ooi and Popov [19], free convection in a complicated cavity was studied by Nasrin and Alim [20], and finally the free convection in a cavity filled with nanofluids was considered by Garoosi et al. [21] where several pairs of coolers and heaters were installed inside the cavity. A comprehensive review on the natural convection of nanofluids in cavities with different structures is performed by Haddad et al. [22].

However, also some experimental works on the natural convection of nanofluids in cavities are observed in the literature.

Wen and Ding [23] during an experimental work on the natural convection of TiO_2/water nanofluid between two parallel disks, concluded that using nanofluids leads to the decrease of the heat transfer rate in the enclosure. They used the nanofluids at low volume concentrations (not more than 0.57%). Nnanna [24] tested Al_2O_3–water nanofluids with volume fractions upto 8% in a partially heated cavity. It was found that using nanofluids with concentrations upto 2% results in the increase in the heat transfer rate while for volume fractions greater than 2%, due the unfavorable effects of viscosity the heat transfer rate decreases. Li and Peterson [25] sought for the possible reasons behind the heat transfer detraction due to using Al_2O_3/water nanofluids (volume fractions upto 6%) in a vertical cylindrical cavity. In separate experiments, they could find that the Brownian motion and thermophoresis phenomena affect the heat transfer rate. In a nice work, Ho et al. [26] examined the natural convection of Al_2O_3/water nanofluid (volume fractions upto 4%) in the vertical cavities with three different aspect ratios. They concluded that increasing the particle loading (more than about 1%) leads to the decrease of the average Nusselt number especially at lower Rayleigh numbers.

As it is seen, although extensive numerical studies have been performed on the natural convection in a cavity using nanofluids, but there has been little experimental works in this field. This is due to the difficulties in the experimental study of such flows. Also, in most of the studies the base fluids were water or ethylene glycol.

The present work aims to provide a comprehensive investigation on the effects of using three different turbine oil (TO) based nanofluids including Al_2O_3, TiO_2, and CuO nanoparticles in a cubic cavity. After preparing the suspensions of nanofluids, the effects of the inclination angle, Rayleigh number, and volume fraction of nanoparticles on the Nusselt number are investigated. Utilizing three different types of nanoparticles let to find out the effects of thermal conductivity, heat capacity, density and thermal expansion of nanoparticles on the heat transfer rate.

Table 1
Properties of nanoparticles and turbine oil in room temperature.

Nanoparticle type	Mean diameter (nm)	Thermal expansion coefficient (1/K)	Density (kg/m^3)	Heat capacity (J/kg K)	Thermal conductivity (W/m K)
TiO_2	20	0.9×10^{-5}	4250	686.2	8.95
CuO	60	1.8×10^{-5}	6400	535.6	76.5
Al_2O_3	20	0.85×10^{-5}	3970	765	40
Turbine oil	–	64×10^{-5}	875	2000	0.133

2. Nanofluid preparation

Nanoparticles of Al_2O_3 (20 nm), TiO_2 (20 nm), and CuO (60 nm) have been purchased from the NIPPON AEROSIL company, Japan while the turbine oil is provided by Behran Oil company, Iran. The thermophysical properties of nanoparticles and turbine oil are presented in Table 1. To prepare a given concentration of the nanofluids, a specified quantity of the nanoparticles is weighed, then it is added to the turbine oil little by little. Simultaneously, by using a magnetic stirrer the suspension is mixed well for 30–45 min. After mixing, the samples are inserted inside an ultrasonic vibrator (Misonix Inc. XL2020) for about 1 h to have a homogenous mixture and breaking down the agglomeration between the nanoparticles.

The samples are provided in three different concentrations including 0.2 wt.%, 0.5 wt.%, and 0.8 wt.%. By converting the concentrations in terms of volume fraction, one can find that the concentrations do not exceed 0.5 vol.%. This reveals that low concentrations of nanofluids used in the present work. Fig. 1 shows the photographs of the prepared samples and the pure turbine oil. It should be noted that the samples were stable during the tests and no sedimentation is observed with naked eyes, but; in general, CuO/TO nanofluids were stable for a shorter time in comparison with TiO_2/TO and Al_2O_3/TO nanofluids. The lower level of stability

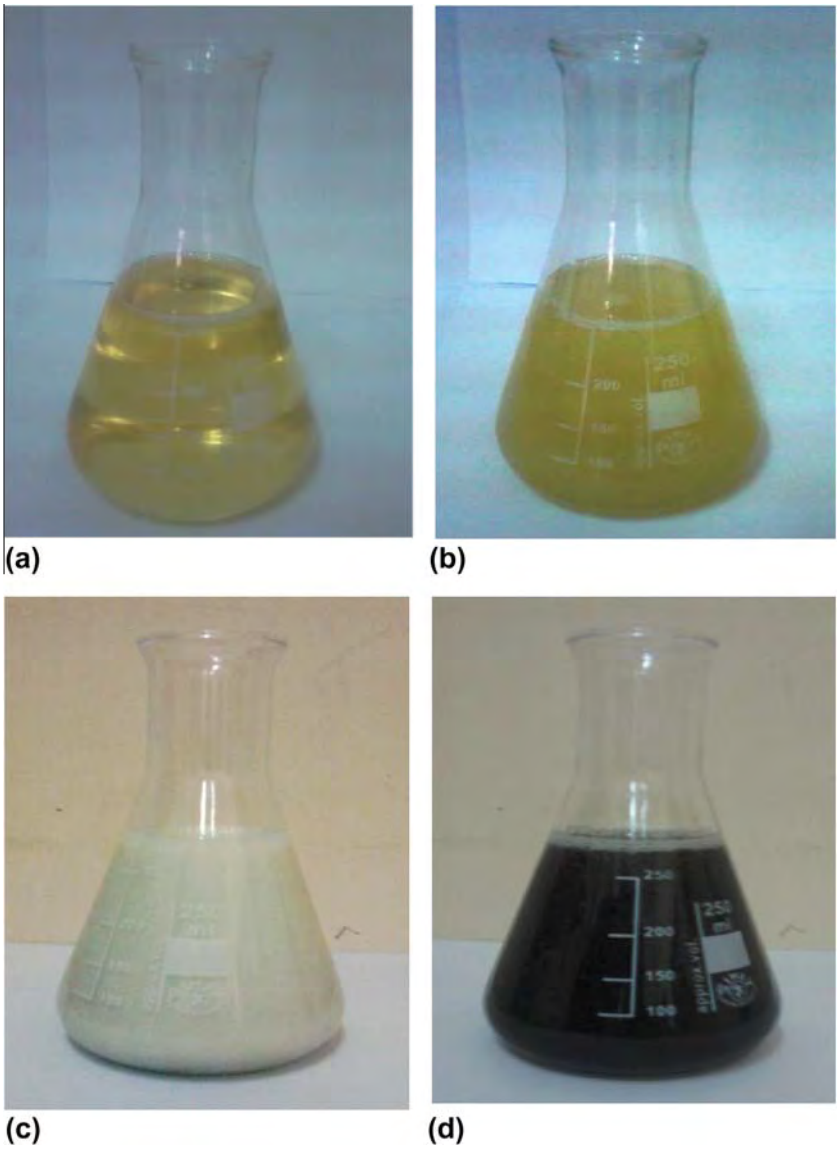

Fig. 1. Photographs of the samples: (a) turbine oil, (b) Al_2O_3/ TO, (c) TiO_2/ TO, and (d) CuO/TO.

of CuO/TO nanofluids may be due to the higher density and bigger size of its particles compared to other ones.

3. Experimental set up and procedure

The schematic view and photograph of the experimental set up is shown in Fig. 2.

The experimental set up is composed of a test cell, insulator materials, nanofluid tank, DC power supply, and electrical panel. The test cell is a cubic cavity with the side size of 10 cm. One of the walls is cooled down by cooling water while another wall at the opposite side is heated by a heating element with the maximum power of 1000 W. The power of heating element is regulated by varying the voltage of DC power supply. The cold and hot walls are made of copper with a thickness of 2 mm, and other walls are made of steel and the thickness of 2 mm. All walls are insulated with a ceramic fiber insulating blanket with a thickness of 50 mm. PT 100 thermocouples with an accuracy of 0.1 °C are used to measure the surface temperature of the hot and cold walls. The thermocouples are calibrated in a constant temperature bath equipped with a digital thermometer with an accuracy of 0.1 °C. After about 3 h the system reaches the steady state conditions so that no change is observed in the temperatures. The temperatures are recorded in the steady state conditions. After each test, the enclosure is cleaned well. The tests are repeated 3–4 times to be sure about the repeatability of the data.

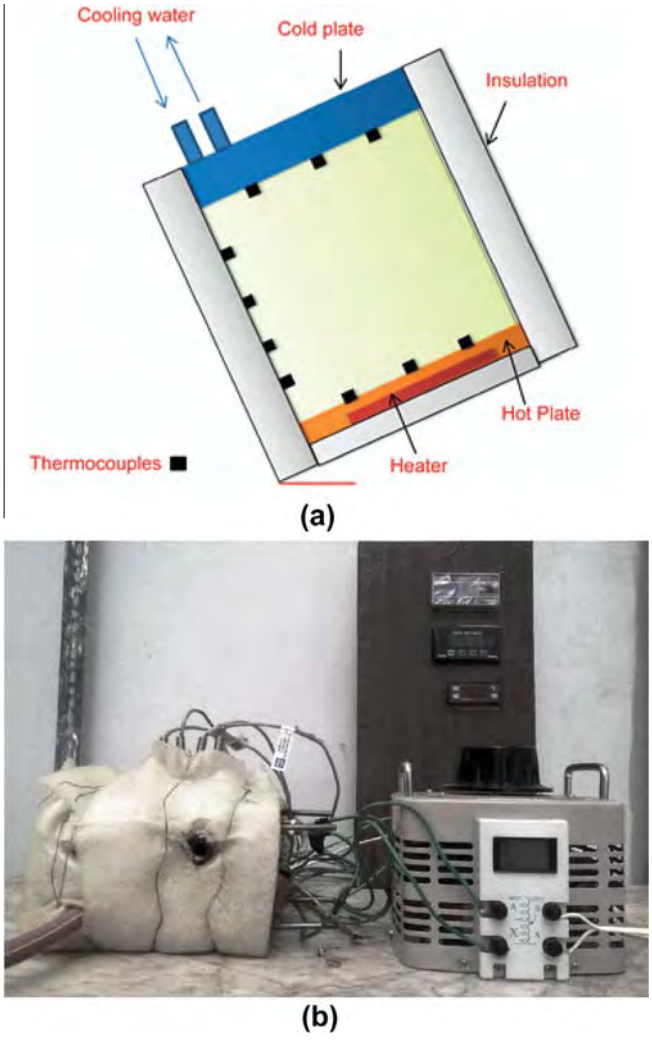

Fig. 2. (a) Schematic view of the inclined cavity, and (b) photograph of the experimental set up.

4. Data reduction

The steady state heat flux applied on the hot wall is obtained by multiplying the voltage (V) and current (I) as follows:

$$q'' = VI \tag{1}$$

Therefore the heat transfer coefficient (h) and the Nusselt number (Nu) can be determined as:

$$\bar{h} = \frac{q''}{A(T_h - T_c)} \tag{2}$$

$$Nu = \frac{\bar{h}l}{k_{nf}} \tag{3}$$

In which T_h and T_c are the temperatures of hot and cold walls, respectively. Also, l is the size of cavity, and k_{nf} is the thermal conductivity of nanofluid.

Also, the Rayleigh number is computed by:

$$Ra = \frac{g\rho_{nf}^2 c_P \beta_{nf}(T_h - T_c)l^3}{k_{nf}\mu_{nf}} \tag{4}$$

The thermophysical properties of the nanofluid are calculated at the mean temperature of the hot and cold walls ($T_h + T_c/2$) as follows. Thermal conductivity is obtained by Hamilton–Crosser equations [27]:

$$K_{nf} = \frac{k_p + (n-1)k_f + (n-1)\phi(k_p - k_f)}{k_p + (n-1)k_f - \phi(k_p - k_f)}k_f \tag{5}$$

Density (ρ_{nf}), heat capacity (C_{nf}) and thermal expansion coefficient (β_{nf}) are calculated by Khanafer and Vafai [28]:

$$\rho_{nf} = \rho_f(1-\phi) + \rho_p\phi \tag{6}$$

$$C_{nf} = \frac{\rho_f C_f(1-\phi) + \rho_p C_p \phi}{\rho_{nf}} \tag{7}$$

$$\beta_{nf} = \frac{(1-\phi)(\rho\beta)_f + \phi(\rho\beta)_p}{\rho_{nf}} \tag{8}$$

The viscosity is determined by the Brinkman relation [29]:

$$\mu_{nf} = \frac{\mu_f}{(1-\phi)^{2.5}} \tag{9}$$

As mentioned the volume concentrations used in the present work do not exceed 0.5%, therefore, as it is confirmed by Ho et al. [3] and Abu-Nada et al. [6] the uncertainties in thermophysical models have no effect on the reported results in low concentrations.

5. Results and discussion

In this section, the effects of concentration, inclination angle, and nanoparticle type in different Rayleigh numbers on the Nusselt number are investigated.

5.1. Effects of concentration

Fig. 3 shows the variations of the Nusselt number with the Rayleigh number for different concentrations of TiO_2/TO, Al_2O_3/TO, and CuO/TO nanofluids and inclination angles of 0, 45, and 90. As it is observed, at all inclination angles for TiO_2/TO nanofluid, the Nusselt number decreases with an increase in the weight fraction of nanoparticles. However, for the two other nanofluids there is

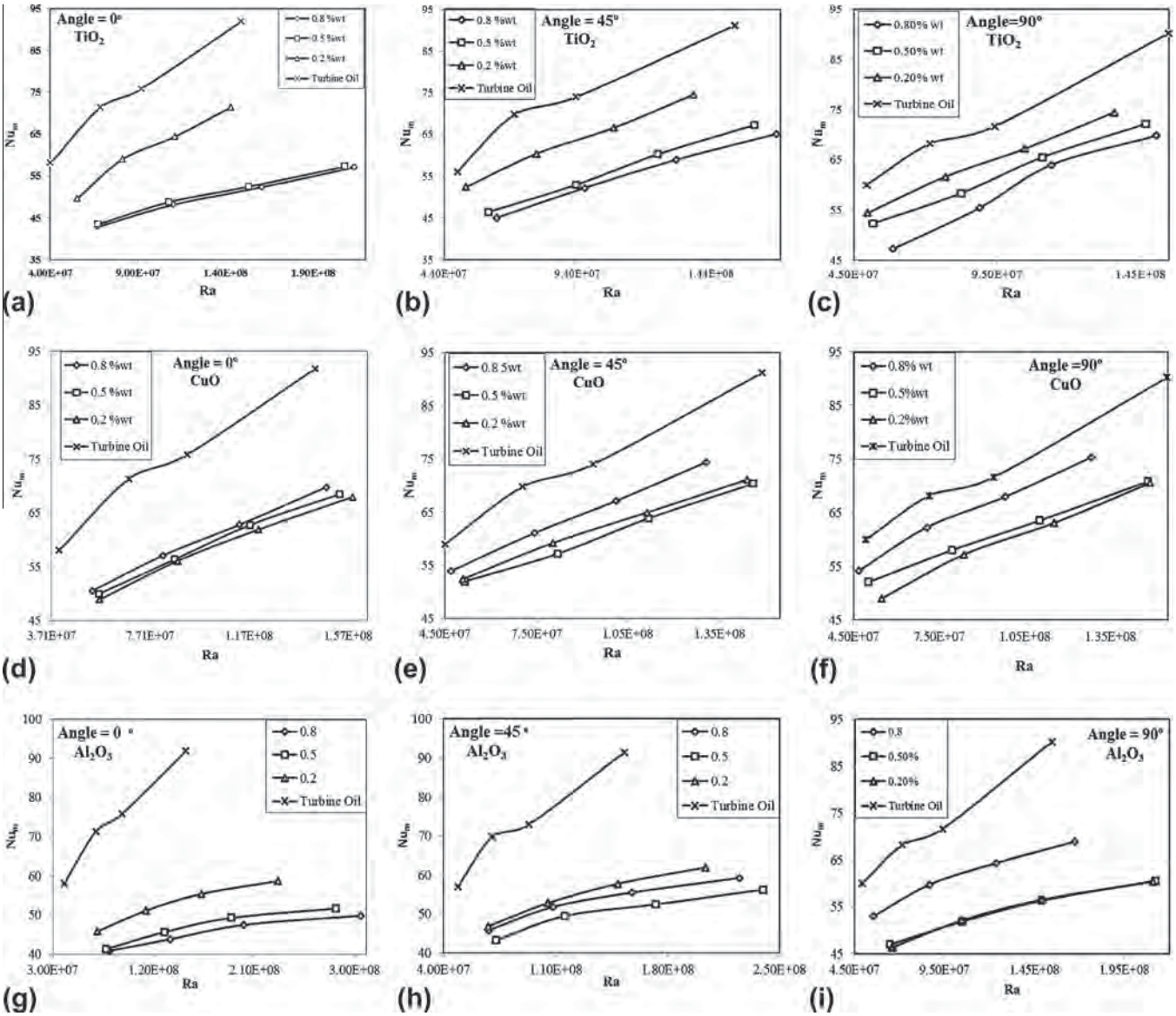

Fig. 3. Effects of concentration on the Nusselt number for different nanoparticles.

no a specified trend for the changes in the Nusselt number. The following relation can help to describe the reasons behind the changes in the Nusselt number [26]:

$$\frac{h_{nf}}{h_f} \approx \left(\frac{\beta_{nf}}{\beta_f}\right)^{n} \left(\frac{\rho_{nf}}{\rho_f}\right)^{2n} \left(\frac{C_{p,nf}}{C_{p,f}}\right)^{n} \left(\frac{k_{nf}}{k_f}\right)^{1-n} \left(\frac{\mu_{nf}}{\mu_f}\right)^{-n} \tag{10}$$

The above relation can be developed in terms of the Nusselt number as follows:

$$\frac{Nu_{nf}}{Nu_f} \approx \left(\frac{\beta_{nf}}{\beta_f}\right)^{n} \left(\frac{\rho_{nf}}{\rho_f}\right)^{2n} \left(\frac{C_{p,nf}}{C_{p,f}}\right)^{n} \left(\frac{k_{nf}}{k_f}\right)^{-n} \left(\frac{\mu_{nf}}{\mu_f}\right)^{-n} \tag{11}$$

or:

$$\frac{Nu_{nf}}{Nu_f} \approx (\beta_r)^{n} (\rho_r)^{2n} (C_{p,r})^{n} (k_r)^{-n} (\mu_r)^{-n} \tag{12}$$

where n is considered equal to 1/3, and the subscript r indicates the ratio of the properties. With an increase in the concentration of nanofluids, the density, thermal conductivity and viscosity ratios increase while the heat capacity and thermal expansion coefficient ratios decrease. However, it should be considered that the power of n for the thermal conductivity and viscosity ratios in the relation is negative. Therefore, the Nusselt number increases with particle loading due to the increase of density ratio. On the other hand, the Nusselt number decreases with particle loading due to the decrease of thermal conductivity, viscosity, heat capacity and thermal expansion coefficient ratios. The outcome of these changes is the decrease of the Nusselt number for the TiO_2/TO nanofluid. For Al_2O_3/TO and CuO/TO nanofluids it is not predictable that which concentration yields the minimum Nusselt number, as shown in figure. More experiments are needed to know the reasons behind these unusual changes. However, the physical and chemical specifications of nanoparticles such as the shape, size, heat absorption and the level of surface activity should be considered as possible reasons. Moreover, CuO and Al_2O_3 particles have higher thermal conductivity compared to TiO_2 particles. This may affect the thermophoresis phenomenon which is occurring in the cavity. Thermophoresis is sensitive to the changes in the temperature gradient and hence the variations of the thermal conductivity. In all cases, the

Nusselt number increases with an increase in the Rayleigh number due to the increases in the buoyancy force. The rate of increase in the Nusselt number for nanofluids is lower than the pure turbine oil. This may happen because of the agglomeration and probable sedimentation of nanoparticles on the hot plate which deteriorates the heat transfer.

5.2. Effects of inclination angle

Now, the aim is to focus on the effects of inclination angle on the Nusselt number for the three types of nanofluids. As it is shown in Fig. 4, for all types of nanofluids and any concentration, the Nusselt number is minimized at the inclination angle of 0° where the hot plate is placed on the ground. This happens because in this case the heat transfer is deteriorated due to the lower velocity of particles that is due to the gravitational effects.

For TiO_2 particles, the maximum heat transfer occurs at the angle of 90°. For Al_2O_3 and CuO the heat transfer is highest at 90° in the weight fractions of 0.8% and 0.5%. However, for 0.2% particle loading, the maximum heat transfer happens at 45° due to the higher migration velocity of particles in this angle compared to 90°.

5.3. Effects of nanoparticle type

Finally, the effects of using different nanoparticles in the cavity on the Nusselt number are investigated. Fig. 5 shows the variation of the Nusselt number with the Rayleigh number at the inclination angle of 90°. As it is seen, for the weight fraction of 0.2%, the use of TiO_2 particles leads to the maximum Nusselt number in the cavity, although its thermal conductivity is the smallest. By increasing the weight fraction of nanoparticles from 0.2% to 0.8%, Cuo/To nanofluid shows a higher Nusselt number compared to TiO_2/TO nanofluid. Also, it is perceived that for the weight fraction of 0.8%, the magnitude of the Nusselt number for Al_2O_3/TO nanofluid is higher than TiO_2/TO nanofluid at lower Rayleigh numbers.

Referring to Eq. (11) and with the development of it for two particles, one can write:

$$\frac{Nu_{nf})_{p_2}}{Nu_{nf})_{P_1}} \approx \left(\frac{\beta_{nf,p_2}}{\beta_{nf,p_1}}\right)^n \left(\frac{\rho_{nf,p_2}}{\rho_{nf},p_1}\right)^{2n} \left(\frac{C_{p,nf,p_2}}{C_{p,nf},p_1}\right)^n \left(\frac{k_{nf},p_1}{k_{nf},p_2}\right)^n \left(\frac{\mu_{nf},p_1}{\mu_{nf},p_2}\right)^n \tag{13}$$

where the subscripts $p_1$and p_2 indicates the particle type #1 and particle type #2. To explain the reasons behind the changes of the

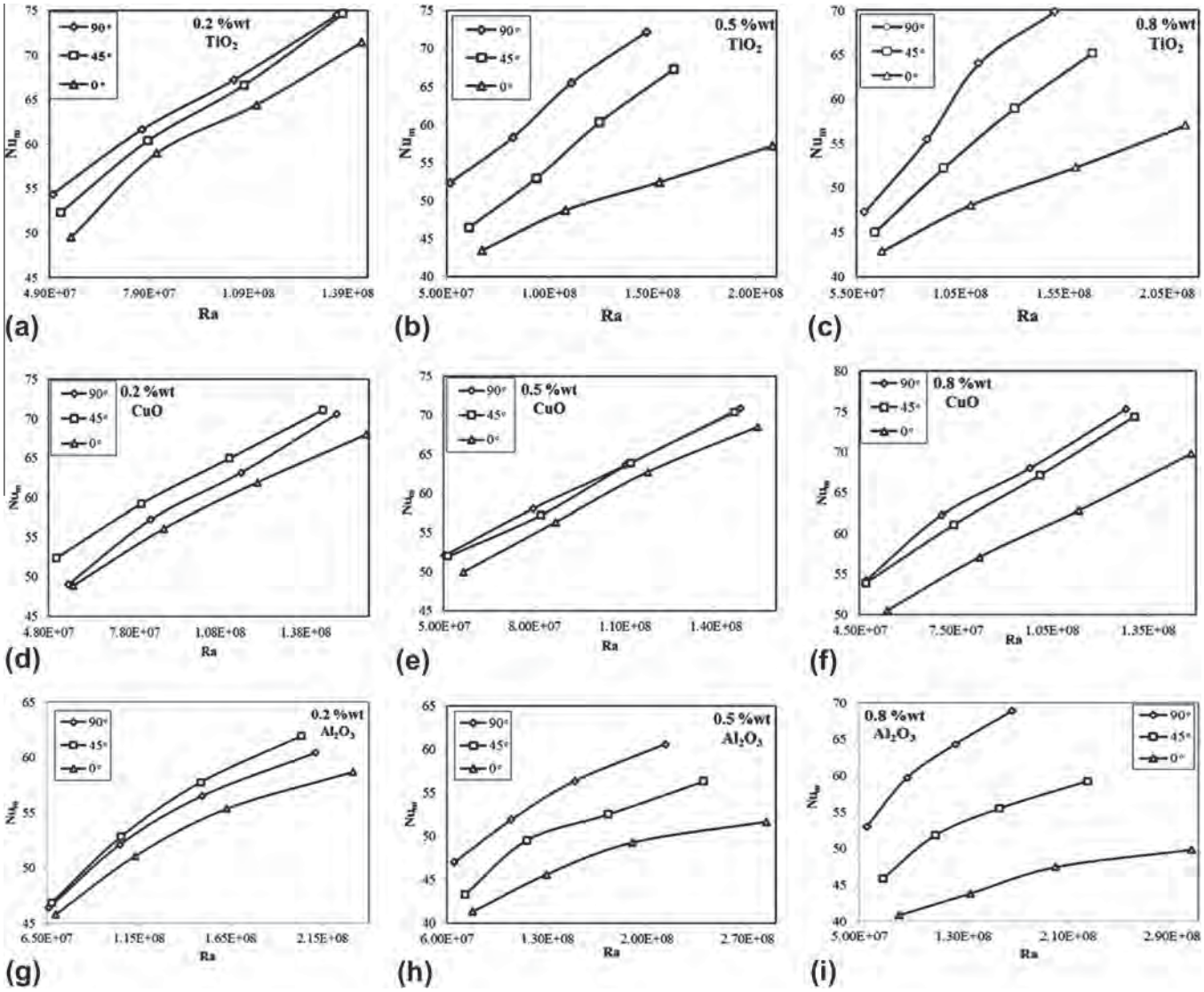

Fig. 4. Effects of inclination angle on the Nusselt number for different nanoparticles.

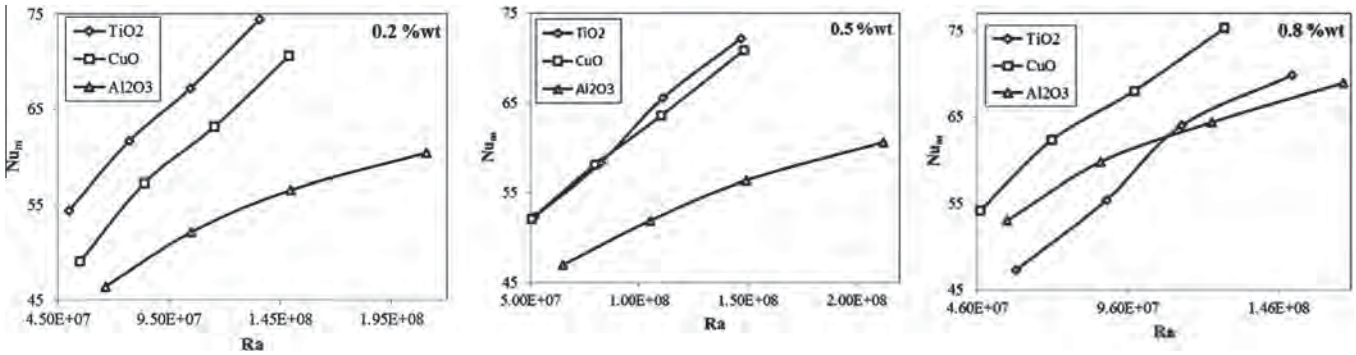

Fig. 5. Effects of different nanoparticles on the Nusselt number for the inclination angle of 90°.

Nusselt number, besides the above relation, the effects of size,-shape, heat absorption, and Brownian motion of nanoparticles should be considered. Also, the van der Waals' forces between the nanoparticles are another important factor. As the van der Waals' forces increase, the agglomeration of nanoparticles increases which it can reduce the effect of buoyancy force and consequently the Nusselt number decreases. Therefore, more experiments in microscopic and macroscopic scales should be done to find out the reasons behind the changes in the Nusselt number for different nano materials.

6. Uncertainty analysis

Uncertainty analysis is performed to determine the percentages of error in each experiment. In the following, the uncertainty analysis for important parameters such as the heat transfer coefficient, Nusselt number, and Rayleigh number is conducted in details.

The maximum possible error (E_{Mi}) in the measurement of parameter M is determined by:

$$E_{Mi} = \frac{X_i}{M}\frac{\partial M}{\partial X_i}E_{x_i} \tag{14}$$

in which X_i is an independent parameter that can be determined directly through the measurements. M is the d that is calculated through X. E_{Xi} is obtained by dividing the measurement accuracy of the device that is used for measuring a parameter to the minimum value of the measured quantity during the tests.

Another form of the above equation is as follows:

$$MaxE_M = \left[\left(\frac{X_1}{M}\frac{\partial M}{\partial X_1}E_{x_1}\right)^2 + \left(\frac{X_2}{M}\frac{\partial M}{\partial X_2}E_{x_2}\right)^2 + \cdots + \left(\frac{X_n}{M}\frac{\partial M}{\partial Xn}E_{x_n}\right)^2\right]^{1/2}$$

6.1. Calculation of errors

In this section, E_{Xi} for all measured parameters are calculated.

The mass of nanoparticle : $E_m = \pm\frac{0.001}{1.752} = \pm 5.71 \times 10^{-4}$

The temperature : $E_{(T_h - T_c)} = \pm\frac{0.1}{22.8} = \pm 4.93 \times 10^{-3}$

The length of cavity : $E_l = \pm\frac{0.001}{0.1} = \pm 0.01$

The surface area of the cavity : $E_A = \pm\left[E_l^2 + E_l^2\right]^{1/2} = \pm 0.014$

Voltage : $E_V = \pm\frac{1}{25} = \pm 0.04$

Current : $E_I = \pm\frac{0.001}{0.648} = \pm 1.54 \times 10^{-3}$

6.2. Maximum error in the estimation of heat transfer parameters

First, the maximum error in the estimation of heat transfer coefficient is determined as follows:

$$MaxE_{\bar{h}} = \pm\left[E_V^2 + E_I^2 + (-E_A)^2 + (-E_{(T_h - T_c)})^2\right]^{1/2} = \pm 0.0426$$

Therefore, the maximum error in the measurement of heat transfer coefficient is 4.26%. In a similar way, the uncertainties in the estimation of the Nusselt number and the Rayleigh number are 7.43% and 9.45%, respectively.

7. Conclusions

A comparative experimental study is conducted to examine the effects of metal oxide nanopowders including TiO_2, CuO, and Al_2O_3 suspended in turbine oil on the natural convection flow inside a titled cube cavity. Three inclination angles of 0, 45, and 90° and three weight fractions of 0.2%, 0.5%, and 0.8% are investigated in the work. The results show that for any inclination angle and the Rayleigh number, the Nusselt number is higher for turbine oil compared to the nanofluids. For TiO_2/TO nanofluids, with increasing the inclination angle from 0 to 90, the Nusselt number increases. In other words, the optimum inclination angle for TiO_2/TO nanofluids is 90°. However, the tests on the two other nanofluids indicate that at the low concentration (i.e. 0.2 wt%), the maximum heat transfer occurs at the inclination angle of 45°. Also, it is found that for the angle of 90°, in the weight fraction of 0.2%, using TiO_2/TO nanofluid results in the maximum Nusselt number while for 0.8% wt.% the maximum Nusselt number is caused by the CuO/TO nanofluid flow. It was concluded that besides some factors such as shape, size, heat absorption, Brownian motion, and physical and chemical properties of the nanoparticles, future experimental studies are needed to know the possible reasons behind the changes in the Nusselt number for different nano materials.

Acknowledgments

The authors acknowledge Iranian Nano Technology Initiative for the financial support of this study. The third author wishes to thank Prof. Somchai Wongwises for the supports during his research at FUTURE, King Mongkut's University of Technology Thonburi, Thailand. The fourth author wishes to thank the National Science and Technology Development Agency, the Thailand Research Fund and the National Research University Project for the support.

References

[1] R. Saidur, K.Y. Leong, H.A. Mohammad, A review on applications and challenges of nanofluids, Renewable Sustainable Energy Rev. 15 (3) (2011) 1646–1668.

[2] O. Mahian, A. Kianifar, S.A. Kalogirou, I. Pop, S. Wongwises, A review of the applications of nanofluids in solar energy, Int. J. Heat Mass Transfer 57 (2013) 582–594.

[3] C.J. Ho, M.W. Chen, Z.W. Li, Numerical simulation of natural convection of nanofluid in a square enclosure: Effects due to uncertainties of viscosity and thermal conductivity, Int. J. Heat Mass Transfer 51 (17–18) (2008) 4506–4516.

[4] E. Abu-Nada, H.F. Oztop, Effects of inclination angle on natural convection in enclosures filled with Cu–water nanofluid, Int. J. Heat Fluid Flow 30 (4) (2009) 669–678.

[5] E. Büyük Öğüt, Natural convection of water-based nanofluids in an inclined enclosure with a heat source, Int. J. Therm. Sci. 48 (11) (2009) 2063–2073.

[6] E. Abu-Nada, Z. Masoud, H.F. Oztop, A. Campo, Effect of nanofluid variable properties on natural convection in enclosures, Int. J. Therm. Sci. 49 (3) (2010) 479–491.

[7] B. Ghasemi, S.M. Aminossadati, Periodic natural convection in a nanofluid-filled enclosure with oscillating heat flux, Int. J. Therm. Sci. 49 (1) (2010) 1–9.

[8] M. Shahi, A.H. Mahmoudi, F. Talebi, Numerical study of mixed convective cooling in a square cavity ventilated and partially heated from the below utilizing nanofluid, Int. Commun. Heat Mass Transfer 37 (2) (2010) 201–213.

[9] K.C. Lin, A. Violi, Natural convection heat transfer of nanofluids in a vertical cavity: effects of non-uniform particle diameter and temperature on thermal conductivity, Int. J. Heat Fluid Flow 31 (2) (2010) 236–245.

[10] K. Kahveci, Buoyancy driven heat transfer of nanofluids in a tilted enclosure, J. Heat Transfer 132 (6) (2010) 1–12.

[11] M. Corcione, Heat transfer features of buoyancy-driven nanofluids inside rectangular enclosures differentially heated at the sidewalls, Int. J. Therm. Sci. 49 (9) (2010) 1536–1546.

[12] A.H. Mahmoudi, M. Shahi, F. Talebi, Effect of inlet and outlet location on the mixed convective cooling inside the ventilated cavity subjected to an external nanofluid, Int. Commun. Heat Mass Transfer 37 (8) (2010) 1158–1173.

[13] A.H. Mahmoudi, M. Shahi, A.H. Raouf, Modeling of conjugated heat transfer in a thick walled enclosure filled with nanofluid, Int. Commun. Heat Mass Transfer 38 (1) (2011) 119–127.

[14] E. Abu-Nada, Rayleigh–Bénard convection in nanofluids: effect of temperature dependent properties, Int. J. Therm. Sci. 50 (9) (2011) 1720–1730.

[15] F.-H. Lai, Y.-T. Yang, Lattice Boltzmann simulation of natural convection heat transfer of Al_2O_3/water nanofluids in a square enclosure, Int. J. Therm. Sci. 50 (10) (2011) 1930–1941.

[16] Z. Haddad, E. Abu-Nada, H.F. Oztop, A. Mataoui, Natural convection in nanofluids: are the thermophoresis and Brownian motion effects significant in nanofluid heat transfer enhancement?, Int J. Therm. Sci. 57 (2012) 152–162.

[17] S. Parvin, R. Nasrin, M. Alim, N. Hossain, Double-diffusive natural convection in a partially heated enclosure using a nanofluid, Heat Transfer – Asian Res. 41 (6) (2012) 484–497.

[18] T. Basak, A.J. Chamkha, Heatline analysis on natural convection for nanofluids confined within square cavities with various thermal boundary conditions, Int. J. Heat Mass Transfer 55 (21–22) (2012) 5526–5543.

[19] E.H. Ooi, V. Popov, Numerical study of influence of nanoparticle shape on the natural convection in Cu–water nanofluid, Int. J. Therm. Sci. 65 (2013) 178–188.

[20] R. Nasrin, M.A. Alim, Free convective flow of nanofluid having two nanoparticles inside a complicated cavity, Int. J. Heat Mass Transfer 63 (2013) 191–198.

[21] F. Garoosi, G. Bagheri, F. Talebi, Numerical simulation of natural convection of nanofluids in a square cavity with several pairs of heaters and coolers (HACs) inside, Int. J. Heat Mass Transfer 67 (2013) 362–376.

[22] Z. Haddada, H.F. Oztop, E. Abu-Nada, A. Mataoui, A review on natural convective heat transfer of nanofluids, Renewable Sustainable Energy Rev. 16 (7) (2012) 5363–5378.

[23] D. Wen, Y. Ding, Formulation of nanofluids for natural convective heat transfer applications, Int. J. Heat Fluid Flow 26 (2005) 855–864.

[24] A.G.A. Nnanna, Experimental model of temperature-driven nanofluid, J. Heat Transfer 129 (2007) 697–704.

[25] C.H. Li, G.P. Peterson, Experimental studies of natural convection heat transfer of Al_2O_3/DI water nanoparticle suspensions (nanofluids), Adv. Mech. Eng. (2010) (Article ID 742739).

[26] C.J. Ho, W.K. Liu, Y.S. Chang, C.C. Lin, Natural convection heat transfer of alumina-water nanofluid in vertical square enclosures: an experimental study, Int. J. Therm. Sci. 49 (8) (2010) 1345–1353.

[27] R.L. Hamilton, O.K. Crosser, Thermal conductivity of heterogeneous two component systems, I&EC Fundam. 1 (1962) 182–191.

[28] K. Khanafer, K. Vafai, A critical synthesis of thermophysical characteristics of nanofluids, Int. J. Heat Mass Transfer 54 (2011) 4410–4428.

[29] H.C. Brinkman, The viscosity of concentrated suspensions and solutions, J. Chem. Phys. 20 (1952) 571.

International Communications in Heat and Mass Transfer 53 (2014) 98–108

Contents lists available at ScienceDirect

International Communications in Heat and Mass Transfer

journal homepage: www.elsevier.com/locate/ichmt

Numerical investigation for the calculation of TiO_2–water nanofluids' pressure drop in plain and enhanced pipes ☆

Ali Celen [a], Nurullah Kayaci [a], Alican Çebi [a], Hakan Demir [a], Ahmet Selim Dalkılıç [a,*], Somchai Wongwises [b]

[a] Heat and Thermodynamics Division, Department of Mechanical Engineering, Yildiz Technical University (YTU), Yildiz, Besiktas, Istanbul 34349, Turkey
[b] Fluid Mechanics, Thermal Engineering and Multiphase Flow Research Lab. (FUTURE), Department of Mechanical Engineering, Faculty of Engineering, King Mongkut's University of Technology Thonburi (KMUTT), Bangmod, Bangkok 10140, Thailand

ARTICLE INFO

Available online 1 March 2014

Keywords:
Pressure drop
Nanofluid
Single-phase flow
CFD
ANN

ABSTRACT

In this investigation, a numerical model having two-dimensional equations was obtained by a CFD program and authors' experimental data were evaluated for the verification procedure of the numerical outputs. The experimental case study includes the single-phase flow of pure water in plain and micro-fin pipes whereas the numerical one has the simulated results of TiO_2 particles suspended in single phase water flow in equivalent pipes at a constant heat flux. Hydrodynamics and thermal behaviors of the water–TiO_2 flow were calculated by constant heat flux and temperature-dependent settings. Physical specifications of nanofluids were calculated by means of the results of authors' previous ANN analyses. This study illustrates local and average values of temperature, pressure, and velocity distributions in the tested pipes; furthermore, comparisons of pressure drop characteristics are given in terms of nanoparticle concentrations and tube types.

© 2014 Elsevier Ltd. All rights reserved.

1. Introduction

The productivity of a fluid regarding heat transfer applications depends on thermal conductivity significantly. Applications in the electronic, automotive, and aerospace industries are affected from traditional heat transfer fluids' (e.g. water, oil, ethylene glycol mixtures) low thermal conductivity values resulting as the restriction for the improvement of productivity and smallness in heat exchangers. Having suspended tiny particles in the base liquid improves the thermal conductivity and thus the increase in heat transfer performance is expected. In case there may be abrasion and clogging problems, the millimeter size suspended particles have not been used for a long time. The particle sizes from 10 to 100 nm are preferred to have uniform and stable suspensions. Some of recent experimental and numerical works on the single-phase flow of nanofluids are given as shown below:

Anoop et al. [1] have done an experimental investigation to determine the effect of particle size in the flow regarding laminar developing region. They had constant heat flux regarding nanofluid flow including 45 nm and 150 nm sized alumina particles suspended in base fluid in the investigated pipe. According to the results, nanofluids have the heat transfer enhancement in comparison to its base fluid; besides smaller sized particles with water mixture has greater heat transfer coefficients than those of larger one. They also obtained higher heat transfer coefficients in the developing region than those in the developed region. Finally, they correlated an equation for heat transfer in the developing region.

Heidary and Kermani [2] prepared a numerical work using nanofluid on the heat transfer and flow field in a wavy channel. They used copper particles in pure water for their simulation study. They studied on the influences of Reynolds number, nano-fluid volume fraction, and wave amplitude on the local and average Nusselt numbers and the skin friction coefficient. Authors validated their results with those in the literature and showed heat transfer increase regarding with the use of nanofluid flow in channels having wavy horizontal walls.

Heidary and Kermani [3] investigated nanofluid's heat transfer in a channel having some specified blocks. Their numerical study was subjected to the parameters of Reynolds number, nanofluid volume fraction and the block number. They studied those parameters' effects on the local and average Nusselt numbers and determined some enhancement on heat transfer using nanofluids flowing in a channel having attached blocks.

Wang and Chen [4] studied the heat transfer rate for flow through a specially designed channel benefitting from the techniques of simple coordinate transformation and the spline alternating-direction implicit numerically. Authors showed the influences on the wavy geometry, Reynolds number and Prandtl number on the skin-friction and Nusselt number. According to their results, the rise in the Reynolds number and the amplitude–wavelength ratio increase the values of the Nusselt number and the skin-friction coefficient.

☆ Communicated by W.J. Minkowycz.

* Corresponding author.
E-mail address: dalkilic@yildiz.edu.tr (A.S. Dalkılıç).

http://dx.doi.org/10.1016/j.icheatmasstransfer.2014.02.022
0735-1933/© 2014 Elsevier Ltd. All rights reserved.

Nomenclature

Cp	specific heat [J kg^{-1} K^{-1}]
D	tube diameter [m]
e	height of fin [m]
f	friction factor
k	thermal conductivity [W m^{-1} K^{-1}]
L	length of test tube [m]
m	mass flow rate [kg s^{-1}]
n	number of fins
p	distance between microfins [m]
Re	Reynolds number
t	thickness [m]
V	velocity [m s^{-1}]
μ	dynamic viscosity [Pa·s]
ρ	density [kg m^{-3}]
ϕ	volume fraction [%]
ΔP	pressure drop [Pa]
α	helix angle [°]

Subscripts

exp	experimental
f	fluid
i	inside
m	mean
nf	nanofluid
num	numerical
o	outside
p	particle
w	water

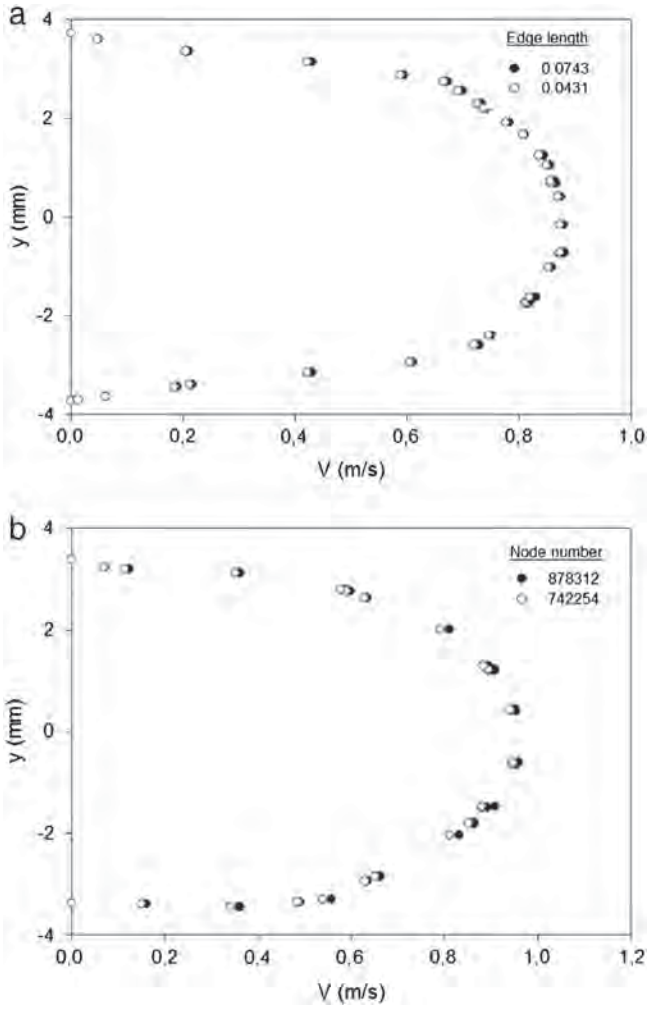

Fig. 1. Achieving the grid independency for velocity profiles of smooth tube 3 (a) and microfin tube (b) for mass flow rate of 0.0312 kg/s.

Yang et al. [5] calculated the heat transfer coefficients during laminar flow of various nanofluids in a horizontal heat exchanger. They used the graphitic particles in nature and reported some enhancement in thermal conductivity values because of used particles. Authors concluded that the experimental heat transfer coefficients have lesser increases than calculated ones.

Khanafer et al. [6] defined a numerical model regarding with the heat transfer enhancement in a two-dimensional enclosure considering solid particle dispersion of nanofluids. They validated and compared their findings with those in their previous work. Their analysis includes the influence of suspended tiny metallic particles on the fluid flow and heat transfer applications within the enclosure on thermal conductivity improvement. Their proposed Nusselt correlation has the parameters of Grashof number and volume fraction.

Xuan and Li [7] presented a theoretical model regarding with the nanofluid flow in a tube considering dispersion of solid particles. Their method includes the preparation of sample nanofluids. They obtained TEM images to show the stability and evenness of suspension. Thermal conductivity values were determined by means of both the hot-wire technique experimentally and their theoretical model. The volume fraction, dimensions, shapes and specifications of the nanoparticles are considered as important parameters in their study.

Shokouhmand et al. [8] performed a numerical simulation study related with Darcy–Brinkman–Forchheimer flow model and convective flow model in an enhanced round micro/nano channel. They considered velocity slip and temperature jump in their model and investigated the influence of Knudsen number and Darcy coefficient on velocity and temperature spreading.

Table 1
Geometrical parameters of the investigated tubes.

Parameter	Unit	Smooth tube 1	Smooth tube 2	Smooth tube 3 (simulated)	Micro-fin tube
Length (L)	mm	1100	1100	1100	1100
Outside diameter (D_o)	mm	8	10	8.48	8
Inside diameter (D_i)	mm	6	8	7.48	7.48
Thickness (t)	mm	1	1	1	0.26
Fin Height (e)	mm	–	–	–	0.22
Fin pitch (p)	mm	–	–	–	0.34
Helix angle (α)	°	–	–	–	35
Number of fins (n)	–	–	–	–	65
e/D	–	–	–	–	0.027

Mohammed et al. [9] concentrated on the influences of the use of louvered strip inserts installed in a round double tube heat exchanger on the thermal and flow fields. They used several kinds of nanoparticles having various sizes and concentrations dispersed in water in their numerical study based on finite volume technique. According to their analyses, the highest Nusselt number was obtained by using SiO_2 nanofluid comparing with Al_2O_3, ZnO, and CuO. Nusselt number decreases with increasing nanoparticle diameter size and the increase in volume fraction of nanoparticles enhances the Nusselt numbers. They also studied the significant parameters' effects on the skin friction coefficient factor.

Moraveji et al. [10] studied the convective nanofluid flow in the developing region of a pipe with constant heat flux numerically. They used numerical (CFD) analyses for the nanoparticles of Al_2O_3 having various sizes and concentrations with its base fluid of water. Their analyses included the influence of particle size on single phase heat transfer

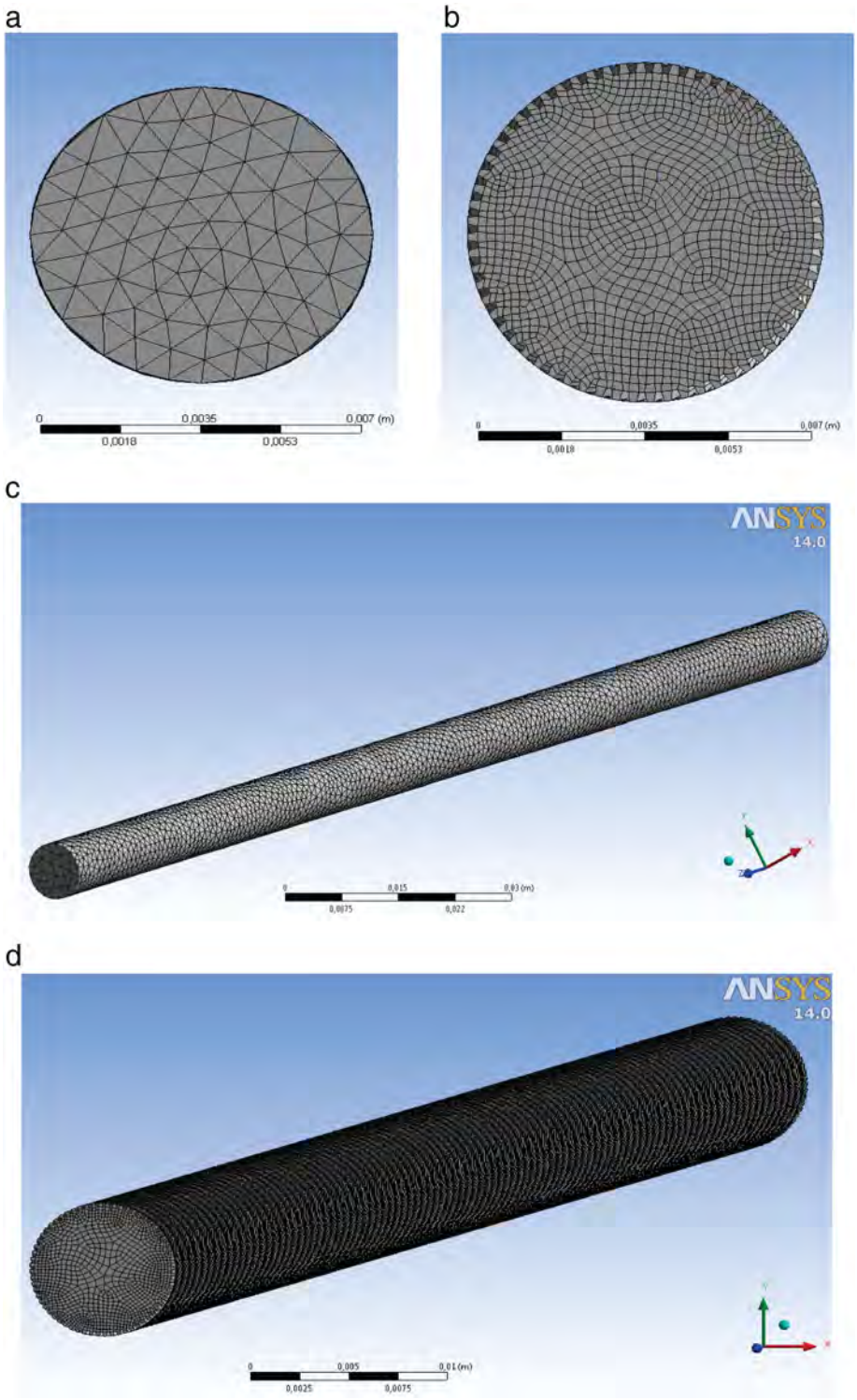

Fig. 2. Grid structures of investigated tubes. (a) Front view of smooth tube 3. (b) Front view of microfin tube. (c) Isometric view of smooth tube 3. (d) Isometric view of microfin tube.

coefficient for a limited range of Reynolds numbers. They proposed a correlation having dimensionless numbers to determine Nusselt numbers as according to their outputs.

A lot of investigations have been prepared to determine the heat transfer augmentation of nanofluids in the literature so far. It should be considered that there have insufficient numbers of studies; including artificial neural network based physical properties [17], on the nanofluid flows in enhanced tubes. Solid Works software [24] was used for the draw of plain and micro-fin pipes and then they were imported into ANSYS Fluent software [25] for CFD analysis. Before the simulation of the smooth and micro-fin tubes in the CFD program, the validation process of experimental data was accomplished for the convective single phase flow of pure water in authors' previous study [23]. The measured data and simulated one for nanofluid flow having TiO_2 particles with its base fluid of water were analyzed by the CFD program to determine the pressure drops, temperature, pressure and velocity distributions in plain and enhanced pipes. Moreover, the measured and numerical outputs were evaluated as a comparison and also their variations with Reynolds number and flow rate were also shown for the investigated tubes in the study. It can be said that this paper is a continuation of authors' previous works on nanofluids [10–23].

2. Experimental apparatus

Additional knowledge on the experimental setup for investigating single phase heat transfer flow of pure water inside plain and microfin horizontal pipes exists in Celen et al. [23]. Specifications of the tested pipes are shown in Table 1. For the comparison of smooth and microfin tubes having the same equivalent diameter, smooth tube 3 is simulated by using smooth tube 1 and 2' experimental data.

3. Data reduction

3.1. Calculation of pressure drop in pipes

In practice, pressure drop is calculated by means of an equation given below. This equation can be used for smooth or rough surfaces, laminar or turbulent flows, smooth or rough surfaces [26].

$$\Delta P = f \cdot \frac{L}{D} \cdot \frac{\rho V_m{}^2}{2}. \tag{1}$$

In Eq. (1) f is friction factor and it can be changed according to the type of flow (laminar or turbulent). The friction factor for fully developed turbulent flow in a smooth tube expressed respectively as follows

$$\begin{aligned} f &= 0.316/Re^{0.25} \text{ for } 2300 < Re < 20000 \text{ and} \\ f &= 0.184/Re^{0.2} \text{ for } 20000 < Re < 400000 \end{aligned} \tag{2}$$

where Reynolds number is determined as follows:

$$Re = \frac{\rho \cdot V_m \cdot D}{\mu}. \tag{3}$$

Detailed list of turbulent friction factor equations for plain and microfin pipes can be seen in Celen et al. [23].

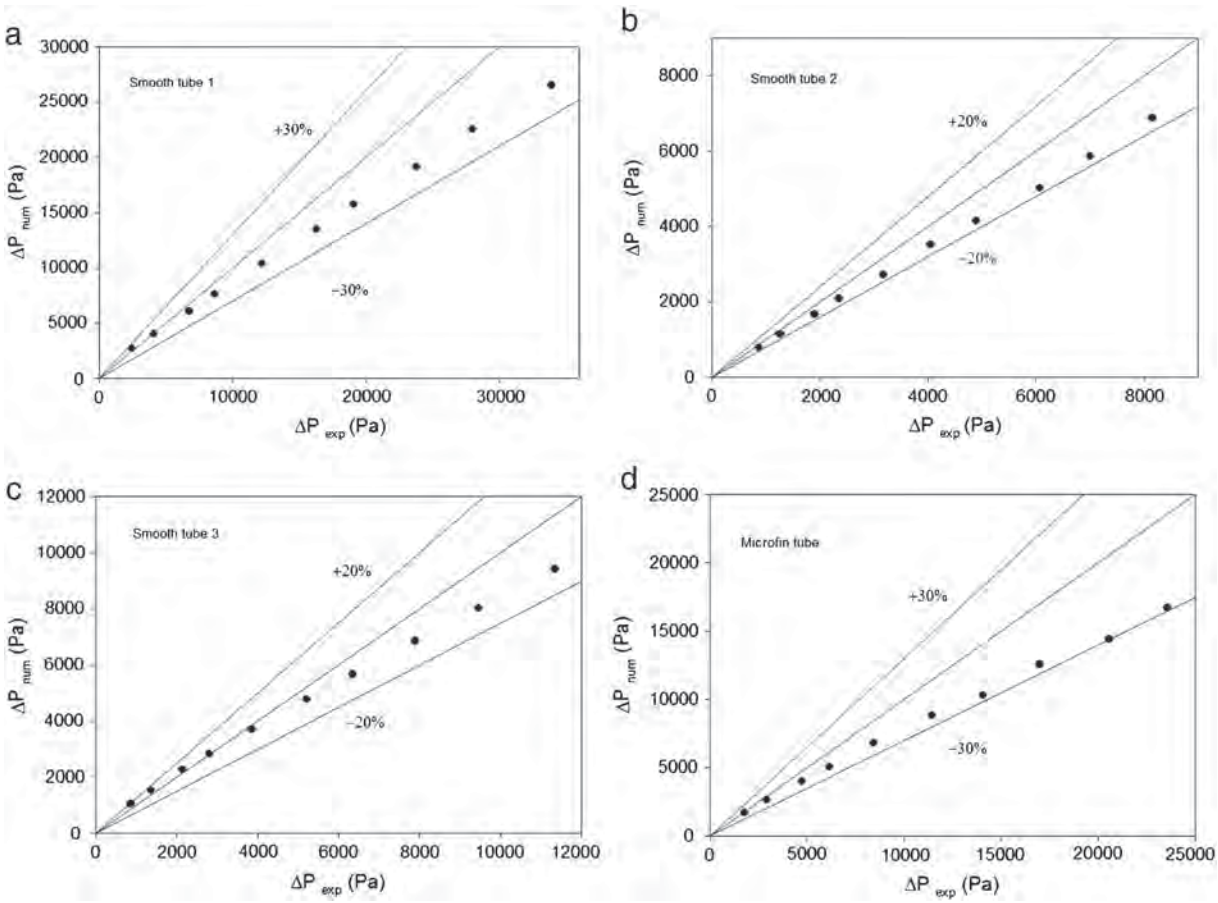

Fig. 3. The comparison of experimental and numerical pressure drop results for smooth tubes 1 (a), 2 (b), 3 (c) and (d) microfin tube.

3.2. Specifications of nanofluids

The greatest confirmed equations were taken from Kayaci et al. [17] and used for the determination of the physical properties of TiO_2–water nanofluids. In their work, they summarized the literature on almost all empirical correlations for nanofluid dynamic viscosity, thermal conductivity and specific heat capacity at constant pressure. They also developed two different ANN models in order to conclude the proper grouping of specifications for the TiO_2 nanofluid. The ANN model 1 inputs were the empirical equations of specifications, the nanoparticle concentration, the velocity of water and the average temperature in the test tube. The outputs of the ANN model 1 were pressure drop, friction factor, shear stress, and convective heat transfer coefficient and heat flux. The ANN model 2 inputs were the empirical equations of physical properties and the inlet and outlet temperatures and velocity of the water in the investigated pipe. The ANN model 2 outputs were the pressure drop and the convective heat transfer coefficient. According to their study, the best agreeable equations were obtained from the ANN 1 model for the specifications (k, μ, Cp) of nanofluids and they are given as follows:

The thermal conductivity of the nanofluid was calculated from Bhattacharya et al. [27] correlation, as:

$$k_{nf} = k_p\phi + (1-\phi)k_f. \tag{4}$$

The dynamic viscosity of the nanofluid was calculated from Wang et al. [28] correlation as:

$$\mu_{nf} = \mu_f\left(306\phi^2 - 0.19\phi + 1\right). \tag{5}$$

The heat capacity of nanofluid was calculated from Maxwell [29] as:

$$Cp_{nf} = (1-\phi)Cp_f\left(1 + 2.5\phi_p\right)\mu_f. \tag{6}$$

The density of the nanofluid was calculated from Pak and Cho's [30] equation, as follows:

$$\rho_{nf} = \rho_p\phi + (1-\phi)\rho_f. \tag{7}$$

3.3. Numerical method — CFD approach

In CFD analysis one of the most used software is the ANSYS Fluent program [25]. The detailed information about the program and its algebraic models exists in the Fluent User's Guide. In order to transform governing equations into algebraic definitions, the control volume theory is used by the program and their numerical solution is possible with giving an important investigation clarification. The control volume method operates with the integration of the governing definitions for each control volume, and at that point by discretizing the formulas that conserve each quantity based on the control volume.

Because leading equations could be given numerical analyses afterward their transformation into a set of algebraic formulas, classic single-phase conservation formulas were presented with a solution in the control volume method. Whole scalar values and velocity components are determined at the center of control volume interfaces, where grid schemes are done widely. The Semi-Implicit Method for Pressure Linked Equations (SIMPLE) was evaluated to match pressure and velocity. A point-implicit (Gauss–Seidel) linear equation solver, in conjunction with an algebraic multigrid method, was applied in the Fluent CFD program to evaluate the linear systems resulting from

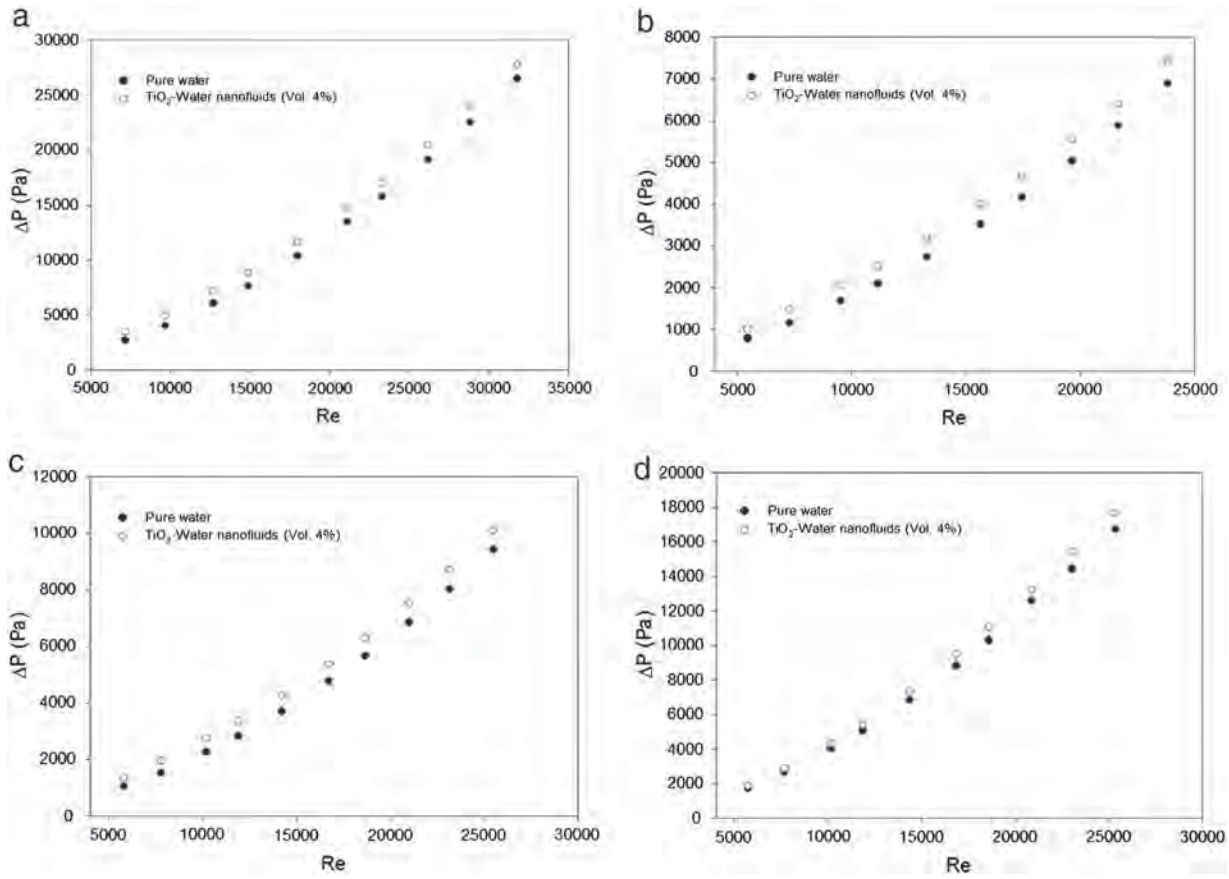

Fig. 4. Numerical pressure drop comparison of water and TiO_2–water nanofluids flowing in smooth tubes 1 (a), 2 (b), 3 (c) and (d) microfin tube.

discretization schemes. k-ε turbulence models were selected as viscous model. In the course of the iterative procedure, residuals were thoroughly observed and all outputs were thought to have converged when the residuals for each governing equation drop below 10^{-6}. Boundary conditions were recognized for the velocity inlet at the tube inlet and for the pressure outlet at the tube exit; turbulence intensity and equivalent diameter were identified for the turbulence parameters. Constant heat flux was determined to the tube surface.

According to Fig. 1(a), in order to display grid-independent solutions in smooth tube 3, two different edge lengths were considered in the tetrahedron grid type for mass flow rate of 0.0312 kg/s. Fig. 1(b) shows grid-independent solutions in micro-fin tubes by using two different node numbers for mass flow rate of 0.0312 kg/s. Fig. 1(a) and (b) shows the velocity profile distributions at the different mesh sizes, which are nearly identical in each other.

4. Results and discussion

In order to confirm the numerical results, some experimental data points was obtained for the single-phase flow of pure water in horizontal smooth and micro-fin tubes with inner diameters of 6, 7.48 and 8 mm at a Mechanical Engineering Lab in YTU. The experiments have been performed by pure water. Evaluation of the outputs is illustrated in sequence in below paragraphs:

In the numerical study, the commercial software package ANSYS Fluent [25] was used for the investigation of pressure drop of plain and microfin pipes. Investigated tubes were created by means of Solid Works program [24] and they were imported to ANSYS Geometry. After this process, meshing process was applied to the tubes by using ANSYS Meshing program. The mesh affects the accuracy, convergence, and speed of the solution. Moreover, the meshing time to develop a model frequently takes an important percentage of the necessary time to obtain outcomes from the analyses; this explanation reveals that the better and extra computerized the meshing tools, the better the solution. Grid structures of investigated tubes are illustrated in Fig. 2.

Fig. 3 depicts the comparison of experimental and numerical pressure drop outputs for plain and microfin pipes. According to Fig. 1, numerical and experimental pressure drop results of smooth tube 1, smooth tube 2, smooth tube 3 and microfin tube were observed in the deviation bands of ±21.8%, ±17.2%, ±20.3% and ±29.8%, respectively.

Fig. 4 shows numerical pressure drop comparison pure water and nanofluids with TiO_2 volume concentrations of 0.4% flowing in smooth and microfin tubes. It is clear that the pressure drop of nanofluid is greater than the pure water for all tested tubes. The maximum augmentation of pressure drop outputs for plain pipe 1, plain pipe 2, plain pipe 3 and microfin pipe were 28.1%, 28.9%, 29.1% and 8%, respectively. The result can be explained with relation between dynamic viscosity and pressure drop of the fluid. Because nanoparticle addition in a base fluid generally increases dynamic viscosity of the fluid, it is obvious that the usage of nanoparticles in water raises pressure drop results.

Fig. 5 shows comparison of numerical pressure drop results of pure water and TiO_2–water nanofluids with 4% volumetric particle concentrations flowing inside plain and micro-fin pipes. As shown in the figure, the pressure drop enlarged regularly as mass flow rate increased for both plain and microfin pipes. It was also observed that the smooth tube 1 had higher pressure drop when it was matched with plain pipes 2 and 3. Compared with plain tube, microfin pipe has higher pressure drop.

Figs. 6(a) and 7(a) represent velocity profiles of pure water and TiO_2–water nanofluids having volume concentration of 4% flowing in smooth tube 3. Figs. 8(a) and 9(a) represent velocity profiles of pure water and TiO_2–water nanofluids having volume concentration of 4% flowing in microfin tube. The velocity of the fluid at the place where fluid and pipe wall contact with each other is zero because of no slip condition. It increases with increasing distance from the pipe wall. The velocity profile of the fluid is related to the surface properties of the pipe wall. The smooth tubes have more uniform velocity profile than the microfin tubes.

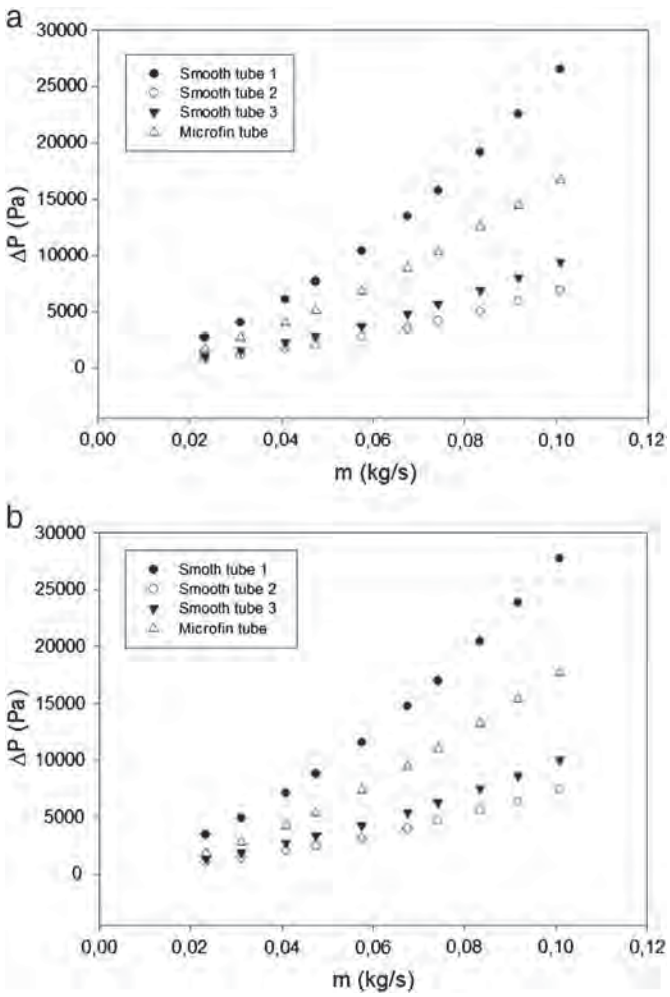

Fig. 5. Comparison of numerical pressure drop results of tubes used in the study. a) Pure water and b) TiO_2–water nanofluids (vol. 4%).

Figs. 6(b) and 7(b) represent temperature profiles of pure water and TiO_2–water nanofluids having volume concentration of 4% flowing in smooth tube 3. Figs. 8(b) and 9(b) represent temperature profiles of pure water and TiO_2–water nanofluids having volume concentration of 4% flowing in microfin tube. The temperature of the fluid has its minimum rate on the wall and maximum rate at the entrance of the tube. Because cold water flows outside of the pipe (annulus side of double pipe heat exchanger), the temperature of the fluid also decreases with increasing distance from the entrance.

Figs. 6(c) and 7(c) represent temperature profiles of pure water and TiO_2–water nanofluids having volume concentration of 4% flowing in smooth tube 3. Figs. 8(c) and 9(c) represent temperature profiles of pure water and TiO_2–water nanofluids having volume concentration of 4% flowing in microfin tube. The fluid pressure has its highest rate at inlet of the tube and it decreases with increasing distance from inlet of the pipe.

It is should be noted that the velocity, temperature and pressure profiles represented in Figs. 6–9 were obtained for mass flow rate of 0.0312 kg/s.

Many figures and tables might be produced from the results of the analyses, but, caused by the space restriction, just characteristic conclusions are illustrated. Moreover, the additional knowledge about the information above and some extra graphics with various experimental factors regarding with the work exists in the authors' published publications previously in open sources.

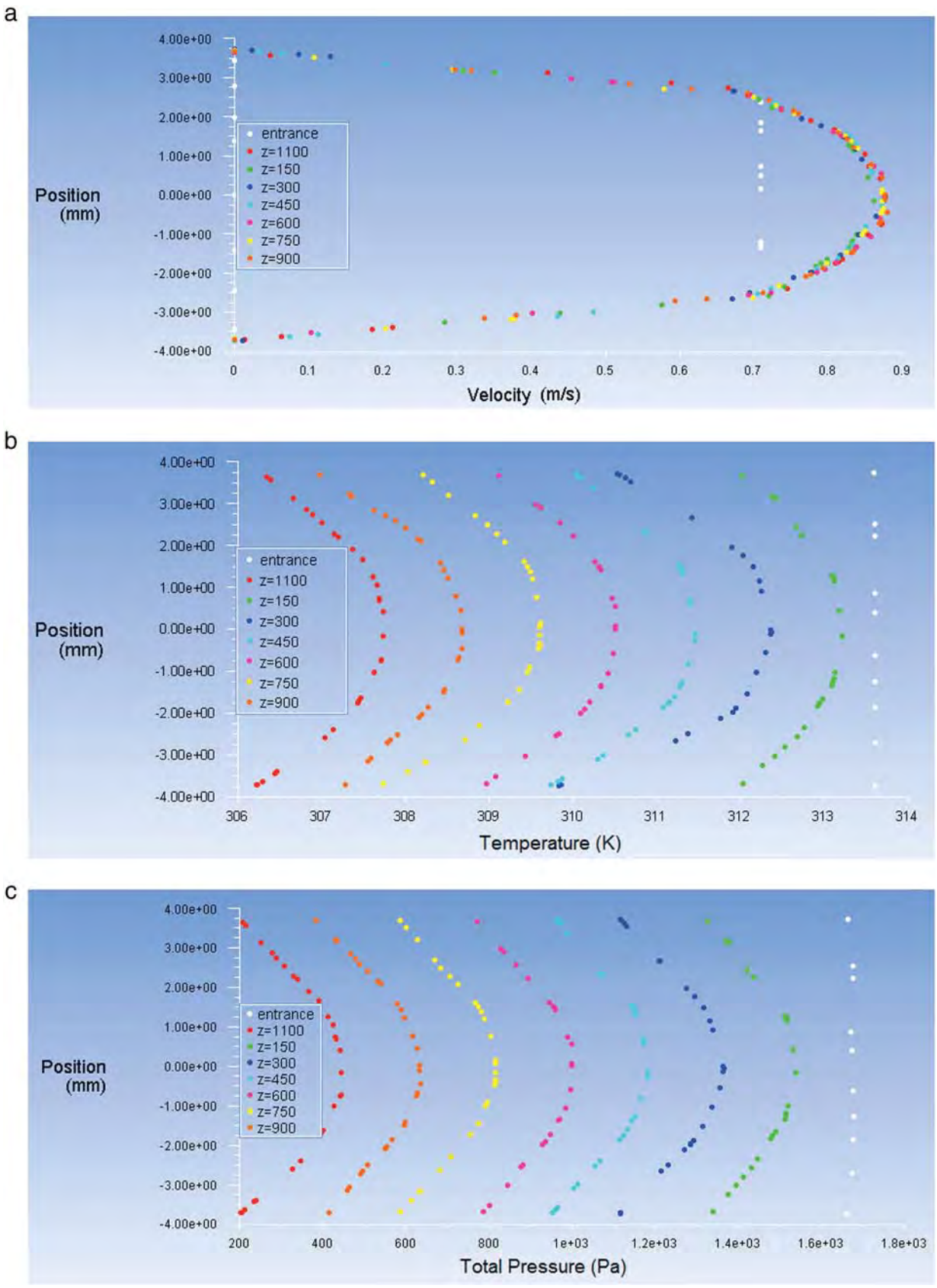

Fig. 6. Velocity (a), temperature (b) and pressure (c) profiles at various locations in smooth tube 3 for pure water.

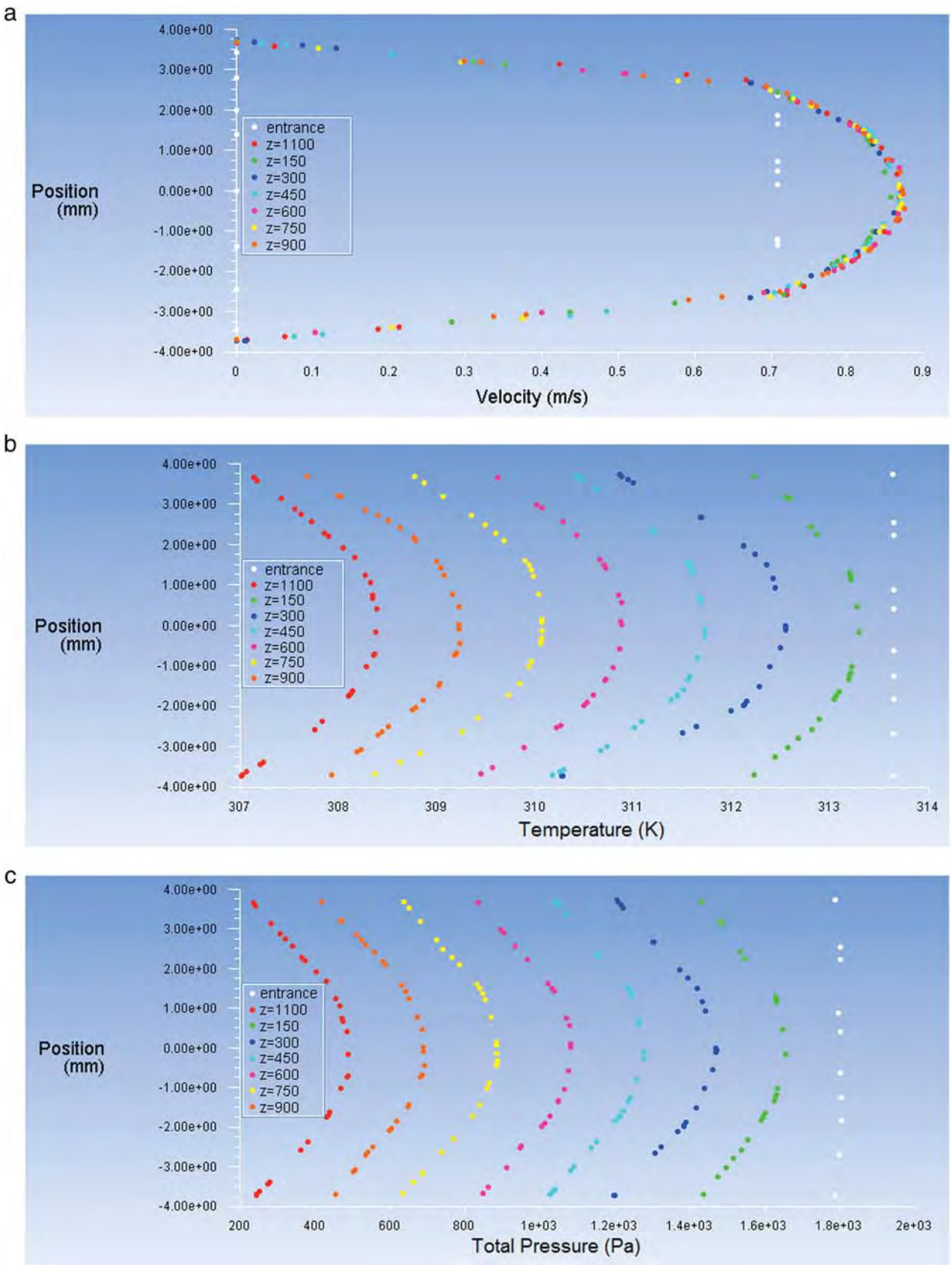

Fig. 7. Velocity (a), temperature (b) and pressure (c) profiles at various locations in smooth tube 3 for TiO_2–water nanofluids (vol. 4%).

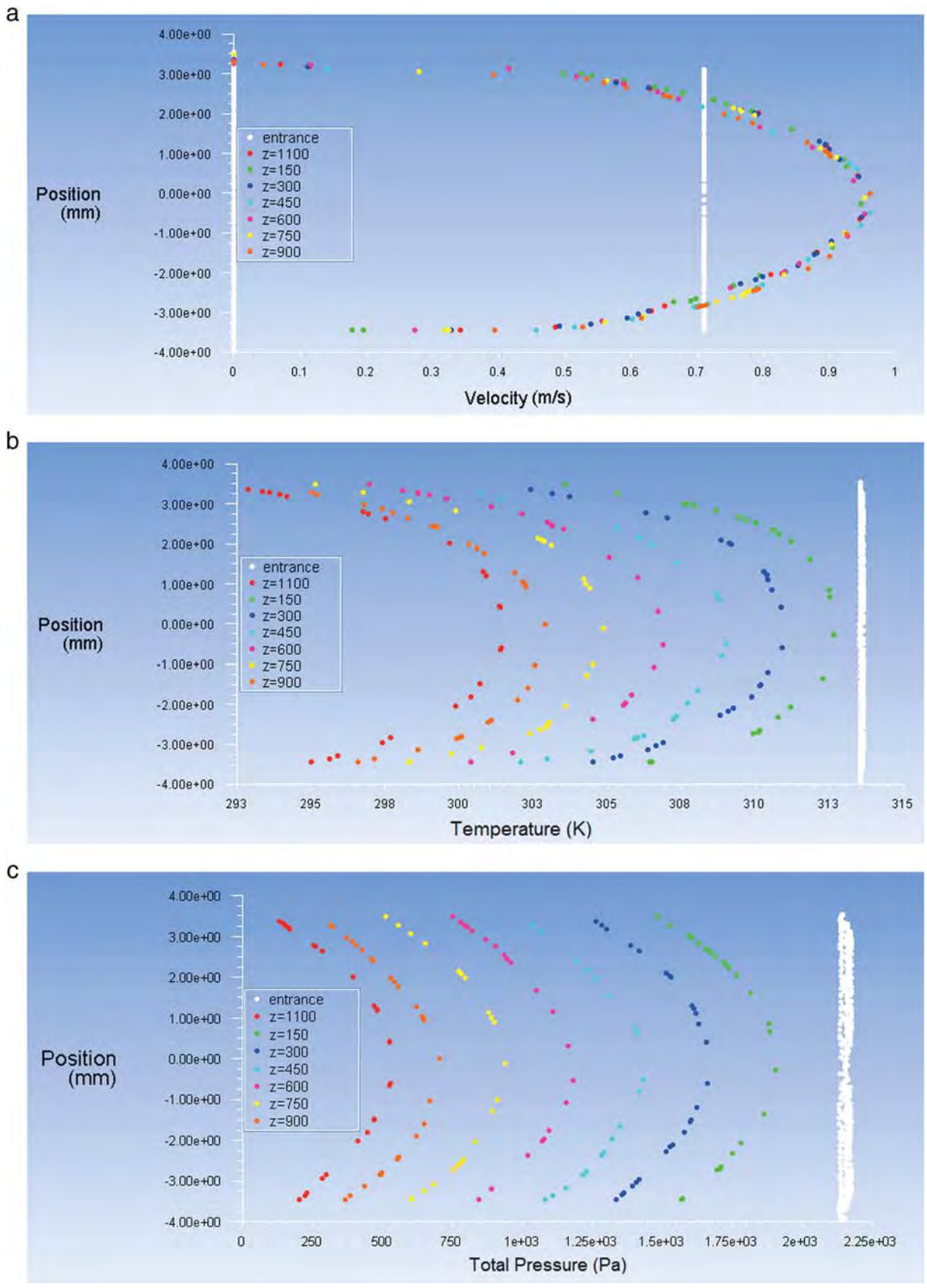

Fig. 8. Velocity (a), temperature (b) and pressure (c) profiles at various locations in microfin tube for pure water.

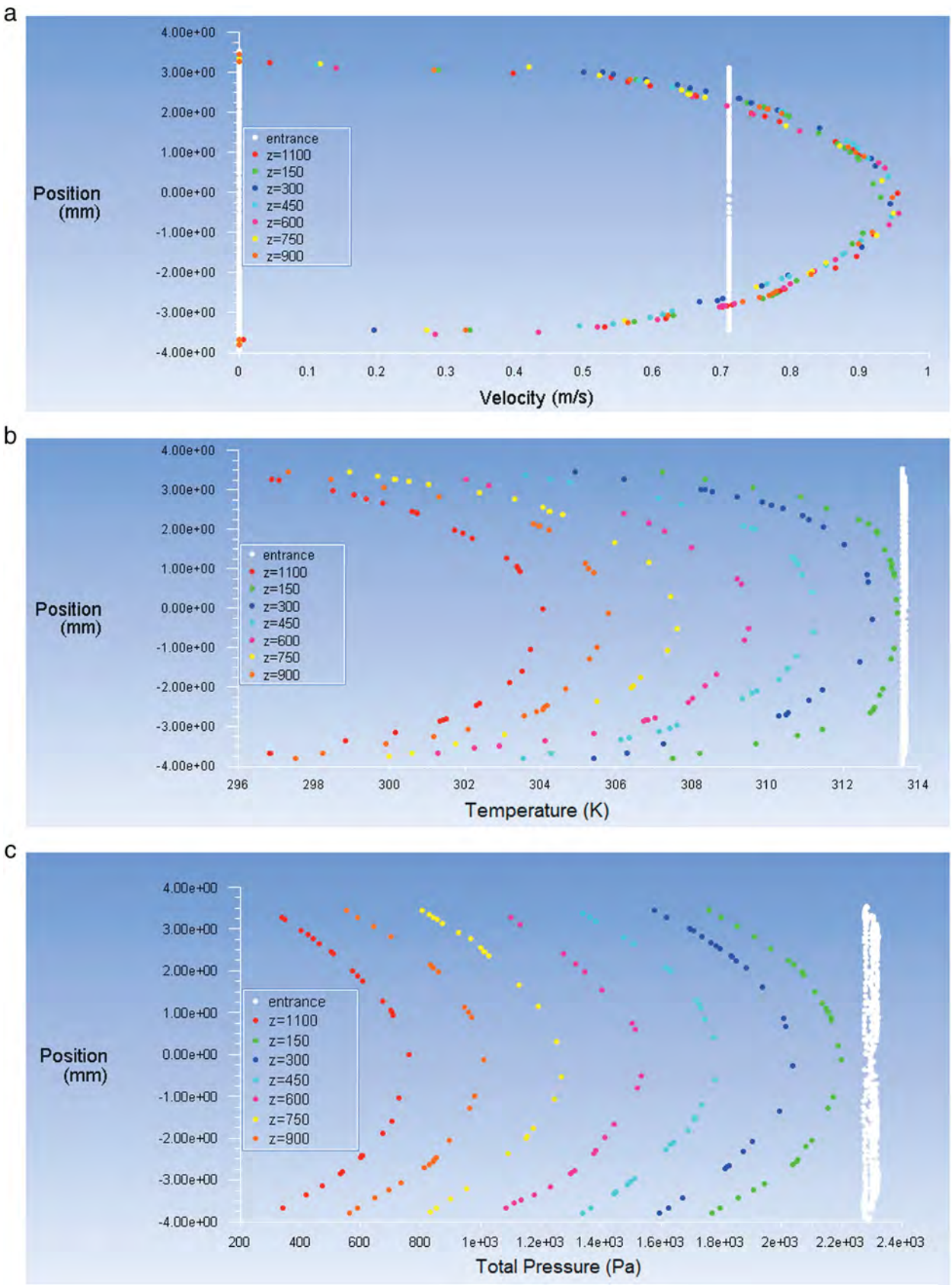

Fig. 9. Velocity (a), temperature (b) and pressure (c) profiles at various locations in microfin tube for TiO_2–water nanofluids (vol. 4%).

5. Conclusion

This investigation studied the pressure drop of pure water and TiO_2–water nanofluid flowing inside plain and micro-fin pipes by means of CFD analysis using authors' accurate and repeatable single-phase flow data. The results of current work are summarized herein below:

a. Experimental and numerical pressure drop results for pure water and TiO_2–water nanofluids were compared and determined in the tolerable range of $\pm 30\%$ for investigated tubes.
b. The numerical pressure drop results of TiO_2–water nanofluids were higher compared to pure water for both plain and microfin pipes.
c. The numerical outcomes showed that the pressure drop in plain pipe having smaller inside diameter was greater than in the plain pipe having larger inside diameter.
d. The numerical pressure drop of pure water flowing in microfin tube was greater than those in the plain one having the same inside diameter.
e. The numerical pressure drop of TiO_2–water nanofluids flowing in microfin tube was greater than plain one having the same inside diameter.
f. The temperature, pressure, and velocity distributions in the smooth and microfin tubes were illustrated by using CFD analysis.

This study indicates that a computational fluid dynamics (CFD) program can be evaluated for the pure water and TiO_2 particles suspended in water mixture flowing in plain and microfin tubes.

Acknowledgments

The fifth author wishes to thank KMUTT for providing him with a Post-doctoral fellowship. The sixth author is indebted to the Thailand Research Fund, the National Research University Project and the National Science and Technology Development Agency for their financial support. This research has been supported by Yildiz Technical University Scientific Research Projects Coordination Department. Project number: 2013-06-01-KAP01.

References

[1] K.B. Anoop, T. Sundararajan, Sarit K. Das, Effect of particle size on the convective heat transfer in nanofluid in the developing region, Int. J. Heat Mass Transfer 52 (2009) 2189–2195.
[2] H. Heidary, M.J. Kermani, Effect of nano-particles on forced convection in sinusoidal-wall channel, Int. Commun. Heat Mass Transfer 37 (2010) 1520–1527.
[3] H. Heidary, M.J. Kermani, Heat transfer enhancement in a channel with block(s) effect and utilizing nano-fluid, Int. J. Therm. Sci. 57 (2012) 163–171.
[4] C.-C. Wang, C.-K. Chen, Forced convection in a wavy-wall channel, Int. J. Heat Mass Transfer 45 (2002) 2587–2595.
[5] Y. Yang, Z.G. Zhang, E.A. Grulke, W.B. Anderson, G. Wu, Heat transfer properties of nanoparticle-in-fluid dispersions (nanofluids) in laminar flow, Int. J. Heat Mass Transfer 48 (2005) 1107–1116.
[6] K. Khanafer, K. Vafai, M. Lightstone, Buoyancy-driven heat transfer enhancement in a two-dimensional enclosure utilizing nanofluids, Int. J. Heat Mass Transfer 46 (2003) 3639–3653.
[7] Y. Xuan, Q. Li, Heat transfer enhancement of nanofluids, Int. J. Heat Fluid Flow 21 (2000) 58–64.
[8] H. Shokouhmand, A.H. Meghdadi Isfahani, E. Shirani, Friction and heat transfer coefficient in micro and nano channels filled with porous media for wide range of Knudsen number, Int. Commun. Heat Mass Transfer 37 (2010) 890–894.
[9] H.A. Mohammed, Husam A. Hasan, M.A. Wahid, Heat transfer enhancement of nanofluids in a double pipe heat exchanger with louvered strip inserts, Int. Commun. Heat Mass Transfer 40 (2013) 36–46.
[10] M.K. Moraveji, M. Darabi, S.M.H. Haddad, R. Davarneja, Modeling of convective heat transfer of a nanofluid in the developing region of tube flow with computational fluid dynamics, Int. Commun. Heat Mass Transfer 38 (2011) 1291–1295.
[11] H. Demir, A.S. Dalkilic, N.A. Kurekci, W. Duangthongsuk, S. Wongwises, Numerical investigation on the single phase forced convection heat transfer characteristics of TiO_2 nanofluids in a double-tube counter flow heat exchanger, Int. Commun. Heat Mass Transfer 38 (2011) 218–228.
[12] M. Balcilar, A.S. Dalkilic, A. Suriyawong, T. Yiamsawas, S. Wongwises, Investigation of pool boiling of nanofluids using artificial neural networks and correlation development techniques, Int. Commun. Heat Mass Transfer 39 (2012) 424–431.
[13] W. Duangthongsuk, A.S. Dalkilic, S. Wongwises, Convective heat transfer of Al_2O_3–water nanofluids in a microchannel heat sink, Curr. Nanosci. 8 (2012) 317–322.
[14] T. Yiamsawas, A.S. Dalkilic, S. Wongwises, Measurement of the thermal conductivity of titania and alumina nanofluids, Thermochim. Acta 545 (2012) 48–56.
[15] A.S. Dalkilic, N. Kayacı, M. Tabatabaei, O. Yıldız, A. Celen, W. Daungthongsuk, S. Wongwises, Forced convective heat transfer of nanofluids — a review of the recent literature, Curr. Nanosci. 8 (2012) 949–969.
[16] T. Yiamsawas, A.S. Dalkilic, S. Wongwises, Measurement of specific heat of nanofluids, Curr. Nanosci. 8 (2012) 939–944.
[17] N. Kayaci, M. Balcilar, M. Tabatabaei, A. Celen, O. Yıldız, A.S. Dalkilic, S. Wongwises, Determination of the single-phase forced convection heat transfer characteristics of TiO2 nanofluids flowing in smooth and micro-fin tubes by means of CFD and ANN analyses, Curr. Nanosci. 9 (2013) 61–80.
[18] W. Duangthongsuk, T. Yiamsawas, A.S. Dalkilic, S. Wongwises, Pool boiling heat transfer characteristics of Al_2O_3–water nanofluids on a horizontal cylindrical heating surface, Curr. Nanosci. 9 (2013) 56–60.
[19] T. Yiamsawas, O. Mahian, A.S. Dalkilic, S. Kaewnai, S. Wongwises, Experimental studies on the viscosity of TiO_2 and Al_2O_3 nanoparticles suspended in a mixture of ethylene glycol and water for high temperature applications, Appl. Energy 111 (2013) 40–45.
[20] P. Nitiapiruk, O. Mahian, A.S. Dalkilic, S. Wongwises, Performance characteristics of a microchannel heat sink using TiO2/water nanofluid and different thermophysical model, Int. Commun. Heat Mass Transfer 47 (2013) 98–104.
[21] T. Yiamsawas, A.S. Dalkilic, O. Mahian, S. Wongwises, Measurement and correlation of the viscosity of water based Al_2O_3 and TiO_2 nanofluids in high temperatures and comparisons with literature reports, J. Dispers. Sci. Technol. 34 (2013) 1697–1703.
[22] A. Suriyawong, A.S. Dalkilic, S. Wongwises, Nucleate pool boiling heat transfer correlation for TiO_2–water nanofluids, J. ASTM Int. 9 (2012) 1–12.
[23] A. Celen, A.S. Dalkilic, S. Wongwises, Experimental analysis of the single phase pressure drop characteristics of smooth and microfin tubes, Int. Commun. Heat Mass Transfer 46 (2013) 58–66.
[24] SolidWorks, SolidWorks Corporation, 300 Baker Avenue, Concord, MA 01742. Available from: http://www.solidworks.com/ .
[25] ANSYS Fluent, ANSYS Inc., 10 Cavendish Court Lebanon, NH 03766 Available from: http://www.ansys.com/ .
[26] Y.A. Çengel, Heat Transfer: A Practical Approach, 3rd ed. McGraw Hill, 2006.
[27] P. Bhattacharya, S.K. Saha, A. Yadav, P.E. Phelan, R.S. Prasher, Brownian dynamics simulation to determine the effective thermal conductivity of nanofluids, J. Appl. Phys. 95 (2004) 6492–6494.
[28] X. Wang, X. Xu, S.U.S. Choi, Thermal conductivity of nanoparticle–fluid mixture, J. Thermophys. Heat Transfer 13 (1999) 474–480.
[29] J.C. Maxwell, Electricity and Magnetism, Clarendon Press, Oxford UK, 1873.
[30] B.C. Pak, Y.I. Cho, Hydrodynamic and heat transfer study of dispersed fluids with submicron metallic oxide particles, Exp. Heat Transfer 11 (1998) 151.

International Communications in Heat and Mass Transfer 53 (2014) 185–194

Contents lists available at ScienceDirect

International Communications in Heat and Mass Transfer

journal homepage: www.elsevier.com/locate/ichmt

Classification of in-tube boiling R134a data belonging to the smooth and corrugated tubes ☆

M. Balcilar [a,*], A.S. Dalkilic [b], A.C. Sonmez [c], S. Wongwises [d]

[a] Computer Engineering Department, Yildiz Technical University,Davutpasa, Esenler, Istanbul 34349, Turkey
[b] Heat and Thermodynamics Division, Department of Mechanical Engineering, Yildiz Technical University (YTU), Yildiz, Besiktas, Istanbul 34349, Turkey
[c] Faculty of Computer and Informatics, Istanbul Technical University, Maslak, 34469, Istanbul, Turkey
[d] Fluid Mechanics, Thermal Engineering and Multiphase Flow Research Lab. (FUTURE), Department of Mechanical Engineering, Faculty of Engineering, King Mongkut's University of Technology Thonburi (KMUTT), Bangmod, Bangkok 10140, Thailand

ARTICLE INFO

Available online 1 March 2014

Keywords:
Artificial intelligence
Machine learning
Pattern classification
Naive Bayes Classifier (NBC)
Quadratic Discriminant Classifier (QDC)
Linear Discriminant Analysis (LDA)
Mahalanobis distance
Principle component
Boiling

ABSTRACT

Different types of tubes have been used to improve cooling systems regarding the performance, cost and compactness. Corrugated tubes are tubes with their inner surface enhanced in these systems. One of the applications of machine learning, named as pattern classification, is often used to separate the human faces, voices, finger prints etc. In this study, it is used to separate the R134a data taken in-tube boiling process in smooth and enhanced tubes automatically. In other words, the developed numerical algorithms enabled artificial intelligence to predict the type of tubes having equivalent diameters used in the experiments. Systematical experiments, including saturation temperatures of 10, 15 and 20 °C, mass fluxes of 200, 300 and 400 kg m^{-2} s^{-1} and heat fluxes of 20, 25 and 30 W m^{-2}, are carried out for the comparisons using smooth and 5 different types of corrugated tubes having various corrugation depths and helix angles. The boiling process in the test tubes has been measured with 300 data points, having 30 individual parameters (inputs) for varying tube types for the reduction process by the Linear Discriminant Analysis (LDA) and Principle Component Analysis (PCA). The classification success rates of the methods of Linear Discriminant Classifier (LDC), Quadratic Discriminant Classifier (QDC), Naive Bayes Classifier (NBC) and Minimum Mahalanobis Distance Classifier (MMDC) by each dimensional reduction and the total area occupying under receiver operating characteristic (ROC) curves are determined according to 3-fold cross validation method. NBC method has the highest classification success with the accuracy of 98.33% as a result of the reduction to 3 dimensions by LDA method. In addition to this, QDC method has the highest area under curve (AUC) with the value of 0.9994 according to the reduction to 3 dimensions by LDA method. Dependency analyses showed that the use of 8 dimensional experimental parameters as the most important input is enough to determine the type of test tubes with a high accuracy.

© 2014 Elsevier Ltd. All rights reserved.

1. Introduction

Machine Learning is a kind of programming concept to optimize a performance criterion using example data or past experience [1]. The act of taking in raw data and making an action, based on the category of pattern, is called as pattern classification [2]. Pattern classification is the most important field of Machine Learning. Humans are able to classify the patterns which they come across in their daily lives very easily. Amongst common examples of pattern classification is the human ability to identify the caller on the phone, to recognize individual persons in a photograph or to read and guess the author of an unfamiliar text without being given any information about the author. The pattern classification problem arises due to the human desire to have the machines do all these tasks which are easily done by human beings. There are a lot of classification methods described in the literature developed utilizing computer science research on how these methods can be applied to different problems.

In pattern classification problems, the methods in use are probability-based methods such as Maximum-likelihood Estimation, Bayesian Estimation, Naïve Bayes Classification, Expectation–Maximization, and Hidden Markov Model, non-parametric models such as Parzen Windows and K-nearest Neighbor [2], linear models such as Linear Discriminant Functions, Probabilistic Discriminant Functions, and Logistic Regression [3], neural network models such as Multi-Layer Perceptron, Radial Basis Function, and Probabilistic Neural Network, non-metric models such as Decision Trees and Decision Forests [2], kernel-based methods such as Support Vector Machines and Quadratic Discriminant Functions [3], minimum distance classifier methods defined accordingly

☆ Communicated by Dr. W.J. Minkowycz.

* Corresponding author: Tel.: +90212835758; fax: +902123835732.
E-mail addresses: muhammet@ce.yildiz.edu.tr (M. Balcilar), dalkilic@yildiz.edu.tr (A.S. Dalkilic).

http://dx.doi.org/10.1016/j.icheatmasstransfer.2014.02.020
0735-1933/© 2014 Elsevier Ltd. All rights reserved.

with several distance metrics [4], and fuzzy logic-based methods such as Fuzzy Classification and Adaptive Neuro Fuzzy Inference System [5].

However, in heat transfer literature, the pattern classification methods have started being utilized very recently. The first example is the study which aimed to detect the faults occurring in the cooling systems by using Bayesian Classification Methods [6]. In the study, the signals obtained from the machine were classified based either on their fault pattern or non-fault pattern characteristics. Another study aimed to classify the heat resistance of steel structure. In this study, the aim was to classify the properties detecting them from images of steel structures [7]. A different study showed that, there is an important difference between fire retardant treated and untreated wood products in terms of heat release and therefore these products can be classified only with measurements and observations. However, a specific classification algorithm was not applied [8]. Another study investigated the classification of different types of milk obtained from different places based on the values measured by electronic nose device. Support vector machine was used in this study [9].

There has been no study in the literature yet to date; investigating the automatic classification of different types of tubes used refrigeration systems during two-phase flows. For this reason, this study is expected to be a model for future studies and fill the gap in the literature.

2. Experimental setup

A schematic diagram of the test apparatus can be seen from author's publications in the literature. The refrigerant loop consists of a preheating loop, test section, heating loop, and chilling loop. For the refrigerant circulating loop, liquid refrigerant is forced by a gear pump which can be adjusted to the flow rate using an inverter. The refrigerant then passes in series through a filter/dryer, a refrigerant flow meter, a preheater, and a sight glass and enters the test section. The pre-heater controls the inlet quality before entering the test section. It consists of a spiral counter-flow tube-in-tube heat exchanger which is designed to supply heat in order to prepare an inlet quality for the vaporization of the refrigerant. Leaving the test section, the refrigerant vapor then condenses inside a sub-cooler and is collected in a receiver. After leaving the chilling loop, the refrigerant returns from a two phase refrigerant to a sub-cooled state. Eventually, the refrigerant returns to the refrigerant pump to complete the cycle.

Details of the test section are shown schematically in Fig. 1a. The test section is a vertical counter-flow double tube heat exchanger with refrigerant flowing downward in the inner tube and heating water flowing upward in the annulus. The test sections are one smooth tube and two corrugated tubes, which are made from copper. The inner diameter and outer diameter of the inner tube are 8.7 and 9.52 mm, respectively. The length of the test section is 500 mm. Fig. 1b shows a sketch of a corrugated tube. T-type thermocouples are installed at the inlet and outlet of the test section to measure the saturation temperature of the refrigerant. Similarly, the differential pressure transducer is installed in order to measure the pressure drop across the test section. The length between the pressure taps is 850 mm. There are 10 thermocouples located at five positions along the test section. All of the wall thermocouples are fixed with special glue having low thermal conductivity. The test section is insulated with rubber foam with a thermal conductivity of 0.04 W/mK. All of the thermocouples are well calibrated by standard thermometers with a precision of 0.1 °C. The refrigerant flow meter is a variable area type and is specially calibrated in the range of 0.2–3.4 LPM for R-134a by the manufacturer, as is the differential pressure transducer. In the experiments, the inlet quality of the test section is varied by small increments. The imposed heat flux, mass flux, and saturation temperature are kept constantly at the desired values. The system is allowed to approach a steady state before any data are recorded. During experiments, the temperature and pressure are continuously recorded along the test section by the data acquisition system.

It should be noted that the detailed information on the experimental setup belonging to the subject tubes in this study can be seen from authors' previous publications [10,11].

3. Methodology

One of the application fields of Machine Learning is pattern classification problem. Definition of this problem is shown mathematically as follows [3].If each value measured by the experiments is represented by x scalar and each vector consisting of the values measured at each point of the experiment is represented by X, m dimensional vector belonging to n number test point can be shown as follows:

$$X_i = \left\{x_{i,1}, x_{i,2}, \ldots\ldots\ldots, x_{i,m}\right\} \quad i = 1 \ldots n \tag{1}$$

X_i vector in Eq. (1) is called as pattern. If the discrete class to which each pattern belongs is named as s_i and if s_i is an element of a set (which consists of C number elements) which has a finite number of elements, this is expressed as follows:

$$s_i \in \{1, 2, 3, \ldots C\} \tag{2}$$

When X_i is known, finding what s_i value corresponding to this vector is called classification problem.

Generally classification problem can be considered as the investigation of a function that takes X_i input to s_i output like the equation below.

$$f(X_i) = s_i \tag{3}$$

In this case, the only difference between the classification problem and regression problem is that function outputs are not continuous but they are members of a discrete set [2].

3.1. Dimensionality reduction

Pattern classification algorithms can directly use the value (which can be named as feature) obtained from the test environment and classify them. Similarly, the success of classification can be increased by reducing some features obtained by dimensionality reduction algorithms to a fewer number of features. This dimension reduction process can be done in two ways, namely feature selection and feature extraction. While feature selection process is done using some of the measured values (features) and not the others, feature extraction process is realized by using some of the combinations of all measured values. The method that will be used to select the linear combinations determines the name of dimensionality reduction algorithm. The number of the combinations to be used indicates the number of dimensions the new features will have. In this study, the main focus is to increase the success of classification methods by using the dimensional reduction through Principal Component Analysis and Linear Discriminant Analysis [12].

3.1.1. Principal Component Analysis (PCA)

Some dimensions (features) of p-dimensional X_i measurements obtained from the experiment environment can have high correlations with each other. In this case, it is quite redundant for the classification algorithm to take each feature with high correlation into consideration, bearing in mind that it may lead to wrong classification results [13]. Under these circumstances, the characteristic vector should have a linear transformation such that new characteristic vector features generated by this transformation could have the lowest correlation possible. New features having minimum correlation are called Principle Components. Principle Component Analysis (PCA) is an orthogonal transformation which changes the p-dimensional X_i feature vector into k-dimensional Y_i vector whose correlation is minimal between these dimensions. Principle Components obtained by PCA are determined as transformation elements through a process which orders

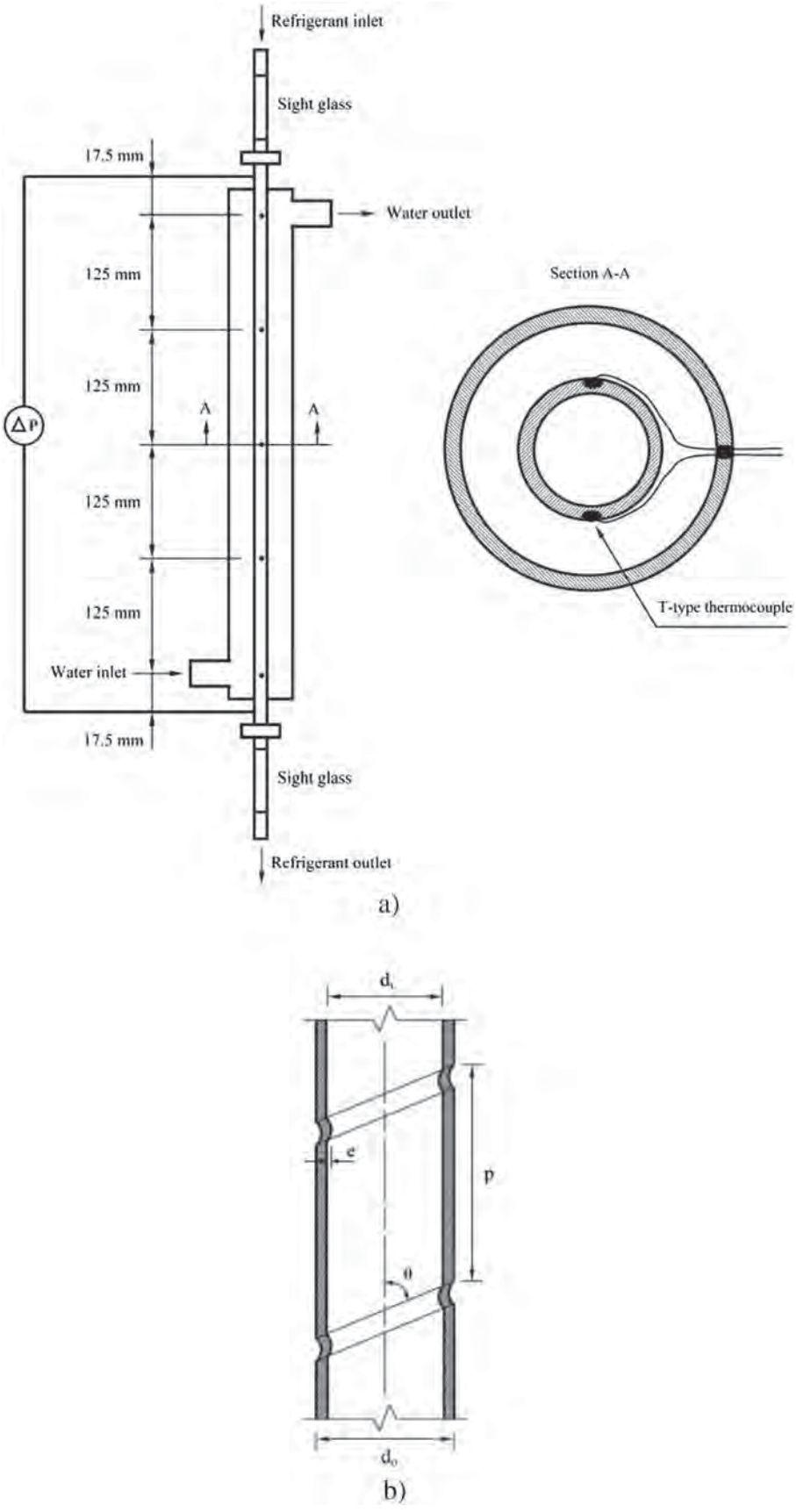

Fig. 1. Schematic diagram of the test section (a) and sketch of a grooved tube (b).
From Aroonrat and Wongwises [10], with permission from Elsevier.

them according to their variance values and gets k number with the highest variance. For the method to become a dimensionality reduction, evidently the relation between k and p must be $k < p$ [2]. Details of method are explained as follows. n number and p dimensional measurements obtained from the test environment are presented in Eq. (4) as:

$$\begin{aligned} X_1 &= \left\{x_{1,1}, x_{1,2}, \ldots, x_{1,p}\right\} \\ X_2 &= \left\{x_{2,1}, x_{2,2}, \ldots, x_{2,p}\right\} \\ X_n &= \left\{x_{n,1}, x_{n,2}, \ldots, x_{n,p}\right\} \end{aligned} \tag{4}$$

If the mean vector of this measurement values is presented by $\bar{X}$, the equation will take its form in Eq. (5) as:

$$\bar{X} = \frac{1}{n}\sum_{i=1}^{n} X_i \tag{5}$$

With subtraction of the measured vector and mean vector of n number vectors, mean zero (0) vectors are obtained as follows:

$$\vec{x}_i = X_i - \bar{X} \tag{6}$$

A matrix, which consists of mean zero feature vectors, n rows and p column, is defined as:

$$A = \begin{bmatrix} \vec{x}_1 \\ \vec{x}_2 \\ \vec{x}_n \end{bmatrix} \tag{7}$$

C matrix is obtained by multiplying the transpose of A matrix and itself.

$$C = A^T A \tag{8}$$

The values of $\vec{x}_i$ and λ_1, corresponding Eq. (9), are found in order to be represented with eigenvalue λ and eigenvector $\vec{x}$.

$$C\vec{x}_i = \lambda_i \vec{x}_i \tag{9}$$

The eigenvectors corresponding to k number of all the resulting eigenvectors, which have the highest value, become the principal components to be found. T matrix consisting of principle components is called as a transformation matrix.

$$T_{PCA} = [\vec{x}_1 \quad \vec{x}_2 \quad \vec{x}_k] \tag{10}$$

PCA dimensions can be obtained by using the obtained T matrix with p row and k column.

$$Y_i = \vec{x}_i \cdot T_{PCA} \tag{11}$$

3.1.2. Linear Discriminant Analysis (LDA)

The PCA method mentioned in the previous section does not use the data class information. However, the LDA method suggests a linear transformation by using the class information from a group in which all data belonging to the same class have the minimum variance, while data coming from different classes have the maximum variance in comparison to each other. This is an example of where within-class variances are minimum while between-class variances are maximum. In this way, the classes can be separated from each other more clearly in the new dimension [13].

The details of the method are summarized in this paragraph [2]. If the feature vector is obtained from the test environment taken as in Eq. (4), then the discrete class to which each of these vectors belong can be represented as in Eq. (2) and the mean of the features vector can be represented as in Eq. (5), and the average of cth class can be represented by $\overline{X}_c$. Similarly, if the number of elements in cth class is taken as n_c and the total experiment points as n, the average of each class can be found as follows:

$$\overline{X}_c = \frac{1}{n_c}\sum_{i=1}^{n} \delta_{ic} X_i \quad c = 1..C. \tag{12}$$

In this equation δ_{ic} is a coefficient which defines whether ith experiment point belongs to c^{th} class and it is expressed as follows:

$$\delta_{ic} = \begin{Bmatrix} 1, & s_i = c \\ 0, & s_i \neq c \end{Bmatrix} \tag{13}$$

When each element is subtracted from the class average it belongs to, experimental points that come from the same class can have 0 averages amongst themselves.

$$\vec{x}_i = X_i - \sum_{c=1}^{c} \delta_{ic} \cdot \overline{X}_c \quad i = 1..n \tag{14}$$

S scatter matrix defining variance belonging to each class is calculated as:

$$S_c = \sum_{i=1}^{n} \delta_{ic} \vec{x}_i^{\,T} \vec{x}_i \quad c = 1..C \tag{15}$$

Within-class scatter matrix defining total variance with-in class is determined as:

$$S_w = \sum_{c=1}^{c} S_c \tag{16}$$

Between-class scatter matrix defining between-class variance is obtained as:

$$S_B = \sum_{c=1}^{c} 2.\left(\overline{X}_c - \overline{X}\right)^T.\left(\overline{X}_c - \overline{X}\right) \tag{17}$$

When within-class variance is minimum and between-class variance is maximum, fitness function reaches its maximum and the fitness function can be expressed as follows:

$$J(W) = \frac{\left|w^T \cdot S_B \cdot w\right|}{\left|w^T \cdot S_W \cdot w\right|} \tag{18}$$

LDA seeks the transformation which is the maximum of the W transformation matrix making function. W vector making J function maximum is the solution of Generalized Rayleigh quotient problem, also very well known in mathematical physics [14]. Analytical solution of this problem is a combination of W_i and λ_i values proving the equation below.

$$S_B W_i = \lambda_i S_w W_i \tag{19}$$

W_i values are eigenvectors of $S_w^{-1} \cdot S_B$ matrix and λ_i values are eigenvalues of $S_w^{-1} \cdot S_B$ matrix. T matrix, which is composed of the eigenvectors corresponding to k number of all eigenvectors having the highest values, is called as LDA transformation matrix.

$$T_{LDA} = [W_1 \quad W_2 \quad W_k] \tag{20}$$

LDA dimensions can be determined by using the subject T matrix with row p and column k in Eq. (21) as:

$$Y_i = (X_i - \bar{X}) T_{LDA} \tag{21}$$

S_w matrix must not be singular in order to define eigenvectors of Eq. (19). However, in some cases S_w matrix can be singular. In this case, first of all, p dimensional number is reduced to d by applying PCA to all the data in the form of determinant of S_w matrix not being equal to 0, and then d dimensional number is reduced to k by applying LDA. Evidently, the relation between dimensional numbers must be $k < d < p$.

3.2. Classification methods

Vectors with new features, which are obtained from dimensional reduction process, are classified by using Linear Discriminant Classifier, Quadratic Discriminant Classifier, Naive Bayes Classifier, and Minimum Mahanolobis Distance Classifier methods, and this section aims to give detailed information on each of these methods.

3.2.1. Linear Discriminant Classifier (LDC)

Discriminant functions are functions which can separate feature vectors and the resulting data point belonging to 2 different classes in the space they are located. They can also separate the space into 2 regions. Linear Discriminant Function is also used in cases where the function in question is linear with regard to the feature comprising the data. In this case, Linear Discriminant Function can be written as below [2].

$$\begin{aligned} g(X) &= w_0 + \sum_{j=1}^{k} w_j x_j \\ g(X) &= w^T \cdot X + w_0 \end{aligned} \tag{22}$$

where X is a vector having k features in the form of $\{x_1, x_2, \ldots\ldots\ldots, x_k\}$, W is the weight vector having k number of weights in the form of $\{w_1, w_2, \ldots\ldots\ldots, w_k\}$, w_0 is the threshold value, and g is the Linear discriminant function. When an element in the form of $x_0 = 1$ is added to the vector X, X becomes $\{1, x_1, x_2, \ldots\ldots\ldots, x_k\}$, and if w_0 value is added to the vector W, it becomes $\{w_0, w_1, w_2, \ldots\ldots\ldots, w_k\}$. In this case, discriminant function can be written as below.

$$g(X) = w^T X \tag{23}$$

If $g(X) > 0$, it means that X feature belongs to vector class 1 and if $g(X) < 0$, it means that X feature belongs to vector class 2. In order to find the values comprising W weight vector in Eq. (23), J error function needs to be defined and try to be minimized. If the cluster of misclassified feature vectors is represented by Y, error function is written as follows.

$$J(W) = \sum_{i \in Y} -w^T X_i \tag{24}$$

Minimization problem can be solved by optimization methods such as Gradient Descent and Newton optimization.

According to Gradient Descent method, the algorithm started from a random W value update w vector in each j step like the update step below.

$$W^{j+1} = W^j - \eta^j \nabla J(W) \tag{25}$$

where ∇J is the gradient vector of error function, and η^j is the amount of step.

According to Newton optimization method, a random W value is taken as a starting point, but in the update step the inverse of Hessian (H) matrix, which is comprised of second order partial derivation of J error function, is used.

$$W^{j+1} = W^j - H^{-1} \nabla J(W) \tag{26}$$

Both methods update W weight vector until the defined stopping criteria are proven. When stopping criteria are proven, the resulting vector W defines boundary separating class 1 from class 2.

In this study, instead of using Gradient Descent and Newton optimization methods, an LDA based method is used. The preferred LDA based method can find the smallest error analytically without using iteration but instead an eigenvector, having taken the mean square errors of the expected class and the actual class is taken as the error function.

In this method, experimental points aiming to separate 2 classes are reduced to one dimension with LDA as mentioned in Section 3.1.2. If resulting value is higher than 0, it belongs to class 1, otherwise, it belongs to class 2. If discriminant function equation, separating 2 classes from each other, is represented by Eq. (22), then equivalent W vector and w_0 can be represented as below.

$$\begin{aligned} W &= n S_w^{-1} (\bar{X}_1 - \bar{X}_2) \\ w_0 &= -\bar{\bar{X}} W \end{aligned} \tag{27}$$

where n is the total element number, S_w is within-class scatter matrix calculated by Eq. (16), $\bar{X}_i$ is the mean of data points belonging to ith class given in Eq. (12), and $\bar{X}$ is the mean of all data points in the Eq. (5).

Above mentioned methods are for determining the boundary lines separating 2 classes from each other. For multi class case, multiple separators of 2 classes need to be taken, 2 different methods in the literature, one of them being one-to-one strategy and the other being one-to-all strategy. In one-to-one strategy, C number discriminant function is used for C number class. Each discriminant function determines whether a vector belongs to that class or one of the all other classes.

$$g_i(X) = w_i^T X + w_{i,0} \qquad i = 1 \ldots C \tag{28}$$

In this case, $\hat{s}$ is the prediction class of X feature vector and found in Eq. (29).

$$\hat{s} = i, \quad if \;\; g_i(X) > g_j(X) \qquad for\ all\ j \neq i \tag{29}$$

In one to one strategy a different discriminant function is written for each pair. $C(C\text{-}1)/2$ number discriminant functions are written for C number class. These functions are expressed in Eq. (30).

$$g_{ij}(X) = W_{ij}^T X + w_{ij,0} \qquad i = 1 \ldots C-1, \quad j = i+1 \ldots C \tag{30}$$

In this case, $\hat{s}$ is the prediction class of X feature vector and found in Eq. (31).

$$\hat{s} = i, \quad if \;\; g_{ij}(X) > 0 \quad for\ all\ j \neq i \tag{31}$$

In this study one-to-all strategy is preferred.

3.2.2. Quadratic Discriminant Classifier (QDC)

The only difference between QDC and LDC method is that in QDC, the discriminant function is not linear with the feature vector while it comprises a second order function. If feature vector X is like $\{x_1, x_2, \ldots\ldots\ldots, x_k\}$, then the discriminant function for QDC is written as follows [2].

$$g(X) = w_0^s + \sum_{j=1}^{k} w_j^l x_j + \sum_{i=1}^{k} \sum_{j=i}^{k} w_{ij}^q x_i x_j \tag{32}$$

where w^s defines a scalar number representing threshold value, w^l defines a vector representing linear coefficients, and w^q defines a matrix representing quadratic coefficients. In order to reduce Eqs. (32) to (22), $w_0 = w_0^s$ substitution is made. Descriptions of X feature vector and W weight vector are changed as below.

$$\begin{aligned} X &= \left\{ x_1, \ldots, x_k, x_1^2, x_1 x_2, \ldots, x_1 x_k, x_2^2, \ldots, x_2 x_k, \ldots x_k^2 \right\} \\ W &= \left\{ w_1^l, \ldots, w_k^l, w_{1,1}^q, w_{1,2}^q, \ldots, w_{1,k}^q, w_{2,2}^q, \ldots, w_{2,k}^q, \ldots, w_{k,k}^q \right\} \end{aligned} \tag{33}$$

In this case, discriminant function of QDC method can be expressed with Eq. (22).

$$g(X) = w^T X + w_0 \tag{34}$$

Further calculations use the same procedure as LDC method.

3.2.3. Minimum Mahalanobis Distance Classifier (MMDC)

MMDC is a distance based method. In addition, it is called the parametric method since the elements of the classes use primary thesis suggesting that they are distributed in space with a normal distribution depending on the mean and covariance of the class. According to this algorithm, first of all, the mean and the covariance of each class need to be predicted. Since the mean and the covariance of the subject training set used are the best predictions of the average and covariance of all classes, these parameters are calculated as a starting point [4].

$\bar{X}_c$ value, which is the mean value of cth class, is calculated with Eq. (12). If the number of the elements in cth class is represented by n_c, the covariance of cth class is calculated by Eq. (35) as:

$$\sum_c = \frac{1}{n_c}\sum_{s_i=c}(X_i-\bar{X}_c)^T(X_i-\bar{X}_c) \qquad c = 1...C \tag{35}$$

Mahalanobis distance between X_i feature vector and cth class (d_{ic}) is calculated as below:

$$d_{ic} = (X_i-\bar{X}_c)\sum_c^{-1}(X_i-\bar{X}_c)^T \quad c = 1...C \tag{36}$$

In this case, $\hat{s}$ is the prediction class of X feature vector, and can be calculated in Eq. (37) as:

$$\hat{s}_i = argmin_c(d_{ic}) \tag{37}$$

3.2.4. Naive Bayes Classifier (NBC)

NBC method is a probability based simple classifier. This method which is based on Bayes theorem has been widely used because of both its simplicity, and better performance compared to more complicated classifiers.

NBC method makes classification with the assumption that all features comprising data are independent from each other. Therefore, the data obtained from the test environment give bad results if applied without dimension reduction. The advantage of this method is that it is highly accurate in small training sets requiring only a few class parameters to be predicted, since all features are taken into account independent from each other, only the mean and the variance of these features need to be predicted. There is no need to predict the variance of the features with respect to one another.

The details of the method are summarized below [15].

If there are data belonging to C number different classes in the training set which have n number of elements, prior probability belonging to each class is defined as

$$p(s_c) = \frac{\sum_{i=1}^{n}\delta_{ic}}{n} c = 1...C \tag{38}$$

The feature vector belonging the test set is represented as $X = \{x_1, x_2,.....,x_k\}$ and its probability to belong to s_c class.

$$p(s_c|X) = p(s_c|x_1, x_2, ..., x_k) \tag{39}$$

Conditional probability can be written by using Bayes theorem as follows.

$$p(s_c|X) = \frac{p(s_c)p(x_1, x_2, ..., x_k|s_c)}{p(x_1, x_2, ..., x_k)} \tag{40}$$

Because measured values cannot be known, all values have an equal probability to be measured; the denominator of Eq. (40) will be the same for all X values. Therefore, probability can be written as below.

$$p(s_c|X) = p(s_c)p(x_1, x_2, ..., x_k|s_c) \tag{41}$$

This method makes conditional independence assumptions. Therefore, if the features comprising joint probability are considered as independent and written in the form of a multiplication, the probability can be expressed as follows:

$$p(s_c|X) = p(s_c)\prod_{j=1}^{k}p(x_j|s_c) \tag{42}$$

where $p(x_j|s_c)$ is the possibility of jth feature of X vector to be in class c. While calculating this value, s_c class can be considered to have a normal distribution according to the mean and variance of j^{th} feature.

In this case, $p(x_j|s_c)$ can be calculated as below:

$$p(x_j|s_c) = \frac{1}{\sqrt{2\pi\sigma_{c,j}^2}}e^{-\frac{(x_j-\mu_{c,j})^2}{2\pi\sigma_{c,j}^2}} \tag{43}$$

where $\mu_{c,j}$ defines the mean of j^{th} feature of cth class, and $\sigma_{c,j}^2$ defines the variance of jth feature of c^{th} class.

With all this definition, the probability of the X vector given in Eq. (42) existing in cth class $p(s_c|X)$ can be calculated. C value making Eq. (42) maximum determines which class X vector will belong to.

If $\hat{s}$ is defined as the predicted class of the X vector being an element of the test set, then it is calculated as:

$$\hat{s} = argmax_c(p(s_c|X)) \tag{44}$$

3.3. Validation and performance criteria

Validation process must be carried out to measure how successful the classification has been. Validation is made by using algorithms that have been utilized in supervised learning method, acquiring data points from the experiment. The most well-known validation methods are Hold-out validation, K-fold cross validation, and Leave-one-out cross validation methods.

In addition, correct classifying ratio (success rate) is used as criteria showing the success of this classification. Similarly, the area under curve (AUC), which is the total area under receiver operating characteristic (ROC) curve showing to what degree the classes can be separated from each other, is used.

3.3.1. K-fold cross validation

According to this method, n number of data obtained from the experiments is divided randomly by k number set in the form of each cluster having equal element and each set being numbered from 1 to k.

$$v_i \in \{1, 2, ..., k\} \qquad i = 1...n \tag{45}$$

First of all, data, whose v_i values are equal to 1, are taken as a test set and data whose values are different from 1 are taken as a training set.

Suggested method is to train with training set and to examine with test set. Then data whose v_i values are 2 are sent to test set, and data whose v_i values are different from 2 are sent to training set. The method is retrained with a new training set and examined with the test set. This process continues until all layers are tested [1].

3.3.2. Success rate

One of the performance criteria used is success rate ratio. This ratio is obtained by the ratio of correctly classified data to total data number.

If the real class of vector represented by feature vector X_i is s_i and predicted class through classification method is $\hat{s}_i$, success rate is calculated as follows.

$$Success\ Rate = \frac{1}{n}\sum_{i=1}^{n}D(s_i, \hat{s}_i) \tag{46}$$

Definition of D function is shown as follows.

$$D = \begin{Bmatrix} 1, & s_i = \widehat{s}_i \\ 0, & s_i \neq \widehat{s}_i \end{Bmatrix} \tag{47}$$

3.3.3. Area under receiver operating characteristic (ROC) curve

If measuring the performance of classification is considered inadequate, then ROC curve could be utilized. ROC curve is a metric curve which measures to what degree the classifier separates the classes from each other and how far the boundaries of classes are away from each other [16].

This curve is the measure of performance for the classifier separating two classes.

Outputs of classifiers classifying data sets consisting of two classes one of which is positive and the other is negative are normalized between [0 1]. In this case, if the classifier generates 0 for X vector, it will be negative and if it generates 1, it will be positive. The probability density function of the values generated in the output by the elements of positive and negative sets can be represented by $L_1(x)$ and $L_0(x)$ respectively. In this case, any threshold value between [0 1] is called a hit rate, connected to $H(t)$, in other words, the rate of the elements which are both in the positive class and classified as positive,

$$H(t) = \int_t^1 L_1(x)dx \tag{48}$$

False alarm rate, $F(t)$, is the rate of the elements which are classified as positive although they are negative,

$$F(t) = \int_t^1 L_0(x)dx \tag{49}$$

The ROC curve is a tool realized by the $\{F(t), H(t)\}$ points in the two dimensional space. Therefore, the area below [0 1] in ROC can be defined as the Area Under Receiver (AUC).

$$AUC = \int_0^1 H(t)dF(t) \tag{50}$$

The AUC value is between 0 and 1. When the value is close to 1, it means that the classes are well separated from each other. When the value is 0.5, this shows that the classifier is of no use at all because the value obtained in random classification is 0.5. Any resulting value under 0.5, shows that the data have been ordered in a reverse manner.

The statement in Eq. (50) is only for the classifier which separates the data set consisting of two classes. In the C-class problem, C-number of classes needs to be defined according to one-to-all strategy in order to apply it to multiclass problems. For each classifier, the class in question is labeled as positive while others are labeled as negative. The AUC value is calculated for each pair of classifiers. This value is defined as the average of calculated AUCs for all classes.

4. Results and discussion

In the data set used in the application, there are 300 data points belonging to six different types of tubes. All test conditions have been kept constant except for the pipes. Names of the pipes used, numbers of the measurements done, depth of corrugation and helix angles are shown in Table 1.

Totally 30 values have been collected for each test point. The values used in the experiment are represented as follows.

Table 1
Tube properties used in the experiment and number of the test points.

Tube name	Number of test points	Depth of corrugation	Helix angle
ST	50	–	–
CT1	51	0.5	53.875
CT2	48	0.75	53.875
CT3	46	1	53.875
CT4	54	1	64.07
CT5	51	1	69.95

Total pressure drop ΔP_{total}; inlet, outlet and average vapor qualities x_{in}, x_{out}, x_{avg} liquid and vapor densities $\rho 1$, ρ_v, liquid and vapor dynamic viscosities μ_1, μ_v; mass flux G, inlet, outlet and average refrigerant temperatures $T_{ref,in}$, $T_{ref,out}$, $T_{ref,avg}$; inlet, outlet and average water temperatures $T_{w,in}$, $T_{w,out}$, $T_{w,avg}$; average wall temperatures $T_{wall,avg}$; enthalpies of liquid, vapor and phase changes i_l, i_v, i_{lv}; thermal conductivity k; specific heat at constant pressure c_p; inlet, outlet and average Zivi's void fractions α_{in}, α_{out}, α_{avg}; equivalent mass flux G_{eq}; equivalent Reynolds number Re_{eq} gravitational pressure drop ΔP_g; the acceleration pressure drop ΔP_a; frictional pressure drop ΔP_f; and friction factor of tube f_{tp}.

In this case, the feature vector to be used is defined as:

$$X = \Big\{\Delta P_{total}, x_{in}, x_{out}, x_{avg}, \rho_l, \rho_v, \mu_l, \mu_v, G, T_{ref,in}, T_{ref,out}, T_{ref,avg}, T_{w,in}, T_{w,out}, T_{w,avg}, T_{wall,avg}, i_l, i_v, i_{lv}, k, c_p, \alpha_{in}, \alpha_{out}, \alpha_{avg}, G_{eq}, Re_{eq}, \Delta P_g, \Delta P_a, \Delta P_f, f_{tp}\Big\} \tag{51}$$

The identified X feature has been subjected to dimension reduction through both PCA and LDA, and via 3-fold validation, the performance of each classifier has been measured according to success rate. Fig. 2 shows the success rate graphics based on the numbers of PCA and LDA's number of dimensions changing with each classifier.

Dimension numbers with the highest success numbers, which are obtained through a PCA and an LDA dimension reduction, and the success rates and AUC values of these models, are given in Table 2a.

According to the table, in all classifier methods, LDA dimension reduction precedes PCA. In addition, the highest classification success has been obtained through the reduction of the values to three dimensions that all the classifiers have. With the reduction of the classifier methods to 3 dimensions through LDA, the details of the resulting AUC values are given in Table 2b.

According to this table, corrugated tube 1 and corrugated tube 5 have been defined with the highest accuracy with regard to all methods. The error of the classification is due to other tubes. With regard to the success rate criteria, NBC has given the worst result when used with PCA, but the best result with LDA. This finding is a result of the fact that the Naïve Bayes method evaluates the features independently. Without doubt, one cannot argue that the features obtained from the test environment are not related. Since the LDA method can separate the classes in the best way possible and find new features that are unrelated to each other, the NBC method is successful with LDA.

Although NBC is the highest in the success rate, QDC is the most successful one according to the AUC metric. The AUC metric tests the ability of the classifier to separate between the classes. In this case, it can be argued that the QDC is the best method to separate between the classes. The reason why it cannot outperform NBC in success rate can be explained by the fact that after the classes are separated, this method can no longer measure the boundary between the classes in an efficient way.

For the investigation of the most effective methods in classification, 3-fold validation success of the data, which was reduced to 3 dimensions through LDA, in LDC method, is used. Through Forward-Sequential feature selection method, the most effective parameters were investigated. According to this method, the feature, which makes the classification

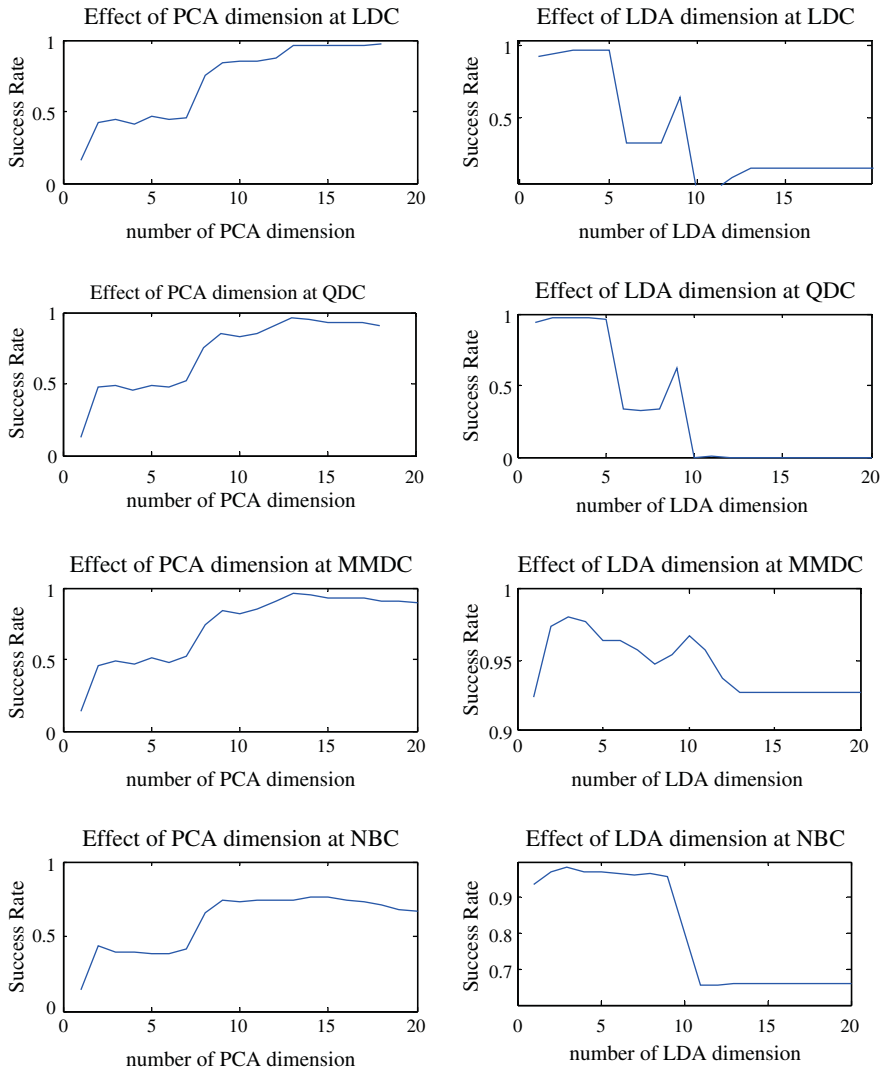

Fig. 2. Success rate graphics according to number of PCA and LDA dimensions changing for each classifier.

Table 2
Success of classification methods (a) and detailed success table of classification methods according to AUC metric (b).

a)

Classification method	Dimensionality reduction	Best dimension	Success rate	Mean AUC
LDC	PCA	18	0.97	0.9985
	LDA	3	0.97	0.9988
QDC	PCA	13	0.96	0.9893
	LDA	3	0.9767	0.9994
NBC	PCA	14	0.7633	0.9272
	LDA	3	0.9833	0.9993
MMDC	PCA	13	0.9567	0.9825
	LDA	3	0.98	0.9959

b)

Classification method	LDC	QDC	NBC	MMDC
ST to other	1.0000	1.0000	1.0000	0.9964
CT1 to other	1.0000	1.0000	1.0000	0.9999
CT2 to other	0.9991	0.9988	0.9999	0.9846
CT3 to other	0.9944	0.9977	0.9958	0.9968
CT4 to other	0.9994	1.0000	0.9998	0.9994
CT5 to other	1.0000	1.0000	1.0000	0.9981
Mean AUC	0.9988	0.9994	0.9993	0.9959

success maximum, is added to the specification subset one by one. When the increase in success stops or does not surpass the threshold value, the choice of specification is finished [17]. The specifications and success obtained from the research are as given in Table 3. Classification success reaches 97% with LDC method by selecting 8 properties from this table.

The pattern how the classifiers divide the 2-d space into regions and how LDA groups the test points in the space are shown in Fig. 3. While this shape was being formed, all data points were put into the training set and reduced to two features through LDA, after which classifiers were applied.

5. Conclusion

The tubes used in refrigeration systems are classified in quite a successful when the suggested features are reduced to three dimensions through the LDA method. In addition, it has been shown in this paper that property cluster can give significantly successful results even with a subset consisting of 8 elements. This study is the first one using classification algorithms to differentiate the type of enhanced tubes from each other during two-phase boiling flow. For that reason, it is expected to fill the gap in the literature presenting the new finding using this technique.

Table 3
8 properties affecting the success of classification most and classification success of these properties when selected cumulatively.

Number of feature	1	2	3	4	5	6	7	8
Adding feature	f_{tp}	ΔP_{total}	x_{out}	$T_{ref,in}$	$T_{w,out}$	$T_{w,in}$	$T_{wall,avg}$	ΔP_a
Success rate (%)	0.45	0.5533	0.5967	0.6367	0.6867	0.9233	0.9567	0.97
AUC	0.8001	0.8837	0.9061	0.9129	0.9327	0.989	0.9961	0.9978

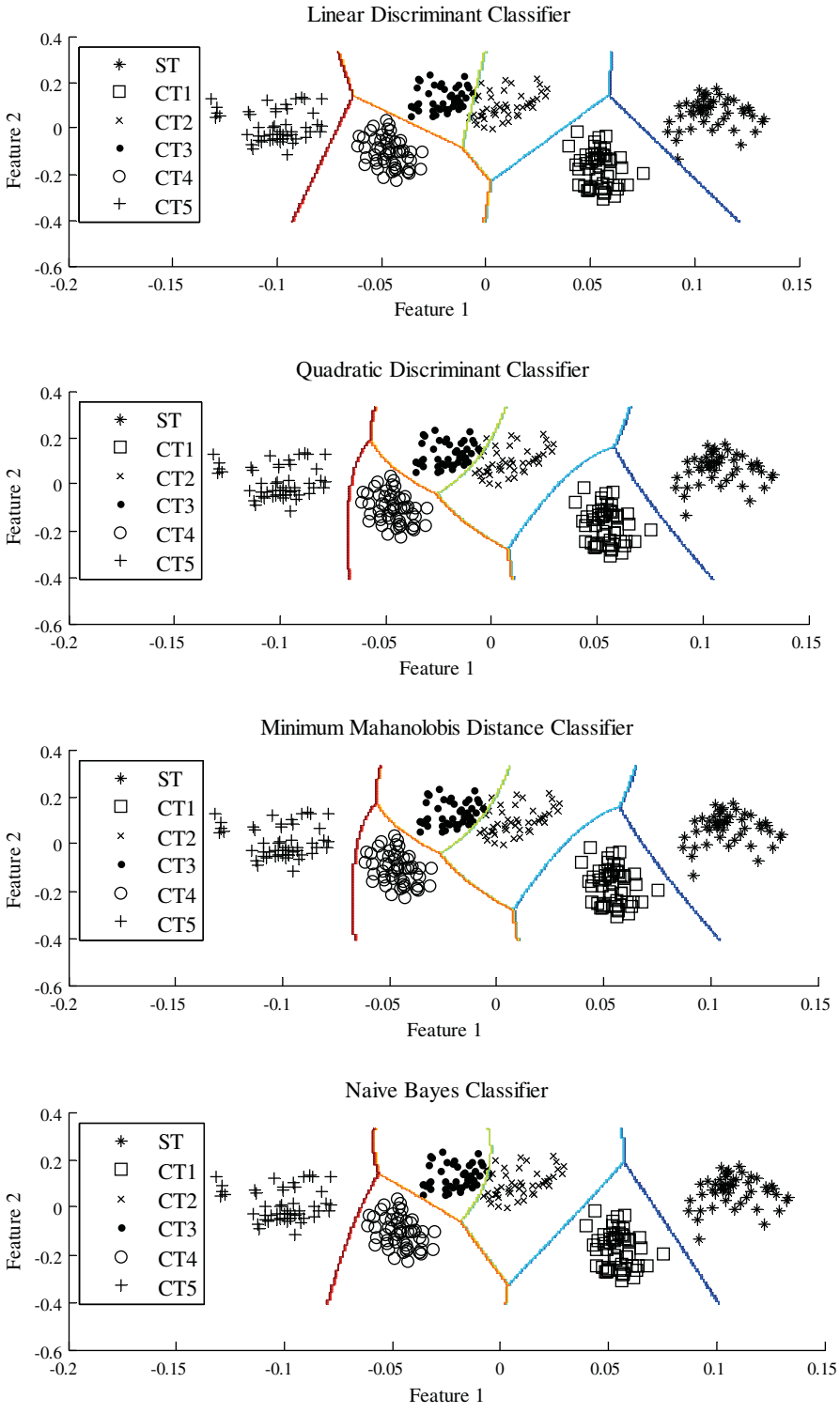

Fig. 3. Locations of experiment points with LDA in 2-d space and boundary lines of classifiers.

Acknowledgment

The second author wishes to thank King Mongkut's University of Technology Thonburi (KMUTT) for providing him with a Post-doctoral fellowship. The fourth author wishes to thank the Thailand Research Fund, the National Research University Project and the National Science and Technology Development Agency.

References

[1] E. Alpaydin, Introduction to Machine Learning, vol. 56, no. 2The MIT Press, 2004. 387–399.
[2] R.O. Duda, P.E. Hart, D.G. Stork, Pattern Classification, vol. 2, no. 6Wiley, 2001. 654.
[3] C.M. Bishop, Pattern Recognition and Machine Learning, vol. 4, no. 4Springer, 2006. 738.
[4] T.M. Mitchell, Machine Learning, vol. 1, no. 3McGraw-Hill, 1997. 414.
[5] J.S.R. Jang, C.T. Sun, E. Mizutani, Neuro-fuzzy and Soft Computing, Prentice Hall, 1997.
[6] Y. Guo, J. Wall, J. Li, S. West, A machine learning approach for fault detection in multi-variable systems, ATES Second International Workshop on Agent technology for Energy Systems, 2011, pp. 23–¯30.
[7] I. Topalova, A. Mihailov, A. Tzokev, Automated classification of heat resistant steel structures based on neural networks, IEEE Convention of Electrical and Electronics Engineers in Israel Proceedings, 2008, pp. 437–440.
[8] T. Yamashita, L.D. Tsantaridis, Heat release and classification of fire retardant wood products, Fire Mater. 19 (1994) (1995) 253–258.
[9] K. Brudzewski, S. Osowski, T. Markiewicz, Classification of milk by means of an electronic nose and SVM neural network, Sensors Actuators B Chem. 98 (2–3) (2004) 291–298.
[10] K. Aroonrat, S. Wongwises, Evaporation heat transfer and friction characteristics of R-134a flowing downward in a vertical corrugated tube, Exp. Thermal Fluid Sci. 35 (1) (2011) 20–28.
[11] S. Laohalertdecha, S. Wongwises, An experimental study into the evaporation heat transfer and flow characteristics of R-134a refrigerant flowing through corrugated tubes, Int. J. Refrig. 34 (1) (2011) 280–291.
[12] I. Guyon, A. Elisseeff, An introduction to variable and feature selection, J. Mach. Learn. Res. 3 (7–8) (2003) 1157–1182.
[13] J. Li, B. Zhao, H. Zhang, J. Jiao, Face recognition system using SVM classifier and feature extraction by PCA and LDA combination, 2009 International Conference on Computational Intelligence and Software, Engineering, 2009, pp. 1–4.
[14] M.A. Golberg, A generalized Rayleigh quotient for eigenvalue problems nonlinear in the parameter, J. Optim. Theory Appl. 11 (2) (1973) 146–158.
[15] H. Zhang, The optimality of naive Bayes, Mach. Learn. 1 (2) (2004) 3.
[16] T. Fawcett, An introduction to ROC analysis, Pattern Recogn. Lett. 27 (8) (2006) 861–874.
[17] A. Marcano-Cedeno, J. Quintanilla-Dominguez, M.G. Corthina-Januchs, D. Andina, Feature selection using sequential forward selection and classification applying artificial metaplasticity neural network, Cell (2010) 2845–2850.

Experimental Thermal and Fluid Science 55 (2014) 54–61

Contents lists available at ScienceDirect

Experimental Thermal and Fluid Science

journal homepage: www.elsevier.com/locate/etfs

Heat transfer characteristics of gas–liquid flow in horizontal rectangular micro-channels

Sira Saisorn [a,c], Piyawat Kuaseng [b], Somchai Wongwises [c,*]

[a] Department of Mechanical Engineering, King Mongkut's Institute of Technology Ladkrabang, Prince of Chumphon Campus, Chumphon 86160, Thailand
[b] Department of Mechanical Engineering, King Mongkut's Institute of Technology Ladkrabang, Bangkok 10520, Thailand
[c] Fluid Mechanics, Thermal Engineering and Multiphase Flow Research Lab. (FUTURE), Department of Mechanical Engineering, Faculty of Engineering, King Mongkut's University of Technology Thonburi, Bangmod, Bangkok 10140, Thailand

ARTICLE INFO

Article history:
Received 17 October 2013
Received in revised form 28 January 2014
Accepted 3 February 2014
Available online 11 February 2014

Keywords:
Flow pattern
Micro-channel
Heat transfer

ABSTRACT

An experimental study of heat transfer characteristics of air–water flow in horizontal micro-channels was carried out in this work. The gas–liquid mixture from a y-shaped mixing chamber was forced to pass through a plenum inlet and entered 21 parallel rectangular micro-channels 40 mm long in the direction of flow. Each channel had a width and a depth of 0.45 and 0.41 mm, respectively. The test runs were done at a heat load of 80 W, with superficial Reynolds numbers of gas and liquid ranging between 54–142 and 131–373, respectively. A Stereozoom microscope and camera system were employed to conduct flow visualization. To explore the dependence of a Nusselt number on the flow characteristics, two inlet sections with different designs were used in this work. The experiments revealed that the formation of small gas slugs instead of gas core flow involves an increase in Nusselt numbers. In this work, the gas–liquid flow gave heat transfer enhancement up to 80% over the liquid flow.

© 2014 Elsevier Inc. All rights reserved.

1. Introduction

Two-phase flow studies have been carried out extensively over the years. However, there have been a relatively small amount of publications dealing with micro-channels when compared with those for ordinarily sized channels. Capillary force is likely to play an important role for two-phase flow characteristics in micro-channels, resulting in flow phenomena significantly different from those observed in ordinarily sized channels. Serizawa et al. [1], for instance, investigated the visualization of the two-phase flow pattern in circular micro-channels. The flowing mixture of air and water in channels of 20, 25 and 100 μm in diameter and that of steam and water in a channel of 50 μm in diameter were conducted experimentally. The study confirmed that the surface wettability had a significant effect on the two-phase flow patterns in very small channels. The discrepancies between micro-scale and macro-scale flows have been reported in the literature [2–7].

Two-phase flow in micro-channels has gained significant attention in engineering due to wide application, extending to such fields as bioengineering, fuel cells, compact heat exchangers, heat sinks, and so on. For cooling purposes, various applications of micro-channels are discussed in detail by Mudawar [8]. Due to the rapid development of modern miniature devices generating large amounts of heat, the single-phase micro-channel flow seems no longer a highly effective cooling method.

Two-phase flow in small channels has become another effective means for dissipating heat. Flow boiling, for instance, involves very high heat transfer rate but backflow and instabilities, which are considered as drawbacks [9], have to be carefully controlled. According to the open literature, two-phase heat transfer in micro-channels have been mainly reported for flow boiling studies. The effects of such parameters as mass flux and heat flux on flow boiling phenomena have been reported in several publications [10–12]. Moreover, the up-to-date comprehensive discussions on flow boiling in micro-scale channels were given by Ribatski [13] and Tibirica and Ribatski [14]. In contrast, the data corresponding to heat transfer characteristics during non-boiling two-phase flow in micro-channels is still limited.

Bao et al. [15] carried out experiments to explore the heat transfer performance of air–water flow in a channel having a diameter of 1.95 mm. They reported that at a fixed liquid flow rate, the heat transfer coefficient increased with the increase in air flow rate caused by the flow pattern transition. Hetsroni et al. [16] performed experiments to study two-phase flow regimes and bubble behavior in triangular parallel micro-channels made from $15 \times 15 \times 0.53$ mm^3 square-shape silicon substrate. In this study, air–water and steam-water were chosen as working fluids and

* Corresponding author. Tel.: +66 24709115; fax: +66 24709111.
E-mail address: somchai.won@kmutt.ac.th (S. Wongwises).

http://dx.doi.org/10.1016/j.expthermflusci.2014.02.006
0894-1777/© 2014 Elsevier Inc. All rights reserved.

Nomenclature

A	area (m^2)
H	height (m)
h	heat transfer coefficient (W/m^2 K)
k	thermal conductivity (W/m K)
m	$(hP/kA_c)^{1/2}$
Nu	Nusselt number
P	perimeter (m)
Q	heat transfer rate (W)
q	heat flux (W/m^2)
Re_{GS}	superficial Reynolds number of gas
Re_{LS}	superficial Reynolds number of liquid
T_f	fluid temperature (K)
T_w	wall temperature (K)
W	width (m)

Greek symbols

η	fin efficiency

Subscripts

b	base
c	cross-section
ch	channel
f	fin
L	liquid phase
TP	two-phase

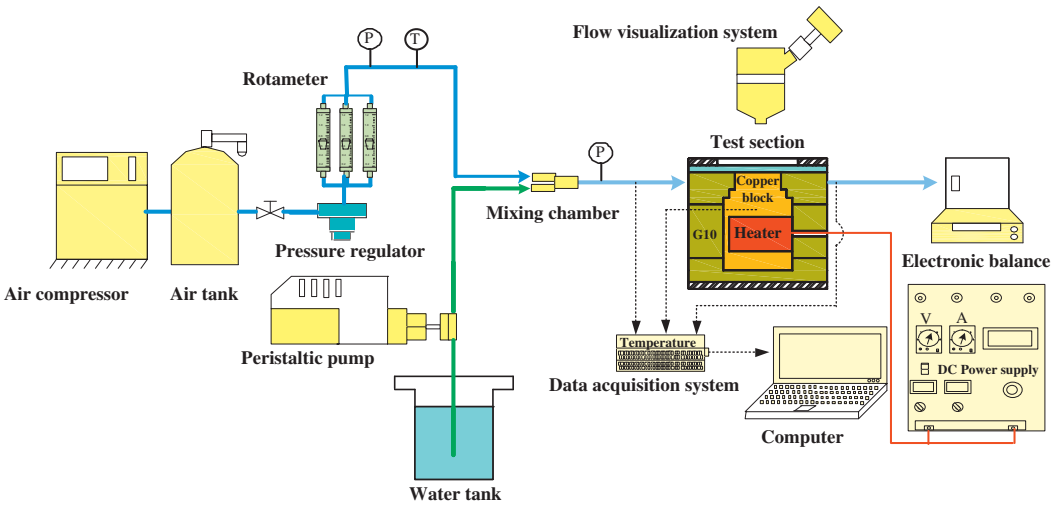

Fig. 1. Schematic diagram of experimental apparatus.

the differences between flow patterns of the two cases were addressed. It is noted from Triplett et al. [17,18] that based on different channel cross-sectional shapes, the adiabatic two-phase air–water flow characteristics in semi-triangular micro-channels were similar to those obtained from circular channels. The heat transfer of an air–water flow in parallel micro-channels of 0.1 mm in hydraulic diameter was experimentally investigated by Hetsroni et al. [19]. Their results showed a decrease in the Nusselt number with an increasing gas flow rate, which was opposite to the results obtained by Bao et al. [15]. Betz and Attinger [20] showed segmented flow, an intermittent pattern of gas bubbles and liquid slugs, resulting in the heat transfer enhancement up to 140% in a micro-channel heat sink when compared with single-phase liquid flow.

Heat transfer characteristics of a non-boiling two-phase flow in micro-channels with different diameters were studied by Choo and Kim [21]. Air and water were used as working fluids to examine the dependence of Nusselt number on the channel diameter. They found that with channel diameters of 0.506 and 0.334 mm, the Nusselt number increased with the increment of gas flow rate, but decreased with increasing gas flow rate when the channel diameters of 0.222 and 0.140 were employed.

Marchitto et al. [22] studied two-phase flow distribution in parallel upward channels. They reported that the phase distribution

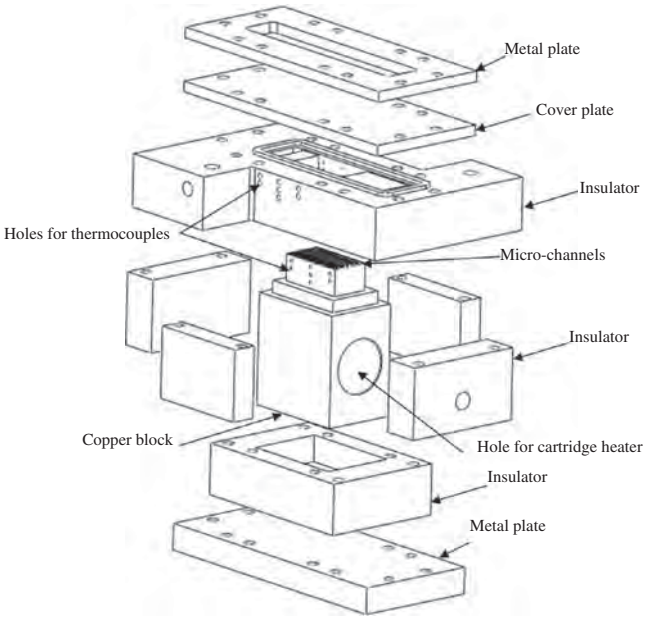

Fig. 2. Schematic diagram of test section assembly.

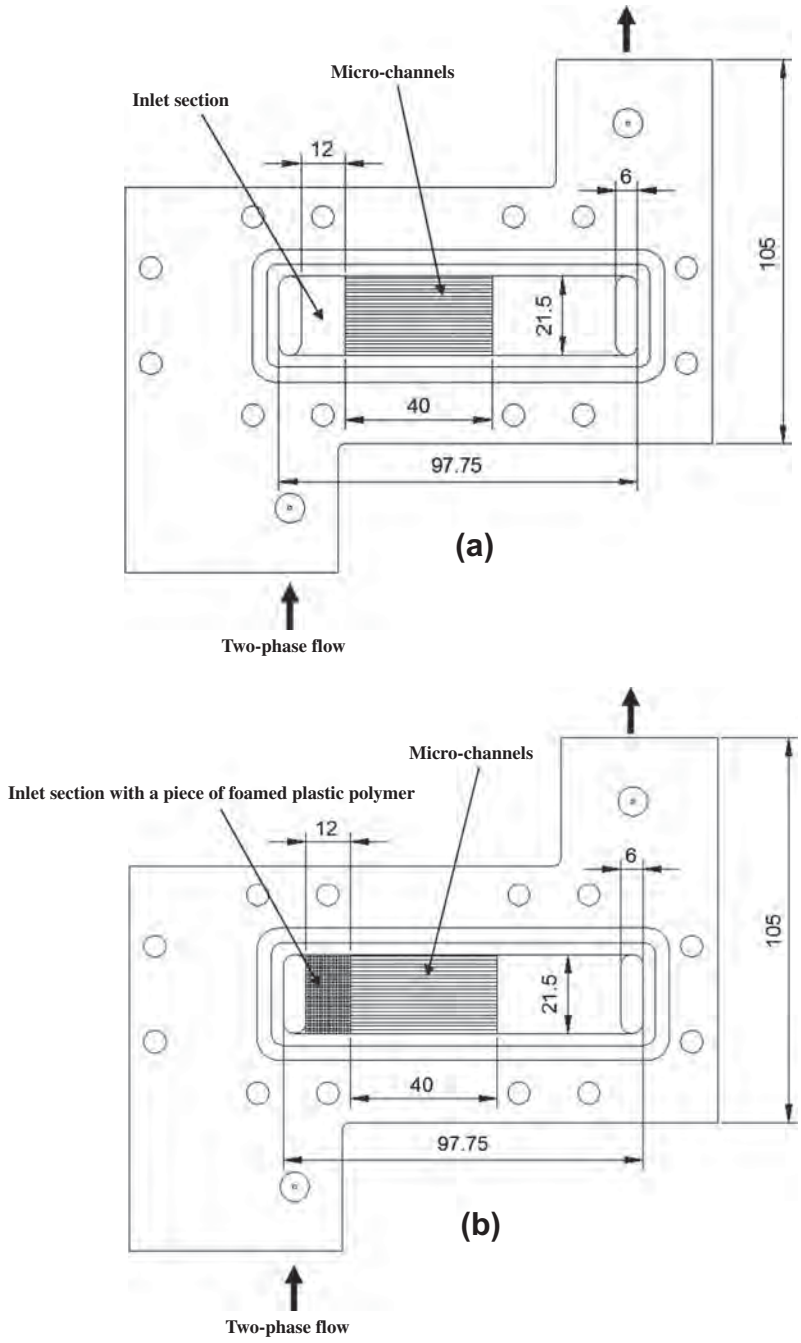

Fig. 3. Schematic diagram of test sections with different inlet sections. (a) Inlet section without a piece of foamed plastic polymer, and (b) inlet section with a piece of foamed plastic polymer.

was improved by using a special fitting, acting as distributor, which was installed inside the header.

Thus, the available results for non-boiling gas–liquid flow in micro-channels are not conclusive. Furthermore, important information associated with flow pattern and heat transfer data is still lacking. Consequently, the aim of this work is to explore heat transfer results for different gas–liquid flow patterns in horizontal micro-channels, an area needed to be clarified. In this paper, the flow pattern behaviors obtained from flow visualization and the heat transfer results are discussed.

Table 1
Experimental uncertainty.

Parameter	Uncertainty
Channel dimensions	±0.01 (mm)
Liquid superficial velocity	±3.3%
Gas superficial velocity	±5.2–10.5%
Heat transfer coefficient	±3.0–6.9%

2. Experimental apparatus and procedure

A schematic diagram of the experimental apparatus is shown in Fig. 1. A peristaltic pump with adjustable flow rate was used to supply liquid flow through the test section. The liquid mass flow rates were determined by using an electronic balance

(320 ± 0.001 g) to measure weight of the liquid flowing from the test section outlet over a sufficient time, whereas the flow rates of gases were measured by three sets of rotameters within the range of 5–50, 50–500, and 200–2500 cm^3/min, respectively. An air–water y-shaped mixer served to introduce fluids smoothly along the test section. Thermocouples and pressure transducers were installed at various positions to monitor the flow condition of the working fluids.

Fig. 2 illustrates an exploded view of the test section. The 21 parallel rectangular micro-channels of 0.45×0.41 mm (width $\times$ depth) with a 0.54 mm wall thickness between each channel were fabricated on the copper block in which a cartridge heater with adjustable input power was installed. The length of the micro-channels was 40 mm. On the top of the test section, the cover plate made of polycarbonate was placed to allow optical access for flow visualization. The copper block was well insulated by G10 epoxy. Metal plates and the insulators were bolted together with the copper block and the cover plate to firm up the assembly.

The cover plate, which is transparent, served as a viewing window for flow visualization. The detailed formation of flow pattern was registered by precise Stereozoom microscope mounted together with a camera having shutter speeds of 1/15–1/10,000 s. An adjustable LED light source was placed perpendicular to the viewing section.

A set of 14 K-type thermocouples was embedded in the copper block. For each side of the test section presented in Fig. 2, there were seven thermocouples inserted at equal distances of 16 mm along the channel length and 4.3 mm along the direction perpendicular to the channel length. These temperature measurements were done to determine surface temperatures at six positions using linear extrapolation. The arithmetic mean of these surface temperatures was used to calculate the average heat transfer coefficient. In addition, T-type thermocouples were installed at the inlet and outlet of the test section to measure the fluid temperature. All thermocouples and relevant instruments installed in the experimental apparatus were well calibrated.

To explore different flow phenomena in micro-channels, different inlet sections were used in the experiments, as shown in Fig. 3. The inlet section, presented in Fig. 3a, led the gas–liquid mixture directly to the micro-channels. For the other, as illustrated in Fig. 3b, the mixture was led to flow through a piece of foamed plastic polymer, a porous material, and subsequently entered the micro-channels.

In this work, the experiments for each inlet section were conducted so the air flow rate increased by small increments while the water flow rate was constant at the desired value. To keep the flow from boiling conditions, the heat load of 80 W was provided by a DC power supply during the experiments. The system was allowed to approach a steady state before the flow pattern and relevant data are recorded. The uncertainties associated with different parameters are given in Table 1.

3. Data reduction

Due to the cover plate, which was made of polycarbonate, an adiabatic fin tip was assumed to obtain the wall heat flux, q_w, calculated based on the effective area, given by

$$q_w = \frac{q_b(W_{ch} + W_f)}{(W_{ch} + 2\eta H_f)} \quad (1)$$

where W_{ch}, W_f, H_f and η represent, respectively, channel width, fin thickness, channel depth and fin efficiency. q_b, which is the heat flux from the heater to the working fluid, was obtained from a steady-flow thermal energy equation with no changes in latent energy.

The average heat transfer coefficient is given by

$$h = \frac{q_w}{T_w - T_f} \quad (2)$$

where T_f is fluid temperature and T_w denotes the average wall surface temperature (at prime surface).

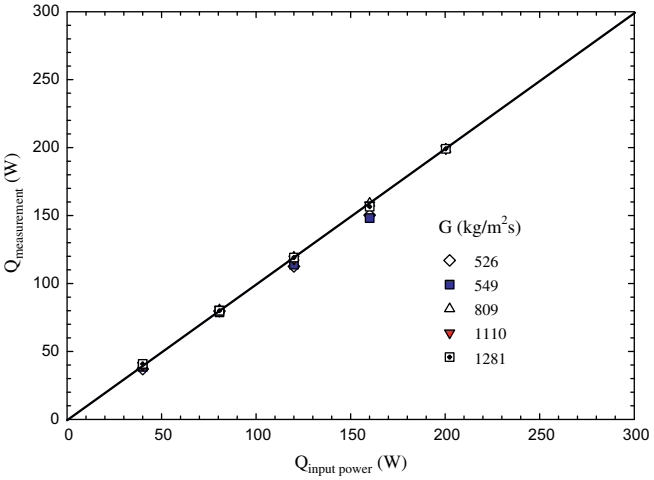

Fig. 4. Energy balance applied on the test section.

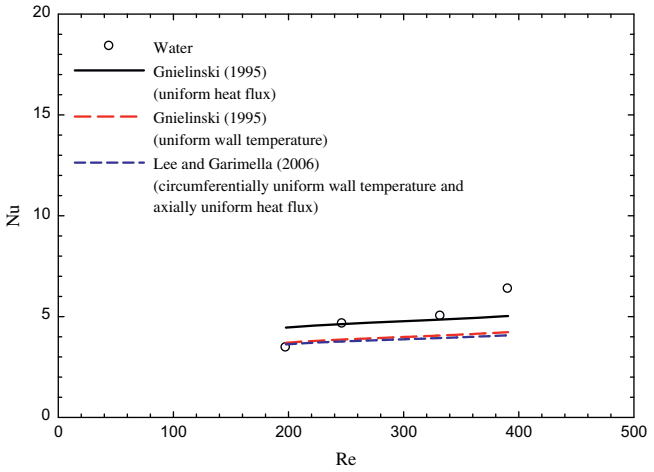

Fig. 5. Theoretical and measured values of Nusselt numbers for single-phase flow versus Reynolds numbers.

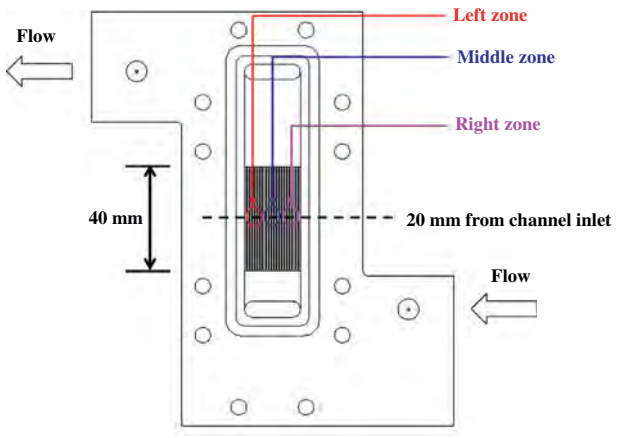

Fig. 6. Locations for flow visualization.

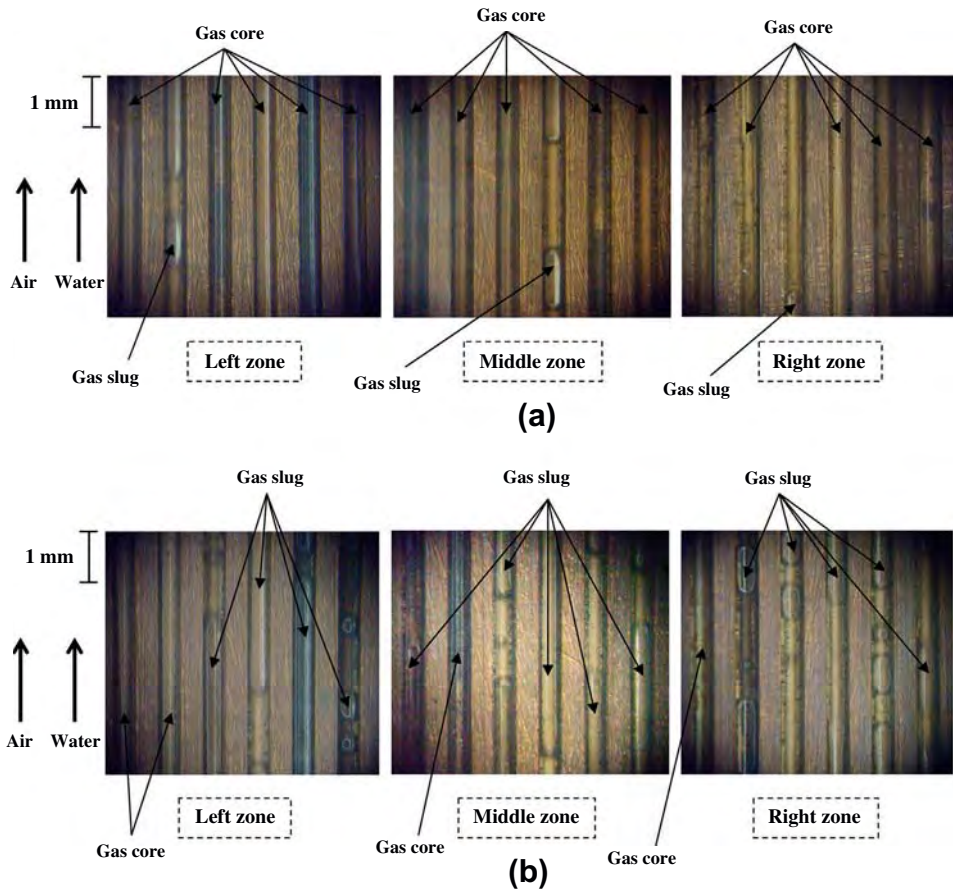

Fig. 7. Flow patterns for different inlet sections (Re_{GS} = 50, Re_{LS} = 132). (a) Inlet section without a piece of foamed plastic polymer, and (b) inlet section with a piece of foamed plastic polymer.

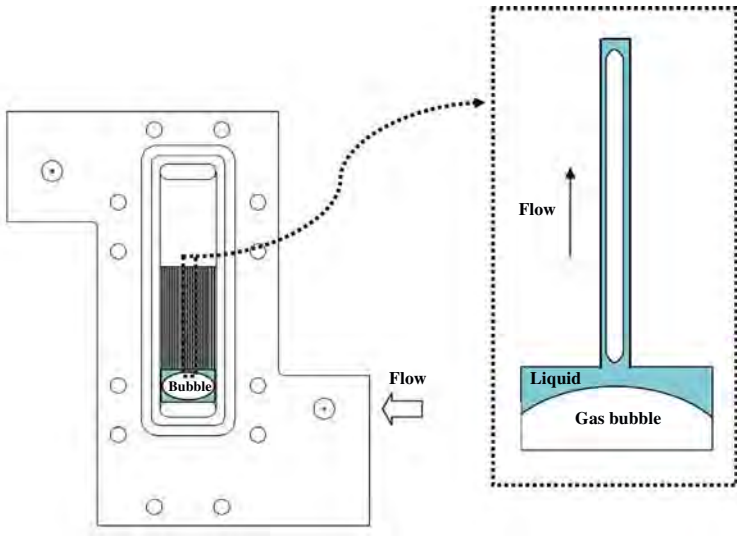

Fig. 8. Schematic diagram of gas core flow formation in micro-channels.

For one dimensional heat conduction with adiabatic fin tip, the fin efficiency is expressed by

$$\eta = \frac{\tanh(mH_f)}{mH_f} \tag{3}$$

where m is defined as

$$m^2 = \frac{hP}{kA_c} \tag{4}$$

In Eq. (4), P stands for fin perimeter, k for thermal conductivity and A_c for fin cross-sectional area.

As suggested by Park and Thome [23], an iteration process for Eqs. (1)–(4) was needed to determine the wall heat flux and heat

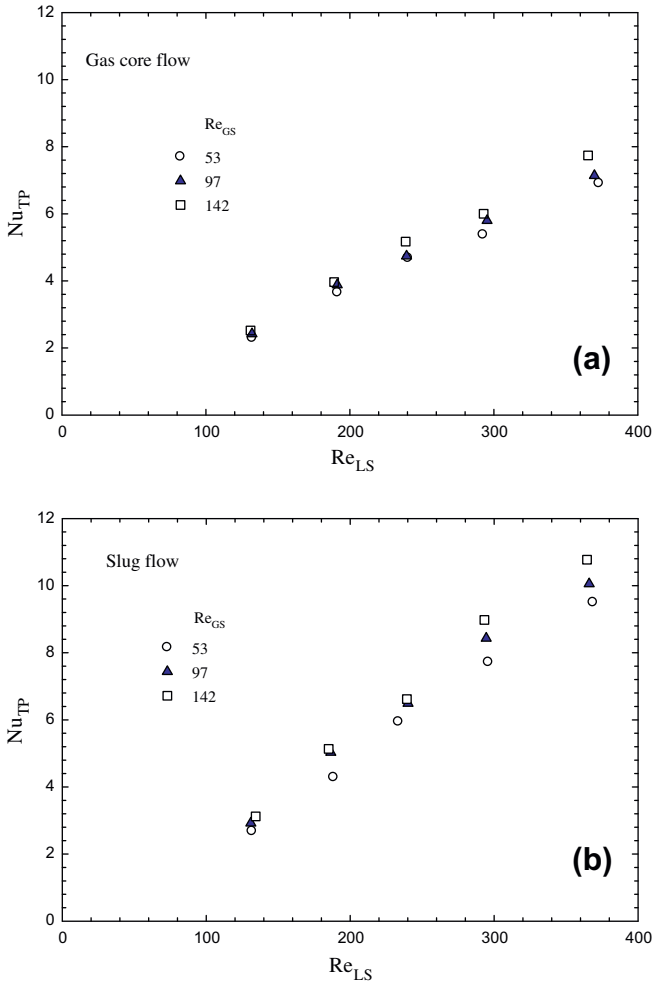

Fig. 9. Heat transfer data for different superficial Reynolds numbers.

transfer coefficient. The process was carried out until the fin efficiency converged to a fixed value.

4. Results and discussion

These single-phase flow experiments were the first to be conducted to check the validity of the experimental system. The energy balance of the test section is illustrated in Fig. 4, indicating the test section, which was well insulated. The single-phase Nusselt numbers were also compared with the prediction methods of Gnielinski [24] and Lee and Garimella [25], which were applied for laminar developing flow. The comparisons presented in Fig. 5 indicate that the experimental results tended to agree fairly with the predictions, corresponding to a uniform heat flux boundary condition.

The following sections present the two-phase flow results, including flow pattern and heat transfer.

4.1. Flow pattern results

A Stereozoom microscope and camera system were employed to conduct flow visualization, carried out at a distance of 20 mm from the channel inlet. Based on this distance, the images were recorded at three different zones: left zone, middle zone, and right zone. Fig. 6 illustrates the locations at which the images were captured.

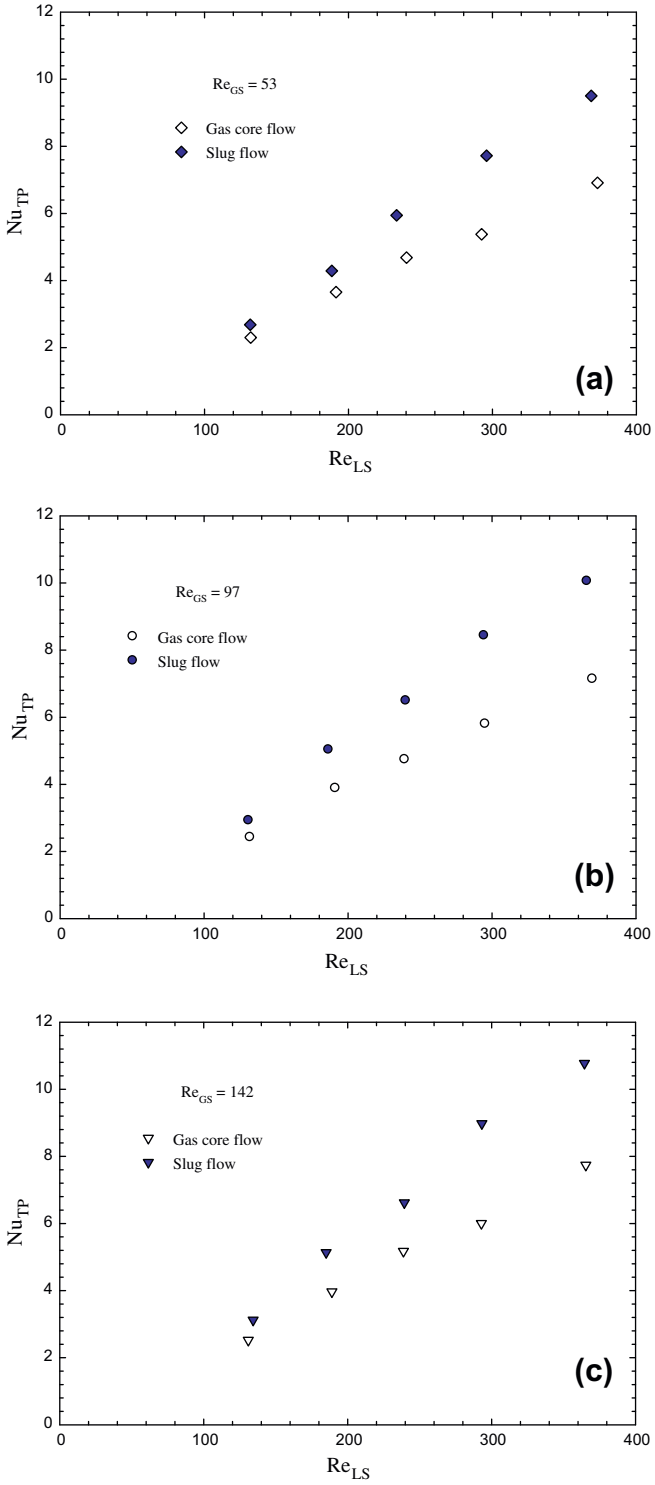

Fig. 10. Effect of flow pattern on gas–liquid heat transfer.

For two-phase flow, Reynolds numbers for gas and liquid phases can be defined respectively by gas superficial Reynolds number, Re_{GS}, and liquid superficial Reynolds number, Re_{LS}, which are expressed by the following equations.

$$Re_{LS} = \frac{\rho_L j_{LS} D_h}{\mu_L} \tag{5}$$

$$Re_{GS} = \frac{\rho_G j_{GS} D_h}{\mu_G} \tag{6}$$

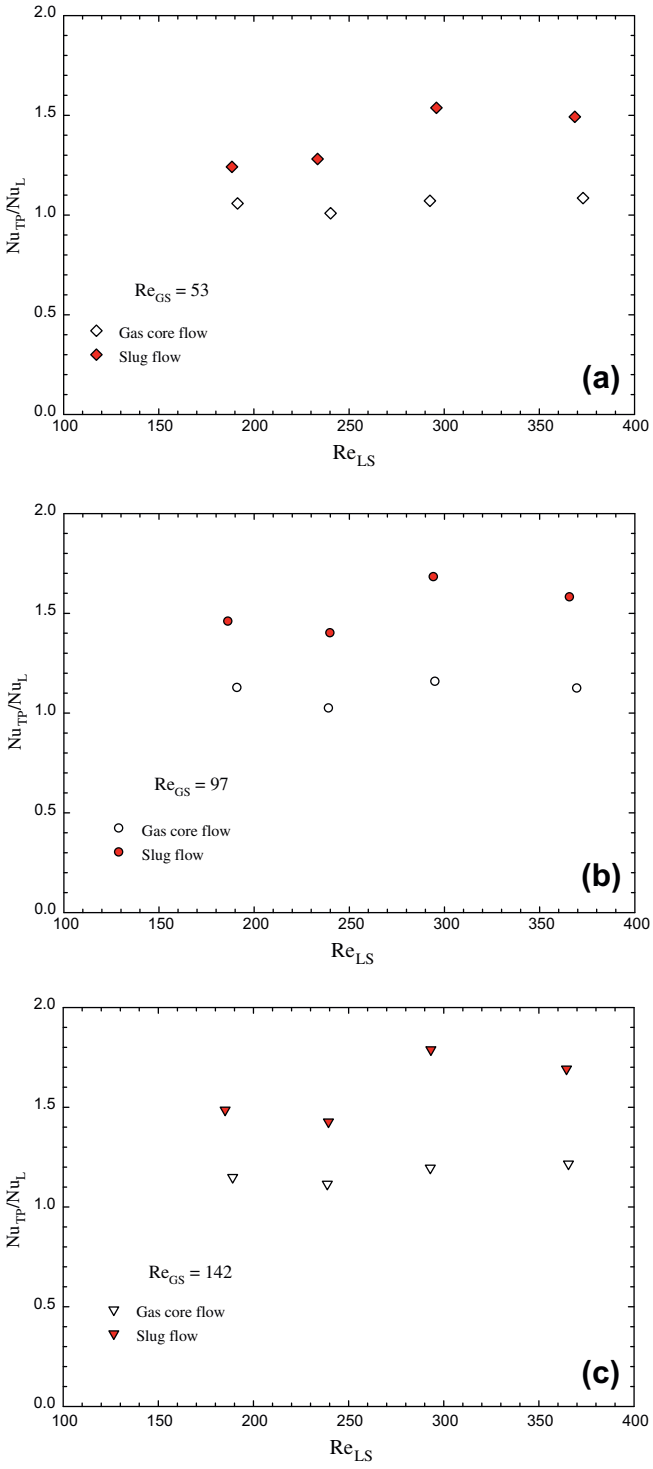

Fig. 11. Heat transfer enhancement ratio for different flow patterns.

From Eqs. (5) and (6), D_h is channel hydraulic diameter, j_{LS} and j_{GS} are liquid and gas superficial velocities, respectively, ρ_L and ρ_G are liquid and gas densities, respectively, and μ_L and μ_G are liquid and gas viscosities, respectively.

The flow visualization indicated that flow behaviors under the present conditions (superficial Reynolds numbers of gas and liquid ranging between 54–142 and 131–373, respectively) can be significantly affected by the change in inlet section. The flow pattern identification was mostly observed under a given flow condition. Fig. 7 shows flow patterns at different locations.

Slug flow, characterized by elongated bubbles flowing in the axial direction, and gas core flow, which is defined as long gas slug occupied over a length of channel, were observed. As shown in Fig. 7a, for the inlet section which led the gas–liquid mixture directly to the micro-channels, large gas bubbles in the chamber could expand along the channel length, leading to gas core flow in most channels. The formation of gas core flow is schematically depicted in Fig. 8. Comparatively, almost all the channels could be occupied by slug flow, as seen in Fig. 7b, when a piece of foamed plastic polymer inserted in the inlet section was used to induce the discrete bubbles before entering the channels.

In this work, the flow pattern results were taken simultaneously with the heat transfer data. Flow patterns were expected to affect the heat transfer phenomena. Different flow patterns may give differences in heat transfer mechanisms during gas–liquid flow. The effect of flow pattern on heat transfer characteristics is discussed next.

4.2. Heat transfer results

The average Nusselt numbers were plotted against superficial Reynolds numbers, as presented in Figs. 9 and 10. As seen in Fig. 9, the results, as expected, showed monotonous increases of the Nusselt numbers with the liquid superficial Reynolds numbers. As also shown in the figure, the Nusselt number increases with increasing the gas superficial Reynolds number. Hetsroni et al. [19] studied heat transfer characteristics in the channels of 0.1 mm in size and reported that an increase in gas superficial Reynolds number involved a decrease in heat transfer, which was opposite to the present results corresponding to micro-channels of 0.4 mm in size. The behavior observed by Hetsroni et al. [19] may be mainly due to, as suggested by Chung and Kawaji [2], significant effects of surface tension as well as liquid viscosity, which prohibit agitation of the gas–liquid interface in very small channels. Such different observations were also reported by Choo and Kim [21]. Based on their work, the heat transfer results for the channels with diameters of 0.14 mm and 0.22 mm revealed the trend similar to that of Hetsroni et al. [19]. On the other hand, for the 0.33 mm and 0.5 mm channels, Choo and Kim [21] reported the Nusselt number increasing with increasing the air flow rate.

The effect of flow pattern on gas–liquid heat transfer is shown in Fig. 10. The Nusselt number was higher for slug flow (Fig. 7b) than for gas core flow (Fig. 7a). This result indicates that the installation of a piece of foamed plastic polymer can improve the distribution of phases in micro-channels. As shown in Fig. 10, the Nusselt number can be enhanced up to 40% at high flow rates. The improvement of heat transfer may be mainly attributed to the small gas slugs contributing to agitation in the liquid film on the wall.

There have been several factors influencing the two-phase flow maldistribution in parallel channels. The relevant factors were recently given in details by Dario et al. [26].

Interestingly, the results based on micro-scale flow boiling involving complex mechanisms, reported by Ong and Thome [27] and Saisorn et al. [6], indicated that slug flow appeared with low heat transfer coefficient in comparison to the vapor core flow.

Fig. 11 illustrates heat transfer enhancement ratio for the present flow conditions. For slug flow, a heat transfer enhancement up to 80% was obtained over the single-phase flow.

5. Conclusions

Heat transfer and fluid flow characteristics of non-boiling gas–liquid flow in horizontal micro-channels were carried out in this work. For a constant heat load with a range of superficial

Reynolds numbers (Re_{GS} = 54–142 and Re_{LS} = 131–373), the experiments were performed in parallel rectangular micro-channels to obtain flow pattern and heat transfer data. The conclusions from this study can be drawn as follows.

1. Slug flow can result in higher heat transfer enhancement in comparison to gas core flow.
2. The Nusselt number increases with the increase in superficial Reynolds numbers.
3. Two-phase gas–liquid flow yields heat transfer enhancement up to 80% when compared with the single-phase liquid flow.

Acknowledgements

The authors would like to express their appreciation to the Thailand Research Fund, the National Science and Technology Development Agency, the National Research University Project and KMITL Research Fund for providing financial support for this study.

References

[1] A. Serizawa, Z. Feng, Z. Kawara, Two-phase flow in micro-channels, Exp. Therm. Fluid Sci. 26 (2002) 703–714.
[2] P.M.-Y. Chung, M. Kawaji, The effect of channel diameter on adiabatic two-phase flow characteristics in microchannels, Int. J. Multiphase Flow 30 (2004) 735–761.
[3] S.G. Kandlikar, Scale effects on flow boiling heat transfer in microchannels: a fundamental perspective, Int. J. Therm. Sci. 49 (2010) 1073–1085.
[4] C.L. Ong, J.R. Thome, Macro-to-microchannel transition in two-phase flow: part 1-two-phase flow patterns and film thickness measurements, Exp. Therm. Fluid Sci. 35 (2011) 37–47.
[5] J.-T. Oh, A.S. Pamitran, K.-I. Choi, P. Hrnjak, Experimental investigation on two-phase flow boiling heat transfer of five refrigerants in horizontal small tubes of 0.5, 1.5 and 3.0 mm inner diameters, Int. J. Heat Mass Transfer 54 (2011) 2080–2088.
[6] S. Saisorn, J. Kaew-On, S. Wongwises, An experimental investigation of flow boiling heat transfer of R-134a in horizontal and vertical mini-channels, Exp. Therm. Fluid Sci. 46 (2013) 232–244.
[7] H. Ide, M. Kawaji, Effect of tube diameters on the flow phenomena of gas-liquid two-phase flow in microchannels, in: ASME 2013 11th International Conference on Nanochannels, Microchannels, and Minichannels (ICNMM2013), Sapporo, Japan, June 16–19, 2013.
[8] I. Mudawar, Two-phase microchannel heat sinks: theory, applications and limitations, J. Electron. Packag. 133 (2011) 1–31.
[9] L. Tadrist, Review on two-phase flow instabilities in narrow spaces, Int. J. Heat Fluid Flow 28 (2007) 54–62.
[10] A.A. Arcanjo, C.B. Tibirica, G. Ribatski, Evaluation of flow patterns and elongated bubble characteristics during the flow boiling of halocarbon refrigerants in a micro-scale channel, Exp. Therm. Fluid Sci. 34 (2010) 766–775.
[11] C.B. Tibirica, G. Ribatski, Flow boiling heat transfer of R134a and R245fa in a 2.3 mm tube, Int. J. Heat Mass Transfer 53 (2010) 2459–2468.
[12] C.L. Ong, J.R. Thome, Macro-to-microchannel transition in two-phase flow: part 2 – flow boiling heat transfer and critical heat flux, Exp. Therm. Fluid Sci. 35 (2011) 873–886.
[13] G. Ribatski, A critical overview on the recent literature concerning flow boiling and two-phase flows inside micro-scale channels, Exp. Heat Transfer 26 (2013) 198–246.
[14] C.B. Tibirica, G. Ribatski, Flow boiling in micro-scale channels – synthesized literature review, Int. J. Refrigeration 36 (2013) 301–324.
[15] Z.Y. Bao, D.F. Fletcher, B.S. Haynes, An experimental study of gas–liquid flow in a narrow conduit, Int. J. Heat Mass Transfer 43 (2000) 2313–2324.
[16] G. Hetsroni, A. Mosyak, Z. Segal, E. Pogrebnyak, Two-phase flow patterns in parallel micro-channels, Int. J. Multiphase Flow 29 (2003) 341–360.
[17] K.A. Triplett, S.M. Ghiaasiaan, S.I. Abdel-Khalik, D.L. Sadowski, Gas–liquid two-phase flow in microchannels part I: two-phase flow patterns, Int. J. Multiphase Flow 25 (1999) 377–394.
[18] K.A. Triplett, S.M. Ghiaasiaan, S.I. Abdel-Khalik, A. LeMouel, B.N. McCord, Gas–liquid two-phase flow in microchannels part II: void fraction and pressure drop, Int. J. Multiphase Flow 25 (1999) 395–410.
[19] G. Hetsroni, A. Mosyak, E. Pogrebnyak, Z. Segal, Heat transfer of gas–liquid mixture in micro-channel heat sink, Int. J. Heat Mass Transfer 52 (2009) 3963–3971.
[20] A.R. Betz, D. Attinger, Can segmented flow enhance heat transfer in microchannel heat sinks?, Int J. Heat Mass Transfer 53 (2010) 3683–3691.
[21] K. Choo, S.J. Kim, Heat transfer and fluid flow characteristics of nonboiling two-phase flow in microchannels, J. Heat Transfer 133 (2011) 1–7.
[22] A. Marchitto, M. Fossa, G. Guglielmini, The effect of the flow direction inside the header on two-phase flow distribution in parallel vertical channels, Appl. Therm. Eng. 36 (2012) 245–251.
[23] J.E. Park, J.R. Thome, Critical heat flux in multi-microchannel copper elements with low pressure refrigerants, Int. J. Heat Mass Transfer 53 (2010) 110–122.
[24] V. Gnielinski, Ein neues berechnungsverfahren fur die warmeubertragung im ubergangsbereich zwischen laminaren und turbulenter rohstromung, Forsch. Ingenieurwesen – Eng. Res. 61 (1995) 240–248.
[25] P.-S. Lee, S.V. Garimella, Thermally developing flow and heat transfer in rectangular microchannels of different aspect ratios, Int. J. Heat Mass Transfer 49 (2006) 3060–3067.
[26] E.R. Dario, L. Tadrist, J.C. Passos, Review on two-phase flow distribution in parallel channels with macro and micro hydraulic diameters: main results, analyses, trends, Appl. Therm. Eng. 59 (2013) 316–335.
[27] C.L. Ong, J.R. Thome, Flow boiling heat transfer of R134a, R236fa and R245fa in a horizontal 1.030 mm circular channel, Exp. Therm. Fluid Sci. 33 (2009) 651–663.

Springer

Dear Author,

Here are the proofs of your article.

- You can submit your corrections **online**, via **e-mail** or by **fax**.
- For **online** submission please insert your corrections in the online correction form. Always indicate the line number to which the correction refers.
- You can also insert your corrections in the proof PDF and **email** the annotated PDF.
- For fax submission, please ensure that your corrections are clearly legible. Use a fine black pen and write the correction in the margin, not too close to the edge of the page.
- Remember to note the **journal title**, **article number**, and **your name** when sending your response via e-mail or fax.
- **Check** the metadata sheet to make sure that the header information, especially author names and the corresponding affiliations are correctly shown.
- **Check** the questions that may have arisen during copy editing and insert your answers/ corrections.
- **Check** that the text is complete and that all figures, tables and their legends are included. Also check the accuracy of special characters, equations, and electronic supplementary material if applicable. If necessary refer to the *Edited manuscript*.
- The publication of inaccurate data such as dosages and units can have serious consequences. Please take particular care that all such details are correct.
- Please **do not** make changes that involve only matters of style. We have generally introduced forms that follow the journal's style.
  Substantial changes in content, e.g., new results, corrected values, title and authorship are not allowed without the approval of the responsible editor. In such a case, please contact the Editorial Office and return his/her consent together with the proof.
- If we do not receive your corrections **within 48 hours**, we will send you a reminder.
- Your article will be published **Online First** approximately one week after receipt of your corrected proofs. This is the **official first publication** citable with the DOI. **Further changes are, therefore, not possible.**
- The **printed version** will follow in a forthcoming issue.

Please note

After online publication, subscribers (personal/institutional) to this journal will have access to the complete article via the DOI using the URL: http://dx.doi.org/[DOI].
If you would like to know when your article has been published online, take advantage of our free alert service. For registration and further information go to: http://www.link.springer.com.

Due to the electronic nature of the procedure, the manuscript and the original figures will only be returned to you on special request. When you return your corrections, please inform us if you would like to have these documents returned.

Metadata of the article that will be visualized in OnlineFirst

Please note: Images will appear in color online but will be printed in black and white.

ArticleTitle	Thermal conductivity of Al_2O_3/water nanofluids: measurement, correlation, sensitivity analysis, and comparisons with literature reports	
Article Sub-Title		
Article CopyRight	Akadémiai Kiadó, Budapest, Hungary (This will be the copyright line in the final PDF)	
Journal Name	Journal of Thermal Analysis and Calorimetry	
Corresponding Author	Family Name	**Esfe**
	Particle	
	Given Name	**Mohammad Hemmat**
	Suffix	
	Division	Faculty of Mechanical Engineering
	Organization	Semnan University
	Address	Semnan, Iran
	Email	m.hemmatesfe@gmail.com
Corresponding Author	Family Name	**Mahian**
	Particle	
	Given Name	**Omid**
	Suffix	
	Division	Young Researchers and Elite Club, Mashhad Branch
	Organization	Islamic Azad University
	Address	Mashhad, Iran
	Email	omid.mahian@gmail.com
Author	Family Name	**Saedodin**
	Particle	
	Given Name	**Seyfolah**
	Suffix	
	Division	Faculty of Mechanical Engineering
	Organization	Semnan University
	Address	Semnan, Iran
	Email	
Author	Family Name	**Wongwises**
	Particle	
	Given Name	**Somchai**
	Suffix	
	Division	Fluid Mechanics, Thermal Engineering and Multiphase Flow Research Lab. (FUTURE), Department of Mechanical Engineering, Faculty of Engineering
	Organization	King Mongkut's University of Technology Thonburi
	Address	Bangmod, 10140, Bangkok, Thailand
	Email	

Schedule	Received	22 October 2013

Revised

Accepted 15 March 2014

Abstract

A considerable number of studies can be found on the thermal conductivity of nanofluids in which Al_2O_3 nanoparticles are used as additives. In the present study, the aim is to measure the thermal conductivity of very narrow Al_2O_3 nanoparticles with the size of 5 nm suspended in water. The thermal conductivity of nanofluids with concentrations up to 5 % is measured in a temperature range between 26 and 55 °C. Using the experimental data, a correlation is presented as a function of the temperature and volume fraction of nanoparticles. Finally, a sensitivity analysis is performed to assess the sensitivity of thermal conductivity of nanofluids to increase the particle loading at different temperatures. The sensitivity analysis reveals that at a given concentration, the sensitivity of thermal conductivity to particle loading increases when the temperature increases.

Keywords (separated by '-') Thermal conductivity - Nanofluid - Correlation - Sensitivity analysis

Footnote Information

J Therm Anal Calorim
DOI 10.1007/s10973-014-3771-x

Thermal conductivity of Al_2O_3/water nanofluids: measurement, correlation, sensitivity analysis, and comparisons with literature reports

Mohammad Hemmat Esfe · Seyfolah Saedodin · Omid Mahian · Somchai Wongwises

Received: 22 October 2013 / Accepted: 15 March 2014
© Akadémiai Kiadó, Budapest, Hungary 2014

Abstract A considerable number of studies can be found on the thermal conductivity of nanofluids in which Al_2O_3 nanoparticles are used as additives. In the present study, the aim is to measure the thermal conductivity of very narrow Al_2O_3 nanoparticles with the size of 5 nm suspended in water. The thermal conductivity of nanofluids with concentrations up to 5 % is measured in a temperature range between 26 and 55 °C. Using the experimental data, a correlation is presented as a function of the temperature and volume fraction of nanoparticles. Finally, a sensitivity analysis is performed to assess the sensitivity of thermal conductivity of nanofluids to increase the particle loading at different temperatures. The sensitivity analysis reveals that at a given concentration, the sensitivity of thermal conductivity to particle loading increases when the temperature increases.

Keywords Thermal conductivity · Nanofluid · Correlation · Sensitivity analysis

M. H. Esfe (✉) · S. Saedodin
Faculty of Mechanical Engineering, Semnan University, Semnan, Iran
e-mail: m.hemmatesfe@gmail.com

O. Mahian (✉)
Young Researchers and Elite Club, Mashhad Branch, Islamic Azad University, Mashhad, Iran
e-mail: omid.mahian@gmail.com

S. Wongwises
Fluid Mechanics, Thermal Engineering and Multiphase Flow Research Lab. (FUTURE), Department of Mechanical Engineering, Faculty of Engineering, King Mongkut's University of Technology Thonburi, Bangmod, Bangkok 10140, Thailand

Introduction

In 1995, Choi [1] called the mixture of very fine particles suspended in common liquids a "Nanofluid." From that time until now, many researchers worldwide have paid attention to this new field of thermal and fluid sciences. The applications of nanofluids have been established in many branches of thermal engineering, such as solar energy, nuclear reactors, medical applications, automobiles, electronic equipment, and so on [2, 3]. The replacement of common heat transfer fluids with nanofluids is reasonable because the thermal conductivity of nanofluids containing solid nanoparticles is higher than that of the usual fluids. As a result, using a fluid with a higher thermal conductivity enhances the heat transfer rate and, consequently, results in a more compact system. Therefore, the measurement of the thermal conductivity of nanofluids and knowing the factors (e.g., temperature, size of particles, etc.) that affect its magnitude are important issues. Based on the literature, aluminum oxide (Al_2O_3) nanoparticles are one of the most common particles that are used to prepare the nanofluids.

In the following, a literature review of the studies on the thermal conductivity of nanofluids containing Al_2O_3 nanoparticles has been conducted. Wang et al. [4] provided Al_2O_3/water and Al_2O_3/ethylene glycol nanofluids in which the particle size was 28 nm. Using the steady-state parallel plates method, the thermal conductivity of nanofluid samples was measured. The thermal conductivity enhancements were approximately 16 % and 24 % for 5.5 % of particle loading in water and 5 % of particle loading in ethylene glycol, respectively.

Das et al. [5] measured the thermal conductivity of Al_2O_3/water nanofluids using the temperature oscillation method at a temperature range between 21 and 51 °C,

Author Proof
UNCORRECTED PROOF

Journal : Large 10973 | Dispatch : 26-3-2014 | Pages : 7
Article No. : 3771 | ☐ LE | ☐ TYPESET
MS Code : JTAC-D-13-01090 | ✔ CP | ✔ DISK

Author Proof

where the volume fractions of particles do not exceed 4 %. The nanoparticle's size in the study was about 38 nm. Their results indicated that with the increase of the temperature and concentration of nanofluids, the effective thermal conductivity increases. For the 4 % volume fraction of nanoparticles and the temperature of 51 °C, the thermal conductivity enhancement was about 24.3 %, as compared to pure water. Putra et al. [6] studied the thermal conductivity of Al_2O_3 nanoparticles with an average size of 131 nm dispersed in water. The steady-state parallel plates approach was utilized to measure the thermal conductivity. The thermal conductivity enhancement was equal to 24 %, for the concentration of 4 %. Masuda et al. [7] investigated the thermal conductivity of Al_2O_3 nanoparticles with the diameter of 13 nm suspended in pure water using the transient hot wire technique. They perceived that the particle loading up to 4.4 % leads to increasing the effective thermal conductivity by 33 %. Lee et al. [8] provided two types of nanofluids containing Al_2O_3 nanoparticles with a diameter of 38.4 nm. These two types are Al_2O_3/water and Al_2O_3/ethylene glycol nanofluids and their thermal conductivities were measured by the transient hot wire procedure. They found that the thermal conductivity of water-based nanofluids increases by 11 % for the 4.3 % volume fraction, while for ethylene glycol-based nanofluids the maximum enhancement of thermal conductivity was 19 % at the concentration of 5 %. Chon et al. [9] examined the thermal conductivity of Al_2O_3/water nanofluids by the transient hot wire method where the temperature changes from 21 to 71 °C and the particle sizes of 11 nm, 47 nm, and 150 nm. They concluded that increasing the particle size results in the decrease of the thermal conductivity enhancement. Also, for the 4 % concentration, a temperature of 71 °C, and a particle size of 47 nm, the enhancement magnitude was 28 %. Li and Peterson [10] studied the effect of the particle size of Al_2O_3 nanoparticles dispersed in water on the thermal conductivity enhancement by the steady-state parallel plates method. They pointed out that for the 6 % volume fraction of nanoparticles, when the size of particles increases from 36 nm to 47 nm, the thermal conductivity enhancement decreases by about 2 % (changes from 28 % to 26 %). Zhang et al. [11] reported an increase of 15 % in the thermal conductivity of the Al_2O_3/water nanofluid with a concentration of 5 % and particle size of 20 nm. The transient hot wire approach was applied for the measurement. Timofeeva et al. [12] evaluated the thermal conductivity enhancement of Al_2O_3/water nanofluids with the maximum particle volume fraction of 5 % by utilizing the transient hot wire method. They found that the enhancements in the thermal conductivity for particle sizes of 11 nm, 20 nm, and 40 nm were 8, 7, and 10 %, respectively. Wong and Kurma [13] showed that the thermal conductivity of the Al_2O_3/water nanofluid at 46.6 °C, compared to water at room temperature, increases by 22 % where the concentration is 8.47 Vol%. The particle size in this study was 36 nm. More research on the thermal conductivity of Al_2O_3/water nanofluids has been done by Ju et al. [14]. The maximum concentration was considered 10 Vol%, where the tests were performed with three different sizes of nanoparticles including 20, 30, and 45 nm. Oh et al. [15] applied the 3ω method to measure the thermal conductivity of Al_2O_3/water and Al_2O_3/ethylene glycol nanofluids. Sommers and Yerkes [16] prepared suspensions of propanol and Al_2O_3 nanoparticles with the size of 10 nm. They indicated that the thermal conductivity changes linearly against the particle loading. Sundar and Sharma [17] measured the thermal conductivity of aqueous suspensions of Al_2O_3 nanoparticles with the size of 47 nm and volume fractions of 0.2, 0.4, and 0.8 %. Longo and Zilio [18] conducted the experiments to determine the thermal conductivity of sonicated and stirred Al_2O_3/water nanofluids with concentrations between 1 and 4 Vol% for the temperature range from 1 to 40 °C. Their results showed that the thermal conductivity enhancement is negative for temperatures close to 1 °C. Yiamsawasd et al. [19] measured the thermal conductivity of Al_2O_3 nanoparticles suspended in a mixture of water and ethylene glycol (80:20 weight ratio) for volume fractions by 8 % and temperatures between 15 and 65 °C. They reported an increase by 30 % for the thermal conductivity in the range of measurements. The size of particles in this work was 120 nm. Recently in a nice work, Barbes et al. [20] measured thermal conductivity of Al_2O_3 nanoparticles suspended in water and ethylene glycol using steady-state coaxial cylinders method.

The aim of the present work is to study of the thermal conductivity of Al_2O_3/water nanofluids at a particle volume fraction range from 0.25 to 5 % and the temperature range between 26 and 55 °C. Based on the best knowledge of the authors, the particle size used in this work is the smallest one used in the literature (i.e., 5 nm). After measuring the thermal conductivity, a model is presented for the thermal conductivity as a function of the temperature and volume fraction. Finally, a sensitivity analysis is conducted on the experimental data.

Nanofluid preparation

The first step for studying the nanofluids and their properties is the preparation of the fluid. Due to the sedimentation and agglomeration of nanoparticles in the base fluid, special methods should be utilized to create a suspension with an acceptable stability. In this work, the nanofluids at volume concentrations of 0.25, 0.5, 1.0, 2.0, 3.0, 4.0, and 5.0 % were prepared by dispersing Al_2O_3 nanoparticles in DI Water as the base fluid.

UNCORRECTED PROOF

Journal : Large 10973 | Dispatch : 26-3-2014 | Pages : 7
Article No. : 3771 | ☐ LE | ☐ TYPESET
MS Code : JTAC-D-13-01090 | ✔ CP | ✔ DISK

Table 1 Characteristics of Al_2O_3 nanoparticles

Nanoparticles (Al_2O_3) purity	99.99 %
Nanoparticles (Al_2O_3) APS	5 nm—very narrow particle size range
Nanoparticles (Al_2O_3) SSA/m^2 g^{-1}	>150
Nanoparticles (Al_2O_3) Morphology	Nearly spherical
Nanoparticles (Al_2O_3) color	White
Specific heat capacity/ J Kg^{-1} K^{-1}	880
Density/Kg m^{-3}	3,890
Bulk Density/g ml^{-1}	0.18

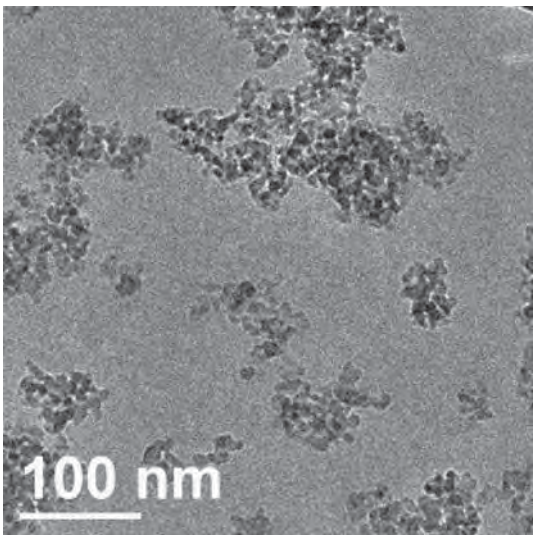

Fig. 1 Transmission electron microscopy (TEM) image of Al_2O_3 nanoparticles

A two-step method was utilized to prepare the nanofluids. The nanoparticles with a diameter of 5 nm were purchased from US Research Nanomaterial, Inc. The properties of the nanoparticles are presented in Table 1. Also, a TEM image of the particles taken from the company is displayed in Fig. 1. As shown in the TEM image, the particles are almost spherical in shape. Nanoparticles are weighed carefully for any volume concentration and then are added to the water little by little. The mixture is stirred for 30 to 45 min, and after that the suspension is inserted inside an ultrasonic vibrator (Hielschercompany, Germany) for 3 h to break down the agglomeration of particles. Using the stirrer and ultrasonic vibrator results in a more stable and uniform nanofluid. No sedimentation in the samples is observed with the naked eyes for a long time (at least 1 week).

Measurement of thermal conductivity

Thermal conductivity of Al_2O_3-water nanofluids with various concentrations and the temperature range between 26 and 55 °C was measured by a KD2 Pro instrument manufactured by Decagon Devices Inc. This instrument acts based on the transient hot wire approach; the KD2 Pro takes measurements at 1 s intervals during a 90 s measurement cycle. The accuracy of the device is ± 5 %. The experiments are repeated three times for each case and the average value is reported. A hot water bath is used to stabilize the temperature and a thermometer with accuracy of 0.1^C is used to measure the temperature.

Results and discussions

The experimental data are compared with the most well-known theoretical models including Hamilton−Crosser and Yu–Choi. One of the basic models to calculate the thermal conductivity of solid–liquid mixtures, k_{eff}, is the Hamilton–Crosser (H–C) model [21]. This model is able to predict the thermal conductivity of solid–liquid mixtures in which the thermal conductivity ratio of the solid phase to the liquid phase is larger than 100; this model is described as follows:

$$\frac{k_{eff}}{k_f} = \frac{k_p + (n-1)k_f + (n-1)\,\varphi\,(k_p - k_f)}{k_p + (n-1)k_f - \varphi(k_p - k_f)}, \quad (1)$$

where k_p, k_f, are the thermal conductivity of particles and fluid, respectively. φ is the volume fraction of nanoparticles and n is the empirical shape factor defined as

$$n = \frac{3}{\psi} \quad (2)$$

in which ψ indicates the sphericity of particles. The sphericity for cylindrical and spherical particles is 0.5 and 1, respectively. Therefore, in the present work, n is considered equal to 3 because of the spherical shape of Al_2O_3 nanoparticles.

Yu and Choi [22] is another model that is considered for the comparative purposes. The relation reads as

$$k_{eff} = \frac{k_p + 2k_f + 2(k_p - k_f)(1+\beta)^3\varphi}{k_p + 2k_f - 2(k_p - k_f)(1+\beta)^3\varphi}\,k_f, \quad (3)$$

where β is the ratio of the nanolayer thickness to the original particle radius; normally it is assumed to be 0.1.

Figure 2 presents a comparison between the experimental data for the dimensionless thermal conductivity (k_{eff}/k_f) and the results obtained by the H–C and Yu–Choi models. The comparison is conducted at different temperatures. As it can be observed from Fig. 2a, at a low temperature (i.e., 26 °C), the Yu–Choi model is able to predict

Author Proof
UNCORRECTED PROOF

Journal : Large 10973 Dispatch : 26-3-2014 Pages : 7
Article No. : 3771 LE TYPESET
MS Code : JTAC-D-13-01090 CP DISK

Author Proof

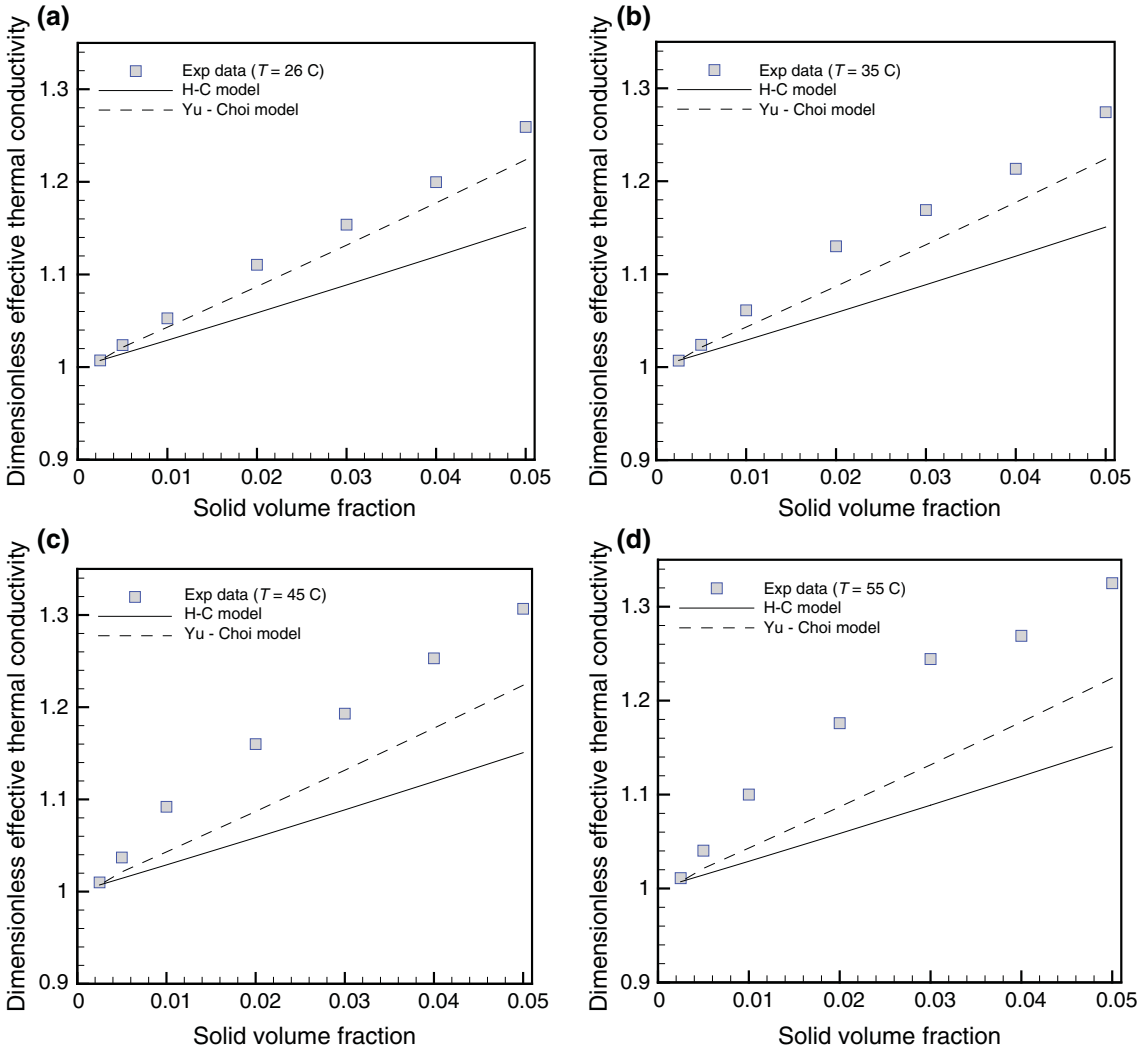

Fig. 2 Comparison between the measured data and the theoretical models

the experimental data. By increasing the temperature, the difference between the measured data and the results of Yu–Choi model increases considerably. Looking at Fig. 2d reveals that the Yu–Choi model underestimates the measured data by about 10 %. Therefore, it is found that the temperature is a significant factor that should be involved in the models that are presented to predict the thermal conductivity.

Figure 3 shows the thermal conductivity enhancement against the solid volume fraction at different temperatures. It is found that the thermal conductivity of nanofluid with the volume concentration of 5 % is enhanced compared to the base fluid (pure water) from 25 % to 32 %, depending on the temperature. A higher temperature results in a bigger enhancement.

Figure 4 is plotted to show the variations of dimensionless thermal conductivity with temperature at different volume fractions. It is seen that for low concentrations of nanofluids (less than 1 %), there is no visible change in the dimensionless thermal conductivity with temperature. Collision between the solid particles is a main factor which determines the thermal conductivity of a nanofluid. By increasing the number of collisions, the internal energy of particles, and hence the effective thermal conductivity of the nanofluid increases. At low concentrations, the number of particles in a given volume of nanofluid is less than at higher concentrations. Consequently, the space between the solid molecules is bigger at low concentrations; this reduces the probability and number of collisions between the particles due to heating. Table 2 provides the values of dimensionless thermal conductivity at different temperatures and concentrations.

Now, the present data are compared with the results of some experimental works on the Al_2O_3/water nanofluids [7, 8, 23–26] at room temperature, as shown in Fig. 5. The data are extracted from the review paper by Khanafer and

Journal : Large 10973 Dispatch : 26-3-2014 Pages : 7
Article No. : 3771 LE TYPESET
MS Code : JTAC-D-13-01090 CP DISK

Author Proof

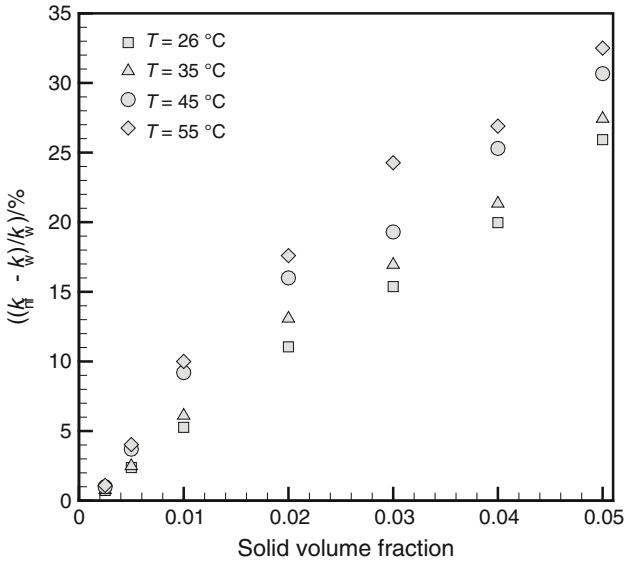

Fig. 3 Thermal conductivity enhancement against the solid volume fraction at different temperatures

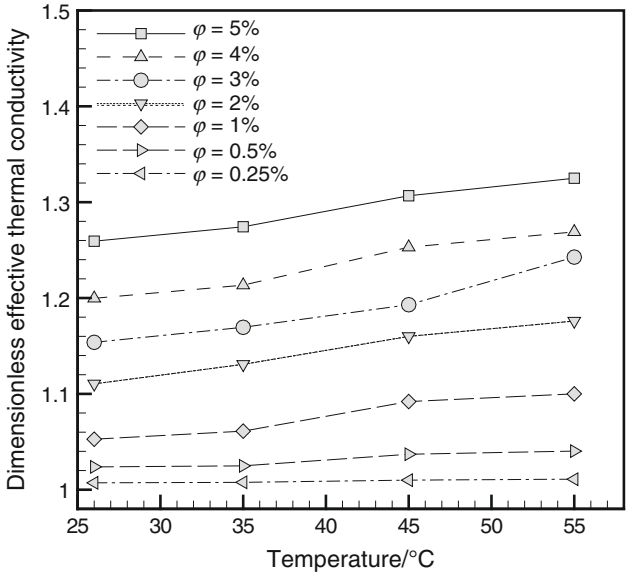

Fig. 4 Variations of dimensionless thermal conductivity with temperature at different volume fractions

Vafai [27] on the thermophysical properties of nanofluids. It is observed from the figure that the present results are very close to the results of Murshed et al. [26], although the nanoparticle size used in the present work is 5 nm and in the study of Murshed et al. [26] it is 80 nm. Also, it is seen that the difference between the present data and the data by Minsta et al. [25] is very high. Besides the difference in size, the differences in preparation method, measurement approaches, and experimental conditions should be considered in the comparisons of various works.

Table 2 Effective thermal conductivity of Al_2O_3/water nanofluids in various temperatures

Volume fraction	T = 26 °C	T = 35 °C	T = 45 °C	T = 55 °C
0.05	1.259	1.274	1.307	1.325
0.04	1.199	1.213	1.253	1.269
0.03	1.153	1.169	1.193	1.243
0.02	1.110	1.130	1.160	1.176
0.01	1.053	1.061	1.092	1.101
0.005	1.023	1.025	1.037	1.040
0.0025	1.007	1.008	1.010	1.011

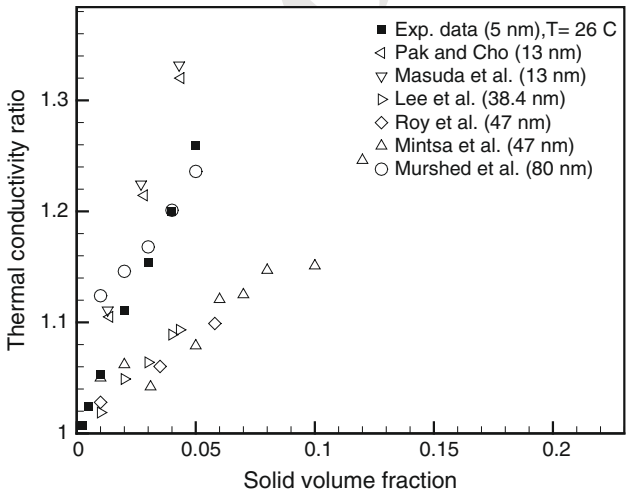

Fig. 5 Comparison between the measured data and other experimental works

Based on the experimental data, a model as a function of temperature and solid volume fraction is proposed. The model is valid for Al_2O_3/water nanofluids, $26 \leq T(^{\circ}C) \leq 55$, and $0.0025 \leq \phi \leq 0.05$. The model is presented as follows:

$$\frac{k_{nf}}{k_f} = 0.911 \times T^{\left(-0.0415-\frac{0.404}{\ln(\varphi)}\right)}. \quad (4)$$

To examine the accuracy of the presented model, the margin of deviation can be defined as follows:

$$\text{Margin of deviation } (\%) = \frac{k_c - k_m}{k_m} \times 100, \quad (5)$$

where k_c is the thermal conductivity calculated through the correlation, and k_m is the thermal conductivity measured during the tests. Figure 6 illustrates the margin of deviation at different temperatures. The margin of deviation does not exceed 2 %, which indicates the acceptable accuracy of the presented model to predict the thermal conductivity.

Journal : Large 10973 Dispatch : 26-3-2014 Pages : 7
Article No. : 3771 LE TYPESET
MS Code : JTAC-D-13-01090 CP DISK

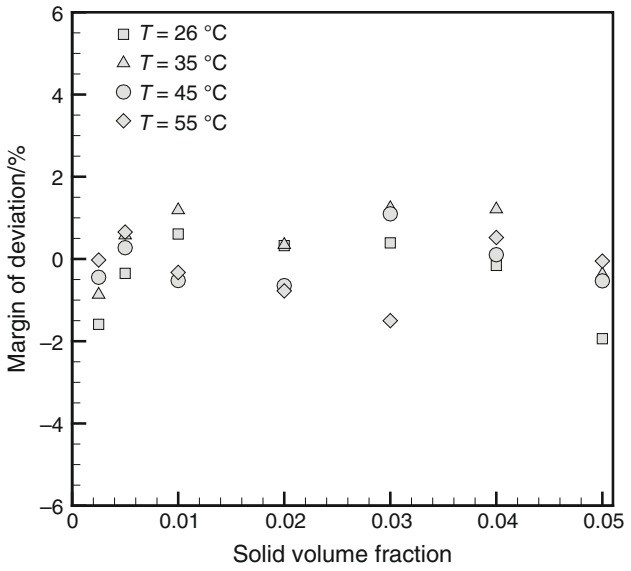

Fig. 6 Margin of deviation of the presented correlation

Finally, a sensitivity analysis is conducted based on Ref.

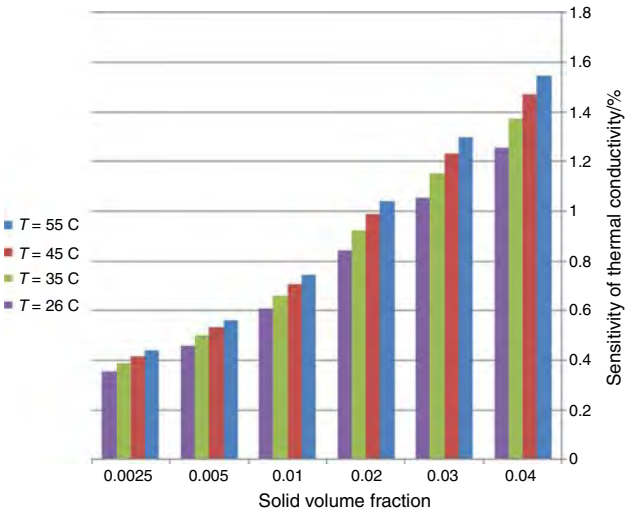

Fig. 7 Sensitivity analysis of thermal conductivity at different temperatures and concentrations

[28]. The sensitivity analysis shows how much the thermal conductivity is sensitive to the changes in particle loading at a given temperature. In the present work, the sensitivity analysis is performed by considering 10 % change in particle loading. For example, consider the volume fraction of 2 % and a temperature of 26 °C. The sensitivity in this temperature can be calculated as follows:

$$\text{Sensitivity } (\%) = \frac{k(\phi = 2.2\%) - k(\phi = 2\%)}{k(\phi = 2\%)} \times 100. \qquad (6)$$

Figure 7 provides the results of the sensitivity analysis. As it can be seen, with an increase in the temperature, the sensitivity of thermal conductivity increases. This means that at a moderate volume fraction, adding a specified amount of nanoparticles to the nanofluid at a high temperature is more effective than at low temperatures.

Conclusions

An experimental study was performed to measure the thermal conductivity of aqueous suspensions of Al_2O_3 nanoparticles with the diameter of 5 nm using the transient hot wire approach. In the work, the temperature changed from 26 to 55 °C, while the solid volume fraction range was between 0.0025 and 0.05. The measured data were compared with the results of theoretical models, including the Hamilton–Crosser and Yu–Choi relations. The comparisons showed that the Yu–Choi model gives acceptable estimations at low temperature, but with increased temperatures, it fails to predict the measured data with an acceptable accuracy. The present data were also compared with the results of other experimental works available in the literature. It was indicated that many factors, such as the particle size, environmental conditions, and methods of preparation and measurement of the thermal conductivity, affect the measured results. Based on the data, a model was proposed as a function of the temperature and solid volume fraction. Finally, the sensitivity analysis of data showed that the thermal conductivity is more sensitive to particle loading at higher temperatures.

Acknowledgements The authors would like to acknowledge the assistance provided by the Nanofluid Laboratory of Semnan University Science and Technology Park for providing necessary instruments to carry out the sample preparation and help in the analysis of samples to complete the article in time. The third and fourth authors wish to thank the National Science and Technology Development Agency and the National Research University Project for the support. Also, Omid Mahian wishes to thank Prof. Somchai Wongwises for his supports during his research at King Mongkut's University of Technology Thonburi, Thailand.

References

1. Choi SUS. Enhancing thermal conductivity of fluids with nanoparticles. Dev Appl Non Newton Flows. 1995;231:99–105.
2. Saidur R, Leong KY, Mohammad HA. A review on applications and challenges of nanofluids. Renew Sust Energ Rev. 2011;15:1646–68.
3. Mahian O, Kianifar A, Kalogirou SA, Pop I, Wongwises S. A review of the applications of nanofluids in solar energy. Int J Heat Mass Transf. 2013;57:582–94.
4. Wang X, Xu X, Choi SUS. Thermal conductivity of nanoparticle-fluid mixture. J Thermophys Heat Transf. 1999;13:474–80.
5. Das SK, Putra N, Thiesen P, Roetzel W. Temperature dependence of thermal conductivity enhancement for nanofluids. J Heat Transf. 2003;125:567–74.
6. Putra N, Roetzel W, Das SK. Natural convection of nano-fluids. Heat Mass Transf. 2003;39:775–84.

Author Proof
UNCORRECTED PROOF

Journal : Large 10973 | Dispatch : 26-3-2014 | Pages : 7
Article No. : 3771 | LE | TYPESET
MS Code : JTAC-D-13-01090 | CP | DISK

Author Proof

7. Masuda H, Ebata A, Teramae K, Hishinuma N. lteration of thermal conductivity and viscosity of liquid by dispersing ultra-fine particles(dispersion of Al2O3, SiO2 and TiO2 ultra-fine particles). Netsu Bussei. 1993;4:227–33.
8. Lee S, Choi SUS, Li S, Eastman JA. Measuring thermal conductivity of fluids containing oxide nanoparticles. J Heat Transf. 1999;121:280–9.
9. Chon CH, Kihm KD, Lee SP, Choi SUS. Empirical correlation finding the role of temperature and particle size for nanofluid (Al2O3) thermal conductivity enhancement. Appl Phys Lett. 2005;87:153107.
10. Li CH, Peterson GP. The effect of particle size on the effective thermal conductivity of Al2O3-water nanofluids. J Appl Phys. 2007;101:044312.
11. Zhang X, Gu H, Fujii M. Effective thermal conductivity and thermal diffusivity of nanofluids containing spherical and cylindrical nanoparticles. J Appl Phys. 2006;100:1–5.
12. Timofeeva EV, Gavrilov AN, McCloskey JM, Tolmachev YV. Thermal conductivity and particle agglomeration in alumina nanofluids: experiment and theory. Phys Rev E. 2007;76:061203.
13. Wong KFV, Kurma T. Transport properties of alumina nanofluids. Nanotechnology. 2008;19:345702.
14. Ju YS, Kim J, Hung MT. Experimental study of heat conduction in aqueous suspensions of aluminum oxide nanoparticles. J. Heat Transf. 2008;130:092403.
15. Oh DW, Jain A, Eaton JK, Goodson KE, Lee JS. Thermal conductivity measurement and sedimentation detection of aluminum oxide nanofluids by using the 3ω method. Int J Heat Fluid Flow. 2008;29:1456–61.
16. Sommers AD, Yerkes KL. Experimental investigation into the convective heat transfer and system-level effects of Al2O3-propanol nanofluid. J. Nanoparticle Res. 2010;12:1003–14.
17. Sundar LS, Sharma KV. Turbulent heat transfer and friction factor of Al2O3 nanofluid in circular tube with twisted tape inserts. Int J Heat Mass Transf. 2010;53:1409–16.
18. Longo GA, Zilio C. Experimental measurement of thermophysical properties of oxide-water nano-fluids down to ice-point. Exp Therm Fluid Sci. 2011;35:1313–24.
19. Yiamsawasd T, Dalkilic AS, Wongwises S. Measurement of the thermal conductivity of titania and alumina nanofluids. Thermochim Acta. 2012;545:48–56.
20. Barbés B, Páramo R, Blanco E, Pastoriza-Gallego MJ, Piñeiro MM, Legido JL, Casanova C. Thermal conductivity and specific heat capacity measurements of Al2O3 nanofluids. J. Thermal Anal Calorim. 2013;11:1615–25.
21. Hamilton RL, Crosser OK. Thermal conductivity of heterogeneous two-component systems. I&EC Fundam. 1962;1:182–91.
22. Yu W, Choi SUS. The Role of Interfacial Layers in the Enhanced Thermal Conductivity of Nanofluids: A Renovated Maxwell Model. J Nanopart Res. 2003;5:167–71.
23. Pak BC, Cho YI. Hydrodynamic and Heat Transfer Study of Dispersed Fluids with Submicron Metallic Oxide Particles. Exp Heat Transfer. 1998;11:151–70.
24. Roy G, Nguyen CT, Lajoie PR. Numerical investigation of laminar flow and heat transfer in a radial flow cooling system with the use of nanofluids. Superlatt Microstruct. 2004;35:497–511.
25. Minsta HA, Roy G, Nguyen CT, Doucet D. New temperature dependent thermal conductivity data for water-based nanofluids. Int J Therm Sci. 2009;48:363–71.
26. Murshed SMS, Leong KC, Yang C. Investigations of thermal conductivity and viscosity of nanofluids. Int J Therm Sci. 2008;47:560–8.
27. Khanafer K, Vafai K. A critical synthesis of thermophysical characteristics of nanofluids. Int J Heat Mass Transf. 2011;54:4410–28.
28. Mahian O, Kianifar A, Wongwises S. Dispersion of ZnO nanoparticles in a mixture of ethylene glycol–water, exploration of temperature-dependent density, and sensitivity analysis. J Clust Sci. 2013;24:1103–14.

UNCORRECTED PROOF

Journal : Large 10973 | Dispatch : 26-3-2014 | Pages : 7
Article No. : 3771 | ☐ LE | ☐ TYPESET
MS Code : JTAC-D-13-01090 | ✔ CP | ✔ DISK

AUTHOR QUERY FORM

ELSEVIER	**Journal: HMT** **Article Number: 10728**	**Please e-mail or fax your responses and any corrections to:** **E-mail: corrections.eseo@elsevier.sps.co.in** **Fax: +31 2048 52799**

Dear Author,

Please check your proof carefully and mark all corrections at the appropriate place in the proof (e.g., by using on-screen annotation in the PDF file) or compile them in a separate list. Note: if you opt to annotate the file with software other than Adobe Reader then please also highlight the appropriate place in the PDF file. To ensure fast publication of your paper please return your corrections within 48 hours.

For correction or revision of any artwork, please consult http://www.elsevier.com/artworkinstructions.

Any queries or remarks that have arisen during the processing of your manuscript are listed below and highlighted by flags in the proof. Click on the 'Q' link to go to the location in the proof.

Location in article	Query / Remark: click on the Q link to go Please insert your reply or correction at the corresponding line in the proof
Q1	Please confirm that given name(s) and surname(s) have been identified correctly.
Q2	Please update the following Ref. [12].

Please check this box if you have no corrections to make to the PDF file ☐

Thank you for your assistance.

International Journal of Heat and Mass Transfer xxx (2014) xxx–xxx

Contents lists available at ScienceDirect

International Journal of Heat and Mass Transfer

journal homepage: www.elsevier.com/locate/ijhmt

Pressure drop during condensation of R134a flowing inside a multiport minichannel

Kittipong Sakamatapan, Somchai Wongwises*

Fluid Mechanics, Thermal Engineering and Multiphase Flow Research Lab. (FUTURE), Department of Mechanical Engineering, Faculty of Engineering, King Mongkut's University of Technology Thonburi, Bangmod, Bangkok 10140, Thailand

ARTICLE INFO

Article history:
Received 1 October 2013
Received in revised form 27 February 2014
Accepted 27 February 2014
Available online xxxx

Keywords:
Condensation
Frictional pressure gradient
R-134a
Multiport minichannel
Correlation

ABSTRACT

This paper is a continuation of the authors' previous work on the condensation of R134a flowing inside a multiport minichannel (Sakamatapan et al., 2013) [22]. The pressure drop's characteristics during condensation were investigated in an experiment for R134a flowing inside a multiport minichannel. The pressure drop characteristics were observed under mass flux range of 345–685 kg/m^2, heat flux of 15–25 kW/m^2, and saturation temperature of 35–45 °C. Two types of multiport minichannels having 14 channels, one with a 1.1 mm hydraulic diameter and another with 8 channels with a 1.2 mm hydraulic diameter, were designed as a counter flow tube in a tube heat exchanger. The results showed that the total pressure drop is dominated by the frictional pressure drop. The frictional pressure gradient increased with the augmentation of mass flux and vapor quality, but the increase of the saturation temperature and channel size play an important role in the decrease of frictional pressure gradient. On the other hand, the heat flux had an insignificant effect on the frictional pressure gradient. Moreover, the miniscale correlations were conducted to predict the frictional pressure gradient, and it was found that only the multiport minichannel correlations gave a reasonable result. A new two-phase friction factor correlation was proposed using the equivalent Reynolds number concept to predict the frictional pressure gradient during condensation.

© 2014 Published by Elsevier Ltd.

1. Introduction

The multiport minichannel is commonly used in automotive air conditioning systems as a condenser. There are many advantages of using the minichannel, such as that it has a high heat transfer area per unit volume, compact size, low refrigerant charge, supported high pressure operation, reduced air-side, and pressure drop; however, sound understanding about heat transfer and pressure drop characteristics during condensation of a refrigerant in a multiport minichannel is still important and requires more attention from researchers. A few studies on pressure drop characteristics in multiport minichannels have been conducted by the following researchers.

Yang and Webb [1] measured adiabatic single and two phase pressure drop of R-12 flowing through 1.56 and 2.64 mm hydraulic diameters, which were made from an extruded aluminum tube with and without microfin, respectively. The tested conditions were conducted within the range of Reynolds number 2500–23,000 for single-phase liquid flow, mass flux 400–1400 kg/m^2 s, and vapor qualities 0.1–0.9 for two-phase flow. For two-phase flow, the pressure drop increased with the augmentation of the mass flux and vapor quality. The pressure drop of the microfin tube was higher than that of the plain tube. They developed the pressure drop correlation by using the equivalent mass velocity concept proposed by Akers et al. [2]. In addition, they concluded that surface tension force had an insignificant effect on frictional pressure drop in the microfin tube.

Single-phase and two-phase pressure drop for R134a, R22, and R404A flow in a multiport extruded aluminum tube with a hydraulic of 2.13 mm, and two circular copper tubes with an inside diameter of 3.25 and 6.25 mm, respectively, were measured by Zhang and Webb [3]. The Blasius correlation [4] was used to predict the single-phase friction factor within a ±10% error rate. The correlation of Friedel [5] was modified by including the employment of reduced pressure for their new two-phase friction factor correlation.

Koyama et al. [6] investigated the condensation of R134a in two multiport extruded tubes. One had 8 channels with a 1.11 hydraulic diameter, and the other had 19 channels with a 0.8 hydraulic diameter. They used pressure-measuring ports to measure the

* Corresponding author. Tel.: +66 2 470 9115; fax: +66 2 470 9111.
E-mail address: somchai.won@kmutt.ac.th (S. Wongwises).

http://dx.doi.org/10.1016/j.ijheatmasstransfer.2014.02.071
0017-9310/© 2014 Published by Elsevier Ltd.

UNCORRECTED PROOF

Nomenclature

c	specific heat at constant pressure (kJ kg^{-1} K^{-1})
d_h	hydraulic diameter (m)
G	mass flux (kg m^{-2} s^{-1})
I	current (A)
i	enthalpy (kJ kg^{-1})
k	thermal conductivity (W m^{-1} K^{-1})
$\dot{m}$	mass flow rate (kg s^{-1})
L	length of multiport minichannel (m)
N	number of channels
P	pressure (kPa)
$\dot{Q}$	heat transfer rate (kW)
q''	heat flux (kW m^{-2})
Re	Reynolds number, $Re = \frac{Gd}{\mu}$
T	temperature (°C)
v	specific volume (m^3 kg^{-1})
V	voltage (V)
x	vapor quality
Greek lettersΔP	
	pressure drop (kPa)
μ	dynamic viscosity (Pa-s)
α	void fraction
ρ	density (kg m^{-3})
σ	surface tension (N m^{-1})
Subscripts$a$	
	acceleration
avg	average
$cont$	contraction
eq	*equivalent*
exp	expansion
f	friction
in	inlet
l	liquid
v	vapor
out	outlet
ref	refrigerant
sat	saturation
tot	total
tp	two phase
TS	test section
w	water

pressure drop at a distance of 191 mm. The positive agreement of the frictional pressure drop was found between the correlation of Mishima and Hibiki [7]. Therefore, the heat transfers' correlation of Haraguchi et al. [8] was modified by calculating the two-phase multiplier from the Mishima and Hibiki correlation [7].

Cavallini et al. [9] discussed the adiabatic two phases of the frictional pressure gradient of R236ea, R134a, and R410A, which were available in a wide range of reduced pressure for the multiport minichannel with a hydraulic diameter of 1.4 mm. The frictional pressure gradient was observed by the saturation temperature drop measurement of the frictional pressure gradient of R410A, which was lower than those of R134a and R236ea, respectively. Moreover, the experimental data were compared with several frictional pressure drop correlations available in the literature. The results showed that the frictional pressure gradient of R134a was in strong agreement but was not accurate for R236ea and R410A.

Garimella et al. [10] developed the multiple flow regime model for predicting pressure drop during all processes of condensation by a combined and modified intermittent and annular regime model, which were developed earlier. When comparing the predicted values with the measured data that was taken from mass flux between 150 and 750 kg/m^2 s in five circular microchannels, 82% of the data were within ±20% error rate.

The pressure drop of CO_2 during condensation was investigated by Park and Hrnjak [11]. This study was conducted at the saturation temperature of −15 and −25 °C by, mass fluxes of 200–800 kg/m^2 s, and wall sub-cooling temperature from 2 to 4 °C for a 0.89 mm microchannel. It was found that the two-phase pressure drop in the adiabatic condition increased with the augmentation of mass flux and vapor quality, but it decreased when saturation temperature increased. The comparison between the values predicted by conventional tubes and small tubes correlations, and the experimental data was also reported. It was shown that several correlations predicted the experimental data well.

Heo et al. [12] investigated the pressure drop of CO_2 during condensation in the multiport microchannel with a hydraulic diameter of 1.5 mm. The experiment was tested under mass flux from 400 to 1000 kg/m^2 s and saturation temperature from −5 to 5 °C. The pressure drop increased with the augmentation of mass flux and vapor quality, but it decreased with the increasing saturation temperature. It was also found that the correlation of Misima and Hibiski [7] could be predicted the data with a mean deviation of 29.1%.

Due to the difficulties in constructing the test section, which is a type of heat exchanger for condensation experiment, the information on heat transfer and pressure drop characteristics during the condensation of working fluids in a multiport minichannel is still limited, compared to the evaporation experiment. As described above, there have been only works carried out by [1,3,6,9–12] dealing with this issue. However, it can be noted that the experimental investigations found in the literature described above focused on the effect of the specific parameter, and the particular detailed investigation is still lacking. To the best of our knowledge, among these works, only one work, which was carried out by Park and Hrnjak [11], reported the effect of all parameters.

Although some information is currently available, there still remains room for further research. In the present study, the working fluid and the test section used are different from those used by the previous study. The effects of all involved parameters are presented for condensing flow, including mass flux, heat flux, saturation temperature, and vapor quality on the pressure drop characteristics, which have never before appeared in the available literature.

2. Apparatus and method

The schematic diagram of the experimental setting, which is also used in the flow boiling heat transfer and pressure drop in the multiport minichannel study [13,14], is presented in Fig. 1. The main system components consisted of the refrigerant loop, cooling water loop, subcooling loop, data acquisition system, and test section.

For the refrigerant circulating loop, as shown in Fig. 1, the liquid refrigerant is pumped by a gear pump through a filter and dryer, refrigerant flow meter, preheater, inlet sight glass tube, test section, again to the outlet sight glass tube, and plate heat exchanger. Then, it is collected in a receiver tank and returned to the refrigerant gear pump to complete the cycle. The refrigerant flow rate is controlled by a gear pump that can be regulated by an inverter. The desired inlet quality of the test section is controlled by the

UNCORRECTED PROOF

Please cite this article in press as: K. Sakamatapan, S. Wongwises, Pressure drop during condensation of R134a flowing inside a multiport minichannel, Int. J. Heat Mass Transfer (2014), http://dx.doi.org/10.1016/j.ijheatmasstransfer.2014.02.071

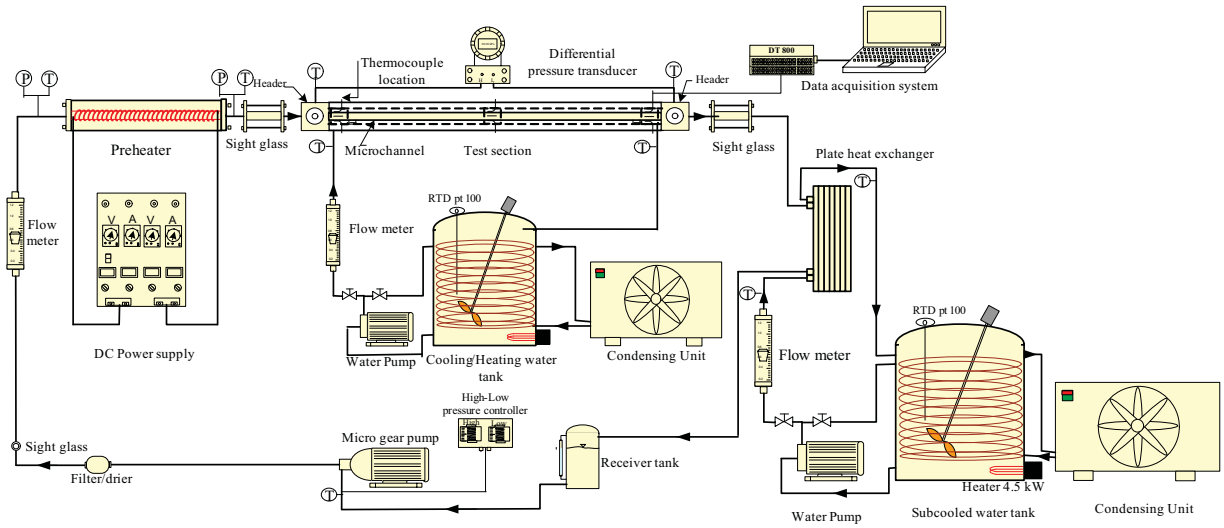

Fig. 1. Schematic diagram of the experimental apparatus. [Sakamatapan et al. [22], with permission from Elsevier]

preheater. A DC power supply is used to supply power to the preheater, which can be controlled by adjusting the supply voltage and current. After leaving the test section, the two-phase refrigerant condenses to a liquid phase in the plate heat exchanger by transferring its heat to the subcooling water loop. To monitor the state of the refrigerant, all of the signals from the thermocouples and differential pressure transducer are collected by a data acquisition. All instruments are installed at various positions, which is clearly seen in Fig. 1.

Fig. 2 shows a schematic diagram of the test section for this study, and the test section is designed as a counter flow tube in the tube heat exchanger with refrigerant flowing in the multiport minichannel and cooling water flowing in the annular gap. The multiport minichannel is aluminum that has 14 channels with a 1.1 mm hydraulic diameter (Type 1) and 8 channels with a 1.2 mm hydraulic diameter (Type 2). The outer tube is made from 12 mm thick clear acrylic and is designed as a rectangular annulus, which is used to absorb heat flux from the tested tubes. The photographs of these multiport minichannels are presented in Fig. 3. In addition, the inlet and outlet saturation temperatures are measured by T-type thermocouples installed at the inlet and outlet points of the test section headers. For measuring the pressure drop, which goes 250 mm across the test section, a differential pressure transducer, which has an accuracy of the differential pressure drop, is ±0.25% of the full scale, or ±0.125 kPa is installed on the other side of the header. The thermocouples are also installed at the inlet and outlet of the water channel to measure the inlet and outlet cooling water temperatures. Moreover, the test section is composed of rubber foam with 0.04 W/m K of thermal conductivity, which provides thermal insulation for this section. The refrigerant flow meter is a variable-area type. The flow meter is specially calibrated in the range of 0.2–1.8 LPM for R134a by the manufacturer. The tested conditions are presented in Table 1. The details of the test section are presented in Table 2. The accuracies of the direct measurements and the uncertainties in the derived experimental values determined by standard method are shown in Table 3.

3. Data reduction

The data reduction is provided for determining the average vapor quality as well as the pressure gradient components of the measured data.

The average vapor quality between the inlet and the outlet vapor quality of the test section can be calculated from the relation

$$x_{ave} = \frac{x_{TS,in} + x_{TS,out}}{2} \quad (1)$$

where $i_{TS,in}$ is the refrigerant enthalpy at the test section inlet, and $i_{TS,out}$ is the refrigerant enthalpy at the test section outlet.

The inlet vapor quality of the test section is determined as follows:

$$x_{TS,in} = \frac{i_{TS,in} - i_{l@TS,in}}{i_{lv@TS,in}} \quad (2)$$

where $i_{l@TS,in}$ is the enthalpy of saturated liquid refrigerant based on the temperature at the test section inlet, and $i_{lv@TS,in}$ is the enthalpy of vaporization based on the temperature at the test section inlet, which is given by

$$i_{TS,in} = i_{l@ph} + \frac{\dot{Q}_{lat}}{\dot{m}_{ref}} \quad (3)$$

where $i_{l@ph}$ is the enthalpy of the saturated liquid refrigerant based on saturation temperature at the preheater, $\dot{m}_{ref}$ is the mass flow rate of the refrigerant, and $\dot{Q}_{lat}$ is the latent heat transfer rate in the preheater, which is calculated as follows:

$$\dot{Q}_{ph} = \dot{Q}_{lat} + \dot{Q}_{sen} \quad (4)$$

where $\dot{Q}_{ph}$ is the electrical power from a heater to the refrigerant flowing through the pre-heater, and $\dot{Q}_{sen}$ is the sensible heat transfer rate in the pre-heater, which is defined as

$$\dot{Q}_{ph} = (VI)_{@ph} \quad (5)$$

$$\dot{Q}_{sen} = \dot{m}_{ref} c_{ref} \left(T_{ph,out} - T_{ph,in}\right) \quad (6)$$

The outlet vapor quality of the test section is also determined from

$$x_{TS,out} = \frac{i_{TS,out} - i_{l@TS,out}}{i_{lv@TS,out}} \quad (7)$$

where $i_{TS,out}$ is the refrigerant enthalpy at the test section outlet, $i_{l@TS,out}$ is the enthalpy of saturated liquid refrigerant based on the temperature of the test section outlet, and $i_{lv@TS,out}$ is the enthalpy of vaporization. As a consequence, the enthalpy of the refrigerant flow at the test section outlet can be determined from

$$i_{TS,out} = i_{TS,in} - \frac{\dot{Q}_{TS}}{\dot{m}_{ref}} \quad (8)$$

UNCORRECTED PROOFS

Please cite this article in press as: K. Sakamatapan, S. Wongwises, Pressure drop during condensation of R134a flowing inside a multiport minichannel, Int. J. Heat Mass Transfer (2014), http://dx.doi.org/10.1016/j.ijheatmasstransfer.2014.02.071

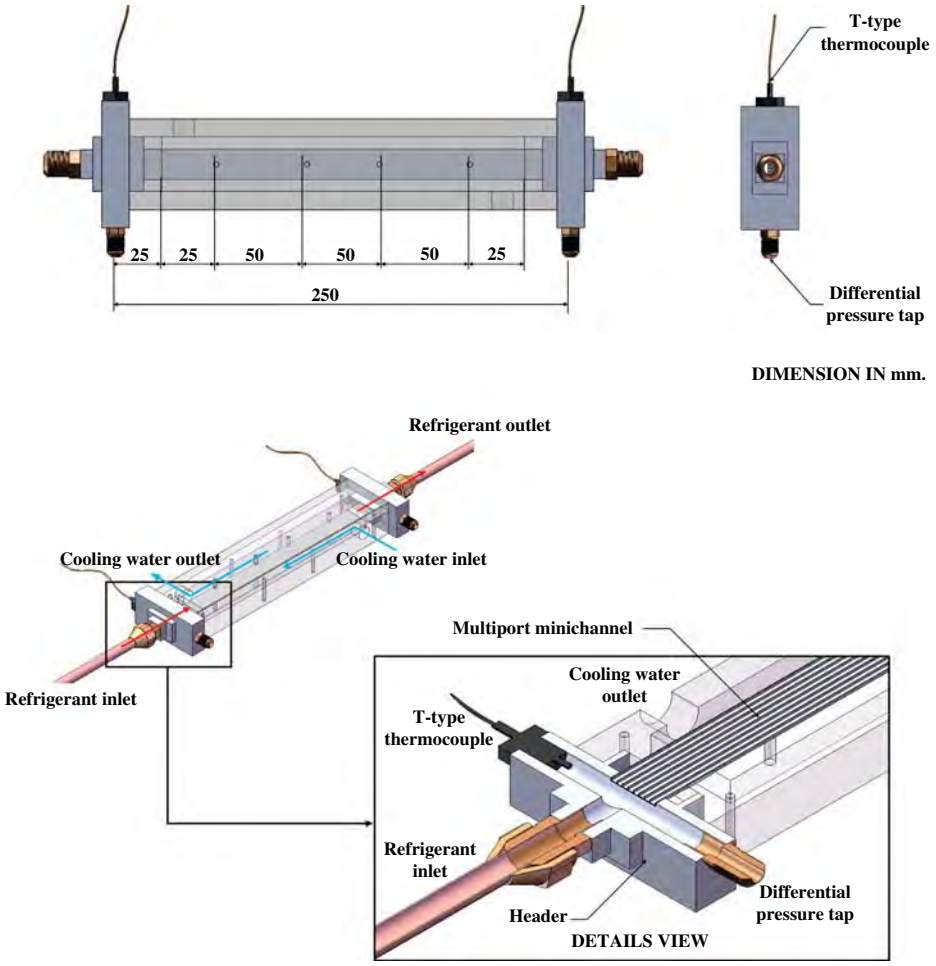

Fig. 2. Schematic diagram of the test section. [Sakamatapan et al. [22], with permission from Elsevier]

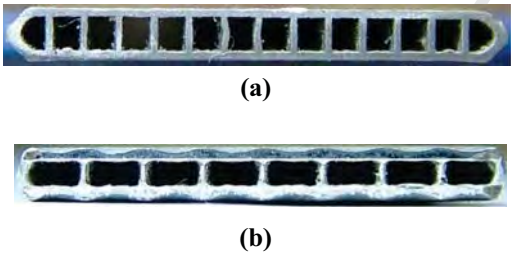

Fig. 3. Photographs of cross section of the multiport minichannels: (a) Type 1 (d_h = 1.1 mm, n = 14), (b) Type 2 (d_h = 1.2 mm, n = 8). [Sakamatapan et al. [22], with permission from Elsevier]

Table 1
The experimental conditions.

Refrigerant	R134a
Hydraulic diameter (mm)	1.1 and 1.2
Number of channels, (N)	8 and 14
Mass flux (kg/m^2 s)	340–680
Heat flux (kW/m^2)	15–25
Saturation temperature (°C)	35–45
Average vapor quality	0.1–0.8
• Inlet vapor quality	0.15–0.85
• Outlet vapor quality	0.05–0.75

where $\dot{Q}_{TS}$ is obtained from the heat and absorbed from the refrigerant to the cooling water, which can be calculated from

$$\dot{Q}_{TS} = \dot{m}_w c_w (T_{w,out} - T_{w,in}) \quad (9)$$

The total pressure drop is the summation of the frictional pressure drop, the sudden contraction and sudden expansion pressure drop due to the headers at the inlet and outlet of the test section, and the momentum or acceleration pressure drop, which can be expressed as follows:

$$\Delta P_{tot} = \Delta P_f + \Delta P_{exp} + \Delta P_{cont} + \Delta P_a \quad (10)$$

The sudden expansion pressure drop at outlet of multiport minichannel is calculated using Eq. (11) [15].

$$\Delta P_{exp} = G^2 \sigma (1-\sigma) v_l \left[\frac{(1-x)^2}{(1-\alpha)^2} + \left(\frac{v_v}{v_l}\right) \frac{x^2}{\alpha} \right] \quad (11)$$

Please note that void fraction is assumed as a constant in Eq. (11).

For the homogeneous model, the sudden contraction pressure drop at inlet of multiport minichannel is calculated from Eq. (12) [15].

$$\Delta P_{cont} = \frac{G^2 v_l}{2} \left[\left(\frac{1}{C_c} - 1 \right)^2 + \left(1 - \frac{1}{\sigma^2} \right) \right] \left[1 + \left(\frac{v_{lv}}{v_l} \right) x \right] \quad (12)$$

where σ is area ratio, and C_c is the coefficient of contraction which is a function of σ.

Please cite this article in press as: K. Sakamatapan, S. Wongwises, Pressure drop during condensation of R134a flowing inside a multiport minichannel, Int. J. Heat Mass Transfer (2014), http://dx.doi.org/10.1016/j.ijheatmasstransfer.2014.02.071

Table 2
The details of multiport minichannel.

Type	Hydraulic diameter (mm)	Number of channels	Channel width (mm)	Channel height (mm)	Aspect ratio	Outer surface (mm^2)	Surface roughness (μm)
1	1.1	14	1	1.25	1.25	5797.5	0.20
2	1.2	8	1.8	1.8	0.5	6171	0.18

Table 3
The accuracies of the direct measurements and the uncertainties in the derived experimental values.

Parameter	Uncertainty
Temperature (°C)	±0.1
Mass flow rate of refrigerant (kg/s)	±2.4%
Differential pressure transducer (kPa)	±125
Heat transfer rate of test section (kW)	±14%
Average quality (–)	±8.6%
Frictional pressure gradient (kPa/m)	±6.4%

Finally, the momentum or acceleration pressure drop is the loss due to the change in quality across the test section, the following equation recommended by Carey [16] is used.

$$\Delta P_a = G^2 \left\{ \left[\frac{(1-x)^2}{\rho_l(1-\alpha)} + \frac{x^2}{\rho_v \alpha} \right]_{out} - \left[\frac{(1-x)^2}{\rho_l(1-\alpha)} + \frac{x^2}{\rho_v \alpha} \right]_{in} \right\} \quad (13)$$

where the void fraction α can be determined by the Zivi [17] correlation, which is expressed as follows:

$$\alpha = \frac{1}{1 + \frac{(1-x)}{x}\left(\frac{\rho_v}{\rho_l}\right)^{2/3}} \quad (14)$$

The frictional pressure gradient can be determined by subtracting the sudden expansion, sudden contraction, and momentum pressure drop into the terms of the total measured pressure drop and dividing the length of multiport minichannel.

4. Results and discussion

The pressure gradient during condensation of R134a flowing inside multiport minichannel from this study under the condition: mass flux 340–680 kg/m^2 s, heat flux 15–25 kW/m^2, and saturation temperature 35–45 °C is presented and discussed in this topic.

It should be noted that the flow pattern of this study was an annular flow, which was predicted by a flow pattern map of Soliman [18], Coleman and Garimella [19,20], and Garimella [21], as presented in the study of condensation heat transfer characteristic inside multiport minichannel [22].

4.1. The pressure gradient components

The total pressure gradient can be expressed as the sum of the four terms of the frictional pressure drop, the sudden contraction pressure drop, the sudden expansion pressure drop, and the momentum or acceleration pressure drop.

The components of the pressure drop with the variation of heat fluxes at the mass flux of 350 kg/m^2 s and saturation temperature of 40 °C are presented in Fig. 4. The results showed that the total pressure drop was dominated by the frictional pressure drop, which was approximately 79.42% of total pressure gradient. It was also found that the sudden contraction pressure drop, the sudden expansion pressure drop, and the momentum pressure drop amount was 22.35%, 4.21%, and 5.98% of total pressure drop, respectively.

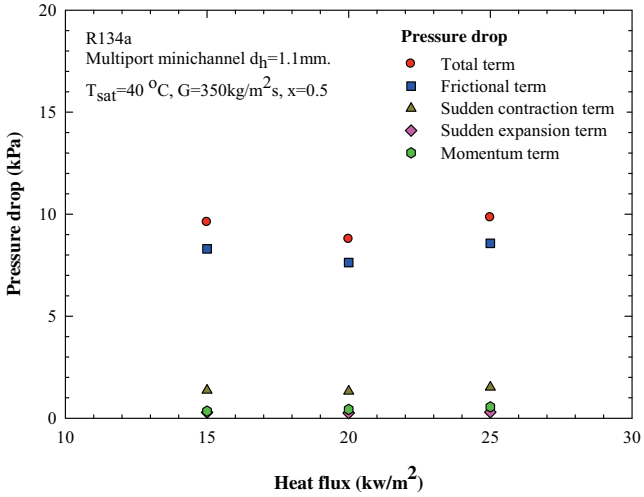

Fig. 4. Heat flux vs. total pressure gradient for various mass fluxes.

4.2. The frictional pressure gradient

Fig. 5 shows the frictional pressure gradient as a function of vapor quality with variation of mass fluxes. It was found that the increasing mass flux had a significant effect on the increase of frictional pressure gradient. Moreover, it was also demonstrated that the frictional pressure gradient increased with the augmentation of vapor quality. The increase of the frictional pressure gradient was due to the effects of higher shear stress. The increasing mass flux and the increasing vapor quality have a direct effect on higher flow velocity and flow velocity differences between liquid and vapor phase. Consequently, it leads to an increase in wall shear stress and interfacial shear, which results in frictional pressure gradient increase.

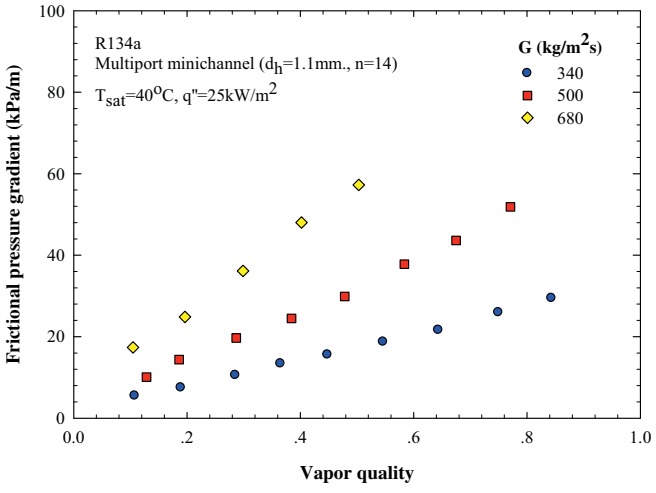

Fig. 5. Average vapor quality vs. frictional pressure gradient for various mass fluxes.

UNCORRECTED

Please cite this article in press as: K. Sakamatapan, S. Wongwises, Pressure drop during condensation of R134a flowing inside a multiport minichannel, Int. J. Heat Mass Transfer (2014), http://dx.doi.org/10.1016/j.ijheatmasstransfer.2014.02.071

The present study, as shown in Fig. 6, shows the variation of frictional pressure gradient in vapor quality for different heat fluxes. It can be clearly seen that the heat flux had an insignificant effect on the frictional pressure gradient. These phenomena may occur from the increase of heat flux, presenting a minimal effect on the viscosity and velocity of the flowing refrigerant.

The influence of saturation temperature on the frictional pressure gradient is presented in Fig. 7. The results showed that the frictional pressure gradient increased with the decreasing saturation temperature. Consider that the property of refrigerant under saturation temperature decreased from 45 to 35 °C. The viscosity ratio (μ_l/μ_v) increased from 11.93 to 14.18, and the density ratio (ρ_l/ρ_v) decreased from 19.51 to 26.88, which makes the quantity of shear stress higher. Therefore, this occurrence causes a frictional pressure gradient increase.

The measured frictional pressure gradient between the two different tubes in all of the similar tested conditions was also compared, as shown in Fig. 8. The frictional pressure gradient of the multiport minichannel of Type 1 was higher than those of Type 2 about 16.4%. The refrigerant velocities in the multiport minichannel of Type 1 are equal to those in Type 2; however, due to the smaller hydraulic diameter, a higher frictional pressure gradient in multiport minichannel Type 1 is obtained.

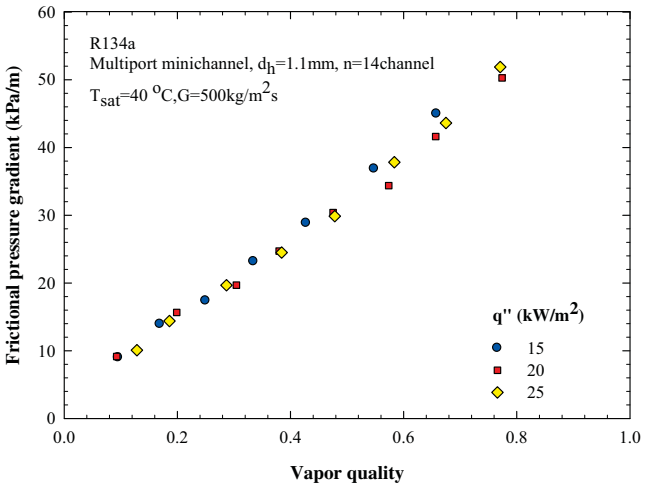

Fig. 6. Average vapor quality vs. frictional pressure gradient for various heat fluxes.

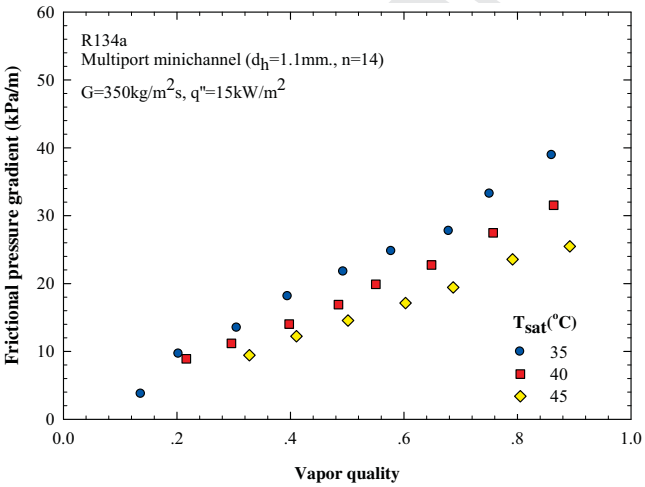

Fig. 7. Average vapor quality vs. frictional pressure gradient for various saturation temperature.

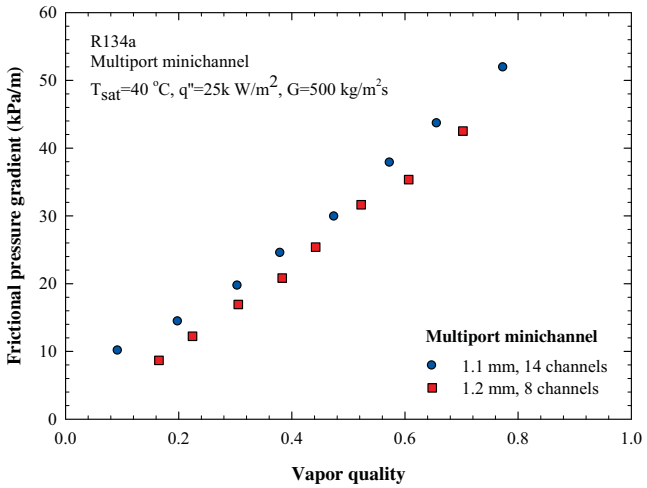

Fig. 8. Comparison of frictional pressure gradient between multiport minichannel Type 1 and multiport minichannel Type 2.

4.3. The comparison with the existing correlations

Experimental data were compared against the five well-known correlations that were particularly developed for predicting frictional pressure gradient in minichannels in both single and multiport, which were proposed by Chen et al. [23], Zhang and Webb [24], Garimella et al. [25], Cavallini et al. [26], Cavallini et al. [30], and Bodal et al. [31]. The available experimental information of the correlations is reviewed in Table 4.

Chen et al. [23] informed the effects of surface tension and gravity by conducting the Bond number and the Webber number of the Friedel correlation [5], when this was used for their single minichannel correlation. The comparison with the Chen et al. correlation [23] is presented in Fig. 9. The Chen et al. [23] correlation underestimated the experimental data as 94% of data had 50% of the errors. The frictional pressure drop in multiport minichannel correlation of Zhang and Webb [24] was also done by including the reduced pressure into the Friedel correlation [5]. In Fig. 10, the Zhang and Webb correlation [24] could predict 72% of the data with ±30% error. Garimella et al. [25] developed the correlation for pressure drops during condensation by combining the correlation of the intermittent flow model and annular flow in both circular and non-circular microchannel, and 87% of the predicted data falling within the ±20% error band as presented in Fig. 11. The correlation was developed by Cavallini et al. [26], which was interpolated from Cavallini et al. [27], Coleman [28], and Zhang [29] regarding the frictional pressure gradient in minichannel correlations. The results of this work found that 82% of the data calculated by the Cavallini et al. [26] correlation was within a ±20% error rate, as shown in Fig. 12. Fig. 13 shows an experimental frictional pressure gradient plotted against predicted frictional pressure gradient obtained from Cavallini et al. [30]. The correlation was improved from the previous one (Cavallini et al. [26]) by including the effect of surface roughness. The plot shows that 71% of the data fall within ±20% of the correlation. Over 75.5% of the calculated data was within 50% of the error rate by comparing with the Bohdal et al. [31] correlation, which was based on the refrigerant R134a and R404A condensing flow in singleport minichannel, as reported in Fig. 14.

4.4. New proposed correlation

To predict the frictional pressure gradient of R134a flowing inside the multiport minichannel, the correlation of the two-phase fiction factor is proposed in this topic. The correlation is one of

Please cite this article in press as: K. Sakamatapan, S. Wongwises, Pressure drop during condensation of R134a flowing inside a multiport minichannel, Int. J. Heat Mass Transfer (2014), http://dx.doi.org/10.1016/j.ijheatmasstransfer.2014.02.071

Table 4
The available experimental information of the correlations.

Author(s)	Working fluid	Hydraulic diameter (mm)	Channel/orientation/conditions	Rang/ applicability
Chen et al. [23]	Air–water	1.02, 3.17, 5.05, 7.02	Single minichannal/horizontal/adiabatic	Room temperature G = 50–3000 kg/ m^2 s x = 0.001–0.9
	R410A	3.17, 5.05, 7.02, 9		T_{sat} = 5, 15 °C G = 50–600 kg/ m^2 s x = 0.1–0.9
Zhang and Webb [24]	R22, R134a and R404A	2.13	Multiport minichannel/horizontal/adiabatic	T_{sat} = 20–65 °C G = 200–1000 kg/ m^2 s
Garimella et al. [25]	R134a	0.5–4.91	Multiport minichannel/horizontal/condensation	T = 52 °C x = 0–1 G = 150–750 kg/ m^2 s
Cavallini et al. [26] and [30]	R236ea, R134a and R410A		Smooth multiport minichannel and rough singleport minichannel horizontal/adiabatic	T_{sat} = 40 °C G = 200–1400 kg/ m^2 s x = 0.25, 0.5, 0.75
Bohdal et al. [31]	R134a and R404A	0.31–3.3	Single minichannal/horizontal/condensation	T_{sat} = 20–40 °C G = 100–1300 kg/ m^2 s x = 0–1

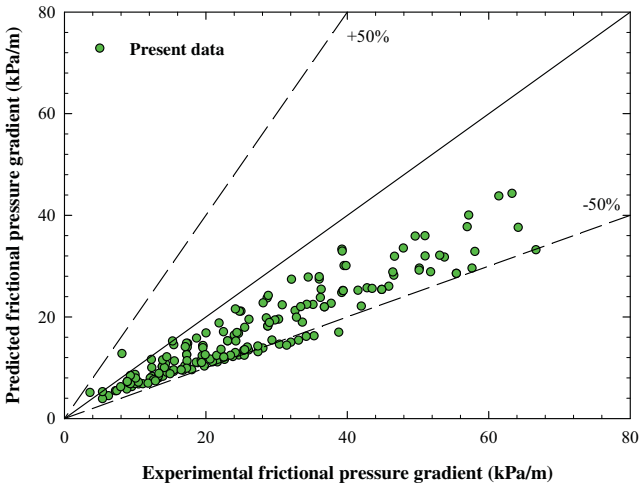

Fig. 9. Comparison of the experimental data with the correlation of Chen et al. [23].

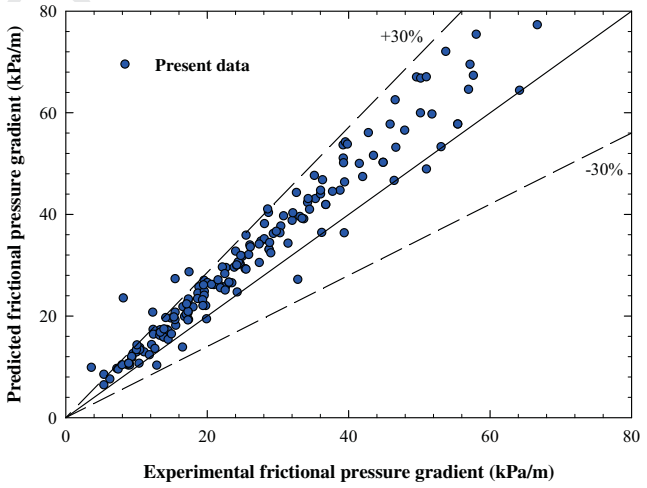

Fig. 10. Comparison of the experimental data with the correlation of Zhang and Webb [24].

the important equipment in order to design the condenser for automobile industrial usage.

Based on the dimensional analysis, the two-phase friction factor correlation was developed by using the equivalent Reynolds number concept of Akers et al. [2] to include the effect of the involved parameter.

The two-phase pressure gradient is calculated by the following equation based on the equivalent Reynolds number.

$$\left(\frac{\Delta P}{L}\right)_f = \frac{2f_{tp}Re_{eq}^2\mu_l^2}{\rho_l d_h^3} \tag{15}$$

where the equivalent Reynolds number is determined by

$$Re_{eq} = \frac{G_{eq}d_h}{\mu_l} \tag{16}$$

and equivalent mass flux is defined as

$$G_{eq} = G\left[(1-x) + x\sqrt{\frac{\rho_l}{\rho_v}}\right] \tag{17}$$

Finally, the two-phase friction factor as a function of the equivalent Reynolds number was fitted to the following correlation:

$$f_{tp} = 6977\mathrm{Re}_{eq}^{-0.337}x^{-0.031}\left[\frac{\rho_l}{\rho_v}\right]^{6.510}\left[\frac{\mu_l}{\mu_v}\right]^{-11.883} \tag{18}$$

Fig. 15 shows the experimental two phase friction factor plotted against the predicted two-phase friction factor calculated from the proposed correlation. It was found that 90% of data fell within a deviation of 20%.

5. Conclusion

The flow characteristics of R134a during the condensing flow inside the multiport minichannel are some of the essential factors

Please cite this article in press as: K. Sakamatapan, S. Wongwises, Pressure drop during condensation of R134a flowing inside a multiport minichannel, Int. J. Heat Mass Transfer (2014), http://dx.doi.org/10.1016/j.ijheatmasstransfer.2014.02.071

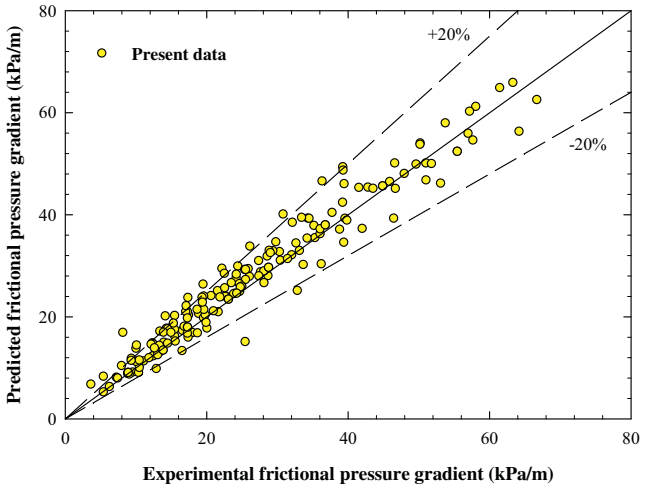

Fig. 11. Comparison of the experimental data with the correlation of Garimella et al. [25].

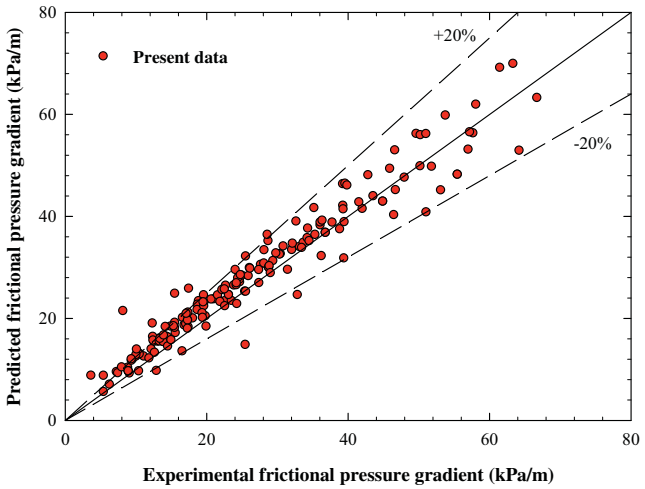

Fig. 12. Comparison of the experimental data with the correlation of Cavallini et al. [26].

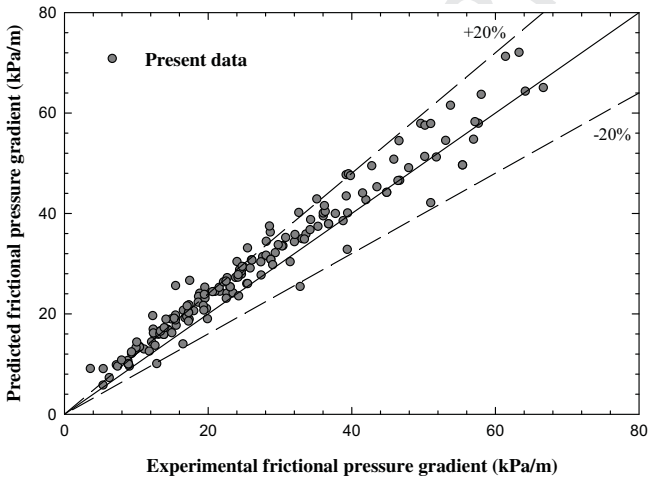

Fig. 13. Comparison of the experimental data with the correlation of Cavallini et al. [30].

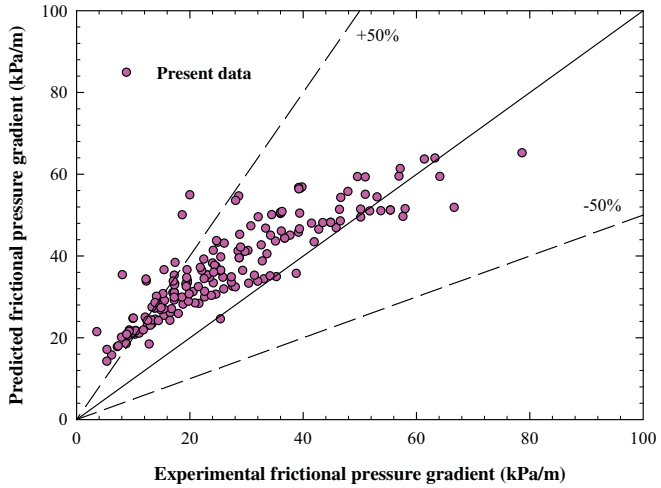

Fig. 14. Comparison of the experimental data with the correlation of Bohdal et al. [31].

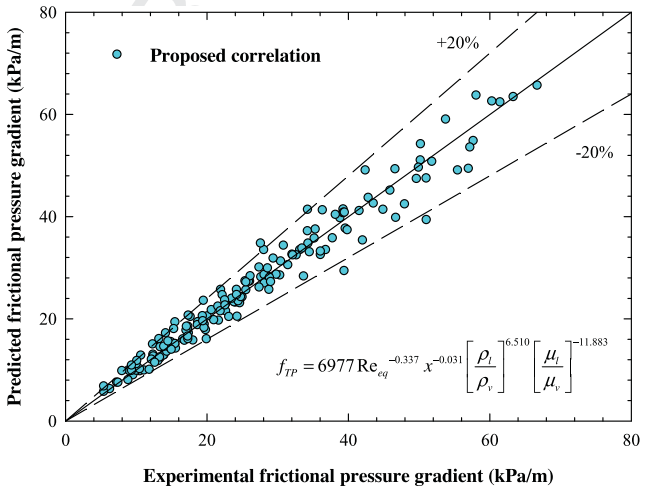

Fig. 15. Comparison of measured with predicted frictional pressure gradient using proposed correlation of two phase friction factor.

of designing the condenser in the automotive air conditioning system. The friction is the main cause of the total pressure drop as the frictional pressure drop, which is 79.42% of the total pressure drop. There are four flow parameters that have an influence on the increase of the frictional pressure gradient, which are increasing the mass flux and vapor quality and decreasing the saturation temperature and size of the channel.

The measured frictional pressure gradient is compared with two types of correlations that were developed for single minichannel and three correlations, specially developed for the multiport minichannel. There are only multiport minichannel correlations that give an accurate prediction, which was not to exceed 20% of the error rate when compared with the measured data. Correlations for the single minichannel give an imprecise prediction with the measured data.

The correlation of the two-phase friction factor for the multiport minichannel under dimension analysis is proposed by using the equivalent Reynolds number to correlate the effects of involved parameters.

Acknowledgement

The authors would like to express their appreciation to the National Science and Technology Development Agency, the Thailand

Please cite this article in press as: K. Sakamatapan, S. Wongwises, Pressure drop during condensation of R134a flowing inside a multiport minichannel, Int. J. Heat Mass Transfer (2014), http://dx.doi.org/10.1016/j.ijheatmasstransfer.2014.02.071

Research Fund and the National Research University Project for providing financial support for this study.

References

[1] C.Y. Yang, R.L. Webb, Friction pressure drop of R-12 in small hydraulic diameter extruded aluminum tubes with and without micro-fins, Int. J. Heat Mass Transfer 39 (1996) 801–809.
[2] W.W. Akers, H.A. Deans, O.K. Crosser, Condensation heat transfer within horizontal tubes, Chem. Eng. Prog. Symp. Ser. 55 (1959) 171–176.
[3] M. Zhang, R.L. Webb, Correlation of two-phase friction for refrigerant in small-diameter tubes, Exp. Therm. Fluid Sci. 25 (2001) 131–139.
[4] P.R.H. Blassius, Das Aehnlichkeitsgesetz bei Reibungvorgangen in Flussigkeiten, Forschungsheft 131 (1913) 1–41.
[5] L. Friedel, Improved friction pressure drop correlations for horizontal and vertical two-phase pipe flow, in: Proceedings of the European Two Phase-Flow Group Meeting, Ispra, Itary, 1979.
[6] S. Koyama, K. Kuwahara, K. Nakashita, K. Yamamoto, An experiment study on condensation of refrigerant R134a in a multi-port extruded tube, Int. J. Refrig. 24 (2003) 425–432.
[7] K. Mishima, T. Hibiki, Effect of inner diameter on some characteristics of air–water two-phase flows in capillary tubes, Trans. JSME 61 (1995) 99–106.
[8] H. Haraguchi, S. Koyama, T. Fujii, Condensation of refrigerants HCFC22, HFC134a and HCFC123 in horizontal smooth tube, Trans. JSME 60 (1994) 245–252.
[9] A. Cavallini, D. Del Col, L. Doretti, M. Matkovic, C. Zilio, Two-phase friction pressure gradient of R236ea, R134a and R410A inside multi-port mini-channels, Exp. Therm. Fluid Sci. 29 (2005) 861–870.
[10] S. Garimella, A. Agarwal, J.D. Killion, Condensation pressure drop in circular minichannels, Heat Transfer Eng. 26 (2005) 1–8.
[11] C.Y. Park, P. Hrnjak, CO_2 flow condensation heat transfer and pressure drop in multi-port microchannels at low temperatures, Int. J. Refrig. 32 (2009) 1129–1139.
[12] J. Heo, H. Park, R. Yun, Condensation heat transfer and pressure drop characteristic of CO_2 in microchannel, *Int. J. Refrig.* (in press).
[13] J. Kaew-On, K. Sakamatapan, S. Wongwises, Flow boiling heat transfer of R134a in the multiport minichannel heat exchangers, Exp. Therm. Fluid Sci. 35 (2011) 364–374.
[14] J. Kaew-On, K. Sakamatapan, S. Wongwises, Flow boiling pressure drop of R134a in the counter flow multiport minichannel heat exchangers, Exp. Therm. Fluid Sci. 36 (2012) 107–117.
[15] J.G. Colliier, J.R. Thome, Convective Boiling and Condensation, third ed., Oxford University Press, Oxford, UK., 1994.
[16] V.P. Carey, Liquid–Vapor Phase-change Phenomena, second ed., Taylor and Francis, New York, USA, 2007.
[17] S.M. Zivi, Estimation of steady-state steam void-fraction by mean of the principle of minimal entropy production, Trans. ASME J. Heat Transfer 86 (1964) 247–252.
[18] H.M. Soliman, Mist-annular transition during condensation and its influence on the heat transfer mechanism, Int. J. Multiphase Flow 12 (1986) 277–288.
[19] J.W. Coleman, S. Garimella, Characterization of two-phase flow patterns in small diameter round and rectangular tubes, Int. J. Heat Mass Transfer 42 (1999) 2869–2881.
[20] J.W. Coleman, S. Garimella, Two-phase flow regime transition in microchannel tubes: the effect of hydraulic diameter, ASME HTD 366 (2000) 71–83.
[21] S. Garimella, Condensation flow mechanisms in microchannels: basis for pressure for pressure drop and heat transfer models, Heat Transfer Eng. 25 (2004) 104–116.
[22] K. Sakamatapan, J. Kaew-On, A.S. Dalkilic, O. Mahian, S. Wongwises, Condensation heat transfer characteristics of R-134a flowing inside the multiport minichannels, Int. J. Heat Mass Transfer 64 (2013) 976–985.
[23] I.Y. Chen, K.S. Yang, Y.J. Chang, C.C. Wang, Two-phase pressure drop of air–water and R-410A in small horizontal tubes, Int. J. Multiphase Flow 27 (2001) 1293–1299.
[24] M. Zhang, R.L. Webb, Correlation of two-phase friction for refrigerants in small-diameter tubes, Exp. Therm. Fluid Sci. 25 (2001) 131–139.
[25] S. Garimella, A. Agarwal, J.D. Killion, Condensation pressure drop in circular microchannels, Heat Transfer Eng. 26 (2005) 1–8.
[26] A. Cavallini, L. Doretti, M. Matkovic, L. Rossetto, Update on condensation heat transfer and pressure drop inside minichannels, Heat Transfer Eng. 27 (2006) 74–87.
[27] A. Cavallini, D. Del Col, L. Doretti, M. Matkovic, L. Rossetto, C. Zilio, Measurement of Pressure Gradient during two-phase flow inside multi-port mini-channel, in: Third International Symposium on Two-phase Flow Modeling and Experimentation, Pisa, 2004, pp. 22–24.
[28] J.W. Coleman, Flow visualization and pressure drop for refrigerant phase change and air–water flow in small hydraulic diameter geometries (Ph.D. thesis), Iowa State University, Ames, Iowa, 2009.
[29] M. Zhang, A new equivalent Reynolds number model for vapor shear-controlled condensation inside smooth and micro-fin tubes (Ph.D. thesis), The Pennsylvania State University, 1998.
[30] A. Cavallini, D. Del Col, M. Matkovic, L. Rossetto, Frictional pressure drop during vapour–liquid–liquid flow in minichannels: modelling and experimental evaluation, Int. Heat Fluid Flow 30 (2009) 131–139.
[31] T. Bohdal, H. Charun, M. Sikora, Comparative investigations of the condensation of R134a and R404A refrigerants in pipe minichannels, Int. J. Heat Mass Transfer 54 (2011) 1963–1974.

UNCORRECTED PROOF

ELSEVIER SCIENCE

INTERNATIONAL JOURNAL OF HEAT AND MASS TRANSFER
INTERNATIONAL COMMUNICATIONS IN HEAT AND MASS TRANSFER

Professor W.J. Minkowycz
Editor-in-Chief
University of Illinois at Chicago
Mechanical Engineering (M/C 251)
842 West Taylor Street, 2049 ERF
Chicago, Illinois 60607-7022
Tel: (312) 996-3467
Fax: (312) 413-0447
E-mail: wjm@uic.edu

March 16, 2014

Dr. Somchai Wongwises
Fluid Mechanics, Thermal Engineering and Multiphase Flow Research Lab
King Mongkut's University of Technology
Thonburi, Bangmod, Bangkok 10140 Thailand
somchai.won@kmutt.ac.th

Subj: CJ14/5834 — "Measurement of Void Fraction of R-134a Flowing Through Horizontal Tube" by R. Srisomba, S. Wongwises

Dear Dr. Wongwises:

Thank you for the above-referenced manuscript which you have submitted for possible publication in the ***International Communications in Heat and Mass Transfer***. I am pleased to advise you that the reviews and recommendations to me from two members of the Board of Editors are favorable. I have also reviewed the paper carefully and find it to be of good quality. Indeed, the quality standard of the paper merits its acceptance for publication without further review and, therefore, I intend to accept your work for the journal.

Please note that the final revision cannot exceed 24 pages, using 1½ space typing, with each individual figure page (which can have separate figures such as Fig. 1, Fig. 2, Fig. 3, ..., properly positioned and cut-and-pasted on the page) being counted as one page of text. Papers using a font size smaller than 11 point will not be accepted. The entire manuscript must be typed in the *same* font face and the *same* font size. Also, please note that color illustrations cannot normally be hard-copy printed in a journal, unless paid by the author. The charge will be determined by the publisher.

Please proofread and revise your paper to make certain that all possible errors have been eliminated. **A Word, Word Perfect or a TeX copy of the manuscript must be included as an attachment by email. The enclosed Manuscript Acceptance Form must also be filled out and returned in a pdf format to this office.** Upon receipt of the above material, the publisher will then advise you of the publication schedule of your paper.

Please note the new revision submission instructions. Hard copy submissions are no longer accepted. Thank you for your cooperation and interest in the ***Communications*** journal.

Sincerely yours,

W.J. Minkowycz
Editor-in-Chief and
James P. Hartnett Professor of Mechanical Engineering

WJM:rms
enclosure

ELSEVIER
MANUSCRIPT ACCEPTANCE FORM

Name of Journal: ***INTERNATIONAL COMMUNICATIONS IN HEAT AND MASS TRANSFER***

Author *(Fill out and return)*

Corresponding author's name: S. Wongwises *Mandatory for Final Acceptance*

Please ensure that the following information is supplied for the corresponding author:

☐ E-mail address: _____

☐ Full postal address: _____

_____

_____

☐ Telephone: _____ ☐ Fax: _____

Checklist:

☐ Are the attachments and the final revised version of the manuscript identical?
☐ Are all text pages supplied?
☐ Are the keywords supplied? *(if appropriate for journal)*
☐ Are all original figures supplied, especially photographs?
☐ Are all figure captions supplied?
☐ Are all tables supplied?
☐ Are all tables captions supplied?
☐ Are copyright permission letters enclosed for any artwork/tables previously published, including those published on the world-wide-web?

If any of the illustrations are to be printed in colour please indicate this below:

Attachments

☐ Yes

Media format:
☐ PC
☐ Mac
☐ Other _____

Electronic text format:
☐ WordPerfect
☐ MS Word
☐ TeX
☐ Other _____

Editor-in-Chief

Name: *Professor W.J. Minkowycz*

Editorial manuscript ref. no: CJ 14/5834
(please ensure this reference is also indicated on the manuscript)

Manuscript date details:
Date ms. received: 1/29/14
Date revised: _____
Date accepted: _____

Section of journal in which manuscript is to appear:
(If applicable)

Editor's Notes *(please indicate any special instructions or requirements)*

Manuscript type:
(please tick one box)
☐ Book review
☐ Correspondence
☐ Discussion
☐ Erratum
☒ Full length article
☐ Review article
☐ Short communication
☐ Other _____

Editor's signature _____ Date _____